Dicle Üniversitesi
Mühendislik Fakültesi

mühendislikdergisi
journal of engineering

Dicle Üniversitesi Mühendislik Fakültesi
mühendislikdergisi
Cilt: 16, Sayı: 4, Aralık 2025 ISSN: 1309-8640

Dicle Üniversitesi Adına yayın Sahibi / Privilige Owner
Mehmet Siraç ÖZERDEM

Baş Editör / Editor-in-Chief
Mehmet Siraç Özerdem

Alan Editörleri / Field Editors
Fevzi Sarıtaş
İdris Bedirhanoğlu
Mustafa Cansız
İbrahim Kaya
Ömer Türk
Atilla Gencer Devecioğlu
Halime Abakay Temel
Nurtekin Özen
Abdulnasır Yıldız
Erkan Bahçe
Hasan Polat
Mehmet Emin Öncü
Fevzi Önen
Resul Daş

Teknik Editör / Technical Editor
Mesut Şeker

Yazışma Adresi
Mühendislik Dergisi, Koordinatörlük ve Yayın Bürosu,
Dicle Üniversitesi, Mühendislik Fakültesi, 21280 Diyarbakır
Telefon : +90-412 241 10 00 (Dahili: 3637)
Elektronik posta : muhendislikdergisi@dicle.edu.tr
web : http://dergipark.gov.tr/dumf, https://duje.dicle.edu.tr/journal/

Dergide yayınlanan yazılar izinsiz başka bir yerde yayınlanamaz veya bildiri olarak sunulamaz.

ISSN Basılı Materyal: 1309-8640
Online ISSN: 2146-4391

Hakem Listesi / *Reviewers List*

Dergimize yayınlanmak üzere gönderilmiş olan makaleleri titiz bir şekilde değerlendiren kıymetli hakem hocalarımıza, değerli katkılarından dolayı teşekkür eder, katkılarının devamını dileriz.

We greatly appreciate the contributions made by the scientists, who worked as reviewers for Dicle University Journal of Engineering (DUJE) and we expect their contributions to the following journal issues.

Yıldır Akkaya (ITU)
Kadir Özakgül (ITU)
Adem Solak (Pamukkale Üniversitesi)
Muhammed Ali Aydın (İstanbul Üniversitesi-Cerrahpaşa)
Yusuf Yaslan (ITU)
Cemanur Aydınalp (ITU)
Mehmet Duman (Düzce Üniversitesi)
Ali Koçak (YTU)
Şahin Güneş (Solihul College and University Centre)
Emine Ekinci Dağtekin (DU)
Murat Çağlayan (Mardin Artuklu Üniversitesi)
Emine Sibel Hattap (Mimar Sinan Güzel Sanatlar Üniversitesi)
Fadi Alyoussef (King Fahd University of Petroleum and Minerals)
Orhan Arpa (DU)
Hüseyin Alperen Dağdögen (Fırat Üniversitesi)
Resul Tugay (Atatürk Üniversitesi)
Suat Toraman (Fırat Üniversitesi)
Ferit Akbalık (Batman Üniversitesi)
Gözde Sarı (Manisa Celal Bayar Üniversitesi)
Pınar Demircioğlu (Aydın Adnan Menderes Üniversitesi)
Volkan Arıkan (Osmaniye Korkut Ata Üniversitesi)
Melis Yurddaşkal (Ege Üniversitesi)
Serhat Çiftçi (İstanbul Gelişim Üniversitesi)
Ramazan Menak (Siirt Üniversitesi)
Hamit Adin (Batman Üniversitesi)
Yaşar Ayaz (İnönü Üniversitesi)
Zehra Çetinkaya (Çukurova Üniversitesi)
Aydan Aksoğan Korkmaz (Malatya Turgut Özal Üniversitesi)
Murat Dal (Munzur Üniversitesi)
Süleyman İpek (Yaşar Üniversitesi)
Çiğdem Tekin (Mimar Sinan Güzel Sanatlar Üniversitesi)
Fuat Kılıç (Balıkesir Üniversitesi)
Hakkı Mollahasanoğlu (Recep Tayyip Erdoğan Üniversitesi)
Gökhan Kahraman (Munzur Üniversitesi)
Cemil Koyunoğlu (Yalova Üniversitesi)
Alişan Gönül (Siirt Üniversitesi)
Ahmet Erdoğan (İnönü Üniversitesi)
Funda Akar (Erzincan Binali Yıldırım Üniversitesi)
İhsan Tuğal (Muş Alparslan Üniversitesi)
Semra Arslan Selçuk (Gazi Üniversitesi)
Tuğçe Çelik (Ostim Teknik Üniversitesi)

Onur Behzat Tokdemir (ITU)
Gürkan Emre Gürcanlı (ITU)
Serkan Aydınlı (Çukurova Üniversitesi)
Esma Ahlatcıoğlu Özerol (YTU)
Neslihan Özsoy (Sakarya Üniversitesi)
Canan Kocabaldır (Çanakkale Onsekiz Mart Üniversitesi)
Ahmet Kabul (Burdur Mehmet Akif Ersoy Üniversitesi)
Mesut Gör (Fırat Üniversitesi)
Babak Karımı (Erzurum Teknik Üniversitesi)
Tayfun Abut (Muş Alparslan Üniversitesi)
Mahmut Daşkın (İnönü Üniversitesi)
Onur Denizhan (Batman Üniversitesi)
Serhat Aksungur (Malatya Turgut Özal Üniversitesi)
Abdullah Turan (Şırnak Üniversitesi)
Mehmet Cebe (DU)
Büşra Sağlam Doruk (Eskişehir Teknik Üniversitesi)
Murat Aslan (Şırnak Üniversitesi)
Musa Kaplan (Şırnak Üniversitesi)
Tahsin Baykal (Kırıkkale Üniversitesi)
Eyüp Şişman (YTU)
Hatice Çırakoğlu (Erciyes Üniversitesi)
Mehmet Onur Kaya (Fırat Üniversitesi)
Gökhan Gürgöze (Elazığ İl Milli Eğitim Müdürlüğü)
İlyas Karasu (Samsun Üniversitesi)
Arif Emre Aktaş (Çukurova Üniversitesi)
Barış Karakaya (Fırat Üniversitesi)
Emrullah Acar (Batman Üniversitesi)

İçindekiler / *Table of Contents*

Elektrik Elektronik Mühendisliği / Electrical and Electronics Engineering

Comparison of Performances of Two Different Antipodal Vivaldi Antennas in Microwave Breast Cancer Detection Systems (Research Article)
Şahin Yıldız, Muhammed Bahaddin Kurt **857**

Dynamic Model Linearization and Model Predictive Control of an Organic Rankine Cycle (Research Article)
Mert Sinan Turgut, Oguz Emrah Turgut **865**

Performance Evaluation of MambaVision in Breast Cancer Detection from Histopathology Images (Research Article)
Hasan Zan **879**

Design of Sodium-Ion Battery Packs in Electric Heavy-Duty Vehicles: A Case Study for Garbage Truck (Research Article)
Burak Fındık, Koray Erhan **889**

Trends in Electric Vehicle Motor Power: A Comparative Study on Performance and Efficiency (Review article)
Ahmet Orhan, Sencer Ünal, Ayhan Akbal, Kıvanç Doğan, Murat Kayaoğlu, Hilal Bıyık **901**

Application of Emotion Analysis in Deep Learning Techniques (Research Article)
Mesut Uysal, Mehmet Fatih Demiral, Ali Hakan Işık **919**

Güneydoğu Anadolu Bölgesi'nde çok kriterli karar verme yöntemleri ile yüzer güneş panelleri için optimal yer seçimi (Araştırma Makalesi)
Optimal site selection for floating solar panels in the Southeastern Anatolia Region using multi-criteria decision making methods (Research Article)
Rıdvan Şen, Şehmus Fidan **937**

Rose Leaf Diseases Detection Using Convolutional Neural Networks with Texture-Based Patch-Wise Selection (Research Article)
Birkan Büyükarıkan, Keziban Yalçın Dokumacı **949**

Comparative Analysis of CNN-Based Deep Learning Architectures for Automatic Plant Disease Classification (Research Article)
Sedat Örenç, Emrullah Acar, Mehmet Siraç Özerdem **961**

FPGA-Based Cosimulation of S-Box Constitution from Fractional Order Liu System (Research Article)
Muhammet Ali Arserim, Ömer Türk **971**

Makina Mühendisliği / Mechanical Engineering

İnceleme: Döküm Alüminyum Alaşımlarında Kalıntı Gerilme Ölçüm Yöntemleri, Nedenleri ve Önleme Çalışmaları (Derleme Makalesi)
Review: Residual Stress Measurement Methods, Reasons and Prevention Studies in Aluminium Cast Alloys (Review Article)
Onur Özaydın, Aytaç Gören,Esra Dokumacı Alkan, Gökçe Gencer **983**

Hibrit Kompozit Kolonlarda Burkulma Analizi (Araştırma Makalesi)
Buckling Analysis of Hybrid Composite Columns (Research Article)
Hüseyin Karaduman, Şemsettin Temiz **1001**

Energy and Exergy Analysis of a Metal Hydride-Based Hydrogen Storage System: A Parametric Approach (Research Article)
Nesrin İlgin Beyazit **1015**

Topology Optimization-Based Lightweight Chassis Design: A Case Study on Structural Efficiency Enhancement for an Autonomous Scale (Research Article)
Kerem Ali Taş, Mehmet Can Karabıyık, Kürşat Tanıver, Mine Ak **1033**

Position and Motor Control of a 3-DoF RRR Robotic Manipulator Using PID and Sliding Mode Control (Research Article)
Hasan Eker, Mesut Hüseyinoğlu **1043**

Multi-Objective Optimization of Axially Flat Finned Cam-Shaped and Elliptical Tube Banks Based on Entropy Generation and Thermal Hydraulic Performance (Research Article)
Mehmet Özkarakoç, Muhammet Nasıf Kuru **1059**

Maden Mühendisliği / Mining Engineering

Bioleaching of Oxidized Zinc Ore Using *Acidithiobacillus ferrooxidans* with Taguchi Approach (Research Article)
Seda Demirci **1067**

İnşaat Mühendisliği / Civil Engineering

Impact of Building Height on Seismic Response, Economic Viability, Environmental Performance, and Social Well-being in Earthquake-Prone Türkiye (Research Article)
Mehmet İshak Yüce, Aydın Oğuz, Talal Faroug Mahgoub Ahmed **1077**

AI-driven anomaly detection for fraud prevention in project monitoring (Research Article)
Mehmet Tahir Sandıkkaya, Onur Behzat Tokdemir **1103**

Hekimoğlu Ali Paşa Türbesi'nin Mevcut Durum Tahkiki Ve Taşıyıcı Kemere Takviye Önerisi (Araştırma Makalesi)
Actual Structural Condition Assessment of Hekimoğlu Ali Pasha Tomb and Reinforcement Recommendation for the Supporting Arch (Research Article)
Erdinç Önen **1113**

Mardin'in Eryeri Mahallesinde Bulunan Geleneksel Evlerin Yapısal Koruma Sorunları (Araştırma Makalesi)
The Structural Conservation Problems of the Traditional Houses in Eryeri, Mardin (Research Article)
Yasemin Ercan Gündüz, Mine Turan, Engin Aktaş **1125**

Diyarbakır Surlarında Tuğla Malzemenin Kullanım Teknikleri ile SEM/EDX (Taramalı Elektron Mikroskobu/Enerji Dağılımlı X-Işını Spektroskopisi) Analizlerinin Değerlendirilmesi (Araştırma Makalesi)
Evaluation of Brick Material Usage Techniques and SEM/EDX (Scanning electron microscopy/Energy dispersive X-ray spectroscopy) Analyses on the City Walls of Diyarbakır (Research Article)
Nursen Işık, Ronay Okutmuştur **1135**

Tuğla Üretiminden Kaynaklı Küresel Isınma Potansiyelinin Çevresel Ürün Beyanları Verileri Bağlamında İncelenmesi (Araştırma Makalesi)
Investigation of Global Warming Potential of Brick Production in the Context of Environmental Product Declarations Data (Research Article)
Yusuf Eşidir, Arzuhan Burcu Gültekin, Hüseyin Yılmaz Aruntaş, Çiğdem Belgin Dikmen **1151**

Understanding the Root Causes of Construction Claims: A Narrative Review of Determinants and Preventive Strategies (Review Article)
Mehmet Kürşat Bahat, Sema Ergönül **1157**

Geri Dönüşümlü Malzemeler ve Doğal Katkıların İnce-Daneli Zeminlerin Stabilizasyonundaki Etkisinin Taguchi Optimizasyon Yöntemi ile İncelenmesi (Araştırma Makalesi)
Investigation of the Effects of Recycled Materials and Natural Additives on the Stabilization of Fine-Grained Soils Using the Taguchi Optimization Method (Research Article)
Yasemin Pekdemir, Ahmet Şahin Zaimoğlu, Fatih Artuk **1171**

Tarihi Yapı Restorasyonunda Enerji Performansı Optimizasyonu: Cami Son Cemaat Bölüm Tasarımları İçin Simülasyon Temelli Bir Karşılaştırma (Araştırma Makalesi)
Energy Performance Optimization in Historic Building Restoration: A Simulation-Based Comparison of Design Alternatives for Mosque Porticoes (Research Article)
Ebru Ulaş Sarıaydın **1185**

Askı Maddesi Boyutunun Askı Maddesi Konsantrasyonu Üzerindeki Etkisinin Doğrusal Karma Regresyon Modeli ile Analizi (Araştırma Makalesi)
Analysis of the Effect of Suspended Sediment Particle Size on Suspended Sediment Concentration Using Linear Mixed-Effects Regression Model (Research Article)
Eyyup Ensar Başakın **1197**

Dicle Üniversitesi Mühendislik Fakültesi (DÜMF) Mühendislik Dergisi yayınlarında varılan sonuçlar veya fikirlerin sorumluluğunu taşımamaktadır. Üniversite'nin, bu yayında ileri sürülen bilgi, alet, ürün veya işlevin doğruluğu, bütünlüğü, uygunluğu ve kullanılırlığı konusunda bir yüklenimi ve iddiası bulunmamaktadır. Bu nedenle herhangi bir şekilde sorumlu tutulamaz.

Bu yayının herhangi bir kısmı, mühendislik dergisinin yazılı izni olmadıkça kaynak gösterilmeden yayınlanamaz, bilgi saklama sistemine alınamaz veya elektronik, mekanik, fotokopi, kayıt veya başka sistemlerle çoğaltılamaz.

Dicle University
Journal of Engineering
https://dergipark.org.tr/tr/pub/dumf
duje.dicle.edu.tr

Research Article

Comparison of Performances of Two Different Antipodal Vivaldi Antennas in Microwave Breast Cancer Detection Systems

Şahin YILDIZ[1*], Muhammed Bahaddin KURT[2]

[1] Dicle University, Electrical-Electronics Engineering Department, sahin.yldz92@gmail.com, Orcid No: 0009-0000-2139-5361
[2] Dicle University, Electrical-Electronics Engineering Department, bkurt@dicle.edu.tr, Orcid No 0000-0001-6983-2081

ARTICLE INFO

Article history:

Received 21 April 2025
Received in revised form 30 August 2025
Accepted 22 September 2025
Available online 30 December 2025

Keywords:

Microwave imaging, Breast cancer, Vivaldi antenna performance, Phantom, Biophysics

Doi: 10.24012/dumf.1679840

* Corresponding author

ABSTRACT

In this study, two different antipodal Vivaldi antennas were designed using CST MWS simulation program. The proposed antipodal Vivaldi antennas were designed using 1.6 mm thick FR4 material. The dielectric constant of this material is 4.4 and the loss tangent value is 0.002. The impedance of the feed port is 50 Ω and the copper thickness is 0.035 µm. The compact size of the first antenna is 30 mm x 36 mm, its gain is 5.04 dB and its directivity is 6.48 dB. The size of the second antenna is 38 mm x 33.5 mm, its gain is 7.68 dB and its directivity is 8.77 dB. In the simulation environment, two phantoms were created by placing spherical tumors with two different diameters, each inside a separate heterogeneous breast phantom. Then, the designed antennas in the simulation environment were tested for tumor detection performance on the phantom using the radar-based microwave breast cancer imaging technique (RMWI). After the signal processing stages, tumor images were obtained. In microwave imaging methods, the performance of two different antennas on tumor detection was observed in terms of gain and directivity. In the breast cancer detection study using RMWI technique, the importance of antenna properties such as gain and directivity was emphasized.

Introduction

Breast cancer is a type of cancer that occurs in 32% of women [1]. It is also the most common cancer in women in approximately 157 countries. The World Health Organization's goal is to reduce global breast cancer deaths by 2.5% per year between 2020 and 2040. This is expected to prevent 2.5 million deaths [2].

Positron emission tomography (PET), ultrasound, mammography and magnetic resonance imaging (MRI) detection are important imaging tools for breast cancer detection [3]. However, imaging techniques have several disadvantages. The MRI imaging technique is not suitable for those with claustrophobia and sensitivity to the contrast materials used, and is a time-consuming, expensive imaging method. The experience of doctors is very important in ultrasound imaging, and the resolution is not good in detecting small masses. Tomography requires experienced physician due to radiation damage and poor resolution. Positron emission tomography imaging has a carcinogenic effect and this method is not suitable for patients with metabolic abnormalities [4].

Normal and malignant tissues in the breast have different electrical properties. Microwave imaging detects tumors by detecting these differences. Microwave imaging is an important alternative to other imaging methods. This system uses electromagnetic waves and the system has no ionizing effect. It uses non-ionizing electromagnetic waves to examine an unknown tumor target based on scattering. Therefore, it has enabled the development of this imaging technique [5].

In microwave imaging, the antenna sends low-power radio-frequency (RF) signals toward the breast and collects the reflected signals. It analyzes the collected signals to reconstruct the image. The antenna used here acts as both a transmitter and a receiver.

RMWI reveals the electrical properties of tissues by solving the inverse scattering problem [6]. The aim of RMWI is to detect objects (tumors) and determine their location. The antenna used as a sensor sends a Gaussian pulse signal to the target (chest). The sum of the reflected signals is the sum of the signals reflected from the tissues in the chest and environmental noise. Using filtering techniques, unwanted parts of the reflected signals are eliminated and the tumor response is obtained [7].

There are many important factors in the RMWI technique. The antenna used in this technique must have features such as bandwidth, directionality (radiance) and gain suitable for

microwave imaging. In addition, factors such as the density of the breast tissue used as a phantom in this system, the size of the tumor and signal processing techniques are important. In these systems, antenna types such as resonant, patch, bowtie, monopole, dipole and antipodal Vivaldi are used [8, 9, 10, 11, 12]. Using antipodal Vivaldi antennas in these systems provides various advantages to other antennas [13]. Antipodal Vivaldi antennas used in these systems are good candidates for these systems due to their high performance (gain, directivity, bandwidth, impedance matching etc.) [14, 15, 16, 17, 18]. There are many antipodal Vivaldi antennas designed with different techniques using microwave imaging system for breast cancer detection in the literature [13, 19, 20, 21, 22, 23, 24, 25, 26, 27].

Rubber, polyimide, silicone, polycarbonate and FR4 are used as substrates in antenna designs. FR4 substrate is ideal for the design of antipodal Vivaldi antennas due to the desired bandwidth, impedance matching, stable radiation values, high gain, good directivity, compact size, low cost and easy availability [28, 29, 30].

The directional performance of antipodal Vivaldi antennas can be improved by changing some of their geometrical properties. The antenna geometry was optimized using particle swarm optimization and the gain and directivity of the Vivaldi antenna were increased [22, 31].

With RMWI system, the signals reflected from the target (breast phantom) are the sum of environmental noises and signals reflected from all breast tissues. To obtain the tumor response, other reflected signals need to be filtered [57, 58, 59]. For this purpose, adaptive Wiener filter is an effective filtering algorithm and has been used in studies in the literature [27, 32, 33, 34, 35]. After the filtering algorithm stage, DAS and DMAS are used as reference image generation algorithms for imaging the tumor response [36, 37]. The DMAS imaging algorithm is an extended version of DAS with higher contrast resolution [38, 39]. Due to this advantage, the DMAS algorithm has been used as an ideal algorithm for tumor detection [27, 37].

In the RMWI system, breast phantom tissues, which are target objects, should be designed in accordance with the electrical properties of the real breast. The design of artificial breast phantom tissues according to appropriate electrical properties in simulation and experimental environments has been presented in scientific studies [40, 41]. In order to model these tissues in the CST MWS environment, a design suitable for the electrical properties of real breast tissues was made [42].

Materials and Methods

The proposed antipodal Vivaldi antennas are designed using FR4 material with a thickness of 1.6 mm. The dielectric constant of this material is 4.4 and the loss tangent value is 0.002. The feed port has an impedance of 50 Ω and the copper thickness is 0.035 μm. All designs and simulations were made using the CST MWS simulation program.

The exponential form (inner and outer edge taper) equations used in the designs of the antipodal Vivaldi antenna:

$$y = C_1 e^{Rx} + C_2 \quad (1)$$

Here R is the angle ratio, y is the curve and C_1 and C_2 geometric parameters are calculated in the following equations.

$$C_1 = \frac{y_2 - y_1}{e^{Rx_2} - e^{Rx_1}} \quad (2)$$

$$C_2 = \frac{y_1 e^{Rx_2} - y_2 e^{Rx_1}}{e^{Rx_2} - e^{Rx_1}} \quad (3)$$

The starting points of the curves in the antennas are y_1 and x_1; the ending points are y_2 and x_2.

The purpose of particle swarm optimization used in antenna design is to determine the direction of particle movement in the solution space. This optimization technique assumes that the particles should move towards the best positions from the calculated positions. To update the particle positions at each step, they can be stored in an M x N matrix, where M is the number of particles in the simulation and N is the number of dimensions of the problem [43, 44]. In this way, the best particle position can be obtained by performing iteration operations. The best positions are represented by the M x N matrices P = (P_{ij}) and G = (g_{ij}), respectively.

The position and velocity of the particles are updated at discrete intervals.

$$Vuptaded = Vprevious + C_1 n_1 (P\text{-}X) + C_2 n_2 (G\text{-}X) \quad (4)$$

The positions and velocities of the particles are updated at discrete intervals in the range $0 \leq n_{1,2} \leq 1$, C_1 and C_2 determine the influences on the trajectories of the particle [45]. Finally, the particles move according to the desired best position.

$$Vuptaded = Vprevious + V.\Delta t \quad (5)$$

Where At is either a unit time step.

In 2002, the Federal Communications Commission allowed unlicensed use of the 3.1-10.6 GHz frequency band, thus increasing interest in studies in this area. Using the above equations, antennas were optimized and designed to cover the allowed frequency operating range.

In this study, two different antipodal Vivaldi antennas were designed. The antenna dimensions are 30 mm x 36 mm and 38 mm x 33.5 mm. The antenna designs were carried out using the CST MWS simulation program.

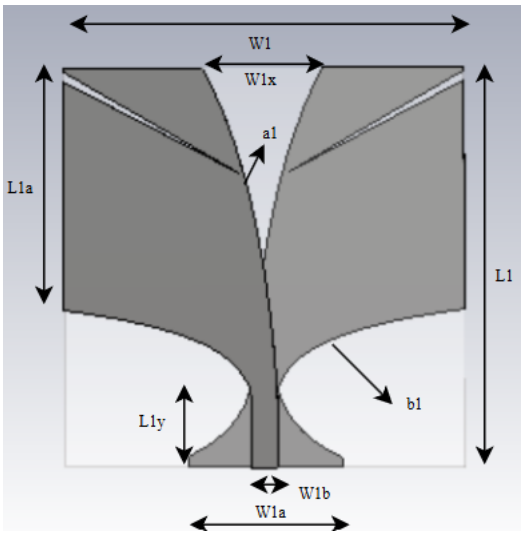

a.

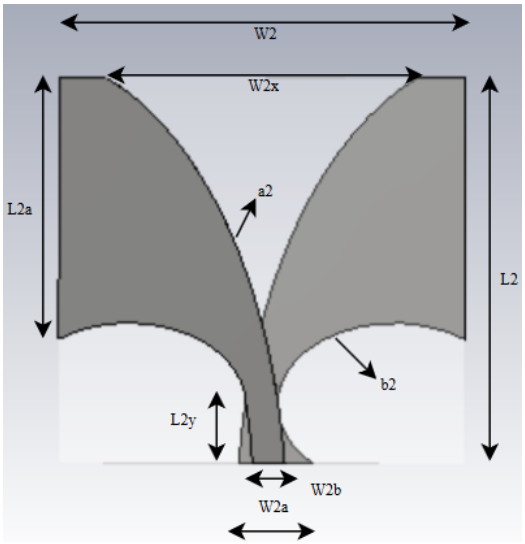

b.

Figure 1. Antipodal Vivaldi antennas configuration: (a) antipodal Vivaldi -1; (b) antipodal Vivaldi-2.

Table 1. Geometric Configurations of Opposite Polarity Antipodal Vivaldi Antennas

Parameter-1	Antipodal Vivaldi antenna value (mm)-1	Parameter-2	Antipodal Vivaldi antenna value (mm)-2
W1 (Antenna width)	30	W2 (Antenna width)	38
L1 (Antenna length)	36	L2 (Antenna length)	33.5
W1x (Spacing width)	10.5	W2x (Spacing width)	26
L1y (Flap length)	22	L2y (Flap length)	23
L1a (Port length)	7	L2a (Port length)	6
W1a (Port width)	14	W2a (Port width)	7
W1b (Port width)	2.4	W2b (Port width)	2.6
a1 (Elliptical edge)	0.3	a2 (Elliptical edge)	0.08
b1 (Elliptical edge)	0.095	b2 (Circular diameter)	11.5

Two different antipodal Vivaldi antennas were designed as seen in Figure 1. The measurement results of the antennas for the S11 over-frequency are as shown in Figure 2.

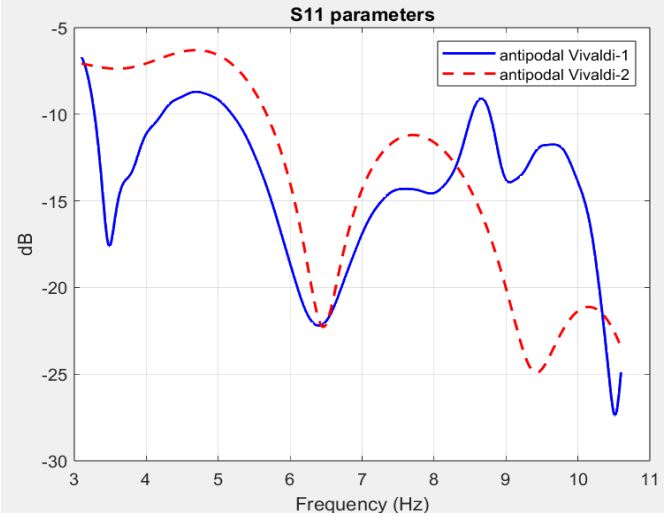

Figure 2. S11 over-frequency parameters: (a) antipodal Vivaldi -1; (b) antipodal Vivaldi -2.

The gain and directivity results of the designed antipodal Vivaldi antennas are shown in Figure 3.

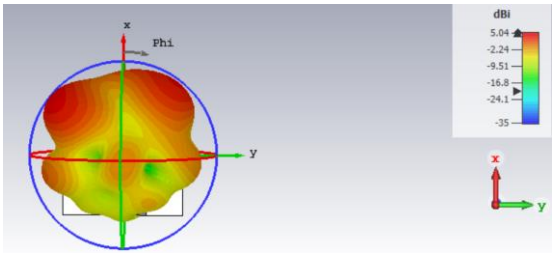

a.

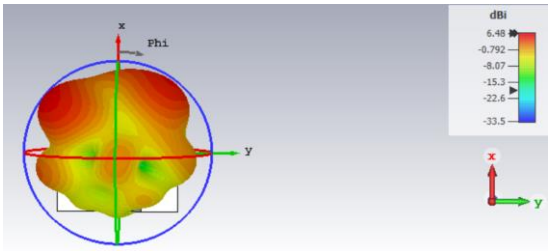

b.

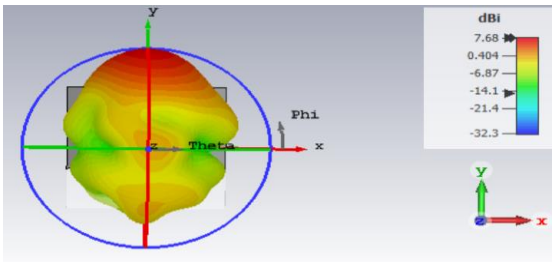

c.

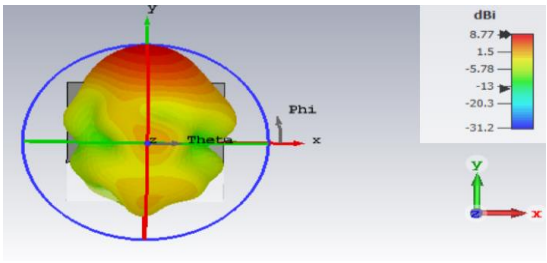

d.

Figure 3. Antenna parameters: (a) gain, antipodal Vivaldi-1; (b) directivity, antipodal Vivaldi-1; (c) gain, antipodal Vivaldi-2; (d) directivity, antipodal Vivaldi-2.

As a result of the operations performed, the first antenna gave the best result at the frequency of 10.3 GHz with a gain of 5.04 dB and a directivity of 6.48 dB; The second antenna gave the best result at the frequency of 10.5 GHz with a gain of 7.68 dB and a directivity of 8.77 dB.

RMWI System and Imaging in Simulation Environment

Female breasts have different tissues (fat, glandular, lymph, muscle and nipple etc.). The electrical properties of the tissues are different at microwave frequencies. Tumor detection with RMWI is based on the high contrast between the relative permittivity and conductivity of healthy tissue and cancerous tissue [46].

In the simulation program, two heterogeneous breast phantoms with electrical properties suitable for breast tissues were created. The first phantom was 100 mm in diameter and its interior was covered with fat (36%), glandular tissue (60%) and a 1 mm diameter tumor; its exterior was covered with 2 mm skin tissue and the nipple was added. The other phantom contained a 10 mm diameter tumor and was designed with fat (36%), glandular tissue (42%), 2 mm skin and the nipple. The phantoms created in Figure 4 are shown in the XY and YZ planes and 12 different measurement positions of the antennas around the phantom are shown in Figure 5.

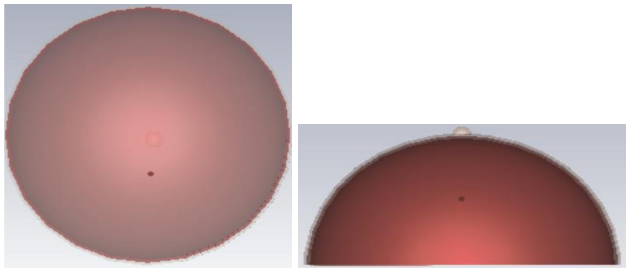

a. b.

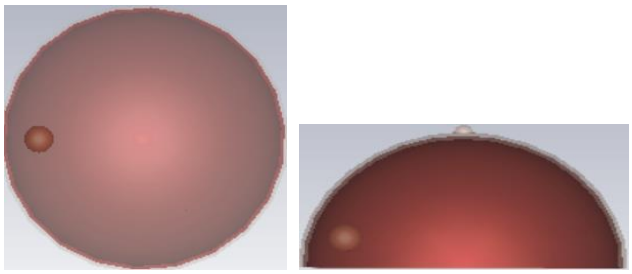

c. d.

Figure 4. CST Heterogeneous breast phantom simulation: (a) XY (1 mm diameter tumor); (b) XZ (1 mm diameter tumor); (c) XY (10 mm diameter tumor); (d) XZ (10 mm diameter tumor).

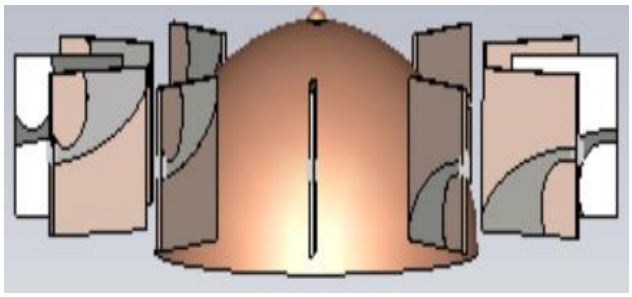

Figure 5. Positioning of antipodal Vivaldi antennas at 12 different points around the phantom.

To detect the tumor in the phantom, a Gaussian signal is sent to the target and the reflected signals are collected. The collected signals are preprocessed to remove artifacts [47]. Then, to find the tumor response, other signals are suppressed and filtered to obtain a low amplitude tumor response.

A RMWI system was developed on CST MWS with antipodal Vivaldi antennas used as a transmitter sending Gaussian pulse signal and a receiver collecting the reflected signals. In this system, antipodal Vivaldi antennas were rotated in twelve different positions around the tumor heterogeneous breast phantom and measurements were made. Calibration process was performed using a tumor-free heterogeneous phantom. The tumor response was found by subtracting the signals reflected from healthy breast tissues from the total signal reflected from the tumorous breast. is the subtraction method stage. The subtraction method is expressed in equation 6:

$$S^{TY} = S^{T} - S^{H} \quad (6)$$

In equation (6); S^{T} represents the signal in each channel, S^{H} represents the signal scattered from the tumor-free breast, and S^{TY} represents the tumor response signal obtained as a result of filtering. The image was enhanced using gauss band-pass filtering to eliminate artifact effects [48]. Hilbert transform was used for integration of the incident wave. Thus, the tumor image was obtained.

The envelope of the signal for the tumor response is obtained by the Hilbert transform. This transformation is expressed in Equation 7.

$$H[s(t)] = \frac{1}{\Pi}\int_{-\infty}^{+\infty} \frac{s(r)}{s(t-r)}\,dr \quad (7)$$

$$S_A(t) = s(t) + jh[s(t)] \quad (8)$$

$$S_A(t) = A(t)e^{j\omega(t)} \quad (9)$$

Here $S_A(t)$ is the analytical signal, $s(t)$ is the filtered real signal, $H[s(t)]$ is the complex composition, and Equation 9 shows the time envelope.

Delay-multiply-sum (DMAS) focusing method was used for tumor detection using ultra-wideband confocal technique. In this method, signals reflected back from the simulated target using finite difference time domain method are shifted in time domain, multiplied double and summed to form a focal point. Difference multiplication operation was performed according to DAS. This method is shown in Equation 10.

$$I(r_0) = \int_0^T [\sum_{m=1}^{M-1} \sum_{j=(m+1)}^{M} x_m(r_m(r_0)) x_j(r_j(r_0))]^2 dt \quad (10)$$

Here, for each pixel, τ_m represents the delay time, x_m represents the tumor response, and the energy of the pixel energy at distance r is expressed as $I(r_0)$.

$I(r)$ is the energy of pixels at location r(x, y, z). Here, v is the wave velocity, Δt is the time steps, and d_i is the distance between the pixel and the antenna. Time delay (Equation 9), distance (Equation 12), speed of the wave (Equation 11) are shown below respectively.

$$r_n(r) = \frac{2}{v\Delta t} d_i \quad (11)$$

$$d_i = \frac{\sqrt{(x-xi)2+(y-yi)2+(z-zi)2}}{v} \quad (12)$$

$$v = \frac{c}{\sqrt{\varepsilon r}} \quad (13)$$

Here, ε_r represents the relative permittivity of the medium and c represents the speed of light.

In the simulation environment, small spherical tumors with diameters of 1 mm and 10 mm were placed in the heterogeneous breast phantom, as seen in Figure 4. After applying signal processing steps to the heterogeneous and dense breast phantom, images obtained from two different antennas were generated, as seen in Figures 6 and 7.

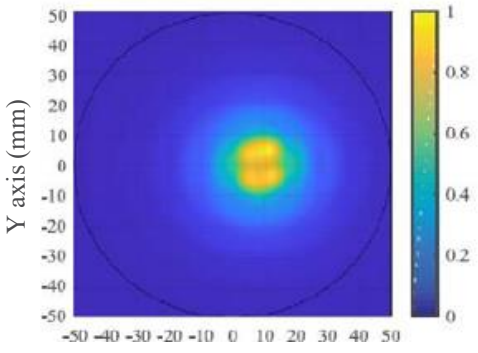

a.

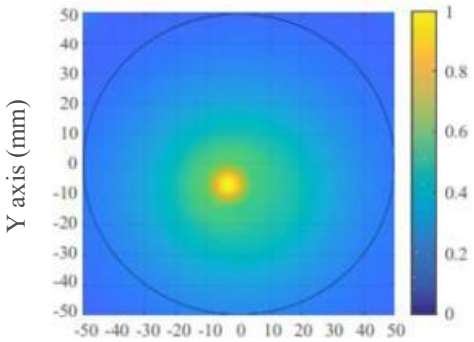

b.

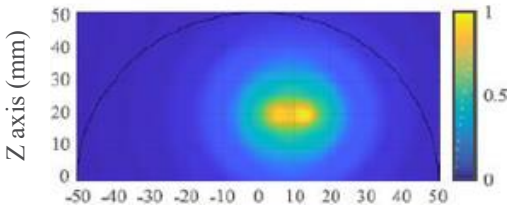

c.

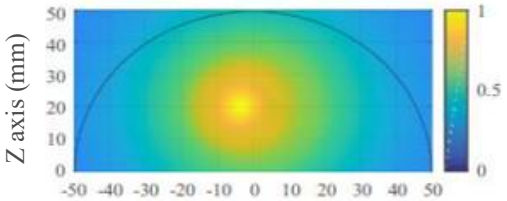

d.

Figure 6. Images of the tumor in the heterogeneous breast model with a diameter of 1 mm in the X-Y and X-Z planes: (a) X-Y, antipodal Vivaldi-1; (b) X-Y, antipodal Vivaldi-2; (c) X-Z, antipodal Vivaldi-1; (d) X-Z, antipodal Vivaldi-2.

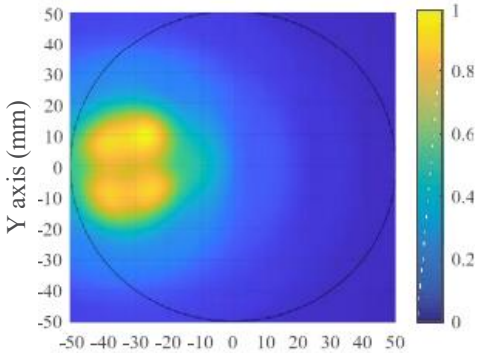

a.

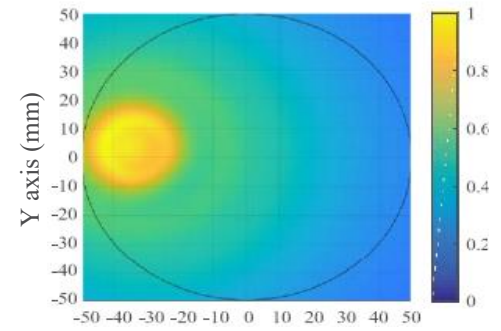

b.

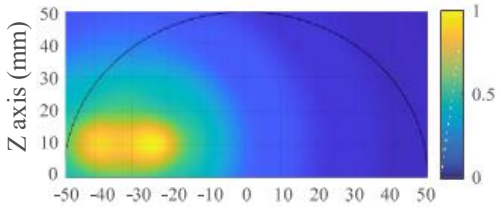

c.

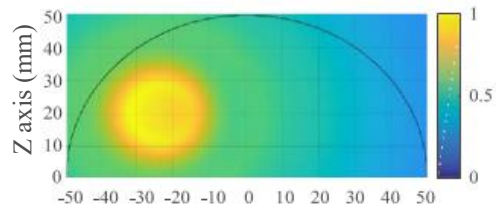

d.

Figure 7. Images of the tumor in the heterogeneous breast model with a diameter of 10 mm in the X-Y and X-Z planes: (a) X-Y, antipodal Vivaldi-1; (b) X-Y, antipodal Vivaldi-2; (c) X-Z, antipodal Vivaldi-1; (d) X-Z, antipodal Vivaldi-2.

The tumor detection performance of two different antipodal vivaldi antennas was compared. In the measurement made with the number one antenna, the tumor image was scattered due to the low focus of the antenna directivity in the tumor image and a double image was obtained. The image of the tumor placed on the created heterogeneous breast model was obtained with a more uniform single-focus image compared to the first antenna due to the high gain and directivity properties of the second antenna. In addition, images close to the tumor location were obtained in the measurements made using two different antennas. However, in the measurements made with the antenna with high gain and directionality, the tumor response was displayed more smoothly and without a scattered focus. This showed us the importance of gain and directionality.

Conclusions

In this study, two different antipodal vivaldi antennas and heterogeneous breast phantoms containing tumors of different sizes were designed using the CST MWS simulation program. A radar-based system was established for breast cancer detection in the simulation environment. Measurements were made by placing spherical tumors of different diameters into the heterogeneous phantom. The tumor detection performances of the designed antennas were tested on phantoms using the RMWI technique. After the signal processing stages, tumor images were obtained. The effects of the gain and directionality of the antennas on tumor detection in microwave imaging methods were investigated. The importance of antenna performances in this imaging technique was determined. As a result, it was emphasized that the gain and directionality of the antennas are very important in breast cancer detection studies using RMWI technique.

Ethics committee approval and conflict of interest statement

"There is no need to obtain permission from the ethics committee for the article prepared"

"There is no conflict of interest with any person / institution in the article prepared"

Reference

[1] American Cancer Society. Key Statistics for Breast Cancer. American Cancer Society, Atlanta, USA. 2023, https://www.breastcancer.org/facts-statistics

[2] World Health Organization. Breast Cancer. World Health Organization, Global Breast Cancer Initiative. 2023, https://www.who.int/news-room/fact-sheets/detail/breast-cancer

[3] B. J. Pomerantz, "Imaging and Interventional Radiology for Cancer." *Surgical Oncology for the General Surgeon, An Issue of Surgical Clinics*, vol. 100, no. 3, pp. 499-506, 2020.

[4] Z. He, Z. Chen, M. Tan, S. Elingarami, Y. Liu, T. Li, Y. Deng, N. He, S. Li, J. Fu and W. Li, "A review on methods for diagnosis of breast cancer cells and tissues." *Cell proliferation*, *53*(7), e12822, 2020.

[5] K. Lalitha and J. Manjula, "Non-invasive microwave head imaging to detect tumors and to estimate their size and location." *Physics in Medicine* 13: 100047, 2022.

[6] A. Naghibi, A. R. Attari, "Near-field radar-based microwave imaging for breast cancer detection: A study on resolution and image quality." *IEEE Transactions on antennas and propagation* 69.3: 1670-1680, 2020.

[7] E. C. Fear, X. Li, S.C. Hagness and M. A. Stuchly, "Confocal microwave imaging for breast cancer detection: Localization of tumors in three dimensions." *IEEE Transactions on biomedical engineering*, *49*(8), 812-822, 2002.

[8] D. Guliato, R. M. Rangayyan, J. D. Carvalho and S. A. Santiago. Polygonal modeling of contours of breast tumors with the preservation of spicules. *IEEE Transactions on Biomedical Engineering*. 55(1), 14-20, 2007.

[9] D. Á. Sánchez-Bayuela, N. Ghavami, G. Tiberi, L. Sani, A. Vispa, A. Bigotti, and A. S. Tagliafico. A multicentric, single arm, prospective, stratified clinical investigation to evaluate MammoWave's ability in breast lesions detection. *PLoS One*. 18(7), e0288312, 2023.

[10] K. Singh, M. Dhayal and S. Dwivedi. Breast cancer detection by terahertz UWB microstrip patch antenna loaded with 6X6 SRR array. *IETE Journal of Research*. 70(5), 5295-5310, 2024.

[11] J. Moll, T. Slanina, J. Stindl, T. Maetz, D. Nguyen H. and V. Krozer. Temperature-induced contrast enhancement for radar-based breast tumor detection at k-band using tissue mimicking phantoms. *IEEE Journal of Electromagnetics, RF and Microwaves in Medicine and Biology*, *7*(3), 251-257, 2023.

[12] A. O. Asok, M. A. Shukoor and S. Dey. Breast cancer detection with metamerial enabled monopole antennas using microwave imaging. In *2022 IEEE International Conference on Emerging Electronics (ICEE)*. pp. 1-4, 2022.

[13] A. Bhaij, A. Haddad, R. Jouali, K. Sabri, and M. Aoutoul, Design and optimization of a vivaldi antenna for early cancer detection: Sar and current density analysis. *Int. J. Tech. Phys. Probl. Eng*. 16, 85-92, 2024.

[14] M. Abbak, M. Çayören and I. Akduman, "Microwave breast phantom measurements with a cavity-backed Vivaldi antenna." *IET Microwaves, Antennas & Propagation* 8.13: 1127-1133, 2014.

[15] A. Lazaro, R. Villarino and D. Girbau. Design of tapered slot Vivaldi antenna for UWB breast cancer detection. *Microwave and Optical Technology Letters*, *53*(3), 639-643, 2011.

[16] M. Salimi, S. Gheitarani Sehrigh and S. Rajebi. Design and analysis of Microstrip Patch Antenna for hyperthermia applications in breast cancer. *International Journal on Technical and Physical Problems of Engineering (IJTPE)*. (41), 71-76, 2019.

[17] J. L. Rajput, A. B. Nandgaonkar, S. L. Nalbalwar, A. E. Wagh and N. G. Huilgol. Performance evaluation of compact rectangular microstrip antenna for breast hyperthermia. *Int. J. Tech. Phys. Probl. Eng*. 48, 87-94, 2021.

[18] M. A. Aldhaeebi and T. S. Almoneef. Dipole array sensor for microwave breast cancer detection. *IEEE Access*. 11, 91375-91384, 2023.

[19] Z. Hood, T. Karacolak, E. Topsakal, "A small antipodal Vivaldi antenna for ultrawide-band applications." *IEEE Antennas and Wireless propagation letters* 7: 656-660, 2008.

[20] A. Hossain, S. Pancrazio, T. Kelley and A. V. Pham. A Compact and Low-Profile High-Gain Multilayer Vivaldi Antenna Based on Gradient Metasurface Superstrates. *IEEE Antennas and Wireless Propagation Letters*. pp. 1-5, 2025.

[21] J. Harel, M. Himdi, O. Lafond, O. Clauzier, O. Vivares. A compact Vivaldi-shaped array using antipodal Vivaldi antennas to stabilize the high-frequency radiation pattern. *IEEE Access*. 13, 29983–29993, 2025.

[22] M. T. Islam, M. Z. Mahmud, N. Misran, J. I. Takada and M. Cho, "Microwave breast phantom measurement system with compact side slotted directional antenna." *IEEE access* 5: 5321-5330, 2017.

[23] R. Natarajan, J.V George, M. Kanagasabai, L. Lawrance and B. Moorthy. Modified antipodal Vivaldi antenna for ultra-wideband communications. *IET Microw. Antennas Propag.* 10, 401–405, 2016.

[24] M.T. Islam, M.Z. Mahmud, M.T Islam, M.T.S. Kibria and M. Samsuzzaman, M. A low cost and portable microwave imaging system for breast tumor detection using UWB directional antenna array. *Sci. Rep.* 9, 15491, 2019.

[25] Z. Katbay, M. Le Roy, C. Olleik, A. Pérennec, S. Sadek and R. Lababidi, R. Bi-Static Time Domain Study for Microwave Breast Imaging. In *2018 18th Mediterranean Microwave Symposium (MMS)* IEEE. pp. 411-414, 2018.

[26] M. Samsuzzaman, M.T. Islam, A.A. Shovon, R.L. Faruque and N. Misran. (2019). A 16-modified antipodal Vivaldi antenna array for microwave-based breast tumor imaging applications. *Microwave and Optical Technology Letters*. 61(9), 2110-2118, 2019.

[27] H. Özmen and M. B. KURT, "Radar-based microwave breast cancer detection system with a high-performanceultrawide band antipodal Vivaldi antenna." *Turkish Journal of Electrical Engineering and Computer Sciences* 29.5: 2326-2345, 2021.

[28] S. Christydass, G. Navaneethakrishnan, R. Palanisamy, C. A. Saleel, and B. S. Arputharaj. Split ring resonators and composite FR4 substrate for analysis and design of tri-band monopole antenna. *Applied Physics Letters*. 125(18), 2024.

[29] S. Z. Ali, K. Ahsan, D. ul Khairi, W. Alhalabi and M. S. Anwar. Advancements in FR4 dielectric analysis: Free space approach and measurement validation. *Plos one*. 19(9), e0305614, 2024.

[30] N. B. Kwe, V. Yadav, M. Kumar, S. V. Savilov, M. Z. A. Yahya, S. K. Singh. A comparative study of dielectric substrate materials effects on the performance of microstrip patch antenna for 5G/6G application. *Journal of Materials Science: Materials in Electronics*, *35*(24), 1617, 2024.

[31] H. B. Lim, N. T. T. Nhung, E. P. Li and N. D. Thang, "Confocal microwave imaging for breast cancer detection: Delay-multiply-and-sum image reconstruction algorithm." *IEEE Transactions on Biomedical Engineering* 55.6: 1697-1704, 2008.

[32] J. Wang, M. Zhang, Y. Bai, H. Xu and Y. Fan. Distance compensation-based dual adaptive artifact removal algorithm in microwave breast tumor imaging system. *Biomedical Signal Processing and Control*. 88, 105598, 2024.

[33] K. V. Ranjitha and T. P. Pushphavathi. Analysis on improved Gaussian-Wiener filtering technique and GLCM based feature extraction for breast cancer diagnosis. *Procedia Computer Science*. 235, 2857-2866, 2024.

[34] R. Saini. Modified weiner filter for improving quality of MRI image for detection of diseases. *Int. J. Adv. Res. Comput. Sci.* 8, 64, 2017.

[35] R. Chakraborty, A. Bairagi, P. Samui and S. Das. Noise removal from digital mammogram. *Eur. J. Pharm. Med. Res.* 6, 312–319, 2019.

[36] M. Pato, R. Eleutério, R. C. Conceição and D. M. Godinho. (2023). Evaluating the performance of algorithms in axillary microwave imaging towards improved breast cancer staging. *Sensors*. 23(3), 1496, 2023.

[37] T. Reimer, M. Solis-Nepote and S. Pistorius. The application of an iterative structure to the delay-and-sum and the delay-multiply-and-sum beamformers in breast microwave imaging. *Diagnostics*. 10(6), 411, 2020.

[38] S. S. KaramFard and B. M. Asl. Fast delay-multiply-and-sum beamformer: Application to confocal microwave imaging. *IEEE Antennas and Wireless Propagation Letters.* 19(1), 14-18, 2019.

[39] M. T. Islam, M. Samsuzzaman and S. Kibria. Experimental breast phantoms for estimation of breast tumor using microwave imaging systems. *IEEE Access*. 6, 78587-78597, 2018.

[40] M. Lazebnik, E. L. Madsen, G. R. Frank, and S. C. Hagness, S. C. Tissue-mimicking phantom materials for narrowband and ultrawideband microwave applications. *Physics in Medicine & Biology*. 50(18), 4245, 2005.

[41] H. Zhang, T. Arslan and B. Flynn. A single antenna based microwave system for breast cancer detection: Experimental results. In *2013 Loughborough Antennas & Propagation Conference (LAPC)*. IEEE. pp. 477-481, 2013.

[42] X. Li and S. C. Hagness. A confocal microwave imaging algorithm for breast cancer detection. *IEEE Microwave and wireless components letters*. 11(3), 130-132, 2001.

[43] Y. Rahmat-Samii, D. Gies and J. Robinson. Particle swarm optimization (PSO): A novel paradigm for antenna designs. *URSI Radio Science Bulletin*. 2003(306), 14-22, 2003.

[44] A. K. Kesarwani, M. Yadav, D. Singh and G. D. Gautam. A review on the recent applications of particle swarm optimization & genetic algorithm during antenna design. *Materials Today: Proceedings*. 56, 3823-3825, 2022.

[45] N. Jin and Y. Rahmat-Samii. Particle swarm optimization for antenna designs in engineering electromagnetics. *Journal of Artificial evolution and applications*. 2008(1), 728929, 2008.

[46] H. K. Bidhendi, H. M. Jafari and R. Genov, "Ultra-wideband imaging systems for breast cancer detection." *Ultra-wideband and 60 GHz communications for biomedical applications*. Boston, MA: Springer US, 83-103, 2013.

[47] A. M. Qashlan, R. W. Aldhaher and K. H. Alharbi, "A modified compact flexible vivaldi antenna array design for microwave breast cancer detection." *Applied Sciences* 12.10: 4908, 2022.

[48] S. Kwon, H. Lee and S. Lee, "Image enhancement with Gaussian filtering in time-domain microwave imaging system for breast cancer detection." *Electronics Letters* 52.5: 342-344, 2016.

Dicle University
Journal of Engineering
https://dergipark.org.tr/tr/pub/dumf
duje.dicle.edu.tr

Research Article

Dynamic Model Linearization and Model Predictive Control of an Organic Rankine Cycle

Mert Sinan TURGUT[1*], Oguz Emrah TURGUT[2]

[1] Izmir Democracy University, Mechanical Engineering Department, mertsinan.turgut@idu.edu.tr, Orcid No: 0000-0002-5739-2119
[2] Izmir Bakırçay University, Industrial Engineering Department, oguzemrah.turgut@bakircay.edu.tr, Orcid No 0000-0003-3556-8889

ARTICLE INFO

Article history:

Received 4 May 2025
Received in revised form 22 October 2025
Accepted 29 October 2025
Available online 30 December 2025

Keywords:

Organic Rankine Cycle, Model Predictive Control, Model Linearization, Energy Efficiency, Thermal Systems

Doi: 10.24012/dumf.1691147

* Corresponding author

ABSTRACT

This research investigates the control of an Organic Rankine Cycle (ORC) system, which consists of four main components: a condenser, a turbine, a pump, and an evaporator. The heat exchangers are designed as double-pipe configurations, and their dynamic behavior is modeled using the moving boundary approach. The pump and turbine, due to their significantly faster dynamics compared to the heat exchangers, are represented with static equations. The cycle's mathematical model is linearized by computing the Jacobian of the nonlinear function with respect to state, input, and disturbance variables. Model validation is performed by generating pseudo-random input sequences and applying them to both the developed ORC model and an Aspen model with identical specifications. The validation results show strong agreement between the two models, with only minor discrepancies. Subsequently, a linear model predictive control framework is established to regulate the linearized ORC model, incorporating several inequality constraints to ensure safe and efficient operation. Four control strategies are introduced, each focusing on distinct objectives such as enhancing thermodynamic efficiency or reducing entropy generation, while all share the common goal of tracking the turbine work output trajectory. Simulation results indicate that all four controllers effectively follow the specified turbine work output trajectory. The first law and second law controllers achieve the highest average efficiencies, with first law efficiency at 0.10250 and second law efficiency at 0.31732, respectively. The turbine work controller exhibits the highest total exergy destruction rate, recorded at 2100.17 W.

Introduction

The ever-increasing energy need by the global population requires the development of sustainable energy solutions and effective usage of energy sources [1]. The Organic Rankine Cycle (ORC) is an advancing technology that can fulfill global energy needs [2]. The ORCs have several important advantages over their traditional steam-based counterparts [3,4]. They are: the ORCs show favorable performance when working with low-grade and environmentally-friendly energy sources, such as solar, waste heat, or geothermal heat, and they can be fit to low temperature and pressure evaporation and applicable primary fluid mass flow rate working conditions since they utilize organic fluids as the main refrigerant [5,6]. Some of the unique qualities of ORCs are that they can be adapted to different kinds of heat sources, are a proven technology, have low complexity, and have huge market potential. The main fields of ORC research can be divided into the following categories: working fluid selection, cycle design configuration, turbomachinery, experimental analysis, design optimization, and dynamic modeling and control of the ORC cycle [7,8]. Upon examination of the literature, it is noted that the majority of studies focus on the design and optimization of ORCs, with less than 10% of the works addressing dynamic modeling and control [9,10]. Despite this, the dynamic modeling and control of ORCs remain a crucial research area, particularly for systems influenced by fluctuating heat source conditions. Both on-grid and off-grid operating ORCs have to react to the changes in the heat load. Numerous heat sources utilized by ORCs, including solar energy and waste heat from industrial processes or internal combustion engines, experience variable mass flow rates or temperatures. The study of dynamic modeling and control of ORCs gains more importance in reacting to the changes in the heat sources since transient heat source utilization can result in overheating, decomposition of the working fluid, and component failure due to stalling or temperature shocks.

Among the pioneering efforts in dynamic modeling of Rankine cycles, Colonna and colleagues [11,12] created a dynamic simulation for a steam-based Rankine cycle, validating it against data from a lab-scale setup. Their results showed a close match between the model predictions and experimental outcomes. Likewise, Quoilin et al. [13] explored the transient behavior of a small-scale ORC driven by a heat source with variable temperature and mass flow. They emphasized the dynamic modeling of heat exchangers, comparing three control strategies and finding

that model predictive control yielded the best performance. Additionally, Quoilin et al. introduced ThermoCycle, a Modelica-based library for simulating thermodynamic systems dynamically [14]. Shu et al. [15] built a dynamic ORC model in Matlab/Simulink, examining 14 working fluids powered by waste heat from a natural gas engine. They evaluated dynamic responses using metrics like rise time, time constant, and settling time, noting that low-temperature fluids reacted more quickly to changes in exhaust temperature and fluid mass flow. Gu et al. [16] developed a comprehensive ORC model based on an experimental system, incorporating processes like start-stop operations. Using the response surface method, they optimized operating conditions, and validation confirmed consistency with existing literature. Their findings indicated that increasing the connected load from 60 W to 120 W raised evaporator pressure by 3.4%, with the ORC achieving a peak output of 832 W at expander and pump speeds of 1400 rpm and 1500 rpm, respectively. Wilberforce and Muhammad [17] studied an integrated system combining a Proton Exchange Membrane (PEM) fuel cell with an ORC, where the fuel cell's waste heat exhibited significant temperature and flow variations, impacting cycle efficiency. They developed a dynamic model and implemented a PID controller to maintain a 10% thermal efficiency, observing a 0.9% power output increase after 2000 seconds, enhancing overall system performance. Kaleibar et al. [18] simulated an ORC dynamically using the moving-boundary approach, uniquely defining initial system states and vector variables. Their model's results aligned closely with experimental data, with a maximum deviation of 11% in net power output. Parametric analyses revealed that higher heat source temperatures and mass flow rates increased evaporator pressure and outlet temperature while reducing the working fluid's mass flow in the evaporator.

Controlling ORCs is a critical area of study due to inevitable variations in heat source temperature and mass flow, as previously noted. Effective control strategies are essential to mitigate the negative impacts of these fluctuations and enhance cycle efficiency. Controllers play a key role in ensuring safe operation while striving to optimize performance [19,20]. A widely used control approach involves adjusting the pump's rotational speed to manage the superheating temperature of the working fluid at the evaporator outlet [21]. Additionally, manipulating the expander's rotational speed or the heat source's mass flow can help achieve the target pressure at the expander inlet. Although research on dynamic modeling and control of ORCs is less extensive than other ORC-related fields, it is a growing discipline with increasing contributions to the literature. Pili et al. [22] explored control strategies for an ORC recovering waste heat from a heavy-duty vehicle's diesel engine, introducing a multi-objective optimization approach to tune a model predictive controller. The optimization focused on minimizing settling time and cumulative controller effort to address measurement noise, revealing a balance between these goals. Their controller effectively managed the ORC, with settling times for heat source mass flow variations serving as a reliable measure of tracking performance, ideally kept below 15 seconds for an absolute mean square error under 2 K. Feng et al. [23] examined a 3 kW ORC in a chemical plant, integrating a control system and analyzing its performance. They used 3400 experimental data points, split into training and validation sets, to train a backpropagation neural network. Six operational parameters were evaluated, showing that startup and stop stages had response times of 300 s and 90 s, respectively. Higher expander inlet temperatures and mass flow, combined with lower outlet temperatures, increased net output work. Liu et al. [24] applied model predictive control to an ORC paired with a 13L heavy-duty diesel engine, targeting fluid temperature regulation, superheating at the evaporator outlet, and maximum waste heat recovery. Their model, linearized around an operating condition, tested both linear and nonlinear model predictive controllers alongside PID algorithms. The predictive controllers outperformed PID, with the linear variant offering faster execution and reduced memory use. Wang et al. [25] investigated control methods for a small-scale ORC's cooling water and working fluid pumps under varying condensing conditions, using R245fa as the working fluid. Their model showed pump efficiencies ranging from 14% to 39% at speeds of 1600 to 2328 RPM. Ambient temperature fluctuations significantly affected thermal efficiency, with winter conditions boosting efficiency by 3.36% and net power by 5.11 kW compared to summer. Saha et al. [26] reviewed prior studies on ORC dynamic modeling and control, proposing innovative modeling and control approaches to address challenges. Their analysis covered energy conversion and control methods, highlighting the effectiveness of model predictive control and the importance of regulating superheat for optimal thermal performance. For further details on ORC dynamic modeling and control, readers may refer to [1,8,27-30].

This research focuses on linearizing a dynamic ORC model and implementing linear model predictive control to manage the system, aiming to meet predefined energy efficiency targets. The ORC system experiences continuous disturbances from varying secondary fluid temperatures in the evaporator and condenser. The ORC comprises four primary components: a pump, a turbine, an evaporator, and a condenser. Dynamic modeling of the heat exchangers employs the moving boundary method, while the pump and turbine are characterized using static algebraic equations. The REFPROP software [31] is used to calculate the thermodynamic and thermophysical properties of the refrigerants. The heat exchanger models are developed and linearized following methods outlined in [15,32]. System linearization is performed in MATLAB, resulting in a linear state-space model with 18 state variables, such as the working fluid's enthalpies and entropies throughout the cycle. The model includes four input variables: the secondary fluid mass flow rates in the heat exchangers, the pump's rotational speed, and the turbine coefficient. Seven output variables are defined, including component exergy destruction, pump power

consumption, and turbine power output. The linearized model is validated against a model with identical specifications built in Aspen Plus Dynamics [33]. Subsequently, four controllers with distinct objectives are designed and applied to the linearized ORC model. All controllers aim to track the work output trajectory, with one focusing solely on tracking work output (TWO). The other three controllers pursue additional goals: maximizing first law efficiency (FLM), maximizing second law efficiency (SLM), and minimizing entropy generation (EGM). The linear model predictive control approach [34,35] is used to adjust input variables to achieve these objectives. The Adam optimization algorithm [36] solves the optimization problem generated by the controller at each time step. The controllers' performance in trajectory tracking and thermal efficiency is evaluated and compared. To the authors' knowledge, detailed studies on linearizing dynamic ORC models are scarce in the literature. Given the emerging nature of dynamic ORC modeling and control, with limited existing research, this study represents a groundbreaking effort in linearizing and controlling ORC systems, addressing a notable gap in the field. Moreover, the current study advances the existing literature by proposing an 18-state model that captures full-cycle transients, including novel entropy states that are absent in current works, such as [15, 32]. The current works do not perform a linearization study with Jacobians. Additionally, the explicit inclusion of secondary fluid temperature disturbances and the proposed controllers have not been previously studied in the literature.

Organic Rankine Cycle System Modeling

The schematic diagram of the ORC considered in this study is depicted in Figure 1. The primary fluid draws heat from the secondary fluid and evaporates to a superheated state in the evaporator between states 1 and 2. Then, it expands and generates work output in the expander between states 2 and 3. Afterward, the fluid enters the condenser, releasing its excessive heat to the secondary fluid and condensing to a subcooled state between states 3 and 4. Finally, the working fluid pressure is raised to the evaporator levels in the pump between states 4 and 1. The mentioned processes carry on during the cycle.

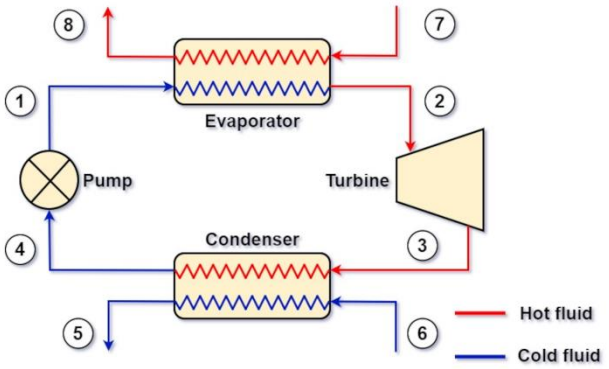

Figure 1. Graphical representation of the ORC.

Table 1. Specifications of the ORC components.

Parameter	Value
Inner diameter of the heat exchanger tube (m)	0.024
Outer diameter of the heat exchanger tube (m)	0.030
Heat exchanger wall thickness (m)	0.002
Heat exchanger tube length (m)	20.0
Heat exchanger wall material	Copper
Volumetric efficiency of pump ($\eta_{vol,pump}$)	0.60
Cylinder volume of pump (V_{pump}) (m^3)	1.30E-05
Turbine constant pressure (P_{const}) (MPa)	1.40
Isentropic efficiency of turbine	0.75
Isentropic efficiency of pump	0.80

The component design specifications of the ORC system and their corresponding values are listed in Table 1. The primary and secondary fluids employed in the cycle are R134a and air, respectively. The temperatures of the cold and hot medium are respectively taken as 305 K and 344 K. Moreover, constant cold and hot medium temperature disturbances are applied to the system throughout its operation. The cold and hot medium disturbance temperatures are respectively considered to be 309 K and 347 K, respectively. The ambient temperature value utilized in the calculations is considered 298.15 K. REFPROP [31] software is utilized to determine the thermodynamic and thermophysical properties of the fluids.

Evaporator and Condenser

The Moving Boundary (MB) approach is used to represent the dynamic behavior of the heat exchangers, with comprehensive details provided in Shu et al. [15] and Rasmussen and Alleyne [32]. The heat exchangers are designed as counter-flow double-pipe systems. In both the evaporator and condenser, the primary refrigerant exists in superheated, two-phase, and subcooled states, with the boundaries of these phase regions shifting over time. The thermodynamic and thermophysical properties of each phase are calculated as lumped parameters. Illustrations of the MB model for the heat exchangers are presented in Figure 2. The evaporation and condensation processes are modeled using the Gungor and Winterton [37] and Shah [38] correlations, respectively. The Gnielinski [39] correlation is applied for single-phase heat transfer, and the Fauske [40] correlation is used to determine the mean void fraction. To simplify the heat exchanger models, several assumptions are adopted:The axial conduction occurring inside the pipes is ignored.

- Axial conduction within the pipes is neglected
- The tubes of the heat exchangers are assumed to be long, thin, and horizontal.
- The flow within the tubes is treated as one-dimensional.

• Pressure losses during flow through the heat exchangers are considered insignificant, eliminating the need for a momentum conservation equation. Many studies in the literature have utilized this approach and found similar results to those in real-world scenarios [15, 32].

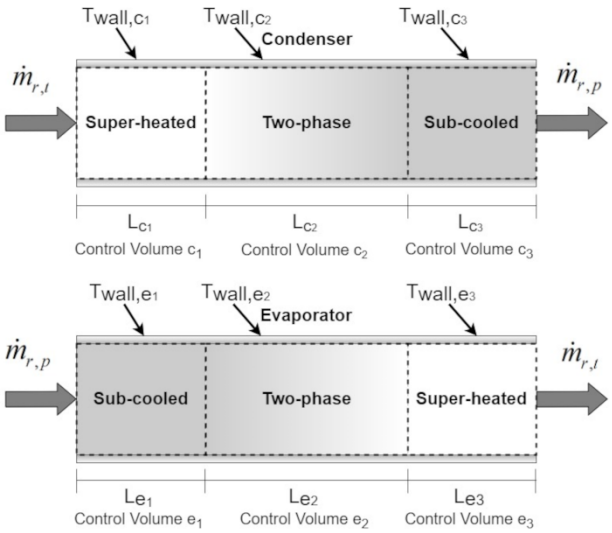

Figure 2. Moving boundary modeling of the heat exchangers.

Three governing partial differential equations are defined for each region in the MB modeling of the heat exchangers. They are the mass and energy balance of the working fluid and the energy balance in the tube wall. These equations are,

$$\int_{L_1}^{L_2} \frac{\partial(A\rho)}{\partial t} + \int_{L_1}^{L_2} \frac{\partial(\dot{m})}{\partial x} = 0 \quad (1)$$

$$\int_{L_1}^{L_2} \frac{\partial(hA\rho - PA)}{\partial t} + \int_{L_1}^{L_2} \frac{\partial(\dot{m}h)}{\partial x} = d_{in}\alpha_{in}\left(T_{wall} - T_{ref}\right) \quad (2)$$

$$(c\rho A)_{wall}\frac{\partial(T)_{wall}}{\partial t} = d_{in}\alpha_{in}\left(T_{ref} - T_{wall}\right) + d_{out}\alpha_{out}(T_{out} - T_{wall}) \quad (3)$$

where A is the cross-sectional area of the inner tube, $\dot{m}$ is the mass flow rate, ρ represents the density, h is the enthalpy, and P denotes the pressure of the fluid. The necessary integrations given in Eqs. (1-3) are performed to obtain the transient behavior of the heat exchangers. The lumped fluid enthalpy and density are calculated by taking the arithmetic average of the phase values at the inlet and outlet of the region boundaries for the single phase-zones. For the two-phase region, these values are determined with the following equations,

$$\rho_{av} = \rho_{vap}\bar{\gamma} + \rho_{liq}(1 - \bar{\gamma}) \quad (4)$$

$$\rho_{av}h_{av} = \rho_{vap}h_{vap}\bar{\gamma} + \rho_{liq}h_{liq}(1 - \bar{\gamma}) \quad (5)$$

where $\bar{\gamma}$ is the mean void fraction which is the volumetric ratio of the gaseous phase and total fluid amount. The Leibniz integration rule is applied to the fluid mass and energy balance equations to simplify and and organize them into matrix structure. The MB model of all working fluid regions present in the heat exchanger (e.g. superheated, two-phase, and subcooled) are obtained as a result of the integration. The mathematical representation of the Leibniz integration rule is given below,

$$\int_{x_1}^{x_2} \frac{\partial f(x,t)}{\partial x}dx = \frac{d}{dt}\int_{x_1}^{x_2} f(x,t)dx - f(x_2,t)\frac{dx_2}{dt} + f(x_1,t)\frac{dx_1}{dt} \quad (6)$$

The exergy destructions occurring in the evaporator and condenser are determined with the following equations,

$$\dot{X}_{evap} = \dot{m}_{turb}\left(h_{out,evap} - T_{amb}s_{out,evap}\right) - \dot{m}_{pump}\left(h_{in,evap} - T_{amb}s_{in,evap}\right) + \dot{m}_{sevap}\left(h_{sevap} - T_H s_{sevap}\right) \quad (7)$$

$$\dot{X}_{cond} = \dot{m}_{pump}\left(h_{out,cond} - T_{amb}s_{out,cond}\right) - \dot{m}_{turb}\left(h_{in,cond} - T_{amb}s_{in,cond}\right) + \dot{m}_{scond}\left(h_{scond} - T_L s_{scond}\right) \quad (8)$$

where *s* denoted the specific entropy of the fluid. The entropy values at the inlet and outlet of the heat exchangers are calculated utilizing the chain rule for the sake of simplification during the linearization procedure,

$$\frac{ds}{dt} = \frac{\partial s}{\partial h}\Big|_{P,h}\frac{dh}{dt} + \frac{\partial s}{\partial P}\Big|_{P,h}\frac{dP}{dt} \quad (9)$$

Pump and Turbine

The pump and turbine exhibit significantly faster dynamics compared to the heat exchangers, so they are modeled using static algebraic equations and treated as non-isentropic, adiabatic components. To streamline the model, the turbine's electro-mechanical variables are omitted [41,42]. The mass flow rate and outlet enthalpy of the working fluid at the turbine are calculated as described in [43],

$$\dot{m}_{turb} = C_{turb}\sqrt{\rho_{out,evap}\left(P_{evap} - P_{const}\right)} \quad (10)$$

$$h_{out,t} = h_{in,t} + \eta_{isen,t}\left(h_{isen,t} - h_{in,t}\right) \quad (11)$$

where C_{turb} is the discharge coefficient of the turbine, P_{evap} is the evaporator pressure, P_{const} is a pre-determined constant pressure value, and $\eta_{isen,t}$ is the isentropic efficiency of the turbine. The work output and exergy destruction of the turbine are calculated as,

$$\dot{W}_{turb} = \dot{m}_{turb}\left(h_{a,out,t} - h_{in,t}\right) \quad (12)$$

$$\dot{X}_{turb} = \dot{m}_{turb}T_{amb}\left(s_{a,out,t} - s_{in,t}\right) \quad (13)$$

The working fluid mass flow rate and outlet enthalpy at the pump are computed as follows,

$$\dot{m}_{pump} = \rho_{in,pump} V_{pump} \eta_{vol,pump} \omega \quad (14)$$

$$h_{out,p} = h_{in,p} + \frac{1}{\eta_{isen,p}} \left(h_{isen,p} - h_{in,p}\right) \quad (15)$$

where V_{pump} is the volumetric displacement, $\eta_{vol,pump}$ and $\eta_{isen,p}$ are the volumetric and isentropic efficiencies and ω is the rotation speed of the pump. The work consumption and exergy destruction of the pump are calculated with the following equations,

$$\dot{W}_{pump} = \dot{m}_{pump}\left(h_{a,out,p} - h_{in,p}\right) \quad (16)$$

$$\dot{X}_{pump} = \dot{m}_{pump} T_{amb}\left(s_{a,out,p} - s_{in,p}\right) \quad (17)$$

The heat transfer rate taking place in the evaporator is determined as,

$$\dot{Q}_{evap} = \dot{m}_{turb} h_{out,evap} - \dot{m}_{pump} h_{in,evap} \quad (18)$$

The overall total exergy destruction in the cycle is computed as,

$$\dot{X}_{tot} = \dot{X}_{evap} + \dot{X}_{cond} + \dot{X}_{turb} + \dot{X}_{pump} \quad (19)$$

The ORC first and second law efficiencies are determined with the following equations,

$$\eta_I = \frac{\dot{W}_{turb} - \dot{W}_{pump}}{\dot{Q}_{evap}} \quad (20)$$

$$\eta_{II} = 1 - \frac{\dot{X}_{tot}}{\dot{W}_{turb} - \dot{W}_{pump}} \quad (21)$$

Linearization of the Cycle Model

The developed MB model of the ORC is highly nonlinear. Linearizing the nonlinear model makes it simpler and easier to control. The linearization of the cycle model is accomplished by taking the partial derivatives of the obtained functions with respect to the states and inputs of the system and eliminating the second and higher-order terms. The nonlinear mathematical representation of the overall cycle is,

$$M(x,u)\dot{x} = f(x,u) \quad (22)$$

The state derivative matrix is obtained by inverting and multiplying the M matrix,

$$\dot{x} = f(x,u)M(x,u)^{-1} = z(x,u) \quad (23)$$

By taking the jacobian of the f matrix and assuming the local linearizations $\partial x = x - x_0$ and $\partial u = u - u_0$, the following linear state-space representations are acquired,

$$\dot{x} = \underbrace{\left(M|_{x_0,u_0}\right)^{-1}\left(\frac{\partial f}{\partial x}\Big|_{x_0,u_0}\right)}_{A}\partial x + \underbrace{\left(M|_{x_0,u_0}\right)^{-1}\left(\frac{\partial f}{\partial u}\Big|_{x_0,u_0}\right)}_{B}\partial u \quad (24)$$

$$y = \underbrace{\left(\frac{\partial z}{\partial x}\Big|_{x_0,u_0}\right)}_{C}\partial x + \underbrace{\left(\frac{\partial z}{\partial u}\Big|_{x_0,u_0}\right)}_{D}\partial u \quad (25)$$

where A is the state matrix, B is the input matrix, C is the output matrix, and D is the feedthrough matrix.

Validation of the Developed Organic Rankine Cycle Model

The model validation study is conducted in the Aspen Plus [33] environment by comparing the outcomes of the two different state variables, i.e., condenser outlet entropy and evaporator subcooled region length, with those of the Aspen model with the same design configurations. Aspen Plus is a well-known process simulator used by top chemical companies worldwide. Both models employ the same working fluids, have the exact design specifications, and are subject to the same reservoir temperature disturbances. A set of pseudo-random input parameters is generated in the Julia environment [44] and applied to both systems. The variations of the input parameters are depicted in Figure 3. The outcomes of the two selected state variables resulting from the inputs applied to the systems are shown in Figures 4a and 4b. The results of both state variables revealed that the developed and Aspen models agree well, and the most significant difference between them is 8.95% in the evaporator subcooled region length. This amount of error is acceptable and indicates that the proposed and Aspen Plus models are coherent [15].

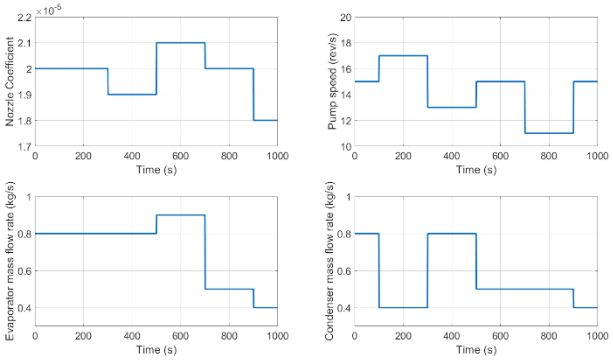

Figure 3. Generated pseudo-random input variables for the model validation.

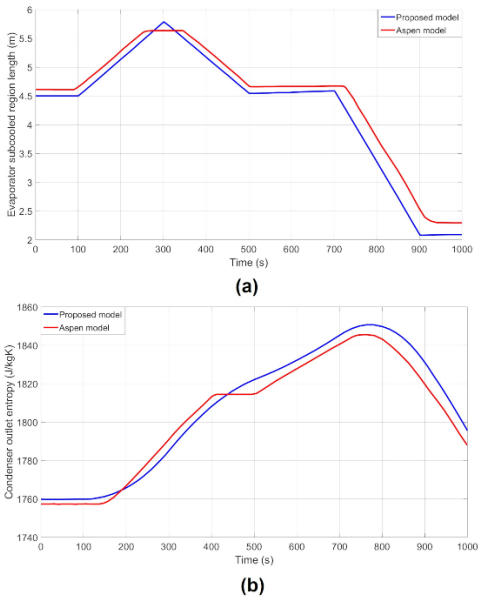

Figure 4. Selected variable outcome comparisons for the Aspen and proposed models.

Model Predictive Controller Design

Model Predictive Control (MPC) is a control technique that utilizes a mathematical model of a system to predict and regulate its future behavior [45]. The schematic of the MPC is depicted in Figure 5. The controller solves a linear or nonlinear optimization problem depending on the form of the mathematical model at each time step and tries to address three main objectives, namely future prediction of the state variables, directing the output through the target trajectory, and computing the most desirable input sequence to reach the target. A considerable amount of real-time computing power is needed to implement a MPC system. However, recent advances in computing technology have significantly improved the speed and accuracy of the calculations [46]. MPC is one of the most acknowledged control techniques due to its prediction-based execution and good balance between computation speed and optimality [47]. The main idea behind the MPC is to predict the future behavior of the model and generate the optimal control input sequence to make the system reach a desirable state. Moreover, the MPC technique can be adapted to linear and nonlinear system model control cases, which increases its desirability. The linear MPC technique is discussed in this section since it is applied to control the ORC system in this study.

Techniques like decentralized and multiloop PID are widely used in the literature to control multi-input multi-output systems. The MPC control system utilized in this study must satisfy limited actuator and process constraints at every sampling time. Given that PID control lacks multi-variable constraint handling for process claims, it is not suitable for use in this study. Moreover, it is not possible to pair or decouple the model to make it ready for decentralized and multiloop PID techniques. For the reasons given above, the MPC control technique is adopted instead of the PID in this study. In terms of qualitative performance, a finely tuned decentralized PID can follow the setpoint, but should encounter (i) higher overshoots and settling times in the presence of disturbances, (ii) more frequent manipulative variable swings as a result of loop interactions, and (iii) possible constraint violations without additional supervisory action. Published comparisons on multivariable benchmark problems, such as double and triple tank systems or distillation columns, show that, for the same type of constraints and under similar conditions, MPC results in minor tracking errors and avoids extensive input switching more effectively than a decentralized PID controller [1, 48].

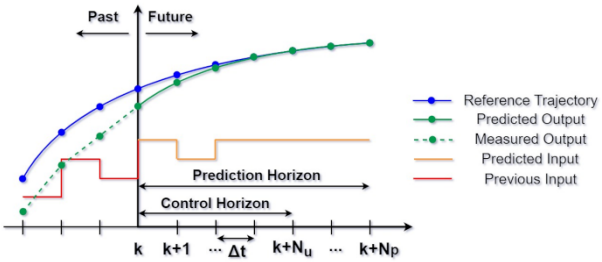

Figure 5. Graphical illustration of the model predictive controller.

Given a linear discrete time-invarient system in the state-space form,

$$x(k+1) = Ax(k) + Bu(k) + B_w w(k) \tag{26}$$

The MPC method attempts to minimize the following cost equation at each time step,

$$\begin{aligned} J(k) = \sum_{0}^{M-1} \left((x_k - x_k^d)^T Q (x_k - x_k^d) + u_k^T R u_k \right) \\ + x_{fin}^T Q_{fin} x_{fin} \\ s.t.\ X_{min} \le x \le X_{max} \\ \Delta U_{min} \le u \le \Delta U_{max} \\ U_{min} \le u \le U_{max} \end{aligned} \tag{27}$$

where Q and R are the weight matrices, M is the prediction horizon, x_k^d is the desired state variable value, U_{min}, U_{max}, represent the minimum and maximum bounds for input variables, X_{min}, and X_{max} denote the limits for state variables, and ΔU_{min} and ΔU_{max} define the lower and upper constraints on the slew rate.

The linear ORC model proposed in this study consists of eighteen state, four input, two disturbance, and seven output variables,

$$\begin{aligned} x = [L_{cond,1}\ L_{cond,2}\ P_{cond}\ h_{cond,o}\ T_{cond,wall,1}\ T_{cond,wall,2} \\ T_{cond,wall,3}\ L_{evap,1}\ L_{evap,2}\ P_{evap}\ h_{evap,o}\ T_{evap,wall,1} \\ T_{evap,wall,2}\ T_{evap,wall,3}\ s_1\ s_2\ s_3\ s_4\ ] \end{aligned} \tag{28}$$

$$u = [\omega\ C_{turb}\ \dot{m}_{scond}\ \dot{m}_{sevap}] \tag{29}$$

$$w = [T_L\ T_H] \tag{30}$$

$$y = [\dot{W}_{pump}\ \dot{W}_{turb}\ \dot{Q}_{evap}\ \dot{X}_{evap}\ \dot{X}_{cond}\ \dot{X}_{pump}\ \dot{X}_{turb}] \tag{31}$$

The following constraints are imposed on the evaporator and condenser working fluid region lengths for the safe operation of the system,

$$L_{evap,1} + L_{evap,2} \leq 0.90.\, L_{evap} \quad (32)$$
$$L_{cond,1} + L_{cond,2} \leq 0.90.\, L_{cond} \quad (33)$$

Moreover, the component exergy destructions are subjected to constraints to ensure that they are nonnegative during the operation of the cycle,

$$\begin{aligned} \dot{X}_{evap} &> 0 \\ \dot{X}_{cond} &> 0 \\ \dot{X}_{turb} &> 0 \\ \dot{X}_{pump} &> 0 \end{aligned} \quad (34)$$

Four controllers are proposed: TWO, FLM, FLM, and EGM controllers. Three of them have unique objectives, but all share a common objective, i.e., turbine work trajectory tracking. The TWO controller only has the common objective of turbine work trajectory tracking. All controllers are named after their distinct objectives: turbine work trajectory tracking, first law efficiency maximization, second law efficiency maximization, and entropy generation minimization. The control and thermal performances of these controllers are compared in this study. The mathematical expressions of the controllers are,

$$J_{turbwork} = |\dot{W}_d - \dot{W}_{turb}|_2 \quad (35)$$
$$J_{firstlaw} = |\dot{W}_d - \dot{W}_{turb}|_2 + \alpha \sum_0^M \eta_I \quad (36)$$
$$J_{secondlaw} = |\dot{W}_d - \dot{W}_{turb}|_2 + \alpha \sum_0^M \eta_{II} \quad (37)$$
$$J_{entgen} = |\dot{W}_d - \dot{W}_{turb}|_2 + \alpha \sum_0^M \dot{s}_{gen} \quad (38)$$

where α is the objective weight. The block diagram of the proposed control system is depicted in Figure 6.

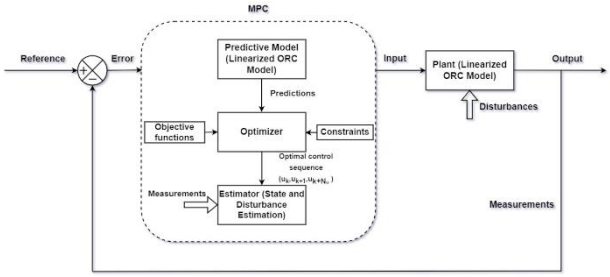

Figure 6. Block diagram of the proposed control system

Results and Discussion

Practical Applications of the Proposed ORC Control System

The proposed linearized ORC model and MPC framework are particularly suited for systems where heat sources exhibit temporal variability, enabling precise trajectory tracking of power output while optimizing thermodynamic performance. Adaptive control is crucial in off-grid and hybrid energy systems, as disturbances such as diurnal solar variability or intermittent industrial emissions can reduce operational efficiency by 10-15%. Some of the potential applications of the proposed ORC control system for real-world applications are as follows. ORC systems recover low-grade heat (50–200°C) from processes in chemical, steel, cement, and glass manufacturing, where exhaust gases vary with production rates. The proposed controllers could regulate pump/turbine speeds to maintain superheat and minimize exergy destruction. In geothermal plants, ORC handles steady but location-specific temperature swings, while solar ORC faces hourly irradiance changes. The proposed disturbance-inclusive controllers could reduce the settling times in the geothermal plants. The proposed controllers, like FLM, could maximize first-law efficiency for biomass-fired ORCs in district heating or power plants. Thus, it has significant potential for use in these types of systems [1].

Simulation Results

The implementation of the controller is accomplished in the Julia programming environment. The control and prediction horizon values are 10 for all controllers. As mentioned in the previous section, the linear MPC controller generates a convex objective function to be optimized at each time step. The ADAM algorithm is utilized to solve the generated convex problem. The step size of the ADAM algorithm is dynamically adjusted, and the maximum number of iterations is selected to be 1000. The time step of the simulation is 0.1 seconds. Moreover, the objective weight values for all controllers are heuristically chosen as one. Tables 2 and 3, respectively, report the minimum and maximum bounds and slew rate of the system inputs. Figure 7 depicts the turbine work output ($\dot{W}_{turb}$) trajectory of the controllers. The desired work output value is 3660 W in the first 400 seconds; then it changes to 3670 W in the next 500 seconds; afterward, it increases to 3690 W between 900 and 1500 seconds, and it rises to 3700 W for the next 300 seconds and falls back to 3690 W for the remaining of the simulation.

Table 2. Lower and upper bounds of the inputs.

Input variable	Lower bound	Upper bound
Evaporator secondary fluid mass flow rate (kg/s)	0.4	1.0
Condenser secondary fluid mass flow rate (kg/s)	0.4	1.0
Nozzle coefficient (-)	1.8E-05	2.2E-05
Pump speed (rev/s)	10.0	20.0

Table 3. Slew rate bounds of the inputs.

Input variable	Bound
Evaporator secondary fluid mass flow rate (kg/s)	±0.1
Condenser secondary fluid mass flow rate (kg/s)	±0.1
Nozzle coefficient (-)	±6.0E-07
Pump speed (rev/s)	±0.5

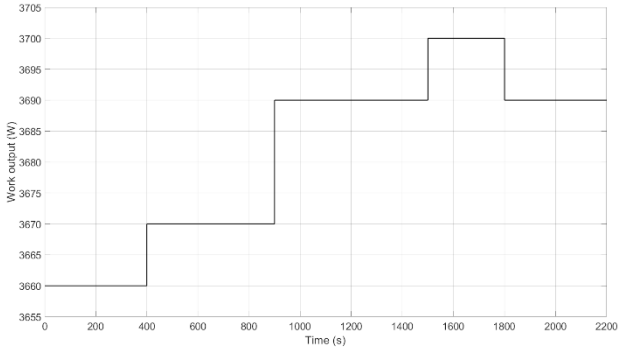

Figure 7. Common trajectory of the controllers.

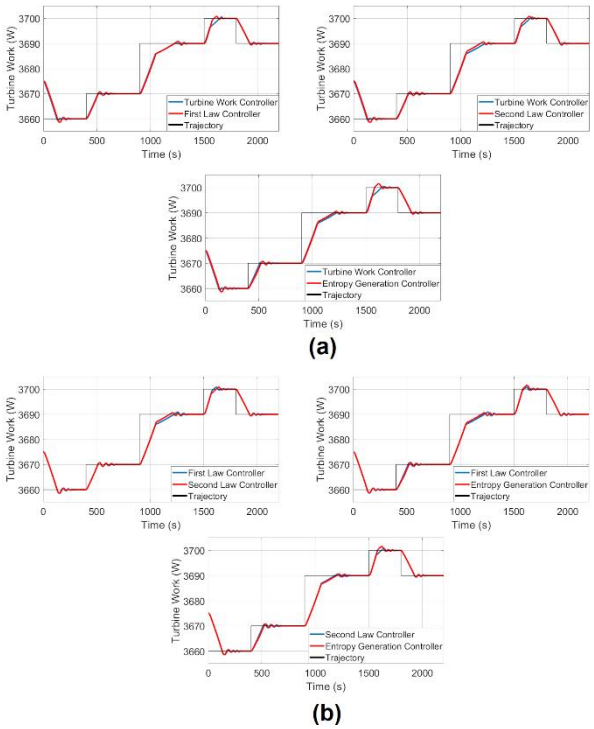

Figure 8. Pair-wise desired turbine work trajectory tracking performance comparison of the controllers.

Figure 8 compares the controllers' ability to track the designated turbine work output trajectory. All controllers follow the specified trajectory effectively, though they exhibit noticeable overshoot and prolonged settling times during convergence to the target set points. These effects stem from disturbances in the heat source temperature affecting the ORC system, which hinder smooth trajectory tracking. The TWO controller demonstrates a longer rise time but significantly reduced maximum overshoot and settling time compared to its counterparts. Conversely, the EGM controller displays greater overshoot and settling time than the others. The FLM and SLM controllers show moderate performance with acceptable convergence characteristics. Figures 9a and 9b present the variations in evaporator and condenser mass flow rate inputs during the simulation. Both inputs initially drop to their minimum values and remain stable thereafter, indicating that secondary fluid mass flow rates have minimal impact on the cycle's thermal efficiency. Figures 10a and 10b depict the changes in turbine coefficient and pump speed inputs over time. The pump speed transitions smoothly during set point adjustments but exhibits zigzag patterns after reaching the set point. The TWO controller follows a noticeably smoother path compared to the others. All controllers fluctuate between the upper and lower limits of the nozzle coefficient, each taking distinct trajectories. Figures 11a and 11b show the exergy destruction rates for the condenser and evaporator across the four controllers. The exergy destruction patterns are similar for both components, with the TWO controller slightly diverging, showing a higher condenser exergy destruction rate and a marginally lower evaporator exergy destruction rate than the others. Figures 12a and 12b illustrate the exergy destruction rates for the pump and turbine throughout the simulation. The TWO controller exhibits a notably higher pump exergy destruction rate, while all controllers perform similarly regarding turbine exergy destruction.

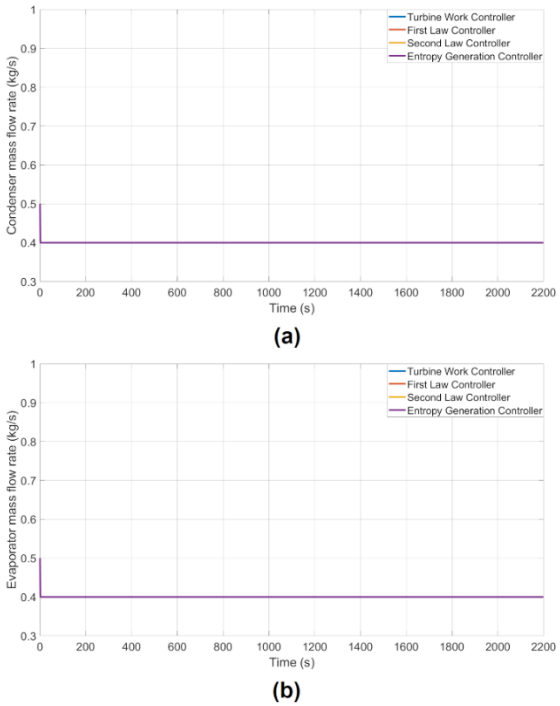

Figure 9. Condenser and evaporator secondary fluid mass flow rate variations over time.

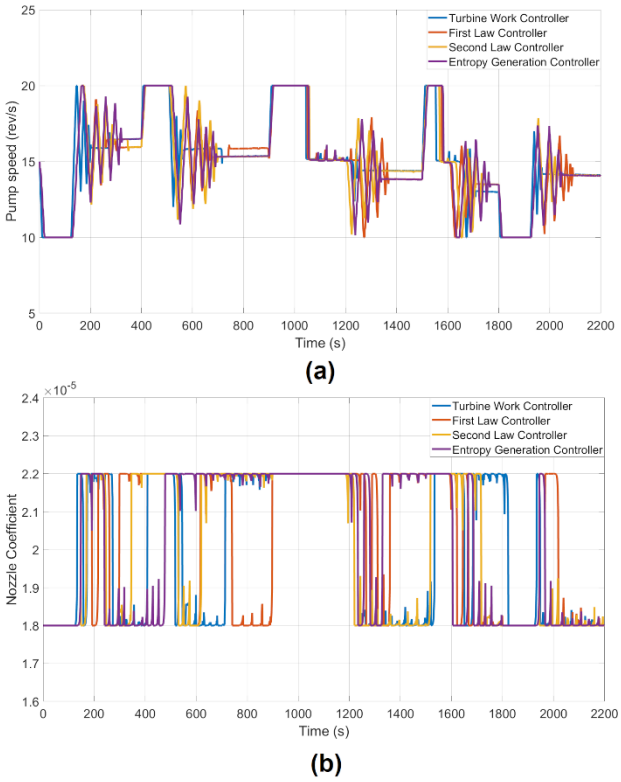

Figure 10. Pump speed and nozzle coefficient input variable variations over time.

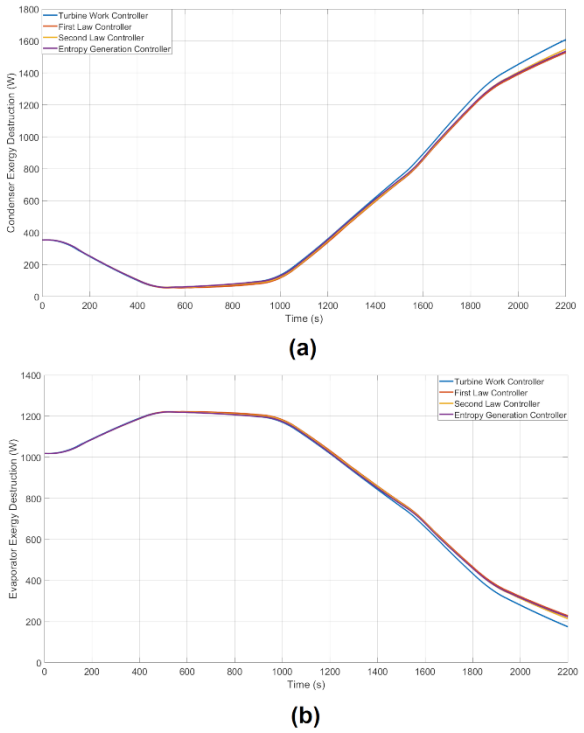

Figure 11. Condenser and evaporator exergy destruction rates over time for the controllers.

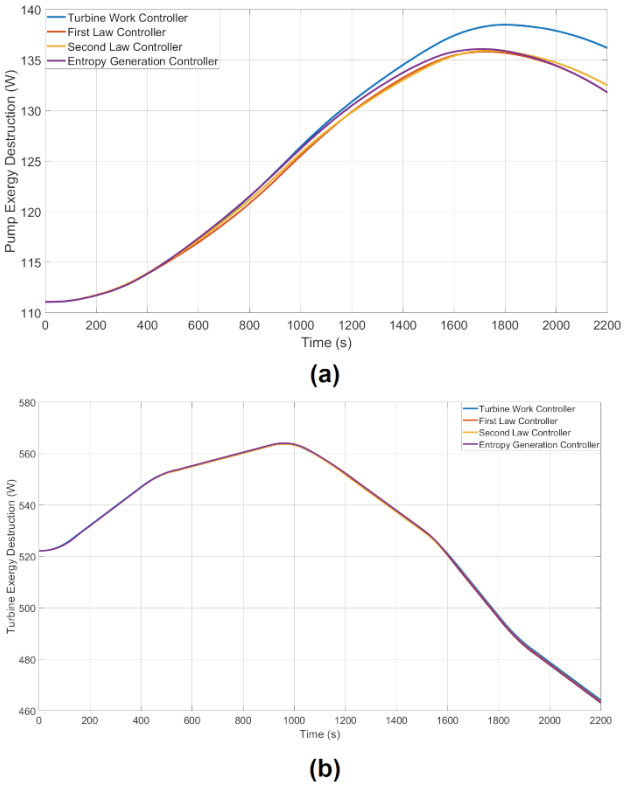

Figure 12. Pump and turbine exergy destruction rates over time for the controllers.

Table 4 presents the time-averaged exergy destruction rates for the ORC components. The evaporator exhibits the highest exergy destruction rates across all controllers, while the pump consistently shows the lowest, aligning with expectations as pumps typically have minimal exergy destruction in ORC systems [49]. On average, the evaporator's exergy destruction rate exceeds that of the condenser by about 66.3%. Additionally, the turbine's exergy destruction rates remain comparable across all controllers. Table 5 summarizes the time-averaged total turbine work, exergy destruction rates, and entropy generation rates for each controller. The TWO controller records the highest total exergy destruction rate at 2100.17 W, surpassing the FLM controller by 0.21%. The SLM and EGM controllers demonstrate lower total exergy destruction rates, reflecting their focus on minimizing exergy loss during control. A similar trend appears in total entropy generation, with the TWO controller reaching 1404.66 W, 1.02% above the FLM controller. The SLM controller generates slightly less entropy than the EGM controller, as it prioritizes entropy minimization more heavily. While all controllers achieve comparable total turbine work outputs, the EGM controller marginally outperforms the others.

Table 4. ORC components' time-averaged exergy destruction rates for the controllers.

Exergy destruction (W)	TWO	FLM	SLM	EGM
Evaporator	882.489	898.222	893.622	892.337
Condenser	560.125	541.547	543.386	545.347
Turbine	530.825	530.564	530.307	530.532
Pump	126.731	125.410	125.535	125.729

Table 5. Total exergy destruction, turbine work output, and entropy generation performances averaged over time for the controllers.

	TWO	FLM	SLM	EGM
Total exergy destruction (W)	2100.17	2095.74	2092.85	2093.94
Total turbine work output (W)	3913.34	3913.40	3914.41	3914.44
Total entropy generation (J/K)	1404.66	1390.17	1386.57	1388.89

Bejan [50] pointed out in his study that minimizing the total entropy generation rate is similar to maximizing the net power output of a power generation cycle. The Gouy-Stadola theorem states that,

$$\dot{W}_{net} = \dot{W}_{rev} - T_L \dot{S}_{gen} \tag{39}$$

where $\dot{W}_{net}$ is the net power output of the cycle and $\dot{W}_{rev}$ is the reversible work. According to the Gouy-Stadola theorem, minimizing the total entropy generation rate is the same as maximizing the net power output for all thermodynamic cycles. However, some generalizations are made while considering this theorem, such as considering all interactions between heat sources as fixed and assuming the hot medium has infinite heating capability. In practice, the hot medium has finite heating capability and can supply changing heat to the cycle. For this reason, the changing heat supply and entropy must be considered in the system model. Organizing and integrating the Gouy-Stadola theorem leads to the following equation,

$$S_{gen} = \left(\left(\frac{1}{T_L} - \frac{1}{T_H} \right) (U_L - U_S) \right) - \frac{1}{T_L} W_{net} \tag{40}$$

Given that all temperature and heat transfer coefficient variables remain constant, it is evident that the cycle's entropy generation and net power output exhibit an inverse relationship. The results presented in Table 5 align with the computations described by Bejan [49]. The EGM controller demonstrates superior work output performance compared to its counterparts. Figures 13a and 13b illustrate the first and second law efficiency trends of the controllers over time. The TWO controller performs noticeably worse than others in terms of first law efficiency. The TWO controller exhibits worse exergy destruction performance due to its focus on trajectory tracking. The EGM shows a significant improvement in the total exergy destruction and entropy generation metrics due to its focus on entropy generation minimization performance. The FLM controller excels in first law efficiency, as it is designed to prioritize its maximization. All four controllers show comparable trends in second law efficiency. The time-averaged first law efficiency values for the TWO, FLM, SLM, and EGM controllers are 0.10247, 0.10250, 0.10248, and 0.10249, respectively. For second law efficiency, the time-averaged values are 0.31720, 0.31726, 0.31732, and 0.31727 for the TWO, FLM, SLM, and EGM controllers, respectively. Although the differences between the time-averaged first and second law efficiency performances of the controllers are minor, the controllers with the highest efficiency values have slight advantages compared to the others. As anticipated, the SLM controller achieves the highest second law efficiency, while the TWO controller performs the least effectively, as its sole focus is tracking the specified turbine work output trajectory.

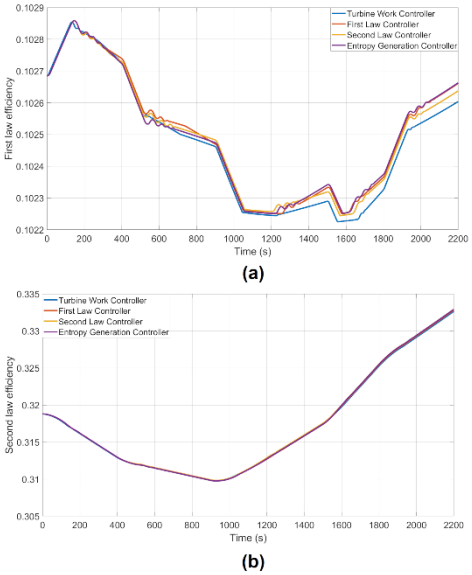

Figure 13. Variations in the first law and second law efficiencies exhibited by the controllers

Conclusions

This study centers on linearizing and controlling a mathematical model of an organic rankine cycle (ORC) system. The ORC system includes four key components: a pump, a turbine, a condenser, and an evaporator. The condenser and evaporator, configured as double-pipe heat exchangers, are modeled dynamically using the moving boundary approach, while the turbine and pump, with faster dynamics, are represented by static equations. In the moving boundary model, each fluid phase is treated as a distinct region, with the model tracking the temporal evolution of phase boundaries. Thermodynamic and thermophysical properties for each phase region are computed as lumped parameters. The cycle's mathematical model is linearized by calculating the Jacobian of the nonlinear function with respect to state, input, and disturbance variables, yielding a linear model with 18 state variables, four inputs, two disturbances, and seven outputs. The model's validity is confirmed by generating pseudo-random input sequences, applying them to both the ORC model and an Aspen model with identical specifications, and comparing two state variables—condenser outlet entropy and evaporator subcooled region length. The comparison shows close agreement with minimal discrepancies. A linear predictive control framework is then implemented to regulate the linearized ORC model, generating a convex objective function at each time step, solved using the Adam algorithm. Inequalities constrain the objective function to ensure safe and efficient cycle operation. Four control strategies are developed to track a predefined turbine work output trajectory, with three controllers pursuing additional goals: maximizing first law efficiency, enhancing second law efficiency, and reducing entropy generation. This study's primary objective is to evaluate these controllers' thermal performance. Simulations reveal that all controllers successfully track the target work output trajectory, though performance varies. The evaporator exhibits exergy destruction rates approximately 66.3% higher than the condenser on average. The TWO controller records the highest time-averaged exergy destruction rate at 2100.17 W, followed by the FLM controller at 2095.74 W. The FLM and SLM controllers achieve the highest time-averaged first law and second law efficiencies, respectively.

Nomenclature

Symbols

A	Area, State matrix [m^2]
B	Input matrix
C	Discharge coefficient
h	Enthalpy [J]
J	Objective function
L	Length [m]
$\dot{m}$	Mass flow rate [kg/sec]
P	Pressure [Pa]
Q	Weight matrix
$\dot{Q}$	Heat transfer rate [J]
R	Weight matrix
S	Entropy [J/K]
t	Time [sec]
T	Temperature [K]
u	Input vector
U	Internal Energy [J]
x	State vector
$\dot{X}$	Exergy destruction rate [W]
W	Work [J]
$\dot{W}$	Work rate [J]
α	Objective weight
$\bar{\gamma}$	Mean void fraction
η	Efficiency
ρ	Density [kg/m^3]
ω	Pump rotation speed [rev/s]

Subscripts

av	Average
cond	Condenser
d	Desired
evap	Evaporator
gen	Generated
H	Hot reservoir
isen	Isentropic
L	Cold reservoir
liq	Liquid
net	Net amount
pump	Pump
ref	Refrigerant
rev	Reversible
turb	Turbine
vap	Vapor
wall	Tube wall
η_I, I	First law efficiency
η_{II}, II	Second law efficiency

Ethics committee approval and conflict of interest statement

There is no need to obtain permission from the ethics committee for the article prepared

There is no conflict of interest with any person / institution in the article prepared

Authors' Contributions

-Study conception and design: M.S. Turgut & O. E. Turgut

-Acquisition of data: M.S. Turgut & O. E. Turgut

-Analysis and interpretation of data: M.S. Turgut & O. E. Turgut

-Drafting of manuscript: M.S. Turgut & O. E. Turgut

-Critical revision: M.S. Turgut & O. E. Turgut

References

[1] M. Imran, R. Pili, M. Usman, and F. Haglind, "Dynamic modeling and control strategies of organic Rankine cycle systems: Methods and challenges," Appl. Energy, vol. 257, p. 115537, Jan. 2020, DOI: 10.1016/j.apenergy.2020.115537.

[2] J. G. Andersen, U. Larsen, T. Knudsen, L. Pierobon, and F. Haglind, "Selection and optimization of pure and mixed working fluids for low grade heat utilization using organic Rankine cycles," Energy, vol. 73, pp. 204–213, Aug. 2014, DOI: 10.1006/j.energy.2014.06.012.

[3] T. C. Hung, T. Y. Shai, and S. K. Wang, "A review of organic Rankine cycles (ORCs) for the recovery of low-grade waste heat," Appl. Energy, vol. 6, pp. 661–667, Jul. 1997, DOI: 10.1016/S0360-5442(96)00165-X.

[4] B. F. Tchanche, G. Lambrinos, A. Frangoudakis, and G. Papadakis, "Low-grade heat conversion into power using organic Rankine cycles—a review of various applications," Renew. Sustain. Energy Rev., vol. 15, no. 8, pp. 3963–3979, Oct. 2011, DOI: 10.1016/j.rser.2011.07.024.

[5] E. Macchi and M. Astolfi, Organic Rankine Cycle (ORC) Power Systems: Technologies and Applications. Cambridge, U.K.: Woodhead Publishing, 2017, DOI: 10.1016/C2014-0-04239-6.

[6] X. Chen, C. Liu, Q. Li, X. Wang, and X. Xu, "Dynamic analysis and control strategies of organic Rankine cycle system for waste heat recovery using zeotropic mixture as working fluid," Energy Convers. Manag., vol. 192, pp. 321–334, Jul. 2019, DOI: 10.1016/j.enconman.2019.04.049.

[7] M. Imran, F. Haglind, M. Asim, and J. Zeb Alvi, "Recent research trends in organic Rankine cycle technology: A bibliometric approach," Renew. Sustain. Energy Rev., vol. 81, pp. 552–562, Jan. 2018, DOI: 10.1016/j.rser.2017.08.028.

[8] C. Wieland, C. Schifflechner, K. Braimakis, F. Kaufmann, F. Dawo, S. Kerellas, G. Besagni, and C. N. Markides, "Innovations for organic Rankine cycle power systems: Current trends and future perspectives," Appl. Therm. Eng., vol. 225, p. 120201, May 2023, DOI: 10.1016/j.applthermaleng.2023.120201.

[9] B. S. Park, M. Usman, M. Imran, and A. Pesyridis, "Review of organic Rankine cycle experimental data trends," Energy Convers. Manag., vol. 173, pp. 679–691, Oct. 2018, DOI: 10.1016/j.enconman.2018.07.097.

[10] A. Landelle, N. Tauveron, P. Haberschill, R. Revellin, and S. Colasson, "Organic Rankine cycle design and performance comparison based on experimental database," Appl. Energy, vol. 204, pp. 1172–1187, Oct. 2017, DOI: 10.1016/j.apenergy.2017.04.012.

[11] P. Colonna and H. van Putten, "Dynamic modeling of steam power cycles: Part I—Modeling paradigm and validation," Appl. Therm. Eng., vol. 27, no. 2–3, pp. 467–480, Feb. 2007, DOI: 10.1016/j.applthermaleng.2006.06.011.

[12] H. van Putten and P. Colonna, "Dynamic modeling of steam power cycles: Part II—Simulation of a small simple Rankine cycle system," Appl. Therm. Eng., vol. 27, no. 14–15, pp. 2566–2582, Oct. 2007, DOI: 10.1016/j.applthermaleng.2007.01.035.

[13] S. Quoilin, R. Aumann, A. Grill, A. Schuster, V. Lemort, and H. Spliethoff, "Dynamic modeling and optimal control strategy of waste heat recovery organic Rankine cycles," Appl. Energy, vol. 88, no. 6, pp. 2183–2190, Jun. 2011, DOI: 10.1016/j.apenergy.2011.01.015.

[14] J. Wornski, V. Lemort, S. Quoilin, I. Bell, and A. Desideri, "ThermoCycle: A Modelica library for the simulation of thermodynamic systems," in Proc. 10th Int. Modelica Conf., Lund, Sweden, 2014, pp. 683–692, DOI: 10.3384/ECP14096683.

[15] G. Shu, X. Wang, H. Tian, P. Liu, D. Jing, and X. Li, "Scan of working fluids based on dynamic response characters for organic Rankine cycle using for engine waste heat recovery," Energy, vol. 133, pp. 609–620, Aug. 2017, DOI: 10.1016/j.energy.2017.05.003.

[16] Z. Gu, K. Feng, L. Ge, and L. Quan, "Dynamic modeling and optimization of organic Rankine cycle in the waste heat recovery of the hydraulic system," Energy, vol. 263, p. 125673, Jan. 2023, DOI: 10.1016/j.energy.2022.125673.

[17] T. Wilberforce and I. Muhammad, "Dynamic modeling and analysis of organic Rankine cycle power units for the recovery of waste heat from 110kW proton exchange membrane fuel cell system," Int. J. Thermofluids, vol. 17, p. 100280, Feb. 2023, DOI: 10.1016/j.ijft.2023.100280.

[18] M. R. Kaleibar, R. K. Saray, and M. Pourgol, "Comprehensive assumption-free dynamic simulation of an organic Rankine cycle using moving-boundary method," Energy, vol. 307, p. 132584, Oct. 2024, DOI: 10.1016/j.energy.2024.132584.

[19] J. Peralez, M. Nadri, P. Dufour, P. Tona, and A. Sciarretta, "Organic Rankine cycle for vehicles: Control design and experimental results," IEEE Trans. Control Syst. Technol., vol. 25, no. 3, pp. 952–965, May 2017, DOI: 10.1109/TCST.2016.2574760.

[20] A. Hernandez, F. Ruiz, S. Gusev, R. De Keyser, S. Quoilin, and V. Lemort, "Experimental validation of a multiple model predictive control for waste heat recovery organic Rankine cycle systems," Appl. Therm. Eng., vol. 193, p. 116993, Jul. 2021, DOI: 10.1016/j.applthermaleng.2021.116993.

[21] P. Pallis, E. Varvagiannis, K. Braimakis, T. Roumpedakis, A.-D. Leontaritis, and S. Karellas, "Development, experimental testing and techno-economic assessment of a fully automated marine organic Rankine cycle prototype for jacket cooling water heat recovery," Energy, vol. 228, p. 120596, Jul. 2021, DOI: 10.1016/j.energy.2021.120596.

[22] R. Pili, C. Wieland, H. Spliethoff, and F. Haglind, "Optimal tuning of model predictive controllers for organic Rankine cycle systems recovering waste heat from heavy-duty vehicles," Appl. Therm. Eng., vol. 220, p. 119803, Feb. 2023, DOI: 10.1016/j.applthermaleng.2022.119803.

[23] Y.-Q. Feng, Q. Zhang, K.-J. Xu, C.-M. Wang, Z.-X. He, and T.-C. Hung, "Operation characteristics and performance prediction of a 3 kW organic Rankine cycle (ORC) with automatic control system based on machine learning methodology," Energy, vol. 263, p. 125857, Jan. 2023, DOI: 10.1016/j.energy.2022.125857.

[24] X. Liu, A. Yebi, P. Anschel, J. Shutty, B. Xu, M. Hoffman, and S. Onori, "Model predictive control of an organic Rankine cycle system," in Proc. Int. Conf. Appl. Energy (Energy Proc.), Cape Town, South Africa, 2017, pp. 184–191, DOI: 10.1016/j.egypro.2017.09.109.

[25] H.-X. Wang, B. Lei, and Y.-T. Wu, "Control strategies of pumps in organic Rankine cycle under variable condensing conditions," Appl. Therm. Eng., vol. 234, p. 121226, Nov. 2023, DOI: 10.1016/j.applthermaleng.2023.121226.

[26] B. K. Saha, B. Chakraborty, J. Mondal, A. Pesyridis, E. M. B. Messini, and P. Kumar, "Design and implementation of a control strategy for a dynamic organic Rankine cycle-based power system in the context of industrial waste heat recovery," Energy Technol., vol. 11, no. 11, p. 2300425, Nov. 2023, DOI: 10.1002/ente.202300425.

[27] H. Enayatollahi, P. Fussey, and B. K. Nguyen, "Control of organic Rankine cycle, a neuro-fuzzy approach," Control Eng. Pract., vol. 109, p. 104728, Apr. 2021, DOI: 10.1016/j.conengprac.2021.104728.

[28] X. Wang, R. Wang, M. Jin, G. Shu, H. Tian, and J. Pan, "Control of superheat of organic Rankine cycle under transient heat source based on deep reinforcement learning," Appl. Energy, vol. 278, p. 115637, Nov. 2020, DOI: 10.1016/j.apenergy.2020.115637.

[29] F. Galuppo, T. Reiche, V. Lemort, P. Dufour, and M. Nadri, "Organic Rankine cycle based waste heat recovery modeling and control of the low pressure side using direct condensation and dedicated fans," Energy, vol. 216, p. 119074, Feb. 2021, DOI: 10.1016/j.energy.2020.119074.

[30] M. Marchionni, M. Usman, L. Chai, and S. A. Tassou, "Inventory control assessment for small scale sCO2 heat to power conversion systems," Energy, vol. 267, p. 126537, Mar. 2023, DOI: 10.1016/j.energy.2022.126537.

[31] E. W. Lemmon, I. H. Bell, M. L. Huber, and M. O. McLinden, "NIST standard reference database 23: Reference fluid thermodynamic and transport properties—REFPROP," Nat. Inst. Stand. Technol., Gaithersburg, MD, USA, Rep. 10.0, 2018, DOI: 10.18434/T4/1502528.

[32] B. P. Rasmussen and A. G. Alleyne, "Dynamic modeling and advanced control of air conditioning and refrigeration systems," Univ. Illinois Air Conditioning Refrigeration Center, Urbana, IL, USA, Tech. Rep. ACRC TR-244, 2006. [Online]. Available: https://hdl.handle.net/2142/12355.

[33] Aspen Plus, Aspen Technol. Inc., Bedford, MA, USA, 2013.

[34] S. Qin and T. Badgwell, "A survey of industrial model predictive control technology," Control Eng. Pract., vol. 11, no. 7, pp. 733–761, Jul. 2003, DOI: 10.1016/S0967-0661(02).

[35] M. L. Darby and M. Nikolaou, "MPC: Current practice and challenges," Control Eng. Pract., vol. 20, no. 4, pp. 328–342, Apr. 2012, DOI: 10.1016/j.conengprac.2011.12.004.

[36] D. P. Kingma and L. J. Ba, "Adam: A method for stochastic optimization," in Proc. Int. Conf. Learning Representations (ICLR), San Diego, CA, USA, 2015.

[37] K. E. Gungor and R. H. S. Winterton, "A general correlation for flow boiling in tubes and annuli," Int. J. Heat Mass Transf., vol. 29, no. 3, pp. 351–358, Mar. 1986, DOI: 10.1016/0017-9310(86)90205-X.

[38] M. M. Shah, "A general correlation for heat transfer during film condensation inside pipes," Int. J. Heat Mass Transf., vol. 22, no. 4, pp. 547–556, Apr. 1979, DOI: 10.1016/0017-9310(79)90058-9.

[39] T. L. Bergman, F. P. Incropera, D. P. DeWitt, and A. S. Lavine, Fundamentals of Heat and Mass Transfer. Hoboken, NJ, USA: Wiley, 2011.

[40] H. K. Fauske, "Some ideas about the mechanism causing two-phase critical flow," Appl. Sci. Res., vol. 13, no. 1, pp. 149–160, Dec. 1964, DOI: 10.1007/BF00382043.

[41] J. M. Jensen and H. Tummescheit, "Moving boundary models for dynamic simulations of two-phase flows," in Proc. 2nd Int. Modelica Conf., Oberpfaffenhofen, Germany, 2002, pp. 235–244. [Online]. Available: http://www.modelica.org/events/Conference2002/papers/p31_Jensen.pdf.

[42] X. Wang, G. Shu, H. Tian, P. Liu, X. Li, and D. Jing, "Engine working condition effects on the dynamic response of organic Rankine cycle as exhaust waste heat recovery system," Appl. Therm. Eng., vol. 123, pp. 670–681, Aug. 2017, DOI: 10.1016/j.applthermaleng.2017.05.088.

[43] M. J. Moran, H. N. Shapiro, D. D. Boettner, and M. B. Bailey, Fundamentals of Engineering Thermodynamics. Hoboken, NJ, USA: Wiley, 2018.

[44] J. Bezanson, A. Edelman, S. Karpinski, and V. B. Shah, "Julia: A fresh approach to numerical computing," SIAM Rev., vol. 59, no. 1, pp. 65–98, Feb. 2017, DOI: 10.1137/141000671.

[45] J. Baillieul and T. Samad, Encyclopedia of Systems and Control. Cham, Switzerland: Springer Nature, 2021, DOI: 10.1007/978-3-030-44184-5.

[46] S. V. Rakovic and W. S. Levine, Handbook of Model Predictive Control. Cham, Switzerland: Springer Nature, 2019, DOI: 10.1007/978-3-319-77489-3.

[47] B. Kovaritakis and M. Cannon, Model Predictive Control: Classical, Robust and Stochastic. Cham, Switzerland: Springer Nature, 2016, DOI: 10.1007/978-3-319-24853-0.

[48] S. Skogestad, I. Pstlethwaite, Multivariable Feedback Control: Analysis and Design, West Sussex: England, Wiley & Sons, 2006, ISBN: 978-0-470-00168-3.

[49] S. Y. Dibazar, G. Salehi, and A. Davarpanah, "Comparison of exergy and advanced exergy analysis in three different organic Rankine cycles," Processes, vol. 8, no. 5, p. 586, May 2020, DOI: 10.3390/pr8050586.

[50] A. Bejan, "The equivalence of maximum power and minimum entropy generation rate in the optimization of power plants," J. Energy Resour. Technol., vol. 118, no. 2, pp. 98–101, Jun. 1996, DOI: 10.1115/1.2792711.

Dicle University
Journal of Engineering
https://dergipark.org.tr/tr/pub/dumf
duje.dicle.edu.tr

Research Article

Performance Evaluation of MambaVision in Breast Cancer Detection from Histopathology Images

Hasan Zan[1*]
[1]Mardin Artuklu University, Department of Computer Engineering, hasanzan@artuklu.edu.tr, Orcid No: 0000-0002-8156-016X

ARTICLE INFO

Article history:

Received 5 May 2025
Received in revised form 18 September 2025
Accepted 9 October 2025
Available online 30 December 2025

Keywords:

Breast Cancer, MambaVision, Histopathological Image Classification, Deep Learning

Doi: 10.24012/dumf.1691671

* Corresponding author

ABSTRACT

Accurate and early diagnosis of breast cancer is critical to improving patient outcomes, and histopathological image analysis remains the gold standard for clinical assessment. In this study, we explore the use of MambaVision, a hybrid visual state space and transformer model, for binary classification of breast histopathology images. Four pretrained MambaVision variants—Tiny, Small, Base, and Large—were fine-tuned and evaluated on a benchmark dataset to distinguish between benign and malignant tissue samples. The proposed models were trained using a two-stage learning rate schedule with cross-entropy loss, and performance was assessed using precision, recall, F1-score, and accuracy. Our experiments demonstrate consistently high classification performance across all model scales, with the Large variant achieving the highest accuracy of 99.7% and perfect recall. Confusion matrix analysis further highlights the models' reliability in minimizing false negatives, a critical consideration in clinical applications. When compared to several existing deep learning approaches in the literature, MambaVision outperforms all competing methods, confirming its effectiveness in modeling both fine-grained cellular features and large-scale tissue context. The results suggest that MambaVision offers a scalable and accurate solution for computer-aided breast cancer diagnosis, with strong potential for deployment in digital pathology workflows.

Introduction

Breast cancer remains one of the most common and fatal malignancies affecting women worldwide, contributing significantly to global cancer-related morbidity and mortality [1]. According to recent estimates, it is the most frequently diagnosed cancer among women and a leading cause of cancer deaths [2]. Early and accurate diagnosis is essential for effective treatment planning, timely intervention, and improved patient outcomes [3]. Among various diagnostic tools, histopathological examination of tissue biopsies continues to be the gold standard for breast cancer diagnosis [4]. This process involves microscopic evaluation of stained tissue samples to assess cellular morphology, structural organization, and pathological abnormalities.

Despite its clinical importance, histopathological analysis is inherently subjective and time-consuming. Manual slide interpretation by pathologists is prone to inter-observer variability, especially when distinguishing between morphologically similar tissue patterns [5]. Moreover, the growing adoption of digital pathology has resulted in an explosion of whole-slide image data, making the analysis process even more labor-intensive and error-prone [6]. These challenges highlight the need for reliable, efficient, and automated diagnostic tools.

To address these limitations, computer-aided diagnosis (CAD) systems have emerged as promising solutions for supporting pathologists in image interpretation and decision-making [7, 8]. While classical machine learning (ML) methods laid the groundwork for computational histopathology, they often relied on handcrafted features and rigid pipelines, limiting their generalization capabilities. More recently, deep learning models—particularly convolutional neural networks (CNNs) and vision transformers—have shown strong performance in medical image analysis, but each comes with its own limitations in capturing multiscale patterns and global dependencies efficiently.

Literature Review

Early CAD systems were grounded in classical machine learning (ML) paradigms [9]. These systems usually used a two-step pipeline. Firstly, they extracted handcrafted features from manually chosen or pre-segmented regions of interest, such as textural [10, 11, 12, 13], graph [12, 13], morphological [10, 12, 14, 15], and intensity features [13, 15]. Secondly, they applied traditional classifiers, such as support vector machines [10, 16], k-nearest neighbors [14],

or ensemble-based classification techniques [11, 17]. While these techniques established the feasibility of computational histopathology, their reliance on domain-specific feature engineering severely limited adaptability across different datasets and imaging conditions.

Moreover, classical methods often failed to capture the complex spatial relationships, scale variance, and nonlinear patterns inherent in histopathological images. They were typically brittle to variations in staining protocols, image resolutions, and anatomical structures, resulting in reduced robustness and generalization [18]. As datasets grew larger and more diverse with the advent of digital pathology, it became increasingly clear that these hand-engineered pipelines could not keep pace with the complexities of real-world diagnostic scenarios.

With the advent of deep learning, convolutional neural networks (CNNs) have significantly advanced histopathological image analysis by learning hierarchical feature representations directly from raw image data [19]. Numerous studies have demonstrated the effectiveness of CNNs in capturing localized morphological patterns critical for accurate breast cancer classification. For instance, Musfequa et al. [20] introduced ADBNet, a deep broad convolutional architecture enhanced with attention modules to improve performance across magnifications, while Chen et al. [21] proposed MDFF-Net, which integrates 1D and 2D features with fusion strategies to strengthen multiscale feature extraction. Other CNN-based innovations include lightweight and mobile-friendly designs like BCHI-CovNet by Daniel et al. [22], and hybrid mechanisms such as GLNET by Saif et al. [23], which combine global and local cues for enhanced representation.

Despite their strengths, CNNs primarily focus on local spatial patterns due to the inherently limited receptive field of convolutional layers. As a result, they may struggle to capture long-range dependencies and broader tissue context, which are crucial for interpreting complex histological structures.

To overcome these limitations, vision transformers (ViTs) have recently gained traction in computational pathology. These models use self-attention mechanisms to model global context, enabling more holistic interpretation of tissue samples. For example, Zhu et al. [24] proposed DecT, a transformer model enhanced with stain-specific color space fusion and attention for subtype classification. Similarly, Pratik et al. [25] used an ensemble of deep models within a fuzzy logic framework to harness the complementary strengths of diverse transformers and CNN backbones. However, transformer-based models are computationally demanding due to the quadratic complexity of self-attention, making them less suitable for high-resolution histopathology images, especially in resource-constrained settings.

To overcome these challenges, this study investigates the use of MambaVision, a hybrid vision backbone that integrates convolutional layers, state space modeling, and transformer components. By leveraging both local and global feature modeling capabilities in a computationally efficient design, MambaVision offers a scalable and accurate framework for histopathological image classification.

The main contributions of this study are as follows:

- We propose a MambaVision-based framework for binary classification of breast cancer using histopathological images.
- We fine-tune and evaluate four MambaVision variants—Tiny, Small, Base, and Large—under identical training conditions to analyze the effect of model scale.
- We achieve state-of-the-art classification accuracy, with the Large model reaching 99.7%, outperforming several existing methods in the literature.
- We provide a detailed performance comparison using standard classification metrics and confusion matrix analysis to interpret model behavior.
- We demonstrate that MambaVision offers a balance between accuracy and computational efficiency, making it suitable for both clinical deployment and resource-limited environments.

The remainder of this paper is organized as follows. Methodology section describes the dataset used in the study and presents the methodology, including the Vision Mamba architecture and training setup. Results and Discussion reports experimental results and provides a comparative discussion. The last section concludes the paper and outlines possible future directions.

Methodology

Dataset

In this study, we employ the benchmark Breast Cancer Histopathological Image Classification (BreakHis) dataset [11] to evaluate the performance of our proposed approach. BreakHis is a widely used public dataset designed to support the development and assessment of automated breast cancer diagnosis systems using histopathological images. It consists of 7,909 color microscopic images collected from 82 patients, captured at four magnification levels: 40×, 100×, 200×, and 400×. All images are stored in RGB format with a fixed resolution of 700×460 pixels. Sample images are depicted in Fig. 1.

Each image in the dataset is labeled as either benign or malignant, representing non-cancerous and cancerous breast tissue, respectively. Benign tissues are characterized by well-organized cellular structures and slow growth, whereas malignant tissues exhibit irregular nuclei, disorganized architecture, and uncontrolled proliferation, often invading surrounding tissues. These visual and structural differences form the basis for histopathological diagnosis, but can be subtle and difficult to discern, especially across varying magnification levels.

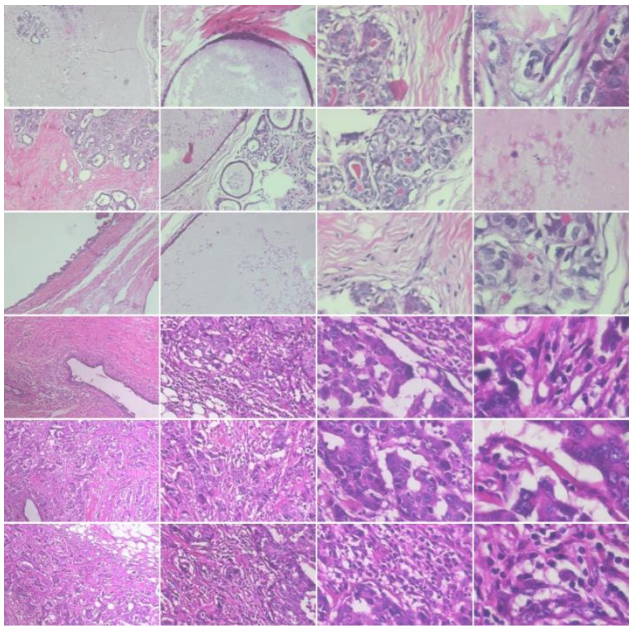

Figure 1. Sample histopathological images from the dataset. Columns represent increasing magnification levels from 40× to 400×. The first three rows show benign samples, while the last three rows show malignant samples.

This section outlines the proposed methodology for breast cancer classification using histopathological images. We begin with an overview of the pipeline, followed by a detailed explanation of the MambaVision architecture. The section also describes the training strategy, evaluation procedures, and experimental settings used to assess model performance.

Method Overview

Our pipeline for histopathological breast cancer classification is illustrated in Fig. 2. The proposed framework leverages MambaVision, a hybrid visual state space and transformer model, fine-tuned for binary classification of breast tissue samples as benign or malignant.

In the first step of the pipeline, input histopathological images are resized to a fixed resolution of 224×224 pixels to match the input size expected by pretrained MambaVision models. These images are then passed through one of four MambaVision variants—Tiny, Small, Base, or Large—each differing in architectural depth, number of parameters, and computational complexity.

The Vision Mamba backbone processes the input in a hierarchical manner. It begins with a stem block, consisting of two convolutional layers, which serves a role similar to patch embedding in vision transformers by projecting the input image into an initial feature space while reducing spatial resolution. Following the stem, the first two stages utilize convolutional blocks to efficiently extract low- and mid-level visual features, capturing local textures and morphological patterns relevant to histopathological structures.

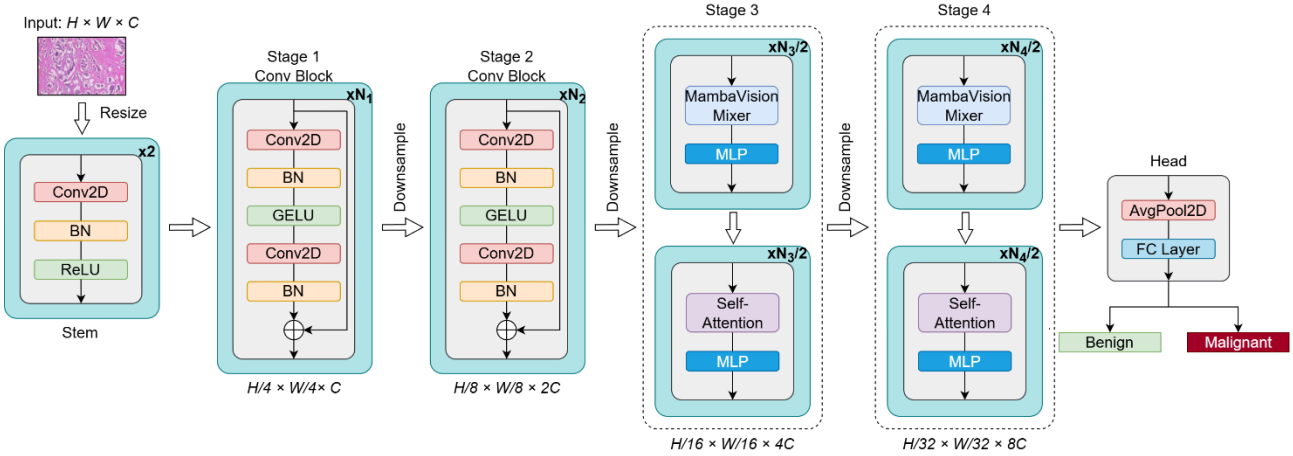

Figure 2. Block diagram of VisionMamba

The final two stages adopt a hybrid design, combining MambaVision mixers with transformer-based self-attention mechanisms, each followed by a multi-layer perceptron (MLP). This configuration enables the model to capture mid-to-long-range dependencies through state space modeling and global contextual information via self-attention. By integrating these components, Vision Mamba effectively learns both fine-grained local details and broader structural patterns critical for accurate histopathological image classification.

Following feature extraction, the output of the backbone is passed through a global average pooling layer and a fully connected classification head, which produces a probability score indicating the likelihood of malignancy.

State Space Models and Mamba

State Space Models (SSMs) offer a mathematical framework for modeling sequential data by defining a hidden state that evolves over time [26]. Traditionally used in control theory and time-series modeling, SSMs describe system dynamics using differential or difference equations. In their continuous-time form, the behavior of the system is governed by

$$\frac{d\mathbf{h}(t)}{dt} = \mathbf{A}\mathbf{h}(t) + \mathbf{B}\mathbf{u}(t)$$
$$\mathbf{y}(t) = \mathbf{C}\mathbf{h}(t) \quad (1)$$

where $\mathbf{h}(t)$ is the hidden state, $\mathbf{u}(t)$ is the input, $\mathbf{y}(t)$ is the output, and $\mathbf{A}$, $\mathbf{B}$, and $\mathbf{C}$ are learnable system matrices. These equations define how the state evolves over time and how the output is generated from both the current state and the input.

In recent years, SSMs have gained renewed attention in machine learning as efficient alternatives to self-attention for sequence modeling, particularly in settings where long-range dependencies are important, but the quadratic complexity of attention mechanisms becomes a computational bottleneck [27].

Mamba is a recent advancement in this direction that introduces a highly efficient and expressive neural SSM architecture [27]. Unlike classical models, Mamba implements selective state updates through input-dependent dynamic gating. This allows the model to control which parts of the sequence to emphasize, improving its capacity to capture important features while maintaining computational efficiency. The continuous-time formulation is discretized and restructured into a convolution-friendly form, enabling parallelization and acceleration on modern hardware.

A key benefit of Mamba is its ability to model long-range dependencies with linear computational complexity relative to sequence length, offering significant speed and memory advantages over attention-based models. This property makes it particularly attractive for processing high-resolution inputs and long sequences, as commonly encountered in computer vision. In the context of histopathological image analysis, Mamba enables efficient and scalable modeling of extended spatial relationships, making it well suited for capturing both fine-grained and global patterns critical to accurate diagnosis.

MambaVision Mixer

To enhance the suitability of Mamba architecture for visual tasks, the MambaVision Mixer was introduced as a redesigned token mixing module [28]. As illustrated in Fig. 3, this component is specifically tailored to image data, where spatial relationships are two-dimensional and inherently bidirectional. Unlike the original Mamba mixer, which employs causal convolutions to enforce directional constraints suited for sequence modeling, MambaVision replaces these with regular convolutions. This change removes unnecessary limitations in spatial processing and allows for a more natural flow of contextual information across image regions.

In addition to modifying the convolutional structure, MambaVision includes a symmetric parallel branch that does not rely on state space modeling. This branch comprises a convolutional layer followed by a non-linear activation and is designed to compensate for any representational loss that may occur due to the sequential nature of the SSM path. Both branches operate in parallel on the same input, and their outputs are concatenated and projected back into the original embedding space using a linear transformation. To preserve computational efficiency, each branch works with a reduced embedding dimension, ensuring the total parameter count remains comparable to that of the original design.

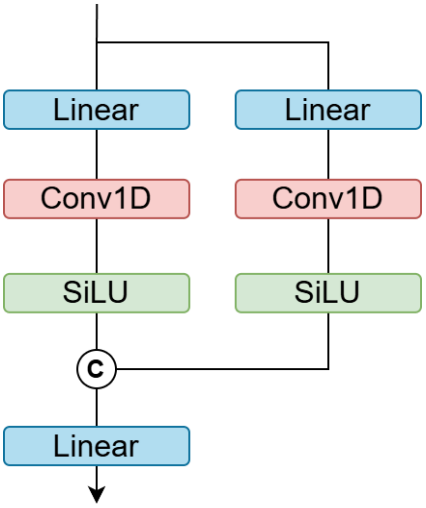

Figure 3. Architecture of MambaVision mixer

This dual-path structure enables the mixer to combine the strengths of both sequential and spatial modeling. The state space path provides efficient long-range dependency modeling, while the symmetric convolutional path reinforces local spatial sensitivity. As a result, the MambaVision Mixer produces richer and more expressive feature representations, which contribute to improved generalization and classification performance in visual domains. This is especially important in histopathological image analysis, where both fine-grained local structures and broader tissue-level context are critical for accurate diagnosis.

Model Variations

To analyze the impact of model capacity on histopathological image classification performance, we experiment with four variants of the MambaVision architecture: **Tiny**, **Small**, **Base**, and **Large**. All variants share the same core design but differ in their embedding dimensions and internal widths, resulting in varying levels of representational power and computational complexity.

Each model operates on input images resized to 224×224 pixels. The embedding dimension increases progressively from Tiny to Large, leading to a corresponding increase in the number of parameters and floating-point operations (FLOPs). The number of parameters grows from approximately 32 million in the Tiny variant to nearly 228 million in the Large variant, while FLOPs scale from 4.4 to 34.9 billion per forward pass. This range allows us to examine the trade-offs between efficiency and accuracy, and to identify models that best balance computational cost with classification performance in medical imaging contexts.

Table 1. Model variations

Variation	Input Size	Embedding Dim	Parameters (M)	FLOPs (G)
Tiny	224	80	31.8	4.4
Small	224	96	50.1	7.5
Base	224	128	97.7	15.0
Large	224	196	227.9	34.9

Model Training

All MambaVision model variants were trained on the training portion of the dataset as defined by the 80:10:10 split. Model optimization was carried out using the Adam optimizer, which has been widely adopted for its adaptive learning capabilities and stable convergence behavior. To balance learning dynamics across different parts of the network, a two-tiered learning rate strategy was employed: the classification head was trained with a learning rate of 10^{-3}, while the remaining layers of the pretrained backbone were fine-tuned using a lower learning rate of 5×10^{-5}. This differential learning rate scheme encourages rapid adaptation of the final classification layer while preserving the general-purpose visual features learned during pretraining. These hyperparameters were selected based on common practice in transfer learning for image classification and were not extensively tuned, as our primary goal was to compare performance across model scales under a uniform training setting.

The models were trained using the cross-entropy loss function, appropriate for binary classification tasks. To prevent overfitting, early stopping was applied based on validation accuracy, with a patience of 30 epochs. This allowed the training process to terminate if no improvement was observed for a sustained period, ensuring efficient use of computational resources.

To improve generalization and robustness, we applied data augmentation during training in the form of random resized cropping. This technique randomly selects a region of the input image, resizes it to the target size (224×224), and feeds it to the network. Specifically, we used the parameter values $\text{scale} = (0.08, 1.0)$ and $\text{ratio} = (0.75, 1.33)$. The scale parameter determines the area of the crop relative to the original image, ranging from 8% to 100%, introducing variation in how much of the image is retained. The ratio parameter controls the aspect ratio of the crop, allowing it to vary between 3:4 and 4:3. Together, these settings encourage the model to learn representations that are invariant to spatial location, zoom level, and aspect ratio distortions.

Fig. 4 shows multiple augmented versions of a single image produced through this process. As depicted, the augmented samples preserve essential tissue characteristics while varying spatial composition and focus. This augmentation strategy proved effective in reducing overfitting and improving the model's robustness to scale and orientation changes in histopathological images. All experiments were conducted using Python 3.12 and PyTorch 2.4, ensuring compatibility with modern deep learning libraries and hardware accelerators [29].

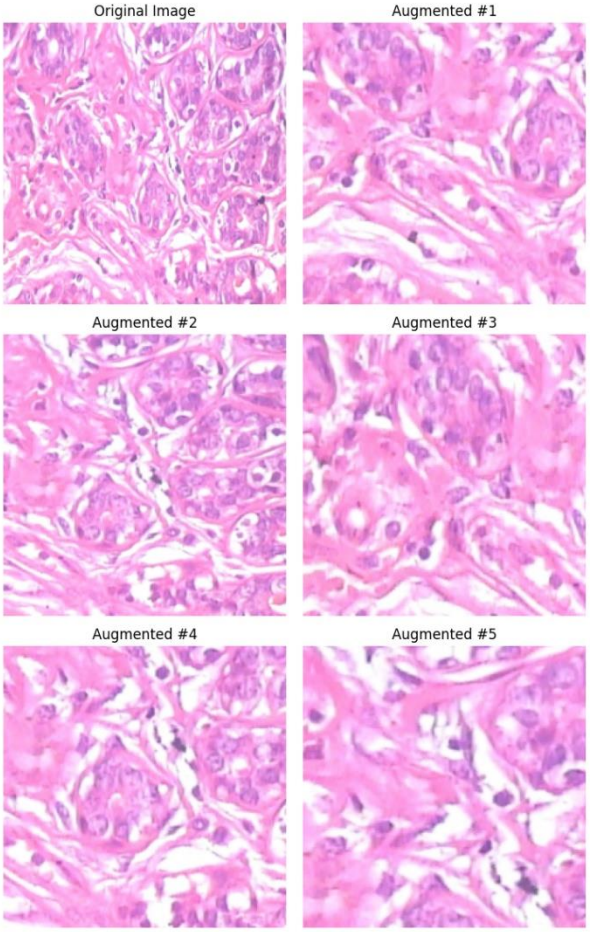

Figure 4. Image augmentation

Model Evaluation

The performance of the MambaVision models was evaluated using standard classification metrics computed on the test set. Specifically, we report accuracy, precision, recall, and F1-score, which provide complementary perspectives on the model's ability to distinguish between benign and malignant tissue samples. These metrics were derived from the counts of true positives (TP), false positives (FP), true negatives (TN), and false negatives (FN), and are defined as follows:

$$\text{Precision (PR)} = \frac{TP}{TP + FP} \tag{2}$$

$$\text{Recall (RE)} = \frac{TP}{TP + FN} \tag{3}$$

$$\text{F1-score (F1)} = \frac{2 \times \text{PR} \times \text{RE}}{\text{PR} + \text{RE}} \tag{4}$$

$$\text{Accuracy (ACC)} = \frac{TP + TN}{TP + TN + FP + FN} \tag{5}$$

Precision quantifies the proportion of correctly predicted malignant cases among all cases predicted as malignant. Recall measures the proportion of actual malignant cases that were correctly identified. The F1-score provides a harmonic mean of precision and recall, offering a single measure that balances both. Accuracy reflects the overall proportion of correctly classified samples.

Results and Discussion

This section summarizes and analyzes the performance of the proposed MambaVision-based models in classifying breast histopathology images as benign or malignant. We evaluate four model variants—Tiny, Small, Base, and Large—based on precision, recall, F1-score, and accuracy. Quantitative results are presented in Table 2, while the confusion matrices for each variant are shown in Figure 4, providing a detailed view of prediction behavior in terms of correctly and incorrectly classified samples.

Table 2. Performance results of model variations

Model	PR	RE	F1	ACC
Tiny	0.994	0.994	0.994	0.992
Small	0.991	0.994	0.993	0.990
Base	0.993	0.998	0.995	0.994
Large	0.996	1.000	0.998	0.997

As summarized in Table 2, all four MambaVision variants demonstrate strong classification performance. The Tiny model achieved a precision of 0.994, recall of 0.994, F1-score of 0.994, and accuracy of 0.992. The Small model slightly underperformed relative to Tiny in precision (0.991) but matched it in recall (0.994), resulting in an F1-score of 0.993 and accuracy of 0.990. The Base variant showed marked improvement, attaining a precision of 0.993, recall of 0.998, and F1-score of 0.995, with an overall accuracy of 0.994. The Large model achieved the best results across all metrics, reaching a precision of 0.996, perfect recall of 1.000, F1-score of 0.998, and accuracy of 0.997. These results indicate a consistent trend: as model complexity increases, so does classification performance, particularly in sensitivity to malignant cases.

To further understand the models' behavior, Fig. 5 presents the confusion matrices for each variant. A confusion matrix is a two-dimensional table that compares the model's predictions against the true class labels. Each matrix contains four values: true positives (bottom-right), true negatives (top-left), false positives (top-right), and false negatives (bottom-left). In addition to raw counts, each cell also shows the corresponding percentage of total predictions for that class. The color shading visually encodes the magnitude of each value, with darker shades indicating higher counts and lighter shades corresponding to fewer samples.

In Fig. 5a, the Tiny model correctly classified 245 out of 248 benign samples and 540 out of 543 malignant samples, resulting in a benign accuracy of 98.8% and malignant accuracy of 99.4%. The Small model, shown in Fig. 5b, had slightly reduced benign precision, correctly identifying 243 benign cases, with a few more false positives. The Base model's confusion matrix (Fig. 5c) shows only one misclassified malignant sample and a slight reduction in benign accuracy. Finally, the Large model (Fig. 5d) achieved perfect classification of all malignant samples and misclassified only two benign instances, reflecting 100% recall and 99.2% precision for the malignant class.

These confusion matrices reinforce the numerical trends observed in Table 2. All models exhibit strong sensitivity to malignant cases, with false negatives kept to a minimum. The Large variant stands out for its perfect recall, which is particularly valuable in medical diagnosis, where failing to identify malignancy can have serious consequences. On the other hand, the Tiny and Small variants offer competitive performance at significantly lower computational cost, making them suitable for deployment in real-time or resource-constrained environments.

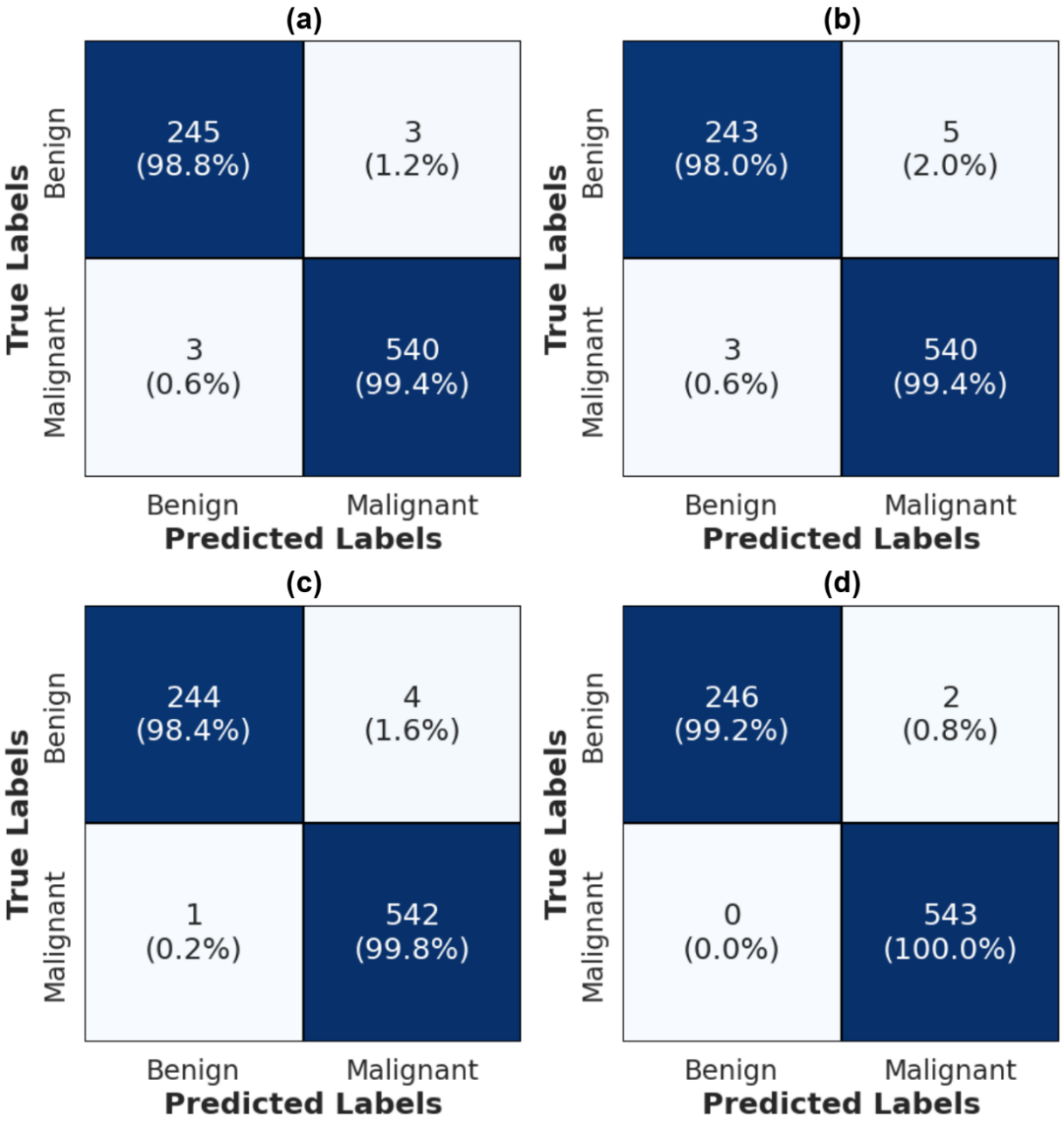

Figure 5. Confusion matrices for (a) Tiny, (b) Small, (c) Base, and (d) Large model

Table 3 lists the performance comparison of the proposed MambaVision models against several existing approaches for histopathological breast cancer classification. The listed methods include CNN-based architectures, hybrid CNN-transformer designs, attention mechanisms, and graph-based networks. Reported accuracies vary, with Li et al. [30] and Khan et al. [23] achieving 0.906 and 0.923, respectively, while other approaches such as Abdulwahhab et al. [31], Xu et al. [21], and Patel et al. [32] report accuracies closer to or equal to 0.989–0.995.

The Tiny variant of MambaVision achieves an accuracy of 0.992, outperforming most listed methods while maintaining a lightweight and efficient architecture. The Large variant reaches an accuracy of 0.997, the highest among all compared methods. These results demonstrate the effectiveness of MambaVision's hybrid architecture, which combines state space modeling and transformer-style attention to learn both local and global features in histopathological images. The consistent performance across scales highlights its adaptability and suitability for medical image classification tasks.

Table 3. Performance comparison of MambaVision with other studies

Study	Method	Precision	Recall	F1-score	Accuracy
Li et al. [30]	Two-branch model based on Swin transformer and ConvNeXt	0.908	0.873	0.887	0.906
Khan et al. [23]	ResNet101 with global-local convolution	-	-	-	0.923
Abdulwahhab et al. [31]	Multi-level attention-based bottleneck model	0.980	0.985	0.985	0.989
Fiaz et al. [33]	Hybrid model based on transformers and CNNs	0.970	0.969	0.977	0.953
Maurya et al. [34]	Multi-level CNN with attention	**1.000**	0.993	0.996	0.995
Xu et al. [21]	CNN with multidimensional feature fusion	0.993	0.991	0.992	0.989
Patel et al. [32]	Graph-based DenseNet121	0.990	0.994	0.992	0.995
Sreelekshmi et al. [35]	Hybrid model based on Swin transformer and CNN	0.977	0.981	0.981	0.981
Liu et al. [36]	Collaborative transfer network	0.983	0.983	0.982	0.983
This study	Tiny MambaVision	0.994	0.994	0.994	0.992
This study	Large MambaVision	0.996	**1.000**	**0.998**	**0.997**

Conclusion

In this study, we investigated the effectiveness of MambaVision, a hybrid visual state space and transformer model, for breast cancer classification using histopathological images. Four pretrained MambaVision variants—Tiny, Small, Base, and Large—were fine-tuned and evaluated on a binary classification task to distinguish between benign and malignant tissue. The results demonstrate that all model variants achieved high accuracy, precision, recall, and F1-scores, with the Large model achieving the highest performance at 99.7% accuracy and 100% recall.

Through comprehensive evaluation, we showed that MambaVision is capable of learning both fine-grained morphological details and global contextual patterns critical for reliable histopathological analysis. The architecture's ability to scale in both performance and computational complexity makes it suitable for a range of clinical and deployment scenarios, from lightweight edge devices to high-performance diagnostic systems.

When compared to existing state-of-the-art methods, MambaVision outperformed most models in terms of classification accuracy, confirming its potential as a strong backbone for digital pathology applications. Future work may explore multi-class classification, whole-slide image processing, and domain adaptation techniques to further expand its clinical utility.

References

[1] D. Trapani, O. Ginsburg, T. Fadelu, N. U. Lin, M. Hassett, A. M. Ilbawi, B. O. Anderson and G. Curigliano, "Global challenges and policy solutions in breast cancer control," *Cancer Treatment Reviews,* vol. 104, p. 102339, 2022.

[2] L. Wilkinson and T. Gathani, "Understanding breast cancer as a global health concern," *The British Journal of Radiology,* vol. 95, no. 1130, 2022.

[3] L. Wang, "Early Diagnosis of Breast Cancer," *Sensors,* vol. 17, no. 7, p. 1572, 2017.

[4] F. A. Zeiser, C. A. da Costa, A. V. Roehe, R. d. R. Righi and N. M. C. Marques, "Breast cancer intelligent analysis of histopathological data: A systematic review," *Applied Soft Computing,* vol. 113, p. 107886, 2021.

[5] T. T. Brunyé, E. Mercan, D. L. Weaver and J. G. Elmore, "Accuracy is in the eyes of the pathologist: The visual interpretive process and diagnostic accuracy with digital whole slide images," *Journal of Biomedical Informatics,* vol. 66, pp. 171-179, 2017.

[6] S. Nam, Y. Chong, C. K. Jung, T.-Y. Kwak, J. Y. Lee, J. Park, M. J. Rho and H. Go, "Introduction to digital pathology and computer-aided pathology," *Journal of Pathology and Translational Medicine,* vol. 54, no. 2, pp. 125-134, 2020.

[7] D. Komura and S. Ishikawa, "Machine Learning Methods for Histopathological Image Analysis," *Computational and Structural Biotechnology Journal,* vol. 16, pp. 34-42, 2018.

[8] A. Jalalian, S. Mashohor, R. Mahmud, B. Karasfi, M. Saripan and A. Ramli, "Foundation and methodologies in computer-aided diagnosis systems for breast cancer detection," *EXCLI Journal,* vol. 16, pp. 113-137, 2017.

[9] C. Kaushal, S. Bhat, D. Koundal and A. Singla, "Recent Trends in Computer Assisted Diagnosis (CAD) System for Breast Cancer Diagnosis Using Histopathological Images," *IRBM,* vol. 40, no. 4, pp. 211-227, 2019.

[10] P. Wang, X. Hu, Y. Li, Q. Liu and X. Zhu, "Automatic cell nuclei segmentation and classification of breast cancer histopathology images," *Signal Processing,* vol. 122, pp. 1-13, 2016.

[11] F. A. Spanhol, L. S. Oliveira, C. Petitjean and L. Heutte, "A Dataset for Breast Cancer Histopathological Image Classification," *IEEE Transactions on Biomedical Engineering,* vol. 63, no. 7, pp. 1455-1462, 2016.

[12] B. Ehteshami Bejnordi, J. Lin, B. Glass, M. Mullooly, G. L. Gierach, M. E. Sherman, N. Karssemeijer, J. van der Laak and A. H. Beck, "Deep learning-based assessment of tumor-associated stroma for diagnosing breast cancer in histopathology images," in *2017 IEEE 14th International Symposium on Biomedical Imaging (ISBI 2017)*, Melbourne, VIC, Australia, 2017.

[13] A. A. Cruz-Roa, J. E. Arevalo Ovalle, A. Madabhushi and F. A. González Osorio, "A Deep Learning Architecture for Image Representation, Visual Interpretability and Automat," in *Medical Image Computing and Computer-Assisted Intervention–MICCAI 2013: 16th International Conference*, Nagoya, Japan, 2013.

[14] R. Kumar, R. Srivastava and S. Srivastava, "Detection and Classification of Cancer from Microscopic Biopsy Images Using Clinically Significant and Biologically Interpretable Features," *Journal of Medical Engineering,* vol. 2015, no. 1, pp. 1-14, 2015.

[15] C. Sommer, L. Fiaschi, F. A. Hamprecht and D. W. Gerlich, "Learning-based mitotic cell detection in histopathological images," in *Proceedings of the 21st International Conference on Pattern Recognition (ICPR2012)*, Tsukuba, Japan, 2012.

[16] S. Issac Niwas, P. Palanisamy, R. Chibbar and W. J. Zhang, "An Expert Support System for Breast Cancer Diagnosis using Color Wavelet Features," *Journal of Medical Systems,* vol. 36, no. 5, pp. 3091-3102, 2012.

[17] A. Basavanhally, S. Ganesan, M. Feldman, N. Shih, C. Mies, J. Tomaszewski and A. Madabhushi, "Multi-Field-of-View Framework for Distinguishing Tumor Grade in ER+ Breast Cancer From Entire Histopathology Slides," *IEEE Transactions on Biomedical Engineering,* vol. 60, no. 8, pp. 2089-2099, 2013.

[18] M. Cooper, Z. Ji and R. G. Krishnan, "Machine learning in computational histopathology: Challenges and opportunities," *Genes, Chromosomes and Cancer,* vol. 62, no. 9, pp. 540-556, 2023.

[19] M. Yusoff, T. Haryanto, H. Suhartanto, W. A. Mustafa, J. M. Zain and K. Kusmardi, "Accuracy Analysis of Deep Learning Methods in Breast Cancer Classification: A Structured Review," *Diagnostics,* vol. 13, no. 4, p. 683, 2023.

[20] M. Rahman, K. Deb, P. K. Dhar and a. T. Shimamura, "ADBNet: An Attention-Guided Deep Broad Convolutional Neural Network for the Classification of Breast Cancer Histopathology Images," *IEEE Access,* vol. 12, pp. 133784-133809, 2024.

[21] C. Xu, K. Yi, N. Jiang, X. Li, M. Zhong and Y. Zhang, "MDFF-Net: A multi-dimensional feature fusion network for breast histopathology image classification," *Computers in Biology and Medicine,* vol. 165, p. 107385, 2023.

[22] D. Addo, S. Zhou, K. Sarpong, O. T. Nartey, M. A. Abdullah, C. C. Ukwuoma and M. A. Al-antari, "A hybrid lightweight breast cancer classification framework using the histopathological images," *Biocybernetics and Biomedical Engineering,* vol. 44, no. 1, pp. 31-54, 2024.

[23] S. U. R. Khan, M. Zhao, S. Asif, X. Chen and Y. Zhu, "GLNET: global–local CNN's-based informed model for detection of breast cancer categories from histopathological slides," *The Journal of Supercomputing,* vol. 80, no. 6, pp. 7316-7348, 2024.

[24] Z. He, M. Lin, Z. Xu, Z. Yao, H. Chen, A. Alhudhaif and F. Alenezi, "Deconv-transformer (DecT): A histopathological image classification model for breast cancer based on color deconvolution and transformer architecture," *Information Sciences,* vol. 608, pp. 1093-1112, 2022.

[25] P. Bhowal, S. Sen, J. D. Velasquez and R. Sarkar, "Fuzzy ensemble of deep learning models using choquet fuzzy integral, coalition game and information theory for breast cancer histology classification," *Expert Systems with Applications,* vol. 190, p. 116167, 2022.

[26] A. Gu, K. Goel and C. Ré, "Efficiently Modeling Long Sequences with Structured State Spaces," *arXiv preprint arXiv:2111.00396,* 2021.

[27] A. Gu and T. Dao, "Mamba: Linear-Time Sequence Modeling with Selective State Spaces," *arXiv preprint arXiv:2312.00752,* 2023.

[28] A. Hatamizadeh and J. Kautz, "MambaVision: A Hybrid Mamba-Transformer Vision Backbone," *arXiv preprint arXiv:2407.08083,* 2024.

[29] A. Paszke, S. Gross, F. Massa, A. Lerer, J. Bradbury, G. Chanan, T. Killeen, Z. Lin, N. Gimelshein, L. Antiga, A. Desmaison, A. Köpf, E. Yang, Z. DeVito, M. Raison, A. Tejani, S. Chilamkurthy, B. Steiner, L. Fang, J. Bai and S. Chintala, "PyTorch: an imperative style, high-performance deep learning library," in *NIPS'19: 33rd International Conference on Neural Information Processing Systems*, Vancouver, BC, Canada, 2019.

[30] J. Li, K. Wang and X. Jiang, "Robust Multi-Subtype Identification of Breast Cancer Pathological Images Based on a Dual-Branch Frequency Domain Fusion Network," *Sensors,* vol. 25, no. 1, p. 240, 2025.

[31] A. H. Abdulwahhab, O. Bayat and A. A. Ibrahim, "HAFMAB-Net: hierarchical adaptive fusion based on multilevel attention-enhanced bottleneck neural network for breast histopathological cancer classification," *Signal, Image and Video Processing,* vol. 19, no. 5, p. 410, 2025.

[32] V. Patel, V. Chaurasia, R. Mahadeva and S. P. Patole, "GARL-Net: Graph Based Adaptive Regularized Learning Deep Network for Breast Cancer Classification," *IEEE Access,* vol. 11, pp. 9095-9112, 2023.

[33] A. Fiaz, B. Raza, M. Faheem and A. Raza, "A deep fusion-based vision transformer for breast cancer classification," *Healthcare Technology Letters,* vol. 11, no. 6, pp. 471-484, 2024.

[34] R. Maurya, N. N. Pandey, M. K. Dutta and M. Karnati, "FCCS-Net: Breast cancer classification using Multi-Level fully Convolutional-Channel and spatial attention-based transfer learning approach," *Biomedical Signal Processing and Control,* vol. 94, p. 106258, 2024.

[35] V. Sreelekshmi, K. Pavithran and J. J. Nair, "SwinCNN: An Integrated Swin Transformer and CNN for Improved Breast Cancer Grade Classification," *IEEE Access,* vol. 12, pp. 68697-68710, 2024.

[36] L. Liu, Y. Wang, P. Zhang, H. Qiao, T. Sun, H. Zhang, X. Xu and H. Shang, "Collaborative Transfer Network for Multi-Classification of Breast Cancer Histopathological Images," *IEEE Journal of Biomedical and Health Informatics,* vol. 28, no. 1, pp. 110-121, 2024.

Dicle University
Journal of Engineering
https://dergipark.org.tr/tr/pub/dumf
duje.dicle.edu.tr

Research Article

Design of Sodium-Ion Battery Packs in Electric Heavy-Duty Vehicles: A Case Study for Garbage Truck

Burak FINDIK[1], Koray ERHAN[2*]

[1] Marmara University, Mechatronics Engineering Department, burak.findik34@gmail.com, Orcid No: 0000-0001-9804-3540
[2] Marmara University, Mechatronics Engineering Department, koray.erhan@marmara.edu.tr, Orcid No: 0000-0003-0505-9389

ARTICLE INFO

Article history:

Received 20 June 2025
Received in revised form 16 October 2025
Accepted 30 October 2025
Available online 30 December 2025

Keywords:

Sodium-ion battery, modular battery pack design, electric heavy-duty vehicle, electric garbage truck, energy storage

Doi: 10.24012/dumf.1719248

* Corresponding author

ABSTRACT

The transition from internal combustion engine vehicles to electric alternatives has become essential to reduce carbon emissions, improve air quality, and mitigate noise pollution, particularly in urban environments. Heavy-duty vehicles, and especially garbage trucks, exhibit highly inefficient operation under low-speed driving cycles, making electrification an urgent requirement. In this context, sodium-ion batteries are investigated as an alternative to lithium-ion batteries for electric heavy-duty vehicle applications. Owing to their advantages in terms of cost, resource availability, environmental sustainability, safety, and thermal stability, sodium-ion batteries have gained growing attention in recent years. This study focuses on the design and performance evaluation of modular sodium-ion battery packs for an electric garbage truck operating at an 800 V voltage level. Within the scope of the research, battery pack configurations were analyzed with respect to energy and power requirements, module topology, equivalent resistance, and system efficiency. The proposed design framework demonstrates the technical feasibility of integrating sodium-ion batteries into heavy-duty electric vehicles and provides a comparative perspective on their potential to complement or replace lithium-ion chemistry in future transportation systems.

Introduction

Internal combustion engine vehicles powered by fossil fuels are planned to be gradually phased out. In this context, the sale of new fossil fuel vehicles and the use of existing ones are to be increasingly restricted. The phase-out process is expected to be accelerated through higher taxation on fossil fuel vehicles and incentives for electric vehicles [1]. Restrictions and bans on the operation of internal combustion engine vehicles, particularly in urban areas, are becoming increasingly widespread worldwide. Access of such vehicles to densely populated city centers is already being prohibited in several regions. The primary drivers of this transition are the objectives of improving urban air quality and reducing carbon emissions. Currently, more than 30 cities worldwide have already implemented bans on internal combustion vehicles. Specific details and conditions regarding these restrictions are presented in Table 1 [1].

Comparison of sodium-ion and lithium-ion batteries

Lithium is a mineral with limited global reserves, and its trade is controlled by a small number of countries. In contrast, sodium is abundantly available worldwide and poses no supply constraints, making it a more reliable raw material for battery manufacturers. Moreover, the unit cost of lithium is significantly higher than that of sodium, and lithium-based battery chemistries contain environmentally harmful components such as nickel and cobalt. Considering these factors, major battery manufacturers predict a substantial increase in the use of sodium-ion batteries in the future. At present, the major drawback of sodium-ion batteries is their specific energy, which is approximately 20%–40% lower than that of lithium-ion batteries [11–14]. However, this gap is expected to narrow with ongoing advancements. Furthermore, studies indicate that sodium-ion batteries are inherently safer than lithium-ion batteries, particularly in terms of storage and transportation. Since sodium-ion batteries can be shipped in a nearly fully discharged state, the fire risk is minimized, thereby reducing transportation costs due to the absence of additional safety requirements. By contrast, lithium-ion batteries must be transported in a partially charged state to avoid electrode dissolution, which elevates the associated safety risks. In addition, the electrolytes used in sodium-ion batteries have a higher flash point, which further reduces the risk of fire. Sodium-ion batteries also demonstrate superior thermal stability compared to lithium-ion batteries, being less flammable and less susceptible to explosion.

Table 1. Cities with bans and restrictions on internal combustion engine vehicles.

City	Year	Covering	Detail
Aachen [2]	2019	Diesel	Old diesel vehicles
Amsterdam [3]	2030	Diesel, Gasoline	All ICE vehicles
Athens [4]	2025	Diesel	All ICE vehicles
Berlin [2]	2019	Diesel	Euro I–V diesel vehicles
Brussels [5,6]	2030-2035	Diesel, Gasoline	All diesel vehicles (2030), all ICE vehicles (2035)
Connecticut	2035	Diesel, Gasoline	All ICE vehicles
Eindhoven	2030	Diesel, Gasoline	All ICE vehicles
Hawaii	2035	Diesel, Gasoline	New ICE vehicles
California [7,8]	2035	Diesel, Gasoline	All ICE vehicles
New York [9]	2040	Diesel, Gasoline	All ICE vehicles
Paris [4]	2025	Diesel	All ICE vehicles
Rome [10]	2024	Diesel	All ICE vehicle historic areas
Washington	2030	Diesel, Gasoline	All ICE vehicles

Continuous advancements are being made in thermal management systems; nevertheless, lithium-ion batteries remain more flammable and prone to thermal runaway events [15]. Figure 1 presents a comparison of gravimetric energy density, cycle life, specific power, energy efficiency, and production cost parameters [16].

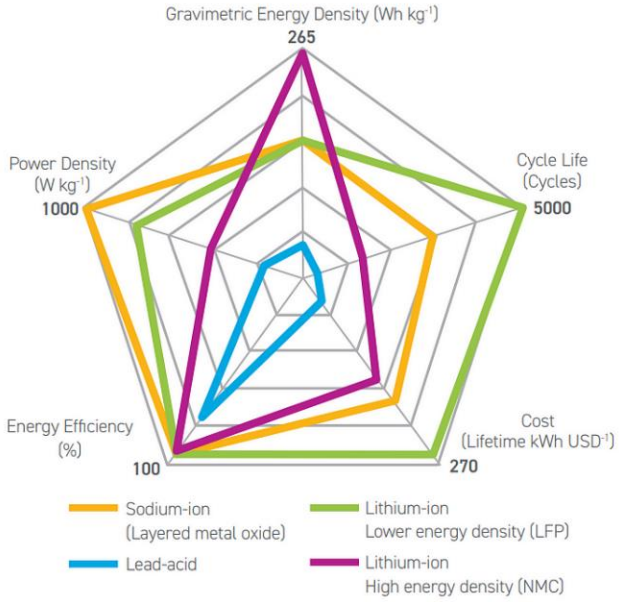

Figure 1. Comparison of sodium-ion, LFP, NMC, and lead-acid batteries [16].

The natural abundance of sodium (Na) the fifth most abundant element, constituting approximately 3% of the Earth's mass is significantly greater than that of lithium (Li), highlighting its potential importance in large-scale battery production. The concentration of sodium in the Earth's crust is about 1,180 times higher than lithium, and in seawater, it is nearly 60,000 times higher. Nevertheless, current sodium-ion batteries face fundamental challenges, including low power density, limited energy storage capacity, and long charging times. These limitations necessitate the development of next-generation materials capable of enabling more efficient energy storage solutions. Recently, KAIST announced the development of a hybrid sodium-ion battery achieving an energy density of 247 Wh/kg and a power density of 34.7 W/kg, with the additional advantage of rapid charging capability [17]. Furthermore, CATL, one of the world's largest lithium battery manufacturers, has introduced a sodium-ion cell ready for mass production, which is expected to be deployed in electric vehicles by 2025. The specific energy of this cell is reported as 160 Wh/kg [18]. The corresponding data are presented in Figure 2.

Figure 2. Technical specifications of the sodium-ion battery developed by CATL [18].

Some technical data comparing sodium-ion and lithium-ion batteries are presented in Table 2 [19–21]. At present, sodium-ion batteries are more cost-effective than lithium-ion batteries; however, they lag behind in terms of specific

energy [22]. Research indicates that the unit cost of sodium-ion batteries will further decrease as production volumes increase. Another advantage of sodium-ion batteries lies in the flexibility available to manufacturers in sourcing raw materials. Lithium ore is extracted and processed by only a limited number of countries, creating supply-chain dependencies that many nations prefer to avoid. By contrast, sodium is abundant and widely accessible, providing a more favorable supply outlook. While the raw material cost of sodium is approximately $290/ton, the corresponding cost of lithium is around $35,000/ton [23, 24].

Table 2. Technical specifications of sodium-ion and lithium-ion batteries [18-21].

	Na-ion	Li-ion
Production cost (kWh)	40-77 $	100-140 $
Volumetric energy density	250–375 Wh/l	200–683 Wh/l
Specific energy	75–247 Wh/kg	120–350 Wh/kg
Specific power	1000 W/kg	340–420 W/kg (NMC) 175–425 W/kg (LFP)
Cycle-life	2000–6000	Up to 4500 cycles
Safety	High	Low (NMC, NCA), High (LFP)
Availability	Rife	Rare
Cycle efficiency	92%	85%-95%
Working temperature	−20 °C / 60 °C	-10 °C / 50 °C

Battery packs used in electric vehicles vary across models, typically consisting of several hundred to as many as 8,000–9,000 cells. To ensure reliable operation of such a large number of cells over many years, a Battery Management System (BMS) is essential. Lithium-based batteries are highly sensitive to extreme temperatures, power demand, current density, and aging. In contrast, sodium-ion batteries demonstrate greater resilience across all these parameters and are characterized by a structure that is easier to operate [25]. Recent studies indicate that sodium-ion cells exhibit energy density values comparable to those of lithium iron phosphate (LFP) chemistry. This suggests that sodium-ion batteries can be applied in all automotive applications currently employing LFP technology [26,27]. In terms of cycle life, sodium-ion and LFP batteries also provide similar performance, with both chemistries achieving between 2,500 and 6,500 cycles [28,29].

The extraction of sodium is less harmful to the environment compared to lithium. Lithium is significantly more toxic, whereas sodium recycling is relatively simpler. In contrast, lithium extraction generates severe environmental concerns, including the contamination of water resources and ecosystem degradation [30]. The chemical properties of sodium and lithium metals are summarized in Table 3.

Although lithium-ion batteries have dominated the electric vehicle market in recent years due to their high energy density and well-established infrastructure, sodium-ion batteries have emerged as a promising alternative, particularly with regard to cost-effectiveness and sustainability.

Table 3. Chemical properties of sodium and lithium metals [31].

Comparison Parameter	Li	Na
Atomic mass	6.94	22.99
Density (kg m^{-3})	534	968
Gravimetric capacity (mAh/g)	3829	1165
Volumetric capacity ($mAhcm^{-3}$)	2062	1131
Abundance on Earth (%)	0.002	2.358

Electric heavy vehicles and driving cycle

In response to industry demands, many automotive manufacturers are now producing electric heavy-duty vehicles, including commercial trucks, construction equipment, and agricultural machinery. Given their inherently high energy consumption, electrification is particularly critical for this vehicle segment. The case study in this research focuses on a garbage truck, which typically operates under an urban driving cycle. Previous studies indicate that electric garbage trucks operate at an average speed of less than 3 km/h for approximately 65% of their duty cycle. Such low-speed operation places conventional diesel garbage trucks within an extremely inefficient performance range. Figure 3 presents a cost comparison of energy consumption between diesel and electric garbage trucks operating under the urban driving cycle. The results demonstrate that the internal combustion engine (ICE) truck consumes approximately 3.5 times more energy than its electric counterpart [32].

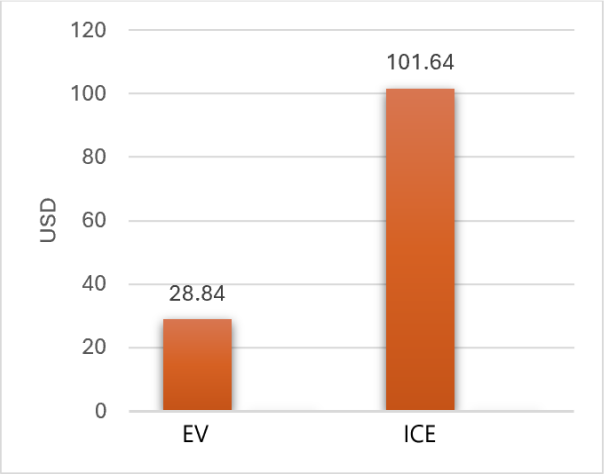

Figure 3. Comparison of fuel consumption costs of BEV and ICE vehicles per 100 km [32].

Within the scope of this study, prior to the design of the battery pack, the battery capacities, voltage levels, pack sizes, and on-board pack placements of heavy-duty vehicles currently in mass production were thoroughly analyzed. Furthermore, the calculation of energy consumption values, considering the driving cycle of a garbage truck, was conducted to accurately determine the required battery capacity. The technical specifications of the analyzed electric trucks are presented in Table 4.

Table 4. Technical specifications of battery packs in mass-produced electric heavy-duty vehicles from different brands [33].

Brand	Model	Battery Pack (Modular- expandable)	Battery Capacity (kWh)	Engine Power (kW)
Mercedes-Benz	eEconic	3	336	330
Volvo	FE Electric	3-4	280-375	225
Scania	EM C1-2	-	416	240
Renault	D Wide	-	200	260
DAF	XD Electric	3-5	315-525	270

Heavy-duty vehicles typically differ in chassis length and number of axles. Consequently, many manufacturers adopt a parallel/expandable battery pack topology in their designs. The advantage of this structure is that it enables flexibility in driving range by integrating varying numbers of identical battery packs into the vehicle. As shown in Table 4, the average capacity of individual battery packs ranges from 80 to 120 kWh, with the total capacity reaching up to 500 kWh. These values provide electric trucks with a driving range of up to 500 km on a single charge. Another critical parameter in battery design is the vehicle's engine power, which determines the maximum current (C-rate) drawn from the battery pack. Based on the data in Table 4, the average engine power of the vehicles is calculated as 265 kW. Accordingly, a power rating of 265 kW is considered in the design of the battery pack for this study.

Battery pack design

In first-generation electric vehicles, a 400 V voltage topology was generally preferred. However, in newer electric vehicle architectures, the voltage level has been increased to 800 V in order to minimize current-related losses and improve charging speed. For electric heavy-duty vehicles, the voltage level can reach up to 1000 V, as their power demands are significantly higher than those of passenger cars. Since higher power results in a proportional increase in current, it consequently leads to greater electrical losses. The relationship between current and power losses is expressed in Equation (1), where the lost power increases proportionally to the square of the current. Thus, halving the current reduces current-related losses by a factor of four. Increasing the system voltage level is therefore an effective method to reduce current and associated losses.

$$P_{loss} = I^2.R_{pack} \quad (1)$$

As the battery voltage increases at constant power, the current decreases, which in turn allows for a reduction in the required conductor cross-section. A smaller conductor cross-section results in both reduced weight and lower cost. Figure 4 illustrates the variation in conductor and insulation cross-sections at different voltage levels, clearly showing that significantly smaller conductor cross-sections are required at higher voltages.

In this design, the battery pack is intended to be compatible with the 800 V topology. However, the batteries do not have a fixed voltage value. The nominal voltage value of sodium-ion batteries is 3.1 V. The maximum voltage value is 3.95 V and the minimum cell voltage is 2 V. These values cause the battery pack voltage value to vary in a wide range during use. A battery pack designed in the 800 V topology operates in the range of approximately 600 – 900 V during use. Table 5 provides the basic characteristics of the CATL brand Na-ion cell used in the battery pack design.

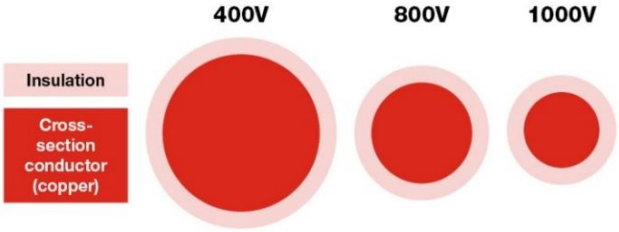

Figure 4. Conductor cross-sections for different voltage levels with the same power loss [34].

In a battery pack, cells form modules with series-parallel connections, and modules form the pack with series-parallel connections. The number of cells in the module, the number of modules in the pack and their connection type change the total electrical equivalent resistance of the pack. In this study, calculations are made for two different module alternatives. Thus, the effect of changing the number of modules on the electrical values can be observed without changing the total number of cells in the pack. As a result of the calculations, different conductor lengths, different package equivalent resistance values and different energy losses occur for the 2 cases examined.

Table 5. Properties of Sodium-Ion Cells Used in Battery Pack Design [18].

Parameter	
Brand	CATL
Min. voltage	3.1 V
Max. voltage	3.95 V
Cut-off voltage	2 V
Specific energy	160 Wh/kg
Capacity	260 Ah
Discharge energy	806 Wh
DCIR	≤ 0.25 mΩ
Weight	~ 5 kg
Dimensions	173x71x203 mm

Pack design for case 1

There are 16 cells in a module and 14 modules in a package. The nominal voltage of the battery pack is 694.4 V. In this

study, in order to reach the targeted package voltage, 260 Ah Na-ion cells, which can be considered quite large, are preferred. When a package suitable for 800 V topology is created with these cells, the total battery pack capacity is calculated as 180.5 kWh. Due to the high-capacity value of the cell, there is a single parallel arm both in the module and in the package. Thus, battery capacity options on a vehicle basis can be 180 kWh and multiples thereof. While a vehicle with 1 package is 180 kWh, a vehicle with 2 packages has a battery capacity of 360 kWh and a vehicle with 3 packages has a battery capacity of 540 kWh. As a result of the calculations, the values of battery pack 1 are given in Table 6.

Table 6. Technical specifications of designed battery pack – 1.

Technical Specifications	CATL Na-Ion
Number of cells in the module	16 series
Number of modules in the pack	14 series
Number of cells in the pack	224
Battery pack nominal voltage	694.4 V
Battery pack maximum cut-off voltage	884.8 V
Battery pack minimum cut-off voltage	448 V
Module weight	80.6 kg
Pack weight	1128.4 kg
Battery module energy capacity	12.9 kWh
Battery capacity	180.5 kWh
Module capacity	260 Ah
Module capacity	806 Wh
Module nominal voltage	49.6 V
Module dimensions	713x305x203 mm
Battery pack dimensions	1451x713x615 mm

The internal structure (module connections) of battery pack – 1 is given in Figure 5. There are 14 serial modules in the battery pack. The modules are placed by taking into account the shortest connection bars.

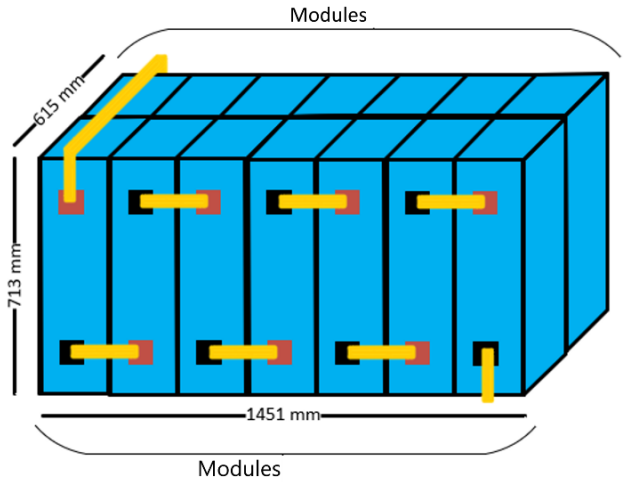

Figure 5. Internal structure of 14S1P battery pack – 1 (3D – modules).

The electrical diagram of 16 series cells is given in Figure 6.

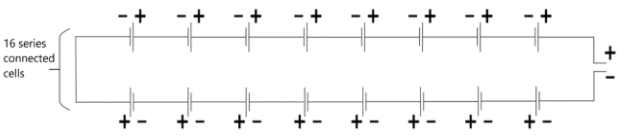

Figure 6. Electrical connection diagram of 16S1P module.

The internal structure of the 16S1P module is given in Figure 7. There are 16 series cells in the module seen in the figure. The cell layout is made by aiming for the connection bars to be as short as possible.

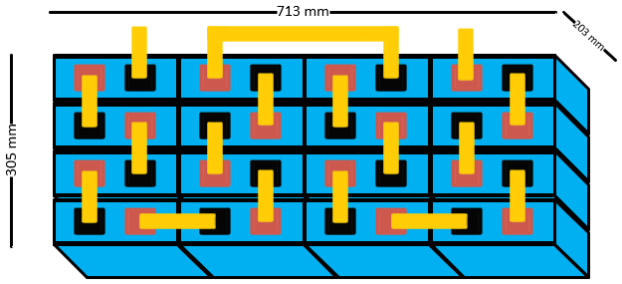

Figure 7. Internal structure of 16S1P module (3D – cells).

Pack design for case 2

A module is created with 8 cells and a battery pack is created with a total of 28 modules. The battery voltage and capacity values are the same as Case 1. The changing parameters are the number of cells in the module and the number of modules in the pack. As a result of the calculations, the values for battery pack 2 are given in Table 7.

Table 7. Technical specifications of designed battery pack – 2.

Technical Specifications	CATL Na-Ion
Number of cells in the module	8 series
Number of modules in the pack	28 series
Number of cells in the pack	224
Battery pack nominal voltage	694.4 V
Battery pack maximum cut-off voltage	884.8 V
Battery pack minimum cut-off voltage	448 V
Module weight	40.3 kg
Pack weight	1128.4 kg
Battery module energy capacity	6.5 kWh
Battery capacity	180.5 kWh
Module capacity	260 Ah
Module capacity	806 Wh
Module nominal voltage	24.8 V
Module dimensions	356x305x203 mm
Battery pack dimensions	1451x713x615 mm

The internal structure (module connections) of battery pack – 2 is given in Figure 8. There are 28 serial modules in the battery pack. The modules are placed by taking into account the shortest connection bars.

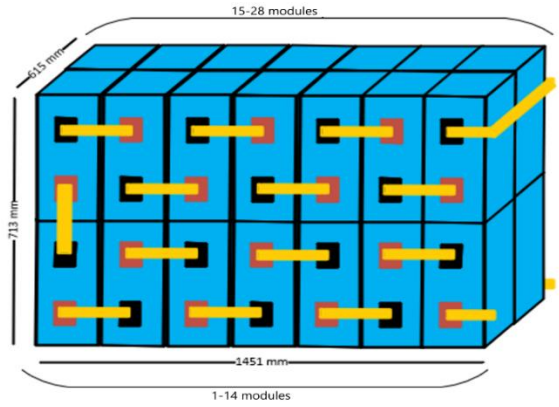

Figure 8. Internal structure of 28S1P battery pack – 2 (3D – modules).

The internal structure of the 8S1P module is given in Figure 9. There are 8 series cells in the module seen in the figure. The cell layout is made by aiming for the connection bars to be as short as possible.

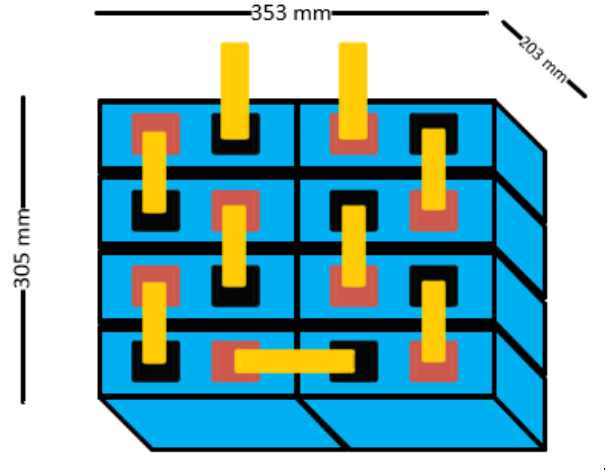

Figure 9. Internal structure of 8S1P module (3D – cells).

The electrical diagram of 8 series cells is given in Figure 10.

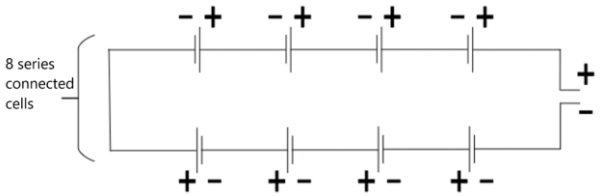

Figure 10. Electrical connection diagram of 8S1P module.

Power calculations

The engine power of the designed vehicle was determined as 265 kW by taking Table 4 into account. Equation (2) gives the minimum current of the motor, Equation (3) gives the nominal current of the motor and Equation (4) gives the maximum current of the motor.

$$I_{min} = \frac{P}{V_{max}} \quad (2)$$

V_{max} = 224 x 3.95 = 884.8 V

I_{min} = 265000 / 884.8 = 299.502 A

$$I_{nom} = \frac{P}{V_{nom}} \quad (3)$$

V_{nom} = 224 x 3.1 = 694.4 V

$$I_{max} = \frac{P}{V_{min}} \quad (4)$$

V_{min} = 2 x 224 = 448 V

I_{max} = P / V_{min} = 591.517 A

Batteries are storage elements that operate at different voltage levels due to their chemical structures. In the designed system, the battery pack has a voltage value of approximately 885 V when fully charged. The minimum battery voltage value is 448 V. The nominal voltage value is calculated as 694 volts. Based on these values, different current values are calculated for the maximum power of the vehicle, which is determined as 265 kW. While the current value drawn when the battery pack is fully charged is calculated as approximately 300 A, this value becomes 592 A when the battery charge rate (SOC) is at 10%. Table 8 shows the minimum, nominal and maximum current values for the maximum, nominal and minimum states of the battery pack voltage level.

Table 8. Battery current values at minimum, nominal, and maximum voltage levels for maximum power (265 kW).

Voltage (V)	Current (A)
884.8	299.5 (min.)
694.4	381.6 (nom.)
448	591.5 (max.)

Considering the selected battery cell and designed battery packs, a 260 Ah battery cell can provide 260 A current at 1C. Thus, 2 battery packs are capable of providing 520 A continuous current, and 3 battery packs are capable of providing 780 A continuous current. Sodium-ion batteries can reach 2-5 C-rate discharge values due to their structure. There are at least 2 battery packs in a vehicle. The maximum current value that can be drawn from a 2-pack system (592 A) corresponds to approximately 1C. This means that the sodium-ion battery used can easily respond to the current requirements of the vehicle. Conductor cross-section calculations between cells and modules are made by taking into account the maximum current value of 592 A.

Battery pack configurations and lay-out on the vehicle

As the number of battery packs increases (total energy capacity increase) while the engine power remains constant, the current drawn per pack decreases. This ensures that the cells are exposed to less electrical stress. The most difficult operating condition is when 265 kW vehicle power is provided by 2 battery packs. Calculations for double battery pack and triple battery pack vehicle configurations are shared.

Vehicle configuration – 1

Energy and power calculations are made for the dual-pack vehicle configuration. In the first case, the battery packs are placed opposite each other on the vehicle, one on the left and one on the right. The packs are electrically connected in parallel. Thus, a vehicle with 2 battery packs has an energy capacity of 360 kWh. The values obtained as a result of the calculations made for Vehicle Configuration – 1 are given in Table 9.

Figure 11 shows the electrical single-line diagram of the battery pack used in Vehicle Configuration-1 Case 1. Each battery pack consists of 14 serially connected 16S1P modules. When two battery packs are connected in parallel, a total of 28 16S1P modules are used.

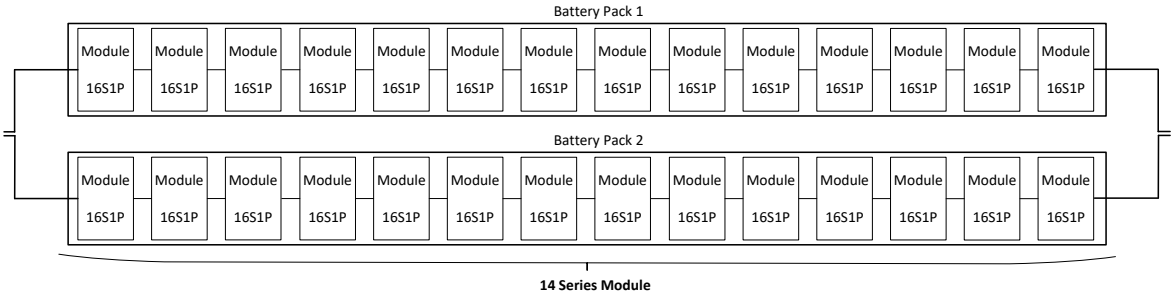

Figure 11. Electrical connection diagram of battery packs for vehicle configuration-1, case 1.

Table 9. Technical specifications of the dual battery pack vehicle configuration.

Technical Specifications	CATL Na-Ion
Number of cells in two pack	448
Number of battery pack on vehicle	2 in parallel
Battery pack maximum cut-off voltage	884.8 V
Battery pack nominal voltage	694.4 V
Battery pack minimum cut-off voltage	448 V
Total energy capacity of battery	361 kWh
Nominal capacity	520 Ah (2x260 Ah)
Nominal Discharge Current (1C)	520 A
Total pack weight	2256.8 kg

Figure 12 shows a 3D representation of the lowest capacity configuration heavy vehicle with dual battery packs. The packs are shown in green. For longer range or usage time, a 3-pack configuration is needed.

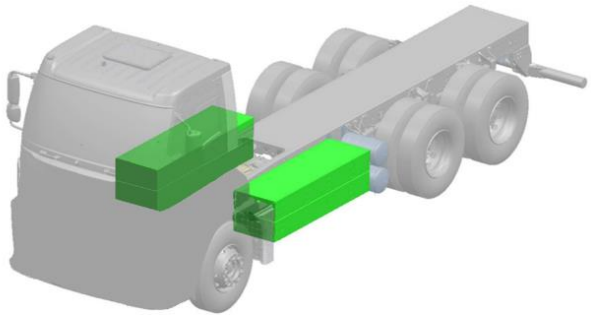

Figure 12. Illustration of a heavy-duty vehicle with two battery packs.

Figure 13 shows the electrical single-line diagram of the battery packs used in Vehicle Configuration-1 Case 2. Each battery pack consists of 28 serially connected 8S1P modules. When two battery packs are connected in parallel, a total of 56 8S1P modules are used.

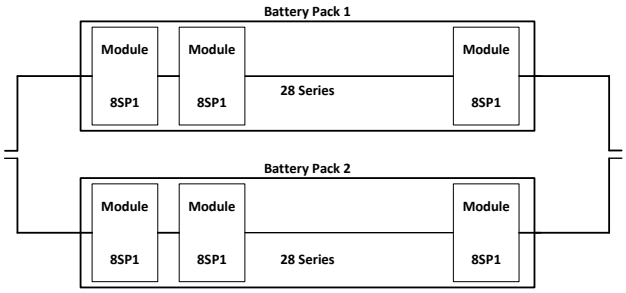

Figure 13. Electrical connection diagram of battery packs for vehicle configuration-1, case 2.

Vehicle configuration – 2

Calculations are carried out for a vehicle with three parallel battery packs: one on the left side, one on the right side, and one in the center of the vehicle. The values obtained from the calculations for Vehicle Configuration – 2 are presented in Table 10. Figure 14 shows the placement of the three battery packs on the vehicle.

Table 10. Technical specifications of the triple battery pack vehicle configuration.

Technical Specifications	CATL Na-Ion
Number of cells in a pack	224
Number of cells in three pack	672 (3x224)
Number of battery pack on vehicle	3 in parallel
Battery pack maximum cut-off voltage	884.8 V
Battery pack nominal voltage	694.4 V
Battery pack minimum cut-off voltage	448 V
Total energy capacity of battery	542 kWh
Nominal capacity	780 Ah (3x260 Ah)
Nominal Discharge Current (1C)	780 A
Total pack weight	3385.2 kg
Battery module energy capacity	12.9 kWh
Battery capacity	180.5 kWh
Module capacity	260 Ah
Module capacity	806 Wh
Module nominal voltage	49.6 V
Battery pack dimensions	1451x713x615 mm
Module dimensions	713x305x203 mm

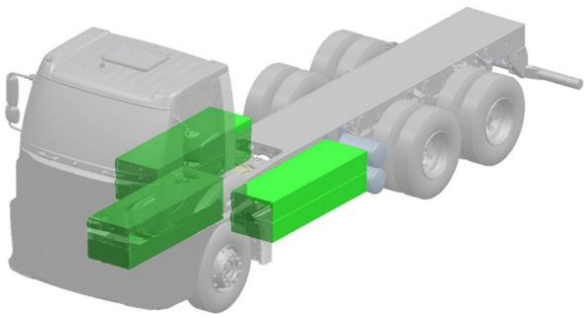

Figure 14. Placement of triple battery packs on the vehicle.

Figure 15 shows the electrical single-line diagram of the battery packs used in Vehicle Configuration-2 Case 1. Each battery pack consists of 14 serially connected 16S1P modules. Three battery packs are connected in parallel, resulting in a total of 42 16S1P modules.

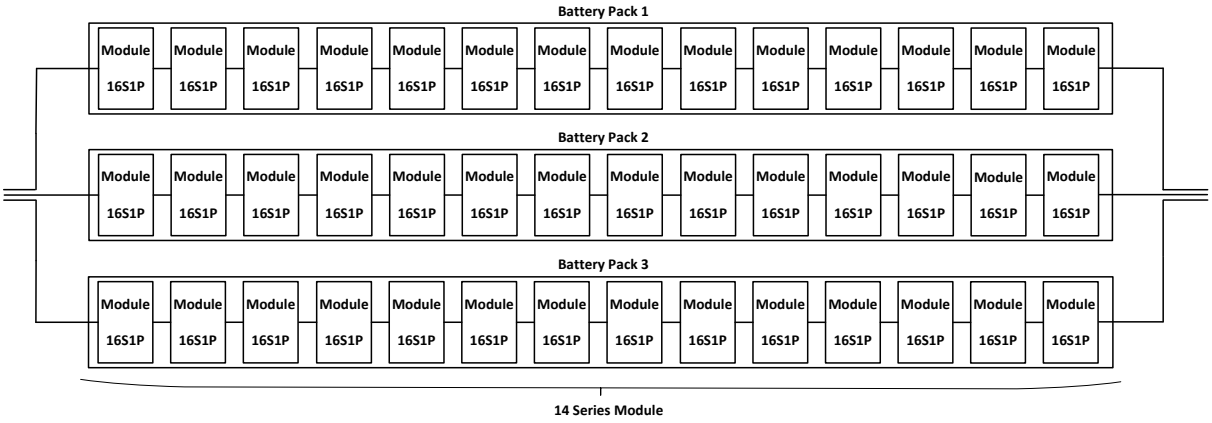

Figure 15. Electrical connection diagram of battery packs for vehicle configuration-2, case 1.

Figure 16 shows the electrical single-line diagram of the battery packs used in Vehicle Configuration-2 Case 2. Each battery pack consists of 28 serially connected 8S1P modules. When three battery packs are connected in parallel, a total of 84 8S1P modules are used.

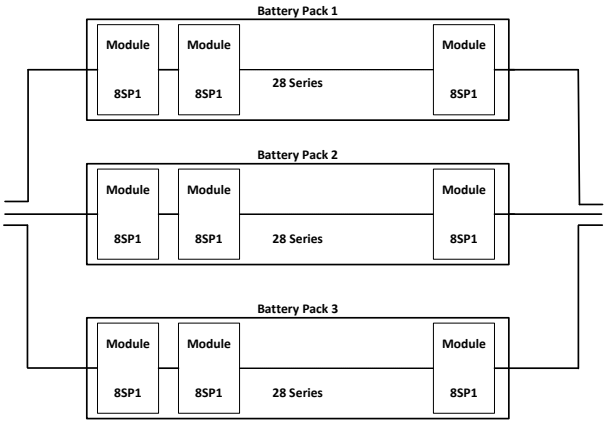

Figure 16. Electrical diagram of parallel connection for three 8S1P battery packs in vehicle configuration-2.

System equivalent resistance and power loss calculation

Minimizing electrical power loss is a critical factor in battery design, as it directly affects key performance metrics such as efficiency, charging time, and driving range. In this study, the vehicle power is assumed to be 265 kW, corresponding to a maximum current of 592 A. Two configurations were analyzed: one with two battery packs and another with three, with the most critical case being the two-pack configuration where each pack must supply 296 A. To calculate the resulting power loss, the electrical resistance points within the system and their corresponding values must be determined, including cell connections, internal cell resistances, conductors, and module connections. Conductor resistance is obtained using Equation (5), while Figure 17 illustrates the current distribution across the battery packs.

$$R_{copper} = \rho * \frac{L}{A} \quad (5)$$

A: Cross-sectional area (mm2), L: Length (m), ρ: Copper resistivity, 0.017 (mm²/mΩ)

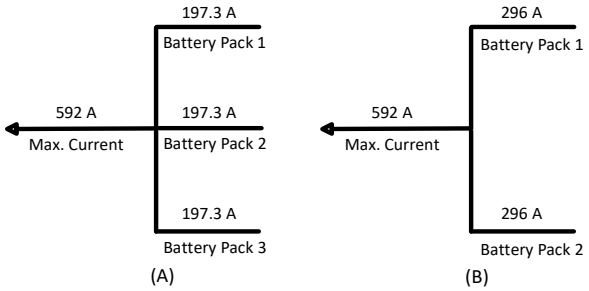

Figure 17. Current distribution diagram (A) for three battery packs, (B) for the two battery packs.

In the calculations, the current-carrying capacity considered for copper conductors is 3 A per 1 mm² cross-sectional area. This value is a standardized figure commonly used in the automotive industry to ensure safe operation. Copper resistance values are calculated separately for all cases and are presented in Table 11, Table 12, Table 13, and Table 14.

The connection of batteries to conductors is typically achieved using spot welding, ultrasonic welding, and laser welding methods. In this design, the welding resistance (Rwelding) for each cell-terminal connection is taken as 0.15 mΩ [29,30]. The internal resistance (Rinternal) of the selected cells in the battery design is accepted as the maximum internal resistance value of 0.25 mΩ [29,30]. This value corresponds to the End of Life (EoL) specification for the cell. To calculate the module resistance, Equation (6) is used; for the battery pack resistance, Equation (7) is applied; and to determine power losses, Equation (8) is utilized. The calculated values are presented in Table 15.

As a result of the calculations, it is observed that configurations using 16S1P modules experience lower power loss. Furthermore, the three-pack system has a lower equivalent resistance compared to the two-pack system, resulting in reduced electrical power loss. This is because, as the number of parallel branches increases, the equivalent resistance decreases. Additionally, since the current drawn from each individual pack is lower, current-dependent losses are also reduced. Consequently, the entire system operates more efficiently.

Table 11. Conductor cross-section and copper resistance calculation during discharge for a dual battery pack with 16S1P modules.

Connection	Current (A)	Required cross section (mm^2)	Conductor size (mm)	Conductor length (cm)	Conductor resistance (μΩ)
Between Cells	296	99	17x6	178.2	297
Between Modules	296	99	25x4	1254	2131.8

Table 12. Conductor cross-section and copper resistance calculation during discharge for a dual battery pack with 8S1P modules.

Connection	Current (A)	Required cross section (mm^2)	Conductor size (mm)	Conductor length (cm)	Conductor resistance (μΩ)
Between Cells	296	99	17x6	74.8	124.6
Between Modules	296	99	25x4	1828	3107.6

Table 13. Calculation of conductor cross-section and copper resistance during discharge for 3 battery packs with 16S1P modules.

Connection	Current (A)	Required cross section (mm^2)	Conductor size (mm)	Conductor length (cm)	Conductor resistance (μΩ)
Between Cells	197.33	66	17x6	178.2	297
Between Modules	197.33	66	25x4	1841	3129.7

Table 14. Calculation of conductor cross-section and copper resistance during discharge for 3 battery packs with 8S1P modules.

Connection	Current (A)	Required cross section (mm^2)	Conductor size (mm)	Conductor length (cm)	Conductor resistance (μΩ)
Between Cells	197.33	66	17x6	74.8	124.6
Between Modules	197.33	66	25x4	2702	4593.4

$$R_{Module} = \left(2.R_{Welding} + R_{internal}\right).\frac{n_{seriescell}}{n_{parallelcell}} + R_{ModuleBusbars}(n_{seriescell} - 1) + 2.R_{poleBusbars} \quad (6)$$

$$R_{pack} = \left(2.R_{Welding} + R_{module}\right).\frac{n_{seriesmodule}}{n_{parallelmodule}} + R_{packBusbars}(n_{seriesmodule} - 1) + 4.R_{poleBusbars} \quad (7)$$

$$P_{loss} = I^2.R_{pack} \quad (8)$$

Table 15. Power losses during discharge for all variations.

	Module resistance (mΩ)	Pack resistance (mΩ)	System resistance (mΩ)	Power loss of system (kW)
2 battery packs - 16S1P	9.097	133.68	66.84	23.42
2 battery packs - 8S1P	4.524	138.179	69.089	24.21
3 battery packs - 16S1P	9.097	134.687	44.895	15.73
3 battery packs - 8S1P	4.524	139.665	46.555	16.32

System evaluation in terms of battery control architecture

The battery control architecture is designed as a Distributed Battery Management System (BMS). Compared to other methods, a distributed BMS provides higher measurement accuracy and has a flexible structure capable of managing a large number of modules. A Module Control Unit (MCU) is the electronic circuit responsible for monitoring and controlling each module. Each MCU has a specific number of voltage and temperature sensing channels. If the number of measurement points is too low, it becomes difficult to accurately assess the health of the cells. On the other hand, having more measurement points allows for more precise monitoring of cell health. However, this also increases the system's electrical and physical complexity. MCUs need to have a higher number of input/output channels, and the wiring becomes more complex—raising the risk of system failure. Therefore, an optimum balance must be achieved. In battery packs using 16S1P modules, each module is

monitored by one MCU, which includes 17 voltage measurement points and 2 temperature sensing points. In battery packs using 8S1P modules, each module is also monitored by one MCU, featuring 9 voltage measurement points and 2 temperature sensing points. The number of voltage measurement points per module is calculated using Equation (9). For temperature measurement, two reference points should be used—one from the hottest and one from the coldest part of each module.

$$n_{Voltage\ measurement} = n_{series} + 1 \quad (9)$$

Table 16 presents the number of MCUs used in vehicles equipped with 2 and 3 battery packs utilizing 16S1P and 8S1P modules.

Table 16. Number of MCUs used in battery packs and measurement points.

Configurations	16S1P module	8S1P module
Number of MCU's per pack	14	28
Voltage measurement points	17	9
Temperature measurement	2	2
Total measurement points	266	308

Usable energy content determination of battery pack (SOC window)

One of the important parameters used in battery packs is the SoC Window (State of Charge Window). Accurate estimation of the current capacity of the battery contributes to preventing over-discharging, protecting the battery and extending its life. To avoid over-discharging and overcharging of the designed battery pack, the State of Charge (SoC) window is limited. This helps maintain the chemical balance of the battery. It also prevents thermal runaways caused by increased heating at full charge. Additionally, the SoC window ensures that cells do not fall below 2 V, avoiding deep discharge damage. Capacity is reserved for regenerative braking, and charging speed is optimized. Therefore, the SoC window is set between 5% and 95%. Thus, only 90% of the total capacity can be used. The SoC Window refines the "Total Energy Throughput" value, which is the total energy that the battery will give throughout its life. Some values for the designed electric vehicle are given in Table 17 [35].

Table 17. Electrical specifications of the designed vehicle.

	Battery pack	Definitions
Maximum voltage	884.8 V	
Nominal voltage	694.4 V	
Minimum voltage	448 V	
Insulation strength	2500 V	IEC 60664
Energy capacity	180.5 kWh	
SoC window	5% – 95%	
Usable energy capacity	162.5 kWh	SoC Window

Comparison of configurations in terms of size and weight

In battery pack design, the weight of the conductors used is one of the important factors affecting the total battery weight. The volumes of the copper bars used were calculated by considering their lengths and cross-sections, and the total conductor weight was calculated by taking the specific gravity of copper as 8.94 g/cm^3. Table 18 shows the conductor weights of the configurations. Although the same number of cells are used in the 16S1P and 8S1P modules, it is seen that the battery pack created with the 16S1P module has less conductor weight due to the connection differences.

Table 18. Weights of conductors and modules.

	16S1P	8S1P
Conductor weight in module (kg)	1.62	1.36
Total Conductor weight between modules (kg)	10.69	16.66
Module weight (kg)	80.6	40.3
Total conductor weight (kg)	33.37	54.74
Pack weight (kg)	1162	1183

When the battery packs designed with 16S1P and 8S1P module configurations are examined, it is seen that the battery pack using 16S1P module uses 21.37 kg less conductor in total by calculating the conductor weights within the module and between the modules. Thus, it is understood that the battery pack created with 16S1P module structure is more efficient in terms of conductor cost and vehicle weight.

Conclusion

This study investigates the electrification of trucks by designing and performing calculations with sodium-ion batteries as an alternative to conventional lithium-ion batteries. Sodium-ion chemistry is considered a noteworthy alternative due to its more environmentally friendly, safer, cheaper, and sustainable characteristics. With recent advancements enabling energy densities around 160 Wh/kg, sodium-ion batteries have started to be preferred especially in electric trucks where battery weight is tolerable and onboard space is not limited. Designs were made for four different configurations operating at an 800 V voltage level. The results were evaluated in terms of range, maximum discharge rate, performance, power loss, conductor weight, cost, and volumetric energy density. The key findings are summarized below:

- For battery pack design, CATL cells with the highest energy density in sodium-ion chemistry were used. Each cell has a nominal voltage of 3.1 V and a capacity of 260 Ah. Therefore, all cells were connected in series with no parallel connections in the pack. A total of 224 cells were used in the battery pack. The total energy capacity is 180.5 kWh; however, since the State of Charge (SoC) window is limited to 5% – 95% to increase battery life, 90% of this capacity is usable, corresponding to 162.5 kWh.
- In the battery control architecture, the 16S1P module structure includes 14 MCUs and 266 measurement points, whereas the 8S1P structure includes 28 MCUs and 308 measurement points. From this perspective, the 16S1P module structure appears more advantageous.
- The technical parameters of the selected battery cell specify a minimum voltage of 2 V, nominal voltage of 3.1 V, and maximum voltage of 3.95 V. Thus, the battery pack voltage is calculated as a minimum of 448 V,

nominal 694.4 V, and maximum 884.8 V. For a power rating of 265 kW, the corresponding current values are 299.5 A (minimum), 381.6 A (nominal), and 592 A (maximum). Therefore, the maximum current required to meet the 265 kW power demand is 592 A.

- In all vehicle designs, battery packs are connected in parallel to allow for extended driving range when needed.
- To meet the maximum power demand of 265 kW, the two-pack configuration requires 296 A at the minimum voltage level (448 V), whereas in the three-pack configuration, the total current is divided by three, requiring only 197 A per pack. This three-pack structure is advantageous in terms of reducing electrical losses in the battery.
- Among the four configurations examined, the one with three battery packs using 16S1P modules exhibits the lowest power loss. This is due to the reduction in equivalent resistance as the number of parallel strings increases. Additionally, the current drawn from each pack decreases, thus reducing current-dependent losses. This leads to a more efficient overall system.
- When evaluating electrical losses, systems composed of 16S1P modules demonstrate lower power loss, while the 8S1P module structure shows higher system resistance.
- Comparing vehicles designed with 16S1P and 8S1P module configurations, the conductor weight within and between modules was calculated. It was found that the battery pack with 16S1P modules uses 21.37 kg less conductor material, indicating that the 16S1P module structure is more efficient in terms of conductor cost and vehicle weight.
- Energy content differs by approximately 20%–30% between lithium and sodium cells of the same volume. Sodium-ion batteries are also heavier. However, this weight increase, amounting to a few hundred kilograms in total, is not significant for trucks. This weight drawback is offset by production cost advantages.
- Sodium batteries cost approximately half as much as lithium batteries.

In conclusion, sodium-ion batteries offer adequate energy and power density for electric truck applications. In addition, sodium-ion chemistry provides notable advantages over lithium-ion technology in terms of resource availability, environmental impact, efficiency, cost, lifespan, safety, and robustness. Nevertheless, it remains inferior to lithium-ion batteries in terms of energy density. The selection of battery chemistry should therefore be determined by the vehicle segment, intended use case, and range requirements. This study demonstrates the technical feasibility of employing sodium-ion cells in electric trucks. Given their numerous advantages, sodium-ion batteries hold significant potential to complement or even replace lithium-ion batteries in heavy-duty vehicle applications in the near future. Furthermore, the findings highlight the importance of developing optimized pack configurations and system architectures to fully exploit the potential of sodium-ion chemistry. Future research should focus on improving the energy density of sodium-ion cells, advancing thermal management strategies, and investigating long-term durability under real driving cycles. Such efforts will accelerate the transition of sodium-ion technology from laboratory-scale innovation to widespread commercial adoption in heavy-duty electric vehicles.

Ethics committee approval and conflict of interest statement

There is no need to obtain permission from the ethics committee for the article prepared.

Authors' Contributions

-Study conception and design: Fındık & Erhan

-Acquisition of data: Fındık

-Analysis and interpretation of data: Fındık & Erhan

-Drafting of manuscript: Fındık & Erhan

-Critical revision: Erhan

References

[1] IEA, Global EV Outlook 2020. Entering the decade of electric drive? International Energy Agency, 2020.

[2] "Factbox: German cities ban older diesel cars," Reuters, [Online]. Date of Access: Dec. 8, 2024. from https://www.reuters.com

[3] "City of Amsterdam to ban polluting cars from 2030," Reuters, [Online]. Date of Access: Dec. 8, 2024. from https://www.reuters.com

[4] F. Harvey, "Four of world's biggest cities to ban diesel cars from their centres," The Guardian, [Online]. Date of Access: Dec. 8, 2024. from https://www.theguardian.com

[5] "Brussel gaat dieselwagens verbannen vanaf 2030, regering wil ook maatregelen tegen benzinewagens," Het Nieuwsblad, [Online]. Date of Access: Dec. 8, 2024. from https://www.nieuwsblad.be

[6] "Vanaf vandaag (strengere) lage-emissiezones in Gent, Antwerpen en Brussel: met welke wagen mag je waar nog binnen?," VRT NWS, [Online]. Date of Access: Dec. 8, 2024. from https://www.vrt.be

[7] L. Sommer, "California Governor Signs Order Banning Sales Of New Gasoline Cars By 2035," NPR, 2020. [Online]. Date of Access: Dec. 8, 2024 from https://www.npr.org

[8] Governor of California, Executive Order N-79-20, [Online]. Date of Access: Sep. 23, 2020. from https://www.gov.ca.gov

[9] The City of New York Office of The Mayor, Executive Order No. 53, 2020. [Online]. Date of Access: Dec. 8, 2024. https://www.nyc.gov

[10] M. Seijdel, "Oude dieselauto's en vervuilende brommers komen centrum Den Haag straks niet meer in," AD.nl, [Online]. Date of Access: Dec. 8, 2024. from https://www.ad.nl

[11] L. J. Hounjet, "Comparing lithium-and sodium-ion batteries for their applicability within energy storage systems," Energy Storage, vol. 4, no. 3, e309, 2022.

[12] A. Nekahi et al., "Comparative issues of metal-ion batteries toward sustainable energy storage: Lithium vs. sodium," Batteries, vol. 10, no. 8, p. 279, 2024.

[13] H. Bai and Z. Song, "Lithium-ion battery, sodium-ion battery, or redox-flow battery: A comprehensive comparison in renewable energy systems," J. Power Sources, vol. 580, p. 233426, 2023.

[14] Y. Soydan, "Electrical and conventional automobile tribology: New trends and applications", DÜMF MD, vol. 7, no. 3, p. 527–536, 2016.

[15] "Sodium-Ion vs. Lithium-Ion Batteries - A Clear Winner?," Solar4RVs, [Online]. Date of Access: Dec. 8, 2024. from https://www.solar4rvs.com.au

[16] S. Lilley, "Sodium-ion Batteries: Inexpensive and Sustainable Energy Storage," Faraday Insights, no. 11, 2021.

[17] J. H. Choi et al., "Low-crystallinity conductive multivalence iron sulfide-embedded S-doped anode and high-surface area O-doped cathode of 3D porous N-rich graphitic carbon frameworks for high-performance sodium-ion hybrid energy storages," Energy Storage Mater., vol. 68, p. 103368, 2024.

[18] "CATL, BYD's sodium-ion batteries both to be in mass production within this year, report says," CNEV Post, [Online]. Date of Access: Apr. 20, 2023. from https://cnevpost.com

[19] J. F. Peters, A. Peña Cruz, and M. Weil, "Exploring the economic potential of sodium-ion batteries," Batteries, vol. 5, no. 1, p. 10, 2019.

[20] K. M. Abraham, "How comparable are sodium-ion batteries to lithium-ion counterparts?," ACS Energy Lett., vol. 5, no. 11, p. 3544–3547, 2020.

[21] G. Taş, "Temperature Prediction of Lithium-ion Battery by CPSO-UKF", DÜMF MD, vol. 15, no. 4, p. 817–825, 2024, doi: 10.24012/dumf.1528158.

[22] Ö. F. Özcan, T. Karadağ, M. Altuğ, ve Ö. Özgüven, "A Review Study on the Characteristics and Advantages of Battery Chemicals Used in Electric Vehicles," Gazi Univ. J. Sci. Part A: Eng. Innov., vol. 8, no. 2, p. 276–298, 2021.

[23] C. Crownhart, "How sodium could change the game for batteries," MIT Technology Review, [Online]. Date of Access: May 11, 2023. from https://www.technologyreview.com

[24] M. Schirber, "Sodium as a green substitute for lithium-ion batteries," Physics, vol. 17, p. 73, 2024.

[25] R. Menak, T. Karadağ, M. Altuğ, ve N. Tan, "A Review Study on Battery Management Systems in Electric Vehicles," Gazi Univ. J. Sci. Part A: Eng. Innov., vol. 8, no. 2, p. 234–275, 2021.

[26] A. Rudola, R. Sayers, C. J. Wright, et al., "Opportunities for moderate-range electric vehicles using sustainable sodium-ion batteries," Nat. Energy, vol. 8, p. 215–218, 2023. doi: 10.1038/s41560-023-01215-w.

[27] Z. N. Kurtulmuş ve A. Karakaya, "Review of lithium-ion, fuel cell, sodium-beta, nickel-based and metal-air battery technologies used in electric vehicles," *Int. J. Energy Appl. Technol.*, vol. 10, no. 2, p. 103–113, 2023. doi: 10.31593/ijeat.1307361.

[28] A. M. Glushenkov, "Recent commentaries on the expected performance, advantages and applications of sodium-ion batteries," *Energy Mater.*, vol. 3, p. 300010, 2023. doi: 10.20517/energymater.2022.70.

[29] M. G. M. Abdolrasol, S. Ansari, I. A. Sarker, S. K. Tiong, ve M. A. Hannan, "Lithium-ion to sodium-ion batteries transitioning: trends, analysis and innovative technologies prospects in EV application," *Prog. Energy*, vol. 7, no. 2, p. 022007, 2025. doi: 10.1088/2516-1083/adbff0.

[30] F. Degen, M. Mitterfellner, and A. Kampker, "Comparative life cycle assessment of lithium-ion, sodium-ion, and solid-state battery cells for electric vehicles," J. Ind. Ecol., vol. 29, no. 1, p. 113–128, 2025.

[31] A. R. Nurohmah et al., "Sodium-ion battery from sea salt: a review," Mater. Renew. Sustain. Energy, vol. 11, no. 1, p. 71, 2022.

[32] B. Fındık and K. Erhan, "Comparative Analysis of Energy Consumption Between an Electrified and A Conventional Garbage Truck According to Urban Driving Cycle," in Proc. 5th Int. Congr. Eng. Sci., Istanbul, Turkey, Oct. 12–13, 2024.

[33] "Electric Trucks 2025: The Big Comparison of Models, Ranges & Applications," IODynamics, [Online]. Date of Access: Dec. 8, 2024. from https://www.iodynamics.de

[34] G. Gartler, "Over 1000 V in the future? Integration of HV battery and drivetrain in the electric car," Inside Automotive, 2023. [Online]. Date of Access: Dec. 8, 2024. from https://www.magna.com

[35] P. Dini, A. Colicelli, and S. Saponara, "Review on modeling and SOC/SOH estimation of batteries for automotive applications," Batteries, vol. 10, no. 1, p. 34, 2024.

Dicle University
Journal of Engineering
https://dergipark.org.tr/tr/pub/dumf
duje.dicle.edu.tr

Review Article

Trends in Electric Vehicle Motor Power: A Comparative Study on Performance and Efficiency

Ahmet ORHAN[1*], Sencer ÜNAL[2], Ayhan AKBAL[3], Kıvanç DOĞAN[4], Murat KAYAOĞLU[5], Hilal BIYIK[6]

[1] Fırat University, Electrical-Electronics Engineering Department, aorhan@firat.edu.tr, Orcid No: 0000-0003-1994-4661, [2] Fırat University, Electrical-Electronics Engineering Department, sencerunal@firat.edu.tr, Orcid No: 0000-0001-5990-933X, [3]Fırat University, Electrical-Electronics Engineering Department, ayhan_akbal@firat.edu.tr, Orcid No: 0000-0003-4820-3563, [4]Fırat University, Electrical-Electronics Engineering Department, kivanc.dogan@firat.edu.tr, Orcid No: 0000-0003-4832-1412, [5]Fırat University, Electrical-Electronics Engineering Department, mkayaoglu@firat.edu.tr, Orcid No: 0009-0004-1327-012X, [6]Fırat University, Electrical-Electronics Engineering Department, hbiyik@firat.edu.tr, Orcid No: 0009-0007-1816-6868

ARTICLE INFO

Article history:

Received 31 July 2025
Received in revised form 19 September 2025
Accepted 22 September 2025
Available online 30 December 2025

Keywords:

Wound Rotor Synchronous Motor, Permanent Magnet Synchronous Motor, Brushless DC Motor, Electric Vehicles, Induction Motor

Doi: 10.24012/dumf.1755155

* Corresponding author

ABSTRACT

Electric vehicles (EVs) have increasingly become central to modern transportation systems due to their advantages in environmental sustainability and energy efficiency. In this development process, electric drive motors play a decisive role in key criteria such as performance, range, energy consumption, and production costs. In this study, three primary motor types commonly used in electric vehicles the Wound Rotor Synchronous Motor (WRSM), Permanent Magnet Synchronous Motor (PMSM), and Induction Motor (IM) are evaluated in a multidimensional manner in terms of their technical performance, energy efficiency, and application segments. Comparative analyses reveal that PMSM motors, in particular, provide an optimal power-to-weight ratio for mid-range vehicles due to their high torque generation and low energy consumption. The compact structure and high efficiency levels of these motors have made them the standard choice for many manufacturers today. On the other hand, WRSM motors offer a strong alternative for long-term sustainability goals by eliminating dependence on rare-earth elements and providing field weakening capability. The high-temperature tolerance, low maintenance requirements, and wide speed range operating capability of WRSM motors indicate their potential for broader adoption in the future. Segment-based evaluations have determined that vehicles in the economic class offer longer range per unit of energy due to lower weight and limited power requirements, representing a significant advantage for compact electric vehicles intended for urban use in terms of energy savings. Conversely, luxury and high-performance segment vehicles demonstrate higher energy consumption despite larger battery capacities; in these segments, factors such as acceleration, traction power, and driving comfort are prioritized over efficiency. The general findings indicate that motor power plays a critical role not only in performance but also in energy consumption, range capacity, and segment-based product positioning. Furthermore, the increasing research and development efforts on alternative motor architectures such as WRSM suggest that these motors may become more attractive both economically and environmentally in the future. In this context, it is recommended that interdisciplinary research on motor technologies be intensified in order to achieve sustainable electric transportation objectives

Introduction

The transportation sector, one of the largest sources of air pollution, is considered the biggest consumer of petroleum [1]. This sector accounts for approximately 20% of global greenhouse gas emissions, with this proportion reaching up to 30% in developed countries [2]. Growing concerns about petroleum availability and its adverse environmental impacts have increased the need for alternative energy options in the transportation sector. At this point, efforts have accelerated toward the development of electric vehicles (EVs), which are regarded as the most suitable option to reduce dependence on fossil fuels [3].

According to data from the International Energy Agency (IEA), while the number of electric vehicles worldwide was 11 million in 2020, it is projected to reach 350 million by 2030 and approximately 2 billion by 2050. In addition, the number of electric two- and three-wheeled vehicles, as well as electric buses, is also expected to quadruple, reaching nearly 50 million. However, not only the increase in the size of the electric vehicle fleet but also the size and capacity of batteries constitute key factors determining the demand for critical minerals and raw materials. Batteries used in light-duty electric vehicles can have capacities ranging from approximately 10 kWh to 200 kWh and specific energy values between 30 and 275 Wh/kg. In electric vehicle models commonly used in the United States, the average battery mass is approximately 350 kg. Unlike internal combustion engine (ICE) vehicles, EVs draw their energy from electricity stored in batteries. Alongside sustainable fuels and advanced powertrain systems, EVs are among the most effective and promising technologies for reducing carbon emissions in road transportation [4]. Minimizing energy consumption is of great importance for the success of this transformation. Traditional ICE vehicles lose about 80% of energy through mechanical friction, heat, and braking before the energy reaches the wheels. In contrast, EVs can recover a portion of this kinetic energy by converting it back into electrical energy through regenerative braking systems. Furthermore, the electric motors used in EVs offer significantly higher energy efficiency compared to ICEs [5]. Therefore, the performance of EVs varies depending on the type and

characteristics of the electric motors employed. In this context, studies focusing on the advantages and disadvantages of different motor types play a significant role in the design and application of EVs [3].

Electric vehicles (EVs) utilize electric motors for propulsion and operate using electricity supplied by onboard batteries. The electricity consumed by EVs can be generated from various energy sources, which allows them to have a lower carbon footprint and reduced emissions compared to conventional internal combustion engine (ICE) vehicles [1]. Additionally, EVs offer numerous benefits, including lower operating and maintenance costs, tax advantages, ease of driving, quiet operation, and the convenience of home charging [6]. Battery electric vehicles (BEVs) are becoming increasingly popular due to technological advancements and their wide applicability. According to the European Automobile Manufacturers Association (ACEA), China currently leads the BEV market ahead of Europe and the United States. However, projections suggest that Europe will surpass other regions by 2030. In BEVs, electric motors replace ICEs; therefore, electric motors must operate over a wide range of torque and speed to enable high-performance power delivery in a vehicle. An electric motor should provide high load power, higher torque at low speeds for starting and climbing, moderate power at high speeds for cruising, and function as a generator during braking. Moreover, electric motors are required to possess high power density, torque density, specific power, a broad and highly efficient operating range, low vibration and noise, high reliability, and a favorable performance-to-cost ratio [7]. Among the motor types commonly used in EVs are permanent magnet synchronous motors (PMSM), induction motors (IM), brushless direct current motors (BLDC), and switched reluctance motors (SRM). Each of these motor types has distinct characteristics that influence EV performance. In particular, PMSMs stand out for their lightweight, high efficiency, and low noise levels [3]. As shown in Table 1, PMSMs are the most widely used type of electric motor in commercially available EVs.

TABLE 1. Technical specifications of commercially available electric vehicles [8], [9], [10], [11], [12], [13], [14], [15], [16], [17]

Model	Motor Type	Torque (Nm)	Motor Power	Range (km)	Total Weight (kg)	Energy Consumption (Wh/km)
Tesla Model S	AC PMSM	440	350 kW	575	2534	120
Nissan Leaf	Synchronous (Nissan EM motor)	280	110 kW	235	1995	166
BMW i3	Synchronous Electric Motor	250	125 kW	235	1710	130–150
Audi e-tron	2 x Synchronous Motor	664	124 kW (front) + 175 kW (back)	336	3040	220–260
Volkswagen ID.3	PMSM	310	110 kW	350	1725	151
Porsche Taycan	PMSM	774	460 kW (max) / 616 hp	412	2345	260
Ford Mustang	PMSM	430	216 kW	480	2605	190
Chevrolet Bolt EV	PMSM	360	149.1 kW	416	1628	156

In addition, numerous studies in the literature have focused on motor types used in electric vehicles. In the study conducted by Sadiki, the application of permanent magnet synchronous motors (PMSM) in electric vehicles and their control methods are emphasized. It is stated that vector control techniques are effective in enhancing the energy efficiency and performance of these motors. The study highlights that appropriate control strategies should be implemented to improve the dynamic performance of electric vehicles utilizing these motors [3]. Cao et al. conducted a review on the classification and performance comparison of alternative electric motors for electric vehicle applications. This study points out that induction motors offer advantages particularly in terms of cost and durability; however, their efficiency is not as high as that of permanent magnet motors. Therefore, when selecting a motor, these factors should be taken into account based on the intended application and vehicle design [17]. Mayuri and Dhamal carried out a detailed review of the motors used in the drive systems of electric vehicles. In their study, criteria such as efficiency, cost, and reliability are listed as key factors to be considered in motor selection. Brushless motors play a significant role in enhancing electric vehicle performance, particularly due to their ability to provide high starting torque and energy efficiency [18]. Qianfan et al. investigated the characteristics of hybrid switched reluctance motors developed for electric vehicles. These motors are reported to offer high efficiency and a wide torque-speed range. However, their application areas may be limited, and they generally require more complex control systems [19]. Xiao et al. proposed the implementation of regenerative braking mechanisms to improve the efficiency of DC motors in electric vehicles. In their study, the

integration of wound rotor synchronous motors (WRSM) with energy recovery mechanisms is discussed in terms of its potential to extend the range of electric vehicles. The study further emphasizes that WRSMs can enhance energy efficiency in electric vehicles by converting kinetic energy into electrical energy during braking [20]. In conclusion, the selection of motor types in electric vehicles is a critical issue in terms of performance, cost, energy efficiency, and environmental impact. The advantages and disadvantages of different motor types should be considered in the design of electric vehicles, and the most suitable motor should be selected according to the intended application. In the current literature, electric vehicle motors are predominantly examined along the axes of PMSM, IM, and BLDC, while studies on WRSM remain limited. However, WRSM emerges as a noteworthy alternative in electric vehicle motor architectures due to its technical advantages such as reducing dependency on rare-earth elements, resistance to magnetic saturation, and field weakening capability. This review aims to address this gap in the literature by comprehensively examining the potential application of WRSM in electric vehicles. Furthermore, by providing a technical comparison of existing motor types, this study seeks to establish a foundation that can guide future research.

The scope of this study includes peer-reviewed journal articles and conference papers published over the last 19 years (2006-2025). The literature review was conducted primarily using the IEEE Xplore, Google Scholar, ScienceDirect, and Scopus databases with keyword combinations such as 'Wound Rotor Synchronous Motor', 'Permanent Magnet Synchronous Motor', 'Induction Motor', 'Brushless DC Motor', 'Switched Reluctance Motor', 'electric vehicles', 'motor efficiency', and similar keyword combinations. This review comprehensively reveals current trends and developments in electric vehicle motor technologies by examining the relevant literature using a systematic approach.

MOTOR TYPOLOGIES IN ELECTRIC VEHICLES

The foundations of electric drive systems date back to the 18th century, when Faraday introduced the principle of electromagnetic induction. This development led to the emergence of Alternating Current (AC) and Direct Current (DC) motors. Electric motors typically consist of components such as the rotor, stator, windings, air gap, and commutator. Various configurations of these components have resulted in the development of different motor types, as illustrated in Figure 1 [21]. In the early stages, electric vehicles relied on DC traction motors, which provided high torque at low speeds, possessed a wide constant power-speed range, and offered relatively simple control. Due to these characteristics, DC motors initially presented a suitable solution for electric transportation. Currently, DC motors are still widely used in low-power applications within the range of 10–30 kW, particularly in micro-mobility solutions such as electric bicycles, mopeds, and three-wheeled vehicles. However, in high-speed applications, DC motors exhibit disadvantages such as limited efficiency and low power density. In contrast, brushless motors offer higher reliability, improved dynamic performance, and greater energy efficiency. Owing to these advantages, AC motors are now preferred in high-power and high-performance electric vehicle applications [7].

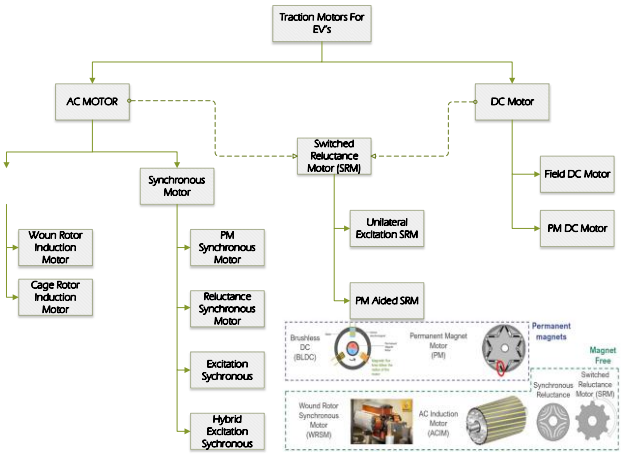

Figure 1. Classification of electric motors for electric vehicles according to power source [22]

As shown in Figure 2, according to the latest report published by IDTechEx covering the years 2024–2034, permanent magnet motors continue to dominate as the leading motor technology in the electric vehicle market. While the market share of permanent magnet motors was 84% in 2021, it is reported that similarly high levels have been maintained in 2024 and beyond. However, due to growing concerns regarding sustainability and supply chain issues, interest in alternative motor types, such as wound rotor synchronous motors (WRSM) and induction motors (IM), has been increasing [23].

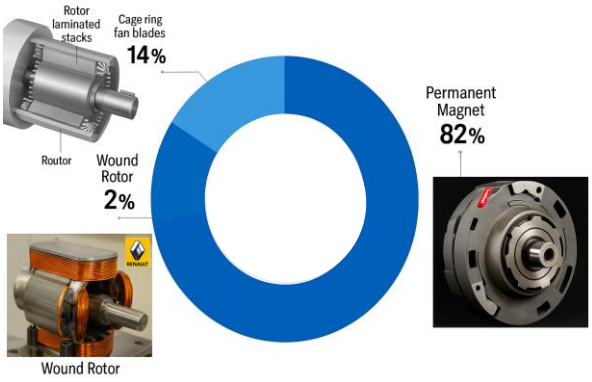

Figure 2. 2024 BEV and PHEV engine type market shares (based on IDTechEx data) [23]

Figure 3 presents an analysis comparing the peak power to mass ratio of different electric vehicle traction motors. PMSM motors are positioned within the range of 2–3 kW/kg, offering a powerful and efficient solution that is widely preferred in current applications. WRSM, on the other hand, exhibits lower power density levels; however, it remains highly popular due to its ability to deliver synchronous motor behavior without the need for rare-earth elements. SRM motors demonstrate moderate performance across a wide range of power and mass values [23].

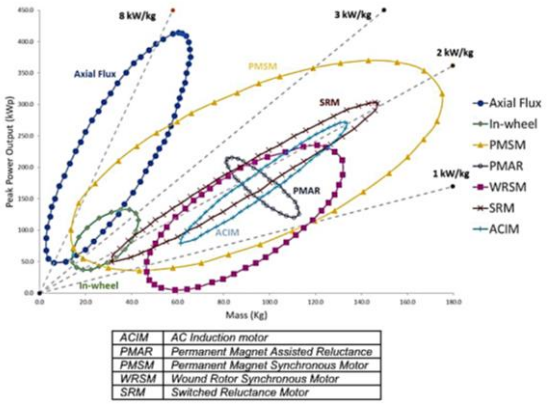

ACIM	AC Induction motor
PMAR	Permanent Magnet Assisted Reluctance
PMSM	Permanent Magnet Synchronous Motor
WRSM	Wound Rotor Synchronous Motor
SRM	Switched Reluctance Motor

Figure 3. Power density comparison of different engine types used in EVs (based on data from IDTechEx) [23]

DC Motors

Today, EVs have secured a significant position among transportation solutions that promote environmental sustainability. The propulsion systems used in these vehicles play a crucial role in terms of performance, energy efficiency, and cost. In this context, DC motors are among the widely preferred motor types in EVs due to the various advantages they offer.

DC motors stand out for their high energy efficiency, simple control mechanisms, and low production costs. In particular, brushless DC (BLDC) motors offer longer service life and lower maintenance requirements compared to conventional brushed motors, as they exhibit less mechanical wear [24]. Their simple structure allows for easy implementation of control systems, and their high torque generation capability directly contributes to EV performance [25]. DC motors also offer significant flexibility in speed and torque control. It is well-known that their dynamic performance can be enhanced through Proportional-Integral-Derivative (PID) control methods [26]. This control flexibility allows EVs to respond instantaneously to variable load conditions. Furthermore, their compatibility with regenerative braking systems enables the conversion of kinetic energy into electrical energy during braking, which can then be fed back into the battery. This process not only contributes to battery recharging but also extends the vehicle's driving range [20],[27].

Another notable advantage of DC motors is their cost-effectiveness. Their lower production and maintenance costs compared to AC motors make EV technologies more accessible to a wider range of consumers [28]. Additionally, their simpler design, containing fewer components, reduces overall system complexity and facilitates ease of design [29]. When combined with bidirectional DC-DC converters, DC motors can operate in both motor and generator modes. Such systems optimize energy flow, enhance efficiency, and minimize energy losses [30],[31]. These converters, widely used in regenerative braking applications, not only recover energy to recharge the battery but also contribute to extending battery life [32],[33].

In fact, since the magnetic field B is generated by the stator windings, not only the motion of the rotor windings relative to the stator but also the movement of the stator excitation becomes possible. This can be achieved by increasing the number of windings. Figure 4 presents a simplified model of a DC motor, in which the stator is assumed to have a single winding. This winding is represented by an inductance (L_e) caused by the windings and a resistance (R_e) resulting from distributed losses in the conductive material. The electrical behavior of this model is described by Equation (1).

$$v_e(t) = L_e \frac{\mathrm{d}i_e}{\mathrm{d}t} + R_e i_e \quad (1)$$

The rotor is assumed to consist of a single winding defined by its inductance (L_a) and resistance (R_a). This electrical behavior is as in Equation 2. However, the hard electromotive force of the motor has to be taken into account [34].

$$v_a(t) = L_a \frac{\mathrm{d}i_a}{\mathrm{d}t} + R_a i_a + e \quad (2)$$

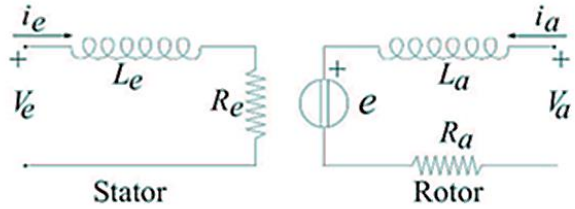

Figure 4. Electrical equivalent scheme of a DC motor [35]

The control of DC motors is typically performed using Pulse Width Modulation (PWM) techniques. Through methods such as field weakening applied for speed control, both low-speed and high-speed performance of the motor can be optimized [36]. These techniques enable the improvement of overall motor efficiency using simple control strategies. Additionally, modeling studies conducted with separately excited DC motors have shown that dynamic performance is influenced by factors such as current and thermal limits. This demonstrates how the flexibility in speed and torque control can be optimized in practical applications [37]. Structurally enhanced DC motors can also deliver effective performance even in low-voltage drive systems through the use of high-gain DC-DC converters [38]. Such innovative designs contribute to improving motor performance in electric vehicles while simultaneously helping to maintain low costs [39]. From an energy management perspective, hybrid energy systems combining batteries and supercapacitors allow the system to exhibit high transient performance even when battery energy density is low [40]. These strategies are critical for increasing the efficiency of DC motors and ensuring the overall robustness of the system. Finally, advanced control algorithms can reduce torque ripple and increase power density. Such algorithms optimize the performance of BLDC motor/generator systems, particularly in hybrid and fully electric vehicles [41].

In conclusion, DC motors used in electric vehicles offer significant advantages for sustainable transportation solutions due to their high energy efficiency, low cost, simple controllability, and integration capabilities with

regenerative energy recovery systems. The design and control strategies of these motors directly affect the overall performance of electric vehicles.

Induction Motors

Induction motors are another widely used motor type in electric and hybrid vehicles, and they have become one of the primary propulsion components in these vehicles today. These motors, which are notable for their durability, low production costs, and minimal maintenance requirements, offer a highly suitable solution for electric vehicle applications. Figure 5 presents the T-shaped equivalent electrical circuit of the induction motor. Through this circuit, the desired parameters of the induction motor can be calculated [42].

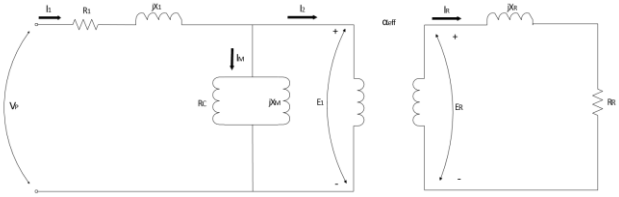

Figure 5. Equivalent circuit of asynchronous motor [42]

The control of induction motors is generally implemented using advanced methods such as field-oriented control. This approach enhances dynamic performance and maximizes energy efficiency by regulating the motor's speed and current loops through PID-based controllers [27]. Since each motor type used in electric vehicles exhibits different structural characteristics, it is essential to analyze their design and control drivers in detail according to their power classes [43]. Research on the energy efficiency of induction motors particularly focuses on how energy recovery is achieved during braking processes. Control strategies such as Direct Torque Control (DTC) enable the conversion of kinetic energy into electrical energy during braking, allowing it to be fed back into the battery [44]. This process reduces the overall energy consumption of electric vehicles, extends driving range, and contributes to energy sustainability.

High torque density and the ability to operate over a wide speed range are among the most prominent advantages of induction motors. Motor designs with high power density exhibit superior performance in terms of both torque and efficiency in electric vehicles [45]. For instance, a newly developed field-oriented control method for hybrid electric vehicles enhances system efficiency by improving the motor's speed and current loops with PID-based controllers [46]. Induction motors also offer significant advantages for regenerative braking. Braking strategies based on the negative slip principle increase the energy recovery capacity of the motor during deceleration, which is particularly critical for vehicles frequently stopping and starting in urban driving conditions. Moreover, induction motors fed by three-phase inverter systems provide cost-effective and energy-efficient solutions for hybrid electric vehicles [47]. One of the primary factors contributing to the widespread adoption of induction motors is their low-cost and durable structure. These motors are made more efficient through various control strategies and design improvements, directly enhancing the overall performance of electric vehicles. In fact, calculation of motor losses and analysis of operating conditions are fundamental factors to be considered during the design phase to improve efficiency [48]. One of the efficiency-enhancing strategies, the Maximum Torque-per-Ampere (MTPA)-based Direct Torque Control method, reduces the current drawn from the inverter under light load conditions, thus saving energy [49]. This reduces energy consumption and extends the driving range. In addition, the use of multiphase induction motors offers higher reliability and power capacity compared to conventional three-phase motors. Such configurations enable electric vehicles to deliver optimal performance under varying driving conditions [50]. From the perspective of control strategies, advanced methods such as sliding mode control improve torque regulation while also enhancing the system's dynamic stability [51]. These control techniques provide more stable and efficient operation by minimizing current and torque fluctuations [52]. Furthermore, the conversion of kinetic energy into electrical energy during braking enables feedback to the battery system, minimizing energy losses while increasing range [20]. The effectiveness of these systems is further enhanced when integrated with motor control algorithms.

Induction motors hold a significant place in electric vehicle technologies due to their energy efficiency, high torque density, low cost, durability, and advanced control strategies. Innovative approaches developed for the design and control of these motors contribute to making electric vehicles more efficient, longer-lasting, and environmentally friendly. Given their combined performance and efficiency, induction motors will continue to play a key role in future electric transportation systems.

Switched reluctance motors (SRM)

Switched Reluctance Motors (SRMs) are among the alternative motor types that have gained significant attention in electric vehicle technologies. Due to their simple structure, low cost, high reliability, and high efficiency potential, SRMs are increasingly attracting interest both in academic research and commercial applications. One of the main advantages of SRMs is their low production cost and high thermal tolerance, owing to rotor structures that do not contain permanent magnets. Additionally, their low rotor inertia, fast response times, and four-quadrant operation capabilities (operating in both motor/generator modes and forward/reverse directions) make SRMs attractive for electric vehicle applications [53]. However, since their torque generation processes are susceptible to abrupt variations and fluctuations, control strategies for SRMs require relatively more complex and precise adjustments. Developed control methods for SRMs include multi-objective optimization, Direct Torque Control (DTC), Fuzzy Logic Control (FLC), Model Predictive Control (MPC), and regenerative braking strategies. For example, an optimized controller design proposed in one study has been evaluated in a simulation environment to enhance the dynamic performance of SRMs

[31]. These control approaches aim to reduce torque ripples while improving energy recovery efficiency [53],[54].

Simulation-based models of SRMs are generally developed in Matlab/Simulink environments. These models are structured based on flux linkage and torque characteristics, allowing predictions of motor behavior under different driving scenarios [55]. In DTC applications, artificial intelligence-based controllers such as fuzzy logic are employed to achieve more precise torque control [56]. Another important advantage of SRMs is their ability to deliver efficient performance over a wide speed range. By comparing instantaneous torque control with average torque control methods, the most effective control strategy can be determined for varying driving conditions [57]. This capability allows SRMs to operate efficiently at both low and high speeds.

The regenerative braking potential of SRMs is particularly prominent in energy recovery at low speeds. For instance, strategies that minimize torque ripples and increase negative torque at low speeds enable greater energy transfer to the battery, thereby extending the driving range of electric vehicles [58],[59]. From a design perspective, SRMs are developed through multi-objective optimization strategies. Design studies for small electric vehicle applications involve optimizing the motor's geometric structure, static parameters, and electromagnetic losses [60],[61]. The absence of permanent magnets is one of the key factors that enhance the cost-effectiveness and environmental sustainability of SRMs [62]. In terms of control systems, research focused on reducing torque ripples is critical for improving driving comfort and energy efficiency in electric vehicles utilizing SRMs. Advanced control strategies such as Model Predictive Control (MPC) minimize torque ripples and provide more stable driving performance [63],[64]. Another advantage of SRMs is their ability to operate under high-temperature conditions. Their reliable performance in high-temperature environments makes them suitable for applications in harsh operating conditions [65]. Structurally simple, these motors also offer reduced maintenance requirements, thereby lowering production costs and making them accessible to a broader range of users [66].

Ultimately, Switched Reluctance Motors stand out in electric vehicle applications due to their high efficiency, low cost, durability, and flexible control capabilities. The design, simulation, and control methods developed for these motors contribute to enhancing the performance and energy efficiency of electric vehicles while supporting the development of sustainable transportation systems. SRMs are poised to play an important role in the future of electric vehicle technologies.

Brushless direct current (BLDC) motors

Brushless Direct Current (BLDC) motors are frequently preferred in dynamic applications such as automotive, pumping, and rolling industries. It is predicted that by 2030, these motors will replace conventional induction motors and become the primary component of power transmission in various industries. The figure 6 illustrates the application areas of BLDC motors [67].

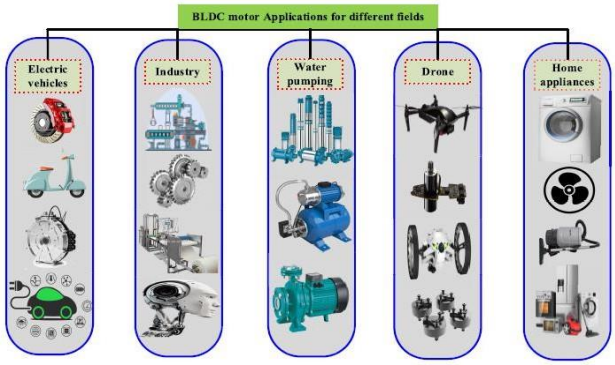

Figure 6. BLDC Motor applications for differend fields [67]

Brushless Direct Current (BLDC) motors are among the widely used motor types in electric vehicles. With their high efficiency, low maintenance requirements, and compact structures, these motors not only enable energy savings but also provide a more reliable driving experience. As electric vehicle technology advances, efficiency and durability have become crucial criteria in motor selection [68]. In this context, the use of BLDC motors offers numerous advantages in terms of both energy efficiency and performance. Due to their high power density, minimal maintenance needs, and superior efficiency, BLDC motors are widely preferred in various EV applications [69].

Compared to conventional brushed DC motors, BLDC motors have a more modern design. While mechanical commutation is employed in brushed motors, BLDC motors utilize electronic commutation. Consisting of permanent magnet rotors and multiphase stator windings, BLDC motors offer high power density and minimize mechanical wear, thereby enabling long service life [70]. Electronic commutation allows for precise speed and torque control, making BLDC motors ideal for electric vehicle applications. By minimizing energy losses, BLDC motors offer higher efficiency than internal combustion engines [71]. Their brushless structure eliminates wear and tear, reducing maintenance costs [72]. Additionally, their compact size makes them an ideal solution for lightweight electric vehicles [73]. BLDC motors can also recover kinetic energy during braking and feed it back into the battery, thereby increasing the vehicle's driving range [5]. Their ability to operate over a wide speed range and respond quickly to sudden load changes are also significant advantages [74].

BLDC motors are widely employed in various segments of electric vehicles. In electric bicycles, scooters, and compact urban vehicles, BLDC motors are preferred to meet low power demands. Typical operating voltages range between 24V and 48V [67]. In passenger electric vehicles, they are commonly used as hub motors [75]. In hub motor applications, magnetic flux distribution and torque production capabilities are optimized, eliminating the need for transmissions. This transmission-free structure enhances efficiency and reduces energy consumption [76]. In commercial vehicles and public transportation systems, BLDC motors are favored due to their high torque capacities and low maintenance requirements [77]. For

hybrid electric vehicles (HEVs), the use of BLDC motor drivers is widely studied to reduce fuel consumption while working in conjunction with internal combustion engines and to optimize battery charging. Research has shown that improvements in BLDC motor driver circuits enhance the state of charge of the battery and improve regenerative braking performance [78].

Currently, various studies are being conducted to further improve the performance and efficiency of BLDC motors. Advanced control techniques such as Direct Torque Control (DTC) and Field-Oriented Control (FOC) are being developed to increase the precision of BLDC motor control [67]. The torque-speed performance of BLDC motors directly affects the operating conditions of the vehicles.

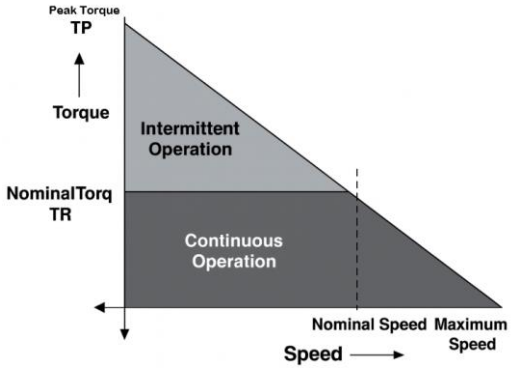

Figure 7. BLDC Motor Torque-Speed Characteristics Brushless direct current (BLDC) motors [79]

BLDC motors operate within two distinct regions: the Continuous Torque Zone and the Intermittent Torque Zone. The Continuous Torque Zone represents the operating range up to the motor's rated speed, during which the motor can operate at its specified nominal torque. Beyond the rated speed, the motor's torque-producing capability decreases while the output power remains largely constant. The Intermittent Torque Zone refers to the maximum torque capacity that the motor can provide for short-duration overload conditions. Due to their ability to deliver constant power over a wide speed range, BLDC motors offer high efficiency and performance in electric vehicle applications. Although these characteristics make BLDC motors highly suitable for electric vehicles, Permanent Magnet Synchronous Motors (PMSMs) also possess notable advantages in similar applications.

Permanent Magnet Synchronous Motor (PMSM)

In electric vehicle applications, PMSMs are considered a critical traction system option due to their ability to provide high torque while minimizing energy losses. For instance, the high power-to-weight ratio of PMSMs makes them an ideal choice for electric vehicles [80]. Additionally, PMSMs are distinguished by their low noise levels and high torque production capabilities, which enhance vehicle performance and improve the driving experience [81]. The structure of PMSMs, featuring permanent magnets in the rotor, provides high efficiency. These motors consist of two main components: the rotor, which is equipped with permanent magnets generating the magnetic field during operation, and the stator, which contains coils that conduct electric current to induce rotor rotation [82]. This structural design makes PMSMs both lighter and more compact, offering significant advantages in electric vehicle design. The operation of PMSMs is optimized through Field-Oriented Control (FOC), which allows independent control of torque and current components, enabling more precise motor operation [83]. This control method enhances speed and torque control, improving dynamic performance and optimizing energy efficiency in electric vehicles [84]. Another important advantage of PMSMs is their regenerative braking capability, which allows energy recovery during braking. In this process, the motor operates as a generator, converting kinetic energy into electrical energy and feeding it back to the battery [84]. This feature extends the driving range of electric vehicles and improves overall energy efficiency. In addition to enhancing vehicle performance, the use of PMSMs contributes to reducing environmental impact. Compared to conventional internal combustion engines, PMSMs produce lower emissions and generate less noise [85], playing a significant role in establishing electric vehicles as sustainable transportation solutions.

The utilization of PMSMs in electric vehicles offers numerous advantages, including high efficiency, low energy consumption, regenerative braking capability, and environmental benefits. Their structure and operating principles significantly enhance vehicle performance and serve as a crucial foundation for sustainable transportation solutions. As electric vehicles gain prominence as environmentally friendly transportation alternatives, the motor technologies at their core hold critical importance for performance, efficiency, and sustainability. In this context, PMSMs have become one of the most preferred motor types for electric vehicles, providing a structural and operational foundation for improving vehicle performance. The high power density and efficiency of PMSMs minimize energy consumption while generating less heat. Studies have shown that control algorithms have been developed to improve the energy efficiency of PMSMs, which function independently of motor parameters and significantly enhance energy savings [86]. Moreover, due to their high torque and power density, PMSMs improve acceleration performance in electric vehicles [87]. Another advantage of PMSMs is their low maintenance requirement. Since permanent magnets are used, these motors experience less wear compared to brushed motors, thereby lowering maintenance costs and extending motor lifespan. The development of control methods aimed at enhancing energy recovery at low speeds enables longer periods of efficient operation [88].

Structurally, PMSMs are ideally suited for electric vehicles. These motors primarily consist of a stator and a rotor, where the stator generates a magnetic field through electric current, and the rotor rotates under the influence of this field. This operational principle allows the motor to function with high efficiency. Studies have indicated that maintaining reactive power at zero can further enhance motor performance [89]. Such optimization techniques play

a critical role in improving the energy efficiency of electric vehicles. The operating principle of PMSMs is based on magnetic field interaction, where current in the stator induces a rotating magnetic field that drives rotor motion. This enables the motor to generate high torque while providing rapid response. It has been suggested that indirect stator control can reduce torque ripple, contributing to vehicle safety [90]. These control methods are considered effective strategies for improving electric vehicle performance. Moreover, PMSMs offer additional advantages through advanced control methods. Modern control techniques include various applications aimed at optimizing motor performance. Newly developed adaptive control methods enhance system robustness against parameter variations, leading to improved motor performance [91]. Such advanced approaches contribute to the efficient and reliable operation of electric vehicles. The figure presents the ideal torque characteristic curves for PMSMs [92].

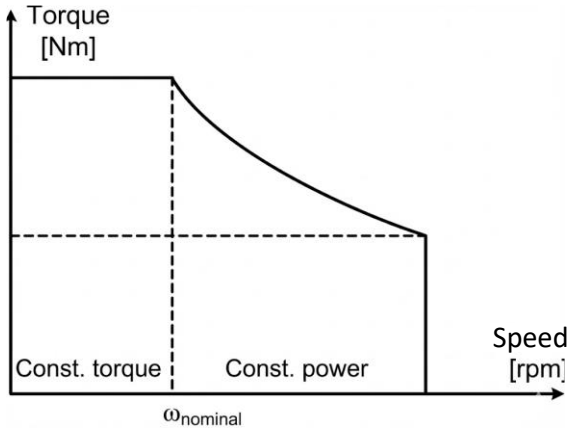

Figure 8. Ideal Torque Characteristic Curves for PMSM [92]

The ideal torque characteristic curve of PMSM motors illustrates two primary operating regions: the constant torque region and the constant power region. In the constant torque region, the motor produces a fixed torque up to its rated speed. This region is particularly important for applications requiring high torque at startup and low speeds. Beyond the rated speed, the motor enters the constant power region, where torque decreases inversely with speed. This characteristic enables the motor to maintain efficient operation even at high speeds. These features of PMSMs provide significant advantages in applications that demand high performance across a wide speed range, such as electric vehicles.

In PMSM design, magnet placement plays a critical role in torque ripple, efficiency, and power density. The optimization of magnetic topology is performed to improve torque production and minimize rotor losses. While conventional surface-mounted PMSMs are widely used due to their high power density and low losses, interior-mounted magnets offer lower harmonic components and improved torque ripple characteristics. The following figures illustrate different magnet placement strategies for PMSMs [93].

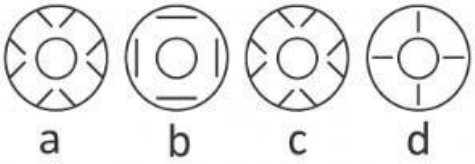

Figure 9. Different configurations of permanent magnet placement in the rotors of electrical machines: (a) V-type; (b) T-type; (c) Delta-type; and (d) Spoke-type arrangements [94].

However, due to the inherent operating principle of PMSMs, having a constant magnetic flux introduces certain operational limitations. Specifically, because of the magnetic properties of permanent magnets, flux-weakening capabilities are restricted, which may lead to power losses at high speeds. In addition, the use of rare-earth magnets in PMSMs presents a significant disadvantage in terms of sustainability, primarily due to their high costs and supply chain uncertainties. At this point, Wound-Field Synchronous Machines (WRSMs) offer considerable advantages compared to PMSMs and have attracted growing attention.

Wound Rotor Synchronous Machines (WRSM)

Wound Rotor Synchronous Machines (WRSMs) have attracted significant attention in the field of electric vehicle (EV) propulsion due to their unique advantages over Permanent Magnet Synchronous Machines (PMSMs). Unlike PMSMs, WRSMs do not rely on rare-earth materials, making them a more sustainable and cost-effective alternative while offering greater control over flux regulation and field weakening capabilities [84]. In WRSMs, field excitation is externally controlled, allowing dynamic adaptation to varying load and speed conditions, which is essential for efficient EV operation[85].

The fundamental principle of WRSMs lies in their ability to generate magnetic fields through rotor windings fed with direct current. This configuration provides a distinct advantage in operational flexibility, particularly in applications requiring high torque density and extended constant power speed range (CPSR) [86]. Traditional WRSMs have historically relied on brushes and slip rings to deliver excitation current to the rotor windings. However, recent advancements in brushless excitation techniques, such as inductive and capacitive power transfer, have significantly enhanced their reliability and efficiency [87]. The introduction of rotary transformer-based excitation systems has further improved field control efficiency while eliminating the maintenance challenges associated with conventional brush-based systems [88].

One of the most significant advantages of WRSMs in EV applications is their superior controllability compared to PMSMs. The ability to actively regulate the field current enables optimal energy usage under varying driving conditions, enhancing overall system efficiency [89]. Unlike PMSMs, whose field weakening capabilities are limited by the characteristics of permanent magnets, WRSMs can achieve a much broader CPSR, making them

ideal for automotive traction applications that demand high torque at low speeds and high efficiency at high speeds [90]. Additionally, WRSMs exhibit better thermal management capabilities due to their external excitation systems, reducing the risk of overheating in high-power applications [91].

Several recent studies have focused on improving the design and performance of WRSMs for EV applications. Research on high-frequency rotor designs has shown that segmented rotor structures can significantly increase power density while maintaining high efficiency [92]. Moreover, efforts to optimize the distribution of electromagnetic forces within the motor have contributed to the reduction of vibration and noise levels critical factors for passenger comfort in modern electric vehicles [93]. Another innovative approach involves the development of hybrid WRSM designs, combining wound field and reluctance torque components to enhance efficiency without the need for rare-earth materials [94].

The adoption of AI-based optimization techniques has also played a crucial role in advancing WRSM technology. Multidisciplinary design optimization (MDO) methods, including finite element analysis (FEA) and genetic algorithms, have enabled researchers to achieve optimal motor configurations that balance efficiency, torque performance, and thermal stability [95]. These computational approaches have been instrumental in the development of next-generation WRSMs capable of competing with PMSMs in terms of power density and operational flexibility [96].

Compared to PMSMs, WRSMs exhibit marginally lower peak efficiency due to additional losses in the rotor excitation system. However, when analyzed over a complete drive cycle, WRSMs demonstrate competitive energy efficiency, particularly under variable load conditions [97]. In real-world driving scenarios, WRSM-based EVs have shown lower overall energy consumption due to their ability to dynamically adjust field excitation and reduce losses during low-torque operation [98]. Additionally, advancements in sensorless control methods, such as mutual stator-rotor inductance techniques, have eliminated the need for physical sensors to estimate rotor position, further improving WRSM efficiency [99].

Many automotive manufacturers have already integrated WRSM technology into EV powertrains. Renault has successfully implemented WRSMs in models like the Renault Zoe, fully utilizing their field control and cost-effectiveness advantages [100]. Similarly, BMW has integrated WRSMs into its iX3 e-drive system, emphasizing their applicability as a high-performance alternative to PMSMs in modern EV architectures [101]. These applications provide strong evidence that WRSMs can meet the demands of automotive traction while addressing sustainability concerns associated with rare-earth-based machines [102]

Despite these advantages, WRSMs still face challenges that require further research. The additional copper losses associated with rotor excitation remain a limiting factor in achieving peak efficiency [103]. The presence of rotor windings in WRSMs brings certain challenges in terms of efficiency and thermal management. Copper losses occurring in rotor windings can potentially reduce the overall efficiency of the machine and cause an increase in internal heat. Therefore, complex cooling systems are required to effectively manage the heat generated in applications requiring high currents. Innovative solutions in cooling systems, such as automatic valve testing and the integration of rapid maintenance mechanisms, have a direct impact on the system's efficiency and reliability [95], [96]. Furthermore, the complexity of excitation control systems necessitates more sophisticated power electronics and control algorithms [104]. Controlling WRSMs in highspeed applications presents a complex challenge because it requires accurate determination of the rotor position. To overcome this challenge and ensure precise control, advanced observer-based control algorithms, such as the Luenberger observer, are being developed. These algorithms can perform high-precision position estimation based on data from low-resolution sensors. Such algorithms optimize the machine's performance under high-speed and variable load conditions, enabling effective use across a wider range of applications [97]. Future research directions should focus on advancing brushless excitation techniques, which play a critical role in overcoming limitations such as maintenance issues related to slip rings and brushes in conventional WRSMs. Another important consideration for WRSMs is the maintenance requirement arising from brush-ring systems. These mechanical contact elements, used to transfer energy to the rotor windings, wear out over time and require periodic maintenance. This situation can make the maintenance cycles of WRSMs more frequent compared to PMSMs and can shorten the system life, especially in high-speed applications. To overcome this challenge, research continues on alternative technologies such as brushless excitation systems and new materials that extend the life of brush-ring systems [97]. Recent developments in subharmonic magnetomotive force (SH-MMF) excitation have shown promising results in achieving brushless operation while maintaining high efficiency. Newly proposed winding schemes for brushless WRSMs enhance system reliability and reduce operational losses by providing efficient field excitation without physical contact [105]. Additionally, further investigation is needed to optimize rotor geometries, as different designs significantly impact electromagnetic performance, efficiency, and mechanical stability at high speeds. The adoption of cylindrical rotor structures has been identified as a viable alternative to traditional salient-pole designs, offering improved mechanical robustness and reduced centrifugal stress in high-speed traction applications [106].

In conclusion, WRSMs are emerging as a viable alternative to permanent magnet synchronous machines (PMSMs) in EV applications due to their cost-effectiveness, sustainability, and controllability. Although challenges such as excitation losses and the complexity of power transmission to the rotor persist, ongoing research on brushless excitation methods, AI-driven optimization, and hybrid excitation strategies is expected to enhance WRSM performance in the coming years [105]. Furthermore, improvements in rotor design, especially with cylindrical

rotor architectures, are projected to increase mechanical durability and operational efficiency, making WRSMs a strong candidate for next generation electric vehicle powertrains [106]. Figure 10 illustrates the structure of a WRSM.

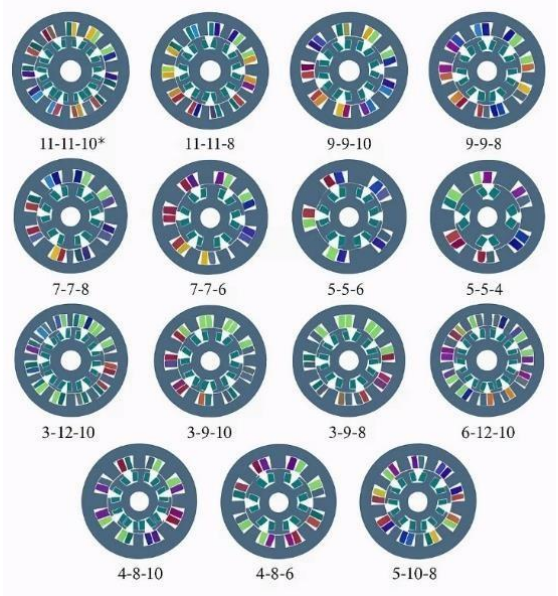

Figure 10. Structure of a Wound Rotor Synchronous Machine (WRSM) [98]

Performance Evaluation By Engine Power, Efficiency And Vehicle Segments

In electric vehicles, key technical parameters such as motor power, energy capacity, and weight have a direct and decisive impact on the vehicle's range, acceleration, and overall driving performance. In this section, a comparative analysis based on three commercially available electric vehicle models with different motor types is presented to examine how motor power varies according to efficiency and vehicle segments. Table 2 shows that the types of motors used in EVs offer different advantages depending on the power range and intended use. The selection of electric drive motors for EVs varies significantly depending on the power range and application type. BLDC motors are the most common choice for light EVs with power requirements between 1–15 kW, and they remain applicable for urban EVs 15–100 kW. However, their efficiency decreases with increasing power, making them unsuitable for large 100–250 kW and commercial (>250 kW) EV applications. PMSMs, owing to their high efficiency and power density, are the dominant motor type for both urban and large EVs and remain applicable for commercial EVs. IMs, although not very efficient at low power, are widely used in urban EVs and are among the best options for heavy-duty commercial EVs due to their robustness and cost-effectiveness. SRMs offer a low-cost solution and are suitable for medium power applications, but they are less preferred for very high-power EVs because of their control complexity. Finally, WRSMs, despite their structural complexity, are considered a viable alternative to PMSMs for power levels between 100–250 kW and are emerging as a strong option for commercial EV applications.

Table 2. Suitability Analysis of Motor Types According to Electric Vehicle Segments [99], [100], [101]

Motor Type	Light EVs (1–15 kW)	Urban EVs (15–100 kW)	Large EVs (100–250 kW)	Commercial EVs (250 kW and above)
BLDC	Most common	Applicable	Inefficient	Inadequate
PMSM	Feasible but costly	Most common	Most common	Applicable
IM	Not very efficient at low power	Common	Common in commercial EVs	Best option for heavy-duty EVs
SRM	Low cost	Suitable for medium power	Applicable, but PMSM or IM more common	Difficult to control at very high power
WRSM	Applicable but complex	Good option for medium power	Preferred as an alternative to PMSM	Strong alternative in commercial EVs

While BLDC motors are commonly preferred in low-power applications, PMSM motors stand out in medium- and high-power segments due to their high efficiency. In applications requiring power above 100 kW, such as commercial vehicles, induction motors (IM) are a significant choice due to their durability and cost advantages. SRM motors are applicable due to their low-cost structure, but they have limited application in high-power systems due to control difficulties. WRSM motors, on the other hand, are considered as an alternative to PMSMs especially in commercial and high-power vehicles, offering a suitable solution for high-torque applications thanks to their controlled magnetic field advantage.

Table 3 presents the technical specifications of commercially available EVs utilizing three different motor types. The WRSM used in the Renault ZOE provides a sustainable solution as it does not require rare-earth elements and offers field weakening capability; however, with its low motor power and limited maximum speed, it is suitable for urban use. The PMSM used in the Tesla Model 3 successfully balances high power output and maximum speed capacity, delivering both high efficiency and performance. Thanks to their high torque and low energy losses, PMSM motors are currently the most widely preferred motor type in electric vehicles. The induction motor used in the front axle of the Tesla Model X offers advantages particularly in situations requiring high load capacity and extended range. While induction motors stand out for their durability and ease of maintenance, they typically serve a supporting role in dual-motor systems due to their lower efficiency compared to PMSMs.

The comparison of these three different motor types clearly demonstrates that motor architecture choices in electric vehicles are shaped not only by performance but also by criteria such as efficiency, cost, and sustainability. WRSM motors offer efficient systems suitable for urban use, PMSM motors provide both range and performance advantages in the mid-segment, while induction motors play a supportive role in heavier and more powerful systems, although they are less efficient than PMSMs.

In recent years, significant innovations have been reported in both the design and control of PMSM, BLDC, and induction motors. In PMSMs, rotor/stator topology

optimization has been applied to improve torque quality, while advanced control algorithms such as MPC and DTC have been introduced to enhance energy efficiency. Parametric optimization studies have also been carried out to meet application-specific performance requirements [102], [103], [104], [105]. In BLDC motors, AI-based control methods, advanced observer designs, and integration into renewable energy systems have attracted attention, while new DTC approaches have been developed to reduce torque ripple [106], [107], [108], [109]. For induction motors, multi-sensor-based fault diagnosis and structural improvements have been proposed to increase reliability and performance [110], [111]. Furthermore, comparative studies between PMSM and BLDC motors under different operating conditions provide useful guidance in selecting the most suitable motor type for specific applications [112].

Table 3. Technical Specifications of Electric Vehicles According to Different Motor Types [8], [9]

Model	Motor Type	Motor Power (kW)	Max. Speed (km/h)	Energy Capacity (kWh)	Range (km)	Weight (kg)
Renault ZOE	WRSM	80	135	41	300	1.468
Tesla Model 3	PMSM (back)	208	261	81.33	487	1.824
Tesla Model X	IMA (front)	196	210	110	576	2.960

The power to weight ratio comparison presented in Figure 11 evaluates the performance capabilities of electric vehicles with different motor types in terms of mass efficiency. When examining the capacity values of the reference WRSM-powered Renault ZOE, it offers a compact structure aligned with the goal of urban driving and low power consumption, but it can be characterized by limited dynamic response and acceleration performance. In comparison, the PMSM powered Tesla Model 3 demonstrates approximately twice the power-to-weight ratio, indicating a better balance between efficiency and performance compared to the other two vehicles. The primary sources of this advantage are the high torque density, low-loss operating principle, and compact design of PMSM motors. Although the induction motor-equipped Tesla Model X provides higher absolute power than the WRSM, it exhibits a lower efficiency profile. This indicates that despite the durability and low maintenance benefits of induction motors, they may present limitations in terms of performance-to-mass efficiency in high-mass systems.

In conclusion, while WRSM motors offer advantages in sustainability and cost, PMSM motors can be considered the most balanced and superior solution in terms of performance and energy density.

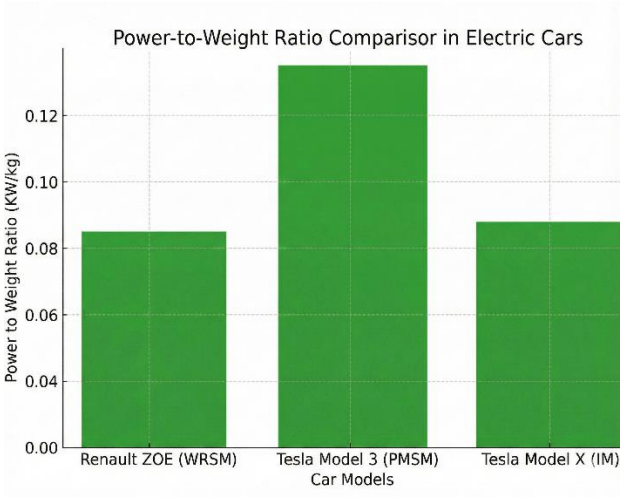

Figure 11. Comparison of Power-to-Weight Ratio by Motor Types in Electric Vehicles

Figure 12 illustrates the relationship between motor power and energy consumption in electric vehicles. As a general trend, it is observed that energy consumption increases with motor power. This is particularly evident in the case of the Tesla Model X, where the 196 kW IM motor demonstrates the high energy demand of powerful systems with an energy consumption of approximately 19.1 kWh per 100 km. In contrast, the Renault ZOE, equipped with an 80 kW WRSM motor, consumes around 13.7 kWh per 100 km, indicating that lower-power motors tend to operate more efficiently in urban driving conditions. However, a notable exception is the Tesla Model 3, which maintains a relatively low energy consumption of 16.7 kWh per 100 km despite its high motor power of 208 kW. This highlights the superior efficiency of PMSM technology, suggesting that PMSM motors offer an optimal balance between performance and energy management.

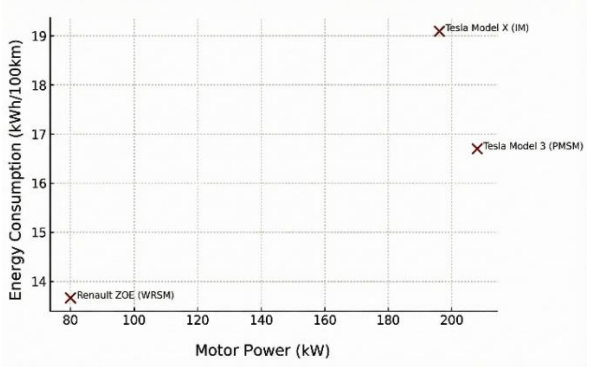

Figure 12. The Relationship Between Motor Power and Energy Consumption in Electric Vehicles

Figure 13 presents the relationship between energy capacity and driving range for the vehicles listed in Table 2 across different segments, using a dual-axis representation. As a general trend, an increase in energy capacity corresponds to an increase in driving range. However, this relationship is not linear, and the efficiency with which each segment utilizes its energy capacity varies significantly. For instance, the Renault ZOE (economy segment) offers a driving range of 300 km with a 41 kWh battery, yielding approximately 7.3 km per kWh and demonstrating a highly efficient energy profile. In contrast, the Tesla Model X (luxury segment) delivers a range of 576 km with a 110 kWh battery, resulting in a lower efficiency of approximately 5.2 km per kWh. The Tesla Model 3 (mid-range segment), equipped with an 81.33 kWh battery, provides a range of 487 km, translating to around 6.0 km per kWh, indicating a balanced performance between the two extremes. This comparison reveals that high battery capacity alone is not sufficient to ensure extended range; vehicle weight, aerodynamic design, motor efficiency, and energy management systems also play a direct and significant role. Economy segment vehicles tend to achieve greater efficiency due to their lighter and simpler construction, whereas luxury segment vehicles, with a focus on comfort and performance, generally exhibit higher energy consumption.

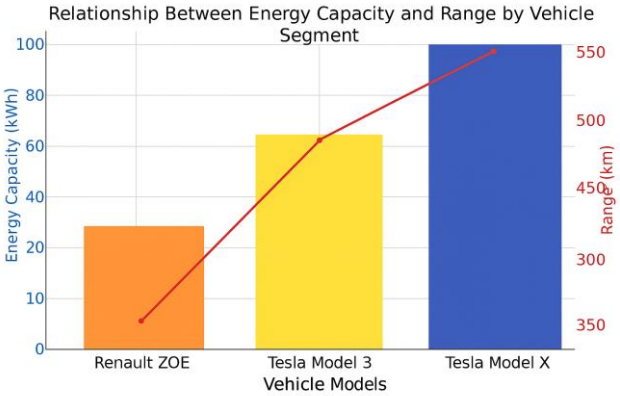

Figure 13. Comparison of Energy Capacity and Driving Range of Vehicles Across Different Segments

In terms of energy efficiency, the distance an electric vehicle can travel per unit of energy (kWh) is measured using the km/kWh metric. This value reflects the effectiveness of both the motor type and the battery management system. The Renault ZOE, with a 41 kWh battery capacity and a driving range of 300 km, achieves approximately 7.32 km/kWh, making it the most efficient model in this comparison. This high efficiency can be attributed to the WRSM motor's stable operation at low speeds, the vehicle's lightweight structure, and its simple, city-focused design.

The Tesla Model 3, with an 81.33 kWh battery and a range of 487 km, yields an efficiency of 5.99 km/kWh. Despite its high power output, the PMSM motor used in this model provides efficient propulsion, offering an impressive balance between efficiency and performance for the mid-range segment. On the other hand, the Tesla Model X delivers a range of 576 km with a 110 kWh battery, resulting in approximately 5.24 km/kWh. While this value is not below expectations for the luxury segment, the vehicle's high weight, aerodynamic drag, and spacious interior design contribute to increased energy consumption.

In conclusion, compact vehicles equipped with WRSM systems stand out in terms of efficiency by delivering longer ranges per unit of energy. Mid-range models using PMSM motors offer higher performance with only a slight compromise in efficiency. In the luxury segment, however, energy efficiency becomes a secondary consideration, with greater emphasis placed on driving comfort and high torque output.

Conclusion

Electric vehicle technologies have become one of the fundamental building blocks of sustainable transportation systems and have garnered significant interest in recent years, both in academic research and industrial applications. In this context, the structure and performance of traction motors play a crucial role in determining the energy efficiency, driving range, and cost-effectiveness of electric vehicles. Considering the technical advantages, limitations, and segment-specific usage scenarios of different motor types, there is a growing need for systematic and multidimensional analyses in this field.

This review study presents a comparative analysis of the most commonly used motor types in electric vehicles Wound Rotor Synchronous Motors (WRSM), Permanent Magnet Synchronous Motors (PMSM), and Induction Motors (IM) in terms of technical characteristics, energy efficiency, and vehicle segments. The analyses reveal that motor power is one of the most critical parameters affecting the performance of electric vehicles; however, this power must be evaluated in conjunction with vehicle weight, battery capacity, motor type, and driving profile. In terms of power to weight ratio, mid-range models equipped with PMSM motors demonstrate the best performance, while WRSM-equipped vehicles, despite having lower power-to-weight ratios, stand out in terms of sustainability and efficiency. In the motor power energy consumption analysis, PMSM motors tend to exhibit low energy consumption despite their high power output, which explains their widespread use in modern electric vehicles. Segment-based evaluations show that economy-class vehicles are the most efficient in terms of driving range per unit of energy, highlighting the advantages of combining low power with lightweight design for urban use. In contrast, vehicles in the luxury and high-performance segments prioritize torque, comfort, and traction capabilities over energy efficiency, as reflected by their lower km/kWh values despite larger battery capacities. Overall, WRSM motor systems present significant potential in terms of sustainability and long-term cost advantages due to their independence from rare earth materials, field weakening capability, and high thermal tolerance.

Although their commercial adoption remains limited, it is likely that WRSM motors will gain a stronger position in

the market in the future, supported by advanced control algorithms and compact cooling systems.

In conclusion, this study demonstrates that motor power in electric vehicles is not only a determinant of performance but also plays a key role in efficiency, energy consumption, and segment-specific design decisions. It emphasizes the need for further research and development efforts to enable the more effective use of alternative motor systems such as WRSM.

Future Prospect

In electric vehicles, Wound Rotor Synchronous Motor (WRSM) technology offers significant environmental and strategic advantages due to a structure that does not require rare earth elements, its controllable magnetic flux, and its ability to operate over a wide speed range. However, despite these benefits, WRSM systems currently have a limited presence in the market. The primary reasons for this include the complexity of commutation, thermal management challenges of rotor windings, the limited lifespan of slip ring systems, and the inadequacy of high-speed control algorithms. These limitations have caused WRSM to lag behind PMSM and IM technologies in commercial applications, despite its potential.

For WRSM technology to achieve broader adoption in the future, the development of new materials and designs that reduce the maintenance requirements of slip ring systems will be critical. In addition, smart cooling systems capable of actively monitoring and managing the thermal loads of rotor windings could facilitate the integration of WRSM into heavy-duty vehicle segments. Furthermore, vector-controlled inverter software and adaptive torque management algorithms that optimize WRSM efficiency could provide significant advantages, particularly in high-speed driving scenarios. The flux-weakening capability of WRSM motors also presents an opportunity for seamless integration with battery management systems to support range extension strategies, creating new possibilities for efficiency- and range-focused vehicle designs.

Considering the increasing sustainability-driven policies in European and Asian markets aimed at reducing dependence on rare earth materials, WRSM-based motor systems are expected to become more widespread in the post-2025 period, particularly in commercial vehicles, fleet transportation, and long-range passenger car segments. In conclusion, when supported by smarter drive algorithms, durable commutation components, and efficient cooling systems, WRSM motors have the potential to establish a strong position within the electric vehicle ecosystem as a sustainable and high-performance alternative

Ethics committee approval and conflict of interest statement

"There is no need to obtain permission from the ethics committee for the article prepared"

"There is no conflict of interest with any person / institution in the article prepared"

Authors' Contributions

Orhan A: Study conception and design, Drafting of manuscript, Critical revision, Other contribution

Ünal S: Study conception and design, Drafting of manuscript, Critical revision, Other contribution

Akbal A: Study conception and design, Drafting of manuscript, Critical revision, Other contribution

Doğan K: Study conception and design, Drafting of manuscript, Critical revision, Other contribution

Kayaoğlu M: Study conception and design, Drafting of manuscript, Critical revision, Other contribution

Bıyık H: Study conception and design, Drafting of manuscript, Critical revision, Other contribution

References

[1] F. Kong and X. Liu, "Sustainable Transportation with Electric Vehicles," *Found. Trends Electr. Energy Syst.*, vol. 2, no. 1, pp. 1–132, 2017, doi: 10.1561/3100000016.

[2] "Metropolleri dönüştürmek ulaşımda zafere işaret eder," Dünya Gazetesi.

[3] A. SADIKI, "Control of Permanent Magnet Syncronous Motor in Electric Vehicles," *Yöktez*, 2022.

[4] A. Dall-Orsoletta, P. Ferreira, and G. Gilson Dranka, "Low-carbon technologies and just energy transition: Prospects for electric vehicles," *Energy Convers. Manag. X*, vol. 16, no. May, 2022, doi: 10.1016/j.ecmx.2022.100271.

[5] W. J. Sweeting, A. R. Hutchinson, and S. D. Savage, "Factors affecting electric vehicle energy consumption," *Int. J. Sustain. Eng.*, vol. 4, no. 3, pp. 192–201, 2011, doi: 10.1080/19397038.2011.592956.

[6] H. J, A. R. Y, P. S, and A. K. L, "Electric vehicle adoption toward sustainable transportation solution: key drivers and implications," *Int. J. Energy Sect. Manag.*, 2024, doi: 10.1108/IJESM-04-2024-0015.

[7] M. Gobbi, A. Sattar, R. Palazzetti, and G. Mastinu, "Traction motors for electric vehicles: Maximization of mechanical efficiency – A review," *Appl. Energy*, vol. 357, p. 122496, Mar. 2024, doi: 10.1016/j.apenergy.2023.122496.

[8] Tesla, "Model 3 2024+ owner's manual," 2024.

[9] Tesla, "Model X 2021-2024 owners manual n.d."

[10] N. Leaf, "Dolu Batarya n.d.".

[11] Türkiye BMW, "Yeni BMW i3 Elektrikli ve Heyecan Verici n.d."

[12] "Audi e-tron."

[13] A. Babangida and P. Szemes, "Electric Vehicle Modeling and Simulation of Volkswagen Crafter with 2.0 TDI CR Diesel Engine," *Rcent Innov Mechatronics 2021*, p. 8, doi: 10.17667/riim.2021.1/1.

[14] A. Garcia, S. Filipe, C. Fernandes, C. Estevão, and G. Ramos, "The new Taycan and the new Taycan Cross Turismo".
[15] Ford, "Ford Mustang," 2024.
[16] Chevrolet, "Bolt EUV Owners Manual 2022".
[17] Z. Cao, A. Mahmoudi, S. Kahourzade, and W. L. Soong, "An Overview of Electric Motors for Electric Vehicles," in *2021 31st Australasian Universities Power Engineering Conference (AUPEC)*, IEEE, Sep. 2021, pp. 1–6. doi: 10.1109/AUPEC52110.2021.9597739.
[18] M. S. Patil and S. S. Dhamal, "A Detailed Motor Selection for Electric Vehicle Traction System," *2019 Third Int. Conf. I-SMAC (IoT Soc. Mobile, Anal. Cloud)*, pp. 679–684, 2019.
[19] Z. Qianfan, C. Shumei, and T. Xinjia, "Hybrid Switched Reluctance Motor Applied in Electric Vehicles," no. 2, pp. 359–363, 2007.
[20] Y. Xiao, M. Nemec, L. J. Borle, V. Sreeram, and H. H. C. Iu, "Regenerative braking of series-wound brushed DC electric motors for electric vehicles," *Proc. 2012 7th IEEE Conf. Ind. Electron. Appl. ICIEA 2012*, pp. 1657–1662, 2012, doi: 10.1109/ICIEA.2012.6360991.
[21] A. Zarma, A. A. Galadima, M. A. Aminu, and E. Engineering, "A Review of Motors for Electric Vehicles," in *International Power Engineering Exhibition & Conference*, 2019, pp. 11–14.
[22] P. Oy, "Sähköautojen moottorien purku ja kierrätys 2023".
[23] J. Edmondson, S. Siddiqi, and M. Takahashi, "Electric Motors for Electric Vehicles 2025-2035: Technologies, Materials, Markets, and Forecasts," IDTechEx.
[24] A. Gupta, T. Kim, T. Park, and C. Lee, "Intelligent direct torque control of brushless DC motors for hybrid electric vehicles," in *5th IEEE Vehicle Power and Propulsion Conference, VPPC '09*, 2009. doi: 10.1109/VPPC.2009.5289860.
[25] Y. Zhu, X. Cao, and S. Cui, "Design of Brushless DC motor Drive System for Electric Vehicle Applications," 2016. doi: 10.2991/ameii-16.2016.219.
[26] M. C. Joshi and S. Samanta, "Modeling and control of bidirectional DC-DC converter fed PMDC motor for electric vehicles," in *2013 Annual IEEE India Conference, INDICON 2013*, 2013. doi: 10.1109/INDCON.2013.6726091.
[27] R. G. Chougale and C. R. Lakade, "Regenerative braking system of electric vehicle driven by brushless DC motor using fuzzy logic," in *IEEE International Conference on Power, Control, Signals and Instrumentation Engineering, ICPCSI 2017*, 2018. doi: 10.1109/ICPCSI.2017.8392101.
[28] N. Hashemnia and B. Asaei, "Comparative study of using different electric motors in the electric vehicles," in *Proceedings of the 2008 International Conference on Electrical Machines, ICEM'08*, 2008. doi: 10.1109/ICELMACH.2008.4800157.
[29] D. M. B. and M. K. Kazimierczuk, "DC-DC CONVERTERS FOR ELECTRIC VEHiCLE APPLICATIONS," *IEEE Trans. Veh. Technol.*, vol. 5, no. 4, pp. 1–1, 2018.
[30] N. A. Metin, A. Boyar, and E. Kabalci, "Design and Analysis of Bi-directional DC-DC Driver for Electric Vehicles," in *Proceedings - 2019 IEEE 1st Global Power, Energy and Communication Conference, GPECOM 2019*, 2019. doi: 10.1109/GPECOM.2019.8778532.
[31] D. Cajander and H. Le-Huy, "Design and optimization of a torque controller for a switched reluctance motor drive for electric vehicles by simulation," *Math. Comput. Simul.*, vol. 71, no. 4–6, pp. 333–344, 2006, doi: 10.1016/j.matcom.2006.02.025.
[32] A. T. Waghe and S. K. Patil, "A bidirectional DC-DC converter fed separately excited DC motor electric vehicle application," in *International Conference on Emerging Trends in Information Technology and Engineering, ic-ETITE 2020*, 2020. doi: 10.1109/ic-ETITE47903.2020.421.
[33] K. Sedef, A. Maheri, A. Daadbin, and M. Yilmaz, "A comparative study of the performance of DC permanent magnet and AC induction motors in urban electric cars," in *2nd International Symposium on Environment Friendly Energies and Applications, EFEA 2012*, 2012. doi: 10.1109/EFEA.2012.6294077.
[34] L. Zaccarian, "DC motors : dynamic model and control techniques Magnetic considerations on rotating coils Magnetic field and conductors".
[35] N. Mahajan and S. Deshpande, "Study of Nonlinear Behavior of DC Motor Using," *Int J Sci Res Publ*, vol. 3, pp. 1–6, 2013.
[36] M. M. Hussain, A. Rashid Mustafa, M. A. Chaudary, and A. Razaq, "Design and Implementation of Hybrid Vehicle using Control of DC Electric Motor," in *2019 54th International Universities Power Engineering Conference, UPEC 2019 - Proceedings*, 2019. doi: 10.1109/UPEC.2019.8893604.
[37] C. S. Hearn, D. A. Weeks, R. C. Thompson, and D. Chen, "Electric vehicle modeling utilizing DC motor equations," in *IEEE/ASME International Conference on Advanced Intelligent Mechatronics, AIM*, 2010. doi: 10.1109/AIM.2010.5695785.
[38] A. Al Mamun, S. Arfin, and S. Khan, "High gain DC-DC converter for three-wheeler electric vehicles," in *2021 IEEE International IOT, Electronics and Mechatronics Conference, IEMTRONICS 2021 - Proceedings*, 2021. doi: 10.1109/IEMTRONICS52119.2021.9422579.
[39] B. Carson Groen, "Investigation of DC Motors for Electric and Hybrid Electric Motor Vehicle Applications Using an Infinitely Variable Transmission Benjamin," Brigham Young University, 2011.
[40] M. C. Joshi, S. Samanta, and G. Srungavarapu, "Battery ultracapacitor based DC motor drive for electric vehicles," in *TENSYMP 2017 - IEEE*

International Symposium on Technologies for Smart Cities, 2017. doi: 10.1109/TENCONSpring.2017.8070057.

[41] T. Kim, H. W. Lee, L. Parsa, and M. Ehsani, "Optimal power and torque control of a brushless DC (BLDC) motor/generator drive in electric and hybrid electric vehicles," in *Conference Record - IAS Annual Meeting (IEEE Industry Applications Society)*, 2006. doi: 10.1109/IAS.2006.256695.

[42] S. I. Urazov, S. A. Ivanova, and O. I. Khalupo, "The calculation of asynchronous motors characteristics based on the T-shaped equivalent circuit according to catalogued data," *IOP Conf. Ser. Earth Environ. Sci.*, vol. 949, no. 1, 2022, doi: 10.1088/1755-1315/949/1/012130.

[43] H. Gokozan, "Traction Motors and Motors Drivers Used in Electric Vehicles," *Eur. J. Sci. Technol.*, vol. 1, no. July, 2020.

[44] P. D. Patel and S. N. Pandya, "Energy Regeneration during Deceleration of Direct Torque Control of Induction Motor Drive for Electric Vehicles," in *Proceedings of 2019 3rd IEEE International Conference on Electrical, Computer and Communication Technologies, ICECCT 2019*, 2019. doi: 10.1109/ICECCT.2019.8869494.

[45] H. B. Ertan, M. S. Siddique, S. Koushan, and B. J. Azuaje-Berbeci, "Designing High Power Density Induction Motors for Electric Propulsion," in *2022 IEEE 20th International Power Electronics and Motion Control Conference, PEMC 2022*, 2022. doi: 10.1109/PEMC51159.2022.9962892.

[46] V. K. Pavuluri, X. Wang, J. Long, G. Zhuo, and W. Lian, "Field Oriented Control of Induction Motors Using Symmetrical Optimum Method with Applications in Hybrid Electric Vehicles," in *2015 IEEE Vehicle Power and Propulsion Conference, VPPC 2015 - Proceedings*, 2015. doi: 10.1109/VPPC.2015.7352948.

[47] A. A. Mahapatra and S. Gopalakrishna, "Regenerative braking in induction motor drives in applications to electric vehicles," in *2014 IEEE Students' Conference on Electrical, Electronics and Computer Science, SCEECS 2014*, 2014. doi: 10.1109/SCEECS.2014.6804425.

[48] S. Cui, C. Liang, and L. Song, "Study on efficiency calculation model of induction motors for electric vehicles," in *2008 IEEE Vehicle Power and Propulsion Conference, VPPC 2008*, 2008. doi: 10.1109/VPPC.2008.4677791.

[49] S. Jose and P. P. Rajeevan, "MTPA Based Direct Torque Control for Energy-Efficient Operation of Induction Motors in Electric Vehicles," in *2021 IEEE Transportation Electrification Conference, ITEC-India 2021*, 2021. doi: 10.1109/ITEC-India53713.2021.9932448.

[50] M. Bagheri, E. Farjah, and T. Ghanbari, "Selective Utilized Phase Number of Multiphase Induction Motors Strategy to Enhance Electric Vehicles' Drive Range," in *2021 12th Power Electronics, Drive Systems, and Technologies Conference, PEDSTC 2021*, 2021. doi: 10.1109/PEDSTC52094.2021.9405866.

[51] T. J. Fu and W. F. Xie, "Torque control of induction motors for hybrid electric vehicles," in *Proceedings of the American Control Conference*, 2006. doi: 10.1109/acc.2006.1657668.

[52] M. Sowmiya and S. H. Thilagar, "Performance Enhancement of Electric Vehicles using Vector Controlled Multiphase Induction Motor," in *Proceedings of 2018 IEEE International Conference on Power Electronics, Drives and Energy Systems, PEDES 2018*, 2018. doi: 10.1109/PEDES.2018.8707930.

[53] P. A. Aaliya Farzana and V. R. Bindu, "Regenerative Braking of Switched Reluctance Motor for Electric Vehicle Application," in *SPICES 2022 - IEEE International Conference on Signal Processing, Informatics, Communication and Energy Systems*, 2022. doi: 10.1109/SPICES52834.2022.9774223.

[54] Y. Zhu, H. Wu, and C. Zhen, "Regenerative braking control under sliding braking condition of electric vehicles with switched reluctance motor drive system," *Energy*, vol. 230, 2021, doi: 10.1016/j.energy.2021.120901.

[55] H. Cheng, H. Chen, Q. Wang, S. Xu, and S. Yang, "Design and control of switched reluctance motor drive for electric vehicles," in *2016 14th International Conference on Control, Automation, Robotics and Vision, ICARCV 2016*, 2016. doi: 10.1109/ICARCV.2016.7838783.

[56] R. M. Abdel-Fadil and L. Számel, "Direct Instantaneous Torque Control of the Switched Reluctance Motor for Electric Vehicles Applications Using Fuzzy Logic Control," *Acta Tech. Jaurinensis*, vol. 12, no. 2, 2019, doi: 10.14513/actatechjaur.v12.n2.496.

[57] X. Wang *et al.*, "Design of a wide speed range control strategy of switched reluctance motor for electric vehicles," in *2015 IEEE International Conference on Information and Automation, ICIA 2015 - In conjunction with 2015 IEEE International Conference on Automation and Logistics*, 2015. doi: 10.1109/ICInfA.2015.7279301.

[58] A. Kumar and B. Singh, "DTC Based Solar fed SRM Drive for Electric Vehicle with Regenerative Braking Employing Zeta Converter," in *2021 IEEE 6th International Conference on Computing, Communication and Automation, ICCCA 2021*, 2021. doi: 10.1109/ICCCA52192.2021.9666314.

[59] M. H. Abhiseka and S. Riyadi, "Implementation of Magnetizing-Freewheeling Control Strategy to Increase SRM Regenerative Braking Performance in a Low-Speed Operation," in *ICITEE 2022 - Proceedings of the 14th International Conference on Information Technology and Electrical Engineering*, 2022. doi: 10.1109/ICITEE56407.2022.9954116.

[60] M. Sun, H. Chen, W. Yan, H. Cheng, and Z. Liu, "Design and Optimization of Switched Reluctance Motor for Propulsion System of Small Electric Vehicle," in *2016 IEEE Vehicle Power and Propulsion Conference, VPPC 2016 - Proceedings*, 2016. doi: 10.1109/VPPC.2016.7791657.

[61] P. Rafajdus, P. Dubravka, A. Peniak, J. Saitz, and L. Szabóo, "Design procedure of switched reluctance motor used for electric car drive," in *2014 International Symposium on Power Electronics, Electrical Drives, Automation and Motion, SPEEDAM 2014*, 2014. doi: 10.1109/SPEEDAM.2014.6871986.

[62] R. M. Pindoriya, B. S. Rajpurohit, R. Kumar, and K. N. Srivastava, "Comparative analysis of permanent magnet motors and switched reluctance motors capabilities for electric and hybrid electric vehicles," in *2018 IEEMA Engineer Infinite Conference, eTechNxT 2018*, 2018. doi: 10.1109/ETECHNXT.2018.8385282.

[63] R. Abdel-Fadil and L. Szamel, "Enhancement of the switched reluctance motor performance for electric vehicles applications using predictive current control," in *CANDO-EPE 2018 - Proceedings IEEE International Conference and Workshop in Obuda on Electrical and Power Engineering*, 2018. doi: 10.1109/CANDO-EPE.2018.8601168.

[64] R. H. S. Vrenken *et al.*, "Switched reluctance motor drive for full electric vehicles - Part I: Analysis," in *2013 8th International Conference and Exhibition on Ecological Vehicles and Renewable Energies, EVER 2013*, 2013. doi: 10.1109/EVER.2013.6521605.

[65] H. Mashiko and K. Akatsu, "Design of Switched Reluctance Motors for electric hand tools," in *Proceedings - 2016 22nd International Conference on Electrical Machines, ICEM 2016*, 2016. doi: 10.1109/ICELMACH.2016.7732733.

[66] V. Indragandhi and L. Ashok Kumar, "Artificial intelligence based speed control of SRM for hybrid electric vehicles," in *2018 8th International Conference on Power and Energy Systems, ICPES 2018*, 2018. doi: 10.1109/ICPESYS.2018.8626982.

[67] D. Mohanraj *et al.*, "A Review of BLDC Motor: State of Art, Advanced Control Techniques, and Applications," *IEEE Access*, vol. 10, pp. 54833–54869, 2022, doi: 10.1109/ACCESS.2022.3175011.

[68] L. Vijayaraja, R. Dhanasekar, K. Harini, T. Hemapriya, S. Subhasri, and R. Kesavan, "Performance Analysis of Electric Vehicle using BLDC Motor Drive," in *2023 7th International Conference on Intelligent Computing and Control Systems (ICICCS)*, IEEE, May 2023, pp. 1832–1836. doi: 10.1109/ICICCS56967.2023.10142305.

[69] Mohd Azri Abd Aziz *et al.*, "A Review on BLDC Motor Application in Electric Vehicle (EV) using Battery, Supercapacitor and Hybrid Energy Storage System: Efficiency and Future Prospects," *J. Adv. Res. Appl. Sci. Eng. Technol.*, vol. 30, no. 2, pp. 41–59, Apr. 2023, doi: 10.37934/araset.30.2.4159.

[70] W. Khan-Ngern, W. Keyoonwong, N. Chatsiriwech, P. Sangnopparat, P. Mattayaboon, and P. Worawalai, "High Performance BLDC Motor Control for Electric Vehicle," in *2018 International Conference on Engineering, Applied Sciences, and Technology (ICEAST)*, IEEE, Jul. 2018, pp. 1–4. doi: 10.1109/ICEAST.2018.8434499.

[71] S. S. Srinivasan, N. R. . Lakshanasri, S. M. Setty, P. Dubey, A. Singh, and S. Senthilmurugan, "BLDC Drive for EV Application," *J. Phys. Conf. Ser.*, vol. 2007, no. 1, p. 012059, Aug. 2021, doi: 10.1088/1742-6596/2007/1/012059.

[72] Lin Bai, "Electric drive system with BLDC motor," in *2011 International Conference on Electric Information and Control Engineering*, IEEE, Apr. 2011, pp. 359–363. doi: 10.1109/ICEICE.2011.5777507.

[73] M. AKAR, M. EKER, and F. AKIN, "BLDC Motor Design and Application for Light Electric Vehicle," *Afyon Kocatepe Univ. J. Sci. Eng.*, Apr. 2021, doi: 10.35414/akufemubid.889877.

[74] M. A. Hassanin, F. E. Abdel-Kader, S. I. Amer, and A. E. Abu-Moubarka, "Operation of Brushless DC Motor to Drive the Electric Vehicle," in *2018 Twentieth International Middle East Power Systems Conference (MEPCON)*, IEEE, Dec. 2018, pp. 500–503. doi: 10.1109/MEPCON.2018.8635158.

[75] P. Vishnu Sidharthan and Y. Kashyap, "Brushless DC Hub Motor Drive Control for Electric Vehicle Applications," in *2020 First International Conference on Power, Control and Computing Technologies (ICPC2T)*, IEEE, Jan. 2020, pp. 448–453. doi: 10.1109/ICPC2T48082.2020.9071469.

[76] N. Shrivastava and A. Brahmin, "Design of 3-Phase BLDC Motor for Electric Vehicle Application by Using Finite Element Simulation," *Int. J. Emerg. Technol. Adv. Eng.*, vol. 4, no. 1, pp. 140–145, 2014.

[77] S. Krishnamoorthy and P. P. K. Panikkar, "A comprehensive review of different electric motors for electric vehicles application," *Int. J. Power Electron. Drive Syst.*, vol. 15, no. 1, p. 74, Mar. 2024, doi: 10.11591/ijpeds.v15.i1.pp74-90.

[78] S.-C. Kim, N. Sangam, S. Pagidipala, and S. R. Salkuti, "Design and Analysis of BLDC Motor Driver for Hybrid Electric Vehicles," 2022, pp. 297–311. doi: 10.1007/978-981-16-7794-6_12.

[79] B. Darmono, H. Pranoto, and Z. Arifin, "Torque Analysis of 2 KW BLDC (Brushless Direct Current) Motor with Speed Variations in Electric Cars E-Falco," *Int. J. Adv. Technol. Mech. Mechatronics Mater.*, vol. 2, no. 2, pp. 76–86,

Nov. 2021, doi: 10.37869/ijatec.v2i2.47.

[80] G. S. Lakshmi, O. Rubanenko, M. L. Swarupa, and K. Deepika, "Analysis of ANPCI & DCMLI fed to PMSM Drive for Electric Vehicles," in *2020 IEEE India Council International Subsections Conference (INDISCON)*, IEEE, Oct. 2020, pp. 254–259. doi: 10.1109/INDISCON50162.2020.00059.

[81] O. E. Özçiflikçi, M. Koç, S. Bahçeci, and S. Emiroğlu, "Overview of PMSM control strategies in electric vehicles: a review," *Int. J. Dyn. Control*, vol. 12, no. 6, pp. 2093–2107, Jun. 2024, doi: 10.1007/s40435-023-01314-2.

[82] R. Morales-Caporal, M. E. Leal-Lopez, J. de Jesus Rangel-Magdaleno, O. Sandre-Hernandez, and I. Cruz-Vega, "Direct torque control of a PMSM-drive for electric vehicle applications," in *2018 International Conference on Electronics, Communications and Computers (CONIELECOMP)*, IEEE, Feb. 2018, pp. 232–237. doi: 10.1109/CONIELECOMP.2018.8327204.

[83] R. Sinha and H. Misra, "Control of PMSM driven Electric Vehicle for Indian Drive Cycle," in *2021 National Power Electronics Conference (NPEC)*, IEEE, Dec. 2021, pp. 01–06. doi: 10.1109/NPEC52100.2021.9672473.

[84] U. Gupta, D. K. Yadav, and D. Panchauli, "Field Oriented Control of PMSM during Regenerative Braking," in *2019 Global Conference for Advancement in Technology (GCAT)*, IEEE, Oct. 2019, pp. 1–5. doi: 10.1109/GCAT47503.2019.8978361.

[85] D. Karboua, T. Belgacem, Z. H. Khan, and C. Kellal, "Robust performance comparison of PMSM for flight control applications in more electric aircraft," *PLoS One*, vol. 18, no. 7, p. e0283541, Jul. 2023, doi: 10.1371/journal.pone.0283541.

[86] Y. Lu, Z. Jiang, C. Chen, and Y. Zhuang, "Energy efficiency optimization of field-oriented control for PMSM in all electric system," *Sustain. Energy Technol. Assessments*, vol. 48, p. 101575, Dec. 2021, doi: 10.1016/j.seta.2021.101575.

[87] R. E. K. Meesala, S. Athikkal, P. Pradhan, S. Prasad, and A. Prasad, "Modified Direct Torque Control of PMSM Drive for Electric Vehicle Application," in *2021 IEEE Madras Section Conference (MASCON)*, IEEE, Aug. 2021, pp. 1–5. doi: 10.1109/MASCON51689.2021.9563576.

[88] K.-M. Choo and J.-H. Lee, "Efficient Regenerative Torque Control Method of PMSM Drive," in *2021 IEEE 93rd Vehicular Technology Conference (VTC2021-Spring)*, IEEE, Apr. 2021, pp. 1–6. doi: 10.1109/VTC2021-Spring51267.2021.9448693.

[89] S. German-Galkin and D. Tarnapowicz, "Optimization of the electric car's drive system with PMSM," in *2020 XII International Science-Technical Conference AUTOMOTIVE SAFETY*, IEEE, Oct. 2020, pp. 1–6. doi: 10.1109/AUTOMOTIVESAFETY47494.2020.9293514.

[90] Y. Wen, H. Zheng, Z. Zhang, J. Huang, X. Zeng, and J. Feng, "Stator Flux Oriented Control of PMSM Applied in Electric Vehicles Traction," in *2019 IEEE Vehicle Power and Propulsion Conference (VPPC)*, IEEE, Oct. 2019, pp. 1–5. doi: 10.1109/VPPC46532.2019.8952447.

[91] R. Xiao, Z. Wang, H. Zhang, J. Shen, and Z. Chen, "A Novel Adaptive Control of PMSM for Electric Vehicle," in *2017 IEEE Vehicle Power and Propulsion Conference (VPPC)*, IEEE, Dec. 2017, pp. 1–8. doi: 10.1109/VPPC.2017.8330877.

[92] T. Rudnicki, R. Czerwinski, D. Polok, and A. Sikora, "Performance analysis of a PMSM drive with torque and speed control," in *2015 22nd International Conference Mixed Design of Integrated Circuits & Systems (MIXDES)*, IEEE, Jun. 2015, pp. 562–566. doi: 10.1109/MIXDES.2015.7208586.

[93] D. K. Athanasopoulos, V. I. Kastros, and J. C. Kappatou, "Electromagnetic analysis of a PMSM with different rotor topologies," in *2016 XXII International Conference on Electrical Machines (ICEM)*, IEEE, Sep. 2016, pp. 306–312. doi: 10.1109/ICELMACH.2016.7732543.

[94] M. Lauerburg, P. Toraktrakul, and K. Hameyer, "Multi-domain analytical rotor model with buried permanent magnets in V-arrangement for high-speed applications," *Arch. Electr. Eng.*, Jan. 2024, doi: 10.24425/aee.2023.146041.

[95] D. Voitekhovskii, "Ultimate Flatness Control Through Advanced Selective Cooling Design and Proactive Maintenance Strategy," in *AISTech 2025 — Proceedings of the Iron & Steel Technology Conference*, Association for Iron & Steel Technology, 2025, pp. 1550–1554. doi: 10.33313/389/168.

[96] A. Shia, L. Zhang, J. Peng, X. Yan, C. Rong, and J. Zheming, "Lecture Notes in Electrical Engineering," in *International Conference of Electrical, Electronic and Networked Energy Systems*, 2024.

[97] W. Ma, M. Rong, F. Yang, W. Liu, S. Wang, and G. Li, "Lecture Notes in Electrical Engineering," in *9th Frontier Academic Forum of Electrical Engineering*, 2021.

[98] H. T. Le Luong, C. Hénaux, F. Messine, G. Bueno-Mariani, N. Voyer, and S. Mollov, "Finite element analysis of a modular brushless wound rotor synchronous machine," *J. Eng.*, vol. 2019, no. 17, pp. 3521–3526, Jun. 2019, doi: 10.1049/joe.2018.8206.

[99] D. Rimpas, S. D. Kaminaris, D. D. Piromalis, G. Vokas, K. G. Arvanitis, and C.-S. Karavas, "Comparative Review of Motor Technologies for Electric Vehicles Powered by a Hybrid Energy Storage System Based on Multi-Criteria Analysis," *Energies*, vol. 16, no. 6, p. 2555, Mar. 2023, doi: 10.3390/en16062555.

[100] A. K. Mondal, S. Basak, and C. Chakraborty, "Excitation Control of Brushless Induction Excited Synchronous Motor with Induction Machine Operating in Deep-Plugging Mode," *Power Electron. Drives*, vol. 9, no. 1, pp. 257–271, Jan. 2024, doi: 10.2478/pead-2024-0017.

[101] V. Dmitrievskii, V. Prakht, E. Valeev, A. Paramonov, V. Kazakbaev, and A. Anuchin, "Comparative Study of Induction and Wound Rotor Synchronous Motors for the Traction Drive of a Mining Dump Truck Operating in Wide Constant Power Speed Range," *IEEE Access*, vol. 11, pp. 68395–68409, 2023, doi: 10.1109/ACCESS.2023.3292244.

[102] J. Wu, X. Zhu, Z. Yang, Z. Xiang, Y. Chen, and L. Quan, "Torque Quality Enhancement Design of an Interior Permanent Magnet Synchronous Motor by Reluctance-Network-Based Topology Optimization," *IEEE Trans. Transp. Electrif.*, vol. 11, no. 2, pp. 5628–5640, Apr. 2025, doi: 10.1109/TTE.2024.3486447.

[103] D. K. Patel and R. P. Mehta, "Modeling and Implementation of Efficient Control for Permanent Magnet Synchronous Motor: A Review," 2025, pp. 109–134. doi: 10.1007/978-981-96-0104-2_9.

[104] K. Selvam, V. Patel, and S. Sahoo, "Impact of Torque Ripple in PMSM on EV Energy Efficiency and Driving Range," in *2025 International Conference on Sustainable Energy Technologies and Computational Intelligence (SETCOM)*, IEEE, Feb. 2025, pp. 1–6. doi: 10.1109/SETCOM64758.2025.10932440.

[105] W. Li, P. Huo, and B. Huang, "Optimization Study of Permanent Magnet Synchronous Motor with External Rotor for Robotic Arm Based on Taguchi's Method," in *2025 6th International Conference on Mechatronics Technology and Intelligent Manufacturing (ICMTIM)*, IEEE, Apr. 2025, pp. 574–577. doi: 10.1109/ICMTIM65484.2025.11040976.

[106] A. K. Moodadla, K. Revathi, M. A. F. Bano, and S. R. Salkuti, "Design of Fuzzy Logic Controller Based BLDC Motor," 2024, pp. 335–348. doi: 10.1007/978-3-031-18389-8_15.

[107] M. Hachem, A. Medero, H. Atoui, and O. Sename, "Modeling and Control of BLDC Motor for Scaled Autonomous Vehicle Application," 2024, pp. 13–28. doi: 10.1007/978-981-99-6523-6_2.

[108] H. Bacem, D. Mehdi, and S. Lassaad, "Control of a Photovoltaic Pumping System with BLDC Motor," 2024, pp. 359–375. doi: 10.1007/978-981-97-6148-7_35.

[109] W. Ding, J. Yang, X. Qiu, W. Hua, L. Hu, and C. Wu, "Research on Torque Ripple Reduction in OW-BLDC Motors with Direct Torque Control," 2025, pp. 457–464. doi: 10.1007/978-981-97-8820-0_49.

[110] S. Ganeriwala, "Induction Motor Diagnostics Using Vibration and Motor Current Signature Analysis," in *Special Topics in Structural Dynamics & Experimental Techniques, Volume 5*, New York: River Publishers, 2025, pp. 199–206. doi: 10.1007/978-3-031-37007-6_21.

[111] J. Parmar, J. Panchal, T. Jhankal, and A. N. Patel, "Selection of Stator Pole Tip for Torque Ripple Reduction of Switched Reluctance Motor," in *2024 IEEE 11th Power India International Conference (PIICON)*, IEEE, Dec. 2024, pp. 1–6. doi: 10.1109/PIICON63519.2024.10995057.

[112] H. Taha, G. Barakat, B. Zbib, and F. Chabour, "Comparison Between Axial Flux BLDC and Axial Flux PMSM for High Speed and Low Power Application," 2025, pp. 179–191. doi: 10.1007/978-3-031-73921-7_15.

Dicle University
Journal of Engineering
https://dergipark.org.tr/tr/pub/dumf
duje.dicle.edu.tr

Research Article

Application of Emotion Analysis in Deep Learning Techniques

Mesut UYSAL[1*], Mehmet Fatih DEMİRAL[2], Ali Hakan Işık[3]

[1] Hatay Mustafa Kemal University, Antakya Vocational School, Department of Database Network Design and Management, mesut.uysal@mku.edu.tr, Orcid No: 0009-0002-1650-8880
[2] Burdur Mehmet Akif Ersoy University, Department of Data Science and Analytics, mfdemiral@mehmetakif.edu.tr Orcid No 0000-0003-0742-0633
[3] Burdur Mehmet Akif Ersoy University, Computer Engineering Department, ahakan@mehmetakif.edu.tr, Orcid No: 0000-0003-3561-9375

ARTICLE INFO

Article history:

Received 3 August 2025
Received in revised form 13 October 2025
Accepted 25 November 2025
Available online 30 December 2025

Keywords:

Emotion recognition, Deep learning, Transfer learning, Facial expression, YOLOv8m-cls

Doi: 10.24012/dumf.1757225

* Corresponding author

ABSTRACT

Emotion recognition has become a pivotal technology in advancing human-computer interaction with applications spanning fields such as healthcare, entertainment, and customer experience. This paper evaluates the performance of five deep learning models—YOLOv8m-cls, ResNet50, EfficientNetB5, MobileNetV2, and DenseNet121—in detecting emotions from facial expressions. Leveraging the AffectNet dataset, which initially contained eight emotional categories, we focused on five emotions after excluding three due to low data availability and similarity. The emotions processed include anger, happiness, sadness, surprise, and fear. The models were fine-tuned through transfer learning, demonstrating that YOLOv8m-cls performed best, balancing accuracy, speed, and generalization, making it suitable for real-time applications. ResNet50 and EfficientNetB5 also performed well, with ResNet50 excelling in handling complex facial features and EfficientNetB5 offering computational efficiency with high accuracy. The study also highlights challenges such as intra-class variability and inter-class similarity, which continue to affect model performance. These findings underscore the importance of selecting model architectures based on specific application requirements and suggest that future research should explore integrating multimodal data to enhance emotion recognition systems.

Introduction[1]

Emotion recognition has emerged as a critical component in advancing human-computer interactions and improving how machines understand human behavior. At the core of emotion recognition is the challenge of deciphering complex emotional states that involve a mix of cognitive, physiological, and behavioral responses. Emotions such as happiness, sadness, anger, fear, surprise, and disgust are often communicated through a variety of channels, including facial expressions, vocal tones, and body language. The ability to accurately identify these emotions has far-reaching implications not only for improving user experiences with technology, but also for advancing fields such as mental health, social robotics, and emotional computing. As one of the most direct and universal indicators of emotion, facial expressions have been a primary focus of emotion recognition systems. Across cultures and contexts, facial expressions serve as a powerful medium for conveying emotional states [[1]]. These expressions consist of complex facial muscle movements that can be deciphered to reveal the underlying emotion. Early research on facial expressions for emotion recognition relied largely on manual annotations and rule-based systems. Such systems used hand-crafted features that tracked specific facial cues and mapped them to corresponding emotions. However, these methods were often limited in their ability to adapt to dynamic environments, such as changes in lighting, occlusions, or differences in individual facial features [[2]].

The practical applications of emotion recognition extend beyond simple human-computer interactions. In healthcare, emotion-detection systems are increasingly being used in mental health diagnostics to monitor emotional states in patients and to help diagnose disorders such as depression, anxiety, and post-traumatic stress disorder (PTSD). In marketing and customer service, companies use emotion recognition to better understand consumers' responses to products or advertisements. These insights can lead to more personalized marketing campaigns and increased customer satisfaction. Emotion recognition also plays an important role in entertainment, particularly in the development of emotionally responsive characters in video games and virtual reality environments [[3]].

[1] This work is based on the master thesis of Uysal(2024)

Over the past two decades, emotion recognition has evolved from simple rule-based systems to more complex, data-driven models. This evolution has been largely driven by advances in artificial intelligence (AI) and machine learning (ML), particularly computer vision. By leveraging large datasets and powerful computational models, modern emotion recognition systems can automatically learn and detect features that correspond to emotional states without the need for extensive manual intervention [[4]]. Such systems have demonstrated remarkable accuracy in identifying emotions across a wide range of conditions, making them highly adaptable and reliable. As one of the main data sources for emotion detection, face recognition continues to dominate the research landscape. Automatic face recognition systems analyze pixel-level data from images or video streams to identify patterns in facial landmarks and textures that correspond to specific emotions. These systems typically rely on sophisticated feature extraction techniques, where key facial landmarks, such as the position of the eyes, mouth, and eyebrows, are tracked and processed using deep learning architectures. However, emotion recognition is not without its challenges. Variability in facial expressions due to cultural differences, individual characteristics, and environmental factors (such as lighting and occlusion) can significantly affect the accuracy of these systems [[5]]. Despite all these difficulties, this study aimed to perform accurate emotion detection on 29,042 images taken from the Kaggle platform by selecting transfer learning models. The performance of each model was measured using various metrics, and the model with the highest accuracy value was selected and its suitability for this study was indicated.

Literature review

Previous studies on emotion detection

Emotion detection has long been a topic of research interest, evolving through various methodologies and technological advancements. The core aim of emotion detection is to interpret emotional states from various forms of data such as facial expressions, voice, text, and physiological signals. Early research on this topic largely relied on handcrafted feature extraction techniques, often based on psychological theories of emotion, such as Ekman's six basic emotions [[1]]. However, with the advancements in machine learning and artificial intelligence, especially deep learning, the field has experienced significant transformations, leading to more accurate and scalable emotion detection systems.

Initial studies in emotion detection focused heavily on the manual interpretation of facial expressions. Pioneering study like Ekman and Friesen introduced the Facial Action Coding System (FACS), which provided a systematic method for describing facial expressions by identifying specific facial muscle movements, known as Action Units (AUs) [[6]]. This system became the foundation for many early facial emotion recognition studies, as researchers sought to decode emotions through observable facial movements. However, these methods were limited in their scope and lacked the computational power to be applied on a large scale.

As computing power increased, so did the ambition of emotion detection research. Early machine learning models, such as Support Vector Machines (SVMs), Naive Bayes classifiers, and Decision Trees, were applied to automate the recognition of emotional states. These models, while offering some level of automation, relied heavily on feature engineering—human intervention to manually define the relevant features for emotion recognition where Tian, Kanade and Cohn proposed a facial expression recognition system that used feature-based SVMs to classify expressions based on geometric and appearance features from the face [[5]]. Although effective under controlled conditions, these models struggled with real-world variability, such as changes in lighting, head poses, and occlusions, limiting their practical applications.

The turn of the century saw a marked shift towards data-driven approaches, facilitated by the rise of large emotion-labeled datasets and advances in deep learning. One such dataset is the Extended Cohn-Kanade (CK+) dataset, which contains labeled facial expressions captured under various conditions [[7]]. This dataset became a benchmark for facial expression recognition and contributed to the development of more robust emotion recognition systems.

The introduction of Convolutional Neural Networks (CNNs) revolutionized the field by enabling automatic feature extraction directly from raw data, such as images and videos, without the need for manual intervention. CNNs consist of multiple layers of processing units that learn hierarchical representations of the input data, making them highly effective for image-based tasks like emotion detection. Notably, the work of Tolias and Chum demonstrated the power of CNNs in facial expression recognition [[8]]. Their proposed deep neural network achieved state-of-the-art performance on several datasets, including FER2013 and AffectNet, two large-scale facial emotion recognition datasets.

CNNs are designed to handle the spatial hierarchies in image data, which is crucial for identifying patterns that exist in local neighborhoods of pixels, such as the shape of a mouth or the orientation of the eyes in facial emotion recognition tasks. The network's ability to learn these spatial hierarchies without manual intervention has made it one of the most powerful tools in image classification. One of the earliest successful applications of CNNs in image classification was the AlexNet model, which won the ImageNet Large Scale Visual Recognition Challenge (ILSVRC) in 2012 by a significant margin [[9]]. AlexNet’s success demonstrated the immense potential of deep learning for image classification and spurred further research into deeper and more efficient networks.

The measurement of the success of secondary school activities conducted by Zilyas and Yılmaz, and their learning by determining negative features, machine learning [[10]]. The recorded data set of a survey results including three questions consisting of 519 students, 246

male and 273 female students, consists of 13 columns and 520 rows. The survey asked 13 questions regarding gender, number of siblings, whether they receive special education, and whether their mother and father are separate/together. The data set; After dividing into 80% training, 20% test, data cleaning and pre-processing steps were passed in order to obtain high performance before training, and training was performed in Random Forest, Multiple Linear Regression, Gradient Boosting Regression, KNN, Bagged Trees, Decision Trees explosions. According to successful learning machine applications, the output acquisition rate is 98% with Random Forest cleaning and 95% with R-squared scores.

The FER2013 dataset, introduced during the ICML 2013 Challenges, is widely used in the emotion recognition community and contains over 35,000 labeled images of faces expressing seven different emotions. The AffectNet dataset is even larger, comprising more than one million facial images annotated with both categorical and continuous emotion labels. These large datasets have been instrumental in training deep learning models that are capable of generalizing across different emotional expressions, individuals, and environmental conditions. CNN-based models trained on these datasets have consistently achieved superior performance compared to traditional machine learning methods, making them the go-to solution for modern emotion detection tasks [[11]].

Despite the success of CNNs, challenges remained, particularly when dealing with sequential data such as video or audio, where temporal dynamics are crucial for understanding emotion. Recurrent Neural Networks (RNNs) and their variants, Long Short-Term Memory (LSTM) networks, emerged as suitable candidates for handling sequential data. Wöllmer et al. applied LSTMs to emotion recognition from speech, demonstrating that RNNs can capture temporal dependencies in emotional expressions, which are often missed by static image-based methods. Similarly, in video-based emotion detection, LSTMs have been used to model the temporal evolution of facial expressions over time, providing more nuanced and accurate predictions [**Hata! Başvuru kaynağı bulunamadı.**].

Transfer learning has further propelled the advancements in emotion detection. Transfer learning allows models pre-trained on large general-purpose datasets, like ImageNet, to be fine-tuned on smaller, domain-specific datasets. This technique has proven highly effective in emotion detection, as emotion-labeled datasets are typically much smaller than general-purpose datasets due to the complexity and cost of labeling emotions. By leveraging pre-trained models such as DenseNet, EfficientNet, MobileNet, researchers have been able to achieve high performance with fewer labeled samples [[12]]. Transfer learning not only reduces the need for extensive computational resources but also accelerates the training process and improves generalization to unseen data. In to facial expression recognition, emotion detection from speech and text has also seen significant progress. In speech-based emotion detection, studies such as Wöllmer et al. and Eyben et al. showed that acoustic features such as pitch, intensity, and speaking rate can be used to infer emotional states [**Hata! Başvuru kaynağı bulunamadı.**, **Hata! Başvuru kaynağı bulunamadı.**]. Similarly, text-based emotion recognition, which focuses on identifying emotions from written content, has gained traction with the rise of social media platforms. Sentiment analysis, a subset of emotion detection, is commonly used to gauge public sentiment on social media posts, product reviews, and other textual data. Natural Language Processing (NLP) techniques, including the use of pre-trained language models like BERT. Devlin et al. have significantly improved the accuracy of text-based emotion detection [[15]]. A growing body of research is also exploring multimodal emotion detection, which combines data from multiple modalities, such as facial expressions, speech, and text, to enhance the accuracy of emotion recognition. For instance, Zadeh et al. proposed a multimodal deep learning model that integrates visual, auditory, and textual cues to predict emotions in video data [**Hata! Başvuru kaynağı bulunamadı.**]. Their model outperformed unimodal approaches, highlighting the importance of considering multiple channels of emotional expression for more comprehensive emotion detection. Despite these advancements, emotion detection remains a challenging task due to the complexity of emotional states and the variability in how individuals express emotions. Factors such as cultural differences, personal traits, and situational contexts can significantly affect the accuracy of emotion recognition systems. Furthermore, ethical concerns regarding the use of emotion detection technologies, particularly in surveillance and privacy, have sparked debates about the potential misuse of such systems. As emotion detection continues to evolve, addressing these challenges will be crucial for the responsible development and deployment of emotion-aware technologies.

Shawi et al. [17] found that ResNet-50 architectural enhancements improved face emotion recognition performance. Introducing hybrid pooling with a learnable α weight and enhancing the Adaptive Leaky ReLU activation function with a parameter led to improved efficiency and flexibility in learning complicated emotional variables. In experiments on the FER2013 and CK+ datasets, the enhanced model attained accuracies of 96.60% and 96.32%, outperforming ResNet-50 alone, ResNet-50 with CBAM, and ResNet-50 with GRU. CK+ had a slightly superior precision-recall balance than FER2013, with an average F1-score of 0.9424 against 0.931. “Happiness” was the most reliably detected emotion, but “Neutral” performed poorly, especially on FER2013. This shows that adding Hybrid Pooling and Adaptive Leaky ReLU to ResNet-50 enhances feature representation and classification, making face emotion identification more accurate and dependable across complicated datasets.

A research by Alshammari, & Alshammari [18] showed that the YOLOv8 framework is a powerful model for emotional facial expression identification that can recognize many emotion categories. The model performed

well on 2,353 pictures labeled with seven emotions—anger, contempt, disgust, fear, pleasure, sorrow, and surprise—with a mean Average Precision (mAP@0.5) of 0.837. Anger (1.00), pleasure (0.95), contempt (0.93), disgust (0.70), and surprise (0.88) were more reliably identified than fear (0.36) and melancholy (0.25). Fear and melancholy performed poorly owing to data imbalance, since these classes included less training examples (75 and 84 photos, respectively). YOLOv8 trained to recognize and categorize emotional expressions with increasing accuracy as its precision, recall, and mAP improved over training epochs. Scatter plot analysis also showed that the model detected centrally situated and bigger facial emotions more effectively, showing face placement and size sensitivity. The results show that YOLOv8 excels at emotion identification, but dataset augmentation and class balance might improve its detection of subtle emotions like melancholy and fear.

Istiqomah, et al. [19] showed that transfer learning using ResNet-50 improves facial emotion recognition over training from scratch. Image improvement and resizing helped the model achieve 99.49% accuracy, 99.49% precision, 99.71% recall, and 99.60% F1-score across seven emotion classes, proving its dependability. Transfer learning outperformed non-transfer learning in classification convergence, stability, and true positive rates. These results demonstrate that transfer learning enhances the model's capacity to handle illumination, viewing angles, and face structures, making it a very successful facial emotion identification method.

Wei Du [20] suggested enhancing ResNet50 for face emotion identification. The suggested ResNet50 model has two fully linked layer blocks. The layer stacking approach with reduced connections is utilized to address deterioration and enhance training flexibility. The enhanced model outperformed ResNet50 by 13.31% on the dataset (FER-2013). ResNets have downsides, such as relying significantly on Batch Normalization, which stabilizes training and lowers Dropout. In residual networks, maintaining information flow over skip links is crucial. Dropout may diminish this value.

To recognize and categorize facial expressions, Liu Luan Xiang et.al., [21] suggested a system using ResNet50 and a convolutional block attention module. Deep learning models (VGG19, ResNet50, and InceptionV3) extensively assessed FER tasks and addressed difficulties. The convolutional block attention module was introduced to improve retrieved features and enhance model performance by hyper parameter adjustment. In experiments, VGG19's accuracy was 71.7% before the module integration, whereas ResNet50's accuracy peaked at 72.4% after integration. However, there are some downsides. Adding CBAM to every ResNet layer (50) will dramatically increase calculations, resulting in: A longer training period is required to calculate attention units for each layer. Higher memory use (VRAM/RAM) occurs with huge datasets or high-resolution photos. A slower inference time may be impractical for real-time applications. Using CBAM in all layers may overemphasize individual characteristics, reducing model generalization and overfitting on fresh data. The use of CBAM at each layer makes it difficult to adjust settings and identify the impact of each attention unit, making analysis challenging.

Deep learning methods, especially hybrid CNN-RNN architectures, are best for face emotion identification because they capture both spatial and temporal qualities of facial emotions. Attention processes and embeddings do not considerably outperform RNN-based models. The study [22] found that dataset size and computing restrictions limit deep network training. Transfer learning and preprocessing methods like noise reduction and contrast enhancement improved recognition accuracy. Additionally, ensemble approaches and adversarial training may minimize mistakes by improving model resilience. Optimization is necessary for hyperparameters including learning rate, batch size, number of layers, dropout rate, and activation function, which greatly affect model performance. Finally, the study found that multimodal approaches that combine facial cues with other emotional signals like ECG or verbal cues can improve emotion detection, and that future research should focus on recognizing continuous, spontaneous, and subtle expressions in real life.

Deep learning-based approaches, particularly hybrid ConvNet-RNN and ConvNet-LSTM architectures, outperform traditional machine learning methods in facial expression recognition (FER) because they automatically extract features and capture spatial and temporal information from images and video sequences. Deep learning allows end-to-end learning from raw photos without face physics-based models like SVM, k-NN, and AdaBoost. Training deep networks is difficult due to restricted sample sizes and processing needs, hence the research emphasizes big, high-quality datasets. 3D datasets and multimodal techniques with temporal and physiological information may enhance identification accuracy, especially for minor emotions and position changes. Deep learning algorithms improve FER performance, but more effort is required to construct models that can handle complicated, real-world expressions and minimize computational cost for practical applications [23].

Literature review

In Section 2.2, the contents, data sources and results of previous studies on sentiment analysis are mentioned.

Table 1. Literature table.

Reference	Algorithm/Libraries	Contents	Data source	Language	Results

Vural et al. [**24**]	Dictionary lexicon	Movie reviews	White screen site	Java	-
Bilgin and Şentürk [**25**]	Doc2Vec, Dm, DBow	Social media comments	Twitter	Python	%34 DM precision %44 DBow precision
Demirci et al. [**26**]	NN, SVM, LR	Political news	Twitter	Python	%81 accuracy (ML) %81,86 accuracy (DL)
Seyfioğlu and Demirezen [**27**]	Semi-supervised learning	Aircraft Customer Reviews	Customer reviews and ratings	Python	%92,5 accuracy
Zilyas and Yılmaz [[10]]	LR, Random Forest, KNN, Btr	Measuring Student Success	Survey results	Python	%88 accuracy
Ayan, Kuyumcu, Ceylan [**28**]	Lineer Ridge Regresyonu ve NB	Islamophobic thoughts	Tweets about Islam on Twitter	Python	%95,4 F1 score
Uyaroğlu Akdeniz and Cebeci [**29**]	Turkish Bert	Municipality Service satisfaction	Twitter comments	Python	%80 accuracy
Tuzcu [**30**]	MLP, NB, LR, DVM	Book Sales	Book sales reviews	Python	%90 DVM accuracy %88 MLP accuracy
Yohanes et al. [**31**]	LSTM, BiLSTM, gru	Researching and grouping people's basic emotions	ISEAR data set	Python	%98,72 accuracy
Zhang and Ananiadou [**32**]	CNN models, Deep learning models	Gender effects on sentiment analysis	ISEAR ve CrowdFlower	-	%99 accuracy
Issa et al. [**33**]	Deep learning models	Identifying emotions from speech	RAVDESS, EMO-DB, IMOCAP	Python	%95,71 EMO-DB accuracy
Yüksel and Tan [**34**].	NLP, Zemberek, Simple Bayesian Algorithm	Feelings about places visited via Foursquare	Comments received from Foursquare	Python	%81 binary classification accuracy %84 triple classification accuracy
Arığ and Turan [**35**]	CNN deep learning model	Video sentiment analysis	Reviews from 61 movies	Python	%85 ML accuracy
Eyipınar et al. [**36**]	Text Mining Techniques	Healthy nutrition and sports	The 6 most watched sports videos	Orange 3	%60 accuracy
Tepecik and Demir [**37**]	Nb, SVM, RF KNN, DT	Sentiment analysis from voice	Common Voice	Python and Rapid Miner	Naive Bayes %70 accuracy SVM %69 accuracy
Sel [**38**]	N-gram method	Opinions on the pandemic	Twitter	Python	%70 accuracy
Uysal [**39**]	Deep learning models	Emotion Detection	Kaagle	Python	%89 accuracy

Methodology

Dataset description

For this study, we used a subset of the widely known AffectNet dataset, which initially consisted of facial expressions categorized into eight different emotional states: anger, contempt, disgust, fear, happiness, neutral, sadness, and surprise. However, due to limited data availability for certain emotions and the similarity between some emotion pairs, we continued with five basic emotions: anger, happiness, neutral, surprise, and sadness. The excluded emotions were disgust, contempt, and fear. The total number of images in the dataset is distributed as follows:

Total number of images in the dataset: 29042

Number of images used in models: 20518

- Anger: 3218 images
- Happiness: 5044 images
- Neutral 5126 images
- Surprise: 4039 images
- Sadness: 3091 images

The images in the dataset were converted from 96*96 to 224*224 so that the model can better analyze the images and gain an advantage in detecting the correct emotion. In addition, the images in BGR format were converted to RGB format before being transferred to the models. No data extraction, deletion or data augmentation was done while editing the dataset.

Preprocessing

AffectNet Training Data is one of the largest and most comprehensive datasets developed for facial emotion recognition studies. Approximately 450,000 images were manually labeled with eight primary emotion labels. The labeled data included Anger, Disgust, Fear, Happiness, Sadness, Surprise, Neutral, and Contempt. Approximately 29,042 images were selected from the 450,000 images without any specific criteria. Our dataset contains a total of 29,042 images, but 20,518 of these were used for training and testing the models. Because the accuracy values for predicting eight emotions were not satisfactory for the project results, we preferred to use five classes that yielded better results. Of these eight classes, the contempt and disgust classes were removed from the dataset due to limited data. Because the fear and sadness classes contained similar data, the fear class was also removed from the dataset in the next stage. The two classes with the fewest data in the dataset were removed, while the classes with the most data were used for training. The data in the dataset was already labeled, so no separate labeling was performed a second time. When creating the Affectnet

dataset, the facial expressions in this dataset were manually labeled by human analysts. This labeling process is based on psychological and visual criteria. Thousands of images are collected from search engines like Google and Bing. Each image is evaluated by at least one analyst, who labels the images with continuous values such as pleasure and arousal [-1,1]. Additionally, landmarks, bounding boxes, and pose information (face angle) were used to create the Afectnet datasets.

Picture 1: Sample Images of Emotional Classes Data Set

Picture 2: Images before and after preprocessing on Restnet50 (Surprise)

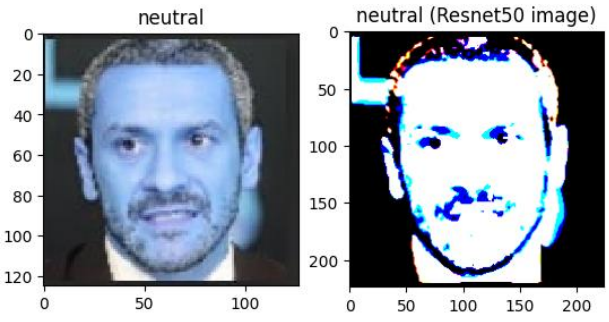

Picture 3: Images before and after preprocessing on Restnet50 (Neutral)

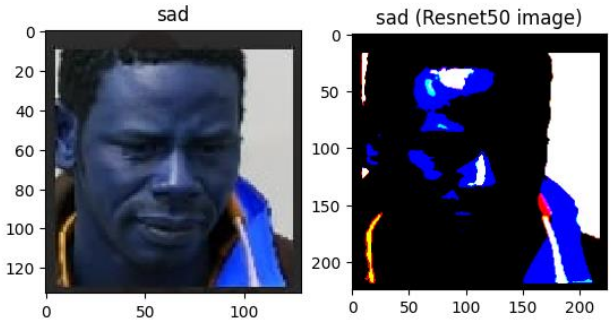

Picture 4: Images before and after preprocessing on Restnet50 (Sad)

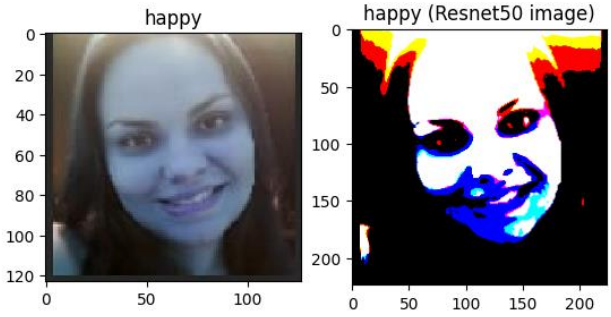

Picture 5: Images before and after preprocessing on Restnet50 (Happy)

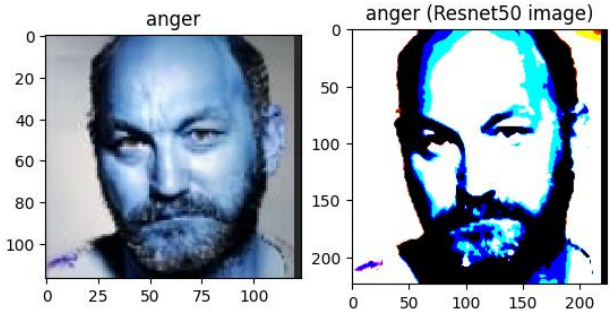

Picture 6: Images before and after preprocessing on Restnet50 (Anger)

The unbalanced representation of emotions like "hate, disgust, and fear" in the dataset created some performance issues. The model struggled to learn certain classes, leading to a decrease in overall model performance during the training process. If all datasets had been assigned equally, a completely different result could have been achieved. However, it performed quite well with happiness and neutral emotions.

Normalization

After resizing, all pixel values of the images were normalized. Image normalization is an essential step in most deep learning tasks, as it scales the pixel intensity values to a fixed range, typically between 0 and 1. In this study, normalization was performed by dividing the pixel values by 255, which is the maximum possible pixel value

in an 8-bit image. This scaling ensures that the inputs to the neural network have a standardized range, helping the models learn more effectively and converge faster during training.

Splitting the dataset

Before the actual training process, the dataset was split into two parts:

- Training Set: 80% of the images were used to train the model.
- Test/Validation Set: 20% of the images were used for both testing and validation. We did not separate a dedicated validation set; instead, the test data was used concurrently for validation during the training process. This combined test/validation set helped monitor the model's performance and prevent overfitting by providing checkpoints to evaluate how well the model was generalizing to unseen data. Because the final test results may not fully reflect generalization ability, it is better to use separate test and validation sets for future studies.

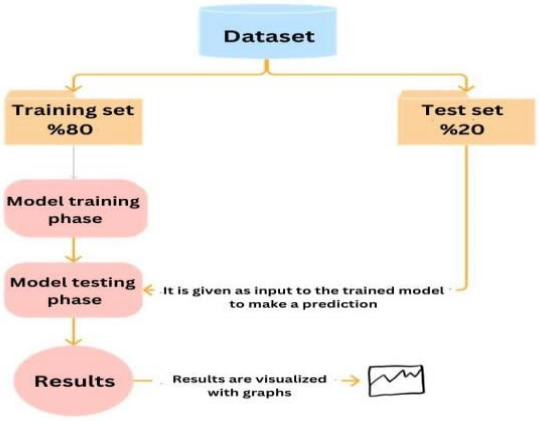

Figure 1. Data distribution percentage.

Model selection

In this section, we explore the selection of six advanced deep learning models that were employed for emotion recognition. These models—DenseNet121, EfficientNetB5, MobileNetV2, ResNet50, VGG16, and YOLOv8m-cls—have been chosen due to their proven performance in image classification tasks and their adaptability to transfer learning techniques.

DenseNet121

DenseNet121 (Densely Connected Convolutional Networks) is a powerful deep learning model that leverages dense connectivity patterns between layers. Unlike traditional convolutional neural networks, where each layer only feeds into the next one, DenseNet121 connects each layer to every other layer in a feed-forward fashion. This connectivity improves the flow of information and gradients throughout the network, addressing the vanishing gradient problem commonly encountered in deep networks [[3]].

DenseNet121 is well-suited for emotion recognition tasks due to its ability to capture intricate details in facial expressions. In this study, the model was fine-tuned using pre-trained weights from the ImageNet dataset and adapted to recognize the eight primary emotion classes. The input shape was set to *224x224 pixels,* and the model utilized *max pooling* and *global average pooling* layers to reduce the dimensionality of the data while retaining critical features for classification.

EfficientNetB5

EfficientNetB5 is a highly efficient and scalable deep learning model designed to balance accuracy and computational complexity. The model uses a compound scaling technique, which uniformly scales network depth, width, and resolution. This allows EfficientNetB5 to achieve superior performance with fewer parameters compared to traditional models.

In this study, EfficientNetB5 was pre-trained on ImageNet and fine-tuned for emotion recognition using the ImageNet dataset. The input images were resized to *224x224 pixels,* and a *softmax classifier* was used to output the probability distribution over the emotion classes.

MobileNetV2

MobileNetV2 is an efficient convolutional neural network optimized for mobile and embedded applications. It employs depthwise separable convolutions to reduce the computational load while maintaining high classification accuracy. MobileNetV2 is especially useful in scenarios where computational power is constrained, such as on smartphones or edge devices [**Hata! Başvuru kaynağı bulunamadı.**].

ResNet50

ResNet50 (Residual Networks) is a deep convolutional neural network that uses residual learning to overcome the vanishing gradient problem and enables training of very deep networks [**Hata! Başvuru kaynağı bulunamadı.**]. ResNet50's architecture consists of 50 layers and includes shortcut connections that skip one or more layers, which makes gradients flow more easily during training. ResNet50 was selected for this study due to its strong performance in image classification and good generalization across different datasets.

VGG16

VGG16 is a deep convolutional neural network that is widely recognized for its success in the ImageNet competition. It uses a simple and consistent architecture consisting of 16 layers consisting primarily of 3x3 convolutional filters followed by max pooling layers [[42]]. The simplicity of VGG16 combined with its deep architecture enables it to capture complex features in images, making it a popular choice for transfer learning tasks.

YOLOv8m-cls

YOLOv8m-cls (version 8 for You Only Look Once classification) is an advanced version of the YOLO object detection framework adapted for image classification tasks. YOLO models are renowned for their speed and accuracy in real-time object detection, making YOLOv8m-cls a suitable choice for emotion detection in dynamic environments such as video streams or live interaction systems [**Hata! Başvuru kaynağı bulunamadı.**]. The primary advantage of YOLOv8m-cls is its ability to process images at high speeds while maintaining high accuracy, making it ideal for real-time emotion recognition applications. In this work, the classification mode of the YOLOv8 architecture developed by Ultralytics was used for image classification.

Table 2. YOLOv8m-cls hyperparameters

Model	YoloV8m-cls
Epoch	20
Lr	0.01
Batch size	16
Optimizer	Adam
İmgsz	96

Training and evaluation

The training and evaluation process is a critical phase in the development of emotion recognition models. In this study, the chosen models (DenseNet121, EfficientNetB5, MobileNetV2, ResNet50, VGG16, and YOLOv8m-cls) were trained and evaluated using the same dataset and preprocessing steps to ensure consistency and comparability across models. The training process for each model involved fine-tuning pre-trained weights on the AffectNet dataset and adapting the models to the emotion recognition task. The key stages in training and evaluation are described below.

Training process

Each model was trained using a training set of 16,414 images, while 4,104 images were reserved for testing. Since there were not many images in the dataset, the test data was also used as validation data. In other words, no separate split was made for validation. The training process involved updating the model weights to minimize the loss function, which measures the difference between the predicted and true emotion labels. The primary loss function used in this study was categorical cross-entropy, which is suitable for multi-class classification tasks such as emotion recognition. This loss function calculates the probability that the correct label is predicted by the model and adjusts the model's weights accordingly to improve its predictions.

In training, each model was trained 30 times and processed 128 data points simultaneously. These parameters were chosen to ensure that the models had sufficient opportunity to learn the complex relationships between facial features and emotions while avoiding overfitting. Overfitting occurs when a model performs well on training data but fails to generalize to unseen data, and is a common problem in deep learning. To reduce this risk, early stopping and learning rate reduction techniques were used.

- Early Stopping: If the performance of the model on the test/validation set has not improved over 5 epochs, training is stopped early to prevent overfitting. In this study, the accuracy metric was monitored.
- Learning Rate Reduction: These metrics are monitored in the loss graph. If the losses in the model are high, the learning rate is reduced by 0.1. The parameter patience=2 specifies the number of rounds to wait before reducing the learning rate.

System architecture

The diagram shows the overall system architecture used for emotion recognition. The process starts with importing the necessary libraries, including TensorFlow, NumPy, and OpenCV. The video camera captures a frame, which is then preprocessed and passed through a deep learning model using transfer learning techniques. The model estimates the emotional state from facial expressions and displays the result on the screen. This architecture efficiently integrates real-time image processing with deep learning to provide accurate emotion detection.

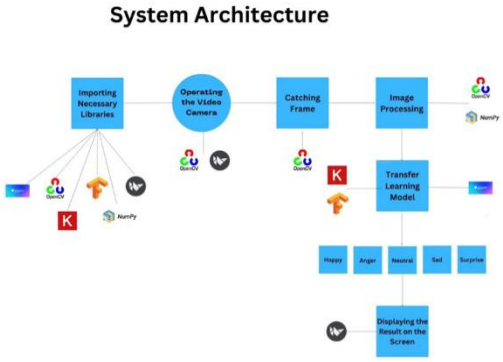

Figure 2. System architecture of the study.

Common metrics for model performance in emotion recognition

In the evaluation of emotion recognition systems, it is crucial to employ a variety of performance metrics to assess how well the models classify emotions and generalize across different datasets and scenarios. These metrics provide insights into the model's accuracy, robustness, and reliability. In particular, confusion matrices, ROC (Receiver Operating Characteristic) curves, accuracy, and loss graphs are some of the most commonly used tools to evaluate model performance in emotion recognition.

Confusion matrix

A complexity matrix is a table used to describe the performance of a classification model, usually by comparing predicted labels to the true labels from the test

data. It provides a breakdown of correct and incorrect classifications for each class.

Each row of the matrix represents examples of true class labels, while each column represents examples of predicted class labels. The diagonal elements of the complexity matrix represent the number of correct predictions, while the off-diagonal elements indicate incorrect classifications, clearly showing where the model made mistakes.

ROC curve

The ROC curve is another valuable metric for evaluating the performance of emotion recognition models, especially in binary or multi-class classification problems. The ROC curve plots the true positive rate (sensitivity) against the false positive rate (1 - specificity) at various threshold settings. A well-performing model will have a ROC curve that hugs the upper left corner of the graph, indicating a high true positive rate with a low false positive rate. The area under the ROC curve (AUC) is calculated to measure the performance of the model. An AUC score close to 1 indicates excellent performance, while a score close to 0.5 indicates that the model is performing no better than random chance.

Accuracy

Accuracy is perhaps the most straightforward and widely recognized performance metric in classification tasks, including emotion recognition. It is defined as the ratio of correctly predicted instances to the total number of instances. Although accuracy provides a general measure of the model's overall performance, it can sometimes be misleading in imbalanced datasets where certain emotion classes are much more frequent than others. Therefore, while accuracy is a useful metric, it is often supplemented by other metrics like precision, recall, and F1-score to provide a more complete picture of the model's performance.

Loss

The loss plot usually plots the training and validation loss over the training epochs. A well-performing model will exhibit decreasing loss for both the training and validation sets. If the validation loss starts to increase while the training loss continues to decrease, this is a sign that overfitting is occurring and regularization techniques or early stopping may be required. In short, it shows the relationships between the model's prediction and the actual data, which is a good guide for optimizing the model.

Results

Comparison of accuracy across models

In this section, the accuracy performance of each deep learning model used in the emotion recognition task is compared. Accuracy is a fundamental metric in classification tasks, providing a measure of how well a model can correctly predict the target labels across all classes. In this case, accuracy represents how effectively the models recognize various emotions from facial images.

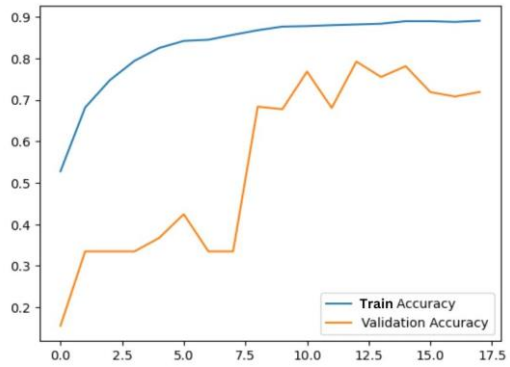

Figure 3. DenseNet-121 accuracy graphs.

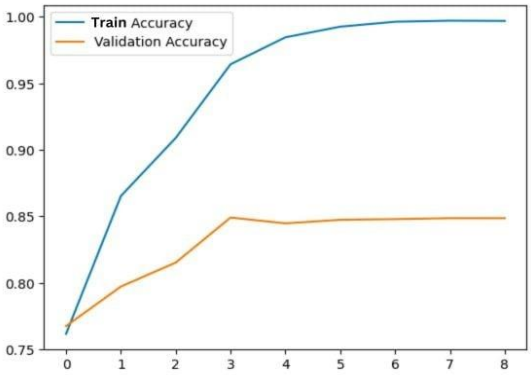

Figure 4. EfficientNet-B5 accuracy graphs.

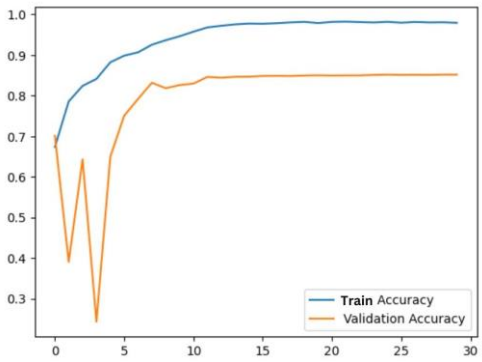

Figure 5. MobilenetV2 accuracy graphs.

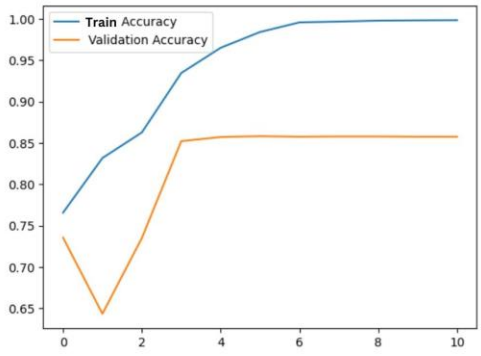

Figure 6. ResNet50 accuracy graphs.

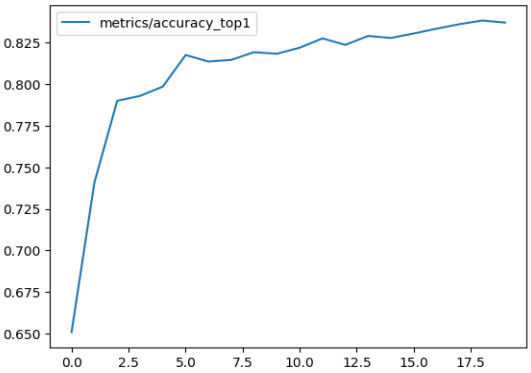

Figure 7. YOLOv8m-cls accuracy graphs.

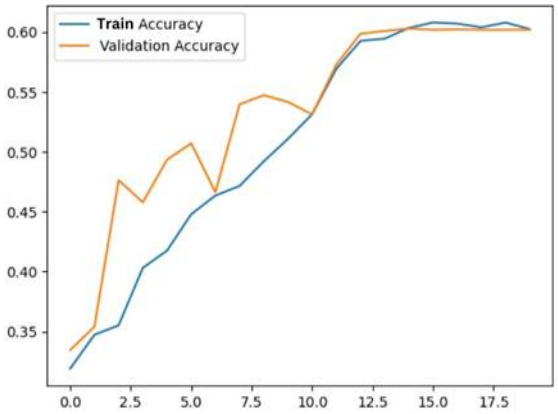

Figure 8. Vgg16 accuracy graphs.

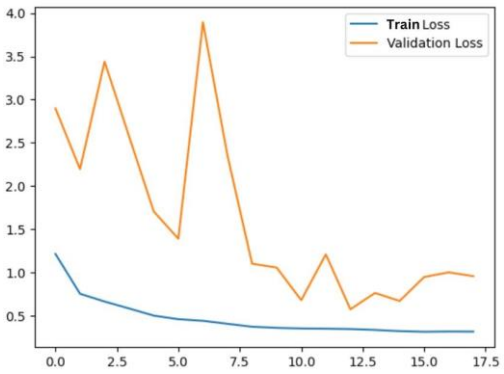

Figure 9. DenseNet121 loss graph.

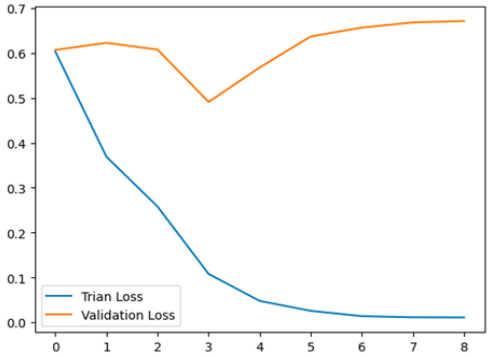

Figure 10. EfficientNet loss graph.

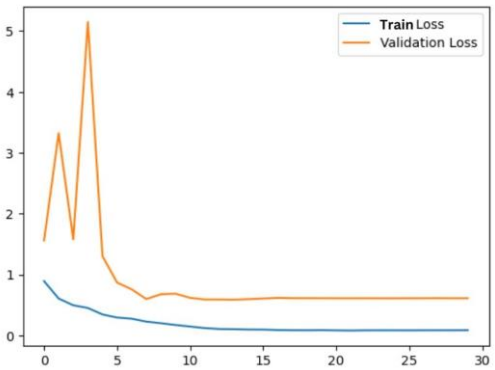

Figure 11. MobilNetV2 loss graph.

Comparison of loss across models

Loss represents the difference between predicted and true values in classification tasks, and lower loss indicates better model performance. During the training process, models try to minimize the loss function, and monitoring both training loss and validation loss provides insights into potential problems such as overfitting or underfitting. Figures 9,10,11,12,13,14,15 show the losses.

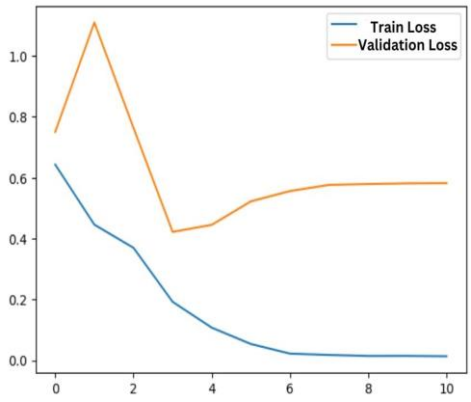

Figure 12. Resnet50 loss graph.

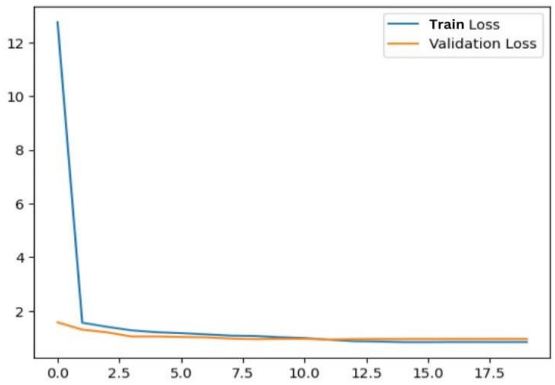

Figure 13. Vgg16 loss graph.

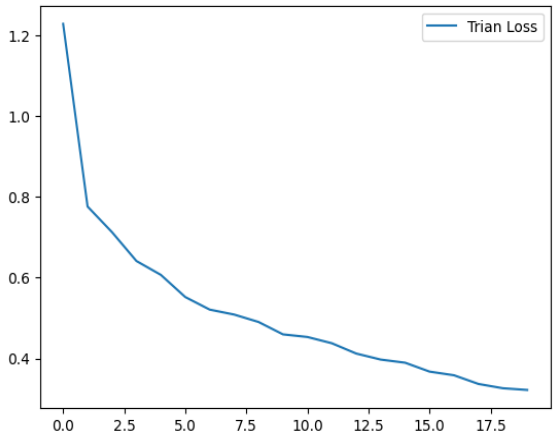

Figure 14. YoloV8m-cls loss graph.

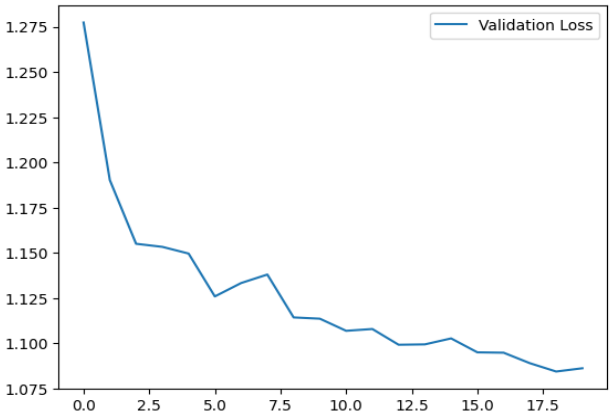

Figure 15. YoloV8-cls val/loss graph.

Table 3. Model loss values.

Model	Loss
DenseNet121	0,57
EfficientNet	0,49
MobilNetV2	0,61
ResNet50	0,52
VGG16	0,96
YoloV8m-cls	0,32

Confusion matrix comparison

The confusion matrix of the models is given in figures 16,17,18,19,20, and 21 below. By looking at this matrix, we can clearly see the relationship between the values predicted by the model and the actual values.

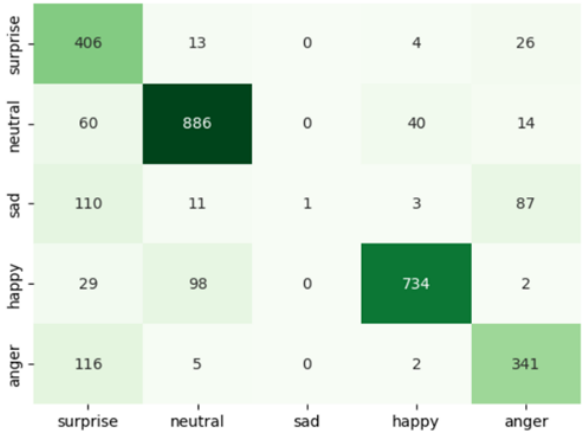

Figure 16. DenseNet121 confusion matrix.

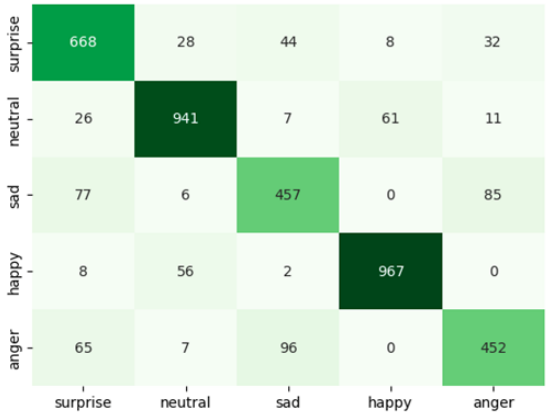

Figure 17. EfficientNet-B5 confusion matrix.

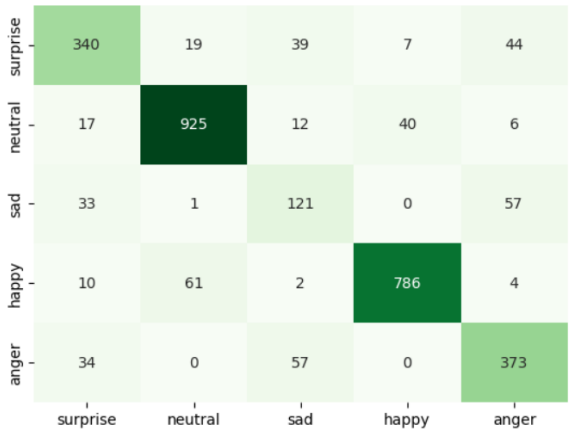

Figure 18. MobileNetV2 confusion matrix.

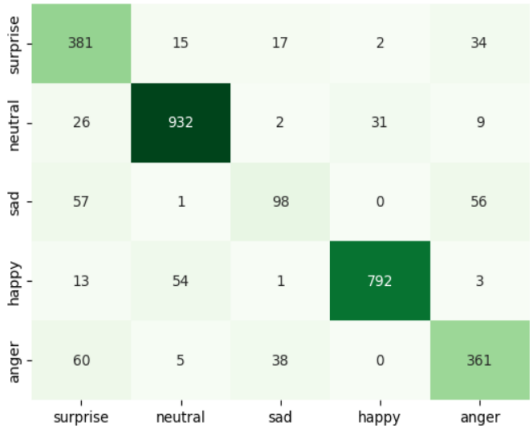

Figure 19. ResNet50 confusion matrix.

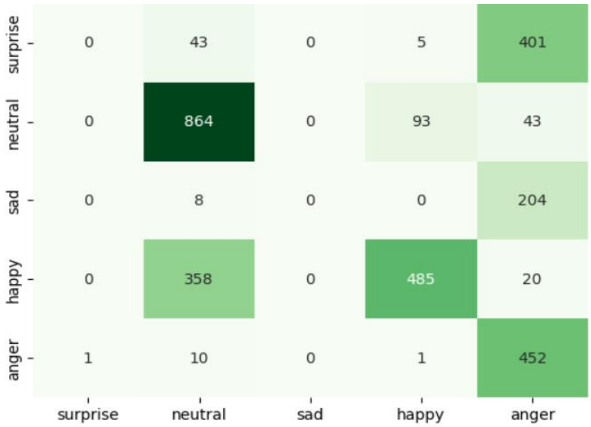

Figure 20. VGG16 confusion matrix.

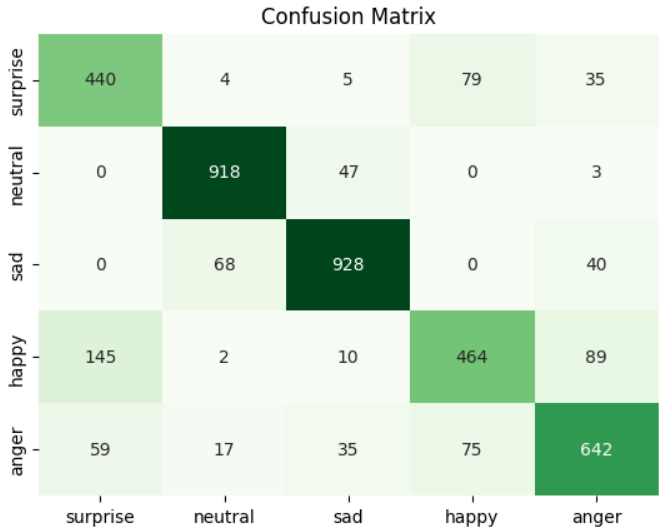

Figure 21. YoloV8m-cls confusion matrix.

The confusion matrix of each model is given in the outputs above. When the results are examined, it is seen that neutral and happy emotions are the best predicted classes in all models.

ROC curve comparison

ROC (Receiver Operating Characteristic) curve is another important metric to evaluate the performance of emotion recognition models. It graphically shows the trade-off between true positive rate (sensitivity) and false positive rate (1 - specificity) across various classification thresholds. Area under the ROC curve (AUC) is a widely used summary measure, where an AUC score closer to 1 indicates better performance. The Roc curve results for the models are given below in Figures 22, 23, 24, 25 and 26.

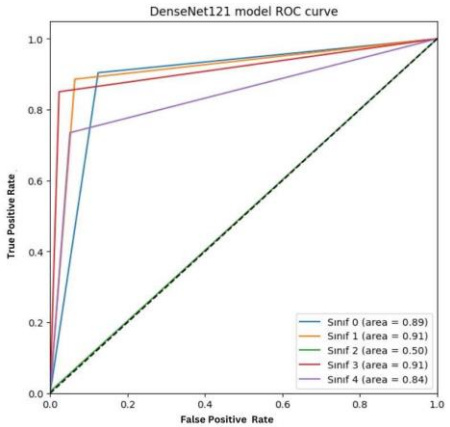

Figure 22. DenseNet121 roc curve.

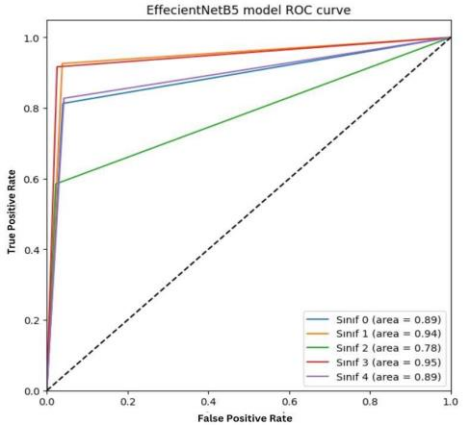

Figure 23. EfficienetNetB5 roc curve.

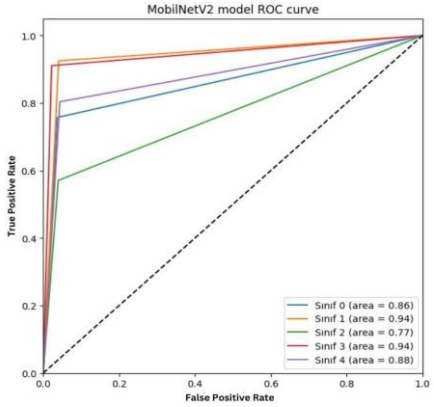

Figure 24. MobilNetV2 roc curve.

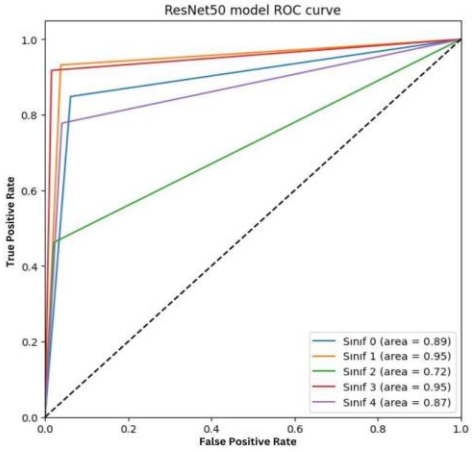

Figure 25. Resnet50 roc curve.

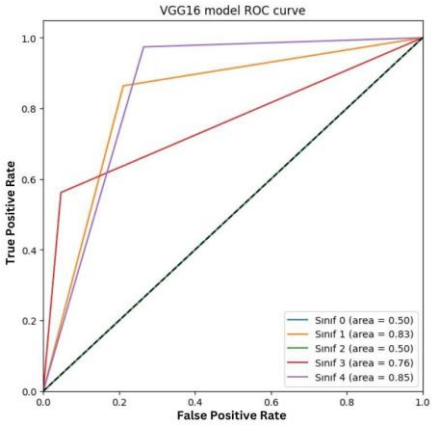

Figure 26. VGG16 roc curve.

The above curves show the Roc curves of all models, and while all models achieved a Roc curve above 0.85, only the VGG16 model achieved a score of around 0.75. The VGG16 model performed worse than the others in distinguishing emotions. It is easier to detect emotions of classes 1 and 3 (neutral and happy). YoloV8-cls was the best discriminator with 0.92.

Model Resource Consumption and Efficiency Analysis

Figure 27: Efficient Resource Consumption Chart

Figure 28. Resnet Resource Consumption Chart

Figure 29. Yolov Resource Consumption Chart

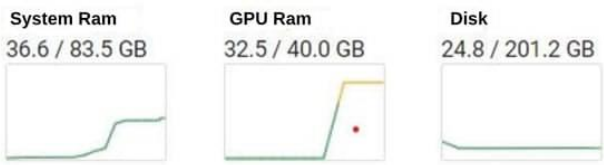

Figure 30. Desnet Resnet Resource Consumption Chart

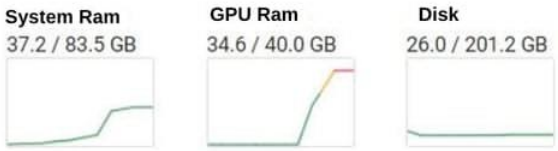

Figure 31. Vgg16 Resnet Resource Consumption Chart

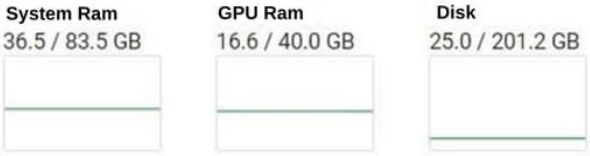

Figure 32. MobilNet Resnet Resource Consumption Chart

Discussion

Table 4 below shows the metric results of all models used in the study. By looking at these results, we can compare the models with each other and form an idea about the loss values.

Table 4. Results of the models.

Model	Accuracy	Loss	Precision	Recall	F1-Score
DenseNet121	0,79	0,57	0,82	0,68	0,64
EfficientNet	0,84	0,49	0,82	0,81	0,82
MobilNetV2	0,85	0,61	0,79	0,79	0,79
ResNet50	0,85	0,52	0,8	0,79	0,79
VGG16	0,6	0,96	0,38	0,48	0,4
YoloV8m-cls	0,89	0,32	0,84	0,87	0,84

Analysis of best performing models

In this study, multiple deep learning models were evaluated for their performance on emotion detection tasks, and YOLOv8m-cls, ResNet50, and EfficientNetB5 emerged as the best performing models based on accuracy, loss values, and confusion matrix results. YOLOv8m-cls showed the highest overall performance, showing excellence in both accuracy and generalization. Its ability to maintain low loss values throughout the training process, combined with minimal misclassifications in the confusion matrix, made it the most reliable model for emotion detection. The strength of YOLOv8m-cls lies in its balance between speed and accuracy, which is crucial for real-time applications where fast detection is required. ResNet50 showed particularly strong results in terms of its ability to process complex facial features. It enabled the model to capture subtle patterns in facial expressions that may be lost in traditional convolutional layers. While ResNet50's training accuracy reached almost perfect levels, its validation accuracy faltered, indicating some overfitting. Despite this, ResNet50's overall performance, especially in distinguishing between subtle emotions such as anger and disgust, positioned it as one of the best performing models. With its efficient scaling of depth, width, and resolution, EfficientNetB5 offered a strong balance between accuracy and computational cost. While it did not outperform YOLOv8m-cls or ResNet50 in absolute terms, its composite scaling made it particularly valuable for scenarios where computational resources are limited. EfficientNetB5 showed a consistent reduction in both training and validation loss with minimal gap between the two, indicating good generalization and resistance to overfitting. MobileNetV2 showed solid performance in terms of speed and efficiency, but fell slightly behind the top three models in terms of accuracy. VGG16 struggled with overfitting, as evidenced by its high training accuracy but low validation accuracy. While VGG16's deep architecture allowed it to perform well on training data, it failed to generalize to unseen data, making it the weakest model in this study. The limitations of VGG16 suggest that it may not be suitable for emotion recognition tasks without further tuning, such as the addition of regularization techniques. YOLOv8m-cls stands out as the best overall performer, especially for real-time applications, while ResNet50 and EfficientNetB5 provide strong alternatives depending on the specific requirements of the task. The efficiency of MobileNetV2 makes it suitable for resource-constrained environments, but significant improvements are required for VGG16 to be applicable for emotion detection tasks.

Limitations of the models

While the deep learning models examined in this study show strong potential for emotion detection, they also exhibit several limitations that need to be addressed for real-world applications. Overfitting remains a persistent problem, especially for models such as VGG16 and DenseNet121. These models achieved high training accuracy but failed to generalize to validation and test sets, suggesting that they memorize training data rather than learn generalizable patterns. Computational cost is another limitation, especially for deep models such as ResNet50 and DenseNet121, which require significant processing power and memory to train and deploy. Although models such as MobileNetV2 and EfficientNetB5 are optimized for efficiency, they may sacrifice some accuracy in favor of lower computational demands. Limited training data is a major limitation. While large datasets such as AffectNet provide a solid foundation for training, emotion recognition datasets are still relatively small compared to datasets for other tasks such as object detection or natural language processing. The scarcity of labeled data makes it difficult for models to learn the full range of human emotional expressions, which can result in lower performance when used in a variety of real-world scenarios. The lack of multimodal data in this study is a limitation. Human emotions are often expressed through multiple channels, including facial expressions, voice, and body language. While this study focused only on facial expressions, future studies can integrate additional modalities to improve emotion recognition performance. Models that include audio or physiological signals, such as heart rate or skin conductance, can capture a more complete picture of emotional states and lead to more

robust and accurate systems. Overfitting, computational cost, limited training data, and the lack of multimodal inputs are important hurdles that future research must address to develop more accurate, generalizable, and efficient emotion recognition systems.

Conclusion

Summary of findings

This study investigated the performance of various deep learning models (YOLOv8m-cls, ResNet50, EfficientNetB5, MobileNetV2, DenseNet121 and VGG16) on the task of emotion recognition from facial expressions. The aim was to identify the most effective model for emotion classification across 5 different emotion categories using transfer learning models. These emotions are Surprise, Neutral, Sad, Happy and Angry. Among the evaluated models, YOLOv8m-cls emerged as the best performing model overall. Its high accuracy, low loss values and strong performance in confusion matrix and ROC curve analysis indicated its suitability for real-time emotion detection tasks. ResNet50 and EfficientNetB5 also showed strong performance; ResNet50 showed excellence in capturing complex facial features and EfficientNetB5 balanced computational efficiency with accuracy. Both models proved to be highly capable of generalizing to unseen data, making them viable options for a range of emotion recognition applications. Despite being slightly behind the top three models, MobileNetV2 showed commendable performance in terms of speed and efficiency, making it a good candidate for mobile or embedded systems where computational resources are limited. DenseNet121 struggled with overfitting issues despite its complex architecture, and VGG16 faced the most significant challenges, especially in generalization due to its tendency to memorize training data rather than learning generalizable patterns. The study also highlighted several key challenges in emotion recognition, including intra-class variability, inter-class similarity, environmental factors, and difficulty generalizing to new datasets. These challenges affected the performance of all models to varying degrees, and while YOLOv8m-cls and ResNet50 handled these challenges better than the others, no model was completely immune to misclassification or overfitting. It highlights the importance of choosing the right model architecture according to the specific needs of the application. It was found that YOLOv8m-cls was the most suitable solution for real-time applications, while ResNet50 and EfficientNetB5, which have different strengths in handling complex features and computational efficiency, offered strong alternatives.

Implications for future research

While the results of this study indicate significant advances in the use of deep learning models for emotion recognition, several areas remain ripe for future research. Addressing the limitations identified in this study, such as overfitting and computational cost, will be important to improve model performance and ensure scalability of emotion detection systems in real-world applications. Future work should focus on improving generalization capabilities. Researchers should explore cross-dataset validation techniques where models are trained on one dataset and evaluated on another dataset to ensure that models can effectively generalize to unseen data. Another promising avenue for future research is the integration of multimodal data. Emotions are often expressed through a combination of facial expressions, audio, and physiological signals, and combining these modalities can significantly improve the accuracy and reliability of emotion recognition systems.

Multimodal models that include audio, text, or physiological data such as heart rate or galvanic skin response can provide a more comprehensive understanding of human emotions. Explainability and ethical concerns also represent important areas for future research. As emotion recognition systems are increasingly used in sensitive applications ranging from mental health to surveillance, the ethical implications of these technologies must be carefully considered. Ensuring privacy, bias reduction, and fairness in emotion recognition systems are important to prevent potential misuse or harm. Future research should focus on developing guidelines and frameworks to ensure these systems are used responsibly and equitably across all demographics.

Author contributions

AHI provided the idea for the software. Reviewed previous studies in this area and made suggestions for development with different methods and methods. MU completed the software part of the study and tested the results, compared them with each other and prepared a report. MFD provided planned progress in the writing phase of the article. Prepared the study according to the draft, taking into account the journal template and rules.

Acknowledgements

We would like to thank our valuable authors who made great efforts in the idea phase of this study, in the planning and software development of the article, and in transforming the results into an original article. We are also grateful to the journal members and referees who took the time to evaluate the article.

Declarations

OpenAccess

This article is licensed under a Creative Commons Attribution-NonCommercial-NoDerivatives 4.0 International License, which permits any non-commercial use, sharing, distribution and reproduction in any medium or format, as long as you give appropriate credit to the original author(s) and the source, provide a link to the Creative Commons licence, and indicate if you modified the licensed material. You do not have permission under this licence to share adapted material derived from this article or parts of it. The images or other third party material in this article are included in the article's Creative Commons licence, unless indicated otherwise in a credit line to the material. If material is not included in the article's Creative Commonslicence and your intended use is not permitted by statutory regulation or exceeds the

permitted use, you will need to obtain permission directly from the copyright holder. To view a copy of this licence, visit http://creativecommons.org/licenses/by-nc-nd/4.0/.

Conflict of interest

The authors affirm that they have no known competing financial interests or personal relationships that might have influenced the work reported in this paper.

Consent to participate

All participants in this study provided informed consent to take part in the research.

Consent for publication

Authors have given their consent for the publication of the research findings and related materials

Financial support

No Financial Support was declared by the authors

References

[1] P. Ekman, "Facial expression and emotion," *Am. Psychol*, vol. 48, no. 4, pp. 384–392, 1993. DOI:10.1037/0003-066X.48.4.384

[2] M. Pantic and L. J. Rothkrantz, "An expert system for recognition of facial actions and their intensity," *AAAI/IAAI*, pp. 1026–1033, 2000.

[3] Z. Zeng, M. Pantic, G. I. Roisman and T. S. Huang, "A survey of affect recognition methods: Audio, visual and spontaneous expressions," *Proceedings of the 9th International Conference on Multimodal Interfaces*, pp. 126–133, 2007.

[4] J. Zhang, Z. Yin, P. Cheng and S. Nichele, "Emotion recognition using multi-modal data and machine learning techniques: A tutorial and review," *Inf Fusion*, 2020. DOI:10.1016/j.inffus.2020.01.011

[5] Y. Tian, T. Kanade and J. F. Cohn, "Facial expression recognition," in *Handbook of Face Recognition*, S. Z. Li and A. K. Jain, Eds., Springer, 2011, pp. 487–519. DOI:10.1007/978-0-85729-932-1_19

[6] P. Ekman and W. V. Friesen, *Facial Action Coding System*. Consulting Psychologists Press, 1978.

[7] P. Lucey, J. F. Cohn, T. Kanade, J. Saragih, Z. Ambadar and I. Matthews, "The extended cohn-kanade dataset (CK+): A complete dataset for action unit and emotion-specified expression," *2010 IEEE Computer Society Conference on Computer Vision and Pattern Recognition – Workshops (CVPRW),* pp. 94–101, 2010. DOI:10.1109/CVPRW.2010.
5543262

[8] G. Tolias and O. Chum, "Asymmetric feature maps with application to sketch-based retrieval," *Proceedings of the IEEE Conference on Computer Vision and Pattern Recognition*, pp. 3155–3164, 2017.

[9] A. Krizhevsky, I. Sutskever and G. E. Hinton, "Imagenet classification with deep convolutional neural networks," *Advances in Neural Information Processing Systems (NeurIPS),* pp. 1097–1105, 2012.

[10] D. Zilyas and A. Yılmaz, "Prediction model of educational success with machine learning methods," *DUMF Engineering Journal*, vol. 14, no. 3, pp. 437–447, 2023. DOI:10.24012/dumf.1322273

[11] I. Goodfellow, Y. Bengio and A. Courville, *Deep Learning*. MIT Press, 2016.

[12] M. Wöllmer, A. Metallinou, F. Eyben, B. Schuller, and S. Narayanan, "Context-sensitive multimodal emotion recognition from speech and facial expression using bidirectional LSTM modeling," *IEEE Transactions on Affective Computing*, vol. 2, no. 1, pp. 42–55, 2010.

[13] A. G. Howard *et al*., "MobileNets: Efficient convolutional neural networks for mobile vision applications," *arXiv preprint, arXiv:1704.04861*, 2017.

[14] F. Eyben *et al*., "The geneva minimalistic acoustic parameter set (GeMAPS) for voice research and affective computing," *IEEE Transactions on Affective Computing*, vol. 7, no. 2, pp. 190–202, 2015.

[15] J. Devlin, "BERT: Pre-training of deep bidirectional transformers for language understanding," *arXiv preprint arXiv:1810.04805,* 2018.

[16] A. Zadeh, M. Chen, S. Poria, E. Cambria and L. P. Morency, "Tensor fusion network for multimodal sentiment analysis," *arXiv preprint, arXiv:1707.07250*, 2017.

[17] R. T. Shawi, A. A. A. Abdulkadhim, and F. N. Abbas, "Facial Emotion Recognition Based on Improved ResNet50 Using Hybrid Pooling and Adaptive Leaky ReLU," *International Journal of Scientific Research in Science, Engineering and Technology*, vol. 12, no. 3, pp. 728–737, 2025.

[18] A. Alshammari and M. E. Alshammari, "Emotional facial expression detection using YOLOv8," *Engineering, Technology & Applied Science Research*, vol. 14, no. 5, pp. 16619–16623, 2024.

[19] A. A. Istiqomah, C. A. Sari, A. Susanto, and E. H. Rachmawanto, "Facial expression recognition using convolutional neural networks with transfer learning ResNet-50," *Journal of Applied Informatics and Computing*, vol. 8, no. 2, pp. 257–264, 2024.

[20] W. Du, "Facial emotion recognition based on improved ResNet," *Applied and Computational Engineering*, vol. 21, pp. 242–248, 2023.

[21] L. L. X. Wei and N. S. Sani, "Enhanced facial expression recognition based on ResNet50 with a

convolutional block attention module," *International Journal of Advanced Computer Science & Applications*, vol. 16, no. 1, 2025.

[22] M. B. Sutar and A. Ambhaikar, "A Comparative Study on Deep Facial Expression Recognition," in *2023 7th International Conference on Intelligent Computing and Control Systems (ICICCS)*, pp. 903–911, May 2023.

[23] N. T. Singh, R. Ritu, C. Kaur, and A. Chaudhary, "Comparative analysis of traditional machine learning and deep learning techniques for facial expression recognition," in *2023 14th International Conference on Computing Communication and Networking Technologies (ICCCNT)*, pp. 1–7, Jul. 2023.

[24] A. G. Vural, B. B. Cambazoğlu, P. Şenkul, and Z. O. Tokgöz, "A framework for sentiment analysis in Turkish: Application to polarity detection of movie reviews in Turkish," in *Computer and Information Sciences III,* E. Gelenbe and R. Lent, Eds., Springer, 2013, pp. 437–445. DOI:10.1007/978-1-4471-4594-3_42

[25] M. Bilgin and İ. F. Şentürk, "Sentiment analysis of document vectors based tweets using supervised and semi-supervised learning," *Journal of Balıkesir University Institute of Science*, vol. 21, no. 2, pp. 822–839, 2019.

[26] G. M. Demirci, S. R. Keskin, and G. Doğan, "Sentiment analysis in Turkish with deep learning," *2019 IEEE International Conference on Big Data (Big Data).* DOI:10.1109/bigdata47090.2019.9006066

[27] M. Seyfioğlu and M. Demirezen, "A hierarchical approach for sentiment analysis and categorization of Turkish written customer relationship management data," *Proceedings of the 2017 Federated Conference on Computer Science and Information Systems (FedCSIS),* IEEE, 2017.

[28] B. Ayan, B. Kuyumcu and B. Ceylan, "Detection of Islamophobic tweets on Twitter using sentiment analysis," *Gazi Univ. J. Sci. Part C Des. Technol.*, vol. 7, no. 2, pp. 495–502, 2019.

[29] F. N. Uyaroğlu Akdeniz and H. I. Cebeci, "Sentiment analysis approach in evaluation of municipal services: Sakarya province example," *J. Intell. Syst. Theory Appl.*, vol. 4, no. 2, pp. 127–135, 2021.

[30] S. Tuzcu, "Classification of online user comments with sentiment analysis," *Eskişehir Turkish World App. Res. Center Informat. J.,* vol. 1, no. 2, pp. 1–5, 2020.

[31] D. Yohanes, J. S. Putra, K. Filbert, K. M. Suryaningrum, and H. A. Saputri, "Emotion detection in textual data using deep learning," *Procedia Comput. Sci.,* vol. 227, pp. 464-473, 2023.

[32] G. Zhang and S. Ananiadou, "Examining and mitigating gender bias in text emotion detection task," *Neurocomputing*, vol. 493, pp. 422–434, 2022. DOI:10.1016/j.neucom.2022.03.051

[33] D. Issa, M. F. Demirci, and A. Yazici, "Speech emotion recognition with deep convolutional neural networks," *Biomedical Signal Processing and Control*, vol. 59, p. 101894, 2020. DOI:10.1016/j.bspc.2020.101894

[34] A. S. Yuksel and F. G. Tan, "Knowledge discovery in social networks with text mining techniques," *J. Eng. Sci. Design*, vol. 6, no. 2, pp. 324–333, 2018. DOI:10.21923/jesd.384791

[35] M. Turan and E. Arığ, "Video sentiment analysis," *Eur. J. Sci. Technol. (EJOSAT) Supplementary Special Issue (HORA),* pp. 34–41, 2021.

[36] C. D. Eyipınar, F. Büyükkalkan and K. Semiz, "Sentiment analysis of YouTube video comments on athlete nutrition," *Int J Phys Educ. Sports Technol*., vol. 2, no. 2, pp. 27–39, 2021.

[37] A. Tepecik and E. Demir, "Analysis of Turkish voice recording data labeled with three emotions using machine learning algorithms," *Gazi Univ. Fac. Eng. Arch. J.,* 39(2):709–716.

[38] A. Sel, "Analysis of public opinion during the pandemic period using sentiment analysis method: The case of Türkiye," *Beykoz Academic Journal*, vol. 10, no. 2, pp. 134–154, 2022.

[39] M. Uysal, "Comparison and applicability of modifying deep learning models for emotion recognition," M.S. thesis, Burdur Mehmet Akif Ersoy Univ., 2024.

[40] M. Sandler, A. Howard, M. Zhu, A. Zhmoginov, and L. C. Chen, "MobileNetV2: Inverted residuals and linear bottlenecks," *Proceedings of the IEEE Conference on Computer Vision and Pattern Recognition (CVPR),* pp. 4510–4520, 2018.

[41] K. He, X. Zhang, S. Ren and J. Sun, "Deep residual learning for image recognition," *Proceedings of the IEEE Conference on Computer Vision and Pattern Recognition (CVPR),* pp. 770–778, 2016.

[42] K. Simonyan and A. Zisserman, "Very deep convolutional networks for large-scale image recognition," *arXiv preprint arXiv:1409.1556,* 2014.

[43] J. Redmon, S. Divvala, R. Girshick and A. Farhadi, "You only look once: Unified, real-time object detection," *Proceedings of the IEEE Conference on Computer Vision and Pattern Recognition (CVPR),* pp. 779–788, 2016.

Dicle University
Journal of Engineering
https://dergipark.org.tr/tr/pub/dumf
duje.dicle.edu.tr

Araştırma Makalesi / Research Article

Güneydoğu Anadolu Bölgesi'nde çok kriterli karar verme yöntemleri ile yüzer güneş panelleri için optimal yer seçimi

Optimal site selection for floating solar panels in the Southeastern Anatolia Region using multi-criteria decision making methods

Rıdvan Şen[1], Şehmus Fidan[2*]

[1] Batman Üniversitesi, Elektrik- Elektronik Mühendisliği Bölümü, ridvan.sen@batman.edu.tr
ORCID: https://orcid.org/0000-0002-5249-7245

[2] Batman Üniversitesi, TBMYO, Elektronik ve Otomasyon Programı, sehmus.fidan@batman.edu.tr
ORCID: https://orcid.org/0009-0003-3374-2393

MAKALE BİLGİLERİ

Makale Geçmişi:

Geliş 25 Ağustos 2025
Revizyon 1 Ekim 2025
Kabul 2 Ekim 2025
Online 30 Aralık 2025

Anahtar Kelimeler:
Çok Kriterli Karar Verme,
Yüzer Güneş Santralleri,
Hidroelektrik Baraj Rezervuarı,
Gündeydoğu Anadolu Bölgesi

ÖZ

Yüzer solar panelleri; suyun soğutma etkisi ile enerji verimliliğini artırması, buharlaşma kayıplarını azaltması ve arazi kullanım gereksinimini ortadan kaldırması gibi çeşitli avantajlar sunmaktadır. Bu faydalar, hem dünyada hem de ülkemizde yüzer solar panel uygulamalarının sayısının her geçen gün artmasına katkı sağlamaktadır. Ancak, Güneydoğu Anadolu Bölgesi özelinde bu sistemlerin kurulacağı en uygun yerin belirlenmesine yönelik çalışmalar oldukça sınırlıdır. Bu araştırma, hidroelektrik santrallerin rezervuar alanlarına yüzer solar panellerinin kurulumu için en uygun lokasyonun belirlenmesine odaklanmaktadır. Bu amaçla, çok kriterli karar verme yöntemleri (AHP, TOPSIS, MABAC, COMET ve SPOTIS) kullanılmıştır. Çok kriterli karar verme yaklaşımları, birden fazla kriterin eşzamanlı olarak dikkate alındığı durumlarda, en uygun seçeneğin tespiti için sistematik ve analitik bir değerlendirme çerçevesi sunmaktadır. Bu yöntemler aracılığıyla farklı kriterlerin önem dereceleri belirlenmekte ve böylece daha objektif ve tutarlı sonuçlar elde edilebilmektedir. Çalışmada, yer seçim sürecinde dikkate alınacak kriterler arasında güneş ışınımı, yıllık günışığı süresi, rüzgâr hızı, bölgesel kalkınma düzeyi, sosyal kabul, sıcaklık, topografik yükselti, su derinliği ile yerleşim alanlarına ve şebeke bağlantı noktalarına uzaklık yer almaktadır. Bu kriterlerin ağırlıkları uzman görüşleri doğrultusunda belirlenmiştir. Yapılan analizler sonucunda, güneş ışınımı ile yıllık günışığı süresinin en kritik kriterler olduğu ortaya çıkmış ve bu değerlendirmeler ışığında Karkamış Barajı en uygun rezervuar alanı olarak belirlenmiştir.

ARTICLE INFO

Article history:

Received 25 August 2025
Received in revised form 1 October 2025
Accepted 2 Oct 2025
Available online 30 December 2025

Keywords:
Multi-Criteria Decision Making,
Floating Solar Power Plants,
Hydroelectric Dam Reservoir,
Southeastern Anatolia Region

Doi: 10.24012/dumf.1762054

ABSTRACT

Floating solar panels offer several advantages, such as increasing energy efficiency through the cooling effect of water, reducing evaporation losses, and eliminating the need for land use. These benefits contribute to the growing number of floating solar panel applications both worldwide and in our country. However, studies focusing on determining the most suitable locations for the installation of such systems in the Southeastern Anatolia Region are quite limited. This research focuses on identifying the optimal location for the installation of floating solar panels on the reservoir areas of hydroelectric power plants. For this purpose, multi-criteria decision-making methods (AHP, TOPSIS, MABAC, COMET, and SPOTIS) were employed. Multi-criteria decision-making approaches provide a systematic and analytical framework for identifying the best option in situations where multiple criteria are considered simultaneously. Through these methods, the relative importance of different criteria can be determined, leading to more objective and consistent results. In this study, the criteria considered for site selection include solar radiation, annual sunshine duration, wind speed, regional development level, social acceptance, temperature, topographic elevation, water depth, and the distance to residential areas and grid connection points. The weights of these criteria were determined based on expert opinions. The analysis revealed that solar radiation and annual sunshine duration are the most critical criteria, and in light of these findings, the Karkamış Dam was identified as the most suitable reservoir area.

* Sorumlu Yazar

Giriş

Günümüzde enerji, yalnızca günlük ihtiyaçların karşılanmasında değil, aynı zamanda ülkelerin stratejik gücünü belirleyen temel bir kaynaktır. Fosil yakıtların çevresel etkileri ve sınırlı rezervleri, yenilenebilir enerji kaynaklarının enerji arzında öncelikli rol oynamasını zorunlu kılmaktadır. Bu süreçte, yenilenebilir enerji kaynaklarını devreye almak büyük önem taşırken, aynı zamanda mevcut enerji kaynaklarının verimliliğini artırarak kayıpları önleyecek yeni çözümlerin geliştirilmesi gerekmektedir. Bu bağlamda, fotovoltaik sistemler (FV), temiz enerji üretiminde önemli bir rol oynarken, teknolojideki gelişmelerle birlikte verimliliklerinin artırılması ve çeşitli uygulama alanlarında yaygınlaştırılması kritik hale gelmiştir. Bu hususta yüzer solar paneller (YSP) geleneksel FV santrallerinden görece daha verimli olduğu, birçok çalışma sonucunda ortaya konulmuştur. Yapılan çalışmalarda elde edilen verilere göre, Brezilya'daki yarı kurak Castanhão, Orós ve Banabuiú rezervuarlarında YSP kurulumları analiz edilmiştir. Bu analizlerde, su yüzeyinden sağlanan soğutucu etki sayesinde YSP'lerin dönüşüm verimliliğinin, karasal tip panellere kıyasla %12,5 daha yüksek olduğu belirlenmiştir [1]. Hindistan'da tarımsal sulama için kurulan küçük ölçekli YSP'ler üzerinde yapılan analizler, coğrafi koşullara bağlı olarak karasal FV sistemlere göre %4 daha fazla verim sağladığını ortaya koymuştur [2]. Endonezya'nın Java Eyaleti'nde YSP sistemlerinin verimliliğini tahmin etmek ve enerji verimini ölçmek amacıyla, uzaktan algılama ölçümleri sonucunda elde edilen veriler kullanılarak bir ekonomik analiz yapılmıştır. Bu analizde, YSP sistemleri karasal FV sistemlerle karşılaştırılmıştır. Uzaktan algılama yöntemiyle elde edilen bulgular, göl yüzeyinin kara yüzeyine kıyasla daha düşük sıcaklığa sahip olduğunu ve yıllık ortalama sıcaklık farkının yaklaşık 8°C olduğunu göstermiştir. Bu fark, YSP sistemlerinin karasal FV sistemlere göre daha düşük sıcaklık stresi altında çalışmasına ve dolayısıyla verimliliklerinin tahmini olarak %0,61 daha yüksek olmasına katkı sağlamaktadır [3]. Sonuç olarak; YSP'ler, karasal güneş enerjisi sistemlerine alternatif olarak son yıllarda dünya genelinde hızla gelişen ve uygulama alanı genişleyen, yenilikçi bir enerji üretim çözümüdür [4].

YSP'ler hakkında bilinen ilk proje 2007 yılında Japonya' nın Aichi kentinde yapılmıştır. Kurulan tesisin 20 kWp gücünde olup araştırmanın ana amacı su üstünde modül sıcaklıklarının FV sistem performansına etkisini incelemektir. Ancak, küçük su rezervuarlarına YSP kurularak üzüm bağlarına enerji sağlama amacıyla ilk kez 2008 yılında ABD'nin Kaliforniya Eyaleti'nde 175 kWp gücünde bir sistem kurulmuştur [5]. Bu öncü çalışmaları takiben, Fransa, Hindistan, Japonya, Güney Kore, Birleşik Krallık, Singapur, Çin ve Amerika Birleşik Devletleri'nde YSP'ler hakkında araştırma ve uygulama projeleri hayata geçirilmiştir. Ayrıca, Brezilya, Pakistan, İspanya ve Yeni Zelanda gibi birçok ülkede, hidroelektrik baraj rezervuarları ile su kanallarına YSP santrallerinin kurulma potansiyeli ve elde edilebilecek enerji miktarına yönelik araştırma projeleri yürütülmektedir [6]. İspanya'da gerçekleştirilen bir çalışmada, mevcut su yüzey alanlarının %10'unun YSP ile kaplanması halinde ülkenin elektrik ihtiyacının yaklaşık %31'inin karşılanabileceği, su yüzey alanlarının tamamının kaplanması durumunda ise fosil kaynaklı elektrik üretiminin %80 oranında azalabileceği ifade edilmiştir [7].

Dünya çapında elektrik enerjisine erişim miktarının %54 ile en az olduğu, ışınım yönünden zengin konumda olan Afrika kıtasında 146 hidroelektrik santrali bulunmaktadır. Bu santrallerin rezervuar alanlarının, %1 den az bir oranda YSP kurulması durumunda, mevcut hidroelektrik santrallerin kurulu güç kapasitesinin iki katına çıkabileceği ve elektrik üretiminin %58 oranında artarak yılda ilave 46,04 TWh enerji üretilebileceğini göstermektedir [8]. Suudi Arabistan'da, proje maliyetini azaltıp maksimum güç elde etmek için AHP yöntemiyle yapılan bir araştırmada, kuzey ve kuzeybatı bölgelerinin FV santral kurulumu için uygun olduğu belirlenmiştir [9]. İran'da FV santralleri için en uygun yerin belirlenmesinde, AHP yöntemiyle güneş radyasyonu, ekonomik, teknik ve coğrafi faktörler gibi birçok kriter değerlendirilmiştir [10]. Etiyopya'da YSP kurulumu için en yüksek potansiyele sahip bölgelerin tespitinde AHP yöntemi kullanılmıştır. Çalışma sonucunda, Amhara bölgesinin sistem kurulumu açısından en yüksek potansiyele sahip olduğu sonucuna ulaşılmıştır [11].

Ülkemizde ise belirli rezerv alanlarda YSP kurulumu üzerine potansiyel değerlendirmeleri ve teorik çalışmaların yapıldığı görülmektedir. Uygulama örneklerinden biri, Büyükçekmece Gölü üzerinde kurulan 90 kWp kapasiteli YSP projesidir. 2017 yılında başlatılan bu projenin amacı, YSP'lerin tasarım, üretim, inşaat ve kurulum süreçlerini ortaya koymak ve bu santralden elde edilen enerji miktarını analiz etmektir [12]. Kayseri yakınlarında bulunan Yamula Barajı'na YSP kurulması ve ortaya çıkacak potansiyelin analizi araştıma konusu olmuştur. Simülasyon programı ile yapılan analiz çalışmasında, rezervuar alanının %10 kadar kısmının YSP ile kapatılması durumunda, 576,4 MW kurulu güç potansiyeli taşıdığı hesaplanmıştır [13]. Diğer bir çalışmada YSP'lerin deniz üstüne kurulumu incelemiştir. Çalışmada, Türkiye'nin kıyı bölgeleri ile durgun su yüzeylerinin YSP'ler için uygun olduğu sonucuna varılmıştır. Uygun rezervuarların %10'unda yapılan kurulumla yıllık 125 TWh elektrik üretimi sağlanabileceğini böylelikle enerji bağımlılığını azaltma potansiyeli taşıdığını belirtmiştir. Türkiye'de bulunan Van Gölü, Tuz Gölü ve Beyşehir göllerine YSP kurulması için yer seçiminde AHP yöntemi kullanılmıştır. Yapılan analizler sonucunda en önemli kriter olarak, küresel yatay ışınım (Global Horizontal Irradiance-GHI) kriterinin belirlenmesi sonucunda, Beyşehir Gölü'nün YSP santrali kurulumu için en ideal seçim olduğu görülmüştür [14]. Farklı bir çalışmada, Türkiye'nin farklı bölgelerinde su rezervuarına sahip sekiz hidroelektrik santralinde, YSP santrali kurulumu potansiyelini belirlemeye yönelik bir araştırma gerçekleştirilmiştir. Bu kapsamda, teknik, ekonomik ve sosyal açıdan tesis kurulumu için alternatifler; AHP yöntemi ile OWA (Ordered Weighted Averaging – Sıralı Ağırlıklı Ortalama) yöntemi kullanılarak

değerlendirilmiştir. Yapılan analizler sonucunda, Aydın ilinde bulunan Kemer HES, YSP kurulumu açısından en uygun alan olarak tespit edilmiştir [15].

Bu çalışma ile Türkiye'nin Güneydoğu Anadolu Bölgesinde bulunan hidroelektrik santrallerinin üzerine YSP kurumunda optimal yer seçimi konusu ele alınmıştır. Yapılan literatür çalışmasında bölge özelinde bu çalışmanın yapılmadığı belirlenmiştir. Yer seçiminin doğruluğunu belirlemek için AHP, TOPSIS, MABAC, COMET ve SPOTIS gibi ÇKKV yöntemleri kullanılmıştır. Ortaya konan sonuçlar, bölgeye yatırım yapmak isteyen kurum ve kuruluşlar için bir ön çalışma niteliğindedir.

Materyal ve Metot

Yüzer solar paneller (YSP)

YSP'ler, karasal alan gereksinimini ortadan kaldırarak su yüzeyleri üzerinde enerji üretimini mümkün kılan yenilikçi fotovoltaik sistemlerdir. Bu sistemler temel olarak dubalar ya da taşıyıcı platformlar, şamandıralar, bağlama sistemleri, FV modüller, kablo ve konnektör bileşenlerinden oluşur. Dubalar ya da taşıyıcı platformlar panellerin su yüzeyinde dengeli şekilde konumlandırılmasını sağlamaktadır. Bu taşıyıcılar genellikle UV ışınlarına ve çevresel etkilere dayanıklı, hafif ancak sağlam malzemelerden üretilir. Şamandıralar ise yapının yüzebilirliğini artırmanın yanı sıra dalga ve rüzgar gibi dış etkenlere karşı sistemin kararlı kalmasına yardımcı olur [5].

Bağlama sistemleri, platformun su yüzeyinde kaymasını ya da savrulmasını önlemek amacıyla zemine sabitlenmesini sağlar; bu sabitleme çelik halatlar, zincirler ve beton bloklarla gerçekleştirilir. FV modüller ise güneş ışığını doğrudan elektrik enerjisine dönüştüren ana bileşenler olup, bu panellerin eğim ve yönü maksimum enerji verimliliği sağlanacak şekilde konumlandırılır. Enerji iletimini sağlayan kablo ve konnektörler, su geçirmez ve dış koşullara dayanıklı şekilde yalıtılmıştır. Sistemde yer alan evirici ise FV modüllerden gelen doğru akımı (DC), şebekede kullanılabilir alternatif akıma (AC) dönüştürerek enerji altyapısına entegrasyonu sağlar. Sonuç olarak, YSP sadece temiz enerji üretimini değil, aynı zamanda su buharlaşmasının azalmasını ve panel sıcaklıklarının düşük tutulması sayesinde verimliliğin artmasını da sağlar. Bu yönüyle YSP'ler hem çevresel hem de ekonomik açıdan sürdürülebilirliğe destek olmaktadır [5].

Çok kriterli karar verme yöntemleri (ÇKKV)

Günümüzde karar verme, birçok alanda giderek daha karmaşık bir süreç hâline gelmektedir. Teknoloji değişimi ve artan bilgi buna bağlı olarak yeni problemler de ortaya çıkarmıştır. Karar verme sırasında; karar vericilerin deneyimleri, kişisel fikirleri, stratejik amaçları dikkate alındığı gibi birçok nicel ve nitel kriterin de sürece dâhil edildiği görülmektedir [17]. Çok kriterli karar verme (ÇKKV) problemleri, birden fazla kriterin dikkate alındığı durumlarda, olası çözüm setleri arasından en uygun alternatifin seçilmesini amaçlayan problemlerdir. Bu tür problemlerin çözümünde uygun yöntemin belirlenmesinde, karar vericinin problemin yapısını ve karar sürecinin özelliklerini dikkate alması gerekmektedir [18]. Çoklu karar vermede birçok yöntem bulunmakla beraber bu çalışmada AHP, TOPSIS, MABAC, COMET ve SPOTIS yöntemleri kullanılmıştır. Bu yöntemlerin kullanılması safhasında seçim cetveli hazırlığı yapılmıştır. Seçim cetveli hazırlanırken YSP ve karasal FV alanında tecrübeli uzmanlardan destek alınmıştır. Ayrıca akademik yayınlardan yararlanarak YSP kurulum yerinin seçiminde etkili olacağı düşünülen teknik, ekonomik ve sosyal kısıtların belirlendiği on kriter seçilmiştir. Daha sonra, belirlenen bu kriterlerin ağırlık oranlarını belirlemek amacıyla, çoğunluğu enerji hakkında çalışan akademisyenlerden oluşan toplam on iki uzmana anketin amacı açıklanarak değerlendirme yapmaları istenmiştir. Ardından uzmanların doldurmuş olduğu seçim cetveline göre her bir kriterin ağırlık oranları belirlenmiştir. Ağırlık oranları ise optimal yer seçimine ilişkin karar verme aşamasında kullanılmıştır.

Analitik hiyerarşi süreci (AHP)

Analitik hiyerarşi süreci (AHP), Thomas L. Saaty tarafından 1980 yılında geliştirilmiş olup, birden fazla kriter barındıran problemlerin çözümüne uygun ÇKKV yöntemidir. Son yıllarda, karar vericilerin sezgi ve hissiyat yerine analitik ve nicel yaklaşımlara yönelmesiyle birlikte, AHP kararların sağlam bir temele dayandırılmasında sıkça kullanılan bir yöntem haline gelmiştir [19]. Bu yöntemde; amaç, kriterler, alt kriterler ve alternatiflerden oluşan hiyerarşik yapı titizlikle oluşturulmalı ve problemler kapsamlı bir şekilde analiz edilmelidir [20].

AHP yönteminde ilk adım, karar problemini anlamak ve bunu hiyerarşik bir modelde düzenlemektir. Bu modelin en üst seviyesinde kararın nihai amacı yer alırken, orta seviyede bu amacı etkileyen kriterler ve gerekirse alt kriterler bulunur. Hiyerarşinin en alt seviyesinde ise değerlendirme yapılacak alternatifler sıralanır. Amaç, kriterler ve alternatifler arasındaki ilişkilerin mantıklı bir düzende organize edilerek, karar probleminin sistematik bir yapıda ifade edilmesi sağlanır. Bu adım, problemin analiz edilmesini ve karar sürecinin kolaylaştırılmasını hedeflemektedir. Kriterler ve alt kriterler belirlendikten sonra, kendi aralarındaki önem derecelerini belirlemek için Denklem 1'de gösterilen karşılaştırma matrisi oluşturulur.

$$A = \begin{bmatrix} 1 & a_{12} & a_{13} & \dots & a_{1n} \\ 1/a_{21} & 1 & a_{23} & \dots & a_{2n} \\ 1/a_{31} & 1/a_{32} & 1 & \dots & a_{3n} \\ \vdots & \vdots & \vdots & \ddots & \vdots \\ 1/a_{n1} & 1/a_{n2} & 1/a_{n3} & \dots & 1 \end{bmatrix} \quad (1)$$

Uygulayıcıların değerlendirmelerine dayanarak, ikili karşılaştırma yöntemi ile her bir kriterin amaca katkısı açısından göreceli önem dereceleri belirlenir. Ardından her bir seçeneğin kriterler bakımından üstünlükleri de ortaya konur. Bu üstünlüklerin tespitinde ise, Saaty tarafından

geliştirilen [19] ve Tablo 1'de sunulan önem ölçeği kullanılmaktadır.

Tablo 1. AHP önem ölçeği

Sayısal Değer	Tanım
1	Kriterler eşit derecede önemli
3	1. kriter 2.'ye göre biraz daha önemli
5	1. kriter 2.'ye göre fazla önemli
7	1. kriter 2.'ye göre çok fazla önemli
9	1. kriter 2.'ye göre aşırı önemli
2,4,6,8	Ara değerler

İkili karşılaştırma matrisleri oluşturulduktan sonra bir sonraki aşama, ilgili matristeki her bir unsurun diğer unsurlara göre önem derecesini gösteren özvektörün hesaplanmasıdır. Matrisin $nx1$ boyutundaki özvektörü aşağıdaki şekilde belirlenir. Özvektör $i = 1,2,3,\dots n$ ve $j = 1,2,3,\dots n$ olmak üzere normalize edilmiş karar matrisi Denklem 2'de, öncelik vektörünün hesaplanması ise Denklem 3'te sunulmuştur.

$$b_{ij} = \frac{a_{ij}}{\sum_{i=1}^{n} a_{ij}} \quad (2)$$

$$w_i = \frac{\sum_{j=1}^{n} b_{ij}}{n} \quad (3)$$

Karar kriterlerinin yüzde bazındaki önem dağılımlarını belirlemek amacıyla sütun vektörlerinin ($w = [w_i]_{nx1}$) hesaplanması gerekmektedir. Bu vektör, Denklem 2'de verilen b_{ij} normalize edilmiş karar matrisinin satır elemanlarının aritmetik ortalaması alınarak elde edilir. Her ikili karşılaştırma matrisi için tutarlılık oranı (TO) hesaplanır ve bu oranın 0,10'u aşmaması beklenir. TO değerinin 0,1'in üzerinde olması, karar vericinin değerlendirmelerinde tutarsızlık bulunduğunu gösterir ve bu durumda yargıların yeniden gözden geçirilip düzeltilmesi gerekmektedir. Tutarlılık oranının (TO) hesaplanması için, A matrisinin en büyük özdeğerini (λ_{max}) hesaplamak gerekir. Bunun için öncelikle Denklem 4'te gösterilen matris hesaplanmalıdır. Ardından Denklem 4'ten elde edilen matris kullanılarak Denklem 5 (λ_{max}) hesaplanmalıdır. Denklem 4 ve 5'te $i = 1,2,3,\dots n$ ve $j = 1,2,3,\dots n$ olmak üzere;

$$D = [a_{ij}]\ x\ [w_i] = [d_i] \quad (4)$$

$$\lambda_{max} = \frac{\sum_{i=1}^{n} \frac{d_i}{w_i}}{n} \quad (5)$$

Tutarlılık oranının hesaplanmasında ihtiyaç duyulan bir başka değer ise rassallık endeksi (RE)'dir. Sabit sayılardan meydana gelen ve n değerine göre belirlenen RE değerinin yer aldığı veriler Tablo 2' de verilmiş olup bu değerler Saaty tarafından belirlenmiştir.

Tablo 2. Rassallık endeksi verileri

n	1	2	3	4	5	6	7	8	9	10
RE	0	0	0,58	0,9	1,12	1,24	1,32	1,41	1,45	1,49

RE belirlendikten sonra TO değerinin hesaplanması gerekir. Bunu yapmak için Denklem 6 kullanılmaktadır.

$$TO = \frac{\lambda_{max} - n}{(n-1).RE} \quad (6)$$

Denklem 2-5 arasında sunulan dört aşama, hiyerarşideki tüm kriterler için uygulanır. Tutarlılık oranı hesaplandıktan sonra, hiyerarşideki n adet kriterin her biri için oluşturulan $mx1$ vektörler bir araya getirilerek mxn boyutunda Denklem 7'de gösterilen DW karar matrisi oluşturulur. Karar matrisi ile kriter ağırlıkları W üstünlük vektörünün çarpımı sonucunda, Denklem 8'de gösterilen R sonuç vektörüne ulaşılır [21].

$$DW = [W_{ij}]_{mxn} \quad (7)$$

$$R = DWxW \quad (8)$$

Denklem 7'de sunulan DW karar matrisi, her alternatifin kriterler açısından göreli üstünlüklerini göstermekte kullanılır. W üstünlük vektörü ise her kriterin ağırlığını, yani karar açısından önemini gösterir. Sonuç olarak R sonuç vektörü, alternatiflerin toplam skorlarını içerir ve hangi alternatifin daha uygun olduğunu gösterir.

İdeal çözüm benzerliğine göre tercih sıralama tekniği (TOPSIS)

TOPSIS yöntemi, 1981 yılında Hwang ve Yoon [21] tarafından geliştirilmiş olup, karar vericinin belirlediği kriterler doğrultusunda en uygun sonucu bulmayı hedefler. Bu yöntemde, her bir alternatifin en iyi çözüme (ideal çözüm) olan yakınlığı ve en kötü çözüme (negatif ideal çözüm) olan uzaklığı hesaplanır. Alternatifler, X_{IJ} ile gösterilen değerlere göre değerlendirilir; burada i alternatifleri, j ise kriterleri temsil eder. İlk olarak, alternatiflerin değerleri normalize edilir. Bu işlem, farklı ölçü birimlerine sahip kriterlerin karşılaştırılabilir hale gelmesini sağlar. Normalizasyon işlemi Denklem 9'da ifade edilmiştir.

$$r_{ij} = \frac{x_{ij}}{\sqrt{\sum_{i=1}^{m} x_{ij}^2}} \quad (9)$$

Burada, r_{ij} normalize edilmiş değer, m ise alternatif sayısıdır. r_{ij} hesaplandıktan sonra her bir kriterin önem derecesine göre ağırlıklandırılmış normalize matris Denklemi (10) oluşturulur.

$$v_{ij} = w_i \cdot r_{ij} \quad (10)$$

Burada r_{ij} normalizasyon matrisi, w_I ise ağırlık matrisi olarak tanımlanır. v_{ij} matrisi, ideal ve negatif ideal çözümün belirlenmesi için önemlidir. İdeal çözüm (A^+) ve negatif ideal çözüm (A^-) Denklem 11 ve 12 ile tanımlanır.

$$A^+ = (max(v_{ij})(benefit), min(v_{ij})(cost))$$
$$A^- = (max(v_{ij})(benefit), min(v_{ij})(cost)) \quad (11)$$

Her alternatifin ideal ve negatif ideal çözüme olan uzaklıkları Öklidyen mesafe ile hesaplanır. Bu durumda Denklem 12 kullanılır.

$$s_i^+ = \sqrt{\sum_{j=1}^{n}\left(v_{ij} - A_j^+\right)^2} \qquad s_i^- = \sqrt{\sum_{j=1}^{n}\left(v_{ij} - A_j^-\right)^2} \tag{12}$$

Burada $S_i{}^+$, i. alternatifin ideal çözüme olan uzaklığı, $S_i{}^-$ ise negatif ideal çözüme olan uzaklığıdır. Alternatiflerin göreli yakınlığı ise Denklem 13'e göre hesaplanır: C_i değeri 0 ile 1 arasında değişir ve en yüksek değere sahip değer en iyi tercih olarak kabul edilir [22].

$$C_i = \frac{s_i^-}{s_i^+ + s_i^-} \tag{13}$$

Çok özellikli sınır yaklaşımı karşılaştırması (MABAC)

2015 yılında Pamučar ve arkadaşları tarafından geliştirilen MABAC yöntemi, diğer ÇKKV yöntemlerine benzer biçimde, alternatiflerin çeşitli kriterler doğrultusunda değerlendirilmesini mümkün kılar. Ancak MABAC'ın ayırt edici özelliği, alternatiflerin sınır yaklaşım alanı (border approximation area) temelinde değerlendirilmesidir [23]. Bu yöntemde, alternatifler $A_1, A_2, \dots, A_m$ olarak kriterler ise $C_1, C_2, \dots C_n$ olarak tanımlanır ve her alternatif için kriterlerin bir değeri olur.

$$X = \begin{pmatrix} x_{11} & \cdots & x_{1j} \\ \vdots & \ddots & \vdots \\ x_i & \cdots & x_{ij} \end{pmatrix} \tag{14}$$

X_{ij} teriminde, i alternatifi, j ise kriteri ifade eder. MABAC yönteminde normalize edilmiş karar matrisi ve ağırlıklı karar matrisi Denklem 14'te gösterildiği gibi bulunur. V_{ij} ağırlıklandırılmış matris hesaplandıktan sonra sınır yaklaşıklık matrisi G_j için Denklem 15 kullanılır.

$$G_j = \frac{1}{m}\sum_{i=1}^{m} v_{ij} \tag{15}$$

Her alternatif için sınır yaklaşıklık alanı ile ilgili performansı hesaplanır: Bu performans göstergesi, alternatiflerin ne kadar iyi olduğunu göstermek için kullanılır.

$$Q_{ij} = v_{ij} - G_j \tag{16}$$

Denklem 16'da Q_{ij} değerleri toplandığında, her alternatif için bir toplam puan elde edilir ve alternatifler sıralanır. En yüksek S_i puanına sahip olan alternatif, en iyi alternatif olarak seçilir [23]. Bu durum Denklem 17'de gösterilmektedir.

$$S_i = \sum_{j=1}^{n} Q_{ij} \tag{17}$$

Karakteristik nesneler yöntemi (COMET)

Bu yöntem, ÇKKV tekniklerinden biri olup, alternatiflerin bağımsız olarak sıralanmasını sağlayan farklı bir yaklaşımdır [24]. COMET yöntemi, karar vericinin önyargılarından bağımsız olarak alternatifleri değerlendirmek için karakteristik nesneleri kullanır. Alternatifler $A_1, A_2, \dots, A_m$ ve kriterler $C_1, C_2, \dots, C_n$ şeklinde tanımlanmakta olup, her alternatifin her kriter için bir değeri bulunmaktadır. Bu değerlere dayanarak karar matrisi oluşturulur ve bu hesaplama, MABAC yönteminde de kullanılan Denklem 18 ile gerçekleştirilir. Her bir alternatif için karakteristik nesnelerin değer fonksiyonu hesaplanır. Örneğin, C_1 kriteri için iki karakteristik nesne, $O_1 = min(x_{i1})$ ve $O_2 = max(x_{i1})$ olarak belirlenir. Denklem 19'da ifade edilen bu fonksiyon, alternatifin karakteristik nesneye olan uzaklığını ölçmek amacıyla kullanılır.

$$X = \begin{pmatrix} x_{11} & \cdots & x_{1j} \\ \vdots & \ddots & \vdots \\ x_i & \cdots & x_{ij} \end{pmatrix} \tag{18}$$

$$v_{ij}(O_k) = f(O_k) \tag{19}$$

Denklem 18 ve 19'da, $v_{ij}(O_k)$, i alternatifin j kriterde k karakteristik nesneye göre değerini ifade eder. Alternatifler, karakteristik nesneler ile karşılaştırılarak olasılık değerleri hesaplanır. Her bir alternatifin performansı, karakteristik nesneler temelinde belirlenen olasılık dağılımları doğrultusunda değerlendirilir. Bu olasılık dağılımı Denklem 20'de gösterilmiştir. Olasılık değerleri esas alınarak alternatifler sıralanır ve en yüksek olasılık değerine sahip alternatif en uygun seçenek olarak seçilir.

$$P(A_i) = \frac{\sum_{k=1}^{n} v_{ij}(O_k)}{\sum_{i=1}^{m}\sum_{k=1}^{n} v_{ij}(O_k)} \tag{20}$$

İdeal çözüme yönelik kararlı tercih sıralaması (SPOTIS)

SPOTIS yöntemi, alternatiflerin ideal çözüme göre değerlendirilmesini sağlayarak tutarlı bir sıralama elde edilmesini mümkün kılar. Bu yöntem, diğer ÇKKV tekniklerinden farklı olarak, alternatiflerin hem fayda hem de maliyet kriterleri açısından referans noktaları olan ideal ve anti-ideal çözümlere olan uzaklıklarını dikkate alır [25]. Diğer yöntemlerde olduğu gibi, alternatifler A, kriterler C ve karar matrisi X şeklinde tanımlanır. Bu süreçte, TOPSIS yöntemine benzer şekilde, Denklem 9, 10 ve 13 kullanılır. Daha sonra ideal çözüm (I_j) ve anti-ideal çözüm (A_j) hesaplanır. İdeal çözümde, fayda kriterleri için en yüksek, maliyet kriterleri için ise en düşük değer seçilirken; anti-ideal çözümde fayda kriterleri için en düşük, maliyet kriterleri için en yüksek değer belirlenir. SPOTIS yönteminde normalizasyon işlemi, her alternatifin belirlenen ideal ve anti-ideal çözümlere olan uzaklığı temelinde gerçekleştirilir. Bu durumda, normalizasyon matrisi Denklem 21'de gösterildiği gibi ifade edilir.

$$z_{ij} = \frac{x_{ij} - A_j}{I_j - A_j} \tag{21}$$

Kriterlerin önem derecelerine göre her kriter için bir ağırlık W_j belirlenir. Her kriter için ağırlıklandırılmış normalizasyon matrisi Denklem 22 ile hesaplanır.

$$d_{ij} = w_j \cdot z_{ij} \quad (22)$$

Her bir alternatifin toplam puanı, Denklem 23'te gösterildiği üzere, tüm kriterlerdeki ağırlıklı normalize edilmiş değerlerin toplamı üzerinden hesaplanır. En düşük toplam puana sahip alternatif, ideal çözüme en yakın olan seçenek olarak değerlendirilir ve en iyi alternatif olarak seçilir.

$$S_i = \sum_{j=!}^{n} d_{ij} \quad (23)$$

Veri kaynağı ve barajların seçimi

Bu çalışmanın temel amacı, araştırma konusu olan hidroelektrik santrallerinde YSP kurulumu için optimal yer seçimini belirlemede ÇKKV yöntemlerini kullanmaktır [27, 28]. Bu amaçla, Güneydoğu Anadolu Bölgesi'nde bulunan, 50 MW ve üstü kurulu güce sahip santraller ele alınmıştır. Yapılan araştırmalarda bu kısıtlama altında 11 adet hidroelektrik santralinin olduğu belirlenmiştir. Bununla birlikte ÇKKV analizlerinin yapılabilmesi için barajlar alternatif olarak ele alınmıştır. Belirlenen santraller Tablo 3'te gösterilmiştir.

Fırat ve Dicle havzalarında yer alan barajlar, YSP kurulumu için ilk bakışta uygun bir profil sunmaktadır. Özellikle Güneydoğu Anadolu Bölgesi'nin yüksek güneşlenme süresi, bu projelerin verimliliğini daha da artıracak önemli bir faktördür. Mevcut baraj altyapısının enerji iletim hatlarına yakın olması, YSP'lerden üretilecek elektriğin sisteme entegrasyonunu kolaylaştırmakta ve maliyetleri düşürmektedir. Bu hibrit model sayesinde hem yenilenebilir enerji üretimi artırılacak hem de buharlaşma yoluyla oluşan su kaybının azaltılması gibi ekosistem faydaları sağlanabilecektir.

Tablo 3. Güneydoğu anadolu bölgesi barajları

	Baraj Adı	Bulunduğu Şehir
1	Atatürk Barajı ve HES	Şanlıurfa
2	Karakaya Barajı ve HES	Diyarbakır
3	Ilısu Barajı ve HES	Şırnak
4	Birecik Barajı ve HES	Şanlıurfa
5	Çetin Barajı ve HES	Siirt
6	Alkumru Barajı ve HES	Siirt
7	Batman Barajı ve HES	Batman
8	Karkamış Barajı ve HES	Gaziantep
9	Dicle Barajı ve HES	Diyarbakır
10	Kralkızı Barajı ve HES	Diyarbakır
11	Garzan Barajı ve HES	Batman

Tablo 3'te verilen barajların sunduğu geniş su yüzeyi alanları, enerji üretim kapasitesini artırmak için değerlendirilebilecek önemli bir kaynak oluşturmaktadır. YSP'lerin su yüzeyini kaplaması, barajlarda buharlaşma kaynaklı su kaybını azaltarak kuraklık yönetimine de katkı sağlayabilir. Ayrıca, bu projeler bölgenin enerji çeşitliliğine katkıda bulunurken, temiz enerji üretiminde yerel bir model oluşturma potansiyeli taşımaktadır.

Listede yer alan her baraj alanı için kullanılacak veriler, Tablo 4'te gösterilen kaynaklardan temin edilmiştir. Doğrudan normal ışınım (DNI), küresel yatay ışınım (GHI) ve dağınık yatay ışınım (DIF) gibi değerler, global solar atlas web sitesi üzerinden çevrimiçi olarak elde edilmiştir. Diğer tüm veriler ise, bağlı bulunduğumuz kamu kurumları olan meteoroloji genel müdürlüğü ve ilgili kuruluşların güncel internet sayfalarından alınarak hazırlanmıştır.

Tablo 4. Veri Kaynağı Listesi [27, 28]

Veri Listesi	Veri Kaynağı
Koordinatlar	Google Earth [29]
Doğrudan Normal Işınım - DNI (kWh/m²)	Global Solar Atlas [30]
Küresel Yatay Işınım - GHI (kWh/m²)	
Dağınık Yatay Işınım - DIF (kWh/m²)	
FV modüllerinin optimum eğimi	
Ortalama Sıcaklık (℃)	
Topografik Yükselti (m)	Topographic-map [31]
Su Derinliği - İşletmeye uygun su kotu (m)	Enerji Atlası [32]
Yerleşim yerlerine uzaklık (m)	Google Earth [29]
Yerel Ortalama Rüzgar hızı (m/s)	Global Wind Atlas [33]
Barajın Göl Alanı (km²)	Enerji Atlası [32]
Ortalama Yağış (m³) - (2009-2019)	Meteoroloji Genel Müdürlüğü [34]
Maksimum Sıcaklık (℃)	
Minimum Sıcaklık (℃)	
Güneşlenme Saati	

Tablo 4'te sunulan veri listesinde sunulan parametreler, YSP'ler için en uygun yer seçiminde kriter olarak değerlendirilmiştir. Her bir parametre, karar sürecinde dikkate alınacak ayrı bir ölçütü temsil etmektedir; örneğin doğrudan normal ışınım (DNI), küresel yatay ışınım (GHI), ortalama sıcaklık, vb. Bu kriterler, karar vericilerin farklı alanları karşılaştırarak en uygun alternatifleri belirlemesine olanak sağlamaktadır. Yazılım geliştirme sürecinde bu parametrelerin hepsi kriter olarak belirlenmiştir.

Analiz ve Bulgular

Tablo 5'te, YSP sistemlerinin kurulumu için teknik, ekonomik ve sosyal kriterlerin karşılaştırmalı ağırlıklandırması sunulmaktadır. Alanında uzman 12 katılımcıdan elde edilen verilerle oluşturulan ağırlıklı grup matrisi, kriterlerin birbirine göre önem derecelerini ortaya koymaktadır. Hesaplama sonucunda en yüksek ağırlığa sahip kriter güneş ışınımı olurken, bunu yıllık gün ışığı saatleri ve ortalama sıcaklık takip etmiştir. Bu sonuç, YSP santrali projelerinde enerji üretim potansiyelini doğrudan etkileyen iklimsel faktörlerin, diğer topoğrafik, altyapısal ve

sosyoekonomik kriterlere kıyasla daha belirleyici olduğunu göstermektedir. Dolayısıyla, YSP'ler için en uygun HES alanı seçiminde güneşlenme süresi ve yoğunluğunun optimizasyonu, teknik verimlilik açısından kritik bir öncelik olarak öne çıkmaktadır. Bu bulgu, uygun iklim koşullarına sahip bölgelerin yatırım geri dönüş süresini kısaltarak projenin ekonomik fizibilitesini de olumlu yönde etkileyebileceğini göstermektedir.

Topografik yükselti (rakım) arttıkça, atmosfer incelir ve bu durum iki temel etki yaratır. Birincisi, hava sıcaklığının düşmesidir; bu soğuk ortam, panellerin aşırı ısınmasını engelleyerek verimliliklerini artırır. İkincisi, artan güneş radyasyonu, doğrudan daha fazla enerji üretim potansiyeli sağlar. Ancak, yüksek rakımın olumsuz yanı, daha yoğun UV ışınlarına ve sert hava koşullarına maruz kalmaktır. Bu durum, panellerin ve yüzer sistem bileşenlerinin daha hızlı yıpranmasına neden olarak sistem ömrünü kısaltabilir. Ayrıca, yüksek rakımlı bölgelerdeki ulaşım ve bakım zorlukları işletme maliyetlerini artırır.

Su derinliği, YSP sistemlerinin maliyetini ve stabilitesini doğrudan etkiler. Çok sığ sular, dip çamurundan kaynaklanan kurulum zorlukları, aşırı su ısınması ve yosunlaşma gibi problemlere yol açarak verimi ve bakımı olumsuz etkiler. Öte yandan, çok derin sular ise çok daha uzun ve güçlü demirleme sistemleri gerektirdiği için kurulum maliyetlerini önemli ölçüde artırır. Ayrıca derin sulardaki bakım işlemleri daha zorlu ve pahalıdır. Bu nedenlerle, genellikle orta derinlikteki sular en uygun maliyet ve performans dengesini sağlar.

Tablo 5. Ağırlıklı Grup Matrisi ve Sıralama [27, 28]

KRİTERLER	Güneş ışınımı	Yıllık Günışığı Saatleri	Ortalama Sıcaklık	Topoğrafik Yükselti	Su Derinliği	Yerleşim Birimlerine Uzaklık	Şebeke Bağlantılarına Uzaklık	Yerel Ortalama Rüzgâr Hızı	Bölgesel Etkiler	Kalkınma ve Yerel Ekonomiler	**Sıralama**
Güneş ışınımı (A1)	1,00	3,85	4,30	6,42	7,25	7,08	6,00	6,44	7,58	7,92	**1**
Yıllık Günışığı Saatleri (A2)	0,92	1,00	5,10	5,92	6,42	7,34	6,34	6,44	7,60	8,17	2
Ortalama Sıcaklık (A3)	1,53	0,63	1,00	5,70	5,34	6,18	3,79	5,34	6,94	7,27	3
Topoğrafik Yükselti (A4)	0,23	0,35	0,88	1,00	3,43	3,96	2,68	2,29	4,80	6,17	4
Su Derinliği (A5)	0,15	0,23	0,86	2,38	1,00	2,32	1,69	1,93	3,54	3,61	7
Yerleşim Birimlerine Uzaklık (A6)	0,21	0,87	0,81	1,80	2,29	1,00	0,48	1,47	2,90	3,32	8
Şebeke Bağlantılarına Uzaklık (A7)	0,29	0,95	1,83	2,83	3,80	4,33	1,00	2,09	3,54	4,98	5
Yerel Ortalama Rüzgâr Hızı (A8)	0,45	0,41	0,84	2,48	3,21	4,89	1,78	1,00	4,59	4,66	6
Bölgesel Etkiler (A9)	0,14	0,70	0,46	1,47	1,34	2,13	1,10	1,52	1,00	1,86	9
Kalkınma ve Yerel Ekonomiler (A10)	0,13	0,12	0,54	0,24	1,66	1,73	0,81	1,27	1,85	1,00	10

Uzmanlar tarafından doldurulan seçim cetvelleri, Python 3.8 programlama dili kullanılarak analiz edilmiş ve pyMCDM 1.3.1 [26] kütüphanesinde yer alan AHP, TOPSIS, MABAC, COMET ve SPOTIS yöntemleri uygulanmıştır. Belirtilen yöntemlerden elde edilen sonuçlar, seçim cetvellerinden elde edilen bulgular ile karşılaştırılarak aralarındaki tutarlılık ve uyum değerlendirilmiştir. Böylece, saha verileri ile ÇKKV yöntemlerinden elde edilen sonuçların birbirini desteklemesi sağlanmış ve analizlerin güvenilirliği ile geçerliliği güçlendirilmiştir.

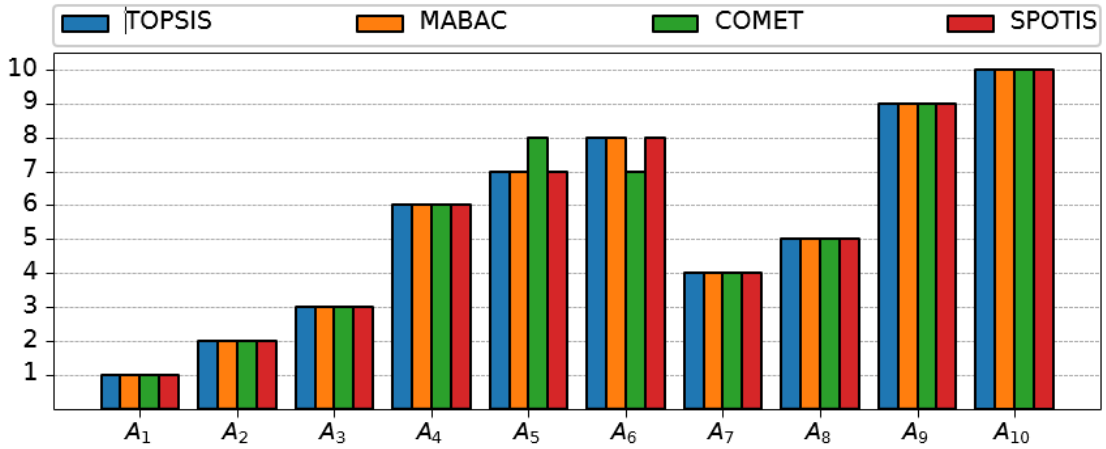

Şekil 1. ÇKKV yöntemleri sıralaması

Geliştirilen yazılımlardan elde edilen veriler dikkate alındığında, ilk üç kriterin en yüksek öneme sahip olduğu tespit edilmiştir. Bu kapsamda, farklı ÇKKV yöntemleri dikkate alındığında karar vericilerin seçtikleri kriterlerde tutarlı tercihler yaptıkları gözlemlenmiştir. Şekil 1'de yer alan sayısal verilere bakıldığında, uygulanan beş yöntemin tamamında ilk üç kriterin aynı kaldığı görülmektedir. Şekil 1'de kriterler sırasıyla A1-A10 olarak isimlendirilmiştir. Bu isimlendirme Tablo 5'te sunulan kriter sütunu ile ilişkilidir. Örneğin: Şekil 1'de gösterilen A1 kriteri Tablo 1'de güneş ışınımı kriterine karşılık gelmektedir.

Bu çalışmada kullanılan TOPSIS, MABAC, COMET, SPOTIS ve AHP gibi ÇKKV yöntemlerinin tamamında, Tablo 6'daki ağırlık analizlerine göre en yüksek önem düzeyine sahip kriterlerin aynı olduğu tespit edilmiştir. Bu durum, farklı ÇKKV yöntemleri arasındaki yakınsamayı ve tutarlılığı açıkça ortaya koymaktadır. Yöntemlerin birbirine benzer sonuçlar üretmesi, elde edilen bulguların güvenilirliğini ve sağlamlığını pekiştirmekte, bu da karar vericilere daha güvenli ve tutarlı bir karar verme süreci sunmaktadır. Bu önemli bulgu, seçilen yöntemlerin veri setine uyumluluğu ve problem yapısını doğru bir şekilde yansıtması açısından da dikkat çekicidir, zira farklı matematiksel prensiplere dayanan bu yöntemlerin aynı kritik faktörleri işaret etmesi, analiz sonuçlarının geçerliliğini artırmaktadır. Ayrıca, bu tutarlılık kriterlerin göreli önem sıralamasının rastlantısal değil, veriye dayalı sistematik bir analizden kaynaklandığını göstermektedir. Böylece, proje planlamasında önceliklendirme yapılırken farklı yöntemler arasında seçim yapılması gerekliliği ortadan kalkmakta, zaman ve kaynak tasarrufu sağlanmaktadır. Sonuç olarak, farklı ÇKKV yöntemlerinden elde edilen paralel sonuçlar, uygulamada daha hızlı ve güvenilir karar mekanizmalarının geliştirilmesine katkı sağlamaktadır. Tablo 6'da gösterilen sonuçlar içinde MABAC yöntemi, bazı kriterler ve alternatifler için negatif değerlere sahip olabilir. Bu durum, söz konusu alternatifin ağırlıklı performansının referans değerlerin altında olduğunu ve diğer alternatiflere göre daha düşük uygunluk düzeyi sergilediğini göstermektedir. TOPSIS yönteminde en büyük değer (0,84) en önemli değeri göstermektedir. COMET yönteminde ağırlıklar 0-1 arasına yayılmaktadır. AHP yönteminde ise tüm kriterlerin toplam değeri 1 olacak şekilde bir yayılım ortaya çıkmaktadır. Tüm yöntemlerde en büyük değer kriterin öneminli olduğuna işaret etmektedir.

Tablo 6. ÇKKV yöntemleri ile kriter ağırlığı tablosu [27, 28]

KRİTERLER	TOPSIS	MABAC	COMET	SPOTIS	AHP
Güneş ışınımı	0,84	0,60	1,00	0,09	0,20
Yıllık Günışığı Saatleri	0,64	0,48	0,87	0,21	0,19
Ortalama Sıcaklık	0,51	0,29	0,54	0,40	0,15
Topografik Yükselti	0,22	-0,08	0,02	0,77	0,09
Su Derinliği	0,15	-0,16	0,01	0,86	0,06
Yerleşim Birimlerine Uzaklık	0,15	-0,18	0,01	0,87	0,05
Şebeke Bağlantılarına Uzaklık	0,26	-0,03	0,06	0,72	0,09
Yerel Ortalama Rüzgâr Hızı	0,23	-0,07	0,03	0,77	0,08
Bölgesel Etkiler	0,11	-0,22	0,01	0,91	0,04
Kalkınma ve Yerel Ekonomiler	0,04	-0,27	0,00	0,97	0,03

Tablo 8'de verilen sıralama, ÇKKV yöntemlerinden TOPSIS kullanılarak üretilmiştir. Çalışmada karar matrisi 12 farklı ikili karşılaştırma matrisinin aritmetik ortalaması alınarak oluşturulmuştur. Ardından, kriter ağırlıkları entropi temelli ağırlıklandırma yöntemi (Entropy Weight Method) ile hesaplanmıştır. Bu yöntemde kriter değerleri, sütun bazlı normalizasyon yaklaşımıyla normalize edilmektedir. Böylece farklı ölçeklerdeki kriterler (örneğin °C, kWh/m², metre) birbirine indirgenmiş ortak bir ölçeğe dönüştürülmektedir. Ardından sıralama, pymcdm kütüphanesi aracılığıyla uygulanan ÇKKV yöntemleri (TOPSIS, MABAC vb.) ile elde edilmektedir. Bu yöntemlerin her biri ayrıca kendi içinde normalizasyon prosedürleri (örneğin TOPSIS'te vektör normalizasyonu, MABAC'ta min–max normalizasyonu) kullanmaktadır. PyMCDM kütüphanesi normalizasyon işleminde birçok alternatif metod önermektedir [35].

ÇKKV yöntemlerinin uygulandığı bu çalışmada, alanında uzman katılımcılara sunulan seçim cetveli ve yapılan hesaplamalar sonucunda en önemli kriter olarak birinci sırada "Güneş Işınımı", ikinci sırada ise "Yıllık Günışığı Saatleri" kriterleri seçilmiştir. Tablo 7'de verilen değerlerden hareketle, YSP santrali kurulumu için en iyi lokasyon seçimi yapılmak istenmesi durumunda Tablo 8'de belirtildiği gibi birinci sıraya Karkamış Barajı yerleşmektedir. Ancak Tablo 7'de gösterildiği üzere doğrudan normal ışınım (DNI), küresel yatay ışınım (GHI) ve dağınık yatay ışınım (DIF) değerleri bakımından Karkamış Barajı'na yakın lokasyonda bulunan Birecik Barajı ve Atatürk Barajı'nın güneş ışınım değeri Karkamış Barajı bölgesi ışınım miktarına çok yakın bir değerde bulunmaktadır. Dolayısıyla YSP santrali kurulum potansiyeli açısından yapılacak olan herhangi bir çalışmada, bu barajların göl rezervuar alanının değerlendirilmeye alınması doğru bir adım olacaktır.

Tablo 7. Baraj bilgileri tablosu

VERİLER	Karkamiş Baraji	Atatürk Baraji	Birecik Baraji
Koordinatlar	36°52'13.4"N 38°01'45.4"E	37°32'19.0"N 38°22'38.6"E	37°03'11.9"N 37°53'29.4"E
Doğrudan Normal Işınım -DNI (kWh/m²)	2185,7	2179,1	2173,7
Küresel Yatay Işınım - GHI (kWh/m²)	1898,4	1877,4	1885,5
Dağınık Yatay Işınım - DIF (kWh/m²)	561,8	544,7	558,3
FV Modül Eğimi	32/180°	32/180°	31/180°
Ortalama Sıcaklık (℃)	19,0	17,3 ℃	18,6
Topografik Yükselti (m)	336	529	353
Su Derinliği - İşletme Su Kotu (m)	336-340	526-542	340-385
Yerleşim Yerlerine Uzaklık (Km)	6,8	24	5
Yerel Ortalama Rüzgar Hızı (m/s)	4,16	4,97	5,51
Baraj Göl Alanı (km²)	28,4	817	56,25
Ortalama Yağış Miktarı (m³)	45,05	33,66	45,05
Max. Sıcaklık (℃)	38,2	41,3	38,2
Min. Sıcaklık (℃)	-1,1	1,3	-1,1
Güneşlenme Saati	5,2	6,5	5,2

Bu çalışmada temel amaç, seçilen hidroelektrik santraller üzerinde YSP kurulumu için ÇKKV yöntemleriyle optimal yer belirlenmesidir. Dolayısıyla analiz, yalnızca barajların uygunluk düzeylerinin karşılaştırmalı değerlendirilmesine odaklanmıştır. Enerji üretim potansiyelinin (örneğin, %10 veya %20 kurulum yapılması durumunda beklenen üretim miktarı) doğrudan hesaplanmaması çalışmanın bir sınırlılığıdır. Bunun nedeni, her bir baraj için ayrıntılı su yüzeyi kullanımı, barajlara ilişkin veriler ve yerel iklim koşullarına bağlı üretim simülasyonlarının bu çalışmanın kapsamı dışında tutulmuş olmasıdır.

Tablo 7, yalnızca ilk üç sırada yer alan barajlara ilişkin temel verileri sunmak amacıyla hazırlanmış olup, seçim cetveli ya da ÇKKV yöntemleriyle yapılan sıralama süreciyle doğrudan ilişkili değildir. Tüm kriterler Tablo 5'te sunulmuş olup karşılaştırmalı olarak araştırmacılara seçim cetveli olarak tercih yapmaları için sunulmuştur. Uzman araştırmacılardan seçim cetveli aracılığıyla toplanan veriler [28] nolu kaynakta el olarak sunulmuştur.

Tablo 8. Kritere göre baraj sıralaması

Baraj Adı	Sıralama
Karkamış Barajı ve HES	**1**
Birecik Barajı ve HES	2
Atatürk Barajı ve HES	3
Ilısu Barajı ve HES	4
Batman Barajı ve HES	5
Kralkızı Barajı ve HES	6
Karakaya Barajı ve HES	7
Alkumru Barajı ve HES	8
Garzan Barajı ve HES	9
Dicle Barajı ve HES	10
Çetin Barajı ve HES	11

Yapılan analizlere göre Karkamış Barajı, yüksek güneş ışınımı (DNI ve GHI değerleri), düşük yerleşim yeri uzaklığı ve uygun su derinliği sayesinde ilk sırada yer almıştır. Birecik Barajı, rüzgar hızı açısından avantajlı olup alan büyüklüğü bakımından da orta seviyede olduğundan ikinci sırada yer almıştır. Atatürk Barajı ise çok geniş göl alanına sahip olmasına rağmen yüksek topoğrafik yükselti, düşük GHI değeri ve yerleşim yerlerine uzaklığının fazla olması sebebiyle üçüncü sırada kalmıştır. Karkamış ve Birecik

Barajları, hem teknik hem de ekonomik olarak daha kısa sürede yatırım geri dönüş potansiyeli sunarken, Atatürk Barajı'nın büyük boyutları uzun vadeli ve yüksek maliyetli bir yatırım gerektirebilir. Bu durum, barajların sıralamasında yalnızca enerji potansiyelinin değil, erişilebilirlik ve kurulum kolaylığı gibi kriterlerin de belirleyici olduğunu göstermektedir. Genel olarak, ilk üç sıradaki barajların hem iklim hem de altyapı açısından diğer barajlara kıyasla YSP sistemleri açısından daha uygun koşullara sahip olduğu görülmektedir.

Tablo 8 oluşturulurken, alternatiflerin değerlendirilmesinde TOPSIS yöntemi tercih edilmiştir. Bu yöntemin seçilmesinin temel nedeni, karar verme sürecinde 'ideal çözüme yakınlık' prensibini esas alması ve literatürde en yaygın kullanılan ÇKKV tekniklerinden biri olmasıdır. Ayrıca, çalışmada kullanılan diğer ÇKKV yöntemleri (MABAC, COMET ve SPOTIS) ile elde edilen sonuçlar karşılaştırıldığında, ilk üç sırada yer alan barajların aynı olduğu görülmüştür. Bu durum, kullanılan yöntemlerin tutarlılığını desteklemekte ve ulaşılan bulguların güvenilirliğini artırmaktadır. Çalışmanın amacı en uygun kurulum yerinin belirlenmesi olduğundan, yalnızca TOPSIS yöntemi ile elde edilen sonuçların sunulması metodolojik açıdan bir sorun teşkil etmemektedir. Bununla birlikte, farklı yöntemlerle yapılan analizlerin de benzer sonuçlar üretmiş olması, bulguların geçerliliğini güçlendiren önemli bir unsurdur.

Sonuç

Bu çalışmada, bilimsel araştırmalarda yaygın olarak kullanılan ve güvenilirliği kanıtlanmış çok kriterli karar verme yöntemlerinden AHP, TOPSIS, MABAC, COMET ve SPOTIS yöntemleri kullanılarak YSP sistemlerinin kurulum potansiyeli değerlendirilmiştir. Bu değerlendirme, karar vericinin öznel görüşleri yerine, bilimsel verilere ve belirlenen kriterlerin ağırlık oranlarına dayanmaktadır. YSP kurulumuna etki eden kriterler, çoğunluğu alanında uzman akademisyenler ve saha tecrübesine sahip profesyonellere danışılarak hazırlanan seçim cetveli aracılığıyla belirlenmiştir. Toplanan seçim cetveli verileri, belirtilen ÇKKV yöntemleri ile analiz edilmiştir. YSP kurulması planlanan her bir baraj bölgesi için teknik, coğrafi ve meteorolojik veriler başta olmak üzere kurulumu etkileyen kriterlerin tespiti amacıyla kamu kurum ve kuruluşları ile birçok santralle doğrudan iletişime geçilerek kapsamlı bir veri toplama süreci yürütülmüştür. ÇKKV yöntemleri sonucunda, karar vericiler tarafından en önemli kriter olarak belirlenen "Güneş ışınımı" faktörüne göre, Güneydoğu Anadolu Bölgesi'ndeki barajlarımızdan Gaziantep ili sınırları içinde yer alan Karkamış Barajı'nın rezervuar alanına YSP santrali kurulması gerektiği sonucuna ulaşılmıştır. Ayrıca, Karkamış Barajı'na yakın lokasyonlarda bulunan ve benzer güneş ışınım değerlerine sahip Atatürk Barajı ve Birecik Barajı rezervuar alanlarına da YSP kurulmasının, mevcut bulgular ışığında ülkemize ve bölgemize önemli katkılar sağlayacağı değerlendirilmektedir.

İlerleyen araştırmalarda, baraj yüzeylerinin farklı bölgeleri için mikro-uygunluk analizleri yapılması ve Coğrafi Bilgi Sistemleri ve ÇKKV entegrasyonunun kullanılması önerilmektedir. Enerji üretim potansiyeli tahminlerinin çalışmaya dahil edilmesi, daha kapsamlı ve uygulanabilir sonuçlar sağlayabilir. Ayrıca barajlara ilişkin bulutluluk indeksi hesaplanarak sunulan analizler yeniden değerlendirilebilir.

Kaynaklar

[1] Sacramento, E.M., Carvalho, P.C.M., Araujo, J.C., Riffel, D.B., Correa, R.M.C. & Neto, J.S.P. (2015), "Scenarios for use of floating photovoltaic plants in Brazilian reservoirs," *The İstitution of Engineering and Technology,* 9, 1019-1024, Doi: 10.1049/iet-rpg.2015.0120.

[2] Anbarasu, P. & Kumar, R.S. (2022), " Performance analysis of polycrystalline floating photovoltaic array: The concept and prototype development for irrigation purpose," *Prog Photovolt Res Appl.* 2023; 31(7), 738 – 749, Doi: 10.1002/pip.3681

[3] Sukarso, A.P. & Kim, K.N. (2020), " Cooling effect on the floating solar PV: Performance and economic analysis on the case of West Java province in Indonesia", *Journal of Energy,* 13, 2126, Doi: 10.3390/en13092126.

[4] Solomin, E., Sirotkin, E., Cuce, E., Selvanathan, S. P. & Kumarasamy, S. (2021), "Hybrid floating solar plant designs: a review," *Energies*, 14(10), 2751,Doi: 10.3390/en14102751.

[5] Trapani, K. & Redón Santafé, M. (2015), "A review of floating photovoltaic installations: 2007–2013," *Progress in Photovoltaics: Research and Applications*, 23(4). 524-532, Doi: 10.1002/pip.2466.

[6] Vodapally, S. N. & Ali, M. H. (2022), "A comprehensive review of solar photovoltaic (PV) technologies, architecture, and its applications to improved efficiency," *Energies*, 16(1), 319, Doi:10.3390/en16010319.

[7] López, M., Soto, F. & Hernández, Z. A. (2022), "Assessment of the potential of floating solar photovoltaic panels in bodies of water in mainland Spain," *Journal of Cleaner Production,* 340, 130752, Doi:10.1016/j.jclepro.2022.130752.

[8] Sanchez, R. G., Kougias, I., Moner-Girona, M., Fahl, F. & Jäger-Waldau, A. (2021), "Assessment of floating solar photovoltaics potential in existing hydropower reservoirs in Africa," *Renewable Energy*, 169, 687-699, Doi:10.1016/j.renene.2021.01.041.

[9] Al Garni, H. Z. & Awasthi, A. (2017), "Solar PV power plant site selection using a GIS-AHP based approach with application in Saudi Arabia," *Applied Energy*, 206, 1225-1240, Doi: 10.1016/j.apenergy.2017.10.024.

[10] Azizkhani, M., Vakili, A., Noorollahi, Y. & Naseri, F. (2017), "Potential survey of photovoltaic power plants using Analytical Hierarchy Process (AHP) method in Iran," *Renewable and Sustainable Energy Reviews*, 75, 1198-1206, Doi:10.1016/j.rser.2016.11.103.

[11] Nebey, A. H., Taye, B. Z. & Workineh, T. G. (2020), "GIS-Based Irrigation Dams Potential Assessment of

Floating Solar PV System," *Journal of Energy*, 2020(1), 1268493, Doi:10.1155/2020/1268493.

[12] Kaymak, M. K. ve Şahin, A. D. (2021), "The first design and application of floating photovoltaic (FPV) energy generation systems in Turkey with structural and electrical performance," *International Journal of Precision Engineering and Manufacturing-Green Technology*, 1-13, Doi:10.1007/s40684-021-00369-w.

[13] Dal, A. R. (2021), "Investigation of the potential of using lakes and dams as solar power plants: the case of yamula dam," *Gazi University Journal of Science Part C: Design and Technology*, 9(4), 726-738, Doi: 10.29109/gujsc.1002791.

[14] Karipoğlu, F., Koca, K. ve İlbahar, E. (2024), "Convenient Site Selection of a Floating PV Power Plant in Türkiye by using GIS-Fuzzy Analytical Hierarchy Process," *Environmental Science and Pollution Research*, 31(15), 23193-23210, Doi: 10.1007/s11356-024-32470-3.

[15] Göllü, K. (2022), "Site selection for floating photovoltaic (PV) panels on 8 HEPP reservoirs in Turkey by using analytical hierarchical process (AHP), Ortadoğu Teknik Üniversitesi, Ankara, Türkiye, 2022, https://open.metu.edu.tr/handle/11511/99486.

[16] Sahu, A., Yadav, N. & Sudhakar, K. (2016). "Floating photovoltaic power plant: A review. Renewable and sustainable" *energy reviews*, 66, 815-824. Doi:10.1016/j.rser.2016.08.051.

[17] Arslankaya, D. ve Göraltay, K. (2019), "*Çok Kriterli Karar Verme Yöntemlerinde Güncel Yaklaşımlar*," İksad Yayınları, 2020, Türkiye,

[18] Dalbudak, E. ve Rençber, Ö. F. (2022), "Çok kriterli karar verme yöntemleri üzerine literatür incelemesi," *Gaziantep Üniversitesi İktisadi ve İdari Bilimler Fakültesi Dergisi*, 4(1), 1-17, Doi:10.55769/gauniibf.1068692.

[19] Aktaş, İ. Ş., (2020), "Akıllı şebekelerde risk analizi," [Yayınlanmış doktora Tezi], Gazi Üniversitesi, Ankara, Türkiye, 2020,

[20] Ekin, E. ve Dolanbay, G. (2024), "AHP Temelli TOPSIS Yöntemi ile Yer Seçim Problemine İlişkin Bir Uygulama," *İstanbul Gelişim Üniversitesi Sosyal Bilimler Dergisi*, 11(1), 301-317, Doi:10.17336/igusbd.1209399.

[21] Supçiller, A. ve Çapraz, O. (2011), "AHP-TOPSIS yöntemine dayali tedarikçi seçimi uygulamasi," *İstanbul University Econometrics and Statistics e-Journal*, (13), 1-22, https://dergipark.org.tr/en/pub/iuekois/issue/8980/112036.

[22] Ustasüleyman, T. (2009), "Bankacılık sektöründe hizmet kalitesinin değerlendirilmesi: Ahs-Topsis Yöntemi," *Bankacılar Dergisi*, 69, 33-43.

[23] Demirtaş, M. C. (2022), "Üniversite rektörlerinin sosyal medya kullanımlarının Mabac yöntemi ile değerlendirilmesi," *Öneri Dergisi*, 17 (57), 102 – 147. Doi: 10.14783/maruoneri.941348.

[24] Sałabun, W. (2014), "Reduction in the number of comparisons required to create matrix of expert judgment in the comet method," *Management and Production Engineering Review*, 5(3), 62-69. Doi: 10.2478/mper-2014-0028.

[25] Dezert, J., Tchamova, A., Han, D. & Tacnet, J. M. (2020, July), "The SPOTIS rank reversal free method for multi-criteria decision-making support," *In 2020 IEEE 23rd International Conference on Information Fusion (FUSION)* (pp. 1-8). Doi: 10.23919/FUSION45008.2020.9190347.

[26] Kizielewicz, B., Shekhovtsov, A., & Sałabun, W. (2023). pymcdm—The universal library for solving multi-criteria decision-making problems. *SoftwareX*, *22*, 101368.

[27] Şen, R., ve Fidan, Ş. (2025). Yüzer fotovoltaik sistemler için AHP yöntemi ile optimal yer seçimi: Güneydoğu Anadolu Bölgesi uygulaması. International Science and Art Research Center (ISARC).

[28] Şen, R. (2025). Güneydoğu Anadolu Bölgesi için çok kriterli karar verme yöntemleri ile yüzer fotovoltaik sistemler için yer seçimi (Yüksek lisans tezi, Batman Üniversitesi). Yükseköğretim Kurulu Ulusal Tez Merkezi. https://tez.yok.gov.tr/UlusalTezMerkezi/TezGoster?key=P3dtmmHrq

[29] Google Earth. (n.d.). Erişim tarihi: 1 Ağustos 2025, https://earth.google.com/

[30] Global Solar Atlas. (n.d.). Erişim tarihi: 10 Ağustos 2025, https://globalsolaratlas.info/

[31] Topographic-map. (n.d.). Erişim tarihi: 3 Ağustos 2025, https://www.topographic-map.com/

[32] Enerji Atlası. (n.d.). Erişim tarihi: 3 Ağustos 2025, https://enerjiatlasi.com/

[33] Global Wind Atlas. (n.d.). Erişim tarihi: 7 Ağustos 2025, https://globalwindatlas.info/

[34] Meteoroloji Genel Müdürlüğü. (n.d.). Erişim tarihi: 9 Ağustos 2025, https://mgm.gov.tr/

[35] https://pypi.org/project/pymcdm/, erişim tarihi 01.10.2025

Dicle University
Journal of Engineering
https://dergipark.org.tr/tr/pub/dumf
duje.dicle.edu.tr

Research Article

Rose Leaf Diseases Detection Using Convolutional Neural Networks with Texture-Based Patch-Wise Selection

Birkan BÜYÜKARIKAN[1*], Keziban YALÇIN DOKUMACI[2]

[1] Isparta University of Applied Sciences, Uluborlu Selahattin Karasoy Vocational School Department of Computer Sciences, birkanbuyukarikan@isparta.edu.tr, Orcid No: 0000-0002-9703-9678
[2] Selçuk University, Agriculture Faculty, Department of Agricultural Machinery and Technologies Engineering, kezibanyalcin@selcuk.edu.tr, Orcid No: 0000-0001-9699-8861

ARTICLE INFO

Article history:

Received 24 August 2025
Received in revised form 21 October 2025
Accepted 27 November 2025
Available online 30 December 2025

Keywords:

Rose leaf disease, patch-wise selection, texture analysis, convolutional neural network, detection, precision spraying

Doi: 10.24012/dumf.1771419

* Corresponding author

ABSTRACT

In agricultural, early detection of leaf diseases enables control targeted at less chemical input, environmental impact, and expense. Towards this end, the see and spray strategy has been sought more intensely in recent decades in applications such as spot/precision spraying and UAV-based treatments. Because roses are converted into high-value medicinal and aromatic products, early identification of leaf diseases prevents quality losses and yield reductions, allowing selective pesticide application and timely intervention. In turn, this optimizes input use and lowers production costs. Convolutional neural networks (CNNs) are widely used for leaf disease detection; however, resizing images to meet fixed input dimensions can cause information loss and hinder the capture of subtle disease cues. To address this limitation, we propose a new approach that combines texture-based patch selection with CNN models for classifying rose leaf diseases. Texture-based patch selection provides a patch-wise pipeline that preserves fine lesion patterns otherwise lost when full images are resized for CNN input. A public rose leaf disease dataset was used. Each dataset image was initially divided into four patches of 224×224 pixels, and the patches with the highest information content were selected using Gray-Level Co-occurrence Matrix (GLCM), Local Binary Patterns (LBP), and Histogram of Oriented Gradients (HOG). The selected patches were classified using nine different CNN models. These CNN models were evaluated using transfer learning and five-fold cross-validation. Experimental results show that LBP-based patch-wise selection combined with DenseNet121 model achieved an accuracy of 95.73 ± 0.87%, while GLCM-based selection with DenseNet201 achieved 95.48 ± 0.70%. The findings indicate that texture-based patch selection can aid the detection of diseased regions on rose leaves and enable targeted pesticide application.

Introduction

Rose (*Rosa spp.*) holds significant value for both commercial production and ornamental landscaping. Cultivated across diverse regions including Asia and North America since antiquity [1, 2] roses face substantial yield threats from foliar diseases such as black spot (*Diplocarpon rosae*), powdery mildew (*Podosphaera pannosa*), and drying syndrome [3-5]. These pathologies frequently evade early farmer detection, leading to reduced flower quality, economic losses, and declining production. Timely intervention through accurate diagnosis could mitigate disease spread and enhance financial returns [1, 6].

One of the major environmental challenges is chemical pollution, which can result in lasting impacts including soil productivity loss and contamination of water resources. Excessive use of chemical pesticides contributes to environmental hazards, as chemical contamination poses a critical concern due to its long term impacts such as soil fertility degradation and water pollution [7]. Currently, farmers often rely on a human centered approach in pesticide application, making spraying decisions based on observations from a limited portion of the field and applying chemicals uniformly across the entire area. As a result, even pest free zones are unnecessarily treated. This practice stems from the lack of real time spatial information on pest infestations, leading to higher production costs and adverse impacts on natural resources due to excessive chemical use [8]. Recent studies highlight that site-specific sprayers equipped with machine vision technology can reduce pesticide application by up to 54% compared to conventional spraying methods [9]. Furthermore, another precision agriculture technique, variable rate application, has been shown to maintain constant spray deposition on target areas while reducing pesticide use by 58% [10]. Artificial intelligence-based approaches can be incorporated into site-specific crop protection practices, enabling variable-rate application and intelligent nozzle control. This integration minimizes pesticide usage while enhancing agricultural sustainability.

Recent advances leverage deep learning architectures to address diagnostic limitations. Convolutional Neural Networks (CNNs) demonstrate particular efficacy in automating disease identification from rose leaf imagery by extracting discriminative visual features [11]. This approach enhances diagnostic precision and operational

efficiency in plant breeding programs, enabling early-stage pathogen detection critical for crop protection. For example, Ma, et al. [6] used CNN to detect black spot disease in rose leaves with an accuracy of 99.95 to 100%. Similarly, Solanki, et al. [12] achieved 98.91% accuracy in identifying diseases in rose leaves using the DenseNet201 model. Additionally, Ashine [13] classified rose leaf diseases with 97.5% accuracy using the VGG16 model. In a different study, Akter, et al. [14] classified rose leaf diseases using the VGG16 model, with an accuracy of 0.975. In their evaluation of the EfficientNet-B7 model's performance in categorizing common rose leaf diseases, Poornima, et al. [15] found that it had an accuracy of 97.992%. Nayan, et al. [16] achieved an accuracy of 97.94% by modifying a CNN model specifically designed for mobile devices. Similarly, Nuanmeesri [17] achieved an accuracy of 88.33% by combining VGG16 and SVM in a hybrid model. Banerjee, et al. [18] proposed a hybrid model using CNN and SVM, achieving an accuracy of 89.3 %. Additionally, Sharma [4] reported an overall accuracy rate of 93% using the Vision Transformer (ViT-B/16) model. These studies highlight the practical applicability of different CNN and ViT architectures by demonstrating how well they classify rose leaf diseases.

High accuracy rates can be attained by CNN models. However, when feature abstraction occurs in the deeper layers, CNNs frequently have trouble maintaining the fine morphological details and spatial relationships on the rose leaf [19, 20]. Furthermore, performance loss may arise from shrinking the image size to fit CNN models, particularly for issues like rose leaf diseases where minute visual variations are crucial. Furthermore, patch-based ViT models can be computationally costly, despite their ability to capture global contexts.

To address these difficulties, especially in studies in the medical field, smaller parts of the images were selected and given as input to CNN models. For instance, Hou, et al. [21] employed a patch selection method based on the Expectation-Maximization algorithm to identify important regions in histopathology images. Similarly, Poudel, et al. [22] adopted a patch-based approach for the segmentation of thyroid ultrasound images. Moreover, Lachaud, et al. [23] developed a method based on entropy and spectral similarity metrics to enhance the effectiveness of the patch selection process. The primary motivation of this study is to integrate texture analysis techniques with CNN models, inspired by approaches in existing literature. This integration ensures that information-rich and distinctive regions contribute more effectively to the CNN-based classification process.

This study's objective is to use CNN models based on a texture-based patch-based selection strategy to classify diseases of rose leaves. This study was used on the Rose Leaf open access dataset. In the proposed method, image patches were selected based on information density using Gray Level Co-occurrence Matrix (GLCM), Local Binary Patterns (LBP), and Histogram of Oriented Gradients (HOG) techniques. These selected patches were then classified using different CNN models. CNN models were evaluated using a transfer learning approach with a 5-fold cross-validation method. The contributions and innovations of this study are summarized follows:

- This study proposes an innovative approach in which high-resolution images of rose leaves were divided into patches, these patches were selected based on their information density using texture-based feature extraction methods, and the selected patches were classified using CNN models.
- Rescaling images to fit the input size of CNN models may lead to the loss of fine details. This study mitigates such loss by selecting only the patches with high disease texture density, rather than downsizing the entire leaf image.
- The study contributes to the classification of diseases in rose leaves and provides practical insights into integrating texture analysis with deep learning for disease classification in different plant species.
- The integration of disease detection outcomes with agricultural mechanization practices provides a robust foundation for site-specific spraying and variable-rate application, facilitating more efficient pesticide use, lowering input costs, and advancing sustainable approaches to crop protection.

Materials and Methods

Overview of the Rose Leaf Dataset

Developed by Jarin Tasmim Jinia, et al. [24], the Rose Leaf dataset is public rose leaf disease dataset and intended for use in studies pertaining to plant pathology, disease prevention, and pest control in rose farming. Four categories comprise the images in this dataset, captured between October 30th and November 6th, 2024. The dataset has a total of 3113 images, all with the same background. They divided into four categories: 1288 images of Black Spot, 818 of Healthy Leaves, 324 of Dry Leaves, and 683 showing Leaf Holes. The images have resolutions of 3264 × 2448 or 2448 × 3264 pixels [24]. A selection of the dataset's images is shown in Fig. 1.

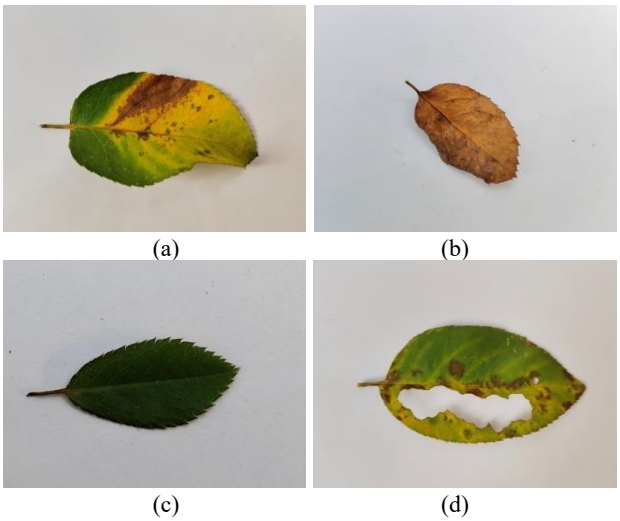

(a) (b) (c) (d)

Figure 1. Sample images from the Rose Leaf dataset: (a) Black Spot, (b) Dry Leaf, (c) Healthy Leaf, (d) Leaf Holes

This study employed a 5-fold cross-validation approach for dataset evaluation. In each iteration, approximately 2490 images were allocated for training and 623 images for testing.

Texture Analysis Models

Texture analysis, one of these features, represents the relevant image surface and structure [25] and is frequently used in many application areas such as textile, medical imaging, agriculture, industrial surface inspection, and remote sensing [26] to recognize the relevant image region [27]. In this study, three texture analysis methods, namely GLCM, LBP, and HOG, were utilized in the patch selection process. These techniques employ a distinct feature extraction strategy. The fundamental working principles of these methods and the types of features they extract are briefly described.

GLCM introduced by Haralick, et al. [28] models spatial relationships between pixel intensities for texture analysis. This method quantifies textural properties including contrast, energy, and homogeneity to characterize global-scale intensity variations and structural patterns [29].

LBP [30] a widely adopted feature extraction technique in computer vision, demonstrates robustness against illumination changes. A sliding window of specified neighborhood size assigns binary labels by thresholding neighboring pixels against the central pixel value. These binary values are arranged clockwise to form an LBP matrix, mathematically representing the texture's statistical and structural properties [31].

The HOG technique, developed by Dalal and Triggs [32] extracts features by encoding image gradient orientations into histograms, enabling detection of contours, edge structures, and shape-based attributes [32].

Models of Convolutional Neural Networks

This study employed pretrained NASNetMobile, MobileNet, MobileNetV2, DenseNet121, DenseNet169, DenseNet201, ResNet50V2, ResNet101V2, and ResNet152V2 models. The DenseNet architecture [33] enhances gradient flow, promotes feature reuse, and improves parameter efficiency by propagating feature maps from all preceding layers to subsequent layers. ResNet50V2, ResNet101V2, and ResNet152V2 [34] were redesigned with modified normalization-activation ordering to achieve more stable training than their original ResNet counterparts. MobileNet [35] and MobileNetV2 [36] utilize depthwise separable convolutions to substantially reduce parameter counts and computational overhead, making them suitable for mobile/embedded devices. NASNetMobile [37] optimized through Neural Architecture Search (NAS), is widely adopted in resource-constrained environments due to its compact size.

For patch feature extraction, convolutional layers of pretrained models were frozen. The following layers were sequentially appended: GlobalAveragePooling2D, BatchNormalization, Dense layer (1000 units) with 0.5 dropout layer and output layer with Softmax activation.

The Proposed Approach for Rose Leaf Disease Classification

In this study, a patch-based DL approach is proposed for the detection of rose leaf diseases. Fig. 2 shows the processing steps of the proposed method. First, each input image was resized to 448 × 448 and then divided into four equal patches of 224 × 224 pixels to match the input size of the CNN models. The information density of the obtained patches was evaluated using texture analysis techniques including GLCM, LBP, and HOG, which enable the identification of diverse texture and morphological features.

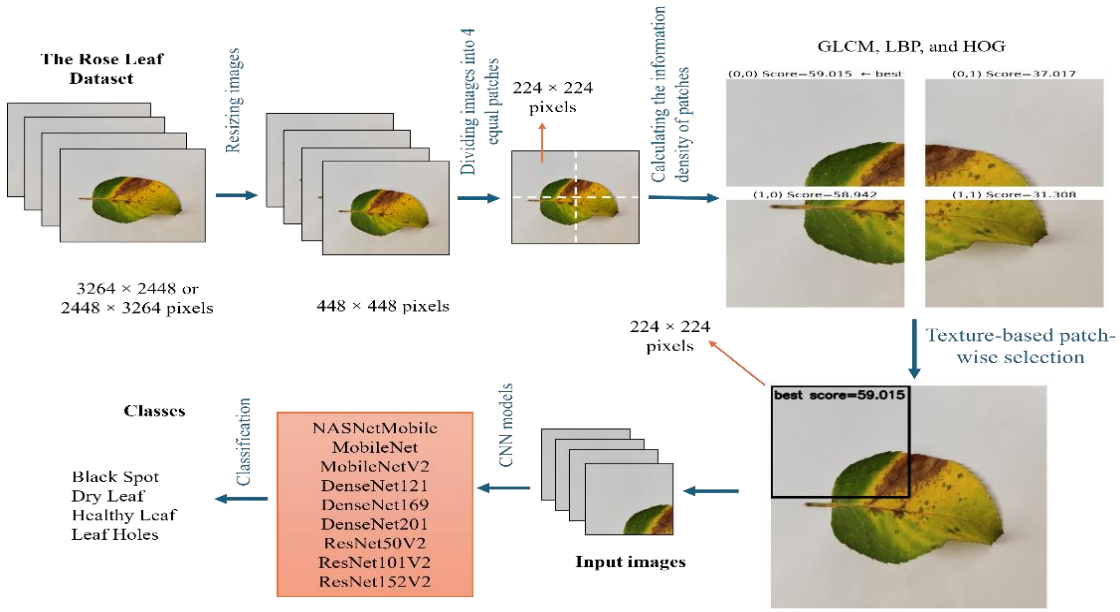

Figure 2. General diagram of the proposed texture-based patch-wise selection and CNN approach (The explanation was made via GLCM)

In the study, RGB color space patches were first converted to grayscale. Then, the following steps were applied for each texture analysis technique:

• In the GLCM technique, a feature matrix was calculated with a 1-pixel distance, 0° angle, and 256 grayscale parameters. From this, contrast and energy values were obtained, and their sum was used as a score for each patch.

• In the LBP technique, a uniform LBP histogram was extracted for each patch with a neighborhood parameter p=8 and a radius r=1. The obtained histogram was then normalized, and its entropy was calculated, which was used as the score.

• In the HOG technique, a HOG vector was created for each patch with a cell size of 8x8 pixels and a block size of 2x2 cells. The L2 norm of this vector was then calculated to obtain the corresponding score.

After calculating each patch's GLCM, LBP, and HoG scores, the patch with the highest score was selected as the best patch. This selected RGB image patch was fed into the CNN model as the input image. The classification process in the study was performed using the pre-trained NASNetMobile, MobileNet, MobileNetV2, DenseNet121, DenseNet169, DenseNet201, ResNet50V2, ResNet101V2, and ResNet152V2 models. These models training were conducted using the 5-fold cross-validation (StratifiedKFold) method. During training, The Adam was employed as the optimization method, with a learning rate of 0.001 and a batch size of 64. All models were trained for 20 epochs. These hyperparameters were determined based on preliminary evaluations. Table 1 lists the parameter values used in the study.

Table 1. Experimental parameters employed in model training

Parameter	Value
Image size	448 × 448
Patch size	224 × 224
Optimizer	Adam
Learning rate	0.001
Epoch	20
Batch size	64
Cross validation	5
Random state	42

All experiments were conducted using the Keras/TensorFlow framework on the Google Colab platform with the Python programming language. Since a time, limit was imposed for the patch selection process, no additional data augmentation was applied. Before training, all image pixels in the selected patches were normalized by dividing their values by 255. The average values of all results were reported in the experiments. The Wilcoxon signed-rank test was used to compare the accuracy results of GLCM-, LBP-, and HOG-based models with their respective baseline CNN classifications. In addition, the Wilcoxon signed-rank Test was applied to the fold-wise accuracy results of the baseline CNN and patch-wise models.

Evaluation Metrics

Accuracy, precision, recall, and F1-score metrics were used to evaluate the classification performance of the proposed models for rose leaf diseases in this study. Of these metrics, accuracy refers to the ratio of correctly predicted samples to the total number of examples. The precision metric represents the proportion of true positive examples among those predicted to be positive. The recall indicates the proportion of correctly identified true positives among all true positives. The F1-score is defined as the harmonic mean of precision and recall. Equations (1)-(4) were used to calculate all these metrics.

$$Accuracy = \frac{TP+TN}{TP+TN+FP+FN} * 100 \quad (1)$$

$$Precision = \frac{TP}{TP+FP} * 100 \quad (2)$$

$$Recall = \frac{TP}{TP+FN} * 100 \quad (3)$$

$$F1 - score = 2 * \frac{\text{PrecisionxRecall}}{\text{Precision+Recall}} * 100 \quad (4)$$

Since the experiments in this study were conducted using a 5-fold cross-validation method, the average values of these metrics are reported throughout the article. Furthermore, to evaluate the discriminative capability of the proposed models between classes, Receiver Operating Characteristic (ROC) curves were plotted for the models that achieved the highest performance results according to different texture analyses, and the corresponding Area Under the Curve (AUC) values were examined.

Experimental Results and Discussion

Results

The results of the patch-wise approach using GLCM-based feature extraction are presented in Table 2. Overall, DenseNet architecture demonstrated the best performance. The DenseNet201 model achieved the best results, with approximately 95% in all metrics. This can be attributed to the dense connectivity structure of the DenseNet architecture, which allows for more effective learning of rich feature representations. In contrast, the ResNet101V2 model recorded the lowest classification performance, with an accuracy of 89.58 ± 1.39%. The NASNetMobile, MobileNet, and MobileNetV2 models performed worse than DenseNet variants, they still demonstrated satisfactory results. In conclusion, the GLCM technique proved most effective when applied with DenseNet architectures. The contrast and energy metrics obtained from the GLCM method accurately captured the visual features of leaf textures, thereby facilitating optimized learning in CNNs.

Table 2. Classification performance results of CNN models using GLCM-based patch-wise selection (%) [a]

Model	Accuracy (Average ± SD)	Precision (Average ± SD)	Recall (Average ± SD)	F1-score (Average ± SD)
NASNetMobile	91.79 ± 0.98	91.86 ± 0.99	91.79 ± 0.98	91.78 ± 0.97
MobileNet	92.72 ± 1.30	92.90 ± 1.15	92.72 ± 1.30	92.64 ± 1.39
MobileNetV2	93.01 ± 0.89	93.06 ± 0.91	93.01 ± 0.89	92.98 ± 0.89
DenseNet121	95.25 ± 1.10	95.38 ± 0.96	95.25 ± 1.10	95.25 ± 1.10
DenseNet169	95.38 ± 0.78	95.44 ± 0.78	95.38 ± 0.78	95.38 ± 0.79
DenseNet201	**95.48 ± 0.70**	**95.50 ± 0.69**	**95.48 ± 0.70**	**95.47 ± 0.70**
ResNet50V2	90.70 ± 1.01	90.83 ± 1.06	90.70 ± 1.12	90.66 ± 1.12
ResNet101V2	89.58 ± 1.39	89.93 ± 1.09	89.60 ± 1.39	89.60 ± 1.36
ResNet152V2	91.76 ± 1.27	91.81 ± 1.26	91.76 ± 1.27	91.71 ± 1.30

[a] The best results are in bold font type. Note: SD: Standard Deviation

Table 3 presents the results of the patch-wise approach evaluated with LBP-based feature extraction. DenseNet-based models outperformed other models. The DenseNet121 model achieved accuracy, precision, recall, and F1-score metrics of 95.73 ± 0.87, 95.77 ± 0.88, 95.73 ± 0.87, and 95.73 ± 0.87%, respectively. The DenseNet121 model is high classified patches selected using the LBP technique. It can be concluded that the LBP technique selected the defining features that distinguish rose leaf disease classes. Conversely, the lowest performance in this technique was achieved by the NASNetMobile and ResNet50V2 models, with approximately 91%

Table 3. Classification performance results of CNN models using LBP-based patch-wise selection (%) [a]

Model	Accuracy (Average ± SD)	Precision (Average ± SD)	Recall (Average ± SD)	F1-score (Average ± SD)
NASNetMobile	91.28 ± 0.89	91.49 ± 0.92	91.28 ± 0.89	98.24 ± 0.88
MobileNet	93.46 ± 1.10	93.59 ± 1.02	93.46 ± 1.10	93.45 ± 1.13
MobileNetV2	92.21 ± 1.37	92.32 ± 1.34	92.21 ± 1.37	92.18 ± 1.37
DenseNet121	**95.73 ± 0.87**	**95.77 ± 0.88**	**95.73 ± 0.87**	**95.73 ± 0.87**
DenseNet169	94.80 ± 0.82	94.98 ± 0.74	94.80 ± 0.82	94.80 ± 0.84
DenseNet201	94.84 ± 2.42	95.04 ± 2.07	94.84 ± 2.42	94.84 ± 2.42
ResNet50V2	91.34 ± 0.95	91.57 ± 0.98	91.34 ± 0.95	91.33 ± 0.96
ResNet101V2	92.21 ± 0.46	92.34 ± 0.48	92.21 ± 0.46	92.19 ± 0.44
ResNet152V2	91.73 ± 0.95	91.88 ± 1.01	91.73 ± 0.95	91.70 ± 0.97

[a] The best results are in bold font type. Note: SD: Standard Deviation

Table 4 reports the classification results of the HOG-based patch-wise selection approach with CNN models. Overall, the HOG-based approach yielded lower classification performance compared to the others. The best results were obtained with the DenseNet201 model, which achieved accuracy, precision, recall, and F1-score values of 91.89 ± 0.59, 92.04 ± 0.59, 91.89 ± 0.59, and 91.88 ± 0.57%, respectively. The lowest performance was recorded with the ResNet50V2 model, which reached an accuracy of 85.18 ± 0.95%. Since the HOG technique primarily relies on edge orientation information, the patches selected using this method did not sufficiently capture distinctive texture features, thereby limiting classification performance.

Table 4. Classification performance results of CNN models using HOG-based patch-wise selection (%) [a]

Model	Accuracy (Average ± SD)	Precision (Average ± SD)	Recall (Average ± SD)	F1-score (Average ± SD)
NASNetMobile	88.45 ± 1.05	88.50 ± 1.07	88.45 ± 1.05	88.38 ± 1.02
MobileNet	89.99 ± 1.51	90.14 ± 1.39	89.99 ± 1.51	89.94 ± 1.53
MobileNetV2	87.33 ± 2.90	87.94 ± 2.12	87.33 ± 2.90	87.23 ± 3.08
DenseNet121	90.31 ± 1.31	90.48 ± 1.36	90.31 ± 1.31	90.32 ± 1.31
DenseNet169	90.22 ± 0.58	90.32 ± 0.47	90.22 ± 0.58	90.20 ± 0.56
DenseNet201	**91.89 ± 0.59**	**92.04 ± 0.59**	**91.89 ± 0.59**	**91.88 ± 0.57**
ResNet50V2	85.18 ± 0.95	85.49 ± 0.86	85.18 ± 0.95	85.12 ± 0.99
ResNet101V2	87.91 ± 1.26	88.04 ± 1.20	87.91 ± 1.26	87.85 ± 1.28
ResNet152V2	88.33 ± 1.16	88.42 ± 1.14	88.33 ± 1.16	88.28 ± 1.15

[a] The best results are in bold font type. Note: SD: Standard Deviation

The confusion matrices obtained from classifying patches selected using GLCM-, LBP-, and HOG-based techniques with DenseNet architectures are presented in Fig. 3. As shown in Fig. 3a, the DenseNet201 model trained with

GLCM-based patch-wise selection demonstrated consistently high predictive accuracy across classes. The model correctly classified nearly all test samples in the Black Spot and Healthy Leaf classes, with only a few misclassifications observed. Most of these errors occurred between the Leaf Holes and Dry Leaf classes, likely due to the visual similarity of the selected patches from these two classes. When comparing the results in Table 2 and Table 3, the LBP-based patch-wise selection approach achieved performance levels similar to those of the GLCM-based approach. Therefore, as shown in Fig. 3b, slightly more misclassifications occurred in the Dry Leaf class compared to GLCM, suggesting that the LBP method is somewhat limited in distinguishing between certain classes. In contrast, the DenseNet201 model trained with HOG-based patch-wise selection produced relatively fewer correct classifications than the other two approaches. In Fig. 3c, this model exhibited notable misclassifications, particularly between the Healthy Leaf and Leaf Holes classes. Although all models demonstrated high success rates, the GLCM-based patch-wise and LBP-based patch-wise methods enabled the selection of more discriminative patches compared to HOG, thereby enhancing classification performance. These findings highlight the importance of texture-based patch selection in improving the effectiveness of CNN-based disease classification.

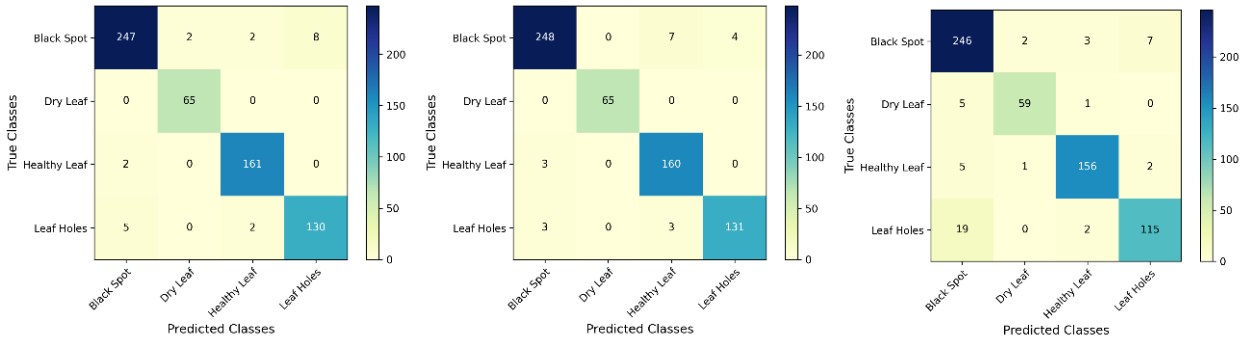

(a) (b) (c)

Figure 3. Confusion matrices of models: (a) GLCM-based with DenseNet201, (b) LBP-based with DenseNet121, (c) HOG-based with DenseNet201

Fig. 4 presents the ROC curves obtained from classifying GLCM-based patch-wise, LBP-based patch-wise, and HOG-based patch-wise selections with DenseNet models. Each curve illustrates the discrimination ability between positive and negative classifications for different classes. In Fig. 4a, the GLCM-based patch-wise selection with the DenseNet201 model remains close to the upper-left corner of the ROC space across all classes, indicating high discriminative power and AUC values approaching 1.0. Similarly, the LBP-based patch-wise selection with the DenseNet121 model also demonstrates strong performance; however, as shown in Fig. 4b, the ROC curve for the Dry Leaf class slightly deviates from the optimal corner, reflecting a marginal reduction in classification performance. The HOG-based patch-wise selection with the DenseNet201 model produces ROC curves that are positioned further from the upper-left corner compared to the other two methods, indicating weaker discrimination, particularly for classes with lower AUC values.

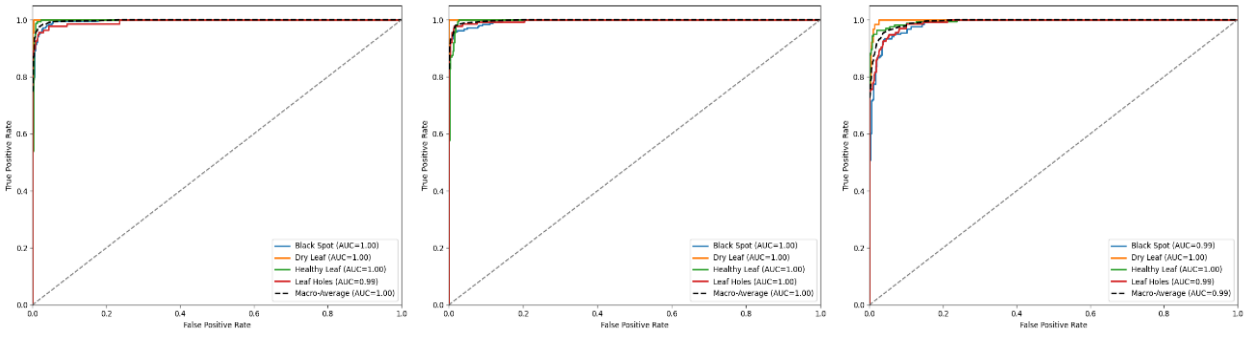

(a) (b) (c)

Figure 4. ROC curves of models, (a) GLCM-based patch-wise selection with DenseNet201, (b) LBP-based patch-wise selection with DenseNet121, (c) HOG-based patch-wise selection with DenseNet201

Fig. 5 presents a comparative graph illustrating the classification results of CNN models based on patch-wise selections performed using three different texture features. According to the graph, the scores obtained with the GLCM- and LBP-based patch-wise selection approaches are closely aligned, and both achieve high performance results. Although the LBP-based approach exhibits a wider distribution across all metrics, it reaches higher values at

the upper limit. In contrast, the HOG-based approach demonstrates significantly lower performance than the other two methods. This suggests that the patches selected using the HOG technique possess limited discriminative power for the classification task, and that the CNN models were unable to achieve sufficient classification performance with these patches.

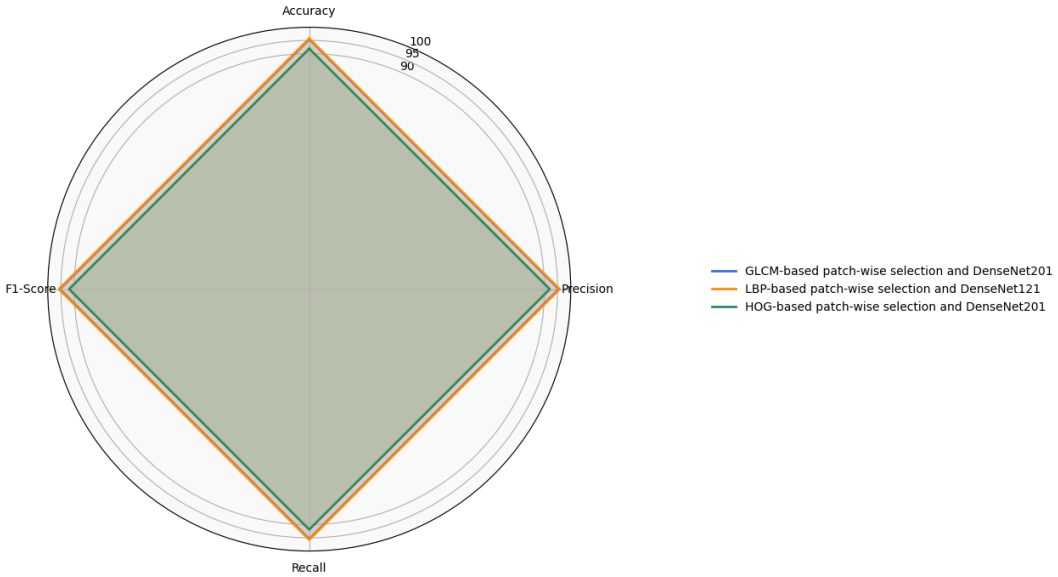

Figure 5. Comparative graph of classification results using GLCM, LBP, and HOG-based patch-wise selection with DenseNet architectures

Table 5 lists the average performance results of the proposed models with precision, recall and F1-score metrics by class. GLCM and LBP-based patch-wise selection with CNN models showed high performance in the "Dry Leaf" class. On the other hand, the HOG-based patch-wise selection and DenseNet201 models achieved higher performance values in the "Healthy Leaf" class than in the other classes.

On the other hand, the GLCM-based DenseNet201 model showed lower performance in the "Leaf Holes" class compared to the other classes. Similarly, the LBP-based DenseNet121 model also achieved low performance results in the "Leaf Holes" class. Furthermore, the HOG-based DenseNet201 model showed a lower performance in the "Dry Leaf" class compared to the other classes.

Table 5. Class-based average performance results of the models (%) [a]

Model	Class	Precision	Recall	Precision
GLCM-based and DenseNet201	Black Spot	95.31	95.20	95.24
	Dry Leaf	**96.63**	**96.59**	**96.57**
	Healthy Leaf	96.39	97.55	96.96
	Leaf Holes	94.24	92.97	93.58
LBP-based and DenseNet121	Black Spot	95.94	94.74	95.33
	Dry Leaf	**97.84**	**97.53**	**97.66**
	Healthy Leaf	95.27	97.80	96.51
	Leaf Holes	95.05	94.29	94.64
HOG-based and DenseNet201	Black Spot	91.67	91.88	91.73
	Dry Leaf	91.11	94.12	92.37
	Healthy Leaf	**93.18**	**95.23**	**94.15**
	Leaf Holes	91.82	86.82	89.18

[a] The best results are in bold font type.

It is observed that the accuracy of baseline CNN models trained with full images were above 98%, while the accuracy values obtained with patch-wise selection strategies remain at 95.48 ± 0.70% for GLCM, 95.73 ± 0.87% for LBP, and 91.89 ± 0.59% for HOG (Table 6). According to the Wilcoxon Signed-Rank Test results, a p-value of 0.0625 was obtained for all compared models, and this value was not found to be statistically significant compared to the $p < 0.05$ threshold. This result indicates that, despite the potential of patch-wise methods to reduce information loss in high-resolution images, they did not significantly improve the basic CNN models in this study. However, it was determined that GLCM and LBP-based approaches exhibited more consistent and higher performance than HOG.

Table 6. Accuracy and statistical comparison of patch-wise selection methods and basic CNN models

Patch selection method	Baseline CNN model	Accuracy (Average ± SD %)	Statistical significance (p-value)
GLCM-based	DenseNet201	95.48 ± 0.70	0.0625
-	DenseNet201	98.7 ± 0.30	-
LBP-based	DenseNet121	95.73 ± 0.87	0.0625
-	DenseNet121	98.5 ± 0.5	-
HOG-based	DenseNet201	91.89 ± 0.59	0.0625
-	DenseNet201	98.7 ± 0.30	-

Note: SD: Standard Deviation

Discussion

The results reported in the existing literature on the classification of rose leaf diseases are compared with those obtained from the proposed texture-based patch-wise selection CNN approach in Table 7. Although both CNN- and ViT-based models have been employed in previous studies, no work with the same methodological structure as the proposed approach has been identified. Therefore, comparisons were made based on model performance to ensure fairness. For instance, Ma, et al. [6] reported nearly 100% accuracy for the classification of black spot disease using CNN models. Similarly, Solanki, et al. [12] achieved 98.91% accuracy for multiple rose leaf diseases with DenseNet201. In comparison, the proposed method achieved 95.48% accuracy using GLCM-based patch-wise selection with DenseNet201. The slightly higher accuracy reported by Solanki, et al. [12] can be attributed to their use of full leaf images as input, whereas the present study focused on texture-based patch extraction.

Ashine [13] reported 98% accuracy using a CNN-based model for rose leaf disease classification. Akter, et al. [14] achieved 97.5% (ratio value 0.975) accuracy with the VGG16 model, while Poornima et al. (2024) obtained 97.992% accuracy using EfficientNet-B7.Nayan, et al. [16] achieved 97.94% accuracy with their proposed CNN model.

Nuanmeesri [17] achieved 83.33% accuracy with a hybrid approach combining VGG16 and SVM. Similarly, Banerjee, et al. [18] obtained 89.35% accuracy with their combined CNN–SVM model. On the other hand, Sharma [4] achieved 93% accuracy using the ViT-B/16 model.

This proposed approach achieved accuracy of 95.73%, despite relying only on patch of the images. This patch-based approach did not provide a statistically significant improvement compared to CNN models trained on the entire image. However, it offered comparable classification performance with the advantages of reduced information loss and increased interpretability. These results suggest that integrating texture-based patch selection with CNN models could be a promising research direction for future studies.

Table 7. Comparison of the classification accuracies of the proposed approach with previous studies

Reference	Classes type	Model	Result (%)
Ma, et al. [6]	Black spot disease	CNN	99.95-100
Solanki, et al. [12]	Diseases of rose leaves	DenseNet201	98.91
Ashine [13]	Diseases of rose leaves	CNN	98
Akter, et al. [14]	Diseases of rose leaves	VGG16	97.5
Poornima, et al. [15]	Diseases of rose leaves	EfficientNet B7	97.992
Nayan, et al. [16]	Diseases of rose leaves	CNN	97.94
Nuanmeesri [17]	Diseases of rose leaves	VGG16 and SVM	88.33
Banerjee, et al. [18]	Diseases of rose leaves	VGG16 and SVM	89.3456
Sharma [4]	Diseases of rose leaves	ViT-B/16	93
This study	Diseases of rose leaves	LBP-based patch-wise selection and DenseNet121	95.73

Limitations of the study

Although the study combines the strengths of both classical image processing and CNN models, several limitations should be noted:

- The Rose Leaf dataset used in this study consists of images captured against a fixed background. In real-world conditions, variations in lighting, shadows, or backgrounds may adversely affect the texture-based patch selection process and, consequently, the classification performance of CNN models.
- The proposed patch selection strategy identifies only a single patch per image. This approach may be insufficient to capture all relevant information when multiple diseased regions are present on a leaf. Moreover, in the dataset used, each image was categorized under only one disease condition, which may limit the generalizability of the method.

- Each image in this study was divided into four equal parts. However, this fixed partitioning approach may lead to incomplete information being extracted if the diseased region falls exactly on a patch boundary. Such cases could negatively influence classification performance.
- The study was evaluated on the original images, and no data augmentation techniques were applied. In addition, the hyperparameters in the training process of CNN models were kept constant to ensure the consistency of the comparisons in the study. Thus, evaluations were performed on the architectural structures of CNN models.

Conclusion and Recommendations

In this study, a texture-based patch-wise selection strategy was integrated with CNN models to classify rose leaf diseases. Each image, resized to 448 × 448 pixels, was divided into four patches, and the patch with the highest information density was selected using GLCM, LBP, and HOG techniques. The selected patches were then evaluated with different CNN architectures. The GLCM-based patch-wise selection combined with the DenseNet201 model achieved an accuracy of 95.48 ± 0.70%, while the LBP-based selection with the DenseNet121 model achieved the highest accuracy of 95.73 ± 0.87%. In contrast, the HOG-based selection combined with the DenseNet201 model resulted in a lower classification accuracy of 91.89 ± 0.59% compared to the other two approaches. It is believed that the HOG technique's focus on edge information results in low accuracy.

The findings of this study indicate that patch-wise disease detection can serve as a decision-support tool for precision spraying machines. By identifying infected leaf regions, sprayers equipped with variable-rate nozzles or intelligent actuation systems can apply pesticides only where needed. This not only increases spraying efficiency but also aligns with the broader goals of sustainable agricultural mechanization by reducing chemical inputs and environmental load. In addition, the study provides a critical bridge between computer vision-based plant disease detection and practical mechanization research, showing how digital tools can be translated into more efficient field operations. Such integration has the potential to minimize chemical overuse, safeguard natural resources, enhance crop productivity, and contribute to global food security. Future studies should focus on integrating the proposed detection framework with diverse spraying platforms, including UAV- and robot assisted systems, to enable fully automated, site-specific crop protection under real field conditions. It is also proposed to implement different patch-wise selection, data augmented and hyperparameter optimization strategies and comprehensively investigate their effects on classification performance.

Ethics committee approval and conflict of interest statement

There is no need to obtain permission from the ethics committee for the article prepared.

There is no conflict of interest with any person / institution in the article prepared.

Data availability

The data used is a public dataset from Mendeley Data and the source has been mentioned in the citation. The dataset is available at the following URL: https://data.mendeley.com/datasets/hmjtdzkfh3/2

Authors' Contributions

Büyükarıkan B: Conceptualization, Investigation, Data curation, Methodology, Software, Validation, Visualization, Formal analysis, Writing – original draft, Writing – review & editing.

Yalçın Dokumacı K: Conceptualization, Writing – original draft, Writing – review & editing.

References

[1] A. Rajbongshi, T. Sarker, M. M. Ahamad, and M. M. Rahman, "Rose diseases recognition using MobileNet," in 2020 4th International Symposium on Multidisciplinary Studies and Innovative Technologies (ISMSIT), Turkey, 2020, IEEE, pp. 1-7.

[2] R. Sobolu, L. Stanca, D. Pusta, I. Pop, and M. Cordea, "Image Processing Technique Applying To Detect Black Spot And Rust Diseases At Roses," Managerial Challenges of the Contemporary Society. Proceedings, vol. 12, no. 1, pp. 68-73, 2019.

[3] S. Sazzad, A. Rajbongshi, R. Shakil, B. Akter, and M. S. Kaiser, "RoseNet: Rose leave dataset for the development of an automation system to recognize the diseases of rose," Data in Brief, vol. 44, p. 108497, 2022.

[4] J. Sharma, "Enhanced Rose Leaf Disease Classification Using Vision Transformer (ViT-B/16) Detecting Black Spot, Downy Mildew, and Healthy Leaves for Improved Plant Health Management," in 2024 5th International Conference on Data Intelligence and Cognitive Informatics (ICDICI), India, 2024, IEEE, pp. 52-56.

[5] E. R. Reddy, S. D. Satturi, M. Harshini, and S. Shaik, "Rose Plant Leaf Disease Recognition Using Machine Learning Methodologies," Asian Journal of Research in Computer Science, vol. 17, no. 11, pp. 65-72, 2024.

[6] J. Ma, L. Pang, L. Yan, and J. Xiao, "Detection of black spot of rose based on hyperspectral imaging and convolutional neural network," AgriEngineering, vol. 2, no. 4, pp. 556-567, 2020.

[7] R. Kaur et al., "Pesticides: An alarming detrimental to health and environment," Science of the Total Environment, vol. 915, p. 170113, 2024.

[8] P. Pokharel, A. Sharda, D. Flippo, and K. Ladino, "Design and systematic evaluation of an Under-Canopy robotic spray system for row crops," Smart Agricultural Technology, vol. 8, p. 100510, 2024.

[9] H. Asaei, A. Jafari, and M. Loghavi, "Site-specific orchard sprayer equipped with machine vision for chemical

usage management," Computers and Electronics in Agriculture, vol. 162, pp. 431-439, 2019.

[10] J. Llorens, E. Gil, J. Llop, and A. Escolà, "Variable rate dosing in precision viticulture: Use of electronic devices to improve application efficiency," Crop protection, vol. 29, no. 3, pp. 239-248, 2010.

[11] S. Sladojevic, M. Arsenovic, A. Anderla, D. Culibrk, and D. Stefanovic, "Deep neural networks based recognition of plant diseases by leaf image classification," Computational intelligence and neuroscience, vol. 2016, no. 1, p. 3289801, 2016.

[12] V. Solanki, R. Ahuja, V. Khullar, and S. Thapliyal, "Optimizing Rose Leaf Disease Detection Performance via Explainable Transfer Learning: A Comparative Analysis," in 2024 International Conference on Electrical Electronics and Computing Technologies (ICEECT), India, 2024, IEEE, pp. 1-6.

[13] T. Ashine, "Image-Based Rose Leaf Diseases Detection Using Deep Learning," St. Mary's University, 2024.

[14] N. Akter, M. N. Ullah, M. S. Rifat, and A. S. Sikder, "Optimized Convolutional Neural Network Architecture for High-Accuracy Classification of Rose Leaf Diseases: Neural Network on Rose Leaf Diseases," International Journal of Imminent Science & Technology., vol. 2, no. 2, 2024.

[15] S. Poornima, R. Divya, R. S. Krishnan, S. Jegadeesan, G. Yamini, and G. V. Rajkumar, "Advancing Rose Disease Diagnosis: A Deep Learning Framework with EfficientNet-B7," in 2024 8th International Conference on I-SMAC (IoT in Social, Mobile, Analytics and Cloud)(I-SMAC), Nepal, 2024, IEEE, pp. 1747-1754.

[16] S. I. Nayan, S. M. Rahman, and N. I. Mahbub, "RoseVision: An Android Application To Detect Rose Leaf Diseases Using Modified Convolutional Neural Network," in 2023 26th International Conference on Computer and Information Technology (ICCIT), Bangladesh, 2023, IEEE, pp. 1-6.

[17] S. Nuanmeesri, "A hybrid deep learning and optimized machine learning approach for rose leaf disease classification," Engineering, Technology & Applied Science Research, vol. 11, no. 5, pp. 7678-7683, 2021.

[18] D. Banerjee, N. Sharma, R. Chauhan, M. Singh, and B. V. Kumar, "Improving Precision in Rose Leaf Disease Recognition with Integrated CNN and SVM Models," in 2024 4th International Conference on Innovative Practices in Technology and Management (ICIPTM), India, 2024, IEEE, pp. 1-6.

[19] S. Sabour, N. Frosst, and G. Hinton, "Matrix capsules with EM routing," in 6th international conference on learning representations, ICLR, Canada, 2018, pp. 1-15.

[20] G. Altan, "Performance evaluation of capsule networks for classification of plant leaf diseases," International Journal of Applied Mathematics Electronics and Computers, vol. 8, no. 3, pp. 57-63, 2020.

[21] L. Hou, D. Samaras, T. M. Kurc, Y. Gao, J. E. Davis, and J. H. Saltz, "Patch-based convolutional neural network for whole slide tissue image classification," in Proceedings of the IEEE conference on computer vision and pattern recognition, 2016, pp. 2424-2433.

[22] P. Poudel, A. Illanes, M. Sadeghi, and M. Friebe, "Patch based texture classification of thyroid ultrasound images using convolutional neural network," in 2019 41st Annual international conference of the IEEE engineering in medicine and biology society (EMBC), Germany, 2019, IEEE, pp. 5828-5831.

[23] G. Lachaud, P. Conde-Cespedes, and M. Trocan, "Patch selection for melanoma classification," in International Conference on Computational Collective Intelligence, 2022: Springer, pp. 148-159.

[24] Jarin Tasmim Jinia, Sakibur Rahman, and M. U. Mojumdar. A Comprehensive dataset on diseases affecting rose leaves: Identification, Symptoms, and Control Strategies. [Online]. Available: https://data.mendeley.com/datasets/hmjtdzkfh3/2

[25] J. Sklansky, "Image segmentation and feature extraction," IEEE Transactions on Systems, Man, and Cybernetics, vol. 8, no. 4, pp. 237-247, 1978.

[26] G. S. Raghtate and S. S. Salankar, "Comparison of classification methods with second order statistical analysis and wavelet transform for texture image classification," in 2015 International Conference on Computational Intelligence and Communication Networks (CICN), India, 2015, IEEE, pp. 312-317.

[27] R. C. Gonzalez and R. E. Woods, Digital image processing (third edition). Pearson, 2007, p. 976.

[28] R. M. Haralick, K. Shanmugam, and I. H. Dinstein, "Textural features for image classification," IEEE Transactions on systems, man, and cybernetics, no. 6, pp. 610-621, 1973.

[29] F. Albregtsen, B. Nielsen, and H. E. Danielsen, "Adaptive gray level run length features from class distance matrices," in Proceedings 15th International Conference on Pattern Recognition. ICPR-2000, 2000, vol. 3: IEEE, pp. 738-741.

[30] T. Ojala, M. Pietikäinen, and D. Harwood, "A comparative study of texture measures with classification based on featured distributions," Pattern recognition, vol. 29, no. 1, pp. 51-59, 1996.

[31] M. Heikkilä, M. Pietikäinen, and C. Schmid, "Description of interest regions with local binary patterns," Pattern recognition, vol. 42, no. 3, pp. 425-436, 2009.

[32] N. Dalal and B. Triggs, "Histograms of oriented gradients for human detection," in 2005 IEEE computer society conference on computer vision and pattern recognition (CVPR'05), 2005, vol. 1: IEEE, pp. 886-893.

[33] G. Huang, Z. Liu, L. Van Der Maaten, and K. Q. Weinberger, "Densely connected convolutional networks,"

in Proceedings of the IEEE conference on computer vision and pattern recognition, Hawaii, 2017, pp. 4700-4708.

[34] K. He, X. Zhang, S. Ren, and J. Sun, "Identity mappings in deep residual networks," in Computer Vision–ECCV 2016: 14th European Conference, Amsterdam, The Netherlands, October 11–14, 2016, Proceedings, Part IV 14, 2016: Springer, pp. 630-645.

[35] A. G. Howard et al., "Mobilenets: Efficient convolutional neural networks for mobile vision applications," arXiv preprint arXiv:1704.04861, 2017.

[36] M. Sandler, A. Howard, M. Zhu, A. Zhmoginov, and L.-C. Chen, "Mobilenetv2: Inverted residuals and linear bottlenecks," in Proceedings of the IEEE conference on computer vision and pattern recognition, USA, 2018, pp. 4510-4520.

[37] B. Zoph, V. Vasudevan, J. Shlens, and Q. V. Le, "Learning transferable architectures for scalable image recognition," in Proceedings of the IEEE conference on computer vision and pattern recognition, USA, 2018, pp. 8697-8710.

Dicle University
Journal of Engineering
https://dergipark.org.tr/tr/pub/dumf
duje.dicle.edu.tr

Research Article

Comparative Analysis of CNN-Based Deep Learning Architectures for Automatic Plant Disease Classification

Sedat ORENC[1*], Emrullah ACAR[2], Mehmet Sirac OZERDEM[3]

[1] Batman University, Electrical-Electronics Engineering Department, sedat.orenc@batman.edu.tr, Orcid No: 0000- 0002-1190-2849
[2] Batman University, Electrical-Electronics Engineering Department, emrullah.acar@batman.edu.tr, Orcid No 0000-0002-1897-9830
[3] Dicle University, Electrical-Electronics Engineering Department, sozerdem@dicle.edu.tr, Orcid No 0000- 0002-9368-8902

ARTICLE INFO

Article history:

Received 3 September 2025
Received in revised form 10 October 2025
Accepted 21 November 2025
Available online 30 December 2025

Keywords:

Image processing, Plant disease, Deep learning models, Apple leaf classification

Doi: 10.24012/dumf.1777471

* Corresponding author

ABSTRACT

Early detection of plant diseases is crucial for ensuring crop health and reducing agricultural losses. Traditional visual inspection presents a key opportunity for enhancement, as its dependence on manual effort naturally limits both its speed and accuracy. To address this challenge, this study conducts a comparative analysis of five convolutional neural network based architectures—DenseNet201, EfficientNetB3, ResNet101, ResNet50, and VGG16—for automatic classification of apple leaf diseases, focusing on healthy, powdery mildew, and rust conditions. A publicly available Kaggle dataset consisting of 1,532 images was augmented to 9,284 samples using techniques such as flipping, brightness adjustment, and rotation. Each model was fine-tuned and evaluated based on accuracy, precision, recall, and F1-score. Among these, EfficientNetB3 and VGG16 demonstrated superior classification performance across all classes, achieving up to 95.00% accuracy with perfect precision and recall (100.00%). These results confirm the effectiveness of transfer learning and data augmentation in enhancing disease detection accuracy, offering a promising foundation for real-time plant health monitoring systems.

Introduction

Plant diseases are a critical challenge to agriculture worldwide, affecting both crop yield and quality. As the global demand for food increases due to population growth and environmental changes, the early detection and effective management of plant diseases have become more essential than ever [1] . Diseases such as rust, powdery mildew, blight, leaf spots, and viral infections significantly threaten various crop species including wheat, tomato, apple, cotton, soybean, and grape. If not diagnosed at early stages, these diseases can spread rapidly across fields, leading to devastating economic losses and a decline in food security [2].

Traditionally, plant disease diagnosis has relied heavily on manual observation and expert knowledge. Agricultural specialists and plant pathologists typically examine visual symptoms such as discoloration, lesion patterns, or deformation on leaves and stems. However, this approach is limited by human error, subjectivity, labor intensity, and scalability. The diagnosis process becomes even more difficult when multiple diseases present similar visual symptoms or when plants are affected by more than one disease at a time [3]. These limitations have paved the way for data-driven and automated approaches to disease detection using computer vision and artificial intelligence [4], [5].

In recent years, deep learning has emerged as a transformative tool in agricultural image analysis. Among deep learning methods, Convolutional Neural Networks (CNNs) have become the backbone of visual classification tasks due to their ability to extract hierarchical features from raw image data [6]. CNNs mimic the human visual system, enabling machines to automatically learn to recognize patterns such as edges, textures, and complex shapes directly from image pixels [7]. Unlike traditional machine learning approaches, CNNs do not require handcrafted features, making them highly suitable for complex and variable datasets such as plant leaf images taken under different lighting conditions, angles, and backgrounds [8].

CNN architectures typically consist of multiple layers, including convolutional layers, pooling layers, and fully connected layers. The convolutional layers are responsible

for detecting local features in the input image, while pooling layers reduce the spatial dimensions, making the model more computationally efficient and less sensitive to small distortions. Fully connected layers at the end of the network are used to map extracted features to the final classification output [9]. Modern CNN models have evolved to include more advanced modules such as batch normalization, residual connections, attention mechanisms, and multi-scale feature extraction, significantly improving classification accuracy and generalization capabilities [10], [11].

In the field of plant disease detection, deep learning models have proven capable of distinguishing between various diseases with high precision and recall. Pre-trained models such as VGG16, ResNet50, InceptionV3, EfficientNet, and DenseNet have been widely adopted through transfer learning, allowing researchers to adapt robust architectures originally trained on large-scale datasets to specific plant disease problems with limited data. These models have been successfully used to identify diseases in a variety of crops, often outperforming traditional algorithms and even expert assessments in terms of speed and accuracy [12], [13], [14].

Moreover, deep learning approaches based on multiple CNN architectures have gained attention for their improved performance and robustness. Comparing different models helps identify their individual strengths and weaknesses, leading to a more comprehensive understanding of how diverse feature representations affect classification accuracy. Such analyses are particularly useful when disease symptoms vary subtly across samples, as is common in early-stage infections or under diverse environmental conditions [11], [15].

Another important factor in building accurate plant disease detection systems is data quality and pre-processing. High-resolution images, proper labeling, and effective data augmentation techniques such as flipping, rotating, and brightness adjustments help address the challenges posed by small datasets. These strategies not only increase the amount of data but also improve the model's ability to generalize across different real-world conditions [2], [3], [13].

The integration of deep learning and image processing into precision agriculture offers promising applications. From smartphone-based diagnostic tools for farmers to autonomous drone systems for real-time field monitoring, these technologies provide scalable, efficient, and accurate solutions to detect plant diseases early, minimize crop loss, and optimize agricultural productivity [4], [5], [16].

This study contributes to the field of plant disease detection by developing a deep learning framework focused on apple leaf diseases, specifically targeting healthy, powdery mildew, and rust categories. The key contributions of this paper are as follows:

- A comprehensive comparison of five state-of-the-art convolutional neural network models was conducted for automatic classification of apple leaf diseases. This comparative approach provides valuable insights into the relative strengths and limitations of widely used CNN architectures in agricultural image analysis.
- A balanced and augmented dataset was developed using horizontal flipping, brightness adjustment, and rotation to expand 1,532 apple leaf images to 9,284 samples. This strategy effectively mitigates data scarcity, enhances generalization, and ensures robust performance under variable lighting and environmental conditions.
- The findings demonstrate the feasibility of integrating CNN-based detection models into real-time plant health monitoring systems, mobile diagnostic tools, and precision agriculture platforms, contributing to scalable and efficient crop management solutions.

Figure 1 presents the methodological workflow employed for plant disease detection in this study. In the image acquisition phase, raw leaf images are collected to establish the primary dataset for subsequent processing. During the preprocessing phase, the images are resized to a standardized resolution to maintain consistency across the dataset, and data augmentation techniques are applied to increase sample diversity and enhance the generalization capability of the models. The dataset is then partitioned into training (80%), validation (10%), and testing (10%) subsets to facilitate robust model training and unbiased performance evaluation. Multiple state-of-the-art deep learning architectures, namely DenseNet201, EfficientNetB3, ResNet101, ResNet50, and VGG16, are implemented for the classification task. Model performance is quantitatively assessed using widely adopted evaluation metrics, including accuracy, precision, recall, and F1-score, ensuring a comprehensive assessment of predictive capability. The results stage provides a visual comparison between the original and predicted images, effectively illustrating the models' ability to accurately identify and classify plant diseases.

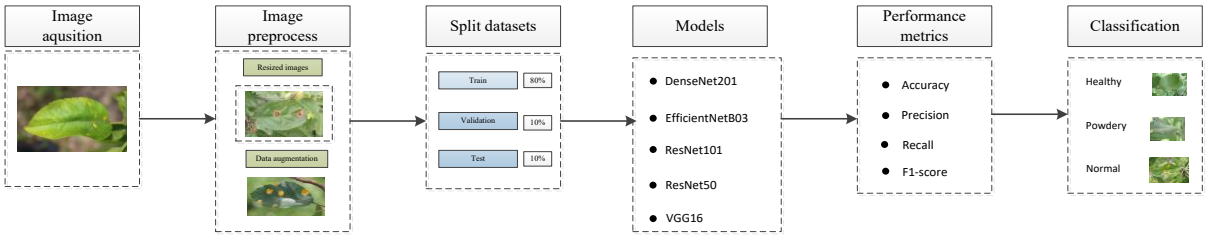

Figure 1. The workflow of plant disease detection using deep learning models

Related Works

Plant disease detection using deep learning and image processing techniques has become a prominent research area in agricultural informatics. Various recent studies have focused on identifying and classifying diseases based on leaf images using CNNs and transfer learning models. Shahoveisi et al. (2023) evaluated the performance of four CNN models (Xception, ResNet50, EfficientNetB4, MobileNet) for detecting rust disease in field crops, where EfficientNetB4 achieved the highest accuracy of 94.29%, highlighting its robustness in real-field conditions [12]. Similarly, Hayit et al. (2021) proposed a CNN-based Yellow-Rust-Xception model for determining the severity of yellow rust in wheat, offering fine-grained classification into five severity levels using a newly constructed dataset [14]. Another study by Sachar and Kumar (2022) introduced the EDL-AMLI framework that combines MobileNetV2, InceptionV3, and ResNet50 for medicinal leaf identification, achieving an average accuracy of 99.9% through fivefold cross-validation [15]. In the domain of tomato plant diseases, Sharma et al. (2023) designed a model by fusing ResNet50 and MobileNetV2 feature maps, reporting over 99.9% accuracy in classifying 10 disease categories [16]. Likewise, Atila et al. (2021) utilized EfficientNet architectures on the PlantVillage dataset and found that EfficientNet-B4 and B5 outperformed other state-of-the- art models in terms of accuracy and precision [13]. Moreover, Wang et al. (2017) applied VGG16 with transfer learning to estimate disease severity stages of apple black rot, achieving 90.4% accuracy, which supports the use of deep learning in fine-grained disease diagnosis [7]. Al-Zubi (2025) also developed a CNN-based model for detecting powdery mildew and rust in apple orchards using a dataset of 1,532 images, achieving over 91% overall accuracy [2]. These studies collectively demonstrate the effectiveness of deep learning, especially CNN-based architectures architectures, in accurately detecting and classifying plant diseases using image data. The integration of augmentation, transfer learning, and optimizer tuning is found to significantly improve performance across diverse plant species and disease types.

Material and Methods

This section outlines the dataset characteristics, image pre-processing steps, augmentation techniques, and performance metrics used in the study. A labeled apple leaf image dataset was prepared by applying various pre-processing operations such as resizing, augmentation, and dataset splitting. Following this, several deep learning models were trained and evaluated using standard classification metrics including accuracy, precision, recall, and F1-score.

Data description

The dataset used in this study was obtained from the open-source Kaggle platform. It contains a total of 1,532 labeled images of apple leaves. These images are divided into three categories: healthy, powdery and rust in Figure 2. Each category represents a different condition of the apple plant. To train and evaluate the model effectively, the dataset was split into three subsets: training, testing, and validation. The division was based on an 80:10:10 ratio. Specifically, 80% of the images were used for training, 10% for testing, and 10% for validation in table 1.

Healthy Powdery Rust

Figure 2. Healthy, powdery and rust leaves on apple leaves

Table 1. The number of healthy, powdery, and rust apple leaf images across dataset subsets

	Type of Apple Leaf Condition			
Data Type	**Healthy**	**Powdery**	**Rust**	**Total**
Training set	458	430	434	1322
Validation set	50	50	50	150
Test Set	50	50	50	150
Grand Total	558	530	534	1622

Table 1 presents the distribution of apple leaf images according to their condition types: healthy, powdery mildew, and rust. The dataset is divided into three subsets: training, validation, and testing. In the training set, there are 458 healthy, 430 powdery mildew, and 434 rust-affected leaf images, totaling 1,322 samples. This subset is used to train the deep learning model. The validation set contains 50 images from each class, making a total of 150 images. This subset helps in tuning the model parameters during training. Similarly, the test set also includes 50 images per class, resulting in another 150 images. This subset is used to evaluate the final performance of the trained model on unseen data. In total, the dataset consists of 558 healthy, 530 powdery mildew, and 534 rust-infected leaf images. The grand total is 1,622 images across all classes and subsets. This balanced distribution ensures reliable model training, validation, and testing.

Image pre-processing

Pre-processing is a critical step in deep learning workflows, especially when dealing with image data. It ensures that all input images are in a consistent format and quality, which improves the efficiency and accuracy of model training. . In this study, several pre-processing techniques were applied prior to training the models. First, all images were resized to a uniform dimension of 128×128 pixels. This resizing step ensures compatibility with the input requirements of pre-trained convolutional neural network architectures. The next step is data augmentation process, and it was performed exclusively on the training dataset to increase data diversity and prevent overfitting. The augmentation techniques included horizontal flipping, rotation by ±15 degrees, and brightness adjustments (both increase and decrease). Finally, the dataset was split into three subsets: training, validation, and test sets, based on an 80:10:10 ratio.

Data augmentation

Data augmentation is a widely used technique in deep learning to address the problem of limited training data. When the available data is insufficient, models tend to overfit. They perform very well on the training set but fail to generalize to new samples. To overcome this issue, data augmentation increases the diversity of the dataset by applying small and meaningful transformations to the original images [17]. In this study, several augmentation techniques were applied only to the training set. These include horizontal flipping, rotation by ±15 degrees, and adjusting brightness by increasing or decreasing it. Each transformation form a slightly different version of the same image and this make helping the model to become more robust and perform better on different input conditions.

Table 2. The number of healthy, powdery, and rust apple leaf images across dataset subsets after augmentation

	Type of Apple Leaf Condition			
Data Type	**Healthy**	**Powdery**	**Rust**	**Total**
Training set	3026	3010	3038	9074
Validation set	20	20	20	60
Test Set	50	50	50	150
Grand total	3096	3080	3108	9284

After the application of data augmentation techniques, the total number of apple leaf images increased significantly from 1,622 to 9,284 in Table 2. This augmentation primarily targeted the training set, which grew from 1,322 to 9,074 images, including 3,026 healthy, 3,010 powdery, and 3,038 rust-infected samples. Such a substantial expansion is critical for improving the generalization ability of deep learning models by exposing them to a more diverse set of examples. Importantly, the validation and test sets were kept relatively small and consistent, with 20 and 50 images per class, respectively. This strategy helps preserve the integrity of model evaluation by preventing overfitting on augmented data and ensuring unbiased validation and testing.

Performance metrics

To evaluate the performance of the proposed deep learning models, several commonly used classification metrics were employed: accuracy, precision, recall, and f1-score. The mathematical expression of these metrics is shown below.

$$\text{Accuracy(Acc)} = \frac{TP+TN}{TP+TN+FP+FN} \quad (1)$$

$$\text{Precision(Prec)} = \frac{TP}{TP+FP} \quad (2)$$

$$\text{Recall(Rec)} = \frac{TP}{TP+FN} \quad (3)$$

$$\text{F1-score(F-sc)} = \frac{2TP}{2TP+FP+FN} \quad (4)$$

True Positive (TP) refers to the number of correctly predicted positive samples. True Negative (TN) denotes the

number of correctly predicted negative samples. False Positive (FP) represents the number of negative samples that are incorrectly classified as positive. False Negative (FN) indicates the number of positive samples that are wrongly predicted as negative.

Hyperparameters configuration for deep learning models

To ensure consistent training across all models, the same set of hyperparameters was applied during the experimental process. The selected models include DenseNet201, EfficientNetB0, ResNet101, ResNet50, and VGG16.

Table 3. Hyperparameter Configuration for Deep Learning Models in Plant Disease Classification

	Models				
Hyper Parameters	DenseNet 201	EfficientNet B03	ResNet 101	ResNet 50	VGG 16
ImageSize	128x128	128x128	128x128	128x128	128x128
Epochs	10	10	10	10	10
BatchSize	16	16	16	16	16
Optimizer	Adam	Adam	Adam	Adam	Adam
Learning Rate	0.001	0.001	0.001	0.001	0.001
Loss Function	Categorical	Categorical	Categorical	Categorical	Categorical
Activation Function	ReLU	ReLU	ReLU	ReLU	ReLU

In this study, the same set of hyperparameters was applied to all deep learning models to ensure a fair and consistent evaluation. All input images were resized to 128×128 pixels, which provides a suitable balance between maintaining relevant visual features and reducing computational cost. Each model was trained for 10 epochs, allowing an initial performance assessment while avoiding extended training times. A batch size of 16 was used, enabling efficient memory usage and stable gradient updates during training. The Adam optimizer was selected for its adaptive learning rate properties and proven effectiveness in image classification tasks. A fixed learning rate of 0.001 was used across all models to ensure consistent convergence behavior. The loss function was set as categorical crossentropy, which is appropriate for multi-class classification problems. Additionally, the ReLU (Rectified Linear Unit) activation function was used in all hidden layers to introduce non-linearity and enhance training efficiency by avoiding the vanishing gradient problem. This consistent hyperparameter configuration ensures reliable comparison among models and supports the overall robustness of the experimental setup.

Methodology

DenseNet201

The denseNet201 architecture was utilized as the primary deep learning model for plant disease classification due to its proven effectiveness in image-based recognition tasks. DenseNet201, a convolutional neural network comprising 201 layers, is known for its dense connectivity pattern, where each layer receives inputs from all preceding layers. This structure enhances feature reuse and significantly reduces the number of parameters, making the model both efficient and accurate in learning complex patterns from visual data [18]. The model was pre- trained on ImageNet, allowing the transfer of learned general features to the plant disease dataset. Fine-tuning was applied by modifying the top layers with additional dense layers to adapt the model for the specific classification task. DenseNet201 has been shown to outperform various CNN models in other visual classification domains, achieving high accuracy, recall, and f1-scores and demonstrating robustness across multiple metrics including specificity and precision [19].These findings support the selection of DenseNet201 as a strong baseline for plant disease identification using leaf images.

EfficientNetB3

EfficientNetB3 is a powerful deep learning model within the EfficientNet family, known for its innovative compound scaling technique that proportionally adjusts the network's depth, width, and input resolution to optimize both performance and efficiency. This balanced scaling allows EfficientNetB3 to extract more meaningful and fine-grained features from input images while keeping the model lightweight and computationally efficient. The architecture of EfficientNetB3 includes depthwise separable convolutions, batch normalization layers, and residual connections, enabling it to learn complex patterns effectively while maintaining a relatively small parameter count compared to traditional CNNs [20]. In the field of medical image analysis, EfficientNetB3 has demonstrated strong performance in disease classification tasks. For instance, in leukemia detection, it has outperformed popular CNN models such as ResNet50 and InceptionV3 in terms of classification accuracy, processing time, and model efficiency. Its ability to maintain high diagnostic precision while reducing computational load makes it a preferred choice for clinical applications and real-time diagnostic systems [21].

ResNet101

ResNet101 is a deep convolutional neural network (DCNN) architecture known for its use of residual learning, which addresses the vanishing gradient problem commonly

encountered in very deep networks [22]. By using shortcut connections that allow the network to learn residual functions instead of direct mappings, ResNet101 improves feature learning and facilitates the training of deeper models. Its 101-layer structure allows it to capture low-, mid-, and high-level features more effectively than shallower variants like ResNet50, making it well-suited for complex image analysis tasks such as plant disease severity assessment. In recent studies, ResNet101 has been employed to evaluate the severity of diseases like early blight in tomato leaves, demonstrating superior performance compared to models like AlexNet, GoogLeNet, and VGG architectures due to its deeper feature extraction capabilities and robust residual learning framework [23].

ResNet50

ResNet50 is a member of the ResNet (Residual Network) family, which is specifically designed to enable the training of very deep neural networks without suffering from vanishing gradient problems [24]. It introduces residual connections that allow the network to bypass one or more layers by directly adding the input of a previous layer to the output of a deeper layer. This mechanism ensures more stable gradient flow and preserves important features during training. ResNet50 consists of 50 layers and uses bottleneck architecture with 1×1, 3×3, and 1×1 convolutions, allowing for efficient computation and faster training. The model effectively balances depth and complexity, making it suitable for various image classification tasks. When applied through transfer learning, ResNet50 can generalize well on smaller, domain-specific datasets by leveraging features learned from large-scale datasets [25].

VGG16

VGG16 is a deep convolutional neural network architecture introduced by Simonyan and Zisserman in 2014, as part of their work on the Visual Geometry Group at the University of Oxford. It gained prominence for its simplicity and high performance in image classification tasks, especially in the ImageNet Large Scale Visual Recognition Challenge (ILSVRC). The architecture consists of 16 weight layers: 13 convolutional layers and 3 fully connected layers. All convolutional layers use small 3×3 filters with a stride of 1, and all max-pooling layers use a 2×2 window with a stride of 2, maintaining a uniform structure throughout the network. One of the defining features of VGG16 is its depth and uniform design, which enable it to extract hierarchical features from input images with increasing abstraction. Although VGG16 has many parameters (approximately 138 million), it performs well in a variety of computer vision tasks, especially when fine-tuned through transfer learning. Due to its relatively straightforward architecture and strong feature extraction capabilities, VGG16 remains a widely used baseline model in medical imaging and plant disease classification studies [26].

Experiments and Results

This section presents the experimental setup, and the performance outcomes of the deep learning models used for plant disease classification. The results are analyzed using standard evaluation metrics to assess the accuracy and robustness of each model.

Table 4. Performance evaluation of deep learning models for plant disease classification

Model	Classification	Accuracy	Precision	Recall	F1-score
DenseNet 201	Healthy	0.89	0.76	1.00	0.86
	Powdery	0.87	0.98	0.86	0.91
	Rust	0.87	0.95	0.76	0.84
EfficientNet B03	Healthy	0.95	0.98	0.98	0.93
	Powdery	0.95	0.98	0.94	0.96
	Rust	0.95	0.98	0.92	0.95
ResNet 101	Healthy	0.92	0.79	1.00	0.88
	Powdery	0.91	0.97	0.76	0.85
	Rust	0.91	1.00	0.96	0.98
ResNet 50	Healthy	0.94	0.91	1.00	0.95
	Powdery	0.94	0.92	0.96	0.94
	Rust	0.94	1.00	0.86	0.92
VGG 16	Healthy	0.95	0.93	1.00	0.96
	Powdery	0.95	0.94	0.94	0.94
	Rust	0.95	0.98	0.90	0.94

The classification results of five deep learning models, DenseNet201, EfficientNetB0, ResNet101, ResNet50, and VGG16, were evaluated on three categories of plant leaf conditions: Healthy, powdery, and rust. The evaluation was based on four standard performance metrics: accuracy, precision, recall, and F1-score. Among the five deep learning models evaluated, EfficientNetB0 and VGG16 demonstrated the most consistent and high-level performance across all disease classes. EfficientNetB0 achieved uniformly high accuracy (0.95) for healthy, powdery, and rust leaves, along with strong precision and recall values, resulting in high F1-scores (0.93–0.96), indicating excellent generalization and balanced classification. Similarly, VGG16 yielded very competitive results, with slightly higher F1-scores for the healthy class (0.96) and equally stable performance for powdery and rust (0.94 each), making it another reliable model. ResNet50

also performed well, especially with perfect recall for healthy and perfect precision for rust, producing overall F1-scores above 0.90, which suggests a robust classification ability. ResNet101showed strength in detecting healthy and rust leaves with high recall (1.00 and 0.96), but its performance for the powdery class was relatively lower in recall (0.76), affecting its F1-score. DenseNet201 displayed the lowest overall performance among the models, particularly with reduced precision in the healthy class (0.76) and lower recall in the rust class (0.76), leading to less balanced F1-scores. In conclusion, while all models showed reasonable accuracy, EfficientNetB0 and VGG16 outperformed the others in terms of both reliability and consistency across all plant disease categories, making them the most effective candidates for real-world plant disease classification tasks.

Figure 3 compares the classification performance of four deep learning models—DenseNet201, EfficientNetB0, ResNet101, and VGG16—based on their confusion matrices for detecting plant leaf conditions. The analysis focuses on each model's ability to correctly classify Healthy, Powdery mildew, and Rust categories.

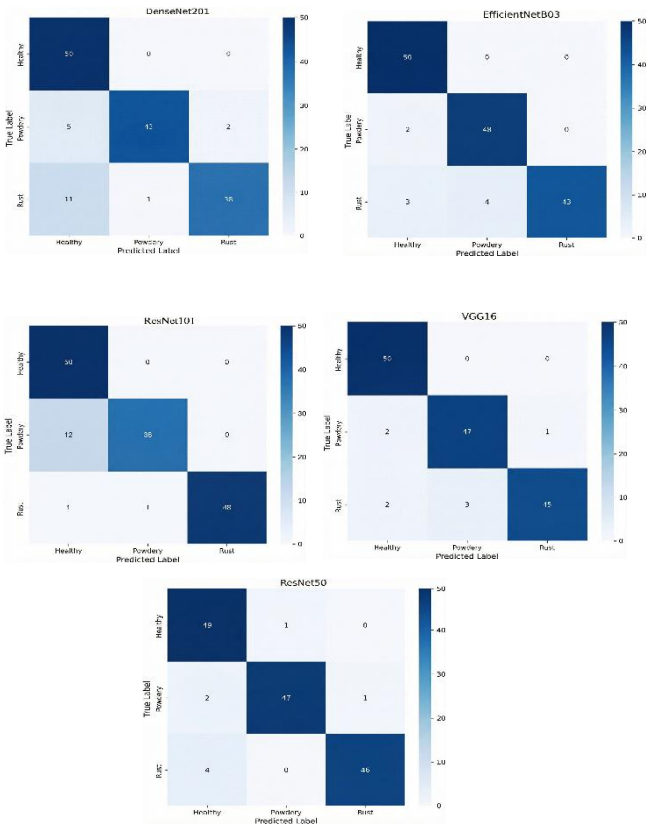

Figure 3. Confusion matrix-based performance analysis of deep learning models in classifying healthy, powdery mildew, and rust leaves

DenseNet201 demonstrates high accuracy in identifying healthy apple leaves. All 50 samples in the test set were correctly classified. In contrast, the model performs less effectively in detecting rust-infected leaves. It misclassified 11 rust samples as healthy and 1 as powdery mildew.

EfficientNetB3 indicates excellent performance in classifying healthy leaves. All healthy samples were correctly identified, demonstrating perfect accuracy for this class. The model also performs strongly in detecting powdery mildew. Out of 50 samples, 48 were correctly classified, with only 2 misclassified. Rust-infected leaves are also well recognized by the model. It correctly predicted 43 out of 50 samples, while 7 were misclassified.

ResNet101 reveals perfect classification of healthy leaf samples. All 50 healthy instances were correctly identified by the model. For rust-infected leaves, the model also performs well. It correctly classified 48 out of 50 samples However, the model shows weaker performance in identifying powdery mildew. It misclassified 12 out of 50 powdery samples as healthy.

The ResNet50 model demonstrates high classification accuracy across all leaf categories. It correctly identified 49 out of 50 healthy samples. For powdery mildew, 47 samples were accurately classified, while 3 were misclassified. In the case of rust-infected leaves, the model correctly predicted 46 out of 50 samples.

The VGG16 model demonstrates excellent classification performance. It achieved perfect accuracy in identifying healthy leaves, with all 50 healthy samples correctly classified. The model also performed well overall, with only 6 misclassifications out of 150 total samples. However, the model showed some difficulty in detecting rust-infected leaves. It misclassified 5 rust samples—2 as healthy and 3 as powdery mildew.

Among the evaluated models, EfficientNetB0 and VGG16 demonstrated the highest overall accuracy. Both models showed minimal misclassifications, especially in identifying healthy leaves. While all models achieved good performance, some models had difficulties distinguishing between disease types. This was particularly evident in the Rust and Powdery mildew categories.

Table 5. The inference time for the deep learning models

Model	inference time	GPU usage
DenseNet201	3.678 s	✓
EfficientNetB03	2.498 s	✓
ResNet101	2.479 s	✓
ResNet50	1.142 s	✓
VGG16	0.489 s	✓

Table 5 demonstrates the inference times of various deep learning models evaluated using GPU acceleration. Among the models, VGG16 achieved the fastest inference with 0.489 seconds, while DenseNet201 showed the slowest performance at 3.678 seconds. The results indicate that model depth and architectural complexity significantly affect computational efficiency, even when GPUs are employed. Therefore, lighter architectures such as VGG16 and ResNet50 are more suitable for real-time or resource-constrained applications compared to deeper models like DenseNet201.

Experimental environment

Training algorithms were implemented on the GPU of an NVIDIA® GeForce RTX 3060 Ti card, using the CUDA® parallel programming platform, in a Windows 10 operating system. The system was equipped with a PowerBoost desktop, an Intel® Core™ i5-10400F CPU @ 2.90 GHz, and 16 GB of RAM. The software environment consisted of Python 3.10.18 and TensorFlow 2.19, executed within the Anaconda/Spyder IDE.

Table 6. A comparative analysis of studies on plant disease classification by using deep learning models

Rerefences	Method	Dataset	Accuracy	Precision	Recall	F1-score
Barbedo (2019) [3]	GoogLeNet + Transfer Learning	XDB (Expanded Dataset: 46,409 cropped symptom images)	94%	–	–	–
Sharma et al. (2025) [27]	CNN-Based Models (ResNet50 + MobileNetV2)	Kaggle tomato leaf disease dataset (11,000 images, 10 classes)	99.91%	99.92%	99.90%	99.91%
Pudumalar & Muthuramalingam (2024) [8]	Hydra (CNN + VGG)	Cotton disease dataset (field-collected, 6 classes)	95.00%	–	–	–
Atila et al. (2021) [13]	EfficientNet-B5	PlantVillage	99.91%	98.42%	–	–
Al-Zubi (2025) [2]	CNN (Sequential)	Kaggle dataset (1532 images: Healthy, Powdery, Rust)	91.34%	0.949 (weighted avg)	0.9479 (weighted avg)	0.9481 (weighted avg)
Our study	CNN-Based Deep Learning Models	Kaggle dataset	95.00%	100.00%	100.00%	95.00%

Table 6 provides a comparative analysis of recent studies that applied various deep learning methods for plant disease classification using different datasets. Performance is evaluated based on metrics such as accuracy, precision, recall, and F1-score.

The highest accuracy was achieved by Atila et al. (2021) and Sharma et al. (2025). Both studies reached 99.91% accuracy. Atila used EfficientNet-B5, while Sharma used CNN-based models such as ResNet50 and MobileNetV2. These results show that deep learning models can perform very well in plant disease classification. Transfer learning methods give excellent results. Sharma et al. also reported very high precision (99.92%) and recall (99.90%). This means their model worked very well across all 10 tomato disease classes. In contrast, Barbedo (2019) achieved 94% accuracy using GoogLeNet and transfer learning on the XDB dataset. However, precision and recall were not given in the study. In our study, we used a CNN- based deep learning models on the Kaggle dataset. Our model reached 95% accuracy, with 100% precision and 100% recall. This means that the model made no mistakes in the test set. Our results are better than Al-Zubi (2025), who used a basic CNN and achieved 91.34% accuracy on the same Kaggle dataset. In conclusion, deep learning models and transfer learning techniques such as ResNet50 and MobileNetV2 are very effective. They are useful tools for automatic plant disease detection, especially when datasets have many classes and varied samples.

Discussion

This study evaluated the performance of five deep learning models in classifying apple leaf diseases using a balanced and augmented Kaggle dataset. Among the models, EfficientNetB0 and VGG16 achieved the most consistent performance across all three disease categories, with high accuracy, precision, and F1-scores. ResNet50 also demonstrated strong classification ability, especially for healthy and powdery mildew samples. However, DenseNet201 showed relatively lower performance, particularly in detecting rust-infected leaves, suggesting its limited generalization on this dataset. The comparison with previous studies revealed that our CNN-based approach

outperformed several existing models on the same dataset, including Al-Zubi (2025), and achieved competitive results compared to state-of-the-art models like ResNet50 and MobileNetV2 applied on larger datasets. The perfect precision and recall values achieved by our model indicate a robust classification capability with no false positives or negatives in the test set.

Conclusion

This study presented a CNN-based deep learning framework for the classification of apple leaf diseases, focusing on healthy, rust, and powdery mildew conditions. The framework utilized transfer learning on five pre-trained CNN architectures and achieved a maximum accuracy of 95%. Compared to individual models and previous works, the proposed method delivered superior precision and recall, demonstrating its strength in handling class imbalance and subtle disease features. Data augmentation and careful preprocessing played a key role in enhancing the generalization performance of the models. The experimental results confirm that CNN-based models are more robust and reliable than single-network approaches in plant disease detection tasks. Furthermore, the balanced and augmented dataset ensured fair evaluation and prevented overfitting. The findings of this study contribute to the development of practical, scalable, and accurate decision-support tools for precision agriculture.

Ethics committee approval and conflict of interest

statement

There is no need to obtain permission from the ethics committee for the article prepared. There is no conflict of interest with any person / institution in the article prepared.

Data availability

Dataset used in this study is publically at Kaggle: https://www.kaggle.com/datasets/rashikrahmanpritom/plant- disease-recognition-dataset

References

[1] K. P. Ferentinos, "Deep learning models for plant disease detection and diagnosis," *Computers and Electronics in Agriculture*, vol. 145, pp. 311–318, Feb. 2018, doi: 10.1016/j.compag.2018.01.009.

[2] A. A. Al-Zubi, "CNN-Based Detection of Powdery Mildew and Rust in Apple Orchards for Optimizing Crop Management," *Journal of Animal and Plant Sciences*, vol. 35, no. 2, pp. 381–389, Apr. 2025, doi: 10.36899/JAPS.2025.2.0032.

[3] J. G. Arnal Barbedo, "Plant disease identification from individual lesions and spots using deep learning," *Biosystems Engineering*, vol. 180, pp. 96–107, Apr. 2019, doi: 10.1016/j.biosystemseng.2019.02.002.

[4] S. Han Lee, H. Goëau, P. Bonnet, and A. Joly, "New perspectives on plant disease characterization based on deep learning," *Computers and Electronics in Agriculture*, vol. 170, p. 105220, 2020, doi: 10.1016/j.compag.2020.105220.

[5] L. Li, S. Zhang, and B. Wang, "Plant Disease Detection and Classification by Deep Learning - A Review," 2021, *Institute of Electrical and Electronics Engineers Inc.* doi: 10.1109/ACCESS.2021.3069646.

[6] S. ÖRENÇ, E. ACAR, and M. S. ÖZERDEM, "Utilizing the Ensemble of Deep Learning Approaches to Identify Monkeypox Disease," *DÜMF Mühendislik Dergisi*, Jan. 2023, doi: 10.24012/dumf.1199679.

[7] G. Wang, Y. Sun, and J. Wang, "Automatic Image-Based Plant Disease Severity Estimation Using Deep Learning," *Computational Intelligence and Neuroscience*, vol. 2017, 2017, doi: 10.1155/2017/2917536.

[8] S. Pudumalar and S. Muthuramalingam, "Hydra: An ensemble deep learning recognition model for plant diseases," *Journal of Engineering Research (Kuwait)*, vol. 12, no. 4, pp. 781–792, Dec. 2024, doi: 10.1016/j.jer.2023.09.033.

[9] S. Örenç, E. Acar, M. S. Özerdem, S. Şahin, and A. Kaya, "Automatic Identification of Adenoid Hypertrophy via Ensemble Deep Learning Models Employing X-ray Adenoid Images," *Journal of Imaging Informatics in Medicine*, 2025, doi: 10.1007/s10278-025-01423-8.

[10] K. Nagasubramanian, S. Jones, A. K. Singh, S. Sarkar, A. Singh, and B. Ganapathysubramanian, "Plant disease identification using explainable 3D deep learning on hyperspectral images," *Plant Methods*, vol. 15, no. 1, Aug. 2019, doi: 10.1186/s13007-019-0479-8.

[11] O. A. D. Ammar *et al.*, "Plant Leaf Disease Detection Using Ensemble Learning and Explainable AI," *IEEE Access*, vol. 12, pp. 156038–156049, 2024, doi: 10.1109/ACCESS.2024.3484574.

[12] F. Shahoveisi, H. Taheri Gorji, S. Shahabi, S. Hosseinirad, S. Markell, and F. Vasefi, "Application of image processing and transfer learning for the detection of rust disease,"

Scientific Reports, vol. 13, no. 1, Dec. 2023, doi: 10.1038/s41598-023-31942-9.

[13] Ü. Atila, M. Uçar, K. Akyol, and E. Uçar, "Plant leaf disease classification using EfficientNet deep learning model," *Ecological Informatics*, vol. 61, Mar. 2021, doi: 10.1016/j.ecoinf.2020.101182.

[14] T. Hayit, H. Erbay, F. Varçın, F. Hayit, and N. Akci, "Determination of the severity level of yellow rust disease in wheat by using convolutional neural networks," *Journal of Plant Pathology*, vol. 103, no. 3, pp. 923–934, Aug. 2021, doi: 10.1007/s42161-021-00886-2.

[15] S. Sachar and A. Kumar, "Deep ensemble learning for automatic medicinal leaf identification," *International Journal of Information Technology (Singapore)*, vol. 14, no. 6, pp. 3089–3097, Oct. 2022, doi: 10.1007/s41870-022-01055-z.

[16] C. K. Sunil, C. D. Jaidhar, and N. Patil, "Systematic study on deep learning-based plant disease detection or classification," *Artificial Intelligence Review*, vol. 56, no. 12, pp. 14955–15052, Dec. 2023, doi: 10.1007/s10462-023-10517-0.

[17] S. Orenc, M. S. Ozerdem, E. Acar, and M. Yilmaz, "Automatic segmentation of chest X-ray images via deep-improved various U-Net techniques," *Digital Health*, vol. 11, May 2025, doi: 10.1177/20552076251366855.

[18] A. Sorayaie Azar, A. Naemi, S. Babaei Rikan, J. Bagherzadeh Mohasefi, H. Pirnejad, and U. K. Wiil, "Monkeypox detection using deep neural networks," *BMC Infectious Diseases*, vol. 23, no. 1, Dec. 2023, doi: 10.1186/s12879-023-08408-4.

[19] S. Matarneh, F. Elghaish, F. Pour Rahimian, E. Abdellatef, and S. Abrishami, "Evaluation and optimisation of pre-trained CNN models for asphalt pavement crack detection and classification," *Automation in Construction*, vol. 160, Apr. 2024, doi: 10.1016/j.autcon.2024.105297.

[20] A. Alshoraihy, "EfficientNetB3 in Leukemia Detection: Advancements in Medical Imaging Analysis," *Medinformatics*, Feb. 2025, doi: 10.47852/bonviewmedin52023293.

[21] P. Utami, R. Hartanto, and I. Soesanti, "The EfficientNet Performance for Facial Expressions Recognition," in *2022 5th International Seminar on Research of Information Technology and Intelligent Systems, ISRITI 2022*, Institute of Electrical and Electronics Engineers Inc., 2022, pp. 756–762. doi: 10.1109/ISRITI56927.2022.10053007.

[22] K. Swetha and A. Seenu, "Deep Learning Approaches for Brain Tumor Detection in MRI Scans: A Comparative Study of DenseNet and ResNet101 Architectures," in *International Conference on Smart Systems for Applications in Electrical Sciences, ICSSES 2024*, Institute of Electrical and Electronics Engineers Inc., 2024. doi: 10.1109/ICSSES62373.2024.10561400.

[23] M. Prabhakar, R. Purushothaman, and D. P. Awasthi, "Deep learning based assessment of disease severity for early blight in tomato crop," *Multimedia Tools and Application*, vol. 79, no. 39–40, pp. 28773–28784, Oct. 2020, doi: 10.1007/s11042-020-09461-w.

[24] M. K. Türkeş and Y. Aydın, "Enhanced Emotion Recognition through Hybrid Deep Learning and SVM Integration," *Bitlis Eren Üniversitesi Fen Bilimleri Dergisi*, vol. 14, no. 1, pp. 348–360, Mar. 2025, doi: 10.17798/bitlisfen.1588046.

[25] L. E. Demir and Y. Canbay, "Deepfake Image Detection with Transfer Learning Models," *Bitlis Eren Üniversitesi Fen Bilimleri Dergisi*, vol. 14, no. 1, pp. 546–560, Mar. 2025, doi: 10.17798/bitlisfen.1610300.

[26] K. Simonyan and A. Zisserman, "Very Deep Convolutional Networks for Large-Scale Image Recognition," Apr. 2015, [Online]. Available: http://arxiv.org/abs/1409.1556

[27] J. Sharma *et al.*, "Deep learning based ensemble model for accurate tomato leaf disease classification by leveraging ResNet50 and MobileNetV2 architectures," *Scientific Reports*, vol. 15, no. 1, Dec. 2025, doi: 10.1038/s41598-025-98015-x.

Dicle University
Journal of Engineering
https://dergipark.org.tr/tr/pub/dumf
duje.dicle.edu.tr

Research Article

FPGA-Based Cosimulation of S-Box Constitution from Fractional Order Liu System

Muhammet Ali ARSERİM[1], Ömer TÜRK[2*]

[1] Dicle University, Electrical-Electronics Engineering Department, marserim@dicle.edu.tr, Orcid No: 0000-0002-9913-5946
[2] Mardin Artuklu University, Computer Engineering Department, omerturk@artuklu.edu.tr, Orcid No: 0000-0002-0060-1880

ARTICLE INFO

Article history:

Received 12 November 2025
Received in revised form 26 November 2025
Accepted 26 November 2025
Available online 30 December 2025

Keywords:

S-box, fractional order systems, Liu chaotic system, FPGA

Doi: 10.24012/dumf.1822418

* Corresponding author

ABSTRACT

Substitution box(S-box) has an important duty in encryption. In recent years plenty of S-box designs by chaotic systems have been studied. In this paper a high speed S-box constitution from fractional order Liu system on FPGA is proposed. The design was implemented by using Xilinx System Generator(XSG) toolbox in MATLAB/Simulink software in single precision floating point numbers format and a low cost Basys 3 FPGA trainer card was used. In addition, numerical fractional order equations was solved by using Grünwald-Letnikov(GL) method with 1024 elements length. The S-box table was constructed about 0.137s. After all performance analyzes as nonlinearity, strict avalanche criterion, differential probability, bits independent criterion, and equiprobable input/output XOR distribution, were performed. The performance analyzes shown that the design was satisfactory.

Introduction

Today, security of digital communication systems becomes very important with the rise of data potential. To achieve this, systems capable of modulation, compression, and encryption should be used [1]. Also one of the systems, which has such potential, is chaotic system.

Chaotic systems depend on initial conditions and have a wide band power spectrum [2]. These systems have random and deterministic properties in themselves [1-2]. Their usage in cryptography has increased, thanks to self-synchronization possibilities of the oscillations that they made [2]. One of these systems is the fractional order chaotic system.

History of fractional order calculus goes back to 1695 based on a famous correspondence between L'Hopital and Leibnitz [3]. Since then, famous scientists as Euler, Lagrange, Laplace, Abel, Liouville, Riemann, Grünwald, Letnikov have worked around fractional calculus [4]. Also scientists as J. Spanier, K. B. Oldham, B. Ross, K. Nishimoto, O. Marichev, A. Kilbas, H. M. Srivastava, R. Bagley, K. S. Miller, M. Caputo, I. Podlubny, and many others contributed to this issue [4].

It can be said that variable order fractional operators can be used to change the system models in time, space or both domains. By the way fractional operators have been applied in various areas such as control, analog filters, chaotic systems, etc. [5]. In addition, such systems can also be implemented on hardware. One of the used device, is FPGA.

Several studies were carried about FPGA implementation of chaotic systems. Ávalos-Ruiz et al [6] studied simulation and control implementation of a class of variable-order fractional chaotic systems by using sliding mode control strategy on a FPGA. FPGA implementation of two multi-scroll chaotic oscillators which produces 2 to 6 scrolls according to maximum Lyapunov exponent was shown [7]. Various fractional chaotic oscillators implementation of FPGA by using Grünwald-Letnikov method was studied [8]. A true random number generator implementation on a FPGA by using a memristive chaotic circuit was carried out [9].

In modern cryptography, one of the chaotic map usage is the Substitution box(S-box) used in confusion principle for encryption. S-box term was first used by Shannon in 1947 [10]. The S-box performs a nonlinear operation in

cryptography. Also several studies were carried out for S-box constitution from chaotic system by using FPGA Parallel Multi-Layer Selector Substitution Boxes based on the Lorenz Chaotic System and its FPGA implementation were carried out [11]. Speech encryption using a chaotic system and an S-box table on FPGA was studied [12-15]. Besides several studies were done on image encryption systems by using chaotic systems based S-box Table implemented on FPGA [16-19].

Some of the recent studies are listed below.

Aydin et al. proposed a new and robust design method for substitution boxes (s-boxes), a critical component of block cipher systems, that meets performance and security requirements. This method enhances the security and efficiency of s-box design by utilizing physical true randomness (phase noise/jitter in ring oscillators) as an entropy source[20]. Garipcan et al. enhanced the randomness obtained from the metastable states of the R-S latch in the proposed method and derived the design inputs from real physical sources at the hardware level via an FPGA. These statistically weak inputs were converted into s-boxes by passing them through four different hash functions (Blake2b, Blake2s, SHA3, and Shake)[21]. Mala et al. focused on the problem of high costs associated with 8×8 S-Boxes, an important component of the AES algorithm, on FPGA platforms. Instead of optimizing the AES S-Box, this study designed a powerful and compact new 8×8 S-Box for FPGA [22]. Hong et al. proposed the efficient implementation of large-scale S-Boxes in hardware using polynomial-based composite field structures. The polynomial-based composite field structure used in the study enabled the optimized implementation of the MK-3 algorithm's 16×16 S-Box on FPGA by increasing the operating frequency while reducing hardware resources [23]. Elrefai et al. presented a hardware-based audio encryption system implemented on an Artix-7 FPGA. The system is based on a dynamic S-Box design and two-dimensional chaotic maps. Three different 2D chaotic maps—logistic–fraction (2D-LF), logistic–sine (2D-LS), and fraction–sine (2D-FS)—were investigated and implemented on the FPGA. The 2D-LF map, which was the most efficient in terms of performance, was used in the encryption system [24].

In this study it is aimed to constitute a FPGA accelerated S-box via fractional order Liu chaotic system. All the system was designed in MATLAB/Simulink software by using Xilinx blockset. Also the main advantage of this model is generating the S-box table about 0.137 s.

The main contributions of this study are as follows:

- The S-box is created by a fractional order Liu chaotic system using the GL method.
- The study was carried out on a low-cost FPGA.
- A real-time applicable system is proposed.
- The proposed S-box structure has sufficiently complex dynamic properties.
- Multiplying the coefficients of the chaotic system by a constant increases the speed of the orbits.

Rest of this article is designed as; fractional order derivatives, numerical solution of fractional order derivatives by using Grünwald-Letnikov method, Fractional order Liu system, and Basys3 FPGA experimental card are introduced in section 2, Simulink model of the S-box constitution from Fractional order Liu system, simulation, cosimulation results and FPGA utilization are given in section 3. Performance analysis tests are given in sections 4 and 5 and the results are discussed in section 6.

2. Materials and Methods

In this section fractional order derivatives, numerical solution of fractional order systems, fractional order Liu system are informed and catalog data of the Basys3 FPGA trainer card is given.

2.1. Fractional Order Derivatives

First of all, it should be mentioned that the most important function is Euler's gamma function,

$$\Gamma(n) = \int_0^\infty t^{n-1}e^{-t}dt \qquad (1)$$

and the general form of the factorial expression is given below [2],

$$\Gamma(n) = (n-1)! \qquad (2)$$

Fractional order derivatives and integrals can be thought as the complimentary of integer derivatives and integrals, and in continuous time it is defined as:

$${}_aD_t^q = \begin{cases} \frac{d^q}{dt^q} & q > 0 \\ 1 & q = 0 \\ \int_a^t (d\tau)^{(-q)} & q < 0 \end{cases} \qquad (3)$$

here q is the fractional order and a, and t are the limits [7]. There are three famous fractional order differintegral definitions as Grünwald-Letnikov(GL), Rieman-Liouvile(RL), and Caputo definitions [2]. In addition, GL derivatives is easy to construct in hardware for numerical calculations. GL fractional order derivative definition can be given as:

$$D_t^q f(t) = \lim_{h\to 0} \frac{1}{h^q} \sum_{j=0}^{\infty} (-1)^j \binom{q}{j} f(t-jh) \qquad (4)$$

and binomial coefficients can be determined by using Euler's gamma function as,

$$\binom{q}{j} = \frac{q!}{j!(q-j)!} = \frac{\Gamma(q+1)}{\Gamma(q+1)\Gamma(q-j+1)} \qquad (5)$$

2.2. Numerical Solution of Fractional Derivatives

Practical implementations need a hardware as DSP, FPGA, microcontroller etc. for processing algorithms. Therefore, numerical solutions of algorithms can be used to execute them in real time applications.

Fractional order derivatives can be solved numerically by using the equation, given below,

$$\left(k-\frac{L_m}{h}\right)D_{t_k}^{q}f(t) \approx h^{-q}\sum_{j=0}^{k}(-1)^j \binom{q}{j} f(t_{k-j}) \quad (6)$$

and $L_m, t_k = kh,$ and $(-1)^j \binom{q}{j}$ denotes memory length, sampling times, sampling period, and binomial coefficients respectively[4, 19]. If binomial coefficients are defined as

$$c_0^{(q)} = 1$$
$$c_j^{(q)} = \left(1-\frac{1+q}{1}\right)c_{j-1}^{(q)} \quad (7)$$

and then, general numerical solution of a fractional order differential equation can be written as;

$$(t_k) = y\big((t_k), t_k\big)h^q - \sum_{j=v}^{k} c_j^{(q)} y\big(t_{k-j}\big) \quad (8)$$

here short time memory can be used for the memory term and for the lower index, v, is chosen as 1 for k< L_m/h and as $k-(L_m/h)$ for k> L_m/h.

2.3. Fractional Order Liu System

Liu et al. [25] offered a new chaotic system similar to Lorentz chaotic map. Differential equations of the chaotic system are given as;

$$\frac{dx(t)}{dt} = -ax(t) - ey^2(t)$$
$$\frac{dy(t)}{dt} = by(t) - kx(t)z(t) \quad (9)$$
$$\frac{dz(t)}{dt} = -cx(t) + mx(t)y(t)$$

and a=1, e=1, b=2.5, k=4, c=5 and m=4 are chosen with (0.2, 0, 0.5) initial conditions.

Also the numerical form can be expressed as;

$$x(t_k) = \big(-ax(t_{k-1}) - ey^2(t_{k-1})\big)h^{q_1} - \sum_{j=v}^{k} c_j^{q_1} x\big(t_{k-j}\big)$$

$$y(t_k) = \big(by(t_{k-1}) - kx(t_k)z(t_{k-1})\big)h^{q_2} - \sum_{j=v}^{k} c_j^{q_2} y\big(t_{k-j}\big) \quad (10)$$

$$z(t_k) = \big(-cz(t_{k-1}) + mx(t_k)y(t_k)\big)h^{q_3} - \sum_{j=v}^{k} c_j^{q_3} z\big(t_{k-j}\big)$$

2.4. Basys3 FPGA trainer card

The Basys3 trainer card, shown in Figure 1., is a low cost digital circuit development platform produced by Digilent firm, based on the latest Artix-7™ FPGA (AMD-Xilinx part number XC7A35T-1CPG236C). It has switches, LEDs and other I/O devices to design quite number of digital circuit designs. In addition, Artix-7 35T FPGA includes 33280 logic cells, 1800 Kbits of fast block RAM, 90 DSP slices, and on chip analog to digital converters(XADC) [21].

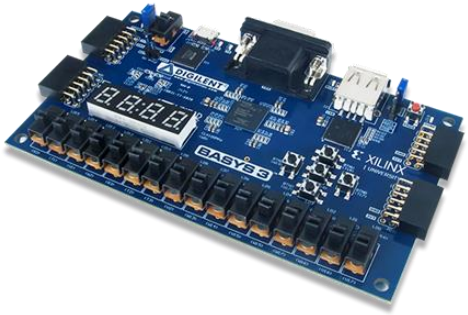

Figure 1. Basys3 trainer card

3. S-box implementation from fractional order Liu system

Xilinx System Generator(XSG) is a very useful tool for programming Xilinx FPGAs by using Matlab/Simulink software. In this study Matlab r2017b and Vivado 2017.4.1 programs were used. Therefore, mathematical operations can be easily programmed by using XSG.

The entire model to constitute S-box from fractional order Liu System using GL method is shown in Figure 2. All the blocks used in the model were belongs to Xilinx blockset and sampling period was 10^{-4} s. Number of the elements used in the GL method was 1024. Also increasing nonlinearity x, y elements of the Liu system was multiplied and this was divided by z element. Thus the result was multiplied by 10^9, converted to 35 bits unsigned integer and eight bit numbers were extracted from the multiplication as the range of 15th and 22nd bit. Therefore, new generated numbers were compared with the numbers stored in a RAM until 256 numbers were completed. After all, cosimulation block of the entire system was created to validate executing the model in Basys3 FPGA. Also the results were saved to MATLAB workspace.

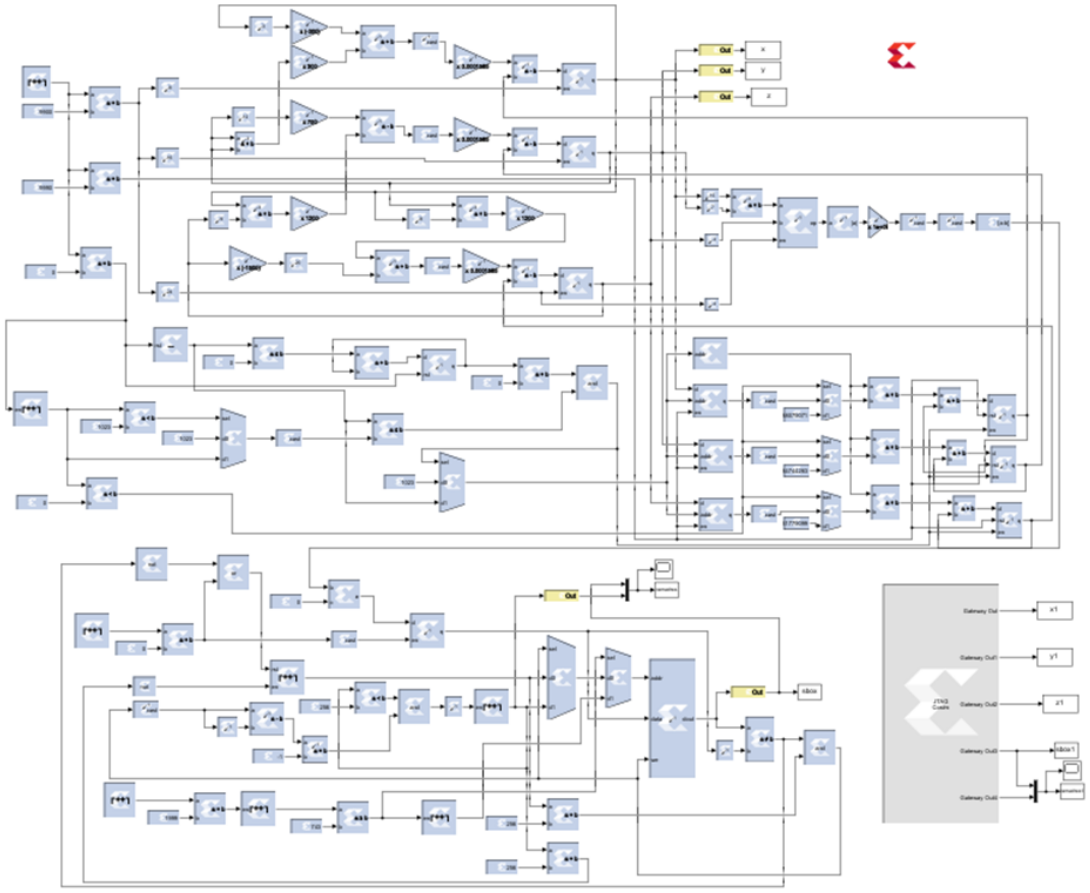

Figure 2. Simulink model of S-box produced by fractional order Liu system

In the model original coefficients of the Liu system was multiplied by constant value of 300 for speeding the orbits to satisfy a faster execution of the system. Also coefficients were chosen as a=300, e=-300, b=750, e=1500, k=1200, m=1200 with (0.32, 0.22, 0.12) initial conditions. The simulation, and cosimulation results of the Liu system is shown in Figure 3. It can be seen that the results are compatible with the Liu system.

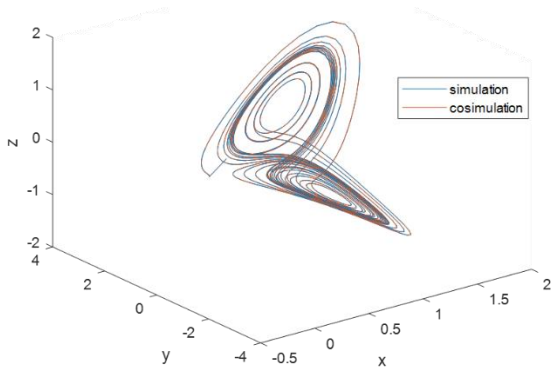

Figure 3. Simulation and cosimulation of fractional order Liu system

Numbers generated and the RAM addresses increase due to storing them in to versus time is shown in Figure 4. This figure shows that S-box table is filled about 0.137s. This means that 0 to 255 numbers are generated from nearly 1370 samples.

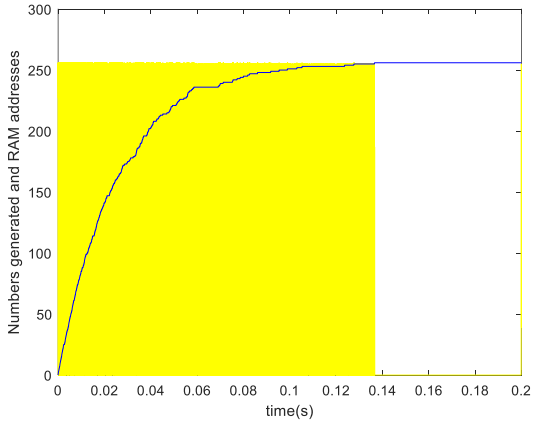

Figure 4. Input values to S-box part and RAM addresses increase

Also simulation was executed 0.2 s and RAM contents were written to MATLAB workspace and plotted as Figure 5.

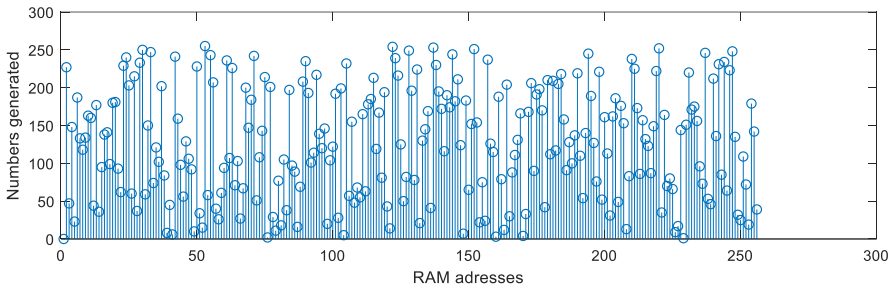

Figure 5. S-box contents

Implemented design schematic of the model is shown in Figure 6. The model was successfully placed in Basys3 trainer card, although it was a heavily design due to G-L method.

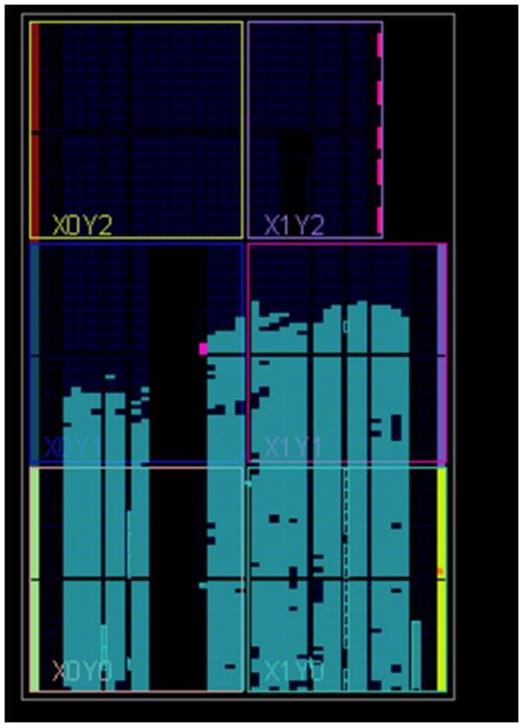

Figure 6. İmplemented design on Basys3

FPGA hardware utilization is shown in Figure 7. It can be seen that nearly half of the LUT resources were used the rest of the resources as LUTRAM, FF, BRAM, DSP, and MMCM usage was much more less. In addition, power consumption is very low.

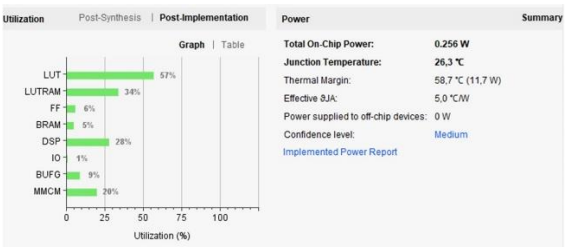

Figure 7. Utilization of FPGA resources

In the next section performance analysis of the S-box table will be discussed.

4. Performance Analyzes of Chaotic S-Box

NIST SP 800-22 test [27] was performed to verify the randomness of the chaotic random sequence before performance analyses of created S-box. Results of the test is shown in Table 1 and it can be seen from the Table 1 that all the tests were passed.

Table 1. NIST randomness analyzes results

NIST test	Result	P-value
Frequency	passed	0.2839
Block Frequency test	passed	0.87154
Run test	passed	0.41564
Longest Run of Ones in a Block	passed	0.41541
Rank Test	passed	0.07987
FFT test	passed	0.67532
Serial Test	passed	0.87442
Approximate entropy test	passed	0.03992
Cumulative Sums (Reverse) Test	passed	0.34745
Cumulative Sums (Forward) Test	passed	0.52150
Non overlapping template matching test	passed	0.38674
Overlapping template matching test	passed	0.26585
Random excursion variant test	passed	0.89431
Random Excursions Test	passed	0.74101
Linear complexity test	passed	0.64271

In addition, values of S-box, generated by the proposed method is shown in Table 2. The S-box contents were written to Matlab workspace and uniqueness of them were checked.

Table 2. S-Box generated by the proposed method

	0	1	2	3	4	5	6	7	8	9	A	B	C	D	E	F
0	0	9	150	156	127	211	86	239	161	5	186	176	209	3	38	26
1	184	207	35	97	136	131	19	203	166	190	149	100	163	76	124	130
2	61	107	94	214	108	40	118	87	48	123	170	200	59	180	248	220
3	64	33	114	233	115	249	99	151	120	202	254	252	103	74	105	234
4	222	195	230	121	164	135	206	72	172	247	32	227	102	245	235	45
5	213	57	129	173	189	182	153	104	187	110	95	226	158	15	91	30
6	133	174	196	6	193	17	243	34	155	113	83	55	89	98	157	198
7	201	144	122	175	217	246	20	54	79	71	1	82	11	208	117	77
8	177	212	132	16	31	128	146	36	88	41	165	92	199	244	241	205
9	63	68	14	183	242	221	225	75	171	229	52	141	2	194	160	80
A	49	125	56	192	179	84	162	65	185	7	223	25	219	109	215	145
B	169	106	28	12	251	231	148	216	147	197	44	228	240	119	69	39
C	237	140	78	137	29	134	10	81	139	111	23	126	154	181	47	168
D	67	250	210	116	96	27	188	21	224	142	70	24	204	66	43	253
E	60	18	62	37	238	51	53	143	58	85	50	112	218	236	232	8
F	178	255	101	152	138	4	46	93	191	167	159	22	13	42	73	90

In the literature, several criteria have been proposed to evaluate the encryption properties of S-boxes. These are Nonlinearity, Bit Independence Criterion (BIC), Strict Avalanche Criterion(SAC) and Input/Output XOR Distribution Table criteria. In this study The criteria tests were performed by using the toolbox, suggested in in the study [28].

4.1. Nonlinearity

According to proposed $f(x): F_2^n \to F_2$ Boole function, nonlinear N_f value of f (x) [29] is determined as in equation (11)

$$N_f = \sum_{l \in L_n} mind_H(f, l) \qquad (11)$$

here L_n denotes affine function set and $d_H(f, l)$ is the Hamming distance between f and l.

In practice, Walsh spectrum, defined as nonlinearity condition, is evaluated by using equation

$$S_f(w) = \sum_{x \in GF(2^n)} (-1)^{f(x) \oplus x \cdot \omega} \qquad (12)$$

and it is dot product of x and ω ($\omega \in GF(2^n)$, $x \cdot \omega \in$ GF (2n)).

For this reason, nonlinearity is calculated according to equation (13)[30],

$$N_f = 2^{n-1}(1 - 2^{-n} \max_{\omega \in GF(2^n)} |S_f(\omega)|) \qquad (13)$$

Nonlinearity values of proposed S-box are shown in Table 3

Table 3. Nonlinearity Values

104	106	108	104	102	108	102	106

4.2. Strict Avalanche Criterion (SAC)

The strict avalanche criterion (SAC) was first introduced by Webster and Tavares [30, 31]. This criterion means that each of the output bits should change with half probability when a single input bit x is changed. Generally, the

dependency matrix is used to test the SAC values of an S-box. If the mean value of each element and matrix is both close to the ideal value of 0.5, the S-box almost fulfills the SAC. The SAC values obtained in the study are shown in Table 4.

Table 4. Strict Avalanche Values (SAC)

0,5156	0,4844	0,4219	0,5156	0,5	0,4375	0,5469	0,5469
0,5625	0,4688	0,4531	0,5	0,5	0,4688	0,5156	0,5
0,4531	0,5938	0,4375	0,5469	0,5625	0,4844	0,5469	0,5469
0,5312	0,4531	0,4844	0,5	0,4375	0,5156	0,5156	0,5156
0,4688	0,5781	0,4688	0,5312	0,625	0,5781	0,5156	0,5156
0,4844	0,4844	0,4375	0,5312	0,5	0,5625	0,4531	0,4688
0,5	0,3594	0,5156	0,5156	0,5156	0,5156	0,5	0,5469
0,5	0,5156	0,4844	0,4531	0,5	0,4531	0,5469	0,5156

The average SAC value of the S-Box proposed in the study was found to be 0.5032. This result is very close to the ideal value that is 0.5.

4.3. Bit Independence Criterion (BIC)

Output bit independence is an another criterion for performance analysis. If Boolean functions in the S-box are supposed as f_1 and f_2 then $f_j \oplus f_k$ ($j = k, 1\ j, k_n$) must be highly non-linear and meet the avalanche criteria. Therefore, BIC can be validated by determining SAC and nonlinearity of $f_j \oplus f_k$ [31] Also, calculated nonlinearity values of BIC for the proposed S-box in the study are given in Table 5.

.

Table 5. BIC Nonlinearity Values

0	104	106	104	104	102	108	104
104	0	104	102	102	104	110	106
106	104	0	104	100	96	104	104
104	102	104	0	106	102	100	98
104	102	100	106	0	98	96	106
102	104	96	102	98	0	104	104
108	110	104	100	96	104	0	102
104	106	104	98	106	104	102	0

The smallest and the highest Nonlinearity Values of the proposed S-Box were obtained as 96 and 110, respectively. Besides the Nonlinearity Values of the S-Box were calculated as 103. The BIC-SAC Values obtained from the proposed S-Box structure are given in Table 6.

Table 6. BIC-SAC Values

0	0,5	0,5059	0,4941	0,5117	0,5	0,4961	0,5098
0,5	0	0,5195	0,5059	0,502	0,4746	0,4883	0,4902
0,5059	0,5195	0	0,4941	0,5078	0,5215	0,5098	0,5312
0,4941	0,5059	0,4941	0	0,4629	0,5215	0,5059	0,5254
0,5117	0,502	0,5078	0,4629	0	0,5078	0,4844	0,5137
0,5	0,4746	0,5215	0,5215	0,5078	0	0,459	0,5234
0,4961	0,4883	0,5098	0,5059	0,4844	0,459	0	0,5098
0,5098	0,4902	0,5312	0,5254	0,5137	0,5234	0,5098	0

4.4. Equiprobable input/output XOR distribution

Biham and Shamir proposed a differential cryptanalysis method, based on the imbalance in the XOR distribution table, for the S-Box [32]. In their proposed method, the XOR of each output should have equal probability with the XOR of each input, and the output variations should be obtainable from the input variations. The differential approximation probability for a given f map can be calculated by measuring the differential resistance according to equation (14),

$$DP_f = \max_{\Delta x \neq 0, \Delta y} \left(\frac{\#\{x \epsilon X | f(x) \oplus f(x \oplus \Delta x) = \Delta y\}}{2^m} \right) \quad (14)$$

where X, and 2^m represents set of all probable input values and number of elements in the set respectively. The Input/Output XOR Distribution Values for the recommended s-box is shown in Table 7.

Table 7. Input/Output XOR Distribution Table

8	8	8	6	0	1	8	8	8	8	8	8	8	8	8	8
8	6	6	6	6	6	6	6	8	6	6	6	6	6	8	6
6	6	6	6	6	6	8	6	8	6	6	6	6	6	8	6
8	4	6	6	6	6	6	6	6	8	6	6	0	6	8	6
8	6	6	8	6	6	6	6	6	6	6	6	0	1	6	6
0	1	6	6	6	8	6	6	6	6	6	6	6	6	8	6
8	6	6	8	8	6	6	6	6	6	6	6	6	6	8	6
6	8	6	6	6	0	8	6	6	6	6	6	6	6	8	8
8	8	6	6	6	6	6	2	1	6	6	6	6	6	6	6
6	6	8	8	6	0	6	6	6	6	6	6	6	6	6	8
0	1	6	8	6	8	8	0	8	2	6	6	6	1	6	6
6	8	0	1	8	8	8	6	6	6	6	6	6	6	6	6
6	6	6	6	6	6	6	6	6	6	6	6	6	8	6	6
8	6	6	6	6	6	8	6	6	6	6	6	6	8	6	6
8	8	8	6	8	6	6	6	0	0	6	6	1	6	8	8
6	6	6	6	6	6	6	6	6	6	6	6	6	6	6	6

5. Performance Comparison

Performance analysis of S-box created by using fractional order Liu system was mentioned above. In literature there are plenty of S-box constitution studies by using different chaotic systems. In this part a comparison of performance analysis of S-box created in this study with the performance analysis of the others in the literature is given in Table 8.

Table 8. Performance comparison of the proposed method with those in literature

S-Box Method	Nonlinearity						Maximum I/O XOR
	SAC	Min.	Max.	Avg	BIC–SAC	BIC-NL	
[33]	0.5058	98	108	104.2	0.5031	104.2	12
[34]	0.5068	108	108	108	0.4950	90	10
[35]	0.49	100	108	104.7	0.5009	103.	12

	78			5		6	
[36]	0.4954	98	108	104	0.4967	102	12
[37]	0.5039	96	106	103	0.5010	100.3	12
[38]	0.5048	100	104	103.2	--	--	10
[39]	0.4915	96	104	102	0.4965	103.5	12
[40]	0.4953	110	112	110.25	0.5021	104.07	10
[41]	0.4988	100	108	104	0.4986	103.57	
[42]	0.5050	96	108	102.25	---	103.5	
[43]	0.5071	96	106	102.5	0.5009	104.29	
Proposed	**0.5032**	**102**	**108**	**105**	**0.5027**	**103**	**12**

It can be seen that, nonlinearity values of the study are higher than the values obtained in [32-34, 37-38], references from the table. Also SAC value was found nearly ideal value as the others.

6. Conclusions

In this study a high speed FPGA model of S-box creation from Fractional order Liu chaotic system was designed. For this aim, coefficients of the Liu system were multiplied by a constant to speed up the orbits. At the same time multiplying x, y componenst and division by z increased nonlinearity. So this yields the S-box constitution about 0.137 s. This design may be used in real time practical systems.

The design used 11837 LUTs, 3225 LUTRAMs, 2328 FFs, 2.5 BRAMs, 25 DSPs, and 1 MMCM. In addition, GL method with 1024 elements was used. Although it was a heavily design, it was successfully placed in Basys3 FPGA trainer card. Therefore, the speed of S-box constitution may be increased by ten times by setting the Simulink system clock 10^{-8}s to 10^{-9}s and with little changes in the design.

Cosimulation results of the model coincided with simulation results. This shows the reliability of real time working on FPGA.

The performance analyzes of the S-box values were found to be satisfactory when compared with those in the literature. Also rearranging the input variable of the S-box may increase the performance of the design.

The design in the study was hard, and time consuming. Therefore, in further studies it will be planned to apply this design to encryption systems in one dimensional signal, and image processing.

Acknowledgement

The authors are thankful to AMD-Xilinx firm for Vivado software license and Basys3 FPGA trainer card donations via university donation program.

References

[1] Kocarev, L. chaos-based cryptography: a brief overview. *IEEE Circuits and Systems Magazine* 2001;*1*(3), 6-21.

[2] Kiani-B A, Fallahi K, Pariz N, Leung H. A chaotic secure communication scheme using fractional chaotic systems based on an extended fractional Kalman filter. Communications in Nonlinear Science and Numerical Simulation 2009;14:863–79. https://doi.org/https://doi.org/10.1016/j.cnsns.2007.11.011.

[3] Zhang X. Relationship between integer order systems and fractional order system and its two applications. IEEE/CAA Journal of Automatica Sinica 2018;5:639–43. https://doi.org/10.1109/JAS.2016.7510205.

[4] Petráš I. Fractional-order nonlinear systems: modeling, analysis and simulation. Springer Science & Business Media; 2011.

[5] Tolba MF, AbdelAty AM, Soliman NS, Said LA, Madian AH, Azar AT, et al. FPGA implementation of two fractional order chaotic systems. AEU - International Journal of Electronics and Communications 2017;78:162–72. https://doi.org/https://doi.org/10.1016/j.aeue.2017.04.028.

[6] Ávalos-Ruiz LF, Zúñiga-Aguilar CJ, Gómez-Aguilar JF, Escobar-Jiménez RF, Romero-Ugalde HM. FPGA implementation and control of chaotic systems involving the variable-order fractional operator with Mittag–Leffler law. Chaos, Solitons & Fractals 2018;115:177–89. https://doi.org/https://doi.org/10.1016/j.chaos.2018.08.021.

[7] Tlelo-Cuautle E, Rangel-Magdaleno JJ, Pano-Azucena AD, Obeso-Rodelo PJ, Nunez-Perez JC. FPGA realization of multi-scroll chaotic oscillators. Communications in Nonlinear Science and Numerical Simulation 2015;27:66–80. https://doi.org/https://doi.org/10.1016/j.cnsns.2015.03.003.

[8] Pano-Azucena AD, Ovilla-Martinez B, Tlelo-Cuautle E, Manuel Muñoz-Pacheco J, de la Fraga LG. FPGA-based implementation of different families of fractional-order chaotic oscillators applying Grünwald–Letnikov method. Communications in Nonlinear Science and Numerical Simulation 2019;72:516–27. https://doi.org/https://doi.org/10.1016/j.cnsns.2019.01.014.

[9] Karakaya B, Gülten A, Frasca M. A true random bit generator based on a memristive chaotic circuit: Analysis, design and FPGA implementation. Chaos, Solitons & Fractals 2019;119:143–9. https://doi.org/https://doi.org/10.1016/j.chaos.2018.12.021.

[10] Shannon CE. Communication Theory of Secrecy Systems. Bell System Technical Journal 1949; 28(4):656–715. DOI: 10.1002/j.1538-7305.1949.tb00928.x.

[11] Saber M, Hagras EAA. Parallel multi-layer selector S-Box based on lorenz chaotic system with FPGA implementation. Indonesian Journal of Electrical Engineering and Computer Science 2020;19:784–92. https://doi.org/10.11591/ijeecs.v19.i2.pp784-792.

[12] Elsafty AH, Tolba MF, Said LA, Madian AH, Radwan AG. FPGA Speech Encryption Realization Based on Variable S-Box and Memristor Chaotic Circuit. 2018 30th International Conference on Microelectronics (ICM), 2018, p. 152–5. https://doi.org/10.1109/ICM.2018.8704019.

[13] Yassin HM, Mohamed AT, Abdel-Gawad AH, Tolba MF, Saleh HI, Madian AH, et al. Speech Encryption on FPGA Using a Chaotic Generator and S-Box Table. 2019 Fourth International Conference on Advances in Computational Tools for Engineering Applications (ACTEA), 2019, p. 1–4. https://doi.org/10.1109/ACTEA.2019.8851086.

[14] ElSafty AH, Tolba MF, Said LA, Madian AH, Radwan AG. Hardware realization of a secure and enhanced s-box based speech encryption engine. Analog Integrated Circuits and Signal Processing 2021;106:385–97. https://doi.org/10.1007/s10470-020-01614-z.

[15] Abd El-Maksoud AJ, Abd El-Kader AA, Hassan BG, Rihan NG, Tolba MF, Said LA, et al. FPGA implementation of sound encryption system based on fractional-order chaotic systems. Microelectronics Journal 2019;90:323–35. https://doi.org/https://doi.org/10.1016/j.mejo.2019.05.005.

[16] Maazouz M, Toubal A, Bengherbia B, Houhou O, Batel N. FPGA implementation of a chaos-based image encryption algorithm. Journal of King Saud University - Computer and Information Sciences 2022. https://doi.org/https://doi.org/10.1016/j.jksuci.2021.12.022.

[17] Hafsa A, Gafsi M, Malek J, MacHhout M. FPGA implementation of improved security approach for medical image encryption and decryption. Scientific Programming 2021;2021. https://doi.org/10.1155/2021/6610655.

[18] Yang CH, Chien YS. FPGA implementation and design of a hybrid chaos-aes color image encryption algorithm. Symmetry 2020;12. https://doi.org/10.3390/sym12020189.

[19] Podlubny I. Fractional differential equations: an introduction to fractional derivatives, fractional differential equations, to methods of their solution and some of their applications. Elsevier; 1998.

[20] Aydin, Y., Garipcan, A. M., & Özkaynak, F. (2025). A novel secure S-box design methodology based on FPGA and SHA-256 hash algorithm for block cipher algorithms. Arabian Journal for Science and Engineering, 50(2), 1247-1260.

[21] Garipcan, A. M., Aydın, Y., & Özkaynak, F. (2025). A novel s-box generation method based on metastable inducing over FPGA for block ciphers. Knowledge-Based Systems, 310, 112968.

[22] Malal, A., & Tezcan, C. (2024). FPGA-friendly compact and efficient AES-like 8× 8 S-box. Microprocessors and Microsystems, 105, 105007.

[23] Hong, R., Zhang, L., Pan, Z., Xiao, C., & Wang, J. (2025). Research and implementation of large-scale S-box for MK-3 algorithm based on polynomial basis: in FPGA. Journal of Cryptographic Engineering, 15(1), 1-13.

[24] Elrefai, H. M., Sayed, W. S., & Said, L. A. (2024). Hardware implementation of a 2D chaotic

map-based audio encryption system using s-box. Electronics, 13(21), 4254.

[25] Liu C, Liu L, Liu T. A novel three-dimensional autonomous chaos system. Chaos, Solitons & Fractals 2009;39:1950–8. https://doi.org/https://doi.org/10.1016/j.chaos.2007.06.079.

[26] https://digilent.com/reference/programmable-logic/basys-3/reference-manual

[27] Rukhin A, Soto J, Nechvatal J, Smid M, Barker E, Leigh S, et al. NIST Special Publication 800-22 (with revisions dated 2001;22.

[28] Özkaynak F. An Analysis and Generation Toolbox for Chaotic Substitution Boxes: A Case Study Based on Chaotic Labyrinth Rene Thomas System. Iranian Journal of Science and Technology - Transactions of Electrical Engineering 2020;44:89–98. https://doi.org/10.1007/s40998-019-00230-6.

[29] Fumy W. On the F-function of FEAL. *Lecture Notes in Computer Science (including subseries Lecture Notes in Artificial Intelligence and Lecture Notes in Bioinformatics)* 1988; 293 LNCS(2):434–437. DOI: 10.1007/3-540-48184-2_38.

[30] Adams C, Tavares S. The structured design of cryptographically good s-boxes. *Journal of Cryptology* 1990; **3**(1):27–41. DOI: 10.1007/BF00203967.

[31] Webster, A.F.; Tavares, S.E. On the design of s-boxes. In Conference on the Theory and Application of Cryptographic Techniques; Williams, H.C., Ed.; Springer: Berlin/Heidelberg, Germany, 1986; pp. 523–534.

[32] Biham E, Shamir A. Differential cryptanalysis of feal and N-hash. Lecture Notes in Computer Science (Including Subseries Lecture Notes in Artificial Intelligence and Lecture Notes in Bioinformatics) 1991;547 LNCS:1–16. https://doi.org/10.1007/3-540-46416-6_1.

[33] Wang X, Teng L, Qin X. A novel colour image encryption algorithm based on chaos. Signal Processing 2012;92:1101–8. https://doi.org/https://doi.org/10.1016/j.sigpro.2011.10.023.

[34] Zhang YQ, Wang XY. Analysis and improvement of a chaos-based symmetric image encryption scheme using a bit-level permutation. Nonlinear Dynamics 2014;77:687–98. https://doi.org/10.1007/s11071-014-1331-3.

[35] Özkaynak F. A novel method to improve the performance of chaos based evolutionary algorithms. Optik 2015;126:5434–8. https://doi.org/https://doi.org/10.1016/j.ijleo.2015.09.098.

[36] Farah T, Rhouma R, Belghith S. A novel method for designing S-box based on chaotic map and Teaching–Learning-Based Optimization. Nonlinear Dynamics 2017;88:1059–74. https://doi.org/10.1007/s11071-016-3295-y.

[37] Khan M, Shah T. A construction of novel chaos base nonlinear component of block cipher. Nonlinear Dynamics 2014;76:377–82. https://doi.org/10.1007/s11071-013-1132-0.

[38] Özkaynak F, Özer AB. A method for designing strong S-Boxes based on chaotic Lorenz system. Physics Letters A 2010;374:3733–8. https://doi.org/https://doi.org/10.1016/j.physleta.2010.07.019.

[39] Özkaynak F. On the effect of chaotic system in performance characteristics of chaos based s-box designs. Physica A: Statistical Mechanics and Its Applications 2020;550:124072. https://doi.org/https://doi.org/10.1016/j.physa.2019.124072.

[40] Wang Y, Zhang Z, Zhang LY, Feng J, Gao J, Lei P. A genetic algorithm for constructing bijective substitution boxes with high nonlinearity. Information Sciences 2020;523:152–66. https://doi.org/https://doi.org/10.1016/j.ins.2020.03.025.

[41] Liu L. Designing a random S-box with the mixed spatiotemporal chaos. Journal of Physics: Conference Series 2021; 1983:0–7. https://doi.org/10.1088/1742-6596/1983/1/012040.

[42] Cassal-Quiroga BB, Campos-Cantón E. Generation of Dynamical S-Boxes for Block Ciphers via Extended Logistic Map. Mathematical Problems in Engineering 2020;2020. https://doi.org/10.1155/2020/2702653.

[43] Türk Ö. FPGA simulation of chaotic tent map-based S-Box design. International Journal of Circuit Theory and Applications n.d.;n/a. https://doi.org/https://doi.org/10.1002/cta.3242.

Dicle University
Journal of Engineering
https://dergipark.org.tr/tr/pub/dumf
duje.dicle.edu.tr

Derleme Makalesi/Review Article

İnceleme: Döküm Alüminyum Alaşımlarında Kalıntı Gerilme Ölçüm Yöntemleri, Nedenleri ve Önleme Çalışmaları

Review: Residual Stress Measurement Methods, Reasons and Prevention Studies in Aluminium Cast Alloys

Onur Özaydın[1*], Aytaç Gören[1], Esra Dokumacı Alkan[2], Gökçe Mehmet Gencer[1]

[1] Dokuz Eylül Üniversitesi, Makine Mühendisliği Bölümü, onur.ozaydin@ogr.deu.edu.tr ORCID: https://orcid.org/0000-0001-6395-7553, aytac.goren@deu.edu.tr ORCID: https://orcid.org/0000-0002-7954-1816 , mehmet.gencer@deu.edu.tr ORCID: https://orcid.org/0000-0003-1084-7240

[2] Dokuz Eylül Üniversitesi, Metalürji ve Malzeme Mühendisliği Bölümü, esra.dokumaci@deu.edu.tr ORCID: https://orcid.org/0000-0003-3886-3963

MAKALE BİLGİLERİ

Makale Geçmişi:

Geliş 13 Mayıs 2025
Revizyon 25 Kasım 2025
Kabul 10 Aralık 2025
Online 30 Aralık 2025

Anahtar Kelimeler:

Döküm Alüminyum Alaşımları, Kalıntı Gerilme, Tahribatlı ve Tahribatsız Ölçüm Yöntemleri.

ÖZ

Bu çalışma, döküm alüminyum alaşımlarında üretim sürecinde ortaya çıkan kalıntı gerilmelerin nedenlerini, ölçüm yöntemlerini ve önleme stratejilerini incelemektedir. Kalıntı gerilmeler; ısıl işlem, talaşlı imalat, kaynak gibi işlemlerden sonra, dış yük olmadan malzeme içinde oluşan elastik gerilmelerdir. Bu gerilmeler, parçanın yorulma ömrünü, mekanik performansını ve boyutsal doğruluğunu doğrudan etkiler. Özellikle T6 gibi ısıl işlem süreçlerinde, su verme sırasında meydana gelen ani sıcaklık değişimleri ciddi kalıntı gerilmeler yaratabilir. Çalışmada delik delme, halka çekirdek ve kontur gibi tahribatlı; X-ışını kırınımı, ultrasonik ve nötron kırınımı gibi tahribatsız yöntemler detaylı şekilde incelenmiş, bunların avantaj ve dezavantajları karşılaştırılmıştır. Ayrıca, sonlu elemanlar analizleriyle yapılan analitik ölçüm yöntemlerine de yer verilmiştir. Yorulma ömrü açısından, çeki kalıntı gerilmeleri zararlı olurken, bası gerilmeleri ömrü artırabilir. Bu nedenle kalıntı gerilmelerin ölçümü kadar kontrolü de önemlidir. Gerilme giderme tavlaması, düşük sıcaklıkta yaşlandırma ve yüzey işlemleri gibi yöntemlerle bu gerilmeler azaltılabilir. Sonuç olarak, kalıntı gerilmelerin dikkatli yönetimi, daha dayanıklı ve güvenilir mühendislik parçaları üretimini mümkün kılar.

ARTICLE INFO

Article history:

Received 13 May 2025
Received in revised form 25 November 2025
Accepted 10 December 2025
Available online 30 December 2025

Keywords:

Cast Aluminum Alloys, Residual Stress, Destructive and Non-Destructive Measurement Methods.

ABSTRACT

This study investigates the causes, measurement methods, and prevention strategies of residual stresses occurring in cast aluminum alloys during the manufacturing process. Residual stresses are elastic internal stresses that form in materials without any external load, typically due to processes like heat treatment, machining, or welding. These stresses directly affect the fatigue life, mechanical performance, and dimensional accuracy of components. In particular, sudden temperature changes during solution treatment and quenching in T6 heat treatment processes can lead to significant residual stresses. The study provides a detailed comparison of destructive methods (e.g., hole-drilling, ring-core, contour methods), non-destructive techniques (e.g., X-ray diffraction, ultrasonic testing, neutron diffraction), and analytical approaches using finite element modeling. The strengths and limitations of each method are discussed. In terms of fatigue performance, tensile residual stresses can be detrimental, while compressive stresses can enhance service life. Thus, accurate measurement and effective control of these stresses are crucial. Techniques such as stress relief annealing, low-temperature aging, and mechanical surface treatments are highlighted as effective in reducing residual stress. In conclusion, managing residual stresses carefully is essential for producing more durable and reliable engineering components.

Doi: 10.24012/dumf.1697102

* Sorumlu Yazar

Giriş

Üretim teknolojilerinin gelişmesiyle daha çok önem kazanan verim artışı, enerji tasarrufu ve maliyet düşürücü faaliyetlerin önemi ortaya çıkmaktadır. Bu faaliyetler kapsamında, yüksek üretim adetleri ve hızlı üretim adımları gerekmektedir. Şüphesiz bu üretim adımları farklı teknik sorunları da beraberinde getirmektedir. Örneğin, artan üretim adetleri sebebiyle ürün başına düşen çevrim süresinin giderek azaltılması hedeflenmekte ve eş zamanlı olarak ürünün performansında herhangi bir düşme olmadan, bilakis ürün performansı arttırma amaçlı farklı imalat prosesleri ve ısıl işlem uygulamaları uygulanabilmektedir.

Kalıntı gerilmeler, farklı imalat prosesleri ve/veya ısıl işlem uygulamaları sonrası yapıda homojen olmayan şekilde oluşan elastik gerilmeler olarak tanımlanabilir. Farklı kaynaklarda, hapsedilmiş (trapped stresses) ya da kilitli (locked stresses) gerilmeler olarak da ifade edilmektedir [1]. Kalıntı gerilmelerin oluşmasında farklı imalat prosesleri mekanik ve termal kökenli sebepler olarak sınıflandırılabilir. Mekanik kökenli etkiler, farklı imalat prosesleri olarak; işleme prosesi, katmanlı imalat ve kaynak prosesi olarak listelenmektedir. Termal kökenli etkiler, ısıl işlem uygulamaları ve termal çevrimler olarak tanımlanmaktadır. Kalıntı gerilmeleri, diğer gerilmelerden ayıran en önemli özellikleri, herhangi bir dış yük (Mekanik ya da termal yükler) olmadan da yapıda var olmalarıdır [1-5]. Esasen, kalıntı gerilmelerin doğrudan ölçümü mümkün olmamakla birlikte, dolaylı olarak şekil değiştirme (deformasyon) değerleri ölçümüyle belirlenebilir.

Kalıntı gerilmelerin büyüklüğünün doğru bir şekilde belirlenmesi, bileşenlerin mekanik performansının anlaşılması için çok önemlidir [4]. Kalıntı gerilmeler, ürün performansını direkt olarak etkileyen mikroyapı, mekanik performans, hata tipleri ve yapısal bütünlük (structural integrity) arasındaki ilişkilerin anlaşılması için de kritik rol oynamaktadır [1]. Endüstriyel uygulamalarda, ilgili parçanın çekme ya da basma yükleri altında çalışması durumuna göre, yapıdaki kalıntı gerilmeler yapının bütünlüğünün bozulması, mikroyapıdaki çatlakların ilerlemesi gibi riskler oluşturabilir [6-7]. Ayrıca, parça içinde kalan kalıntı gerilmenin de çeki ya da bası kalıntı gerilmesi olması durumu da parçaya uygulanacak gerilmelerin gerçek yükleme altında hesaplanandan farklı şekilde ortaya çıkmasına sebep olabilir. Örneğin, yapıdaki çeki kalıntı gerilmeleri, yorulma şartları altında çalışan parçanın servis ömrünü azaltarak yorulma hasarlarına sebep olabilirken, yapıdaki bası kalıntı gerilmeleri ise yine aynı yorulma şartları altında çalışan parçanın servis ömrünü arttırabilir. Ek olarak, aynı parçanın tasarımına ve imalat sürecine göre bir bölgesinde çeki kalıntı gerilmeleri görülürken, diğer bölgesinde bası kalıntı gerilmeleri meydana gelebilir. Bu sebeple, kalıntı gerilmelerin kesin ve doğru (accurate) ölçümü büyük önem kazanmaktadır. Bu ölçüm, parçanın tasarımında, üretim ve ısıl işlem parametrelerinin belirlenmesinde etkilidir. Ayrıca kalıntı gerilmeler, parçanın boyutsal doğruluğunu da etkileyebileceğinden, endüstriyel uygulamalarda ölçümü önemli bir adım haline gelmektedir.

Kalıntı gerilme ölçümleri, endüstride kullanılan metalik, seramik ve kompozit malzemelere uygulanabilir [8-9]. Kalıntı gerilme ölçümleri malzeme türlerine göre en büyük oranda metalik malzemelere uygulanırken, onu metal matrisli kompozitler (MMC: Metal Matrix Composite), seramik ve polimer malzemeler takip etmektedir [10]. Ek olarak, sektöre göre de Ar-Ge ve akademik çalışmalar, havacılık, enerji-güç üretimi ve otomotiv endüstrisinde geniş uygulama alanı bulmaktadır. Sektör uygulamalarında; otomotiv motor pistonları, motor silindir blokları – kapakları, süspansiyon parçaları örnek olarak verilebilir [11].

Çalışmada, farklı imalat prosesleri nedeniyle kalıntı gerilimlerin tasarlanan parça yapısında sıklıkla oluştuğu alüminyum alaşımdan üretilen döküm parçalar ve diğer mühendislik malzemeleri incelenmiştir. Buna ilaveten, metalik alaşımlarda oluşan kalıntı gerilimlerin ölçüm yöntemleri, neden oluştukları ve malzemeye etkileri ile bu gerilimlerin üretilen mühendislik parçaları içindeki önleme çareleri de araştırılmıştır.

Alüminyum Döküm Alaşımları

Temelde makro ve mikro seviyede incelenebilen kalıntı gerilmeler için üç farklı stres seviyesi tanımlanmıştır; bu stres tiplerinin ilki Tip 1 olarak adlandırılan, makro seviyede üretim prosesi esnasında malzeme tane boyutundan daha büyük ölçekte oluşan gerilmelerdir. İkincisi, Tip 2 olarak adlandırılan, mikro seviyede üretim prosesi esnasında tane boyutunda oluşan mikro kalıntı gerilmelerdir. Sonuncusu ise Tip 3 olarak adlandırılan, mikro seviyede tane içinde yer alan kristal kusurlarından oluşan mikro kalıntı gerilmelerdir [1].

Kalıntı gerilmeler, farklı imalat ve kaynak uygulamaları sebepli oluşması yanında, alüminyum döküm parçaları için kalıntı gerilmelerin önemli bir miktarının ısıl işlem sürecinde oluştuğu not edilmiştir [1]. Çözeltiye alma – su verme – yapay yaşlandırma adımlarının olduğu (T6 gibi) ısıl işlem süreçlerinde, özellikle çözeltiye alma ile su verme adımları arasındaki gibi çok kısa zamanda yüksek sıcaklık farkı oluşan adımlarda yapı içinde kalıntı gerilmeler oluşabilir. Yapıdaki bu kalıntı gerilmeler Tip 1 olarak adlandırılan makroskobik seviyede oluşabilir [1].

Diğer Malzemeler

Önceden bildirildiği gibi, bu çalışmada döküm alüminyum alaşımları için yapılan kalıntı gerilme ölçümü işlemleri detaylandırılacaktır. Metal dışı malzemelerdeki en yüksek kullanım oranı, metal matrisli kompozitler (MMC: Metal Matrix Composite), polimerler ve polimer matrisli kompozitler (PMC: Polymer Matrix Composite), seramikler ve seramik matrisli kompozitlerdir (CMC: Ceramic Matrix Composite) [10]. Alüminyum dökme alaşımlarına benzer şekilde, kompozit yapılar için de farklı stres tipleri tanımlanmıştır; Tip 1 tabaka (laminate) kalınlığı boyunca yapıdaki değişim sebepli oluşan kalıntı gerilmelerdir. Tip 2 ise anizotropik farklılıklardan (farklı yönlerdeki dış etkilere farklı özellik gösteren yapılar) dolayı oluşan makro

seviyedeki kalıntı gerilmelerdir. Son olarak, Tip 3 ise matris aralarında oluşan mikro seviyedeki kalıntı gerilmelerdir [1].

Daha önce tamamlanmış çalışmalar kalıntı gerilmelerin farklı mühendislik yapılarının performanslarına etki edebileceği ve değiştirebileceğini göstermiştir [10-11]. Endüstriyel uygulamalarda ilgili çalışma ya da test şartları altında çalışan parça, yapı içindeki kalıntı gerilmenin oluştuğu bölge ve tipine göre, beklenenden daha kısa sürede hasara uğrayabilir. Diğer taraftan, bu durumun tam aksine çalışma ve test şartlarına göre yapıda farklı yönde oluşturulabilecek kalıntı gerilmeler parça ömrünü arttırabilir. Bu durum, kalıntı gerilme ölçümünün önemini bir kez daha göstermiştir.

Ölçüm Yöntemleri

Literatürdeki çalışmalara göre kalıntı gerilimlerin ölçüm yöntemleri deneysel ve analitik yöntemler olmak üzere iki grupta incelenmektedir. Deneysel yöntemler, "tahribatlı (destructive)", "yarı-tahribatlı (semi-destructive)" ve "tahribatsız (non-destructive)" başlıkları altında incelenebildiği gibi [1], bazı çalışmalara göre, yarı-tahribatlı örnekler tahribatlı örnekler içinde de incelenebilmektedir. [3-10-12-13]. Bu sınıflandırmalar içerikleri bakımından yakın oldukları ve her iki yaklaşımda da benzer sonuçların elde edileceği öngörüldüğü için, çalışmada tüm ölçüm yöntemleri; tahribatlı deneysel teknikler, tahribatsız deneysel teknikler ve analitik teknikler olarak sınıflandırılmıştır.

Sınıflandırılan yöntemleri içerdikleri teknikler açısından, delik delme (hole-drilling) yöntemi, halka çekirdek (ring-core) yöntemi, derin delik delme (deep hole drilling) yöntemi, kontur-kesit profili (contour) yöntemi, katman kaldırma (layer removal / curvature) yöntemi ve kesit alma (sectioning) yöntemi gibi tahribatlı deneysel teknikler; X-ışını kırınımı (XRD: X-Ray diffraction) yöntemi, ultrasonik (ultrasonic) yöntem, nötron kırınımı (neutron diffraction) yöntemi ve manyetik (magnetic) yöntem gibi tahribatsız deneysel teknikler ve analitik ve sonlu elemanlar modelleri ile kalıntı gerilme ölçümünü içeren yöntemler analitik (analytical) teknikler olarak incelenmektedir [14].

Tahribatsız yöntemler, diğer yöntemlere kıyasla daha kesin (accurate) sonuçlar vermesine rağmen daha pahalılardır [1]. Bu sebeple, endüstriyel uygulamalarda nispeten daha uygun fiyatlı ve yüksek teknoloji gerektirmeyen ölçüm cihazlarıyla yerinde ölçüm imkânı sunan tahribatlı ölçüm yöntemleri avantajlı hale gelmektedir.

Kandil ve ekibi yayınladığı raporda, Birleşik Krallık'taki endüstriyel kurumların kalıntı gerilmelerin belirlenmesinde kullandığı yöntemleri kullanım oranlarına göre listelenmiştir, %30 oran ile en çok kullanılan yöntemin delik delme yöntemi olduğu belirtilmiştir. Delik delme yöntemini, %26 oranla X-ışını kırınımı yöntemi izlemektedir. Bu iki yöntem sırasıyla tahribatlı ve tahribatsız ölçüm yöntemlerinin en çok tercih edilen örnekleri olmuştur. Bu iki yöntemi ise sırasıyla, nötron kırınımı (%19), katman kaldırma (%16) ve manyetik ve ultrasonik gibi diğer yöntemler (%9) izlemektedir [10]. Bu değerler her ne kadar Birleşik Krallık'taki endüstriyel kurumları örnek gösterse de diğer endüstri alanları için de fikir verici olabilir.

Tahribatlı Deneysel Teknikler

Prensip olarak, iş parçasının gerilmeleri farklı yaklaşımlarla serbest bırakılır ve ölçülür. Bölgenin şekil değiştirmesi veya yer değiştirmesi ölçülerek, elastik mekanik prensiplerine göre kalıntı gerilme durumu belirlenebilir [12]. Tahribatlı teknikler, numunelerde hasara sebep oldukları için ilk aşamada daha az çekici görünseler de çok yönlü kullanımı (versatility) ve güvenilirlikleri (reliability) ile iyi bir tercih olarak öne çıkarlar [16]. Tahribatlı ve yarı-tahribatlı teknikler, genellikle maliyet etkin (cost-effective) ve yüksek teknoloji gerektirmeyen yöntemler olarak bilinir [15]. Tahribatlı ölçüm yöntemlerinde, test edilen parçadaki tahribat, kademeli olarak malzeme kaldırılarak oluşan deformasyonlar, gerinim ölçer (straingage) ya da Dijital Görüntü Korelasyonu (DIC: Digital Image Correlation) gibi optik yöntemler kullanılarak belirlenebilir [1].

Mekanik uygulama teknikleri, gerilme gevşemesi (stress-relaxing) yöntemleri olarak da bilinir ve metal parçadan alınan malzemenin oluşturduğu gevşeme (relaxation) miktarının analizi temeline dayanır. Mekanik uygulama öncesi ve sonrası karşılaştırılarak parçadaki kalıntı gerilmeler analiz edilir [14].

Tahribatlı teknikler, mekanik gevşeme (mechanical relaxation) ölçümleri ile uygulandığında, aynı parça üzerinde tekrarlanamaz ve birçok parça gerektirir [1].

Delik Delme (Hole-drilling) Yöntemi

Delik delme (hole-drilling) yöntemi farklı kaynaklarda "merkezi ya da kör delik delme (central or blind hole drilling)" [17] ve "artımlı ya da derin delik delme (incremental or deep hole drilling)" [18] yöntemi olarak da bilinmektedir.

Delik delme yöntemi, basit ve hızlı bir yöntem olması sebebiyle, en çok tercih edilen tahribatlı ölçüm yöntemidir. Rossini ve arkadaşları, bu yöntemi ölçüm için açılan deliklerin küçük (Yaklaşık 1,8 mm çapında ve en fazla yaklaşık 2,0 mm derinliğinde) ve tamir edilebilir boyutlarda olması sebebiyle, farklı kaynaklarda yarı-tahribatlı yöntemler altında da listelemiştir. En önemli avantajı, kesinlik (accuracy), güvenilirlik (reliability), standardize edilmiş test prosedürleri ve uygulamadaki kolaylık olarak gösterilebilir [14]. Bu etkili yöntem, ilk olarak 1934 yılında Alman bilim insanı Mather tarafından önerilmiştir. Zamanla iyi bir şekilde yerleşmiş ve kabul görmüş, 2015 yılında Amerikan Test ve Malzeme Derneği (ASTM) tarafından bir standart test prosedürü olarak yayımlanmıştır [13]. Test metodu 1981'de tanıtılarak ASTM Standard Test Metodu E837 ile standardize edilmiştir. Bu yöntem, temelde tüm parçayı etkileyecek kadar derin olmayan, sınırlı bir alanda uygulandığı için endüstriyel uygulamalarda geniş bir kullanım alanına sahiptir [1,19,20]. Bu yöntem endüstride daha çok metalik malzemelere uygulanırken, Magnier ve arkadaşları çalışmalarında plastik

malzemeler için [19]; Wu ve arkadaşları ise metal-karbon fiber ile güçlendirilmiş plastikler gibi hibrid malzemelerde delik delme yöntemini kullanmışlardır [20].

Bu yöntemde potansiyel hataları, özellikle delme işlemi sırasında oluşan gerilme etkilerini göz önünde bulundurmak önemlidir. M. T. Flaman, bu etkilerin, özellikle düşük hızla delme işleminde, ölçülen toplam gerilmelere önemli ölçüde katkıda bulunabileceğini bulmuştur. Sonuç olarak, delik delme yönteminde üstün performansı nedeniyle ultra yüksek hızlı bir matkap (20.000 devir/dakikadan, 400.000 devir/dakikaya) kullanımı tercih edilir. [13,21]. Scafidi ve arkadaşları, başlıca hata kaynaklarının analizinde, eksantrikliğin (eccentricity) en büyük etkenlerden biri olduğunu vurgulamıştır. Tipik deneysel koşullar altında, yalnızca eksantriklikten kaynaklanan hatalar %10'u aşabilmektedir. Ancak, ölçüm doğruluğunu etkileyen en kritik faktörün, operatörün yeteneği olduğu muhtemeldir [22,23].

Literatürdeki farklı çalışmaların temel alındığı bir başka standartta (ASTM E837-20 Delik Delme Gerinim Ölçer Yöntemi ile Kalıntı Gerilmelerin Belirlenmesi için Standart Test Yöntemi; ASTM E837-20 Standard Test Method for Determining Residual Stresses by the Hole-Drilling Strain-Gage Method) delik delme yönteminin gereklikleri standart şekilde paylaşılmıştır. En yaygın delme tekniği, en sert malzemeler hariç tümü için uygun olup, 20.000 ila 400.000 devir/dakika hızında dönen yüksek hızlı bir hava türbini veya elektrik motoru ile çalışan karbür frezeler veya uç frezelerin kullanılmasını içerir [24].

Delik çevresinde ölçülen gerilmelerden, uygun kalibrasyon sabitleri kullanılarak kalıntı gerilmeler hesaplanır. Bu sabitler, kullanılan gerinim ölçer rozetinin türüne ve beklenen gerilme türüne en uygun analiz prosedürüne dayanır [10]. Şekil 1, şematik olarak gerinim ölçer (straingage) rozetlerini göstermektedir. Şekil 1'deki merkezi daire delme yapılacak alanı, pozitif x yönü gerinim ölçer 1'in ekseni boyunca, negatif y yönü ise gerinim ölçer 3'ün ekseni boyunca uzanır (Şekil 2). Bu işlem sonucunda oluşan serbest bırakılmış deformasyonlar, üç gerinim ölçer tarafından kaydedilir [2].

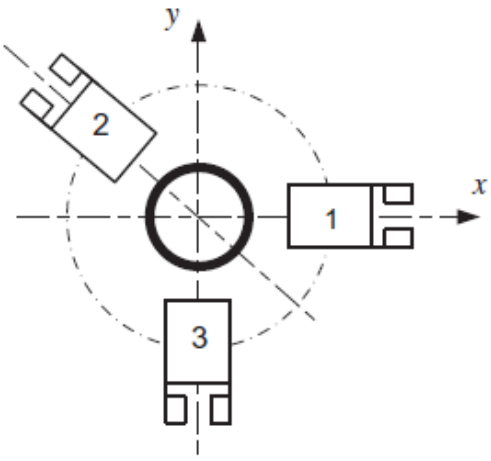

Şekil 1. Bir rozetin tipik geometrisi. [2]

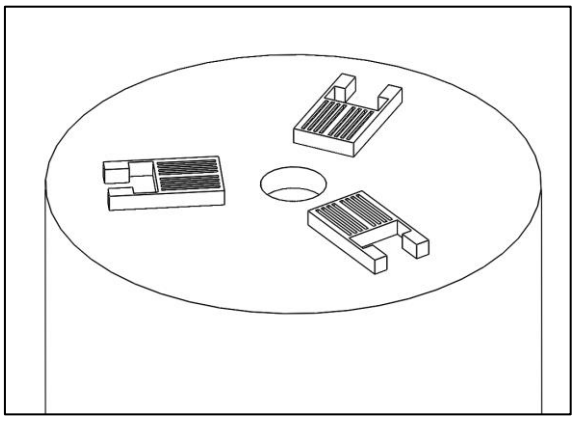

Şekil 2. Delik Delme yöntemi şematik gösterimi.

Elastik değerler için gerilme-gerinim (Stress-strain) ilişkisine dayalı Eşitlik (1) kullanılırken, düzlem gerilme durumundaki kalıntı asal gerilmenin büyüklük ve yönü için ise Eşitlik (2) kullanılır. Gerinim serbest bırakma (Strain relase) katsayıları A ve B, doğruluğu etkileyen en kritik faktörlerden biridir ve tam delik yöntemiyle doğrudan Kirsch teorisi kullanılarak hesaplanabilir [12]. A ve B Gerinim serbest bırakma (strain release) katsayıları, Eşitlik (3)'te gösterilmiştir. Burada ν, a ve r sırasıyla Poisson oranını, deliğin yarıçapını ve strain (gerinim) ölçüm cihazının deliğin merkezine olan mesafesini temsil etmektedir [13]. Buna karşın, kör delik yöntemi için kalibrasyon deneyleri gereklidir [12].

$$\varepsilon = A(\sigma 1 + \sigma 2) + B(\sigma 1 - \sigma 2)\cos 2\theta \tag{1}$$

$$\sigma_{1,2} = (1/4A)(\varepsilon_0 + \varepsilon_{90}) \pm (\sqrt{2}/4B)\sqrt{((\varepsilon_0 - \varepsilon_{135})^2 + (\varepsilon_{90} - \varepsilon_{135})^2)}$$

$$\tan 2\theta = (\varepsilon_0 + \varepsilon_{90} - 2\varepsilon_{135}) / (\varepsilon_0 - \varepsilon_{90}) \tag{2}$$

$$A = -(1 + \nu)/2 \times (a^2 / r^2)$$

$$B = (1/2) \times [\, 3(1 + \nu) \times (a^4 / r^4) - (4a^2 / r^2) \,] \tag{3}$$

Eşitlik (1) ve (2)'de, ε, ε_0, ε_{90} ve ε_{135} radyal gerilmeleri; σ1 ve σ2 ana (principal) gerilmeleri; θ, 0° gerinim (strain) ölçüm cihazı ile ilk başlıca gerilme yönü arasındaki açıyı, E, elastisite modülünü (Young modülü) temsil etmektedir [12,13].

Li ve arkadaşlarına göre, ölçümlerdeki tüm bu gelişmeler, delik delme tekniğinde önemli kolaylıklar ve iyileştirmeler sağlamıştır. Ancak gerinim ölçerlerin bazı sınırlamaları bulunmaktadır; bu sınırlamalar arasında zaman alıcı bir kurulum, sınırlı ölçüm noktaları ve delik delme yönteminde rozet içindeki deliğin yerleştirilmesindeki küçük sapmalardan kaynaklanan doğruluk problemleri yer almaktadır. Optik

yöntemler bu adımda umut vadedici alternatifler sunmuştur. Ayrıca, optik tekniklerin temassız yapısı, gerinim ölçerler ve diğer ölçüm cihazlarının zahmetli kurulumunu gereksiz kılar [13]. Numunenin yüzeyinde küçük bir delik açmayı ve geleneksel olarak gerinim ölçerler ve daha yakın zamanda Moiré interferometresi (Moiré interferometry), Elektronik Nokta Deseni İnterferometrisi (ESPI: Electronic Speckle Pattern Interferometry) ve Dijital Görüntü Korelasyonu (DIC: Digital Image Correlation) gibi tam alan optik teknikleri kullanarak çevreleyen yüzeyin deformasyonlarını ölçmeyi içerir. Delik delme yöntemi, birçok numune türünde güvenilir ve hızlı sonuçlar verebildiği ve yalnızca lokalize ve genellikle tolere edilebilir hasar yarattığı için yaygın olarak kullanılmaktadır [15].

Kim ve Jung, ESPI'yi Dijital Nokta Desen İnterferometrisi (DSPI: Digital speckle pattern interferometry) olarak da adlandırır ve yöntem örnek üzerindeki bir bölgenin tutarlı ışıkla aydınlatılmasını içerir. Bir ışın ayırıcı, lazer kaynağından çıkan ışını iki simetrik ışına böler; bu ışınlar, çoklu aynalar tarafından yansıtılır ve lensler aracılığıyla dağıtılır [25]. Cao ve ekibi ise Moiré interferometrisini örnek yüzeyine yerleştirilen veya üzerinde üretilen ince çizgilerden oluşan bir kırınım ızgarası kullanarak girişim oluşturduğunu ifade etmişlerdir. Elde edilen "sanal ızgaralar", örnek yüzeyinin gerinim bilgilerini taşır [26]. Yoon ve arkadaşları ise DIC'nin temel prensibini, referans görüntü ile farklı yük seviyeleri altındaki şekil değiştirmiş görüntüler arasında görüntü korelasyonları kurmayı içerdiğini söyleyerek açıklamışlardır [27].

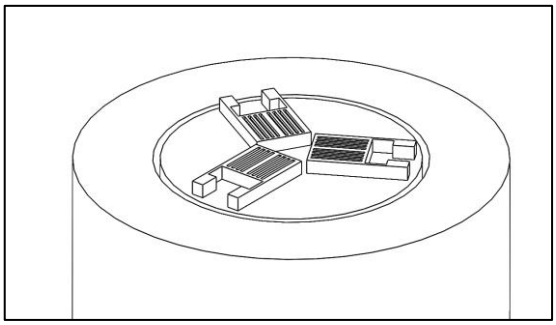

Şekil 3. Halka çekirdeği yöntemi şematik gösterimi.

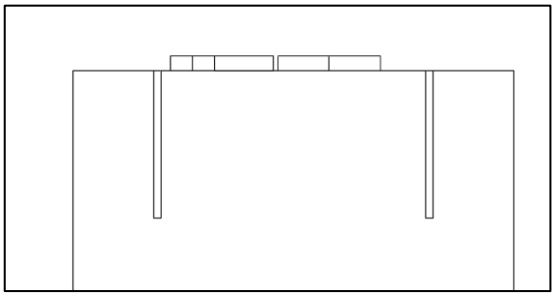

Şekil 4. Halka çekirdeği yöntemi şematik kesit gösterimi.

Halka çekirdeği yöntemi (Şekil 3 ve 4), delik delme yönteminin bir varyasyonu olarak değerlendirilebilir. Delik delme yönteminde, gerinim ölçerin tam merkezine bir delik açılırken, halka çekirdeği yönteminde gerinim ölçerin çevresinde bir halka oluşturulur. Bu süreçte ortaya çıkan şekil değişimleri ölçülerek kalıntı gerilmeler hesaplanır. Halka çekirdeği yönteminin, delik delme yöntemine kıyasla, daha büyük şekil değişimlerini tespit edebilmesi ve bu sayede daha yüksek kalıntı gerilmeleri ölçme imkânı sağlaması önemli bir avantajdır. Ancak, bu yöntem ölçüm yapılan malzemede daha fazla hasara yol açması ve uygulama zorlukları nedeniyle delik delme yöntemine oranla daha az tercih edilmektedir. Halka çekirdeği yöntemi, malzemenin belirli bir derinliği boyunca kalıntı gerilmeleri ölçmeye olanak tanıyan tahribatlı bir yöntemdir. Malzemeden talaş kaldırıldığında, içindeki kalıntı gerilmeler serbest kalır ve bu değişiklikler ölçülür. Delik delme işlemi sırasında oluşan gerinim değişimleri, bilgisayar tarafından derinlik boyunca kaydedilir. Daha sonra bu veriler kullanılarak kalıntı gerilmeler hesaplanır. Halka çekirdeği yöntemi, elastik teorinin geçerli olduğu metaller, seramikler ve polimerler gibi çeşitli malzemelerde uygulanabilir [28].

Baldi, halka çekirdek yönteminin prensip olarak yeniden başlatılabilir olması sebebiyle (çekirdeğin çıkarılıp gerinim ölçer rozetinin yeniden takılmasıyla) bu avantaja sahip nadir bir yöntem olduğundan bahsetmiştir. Bu özelliği sayesinde, diğer yöntemlere kıyasla kalıntı gerilmenin çok daha derinlerde ölçebildiği ve gerinim ölçümünde yöntemin daha hassas olduğunu bildirmiştir. Fakat, bu ilgi çekici fikrin pratik olarak uygulanmasının çok zor olduğunu fark ederek, özellikle derinlik arttıkça gerinim ölçer (strain gauge) rozetlerinin yeniden takılıp kablolamasının deneysel olarak zorluğunu ortaya koyarak, optik bir ölçüm yolu tercih edilmesini önermiştir [38].

Maslákova ve arkadaşları, halka çekirdek yöntemi kullanılarak kalıntı gerilmelerin belirlenmesi için gerinim ölçer (strain gauge) uygulaması çalışmalarında tüm gereklilikleri adım adım açıkladıktan sonra, yöntemin dezavantajları arasında, delik delme yöntemine kıyasla daha hassas/duyarlı olduğunu not etmişlerdir. Bunun yanında, delik delme yöntemine göre bir avantaj olarak deliğin çapındaki küçük hatalara veya eksantrikliğe karşı daha az hassastır. Şüphesiz, halka derinliği, delik delme yöntemine göre daha fazla olduğundan parçaya verilen hasar daha fazladır [39].

Derin Delik Delme (Deep hole drilling) Yöntemi

Derin delik delme yöntemi, delik delme yöntemi ile halka çekirdek yönteminin bir ara formudur. Bu yöntemin uygulamasında, öncelikle iş parçasında boylu boyunca bir delik açılır ve delik çapının ölçümü alınır. Daha sonra, halka çekirdek yöntemine benzer şekilde, deliğin etrafındaki parça çıkarılır. İlk durumda ölçülen delik çapı tekrar ölçülerek, çapta oluşan farktan kalıntı gerilme hesabı yapılır. Bu yöntem genellikle, büyük ölçekli döküm parçalarda kullanılır [28,29].

Shokrieh ve Ghasemi çalışmalarında, ortotropik (mekanik özellikleri üç birbirine dik eksen yönünde bağımsız ve özgün)

plakalar için delik delme yöntemiyle ölçülen serbest kalan gerinimlerin, kesin çözüm yöntemleri kullanılarak kalıntı gerilmelere dönüştürülmesini ele almışlardır [40].

Hosseinzadeh ve arkadaşları çalışmalarında, paslanmaz çelik silindir ve halkaları, gerilme oluşturmak amacıyla suyla soğutmuş ve bu gerilmelerin, akma gerilmelerine eşit veya daha büyük seviyelere ulaşmasını sağlamışlardır. Kalıntı gerilmeleri, nötron kırınımı ve iki mekanik gerilme rahatlatma (relaxation) yöntemi olan derin delik delme ve artımlı merkez delik delme ile ölçmüşlerdir. Bu ölçümlerde, sonlu elemanlar analiziyle yapılan soğutma tahminleriyle karşılaştırıldığında, benzer eğilimler olmasına rağmen büyüklükler arasında sınırlı bir uyum bulmuşlardır. Yeniden oluşturulan gerilmeler ile yapılan ölçümlerde ise daha iyi bir uyum yakalamışlardır. Şaşırtıcı bir şekilde, derin delik delme ve nötron kırınımı ölçümleri arasında ise oldukça iyi bir uyum olduğunu tespit etmişlerdir [41].

Kontur-Kesit Profili (Contour) Yöntemi

Kontur yöntemi, ilk olarak Prime tarafından 2000'li yılların başında önerilmiştir [30, 31] ve stresin iki boyutlu olarak değerlendirilmesi amacıyla uygulanmıştır. Bu yöntemin, tüm kesitindeki kalıntı gerilmelerin görselleştirilmesini sağlaması nedeniyle, kontur yöntemi sonuçları genellikle tahribatsız nötron kırınımı ölçümleriyle karşılaştırılır [1, 28].

Yöntem, Bueckner prensibine dayanır ve özet olarak şunu ifade eder: "Çatlak kapatma kuvvetleri, çatlak içermeyen bir cismin aynı koşullardaki gerilme dağılımına eşdeğer olmalıdır." [30] Ölçüm prosesi ise numunenin kesilmesi, yüzey profilinin çıkarılması, veri toplanması ve gerilme ölçülmesi şeklinde özetlenebilir. Profilin doğru çıkarılması için, bu yöntemde kesilen yüzeyin kalitesi önemli bir rol oynar. Bu sebeple, kesmede geleneksel kesme takımları yerine tel erozyon yöntemi tercih edilir. Diğer proses parametreleri de ölçümde önemli rol oynar. Bu parametreler, malzeme, tel erozyon proses parametreleri, parça kompleksitesi olarak listelenebilir [16, 30].

Hacini ve arkadaşları çalışmalarında, kaynaklı bileşenler, kaynak dikişi çevresinde yüksek gerilmeli kalıntı gerilmelerine maruz kaldığı temeline göre, bu gerilmelerin erken çatlamanın kaynağı olabileceğine dikkat çekmişlerdir. Laboratuvarlarında kurulu robotlu çekiçleme ile, başlangıçta gerilmesiz olan östenitik paslanmaz çelik 304L örneklerinde kompresif kalıntı gerilmeleri indüklemek için kullanılmışlar ve elde edilen kalıntı gerilmeleri, kontur tekniği ile değerlendirilmiştir [30].

Brown ve arkadaşları, kaynaklanmış silindirdeki kalıntı gerilmelerin ölçüm sonuçlarını, kontur ve nötron kırınımı yöntemleriyle karşılaştırmıştır. Sonuçlar, nötron kırınımının, kontur yöntemine göre 50 MPa daha düşük gerilmeler değerlendirdiğini göstermiştir [42].

Son yıllarda yapılan çalışmalarda, kesit profilinin ölçümünde yeni yöntemler kullanıldığı görülmüştür. D'Elia ve arkadaşları, kalıntı gerilme değerlendirmesi için kullanılan kontur yönteminin laboratuvarlar arası yeniden üretilebilirliğini inceleyen çalışmalarında, süreç simülasyonundan elde edilen yüzey topografyası verilerini kullanmışlardır [43].

Wang ve arkadaşları ise karmaşık geometrilere sahip yapısal parçalarda kesit kalıntı gerilmelerini belirlemek için 3D tarayıcı kullanarak kontur ölçümü olarak yeni bir yöntem sunmuşlardır. Önerilen yöntem, farklı özellikteki bir boru kaynağındaki eksenel kalıntı gerilme dağılımını değerlendirmek için uygulanmış ve elde edilen sonuçlar, doğrulama amacıyla referans kontur ölçüm makinesi (CMM) ile karşılaştırılmıştır. İki yöntem arasında hem ölçülen konturlar hem de hesaplanan kalıntı gerilmeleri açısından nicel bir uyum sağlanmıştır. Bu yöntem, referans yönteme kıyasla ölçüm süresini yaklaşık %99 oranında kısaltmaktadır [44]. Özetle, Kontur-Kesit Profili (Contour) yöntemiyle ilgili yeni bakış açıları, karmaşık geometrilere sahip parçalar için kesit kalıntı gerilmelerini belirlemek amacıyla 3D tarayıcı kullanılarak, geleneksel yönteme kıyasla ölçüm süresinde önemli bir azalma sağlamıştır.

Kesit Alma (Sectioning) Yöntemi

Bu yöntem farklı kaynaklarda, Kesit alma (Sectioning), Yarma (Slitting) ya da Dilimleme (Slicing) gibi farklı isimlerle sınıflandırılmışlardır [1,14,32]. Kesit alma tekniği test edilecek parçadan belirli bir kütle/hacim çıkarılması sırasında kalıntı gerilmelerin serbest bırakılmasından kaynaklanan deformasyonun ölçülmesine dayanan tahribatlı bir yöntemdir (Şekil 5 ve 6).

Bu teknik, Tebedge ve arkadaşları tarafından genel yapı çeliği, alüminyum alaşımları ve paslanmaz çelik malzemelerin kesitlerindeki kalıntı gerilmeleri analiz etmek için kullanılmıştır [33].

Rossini ve arkadaşları da kesit alma yöntemini, fiziksel büyüklükleri ölçülüp kaydedilmiş bir plakada kesim yaparak kesim hattında mevcut olan kalıntı gerilmeleri serbest bırakarak belirlemiştir. Çalışmaya göre, kullanılan kesim işlemi, plastik deformasyon veya ısı oluşturmamalıdır, böylece kesim yüzeylerindeki plastik deformasyon etkileri olmadan orijinal kalıntı gerilmeler doğru bir şekilde ölçülebilir. Kesme işlemi sırasında açığa çıkan gerinimler genellikle mekanik ve elektriksel gerinim ölçerler kullanılarak ölçülür [14, 33].

Ekmekçi çalışmasında, kesit alma yöntemini gerilme altındaki nesne kesilir ve gerilmeler serbest bırakılır şeklinde özetlemiştir. Her durumda, çıkarılan malzeme miktarına bağlı olarak ortalama deformasyon değerleri ölçülür ve bunun serbest bırakılan gerilmenin büyüklüğünü belirleyeceği not edilmiştir [32].

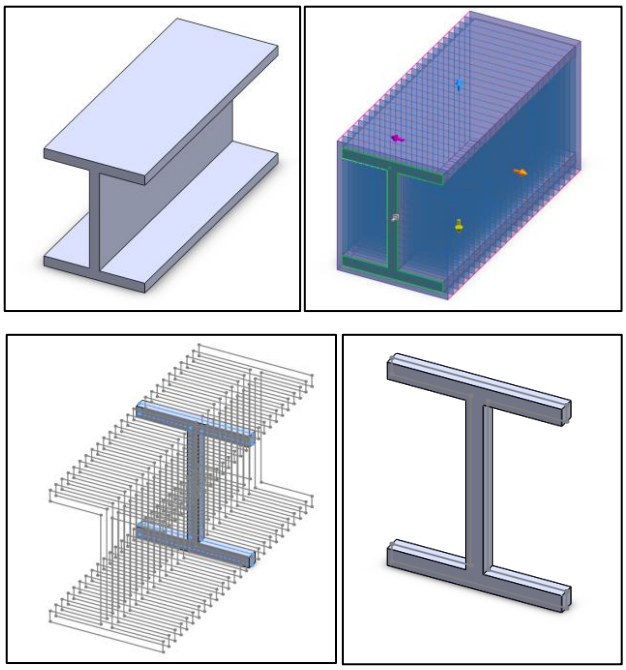

Şekil 5. Kesit alma yönteminde I Profilinin şematik gösterimi.

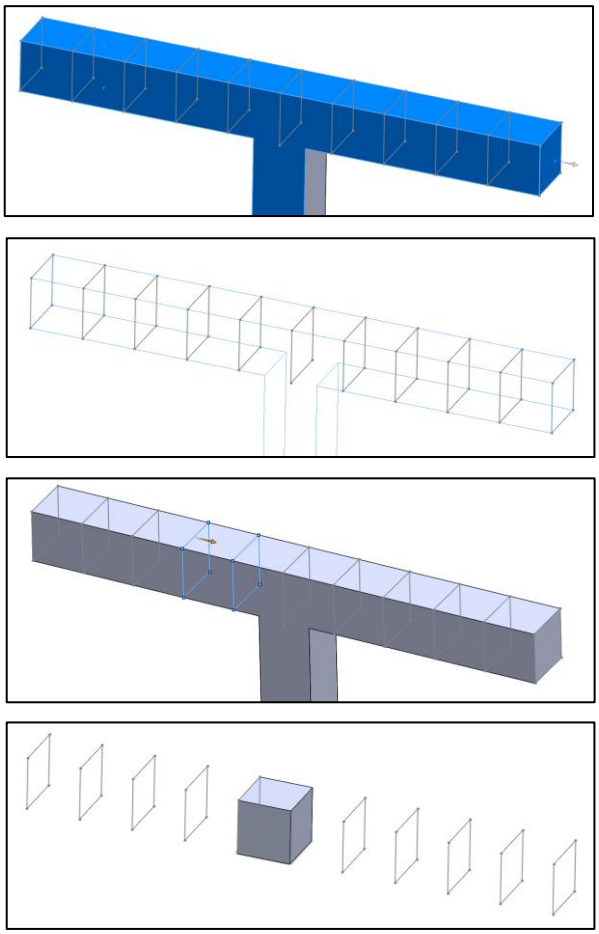

Şekil 6. Kesit alma yönteminde I Profilinin şematik gösterim detayı.

Tahribatsız Deneysel Teknikler

Son yıllarda, tahribatsız değerlendirme (NDT: Non-Destructive Testing) yöntemleri gibi yeni muayene çözümleri geliştirilmiştir. Bu yöntemler sadece maliyet açısından etkili, güvenilir ve uygulaması kolay olmakla kalmaz, aynı zamanda test prosedürü sırasında yüksek bir güvenlik seviyesi de sağlar [1].

Tahribatsız yöntemlerin temeli elastik değişimlerin ölçümüne dayanır. Buradaki en temel fark, malzemeye zarar vermeden yapılan bir ölçüm olmasıdır. Literatürde ve sanayide karşılaşılan en yaygın yöntemler: X-Işını Kırınımı (XRD: X-Ray Diffraction) yöntemi, Ultrasonik yöntem, Nötron kırınımı ve Manyetik (Barkhause gürültüsü) yöntemidir.

X-Işını Kırınımı (XRD: X-Ray Diffraction) Yöntemi

Kalıntı gerilmesi hesaplama yöntemleri arasında en çok X-ışını kırınımı (XRD) yöntemi kullanılmaktadır [33]. X-Işını kırınımı, malzemelerdeki yüzey kalıntı gerilmelerini ölçmek için kullanılan tahribatsız bir yöntemdir (Şekil 7). Bu yöntem, malzemenin gerilme altında veya kalıntı gerilmeleri mevcut olduğunda meydana gelen elastik şekil değişikliklerinin, atomik düzlemler arasındaki mesafeyi değiştirmesi prensibine dayanır. X-Işını kırınımı ile atomik düzlemler arasındaki mesafe ölçülerek, daha sonra bu şekil değişiklikleri hesaplanabilir ve kalıntı gerilme değeri belirlenebilir [28].

Kırınım yöntemleri, elastik deformasyonu belirlemeye dayanır; bu deformasyon, düzlemler arası mesafe d'yi, gerilmesiz değeri d_0 'ya değiştirecektir. Ardından, Eşitlik (4)'te verilen Bragg yasası kullanılarak gerilme hesaplanabilir: [14,32]

$$\lambda = 2d \sin\theta \tag{4}$$

Burada λ X-ışınlarının dalga boyunu, d kristal düzlemleri arası mesafe ve θ kırınım açısını temsil etmektedir [32].

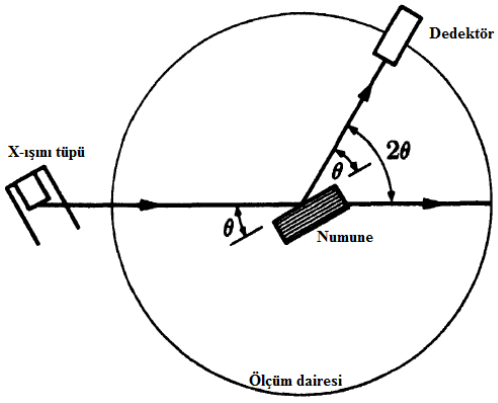

Şekil 7. Geleneksel XRD Yöntemi [34,35].

X-ışını kırınımı ile kalıntı gerilmesi ölçümü, kristalin özelliklere sahip, nispeten ince taneli olan ve numune yüzeyinin her yönü için kırınım üreten malzemelere uygulanabilir. Numune metalik veya seramik olabilir [36]. Ramana ve arkadaşları, X-ışını yöntemini, maraging çeliği ile su verilip tavlanmış alaşımlı orta karbonlu çelik arasındaki farklı metallerin kalıntı gerilme dağılımını değerlendirmek için kullanmışlardır [37]. Bu yöntemin avantajı tüm kalıntı gerilme tiplerinin ölçülebilmesi iken, yüksek cihaz maliyeti ve sınırlı numune boyutu ise dezavantajı olarak görülebilir [28]. Bu çalışmada, tüm detaylarına girilmemekle birlikte, X-ışını kırınımı (XRD) ölçümü için literatürde farklı ölçüm yöntemlerine değinilmiştir. Bu yöntemler: Williamson-Hall yöntemi, Warren-Averbac yöntemi ve Rocking yöntemi olarak listelenmiştir [34].

Robinson ve Redington, XRD yöntemini kullanarak yüzeye yakın kalıntı gerilmeleri ölçmüş ve bunları ısıl işlem görmüş alüminyum alaşımlarındaki mukavemet ve sertlik özellikleriyle ilişkilendirmeye çalışmışlardır. Bu çalışmada incelenen tüm alüminyum alaşımlar için kalınlık boyunca kalıntı gerilme dağılımının aynı deseni takip ettiği ve iç kısımlarda çekme gerilmeleri, yüzeyde ise bası gerilmeleri oluştuğu gözlemlenmiştir. Alaşım mukavemetinin etkisi, gözlenen kalıntı gerilme büyüklüklerinde değişim olarak kendini göstermiştir. Ayrıca, yüzey kalıntı gerilmelerinin su verme sonrası sertlik (Vickers) ve mukavemet ile doğrusal bir ilişkiye sahip olduğu tespit edilmiştir [45].

Ultrasonik (Ultrasonic) Yöntem

Ultrasonik yöntemlerde, katı içerisindeki gerilme seviyelerinin etkisiyle hareket eden ultrason dalgalarının hızındaki değişiklikler kullanılarak kalıntı gerilmeler hesaplanabilir. Bir malzeme, kalıntı gerilme altında ve gerilmesiz durumda farklı ultrason dalga hızlarına sahip olur. Malzeme elastik özellik gösterdiği sürece, dalga hızı malzemedeki kalıntı gerilme durumuna bağlı olarak değişir [34].

Malzeme içindeki kalıntı gerilmeler, ses dalgalarının hareketine engel olarak dalga hızlarını düşürür. Bu nedenle, malzeme içinde ilerleyip arka yüzeyden yansıyan ses dalgalarının gidiş geliş mesafesi, kalıntı gerilmesi olmayan bir malzemeye göre farklılık gösterir. Bu fark nano saniye düzeyinde olduğundan, ölçüm yapabilmek için son derece hassas cihazlar kullanmak gereklidir [28].

Kalıntı gerilmelerinin dalga hızı üzerindeki etkisi, Eşitlik (5) ile kavramsal olarak açıklanabilir:

$$V = V_0 + K\sigma \tag{5}$$

Burada, V_0 gerilmesiz ortamda bir dalganın hızını, σ gerilmeyi ve K ise malzemeye bağlı bir parametre olan akustik elastik sabiti ifade eder.

Javadi ve arkadaşları, sonlu elemanlar ve ultrasonik yöntem kullanarak östenitik paslanmaz çelik plakalarda kalıntı gerilmelerin, kaynaklı parca kalınlıkları boyunca değerlendirilmesi üzerine çalışmışlardır. Öncelikle, sonlu elemanlar modelini, delik delme yöntemi ile karşılaştırmışlar, daha sonra da bu modeli ultrasonik yöntemle karşılaştırmışlardır [46].

Zhan ve arkadaşları da kalıntı gerilmelerin lazer ultrasonik ölçümü için deneysel ve sayısal simülasyonunu yapmışlardır. Numunenin kaynak kalıntı gerilmesi, sayısal simülasyon (ABAQUS) fonksiyon modülü kullanılarak önceden tanımlanmış alanla gerçekleştirilmiştir. Sonlu elemanlar analizi sonuçları, deneysel yöntemle oldukça uyumlu çıkmıştır [47].

Literatürde karşılaşılan örneklere göre, ultrasonik yöntemin genellikle kaynaklı parçalar ve kaynak işleminin neden olduğu kalıntı gerilmenin ölçümünde tercih edildiği not edilebilir.

Nötron Kırınımı (Neutron Diffraction) Yöntemi

Nötron kırınımı yöntemi, X-ışını kırınımı yöntemine benzer şekilde, malzemenin kristal yapısındaki atomik düzlemler arasındaki mesafeyi ölçerek kalıntı gerilmeleri belirler. Bu yöntemin avantajı, X-ışınları yerine daha güçlü ve yüksek penetrasyona sahip nötronlar kullanılmasıyla nüfuziyet derinliğinin daha fazla olmasıdır. Bu sayede ölçüm derinliği, alüminyumda 200 mm, çelikte 25 mm ve titanyumda 25 mm'ye kadar ulaşabilir [28].

Daha önce de not edildiği üzere, Brown ve arkadaşları, kaynaklanmış parçada, kontur ve nötron kırınımı yöntemleriyle karşılaştırmıştır. Sonuçlar, nötron kırınımı, kontur yöntemine göre 50 MPa daha düşük gerilmeler vermiştir [42]. Arada oluşan farkın temel sebebi; kontur yönteminde tüm kesitteki deformasyona bağlı sonuç hesaplanırken, nötron kırınımı yönteminde ise hacimsel ortalama ile sonuçlara ulaşılmasıdır. Bu fark, malzeme yoğunluğu ve tanesel arası gerilmelerin olduğu bölgelerde daha fazla olabilir.

Smith ve arkadaşları, Brown ve arkadaşlarının çalışmasına benzer bir karşılaştırmayı türbin ve kompresörlerde kullanılan Nikel bazlı alaşımların lineer sürtünmeli kaynak işlemi sonrası nötron kırınımı ve kontur yöntemine göre karşılaştırmışlardır. Nötron kırınımı ile yapılan kalıntı gerilme değerlendirmelerinin, ölçüm hatalarını azaltma ve doğruluğu artırma konusunda büyük bir potansiyele sahip olduğunu vurgulamıştır [48].

Analitik (Analytical) Teknikler

Son yıllarda, makroskobik yüzey gerilme ölçüm yöntemlerinde büyük gelişmeler gerçekleşmiştir. Bu gelişmelerden biri, analitik tekniklerden sonlu elemanlar yöntemi (FEM) alanındaki gelişmelerdir. Bu yöntem, kritik gerilme gevşemesi (critical stress relief) katsayısının

kalibrasyon sürecini büyük ölçüde basitleştirerek ölçüm doğruluğunu artırmıştır [13].

Tahribatlı ve tahribatsız deneysel teknikler, kalıntı gerilme analizi için öncelikli olarak tanımlanmıştır. Bununla birlikte, endüstri uygulamalarında artan ölçüm aletleri, kurulum, zaman gibi maliyetler sebebiyle analitik ve sonlu elemanlar modelleri geliştirilmeye ve kullanılmaya başlanmıştır. Bu yöntemin en önemli avantajları, nispeten daha düşük işlem sürelerinde gerçekleştirilmesi ve ölçüm aletleri ve kurulum maliyetlerinin olmamasıdır. Bunun yanında en önemli dezavantajı ise gerçek koşulların tümüyle modellenememesidir.

Özel ve arkadaşları çalışmalarında, kalıntı gerilmelerin analitik yöntemlerle kesin olarak hesaplanmasının zor olduğunu, bu sebeple genellikle deneysel tekniklerle beraber kullanılarak, kesin hesaplama olmasa da iyi bir yaklaşım sunabileceğini belirtmişlerdir. Kalıntı gerilmelerin hesaplanmasının sayısal çözüm yöntemi olan sonlu elemanlar yöntemi ile yapılabileceğini belirtmişlerdir [49].

Zhang ve arkadaşları, karbon fiber takviyeli polimer (CFRP: Carbon Fiber Reinforced Plastic) ve Alüminyum birleşimlerinde oluşan kalıntı gerilmeleri tahmin etmek için bir model geliştirmiştir. Model, deneysel ve sonlu elemanlar sonuçları ile karşılaştırılarak başarılı bir şekilde doğrulanmıştır. Fakat bu doğrulama, birçok varsayıma bağlıdır. Kalıntı gerilmenin düzlem gerilmesi olması, kalıntı gerilmenin bir tork oluşturmadığı, farklı malzemeyi birleştiren yapıştırıcı (adhesive) malzemenin elastik bir malzeme olması ve CFRP ve alüminyumdan farklı malzemelerin aynı deformasyona sahip olması gibi bir dizi varsayımlara bağlıdır [50].

Shokrieh ve Ghasemi, delik delme ve yarma (slitting) yöntemlerinin simülasyonu için temel oluşturabilecek eşitlikleri not etmişlerdir [40].

Literatürdeki birçok çalışma, kullanılan malzemenin - özellikle kompozit parçalar için- farklı sonlu eleman modelleri oluşturarak, deneysel sonuçlara yaklaşmaya çalışmışlardır. Tabatabaeian ve arkadaşları, plastik kompozitler için kullanılan modelleri: Elastik çözüm, Silindir teorisi, Elshelby teorisi, Enerji yöntemi, Kür sertleşmesi anlık doğrusal elastik (CHILE) modeli, Viskoelastik model olarak listelemişlerdir [1].

Cai ve arkadaşları çalışmalarında, AlSi7Cu0.5Mg (A356) alüminyum alaşımının T4 ve T6 ısıl işlem görmüş hallerinde gelişen kalıntı gerilmeleri değerlendirmeyi amaçlamıştır. Farklı ölçüm teknikleriyle yapılan analizlerde, kontur yöntemi ve artımlı delik delme yöntemlerinin T6 uygulanan alaşımlar için en uygun olduğu, T4 uygulanan alaşımlarda ise tüm yöntemlerin eşit derecede etkili olduğu bulunmuştur. Ayrıca, işlem görmemiş (as-cast) ve ısıl işlem görmüş örnekler arasındaki farkların, çökeltme ısıl işlemi ve su vermeden kaynaklandığı öne sürülmüştür [51].

Johnson ve arkadaşları, gri dökme demir örneği için döküm sürecindeki kalıntı gerilmelerin gelişimini incelemek amacıyla MAGMAstress paketini kullanmışlardır. Simülasyonlarında sıcaklık bağımlı termofiziksel özelliklere sahip termo-elastoplastik malzeme modeli kullanmışlardır. Simülasyon sonuçları, parça üzerindeki farklı konumlarda nötron kırınımı tekniğiyle karşılaştırılmış ve doğrulanmıştır [52].

Menne ve arkadaşları, Ford'un bazı motor projelerinde, döküm ve ısıl işlem süreçlerinin son mekanik özellikleri, kalıntı gerilme dağılımını ve olası hataları tahmin etmek için sonlu elemanlar modellemesinin önemini vurgulamışlardır. Çalışma, motor bloğu üretimi öncesinde döküm sürecinin bilgisayar destekli mühendisliğin bir parçası olarak sonlu elemanlar metodu modellemesinin, zaman ve maliyetini %50'ye kadar azaltabileceğini ve ürünlerin kalite ve dayanıklılığını iyileştirebileceğini sonucuna varmıştır. Analiz için MAGMA ticari yazılım paketi kullanılmıştır; ancak modelleme parametreleri, sınır koşulları veya malzeme özellikleri gibi detaylar raporda tartışılmamıştır [53].

Tüm bu yöntemler, Tablo 1'de yöntem grubu (Tahribatlı, Tahribatsız ve Analitik) olarak sınıflandırılarak avantaj, dezavantaj ve uygulama alanları olarak kaşılaştırılarak tablolaştırılmıştır.

Tablo 1. Tüm Ölçüm Yöntemlerinin Karşılaştırılması

Yöntem Grubu	Yöntemler	Avantajlar	Dezavantajlar	Uygulama Alanları
Tahribatlı	Delik Delme	Basit, hızlı, standart, küçük hasar	Operatör etkisi, eksantriklik riski	Metaller, plastikler
	Halka Çekirdek	Yüksek kalıntı gerilme ölçebilme	Daha fazla hasar, zor uygulama	Metaller, seramikler
	Derin Delik Delme	Büyük parçalarda etkili	Karmaşık, çok tahribat oluşturması	Büyük döküm parçalar
	Kontur	Kesit boyunca 2D dağılım	Tam kesit tahribatı	Kaynaklı yapılar
	Kesit Alma	Basit uygulama	Tam tahribat	Çelik/Alüminyum
Tahribatsız	XRD	Kesin, yaygın	Pahalı, yüzeyle sınırlı	Metalik/seramik
	Ultrasonik	Zararsız, kaynaklı parçalarda etkili	Yüksek hassasiyet gerektirir	Kaynaklı parçalar
	Nötron	Derin nüfuziyet	Yüksek maliyet	Kalın metal parçalar
	Manyetik	Kolay, zararsız	Sadece ferromanyetik malzemelerde uygulama	Manyetik malzemeler
Analitik	Analitik ve FEM Yakşalımı	Düşük maliyet, hızlı	Gerçek tam modellenemez	Döküm/ısıl işlem simülasyonları

Nedenler ve Etkiler

Nedenler

Tabatabaeian ve arkadaşları, kalıntı gerilme oluşturan nedenleri; Termal (Isıl işlemler) işlem, Kaynak işlemi, Kaplama işlemleri, Talaşlı imalat ve Katmanlı imalat işlemi olarak listelemişlerdir. Termal süreçler altında kürleme işlemi, kaynak işlemi, termal sprey işlemleri incelenirken, mekanik işlemler altında ise talaşlı imalat ve katmanlı imalat işlemleri detaylı olarak incelenmiştir [1].

Özellikle otomotiv endüstrisinde yaygın olarak kullanılan alüminyum alaşımlı jantlar, silindir kapakları/blokları gibi alüminyum döküm parçalara uygulanan imalat adımlarının sebep olduğu nedenler dikkate alındığında, iki imalat adımı öne çıkmaktadır. Bunlar, ürünlerin mekanik özelliklerini arttırmaya yönelik yapılan ısıl işlemler (T6 Isıl işlemleri gibi) ve ürünlerin son haline getirilmesi amacıyla yapılan talaşlı imalat işlemleridir.

Isıl İşlemler

Kalıntı gerilmelerin oluşmasının ana nedenlerinden biri, sıcaklık alanındaki ani değişikliklerdir.

Li ve arkadaşları, kalıntı gerilmelerin, çeşitli imalat ve kaynak işlemleri sonucunda meydana gelebileceği gibi, alüminyum döküm parçalarında önemli bir kısmının ısıl işlem sırasında oluştuğu gözlemlemiştir [11]. Çalışmalarına göre, T6 gibi çözeltiye alma, su verme ve yapay yaşlandırma aşamalarını içeren ısıl işlem süreçlerinde, özellikle çözeltiye alma ve su verme adımları arasında meydana gelen ani sıcaklık değişimleri, yapı içinde kalıntı gerilmelerin oluşmasına yol açabilir. Bu tür kalıntı gerilmeler, makroskobik ölçekte ortaya çıkabilir [11].

Jiang ve arkadaşları, ısıl işlemler esnasında çok kısa zaman dilimlerinde çok yüksek sıcak farklılıkları sebebiyle ortaya çıkan termal farklılıkların yapıda kalıntı gerilme oluşturması sebebiyle plastik deformasyona yol açabileceğini bildirmiştir [54].

Isıl işlemler sürecinde oluşan kalıntı gerilmelerin giderilmesi için bilinen en iyi yöntem nispeten düşük sıcaklıklarda uygulanacak ek bir ısıl işlem olabilmektedir. [55] Bu ikincil ısıl işlem, gerilme giderme tavı olarak da bilinmekle birlikte (malzeme ve parça geometrisine göre farklılık gösterir) alüminyum alaşımlı döküm parçalarında 250 °C civarında uygulanabilir.

Jiang ve arkadaşları, AlSi10Mg alaşımındaki kalıntı gerilmenin sıcaklığın azalmasıyla kademeli olarak düştüğünü ve 250 °C'de minimum seviyeye ulaştığını göstermektedir [54]. Bu durum, alaşımlarda kalıntı gerilmelerin azaltılması amacıyla yapılan ikincil ısıl işlemin önemini ortaya koymaktadır.

Robinson ve arkadaşları, alüminyum alaşımı malzemenin ısıl işlem sonrası kalıntı gerilmelerinin yeniden dağılım mekanizması üzerine bir çalışma yapmışlardır ve malzeme kaldırmanın, kalıntı gerilmelerinin katman katman yeniden dağılımına neden olduğunu bulmuşlardır [56].

Li ve arkadaşları, A356 malzemeli jantlarda, T6 ısıl işlemindeki su verme aşamasından kaynaklanan kalıntı gerilmelerinin bir modelini geliştirilmiştir. Elde edilen tahminler, su verme işleminden geçirilen jantlar üzerinde gerinim ölçer (strain gauge) konumlandırıp, kesit alma tekniği ile yapılan kalıntı gerilmesi ölçümleriyle karşılaştırılmıştır. Çalışmadaki model, T6 Isıl işlemindeki su verme işlemi sırasında kalıntı gerilmenin durumu ve işleme aşamasındaki malzeme kaldırma (talaşlı imalat) nedeniyle kalıntı gerilmelerinin yeniden dağılımını dikkate almıştır. Su verme sırasında oluşan kalıntı gerilme, esas olarak 200 °C ile 350 °C arasında değişebildiği görülmüştür [57].

Godlewski ve arkadaşları, Alüminyum döküm alaşımlarının işlem döngüsündeki su ile soğutmanın, döküm parçanın bazı bölgelerinde yüksek kalıntı gerilmeleri oluşturma potansiyeline sahip olduğunu not etmişlerdir. Döküm parçanın ömrüne katkı sunacağı düşünülerek, bu kalıntı gerilmenin giderilmesi için farklı sıcaklıklarda gerilme giderme tavlaması uygulanarak sıcaklık arttıkça, kalıntı gerilme gidermenin daha başarılı olduğunu bildirmişlerdir [58].

Talaşlı İmalat

Alüminyum döküm parçalarında talaşlı imalat esnasında oluşan yüzeysel kalıntı gerilimler parçanın yorulma dayanımını etkileyebileceğinden ömrünü de direkt olarak etkileyecektir. Ayrıca talaşlı imalat, yüzey pürüzlüğü ve bütünlüğünü de etkileyebilir. Bu sebeple, talaşlı imalat ısıl işlem sürecinin yanında önemli bir rol oynayan işlemdir. Bu sebeple, talaşlı imalat işlemi, kalıntı gerilme durumu için mutlaka göz önünde bulundurulmalıdır.

Tabatabaeian ve arkadaşları, özellikle uçak endüstrisinde, parça distorsiyonların düzeltilmesi için yüksek maaliyetler olduğunu not etmişlerdir. 2001'de yayınlanan bir çalışmaya dayandırdıkları bir bilgiye göre, Boeing şirketinin işlenmiş bileşenlerdeki distorsiyonu telafi etmek için yaklaşık 290 milyar USD harcadığını belirtmişlerdir [1]

Bu çalışmada daha önce de belirtildiği gibi, yapıda oluşan kalıntı gerilmelerin çeki ya da bası olması, çalışma şartlarına göre değişiklik gösterse de-, bası kalıntı gerilmesine sahip işlenmiş parçaların, işlenmemiş ham parçalara göre daha uzun bir yorulma ömrüne sahip olduğu not edilebilir. Bu sebeple, işleme planında bu durumun göz önüne alınması fayda sağlayabilir.

Zhang ve arkadaşları, ince cidarlı parçaların işlenmesinde kalıntı gerilmelerin iş parçası distorsiyonuna ve boyutsal kararsızlığa neden olduğunu göstermişlerdir [59].

Amini ve arkadaşları, ince cidarlı alüminyum alaşımlarının işleme sonrası kalıntı gerilmelerini incelemiş ve kesme kuvveti ve sıcaklığın kalıntı gerilme ile doğrudan ilişkili olduğunu belirtmişlerdir. Isıl etki, iş parçasında kalıntı gerilme oluşturabilir; bu nedenle, bu parçaların işlenmesi daha fazla distorsiyona ve üretim hatalarına yol açmaktadır [60].

Mantle ve Aspinwall, işleme sürecinde farklı faktörlerin kalıntı gerilmeler üzerindeki etkisini kapsamlı bir şekilde incelemişlerdir. Kesme hızı, ilerleme oranı, eksenel ve radyal kesme derinliği, iş parçası açısı, aşınma ve frezeleme yönü gibi işleme parametrelerinin kalıntı gerilme profili üzerinde büyük bir etkiye sahip olduğunu ortaya koymuşlardır [61].

Liu ve Guo, ikinci kesme işleminin rasyonel optimizasyonu ile yüzeydeki kalıntı gerilmenin çeki gerilmesinden bası gerilmesine dönüştürülebileceğini not etmişlerdir [62].

Tabatabaeian ve arkadaşları, işlenmiş numunenin daha yüksek yüzey kalitesi, bası kalıntı gerilmelerinin varlığını gerektireceğini, işleme operasyonlarında, bası kalıntı gerilmeleri mekanik yüklerin, çekme kalıntı gerilmeleri ise termal yüklerin bir sonucu olarak oluştuğunu bildirmişlerdir [1].

Kalıntı Gerilmelerin Parça Ömrüne Etkileri

Yorulma/Kırılma Üzerine Etkiler

M.B. Prime, Kalıntı gerilmelerin yorulma ve kırılma üzerindeki etkilerinin açık olduğunu ve kırılma mekaniği kavramlarının kalıntı gerilim ölçümleri ile iç içe geçmiş olduğunu belirtmiştir. Ayrıca, kalıntı gerilmelerin, tıpkı harici bir yük gibi davrandığını ve çeki ya da bası gerilmeleri olmasına bağlı olarak hasar süreçlerini hızlandırıp yavaşlatabileceğini bildirmiştir. Ek olarak, nispeten daha az bilinen bir örnek etkiyi; kalıntı gerilmelerin, malzemelerin gerçek mekanik özelliklerini, özellikle kırılma tokluğunu ölçmeyi son derece zorlaştırabileceğini bildirmiştir [63].

Tabatabaeian ve arkadaşları, Kalıntı gerilmelerin yorulma / kırılma üzerine olan etkilerini Eşitlik (6) da ifade etmişlerdir:

$$(K1)applied + (K1)rs > K1c \quad (6)$$

Burada:

- $(K1)applied$: Uygulanan mod gerilme yoğunluk faktörü,

- $(K1)rs$: Kalıntı gerilmeden kaynaklanan mod gerilme yoğunluk faktörü,
- $K1c$: Malzemenin kırılma tokluğu sınırı (kırılma mukavemetine karşı dayanıklılık).

$(K1)rs$, negatif değerlere (bası gerilmeleri) sahip olduğunda faydalı, pozitif değerlere (çekme gerilmeleri) sahip olduğunda ise zararlı olabileceğini göstermektedir [1].

M.B. Prime, kalıntı gerilmelerin yüksek çevrimli yorulmaya kıyasla yorulma çatlağı büyümesi üzerinde daha güçlü bir etkiye sahip olduğunu ortaya koymuştur [63].

Prabhakar ve arkadaşları, kritik bölgelerde lokalize bası kalıntı gerilmeleri uygulayarak bileşenlerin yorulma ömründe %88'lik önemli bir iyileşme sağlanabileceğini ortaya koymuştur [64].

Daha önce bildirildiği üzere, Li ve diğerleri, AlSi7Mg0.3 alaşımlı jantların su verme (quenching) işlemi sırasında oluşan gerilmeler sonrası, bu gerilmelerin yorulma ömrü üzerindeki etkilerini incelemişlerdir. Su verme işlemi sırasında oluşan gerilmelerin, yüzeyde bası, çekirdek kısmında ise çeki olduğu belirtilmiştir. Ayrıca, su verme hızının düşürülmesiyle birlikte, çeki tipi gerilmeler nedeniyle kalıntı gerilmelerin azaldığını ve bunun sonucunda yorulma ömrünün arttığı belirtmişlerdir [57].

Kutsal ve arkadaşları, AlSi7Mg0.3 alüminyum alaşımlı jantların, T6 ısıl işlemlerini simüle ederek, bu ısıl işlem adımlarının farklı adımlarda oluşturduğu kalıntı gerilme değerlerini yazılım yardımıyla hesaplamışlardır. İlk aşamada, üç farklı koşulda (döküm, su verme ve yapay yaşlandırma) mikroyapısal incelemeler ve mekanik test çalışmaları yapılmıştır. Ayrıca, 3D tarayıcı test sonuçlarına göre, her ısıl işlem adımında üç farklı bölgedeki boyutsal değişiklikler gözlemlenmiştir. Su verme işleminden sonra, jantın yüzeyinde çoğunlukla bası gerilmesi gözlemlenmiştir ve yapay yaşlandırma adımında kalıntı gerilimde az ve yetersiz bir düşüş görülmüştür [65].

Kalıntı Gerilmeleri Önleme (Kontrol) Yöntemleri

Kalıntı gerilmeler metallerin yanında; seramikler ve kompozit malzemeleri de önemli ölçüde etkilemektedir.

Kalıntı gerilmelerin, yorulma ömrünü azaltması, yüzeyde çatlak/kırılma oluşturması ya da parçanın şekilsel bütünlüğünü bozması gibi yapıya verdiği hasarlar üstte detaylıca tartışılmıştır. Bu olası hasarları önlemek ise, hem ilgili parçanın uygun şartlar altında çalışılması, hem olası maddi hasarların önüne geçilmesi, hem de tasarım aşamasında tasarımcılara daha optimum ve hafif tasarım yapmalarına yardımcı olacaktır. Endüstriyel uygulamalarda, kalıntı gerilmelerin tamamen önlenmesi mümkün olmasa da azaltılması/yönlendirilmesi ya da kontrol altına alınması maliyet ve parça ömrü açısından önemli bir kazanç sağlar.

Bu önleme faaliyetleri, kompozit ya da seramik malzemeler için farklılık gösterse de bu çalışmada metal ve alüminyum alaşımları için örnekler incelenmiştir.

Isıl İşlemler

Alüminyum alaşımlarında görülen kalıntı gerilmeler için önemli önleme yöntemlerinden ilki ısıl işlem uygulamalarıdır.

Alümiyum alaşımlı parçalarda yapılan kaynak uygulamaları, çok kısa zamanda yüksek sıcaklık farkları oluşturması sebebiyle, kaynak bölgesine yapılacak soğutma işlemleriyle nispeten önlenebilir. Lin ve arkadaşları, kaynaklanan alüminyum alaşımları gibi bazı hassas malzemeler için yerel veya genel olarak uygulanabilen soğutma işleminin daha uygun olduğunu göstermektedir. Araştırma bulguları, çoklu elektron ışını (multi electron beam heating) ile ısıtma yöntemi kullanılarak kalıntı kaynak gerilmelerde yaklaşık %48 oranında azalma sağlanabileceğini ortaya koymaktadır [66].

Bu çalışmanın da merkezinde yer alan, alüminyum alaşımlı döküm parçaların ergitme-döküm-ısıl işlem (T6 Isıl işlem gibi) üretim adımlarında, imalatın doğası gereği sınırlı olarak müdahale edilebilen adımları sonrası, ek ısıl işlemlerle gerilme giderme uygulamaları yapılabilir. Yang ve arkadaşları, alüminyum alaşımlarının su verme işlemi sonrası oluşan kalıntı gerilmelerini incelemek için bir sonlu elemanlar simülasyon modeli geliştirmiştir. Çalışma, su verme sıcaklığının artmasıyla birlikte, su verilmiş silindirik çubuklardaki maksimum çeki ve bası kalıntı gerilmelerin azaldığını ortaya koymuştur [67].

Wyatt ve arkadaşları, A356 alüminyum alaşımından üretilen parçanın yüzeyinde oluşan kalıntı gerilmeleri belirlemek için düşük maliyetli yeni bir yöntem kullanmıştır. Mikro sertlik izleri arasındaki mesafe değişimini ölçerek gerilme seviyeleri hesaplanmış ve kesme ile ısıl gerilme giderme teknikleri karşılaştırılmıştır. Döküm parçalar daha sonra 250°C'de 200 dakika süren bir ısıl işlemle gerilme giderme işlemine tabi tutulmuş ve ısıl gerilme giderme teknikleri karşılaştırılmıştır [69].

Godlewski ve arkadaşları, alüminyum alaşımlı döküm parçalara uygulanan ısıl işlemler adımlarından, çözeltiye alma ile su verme arasındaki hızlı sıcaklık değişimi gerçekleşen bölgeyi işaret ederek kalıntı gerilmelerin oluştuğu adımı belirtmişlerdir. Bu kalıntı gerilmelerin olumsuz etkilerini azaltmak için de farklı yaşlandırma adımları üzerinde çalışmışlardır. Çalışmada dört farklı sıcaklık (190 °C, 220 °C, 240 °C ve 260 °C) ve geniş bir yaşlandırma süresi aralığı (0.3 ila 336 saat) incelenmiştir. Sonuçlar, yaşlandırma sıcaklığı arttıkça kalıntı gerilmelerin azaldığını da göstermiştir [58].

Mohamed ve arkadaşları, gerilim giderme işleminin, bir parçanın uygun bir sıcaklığa eşit şekilde ısıtılması, belirli bir süre boyunca bu sıcaklıkta tutulması ve ardından termal gerilmelerin yeniden oluşmasını önlemek için yavaş

soğutulmasıyla gerçekleştirileceğini not etmişlerdir. Uygun sıcaklığı belirlerken de yüksek sıcaklıklarda (Çözeltiye alma sıcaklığı gibi) kalıntı gerilmelerde büyük bir azalma meydana gelse de malzemenin mekanik özelliklerinde de önemli kayıplar gözlemlenebileceğini ve bunun nedeninin, tavlama işlemi sırasında çökeltilerin irileşerek sertleşme özelliklerini kaybetmesi olacağını bildirmişlerdir. Bu yüksek sıcaklıklarda, gerilme giderme mümkün olmayacağı için, gerilim giderme için gerekli sıcaklık, ikinci faz bileşenlerinin çökelmesini teşvik eden sıcaklıkla örtüşeceği ve bu nedenle, gerilim giderme işlemi daha düşük sıcaklıklarda, yani yaşlandırma sırasında gerçekleştirilmesi gereği sonucuna varmışlardır. Deneysel çalışmalarında, T6 ısıl işlemiyle giderilen kalıntı gerilme miktarı yalnızca sınırlı bir azalma sağlarken, 250°C'de yapılan yaşlandırma işlemi en az %75 oranında kalıntı gerilme gevşemesi sağladığını görmüşlerdir. Yaşlandırma süresi arttıkça, kilitlenmiş kalıntı gerilmelerin büyük bir kısmının tamamen ortadan kaldırılabildiğini not etmişlerdir [72].

Benzer ısıl işlem ile gerilme giderme uygulamaları, farklı imalat yöntemleri ile üretilen alüminyum alaşımları için de uygulanmaktadır. Roveda ve arkadaşları, katmanlı imalat yöntemi ile ürettikleri AlSi10Mg malzemeli parça için düşük sıcaklıkta tavlama ısıl işlemi (265 °C, 1 saat ve 300°C, 2 saat) uygulayıp, kalıntı gerilme gevşemesini (relaxition) X-Işını kırınımı ve nötron kırınımı yöntemleriyle incelemişlerdir. Yorulma çatlağı ilerleme limitinde, 265 °C, 1 saat işleminden sonra %60'a ve 300 °C, 2 saat işleminden sonra %120'ye varan iyileşme görülmüştür. 2. Isıl işlem sürecinde (300 °C, 2 saat) aluminyum matris içindeki silikon partiküllerinin daha homojen dağılmış olması sebebiyle, daha sünek bir yapı oluşturduğu, bu sebeple de bu sünek yapının daha yüksek bir yorulma çatlağı ilerleme limiti verdigi ifade edilmiştir [70].

Robinson ve Tanner, yüksek dayanımlı alüminyum alaşımı (7010) için; Su verme işlemini farklı su sıcaklıklarında ve soğutma işlemlerini farklı fırın sıcaklıklarında yapılmıştır. Ayrıca, yeniden yaşlandırma işlemleri ile standart ısıl işlemlerle (Doğal yaşlandırma, T6, T74 ısıl işlemleri) kalıntı gerilmelerdeki azalma miktarları belirlenmiştir. 175 °C, 200 °C ve 240 °C gibi daha yüksek sıcaklıkları içeren yaşlandırma işlemleri tutarlı olarak %20'den fazla azalma sağlamaktadır [71].

İmalat

Mekanik yöntem, çekiçleme veya titreşimle gerilim giderme yöntemleri ile gerçekleştirilmektedir. Üretim aşamasında kalıntı gerilmeleri azaltmanın etkili bir yolu, bilyeli dövme (shot peening), derin haddeleme ve ultrasonik nano-kristal yüzey modifikasyonu (UNSM) gibi mekanik yüzey işlemlerini uygulamaktır. Bu yüzey işlemleri, bası kalıntı gerilmeleri oluşturarak çekme kalıntı gerilmelerinin neden olduğu çatlak başlangıcını geciktirmekte ve böylece yorulma direncini belirli bir ölçüde artırmaktadır [68].

Tabatabaeian ve arkadaşları, kaynak uygulamalarında, kaynak hattı boyunca bası kalıntı gerilmeleri oluşturabilecek yeterli bir yük uygulamanın avantajlarından bahsetmişlerdir. Bu yöntem, tahrip edici çeki kalıntı gerilmelerinin azaltılmasında önemli bir etkiye sahip görünmektedir. Bununla birlikte, uygulanan yükün miktarı da dikkat edilmesi gereken parametrelerdendir, aksi halde yapıda çatlak oluşturacak ya da mevcut çatlakların ilerleyerek yapı hasarına sebep olabilir [1].

Sonuç ve Değerlendirme

Bu çalışma, alüminyum alaşımlı döküm parçalarındaki kalıntı gerilmelerin oluşum sebeplerini, bunların ürün performansına olan etkilerini ve bu gerilmelerin ölçülmesinin önemini ele almaktadır.

Çalışmada, kalıntı gerilimlerin oluşum sebepleri, ürün ömrüne etkileri, bu gerilimlerin ölçüm ve giderilme yöntemleri üzerinde durulmuştur. Çalışmada elde edilen bulgulara göre:

1. Kalıntı gerilmeler, özellikle hızlı üretim süreçleri ve ısıl işlem uygulamaları sırasında ortaya çıkan, dış yük olmaksızın yapıda var olabilen iç gerilmelerdir. Bu gerilmelerin doğru bir şekilde ölçülmesi, ürünün mekanik performansını, mikroyapısal bütünlüğünü ve servis ömrünü doğrudan etkileyen kritik bir faktördür.
2. Kalıntı gerilme ölçüm yöntemleri, deneysel ve analitik teknikler olarak iki ana grupta sınıflandırılmaktadır. Deneysel yöntemler, tahribatlı ve tahribatsız olarak ayrılırken, Delik delme ve X-ışını kırınımı yöntemleri, sırasıyla tahribatlı ve tahribatsız yöntemlerin en çok tercih edilen örnekleri olarak öne çıkmaktadır.
3. Delik delme yöntemi, tahribatlı yöntemler arasında yaygın kullanımı ve hızlı uygulama avantajı ile dikkat çekmektedir. Ancak, bu yöntemde operatör hatalarının etkisi ve delme sırasında oluşan gerilme etkileri gibi sorunlar göz önünde bulundurulmalıdır.
4. X-ışını kırınımı yöntemi, tahribatsız yöntemler arasında; Hızlı ve yüksek hassasiyetle ölçüm yapabilme, karmaşık malzemeler için uygun olması sebebiyle öne çıkmaktadır. Ancak, yüksek maliyet/ekipman gereksinimi ve uzun süreli ve ileri düzey hazırlık gerektirmektedir.
5. Kalıntı gerilmelerin oluşmasının başlıca nedenleri arasında termal işlemler, kaynak işlemleri, talaşlı imalat ve katmanlı imalat yer almaktadır.
6. Isıl işlemler sırasında meydana gelen ani sıcaklık değişiklikleri, alüminyum alaşımlarındaki kalıntı gerilmeleri artırabilir. Örneğin, T6 ısıl işlemi sırasında su verme ve yapay yaşlandırma aşamaları sırasında gerilmeler oluşabilir. Bu gerilmeler, parçalarda plastik deformasyona yol açabilir.

Kalıntı gerilmelerinin giderilmesi için genellikle ek bir ısıl işlem (gerilme giderme tavı) uygulanır.

7. Talaşlı imalat sırasında yüzeyde oluşan kalıntı gerilmeler, parçalarda distorsiyona ve boyutsal hatalara yol açabilir. Ayrıca, ince cidarlı alüminyum alaşımlarında, işleme sırasında oluşan gerilmeler, parçaların distorsiyonuna ve üretim hatalarına neden olabilir. Bu süreçlerin dikkatle yönetilmesi, ürün ömrünü uzatmaya yardımcı olabilir.
8. Kalıntı gerilmelerinin, özellikle yorulma ve kırılma üzerinde önemli etkileri vardır. Çeki gerilmeleri, malzemelerin yorulma ömrünü kısaltabilirken, bası gerilmeleri bu ömrü uzatabilir. Bu nedenle, kalıntı gerilmelerinin dikkatle yönetilmesi, malzeme ömrünü uzatmada kritik bir faktördür.
9. Endüstriyel uygulamalarda kalıntı gerilmelerin tamamen önlenmesi mümkün olmasa da, azalması ve kontrol altına alınması, maliyet ve parça ömrü açısından önemli faydalar sağlar. Isıl İşlemler adımında; Su verme ve yaşlandırma işlemleri kalıntı gerilmelerin azalmasını sağlar. İmalat İşlemleri adımında; Bilyeli dövme ve yüzey işlemleri kalıntı gerilmelerin azalmasını sağlar.
10. Yeni araştırmalar; tahribatlı ve tahribatsız yöntemleri birlikte kullanabilen hibrit modellerin geliştirilmesine, karmaşık geometriler için 3D tarama destekli analitik/FEM yaklaşımlarındaki varsayım kaynaklı hataları azaltacak yapay zekâ tabanlı tahmin modellerine odaklanabilir. Ayrıca endüstriyel maliyetleri düşürmek için hızlı, yerinde uygulanabilir ve sensör entegrasyonlu kalıntı gerilme ölçüm çözümleri araştırılarak geliştirilebilir.

Kaynaklar

[1] Tabatabaeian, A., Ghasemi, A. R., Shokrieh, M. M., Marzbanrad, B., Baraheni, M., & Fotouhi, M. (2022). Residual Stress in Engineering Materials: A Review. In *Advanced Engineering Materials* (Vol. 24, Issue 3). https://doi.org/10.1002/adem.202100786

[2] Akbari, S., Taheri-Behrooz, F., & Shokrieh, M. M. (2014). Characterization of residual stresses in a thin-walled filament wound carbon/epoxy ring using incremental hole drilling method. *Composites Science and Technology*, *94*, 8–15. https://doi.org/10.1016/j.compscitech.2014.01.008

[3] Ahn, S. min, Park, S. Y., Kim, Y. C., Lee, K. S., & Kim, J. Y. (2015). Surface residual stress in soda-lime glass evaluated using instrumented spherical indentation testing. *Journal of Materials Science*, *50*(23), 7752–7759. https://doi.org/10.1007/s10853-015-9345-x

[4] Serrano-Munoz, I., Fritsch, T., Mishurova, T., Trofimov, A., Apel, D., Ulbricht, A., Kromm, A., Hesse, R., Evans, A., & Bruno, G. (2021). On the interplay of microstructure and residual stress in LPBF IN718. *Journal of Materials Science*, *56*(9), 5845–5867. https://doi.org/10.1007/s10853-020-05553-y

[5] Carpenter, H. W., Reid, R. G., & Paskaramoorthy, R. (2015). The effect of residual stresses and wind configuration on the allowable pressure of thick-walled GFRP pipes with closed ends. *International Journal of Mechanics and Materials in Design*, *11*(4), 455–462. https://doi.org/10.1007/s10999-014-9280-z

[6] Alipooramirabad, H., Kianfar, S., Paradowska, A., & Ghomashchi, R. (2024). Residual stress measurement in engine block—an overview. In *International Journal of Advanced Manufacturing Technology* (Vol. 131, Issue 1, pp. 1–27). Springer Science and Business Media Deutschland GmbH. https://doi.org/10.1007/s00170-024-13071-3

[7] Carrera, E., Rodríguez, A., Talamantes, J., Valtierra, S., & Colás, R. (2007). Measurement of residual stresses in cast aluminium engine blocks. *Journal of Materials Processing Technology*, *189*(1–3), 206–210. https://doi.org/10.1016/j.jmatprotec.2007.01.023

[8] Olson, M. D., DeWald, A. T., & Hill, M. R. (2022). Measurement Layout for Residual Stress Mapping Using Slitting. *Experimental Mechanics*, *62*(3), 393–402. https://doi.org/10.1007/s11340-021-00791-w

[9] Reid, R. G., & Paskaramoorthy, R. (2009). A novel method to measure residual stresses in unidirectional GFRP. *Composite Structures,* Volume 88, Issue 3, May 2009, Pages 388-393. https://doi.org/10.1016/j.compstruct.2008.04.015

[10] Kandil, F. A., Lord, J. D., Fry, A. T., & Grant, P. v. (2001). *A Review of Residual Stress Measurement Methods-A Guide to Technique Selection. by*.

[11] Li, K., Xiao, B., & Wang, Q. (2009). Residual Stresses in As-Quenched Aluminum Castings. *International Journal of Materials and Manufacturing*, *1*(1), 725–731. https://doi.org/10.2307/26282709

[12] Guo, J., Fu, H., Pan, B., & Kang, R. (2021). Recent progress of residual stress measurement methods: A review. In *Chinese Journal of Aeronautics* (Vol. 34, Issue 2, pp. 54–78). Elsevier B.V. https://doi.org/10.1016/j.cja.2019.10.010

[13] Li, X., Liu, J., Wu, H., Miao, K., Wu, H., Li, R., Liu, C., Fang, W., & Fan, G. (2024). Research progress of residual stress measurement methods. In *Heliyon* (Vol. 10, Issue 7). Elsevier Ltd. https://doi.org/10.1016/j.heliyon.2024.e28348

[14] Rossini, N. S., Dassisti, M., Benyounis, K. Y., & Olabi, A. G. (2012). Methods of measuring residual stresses in components. In *Materials and Design* (Vol. 35, pp. 572–588). https://doi.org/10.1016/j.matdes.2011.08.022

[15] Wong, W., & Hill, M. R. (2013). Superposition and Destructive Residual Stress Measurements. *Experimental Mechanics*, *53*(3), 339–344. https://doi.org/10.1007/s11340-012-9636-y

[16] Schajer, G. S. (2010). Relaxation Methods for Measuring Residual Stresses: Techniques and Opportunities. *Experimental Mechanics*, *50*(8), 1117–1127. https://doi.org/10.1007/s11340-010-9386-7

[17] Shokrieh, M. M., & Ghasemi K., A. R. (2007). Determination of calibration factors of the hole drilling method for orthotropic composites using an exact solution. *Journal of Composite Materials*, *41*(19), 2293–2311. https://doi.org/10.1177/0021998307075443

[18] Ghasemi, A. R., Taheri-Behrooz, F., & Shokrieh, M. M. (2014). Determination of non-uniform residual stresses in laminated composites using integral hole drilling method: Experimental evaluation. *Journal of Composite Materials*, *48*(4), 415–425. https://doi.org/10.1177/0021998312473858

[19] Magnier, A., Scholtes, B., & Niendorf, T. (2017). Analysis of residual stress profiles in plastic materials using the hole drilling method – Influence factors and practical aspects. *Polymer Testing*, *59*, 29–37. https://doi.org/10.1016/j.polymertesting.2016.12.025

[20] Wu, T., Tinkloh, S. R., Tröster, T., Zinn, W., & Niendorf, T. (2020). Determination and validation of residual stresses in CFRP/metal hybrid components using the incremental hole drilling method. *Journal of Composites Science*, *4*(3). https://doi.org/10.3390/jcs4030143

[21] Flaman, M.T. Brief investigation of induced drilling stresses in the center-hole method of residual-stress measurement. *Experimental Mechanics,* 22, 26–30 (1982). https://doi.org/10.1007/BF02325700

[22] Scafidi, M., Valentini, E., & Zuccarello, B. (2011). Error and uncertainty analysis of the residual stresses computed by using the hole drilling method. *Strain*, *47*(4), 301–312. https://doi.org/10.1111/j.1475-1305.2009.00688.x

[23] Beghini, M., Bertini, L., & Mori, L. F. (2010). Evaluating non-uniform residual stress by the hole-drilling method with concentric and eccentric holes. Part II: Application of the influence functions to the inverse problem. *Strain*, *46*(4), 337–346. https://doi.org/10.1111/j.1475-1305.2009.00684.x

[24] *Test Method for Determining Residual Stresses by the Hole-Drilling Strain-Gage Method*. (2020). ASTM International. https://doi.org/10.1520/E0837-20

[25] Kim, K., & Jung, H. (2016). Nondestructive Testing of Residual Stress on the Welded Part of Butt-welded A36 Plates Using Electronic Speckle Pattern Interferometry. *Nuclear Engineering and Technology*, *48*(1), 259–267. https://doi.org/10.1016/j.net.2015.10.008

[26] Cao, Q., Li, Y., & Xie, H. (2020). Orientation-Identified virtual fields method combined with moiré interferometry for mechanical characterization of single crystal Ni-based superalloys. *Optics and Lasers in Engineering*, *125*. https://doi.org/10.1016/j.optlaseng.2019.105854

[27] Yoon, S., Jung, H. J., Knowles, J. C., & Lee, H. H. (2021). Digital image correlation in dental materials and related research: A review. In *Dental Materials* (Vol. 37, Issue 5, pp. 758–771). Elsevier Inc. https://doi.org/10.1016/j.dental.2021.02.024

[28] Akdeniz, Y. (2012). Taşlama Sonrası Kalın Camsı Metalde Olusan Kalıntı Gerilmenin Delik Delme Yöntemiyle İncelenmesi. Yüksek Lisans Tezi, İstanbul Teknik Üniversitesi Fen Bilimleri Enstitüsü, İstanbul

[29] Leggatt, R. H., Smith, D. J., Smith, S. D., & Faure, F. (1996). Development and experimental validation of the deep hole method for residual stress measurement. *The Journal of Strain Analysis for Engineering Design*. Volume 31, Issue 3 https://doi.org/10.1243/03093247V313177

[30] Hacini, L., van Lê, N., & Bocher, P. (2009). Evaluation of residual stresses induced by robotized hammer peening by the contour method. *Experimental Mechanics*, *49*(6), 775–783. https://doi.org/10.1007/s11340-008-9205-6

[31] Prime, M. B. (2001). Cross-sectional mapping of residual stresses by measuring the surface contour after a cut. *Journal of Engineering Materials and Technology*, *123*(2), 162–168. https://doi.org/10.1115/1.1345526

[32] Ekmekçi, B. (2004). Theoretical and Experimental Investigation of Residual Stresses in Electric Discharge Machining. PhD Thesis, Middle East Technical University, Graduate School of Natural And Applied Sciences, Ankara

[33] Tebedge, N., Alpsten, G. & Tall, L. (1973) Residual-stress measurement by the sectioning method. *Experimental Mechanics* 13, 88–96. https://doi.org/10.1007/BF02322389

[34] Dege, B. (2013). TiN İnce Filmlerde Bias Voltajına Bağlı Olarak Kalıntı Gerilme Değişiminin İncelenmesi. Yüksek Lisans Tezi, İstanbul Teknik Üniversitesi Fen Bilimleri Enstitüsü, İstanbul

[35] Arnold, D. Gordon., Beauchamp, T. L., & Bowie, N. E. (2014). *Ethical theory and business*. Pearson Education Limited.

[36] Prevéy, P. S. (1986). X-Ray Diffraction Residual Stress Techniques. *Metals Handbook, 10*, American Society for Metals, 1986, pp. 380-392.

[37] Venkata Ramana, P., Madhusudhan Reddy, G., Mohandas, T., & Gupta, A. V. S. S. K. S. (2010). Microstructure and residual stress distribution of similar and dissimilar electron beam welds - Maraging steel to medium alloy medium carbon steel. *Materials and Design*, *31*(2), 749–760. https://doi.org/10.1016/j.matdes.2009.08.007

[38] Baldi, A. (2016). Using Optical Interferometry to Restart the Ring-Core Method. *Experimental Mechanics*, *56*(7), 1191–1202. https://doi.org/10.1007/s11340-016-0163-0

[39] Masláková, K., Trebuňa, F., Frankovský, P., & Binda, M. (2012). Applications of the strain gauge for determination of residual stresses using Ring-core method. *Procedia Engineering*, *48*, 396–401. https://doi.org/10.1016/j.proeng.2012.09.531

[40] Shokrieh, M. M., & Ghasemi K., A. R. (2007). Determination of calibration factors of the hole drilling method for orthotropic composites using an exact solution. *Journal of Composite Materials*, *41*(19), 2293–2311. https://doi.org/10.1177/0021998307075443

[41] Hosseinzadeh, F., Hossain, S., Truman, C. E., & Smith, D. J. (2014). Measurement and Prediction of Residual Stresses in Quenched Stainless Steel Components. *Experimental Mechanics*, *54*(7), 1151–1162. https://doi.org/10.1007/s11340-014-9890-2

[42] Brown, D. W., Holden, T. M., Clausen, B., Prime, M. B., Sisneros, T. A., Swenson, H., & Vaja, J. (2011). Critical comparison of two independent measurements of residual stress in an electron-beam welded uranium cylinder: Neutron diffraction and the contour method. *Acta Materialia*, *59*(3), 864–873. https://doi.org/10.1016/j.actamat.2010.09.022

[43] D'Elia, C. R., Carlson, S. S., Stanfield, M. L., Prime, M. B., Araújo de Oliveira, J., Spradlin, T. J., Lévesque, J. B., & Hill, M. R. (2020). Interlaboratory Reproducibility of Contour Method Data Analysis and Residual Stress Calculation. *Experimental Mechanics*, *60*(6), 833–845. https://doi.org/10.1007/s11340-020-00599-0

[44] Wang, H., Kim, D. K., Woo, W., Choi, S. H., Lee, S. Y., & Hwang, S. K. (2020). A new contour method for rapid evaluation of the cross-sectional residual stress distribution in complex geometries using a 3D scanner. *Journal of Mechanical Science and Technology*, *34*(5), 1989–1996. https://doi.org/10.1007/s12206-020-0420-0

[45] Robinson, J. S., & Redington, W. (2015). The influence of alloy composition on residual stresses in heat treated aluminium alloys. *Materials Characterization*, *105*, 47–55. https://doi.org/10.1016/j.matchar.2015.04.017

[46] Javadi, Y., Akhlaghi, M., & Najafabadi, M. A. (2013). Using finite element and ultrasonic method to evaluate welding longitudinal residual stress through the thickness in austenitic stainless steel plates. *Materials and Design*, *45*, 628–642. https://doi.org/10.1016/j.matdes.2012.09.038

[47] Zhan, Y., Liu, C., Kong, X., & Lin, Z. (2017). Experiment and numerical simulation for laser ultrasonic measurement of residual stress. *Ultrasonics*, *73*, 271–276. https://doi.org/10.1016/j.ultras.2016.08.013

[48] Smith, M., Levesque, J. B., Bichler, L., Sediako, D., Gholipour, J., & Wanjara, P. (2017). Residual stress analysis in linear friction welded in-service Inconel 718 superalloy via neutron diffraction and contour method approaches. *Materials Science and Engineering: A*, *691*, 168–179. https://doi.org/10.1016/j.msea.2017.03.038

[49] Özel, A., Sadri S. (1998). Effects of Residual Stresses Caused by Different Types of Loading on Silent Chain Strength. *Turkish Journal of Engineering and Environmental Sciences* 22 461-470.

[50] Zhang, K., Yang, Z., & Li, Y. (2013). A method for predicting the curing residual stress for CFRP/Al adhesive single-lap joints. *International Journal of Adhesion and Adhesives*, *46*, 7–13. https://doi.org/10.1016/j.ijadhadh.2013.05.010

[51] Cai, Z., Mayr, P., Fernandez, R., Robbe, S., Usmial, E., Lefebvre, F., To, L., Schajer, G. S., Withers, P. J., & Roy, M. J. (2024). Residual Stress Determination of Cast Aluminium Benchmark Components Using Strain Relief Techniques. *Experimental Mechanics*, *64*(3), 441–452. https://doi.org/10.1007/s11340-024-01033-5

[52] Johnson, E. M., Watkins, T. R., Schmidlin, J. E., & Dutler, S. A. (2012). A benchmark study on casting residual stress. *Metallurgical and Materials Transactions A: Physical Metallurgy and Materials Science*, *43*(5), 1487–1496. https://doi.org/10.1007/s11661-011-0907-5

[53] Menne, R.J., Weiss, U., Brohmer, A., Egner-Walter A., Weber M., P. Oelling P. (2007) Implementation of Casting Simulation for Increased Engine Performance and Reduced Development Time and Costs-Selected Examples from FORD R&D Engine Projects. (n.d.). *28. Internationales Wiener Motorensymposium.*

[54] Jiang, X., Kong, X., Zhang, Z., Wu, Z., Ding, Z., & Guo, M. (2020). Modeling the effects of Undeformed Chip Volume (UCV) on residual stresses during the milling of curved thin-walled parts. *International Journal of*

Mechanical Sciences, *167*. https://doi.org/10.1016/j.ijmecsci.2019.105162

[55] Moon, J. H., Baek, S. M., Lee, S. G., Seong, Y., Amanov, A., Lee, S., & Kim, H. S. (2019). Effects of residual stress on the mechanical properties of copper processed using ultrasonic-nanocrystalline surface modification. *Materials Research Letters*, *7*(3), 97–102. https://doi.org/10.1080/21663831.2018.1560370

[56] Robinson, J. S., Tanner, D. A., Truman, C. E., & Wimpory, R. C. (2011). Measurement and Prediction of Machining Induced Redistribution of Residual Stress in the Aluminium Alloy 7449. *Experimental Mechanics*, *51*(6), 981–993. https://doi.org/10.1007/s11340-010-9389-4

[57] Li, P., Maijer, D. M., Lindley, T. C., & Lee, P. D. (2007). Simulating the residual stress in an A356 automotive wheel and its impact on fatigue life. *Metallurgical and Materials Transactions B: Process Metallurgy and Materials Processing Science*, *38*(4), 505–515. https://doi.org/10.1007/s11663-007-9050-5

[58] Godlewski, L. A., Su, X., Pollock, T. M., & Allison, J. E. (2013). The effect of aging on the relaxation of residual stress in cast aluminum. *Metallurgical and Materials Transactions A: Physical Metallurgy and Materials Science*, *44*(10), 4809–4818. https://doi.org/10.1007/s11661-013-1800-1

[59] Zhang, Z., Li, L., Yang, Y., He, N., & Zhao, W. (2014). Machining distortion minimization for the manufacturing of aeronautical structure. *International Journal of Advanced Manufacturing Technology*, *73*(9–12), 1765–1773. https://doi.org/10.1007/s00170-014-5994-1

[60] Masoudi, S., Amini, S., Saeidi, E., & Eslami-Chalander, H. (2015). Effect of machining-induced residual stress on the distortion of thin-walled parts. *International Journal of Advanced Manufacturing Technology*, *76*(1–4), 597–608. https://doi.org/10.1007/s00170-014-6281-x

[61] Mantle, A. L., & Aspinwall, D. K. (2001). Surface integrity of a high speed milled gamma titanium aluminide. *Journal of Materials Processing Technology*. Volume 118, Issues 1–3, 3 December 2001, Pages 143-150. https://doi.org/10.1016/S0924-0136(01)00914-1

[62] Liu, C. R., & Guo, Y. B. (2000). Finite element analysis of the effect of sequential cuts and toolchip friction on residual stresses in a machined layer. In *International Journal of Mechanical Sciences* (Vol. 42).

[63] Prime, M. B. (2018) The Two-Way Relationship Between Residual Stress and Fatigue Fracture. *Fracture, Fatigue, Failure and Damage Evolution, Volume 7*, Springer International Publishing

[64] M, P., Prasad, A. K., & Paswan, M. K. (2020). Durability improvement of axle housings by compressive residual stress inducement. *Applied Materials Today*, *19*. https://doi.org/10.1016/j.apmt.2020.100584

[65] Kutsal, U., Arslan, Y., Ozaydin, O., Akyildiz, Y., Yigit Kaya, A., & Ertugrul, O. (2024). Heat Treatment Simulation of Aluminum Alloy Wheels and Investigation of Process Steps. *International Journal of Metalcasting*, *18*(2), 1556–1572. https://doi.org/10.1007/s40962-023-01132-4

[66] Lin, J., Ma, N., Liu, X., & Lei, Y. (2020). Modification of residual stress distribution in welded joint of titanium alloy with multi electron beam heating. *Journal of Materials Processing Technology*, *278*. https://doi.org/10.1016/j.jmatprotec.2019.116504

[67] Yang, X., Zhu, J., Nong, Z., Lai, Z., & He, D. (2013). FEM simulation of quenching process in A357 aluminum alloy cylindrical bars and reduction of quench residual stress through cold stretching process. *Computational Materials Science*, *69*, 396–413. https://doi.org/10.1016/j.commatsci.2012.11.024

[68] Kattoura, M., Telang, A., Mannava, S. R., Qian, D., & Vasudevan, V. K. (2018). Effect of Ultrasonic Nanocrystal Surface Modification on residual stress, microstructure and fatigue behavior of ATI 718Plus alloy. *Materials Science and Engineering: A*, *711*, 364–377. https://doi.org/10.1016/j.msea.2017.11.043

[69] Wyatt, J. E., Berry, J. T., & Williams, A. R. (2007). Residual stresses in aluminum castings. *Journal of Materials Processing Technology*, *191*(1–3), 170–173. https://doi.org/10.1016/j.jmatprotec.2007.03.018

[70] Roveda, I., Serrano-Munoz, I., Haubrich, J., Requena, G., & Madia, M. (2023). Influence of post-process heat treatments on the fatigue crack propagation behaviour of a PBF-LB/M AlSi10Mg alloy. *International Journal of Fatigue*, *175*. https://doi.org/10.1016/j.ijfatigue.2023.107808

[71] Robinson, J. S., & Tanner, D. A. (2003). Residual stress development and relief in high strength aluminium alloys using standard and retrogression thermal treatments. *Materials Science and Technology*, *19*(4), 512–518. https://doi.org/10.1179/026708303225001939

[72] Mohamed, Serageldin & Samuel, A. & Doty, H. & Valtierra, Salvador & Samuel, Fawzy. (2020). Generation and Relaxation of Residual Stresses in Automotive Cylinder Blocks. *Automotive System Engineering-New Methods and Optimal Solutions* 10.5772/intechopen.93664.

Dicle University
Journal of Engineering
https://dergipark.org.tr/tr/pub/dumf
duje.dicle.edu.tr

Araştırma Makalesi / Research Article

Hibrit Kompozit Kolonlarda Burkulma Analizi

Buckling Analysis of Hybrid Composite Columns

Hüseyin KARADUMAN[1*], Şemsettin TEMİZ[2]

[1] İnönü Üniversitesi, Mühendislik Fakültesi, Makine Mühendisliği Anabilim Dalı, huseynkrdmn44@gmail.com
ORCID: https://orcid.org/0009-0000-9144-7040

[2] İnönü Üniversitesi, Mühendislik Fakültesi, Makine Mühendisliği Anabilim Dalı, semsettin.temiz@inonu.edu.tr
ORCID: https://orcid.org/0000-0002-6737-3720

MAKALE BİLGİLERİ

Makale Geçmişi:

Geliş 17 Haziran 2025
Revizyon 14 Ekim 2025
Kabul 27 Ekim 2025
Online 30 Aralık 2025

Anahtar Kelimeler:

kompozit, burkulma, ansys, sayısal analiz, hibrit

ÖZ

Bu çalışma, betonarme kolonların burkulma dayanımını artırmak amacıyla hibrit kompozit kaplama sistemlerinin performansını sonlu elemanlar yöntemiyle incelemektedir. Burkulma, özellikle deprem etkileri altında uzun ve ince elemanlarda kritik bir stabilite problemi oluşturmaktadır. Çalışmada, 28.5 mm çapında ve 300 mm uzunluğunda C30 beton çekirdek ve dört adet S355 çelik donatı içeren kolon modeli referans alınmış, dış yüzeye altı katmanlı karbon, kevlar ve cam fiber/epoksi kaplama uygulanmıştır. Tüm modeller ANSYS 2024 R2 ortamında ACP modülü kullanılarak hazırlanmış; fiber yönelimleri eksenel (0°) ve enine (90°) olarak belirlenmiş ve kritik burkulma yükleri hesaplanmıştır. Sonuçlar, fiber yönelimi ve malzeme diziliminin burkulma dayanımı üzerinde belirleyici olduğunu göstermektedir. 0° yönelimli yapılarda kapasite referansa göre %161'e kadar artmış, en yüksek değer tamamen karbon esaslı (CCCCCC) konfigürasyonda 892.69 kN olarak elde edilmiştir. Kevlar esaslı yapı %41.6, cam fiberli yapı %0.9 artış sağlamıştır. Hibrit dizilimlerden GGAACC (%74.4), AGCAGC (%71.2) ve GACGAC (%71.8) optimum rijitlik ve enerji yutma dengesi sunmuştur. Buna karşılık, 90° yönelimli tüm konfigürasyonlar referansın altında kalmış, en düşük değer Kevlar esaslı yapıda %19.7 düşüşle elde edilmiştir. Sonuç olarak, karbon fiber yüksek elastisite modülü sayesinde en etkin katkıyı sağlamış, kevlar süneklik ve enerji sönümleme özellikleriyle destekleyici rol oynamış, cam fiber ise hibrit yapılarda dengeleyici bir etki göstermiştir. Bu yönüyle çalışma, betonarme kolonlarda hibrit fiber dizilimlerinin burkulma davranışına etkisini sayısal olarak inceleyen güncel ve özgün bir araştırmadır.

ARTICLE INFO

Article history:

Received 17 June 2025
Received in revised form 14 October 2025
Accepted 27 October 2025
Available online 30 December 2025

Keywords:

composite, buckling, ansys,numerical simulation, hybrid

Doi: 10.24012/dumf.1721326

* Sorumlu Yazar

ABSTRACT

This study investigates the performance of hybrid composite coating systems to enhance the buckling resistance of reinforced concrete columns through numerical analyses based on the finite element method. Buckling is a critical stability issue, particularly for slender members under seismic loading. In this research, a column model consisting of a C30 concrete core with a diameter of 28.5 mm and a length of 300 mm, reinforced by four S355 steel bars, was considered as the reference. The outer surface was coated with six layers of carbon, Kevlar, and glass fiber/epoxy composites. All models were developed using the ACP module of ANSYS 2024 R2, where fiber orientations were defined as axial (0°) and transverse (90°), and the critical buckling loads were calculated. The results indicate that fiber orientation and material sequence have a decisive influence on buckling strength. In 0°-oriented structures, the load-carrying capacity increased up to 161% compared to the reference, reaching the maximum value of 892.69 kN in the fully carbon-based configuration (CCCCCC). Kevlar- and glass-fiber-based configurations exhibited increases of 41.6% and 0.9%, respectively. Among hybrid sequences, GGAACC (74.4%), AGCAGC (71.2%), and GACGAC (71.8%) provided optimal rigidity–energy absorption balance. Conversely, all 90°-oriented configurations performed below the reference, with the lowest capacity (−19.7%) observed in the Kevlar-based structure. Overall, the results demonstrate that carbon fibers provide the most effective enhancement due to their high elastic modulus, Kevlar fibers contribute ductility and energy absorption, and glass fibers play a balancing role in hybrid structures. Hence, this study presents a recent and original numerical investigation addressing the effect of hybrid fiber configurations on the buckling behavior of reinforced concrete columns.

Giriş

Kompozit malzemeler, hafif yapılarıyla birlikte yüksek dayanım sunmaları ve farklı çalışma koşullarına uyum gösterebilmeleri nedeniyle mühendislik uygulamalarında önemli bir yer edinmiştir [1]. Farklı fiziksel ve kimyasal özelliklere sahip birden fazla bileşenin bir araya getirilmesiyle oluşturulan bu çok fazlı yapılar, hem mekanik hem de çevresel performansı artırmak amacıyla tasarlanmaktadır. Matris ve takviye fazlarının kombinasyonu sayesinde bu malzemeler, hem taşıma kapasitesi hem de şekillendirme açısından önemli avantajlar sunmaktadır [2].

Günümüzde kompozit malzemeler; havacılık, otomotiv, inşaat ve savunma sanayii gibi yüksek performans gerektiren birçok sektörde yaygın şekilde kullanılmaktadır. Bu malzemelerin anizotropik yapısı, fiber yönelimi, katman dizilimi ve üretim süreci gibi parametrelerle optimize edilebildiğinden, belirli mühendislik ihtiyaçlarına özel çözümler geliştirilmesine olanak sağlamaktadır [1], [2].

Kompozit bir yapının burkulma gibi stabilite sorunları altındaki performansı; sadece malzeme özelliklerine değil, aynı zamanda iç yapının geometrisine, katman konfigürasyonuna ve üretim tekniğine de bağlıdır. Özellikle uzun ve ince yapı elemanlarında karşılaşılan burkulma, eksenel yükleme altında ani stabilite kaybı ile ortaya çıkar. Bu nedenle, kompozitlerle güçlendirilmiş yapıların burkulma davranışının doğru şekilde modellenmesi ve değerlendirilmesi, yapısal güvenlik açısından büyük önem taşımaktadır. Bu doğrultuda teorik yaklaşımların yanı sıra sonlu elemanlar yöntemi gibi sayısal analiz teknikleri de yaygın olarak kullanılmaktadır [3].

Literatürde bu konuyla ilgili birçok çalışma mevcuttur. Kompozit plakaların burkulma analizi yapılmış, simetrik lif yönelimi ve belirli katman sıralamalarının dayanım açısından avantaj sağladığı tespit edilmiştir [4]. Farklı çekirdek geometrilerine sahip bal peteği sandviç yapılar üzerinde yapılan analizlerde, çekirdek kalınlığının yapısal dayanım üzerinde önemli etkiler yarattığı ortaya konmuştur [5]. Doğal fiber bazlı hibrit yapıların darbe dayanımı açısından karbon fiber alternatifi olarak değerlendirilebileceği belirtilmiştir [6]. EPS köpük çekirdekli sandviç kirişlerin burkulma davranışı sayısal ve deneysel olarak incelenmiş, doğrusal olmayan analizlerle yüksek doğruluk elde edilmiştir [7]. İnce cidarlı silindirik kabukların eksenel yük altındaki davranışları detaylı parametre analizleriyle değerlendirilmiştir [8]. Ankastre mesnetli kompozit kirişlerin burkulma davranışı hem deneysel hem de sayısal olarak analiz edilmiş, model doğruluğu test edilmiştir [9]. Kompozit plakaların burkulma sonrası davranışlarında sayısal yöntemlerin deneysel verilerle örtüştüğü görülmüştür [10]. Fiber açısının ve kesit oranlarının burkulma üzerindeki etkileri, dikdörtgen kesitli tüplerde sonlu elemanlar yöntemiyle modellenmiştir [11]. Hibrit fiberli kirişlerin yanal burkulma dayanımı test edilmiş ve bazı dizilimlerin daha yüksek kritik yüklere ulaştığı belirlenmiştir [12]. Eğri çubuklarda fiber yönelimi ve eğrilik parametrelerinin burkulma ve doğal frekans üzerindeki etkileri değerlendirilmiştir [13]. Köpük dolgulu petek yapıların burkulma dayanımında deneysel olarak artış sağlandığı gösterilmiştir [14]. Farklı fiber açılarında yapılan sayısal analizlerde, 0° fiber yöneliminin en yüksek dayanımı ve doğal frekansı sağladığı, buna karşın 45° ve 90° yönelimlerin daha düşük mukavemet sergilediği rapor edilmiştir [15]. Tip V hidrojen depolama tanklarında Kevlar, Cam elyaf, Karbon ve Bazalt/epoksi kompozitleri karşılaştırılmış; Kevlar'ın düşük yoğunluğu sayesinde en yüksek yapısal verimliliği sunduğu, E-glass'ın ise orta düzeyde mekanik performans sağladığı görülmüştür [16]. Son yıllarda kompozit malzemeler, özellikle havacılıkta kullanılan rijitlendirilmiş panellerde, yüksek özgül dayanım ve hafiflik avantajları nedeniyle yaygın olarak tercih edilmektedir. Bu panellerin burkulma ve burkulma sonrası davranışlarını deneysel, analitik ve sayısal açıdan inceleyen kapsamlı çalışmalar, tasarım optimizasyonu için önemli veriler sunmuştur [17]. Non-hibrit ve hibrit FRP'lerle (C, G, A; AC, GA, CG) güçlendirilmiş beton numunelerde yapılan deneylerde, FRP sarımlarının basınç, eğilme ve çekme dayanımını önemli ölçüde artırdığı ve özellikle hibrit kombinasyonların süneklik kazandırarak kırılma davranışını iyileştirdiği belirlenmiştir [18]. Farklı fiber türlerinin ve dokuma yoğunluklarının çekme, eğilme ve darbe özelliklerini doğrudan etkilediği; bazalt ile Kevlar katkısının darbe dayanımını belirgin şekilde artırdığı tespit edilmiştir [19]. Aramid ve cam fiberlerin farklı tabaka dizilimlerinin burkulma yükü üzerinde belirleyici olduğu, aramid dış katmanlı yapıların yaklaşık %25–30 daha yüksek dayanım sağladığı rapor edilmiştir [20]. Epoksi matrisli selüloz mikrofibril takviyeli kompozitlerde yapılan analizlerde, optimum parametrelerle doğal fiber takviyeli kompozitlerin sentetik kompozitlerle benzer burkulma dayanımı gösterebildiği ortaya konmuştur [21]. Trapezoidal şekilli kompozit plakalarda cut-out oranı ve geometrik formun kritik burkulma yükü üzerindeki etkilerinin sonlu eleman ve RSM analizleriyle optimize edildiği görülmüştür [22]. Cam ve mısır sapı fiberleriyle güçlendirilmiş epoksi matrisli hibrit kompozitlerin mekanik ve yapısal özellikleri incelenmiş; 25 wt% cam + 5 wt% mısır sapı içeren numunenin en yüksek basma dayanımı ve elastisite modülünü sağladığı rapor edilmiştir [23]. Örgü desenine bağlı olarak fiber yollarının kompozit tabakalardaki burkulma davranışına etkisi analitik, deneysel ve sayısal olarak incelenmiş; hibrit takviyeli numunelerin kritik burkulma yüklerinin, uniform tabakalara göre daha yüksek olduğu belirlenmiştir [24]. Sandviç kompozit panellerin burkulma davranışını incelemek için geliştirilen değişken kinematik temelli sonlu eleman modellerinde, hem küresel hem de yerel burkulma modlarının yüksek doğrulukla tespit edildiği görülmüştür [25].

Literatürde kompozit yapıların burkulma davranışına ilişkin çok sayıda çalışma bulunmakla birlikte, bu araştırmalar çoğunlukla plakalar, kabuklar veya sandviç yapılar gibi idealize edilmiş elemanlarla sınırlı kalmıştır. Betonarme kolonların hibrit kompozit kaplamalarla güçlendirilmesi üzerine yapılan çalışmalar ise oldukça sınırlıdır. Mevcut araştırmaların büyük bölümü yalnızca tek tip fiber takviyesine odaklanmış, çok katmanlı hibrit konfigürasyonların burkulma davranışı üzerindeki karmaşık etkileri yeterince incelenmemiştir. Ayrıca, çoğu çalışmada fiber yönelimi tek eksenli olarak ele alınmış, farklı fiber tiplerinin yönelim kombinasyonları arasındaki etkileşimler araştırma dışında bırakılmıştır.

Bu çalışma, literatürdeki bu boşluğu doldurmayı ve hibrit kompozit kaplamalı betonarme kolon sistemlerine ilişkin kapsamlı bir değerlendirme sunmayı hedeflemektedir.

Çalışmada, C30 beton çekirdek ve S355 çelik donatıdan oluşan kolonların dış yüzeyine altı katmanlı hibrit kompozit kaplamalar uygulanmış; karbon, kevlar ve cam fiber/epoksi tabakalar hem saf hem de hibrit konfigürasyonlarla modellenmiştir. Fiber yönelimleri 0° ve 90° olacak şekilde sistematik biçimde değiştirilerek, farklı malzeme dizilimlerinin burkulma dayanımı, eksenel rijitlik, süneklik ve enerji yutma kapasitesi üzerindeki çok boyutlu etkileri ortaya konmuştur.

Bu çalışmanın en önemli yeniliği, hibrit kompozit kolon kavramının hem malzeme hem de analiz düzeyinde bütüncül olarak ele alınmasıdır. ANSYS 2024 R2 ortamında gerçekleştirilen sonlu eleman analizleri, teorik Euler tabanlı burkulma hesaplamalarıyla karşılaştırılarak doğrulanmış; böylece sayısal modelin hem geometrik hem de malzeme bazlı güvenilirliği sağlanmıştır. Ayrıca, bu yaklaşım, literatürde genellikle yalnızca tek eksenli doğrusal analizlerle sınırlı olan burkulma çalışmalarına kıyasla, çok katmanlı ve çok yönlü hibrit fiber konfigürasyonlarının etkisini kapsamlı biçimde değerlendiren özgün bir metodolojik çerçeve sunmaktadır.

Elde edilen bulgular, hibrit fiber kaplamaların özellikle deprem bölgelerinde yer alan betonarme kolonların burkulma dayanımını ve enerji sönümleme kapasitesini anlamlı ölçüde artırdığını göstermektedir. Bu sonuçlar, yalnızca teorik düzeyde bilgi üretmekle kalmayıp, retrofitting (güçlendirme) uygulamalarında kullanılabilecek yeni nesil hibrit kompozit sistemlerin tasarımına yönelik somut mühendislik önerileri sunmaktadır. Böylece çalışma, kompozit malzeme teknolojisi ile betonarme yapı mühendisliği arasındaki etkileşimi birleştiren, güncel ve uygulamaya dönük bir araştırma yaklaşımı ortaya koymaktadır.

Materyal ve Metot

Bu çalışmada, betonarme çekirdek üzerine çok katmanlı kompozit kaplama uygulanmış hibrit silindirik yapıların burkulma dayanımları, sonlu elemanlar yöntemi (Finite Element Method – FEM) kullanılarak analiz edilmiştir. Geliştirilen model, beton–çelik–kompozit etkileşimini birlikte değerlendiren üç temel bileşenden oluşmaktadır; C30 sınıfı beton çekirdek, S355 yapı çeliği donatı çubukları ve Çok katmanlı fiber takviyeli kompozit dış kaplama.

Modelin genel görünümü Şekil 1'de verilmiştir. İç çekirdek, 28.5 mm çapında ve 300 mm uzunluğunda olup, C30 sınıfı beton malzemeyle modellenmiştir. Çekirdek içinde, merkez eksenden 7.5 mm uzaklıkta ve birbirine göre 90° simetrik olarak konumlandırılmış dört adet Ø4 mm S355 çelik donatı yer almaktadır. Bu donatılar, kolonun eksenel rijitliğini artırarak betonun süneklik davranışına katkı sağlamaktadır. Yapının en dış tabakası, 1.5 mm kalınlığında çok katmanlı kompozit kaplama olarak modellenmiştir. Bu kaplama, her biri 0.25 mm kalınlığında olmak üzere altı katmandan oluşmaktadır. Katmanlar; Epoksi–Karbon Fiber, Epoksi–Kevlar (Aramid) Fiber ve Epoksi–Cam Fiber malzemelerden oluşan saf veya hibrit kombinasyonlar şeklinde tanımlanmıştır. Bu malzemeler, farklı elastisite modülleri ve yoğunluk değerleri sayesinde sistemin burkulma rijitliğini çeşitli oranlarda etkileyebilmektedir.

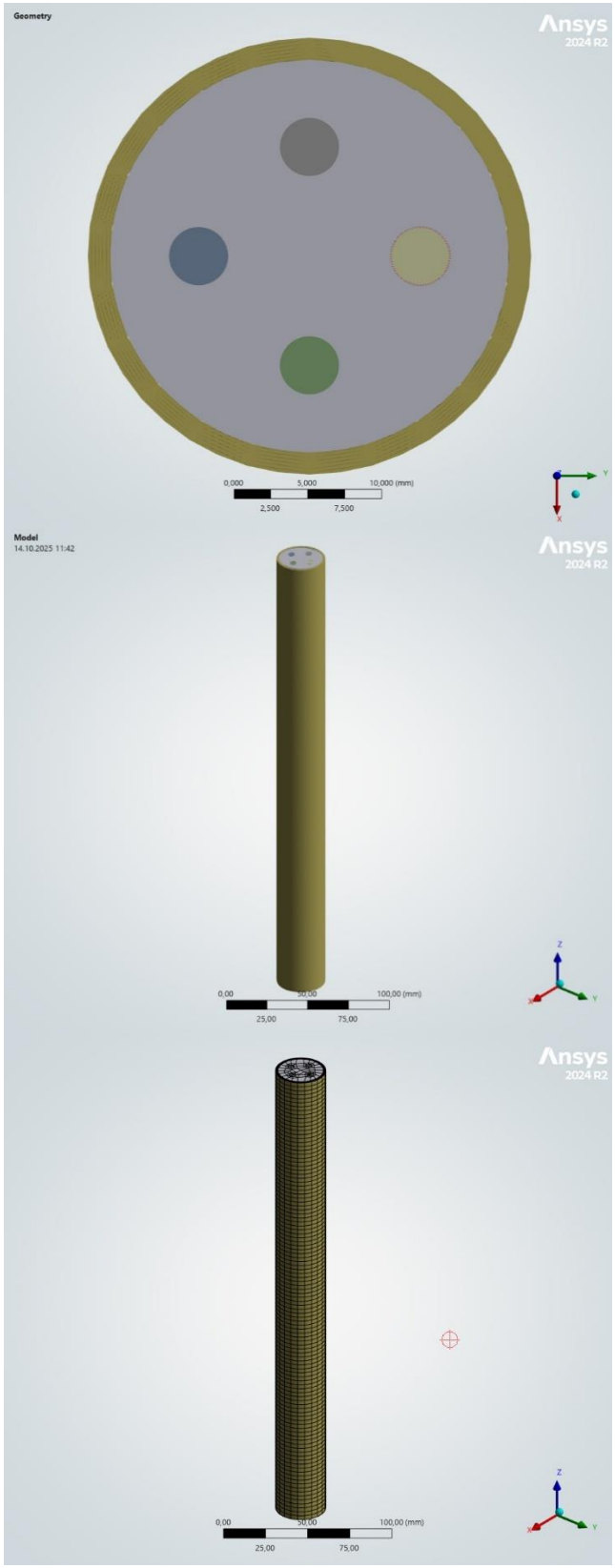

Şekil 1. Modelin görünümleri ve mesh görüntüsü

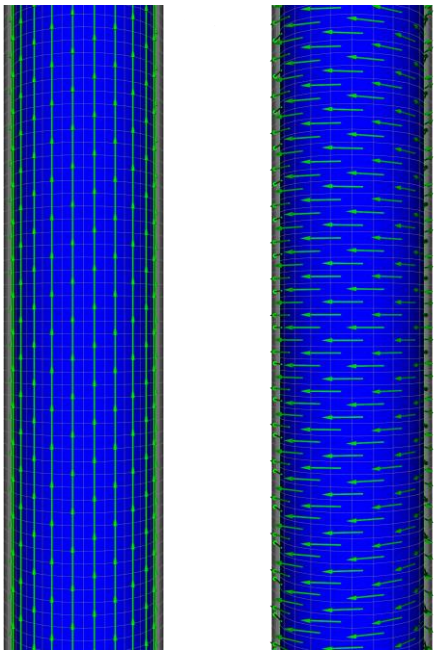

Şekil 2. Fiber açılarının görünümü (0°- 90°)

Fiber yönelimleri Şekil 2'de gösterildiği üzere 0° (eksenel) ve 90° (enine) olmak üzere iki farklı konfigürasyonda değerlendirilmiştir.

0° yönelimi, yük eksenine paralel fiberlerin eksenel taşıma kapasitesini artırdığı durumları,

90° yönelimi ise çevresel (hoop) doğrultuda yerleşen fiberlerin kabuk rijitliği üzerindeki etkilerini temsil etmektedir.

Her analiz senaryosunda, tüm katmanlara aynı fiber yönelimi atanmış ve bu sayede farklı malzeme türleri arasında doğrudan karşılaştırma yapılması sağlanmıştır.

Modelleme çalışmaları ANSYS 2024 R2 yazılımı içerisinde yer alan ACP (Composite PrepPost) modülü kullanılarak gerçekleştirilmiştir. Kompozit katmanlar tek tek tanımlanmış, fiber yönelimleri, dizilim sıraları ve malzeme türleri analiz senaryolarına göre değiştirilmiştir.

Meshleme işlemi, çözüm süresi ile doğruluk arasında optimum denge sağlanacak şekilde yapılmıştır. Model, üç boyutlu 8 düğüm noktalı hexahedral (SOLID186) elemanlarla ağ yapısına kavuşturulmuştur. Ortalama eleman boyutu 5 mm olarak belirlenmiş, burkulma modlarının doğru yakalanabilmesi için yüksek gerilme yoğunluklu bölgelerde ağ yoğunluğu artırılmıştır.

Bu yaklaşım, hem çözüm kararlılığını hem de mod şekillerinin sayısal doğruluğunu yükseltmiş; farklı fiber yönelimleri ve malzeme kombinasyonları arasında hassas kıyaslama yapılmasına olanak tanımıştır. Şekil 3'te, burkulma analizine ait ANSYS Workbench proje düzeni, Şekil 1'de ise modelin genel mesh yapısı sunulmuştur.

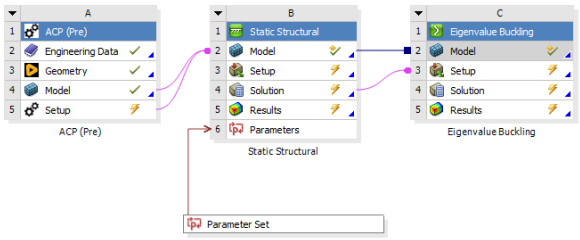

Şekil 3. Ansys proje düzeni

Sınır koşulları Şekil 4'te verilmiştir. Modelin alt ucu tüm yönlerde tam ankastre (x = 0, y = 0, z = 0) olacak şekilde sabitlenmiş; üst ucu ise yalnızca z ekseni doğrultusunda serbest bırakılmıştır. Bu sınır koşulu, bir ucu ankastre, diğer ucu pimli kolon davranışını temsil etmektedir.

Her analizde modele 1 N'luk referans eksenel yük uygulanmış ve ANSYS tarafından hesaplanan yük çarpanı (load multiplier) değeriyle çarpılarak kritik burkulma yükü elde edilmiştir.

Analizler sonucunda her konfigürasyon için ilk burkulma modu ve bu moda karşılık gelen kritik yük değeri belirlenmiştir. Burkulma mod şekilleri görsel olarak değerlendirilmiş ve kritik yük artışları, referans (kaplamasız) yapı ile karşılaştırılarak yorumlanmıştır.

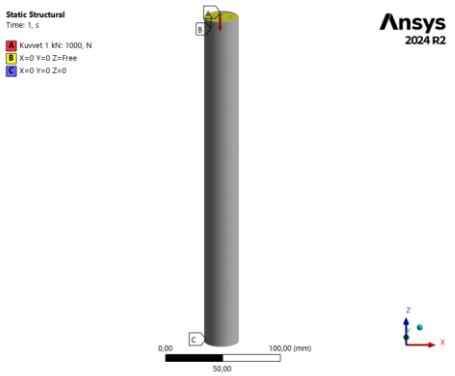

Şekil 4. Modelin sınır şartları

Tablo 1. Ortotropik Malzemelerin Mekanik Özellikleri

	Epoksi Cam Fiber [16]	**Epoksi Karbon Fiber [15]**	**Epoksi Kevlar Fiber [16]**
Yoğunluk (ρ) (kg/m³)	1800	1800	1380
Elastisite (GPa) (Ex/Ey/Ez)	30.9/7.33/7.33	230/23/23	80/5.5/5.5
Poisson Oranı (vxy/vyz/vxz)	0.281/0.448/0.281	0.2/0.4/0.2	0.34/0.4/0.34
Kayma Modülü (GPa) (Gxy/Gyz/Gxz)	2.69/2.53/2.69	9/8/9	2.2/1.8/2.2

Tablo 2. İzotropik Malzemelerin Mekanik Özellikleri

	Beton(C30) [27]	**S355 [26], [28], [29]**
Yoğunluk (ρ) (kg/m³)	2500	7850
Elastisite (GPa)	32	210
Poisson Oranı	0.2	0.3
Akma Mukavemeti (MPa)	-	355
Çekme Mukavemeti (MPa)	1.9	510
Basınçta Akma Mukavemeti (MPa)	30	-

Malzemelerin mekanik özellikleri Tablo 1 ile Tablo 2'de izotropik ve otrotropik olarak belirtilmiştir. Bu çalışmada kullanılan malzemeler, hem ulusal/uluslararası standartlar hem de güncel literatürde rapor edilen mekanik özellikler dikkate alınarak seçilmiştir. Betonarme çekirdek malzemesi olarak C30 sınıfı beton, Türkiye'de betonarme yapıların tasarımında temel referans olan TS500 – Betonarme Yapıların Tasarım ve Yapım Kuralları standartlarından seçilmiştir. Donatı malzemesi olarak seçilen S355 yapı çeliği, hem Avrupa standardı Eurocode 3 (EN 1993-1-1) kapsamında çelik yapıların genel tasarım kurallarıyla uyumlu, hem de TS EN 10025-2 ve TS EN 10025-3 standartlarında mekanik özellikleri, çekme dayanımı ve akma sınırları ayrıntılı şekilde tanımlanmış bir çelik sınıfıdır ve bu standartlardan mekanik özellikleri seçilmiştir. Dış kaplama malzemeleri ise literatürde rapor edilen üstünlükleri nedeniyle tercih edilmiştir: Karbon fiber/epoksi, yüksek elastisite modülü ve rijitliği sayesinde burkulma dayanımını artırma potansiyeliyle öne çıkmaktadır ve kaynakçada 15 numaralı makaleden mekanik özellikleri seçilmiştir (Noman ve ark., 2023); Kevlar (aramid) fiber/epoksi, düşük yoğunluğu ve enerji yutma kapasitesi sayesinde kaynakçada 16 numaralı makaleden mekanik özellikleri seçilmiştir (Jaber ve ark., 2024) ; Cam fiber/epoksi ise orta düzey mekanik özellikleri hibrit yapılarda dengeleyici takviye olduğundan özellikleri yine kaynakçada 16 numaralı makaleden seçilmiştir (Jaber ve ark., 2024) . Böylece seçilen malzemeler, standartlara uygunluğu ve literatürdeki bilimsel bulgularla desteklenmiş özellikleriyle, hibrit kompozit sistemlerin burkulma performansını değerlendirmek için sağlam bir temel oluşturmuş ve elde edilen mekanik özellikler Engineering Data içerisine manuel olarak girilmiş, ACP modülü içerisinde katman tanım aşamasında doğru malzeme olarak referans verilerek kullanılmıştır. Malzeme tanımlamaları, ANSYS Engineering Data modülünde yapılmıştır. İzotrop ve ortotropik malzemeler için ilgili elastisite modülleri (Ex, Ey, Ez), kayma modülleri (Gxy, Gyz, Gxz), Poisson oranları (vxy, vyz, vxz) ve yoğunluk (ρ) gibi tüm parametreler ayrı ayrı girilmiştir. C30 beton ve S355 çeliği için izotropik özellikler atanırken, kompozit malzemeler (Epoksi Kevlar Fiber, Epoksi Karbon Fiber, Epoksi Cam Fiber) ortotropik olarak tanımlanmıştır.

Kıyaslama amacıyla, Şekil 5'te gösterilen referans model oluşturulmuştur. Bu model, kompozit kaplama içermeyen ancak aynı boyutlara sahip bir betonarme kolon sistemidir. Dıştan dışa 30 mm çapında, 300 mm uzunluğunda ve C30 betondan oluşan çekirdek içinde, aynı konumlarda dört adet Ø4 mm S355 donatı bulunmaktadır.

Bu referans yapı, tüm kompozit kaplamalı modellerle aynı sınır koşulları altında analiz edilmiştir. Böylece, farklı fiber kombinasyonlarının burkulma dayanımı üzerindeki katkısı, referans modelle oransal olarak karşılaştırılmıştır. Elde edilen kritik yük değerleri, hibrit kompozit kaplamaların burkulma performansını artırmadaki etkinliğini açıkça ortaya koymuştur.

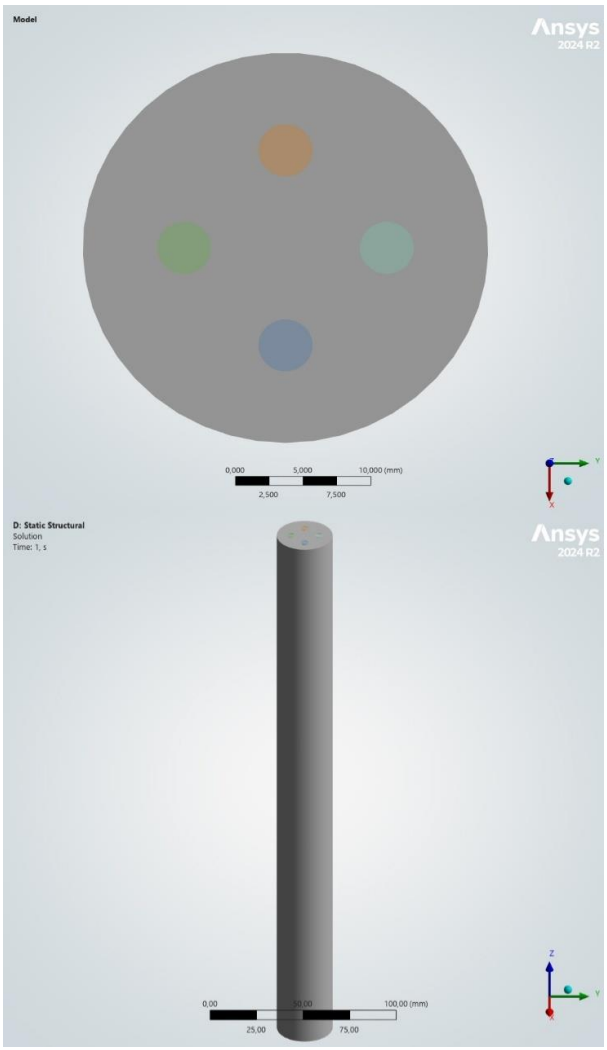

Şekil 5. Referans model

Katman tanımı

Modelde anlaşılır kolaylık amacıyla katman isimleri kısaltmalara kategorize edilip, açıklamaları Tablo 3'te detayları ile belirtilmişitir.

A: Epoksi Kevlar Fiber (Aramid)

C: Epoksi Karbon Fiber

G: Epoksi Cam Fiber

Tablo 3. Katman dizilimleri ve açıklamaları

Katman Dizilimi	Anlamı (İçten dışa)
AAAAAA	Tüm katmanlar Kevlar
CCCCCC	Tüm katmanlar Karbon
GGGGGG	Tüm katmanlar Cam
AACCGG	İçte Kevlar, ortada Karbon, dışta Cam
ACGACG	Kevlar–Karbon–Cam dizilimi, 2 kez tekrar
AGCAGC	Kevlar–Cam–Karbon dizilimi, 2 kez tekrar
CAGCAG	Karbon–Kevlar–Cam dizilimi, 2 kez tekrar
CCGGAA	İçte Karbon, ortada Cam, dışta Kevlar
GACGAC	Cam–Kevlar–Karbon dizilimi, 2 kez tekrar
GGAACC	İçte Cam, ortada Kevlar, dışta Karbon
REFERANS	Kompozit kaplama yok; sadece beton ve çelik çekirdek

ACP (ANSYS Composite PrepPost) modülünde tanımlanan kompozit kaplamalı yapının dış yüzey kalınlık dağılımı, Şekil 6'da gösterilmiştir. Dış kaplama, toplam altı katmandan (ply) oluşacak şekilde modellenmiş ve her bir katmanın kalınlığı 0.25 mm olarak belirlenmiştir. Böylece, tüm katmanların toplam kalınlığı 1.5 mm olacak biçimde sabit tutulmuştur.

Bu kalınlık, modelin gerçekçi kompozit kaplama davranışını temsil etmesi ve fiber-matris oranının (fiber volume fraction) literatürde önerilen sınırlar içinde kalması açısından uygun bulunmuştur. Katman kalınlıklarının eşit seçilmesi, analizlerde homojen bir çevresel dağılım elde edilmesini sağlamış; bu sayede burkulma davranışının yalnızca malzeme kombinasyonuna ve fiber yönelimine bağlı değişimini izole edebilmek mümkün olmuştur.

Kaplama kalınlığı, çekirdek etrafında 360° boyunca eşit olacak şekilde tanımlanmış ve toplam dış çap 30 mm olarak modellenmiştir. Bu yaklaşım, hem malzeme sürekliliğini (material continuity) hem de analiz doğruluğunu artırmakta; ayrıca, beton–çelik–kompozit etkileşiminde oluşabilecek gerilme süreksizliklerinin sayısal olarak dengelenmesini sağlamaktadır. Böylece sistem, burkulma analizi açısından geometrik olarak ideal silindirik forma sahip, eksene simetrik bir hibrit yapı olarak modellenmiştir.

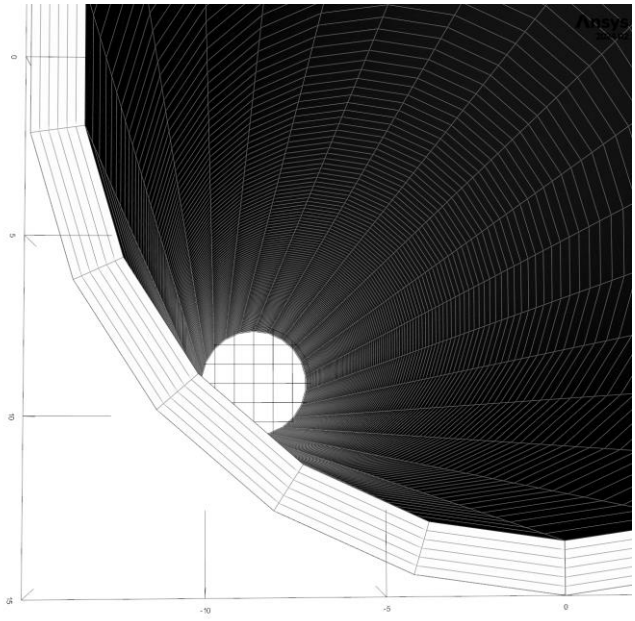

Şekil 6. Kompozit katmanların görünümü

Modellemenin doğruluğunun değerlendirilmesi

Modellemenin doğruluğunu değerlendirmek amacıyla, burkulma analiz sonucu Şekil 7'de verilen çapı 30 mm ve uzunluğu 300 mm olan S355 yapı çeliğinden bir çubuğun kritik burkulma yükü hem teorik yöntemlerle hem de ANSYS simülasyonu ile hesaplanmıştır. Teorik hesaplamalar sonucunda elde edilen 1868.681 kN büyüklüğündeki kritik burkulma kuvveti ile ANSYS analizinden elde edilen 1815.300 kN'luk sonuç arasında yüksek bir örtüşme oranı olan %97'lık bir örtüşme gözlemlenmiştir. Bu yakınlık, oluşturulan sonlu elemanlar modelinin hem doğru hem de güvenilir bir şekilde çalıştığını ortaya koymakta; analitik ve sayısal yöntemlerin uyum içinde olduğunu göstermektedir.

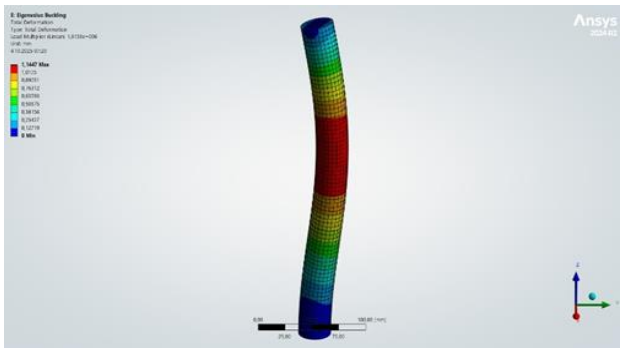

Şekil 7. S355 çeliği burkulma analizi

Sonuçlar ve Tartışma

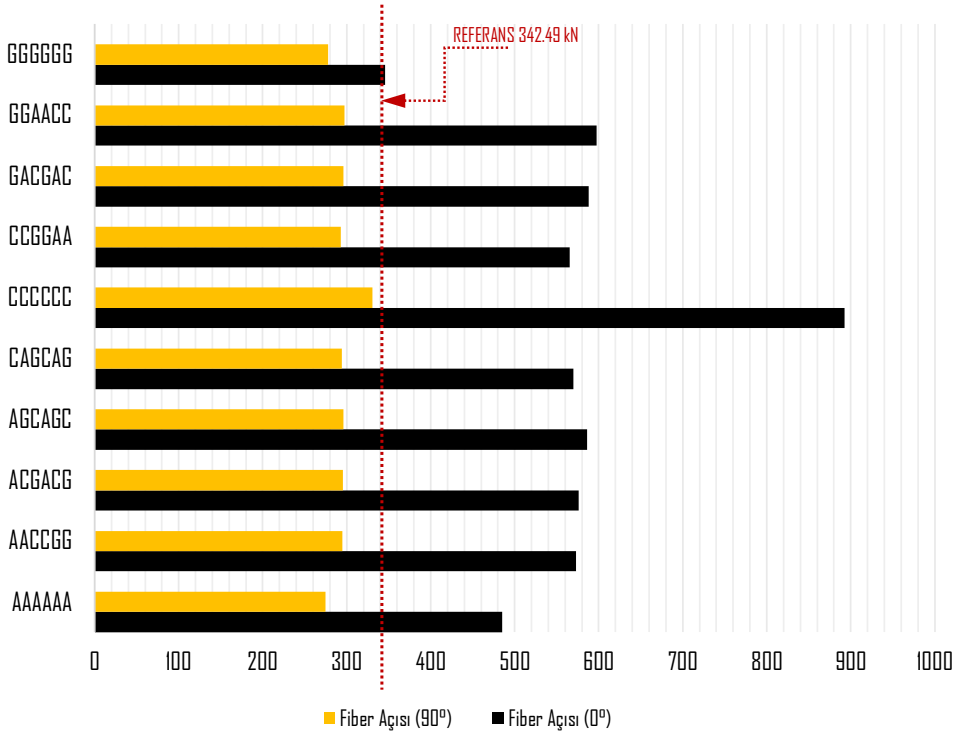

Şekil 8. Burkulma analizi grafiği (Pcr, kN) 0°/90°

Bu bölümde, altı katmandan oluşan kompozit kaplamalı hibrit yapıların farklı malzeme kombinasyonları ve fiber yönelimlerine göre elde edilen kritik burkulma yükleri değerlendirilmiştir. Analizler sonucunda elde edilen sayısal veriler Şekil 8'de grafiksel olarak, Tablo 4'te ise sayısal olarak sunulmuştur. Grafikte her bir yapı konfigürasyonu için 0° (eksenel) ve 90° (enine) fiber yönelimleri altında elde edilen burkulma yükleri karşılaştırmalı olarak verilmiştir.

Verilere göre, 0° fiber yönelimi altında en yüksek burkulma dayanımı 892.69 kN ile CCCCCC konfigürasyonunda elde edilmiştir. Bu yapı, yüksek elastisite modülüne sahip epoksi/karbon fiber tabakalarının eksenel yönde hizalanması sayesinde, referans modele (342.49 kN) göre yaklaşık %161 daha yüksek dayanım sunmuştur.

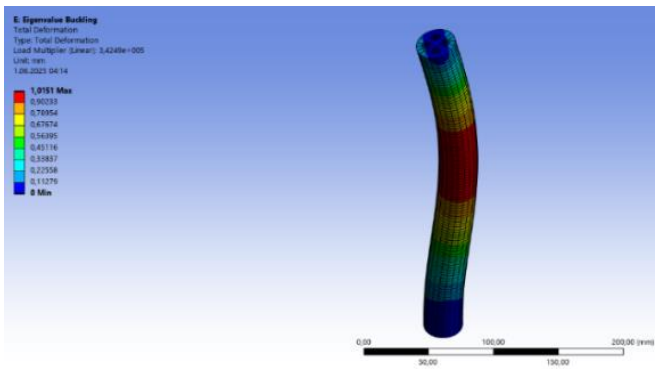

Şekil 9. Referans yapı burkulma analizi

Tablo 4. Burkulma analizi sonuçları

Konfigürasyon	Fiber Açısı 0° (kN)	Fiber Açısı 90° (kN)
AACCGG	573.27	295.06
ACGACG	576.42	295.2
AGCAGC	586.16	296.29
CAGCAG	569.78	294.25
CCCCCC	892.69	330.57
CCGGAA	565.39	293.14
GACGAC	588.31	296.2
GGAACC	597.35	297.11
GGGGGG	345.65	277.65
REFERANS		342.49

İkinci en yüksek değer, 597.35 kN ile GGAACC konfigürasyonunda gözlenmiştir. Bu yapı, cam, karbon ve Kevlar fiberlerinin dengeli dağılımı sayesinde hem rijitlik hem de enerji yutma kapasitesi sağlamıştır. Diğer başarılı hibrit kombinasyonlar arasında GACGAC (588.31 kN), AGCAGC (586.16 kN) ve ACGACG (576.42 kN) dizilimleri yer almaktadır. Bu sonuçlar, malzeme kombinasyonlarının uygun şekilde optimize edilmesi durumunda hibrit yapıların oldukça yüksek performans sergileyebileceğini göstermektedir.

Tablo 5. Referans yapıya göre burkulma kuvvetlerinin yüzdesel karşılaştırılmaları

Konfigürasyon	Fiber Açısı 0° (%)	Fiber Açısı 90° (%)
AAAAAA	41.65	-19.75
AACCGG	67.4	-13.85
ACGACG	68.33	-13.81
AGCAGC	71.18	-13.49
CAGCAG	66.35	-14.09
CCCCCC	160.69	-3.48
CCGGAA	65.07	-14.41
GACGAC	71.79	-13.51
GGAACC	74.4	-13.25
GGGGGG	0.92	-18.94

Not: Referans yapı 342.49 kN'dur ve bu değere göre yüzdesel sonuçlar karşılaştırılmıştır.

Yapılan karşılaştırmalı değerlendirmede CCCCCC konfigürasyonu, ortalama olarak tüm hibrit dizilimlerden %45–60 daha yüksek kapasiteye sahiptir. Bununla birlikte, GGAACC, GACGAC ve AGCAGC dizilimleri arasında fark yalnızca %0.3–1.8 düzeyinde olup, bu üç konfigürasyon yüksek rijitlik–enerji yutma dengesi bakımından optimum yapısal davranış göstermiştir. En yakın performanslı çiftlerden AGCAGC–GACGAC arasındaki fark %0.37, ACGACG–AACCGG arasındaki fark ise %0.55 olarak belirlenmiştir. Bu da hibrit konfigürasyonların belirli bir aralıkta benzer performans gösterdiğini ve küçük malzeme dağılım değişimlerinin dayanım üzerinde sınırlı etki yarattığını göstermektedir.

Fiberlerin eksenel doğrultuda hizalanması (0°), yüklemenin uygulandığı eksende maksimum rijitlik sağladığı için genel olarak tüm 0° fiber yönelimli yapıların daha yüksek burkulma dayanımı elde ettiği gözlemlenmiştir. Diğer yandan, 90° fiber yönelimiyle düzenlenen tüm konfigürasyonlarda elde edilen kritik burkulma yükleri, referans yapının burkulma dayanımı olan 342.49 kN'un altında kalmıştır. Bu durum, yüklemenin eksenel doğrultuda uygulandığı sistemlerde fiberlerin enine yerleşiminin yapısal rijitliğe yeterli katkı sağlamadığını ve bu yöndeki elastisite modülünün düşük olması nedeniyle burkulma direncinin azaldığını göstermektedir.

Örneğin; CCCCCC (330.57 kN), GGAACC (297.11 kN), GACGAC (296.20 kN), AGCAGC (296.29 kN) ve ACGACG (295.20 kN) gibi yüksek performanslı 90° konfigürasyonlar dahi referans yapının altında kalmıştır. Özellikle AAAAAA (Kevlar) konfigürasyonu 274.86 kN ile en düşük kritik burkulma yükünü vermiştir. Kevlar fiberlerin eksen dışı yönlerdeki düşük rijitliği ve enerji sönümleyici yapısı nedeniyle burkulma direncinde sınırlı performans sergilediği gözlenmiştir.

Yönelim değişimi açısından değerlendirildiğinde, 0°'den 90°'ye geçildiğinde en yüksek düşüş CCCCCC yapısında %61.7, hibritlerde ise ortalama %48–50 seviyesindedir. Bu durum, tamamen karbon içeren sistemlerin maksimum rijitlik sağlarken, yönelim değişimine karşı en hassas yapı olduklarını; buna karşılık hibrit konfigürasyonların yük yönü değişimlerine daha dayanıklı ve kararlı bir davranış sergilediğini göstermektedir.

Özellikle Epoksi Kevlar Fiber esaslı AAAAAA konfigürasyonu, 274.86 kN ile en düşük kritik burkulma yükünü vermiştir. Bu yapı, Kevlar'ın eksen dışı yönlerdeki düşük rijitliği ve enerji sönümleyici yapısı nedeniyle burkulma direncinde sınırlı performans sergilemiştir. Bu bulgular, fiber yöneliminin yapısal performans üzerindeki etkisini net biçimde ortaya koymakta ve fiber yerleşiminin eksenel yükleme doğrultusuna göre optimize edilmesi gerektiğini göstermektedir. Şekil 10'da en yüksek ve en düşük değere sahip burkulma analizi sonuç görüntüleri verilmiştir.

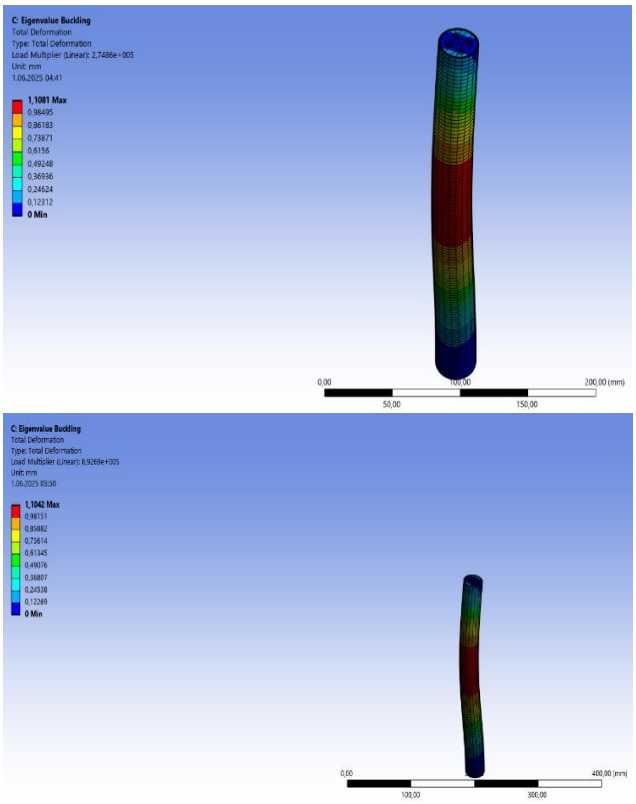

Şekil 10. En yüksek ve en düşük burkulma değerleri

Bu bulgular, 0° fiber yöneliminin burkulma dayanımını artırmada ne kadar etkili olduğunu açıkça ortaya koymaktadır. Eksenel yönde hizalanmış fiberlerin, yükleme doğrultusuyla paralel bir yapı oluşturması nedeniyle taşıma kapasitesi anlamlı şekilde yükselmiştir. Ayrıca, malzeme çeşitliliği ve katman dizilim kombinasyonlarının da yapısal performans üzerinde önemli rol oynadığı görülmektedir. Özellikle karbon fiber içeren konfigürasyonlar yüksek rijitlik

sağlamış, Kevlar ve cam takviyelerinin dengeli şekilde kullanıldığı hibrit yapılar ise hem dayanım hem de enerji yutma açısından optimum mühendislik performansı sunmuştur.

Genel olarak, karbon fiber tabakalarının oranı arttıkça burkulma kapasitesi belirgin şekilde yükselmiş; Kevlar oranı arttıkça süneklik artmış fakat rijitlik azalmıştır. Cam fiberler ise ara faz davranışı göstererek hibrit sistemlerde dengeleyici bir katkı sunmuştur. Bu durum, tasarım aşamasında hedeflenen yapısal özelliklere göre fiber dizilim oranlarının dikkatle optimize edilmesi gerektiğini göstermektedir.

Bu çalışmada elde edilen sonuçlar, hibrit kompozit kolon sistemleri üzerine yapılmış literatürdeki pek çok güncel araştırmayla genel olarak örtüşmekte, bazı yönleriyle ise yeni ve özgün bulgular sunmaktadır.

Fiber yönelimi açısından bakıldığında, literatürde hem sayısal hem deneysel çalışmalar 0° yönelimli fiberlerin burkulma dayanımını belirgin biçimde artırdığını göstermektedir. [4], [15] ve [20] gibi çalışmalarda 0° fiber doğrultusunun yük aktarımında en etkin yön olduğu rapor edilmiştir. Bu çalışma da aynı eğilimi doğrulamış, 0° yönelimli karbon tabakalı sistemlerin referansa göre %161 daha yüksek burkulma dayanımı sunduğunu göstermiştir. Ancak bu araştırma, söz konusu eğilimi betonarme çekirdekli hibrit kolon sistemi üzerinde göstermesiyle literatürdeki plaka veya panel temelli çalışmalardan ayrılmaktadır.

Malzeme bazında karşılaştırma yapıldığında, literatürde karbon fiberin yüksek elastisite modülüyle rijitliği, Kevlar'ın enerji sönümleme kapasitesiyle sünekliği, cam fiberin ise ara faz etkisiyle deformasyon dengeleme özelliğini artırdığı belirtilmektedir [6], [12], [16]. Bu çalışma da aynı doğrultuda sonuç vermiş; Kevlar tabakalarının tek başına %41.6 artışla sınırlı katkı sağladığı, cam fiberin ise referans seviyesinde kaldığı (%0.9 artış) belirlenmiştir. Farklı olarak, bu araştırma bu üç malzemenin kombinasyonunu aynı kolon sisteminde analiz ederek, karbon–kevlar–cam etkileşimini bütüncül biçimde değerlendirmiştir.

Hibrit konfigürasyonların etkisi bakımından önceki çalışmalarda [17], [18], [24] tabaka diziliminin burkulma kapasitesini doğrudan etkilediği, yüksek modüllü tabakaların dışta, düşük modüllülerin içte konumlandırılmasının optimum performans sağladığı rapor edilmiştir. Bu çalışmada da benzer biçimde, GGAACC, GACGAC ve AGCAGC konfigürasyonlarının rijitlik–enerji yutma açısından en dengeli kombinasyonlar olduğu görülmüştür. Ancak mevcut literatürden farklı olarak bu çalışmada tabaka yönelimlerinin tamamı 3B kolon geometrisi üzerinden değerlendirilmiş; burkulma davranışı yalnızca plaka stabilitesiyle değil, çekirdek-kaplama rijitlik etkileşimiyle ilişkilendirilmiştir. Bu yönüyle, sonuçlar klasik kompozit levha analizlerinin ötesine geçmektedir.

Yönelime bağlı performans kayıpları açısından, literatürde 90° fiber yöneliminin kapasiteyi düşürdüğü rapor edilmiştir [8], [9]. Bu çalışma da bu bulguyu doğrulamış, 90° yönelimde bütün konfigürasyonların referansın altında kaldığını göstermiştir. Ancak, karbon tabakalı yapıların düşüş oranı %61.7 iken, hibrit kombinasyonlarda bu kaybın %45–50 aralığında sınırlı kalması, bu çalışmanın hibrit sistemlerin yönelim değişimlerine karşı dayanıklılığını ilk kez bu düzeyde nicel olarak ortaya koyduğunu göstermektedir.

Burkulma sonrası davranış ve rijitlik sürekliliği açısından literatürde [17], [25] tarafından yapılan incelemelerde rijit yüzey tabakalarının lokal burkulmayı bastırarak genel stabiliteyi artırdığı rapor edilmiştir. Bu araştırmada da karbon tabakalarının yüzeyde kullanılması, kolonun hem global hem lokal burkulma modlarını bastırarak stabiliteyi artırmıştır. Ancak literatürdeki çalışmalar çoğunlukla ince cidarlı kabuklar veya sandviç plakalar üzerinde yürütülürken, bu çalışmada beton çekirdekli kompozit kolon sistemlerinde aynı etkinin doğrulanması özgün bir katkı olarak öne çıkmaktadır.

Süneklik ve enerji yutma kapasitesi açısından literatürde hibrit FRP sistemlerinin deformasyon altında sünekliği artırdığı ve kırılma öncesi enerji birikimini desteklediği belirtilmiştir [12], [18]. Bu çalışma da aynı yönde sonuç vermiş; özellikle Kevlar ve cam tabakalarının karbon ile birlikte kullanılması, yük yönü değişimlerinde rijitliğin korunmasını sağlamıştır. Bu durum, hibrit dizilimlerin sadece yüksek dayanım değil, yük tekrarı altında yapısal kararlılık açısından da avantaj sağladığını göstermektedir.

Sonuç olarak, mevcut literatürde fiber yönelimi, malzeme türü ve katman diziliminin burkulma dayanımına etkisi farklı geometrilerde araştırılmış olsa da; bu çalışma, söz konusu etkileri betonarme çekirdekli hibrit kolon yapısı üzerinde incelemesi, her üç fiber tipini tek sistemde değerlendirmesi ve 0°/90° yönelim farklarını nicel olarak karşılaştırması bakımından özgün bir nitelik taşımaktadır. Bu yönüyle araştırma, literatürde rapor edilen eğilimleri doğrulamakla kalmamış, aynı zamanda hibrit sistemlerin yönelime duyarlılığını azaltarak daha kararlı ve enerji sönümleyici kolonlar oluşturabileceğini göstermiştir.

Sonuç

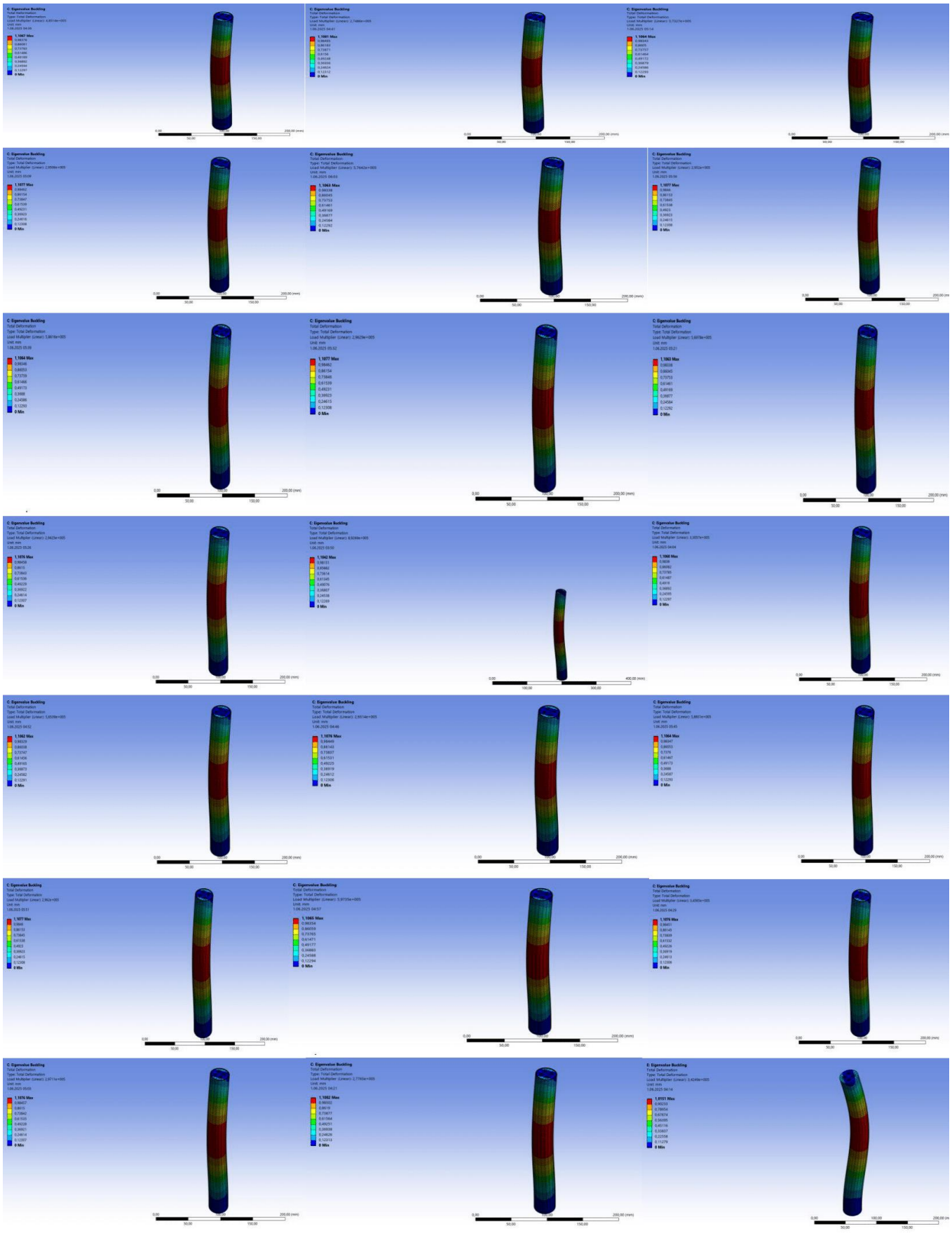

Şekil 11. Burkulma analizleri genel görünüm

Bu çalışma, deprem etkilerine maruz kalabilecek taşıyıcı elemanlarda sıkça karşılaşılan burkulma probleminin, hibrit kompozit kaplama sistemleriyle iyileştirilmesini sayısal olarak analiz etmiştir. C30 beton çekirdek, dört adet S355 çelik donatı ve altı katmanlı fiber takviyeli kompozit kaplamadan oluşan silindirik kolon modeli; farklı malzeme kombinasyonları ve fiber yönelimleri dikkate alınarak toplam yirmi farklı konfigürasyon için ANSYS 2024 R2 ortamında sonlu elemanlar yöntemiyle değerlendirilmiştir. Analiz sonuçları Tablo 4–5 ve Şekil 11'de özetlenmiş, elde edilen burkulma yükleri hem sayısal hem de görsel olarak karşılaştırılmıştır.

Analiz sonuçlarına göre fiber yönelimi, burkulma dayanımı üzerinde en kritik parametre olmuştur. 0° (eksenel) yönelimde tüm konfigürasyonlarda burkulma kapasitesi önemli ölçüde artarken, 90° (enine) yönelimde bu kapasite belirgin biçimde azalmıştır.

En yüksek burkulma yükü, 892.69 kN değeriyle CCCCCC konfigürasyonunda elde edilmiş olup, bu değer referans modelin (342.49 kN) yaklaşık %160.7 üzerinde bulunmuştur. Bu artış, karbon fiberlerin yüksek elastisite modülüne sahip olması ve yükleme ekseniyle paralel yerleşimi sayesinde eksenel rijitliği artırmasından kaynaklanmaktadır.

Buna karşılık, 90° yönelimli tüm modellerde burkulma kapasitesi referans modelin altında kalmıştır. En yüksek değer CCCCCC konfigürasyonunda 330.57 kN (%3.48 düşüş), en düşük değer ise AAAAAA konfigürasyonunda 274.86 kN (%19.7 düşüş) olarak kaydedilmiştir. 0°→90° yön değişiminde kapasite kaybı karbon esaslı yapı için %61.7, hibrit yapılar için ise %48–50 aralığında gerçekleşmiştir. Bu sonuç, hibrit kompozitlerin fiber yönelim değişimlerine karşı daha kararlı ve daha sünek bir davranış sergilediğini açıkça göstermektedir.

Tekil kompozit kaplamalar arasında karbon fiber tabakalar rijitliği en fazla artıran malzeme olmuştur (+%160.7). Kevlar fiberler enerji sönümleme açısından avantaj sağlamış, ancak rijitlik katkısı sınırlı kalmıştır (+%41.6). Cam fiber ise düşük elastisite modülü nedeniyle referans modele oldukça yakın bir değer göstermiştir (+%0.9).

Hibrit dizilimlerde rijitlik ve süneklik dengesi ön plana çıkmıştır.
En başarılı hibrit kombinasyonlar şu şekilde belirlenmiştir:

GGAACC → 597.35 kN (+%74.4),
GACGAC → 588.31 kN (+%71.8),
AGCAGC → 586.16 kN (+%71.2).

Bu üç konfigürasyon arasındaki fark yalnızca %0.3–1.8 düzeyindedir. Bu durum, katman sırasındaki küçük farklılıkların genel burkulma davranışı üzerindeki etkisinin sınırlı olduğunu göstermektedir. Hibrit konfigürasyonlar arasında GGAACC dizilimi, hem yüksek rijitlik hem de optimum enerji yutma kabiliyetiyle öne çıkmıştır. Ayrıca GGAACC konfigürasyonu, AAAAAA'ya göre %23.1, GGGGGG'ye göre ise %72.8 daha yüksek burkulma kapasitesine ulaşmıştır.

Elde edilen bulgular, karbon fiber oranının artmasıyla rijitliğin doğrusal olmayan bir şekilde yükseldiğini; Kevlar ve cam fiber tabakalarının ise sistemin sünekliğini artırarak kırılgan davranışı baskıladığını göstermektedir.

Yeni kolon tasarımlarında, 0° yönelimli karbon ağırlıklı konfigürasyonlar en yüksek dayanımı sağlamaktadır. Önerilen optimum malzeme oranı; %30–40 karbon, %30 Kevlar ve %30 cam olacak şekilde, dışta karbon ve içte Kevlar–cam tabakalarının yer aldığı dizilimdir. Güçlendirme (retrofitting) uygulamalarında ise rijitliğin yanı sıra enerji sönümleme kapasitesi önem kazandığından, dışta karbon ve içte Kevlar/cam kombinasyonları önerilmektedir.

Ekonomik optimizasyon açısından değerlendirildiğinde, karbon tabaka oranının %33'ün üzerinde artırılması burkulma kapasitesini yaklaşık %10 yükseltirken, maliyeti orantısız biçimde artırmaktadır. Bu nedenle GGAACC tipi dizilim, performans–maliyet dengesi açısından optimum çözüm olarak değerlendirilmiştir. Hibrit yapılarda ortalama kapasite artışı %69.2, standart sapma ise ±%3.5 olarak hesaplanmıştır. Bu durum, sistemin kararlı ve öngörülebilir bir mühendislik davranışı sunduğunu kanıtlamaktadır.

Elde edilen sonuçlar, kompozit malzeme mekaniği ile betonarme yapı mühendisliği arasında güçlü bir bağ kurmaktadır. 0° yönelimli karbon tabakalar yük taşıma kapasitesini artırarak global burkulmayı geciktirirken, Kevlar tabakalar tekrarlı yükler altında enerji sönümleme sağlamakta, cam tabakalar ise gerilme geçişlerinde deformasyon dengelemesi yapmaktadır. Bu üç etkinin hibrit bir yapı içerisinde bir araya getirilmesi, özellikle deprem etkisi altındaki kolonlarda hem rijitliği hem de sünekliği aynı anda geliştiren karma bir dayanım mekanizması oluşturmaktadır.

Bu nedenle hibrit kompozit sistemler, hem yeni yapı tasarımlarında hem de mevcut betonarme kolonların dıştan sarılarak güçlendirilmesinde etkin bir çözüm olarak önerilmektedir. Bu tür çalışmalar, hibrit kompozit kolonların gerçek ölçekli davranışlarını daha doğru biçimde modelleyerek tasarım standartlarının geliştirilmesine katkı sağlayacaktır. Sonuç olarak, 0° yönelimli karbon esaslı kompozit kaplamalar kolonların burkulma kapasitesini önemli ölçüde artırmakta; hibrit sistemler ise rijitlik–süneklik dengesini optimize ederek deprem bölgelerinde hem yeni tasarım hem de güçlendirme (retrofitting) uygulamaları için hafif, güvenli ve yüksek performanslı bir mühendislik çözümü sunmaktadır.

Yazar katkı beyanı

İlk gönderimde yazar bilgisi istenmediğinden detay verilmemiştir

Etik kurul onayı ve çıkar çatışması beyanı

"Hazırlanan makalede etik kurul izni alınmasına gerek yoktur". "Hazırlanan makalede herhangi bir kişi/kurum ile çıkar çatışması bulunmamaktadır".

Kaynakça

[1] Abramovich, H. (2017). *Introduction to composite materials*. In *Stability and vibrations of thin-walled composite structures* (pp. 1-47). Woodhead Publishing/Elsevier. https://doi.org/10.1016/B978-0-08-100410-4.00001-6

[2] Phiri, R. (2024). Advances in lightweight composite structures and manufacturing methods. *Heliyon*, 10, Article e15692. https://doi.org/10.1016/j.heliyon.2024.e39661

[3] Al-Masri, R., Rasheed, H. A., & Alali, B. (2025). Buckling Solution of Fixed–Free Anisotropic Laminated Composite Columns Under Axial Loading. *Fibers*, *13*(4), 35. https://doi.org/10.3390/fib13040035

[4] Ahmad, S., & Rajput, L. (2020). Buckling analysis of inter-ply hybrid composite plate. *Materials Today: Proceedings, 21*, 1313–1319. https://doi.org/10.1016/j.matpr.2020.01.168

[5] Öztemiz, H. M. (2024). *Farklı geometriye sahip S şekilli çekirdekli bal peteği sandviç kompozitlerin mekanik davranışlarının araştırılması* (Doktora tezi, İnönü Üniversitesi, Fen Bilimleri Enstitüsü, Makine Mühendisliği Anabilim Dalı).

[6] Çelik, O. (2022). *Karbon fiber kompozitlere alternatif olarak doğal fiber takviyeli hibrit kompozit malzemelerin özellikleri* (Yüksek lisans tezi, Çukurova Üniversitesi, Fen Bilimleri Enstitüsü, Otomotiv Mühendisliği Anabilim Dalı).

[7] Alkeflawi, D. A. H. H. (2018). *Polimerik köpük çekirdekli metal sandviç kirişlerin burkulma ve burkulma sonrası davranışları* (Yüksek lisans tezi, Erciyes Üniversitesi, Fen Bilimleri Enstitüsü, Makine Mühendisliği Anabilim Dalı).

[8] Özgen, C. (2022). *İnce cidarlı kompozit silindirik kabukların statik ve dinamik burkulma analizi üzerine bir çalışma* (Yüksek lisans tezi, İstanbul Teknik Üniversitesi, Lisansüstü Eğitim Enstitüsü, Uçak ve Uzay Mühendisliği Anabilim Dalı).

[9] Eryiğit, E. (2006). *Tabakalı kompozit çubuklarda yanal yük etkisi ile oluşan burkulma* (Yüksek lisans tezi, Dokuz Eylül Üniversitesi, Fen Bilimleri Enstitüsü, Makine Mühendisliği Anabilim Dalı, Mekanik Bilim Dalı).

[10] Namdar, Ö. (2012). *Basma yüklemesi altındaki tabakalı kompozit plakaların burkulma, burkulma sonrası ve ileryen kırılma analizleri* (Yüksek lisans tezi, Orta Doğu Teknik Üniversitesi, Fen Bilimleri Enstitüsü, Makine Mühendisliği Anabilim Dalı).

[11] Alar Öner, G. (2013). İnce cidarlı, tek ve iki hücreli, tabakalı kompozit tüplerde sonlu elemanlar yöntemi ile burulmalı burkulma analizi. *EÜFBED - Fen Bilimleri Enstitüsü Dergisi, 6*(2), 277–300. https://dergipark.org.tr/tr/pub/erzifbed/issue/6027/80710

[12] Öndürücü, A., & Kayıran, H. F. (2018). Hibrit kompozit kirişlerin yanal burkulma davranışlarına soğuk ortamın etkisi. *Süleyman Demirel Üniversitesi Fen Bilimleri Enstitüsü Dergisi, 22*(Özel Sayı), 156–164. https://dergipark.org.tr/tr/pub/sdufenbed/issue/39695/470049

[13] Günyar, A., Öztürk, H., & Sabuncu, M. (2012). Kompozit eğri çubukların doğal frekans ve burkulma yükü analizi. *DEÜ Mühendislik Fakültesi Mühendislik Bilimleri Dergisi, 14*(42), 33–42. https://dergipark.org.tr/tr/pub/deumffmd/issue/40820/492514

[14] Solmaz, M. Y., & Kaman, M. O. (2010). Petek yapılı sandviç yapılarda köpük dolgusunun kritik burkulma yüküne etkisi. *e-Journal of New World Sciences Academy Engineering Sciences, 5*(1A), 24–34. https://dergipark.org.tr/tr/pub/nwsaeng/issue/19863/212873

[15] Noman, A. A., Shohel, S. M., Riyad, S. H., & Sen Gupta, S. (2023). Investigate the mechanical strength of laminated composite carbon fiber with different fiber orientations by numerically using finite element analysis. *Materials Today: Proceedings*. https://doi.org/10.1016/j.matpr.2023.02.132

[16] Jaber, M., Yahya, A., Arif, A. F., Jaber, H., & Alkhedher, M. (2024). Burst pressure performance comparison of type V hydrogen tanks: Evaluating various shapes and materials. *International Journal of Hydrogen Energy, 81*, 906–917. https://doi.org/10.1016/j.ijhydene.2024.07.315

[17] Zhang, Q., Xu, H., Jia, X., Zu, L., Cheng, S., Wang, H., & Chen, M. (2024). Buckling and post-buckling analysis of composite stiffened panels: A ten-year review (2014–2023). *Thin-Walled Structures, 205,* 112525. https://doi.org/10.1016/j.tws.2024.112525

[18] F. Cakir, M.R. Aydin, V. Acar, P. Yildirim, Impact of hybrid and non-hybrid fiber reinforced polymers on mechanical performance of concrete. Constr. Build. Mater. 451, 138806 (2024). https://doi.org/10.1016/j.conbuildmat.2024.138806

[19] Jinwon Cho and Jaehyeung Park 2021 Mater. Res. Express 8 125304 https://doi.org/10.1088/2053-1591/ac406f

[20] Aydin, M.R. A Comprehensive Experimental and Numerical Analysis on Free Vibration and Axial Buckling Behavior of Hybrid Composites. Fibers Polym 26, 4069–4086 (2025). https://doi.org/10.1007/s12221-025-01071-3

[21] Gopalan, V., Vardhan, M. S., Thakur, V., Krishnamoorthy, A., Pragasam, V., Degalahal, M. R., Velu, P. S., Raja Annamalai, A., & Jen, C.-P. (2023). Studies on Numerical Buckling Analysis of Cellulose Microfibrils Reinforced Polymer Composites. Materials, 16(3), 894. https://doi.org/10.3390/ma16030894

[22] Ranjere, M., Rajanna, T. & Arya, B. Influence of Trapezoidal Shapes and Linearly varying Edge Loads on the Buckling Characteristics of Plates with

Cutouts. *J. Inst. Eng. India Ser. C* 102, 1231–1249 (2021). https://doi.org/10.1007/s40032-021-00735-2

[23] Risa, A.G., Wolla, D.W. Characterization and Finite Element Analysis of Hybrid Glass–Maize Stalk Fibers–Epoxy Composite for Bone Plate Application. *Fibers Polym* 26, 2543–2556 (2025). https://doi.org/10.1007/s12221-025-00964-7

[24] Dabiryan, H., Mazloomi, Z.S. & Sharif-Deljuee, O. Effect of Fiber Path on the Buckling Behavior of Delaminated Composites Reinforced with Woven Fabrics; Analytical and Numerical Study. *Fibers Polym* 25, 1047–1059 (2024). https://doi.org/10.1007/s12221-023-00435-x

[25] Di Cara, G., D'Ottavio, M., & Polit, O. (2024). Variable kinematics finite plate elements for the buckling analysis of sandwich composite panels. Composite Structures, 330, 117856. https://doi.org/10.1016/j.compstruct.2023.117856

[26] European Committee for Standardization (CEN). (2005). *EN 1993-1-1: Eurocode 3: Design of steel structures – Part 1-1: General rules and rules for buildings*. Brussels: CEN. https://www.phd.eng.br/wp-content/uploads/2015/12/en.1993.1.1.2005.pdf

[27] Türk Standartları Enstitüsü. (2000). *TS500 – Betonarme Yapıların Tasarım ve Yapım Kuralları*. Ankara, Türkiye. https://staff.emu.edu.tr/cemalgenes/Documents/courses/INSA471_2019_20_Bahar/TS500.pdf

[28] Türk Standartları Enstitüsü (TSE). (2019). *TS EN 10025-2: Sıcak haddelenmiş yapı çelik ürünleri – Bölüm 2: Teknik teslim şartları için tablo özellikleri* (Standard No. TS EN 10025-2). Ankara, Türkiye: Türk Standartları Enstitüsü.

[29] Türk Standartları Enstitüsü (TSE). (2019). *TS EN 10025-3: Sıcak haddelenmiş yapı çelik ürünleri – Bölüm 3: Normalize/normalize haddeleme sonrası su verme ile işlenmiş yüksek dayanımlı çeliklerin teknik teslim şartları* (Standard No. TS EN 10025-3). Ankara, Türkiye: Türk Standartları Enstitüsü.

[30] Beer, F. P., Johnston, E. R., DeWolf, J. T., & Mazurek, D. F. (2015). *Mechanics of materials* (7th ed.).

[31] Kaw, A. K. (2005). *Mechanics of composite materials* (2nd ed.)

Dicle University
Journal of Engineering
https://dergipark.org.tr/tr/pub/dumf
duje.dicle.edu.tr

Research Article

Energy and Exergy Analysis of a Metal Hydride-Based Hydrogen Storage System: A Parametric Approach

Nesrin İLGİN BEYAZİT[1*]

[1]Dicle University, Electrical-Electronics Engineering Department, nesrinilgin@gmail.com, Orcid No: 0000-0003-4708-9615

ARTICLE INFO

Article history:

Received 1 August 2025
Received in revised form 3 November 2025
Accepted 19 November 2025
Available online 30 December 2025

Keywords:

Hydrogen storage, Metal hydride reactor, Energy analysis, Exergy efficiency, Parametric study, Thermal management

Doi: 10.24012/dumf.1756471

* Corresponding author

ABSTRACT

Hydrogen is considered a promising energy carrier for the global energy transition due to its high energy density and environmental sustainability. However, the efficient storage of hydrogen remains a major technical challenge that limits its large-scale deployment. Metal hydrides (MHs) offer a safe and compact solution, but their thermal management strongly influences storage efficiency.This study conducts a comprehensive energy and exergy analysis of a magnesium hydride (MgH_2)-based storage system to evaluate the combined influence of key parameters: reactor number, outlet temperature, coolant mass flow rate, pump efficiency, ambient temperature, heat transfer coefficient, hydrogen capacity, and the volume-to-surface (V/A) ratio. The numerical model integrates energy–exergy formulations to quantify performance under different operating conditions.The results reveal that increasing the number of reactors enhances exergy efficiency from 21.5% to 64.9%, while higher outlet temperatures and mass flow rates reduce efficiency due to thermal imbalance and pumping losses. In contrast, improving the heat transfer coefficient up to 3000 $W/m^2 \cdot K$ increases efficiency to 73.9%, demonstrating the critical role of thermal design.These findings provide design guidelines for optimizing reactor configuration, flow management, and material selection. The study offers practical insights for engineering applications and supports the development of scalable, high-efficiency MH-based hydrogen storage systems.

Introduction

The global transition toward sustainable energy systems has intensified efforts to reduce dependence on fossil fuels and mitigate environmental degradation. In this context, hydrogen has emerged as a promising energy carrier due to its high gravimetric energy density, environmental friendliness, and flexibility in various applications such as transportation, power generation, and industrial processes [1], [2]. However, one of the major challenges hindering its large-scale adoption is the safe, efficient, and compact storage of hydrogen [3], [4].

Hydrogen can be stored through different methods, including compressed gas, cryogenic liquid storage, chemical carriers, and solid-state materials such as metal hydrides (MHs) [5], [6]. Among these, MH-based systems are particularly attractive because they can store hydrogen at moderate pressures with high volumetric density and enhanced operational safety [7]. Recent developments in MgH_2- and TiFe-based materials, driven by nanostructural engineering and alloy modification, have enhanced reaction kinetics and cycling stability [8]–[10]. In parallel, high-entropy alloys (HEAs) have emerged as new candidates for reversible hydrogen storage due to their tunable thermodynamic and mechanical properties [11]–[13].

Thermal management is a key factor that determines the performance of MH reactors. Efficient removal or supply of heat during absorption and desorption directly influences hydrogen kinetics and overall system efficiency [14], [15]. Hence, parameters such as reactor configuration, heat exchanger geometry, coolant mass flow rate, ambient temperature, and the volume-to-surface area (V/A) ratio are crucial for optimizing energy and exergy performance [16]–[18].

Numerous experimental and numerical studies have explored these aspects. For example, Jana and Muthukumar developed a 19-tube bundle reactor (TBR) capable of storing 369 g of hydrogen with 64% energy efficiency under moderate pressures [19], [20]. Parashar and Muthukumar (2024) achieved 82.3% efficiency in a compact multi-tube reactor using Ti–Zr–Mn–V–Fe alloys [21]. Raju and Kumar (2011) demonstrated that helical tube designs, simulated through COMSOL–MATLAB coupling, provide superior heat transfer performance compared to straight tubes [22]. Bai et al. (2021) optimized fin geometries and reduced absorption time by 20.7%, while Liu et al. (2022) showed that multi-heat-transfer-tube (MHTT) designs further improve heat distribution and overall efficiency [23], [24].

Despite these advancements, most existing research has primarily focused on geometric optimization or material enhancement [18], [25]. Comprehensive exergy-based evaluations that simultaneously consider multiple design and operating parameters remain limited [26]. Only a few studies—such as Nyallang and Tolj (2021)—have examined trade-offs between pump power and efficiency, emphasizing the necessity of a comprehensive performance assessment [27].

Therefore, this study comprehensively analyzes the effects of key parameters — such as the number of reactors, inlet temperature of the cooling fluid, mass flow rate, pump efficiency, ambient temperature, heat transfer coefficient, hydrogen loading capacity, and reactor volume-to-surface (V/A) ratio — on the energy and exergy performance of the system. In this context, not only the first-law efficiency but also the second-law (exergy) efficiency is evaluated from a multi-dimensional perspective.

In particular, the combined evaluation of the V/A ratio and pump efficiency, which has been scarcely addressed in the existing literature, quantifies the impact of these parameters on system performance. Hence, this study contributes to the limited body of research by presenting a detailed numerical assessment of their effects.

The remainder of this paper is organized as follows: Section 2 presents the methodology and modeling framework; Section 3 discusses the parametric results; and Section 4 summarizes the main conclusions and engineering implications.

Materials and Methods

In this section, the overall configuration of the metal hydride-based hydrogen storage system investigated in the study is described. The assumptions and boundary conditions employed for the modeling are presented, followed by a detailed formulation of the thermodynamic and exergy equations. Finally, the model validation approach is evaluated. Accordingly, the methodology has been structured not only to outline the computational procedure but also to highlight the similarities and differences of the system with real engineering applications.

System Description and Components

The system analyzed in this work is a compact hydrogen storage configuration consisting of N series-connected metal hydride reactors, a pump, temperature sensors, a coolant reservoir, and pipelines (Fig. 1) [19], [21]. The pump circulates the coolant through the reactors, removing the heat released during the absorption process and maintaining the thermal balance of the system. This configuration is consistent with the experimental multi-tube reactor designs reported in the literature [19], [21].

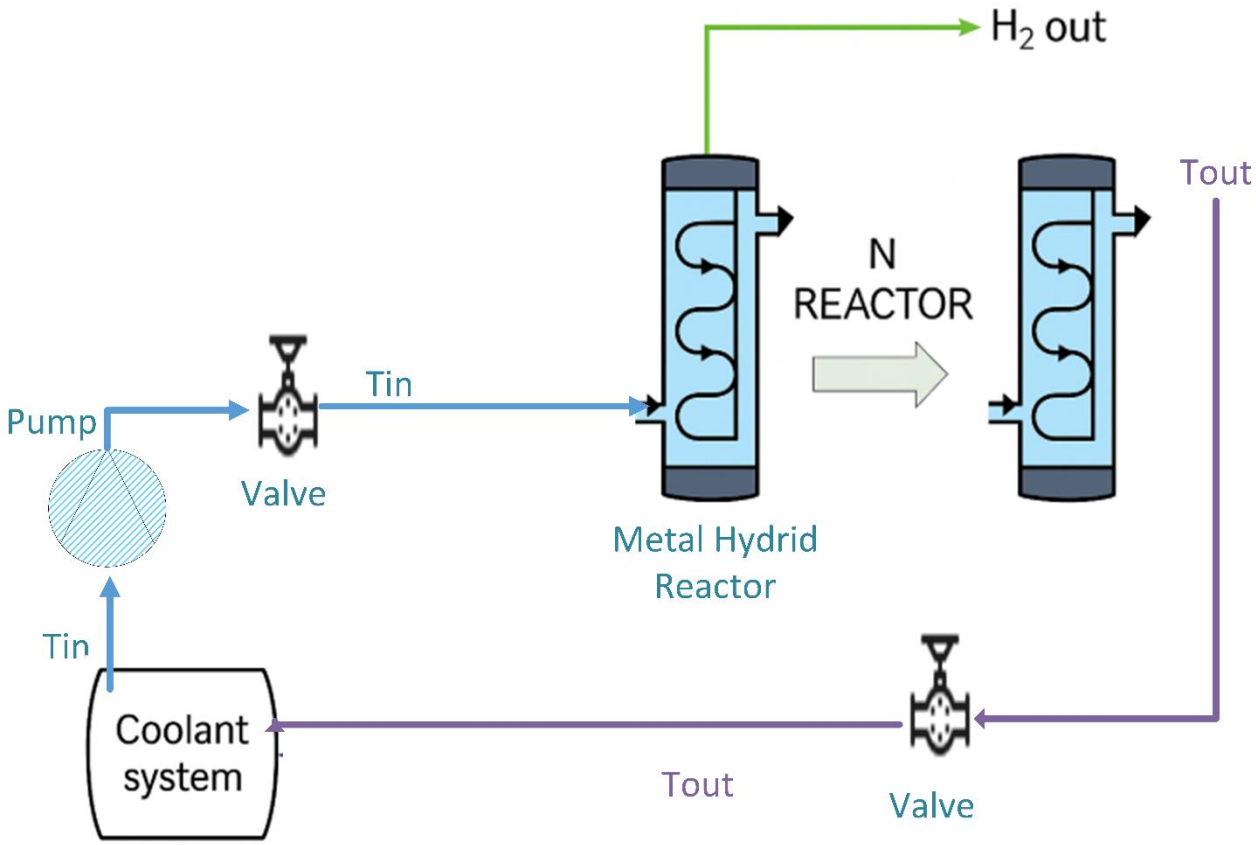

Figure 1. Schematic representation of the metal hydride-based hydrogen storage system

The model systematically investigates the influence of parameters such as ambient temperature, pump efficiency, and reactor volume-to-surface area (V/A) ratio on exergy efficiency, which are often neglected in the literature. Similar approaches have previously been conducted using CFD-based software (e.g., COMSOL, ANSYS Fluent) [22], [24], [25]; however, these studies have typically focused on a single parameter, such as tube geometry or fin configuration. In contrast, the present work addresses this gap by providing a comprehensive multivariable exergy analysis [14], [25].

Assumptions and Boundary Conditions

The main assumptions employed in the model are summarized as follows:

- The metal hydride bed was assumed to be homogeneous, and its thermophysical properties were considered constant. This simplification is consistent with literature where local thermal and mass transfer equilibrium among hydride particles is assumed [19], [25].
- The reactor shell was modeled as adiabatic, and external heat losses were neglected. This assumption is justified by studies reporting that heat losses contribute less than 2% of the total system energy in well-insulated configurations. In the exergy analysis, the ambient temperature was only varied as a reference state, and no physical heat loss to the environment was considered [21], [25].
- The ambient temperature (T_0) was initially taken as 298.15 K but was treated as a variable parameter in the sensitivity analysis to examine the dependence of exergy efficiency on environmental conditions [28].
- Water was selected as the cooling fluid and modeled using forced convection correlations [29]. The choice of water was based on its high specific heat capacity (4.18 kJ/kg·K) and low viscosity, which together maximize heat transfer efficiency inside the reactor.
- The enthalpies of absorption/desorption and the hydrogen storage capacity were adopted from literature data . These represent average values for MgH_2-based systems and were used as reference parameters for comparative evaluation [19], [21].
- The diameter of the cooling channel was assumed to be *d = 0.02 m*, ensuring a forced convection regime while avoiding transition to turbulence, in agreement with similar configurations reported in previous studies[17], [18].

These assumptions are consistent with those applied in comparable experimental and numerical investigations [19], [21], [25]. Each assumption was selected to preserve the physical integrity of the system while reducing computational complexity and ensuring an accurate representation of overall system behavior.

Thermodynamic Modeling

The modeling process was defined to preserve the physical meaning of the energy and exergy equations.

The energy requirement per reactor is expressed as follows [29]:

$$\mathrm{Q_{reactor}} = m_{MH} * \Delta\mathrm{H} * \mathrm{CH2} \quad (1)$$

where m_{MH} is the mass of the metal hydride in the reactor (kg), ΔH is the hydrogen absorption enthalpy (kJ/mol), and C_{H2} is the hydrogen storage capacity per unit mass of MH (mol/kg).

Equation (1) forms the basis of the system's heat balance and represents the change in chemical bond energy during the absorption/desorption process. The energy requirement is directly proportional to the hydrogen saturation capacity of the material [20], [21].

The total system requirement is calculated according to the number of reactors [29]:

$$E_{out} = \mathrm{N} * \mathrm{Q_{reactor}} \quad (2)$$

This equation forms the basis of scalability analysis in multi-reactor systems. While increasing the number of reactors linearly enhances the total energy capacity, it may impose certain limitations on exergy efficiency[25].In this study, it was noted that metal hydrides are not fully utilized in practical applications to their theoretical capacity. Therefore, a conversion ratio (X) was added to the storage unit used in the programming, and this ratio was chosen within the range of 0.5–0.8, typical values reported in the literature. Thus, the usable capacity of the system was modeled similarly to the charge-discharge characteristics of existing batteries.

This approach accounts for the reduction in storage capacity that occurs in practical systems due to material saturation, surface oxidation, and heat transfer limitations [19], [21], [30]. Consequently, the proposed model characterizes the energy storage effectiveness in a manner analogous to the usable charge–discharge ratio observed in electrochemical battery systems.

The governing energy equations in this section were solved through a modular computational algorithm developed in MATLAB R2021a. Each equation was solved iteratively as a function of the system's physical parameters, ensuring both numerical stability and physical consistency. The comparative results of these simulations are illustrated in Figures 2–9 [25], [31].

Heat Transfer Analysis

The heat transfer surface was modeled according to Newton's law of cooling, which establishes the relationship between the convective heat flux and the temperature difference between the surface and the surrounding fluid:

$$\mathrm{h} = \frac{(E_{out} * 1000)}{(\mathrm{A} * \Delta\mathrm{T})} \quad (3)$$

where h is the heat transfer coefficient (W/m²·K), A is the heat transfer area (m²), and ΔT is the temperature difference (K).

The heat transfer coefficient (h) was calculated using forced convection correlations and is directly dependent on the thermophysical properties of the working fluid, including specific heat capacity, density, viscosity, and thermal

conductivity [28], [29], [31]. The classical relationship between the Nusselt (Nu), Reynolds (Re), and Prandtl (Pr) numbers was employed in the correlations.

$$Nu = 0.023 * Re^{0.8} * Pr^{0.4} \quad (4)$$

This expression corresponds to the Dittus–Boelter correlation, commonly applied for estimating the convective heat transfer coefficient in turbulent flow regimes [33]. It provides an empirical relation between the Nusselt number and the Reynolds and Prandtl numbers, ensuring accurate modeling of forced convection heat transfer.

The energy carried by the coolant is given as:The energy carried by the coolant is expressed as:

$$E_{\text{in}} = \dot{m} * cp * (\text{T}_{in} - \text{T}_{out}) * \text{t} \quad (4)$$

where $\dot{m}$ is the mass flow rate of the coolant (kg/s), cp, is the specific heat capacity of the coolant (kJ/kg·K), T_{in} is the inlet temperature (K), and T_{out} is the outlet temperature (K), and t is the cycle time of a reactor (s).

The thermal adequacy of the system was assessed by comparing Ein and Eout. When Ein<Eout , the system is at risk of overheating, whereas for Ein>Eout, cooling is safe but may lead to reduced efficiency.

In this study, in order to better reflect the impact of the heat transfer coefficient (h) on exergy efficiency, the cycle time (t) was assumed to be inversely proportional to hhh (t∝1/h). As h increases, the cycle time decreases, the energy transferred per unit time through the Ein equation rises, and the exergy efficiency of the system improves. This relation represents a simplified model reflecting the trend reported in the literature [19], [21], although in real systems it may vary depending on material properties, reactor geometry, and fluid conditions.

Pump Power Calculation

The power consumed by the pump is expressed as [33]:

$$\text{W}_{\text{pump}} = \frac{\dot{\text{m}} \cdot \Delta\text{P}}{\eta_{\text{pump}} * \rho} \quad (5)$$

where η_{pump} is the pump efficiency, and ρ is the fluid density.

Exergy Analysis

The inlet exergy of the coolant is given as [34]:

$$Exin = \dot{\text{m}} * cp * \left[(\text{T}_{out} - \text{T}_o) - (\text{T}_{in} - \text{T}_o) - \text{T}_o * \ln\left[\frac{\text{T}_{in}}{\text{T}_o}\right]\right] \quad (6)$$

where $\dot{m}$ is the mass flow rate (kg/s), T is the inlet temperature of the coolant (K), T_0 is the ambient temperature (K), and cp is the specific heat capacity at constant pressure (kJ/kg·K).

The useful exergy is calculated as:

$$E_{\text{x,useful}} = \text{Q}_{\text{total}} * \left(1 - \left(\frac{\text{T0}}{\text{Tavg}}\right)\right) \quad (7)$$

With

$$\text{Tavg} = \frac{(\text{Tin} + \text{Tout})}{2} \quad (8)$$

This formulation defines the portion of thermal energy that can be converted into useful work, with reference to the ambient temperature T_0. In the present analysis, the ambient temperature was taken as T_0= 298.15 K (25 °C) as a baseline, but was also varied as a parameter in the Second Law analysis to investigate its influence on exergy efficiency.

The exergy efficiency of the system is defined as the ratio of the net useful work obtained to the total input exergy. In this study, the net work output (W_{net}), the pump power (W_{pump}), and the input exergy supplied by the coolant (Ex_{in}) were used to calculate the exergy efficiency [28]:

$$\text{n}_{\text{ex}} = \frac{E_{\text{x,useful}}}{E_{\text{x.in}} + W_{pump}} \quad (9)$$

The total exergy destruction in the system was determined to evaluate the Second Law losses, using the following expression[28], [34];

$$\text{Ex}_{\text{D}} = E_{\text{x.in}} - E_{\text{x,useful}} \quad (10)$$

Where Ex_{in} is the total inlet exergy carried by the coolant (kJ/s), and Ex_{useful} is the exergy amount effectively converted into useful output (kJ/s).

These analyses allow the energy and exergy performance of the system to be evaluated under different operating scenarios.

Error Analysis

An error analysis was conducted to evaluate the consistency of the model outputs with the experimental data reported in the literature. In this context, the root mean square error (RMSE) and the relative error (Δ%) were calculated as follows:

$$\text{RMSE} = \sqrt{\frac{1}{n}\sum_{i=1}^{n}\left(\eta_{ex,\text{i}}^{model} - \eta_{ex,\text{i}}^{exp}\right)} \quad (11)$$

$$\%\Delta = \frac{\eta_{ex}^{model} - \eta_{ex}^{exp}}{\eta_{exp}} * 100 \quad (12)$$

where η_{ex} refers to the exergy efficiency, with superscripts "model" and "exp" denoting the values obtained from the model and experimental data, respectively. RMSE indicates the overall level of agreement, while the relative error highlights local deviations.

The reliability of the model was assessed in the Results section through an error analysis based on RMSE and relative error, using literature data as reference.

Parametric Analyses

The engineering and thermodynamic parameters used in this study were determined based on a magnesium hydride (MgH_2)–based metal hydride reactor system. Each parameter employed in the model was directly linked to the assumptions defined in Sections 2.2–2.4 and solved using a computational algorithm developed in MATLAB R2021a.

Table 1 presents the fixed assumptions, material properties, and system boundary conditions adopted from the literature. These parameters were selected within the ranges commonly reported in previous studies to ensure both scientific validity and comparability of the model results.

The selection of parameter ranges followed the recommendations of recent works [19], [21], [32], thereby maintaining consistency with established experimental and numerical data. The pump efficiency (η_{pump}) was fixed at 0.7 in the baseline analysis, consistent with the 0.6–0.8 range reported by [25], [29]. To evaluate the system's sensitivity to pump performance, η_{pump} was varied between 0.6 and 0.8, and the resulting trends are illustrated in Figure 5.

The absorption enthalpy of MgH_2, approximately −75 kJ mol^{-1} H_2, is a critical parameter governing the system's heat requirement and forms the thermodynamic basis for both the energy and exergy analyses. This value was used to calculate the temperature-dependent components of the energy balance and exergy efficiency, ensuring physical consistency with the literature.

Table 1. Thermodynamic parameters and assumptions for the MgH_2-based system

Parameter	Symbol	Value	Unit	Description	Source/Note
Mass of metal hydride (per reactor)	m_{MH}	2	kg	Assumed constant per reactor	Assumption
Hydrogen absorption enthalpy	ΔH	−75	kJ/mol H_2	Typical reaction enthalpy for MgH_2	[32]
H_2 storage capacity	C_{H2}	7.6 wt% (≈ 38)	wt% / mol·kg^{-1}	Maximum theoretical H_2 capacity of MgH_2; wt% converted to mol/kg	[32]
Specific heat (water)	cp	4.18	kJ/kg·K	Water used as coolant	[29]
Fluid density (water)	ρ	997	kg/m^3	Assumed constant at 25–30 °C	[29]
Coolant outlet temperature	T_{out}	333.15	K	Varied in the range 50–70 °C	Assumption
Coolant inlet temperature	T_{in}	313.15	K	Assumed as 40 °C	Assumption
Ambient temperature	T_0	298.15	K	Reference temperature (25 °C)	Assumption
Heat transfer coefficient	h	2000	W/m^2·K	Average value for MH heat transfer analyses	[31]
Pump efficiency	η_{pump}	0.7	–	Typical efficiency range in practical systems	Assumption
Pump pressure difference	ΔP	2×10^5	Pa	Typical value for compact systems	Assumption
Average flow velocity	v	1.5	m/s	In-pipe liquid velocity	Assumption
Chemical formula of MH	–	MgH_2	–	Active storage material	Assumption
Pump efficiency	ηpump	0.5	–	Assumed baseline value for pump performance	Assumption

While most studies in the literature focus on single-parameter or limited-variable analyses [19], [21], this study adopts a multi-parameter approach. Parameters including reactor number, inlet temperature, mass flow rate, pump efficiency, ambient temperature, heat transfer coefficient, and the volume-to-surface (V/A) ratio were systematically analyzed from an exergy perspective. This holistic approach not only examines the energy balance but also provides a multidimensional evaluation of Second Law (exergy) efficiency, which is rarely addressed in the literature [22], [24], [25].

Efficiency with Respect to Reactor Number

In metal hydride (MH)-based hydrogen storage systems, the number of reactors is a key design parameter that directly affects the energy and exergy performance.Increasing the number of reactors enhances both the total storage capacity and the available energy output of the system, without

causing a significant change in pump power requirements. This indicates that multi-reactor configurations can offer more sustainable and efficient solutions, particularly for industrial-scale applications. Table 2 presents the MgH_2-based model results for different reactor numbers and allows for comparison with previous studies in the literature. In particular, parameters such as energy output (Eout), pump power (Wpump), and exergy efficiency (ηex) are analyzed to describe the performance variations in detail. Accordingly, the performance improvements achieved with higher reactor numbers can be clearly observed.

Table 2. System performance as a function of reactor number and comparison with literature

System / Study	Reactor Number (N)	Total MH Mass (kg)	Hydrogen Storage (g)	E_{out}	W_{pump} (kJ/s)	η_{ex} (%)
This Study (MgH_2, modeling)	2	10	–	31.67	0.286	21.5
This Study (MgH_2, modeling)	4	20	–	63.33	0.286	43.2
This Study (MgH_2, modeling)	6	30	–	95.00	0.286	64.9
Jana & Muthukumar (2023, TBR) [19]	19	26.5 ($La_{0.8}Ce_{0.2}Ni_5$)	369.1	0.8–1.7	–	58–64
Parashar & Muthukumar (2024, multi-tube compact) [35]	Multi-tube compact	Ti–Zr–Mn–V–Fe alloy	164.3(abs) / 153.6(des)	0.095	–	82.3

The results in Table 2 indicate that the energy output increases almost linearly with the number of reactors, while the exergy efficiency shows a notable improvement. For instance, the exergy efficiency (ηex) increases from 21.5% in the two-reactor system to 64.9% in the six-reactor configuration. The experimental study by Jana and Muthukumar (2023) [19], along with the compact design proposed by Parashar and Muthukumar (2024) [21], demonstrates that high efficiency values can be achieved using alternative alloys and configurations. In this context, although the model results are lower than the literature values at low reactor numbers, they gradually converge with experimental data as the reactor number increases. This trend indicates that the model is scalable.

To further evaluate the model's reliability, Table 2a presents an error analysis in comparison with the literature data reported by Jana (2023) [19], Parashar (2024) [21], and Eisapour (2025) [36]. The root mean square error (RMSE) and relative error (%) values are reported to quantify the level of agreement.

Table 2a. Error analysis of model results compared to literature data (RMSE and relative error)

η_{ex}	$\eta_{Jana2023}$	RMSE (Jana)	Rel. Error (Jana, %)	$\eta_{Parashar2024}$	RMSE (Parashar)	Rel. Error (Parashar, %)	$\eta_{Eisapour2025}$	RMSE (Eisapour)	Rel. Error (Eisapour, %)
17.67	61.0	43.33	−71.04	82.3	64.63	−78.53	31.5	13.83	−43.92
35.33	61.0	25.67	−42.08	82.3	46.97	−57.07	31.5	3.83	12.17
53.00	61.0	8.00	−13.12	82.3	29.30	−35.60	31.5	21.50	68.25

The results in Table 2a indicate that the discrepancies between the model and literature data decrease with an increasing number of reactors. For instance, the relative error with Jana (2023) [19] decreases from −71.04% at two reactors to −13.12% at six reactors. Likewise, when compared with Parashar (2024) [21], the error decreases from −78.53% to −35.60%. The comparison with Eisapour (2025) [36] shows smaller deviations, confirming that the model converges well with literature trends for specific parameters. Therefore, Table 2a demonstrates the model's scalability potential and its ability to align with literature data.

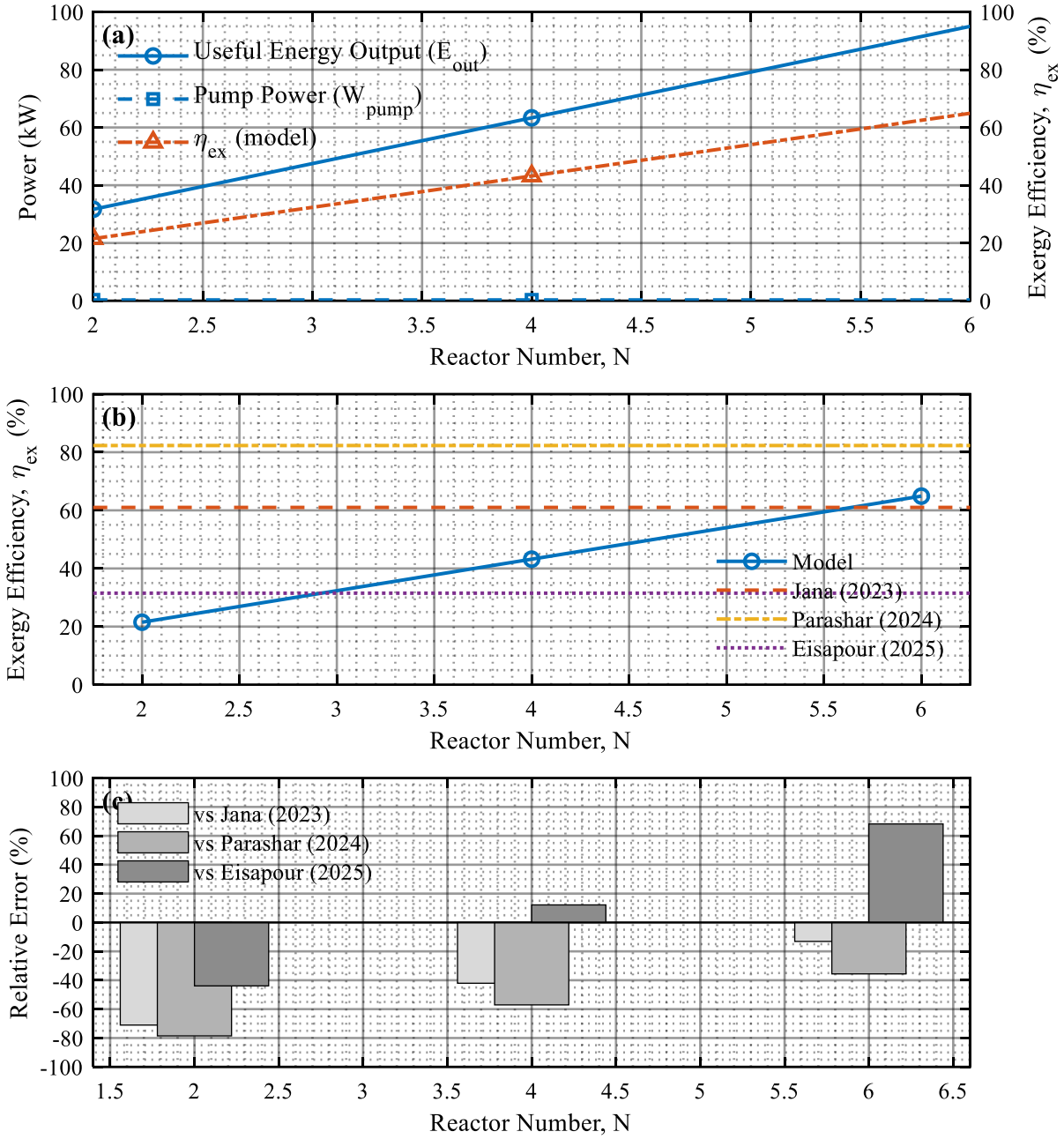

Figure 2. Effect of reactor number on system performance

Figure 2a compares the useful exergy (Exuseful), exergy efficiency (ηex), and pump power (Wpump). As the number of reactors increases, both useful exergy and efficiency increase steadily, while pump power remains almost constant. Figure 2b presents a comparison between the model results and literature data (Jana 2023 [19]; Parashar 2024 [35]; Eisapour 2025 [36]. The model shows closer agreement with literature values as the reactor number increases. Figure 2c depicts the relative error analysis, where deviations are significant at low reactor numbers but decrease markedly at higher ones. These results confirm that the model is scalable and highly consistent with literature data for multi-reactor systems.

Effect of Outlet Temperature

In MH reactors, the outlet temperature is a key factor affecting the system's exergy performance. Hydrogen absorption and desorption are directly dependent on temperature; therefore, variations in outlet temperature strongly impact both available exergy and system efficiency. Analyzing model results at different outlet temperatures (50–70 °C) is essential to identify the optimum operating range. Table 3 presents the results for exergy input (Exin), useful exergy (Exuseful), pump power (Wpump), and exergy efficiency (ηex). It also lists comparative data from Askri (2019) [37], Alqahtani (2024) [38], and Ayub (2020) [39], enabling direct comparison with previous experimental and theoretical studies.

Table 3. Effect of outlet temperature and comparison with literature

T_{out}(°C)	Ex_{in}(kJ/s)	W_{pump}(kJ/s)	η_{ex}(%)
50	2.6166	0.4	65.99
60	6.4236	0.4	35.90
70	11.3507	0.4	24.64
Askri(2019) [37], ~60 °C	–	–	30–40
Alqahtani(2024)[42], 50–70 °C	–	–	32–38
Ayub(2020)[39], 70–80 °C	–	–	35–40

Table 3 shows that exergy efficiency decreases notably as the outlet temperature increases. Efficiency drops from 65.99% at 50 °C to 24.64% at 70 °C. This decline results from slower absorption kinetics and higher heat transfer demand at elevated temperatures. Reported literature values range between 30–40% around 60 °C (Askri, 2019) [37], 32–38% within 50–70 °C (Alqahtani, 2024) [38], and 35–40% for 70–80 °C (Ayub, 2020) [39]. The model results align well with these studies, particularly in the 50–60 °C range. At 70 °C, the efficiency is slightly lower due to absorption limitations. Figure 3 presents the combined influence of outlet temperature on overall system performance.

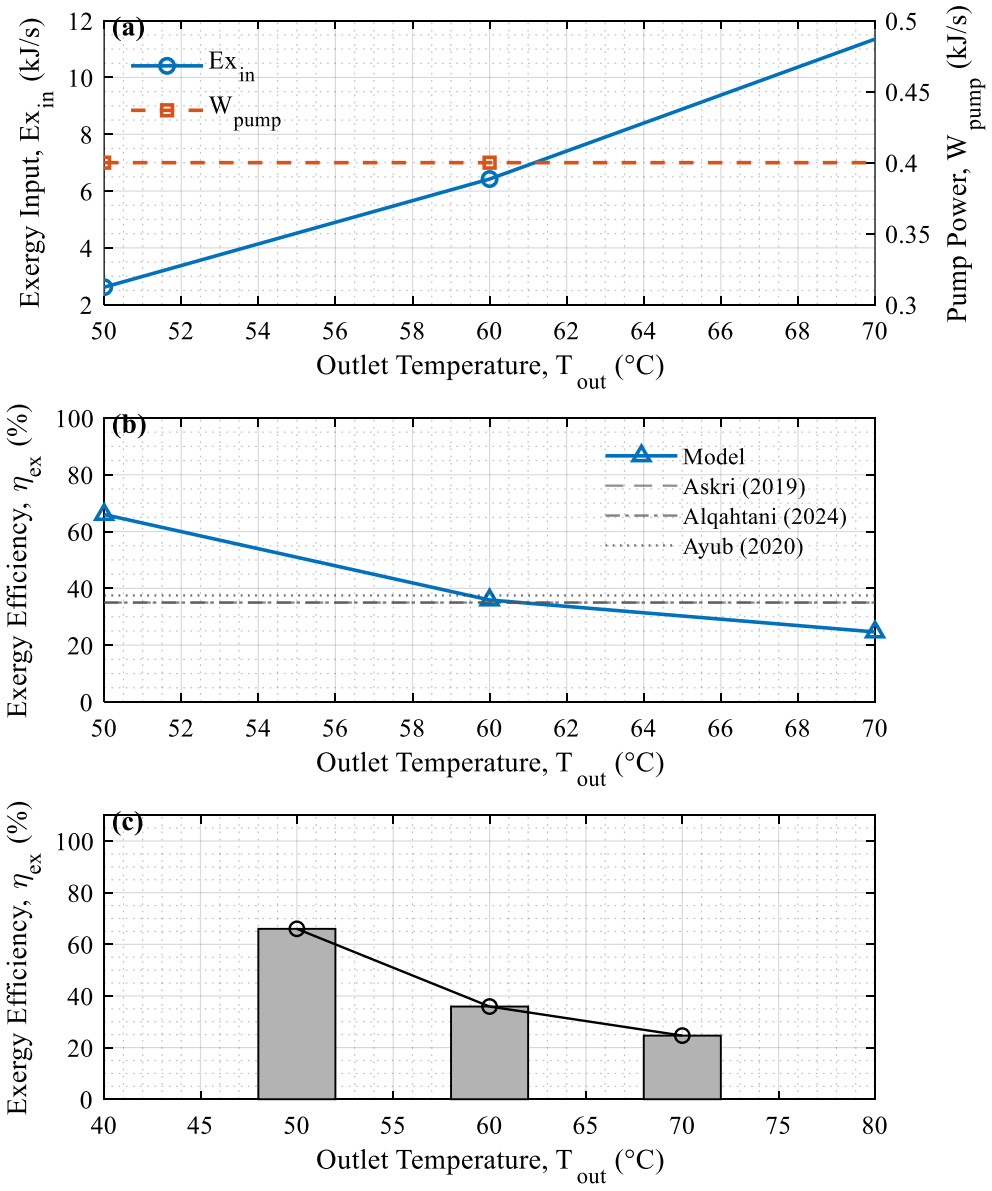

Figure 3. Variation of reactor number and exergy efficiency with outlet temperature

Figure 3 shows that the optimum absorption temperature lies within the 50–60 °C range. Beyond this range, the system's exergy performance declines noticeably. Figure 3(a) presents the relationship between exergy input (Ex_in) and pump power (W_pump) as outlet temperature increases. Exergy input rises with temperature, while pump power remains constant, reflecting greater energy demand at higher temperatures. Figure 3(b) compares the model results with previous studies by Askri (2019) [37], Alqahtani (2024) [38], and Ayub (2020) [39]. The model aligns well with literature data at lower temperatures, but efficiency deviations appear at higher temperatures due to limited absorption kinetics. Figure 3(c) shows the variation of exergy efficiency with reactor number. Efficiency improves as the reactor number increases; however, this trend weakens at higher temperatures, particularly at 70 °C.

In MH-based hydrogen storage systems, the coolant mass flow rate is a key parameter influencing heat transfer and overall system performance. As the flow rate increases, more fluid passes over the heat transfer surface, which enhances heat removal during absorption. However, the higher flow rate also increases pump power demand and reduces exergy efficiency. Evaluating the system under different mass flow rates is therefore essential to determine the optimum operating range. Table 4 presents the effect of mass flow rate variation (0.5–1.5 kg/s) on system parameters. In this study, the mass flow rate (ṁ), volumetric flow rate (V), pump power (Wpump), exergy input (Exin), useful exergy (Exuseful), and exergy efficiency (ηex) were calculated. These parameters provide a quantitative basis for assessing how flow rate changes affect the system's exergy performance.

Effect of Mass Flow Rate

Table 4. Effect of mass flow rate

$\dot{m}$(kg/s)	V (m³/s)	W_{pump} (kJ/s)	Ex_{in} (kJ/s)	Ex_{useful} (kJ/s)	η_{ex} (%)
0.5	0.0005015	0.2006	5.6924	2.895	49.13
1.0	0.001003	0.4012	11.385	2.895	24.56
1.5	0.0015045	0.6018	17.077	2.895	16.38

Table 4 shows that exergy efficiency decreases notably as the mass flow rate increases. For example, efficiency is 49.13% at 0.5 kg/s and drops to 16.38% at 1.5 kg/s. This decline results from the higher pump power required at greater flow rates. Similar trends are reported in the literature. Nyamsi (2021) [27] and Krane (2022) [40] observed that increasing the flow rate beyond a threshold enhances heat transfer but lowers exergy efficiency due to higher energy losses. Accordingly, the model results in Table 4 align well with the literature and indicate that the optimum flow rate lies within the low-to-medium range.

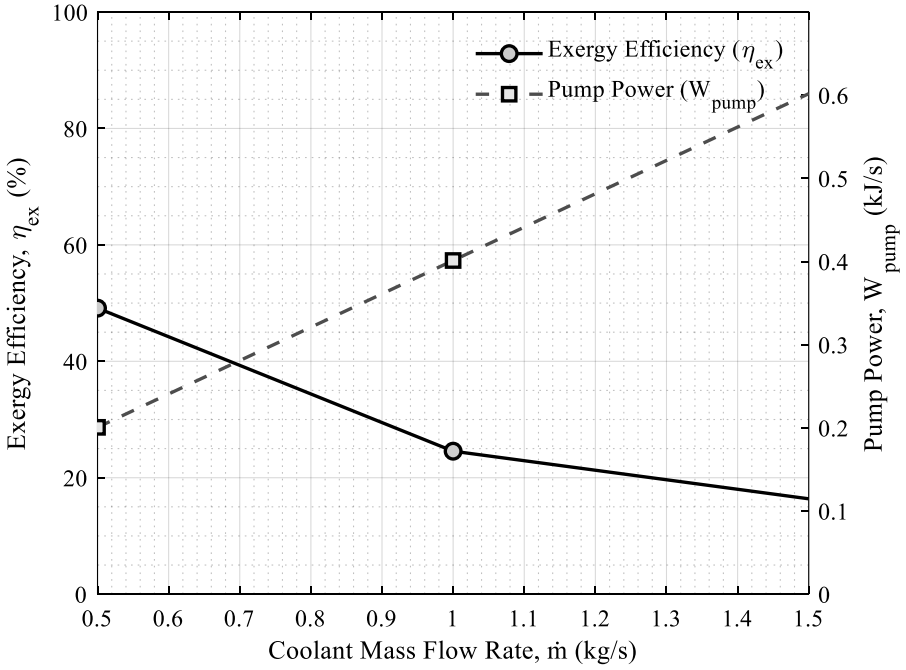

Figure 4. Effect of coolant mass flow rate on exergy efficiency

Figure 4 shows that exergy efficiency decreases as the flow rate increases. At lower flow rates (0.5 kg/s), higher efficiencies are obtained, but efficiency declines sharply at higher flow rates. This behavior agrees with literature findings. Krane (2022) [40] reported that higher flow rates improve heat transfer but lower efficiency due to greater pump power demand. Figure 4 therefore provides clear evidence for the optimum mass flow rate and confirms that the model aligns with literature trends.

Effect of Pump Efficiency on System Performance

Pump efficiency is a key parameter that indirectly influences the exergy performance of hydrogen storage systems. Higher pump efficiency increases the effective power delivered to the system and reduces pump-related losses. Variations in efficiency therefore play an important role in assessing overall exergy performance. To examine this effect, calculations were performed for different ηpump values. The related parameters—pump power (Wpump), exergy input (Exin), useful exergy (Exuseful), exergy destruction (ExD), and exergy efficiency (ηex)—were calculated. The summarized results are presented in Table 5.

Table 5. Effect of pump efficiency on exergy and power

η_{pump}	Wpump (kJ/s)	Ex_{in} (kJ/s)	Ex_{useful} (kJ/s)	Ex_D (kJ/s)	η_{ex} (%)
0.6	0.3333	11.351	2.895	8.4556	24.78
0.7	0.2857	11.351	2.895	8.4556	24.88
0.8	0.2500	11.351	2.895	8.4556	24.96

Table 5 shows that increasing pump efficiency from 60% to 80% reduces pump power consumption from 0.3333 kJ/s to 0.2500 kJ/s. In parallel, exergy efficiency rises slightly from 24.78% to 24.96%. These results indicate that the direct influence of pump efficiency on overall system performance is limited but positive. Literature studies report similar trends, showing that auxiliary components such as pumps make a small yet meaningful contribution to the performance of MH-based storage systems [27], [40]. Therefore, pump selection should account for both energy consumption and its effect on overall exergy efficiency.

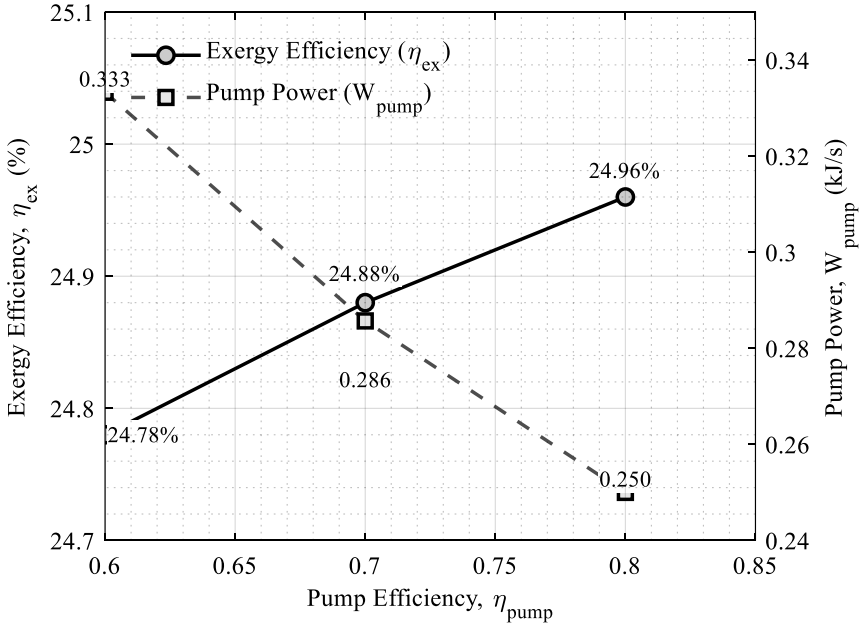

Figure 5. Effect of pump efficiency on exergy efficiency

Figure 5 shows that exergy efficiency increases slightly but linearly as pump efficiency improves. At 60% pump efficiency, exergy efficiency is about 24.78%, and it rises to 24.96% at 80%. This small change helps reduce energy losses during long-term operation. Krane (2022) [40] and Nyamsi (2021) [27] also reported that pumps and other auxiliary components have an indirect but notable effect on overall energy and exergy performance. These findings confirm that high-efficiency pumps are crucial for sustainable hydrogen storage systems.

Effect of Ambient Temperature on Exergy

Ambient temperature (T_0) is a key environmental parameter influencing the performance of thermodynamic processes. In exergy analysis, it defines the reference condition and serves as a basis for calculating exergy input, destruction, and efficiency. Three scenarios were analyzed in this study with ambient temperatures of 20 °C, 25 °C, and 30 °C. For each case, the exergy input (Exin), exergy destruction (ExD), useful exergy (Exuseful), pump power (Wpump), and exergy efficiency (ηex) were computed. The summarized results are presented in Table 6.

Table 6. Effect of ambient temperature on exergy efficiency

T_0 (°C)	Ex_{in} (kJ/s)	Ex_D (kJ/s)	Ex_{useful} (kJ/s)	W_{pump} (kJ/s)	η_{ex} (%)
20	13.257	9.8794	3.3775	0.2857	24.94
25	11.351	8.4556	2.895	0.2857	24.88
30	9.4444	7.0318	2.4125	0.2857	24.79

Table 6 shows that a rise in ambient temperature slightly decreases the system's exergy performance. For instance, exergy efficiency declines from 24.94% at 20 °C to 24.79% at 30 °C. This decline occurs because higher ambient temperatures reduce the exergy gradient with the surroundings and lower the amount of useful exergy. Similar patterns are reported in the literature. Nyamsi (2021) [27] and Krane (2021) [41] observed that changes in ambient conditions alter the system's thermodynamic potential and cause small efficiency variations. These results emphasize the need to consider ambient temperature in long-term operational analyses.

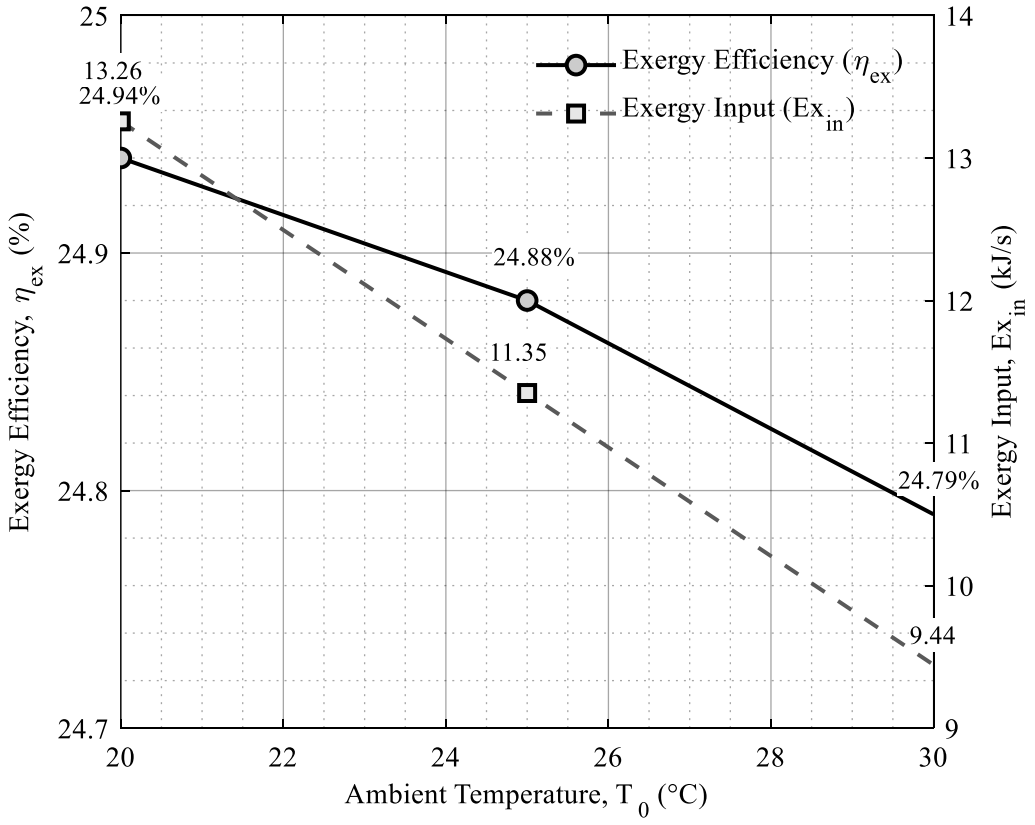

Figure 6. Effect of ambient temperature on exergy efficiency

Figure 6 shows that exergy efficiency decreases linearly as ambient temperature increases. The system exhibits higher exergy potential at lower ambient temperatures, but this potential declines under warmer conditions. Krane (2021) [41] noted that environmental factors, especially fluid inlet and ambient temperatures, strongly affect system

performance. Likewise, Nyamsi (2021) [27] found that environmental parameters cause small changes in both energy and exergy efficiency. These findings confirm that the model results align with the literature and emphasize the need to consider ambient temperature in design optimization.

Effect of Heat Transfer Coefficient (h) on System Performance

The absorption process is the main mechanism that enables hydrogen storage in MH reactors, where an exothermic reaction occurs. If the released heat is not removed effectively, the absorption rate drops and system performance declines. The heat transfer coefficient (h) is therefore a key parameter influencing efficiency during absorption. For different h values, total heat transfer (Qtotal), exergy input (Exin), useful exergy (Exuseful), pump power (Wpump), and exergy efficiency (ηex) were computed. The results are presented in Table 7.

Table 7. Effect of heat transfer coefficient on system performance

h (W/m²·K)	Qtotal (kJ/s)	Exin (kJ/s)	Exuseful (kJ/s)	Wpump (kJ/s)	η_{ex} (%)
1000	31.667	11.351	2.895	0.400	24.64
2000	63.333	11.351	5.790	0.400	49.27
3000	95.000	11.351	8.685	0.400	73.91

Table 7 shows that a higher heat transfer coefficient (h) during absorption directly improves system performance. At h = 1000 W/m²·K, exergy efficiency is 24.64%, and it rises to 73.91% at h = 3000 W/m²·K. This improvement indicates that larger h values enable more effective heat removal from the reactor and accelerate the absorption process, leading to higher exergy efficiency. Literature studies confirm this trend. Jana (2023) [19] found that greater surface areas in tube bundle reactors shorten absorption time. Parashar (2024) [21], [35] reported that enhanced heat transfer in compact multi-tube reactors increases absorption capacity. Likewise, Eisapour (2025) [36] showed that PCM-integrated conical heat exchangers reduce charging times by 30–69% during absorption. These findings confirm that the model results agree well with the literature.

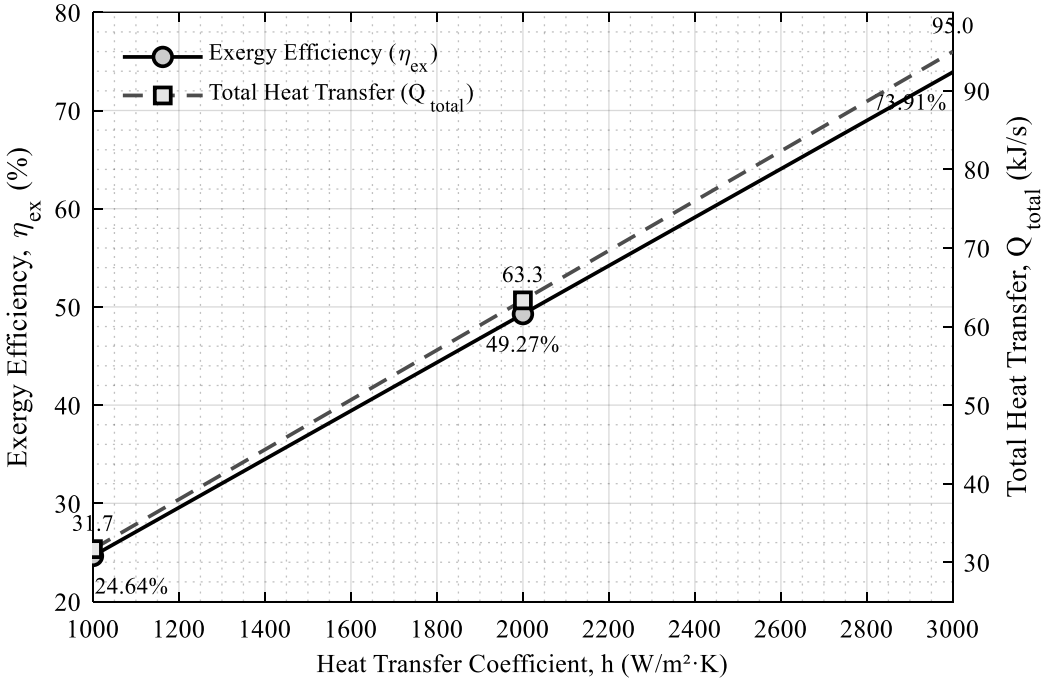

Figure 7. Effect of heat transfer coefficient on exergy efficiency

Figure 7 shows that exergy efficiency increases linearly with the heat transfer coefficient (h) during absorption. At low h values, poor heat removal restricts the absorption rate. At higher h values, effective heat dissipation allows faster and more efficient hydrogen storage. Literature studies confirm this trend. Jana (2023) [19], Parashar & Muthukumar (2024) [21], [35], and Eisapour (2025) [36] found that improving the heat transfer coefficient reduces absorption time and increases storage capacity, leading to higher efficiency. Reactor designs that achieve high h values—such as multi-tube configurations, conical heat exchangers, and PCM-integrated systems—are therefore essential for improved performance.

Effect of Hydrogen Loading Capacity (C_{H2}) on System Performance

In MH-based hydrogen storage systems, the hydrogen loading capacity of the material (CH_2) is a key parameter influencing storage density and overall exergy performance. Materials with higher hydrogen capacity can store more hydrogen and thus yield greater useful exergy, leading to improved system efficiency. Three hydrogen loading capacities—20, 30, and 40 mol/kg—were analyzed in this study. For each case, the exergy input (Exin), useful exergy (Exuseful), pump power (Wpump), exergy destruction (ExD), and exergy efficiency (ηex) were computed. The summarized results are presented in Table 8.

Table 8. Effect of hydrogen loading capacity on exergy efficiency

C_{H2} (mol/kg)	Ex_{in} (kJ/s)	Ex_{useful} (kJ/s)	W_{pump} (kJ/s)	Ex_D (kJ/s)	η_{ex} (%)
20	11.351	0.762	0.286	10.589	6.55
30	11.351	1.143	0.286	10.208	9.82
40	11.351	1.524	0.286	9.827	13.09

Table 8 shows that higher hydrogen capacity significantly enhances system performance. For instance, exergy efficiency (ηex) is 6.55% at CH_2 = 20 mol/kg and increases to 13.09% at CH_2 = 40 mol/kg. This improvement occurs because storing more hydrogen raises useful exergy and lowers exergy destruction. Literature studies confirm this trend, showing that MH materials with greater hydrogen capacity lead to higher efficiency and improved energy conversion [19], [21], [35], [36]. These results confirm that hydrogen capacity is a key factor in material selection.

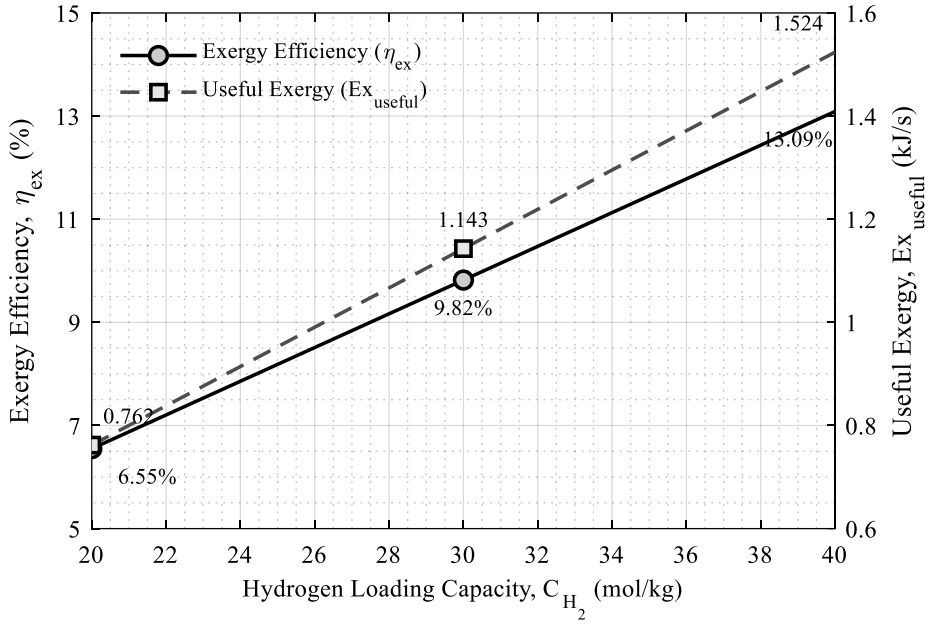

Figure 8. Variation of exergy efficiency with hydrogen loading capacity

Figure 8 shows a nearly linear relationship between hydrogen capacity and exergy efficiency. As capacity increases from 20 mol/kg to 40 mol/kg, efficiency almost doubles. This trend indicates that materials with higher capacities store more hydrogen and use energy more effectively during absorption. Similar results are reported in the literature. Jana (2023) [19] highlighted the importance of high capacity in tube bundle reactors. Parashar (2024) [21], [35] observed similar behavior in multi-tube compact reactors, while Eisapour (2025) [36] found improved charge–discharge efficiency in PCM-integrated systems. Therefore, increasing hydrogen capacity is a critical factor for system design, supported by both the model and literature evidence.

Effect of Reactor Volume-to-Surface Area (V/A) Ratio on Exergy Performance

The volume-to-surface area (V/A) ratio is a key design parameter in MH reactors because it affects heat transfer characteristics. A lower V/A ratio provides a larger surface area for heat exchange and enables faster removal of heat during absorption. In contrast, a higher V/A ratio restricts heat transfer and reduces overall system performance. In this study, the influence of the V/A ratio on exergy performance was analyzed. For V/A ratios of 0.05, 0.075, and 0.10 m, exergy input (Exin), useful exergy (Exuseful), pump power (Wpump), and exergy efficiency (ηex) were computed. The summarized results are presented in Table 9.

Table 9. Effect of V/A ratio on exergy efficiency

V/A Ratio (m)	Ex_{in} (kJ/s)	Ex_{useful} (kJ/s)	W_{pump} (kJ/s)	η_{ex} (%)
0.05	11.351	0.274	0.400	2.33
0.075	11.351	0.183	0.400	1.56
0.10	11.351	0.137	0.400	1.17

Table 9 shows that exergy efficiency decreases significantly as the V/A ratio increases. At V/A = 0.05 m, the exergy efficiency (ηex) is 2.33%, but it falls to 1.17% at V/A = 0.10 m. This reduction occurs because a smaller surface area limits heat dissipation and slows hydrogen storage kinetics. Literature studies confirm this trend. Lower V/A ratios enhance heat transfer and increase overall efficiency, while higher ratios lead to noticeable performance losses [19],[21],[35],[36]. These results emphasize the need to optimize the V/A ratio during reactor design.

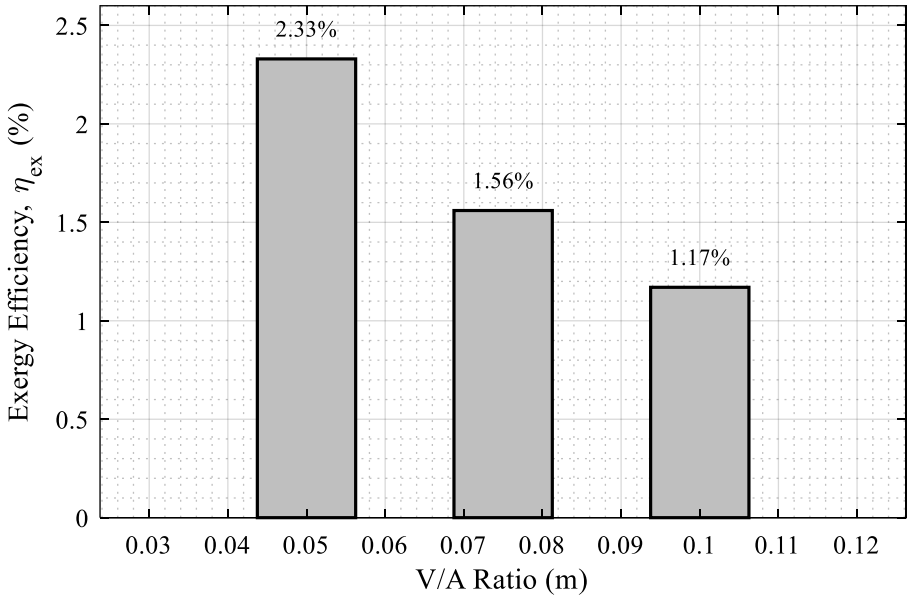

Figure 9. Variation of exergy efficiency with V/A ratio

Figure 9 shows that exergy efficiency decreases as the V/A ratio increases during absorption. Lower ratios provide a larger surface area for heat transfer and enable faster absorption. In contrast, higher ratios restrict heat dissipation and lower overall efficiency. Similar findings are reported in the literature. Jana (2023) [19] observed this effect in tube bundle reactors, Parashar (2024) [35] noted it in multi-tube compact designs, and Eisapour (2025) [36] confirmed it in PCM-integrated systems. These results verify that the model outcomes align well with literature trends.

Discussion

The multi-parametric exergy analysis conducted in this study provides a comprehensive evaluation of MgH_2-based metal hydride systems, extending beyond the single-variable approaches commonly found in the literature. The results reveal that both energy and exergy performances are highly sensitive to multiple engineering parameters, including reactor number, outlet temperature, mass flow rate, pump efficiency, ambient temperature, heat transfer coefficient, hydrogen capacity, and the reactor's volume-to-surface (V/A) ratio.

The findings related to the number of reactors are consistent with the trends reported by Jana (2023) [19] and Parashar (2024) [35], confirming that an increased number of reactors leads to a nearly linear improvement in exergy efficiency, particularly in large-scale configurations. This demonstrates the scalability potential of the proposed model. Regarding outlet temperature, the optimum absorption range was determined to be between 50 °C and 60 °C, which agrees well with the thermal equilibrium ranges reported by Askri (2019) [37] and Alqahtani (2024) [42].

The analysis of mass flow rate showed that exergy efficiency decreases as flow rate increases, mainly due to

the dominant effect of pump power consumption at higher flow conditions. This observation is in strong agreement with the concept of an "optimum flow rate window" highlighted by Krane (2022) [40] and Nyamsi (2021) [27]. Although the variation of pump efficiency (η_{pump}) did not produce large numerical changes, its indirect influence on the overall energy quality was evident. This result supports previous studies emphasizing that the efficiency of auxiliary components, such as pumps, can have a limited but meaningful impact on overall system performance.

The results related to the heat transfer coefficient strongly support the trend reported by Jana (2023) [19], Parashar (2024) [35], and Eisapour (2025) [36], indicating that higher *h* values significantly enhance the absorption rate. Notably, the exergy efficiency of 73.91% achieved at h = 3000 W/m²·K demonstrates that improving the system's heat management capability can substantially increase overall performance. Similarly, the improvements obtained by increasing hydrogen storage capacity and reducing the V/A ratio are consistent with the studies of Parashar (2024) [35] and Eisapour (2025) [36], which emphasize the importance of larger surface areas and higher storage densities in achieving superior system efficiency.

Overall, the model results exhibit strong consistency with the literature, while minor discrepancies can be attributed to differences in material composition (e.g., MgH_2 versus $LaNi_5$ or Ti–Zr alloys), temperature regimes, and heat transfer conditions. These differences do not undermine the model's validity; rather, they highlight its robustness and adaptability under varying operational scenarios.

This study represents one of the first comprehensive models to analyze the multi-dimensional interaction between energy and exergy parameters in MgH_2-based systems. It quantitatively captures the combined influence of interdependent variables, providing an integrated framework that has been largely overlooked in previous research.

In conclusion, the multi-parametric analysis clearly demonstrates that system performance must be evaluated through the coupled interaction of all governing variables. The findings not only confirm the existing trends in the literature but also yield directly applicable engineering insights for design optimization. Consequently, this work establishes the analytical foundation for the results and recommendations presented in the following section.

Conclusions and Recommendations

A comprehensive energy and exergy analysis was carried out for a magnesium hydride (MgH_2)–based metal hydride (MH) hydrogen storage system. The findings quantitatively demonstrate the influence of key design and operating parameters on system performance and provide optimization criteria relevant to engineering-scale applications.

1. Number of Reactors: Increasing the number of reactors was found to be one of the most significant factors enhancing system performance. The exergy efficiency (η_{ex}) increased from 21.5% for two reactors to 64.9% for six reactors. This improvement indicates that multi-reactor configurations are advantageous for industrial-scale hydrogen storage systems, as they enhance heat management and overall energy efficiency.
2. Outlet Temperature: As the outlet temperature increased, the absorption efficiency decreased. The η_{ex} value declined from 65.99% at 50 °C to 24.64% at 70 °C. This highlights the strong sensitivity of the absorption process to thermal balance and defines an optimal operating temperature range of 50–60 °C, which serves as a key reference for thermal management in MH reactor design.
3. Coolant Mass Flow Rate: Although increasing the coolant flow rate improves heat transfer, it simultaneously raises pump power losses, reducing overall efficiency. At 0.5 kg/s, η_{ex} was 49.13%, but it fell to 16.38% at 1.5 kg/s. These results suggest that operating at low-to-moderate flow rates provides a better energy–exergy trade-off and that pump design should consider both thermodynamic and economic performance.
4. Pump Efficiency: Increasing pump efficiency from 60% to 80% slightly raised η_{ex} from 24.78% to 24.96%. Although the gain is modest, improving auxiliary equipment efficiency has a positive cumulative effect on overall system performance. Therefore, the use of high-efficiency pumps and circulation units is recommended to minimize long-term operational losses.
5. Ambient Temperature: When the ambient temperature rose from 20 °C to 30 °C, η_{ex} decreased marginally from 24.94% to 24.79%. While this variation is relatively small, it shows that environmental conditions have a measurable effect on thermodynamic behavior. Thus, MH storage systems should be thermally insulated and climate-adapted to mitigate environmental fluctuations.
6. Heat Transfer Coefficient The heat transfer coefficient (h) exhibited the strongest influence on system performance. When h increased from 1000 W/m²·K to 3000 W/m²·K, η_{ex} improved markedly from 24.64% to 73.91%. This confirms that effective heat removal is the dominant factor controlling hydrogen absorption. Therefore, advanced heat exchanger designs—such as multi-tube reactors, conical exchangers, or PCM-integrated systems—should be prioritized in MH reactor engineering.
7. Hydrogen Storage Capacity: Enhancing hydrogen loading capacity (C_H_2) significantly increased system efficiency. When C_H_2 rose from 20 mol/kg to 40 mol/kg, η_{ex} increased from 6.55% to 13.09%. This finding underscores the importance of high-capacity MgH_2-based and hybrid materials. In materials engineering, capacity improvements achieved through nanostructuring or alloying directly enhance both performance and design flexibility.
8. Volume-to-Surface Area Ratio (V/A): As the V/A ratio increased, heat transfer deteriorated, leading to lower exergy efficiency. At V/A = 0.05 m, η_{ex} was 2.33%, while at V/A = 0.10 m, it dropped to 1.17%. Lower V/A ratios promote better internal heat distribution and faster absorption. Therefore, maintaining a low V/A ratio is essential for improving heat transfer and reactor performance.

Engineering Applications and Future Work:

The results identify the most critical parameters governing the design and scalability of MH-based hydrogen storage systems. Among these, the number of reactors, heat transfer coefficient, and hydrogen storage capacity are dominant factors determining energy and exergy performance.
Future research should integrate economic and environmental assessments into the present model, explore hybrid heat management concepts (e.g., PCM-assisted, nanofluid, or multi-channel designs), and develop automated control and optimization algorithms for dynamic operation.
By incorporating these developments, MgH_2-based systems can evolve into next-generation, high-efficiency, and sustainable hydrogen storage technologies suitable for large-scale clean energy applications. Within this context, parameters such as reactor number, pump efficiency, and the V/A ratio were jointly evaluated under a multi-parametric exergy framework. This integrated approach contributes to the limited literature addressing these interactions simultaneously, and the results are expected to serve as a reference for future optimization and design studies on metal hydride-based hydrogen storage systems.

Ethics Committee Approval and Conflict of Interest Statement

There is no need to obtain permission from the ethics committee for the article prepared.
There is no conflict of interest with any person / institution in the article prepared.

Authors' Contributions

Beyazit İlgin: Study conception and design; Acquisition of data; Analysis and interpretation of data; Drafting of manuscript; Critical revision.

Acknowledgement

Not applicable.

References

[1] İ. Dinçer and C. Acar, "Review and evaluation of hydrogen production methods for better sustainability," International Journal of Hydrogen Energy, vol. 40, no. 34, p. 11094, Jan. 2015, doi: 10.1016/j.ijhydene.2014.12.035.

[2] M. Ball and M. Weeda, "The hydrogen economy – Vision or reality?," International Journal of Hydrogen Energy, vol. 40, no. 25, p. 7903, May 2015, doi: 10.1016/j.ijhydene.2015.04.032.

[3] M. Lototskyy, V. A. Yartys, B. G. Pollet, and R. C. Bowman, "Metal hydride hydrogen compressors: A review," International Journal of Hydrogen Energy, vol. 39, no. 11, p. 5818, Feb. 2014, doi: 10.1016/j.ijhydene.2014.01.158.

[4] L. Schlapbach and A. Züttel, "Hydrogen-storage materials for mobile applications," Nature, vol. 414, no. 6861, p. 353, Nov. 2001, doi: 10.1038/35104634.

[5] A. Züttel, "Hydrogen storage methods," The Science of Nature, vol. 91, no. 4, p. 157, Apr. 2004, doi: 10.1007/s00114-004-0516-x.

[6] B. Sakintuna, F. Lamari-Darkrim, and M. Hirscher, "Metal hydride materials for solid hydrogen storage: A review," International Journal of Hydrogen Energy, vol. 32, no. 9, p. 1121, Jan. 2007, doi: 10.1016/j.ijhydene.2006.11.022.

[7] I. P. Jain, C. Lal, and A. Jain, "Hydrogen storage in Mg: A most promising material," International Journal of Hydrogen Energy, vol. 35, no. 10, p. 5133, Oct. 2009, doi: 10.1016/j.ijhydene.2009.08.088.

[8] R. Paramonov, T. Spassov, P. Nagy, and Á. Révész, "Synergetic Effect of FeTi in Enhancing the Hydrogen-Storage Kinetics of Nanocrystalline MgH2," Energies, vol. 17, no. 4, p. 794, Feb. 2024, doi: 10.3390/en17040794.

[9] A. K. Patel et al., "Study of the Microstructural and First Hydrogenation Properties of TiFe Alloy with Zr, Mn and V as Additives," Processes, vol. 9, no. 7, p. 1217, Jul. 2021, doi: 10.3390/pr9071217.

[10] L. Ren et al., "Nanostructuring of Mg-Based Hydrogen Storage Materials: Recent Advances for Promoting Key Applications," Nano-Micro Letters, vol. 15, no. 1, Apr. 2023, doi: 10.1007/s40820-023-01041-5.

[11] A. Mohammadi et al., "High-entropy hydrides for fast and reversible hydrogen storage at room temperature," Acta Materialia, vol. 236, p. 118117, Jun. 2022, doi: 10.1016/j.actamat.2022.118117.

[12] S. Dangwal and K. Edalati, "High-entropy alloy TiV2ZrCrMnFeNi for hydrogen storage at room temperature," Scripta Materialia, vol. 238, p. 115774, Sep. 2023, doi: 10.1016/j.scriptamat.2023.115774.

[13] Y. Kozhakhmetov et al., "High-Entropy Alloys: Innovative Materials with Unique Properties for Hydrogen Storage," Metals, vol. 15, no. 2, p. 100, Jan. 2025, doi: 10.3390/met15020100.

[14] V. K. Kukkapalli, S. Kim, and S. A. Thomas, "Thermal Management Techniques in Metal Hydrides for Hydrogen Storage Applications: A Review," Energies, vol. 16, no. 8, p. 3444, Apr. 2023, doi: 10.3390/en16083444.

[15] G. Miao et al., "Review of thermal management technology for metal hydride reaction beds," Sustainable Energy & Fuels, vol. 7, no. 9, p. 2025, 2023, doi: 10.1039/d2se01690g.

[16] P. Larpruenrudee et al., "The enhancement of metal hydride hydrogen storage performance using novel triple-branched fin," Journal of Energy Storage, vol. 123, p. 116659, Apr. 2025, doi: 10.1016/j.est.2025.116659.

[17] R. Ran, J. Wang, F. Yang, and R. Imin, "Fast Design and Numerical Simulation of a Metal Hydride Reactor," Energies, vol. 17, no. 3, p. 712, Feb. 2024, doi: 10.3390/en17030712.

[18] V. N. Kudiiarov, R. R. Elman, N. S. Pushilina, and N. Kurdyumov, "State of the Art in Development of Heat Exchanger Geometry Optimization," Materials, vol. 16, no. 13, p. 4891, Jul. 2023, doi: 10.3390/ma16134891.

[19] S. Jana and P. Muthukumar, "Design, development and hydrogen storage performance testing of a tube bundle metal hydride reactor," Journal of Energy Storage, vol. 63, p. 106936, Mar. 2023, doi: 10.1016/j.est.2023.106936.

[20] G. Mohan, M. P. Maiya, and S. Srinivasamurthy, "Performance simulation of metal hydride hydrogen storage device," International Journal of Hydrogen Energy, vol. 32, no. 18, p. 4978, Oct. 2007, doi: 10.1016/j.ijhydene.2007.08.007.

[21] S. Parashar, P. Muthukumar, and A. K. Soti, "Experimental study on absorption and desorption behavior of a novel metal hydride reactor," International Journal of Hydrogen Energy, vol. 94, p. 1224, Nov. 2024, doi: 10.1016/j.ijhydene.2024.11.058.

[22] M. Raju and S. Kumar, "Optimization of heat exchanger designs in metal hydride based hydrogen storage systems," International Journal of Hydrogen Energy, vol. 37, no. 3, p. 2767, Aug. 2011, doi: 10.1016/j.ijhydene.2011.06.120.

[23] X.-S. Bai et al., "Optimization of tree-shaped fin structures towards enhanced absorption performance," Energy, vol. 220, p. 119738, Dec. 2020, doi: 10.1016/j.energy.2020.119738.

[24] Y. Liu et al., "Numerical investigation of metal hydride heat storage reactor with multiple tubes," Energy, vol. 253, p. 124142, May 2022, doi: 10.1016/j.energy.2022.124142.

[25] V. Pandey, K. V. Krishna, and M. P. Maiya, "Numerical modelling and heat transfer optimization of large-scale reactors," International Journal of Hydrogen Energy, vol. 48, no. 42, p. 16020, Jan. 2023, doi: 10.1016/j.ijhydene.2023.01.058.

[26] S. Shafiee, "Operational principles and effect of operating parameters on performance of metal hydride heat pumps," International Journal of Refrigeration, vol. 120, p. 22, Aug. 2020, doi: 10.1016/j.ijrefrig.2020.08.025.

[27] S. N. Nyamsi and I. Tolj, "The Impact of Active and Passive Thermal Management," Energies, vol. 14, no. 11, p. 3006, May 2021, doi: 10.3390/en14113006.

[28] I. Dincer and M. A. Rosen, Exergy: energy, environment and sustainable development. Newnes, 2012. Available: http://ci.nii.ac.jp/ncid/BA8326393X

[29] Y. A. Cengel and M. A. Boles, Thermodynamics: An engineering approach, 8th ed. McGraw-Hill Education, 2015.

[30] V. Bahrs, F. Franke, S. Kazula, and S. de Graaf, "Analysis of the potential of metal hydride-based range extenders," CEAS Aeronautical Journal, Dec. 2024, doi: 10.1007/s13272-024-00784-0.

[31] T. L. Bergman, Fundamentals of heat and mass transfer. John Wiley & Sons, 2011. [Online]. Available: https://ci.nii.ac.jp/ncid/BB01294600

[32] B. Galey et al., "Improved hydrogen storage properties of Mg/MgH2," International Journal of Hydrogen Energy, vol. 44, no. 54, p. 28848, Oct. 2019, doi: 10.1016/j.ijhydene.2019.09.127.

-[33] Y. A. Cengel and J. M. Cimbala, Fluid mechanics: Fundamentals and applications, 3rd ed. McGraw-Hill Education, 2014.

[34] A. Bejan, Advanced engineering thermodynamics, 4th ed. John Wiley & Sons, 2016, doi: 10.1002/9781119245964.

[35] S. Parashar, P. Muthukumar, and A. K. Soti, "Design optimization and numerical investigation," Thermal Science and Engineering Progress, vol. 49, p. 102468, Feb. 2024, doi: 10.1016/j.tsep.2024.102468.

[36] A. H. Eisapour et al., "Enhancing hydrogen storage efficiency," International Journal of Hydrogen Energy, vol. 109, p. 1090, Feb. 2025, doi: 10.1016/j.ijhydene.2025.02.146.

-[37] F. Askri et al., "Numerical investigation of high temperature metal hydride water pumping system," International Journal of Hydrogen Energy, vol. 44, no. 31, p. 16777, May 2019, doi: 10.1016/j.ijhydene.2019.04.263.

[38] T. Alqahtani, S. Mellouli, F. Askri, S. Algarni, B. M. Alshammari, and L. Kolsi, "Numerical Investigation on Thermal Performance of Three Configurations of Solar Thermal Collector Integrated with Metal Hydride," Case Studies in Thermal Engineering, p. 105314, Oct. 2024, doi: 10.1016/j.csite.2024.105314.

[39] I. Ayub et al., "Performance improvement of solar bakery unit," Renewable Energy, vol. 161, p. 1011, Aug. 2020, doi: 10.1016/j.renene.2020.07.133.

[40] P. Krane et al., "Dynamic modeling and control of a two-reactor metal hydride energy storage system," Applied Energy, vol. 325, p. 119836, Sep. 2022, doi: 10.1016/j.apenergy.2022.119836.

[41] P. Krane et al., "Assessment of metal-hydride energy storage coupled with heat pumps and solar PV," Purdue Univ., 2021. [Online]. Available: https://docs.lib.purdue.edu/cgi/viewcontent.cgi?article=1372&context=ihpbc.

[42] T. Alqahtani et al., "Numerical Investigation on Thermal Performance of Solar Collector with Metal Hydride," Case Studies in Thermal Engineering, p. 105314, Oct. 2024, doi: 10.1016/j.csite.2024.105314.

Dicle University
Journal of Engineering
https://dergipark.org.tr/tr/pub/dumf
duje.dicle.edu.tr

Research Article

Topology Optimization-Based Lightweight Chassis Design: A Case Study on Structural Efficiency Enhancement for an Autonomous Scale

Kerem Ali TAŞ[1], Mehmet Can KARABIYIK[2] , Kürşat TANRIVER [3*], Mine AK[4]

[1]Istanbul Health and Technology University, Mechatronic Engineering Department, kerem.tas@istun.edu.tr, Orcid No: 0009-0002-4286-4352

[2]Istanbul Health and Technology University, Mechatronic Engineering Department, mehmet.karabiyik@istun.edu.tr, Orcid No: 0009-0002-1467-0454

[3]Istanbul Health and Technology University, Mechatronic Engineering Department, kursat.tanriver@istun.edu.tr, Orcid No: 0000-0002-1723-4108

[4]Istanbul Health and Technology University, Mechatronic Engineering Department, mine.ak@istun.edu.tr, Orcid No: 0000-0003-1131-5529

ARTICLE INFO

Article history:
Received 9 August 2025
Received in revised form 4 October 2025
Accepted 7 October 2025
Available online 30 December 2025

Keywords:

autonomous vehicle, FEM, SIMP method, structural analysis, topology optimization

Doi: 10.24012/dumf.1761538

* Corresponding author

ABSTRACT

This study aims to enhance structural efficiency and achieve material savings by employing the topology optimization method for the lightweight design of an autonomous model vehicle chassis. During the design process, the penalty-based Solid Isotropic Material with Penalization (SIMP) method, available within ANSYS Academic software, was utilized. Initially, a structural analysis of the chassis was conducted, followed by the application of topology optimization based on the finite element method (FEM) results. Through iterative solutions under specified loading conditions and boundary constraints, a mass reduction of approximately 27% was achieved compared to the initial geometry. Despite the reduction in mass, the design maintained its structural integrity. Graphical analyses indicated that the optimization process reached convergence after the fifth iteration, with a stabilized distribution of material. The results demonstrate the potential of topology optimization to develop low-cost, lightweight, yet robust structural solutions, emphasizing its effectiveness as an engineering tool in systems where weight reduction is critical, such as autonomous model vehicles.

.

Introduction

In contemporary engineering design processes, the scope has expanded beyond merely fulfilling functional requirements. It now encompasses multi-dimensional criteria such as efficient resource utilization, lightweight construction, structural integrity, and manufacturability. These considerations are especially critical in sectors such as automotive, aerospace, defense, and structural engineering, necessitating the adoption of more comprehensive design approaches. Among the various methods developed to address these needs, topology optimization has emerged as a prominent strategy.

Topology optimization is an engineering approach that aims to determine the optimal distribution of material within a given design domain. It goes beyond traditional sizing and shape optimization by enabling the discovery of non-intuitive, high-performance structural layouts. This study focuses on the design process of a chassis intended for use in an autonomous model vehicle, employing topology optimization to achieve both weight reduction and cost efficiency. Within this context, topology optimization stands out as a numerical method that seeks the most effective material distribution under predefined loading and boundary conditions.

With the advancement of computational techniques, topology optimization has evolved through integration with the Finite Element Method (FEM), isogeometric analysis, and artificial intelligence-based algorithms, thereby facilitating innovative engineering solutions. In this study, the effects of topology optimization across various application domains are evaluated in light of leading works in literature.

Numerous studies have explored the applicability of topology optimization to a wide range of engineering problems. For instance, Chen et al. [1] integrated FEM and BEM techniques with isogeometric analysis to achieve broadband optimization in structural-acoustic interactions, significantly improving computational efficiency. In the

automotive sector, Mete and Başak [2] optimized a critical safety component the tie rod while Nazlı and Özsoy [3] reported up to 57% weight reduction in a control arm. Karamert and Demir [4] analyzed the correlation between torsional stiffness and topological structure in commercial bus chassis to propose design improvements. In aerospace applications, Saraç and Koçak [5] demonstrated that topology optimization in aircraft engine bracket design could yield nearly 80% material savings without compromising structural adequacy. Korkut et al. [6] conducted composite-based structural design for aircraft wing sections using Hypermesh-assisted analysis. From a manufacturing technology perspective, studies by Çalık and Uzun [7] and Canlıdinç [8] have shown that combining metal additive manufacturing with topology optimization yields positive impacts on both production flexibility and material efficiency. Furthermore, Arat et al. [9] reported a 35% weight reduction and a 42% improvement in structural efficiency through topology optimization of pneumatic gripper systems. A study by Cai et al. [10] employing mixed-integer programming addressed the effects of kinematic instability in lattice structures, contributing mathematical formulations to the field. Tuğsal and Deniz [11] investigated the structural behavior of industrial storage rack systems with varying heights under seismic loading and evaluated the contribution of beam-to-column connections to overall system safety. The results obtained from both linear and nonlinear analyses revealed that the detailing of beam-to-column joints plays a critical role in ensuring seismic safety.

Akdağ and Çelebi [12] performed weight optimization of a three-phase, 50 Hz, 50 kVA, 34.5/0.4 kV, delta–wye connected oil-type transformer using the Firefly Algorithm. Based on 200 repeated simulations conducted in the MATLAB environment, optimization of the current density and core cross-section suitability factor resulted in an approximately 1% reduction in the transformer's weight. Parla et al., [13] focused on maximum power control and optimization in 8/6 pole switched reluctance generators (SRG) operating under variable wind conditions. In the study conducted in the MATLAB/Simulink environment, it was reported that optimal angles and MPPT control strategies increased power output and ensured system stability. Dündar, İzci et al.,[14] improved the Levy Flight Distribution (LFD) algorithm using the Nelder–Mead (NM) method and developed three different strategies. These strategies optimized the balance between global and local search, enhancing performance in function optimization problems, which was validated through statistical tests. Altay and Altay [15] examined the performance of the Slime Mould Algorithm (SMA) and its hybrid versions in global optimization problems. It was found that hybrid methods such as LSMA and ESMA mitigated SMA's slow convergence and local optima entrapment issues, achieving higher success rates in CEC2020 test functions.

This study addresses a notable gap in the literature by integrating topology optimization into the design of an autonomous vehicle chassis an area where structural optimization applications for lightweight model vehicles remain significantly underexplored. The novelty of the work lies not only in the combined application of FEM-based analysis and the SIMP method, but also in the detailed graphical analysis of the optimization process, including iteration-based convergence observations. While existing research has predominantly focused on aerospace and civil engineering applications, this paper provides an original contribution by presenting a cost-effective and lightweight chassis solution tailored for ground vehicles. The achievement of a 27% mass reduction without compromising the safety factor demonstrates that structural efficiency and material economy can be attained simultaneously. This finding sets the study apart from prior work and highlights the effectiveness of topology optimization in lightweight vehicle design.

The primary aim of this study is to develop a lightweight and structurally efficient chassis design for an autonomous model vehicle by employing the topology optimization method. Using the SIMP approach integrated into the finite element framework, the study focuses on reducing the overall mass of the chassis while ensuring that its load-carrying capacity, stiffness, and safety factor remain within acceptable limits. By doing so, this work seeks to demonstrate the practical applicability of topology optimization in ground vehicle design, highlighting its potential as a cost-effective and computationally efficient engineering tool for achieving material savings without compromising structural integrity.

Optimization

Fundamentally, optimization refers to the process of finding the best solution(s) to one or more problems under a set of predefined conditions. It provides a systematic framework to enhance performance, reduce costs, and ensure efficiency in engineering applications. Today, both classical and heuristic methods are commonly employed to solve such problems [16]. Classical approaches such as linear and nonlinear programming are effective for continuous and differentiable functions, whereas heuristic and metaheuristic methods including Genetic Algorithms, Particle Swarm Optimization, and Ant Colony Optimization offer robust solutions for complex and nonlinear problems. Depending on the problem, optimization can also be classified as deterministic or stochastic, single- or multi-objective, and discrete or continuous. Among these approaches, topology optimization has emerged as a particularly powerful method, as it determines the optimal material distribution within a design domain rather than merely adjusting size or shape.

This capability enables the development of lightweight, high-performance structures in manufacturing, aerospace, and automotive engineering. In this manuscript, topology optimization is used to lightweight a model autonomous vehicle chassis.

A. Topology Optimization

Topology optimization methods not only provide optimal geometries but also minimize material usage, thereby offering cost-effective solutions [17]. An illustration of the topology optimization process is presented in Fig. 1.

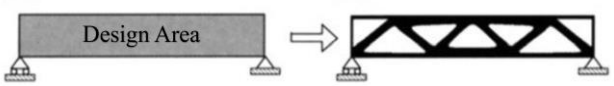

Figure 1. Topology optimization

Topology optimization is one of the most advanced structural design methods, aiming to automatically determine the optimal material layout within a design domain under specified loading conditions and design constraints [18]. The first general and numerical approach in this field was introduced by Cheng and Olhoff [19] for the optimal design of solid elastic plates. Following the seminal work of Bendsøe et al. [20], topology optimization gained significant momentum, introducing a homogenization-based perspective to the methodology.
In subsequent years, several numerical techniques have been developed and widely adopted, including the penalty-based Solid Isotropic Material with Penalization (SIMP) method [21,22]. Evolutionary Structural Optimization (ESO) [23,24], and the Level-Set approach [25,26].
In this manuscript, the penalty-based SIMP method is adopted and implemented for structural optimization purposes.

B. OPTIMIZATION PROBLEM WITH SIMP

This section briefly introduces the topology optimization problem involving both topology and thickness control, which will be addressed in numerical examples.
The penalized Solid Isotropic Material with Penalization (SIMP) approach is a topology optimization technique based on variable density methods. In this method, the design domain is discretized into a finite element mesh composed of isotropic solid microstructures.
The density field (ρ) of the structure is used to transform the topology optimization into a structural continuity optimization problem. The objective of the optimization is to minimize structural compliance under a prescribed volume constraint.
Within the SIMP framework, the optimization problem is mathematically expressed as follows [27].

$$min: f(\Omega, \rho) = U^t K U = \sum E_e(\rho_e)\, {u_e}^t\ {k_e}^o\ u_e \quad (1)$$

$$Subject\ to: KU = F$$
$$\sum \rho_e\ u_e \le V_{max}$$
$$0 \le \rho \le 1$$

Here,

- $\boldsymbol{\Omega}$ denotes the structural design domain, which defines the region where the material distribution is to be optimized.
- $\boldsymbol{\rho}$ is the density field of the structural finite element mesh, representing the relative material presence in each element (0 for void and 1 for solid material).
- $\mathbf{U}$ represents the global displacement field obtained from the finite element analysis, describing the deformation of the entire structure under applied loads.
- $\mathbf{F}$ is the external load vector, which contains the forces or boundary conditions applied to the design domain.
- $\mathbf{K}$ is the global stiffness matrix, relating nodal displacements to applied loads in the finite element formulation.
- $\mathbf{u_e}$ is the displacement vector of an individual element, extracted from the global displacement field.
- $\mathbf{k_e^0}$ is the element stiffness matrix corresponding to unit Young's modulus, which is later scaled by the penalized material properties.
- $\boldsymbol{\rho_e}$ is the elemental density variable that controls whether material exists in a specific element.
- $\boldsymbol{V_{max}}$ represents the upper bound of the total allowable volume, enforcing the volume constraint during optimization.

The density penalization model is expressed by the following equation:

$$E_e(\rho_e) = E_{min} + (\rho_e)^p\ (E_0 - E_{min}) \quad (2)$$
$$\rho_e \in [0,1]$$

Here,

- $\boldsymbol{E_0}$ represents the stiffness of the base material
- $\boldsymbol{E_{min}}$ is the artificial minimum stiffness value assigned to void elements to prevent singularities in the numerical solution.
- $\boldsymbol{p}$ is the penalization factor, which pushes intermediate densities toward either 0 (void) or 1 (solid), thereby promoting a clear black-and-white design.
- $\boldsymbol{\rho_e} \in [\mathbf{0}, \mathbf{1}]$ defines the range of possible material densities, from fully void (0) to fully solid (1).

In the initial preparation stage, the design domain, loading conditions, boundary constraints, and initial design variables are defined. Based on this setup, a numerical solution is performed to determine the structural behavior of the system—typically using the Finite Element Method (FEM).
Following the structural response analysis, a sensitivity study is carried out to assess the influence of design variables on the objective function (e.g., compliance or stiffness), thereby defining the optimization direction. Numerical instabilities that may arise from discretization or interpolation are subsequently mitigated using

techniques such as filtering or penalization to maintain the physical validity of the solution. The design variables are then updated according to the optimization algorithm, and the new configuration is evaluated for convergence. If convergence is not achieved, the process iterates until the optimized material distribution is obtained. The overall SIMP optimization procedure is illustrated in Fig. 2.

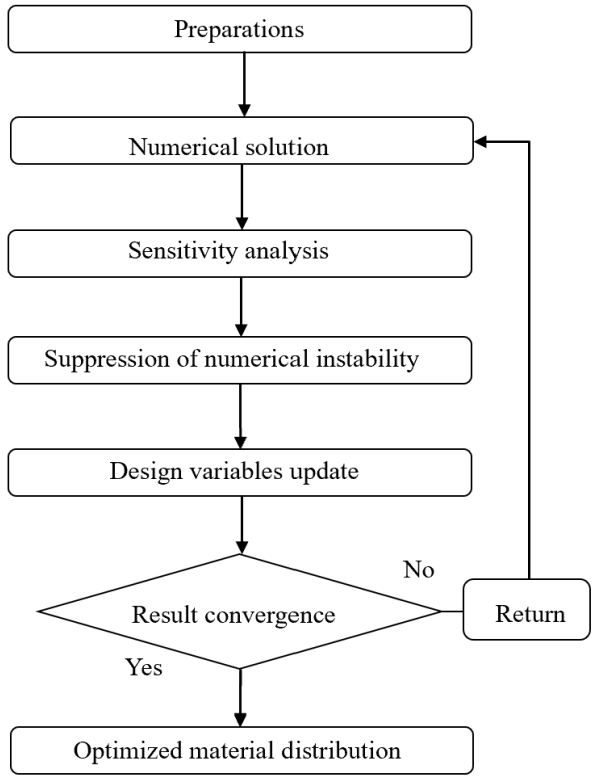

Figure 2. SIMP Flowchart

The stages in Figure 2 are detailed step by step below.

- **Preparations**

In this initial stage, the design domain is defined, including the applied loads, boundary conditions, and material properties. The finite element mesh is generated, and an initial density distribution is assigned across the elements. In addition, the optimization parameters such as the volume fraction, penalty factor, and filter radius are specified to ensure a stable and well-posed problem.

- **Numerical solution**

Based on the current material distribution, a numerical analysis is performed, most commonly using the finite element method. This step provides the system response, such as displacements, stresses, or strain energy, which forms the basis for evaluating the performance of the design.

- **Sensitivity analysis**

The sensitivities of the objective function and the constraints with respect to the design variables are computed. This analysis indicates how the material distribution influences the structural response and guides the optimization algorithm in updating the design variables effectively.

- **Suppression of numerical instability**

To eliminate potential numerical instabilities, such as checkerboard patterns or mesh dependency, filtering or projection techniques are applied. These stabilization measures ensure that the resulting material distribution is physically meaningful and manufacturable.

- **Design variables update**

The design variables (element densities) are updated according to the sensitivity information obtained in the previous step. This iterative update process progressively improves the material layout toward the optimal solution.

- **Result convergence**

Convergence criteria are checked by monitoring changes in the objective function and design variables between successive iterations. If the variation falls below a predefined threshold, the solution is considered converged. Otherwise, the process returns to the numerical solution step and continues iteratively.

- **Optimized material distribution**

Once convergence is achieved, the final optimized material distribution is obtained. This distribution represents the most efficient structural layout within the defined design space and constraints.

Material and Method

A. Material

PLA-based polymer material was used for the vehicle chassis to ensure manufacturability using a 3D printer. The dimensions of the chassis are 10 × 75 × 210 mm. The technical information provided by the manufacturer is indicated in Table 1 [28]. The 3D model of the vehicle chassis is presented in Fig. 3.

Table 1. Mechanical properties of polylactic acid (PLA) [28]

Mechanical Property	Value
Yield strength	60 MPa
Elongation at break	6%
Tensile modulus	3600 MPa
Flexural strength	83 MPa
Flexural modulus	3800 MPa

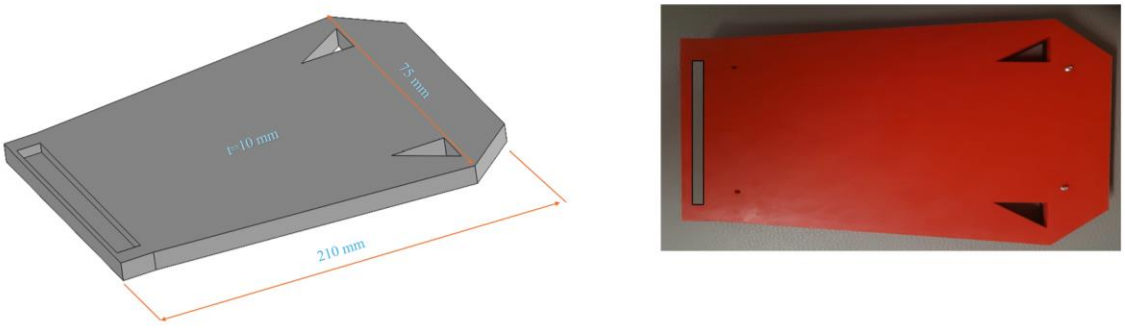

a. b.

Figure 3. Vehicle chassis model (a) 3D CAD design (b) Physical model fabricated using a 3D printer.

B. METHOD

All components of the vehicle were modeled in 3D using the student version of SolidWorks. For topology optimization, the academic version of ANSYS software was utilized. The optimization process was carried out using the topology optimization module available within the structural optimization environment of ANSYS.
The method employed was the Solid Isotropic Material with Penalization (SIMP) technique, which is integrated into the software. In this study, force and moment distributions were applied in a manner that realistically reflects actual driving scenarios.

Results and Discussion

Topology optimization was employed in the design of the vehicle chassis. This approach enabled a reduction in structural weight while maintaining durability and overall performance. The topology optimization analyses were performed using ANSYS software.

A. Structural Analysis Result

Prior to conducting topology optimization, a structural analysis of the vehicle was performed. The analysis utilized 15,096 elements and 76,871 nodes. Subsequently, a Quality Mesh Analysis was conducted, yielding a minimum mesh quality value of 0.31446, which is considered acceptable for the model vehicle chassis. The mesh structure is illustrated in Fig. 4.

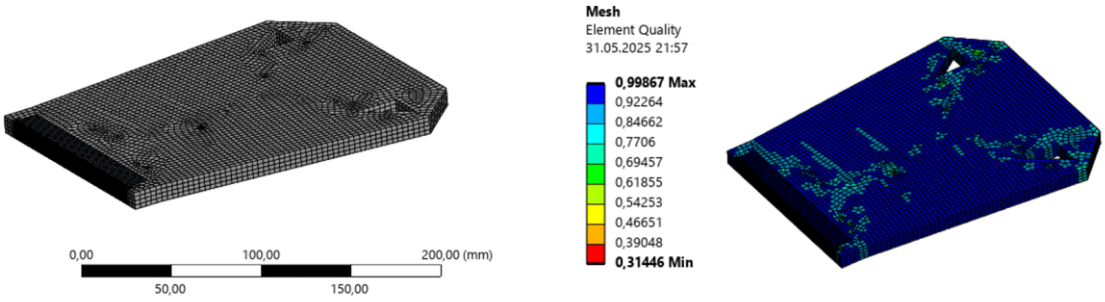

a. b.

Figure 4. Mesh detail (a) Mesh design (b) Mesh element quality

For the structural design of the vehicle chassis, fixed supports were applied at the base points where the wheel axles are mounted. A 5 N vertical load was applied from the top, and the analysis was performed accordingly. The results showed a maximum deformation of 0.00065133 mm. The von Mises stress ranged from a minimum of 5.2505×10^{-5} MPa to a maximum of 0.31043 MPa.

These values indicate that the system operates with a safety factor of approximately 15, confirming its structural safety. Details of the analysis are illustrated in Fig. 5.

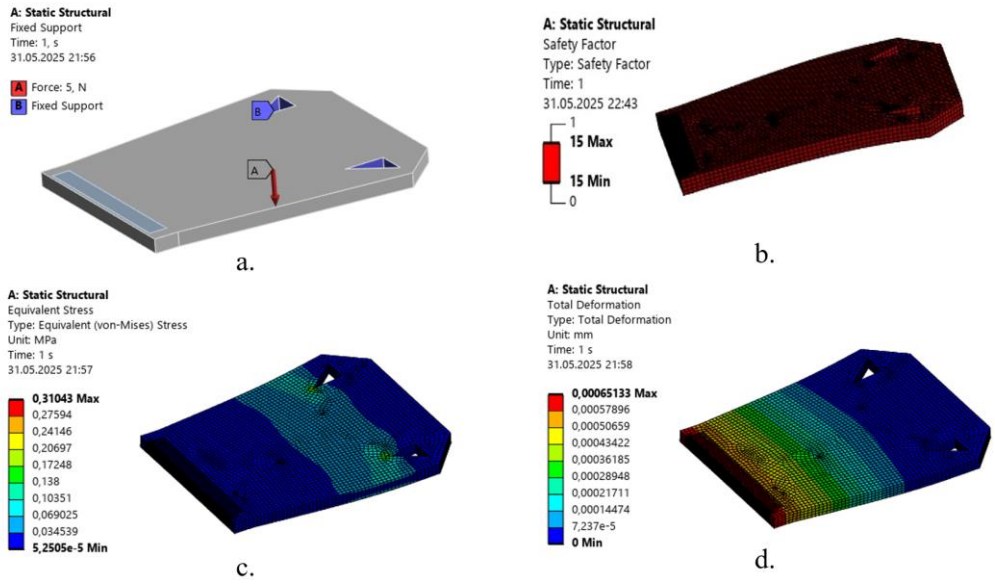

Figure 5. Analysis detail (a) Boundary conditions (b) Safety Factor (c) Von-Mises Stress (d) Total deformation

B. Topology Optimization Result

Following the structural analysis, the results were transferred to the Structural Optimization module within the ANSYS software. The design setup and integration details are presented in Fig. 6.

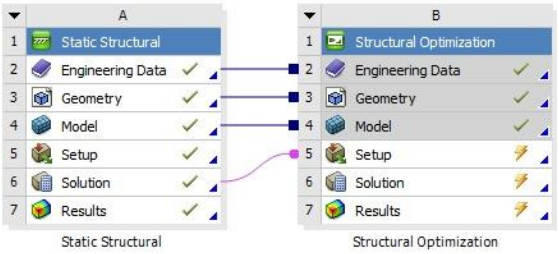

Figure 6. Design detail

From this point onward, topology optimization was performed using the SIMP method, while keeping the boundary conditions and mesh settings unchanged. The results of the topology optimization are presented in Fig. 7.

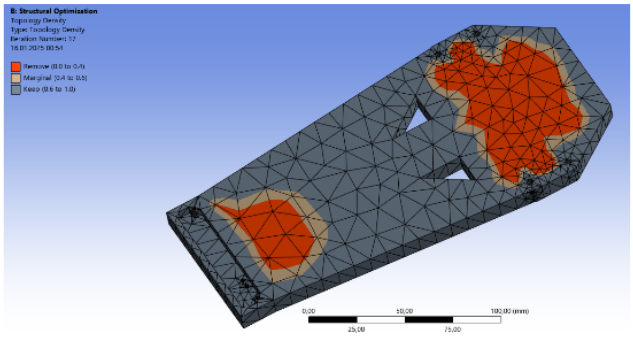

Figure 7. Topology optimization result screen

Based on the results of the topology optimization, a 27% reduction in mass was achieved after 15 iterations compared to the initial model. The optimized design produced lower maximum stress under the same loading conditions compared to the conventional solid chassis. Graphical analyses revealed that the optimization process reached convergence starting from the 5th iteration, indicating a stabilized material distribution. On average, each iteration required approximately 30 seconds, resulting in a total optimization time of about 7.5 minutes. In terms of computational cost, the analyses were performed on a standard workstation equipped with an Intel i7 processor (3.40 GHz) and 16 GB RAM, using ANSYS Academic software. The finite element model consisted of 15,096 elements and 76,871 nodes, which indicates that the proposed topology optimization framework is computationally efficient and feasible for lightweight

design applications. The plot of iteration versus topology density is presented in Fig. 8.

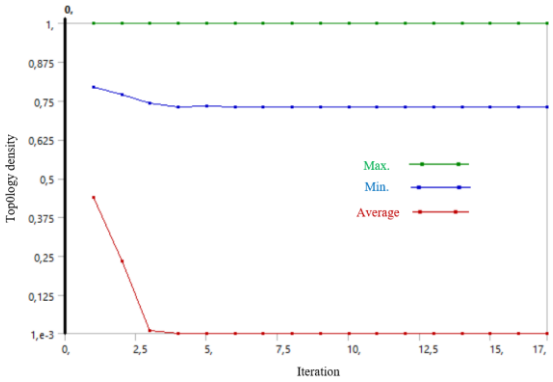

Figure 8. Iteration – Topology density

The graph demonstrates that unnecessary material was effectively removed during the mass optimization process, while material density remained constant in critical regions to preserve structural integrity.

These findings indicate that the applied topology optimization was effective and that further iterations beyond a certain point did not yield additional improvements.

The results of this study were observed to be consistent with the literature [29,30]. A comparison of the literature is shown in Table 2.

Tablo 2. Comparison of the literature

Feature	This Study	Erőss and Markovits [29]	Güney and Uzun [30]
Material	PLA	Ti6Al4V Titanium Alloy	Aluminum alloy (UAV frame structure)
Method	SIMP Topology Optimization	Stiffness-based topology optimization	SIMP-based and BESO (Bi-directional Evolutionary Structural Optimization) methods
Mass Reduction (%)	27% (depending on boundary condition and load case)	Approximately 70–80% (depending on boundary condition and load case)	24–33% (depending on boundary condition and load case)
Number of Iterations	15 (converged after 5)	100 iterations (converged after 10)	40–60 (SIMP converged after 40, BESO after 60)
Maximum Stress	Reduction	Reduction	Reduction in all load cases; stress concentration minimized near support regions
Computation Time	7.5 minutes (standard hardware)	Variable depending on algorithmic and hardware improvements	8–10 minutes (ANSYS Workbench, mid-range CPU)
Software	ANSYS Workbench 2024 R2	Unspecified	ANSYS Workbench 2022 R2
Field	Structural optimization	Structural optimization	UAV lightweight structural optimization
Optimization Type	Single-objective (stiffness maximization)	Single-objective (stiffness and weight trade-off)	Multi-objective (mass minimization and stiffness maximization)
Boundary Conditions	Fixed supports, distributed load	Fixed–cantilever beam constraint	Clamped UAV arm with distributed lift forces
Mesh/Element Size	Medium density mesh (~10^5 elements)	High-resolution mesh (~10^6 elements)	Variable mesh density (~10^5–10^6 elements)
Validation Method	FEA-based convergence validation	Numerical validation with AM compatibility check	FEA and literature-based comparison
Manufacturing Method	FDM (3D printing validation)	SLM (Selective Laser Melting)	CAD-integrated topology optimization (AM-oriented design)
Performance Improvement (%)	Stress reduction ≈12%, weight reduction 27%	Stiffness improvement ≈15%, mass reduction up to 80%	Strength-to-weight ratio improved by ≈20–25%
Objective Function	Minimize compliance (maximize stiffness)	Minimize compliance subject to volume constraint	Minimize compliance and displacement under load constraints

A comparative analysis of the present study with the works of Erőss and Markovits [29] and Güney and Uzun [30] reveals significant variations in material selection, optimization methodology, and computational performance. In this study, PLA material was used, whereas Ti6Al4V titanium alloy and aluminium alloy were

employed in the referenced works for additive manufacturing and UAV structural applications, respectively. The use of PLA in this study highlights a focus on polymer-based lightweight modelling and rapid validation through additive manufacturing, contrasting with the metal-based optimization strategies adopted in the other two studies.

From a methodological standpoint, this research utilizes the SIMP topology optimization technique, while Erőss and Markovits [29] applied a stiffness-based topology optimization, and Güney and Uzun [30] integrated both SIMP and BESO (Bi-directional Evolutionary Structural Optimization) methods. The combination of SIMP and BESO in [30] provides a hybrid framework capable of balancing material distribution and element addition–removal strategies, enhancing convergence precision.

In terms of mass reduction, the current study achieved 27%, which is moderate compared to the 70–80% reported by Erőss and Markovits [29] and the 24–33% range found by Güney and Uzun [30]. The relatively higher mass reduction in [29] is attributed to the use of high-strength titanium alloys and the allowance of greater material removal under similar boundary constraints. In contrast, the mass reduction range obtained by Güney and Uzun [30] reflects a balance between lightweight design and maintaining UAV structural rigidity.

Regarding convergence performance, the present study reached stability after five iterations out of fifteen total, whereas Erőss and Markovits [29] required approximately ten iterations out of one hundred, and Güney and Uzun [30] reported convergence between forty and sixty iterations depending on the optimization method (SIMP or BESO). This outcome indicates a faster convergence trend in the current study, primarily due to simpler geometric constraints and reduced mesh complexity.

All studies demonstrated stress reduction as a key result, though with varying degrees of improvement. The maximum stress reduction observed in the current work is about 12%, while Erőss and Markovits [29] and Güney and Uzun [30] achieved greater reductions due to the utilization of metallic materials with higher stiffness and optimized boundary configurations. Moreover, in [30], the stress concentration near support regions was effectively minimized by combining SIMP and BESO strategies.

In terms of computational efficiency, the present analysis required an average of 7.5 minutes on standard hardware, whereas Erőss and Markovits [29] reported variable durations dependent on algorithmic and hardware performance, and Güney and Uzun [30] achieved convergence within 8–10 minutes using ANSYS Workbench on mid-range CPUs. These results confirm that computational time is primarily influenced by material complexity and mesh resolution rather than optimization methodology alone.

From the software and validation perspective, all three studies utilized the ANSYS Workbench environment for simulation and optimization. However, while this study and Güney and Uzun [30] explicitly specified the software versions (2024 R2 and 2022 R2, respectively), Erőss and Markovits [29] did not. Validation methods also differed: the present study performed FEA-based convergence validation and experimental confirmation via 3D printing, while Erőss and Markovits [29] conducted numerical validation with additive manufacturing compatibility, and Güney and Uzun [30] carried out literature-based and simulation-based validation.

Finally, while all studies pursued structural optimization, the objective functions slightly differed. The present study and Erőss and Markovits [29] aimed to minimize compliance (thus maximizing stiffness), whereas Güney and Uzun [30] conducted a multi-objective optimization balancing both mass minimization and stiffness maximization, which is more suitable for UAV lightweight design requirements.

If further weight reduction is desired without compromising structural stability, alternative optimization constraints or loading scenarios may be considered.

Conclusion

The findings of this research demonstrate the effectiveness of topology optimization in achieving lightweight and structurally efficient chassis designs. The initial finite element analysis, which employed a mesh of 15,096 elements and 76,871 nodes, confirmed the structural adequacy of the baseline design under applied boundary conditions. A maximum deformation of 0.00065133 mm and von Mises stress values ranging from 5.25×10^{-5} MPa to 0.31043 MPa indicated a safety factor of approximately 15, ensuring reliability for practical use.

Subsequently, the application of the SIMP-based topology optimization approach resulted in a 27% reduction in mass compared to the initial geometry. Importantly, this reduction did not compromise the load-carrying capacity or durability of the chassis. Iteration-based analyses revealed that convergence was achieved after 15 iterations, with material distribution stabilizing from the 5th iteration onward. The optimized configuration also exhibited lower maximum stress values compared to the conventional solid chassis, confirming that weight reduction was achieved without sacrificing mechanical performance.

From a computational perspective, the optimization process proved to be efficient. Each iteration required approximately 30 seconds, with a total optimization time of about 7.5 minutes on a standard workstation (Intel i7, 3.40 GHz, 16 GB RAM). This demonstrates that the proposed framework is not only effective but also feasible for real-world engineering applications in terms of computational cost.

Overall, this study confirms that topology optimization can deliver lightweight, cost-effective, and structurally robust solutions for autonomous vehicle chassis design. The method provides a balance between material savings and structural safety, making it highly suitable for engineering applications where weight reduction is a critical design criterion.

In future studies, the optimization framework can be extended in several directions. First, different materials such as composites, lightweight alloys, or advanced

polymers may be investigated to evaluate their influence on the structural performance and manufacturability of the chassis. Second, alternative manufacturing methods, including additive manufacturing or hybrid production techniques, could be explored to validate the practicality of the optimized designs and assess their cost–benefit ratios. Furthermore, multi-objective optimization approaches may be employed to simultaneously consider multiple criteria such as stiffness, weight reduction, vibration performance, and fatigue life, thereby providing a more comprehensive evaluation of design trade-offs. Finally, the integration of experimental validation and hardware-in-the-loop testing will be beneficial to verify numerical predictions and to ensure the real-world applicability of the proposed design methodology.

Ethics committee approval and conflict of interest statement

There is no need to obtain permission from the ethics committee for the article prepared.

There is no conflict of interest with any person / institution in the article prepared.

Declaration of Ethical Standards

The authors remained faithful to all ethical rules

Credit Authorship Contribution Statement

Taş KA: Software, Investigation, Writing – original draft, Methodology,

Karabıyık MC: Software, Investigation, Writing – original draft, Methodology,

Tanriver K: Writing – review and editing, Validation, Conceptualization,

Ak M: Writing – review and editing, Validation, Conceptualization,

References

[1]. Chen, L., Lian, H., Dong, H.-W., Yu, P., Jiang, S., & Bordas, S. P. A. (2024). Broadband topology optimization of three-dimensional structural-acoustic interaction with reduced order isogeometric FEM/BEM. *Journal of Computational Physics, 509*, 113051. https://doi.org/10.1016/j.jcp.2024.113051

[2]. Mete, E., & Başak, H. (2024). Topoloji optimizasyonu kullanılarak rot başı tasarımı, analizi ve doğrulanması. *Politeknik Dergisi, 27*(3), 1053–1068. https://doi.org/10.2339/politeknik.1198353

[3]. Nazlı, A., & Özsoy, N. (2024). Bir otomobil salıncağının topoloji optimizasyonu. *Uludağ Üniversitesi Mühendislik Fakültesi Dergisi, 29*(2). https://doi.org/10.17482/uumfd.1431634

[4]. Karamert, S., & Demir, A. (2022). Ticari otobüs gövde yapısında topoloji optimizasyonu çalışması. *International Journal of Advanced Engineering and Pure Sciences, 34*(2), 229–234. https://doi.org/10.7240/jeps.988228

[5]. Saraç, İ., & Koçak, A. T. (2024). Topology optimization and numerical verification in an aircraft engine bracket. *Gümüşhane University Journal of Science, 14*(1), 325–335. https://doi.org/10.17714/gumusfenbil.1329278

[6]. Korkut, H., Altay, M., & Aydın, H. (2023). Uçak kanadı tasarımı, analizi ve yapı elemanlarının topoloji optimizasyonu. *Yüzüncü Yıl Üniversitesi Fen Bilimleri Enstitüsü Dergisi, 28*(3), 1091–1106. https://doi.org/10.53433/yyufbed.1250545

[7]. Çalık, B., & Uzun, G. (2024). Metal eklemeli imalatta topoloji optimizasyonu uygulamaları. *Gazi University Journal of Science Part C: Design and Technology, 12*(4), 832–844.

[8]. Canlıdinç, M. (2023). Topoloji optimizasyonu ile metal eklemeli imalat yönteminin endüstriyel uygulamaları. *Kırklareli Üniversitesi Mühendislik ve Fen Bilimleri Dergisi, 9*(2), 552–565. https://doi.org/10.34186/klujes.1404647

[9]. Arat, Ö., Duran, A., Erman, B., & Kibar, A. (2025). Structural investigation of pneumatic grippers for handling automotive parts using finite element analysis and topology optimization. *KSÜ Mühendislik Bilimleri Dergisi, 28*(1).

[10]. Cai, Q., Feng, R., Zhang, Z., & Wang, X. (2024). Topology optimization of truss structure considering kinematic stability based on mixed-integer programming approach. *Structural and Multidisciplinary Optimization, 67*, 112. https://doi.org/10.1007/s00158-024-03827-6

[11]. Tuğsal, Ü. M., & Deniz, A. (2024). Endüstriyel depo raf sistemlerinin yapısal güvenliğinin dinamik etkiler altında incelenmesi. *DÜMF Mühendislik Dergisi, 15*(1), 209–221. https://doi.org/10.24012/dumf.1286960

[12]. Akdağ, M., & Çelebi, M. (2022). Ateş Böceği algoritması ile yağlı tip transformatörün ağırlık optimizasyonu. *Dicle University Journal of Engineering, 13*(2), 169–180.

[13]. Parla, G., Yıldırım, M., & Özdemir, M. (2023). Maximum power control and optimization of switched reluctance generators for wind turbines. *Dicle Üniversitesi Mühendislik Fakültesi Mühendislik Dergisi, 14*(1), 55–64. https://doi.org/10.24012/dumf.1232026

[14]. Dündar, A., İzci, D., Ekinci, S., & Eker, E. (2021). A novel modified Lévy flight distribution algorithm based on Nelder–Mead method for function optimization. *Dicle Üniversitesi Mühendislik Fakültesi Mühendislik Dergisi, 12*(3), 487–497. https://doi.org/10.24012/dumf.955645

[15]. Altay, O., & Altay, E. V. (2022). Investigation of slime mould algorithm and hybrid slime mould algorithms' performance in global optimization problems. *Dicle Üniversitesi Mühendislik Fakültesi Mühendislik Dergisi, 13*(4), 661–671. https://doi.org/10.24012/dumf.1177288

[16]. Sucuoğlu, H. S., Böğrekci, İ., Demircioğlu, P., & Aksoy, B. (2025). Design and development of effective furrower mounting bracket using topology optimization.

DÜMF Mühendislik Dergisi, 16(2), 377–383. https://doi.org/10.24012/dumf.1584851

[17]. Gao, Y., Zhou, S., & Li, M. (2025). Structural topology optimization based on deep learning. *Journal of Computational Physics, 520*, 113506. https://doi.org/10.1016/j.jcp.2024.113506

[18]. Yingjun, W., Xining, L., Kai, L., & Peng, W. (2023). Open-source codes of topology optimization: A summary for beginners to start their research. *Computer Modeling in Engineering & Sciences, 137*(1.1), 1526–1506. https://doi.org/10.32604/cmes.2023.027603

[19]. Cheng, K. T., & Olhoff, N. (1981). An investigation concerning optimal design of solid elastic plates. *International Journal of Solids and Structures, 17*(3), 305–323. https://doi.org/10.1016/0020-7683(81)90065-2

[20]. Bendsøe, M. P., & Kikuchi, N. (1988). Generating optimal topologies in structural design using a homogenization method. *Computer Methods in Applied Mechanics and Engineering, 71*(2), 197–224. https://doi.org/10.1016/0045-7825(88)90086-2

[21]. Bendsøe, M. P. (1989). Optimal shape design as a material distribution problem. *Structural Optimization, 1*(4), 193–202.

[22]. Bendsøe, M. P., & Sigmund, O. (2003). *Topology optimization: Theory, methods, and applications.* Berlin, Germany: Springer.

[23]. Xie, Y. M., & Steven, G. P. (1993). A simple evolutionary procedure for structural optimization. *Computers & Structures, 49*(5), 885–896. https://doi.org/10.1016/0045-7949(93)90035-C

[24]. Querin, O., Steven, G., & Xie, Y. (1998). Evolutionary structural optimisation (ESO) using a bidirectional algorithm. *Engineering Computations, 15*(8), 1031–1048. https://doi.org/10.1108/02644409810244129

[25]. Wang, M. Y., Wang, X., & Guo, D. (2003). A level set method for structural topology optimization. *Computer Methods in Applied Mechanics and Engineering, 192*(1), 227–246. https://doi.org/10.1016/S0045-7825(02)00559-5

[26]. Allaire, G., Jouve, F., & Toader, A. M. (2004). Structural optimization using sensitivity analysis and a level-set method. *Journal of Computational Physics, 194*(1), 363–393. https://doi.org/10.1016/j.jcp.2003.09.032

[27]. Gao, Y., Zhou, S., & Li, M. (2025). Structural topology optimization based on deep learning. *Journal of Computational Physics, 520*, 113506. https://doi.org/10.1016/j.jcp.2024.113506

[28]. Travieso-Rodriguez, J. A., Jerez-Mesa, R., Llumà, J., Traver-Ramos, O., Gomez-Gras, G., & Roa Rovira, J. J. (2019). Mechanical properties of 3D-printing polylactic acid parts subjected to bending stress and fatigue testing. *Materials, 12*(23), 3859. https://doi.org/10.3390/ma12233859

[29]. Erőss, L. D., & Markovits, T. (2024). Mass reduction method for topology optimisation of a Ti6Al4V part for additive manufacturing. *Production Engineering Archives, 30*(3), 354–360. https://doi.org/10.30657/pea.2024.30.35

[30]. Güney, E., & Uzun, G. (2024). Investigation of the effects of topology optimization methods on rotary wing unmanned aerial vehicle design. *Gazi Journal of Engineering Sciences, 10*(3), 496–521. https://doi.org/10.30855/gmbd.0705AR04

Dicle University
Journal of Engineering
https://dergipark.org.tr/tr/pub/dumf
duje.dicle.edu.tr

Research Article

Position and Motor Control of a 3-DoF RRR Robotic Manipulator Using PID and Sliding Mode Control

Hasan EKER[1], Mesut HÜSEYİNOĞLU[2*]

[1] Dicle University, Mechanical Engineering Department, hasan.eker@dicle.edu.tr, Orcid No: 0009-0005-0195-090X
[2] Dicle University, Mechanical Engineering Department, mesuth@dicle.edu.tr, Orcid No 0000-0002-6130-6658

ARTICLE INFO

Article history:

Received 20 August 2025
Received in revised form 20 September 2025
Accepted 15 December 2025
Available online 30 December 2025

Keywords:

RRR robotic manipulator, sliding mode control, PID control, kinematic modeling, dynamic modeling

Doi: 10.24012/dumf.1769134

* Corresponding author

ABSTRACT

This study addresses this challenge by investigating the position and motor control of a 3-degree-of-freedom (3-DoF) RRR robotic manipulator, offering a comparative analysis of two advanced control strategies: Proportional-Integral-Derivative (PID) control and Sliding Mode Control (SMC). The novelty of this work lies in the comprehensive implementation and direct comparison of these controllers on the same manipulator platform, providing practical insights for applications. To assess Kinematic modeling, Denavit-Hartenberg parameters is used, while dynamic modeling was achieved through Lagrangian formulation. Extensive MATLAB/Simulink simulations demonstrated that PID tuning significantly improves dynamic characteristics, enhancing stability and reducing overshoot and reliable reference tracking. For Joint1, the tuner prioritized stability over raw speed; it significantly reduced the overshoot by 50.1% to achieve a smoother response, accepting an increase in rise and settling times as a trade-off. For Joint 2, the improvements were exceptionally dramatic: settling time was reduced by 99.96%, rise time by 67.4%, and overshoot by 56.7%. Joint 3 also showed outstanding results, with overshoot reduced by 62.3%, rise time by 84.7%, and settling time by 94.7%. Furthermore, SMC exhibited remarkable efficacy in handling system uncertainties and disturbances. This research provides valuable guidelines for selecting appropriate control strategies based on which specific application requirements.

Introduction

The field of robotics has witnessed significant advancements, particularly in industrial automation, where robotic manipulators play a crucial role in enhancing productivity and precision. Among the various types of robotic manipulators, the 3-DoF RRR configuration is widely employed due to its versatility and ability to perform complex tasks in a three-dimensional workspace. Controlling these manipulators, however, presents a considerable challenge due to their inherent nonlinear dynamics, uncertainties, and time-varying characteristics [1]. To address these challenges, advanced control strategies such as Proportional-Integral-Derivative (PID) control and Sliding Mode Control (SMC) are frequently employed to ensure accurate and stable trajectory tracking [2]. The design and implementation of such control systems necessitate a thorough understanding of both the kinematic and dynamic models of the robotic manipulator. Kinematic modeling is often achieved using the Denavit-Hartenberg (DH) parameter convention. This approach provides a mathematical description of the manipulator's geometry and determines the relationship between joint angles and the end-effector's position and orientation**.** Dynamic modeling, on the other hand, captures the forces and torques acting on the manipulator, enabling the prediction of its motion under different operating conditions; the Lagrangian formulation is a powerful tool for deriving these dynamic equations [3]. Effective control of robotic manipulators requires a comprehensive approach that integrates accurate modeling, robust control algorithms, and thorough simulation to validate performance and ensure stability.

Model-based control techniques, such as computed torque control, offer a robust theoretical framework for controlling robotic manipulators [4]. However, their practical application can be limited by the accuracy of the dynamic models used and the presence of external disturbances. PID control is a widely used feedback control technique due to its simplicity and ease of implementation [5]. However, PID control may struggle to provide satisfactory performance when dealing with highly nonlinear systems or systems with significant uncertainties. Advanced control strategies, such as adaptive control and robust control, have been developed to address the limitations of traditional control techniques in the presence of uncertainties and disturbances. SMC is a nonlinear control technique that offers robustness against

uncertainties and disturbances. The fundamental principle behind SMC involves driving the system's state trajectory onto a predefined sliding surface in the state space and maintaining it on this surface. The design of the sliding surface is crucial for achieving desired performance characteristics, such as stability and tracking accuracy [6].

Optimal control methods such as linear quadratic regulators and model predictive control methods are less used when models' level of details is increasing, and nonlinearities become more important [7]. Model Predictive Control (MPC) has emerged as a widely accepted advanced industrial control technique, offering improved precision over traditional feedback approaches [8]. While MPC improves precision over conventional feedback control, it inherently requires accurate When Fig. 7 is examined, it becomes evident that the initially defined or manually assigned PID gains are inadequate for ensuring stable system behavior, thereby requiring the controller parameters to be retuned rate modeling of the system and involves high computational costs, making real-time implementation challenging [9]. While LQR (Linear Quadratic Regulator) control can be used to tune a PID controller, combining the control techniques to control systems in simulations and real-world scenarios [10]. PID controllers are often unable to cope with complex and highly nonlinear systems, and MPC frameworks can encounter local minima and infeasibility when using black-box machine learning models [11].

Modern control strategies integrate artificial intelligence, edge computing, and other innovations to shape the future of industrial control systems [12]. The integration of model predictive control with deep reinforcement learning offers a pathway to robust thermal management [13]. PID control will likely continue to be used [14]. The growing capabilities of soft sensors and data-driven modeling further complement PID control schemes [12]. Model Predictive Control~ is a powerful control strategy widely utilized in domains like energy management, building control, and autonomous systems [15]. The MPC strategy has been applied to the Benchmark Simulation Model simulation benchmark of wastewater treatment process [16]. MPC has also been used in thermal comfort-in-loop controllers [17].

The significance of this study comes from its focus on robust and precise control of a 3-DoF RRR robotic manipulator, which remains a challenging task in industrial and the other fields robots used. The novelty of the work is that it systematically evaluates PID and SMC under the same modeling and simulation environment, clearly demonstrating their comparative advantages in terms of stability, robustness, and tracking accuracy. This dual perspective contributes both to the theoretical understanding and to the practical implementation of advanced control strategies. In the following sections, kinematic modeling, dynamic modeling and design of control systems and simulation results and discussion sections are included, respectively.

Kinematic and dynamic modeling

The kinematic model of a 3-DoF RRR manipulator describes relationship between the joint angles and the position and orientation of the end-effector. The Denavit-Hartenberg parameter convention is a systematic approach for establishing coordinate frames at each joint of the manipulator and deriving the transformation matrices that relate these frames. Each link is assigned a coordinate frame, and four parameters are defined for each frame: the link length, link twist, joint angle, and joint offset. These parameters are used to construct a homogeneous transformation matrix that represents the transformation from one coordinate frame to the next. By multiplying these transformation matrices sequentially, the overall transformation matrix from the base frame to the end-effector frame can be obtained, providing the forward kinematics solution. The inverse kinematics problem, which involves determining the joint angles required to achieve a desired end-effector position and orientation, is more complex and may not have a unique solution.

Kinematic modeling

The first step in forward kinematics is to determine the position and orientation of the end-effector given the joint variables. Modern industrial and research applications need robotic manipulators, especially systems with multiple degrees of freedom such as 3-link, 3-revolute robots, that need precise manipulation and trajectory tracking. The DH parameters for each joint are generally based on the robot's physical structure. DH parameters are used to determine the robot's forward kinematics. The forward kinematics of a serial RRR robot arm that consists of three revolute joints can be represented in matrix form.

The model of the 3 DoF robotic arm used as reference in this study is shown in Fig. 1.

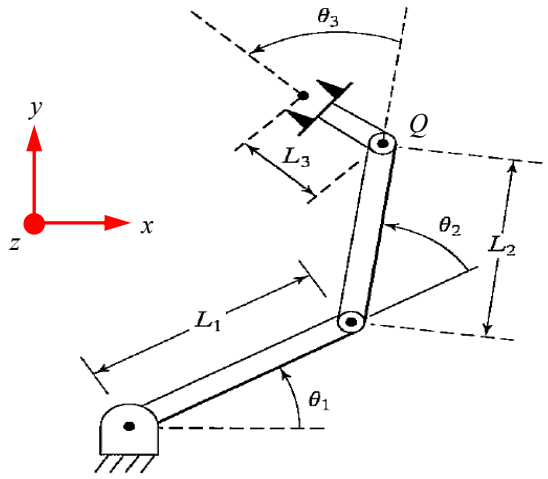

Figure 1. The model of the 3 DoF robotic arm

Figure 1 illustrates the 3-DoF RRR robotic manipulator with clearly labeled joints and coordinate frames. **Joint 1** is

located at the base and provides rotation about the z_0-axis. **Joint 2** is positioned at the connection between the first and second links, rotating about the z_1-axis. **Joint 3** is situated at the wrist connection between the second and third links, rotating about the z_2-axis. All joints are revolute, as indicated by the RRR designation. The coordinate frames follow the Denavit-Hartenberg convention, with each z-axis aligned with the joint rotation axis. The link lengths $L_1, L_2,$ and L_3 represent the distances between consecutive joint axes, while $\theta_1, \theta_2,$ and θ_3 denote the joint angles that define the manipulator's configuration.

The Denavit-Hartenberg (D-H) parameters consist of four fundamental transformation variables:

d: The offset along the previous z-axis to the common normal.

θ: The rotation angle about the previous z-axis from the old x-axis to the new x-axis.

a: The length of the common normal. In the case of a revolute joint, this represents the radius about the previous z-axis.

α: The rotation angle about the common normal from the old z-axis to the new z-axis.

L_i: Denotes length of each link

The DH table created using joint parameters determined by taking into account the axis sets of the joints is given in Table 1.

Table 1. D-H parameters for 3 DoF robotic arm

i	θ_i	α_{i-1}	a_{i-1}	d_i
1	θ_1	0	0	0
2	θ_2	0	L_1	0
3	θ_3	0	L_2	0
4	0	0	L_3	0

When defining coordinate frames, there is flexibility in choosing which x-axis is aligned with the common normal. In some arrangements, multiple links can extend outward from a shared point, which is advantageous in branching structures. The most widely used convention, however, aligns each down-chain x-axis collinear with the common normal, forming the basis for the transformation calculations that follow.

For each link, the corresponding D–H parameters (d, θ, r, α) are inserted into the standard transformation matrix formulation, which includes translations and rotations about and along the defined axes, to obtain the transformations of the axes relative to each other as follows:

$$T = Rot(z,\theta).Trans(z,d).Trans(x,a).Rot(x,\alpha) \quad (1)$$

$Rot(z,\theta)$ denotes rotation around Z-axis, $trans(z,d)$ denotes translation along Z-axis $trans(x,a)$ denotes translation along X-axis, $Rot(x,a)$ denotes rotation around X-axis.

After the relevant matrix multiplications are performed, the homogeneous transformation matrix is calculated as follows:

$$ {}^{i-1}_{i}T = \begin{bmatrix} cos\theta_i & -sin\theta_i & 0 & a_0 \\ \sin\theta_i\cos\alpha_{i-1} & \cos\theta_i\cos\alpha_{i-1} & -\sin\alpha_{i-1} & -sin\alpha_{i-1}d_i \\ \sin\theta_i\sin\alpha_{i-1} & \cos\theta_i sin\alpha_{i-1} & \cos\alpha_{i-1} & cos\alpha_{i-1}d_i \\ 0 & 0 & 0 & 1 \end{bmatrix} \quad (2)$$

Taking into account the parameters given in the D-H table, the 2 equations can be written for each row as follows:

$$ {}^{0}_{1}T = \begin{bmatrix} cos\theta_1 & -sin\theta_1 & 0 & 0 \\ \sin\theta_1 & \cos\theta_1 & 0 & 0 \\ 0 & 0 & 1 & 0 \\ 0 & 0 & 0 & 1 \end{bmatrix} \quad (3)$$

$$ {}^{1}_{2}T = \begin{bmatrix} cos\theta_2 & -sin\theta_2 & 0 & L_1 \\ \sin\theta_2 & \cos\theta_2 & 0 & 0 \\ 0 & 0 & 1 & 0 \\ 0 & 0 & 0 & 1 \end{bmatrix} \quad (4)$$

$$ {}^{2}_{3}T = \begin{bmatrix} cos\theta_3 & -sin\theta_3 & 0 & L_2 \\ \sin\theta_3 & \cos\theta_3 & 0 & 0 \\ 0 & 0 & 1 & 0 \\ 0 & 0 & 0 & 1 \end{bmatrix} \quad (5)$$

$$ {}^{3}_{4}T = \begin{bmatrix} 1 & 0 & 0 & L_3 \\ 0 & 1 & 0 & 0 \\ 0 & 0 & 1 & 0 \\ 0 & 0 & 0 & 1 \end{bmatrix} \quad (6)$$

By multiplying these matrices from the base frame to the end-effector frame in order, the cumulative transformation is obtained, providing a complete mathematical representation of the manipulator's spatial configuration.

$$T = {}^{0}_{4}T = {}^{0}_{1}T.{}^{1}_{2}T.{}^{2}_{3}T.{}^{3}_{4}T \quad (7)$$

$$ {}^{0}_{4}T = \begin{bmatrix} c_{12}c_3 & -s_{12}c_3 - c_{12}s_3 & -s_{12}s_3 + c_{12}s_3 & L_3(c_{12}c_3 - s_{12}s_3) + L_2c_{12} + L_1c_1 \\ s_{12}c_3 + c_{12}s_3 & c_{12}c_3 - s_{12}s_3 & 0 & L_3(s_{12}c_3 - c_{12}s_3) + L_2s_{12} + Ls_1 \\ 0 & 0 & 1 & 0 \\ 0 & 0 & 0 & 1 \end{bmatrix} \quad (8)$$

The expansions of the elements of the matrix given in Eq. 8 are given below.

$$\begin{aligned} c_{12} &= \cos(\theta_1 + \theta_2) = cos\theta_1 cos\theta_2 - sin\theta_1 sin\theta_2 \\ s_{12} &= \sin(\theta_1 + \theta_2) = sin\theta_1 cos\theta_2 + cos\theta_1 sin\theta_2 \\ c_{12}c_3 - s_{12}s_3 &= \cos(\theta_1 + \theta_2 + \theta_3) = \cos(\theta_{123}) \end{aligned} \quad (9)$$

$$s_{12}c_3 + c_{12}s_3 = \sin(\theta_1 + \theta_2 + \theta_3) = \sin(\theta_{123})$$

After making the necessary simplifications, the position of the end effector for the forward kinematic solution is obtained as follows.

$$\begin{aligned} P_x &= L_1 cos\theta_1 + L_2 \cos(\theta_1 + \theta_2) + L_3 \cos(\theta_1 + \theta_2 + \theta_3) \\ P_y &= L_1 sin\theta_1 + L_2 \sin(\theta_1 + \theta_2) + L_3 \sin(\theta_1 + \theta_2 + \theta_3) \end{aligned} \quad (10)$$

P is the position vector of the robot's end-effector. The given equations calculate $x\ and y$ component of this position vector.

$L_1 cos\theta_1$: Projection of the first arm on the x-axis

$L_2\ cos(\theta_1\ +\ \theta_2)$: Projection of the second arm onto the x-axis. The angle that the second arm makes with the global x-axis is the sum of the first and second joint angles $(\theta_1\ +\ \theta_2)$

$L_3\ cos(\theta_1\ +\ \theta_2\ +\ \theta_3)$: Projection of the third arm onto the x-axis. The angle that the third arm makes with the global x-axis is the sum of all joint angles $(\theta_1\ +\ \theta_2\ +\ \theta_3)$.

Terms with $L_i.sin$ denote projections of y- axis

Inverse kinematics is the process of determining the joint variables of a robotic manipulator that will achieve a desired position and orientation of the end-effector. Unlike forward kinematics, where the end-effector pose is directly computed from known joint parameters, inverse kinematics requires solving a set of nonlinear equations, which may have multiple, single, or no solutions depending on the manipulator's geometry and constraints. Analytical methods can be used for manipulators with simple structures, providing exact closed-form solutions, while numerical methods, such as iterative algorithms, are preferred for more complex configurations. The solution of inverse kinematics is essential for precise path planning, obstacle avoidance, and achieving specific task requirements in robotics applications.

For the inverse kinematic solution, it is necessary to find the joint variables θ_1, θ_2 and θ_3. For this, p_x and p_y will be used, along with the angle, φ, with the x axis. Eq. 11 can be written for the orientation.

$$\varphi = \theta_1 + \theta_2 + \theta_3 \quad (11)$$

φ, refers to the orientation angle of the end-effector.φ is the cumulative sum of local rotations of all joints.

If the φ angle is not specified, the inverse kinematics problem will have an infinite number of solutions. The following equations can be obtained:

$$\varphi = \theta_1 + \theta_2 + \theta_3 \quad (12)$$

In this case, the equations can be written as follows:

$$\begin{aligned} P_{Qx} &= P_x - L_3 c_\varphi = L_1 c_1 + L_2 c_{12} \\ P_{Qy} &= P_y - L_3 s_\varphi = L_1 s_1 + L_2 s_{12} \end{aligned} \quad (13)$$

These equations express the location of point Q of the second axis assembly. This location depends only on the angle of the first two joints. If the above equations are squared and summed:

$$P_{Qx}^2 + P_{Qy}^2 = L_1^2 + L_2^2 + 2L_1 L_2 c_2 \quad (14)$$

and from here the expression is obtained:

$$c_2 = \frac{P_{Qx}^2 + P_{Qy}^2 - L_1^2 + L_2^2}{2L_1 L_2} \quad (15)$$

The existence of a solution requires that $-1 < c_2 < 1$. Otherwise, the given point is not within the reachable working space of the arm. An expression can be written from trigonometry as follows:

$$s_2 = \mp\sqrt{1 - c^2} \quad (16)$$

Here, angle θ_2 is;

$$\theta_2 = atan2(s_2, c_2) \quad (17)$$

Substituting θ_2 into Eq. 13 yields two unknowns and two equations. The solution of these equations is:

$$s_1 = \frac{(L_1 + L_2 c_2)P_{Qy} - L_2 s_2 P_{Qx}}{P_{Qx}^2 + P_{Qy}^2} \quad (18)$$

$$c_1 = \frac{(L_1 + L_2 c_2)P_{Qx} - L_2 s_2 P_{Qy}}{P_{Qx}^2 + P_{Qy}^2} \quad (19)$$

Here, similar to Eq. 16, θ_1 can be written as follows:

$$\theta_1 = atan2(s_1, c_1) \quad (20)$$

Finally, θ_3 is calculated as follows:

$$\theta_3 = \varphi - \theta_1 - \theta_2 \quad (21)$$

Dynamic modeling

The dynamic model of the 3-DoF RRR manipulator describes relationship between the joint torques and the joint motions. The Lagrangian formulation is a powerful method for deriving the dynamic equations of motion. The Lagrangian is defined as the difference between the kinetic energy and the potential energy of the system. The equations of motion are then obtained by applying the Euler-Lagrange equations, which relate the Lagrangian to the generalized coordinates (joint angles) and their time derivatives (joint velocities and accelerations). These equations can be expressed in a matrix form, where the mass matrix represents the inertia properties of the manipulator, the Coriolis and centrifugal forces matrix accounts for the velocity-dependent forces, and the gravity vector represents the gravitational forces acting on the links. Friction forces, which are often present in robotic manipulators, can also

be included in the dynamic model. Accurate estimation of the dynamic parameters, such as link masses, moments of inertia, and friction coefficients, is essential for achieving high-performance control [18].

A dynamic model of a manipulator provides relationship between the moments of the joint actuators and the motion of the structure. The Lagrangian formulation allows the equations of motion to be obtained independently of the reference axis set. The Lagrange function is given as follows:

$$L = T - V \tag{22}$$

Here T denotes the total kinetic energy of the system, and V denotes the total potential energy. Lagrange's equations can be expanded as follows;

$$\frac{d}{dt}\left(\frac{\partial L}{\partial \dot{q}_k}\right) - \frac{\partial L}{\partial q_k} = Q_k \tag{23}$$

Here q_k represents the generalized coordinate and Q_k represents the generalized force. q_k , These coordinates are the minimum number of coordinates sufficient to completely describe the position of the system. The index k represents each of these coordinates. Q_k This term on the right side of the equation represents all external forces and moments acting on the system that cannot be derived from potential energy. Q_k corresponds to a linear force, while for revolute joints, it corresponds to a torque. In the case of the 3-DoF RRR manipulator considered in this study, all joints are revolute, and thus Q_k specifically denotes joint torque. $\mathrm{d}/\mathrm{dt}\,(\,\partial \mathrm{L}\,/\,\partial \dot{\mathrm{q}}_{\mathrm{k}}\,)$ denotes change in generalized momentum over time. This term represents the inertia (acceleration) component of motion. The expression $\partial L\,/\,\partial \dot{q}_{\mathrm{k}}$ gives the momentum associated with $\dot{q}_{\mathrm{k}}$. $\partial L\,/\,\partial q_{\mathrm{k}}$ denotes generalized force (derived from conserved forces). This term generally represents forces derived from potential energy, such as gravitational and spring forces. The expressions for potential and kinetic energy are written in the equations below.

$$V = \sum_{i=1}^{3} m_i g y_i \tag{24}$$

$$T = \sum_{i=1}^{3} \left[\frac{1}{2} m_i (\dot{x}^{\,2} + \dot{y}^2) + \frac{1}{2} I_i \dot{\theta}_i\right] \tag{25}$$

The equation of motion is written as below considering the rigid body dynamic.

$$\bar{M}(q)\ddot{q} + \bar{C}\,(q,\dot{q})\dot{q} + \bar{g}(q) = \tau \tag{26}$$

where $\bar{M}(q)$ represents the inertia matrix, $\bar{C}(q,\dot{q})$ represents the coriolis matrix and $\bar{g}(q)$ represents the gravity matrix. The inertia, coriolis and gravity matrices along with their elements are given below.

$$\bar{M}(q) = \begin{bmatrix} m_{11} & m_{12} & m_{13} \\ m_{21} & m_{22} & m_{23} \\ m_{31} & m_{32} & m_{33} \end{bmatrix} \tag{27}$$

$$\bar{C}\,(q,\dot{q}) = \begin{bmatrix} c_{11} & c_{12} & c_{13} \\ c_{21} & c_{22} & c_{23} \\ c_{31} & c_{32} & c_{33} \end{bmatrix} \tag{28}$$

Equation (29) defines the inertia matrix $M(q)$, which characterizes the mass and inertia distribution of the manipulator.

$$\begin{gathered} m_{11} = p_1 + 2p_2\cos(q_2) + 2p_3\cos(q_3) + 2p_4\cos(q_2+q_3) \\ m_{12} = p_5 + p_2\cos(q_2) + 2p_3\cos(q_3) + p_4\cos(q_2+q_3) \\ m_{13} = p_6 + p_3\cos(q_3) + p_4\cos(q_2+q_3) \\ m_{21} = m_{12} \\ m_{22} = p_5 + 2p_3\cos(q_2+q_3) \\ m_{23} = p_6 + p_3\cos(q_3) \\ m_{31} = m_{13} \\ m_{32} = m_{23} \\ m_{33} = p_6 \end{gathered} \tag{29}$$

$p_{i,j}$ are constant coefficients consisting of the robot's physical properties such as mass, length, moment of inertia, and center of mass.

Equation (30) defines the Coriolis and centrifugal matrix $C(q,\dot{q})$, which models the velocity-dependent forces acting on the joints

$$\begin{gathered} c_{11} = -p_2\sin(q_2)\,\dot{q}_2 - p_3\sin(q_3)\,\dot{q}_3 - p_4\sin(q_2+q_3)(\dot{q}_2+\dot{q}_3) \\ c_{12} = -p_2\sin(q_2)\,(\dot{q}_1+\dot{q}_2) - p_3\sin(q_3)\,\dot{q}_3 - p_4\sin(q_2+q_3)\,(\dot{q}_1+\dot{q}_2+\dot{q}_3) \\ c_{13} = -p_3\sin(q_3)\,(\dot{q}_1+\dot{q}_2+\dot{q}_3) - p_4\sin(q_2+q_3)\,(\dot{q}_1+\dot{q}_2+\dot{q}_3) \\ c_{21} = p_2\sin(q_2)\,\dot{q}_1 - p_3\sin(q_3)\,\dot{q}_3 + p_4\sin(q_2+q_3)\,\dot{q}_1 \\ c_{22} = -p_3\sin(q_3)\,\dot{q}_3 \\ c_{23} = -p_3\sin(q_3)(\dot{q}_1+\dot{q}_2+\dot{q}_3) \\ c_{31} = p_3\sin(q_3)\,(\dot{q}_1+\dot{q}_2) + p_4\sin(q_2+q_3)\,\dot{q}_1 \\ c_{32}\sin(q_3)(\dot{q}_1+\dot{q}_2) \\ c_{33} = 0 \end{gathered} \tag{30}$$

Equation (31) defines the gravity vector $G(q)$, representing the gravitational forces acting on the links of the manipulator.

$$\begin{gathered} g_1 = p_7\cos(q_1) + p_8\cos(q_1+q_2) + p_9\cos(q_1+q_2+q_3) \\ g_2 = p_8\cos(q_1+q_2) + p_9 cos\,(q_1+q_2+q_3) \\ g_3 = p_9 cos\,(q_1+q_2+q_3) \end{gathered} \tag{31}$$

Equation (32) $M(q)$ is the inertia matrix of the manipulator. The elements of the matrix are denoted as p_i, and each p_i is derived from the mass, center-of-mass location, and moments of inertia of the system.

$$\begin{gathered} p_1 = m_1 l_{c,i}^2 + I_{n1} + m_2 l_1^2 + m_c l_{c,2}^2 + I_{n2} + m_3 l_1^2 + m_3 l_2^2 \\ p_2 = m_2 l_1 l_{c,2} + m_3 l_1 l_2 \\ p_3 = m_3 l_2 l_{c,3} \\ p_4 = m_3 l_2 l_{c,3} \\ p_5 = m_2 l_{c,2}^2 + I_{n2} + m_3 l_2^2 + m_c l_{c,3}^2 + I_{n3} \\ p_6 = m_3 l_{c,3} + I_{n3} \\ p_7 = m_2 g l_{c,2} + m_3 g l_2 \\ p_8 = m_2 g l_{c,2} + m_3 g l_2 \\ p_9 = m_3 g l_{c,3} \end{gathered} \tag{32}$$

The Jacobian matrix serves as a mathematical tool that connects joint motion to the movement of the end-effector. For planar robots, the Jacobian matrix is a mathematical model that relates the velocities of the

joints to the linear and angular velocity of the end-effector within the plane of motion. Since the movement is confined to two dimensions, the Jacobian typically takes the form of a $3xn$ matrix for an n -joint planar manipulator. The first two rows represent the x and y components of linear velocity, and the third row corresponds to the angular velocity about the axis perpendicular to the plane.

This relationship can be expressed as:

$$\dot{x} = J(q)\dot{q} \tag{33}$$

In planar systems, the Jacobian is essential for differential kinematics, trajectory control, and force transmission analysis. It also helps identify singular points, where the manipulator loses mobility in certain directions, which is crucial for safe and efficient motion planning.

The Jacobian matrix and elements are given Eqs. 34 and 35.

$$J(q) = \begin{bmatrix} j_{11} & j_{12} & j_{13} \\ j_{21} & j_{22} & j_{23} \\ j_{31} & j_{32} & j_{33} \end{bmatrix} \tag{34}$$

$$\begin{gathered} j_{11} = -l_1 \sin(q_1) - l_2 \sin(q_1 + q_2) - l_3 \sin(q_1 + q_2 + q_3) \\ j_{12} = -l_2 \sin(q_1 + q_2) - l_3 \sin(q_1 + q_2 + q_3) \\ j_{13} = -l_3 \sin(q_1 + q_2 + q_3) \\ j_{21} = l_1 \cos(q_1) + l_2 \cos(q_1 + q_2) + l_3 \cos(q_1 + q_2 + q_3) \\ j_{22} = l_2 \cos(q_1 + q_2) + l_3 \cos(q_1 + q_2 + q_3) \\ j_{23} = l_3 \cos(q_1 + q_2 + q_3) \\ j_{31} = 1 \\ j_{32} = 1 \\ j_{33} = 1 \end{gathered} \tag{35}$$

Control system design: PID and Sliding Mode Control

The subsequent sections will delve into the theoretical underpinnings and practical implementation of both PID control and SMC for the precise position and motor control of the 3-DoF RRR robotic manipulator. This investigation will analyze the comparative performance of these two control paradigms, particularly in terms of their robustness against disturbances and their capacity for precise trajectory tracking. The chosen control strategies aim to address the inherent nonlinearities and uncertainties present in robotic systems, which are often compounded by factors such as model inaccuracies and external perturbations. Furthermore, the proposed control strategies will be rigorously tested through simulations in MATLAB/Simulink, providing a comprehensive assessment of their effectiveness in achieving stable and accurate manipulation for this specific robotic platform.

PID control

The PID controller is a widely adopted feedback control mechanism due to its structural simplicity and ease of implementation in various industrial and medical robotic applications. Its widespread use stems from its ability to provide stable and accurate control through a combination of present error (proportional), accumulated past errors (integral), and predicted future errors (derivative). The PID controller generates a control output based on the proportional, integral, and derivative terms of the error signal, each addressing a specific aspect of system response. Specifically, the proportional term responds to the current error, the integral term compensates for steady-state errors by accumulating past errors, and the derivative term anticipates future errors by considering the rate of change of the error signal. The fundamental mathematical expression of the PID controller is written as follows:

$$u(t) = K_P e(t) + K_I \int_0^{\tau} e(t)dt + K_D \frac{de(t)}{dt} \tag{36}$$

Here, $u(t)$, represents the controller output, while K_P, K_I and K_D denote the proportional, integral, and derivative gains, respectively. The term $e(t)$ refers to the error signal. A schematic representation of the PID feedback control system is provided in Fig. 2.

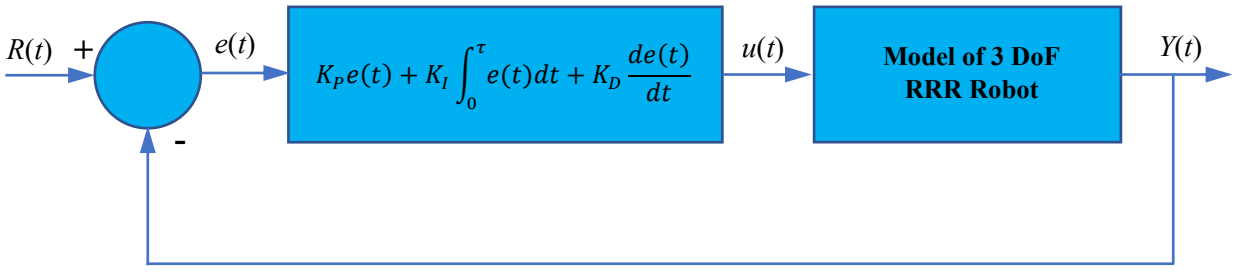

Figure 2. Block diagram of the PID control

In this control architecture, the reference input $(R(t))$ defines the desired motion or position of the end-effector. The actual output $(Y(t))$ of the robot is continuously compared with the reference signal, and the resulting difference constitutes the error signal $(e(t))$. This error is processed by a PID controller, where the proportional term (K_P) reacts to the instantaneous error, the integral term (K_I) compensates for the accumulation of past errors, and the derivative term (K_D) anticipates future error trends based on the rate of change. The combined control action $(u(t))$ generated by the PID controller is applied to the dynamic model of the 3-DoF RRR robot,

producing the system output ($y(t)$). Through the feedback loop, this output is continuously monitored and compared to the reference, enabling real-time error minimization and precise trajectory tracking.

Sliding mode control

The sliding mode control strategy, conversely, represents a class of robust nonlinear control methods particularly well-suited for systems with uncertainties and disturbances, offering a deterministic approach to achieve precise trajectory tracking. This approach is characterized by its ability to drive the system states onto a pre-defined sliding surface in the state space and maintain them there, thereby exhibiting insensitivity to matched uncertainties and disturbances [19]. The design of an SMC typically involves two main steps: the selection of a suitable sliding surface that defines the desired system behavior and the design of a control law that ensures the system states converge to and remain on this surface [20]. The robustness of SMC stems from its high-speed switching control action, which actively compensates for modeling inaccuracies and external perturbations [21]. This inherent robustness makes SMC an attractive option for controlling complex robotic systems, such as the 3-DoF RRR manipulator, where precise and stable control is paramount despite dynamic uncertainties and external loads.

The SMC method is also implemented in this study. In this approach, the robot's joint angles are selected as the primary control variables of the system. The control strategy is designed to regulate these joint angles effectively, even under the influence of external disturbances and model uncertainties. Fig. 3 illustrates the block diagram of the SMC framework, highlighting the feedback structure and the manner in which the control law maintains system stability and tracking performance despite perturbations.

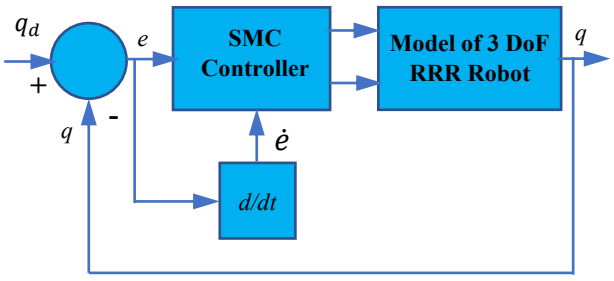

Figure 3. Block diagram of the SMC method

Fig. 4 illustrates the concept of the sliding surface used in the SMC method. In this representation, the horizontal axis denotes the position, while the vertical axis represents the speed. The diagonal line marked as $S = 0$ defines the sliding surface, which represents the desired dynamic behavior of the system. The control objective in SMC is to drive the system states toward this surface and maintain their motion along it. The curved arrows indicate the corrective control actions that force the trajectory toward the sliding surface from either side. Once the system states reach $S = 0$, they "slide" along this surface toward the equilibrium point, ensuring stable convergence to the desired position and speed despite disturbances or modeling uncertainties.

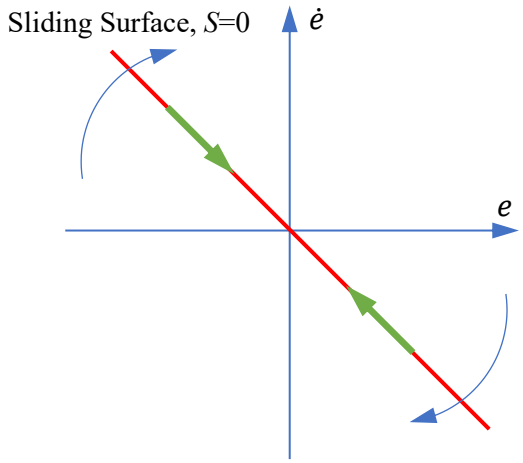

Figure 4. System trajectory and the sliding surface ($S = 0$) for SMC.

The tracking error and its time derivative are defined in Eqs. 37 and 38:

$$e(t) = q_d(t) - q(t) \tag{37}$$

$$\dot{e}(t) = \dot{q}_d(t) - \dot{q}(t) \tag{38}$$

where q_d is the desired joint trajectory and q is the actual trajectory. First and second order derivatives are considered in Eq. 37. The sliding surface is defined as:

$$S = \dot{e} + \lambda e \tag{39}$$

where S is the sliding surface, λ is a positive definite symmetric matrix, and the control signal u is given in Eq. 40.

$$u = -k \times \text{sign}(s)$$
$$sat(s/\varphi) = \begin{cases} \frac{s}{\varphi}, & \left|\frac{s}{\varphi}\right| \le 1 \\ \text{sign}\left(\frac{s}{\varphi}\right), & \left|\frac{s}{\varphi}\right| > 1 \end{cases} \tag{40}$$

To mitigate chattering, a saturation function is employed, where φ defines the boundary layer thickness, k is a constant gain, and $sign()$ acts as a switching function. System stability is ensured using Lyapunov's criterion.

Numerical simulations

Simulation studies are performed in this section using the dynamic equations of the system, and the graphical results demonstrate the performance differences between SMC and PID control strategies. The simulations are implemented in MATLAB/Simulink.

Numerical simulation for PID control

To facilitate real-time adjustments of the PID gains, the "Slider Gain" graphical user interface (GUI) component was employed. This allowed the effects of different gain values on the motion performance of the robot joints to be observed instantaneously. The dynamic response of the robot was recorded using "Scope" blocks, providing a detailed analysis of joint angles and velocities over time. Furthermore, the 'PID Tuner' tool was utilized to evaluate the system's response characteristics, including rise time, settling time, and overshoot. This enabled a quantitative assessment of how the gain settings affect system stability and reference tracking performance. The results demonstrate how different combinations of K_P, K_I and K_D gains influence the performance of each joint and aid in identifying optimal gain values. Overall, the proposed methodology provides a systematic approach for both the design and simulation stages of the PID control system, offering an effective solution for precise position control of robot manipulators. Fig. 5 illustrates the Simulink block diagram of the PID-controlled robot manipulator.

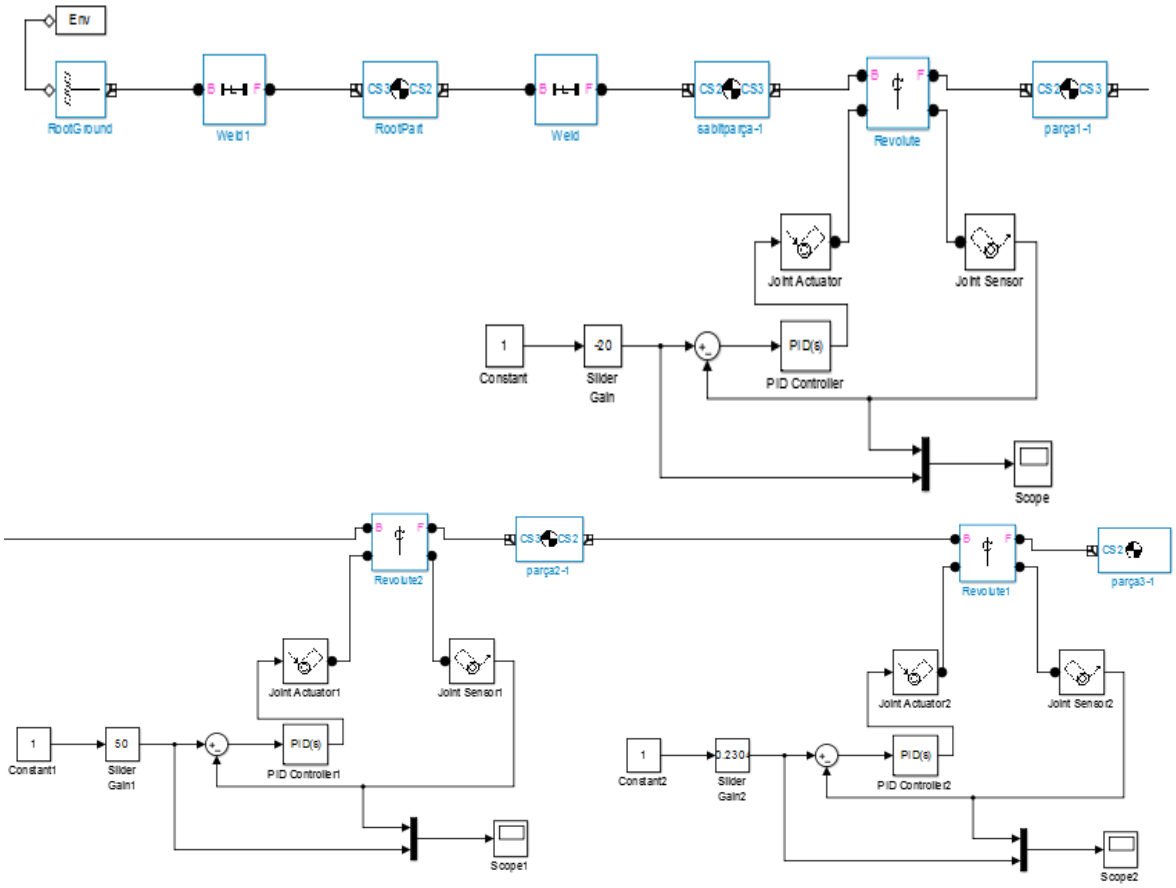

Figure 5. The simulink block diagram for PID control

In the MATLAB/Simulink-based simulation environment, several interface components are employed to analyze and adjust the performance of the robot manipulator under PID control. The Robot Simulation (Robotsim) window (Fig. 6-a) provides a three-dimensional visualization of the manipulator, enabling real-time observation of its physical movements and joint positions (assumed as Joint 1, Joint 2, and Joint 3) in response to varying PID gain settings. The Slider Gain windows (Slider Gain, Slider Gain1, Slider Gain2) serve as graphical user interface elements that allow real-time adjustment of the proportional (K_P), integral (K_I), and derivative (K_D) gains assigned to each joint or control block. Each slider is defined by a minimum (Low) and maximum (High) numerical value, while the current slider position corresponds to the gain value actively used by the system, which can be dynamically modified during simulation. The PID tuner functions as MATLAB's automatic PID tuning tool, providing step response plots, adjusted gain values and quantitative performance metrics such as rise time, settling time, overshoot, peak value, gain margin, phase margin, and closed-loop stability. This interface enables systematic evaluation of controller performance when the PID parameters converge toward near-optimal values. Additionally, the Scope windows are utilized to visualize time-domain behaviors of various control signals, including joint positions, velocities, error signals, and control outputs (Fig. 6-b). Typically, the yellow trace represents the reference input, while the purple trace denotes the actual system response of the manipulator. Empty scopes indicate that no simulation has been executed or the data have been reset, as reflected by static lines in Fig. 6-b, whereas the active plots presented in Fig. 7 correspond to real-time responses recorded during dynamic simulations.

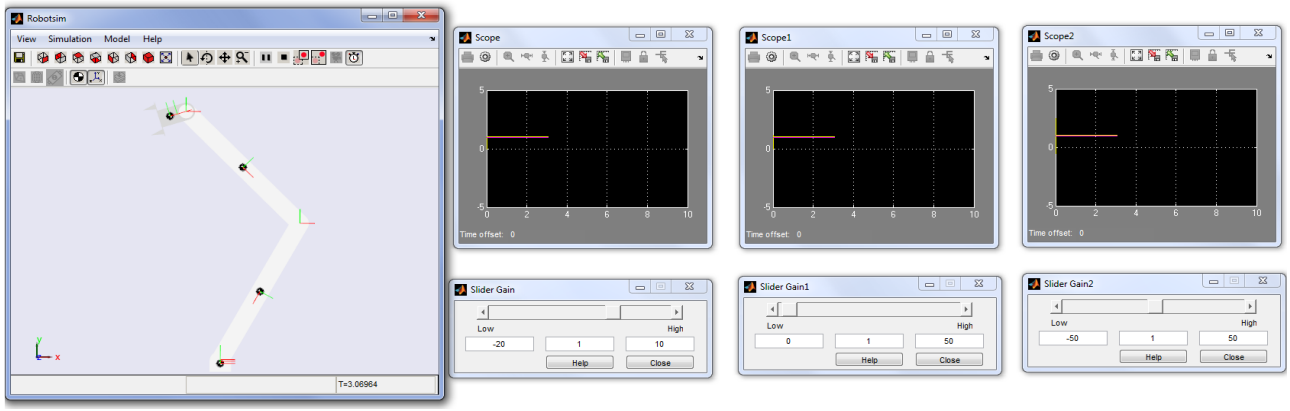

(a) (b)

Figure 6. Robotsim, scope and slider gain windows

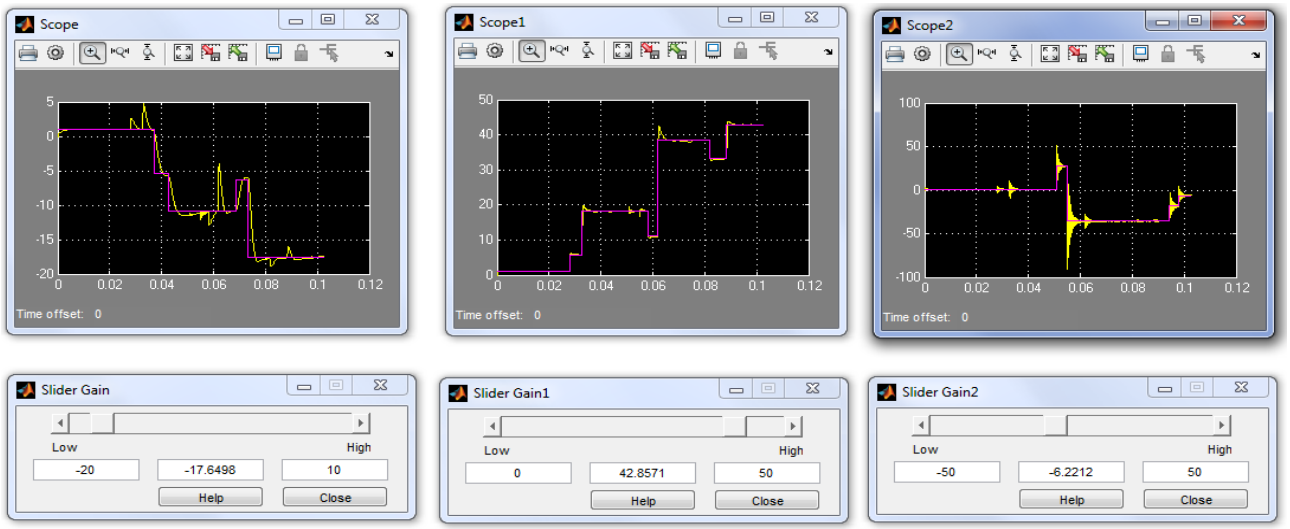

Figure 7. Simulation graphs for joint 1, joint 2 and joint 3

When Fig. 7 is examined, it becomes evident that the initially assigned PID gains are inadequate for ensuring stable system behavior. Therefore, the controller parameters must be returned to achieve stability. The rising peaks observed in the plot further highlight the uncontrolled and oscillatory response of the system, providing a clear indication of instability.

The simulation results presented in the figures illustrate the stability analysis and performance improvement achieved through PID tuning for each joint of the robot manipulator. In Fig. 8-a (Joint 1), the tuned response demonstrates a fast rise time and minimal overshoot, indicating that the controller successfully drives the system to the reference value in a short time while maintaining stability. The performance indices reported in the PID Tuner interface confirm that the joint reaches steady-state quickly with satisfactory accuracy.

Fig. 8-b (Joint 2) presents both the unstable initial response and the stabilized tuned response on the same plot. The initial response exhibits oscillatory behavior with pronounced overshoot, which highlights the inadequacy of the initial PID gains for stable operation. After tuning, the improved response is clearly observed, with oscillations eliminated, overshoot reduced, and the system achieving a stable convergence toward the reference signal. This comparison underscores the effectiveness of the tuning process in enhancing stability and damping characteristics.

Finally, Fig. 8-c (Joint 3) displays the tuned response for the third joint, which is characterized by smooth and well-damped behavior. The system shows a slightly slower rise compared to Joint 1, yet it achieves convergence with negligible overshoot and a short settling time, confirming robust and stable performance.

Overall, the results for all three joints demonstrate that the PID tuning process successfully improved the dynamic characteristics of the manipulator, leading to enhanced stability, reduced overshoot, and reliable reference tracking. These findings validate the effectiveness of the tuning methodology in achieving precise closed-loop control across different joints of the robotic system.

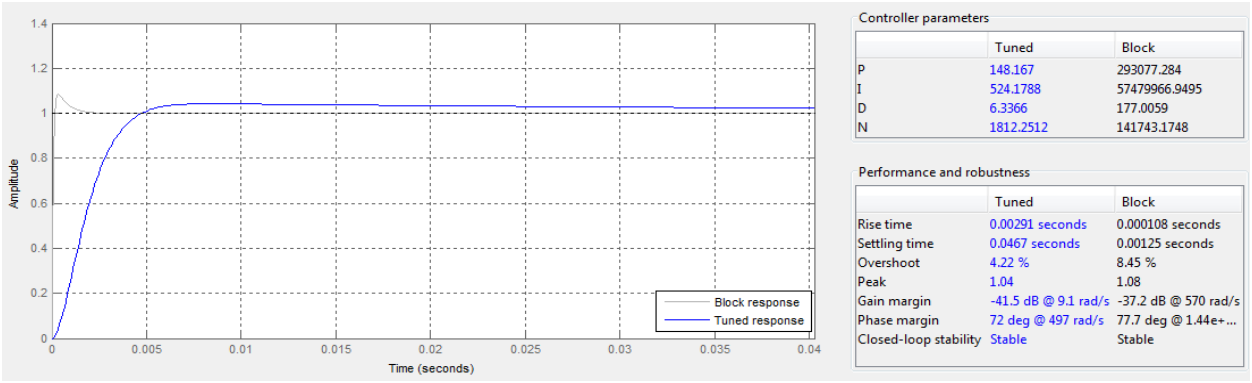

(a)

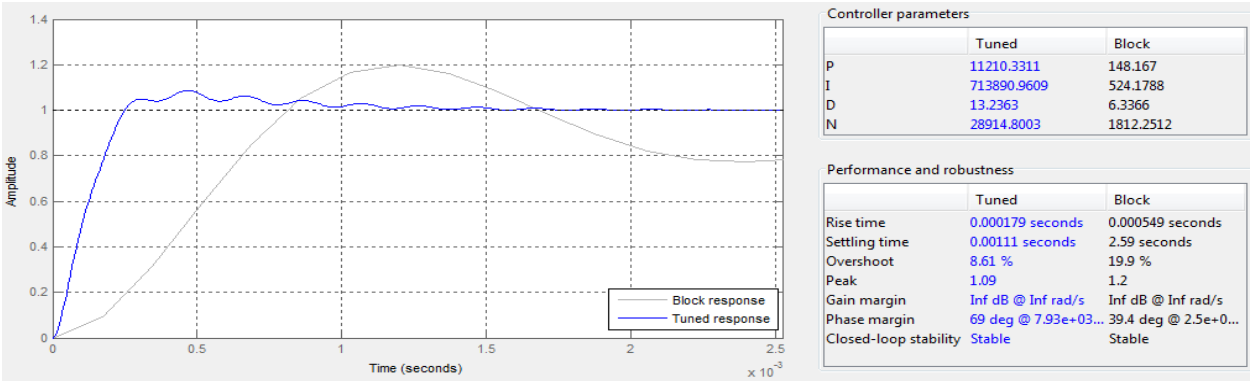

(b)

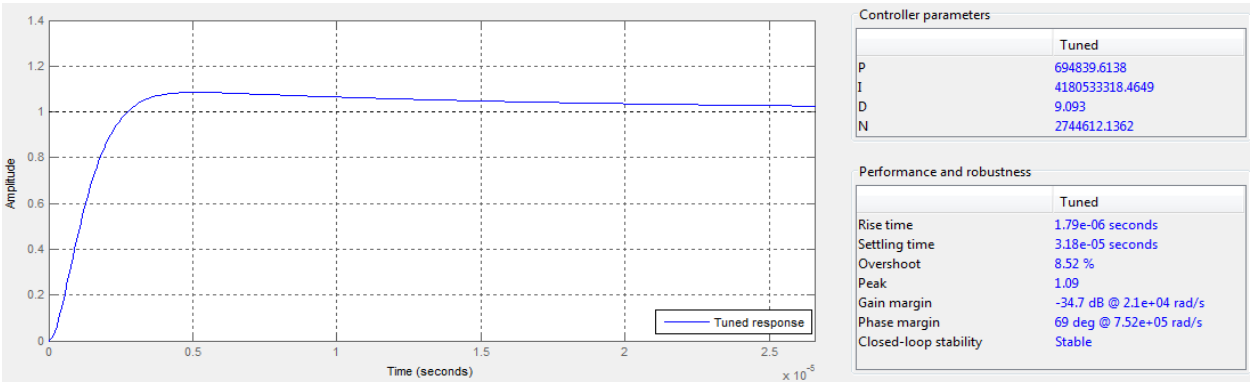

(c)

Figure 8. PID-tuned responses of the three manipulator joints

The effectiveness of the PID tuning process is quantitatively summarized in Table 2, which compares the key performance metrics before and after tuning for each joint.

Table 2. The effectiveness of the PID tuning process

Performance Metric	Joint	Initial (Block)	After Tuning (Tuned)	Improvement (%)
Rise Time (s)	1	0.000108	0.00291	-96.3% ↑
	2	0.000549	0.000179	+67.4% ↓
	3	1.17e-05	1.79e-06	+84.7% ↓
Settling Time (s)	1	0.00125	0.0467	-96.3% ↑
	2	2.59	0.00111	+99.96% ↓
	3	6.07e-04	3.18e-05	+94.7% ↓
Overshoot (%)	1	8.45	4.22	+50.1% ↓
	2	19.9	8.61	+56.7% ↓
	3	22.6	8.52	+62.3% ↓

As quantitatively demonstrated in Table 2, the PID tuning process yielded significant performance enhancements across all three joints, albeit with different strategic emphases. For Joint 2, the improvements were exceptionally dramatic: settling time was reduced by 99.96%, rise time by 67.4%, and overshoot by 56.7%. Joint 3 also showed outstanding results, with overshoot reduced by 62.3%, rise time by 84.7%, and settling time by 94.7%. For Joint 1, the tuner prioritized stability over raw speed; it significantly reduced the overshoot by 50.1% to achieve a smoother response, accepting an increase in rise and settling times as a trade-off. These results underscore that the PID tuning process is a powerful tool for systematically shaping the dynamic response of each joint, allowing for tailored performance characteristics that balance speed, stability, and overshoot based on specific application requirements.

Numerical simulation for SMC

Fig. 9 illustrates the MATLAB/Simulink model of the manipulator designed for the implementation of SMC. The model incorporates the dynamic equations of the manipulator, the defined sliding surfaces, and the control laws, allowing for numerical simulation and analysis of the system's closed-loop performance under SMC.

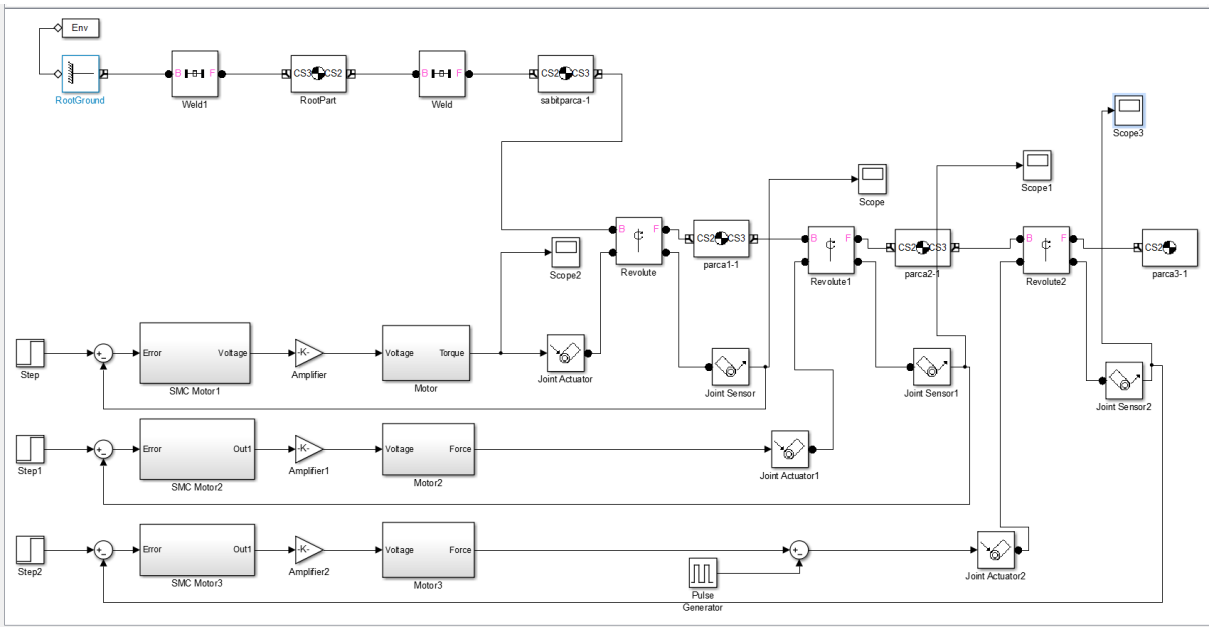

Figure 9. MATLAB/Simulink model of the manipulator for SMC

Fig. 10 presents the model of the servo motors. The model incorporates the motors' dynamic characteristics, enabling accurate simulation of their behavior within the manipulator system. Fig. 11 illustrates the sliding mode control (SMC) model, where the motor dynamics are integrated with the control algorithm, allowing for evaluation of closed-loop performance, reduction of tracking error, and assessment of system stability under SMC.

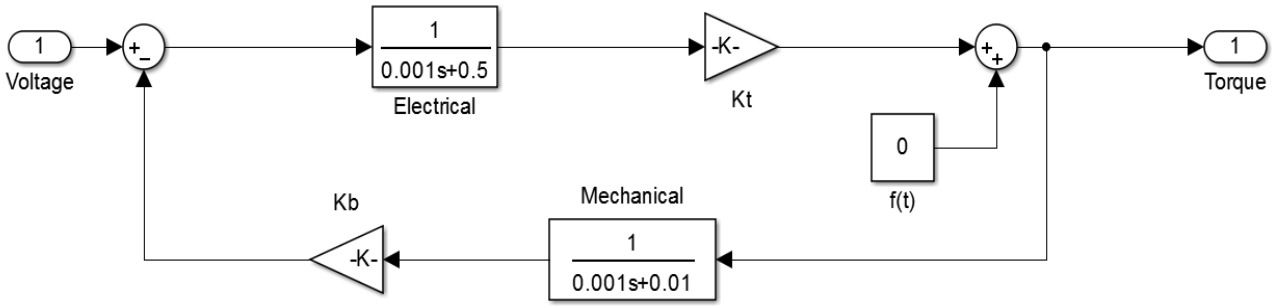

Figure 10. Simulink model of the servo motors

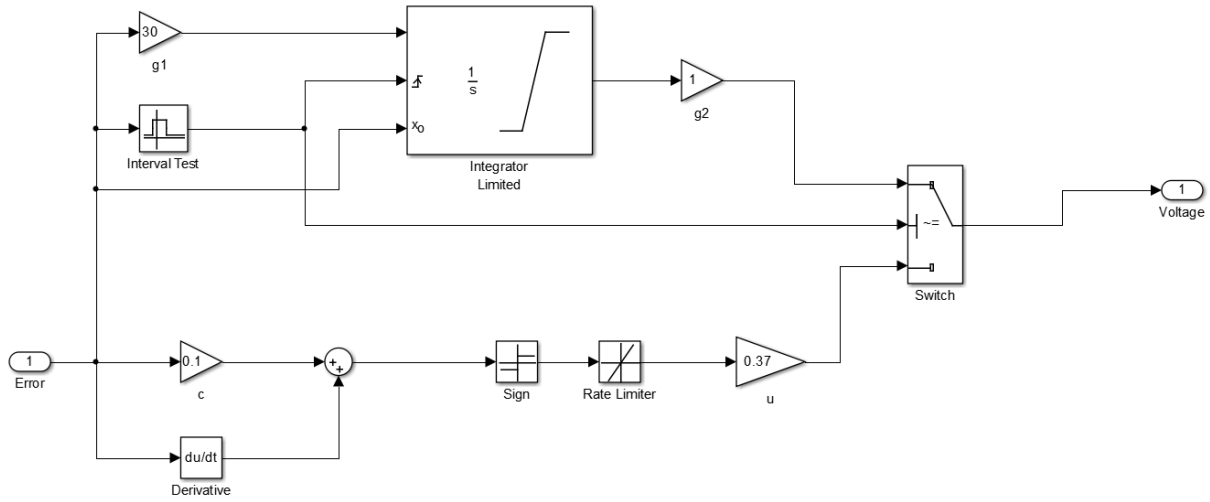

Figure 11. Simulink model of the SMC

Table 3. Physical parameters of the servo motors

Parameters	L $[H]$	R $[\Omega]$	J $[kg.m2]$	B $[Nm/s]$	K_t $[Nm/A]$	K_b $[V/(rad/s)]$
Value	1	0.5	0.001	0.01	0.008	0.68

The physical parameters used in the simulations were selected based on commonly referenced values in the literature for small-scale DC servo motors applied to robotic manipulators. These values (Table 3) provide a realistic yet computationally manageable representation of actuator dynamics, ensuring that the simulation reflects practical system behavior while maintaining tractability. Similarly, link lengths and masses were chosen to match typical dimensions of a laboratory-scale 3-DoF RRR manipulator, where each link length was normalized to facilitate comparison of control performance rather than focus on a specific robot model. The PID gains were initially tuned using MATLAB's 'PID Tuner' tool, and fine adjustments were performed via the 'Slider Gain' interface to illustrate the sensitivity of system performance to parameter variation.

The controller processes the error signal through the interval test block, which performs a switching operation. If the error remains outside the desired range, this indicates that the sliding surface has not yet been reached, and the upper part of the algorithm operates to drive the system toward the sliding surface. Once the sliding surface is reached, the lower part of the algorithm functions to keep the error close to this surface. The overall system consists of three step inputs, one impulse disturbance acting on the end-effector, three sliding mode controllers, three motors, and the robot arm blocks. The difference between the actual and desired forces is provided as the input to the controller.

A trajectory was defined by applying a step input of 10 units to each link. The control parameters were adjusted to regulate overshoot, settling time, and steady-state error. For the first and second links of the robot, a stable output was achieved after an initial transient oscillation. In the case of the third link, an impulse disturbance of amplitude –10 with a duration of 0.1 s was introduced into the system. As a result, the SMC effectively attenuated the disturbance, ensuring progressively improved damping of the force response over time. The torque responses of Links 1, 2, and 3 are illustrated in Fig. 12.

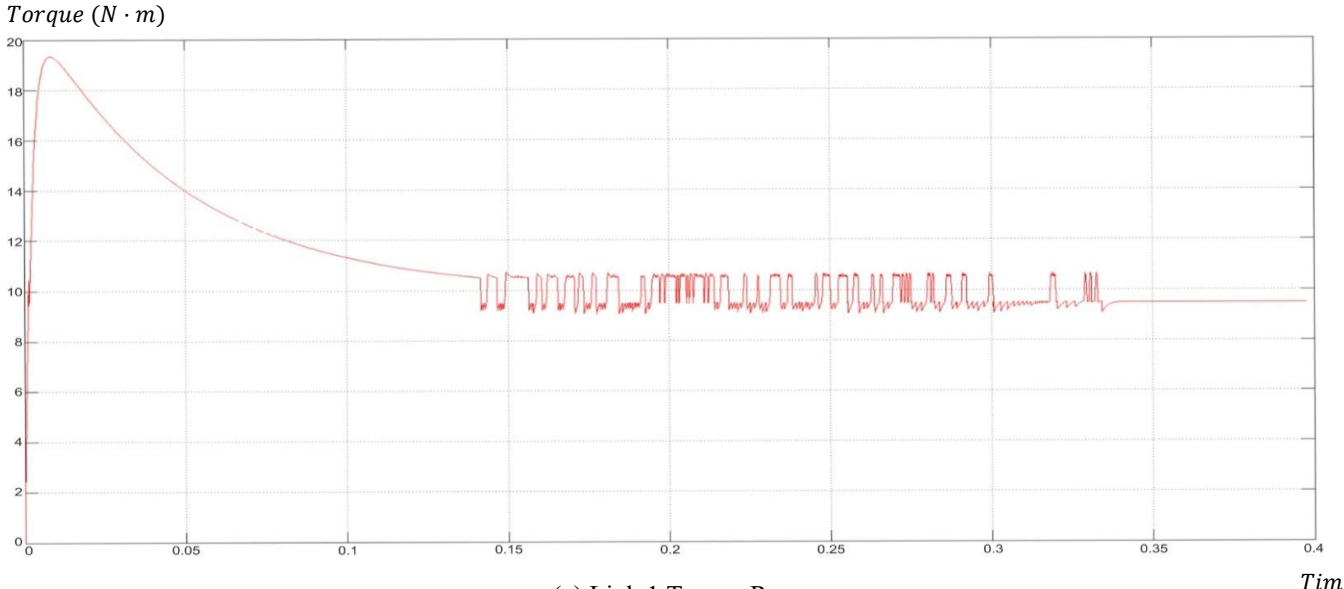

(a) Link 1 Torque Response

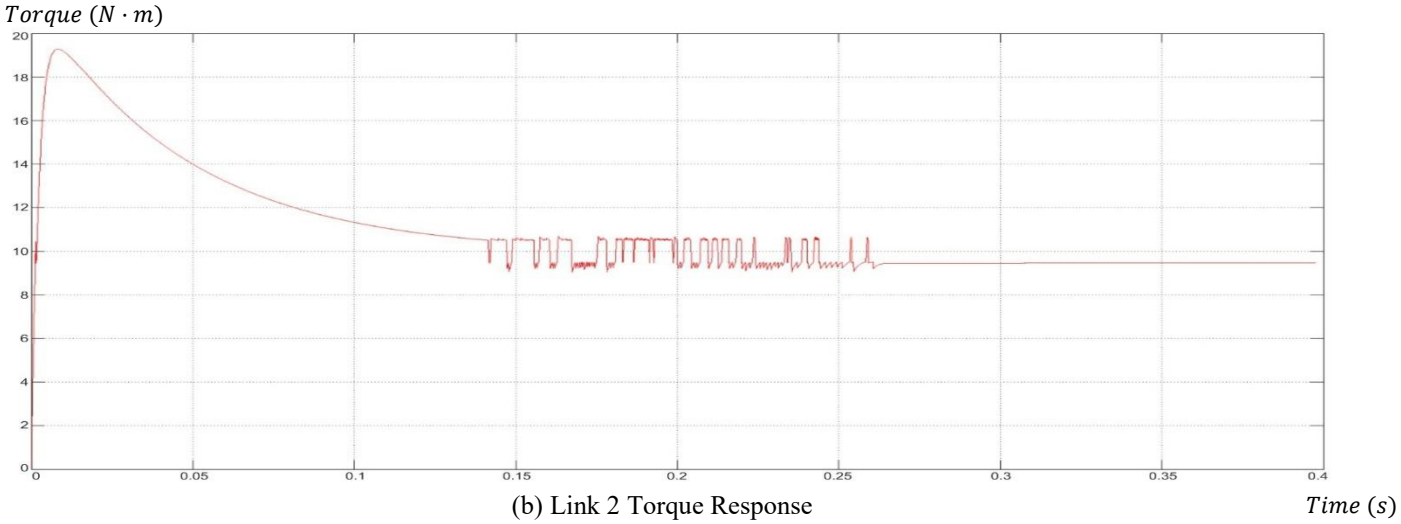

(b) Link 2 Torque Response

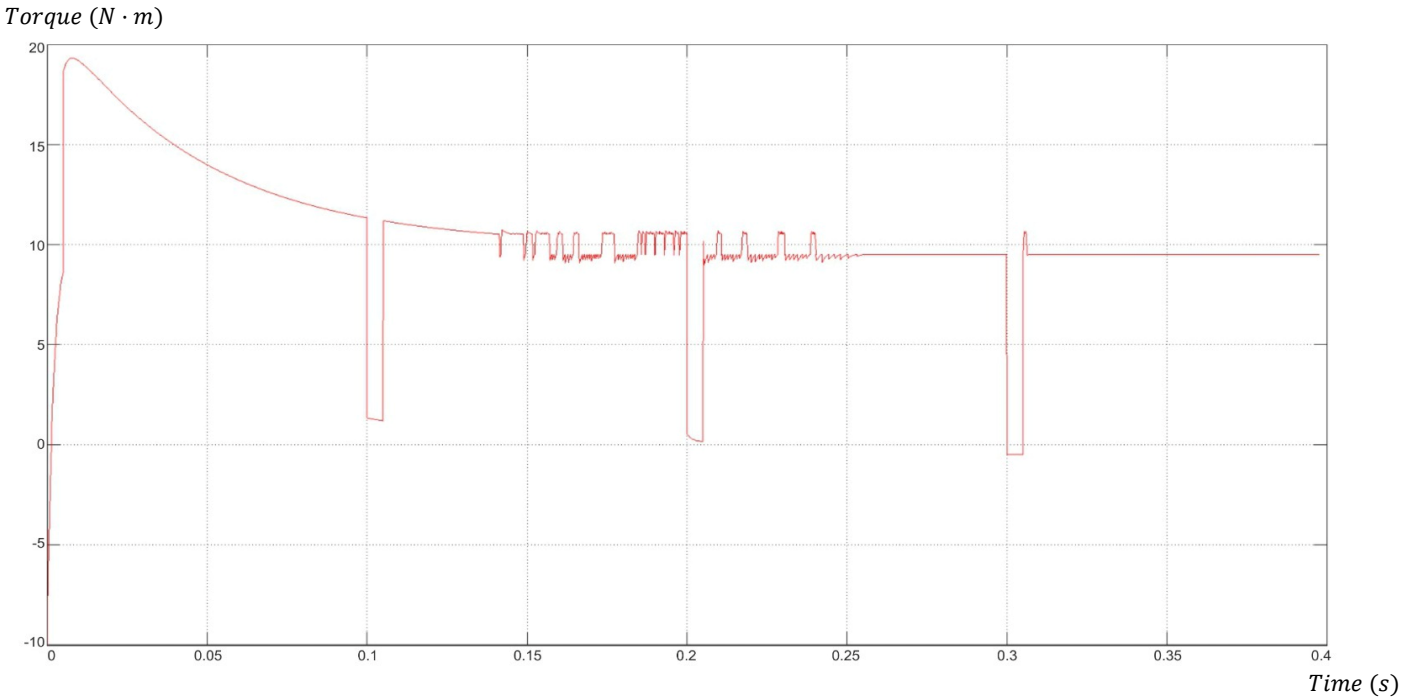

(c) Link 3 Torque Response

Figure 12. The torque responses of Links 1, 2, and 3

The torque responses of the robotic arm controlled with SMC exhibit a varying yet consistent control behavior in accordance with the dynamic characteristics of each joint. The torque response of all joints began with a high transient peak torque of approximately 19-20 Nm at time t=0, generated to overcome the system's inertia and rapidly reset the initial error. This rapid rise and decay within approximately 0.1 s demonstrate the controller's rapid response time and the system's good damping. The low-amplitude and symmetric chattering observed in Link 1 demonstrates that the controller can achieve stability with a relatively low control effort, thanks to the dynamic isolation provided by its high inertia. In contrast, the high-amplitude and asymmetric oscillations in Link 2 demonstrate that this joint is subject to severe dynamic coupling resulting from both base movements and the end load it carries. The fact that the controller must constantly apply high, directionally shifting torques to compensate for these complex forces highlights the robustness of the SMC but also indicates the mechanical strain on the system. The response of Link 3 is characterized by periodic, large torque dips, particularly around 0.1 s, 0.2 s, and 0.3 s, indicating that the motor quickly adapts to changes in the load dynamics and/or sharp turns in the trajectory. It provides stable control with a moderate level of chattering to maintain end-effector sensitivity.

Discussion

The simulation results reveal distinct performance characteristics and practical implications for each control strategy in robotic manipulator applications. PID control demonstrated exceptional performance in scenarios with well-defined system parameters and minimal external disturbances. The systematic tuning process proved critical, as improperly tuned PID gains led to significant

oscillations and instability, as evident in the initial responses shown in Figure 7. However, once optimized, PID controllers provided smooth trajectory tracking with minimal overshoot and fast settling times, particularly suitable for applications where system dynamics are accurately known and consistent. For Joint 1, the tuner explicitly made a stability-speed trade-off. To ensure a smooth, predictable response and mitigate oscillations, the control loop was damped, slashing overshoot by 50.1%. The consequent increases in rise and settling times were an accepted and calculated performance cost for achieving this greater robustness.

The results for Joint 2 represent a paradigm shift in performance, moving from a previously sluggish or oscillatory system to a highly responsive one. The 99.96% improvement in settling time is a clear indicator of a system that now converges on its target value almost instantaneously. When combined with the substantial gains in rise time (67.4%) and overshoot (56.7%), it demonstrates a comprehensive optimization of the joint's dynamic agility.

Joint 3's performance was transformed, with results highlighting a system that is now both fast and stable. The 84.7% improvement in rise time shows a much quicker initial response to command signals, while the 94.7% reduction in settling time and 62.3% lower overshoot confirm that this speed is effectively managed without introducing instability, indicating a well-tuned and high-performance servo loop.

In contrast, Sliding Mode Control exhibited remarkable robustness against uncertainties and external disturbances. The impulsive disturbance applied to Link 3, simulating real-world operational challenges, was effectively rejected by the SMC controller while maintaining system stability. This robustness stems from SMC's inherent ability to handle matched uncertainties through its discontinuous control law. However, this advantage comes with the challenge of chattering, which was mitigated in this study through boundary layer implementation at the cost of slightly reduced tracking precision near the sliding surface.

The comparative analysis suggests a clear trade-off between performance optimization and robustness. PID controllers offer simpler implementation and excellent performance under nominal conditions but require accurate system modeling and are vulnerable to parameter variations. SMC, while more complex to design, provides inherent robustness making it preferable for applications with significant uncertainties or varying operating conditions. This dichotomy highlights that controller selection should be driven by specific application requirements rather than seeking a universally superior solution.

From an implementation perspective, the computational demands also differ substantially. PID control requires minimal computational resources, facilitating real-time implementation on standard hardware. SMC, with its more complex algorithm, demands higher processing capabilities, which may influence hardware selection in practical applications. These practical considerations are crucial for engineers designing control systems for industrial robotic manipulators.

Conclusions

This study aims to develop, implement and compare PID and Sliding Mode Control strategies for a 3-DoF RRR robotic manipulator. Through detailed kinematic and dynamic modeling and comprehensive MATLAB/Simulink simulations, the performance of both controllers was validated. The research confirmed that a well-tuned PID controller can achieve excellent stability and reference tracking, while SMC provides superior robustness against system uncertainties and external disturbances. This comparative analysis validates that both methodologies offer powerful solutions for achieving high-performance control in robotic manipulators, vital for modern industrial and medical applications. Future work could explore adaptive or AI-integrated control methods to further enhance performance in dynamic environments.

Ethics committee approval and conflict of interest statement

There is no need to obtain permission from the ethics committee for the article prepared

There is no conflict of interest with any person / institution in the article prepared

Authors' Contributions

Eker H: The MATLAB/Simulink simulation environment was developed; the 3-DoF RRR manipulator model was implemented; forward and inverse kinematics based on the DH convention were formulated; PID and Sliding Mode Control structures were implemented and tuned; numerical simulations were carried out; simulation data were analyzed; figures and tables were prepared; and the manuscript was drafted.

Huseyinoglu M: The study was conceptualized and supervised; the kinematic and dynamic modeling framework based on the Lagrangian formulation was established; the control methodology and comparative evaluation strategy were defined; the interpretation of stability and robustness results was guided; and the manuscript was critically reviewed and finalized.

References

[1] Z. Kuang, X. Zhang, L. Sun, H. Gao, and M. Tomizuka, "Feedback-based Digital Higher-order Terminal Sliding Mode for 6-DoF Industrial Manipulators," arXiv (Cornell University), Jan. 2021, doi: 10.48550/arxiv.2102.03531.

[2] K. Jayaswal, D. K. Palwalia, and S. Kumar, "Performance investigation of PID controller in trajectory control of two-link robotic manipulator

in medical robots," Journal of Interdisciplinary Mathematics, vol. 24, no. 2, p. 467, Feb. 2021, doi: 10.1080/09720502.2021.1893444.

[3] G. Sherif, S. Ahmad, M. Saad, and G. Fayez, "Dynamic Modelling with a Modified PID Controller of a Three Link Rigid Manipulator," International Journal of Computer Applications, vol. 179, no. 34, p. 37, Apr. 2018, doi: 10.5120/ijca2018916772.

[4] S. Hasan, "A Realistic Model Reference Computed Torque Control Strategy for Human Lower Limb Exoskeletons," arXiv (Cornell University), Sep. 2024, doi: 10.48550/arxiv.2410.07200.

[5] C. Ma and Z. Zhang, "Predictive reinforcement learning based adaptive PID controller," 2025, doi: 10.48550/ARXIV.2506.08509.

[6] V. T. Aghaei, A. Seyyedabbasi, J. Rasheed, and A. M. Abu-Mahfouz, "Sand cat swarm optimization-based feedback controller design for nonlinear systems," Heliyon, vol. 9, no. 3, Feb. 2023, doi: 10.1016/j.heliyon.2023.e13885.

[7] J. Shanbhag et al., "Methods for integrating postural control into biomechanical human simulations: a systematic review," Journal of NeuroEngineering and Rehabilitation, vol. 20, no. 1. BioMed Central, Aug. 21, 2023. doi: 10.1186/s12984-023-01235-3.

[8] A. Ashoori, B. Moshiri, A. K. Sedigh, and M. Bakhtiari, "Optimal control of a nonlinear fed-batch fermentation process using model predictive approach," Journal of Process Control, vol. 19, no. 7, p. 1162, Apr. 2009, doi: 10.1016/j.jprocont.2009.03.006.

[9] N. Gafurov, S.-Y. Lee, U. Ali, M. Irfan, I. Kim, and T. Lee, "AI-driven digital twin for autonomous web tension control in Roll-to-Roll manufacturing system," Scientific Reports, vol. 15, no. 1, Jul. 2025, doi: 10.1038/s41598-025-09813-2.

[10] P. Saraf, M. Gupta, and A. M. Parimi, "A Comparative Study Between a Classical and Optimal Controller for a Quadrotor," 2021 IEEE 18th India Council International Conference (INDICON), p. 1, Dec. 2020, doi: 10.1109/indicon49873.2020.9342485.

[11] N. Sitapure and J. S. Kwon, "Require Process Control? LSTMc is all you need!," arXiv (Cornell University), Jan. 2023, doi: 10.48550/arxiv.2306.07510.

[12] G. Bujgoi and D. Şendrescu, "Tuning of PID Controllers Using Reinforcement Learning for Nonlinear System Control," Processes, vol. 13, no. 3, p. 735, Mar. 2025, doi: 10.3390/pr13030735.

[13] K. M. S. Mamani and A. Prado, "Integrating Model Predictive Control with Deep Reinforcement Learning for Robust Control of Thermal Processes with Long Time Delays," Processes, vol. 13, no. 6, p. 1627, May 2025, doi: 10.3390/pr13061627.

[14] K. J. Åström and T. Hägglund, "The future of PID control," Control Engineering Practice, vol. 9, no. 11, p. 1163, Nov. 2001, doi: 10.1016/s0967-0661(01)00062-4.

[15] R. Wu, J. Ai, and T. Li, "InstructMPC: A Human-LLM-in-the-Loop Framework for Context-Aware Control," 2025, doi: 10.48550/ARXIV.2504.05946.

[16] W. Shen, X. Chen, M. Pons, and J. Corriou, "Model predictive control for wastewater treatment process with feedforward compensation," Chemical Engineering Journal, vol. 155, p. 161, Jul. 2009, doi: 10.1016/j.cej.2009.07.039.

[17] Pandey, B. Bohara, R. Pungaliya, S. C. Patwardhan, and R. Banerjee, "A thermal comfort-driven model predictive controller for residential split air conditioner," Journal of Building Engineering, vol. 42, p. 102513, Apr. 2021, doi: 10.1016/j.jobe.2021.102513.

[18] L. Zollo, E. Lopez, L. Spedaliere, N. García-Aracil, and E. Guglielmelli, "Identification of Dynamic Parameters for Robots with Elastic Joints," Advances in Mechanical Engineering, vol. 7, no. 2, Dec. 2014, doi: 10.1155/2014/843186.

[19] M. Božić, M. Vasiljević-Toskić, M. Bodić, and V. Rajs, "Advantages of a combination of PD and PID controller over PID controller in the example of quadcopter control and stabilization," IJEEC - INTERNATIONAL JOURNAL OF ELECTRICAL ENGINEERING AND COMPUTING, vol. 4, no. 1, Jan. 2020, doi: 10.7251/ijeec2001043b.

[20] M. Fliess and C. Join, "An alternative to proportional-integral and proportional-integral-derivative regulators: Intelligent proportional-derivative regulators," International Journal of Robust and Nonlinear Control, vol. 32, no. 18, p. 9512, Jul. 2021, doi: 10.1002/rnc.5657.

[21] L. A. Tuấn and S. Lee, "3D cooperative control of tower cranes using robust adaptive techniques," Journal of the Franklin Institute, vol. 354, no. 18, p. 8333, Nov. 2017, doi: 10.1016/j.jfranklin.2017.10.026.

Dicle University
Journal of Engineering
https://dergipark.org.tr/tr/pub/dumf
duje.dicle.edu.tr

Research Article

Multi-Objective Optimization of Axially Flat Finned Cam-Shaped and Elliptical Tube Banks Based on Entropy Generation and Thermal Hydraulic Performance

Mehmet ÖZKARAKOÇ[1*], Muhammet Nasıf KURU[2]

[1] Tarsus University, Department of Mechanical Engineering, mehmetozkarakoc@gmail.com, Orcid No: 0009-0000-0312-6707
[2] Tarsus University, Vocational School of Technical Sciences, mnasifkuru@tarsus.edu.tr, Orcid No: 0000-0002-5941-1221

ARTICLE INFO

Article history:

Received 23 October 2025
Received in revised form 16 December 2025
Accepted 16 December 2025
Available online 30 December 2025

Keywords:

Tube bank, axially flat fin, cam-shaped tube, elliptical tube, multi-objective optimization

Doi: 10.24012/dumf.1809125

* Corresponding author

ABSTRACT

The use of different tube geometries in tube bank heat exchangers has a significant impact on thermal hydraulic performance and entropy generation. This study determined the geometric dimensions and operating conditions of a tube bank with in-line arrangement of cam-shaped and elliptical tubes with axially fins using a numerical optimization method. In order to maintain equal heat transfer surface areas, equivalent diameters (12.7 mm) were assumed for the tube geometries (cam and elliptical). The longitudinal and transversal configurations consist of four tubes. Diagrams of the multi-objective optimization workflow were established for two different tube geometries. The objective functions selected here were the reduction of entropy generation and the increase in thermal hydraulic performance. The geometric optimization variables – transversal tube spacing, longitudinal tube spacing and longitudinal fin length – vary by 1/4 of the equivalent diameter and by equivalent diameter. The average velocity at the channel inlet is used as an optimization variable for the operating condition and varying within between 1 m/s and 6 m/s. Consequently, when the Pareto designs derived for the optimization problems under investigation are examined, the smallest entropy generation values obtained are lower for the cam-shaped tube bank (5.05%), while the largest thermal hydraulic performance obtained are higher for the elliptical tube bank (1.66%).

Introduction

Tube bank heat exchangers are widely used in many areas such as energy production, heating, cooling and air conditioning. These systems are preferred due to their efficiency and high applicability. However, rising energy and raw material costs have forced the development of various techniques aimed at reducing investment and operating costs. In this framework, while improving heat transfer performance using active and passive methods, the aim is also to minimize pressure losses. In particular, experimental, numerical, and analytical studies on passive improvement methods that do not require energy consumption are noteworthy in the literature. These studies aim to increase heat transfer and reduce pressure losses by using different tube geometries.

Hilpert [1] and Grimison [2] developed empirical relationships for determining the average Nusselt number in circular cross-section tube banks. Bergelin et al. [3, 4] provided a comprehensive evaluation by compiling studies conducted in low and medium Reynolds number ranges. Žukauskas [5, 6] investigated the effects of dimensionless parameters such as Reynolds and Prandtl numbers on heat transfer and flow in tube banks with in-line and staggered arrangements. Shaboury and Ormiston [7] numerically analysed the effect of the Reynolds number and dimensionless pitch on heat transfer in in-line arrangement circular tube banks. Khan et al. [8] analytically addressed heat transfer in both in-line and staggered arrangement circular tube banks, determining that an increase in transversal tube pitch has a greater effect than an increase in longitudinal tube pitch. Gaddis [9] developed detailed expressions for calculating pressure losses in in-line and staggered tube banks. Yılmaz and Yılmaz [10] evaluated the entropy production associated with heat transfer and pressure drop in circular tube bank and showed that the effect of heat transfer on entropy generation is more dominant at low velocities.

Circular cross-section tubes are widely used due to the ease of their production processes. However, in recent years, researchers have focused on alternative tube geometries to optimize flow and heat transfer. In this context, studies on tube designs that increase flow mixing, thereby promoting boundary layer renewal and reducing friction resistance, have gained momentum. Horvat et al. [11] analysed flow and heat transfer over time in tubes of circular, elliptical, and wing-shaped tube with staggered arrangement. The investigations revealed that the average Stanton number and drag coefficient decreased as the Reynolds number increased. Furthermore, when evaluated in terms of

pressure drop, wing-shaped tubes were found to perform better than elliptical and circular tubes.

Bayat et al. [12] experimentally investigated the flow and heat transfer performance in cam-shaped tube banks with staggered arrangement and observed that the amount of heat transfer increased with the increase in the dimensionless pitch. Compared to circular tubes with the same surface area, cam-shaped tubes were found to provide $5-11\%$ lower heat transfer, but the friction factor decreased by 64%. Furthermore, it was concluded that the thermal hydraulic performance and area goodness factor of cam-shaped tube banks were 5 and $12-14$ times higher than those of circular tube banks, respectively.

Mangrulkar et al. [13] numerically investigated heat transfer and friction factors in in-line arrangement cam-shaped tube banks in the range of $11.500 \leq \mathrm{Re_D} \leq 42.500$. The analyses revealed that increasing the Reynolds number and the longitudinal pitch ratio enhances turbulence and consequently improves heat transfer. It was found that increasing the longitudinal pitch distance expands the recirculation zone, which increases both heat transfer and pressure losses but reduces the overall efficiency of the system. Furthermore, it was determined that the use of cam-shaped tubes increased the area goodness factor by $9-10$ times compared to circular tubes and reduced the friction factor by $85-89\%$.

Khan et al. [14] analytically investigated the total heat transfer and drag coefficient in elliptical tube banks. Calculations performed under constant surface temperature and constant heat flux boundary conditions showed that the drag coefficient of tubes with an elliptical axis ratio of 0.5 was 66.7% lower than that of circular tubes, while tubes with an elliptical axis ratio of 0.25 had a drag coefficient that was 83.3% lower. Sayed Ahmed et al. [15] experimentally and numerically analysed the flow and heat transfer in staggered arrangement wing-shaped tube banks and found that wing-shaped tubes provided higher heat transfer compared to circular tubes by 34% and caused lower pressure drop by 37%.

Numerous studies have been conducted on tube bank design with the aim of increasing heat transfer and reducing pressure drop. These studies have generally focused on optimizing the performance of tube banks using predetermined geometric dimensions. Furthermore, optimization studies between specific geometric parameters are also noteworthy.

Matos et al. [16] performed a numerical optimization process to achieve maximum heat transfer under specific flow and volume constraints in elliptical and circular tube banks with staggered arrangement. In this study, the parameters that yielded the best results with the $\mathrm{Re_L} = 665$, such as the elliptical axis ratio and inter-tube distances, were examined. According to the results of this analysis, it was found that the elliptical tube bank provided more heat transfer than the circular tube bank by 13%.

Yılmaz et al. [17] analytically investigated circular tube banks using the Gnielinski-Gaddis method to optimize heat transfer in staggered arragement tube bank under specific pressure drop and volume conditions. In this study, design parameters such as the number of longitudinal tubes, tube diameter, and dimensionless tube spacing were analysed. The results showed that heat transfer decreased with an increase in the dimensionless tube diameter, but more efficient results could be obtained by optimizing the dimensionless spacing and number of tubes. Changes in the dimensionless tube diameter, tube spacing, and tube number significantly affect heat transfer performance.

Gharbi et al. [18] investigated the effect of circular, elliptical, and wing-shaped tube banks on entropy generation. In this numerical optimization study, it was determined that elliptical tube banks provided lower entropy generation and yielded better results than circular tube banks.

Similarly, Yılmaz and Yılmaz [19] used an analytical approach to optimize heat transfer in in-line arrangement circular tube banks. The study analysed parameters such as the number of tubes, dimensionless tube diameter, and tube spacing, demonstrating that an increase in dimensionless tube diameter has a negative effect on heat transfer. Furthermore, it was determined that changes in the number of tubes and tube spacing are important factors affecting heat transfer.

According to studies in the literature, the shape of the tubes has significant effects on heat transfer, pressure drop, entropy generation, and tube bank volume. Although various studies exist on cam-shaped and elliptical tubes, the specific optimization of these geometries integrated with axially flat fins has not been extensively covered in the literature. This study fills this gap by determining the optimal geometric parameters for these specific finned configurations. In this study, unlike previous studies, the aim was to maximize thermal hydraulic performance and minimize entropy generation in the tube bank design for the longitudinal and transversal spaces and fin length values presented in Table 1, using in-line arrangement of axially flat finned elliptical and cam-shaped tubes. Within this scope, numerous Pareto designs have been obtained.

Parametric Modelling and Numerical Optimization Procedures

Physical Geometries

The axially flat finned cam and elliptical tube cross-sections are shown in Figures 1a and 1b, with the geometric dimensions given in Table 1. The solution domains and boundary conditions for the tube banks are shown in Figures 2a, 2b, 3a, and 3b. The geometric dimensions and operating conditions of the tube bank are presented in Table 2. The heat transfer surface area is equal for cam and elliptical tubes, and the equivalent diameter is $\mathrm{D_e} = 12.7$ mm.

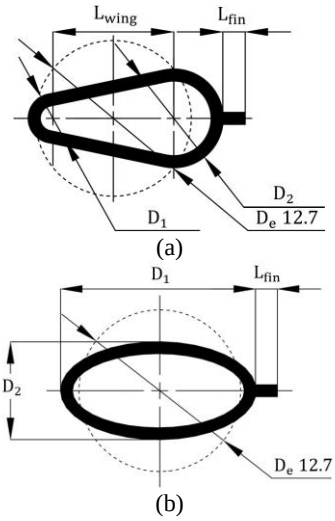

Figure 1. Axially flat finned (a) cam, (b) elliptical tube cross-section

Table 1. Geometric dimensions of axially flat finned tubes used in tube banks

Tube shape	D_e [mm]	D_1 [mm]	D_2 [mm]	L_{wing} [mm]
Tube wall thickness and axially flat fin height are 1 mm.				
Cam	12.7	4.11	8.22	10.054
Elliptical	-	16.44	8.22	-

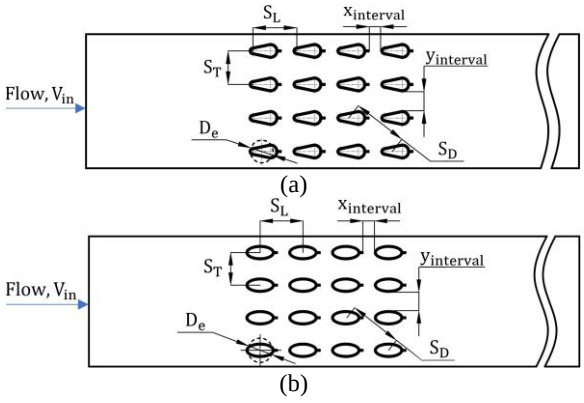

Figure 2. Parametric models of axially flat finned (a) cam-shaped, (b) elliptical tube bank with in-line arrangement

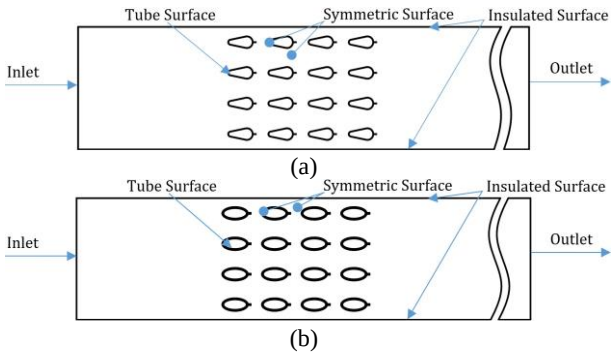

Figure 3. Boundary conditions for axially flat finned (a) cam-shaped, (b) elliptical tube bank with in-line arrangement

Table 2. Geometric dimensions and operating conditions of tube banks in axially flat finned tube bank studies

Parameter	**Symbol**	**Value**
Geometric dimensions of the channel		
Channel height	H_{ch}	$4 * s_T$ mm
Channel width	W_{ch}	210 mm
Geometric dimensions of the tube bank		
Equivalent diameter	D_e	12.7 mm
Number of longitudinal tubes	N_L	4
Number of transversal tubes	N_T	4
Fin length	L_{fin}	$\frac{D_e}{4}$ mm $\leq L_{fin} \leq D_e$ mm, increment $= \frac{D_e}{4}$ mm
Transversal spacing between tubes	$y_{interval}$	$\frac{D_e}{4}$ mm $\leq y_{interval} \leq D_e$ mm, increment $= \frac{D_e}{4}$ mm
Longitudinal spacing between tubes	$x_{interval}$	$\frac{D_e}{4}$ mm $\leq x_{interval} \leq D_e$ mm, increment $= \frac{D_e}{4}$
Operating conditions		
Average inlet air velocity	V_{in}	1 m/s $\leq V_{in} \leq$ 6 m/s, increment = 1 m/s
Inlet temperature	T_{inlet}	25 °C
Tube surface temperature	T_{wall}	45 °C

The inlet velocity range of 1 to 6 m/s was chosen to reflect the typical operating conditions encountered in industrial air-cooled heat exchangers and HVAC systems. $T_{film} = (T_{inlet} + T_{wall})/2$, the thermophysical properties of air at film temperature were obtained using the Engineering Equation Solver (EES) [20] programme and are listed in Table 3.

Table 3. Thermophysical properties of air at the $T_{film} = 35$ °C

Property	**Value**
Thermal conductivity coefficient (k) [W/m K]	0.02699
Density (ρ_{air}) [kg/m^3]	1.146
Specific heat capacity (c_p) [J/kg K]	1007
Kinematic viscosity (μ) [N s/m^2]	1.893×10^{-5}

Mesh

The RNG k-epsilon turbulence model was selected for the numerical simulations due to its superior performance in predicting swirling flows and flow separation in tube banks. The pressure-velocity coupling was handled using the COUPLED algorithm. To ensure a high-accuracy solution, a second-order discretization scheme was implemented for the governing equations of both the turbulent kinetic energy and momentum. Convergence

criteria of 10^{-8} for the energy equations and 10^{-5} for the continuity and other flow equations were established. Regarding the computational domain, a triangular mesh was used in the regions surrounding the tubes (Figure 4). Importantly, the grid was refined near the heat-transfer walls using quadrilateral cells to keep the $y+$ values within the viscous sublayer range of 1 to 5.

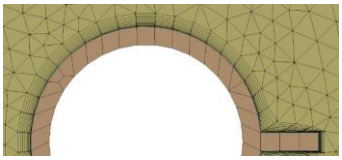

Figure 4. Mesh structure in an axially flat finned tube bank

A mesh independence study was conducted on an in-line arrangement circular tube bank with a channel width of $\mathbf{2\ mm}$ and $\mathbf{V_{in} = 4\ m/s}$. The results for five different element numbers are given in Table 4. The difference in pressure drop ($\mathbf{\Delta P}$) and heat transfer ($\mathbf{Q}$) between mesh structures $\mathbf{4}$ and $\mathbf{5}$ is $\mathbf{0.69}$% and $\mathbf{0.88}$%, respectively. Mesh 4 was used to reduce the calculation time.

Table 4. Mesh independence study for the value of the pressure drop ($\boldsymbol{V_{in} = 4\ m/s}$) for different number of elements

Nu.	Number of Elements	ΔP [Pa]	Q [W]
1	3579	107.6396	1.13867
2	6542	66.13183	1.401459
3	21012	81.12265	4.433381
4	53264	89.88429	4.227593
5	94980	90.50079	4.26483

Data Analysis

The longitudinal pitch of a tube bank is defined as follows (s_L);
For a cam-shaped tube bank,

$$s_L = L_{wing} + \frac{D_2}{2} + L_{fin} + x_{interval} + \frac{D_1}{2} \quad (1)$$

for an elliptical tube bank,

$$s_L = D_1 + L_{fin} + x_{interval} \quad (2)$$

The transversal pitch of a tube bank (s_T) is defined as follows;
For the elliptical and cam-shaped tube bank,

$$s_T = D_2 + y_{interval} \quad (3)$$

The longitudinal dimensionless pitch is defined as follows (s_L^*);
For a cam-shaped tube bank,

$$s_L^* = \frac{s_L}{\left(\frac{D_1}{2} + L_{wing} + \frac{D_2}{2}\right)} \quad (4)$$

For an elliptical tube bank,

$$s_L^* = \frac{s_L}{D_1} \quad (5)$$

The transversal dimensionless pitch is defined as follows (s_T^*);
For the elliptical and cam-shaped tube bank,

$$s_T^* = \frac{s_T}{D_2} \quad (6)$$

The channel height (H_{ch}) is defined as follows,

$$H_{ch} = 4 * s_T \quad (7)$$

The pressure drop (ΔP) is equal to the difference between the pressure at the channel inlet (P_{in}) and the pressure at the channel outlet (P_{out}),

$$\Delta P = P_{in} - P_{out} \quad (8)$$

The channel cross-sectional area (A) is defined as follows;

$$A = N_T * s_T \quad (9)$$

For a tube bank volume

$$V = N_L\ s_L\ N_T\ s_T\ W_{ch} \quad (10)$$

is calculated, and the mass flow rate is obtained from the average air inlet velocity (V_{in}) .

$$\dot{m} = \rho_{air}\ V_{in}\ A \quad (11)$$

The volumetric flow rate ($\dot{V}$) is obtained as follows.

$$\dot{V} = A * V_{in} \quad (12)$$

The pumping power (W_P) is calculated as follows:

$$W_p = \dot{V} * \Delta P \quad (13)$$

The logarithmic temperature difference (ΔT_{lm}); the tube surface temperature (T_{wall}), the inlet (T_{inlet}) and outlet (T_{outlet}) temperatures of the channel are calculated as follows based on the average air temperatures,

$$\Delta T_{lm} = \frac{(T_{outlet} - T_{inlet})}{\ln\left(\frac{(T_{wall} - T_{inlet})}{(T_{wall} - T_{outlet})}\right)} \quad (14)$$

The total heat transfer occurring in the tube bank ($\mathbf{Q}$) is calculated as follows based on the heat flux occurring in a single tube ($\mathbf{q}^{"}$),

$$\mathbf{Q = q^{"}\ \pi\ D_e\ N_L\ N_T\ W_{ch}} \quad (15)$$

The entropy generation (S_{gen}) is calculated as follows based on the total heat transfer (Q) :

$$S_{gen} = \frac{Q * \Delta T_{lm}}{T_{inlet} * T_{wall}} + \frac{\dot{m} * P_{in}}{\rho_{air} * T_{out}} \quad (16)$$

Thermal hydraulic performance (THP) is calculated as follows based on the reference heat transfer (Q_0) and pumping power (W_{p_0}) values [21],

$$THP = \frac{Q/Q_0}{W_p/W_{p_0}} \quad (17)$$

In the thermal hydraulic performance calculation, the lowest heat transfer rate obtained in a circular tube bank with axially flat finned with in-line arrangement under the geometric dimensions and operating conditions presented

in Table 2 was taken as a reference ($Q_0 = 120.7076$ W), as was the pumping power obtained in this design ($W_0 = 0.050526$ W). These reference values correspond to the specific geometric configuration ($x_{inteval} = 3.175$ mm, $y_{interval} = 12.7$ mm, $L_{fin} = 3.175$ mm,) that yielded the minimum heat transfer rate within the investigated range.

Multi-Objective Optimization Problem

The optimal design of the tube bank was investigated numerically with the objective functions of minimizing entropy generation and maximizing thermal hydraulic performance. The optimization variables for the tube bank are $x_{interval}, y_{interval}, L_{fin}$. Table 5 shows the scenario containing the optimization variables, such as tube bank shapes, objective functions, increments, and lower and upper limits.

Table 5. Multi-objective optimization problem, objective functions and optimization variables for tube banks

Multi-Objective Optimization Problem	
Elliptical tube bank with in-line arrangement	Cam-shaped tube bank with in-line arrangement
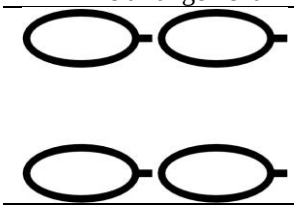	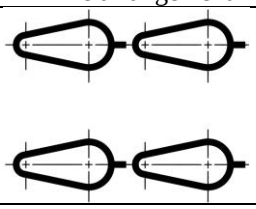
Objective Functions	
Minimize S_{gen} Maximize THP	
Optimization Variables	
$\frac{D_e}{4}$ mm $\leq x_{interval} \leq D_e$ mm, increment $= \frac{D_e}{4}$ mm	
$\frac{D_e}{4}$ mm $\leq y_{interval} \leq D_e$ mm, increment $= \frac{D_e}{4}$ mm	
$\frac{D_e}{4}$ mm $\leq L_{fin} \leq D_e$ mm, increment $= \frac{D_e}{4}$ mm	

The commercial optimization programme modeFRONTIER [22] was worked in coupled with Ansys Workbench HAD [23] software to determine the optimal dimensions of the tube banks. The optimization programme performs numerical calculations at each iteration of the process, using a multi-objective genetic algorithm and generating geometry and mesh by invoking Ansys Workbench. These techniques are shown as flow diagrams in Figures 5 and 6. To begin with, an initial population is created for the optimization studies (Design of Experiments or DOE), and the optimization algorithm attempts to find the optimal designs based on this population. The provided optimization variables ($x_{interval}, y_{interval}, L_{fin}$) are used to create the geometry and generate the tube bank mesh; this process is performed in the simulation using the Ansys Workbench node. Subsequently, another optimization variable (V_{in}) is provided as an input parameter using Fluent's Text User Interface (TUI), and numerical results are obtained. The following were monitored during the optimization studies: temperature at the channel outlet cross-section (T_{outlet}), pressure at the inlet cross-section (P_{in}), pressure at the outlet cross-section (P_{out}), maximum dimensionless wall distance (y^+_{max}), energy conservation (E_{conv}), and mass conservation (m_{conv}). After the final operations are completed, the fitness and objective functions (S_{gen}, THP) are evaluated. The optimization process (selection, crossover, and mutation) continues until the maximum number of iterations specified in the algorithm optimization programme is reached. At the end of the optimization process, Pareto designs are selected from among the feasible solutions in such a way that increasing the value of one objective does not decrease the value of the other.

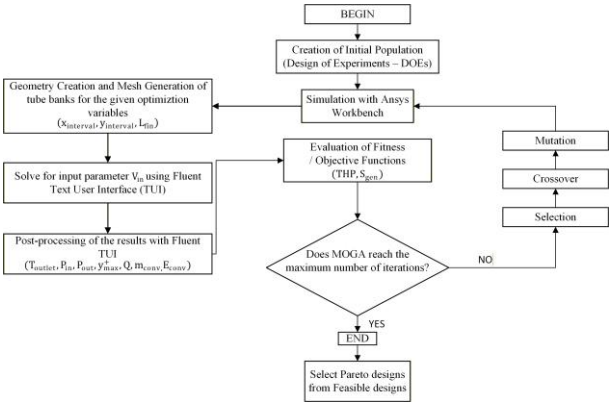

Figure 5. Numerical optimization scheme for axially flat finned tube banks with in-line arrangement

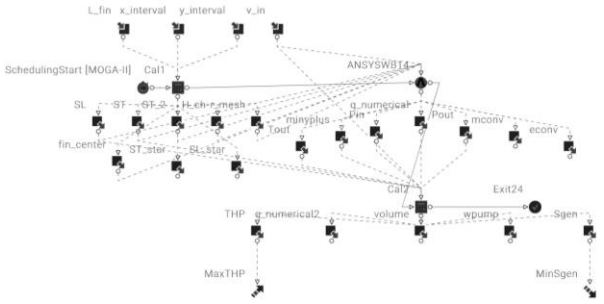

Figure 6. ModeFRONTIER optimization scheme for axially flat finned tube bank with in-line arrangement

According to the designer's decision, one of the designs in the Pareto design set can be selected as the most suitable design.

Results and Discussions

This section focuses on the results of multi-objective optimization studies for axially flat finned elliptical and cam-shaped tube banks with in-line arrangement. Table 6 presents the number of feasible and pareto designs. According to the results obtained, it is possible to create more designs within the given geometric constraints for the axially flat finned elliptical tube bank with in-line arrangement.

Table 6. Pareto and feasible design numbers obtained for axially flat finned tube banks

Tube Bank Type	Feasible Designs	Pareto Designs
Cam-Shaped	282	7
Elliptical	283	8

Entropy generation (S_{gen}), and thermal hydraulic performance (THP) values obtained in Pareto designs for tube bank types are presented in Table 7.

Table 7. Entropy generation (S_{gen}) and thermal hydraulic performance (THP) values obtained in Pareto designs for axially flat finned tube banks

Axially Flat Finned Cam-Shaped Tube Bank with In-line Arrangement			Axially Flat Finned Elliptical Tube Bank with In-line Arrangement		
Nu.	THP	$S_{gen\ [W/K]}$	Nu.	THP	$S_{gen\ [W/K]}$
1	0.348464	0.017597	8	1.812899	0.022225
2	0.352099	0.017678	9	1.757308	0.021774
3	0.355188	0.018748	10	1.746473	0.021087
4	1.679701	0.02068	11	1.686239	0.020521
5	1.720239	0.022059	12	1.684936	0.019943
6	1.775012	0.023415	13	1.648495	0.018603
7	1.842986	0.024642	14	0.300512	0.018562
			15	0.299541	0.018532

The comparison of entropy generation according to thermal hydraulic performance of Pareto design points is shown in Figure 7.

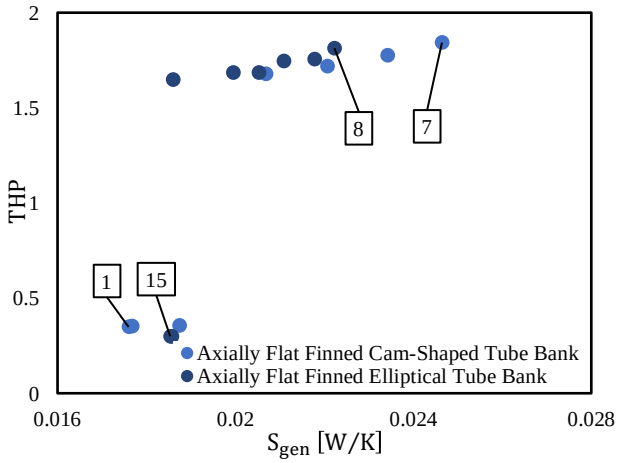

Figure 7. Variation in the thermal hydraulic performance of the Pareto designs according to the entropy generation

Conclusions

In this study, the geometric dimensions and operating conditions of axially flat finned cam-shaped and elliptical tube banks with in-line arrangement were determined using a numerical optimization method. As a result,

- When examining the Pareto designs, the lowest entropy generation value occurred in the cam-shaped tube bank with dimensions $V_{in} = 1\ m/s$, $s_L^* = 2.17455$, $s_T^* = 1.38625$, $L_{fin} = 12.7\ mm$, and a value of $0.017597\ W/K$. This value is lower than the smallest entropy generation value occurring in the cam-shaped tube bank, which is 5.05% .
- When examining the Pareto designs, the highest thermal hydraulic performance value occurring at $V_{in} = 1\ m/s$, $s_L^* = 1.97879$, $s_T^* = 2.54501$, and $L_{fin} = 12.7\ mm$ was obtained in the cam-shaped tube bank at 1.842986. This value is higher than the highest thermal hydraulic performance value occurring in the cam-shaped tube bank by 1.66%.
- Thermal efficiency performance increases with increase in entropy generation.

Ethics Committee Approval

There is no need to obtain permission from the ethics committee for the article prepared.

Conflict of Interest

There is no conflict of interest with any person / institution in the article prepared.

Authors' Contributions

Ozkarakoc M: Study conception and design, acquisition of data, drafting of manuscript

Kuru MN: Supervision, critical revision, project administration, funding acquisition

Acknowledgement

This research was supported by the TUBITAK ARDEB 1001 Research Programme with project number 123M484.

Nomenclature

c_p : Specific heat, J/kg K
D : Diameter of circular tube, mm
D_e : Equivalent tube diameter, mm
D_1 : Streamwise diameter of cam-shaped tube, major axis length of elliptical tube, mm
D_2 : Downstream diameter of cam-shaped tube minor axis length of elliptical tube, mm
H_{ch} : Channel height, mm
k : Thermal conductivity, W/m K
L_{fin} : Axially fin length, mm
L_{wing} : Length of distance between circles, mm
L_{ch} : Channel length, mm
$\dot{m}$: Mass flow rate, kg/s
N_L : Number of longitudinal tubes
N_T : Number of transversal tubes
P_{in} : Inlet pressure, Pa
P_{out} : Outlet pressure, Pa
Q : Heat transfer, W
q" : Heat flux, W/m^2

s_D : Diagonal pitch, mm
S_{gen} : Entropy generation, W/K
s_L : Longitudinal pitch, mm
s_L^* : Longitudinal dimensionless pitch
s_T : Transversal pitch, mm
s_T^* : Transversal dimensionless pitch
T_{film} : Film temperature, °C
T_{in} : Average temperature of the fluid at inlet section, °C
T_{out} : Average temperature of the fluid at outlet section, °C
T_{wall} : Surface temperature of tubes, °C
V : Total volume of tube bank, m^3
V_{in} : Average inlet velocity, m/s
W_p : Pumping power, W
W_{ch} : Channel width, mm
$x_{interval}$: Transversal spacing between tubes, mm
$y_{interval}$: Longitudinal spacing between tubes, mm
y^+_{max} : Dimensionless wall distance

Greek symbols
ρ_{air} : Density, kg/m^3
ΔP : Pressure drop, Pa
ΔT_{lm} : Logarithmic mean temperature difference, K
μ : Dynamic viscosity, kg m/ s

Subscripts
In : Inlet
max : Maximum
out : Outlet
TUI : Text user interface

Abbreviations
DOEs : Design of Experiments
MOGA: Multi-Objective Genetic Algorithm
RNG : Re-Normalization Group

References

[1] R. Hilpert, "Waermeabgabe von geheizten rohren and graehten," *Forschung Auf Dem Gebeit Des Ingenieurwesens*, 1933, 4, 1027-1038.

[2] E. D. Grimison, "Correlation and utilization of new data on flow resistance and heat transfer for cross flow of gases over tube banks," *Trans. ASME.*, 1937, 59, 583-594.

[3] O. P. Bergelin, G. A. Brown, H. L. Hull, F. W. Sullivan, "Heat transfer and fluid friction during viscous flow across banks of tubes-III: a study of tube spacing and tube size," *Trans. A. Sot. Mech. Engrs.*, 1950, 72, 881-888.

[4] O. P. Bergelin, G. A. Brown, S. C. Doberstein, "Heat transfer and fluid friction during flow across banks of tubes-IV: a study of the transition zone between viscous and turbulent row," *Trans. A. Sot. Mech. Engrs.*,1952, 74, 953-960.

[5] A. Žukauskas, "Heat transfer from tubes in crossflow," *Advances in Heat Transfer*, 1972, 8, 93–160.

[6] A. Žukauskas, R. Ulinskas, "Efficiency parameters for heat transfer in tube banks," *Heat Transfer Engineering*, 1985, 6, 19-25.

[7] A. M. F. El-Shaboury, S. J. Ormiston, "Analysis of laminar forced convection of air crossflow in ın-line tube banks with nonsquare arrangements," *Numerical Heat Transfer*, 2005, 48, 99-126, https://doi.org/10.1080/10407780590945452

[8] W. A. Khan, J. R. Culham, M. M. Yovanovich, "Convection heat transfer from tube banks in crossflow: analytical approach," *International Journal of Heat and Mass Transfer*, 2006, 49, 4831–4838, https://doi.org/10.1016/j.ijheatmasstransfer.2006.05.042

[9] E. S. Gaddis, "Pressure drop of tube bundles in cross flow," *VDI Heat Atlas, Berlin*, 2010, 1076-1091.

[10] A. Yılmaz, T. Yılmaz, "Analytical and experimental investigation of entropy generation for an in-line cross-flow tube bank," *Journal of Cukurova University Faculty of Engineering-Architecture*, 2016, 31, 223-230, https://doi.org/10.21605/cukurovaummfd.317805

[11] A. Horvart, M. Leskovar, B. Mavko, "Comparison of heat transfer condition in tube bundle cross-flow for different tube shapes," *International Journal of Heat and Mass Transfer*, 2006, 49, 1027-1038, https://doi.org/10.1016/j.ijheatmasstransfer.2005.09.030

[12] H. Bayat, A. M. Lavasani, T. Maarefdoost, "Experimental study of thermal-hydraulic performance of cam-shaped tube bundle with staggered arrangement," *Energy Conversion and Management*, 2014, 85, 470-476, https://doi.org/10.1016/j.enconman.2014.06.009

[13] C. K. Mangrulkar, A. S. Dhoble, A. R. Deshmukh, S. A. Mandavgane, "Numerical ınvestigation of heat transfer and friction factor characteristics from in-line cam shaped tube bank in crossflow," *Appl. Therm. Eng.*, 2017, 110, 521-538, https://doi.org/10.1016/j.applthermaleng.2016.08.174

[14] W. A. Khan, J. R. Culham, M. M. Yovanovich, "Fluid flow and heat transfer from elliptical cylinder: analytical approach," *37th AIAA Thermophys. Conf.*, 2004, 19.

[15] S. A. E. Sayed Ahmed, O. M. Mesalhy, T. M. Khass, A. H. Hassan, "Parametric study of air cooling process via water cooled bundle of wing-shaped tubes," *Egyptian International Journal of Engineering Sciences and Technology*, 2012, 15, 1172-1184, 10.21608/eijest.2012.96756

[16] R. S. Matos, J. V. C. Vargas, T. A. Laursen, F. E. M. Saboya, "Optimization study and heat transfer comparison of straggered circular and elliptic tubes in forced convection," *International Journal of Heat and Mass Transfer*, 2001, 44, 3953–3961, https://doi.org/10.1016/S0017-9310(01)00006-0

[17] A. Yılmaz, M. T. Erdinç, T. Yılmaz, "Optimization of crossflow staggered tube banks for prescribed pressure loss and effectiveness," *JTHT Thermophysics Heat Transfer*, 2017, 31, 878–888, https://doi.org/10.2514/1.T5033

[18] N. Gharbi, A. Kheiri, M. Ganaoui, R. Blanchard, "Numerical optimization of heat exchangers with circular and non-circular shapes," *Case Studies in Thermal Engineering*, 2015, 6, 194–203, https://doi.org/10.1016/j.csite.2015.09.006

[19] A. Yılmaz, T. Yılmaz, "Optimum design of cross-flow ın-line tube banks at constant wall temperature," *Heat Transfer Engineering*, 2016, 37, 523–534, https://doi.org/10.1080/01457632.2015.1060753

[20] Engineering Equation Solver, F-Chart Software, 2018.

[21] M. T. Erdinç, "Computational thermal-hydraulic analysis and geometric optimization of elliptic and circular wavy fin and tube heat exchangers," *International Communications in Heat and Mass Transfer*, 2023 140, 106518, https://doi.org/10.1016/j.icheatmasstransfer.2022.106518

[22] modeFRONTIER, Esteco S.p.A., 2023.

[23] Ansys Fluent User's Guide, 2021.

Dicle University
Journal of Engineering
https://dergipark.org.tr/tr/pub/dumf
duje.dicle.edu.tr

Research Article

Bioleaching of Oxidized Zinc Ore Using *Acidithiobacillus ferrooxidans* with Taguchi Approach

Seda DEMİRCİ[1*]

[1] Cukurova University, Aladağ Vocational School, Department of Mining and Mining Extraction, demircis@cu.edu.tr, Orcid No: 0000-0001-9577-4970

ARTICLE INFO

Article history:

Received 23 July 2025
Received in revised form 23 November 2025
Accepted 2 December 2025
Available online 30 December 2025

Keywords:

Oxidized Zinc, bioleaching, Acidithiobacillus ferrooxidans

Doi: 0.24012/dumf.1748240

* Corresponding author

ABSTRACT

Zinc is a strategically important metal used in galvanizing, battery, paint, and cosmetic industries. Due to environmental issues associated with sulfide ore processing, interest has shifted toward oxidized zinc ores such as smithsonite. Traditional flotation and acid leaching methods often suffer from low selectivity and generate hazardous wastes, whereas bioleaching offers an energy-efficient and environmentally friendly alternative. This study evaluates the bioleaching performance of smithsonite ore from the Horzum (Adana–Kozan, Türkiye) region using *Acidithiobacillus ferrooxidans*. A Taguchi L9 (3^2) design was applied to assess the effects of solid concentration (10–20%) and leaching time (6–18 days) on Zn and Fe dissolution. The highest recoveries—54.70% Zn and 63.14% Fe—were obtained at a 10% solid ratio and 12 days. ANOVA confirmed solid concentration as the most influential factor. XRD results showed clear mineralogical degradation consistent with metal solubilization. Pb remained largely insoluble under the tested conditions. Overall, the Taguchi-based optimization demonstrated that *A. ferrooxidans* can effectively enhance Zn and Fe dissolution from smithsonite, providing a promising approach for the sustainable processing of oxidized zinc ores.

Introduction

Zinc is one of the metals widely used in many fields such as galvanizing, stainless-steel production, battery production, automotive, white goods, and the chemical industry [1-3]. Sulfide ores constitute the primary source of zinc production [4-7]. The depletion of easily processed sulfide ores and the sulfur emissions generated during metallurgy have led to the enrichment of oxide zinc ores gaining importance in recent years [8-12]. Smithsonite ($ZnCO_3$), willemite (Zn_2SiO_4), hydrozincite ($Zn_5(CO_3)_2(OH)_6$), zincite (ZnO), and hemimorphite ($Zn_4Si_2O_7(OH)_2 \cdot H_2O$) are some of the oxidized ores that are important zinc-bearing ores alternative to sulfide ores [13]. Significant amounts of oxidized ore are found in the Kayseri, Niğde, Adana, Konya, and Malatya regions of Türkiye. Smithsonite, an oxidized ore, is not found alone in the Taurus Mountains in Türkiye, but together with lead-carbonate and zinc deposits [14]. The widely occurring oxidized zinc mineral smithsonite is found in association with minerals such as quartz, dolomite, and calcite [15-18]. The general composition of smithsonite is 52% Zn, Fe, and Mn [19]. Flotation and leaching methods are used in the enrichment of smithsonite [20, 21]. In previous studies conducted using flotation, Liu et al. (2020) [22] achieved a recovery rate of over 90% for smithsonite by using lauryl phosphate as a collector at pH 9. In the study by Wu et al. (2017) [23], Zn was obtained with a 70% yield and a 13.54% grade using isoamyl xanthate as a collector. Wang et al. (2019) [16] determined the Zn recovery yield to be 92% in a flotation experiment conducted by creating a mixture with sodium oleate and benzoic acid.

In leaching studies, the effects of parameters such as acid concentration, temperature, ore particle size, air pressure, leaching time, and solid-liquid ratio on dissolution have been investigated. In sulfuric acid leaching, Zn dissolution rates were found to range between 69% and 84% at a 1M H_2SO_4 concentration [24]. Studies have also begun on leaching with organic acids other than sulfuric acid. In leaching experiments using aqueous gluconic acid, the dissolution kinetics were investigated according to temperature, acid, and ore size parameters (Hurşit et al., 2009). When inorganic acids such as H_2SO_4, HNO_3, and HCl are used, undesirable impurities, particularly iron, can be significantly dissolved during the leaching process [25, 26]. The low Zn content of ores causes high energy consumption in pyrometallurgical processes because gangue removal requires heating at high temperatures [26]. In the flotation method, inorganic and organic suppressant phosphates and polyethers are used for effective separation from calcite [27]. Highly used reagents cause water

pollution and filtration problems. High silica content is associated with the entry of Zn and silica gel into the solution when hydrometallurgical methods are used. Silica gel formation makes filtration difficult. Due to the intensive use of chemicals in flotation and traditional leaching methods, as well as the increase in energy costs caused by temperature and pressure, bioleaching can be considered as an alternative method. Its environmental friendliness and low energy costs compared to other methods make it advantageous for low-grade and complex ores. However, the slow progress of the process and the need for continuous monitoring constitute its disadvantages. Ilyas et al. (2012) [28]. Demonstrated the bioleaching potential of carbonate-based zinc minerals by achieving 70% Zn recovery in a 212-day study on low- and high-grade smithsonite ores using *Sulfobacillus thermosulfidooxidans* and *Thermoplasma acidophilum*. More recent studies further highlight the applicability of bioleaching to diverse zinc-bearing materials: Abdollahi et al. (2022) [29] reported 82% Zn recovery from an iron-rich sphalerite sample under mesophilic conditions: Bulaev and Melamud (2022) [30] achieved 78% Zn dissolution during thermophilic bioleaching of a Cu–Zn concentrate; and Barkusaraey et al. (2021) [31] documented a 28.71% reduction in Zn concentration in automotive paint sludge using *Pseudomonas aeruginosa*. In bioleaching systems, *A. ferrooxidans* plays a central mechanistic role by oxidizing Fe^{2+} to Fe^{3+}, with the generated ferric ions acting as strong oxidants that dissolve metal-bearing minerals; simultaneously, proton generation during Fe^{2+} oxidation helps maintain the acidic conditions required for efficient metal solubilization [32].

Although these findings collectively indicate that bioleaching is effective across a wide range of feedstocks, comprehensive quantitative assessments focusing on the influence of process parameters in Fe-oxide-rich and mineralogically complex smithsonite ores remain limited. In this context, the novelty of the present study lies in elucidating the effects of solid concentration and leaching duration on Zn and Fe dissolution from an Fe-rich smithsonite ore from the Kozan–Horzum region using a Taguchi L9 orthogonal design, thereby identifying the dominant parameters governing bioleaching performance. The use of an Fe-free 9K medium, selected to minimize iron-related interferences during dissolution, further reinforces the methodological distinctiveness of this work.

Material and Methods

Smithsonite Sample

The zinc oxide ore mineral smithsonite was obtained from the Kozan-Horzum region of Adana Province. After being dried in an oven, the ore was crushed to less than 1 cm in a laboratory-scale jaw crusher. The crushed ore was ground in a laboratory-scale ball mill and passed through a 75 μm sieve.

The sample used in the experimental study was chemically analysed in the Chemistry Laboratory of the Department of Mining Engineering at, Cukurova University using a Minipal 4 Panalytical brand XRF (X-ray fluorescence spectrometer) device. The chemical composition of the ore is presented in Table 1.

Table 1. Chemical composition of sample

Al_2O_3	SiO_2	SO_3	K_2O	CaO	TiO_2	Cr_2O_3
12	9.1	0.4	0.82	8.58	0.26	0.02
MnO	**Fe_2O_3**	**CuO**	**ZnO**	**PbO**	**Others**	**LOI**
0.43	39.89	0.13	11.18	0.33	2.61	14.25

Bacterial Culture and Experimental Study

In the bioleaching experiments, *Acidithiobacillus ferrooxidans* (DSM 583) was obtained as a pure culture from the Deutsche Sammlung von Mikroorganismen und Zellkulturen (DSMZ) culture collection and used.

Acidithiobacillus ferrooxidans was cultured in a 9K medium without iron. This medium contained 0.4 g/L $(NH_4)_2SO_4$, 0.4 g/L $MgSO_4 \cdot 7H_2O$, 0.2 g/L KH_2PO_4, and 0.1 g/L KCl. The pH value was adjusted to between 1.8 and 2, the bacterium's growth environment, using sulphuric acid. Analytically pure chemicals and distilled water were used in the experiments.

The use of an Fe-free 9K medium was intentional and methodologically necessary. The addition of $FeSO_4$ in systems containing carbonate-bearing minerals such as smithsonite often leads to the formation of ferric iron precipitates (e.g., jarosite or $Fe(OH)_3$, which may coat the mineral surface and inhibit bacterial activity. Excess Fe^{2+}/Fe^{3+} also causes pH instability and interferes with the interpretation of metal dissolution behavior due to interactions with the naturally released iron from the ore. Similar observations have been reported in the literature, where Fe supplementation was shown to accelerate jarosite formation and reduce metal solubilization in mesophilic bioleaching. Therefore, Fe-free 9K medium was used to minimize iron-related interferences and to accurately assess the effects of solid concentration and leaching duration on bioleaching performance [29].

The experiments were conducted in 250 mL Erlenmeyer flasks with a total working volume of 100 mL of this volume, 90 mL was culture medium and 10 mL was starter culture. Prior to inoculation, the pH of the culture was adjusted with 15% sulphuric acid, and the culture media were sterilised in an autoclave at 121°C and 1 atm pressure for 15 minutes. The cultures were incubated at 150 rpm and 25°C (±5) in shaking incubators.

An abiotic (bacteria-free) control test was also conducted under identical experimental conditions to distinguish chemical dissolution from microbial activity.

All experiments were conducted in triplicate, and the results were expressed as mean ± standard deviation.

In the bioleaching experiments, zinc, lead and iron concentrations; pH, mV (oxidation-reduction potential) (WTW S-720) and bacterial populations were observed. Bacteria counts were performed using a Petroff-Hausser

slide. A Nikon YS-100 model microscope was used for observations.

During the bioleaching experiments, 5 mL samples were taken from the solutions every 6 days and separated into solid and liquid phases using a 0.2-micron membrane filter. Zinc, lead and iron concentration values were determined using a Perkin Elmer PinAAcle 900 H Atomic Absorption Spectrometer (AAS).

Experimental Design and Taguchi Method

Taguchi design, which is used to determine the effective levels of various parameters in a process, is a simple and systematic approach that provides optimization in terms of cost and performance. It is an effective tool for determining the best combination with a limited number of experimental designs [33].

Taguchi design uses the signal-to-noise (S/N) ratio to evaluate performance. The experimental results are categorized as follows based on the S/N ratio: (i) the largest is the best, (ii) the smallest is the best, (iii) normal is the best [34].

The aim of this study is to ensure the dissolution of zinc into solution by selecting the most suitable parameters using the Taguchi technique. For this reason, the "the largest is the best" approach was used as the output.

Since the response value (Zn and Fe dissolution) was evaluated based on the "larger-the-better" criterion, the signal-to-noise (S/N) ratio was calculated using the following Taguchi expression:

$$S/N = -10\log\left(\frac{1}{n}\sum_{i=1}^{n}\frac{1}{y_i^2}\right) \quad (1)$$

where *yi* represents the measured response value and *n* denotes the number of experiments [35-37].

The number of experiments was determined as 9 experiments using a Taguchi L9 design with 2 factors and 3 levels determined within the leaching process conditions. The experiments were performed in duplicate. Table 2 shows the factors, levels, and design of the experiments for the leaching processes. Statistical analyses were performed using MINITAB 18 software.

Table 2. Experimental parameters and levels conducted with Taguchi L9 (3^2) design

Parameters	Level 1	Level 2	Level 3
Solid Ratio (%)	10	15	20
Time (Days)	6	12	18
Experiment No	**Solid Ratio (%)**	**Time (Days)**	
1	10	6	
2	10	12	
3	10	18	
4	15	6	
5	15	12	
6	15	18	
7	20	6	
8	20	12	
9	20	18	

During the bioleaching test, zinc (Zn) and iron (Fe) recovery in the leach solution were used as performance indicators. The following formula was used to calculate leach efficiency.

$$R = \frac{V \times v}{A \times a} \times 100 \quad (2)$$

Where *R* represent the metal Recovery efficiency, *V* is the volume of the leach solution(mL), *v* is metal concentration in the leach solution(mg/L), *A* represent the mineral mass of the smithsonite sample (kg) and *a* is the metal concentration in the smithsonite sample (mg/kg).

Results and Discussion

The bioleaching experiment was conducted at three levels using solid ratio and leaching time parameters in accordance with the Taguchi L9(3^2) method. In addition, control experiments were conducted at each solid ratio to understand bacterial activity. During the experiment, pH, mV, and bacterial count measurements were taken. The pH changes observed during the bioleaching experiments conducted using *A. ferrooxidans* bacterial culture are presented in Figure 1.

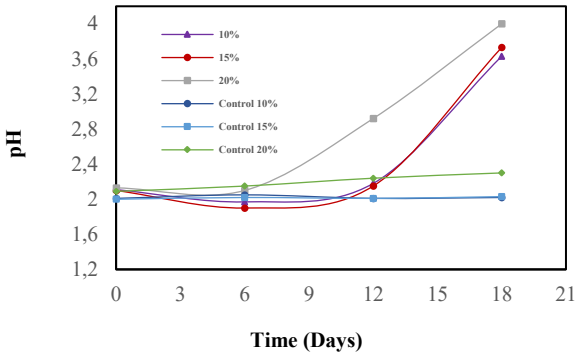

Figure 1. pH change measured according to solid ratios in bioleaching experiments

In the bioleaching experiments, pH values decreased during the first 6 days of the experiment at solid ratios of 10% and 15%. From the 6th day onwards, they began to rise at a visible level. As the solid ratio increased, the pH value also increased. In this case, it can be said that bacterial activity decreased from the 6th day onwards. Additionally, as shown in Figure 2, the mV values decreased as the pH value increased. The bacteria added to the solution increased the acidity of the environment by oxidizing iron and sulfur. In control tests without bacteria, no difference was observed in the pH and mV values. This is due to the absence of microorganisms capable of oxidation in the environment. Based on the dissolution rates and measurement results in the bioleaching tests, it can be concluded that *A. ferrooxidans* is effective.

Mechanistically, the observed trends in pH and redox potential are consistent with the classical Fe^{2+}/Fe^{3+} cycle mediated by *A. ferrooxidans*. The bacterium oxidizes Fe^{2+} to Fe^{3+}, and the resulting Fe^{3+} contributes to the indirect dissolution of $ZnCO_3$ through acidic and oxidative attack.

After the sixth day—particularly at higher solid ratios—the increase in pH leads to a decline in Fe^{3+} concentration, making it insufficient to maintain a high redox potential, which indicates reduced microbial activity. Under these conditions, Fe^{3+} can precipitate as jarosite-type compounds, forming passivation layers on mineral surfaces and inhibiting metal solubilization, as widely reported in mesophilic bioleaching studies [38-40].

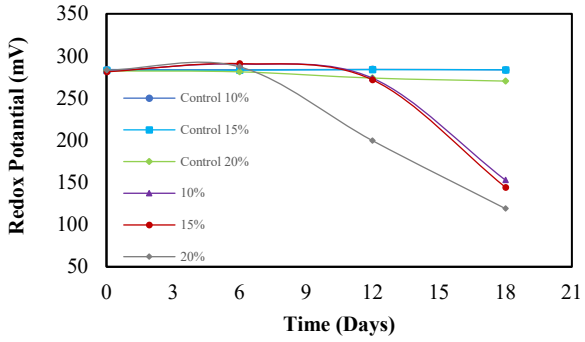

Figure 2. Redox potential change in solid ratios during bioleaching experiments

The pH and mV measurement results are consistent with the bacterial count measurement results. Figure 4 shows the bacterial counts of samples taken at intervals during the period. The bioleaching experiments were initiated by adding an average of $25.8x10^6$ cells/mL *A. ferrooxidans* bacteria to all solid ratios. After 6 days, the bacterial count was determined to be $74.67x10^6$ cells/mL at a 10% solid ratio, $70.3x10^6$ cells/mL at a 15% solid ratio, and $61.5x10^6$ cells/mL at a 20% solid ratio (Figure 3). Based on the bacterial counts, it was determined that the bacteria were in the log phase between 0 and 6 days. It was observed that the bacterial count in the medium decreased as the solid ratio increased. This can be explained by the increase in mineral matter and metal concentration in the medium due to the increasing solid ratio, which inhibits the growth of bacteria. This finding is supported by studies in the literature [41-43].

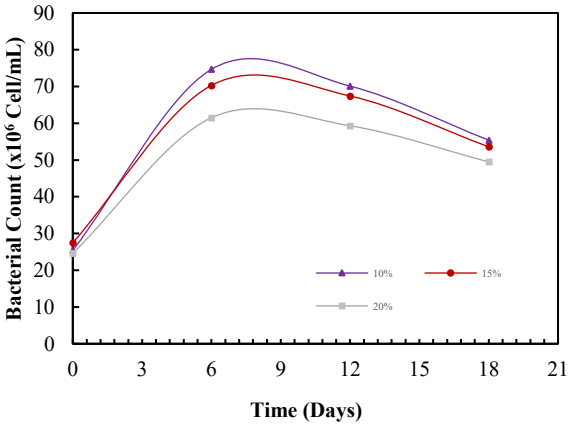

Figure 3. *A. ferrooxidans* counts obtained at different solid ratios in bioleaching experiments.

As presented in Figure 4, the XRD patterns reveal a pronounced mineralogical alteration in the smithsonite ore after bioleaching. The sharp and intense $ZnCO_3$ (smithsonite) peaks observed around $2\theta \approx 30°$ in the raw sample significantly diminished following bioleaching, indicating substantial dissolution of the smithsonite phase and the release of Zn^{2+} ions into the solution. A general decrease in the peak intensities of kaolin, calcite, hematite, corundum, quartz, and montmorillonite further suggests progressive breakdown of the mineral matrix under acidic bioleaching conditions.

The absence of any newly formed crystalline phases after leaching implies that the dissolved species did not recrystallize but remained in either an amorphous state or the solution phase. Overall, the mineralogical transformations observed in the XRD patterns strongly support the effective bioleaching activity of *A. ferrooxidans*, consistent with the enhanced Zn and Fe recoveries obtained experimentally.

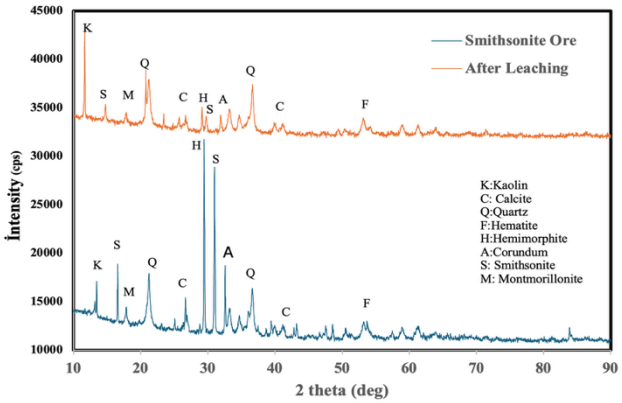

Figure 4. Pre- and post-bioleaching sample XRD pattern

As a result of the bioleaching experiments, the solution analyses indicated that *A. ferrooxidans* did not solubilize lead (Pb) from the smithsonite ore under the studied conditions.This lack of Pb dissolution is attributed to the formation of highly insoluble lead phases, particularly $PbSO_4$ due to sulfate generation by A. *ferrooxidans* and $PbCO_3$ due to the carbonate-rich nature of the ore. The very low solubility product constants of these compounds prevent Pb from entering the leach solution [45].

These results indicate that Pb solubilization is thermodynamically limited under the studied conditions rather than being controlled by bacterial activity. In the experimental results, the zinc and iron values taken into the liquid were converted to the S/N (signal-to-noise) ratio in accordance with the Taguchi L9 (3^2) method. The S/N ratio values are presented in Table 3. The S/N ratio values for zinc and iron recovery efficiency from smithsonite are shown in Figure 5. The parameters affecting Fe recovery efficiency are the solid ratio with a delta value of 3.96 and the leaching time with a delta value of 1.15. For zinc, the S/N ratio values were determined to be the solid ratio with a delta value of 6.76, followed by the leaching time with a delta value of 1.53.

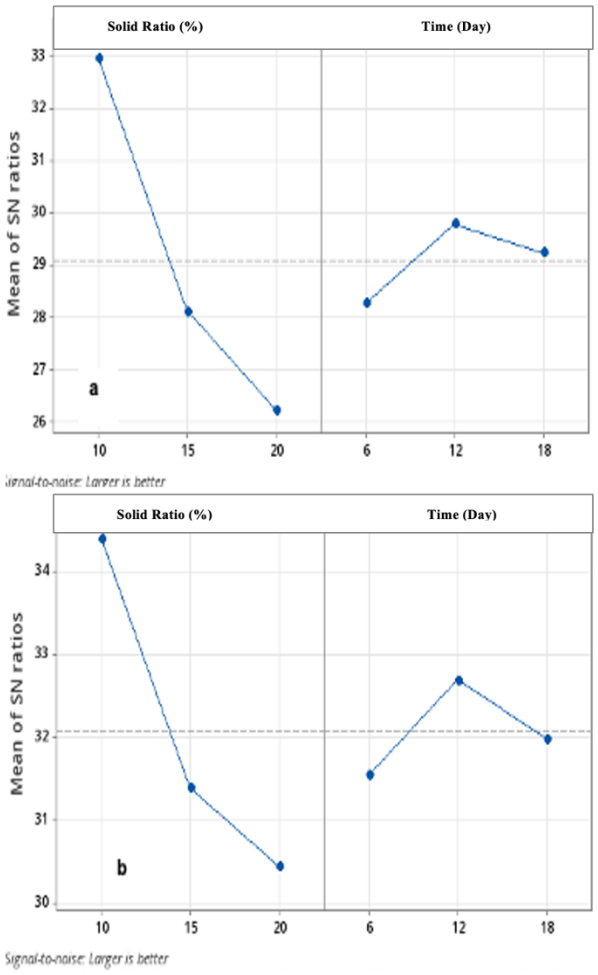

Figure 5. Basic effect graphs of S/N ratios for Zn (a) and Fe (b) recovery efficiency

The results of the bioleaching experiments conducted with *A. ferrooxidans* bacteria under different conditions according to Taguchi design are presented in Table 3. Considering the recovery efficiency of the bacteria, the best results were determined as 54.70% Zn and 63.14% Fe, respectively. The zinc recovery values obtained in this study (~55% Zn in 12 days) demonstrate a considerably faster dissolution rate compared with long-term bioleaching studies reported in the literature. For instance, Ilyas et al. (2012) [28], achieved ~70% Zn recovery from smithsonite ore only after 212 days, whereas in the present work, substantial zinc dissolution was obtained within a much shorter period due to the optimized conditions established by the Taguchi approach. Similarly, although higher dissolution efficiencies (78–82%) have been reported in bioleaching studies conducted on sphalerite or Cu–Zn concentrates [29, 30], these values generally require longer leaching periods or thermophilic conditions. These comparisons indicate that, although the maximum Zn recovery obtained in this study is lower than some literature reports, the dissolution rate is remarkably high, demonstrating the effectiveness of the short-term Fe-free bioleaching strategy employed herein. These results were obtained in an experiment conducted under conditions of a 10% solid ratio and 12 days (Table 3, Experiment No. 2).

Table 3. Test Results and S/N Ratios

Exp. No	Solid Ratio (%)	Time (Days)	Recovery Zn (%)	S/N (Zn)	Recovery Fe (%)	S/N (Fe)
1	10	6	36.48	31.24	44.34	32.93
2	10	12	54.70	34.76	63.14	36.01
3	10	18	44.11	32.89	51.45	34.23
4	15	6	23.60	27.45	35.17	30.93
5	15	12	25.57	28.15	37.68	31.52
6	15	18	27.31	28.72	38.45	31.69
7	20	6	20.17	26.09	34.46	30.74
8	20	12	21.03	26.45	33.64	30.53
9	20	18	20.08	26.05	31.68	30.02

Figures 6-7 show contour (isohypse) diagrams illustrating the effect of the combination of solid ratio and leaching time on Zn and Fe recovery efficiency. According to the contour diagram, in the dark green region, it is observed that the recovery efficiency of Zn (a) above 50% and Fe (b) above 60% decreases as the solid ratio and leaching time increase.

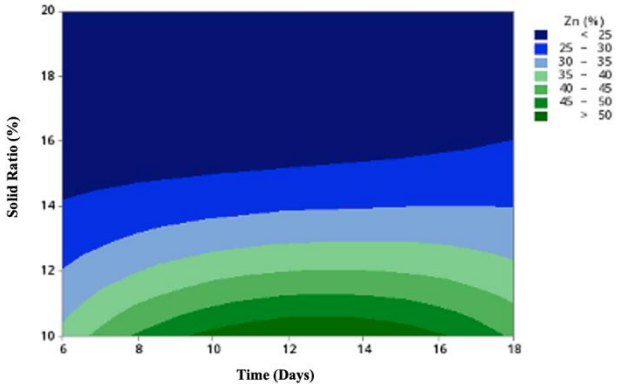

Figure 6. Contour plot illustrating the combined effect of solid ratio (%) and leaching time (days) on Zn recovery efficiency (The color gradient represents Zn recovery ranges, where dark blue regions correspond to lower recoveries (<25%), and progressively lighter blue and green regions indicate higher recoveries (>50%). Maximum Zn dissolution (>50%) was achieved at lower solid ratios (10–12%) and intermediate leaching durations (10–14 days). An increase in solid ratio and prolonged leaching time resulted in a decline in Zn recovery).

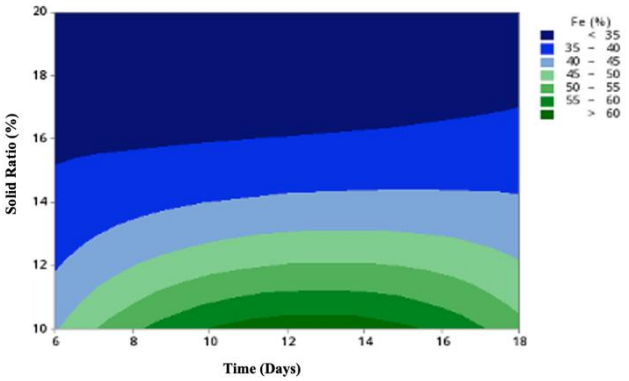

Figure 7. Contour plot illustrating the combined effect of solid ratio (%) and leaching time (days) on Fe recovery efficiency (The contour colors represent Fe recovery intervals, with dark blue areas indicating low recovery (<35%) and light blue-to-green gradients reflecting progressively higher recovery levels (>60%). The highest Fe dissolution (>60%) occurred at low solid ratios (10–12%) and moderate leaching times (10–14 days). Increasing both the solid ratio and the leaching duration reduced Fe recovery due to decreased bacterial activity and limited mass transfer).

The analysis of variance (ANOVA) performed according to the Taguchi method shows the relationship between the study parameters and the observed values [44]. The main purpose of ANOVA is to examine in more detail which parameter and level significantly affect Zn recovery efficiency.

Within the scope of this study, parameters such as solid ratio and leaching time were analyzed as factors, and the ANOVA method was used to evaluate their effects on Zn recovery efficiency [46-49]. The ANOVA analysis was conducted with a 95% confidence level and a 5% error margin. The percentage contribution ratios obtained from the ANOVA analysis are presented in Table 4.

According to the variance analysis performed using the Taguchi method, the factor most affecting zinc recovery efficiency was the solid ratio with a contribution ratio of 85.35%, while for iron, this ratio was calculated as 77.52%. This result indicates that the solid ratio must be carefully optimized to increase bioleaching efficiency.

The practical implication of the high contribution (85.35%) of the solid ratio is associated with several known limitations occurring at elevated pulp densities. High solid ratios restrict mass transfer and oxygen availability, increase slurry viscosity, and elevate dissolved metal concentrations, all of which inhibit the metabolic activity of *A. ferrooxidans.* Consequently, bacterial growth and Fe^{2+} oxidation rates decrease, leading to lower Zn and Fe dissolution. These findings highlight the critical importance of optimizing pulp density in bioleaching operations to prevent bacterial inhibition and ensure efficient metal solubilization [50, 51].

Table 4. ANOVA results based on S/N ratios (signal-to-noise ratios) regarding the effect of factors studied on Zn (a) and Fe (b) recovery.

Source	df	Sum of Squares	Mean Square	F Value	Percentage Distribution (%)	P-Value
(a)						
Solid Ratio	2	1018.67	509.33	20.19	85.35	0.008
Time	2	73.98	36.99	1.47	6.20	0.333
Error	4	100.91	25.23		8.45	
Total	8	1193.55			100	
(b)						
Solid Ratio	2	655.57	327.78	11.05	77.52	0.024
Time	2	71.42	35.71	1.20	8.45	0.390
Error	4	118.69	29.67		14.04	
Total	8	845.68			100	

Conclusion

This study involved the recovery of zinc and iron from smithsonite ore sourced from the Kozan-Horzum region using the bioleaching method. The experiments were optimized using *A. ferrooxidans* bacteria and the Taguchi L9 (3^2) experimental design. According to the experimental results, the solid ratio and leaching time parameters were found to be effective on metal recovery. The optimal bioleaching conditions determined in this study were a 10% solid ratio and a 12-day leaching time, under which the maximum Zn and Fe recoveries reached 54.70% and 63.14%, respectively (Experiment No. 2). These conditions were identified as optimal based on the Taguchi L9 design and S/N ratio analysis.

Based on pH, mV, and bacterial count measurements conducted during the bioleaching process, bacterial activity increased during the first 6 days. From the 12th day onwards, measurements indicated an increase in pH and a decrease in redox potential, suggesting a reduction in bacterial oxidative activity. Additionally, it was observed that as the solid ratio increased, the recovery efficiency of Zn and Fe decreased.

In conclusion, the bioleaching method using *A. ferrooxidans* demonstrated that zinc and iron can be effectively recovered from smithsonite ore, but it is not effective in lead recovery. The experimental design using the Taguchi approach provides an advantage in terms of process efficiency by determining the optimal parameters through the number of experiments. Moreover, bioleaching offers important environmental advantages, including low energy consumption, minimal use of hazardous chemicals, and reduced generation of secondary wastes, making it a sustainable alternative to conventional mineral processing methods.

The activity of the *A. ferrooxidans* bacteria used in this study was examined within the optimal temperature range reported in the literature. The data obtained at the laboratory scale indicate that bacterial activity has a positive effect on metal solubility. However, further

studies are recommended to comprehensively investigate the effects of different microorganism types, pH values, and temperature conditions on the system's kinetics and recovery efficiency.

For industrial-scale application, technical and economic evaluations of process parameters such as reactor design, microbial production capacity, nutrient requirements, air supply system, temperature control, and reaction time are necessary. In this context, process optimization through pilot-scale studies will facilitate the industrial-scale application of the bioleaching method.

Future studies should focus on developing detailed kinetic models to better understand the dissolution mechanisms of Zn and Fe during bioleaching. In addition, pilot-scale and industrial scale-up investigations are recommended to evaluate process feasibility, optimize operational parameters, and assess the economic and technical viability of applying *A. ferrooxidans*–based bioleaching to smithsonite ores.

Ethics Committee Approval and Conflict of Interest Statement

There is no need to obtain permission from the ethics committee for the article prepared

There is no conflict of interest with any person / institution in the article prepared

Acknowledgement

The author would like to extend their sincere appreciation to Prof. Dr. Mahmut ALTINER for his invaluable guidance, continuous support throughout the course of this research.

References

[1] Liu, C., Zhang, W., Song, S., Li, H., Liu, Y. *Flotation separation of smithsonite from calcite using 2-phosphonobutane-1,2, 4-tricarboxylic acid as a depressant*. Powder Technol. 352, 11–15, 2019a.

[2] Ghosh, M.K., Das, R.P., Biswas, A.K. *Oxidative ammonia leaching of sphalerit. Part I. Noncatalytic kinetics.* Int. J. Miner. Process., 66, 241–254, 2002.

[3] Shirin, E., Fereshteh, R., Sadrnezhaad, S.K., *Hydrometallurgical treatment of tailings with high zinc content*. Hydrometallurgy 82, 54–62, 2006.

[4] Albrecht, T.W.J., Addai-Mensah, J., Fornasiero, D. *Critical copper concentration in sphalerite flotation: Effect of temperature and collector.* Int. J. Miner. Process. 146, 15–22, 2016.

[5] Bai, S.J., Li, C.L., Fu, X.Y., Ding, Z., Wen, S.M. *Promoting sulfidation of smithsonite by zinc sulfide species increase with addition of ammonium chloride and its effect on flotation performance.* Miner. Eng., 125, 190–199, 2018a.

[6] Bai, S.J., Li, C.L., Fu, X.Y., Liu, J., Wen, S.M., *Characterization of zinc sulfide species on smithsonite surfaces duringsulfidation processing: Effect of ammonia liquor.* J. Ind. Eng. Chem., 61, 19–27, 2018b.

[7] Irannajad, M., Ejtemaei, M., Gharabaghi, M. *The effect of reagents on selective flotation of smithsonite–calcite–quartz*. Miner. Eng. 22, 766–771, 2009.

[8] Liu, C., Feng, Q., Zhang, G., Ma, W., Meng, Q., Chen, Y. *Effects of lead ions on the flotation of hemimorphite using sodium oleate.* Miner. Eng. 89, 163–167, 2016a.

[9] Liu, C., Feng, Q., Zhang, G., Chen, W., Chen, Y., *Effect of depressants in the selective flotation of scheelite and calcite using oxidized paraffin soap as collector*. Int.J. Miner. Process. 157, 210–215, 2016b.

[10] Chen A., Zhao W. Z., Ji X., Long S., Huo G., Chen X. *Alkaline leaching Zn and its concomitant metals from refractory hemimorphite zinc oxide ore*. Hydrometallurgy 97, 228-232, 2009. https://doi.org/10.1016/j.hydromet.2009.01.005.

[11] Shi, Q., Feng, Q., Zhang, G., Deng, H. *Electrokinetic properties of smithsonite and its floatability with anionic collector.* Colloids Surf. A Physicochem. Eng. Aspects 410 (410), 178–183, 2012.

[12] Zhao, Z. *Mechanochemical leaching of refractory zinc silicate (hemimorphite) in alkaline solution*. Hydrometallurgy 99 (3), 255–258, 2009.

[13] Zhao, Y. and R. Stanforth. ‘‘*Production of Zn Powder by Alkaline Treatment of Smithsonite Zn–Pb Ores*,’’ Hydrometallurgy, 56, 237, 2000.

[14] Hurşit M., Laçin O., Saraç H. *Dissolution kinetics of smithsonite ore as an alternative zinc source with an organic leach reagent.* Journal of the Taiwan Institute of Chemical Engineers, Volume 40, Issue 1,Pages 6-12, 2009. ISSN 1876-1070, https://doi.org/10.1016/j.jtice.2008.07.003.

[15] Liu, C., Zhu, G., Song, S., Li, H. *Flotation separation of smithsonite from quartz using calcium lignosulphonate as a depressant and sodium oleate as a collector.* Miner. Eng., 131, 385–391, 2019b.

[16] Wang L., Hu G.Y., Sun W., Khoso S.A., Liu R.Q., Zhang X.F. *Selective flotation of smithsonite from dolomite by using novel mixed collector system*, Trans. Nonferrous Met. Soc. China 29, 1082–1089, 2019.

[17] Araújo, A.C.A., Lima, R.M.F. *Influence of cations Ca2+, Mg2+ and Zn2+ on the f lotation and surface charge of smithsonite and dolomite with sodium oleate and sodium silicate*. Int. J. Miner. Process. 167, 35–41, 2017.

[18] Kashani, A.H.N., Rashchi, F. *Separation of oxidized zinc minerals from tailings: influence of flotation reagents.* Miner. Eng. 21, 967–972, 2008.

[19] DPT. *Metal Madenler (Kurun, Çinko, Kadmiyum). 8. Be Yıllık Kalkınma Planı, Madencilik Özel ihtisas Komisyonu Metal Madenler Alt Komisyonu Kurun-Çinko-Kadmiyum Çalıma Grubu Raporu*, DPT: 2628- ÖDK 639, Ankara, 2001.

[20] Ciccu, R., Curreli, L., Ghiani, M. *The beneficiation of lean semi oxidized lead–zinc ores. In: Proc. 13th Int. Minerals Process. Cong., Processing of Oxidized and Mixed Oxide–Sulfide Lead–Zinc Ores*, Warsaw, pp. 125–145, 1979.

[21] Pereira, C.A., Peres, A.E.C. *Reagents in calamine zinc ores flotation.* Miner. Eng. 18, 275–277, 2005.

[22] Liu W.P., Wang Z.X., Wang X.M., Miller J.D. *Smithsonite flotation with lauryl phosphate*. Miner. Eng. 147, 106155, 2020.

[23] Wu D. D., Ma W.H., Wen S.M., Deng J.S., Bai S.J., *Enhancing the sulfidation of smithsonite by superficial dissolution with a novel complexing agent*, Miner. Eng. 114, 1–7, 2017.

[24] Top S. *Dıssolvıng Zınc From Smıthsonıte Mıneral By Dırect Leachıng Method.* IV. Internatıonal Istanbul Scıentıfic Research Congress Aprıl 2-4, 2021.

[25] Abdel-Aal, E. A. ''*Kinetics of Sulfuric Acid Leaching of Low-grade Zinc Silicate Ore*,'' Hydrometallurgy, 55, 247, 2000.

[26] Souza A.D., Peina P.S., Lima E.V.O., Dasilva C.A., Leao V.A. *Kinetics of sulphuric acid leaching of a zinc silicate calcine*. Hydrometallurgy 89, 337-345, 2007. https://doi.org/10.1016/j.hydromet.2007.08.005.

[27] Irannajaad, M., Meshkini, M., Azadmehr, A. R. *Leaching of zinc from low grade oxide ore using organic acid.* Physicochemical Problems of Mineral Processing, 49(2), 547-555, 2013. https://doi.org/10.5277/ppmp130215

[28] İlyas, S., Chi, R., Bhatti, H.N. *Column bioleaching of low-grade mining ore containing high level of smithsonite, talc, sphaerocobaltite and azurite.* Bioprocess Biosyst Eng 35, 433–440, 2012. https://doi.org/10.1007/s00449-011-0582-3.

[29] Abdollahi H., Mirmohammadi M., Ghassa S., Jozanikohan G., Boroumand Z., Tuovinen O. H., *Acid bioleaching of select sphalerite samples of variable Zn- and Fe-content*s. Hydrometallurgy, Volume 212, 105897, ISSN 0304-386X, 2022. https://doi.org/10.1016/j.hydromet.2022.105897.

[30] Bulaev, A., & Melamud, V. *Two-Stage Oxidative Leaching of Low-Grade Copper–Zinc Sulfide Concentrat*e. Microorganisms, 10(9), 1781, 2022. https://doi.org/10.3390/microorganisms1009178

[31] Barkusaraey B., Mafigholami F., Faezi Ghasemi R., M., Khayati, G. *Zn bio extraction from a zinc rich paint sludge by indigenous Pseudomonas aeruginosa*. Chemical Engineering Communications, 209(10), 1397–1412, 2021. https://doi.org/10.1080/00986445.2021.1974410

[32] Moinier, D.; Byrne, D.; Amouric, A.; Bonnefoy, V. *The Global Redox Responding RegB/RegA Signal Transduction System Regulates the Genes Involved in Ferrous Iron and Inorganic Sulfur Compound Oxidation of the Acidophilic Acidithiobacillus ferrooxidans*. Front. Microbiol. 8, 16, 2017.

[33] Basavarajappa S, Chandramohan G,Paulo Davim J."*Application of taguchi techniques to study dry sliding wear behaviour of metal matrix composite*s.Mater Des;28(4): 1393-8, 2007.

[34] Mohapatra, S., Bohidar, S., Pradhan, N., Kar, R.N., Sukla, L.B. *Microbial extraction of nickel from Sukinda chromite overburden by Acidithiobacillus ferrooxidans and Aspergillus strains*, Hydrometallurgy, 85, 1–8, 2006.

[35] Kır H., Apay S.*Optimization of coating parameters in hard chrome coated structural steel by electrolytic method with taguchi method GUSTIJ,* 10 (1), pp. 7-14, 2020.

[36] Korkmaz, A.A. *Optimization of Smokeless Fuel Production from Lignite by Taguchi Orthogonal Design*. Solid Fuel Chem. 55, 444–449, 2021. https://doi.org/10.3103/S0361521921060082.

[37] Başar C., A., Korkmaz A., A., Önal Y., Utku T., *Evaluation of optimum carbonization conditions of the blended domestic polymeric waste, biomass and lignite in the presence of catalyst by Taguchi and ANOVA optimization analysis,* Journal of Hazardous Materials Advances, Volume 8, 100164, 2022, ISSN 2772-4166, https://doi.org/10.1016/j.hazadv.2022.100164.

[38] Li, W., Feng, Q., & Li, Z. *Isolation and Characterization of a Novel Iron–Sulfur Oxidizing Bacterium Acidithiobacillus Ferrooxidans YQ-N3 and its Applicability in Coal Biodesulfurization*. Minerals, 2023. https://doi.org/10.3390/min13010095.

[39] Feng, Y., Wang, H., Li, H., Chen, X., Du, Z., & Kang, J. *Effect of iron transformation on Acidithiobacillus ferrooxidans bio-leaching of clay vanadium residue*. Journal of Central South University, 26, 796-805, 2019. https://doi.org/10.1007/s11771-019-4049-z.

[40] Chen, H., Zhang, D., Nie, Z., Xia, J., Li, Q., Zhang, R., Yin, H., & Pakostova, E. *Reductive dissolution of jarosite by inorganic sulfur compounds catalyzed by Acidithiobacillus thiooxidans*. Hydrometallurgy. 2022. https://doi.org/10.1016/j.hydromet.2022.105908.

[41] Çiftçi, H., & Atik, S. *Lateritik Cevherlerden Nikel Kazanımında Biyoliç Yöntemi.* Erciyes Üniversitesi Fen Bilimleri Enstitüsü Fen Bilimleri Dergisi, 30(4), 275-284, 2014.

[42] Astudillo, C., Acevedo, F. *Adaptation of Sulfolobus metallicus to high pulp densities in the biooxidation of a flotation gold concentrate*. Hydrometallurgy 92, 11e15, 2008.

[43] Nemati, M., Harrison, S.T.L. *Effect of solid loading on thermophilic bioleaching of sulfide minerals.* J. Chem. Technol. Biotechnol75, 526e532, 2000.

[44] Roy R.K. *Design of Experiments Using the Taguchi Approach.* G. Taguchi, System of experimental design, quality resources. 1987.

[45] Li, X., Azimzadeh, B., Martínez, C., & McBride, M. *Pb Mineral Precipitation in Solutions of Sulfate, Carbonate and Phosphate: Measured and Modeled Pb Solubility and Pb2+ Activity. Minerals*. 2021. https://doi.org/10.3390/min11060620.

[46] Unal R., and Dean E. B. "*Taguchi approach to design optimization for quality and cost: an overview*," International Society of Parametric Analysts, pp. 1 -10, 1990.

[47] Kashani, A.H.N., Rashchi, F. *Separation of oxidized zinc minerals from tailings: influence of flotation reagents*. Miner. Eng. 21, 967–972, 2008.

[48] Montgomery D. C. *Design and analysis of experiments. Global trends and environmental issues in nickel mining Sulfides versus laterites*, Ore Geology Reviews, 38, 9–26, 2017.

[49] Tiwary V. K., Padmakumar A., and Malik V. R. "*Investigations on FSW of nylon micro -particle enhance 3D printed parts applied to a Clark -Y UAV wing,*" Welding International, vol. 36, no. 8, pp. 474 -488, 2022.

[50] Bayat, O., Sever, E., Bayat, B., Arslan, V., & Poole, C. *Bioleaching of Zinc and Iron from Steel Plant Waste using Acidithiobacillus Ferrooxidans. Applied Biochemistry and Biotechnology, 152, 117-126. https://doi.org/10.1007/s12010-008-8257-5, 2009.*

[51] Heydarian, A., Vakilchap, F., Mousavi, S., & Mousavi, S. *Bacterial acidic agents-assisted multi-elemental (Ni, Co, and Li) leaching of used lithium-ion batteries at high pulp densities*. *Scientific Reports*, 15. 2025, https://doi.org/10.1038/s41598-025-00660-9.

Dicle University
Journal of Engineering
https://dergipark.org.tr/tr/pub/dumf
duje.dicle.edu.tr

Research Article

Impact of Building Height on Seismic Response, Economic Viability, Environmental Performance, and Social Well-being in Earthquake-Prone Türkiye

Mehmet İshak YÜCE[1], Aydın OĞUZ[2*], Talal FAROUG MAHGOUB AHMED[3]

[1] Gaziantep University, Civil Engineering Department, yuce@gantep.edu.tr, Orcid No: 0000-0002-6267-9528
[2*] International Dublin University, Civil Engineering Department, ceaoguz@hotmail.com, Orcid No 0009-0003-6124-1844
[3] International Dublin University, Public Health Department, tamahgoub@gmail.com, Orcid No 0009-0009-1141-8270

ARTICLE INFO

Article history:

Received 12 December 2024
Received in revised form 24 June 2025
Accepted 22 December 2025
Available online 30 December 2025

Keywords:

Seismic Resilience, Building Typologies, Life Cycle Cost Analysis (LCCA), Environmental Impact, Social Well-being, Sustainable Urban Development

Doi:1 0.24012/dumf.1599942

* Corresponding author

ABSTRACT

This study presents a comprehensive comparative evaluation of high-rise and low-rise building typologies in Türkiye's seismically active regions, addressing their seismic behavior, economic viability, environmental footprint, and socio-psychological impacts. Utilizing Finite Element Method (FEM) simulations and Life Cycle Cost Analysis (LCCA), the research integrates structural modeling with long-term performance metrics, supported by generalized data derived from the 2023 Kahramanmaraş earthquake and national statistical sources. In accordance with TBDY-2018, high-rise buildings are defined as those exceeding 15 stories or 60 meters in height, while low-rise buildings typically fall below this threshold. The analysis indicates that, under normalized seismic loading conditions, low-rise buildings exhibit lower inter-story drift and base shear demands, reflecting different dynamic responses. Economically, high-rise developments are associated with 20–30% higher life-cycle costs, primarily due to maintenance, vertical transportation systems, and energy-intensive infrastructure requirements. From an environmental perspective, high-rise structures consume approximately 30% more operational energy and emit up to 35% more CO_2 over their lifespan, attributed to mechanical system dependence and higher embodied carbon in construction materials. Additionally, socio-psychological assessments reveal that high-rise living often correlates with increased social isolation, reduced neighborhood interaction, and adverse effects on mental well-being, whereas low-rise environments tend to support stronger community ties. While recognizing the inherent design and regulatory distinctions between these typologies, this study employs harmonized analytical methods to derive context-specific insights, offering guidance for urban planners and policymakers seeking to align seismic safety with sustainable, livable development strategies.

1. Introduction

Urban development in seismically active regions presents a multitude of challenges, particularly in areas experiencing rapid population growth and land scarcity. As cities around the world expand, vertical urbanization, characterized by the construction of high-rise buildings, has become a common solution for optimizing land use in densely populated areas. Countries such as Japan and Chile, along with regions like California in the United States—all highly prone to seismic activity—have been at the forefront of adopting high-rise construction practices while simultaneously implementing stringent seismic building codes to safeguard public safety. Despite these advances, high-rise buildings continue to face heightened risks during earthquakes, alongside long-term economic and environmental concerns. Furthermore, high-rise living has notable sociological implications, including increased social isolation and mental health issues, which further complicate urban planning strategies for sustainable development.

In Türkiye, the situation is particularly acute. The country lies along major fault lines, including the North Anatolian Fault and the East Anatolian Fault, making it one of the world's most seismically vulnerable regions [1]. Recent events, such as the 2023 Kahramanmaraş earthquake, which caused over 50,000 fatalities and widespread destruction, have brought these vulnerabilities to the forefront [2]. Türkiye's rapid urbanization, especially in cities like Istanbul, Ankara, and Izmir, has resulted in the proliferation of high-rise buildings, which are particularly susceptible to seismic forces. This has raised significant concerns regarding the seismic resilience, long-term economic costs, and environmental sustainability of such structures in the country's most populous regions.

1.1. Global Context of Seismic Vulnerability and Sustainability in Urban Planning

Globally, regions with high seismic activity, such as Japan, Chile, and the state of California in the United States, have emphasized seismic resilience in their urban planning and construction practices. Both Japan and Chile have implemented advanced seismic building codes and retrofitting technologies aimed at reducing the risk of structural failure during earthquakes [3]. Despite these innovations, high-rise buildings continue to present challenges due to their increased height and susceptibility to lateral forces during seismic events [4]. In California, significant investments have been made in early warning systems and retrofitting older structures to enhance

earthquake resilience. However, recent seismic events, such as the 2019 Ridgecrest earthquakes, underscore the persistent vulnerabilities associated with high-rise buildings in seismically active regions [5].

While high-rise buildings remain a necessary response to land constraints, their seismic performance varies significantly depending on structural design, materials, and retrofitting efforts. Global studies in Japan, Chile, and the U.S. have shown that high-rise seismic performance requires targeted engineering strategies to mitigate collapse risks, making comparative evaluations with low-rise structures essential for strategic urban planning [3, 5–7]. Additionally, from an environmental perspective, high-rise buildings have been identified as significant contributors to urban carbon footprints due to their reliance on energy-intensive materials like steel and concrete and the high energy consumption required for vertical transportation and climate control [8]. Studies emphasize the need for sustainable urban development strategies that incorporate both seismic resilience and environmental sustainability [9].

1.2. Seismic Vulnerability of High-Rise Buildings in Türkiye

Türkiye's position along multiple fault lines makes it one of the most seismically active countries globally. Over 70% of the population lives in high-risk seismic zones, and more than 60% of the country's land area is exposed to significant seismic activity [2]. The 2023 Kahramanmaraş earthquake revealed vulnerabilities in some multi-story buildings, particularly older structures with limited compliance to updated seismic codes. Conversely, structures designed under modern engineering standards generally exhibited improved performance. Despite the introduction of modern engineering standards, the lateral displacement of high-rise buildings during the earthquake led to widespread structural damage, increasing the risk of collapse [10]. In contrast, low-rise buildings, due to their simpler design and lower center of gravity, were generally more resilient to the seismic forces. Figure 1 highlights the seismic risk distribution across Türkiye, underscoring the urgency of re-evaluating the country's urban planning strategies, particularly in relation to high-rise construction.

Damage observed in several high-rise structures during the 2023 Kahramanmaraş earthquake has renewed discussions on urban density and seismic safety. The integration of high-rise buildings into Türkiye's urban landscapes has prompted an urgent need for comparative studies that evaluate the performance of both high-rise and low-rise buildings under seismic stress. These evaluations are critical to developing effective policies that balance urban growth with safety considerations.

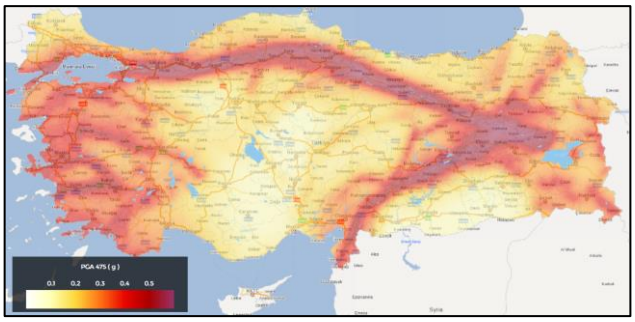

Figure 1. Seismic Risk Distribution in Türkiye [2].

1.3. Economic Costs of High-Rise Buildings: Land, Construction, and Emergency Services

While high-rise buildings offer a practical solution to land scarcity in urban areas, they come with substantial economic costs, particularly in seismically active regions. Land acquisition in cities like Istanbul can account for up to 35% of total construction costs for high-rise developments, a stark contrast to the 10-15% typical for low-rise buildings in suburban areas [11]. In addition, the complexity of constructing high-rise structures—requiring advanced engineering techniques and specialized materials such as high-strength steel—results in significantly higher initial costs [12]. Furthermore, the cost of maintaining high-rise buildings escalates over time, with annual maintenance increasing by approximately 5% due to the need for specialized equipment and systems, such as elevators, HVAC systems, and fire suppression technologies [11].

Emergency services for high-rise buildings also impose a significant financial burden on municipalities. The infrastructure required for vertical rescue operations, fire suppression in high-rise environments, and emergency evacuations necessitates highly specialized equipment and trained personnel, which increases operational costs for city governments [13]. Table 1 provides a detailed comparison of the economic costs associated with high-rise and low-rise buildings, highlighting the long-term financial implications of high-rise urbanization.

Table 1. Comparison of Cost Structure Between High-Rise and Low-Rise Buildings [14].

Cost Type	High-Rise Buildings	Low-Rise Buildings
Land Acquisition	30-35%	10-15%
Construction Complexity	High	Moderate
Long-Term Maintenance	High	Low
Emergency Service Costs	High (specialized)	Low (standard)

1.4. Psychological and Sociological Impacts of High-Rise Living

The psychological and sociological impacts of high-rise living have been the subject of increasing academic attention, particularly in densely populated cities such as New York, Hong Kong, and Tokyo. Studies have consistently found that residents in high-rise buildings report higher levels of social isolation, a lack of community engagement, and increased mental health issues, including anxiety and depression [15,16]. The World Health Organization (WHO) defines social isolation as a lack of meaningful social interactions and connections, which can have significant implications for both mental and physical health [17].

In Türkiye, where community cohesion is a key aspect of social life, the shift to high-rise living has weakened traditional neighborhood relationships. A study by [18] found that 45% of high-rise residents reported feelings of social isolation, compared to only 18% of residents in low-rise buildings. This disparity can be attributed to the lack of communal spaces in many high-rise buildings, which reduces opportunities for interaction and contributes to a sense of alienation. Moreover, the absence of green spaces and outdoor areas exacerbates mental health challenges, with residents in high-rise buildings reporting higher rates of depression and anxiety than their low-rise counterparts [19].

1.5. Environmental Impact and Sustainability Challenges

From an environmental perspective, high-rise buildings pose substantial challenges. According to the United Nations Environment Programme [8], high-rise structures consume 30% more energy for heating, cooling, and vertical transportation than low-rise buildings. This increased energy demand is driven by the need for elevators, HVAC systems, and water pumping equipment, all of which require continuous energy input. Furthermore, the construction of high-rise buildings is resource-intensive, relying heavily on steel and concrete—materials with high embodied carbon—contributing significantly to global CO_2 emissions [20].

As shown in Figure 2, high-rise buildings have a larger environmental footprint over their lifecycle compared to low-rise structures. The environmental impact of high-rise developments is compounded by their inability to easily integrate renewable energy solutions, such as solar panels, due to the lack of available surface area for installation. Consequently, the carbon emissions of high-rise buildings remain disproportionately high throughout their operational lifetime.

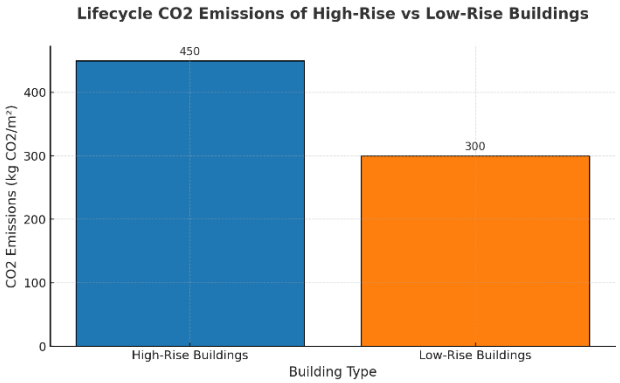

Figure 2. CO_2 Emissions of High-Rise vs Low-Rise Buildings Over Their Lifecycle [8].

1.6. Research Gap and Objectives

Despite significant advancements in seismic engineering and sustainable urban planning, critical gaps remain in understanding the comparative performance of high-rise and low-rise buildings in seismic zones like Türkiye. Previous research has predominantly focused on either seismic resilience or environmental sustainability, with few studies offering a comprehensive analysis that integrates seismic, economic, environmental, and social factors. This study aims to address these gaps by conducting a holistic comparison of high-rise and low-rise buildings, providing insights into their seismic performance, economic costs, environmental impacts, and sociological implications.

The specific research questions guiding this study are:

1. How do high-rise and low-rise buildings compare in terms of seismic resilience in Türkiye?

2. What are the long-term economic costs associated with high-rise versus low-rise developments?

3. How do these building typologies impact social isolation, mental health, and community cohesion?

4. What is the environmental impact of high-rise versus low-rise buildings in terms of energy consumption and carbon emissions?

5. How can urban planners balance sustainability, safety, and social well-being in seismic regions?

By investigating these questions, this study seeks to contribute to the global dialogue on sustainable urban development and offer policy recommendations that prioritize community well-being, seismic safety, and environmental sustainability.

This study uses observational data from the 2023 Kahramanmaraş earthquake strictly for academic modeling and simulation purposes. The intent is to understand generalized structural behavior in seismic scenarios, not to evaluate or assign responsibility to specific engineers, contractors, or construction firms. References to performance outcomes are anonymized and contextually framed to ensure ethical neutrality. The authors acknowledge that many buildings in the affected region

were compliant with existing codes, and that observed failures often involved older structures or exceptional circumstances.

1.7. Definition of High-Rise and Low-Rise Buildings

The classification of buildings as high-rise or low-rise varies significantly across disciplines and regulations. According to TBDY-2018, a high-rise building is defined as a structure exceeding 60 meters in height or more than 15 stories. This definition serves as the regulatory basis for advanced seismic design requirements, including nonlinear dynamic analysis and higher ductility detailing. In contrast, low-rise buildings, typically defined as one to five stories, are subject to simplified seismic analysis methods and different performance expectations [21].

International building codes introduce variations in this classification. For example, the International Building Code (IBC) in the United States defines high-rise structures based on fire safety access, specifically as buildings with an occupied floor located more than 75 feet (approximately 23 meters) above the lowest level of fire department vehicle access [22]. Similarly, European design guidelines vary depending on national regulations, with classification thresholds influenced by factors such as risk category and local seismicity; for instance, buildings over 18 meters in the United Kingdom or 22 meters in Germany are typically designated as high-rise due to fire protection and evacuation considerations [23]. In global urban centers, buildings exceeding 40 stories are commonly referred to as high-rise in architectural discourse, although these structures function within vastly different urban and infrastructural contexts compared to typical Turkish reinforced concrete frames of 8 to 15 stories.

Furthermore, from a socio-environmental perspective, the perception of “height” is not solely based on structural metrics. Studies in environmental psychology suggest that buildings exceeding five to six stories may already induce psychological detachment and community disconnection, particularly when they lack integrated green and social spaces [16, 24]. Such vertical separation has been shown to negatively affect social cohesion, perceived safety, and mental well-being, especially in high-density environments [25]. Similarly, environmental impact studies associate increasing height with higher embodied carbon, greater operational energy consumption, and diminished potential for natural ventilation, due to increased reliance on mechanical systems and denser structural requirements [26-27].

In this study, the term “high-rise” is primarily used in alignment with TBDY-2018 for structural modeling and code analysis. However, in discussions involving urban livability, social perception, or environmental performance, the term may encompass buildings that do not strictly meet the height threshold but function similarly in vertical urban contexts. This layered approach ensures definitional clarity across engineering, environmental, and sociological dimensions.

2. Literature Review

Urban growth and increasing housing demands have led to the rapid rise of high-rise buildings in many cities worldwide. However, high-rise buildings present substantial challenges, particularly in seismically active regions like Türkiye. These challenges include seismic vulnerability, economic sustainability, environmental impacts, and sociological consequences. The following sections provide an updated analysis of recent literature from 2019 to 2024, highlighting both international studies and Türkiye's specific context.

2.1. Seismic Vulnerability of High-Rise Buildings

International Studies on Seismic Resilience

The seismic vulnerability of high-rise buildings remains a critical focus of research, especially in earthquake-prone regions. Recent studies have demonstrated that taller structures experience higher sway and seismic forces, increasing the risk of collapse. [7] explored how dynamic soil-structure interaction (SSI) can amplify base shear and lateral displacement, making tall buildings more vulnerable to seismic activity when SSI is not adequately accounted for. This finding is consistent with research by [28], who evaluated the effectiveness of base isolation techniques, such as friction pendulum isolators, in reducing seismic sway and improving the overall stability of high-rise structures.

In regions like Japan and California, where seismic risks are well-known, base isolation and tuned mass dampers have been successfully implemented in high-rise buildings. These techniques, while effective, have been underutilized in countries like Türkiye due to financial and regulatory constraints. Recent studies, such as [29], propose retrofitting older high-rise buildings with modern isolation systems like lead-core rubber bearings, which can reduce base shear by 30% and inter-story drift by 50%.

Seismic Performance in Türkiye

Türkiye's high seismic risk, especially in cities like Istanbul, underscores the importance of structural resilience in high-rise buildings. Over 70% of the population lives in regions prone to seismic activity, and the 2023 Kahramanmaraş earthquake highlighted the vulnerability of Türkiye’s older high-rise building stock. [29] found that low-rise buildings, due to their simpler designs and lower centers of gravity, performed better during seismic events. In contrast, many high-rise buildings constructed before the enforcement of modern seismic codes experienced structural challenges to withstand the tremors effectively, emphasizing the need for retrofitting.

2.2. Economic Impacts: Land, Construction, and Maintenance Costs

Global Economic Studies

High-rise buildings offer a solution to land scarcity in urban areas, but their economic sustainability is debated. According to [30], long-term maintenance costs for high-

rise buildings account for 30-35% of total lifecycle costs, compared to 20% for low-rise buildings. This disparity is driven by the need for specialized infrastructure, such as elevators and HVAC systems, which require regular upgrades and maintenance.

Further studies have examined the high costs associated with emergency services in high-rise buildings. [31] reported that emergency service costs, including fire suppression and vertical rescue operations, are approximately 30% higher for high-rise buildings than for low-rise structures, largely due to the need for advanced equipment and specialized personnel.

Türkiye's Economic Context

In Türkiye, land acquisition for high-rise developments in cities like Istanbul is a significant financial burden. [14] data shows that land acquisition can account for up to 35% of total construction costs for high-rise projects, compared to only 10-15% for low-rise buildings in suburban areas. This discrepancy is further compounded by the engineering complexities and higher maintenance costs associated with high-rise buildings. Studies suggest that, while low-rise buildings are more financially viable due to lower construction and maintenance costs, high-rise structures in Türkiye's urban centers remain a necessary response to land constraints.

2.3. Environmental Sustainability

Energy Use and CO_2 Emissions in High-Rise Buildings

High-rise buildings are major contributors to energy consumption and carbon emissions. Recent studies have found that high-rise buildings consume up to 30% more energy than low-rise structures, primarily due to the demands of heating, cooling, and vertical transportation. [32] highlighted that high-rise buildings rely heavily on energy-intensive materials, such as steel and concrete, which increase their embodied carbon and operational energy consumption.

To address these concerns, retrofitting high-rise buildings with energy-efficient systems, such as smart HVAC and energy-efficient glazing, has been recommended. [33] reported that energy consumption in high-rise buildings could be reduced by 28% through the use of these technologies, making them more sustainable in the long term.

Life Cycle Assessment (LCA) in Seismic Zones

[34] conducted a Life Cycle Assessment (LCA) on high-rise and low-rise buildings in seismic zones, finding that high-rise buildings emit 35% more CO_2 over their lifecycle than low-rise buildings. This is due to both the embodied carbon in the construction materials and the higher energy demands of high-rise structures. These findings emphasize the need for sustainable building materials and practices in future high-rise construction, particularly in regions like Türkiye where seismic risks further complicate the environmental impact of these buildings.

Environmental Impact in Türkiye

In Türkiye, the environmental sustainability of high-rise buildings has become a growing concern. [35] reported that high-rise buildings in urban centers like Istanbul contribute significantly to carbon emissions, largely due to their reliance on non-renewable energy sources. Researchers have suggested that adopting renewable energy systems and sustainable construction practices could mitigate the environmental impact of high-rise buildings in Türkiye's cities, but implementation remains slow.

2.4. Psychological and Sociological Impacts of High-Rise Living

International Research on Social Isolation

Several studies have linked high-rise living to increased social isolation and mental health issues. [15] found that residents of high-rise buildings in cities like New York and Hong Kong reported higher levels of social isolation and stress compared to those in low-rise communities. [16] also highlighted that the lack of communal spaces in high-rise environments reduces social interaction opportunities, contributing to feelings of isolation and depression.

Türkiye's Sociological Context

In Türkiye, where community cohesion is a central aspect of social life, high-rise living has disrupted traditional neighborhood structures. [18] found that 45% of high-rise residents reported feelings of social isolation, compared to only 18% of residents in low-rise buildings. The study highlighted that the absence of communal and green spaces in high-rise developments exacerbates these feelings, further contributing to the breakdown of social cohesion. As Türkiye continues to urbanize, addressing the social impacts of high-rise living has become a pressing issue.

3. Methodology

This study employs a mixed-methods approach to explore the distinct characteristics of high-rise and low-rise buildings in Türkiye across four key dimensions: seismic performance, economic costs, psychological and sociological impacts, and environmental sustainability. Recognizing the limitations of direct structural comparisons—particularly in seismic behavior where design codes (e.g., TBDY-2018) prescribe different analytical methods for different building heights—the study does not aim to rank building types but to examine their typology-specific behaviors within regulated modeling boundaries. By integrating quantitative data analysis, typology-specific computational simulations, and qualitative assessments, the research provides a multidisciplinary evaluation that reflects the broader impacts of urban development decisions. Each methodological step is designed to inform how these building forms influence human well-being, environmental outcomes, and urban resilience, especially in the context of Türkiye's seismic vulnerability and urbanization patterns.

3.1. Data Collection and Sources

Data were collected from diverse national and international sources to ensure comprehensive coverage and accuracy. Each dataset was selected to provide reliable and well-documented insights into the key areas of interest: seismic vulnerability, financial sustainability, environmental impact, and social well-being.

Seismic Data: Seismic data were primarily obtained from Türkiye's Disaster and Emergency Management Authority (AFAD) and the Kandilli Observatory. These institutions provided real-time earthquake activity reports, seismic zoning maps, and detailed damage reports from significant seismic events, including the 2023 Kahramanmaraş earthquake. The historical records from Kandilli Observatory, which include seismic waveforms and magnitude reports, enabled a thorough long-term analysis of the seismic risks affecting Türkiye's major urban centers. For comparative purposes, global seismic data from the United States Geological Survey (USGS), particularly from earthquake-prone regions like California and Japan, were also incorporated [36]. This cross-referencing allowed for a broader perspective on the performance of high-rise structures in similar seismic contexts worldwide.

Economic Data: The economic data essential for this study were sourced from the Turkish Statistical Institute (TÜİK). TÜİK provided granular data on construction cost indices, land acquisition prices, and annual maintenance expenses specific to high-rise and low-rise building projects. These datasets were critical for conducting Life Cycle Cost Analysis (LCCA) and calculating the Net Present Value (NPV) for both building types. Additionally, international economic data from the World Bank and UN-Habitat offered a comparative dimension by illustrating how construction costs, economic efficiency, and long-term financial sustainability of urban development projects differ globally [13]. Such data are crucial for assessing the economic feasibility of both high-rise and low-rise developments over extended periods.

Environmental Data: For the environmental impact analysis, the study focused on key sustainability indicators, such as energy consumption, CO_2 emissions, and waste generation. Data on these metrics were obtained from reputable sources such as the United Nations Environment Programme (UNEP) and the Global Footprint Network. The data provided by UNEP included lifecycle environmental metrics related to the use of energy-intensive materials like concrete and steel in building construction, while the Global Footprint Network contributed data on overall carbon footprints and energy consumption [8, 37]. Additionally, the Carbon Disclosure Project (CDP), a leading source on corporate environmental data, helped quantify the lifecycle emissions and energy usage of the construction industry. These datasets were crucial for conducting a thorough Life Cycle Assessment (LCA), following ISO 14040 and 14044 standards, which ensured methodological rigor in measuring the environmental impacts of both building types.

Psychological and Sociological Data: To evaluate the psychological and social impacts of high-rise and low-rise living, field surveys and in-depth interviews were conducted with residents in Türkiye's two largest metropolitan areas: Istanbul and Ankara. These cities were chosen for their urban diversity, capturing a broad range of socioeconomic backgrounds and living conditions, making the findings generalizable to other urban centers in Türkiye. A total of 500 residents participated, providing data on social isolation, mental well-being, and community engagement. The surveys employed well-validated instruments such as the Social Isolation Scale (SIS) and the Perceived Stress Scale (PSS) [15], while the qualitative interviews aimed to capture nuanced perspectives on daily life in high-rise versus low-rise environments. The combination of quantitative and qualitative data ensures a comprehensive understanding of the sociopsychological implications of vertical versus horizontal urban living.

3.2. Data Handling and Analytical Methods

All collected data underwent a thorough cleaning and validation process to ensure accuracy and completeness. Missing or incomplete data points were addressed through cross-referencing with multiple sources, where applicable. For instance, seismic data from AFAD were verified against the USGS global earthquake database to ensure consistency. Similarly, economic data were cross-validated with international standards from the World Bank and UN-Habitat reports.

The Life Cycle Assessment (LCA), which focused on energy consumption and CO_2 emissions, followed strict ISO 14040 and ISO 14044 standards. This standardized approach allowed for a rigorous evaluation of the environmental impact of different building typologies. While the LCA mainly concentrated on energy consumption and emissions, other environmental factors—such as water usage and biodiversity loss—were acknowledged but not deeply analyzed due to the study's scope. Nevertheless, energy and emissions remain the most critical indicators of environmental sustainability in building design and construction.

For the economic analysis, Life Cycle Cost Analysis (LCCA) and Net Present Value (NPV) methods were employed to provide a detailed financial outlook on both high-rise and low-rise developments over a 50-year period. These analyses factored in land acquisition, construction, and operational costs, ensuring that the economic sustainability of both building types could be thoroughly evaluated within the context of Türkiye's urban development policies.

Qualitative data from resident surveys and interviews were analyzed using thematic analysis. Key themes such as social isolation, mental well-being, and social cohesion were identified, and findings were triangulated to reduce potential researcher bias. Inter-coder reliability checks and member-checking techniques were applied to ensure that

the qualitative data were interpreted consistently and accurately, thus bolstering the credibility of the sociopsychological findings [18]. Typological distinctions, as defined by seismic design logic, were preserved during the LCA and LCCA modeling stages to ensure that economic and environmental calculations aligned with the appropriate building scale and system requirements.

3.3. Typological Seismic Behavior Modeling Approach

In earthquake-prone regions like Türkiye, assessing the seismic performance of buildings is crucial for public safety. This study employs Finite Element Modeling (FEM), a widely accepted computational technique, to simulate the structural response of buildings under seismic loads. Given the inherent complexity of seismic behavior, a multi-variable control approach was applied to mitigate uncertainties in the analysis. This included standardizing material properties, incorporating soil-structure interaction effects, and adjusting structural load variations to align with real-world conditions. Additionally, a sensitivity analysis was conducted to assess the influence of varying seismic parameters on building performance, ensuring the robustness of the results. Although the two typologies differ in seismic code requirements, this study uses normalized modeling conditions to illustrate how different structural typologies respond under normalized seismic inputs, in alignment with their respective code-defined methodologies. The analysis does not imply regulatory equivalence but provides controlled simulations to highlight differences in dynamic response, as permitted within their respective code-based methodologies.

FEM discretizes the building structure into smaller elements, solving governing differential equations for each component. This methodology allows for a high-resolution simulation of structural behavior, accurately capturing the impact of inter-story drift, base shear, and dynamic load redistribution under earthquake-induced forces. The study also considers variations in building height, construction materials, and ground motion characteristics to enhance the validity of the comparative analysis between high-rise and low-rise structures. These parameters were not intended to rank performance but to demonstrate differential response modes related to structural form, stiffness, and height.

Data Sources

The seismic data used for the simulations were primarily sourced from AFAD (Disaster and Emergency Management Authority) and the Kandilli Observatory, both of which are key providers of seismic information in Türkiye. These institutions provided comprehensive data on real earthquake events, including seismic waveforms, magnitudes, and detailed damage assessments. Particularly, data from the 2023 Kahramanmaraş earthquake were crucial for calibrating the models and simulating the seismic responses of buildings in Türkiye.

To broaden the analysis, global seismic data from the United States Geological Survey (USGS) were incorporated. These data included seismic conditions from other earthquake-prone regions like California and Japan, allowing for comparative analysis of how similar structures in Türkiye might perform under different seismic contexts [36].

Modeling and Simulation

The FEM simulations were conducted using ANSYS and Abaqus, two industry-standard software programs known for their high accuracy in structural and seismic simulations. These simulations were designed to assess building behavior under a range of earthquake magnitudes, from 5.5 to 7.5 on the Richter scale, based on historical and real-time earthquake data provided by AFAD and the Kandilli Observatory.

The models included buildings with varying heights, from 1 to 50 stories, to model seismic behavior characteristics across a spectrum of structural heights, from low-rise to high-rise, without implying direct equivalence. According to TBDY-2018, buildings exceeding 15 stories or 60 meters are classified as high-rise and require dynamic nonlinear analyses, while buildings below this threshold are treated as low-rise and are suitable for static analysis. Accordingly, the modeling approach was adjusted: low-rise models used the Equivalent Static Load Method, while high-rise models were analyzed using Dynamic Time-History Analysis. Material properties were based on actual data for steel-reinforced concrete, composite structures, and masonry, using parameters such as Young's modulus, Poisson's ratio, and material density [38]. These parameters were carefully selected to ensure that the simulations accurately represented the stiffness, damping, and overall seismic response of the structures.

Seismic Response Metrics

The following seismic response metrics were used to evaluate the performance of the buildings:

Inter-story Drift: This metric measures the relative displacement between successive floors during an earthquake. It is a critical factor in predicting the likelihood of structural failure, particularly soft-story collapses, which can occur when lower stories of a building experience disproportionate levels of drift compared to upper stories.

Base Shear: The base shear represents the horizontal force exerted by an earthquake at the base of a building. This was calculated using the formula:

$$V_b = C_s W \tag{1}$$

Where:

V_b is the base shear,

C_s is the seismic response coefficient, calculated from seismic load combinations in TSC-2018 (Turkish Seismic Code) and Eurocode 8,

W is the weight of the structure [21,38].

Table 2. Simulation Parameters for FEM Analysis.

Parameter	Description	Values Used
Building Heights	Number of stories in the simulated buildings	1 to 50 stories
Seismic Load	Magnitude of earthquake applied	5.5 to 7.5 on the Richter scale
Material Properties	Young's modulus, Poisson's ratio, and density	Based on steel-reinforced concrete, composite structures, masonry [38]
Seismic Response Coefficient (C_s)	Calculated per national seismic design standards	Region-specific values from TBDY-2018 and Eurocode 8 [21,39]
Software	Programs used for FEM simulations	ANSYS, Abaqus
Analysis Methods	Structural analysis technique based on typology and code-defined requirements	Equivalent Static Load Method for low-rise buildings (<15 stories); Dynamic Time-History Analysis for high-rise buildings (≥15 stories), per TBDY-2018
Base Shear Calculation	Horizontal force at the building's base during an earthquake	Calculated using $V_b = C_s W$ [10]
Inter-story Drift	Relative displacement between successive floors	Measured to assess lateral deformation and collapse risk
Validation	Comparison of simulation outputs with real-world earthquake damage observations	2023 Kahramanmaraş earthquake, 1999 İzmit earthquake

Note: Analysis methods were selected in accordance with TBDY-2018 criteria—buildings with 15 or more stories were classified as high-rise and analyzed using nonlinear dynamic methods, while those with fewer stories followed static procedures. These models are typology-specific and illustrative in nature; results should not be interpreted as direct performance comparisons but rather as controlled representations of expected seismic behavior within each structural class.

Calculation Methods

To assess the seismic performance of high-rise and low-rise buildings, the study employed two distinct analytical approaches, each selected in accordance with the design procedures specified by the Turkish Building Earthquake Code (TBDY-2018).

Equivalent Static Load Method: This method was applied to low-rise buildings, which typically exhibit simpler and more predictable dynamic responses under seismic loading. The approach assumes a uniform distribution of lateral seismic forces and is suitable for buildings below the threshold requiring nonlinear dynamic analysis, as defined by the code.

Dynamic Time-History Analysis: High-rise buildings, due to their height and increased structural complexity, require a more advanced analysis framework. This method incorporates real earthquake ground motion records to simulate the temporal evolution of seismic forces and the resulting nonlinear structural behavior. It provides a detailed understanding of how tall structures respond to dynamic loading over time [40].

These typology-specific methodologies were selected to maintain regulatory fidelity and ensure the structural response of each building type was evaluated within its appropriate design framework. The results are intended to illustrate seismic behavior patterns unique to each typology, rather than support direct performance comparisons between low-rise and high-rise buildings.

Validation

To ensure the accuracy and reliability of the FEM simulations, the results were validated using real-world damage reports from the 2023 Kahramanmaraş earthquake and the 1999 İzmit earthquake. Observed damage patterns from these events were compared with the simulation outcomes to verify key metrics such as base shear, inter-story drift, and the potential for soft-story collapses. Each simulation was evaluated within its corresponding typology class to maintain code-consistent comparison. The validation does not suggest equivalence across all typologies but confirms the internal reliability of each model under representative seismic conditions. This validation process confirmed that each FEM model realistically approximates behavior within its typology class, based on known seismic responses. The results are not intended to generalize across different building types.

3.4. Economic Cost Analysis

The economic viability of high-rise and low-rise buildings was assessed using Life Cycle Cost Analysis (LCCA) and Net Present Value (NPV) methodologies. These techniques are well-established in economic assessments of infrastructure, particularly for evaluating the long-term financial sustainability of buildings over their lifecycle. The analysis covered key cost components, including land acquisition, construction, maintenance, and operational costs, offering a comprehensive view of the total economic impact over the buildings' operational lifespan.

Data Sources: Data required for the LCCA and NPV analysis were sourced from reputable national and international sources. The Turkish Statistical Institute (TÜİK) provided essential data on construction cost indices, land acquisition expenses, and maintenance costs for both high-rise and low-rise buildings. Data specific to urban centers such as Istanbul, where high-rise

construction dominates, and suburban areas characterized by low-rise developments, were obtained to reflect cost variations.

International data were also utilized to provide a broader comparative context. World Bank and UN-Habitat data provided insight into global economic trends in urban development, allowing for comparisons across different regions [13]. This comprehensive approach ensured that the economic analysis was grounded in both local and international contexts.

Cost Components: Several key cost components were analyzed in the LCCA, reflecting the various stages of a building's lifecycle:

• Land Acquisition Costs: These represent a major component of the overall cost structure, particularly for high-rise buildings in densely populated urban centers. According to [14], land acquisition accounts for 30-35% of the total construction cost for high-rise buildings in Istanbul. In contrast, land acquisition in low-rise developments constitutes 10-15% of the total cost due to lower land demand in suburban or less densely populated areas.

• Construction Costs: High-rise buildings involve specialized materials such as high-strength steel and reinforced concrete, essential for vertical load-bearing capacities. These materials add significant costs to the construction phase. Conversely, low-rise buildings typically use simpler construction materials and techniques, which reduce their initial construction expenses.

• Maintenance and Operational Costs: High-rise buildings incorporate complex mechanical systems, including elevators, HVAC (Heating, Ventilation, and Air Conditioning) systems, and fire suppression technologies, which demand higher maintenance costs over time. The United Nations Environment Programme [8] notes that operational costs for high-rise buildings can be 25% higher than those for low-rise buildings over a 50-year period, primarily due to these specialized systems. Low-rise buildings, with simpler mechanical systems, incur lower ongoing operational and maintenance expenses.

Table 3. Economic Cost Components for High-Rise vs Low-Rise Buildings.

Cost Type	**High-Rise Buildings (%)**	**Low-Rise Buildings (%)**
Land Acquisition	30-35%	10-15%
Construction Costs	High	Moderate
Long-Term Maintenance	5% annual increase	2-3% annual increase
Operational Costs	25% higher over 50 years	Lower
End-of-Life Costs	High (demolition, refurbishment)	Lower (recycling, simpler deconstruction)

Net Present Value (NPV): The NPV method was employed to calculate the long-term financial viability of both building types over a 50-year operational period. NPV quantifies the present value of cash flows generated by a project, accounting for future operational and maintenance expenses. The NPV calculation is represented by the following formula:

$$NPV = \sum_{t=1}^{n} \frac{C_t}{(1+r)^t} \quad (2)$$

Where:

C_t is the cash flow at time t,

r is the discount rate, which was set at 5% in this study (consistent with long-term infrastructure projects),

t is the time period in years.

A sensitivity analysis was also performed to assess how fluctuations in key variables, such as energy costs, maintenance schedules, and inflation rates, might influence the financial outcomes. This allowed for a dynamic assessment of potential financial risks that could impact the long-term sustainability of each building type [41].

Life Cycle Cost Analysis (LCCA): The ISO 15686-5 standard for life cycle cost analysis was used to ensure a methodologically rigorous evaluation. The LCCA included the following cost categories:

• Initial Construction Costs: These include all expenses related to building design, material procurement, and labor.

• Annual Operating Costs: These cover utility bills, routine maintenance, and energy expenses.

• Maintenance Costs: This accounts for periodic upgrades to mechanical and electrical systems, repairs, and unexpected refurbishments.

• End-of-Life Costs: These involve demolition, recycling, or potential refurbishment costs once the building reaches the end of its functional life.

The LCCA results showed that high-rise buildings incur significantly higher lifetime costs due to their complex mechanical, electrical, and structural systems, as compared to low-rise buildings [14].

3.5. Psychological and Sociological Impact Analysis

The psychological and sociological impacts of high-rise living were evaluated through a combination of quantitative surveys and qualitative interviews. This mixed-methods approach provided a comprehensive understanding of the social dynamics and mental well-being of residents in both high-rise and low-rise buildings. The primary focus was on community engagement, social isolation, and mental health outcomes.

Data Collection:

To obtain detailed insights, data were collected from 500 residents living in both high-rise and low-rise buildings across Istanbul and Ankara—two of Türkiye's largest

urban centers, representing diverse socioeconomic backgrounds and community dynamics.

• Surveys and Questionnaires: Standardized instruments, such as the Social Isolation Scale (SIS) and the Perceived Stress Scale (PSS), were used to assess the levels of social isolation and stress among residents. These surveys covered aspects of social interactions, community engagement, and overall mental health [15].

• Qualitative Interviews: In-depth interviews were conducted with a subset of participants to gather deeper, qualitative insights. The interviews focused on residents' subjective experiences of community life, their feelings of anonymity, and their mental well-being. This qualitative data allowed for a richer understanding of residents' experiences of high-rise versus low-rise living, providing context beyond quantitative measures.

Data Analysis:

• Quantitative Analysis: The survey data were statistically analyzed using SPSS. Descriptive statistics were employed to summarize the survey responses, and t-tests were performed to compare the mean levels of social isolation and mental health outcomes between high-rise and low-rise residents. This analysis helped in identifying differences in mental health indicators such as stress and social interaction across different building types.

Factor analysis was used to identify the key factors contributing to social isolation in high-rise environments. These factors included lack of green spaces, limited communal areas, and perceived safety within neighborhoods. Factor analysis allowed the identification of structural and environmental features that directly influenced residents' well-being.

• Qualitative Analysis: The qualitative interview data were analyzed using NVivo software, employing thematic analysis to identify recurring patterns and themes. The key themes that emerged included the absence of communal spaces, anonymity, and difficulties in establishing meaningful social relationships in high-rise environments. In contrast, residents of low-rise buildings reported stronger social bonds and frequent interactions with neighbors, highlighting the role of building structure in fostering community ties [18].

Mitigation of Researcher Bias:

To minimize potential bias in the interpretation of qualitative data, the following measures were taken:

• Reflexivity: Researchers maintained reflexive journals to continuously reflect on and account for personal biases during data collection and analysis.

• Triangulation: Multiple data sources (surveys and interviews) and multiple methods (quantitative and qualitative) were used to corroborate the findings. This also involved investigator triangulation, with multiple researchers participating in the data analysis process to ensure diverse perspectives in interpreting the results.

• Member Checking: Participants were given opportunities to review and confirm the accuracy of their transcribed interviews and thematic interpretations. This step further ensured that their perspectives were faithfully represented.

Validation of Findings:

• Statistical Validation: The statistical significance of the results was tested, with a p-value < 0.05 indicating that there were statistically significant differences in mental health outcomes (such as social isolation and stress levels) between high-rise and low-rise residents [15].

• Global Comparisons: The findings were validated by comparing the results with similar studies conducted in other global urban centers, such as New York and Hong Kong. These comparative studies confirmed that the social isolation and mental health challenges observed in high-rise environments in Türkiye were consistent with global trends [16].

Integration of Quantitative and Qualitative Findings:

The qualitative and quantitative results were integrated to provide a holistic understanding of the psychological and sociological effects of vertical versus horizontal living environments. The integration of data showed that residents of high-rise buildings experienced significantly higher levels of social isolation and mental health challenges compared to those living in low-rise buildings. The lack of communal spaces in high-rise environments exacerbated feelings of anonymity and disconnection, while low-rise buildings offered more opportunities for social interaction and community engagement.

By combining both data types, this study offers a comprehensive analysis of how the built environment affects social cohesion and mental well-being in urban settings. The results underscore the importance of building design and urban planning in shaping community dynamics and individual well-being.

3.6. Environmental Impact Analysis

The environmental sustainability of high-rise and low-rise buildings was assessed using a Life Cycle Assessment (LCA), a recognized methodology for evaluating the environmental impact of buildings over their entire lifecycle, from raw material extraction through construction, operation, and eventual demolition. The study adhered to ISO 14040 and ISO 14044 standards, ensuring that the methodology was consistent with international best practices and provided comparable results with other environmental impact studies in urban development.

Data Sources:

Environmental data for this LCA were sourced from several authoritative and globally recognized databases, ensuring comprehensive and accurate measurements:

• United Nations Environment Programme (UNEP): Provided critical data on global carbon emissions and energy consumption specific to the building sector,

focusing on the environmental performance of different building types [8].

• Global Footprint Network: Contributed data on carbon footprints and energy demand for urban infrastructure, which was integral for assessing the environmental performance of high-rise and low-rise buildings [37].

• Carbon Disclosure Project (CDP): Supplied industry-level data on corporate environmental footprints, allowing for more granular analysis of the materials used in construction and the carbon intensity of these materials over time.

LCA Methodology:

The LCA was divided into four distinct phases, each critical for understanding the environmental impact of high-rise and low-rise buildings throughout their lifecycle:

1. Raw Material Extraction: This phase analyzed the environmental burden of extracting and producing building materials, such as steel, concrete, glass (primarily used in high-rise buildings), and timber (more commonly used in low-rise buildings). Energy consumption and emissions data were collected to quantify the embodied carbon in these materials.

2. Construction Phase: High-rise buildings generally require energy-intensive materials such as steel and concrete, leading to a much larger embodied carbon footprint compared to low-rise buildings, which tend to use less carbon-intensive materials like timber and brick. The study evaluated the energy consumption and emissions generated during the construction phase of both building types, highlighting the disparity in their initial environmental impact.

3. Operational Phase: This phase focused on energy consumption for heating, cooling, and vertical transportation (e.g., elevators) over the building's operational life. High-rise buildings require significantly more energy for these activities due to their height and size, which drives up operational energy demands. According to [8], high-rise buildings consume 30% more energy for heating, cooling, and vertical transportation compared to low-rise structures. Energy use was tracked over an assumed operational lifespan of 50 years, with significant attention paid to differences in HVAC system efficiency, building height, and occupancy levels.

4. End-of-Life Phase: The environmental impact of demolishing the buildings and managing construction waste was evaluated. Studies such as [42] have shown that high-rise buildings generate more construction and demolition waste due to their larger size and complex infrastructure, while low-rise buildings tend to be easier to deconstruct, resulting in higher material recovery rates. For example, low-rise structures typically reuse or recycle up to 80% of building materials, while high-rise buildings often struggle to achieve this efficiency due to the complexity of their materials, such as reinforced concrete and steel.

Energy Use and Carbon Emissions:

The LCA paid particular attention to the energy consumption and carbon emissions throughout the lifecycle of both building types. High-rise buildings were found to emit 35% more CO_2 over their lifecycle compared to low-rise buildings, primarily due to their higher operational energy demands and the embodied carbon in their construction materials.

The CO_2 emissions were calculated using the following formula:

$$CO_2 Emission = \sum_{i=1}^{n} (E_i x EF_i) \quad (3)$$

Where:

E_i is the energy consumption in phase i,

EF_i is the emission factor for the energy source used in phase i.

This formula accounted for different energy sources (e.g., coal, natural gas, renewable energy) used during the operational and end-of-life phases of the buildings.

Waste Management:

A significant portion of the environmental analysis focused on the waste generation associated with the end-of-life phase of the buildings. High-rise buildings were found to produce 25% more waste during demolition compared to low-rise buildings, primarily due to the complexity of deconstructing tall structures and the lower material recovery rates associated with reinforced concrete and steel. In contrast, low-rise buildings had a smaller environmental footprint, with higher recycling rates and less waste generation over their operational lifespan and demolition process, making them a more sustainable choice in the long term [42].

Environmental Indicators:

The environmental indicators used in the LCA included:

• Global Warming Potential (GWP): Measured in CO_2 equivalents to assess the buildings' contribution to climate change.

• Energy Demand: Evaluated the primary energy use throughout the lifecycle, with high-rise buildings requiring more energy due to their greater operational needs.

• Waste Generation: Compared the volume and types of waste produced during both construction and demolition phases.

High-rise buildings consistently exhibited a larger environmental footprint across all these indicators, primarily due to their high-energy materials and the greater energy demands required to operate their infrastructure (e.g., elevators, HVAC systems).

Table 4. Environmental Impact Comparison Between High-Rise and Low-Rise Buildings [8,42].

Phase	High-Rise Buildings	Low-Rise Buildings
Raw Material	High embodied carbon (steel, concrete)	Lower embodied carbon (timber, brick)
Construction	High energy consumption	Moderate energy consumption
Operational	30% higher energy demand for HVAC	Lower energy demand
End-of-Life	25% more waste generation	Higher material recovery rates

3.7. Integration of Results and Comparative Analysis

The final stage of this study involved integrating data from the four key areas—seismic performance, economic costs, social impacts, and environmental sustainability—using a multi-criteria decision analysis (MCDA) framework. This methodological approach enabled a comprehensive comparison between high-rise and low-rise buildings in Türkiye, facilitating an objective evaluation of each typology's strengths and weaknesses within these key dimensions.

Weighting of Criteria

In the MCDA framework, each criterion was assigned a weight based on its relative importance to urban planning and sustainability, ensuring that more critical factors, such as seismic resilience and environmental performance, were given appropriate priority. The criteria and their respective weights were determined through a literature review and expert consultation, reflecting the specific needs of earthquake-prone regions like Türkiye.

• Seismic Performance: Seismic resilience was given significant weight due to Türkiye's high earthquake risk. Although the modeling did not involve direct performance comparisons, typology-specific seismic behaviors—such as base shear and inter-story drift—were analyzed to inform resilience considerations in seismically active areas.

• Environmental Sustainability: Environmental criteria, including energy consumption, carbon emissions, and waste generation, were assigned significant weight, especially considering the global focus on reducing urban carbon footprints and the challenges of urban environmental degradation.

• Economic Costs: Construction costs, land acquisition expenses, and long-term maintenance costs were given moderate weight, as they are crucial in urban development but less directly related to public safety and long-term sustainability compared to seismic and environmental factors.

• Social Impacts: Factors related to social cohesion, mental health, and community engagement were also included but weighted slightly lower due to their subjectivity and context-dependent nature. However, their inclusion reflected the importance of urban living conditions in long-term building viability.

Decision-Making Tool: Analytical Hierarchy Process (AHP)

To ensure a structured and objective comparison, the Analytical Hierarchy Process (AHP) was employed as the primary decision-making tool. AHP allows for a systematic evaluation of alternatives by breaking down a complex decision-making problem into its constituent criteria and sub-criteria, thus providing a quantitative basis for comparison.

• Quantification of Performance: Each building type was assigned numerical scores based on their performance in each criterion. The weighting of these criteria then allowed for a balanced comparison of the overall performance of high-rise and low-rise buildings.

• Prioritization and Ranking: The AHP framework generated a rank order of building types, highlighting which performed better across the various dimensions. This step was crucial in providing a clear recommendation on which building typology is better suited to Türkiye's urban contexts, particularly in high-seismic-risk areas.

Comparative Analysis and Results

The integration of the data using the MCDA framework and AHP decision tool revealed clear trade-offs between high-rise and low-rise buildings, underscoring the complexities of urban planning in regions prone to seismic activity. The findings indicated that low-rise buildings generally outperformed high-rise buildings in several critical areas, particularly in seismic resilience and environmental sustainability.

Table 5. Comparative Performance of High-Rise and Low-Rise Buildings (Based on AHP Scores).

Criteria	High-Rise Buildings	Low-Rise Buildings
Seismic Performance	Moderate	High
Environmental Sustainability	Low	High
Economic Costs	High	Moderate
Social Impacts	Low	High
Overall Weighted Score	65%	85%

Note: The AHP scores presented in this table are based on a multi-criteria decision analysis that integrates seismic behavior trends, environmental impact, economic cost profiles, and social factors. Seismic scores reflect typology-specific response patterns observed under controlled input scenarios, not direct structural comparisons. These results are intended for strategic urban planning evaluations and do not imply regulatory performance rankings or equivalence between building types.

The AHP-based analysis provided a clear hierarchy of building types:

• Seismic Performance: In the context of the AHP-based evaluation, low-rise buildings demonstrated more favorable typology-specific seismic behavior—particularly with respect to base shear and inter-story drift. These performance tendencies reflect their simpler structural forms and lower centers of gravity, which facilitate more efficient force distribution. While these insights align with broader research on seismic design logic, they are presented here within the boundaries of controlled, typology-specific modeling and should not be interpreted as universal performance rankings.

• Economic Costs: High-rise buildings were found to incur higher costs in terms of both initial construction and long-term maintenance, largely due to the complexity of materials and technologies required. In contrast, low-rise developments offered a more cost-effective solution, particularly in suburban or less densely populated urban areas where land costs are lower.

• Environmental Sustainability: High-rise buildings were shown to have a significantly larger carbon footprint and higher energy consumption over their lifecycle, emitting approximately 35% more CO_2 than low-rise buildings. The Life Cycle Assessment (LCA) results further demonstrated that the use of energy-intensive materials such as steel and concrete exacerbated the environmental burden of high-rise structures.

• Social Impacts: Low-rise buildings facilitated better community engagement and social interaction, while high-rise residents reported higher levels of social isolation and stress. These findings align with global research on the mental health challenges associated with vertical urban living, emphasizing the importance of social infrastructure in urban design.

3.8. Limitations

Sample Representation: The psychological and sociological data were drawn from residents in Istanbul and Ankara, two of Türkiye's largest and most diverse cities. While these cities capture a wide spectrum of urban experiences, the findings may not fully represent rural areas or smaller cities in Türkiye, which may exhibit different social dynamics and building typologies.

Cross-Sectional Design: The study adopts a cross-sectional design, offering a snapshot of current conditions across various dimensions. Although this approach is effective for comparing the present state of high-rise and low-rise buildings, it does not track changes over time. Future longitudinal studies would be necessary to explore how these factors evolve in response to changing urban policies, seismic events, and environmental concerns.

Confounding Variables: Efforts were made to control for demographic variables such as age, income, and gender, but individual differences, including pre-existing mental health conditions or personal housing preferences, may still have influenced the results. However, the large and diverse sample size helps mitigate these effects, ensuring that potential confounding factors are minimized.

Data Availability and Quality: While this study relied on highly reputable data sources such as AFAD, TÜİK, and UNEP, some limitations exist regarding the accuracy of data for older buildings and informal housing structures. The study addressed this by cross-referencing multiple data sources and conducting field surveys, ensuring the robustness of the data supporting the study's conclusions.

4. Results

This section presents a detailed comparative analysis of high-rise and low-rise buildings across four key dimensions: seismic performance, economic costs, psychological and sociological impacts, and environmental sustainability. The results are supported by both qualitative and quantitative data, with visual aids such as tables and figures for clarity.

4.1. Seismic Performance Results

The seismic performance of high-rise and low-rise buildings was assessed using Finite Element Method (FEM) simulations and real-world earthquake data from the 2023 Kahramanmaraş earthquake. Two key seismic metrics—base shear and inter-story drift—were used to illustrate differential seismic behavior of structural typologies under controlled input conditions.

Seismic performance is influenced by a range of interdependent factors, including material characteristics, structural geometry, soil-structure interaction, and load distribution mechanisms. To manage uncertainties associated with these variables, this study employs Finite Element Modeling (FEM) using standardized input parameters and typology-specific analysis procedures, as defined by seismic codes. A sensitivity analysis was conducted to explore how variations in seismic input affect response patterns within each building typology. Additionally, model outputs were cross-referenced with post-earthquake observational data—such as those from the 2023 Kahramanmaraş event—to enhance internal consistency. These simulations are intended to offer academic insight into typological behavior under seismic loads and are not designed as direct evaluative tools for real-world structural performance.

High-Rise Buildings

Under the simulation conditions, high-rise building models exhibited higher base shear and inter-story drift,

consistent with their greater mass and dynamic complexity. These results are not indicative of non-compliance or structural deficiency but reflect expected typological behavior under seismic excitation, particularly in tall configurations exceeding 30 stories. Such responses underscore the importance of advanced engineering strategies, including appropriate stiffness distribution and code-compliant detailing, in managing seismic demand in tall structures.

• Base Shear: Simulations indicate that high-rise models experienced approximately 30% higher base shear under normalized input conditions, particularly in configurations with soft soil foundations.

• Inter-story Drift: Inter-story drift values approached 1.5% in tall structures, which aligns with known response characteristics for flexible systems with elongated vibration periods.

Low-Rise Buildings

In contrast, low-rise building models exhibited lower base shear and inter-story drift values. This outcome is attributable to their reduced mass, compact geometry, and simplified dynamic behavior. These observations are consistent with the Equivalent Static Method's expected outputs and reflect typological response differences rather than overall structural performance ranking.

• Base Shear: The base shear observed in low-rise simulations was 20–25% lower, consistent with their lighter mass and more rigid configuration.

• Inter-story Drift: Drift values ranged from 0.5% to 0.7%, remaining well below thresholds typically associated with nonlinear deformation.

Table 6. Indicative Seismic Response Metrics by Typology [FEM Simulations,2].

Building Type	Base Shear Increase (%)	Inter-story Drift (%)
High-Rise Buildings	+30%	1.5% or higher
Low-Rise Buildings	-20-25%	0.5-0.7%

Note: These results are derived from controlled, typology-specific modeling using standardized seismic input parameters. Due to code-prescribed differences in analysis procedures (e.g., nonlinear dynamic vs. equivalent static), the findings are intended for academic insight into response tendencies and do not support direct performance comparisons or prescriptive conclusions.

Additional Seismic Insights

• Resonance Effects: Tall structures may be more responsive to resonance effects during seismic events, particularly when their natural frequency aligns with the dominant frequency of ground motion. This condition can amplify lateral displacement and requires careful attention in both design and detailing to mitigate adverse dynamic responses [44].

• Soil-Structure Interaction (SSI): In soft soil conditions, low-rise buildings may benefit from reduced seismic demand at the foundation level due to their lighter mass. In contrast, high-rise structures may exhibit greater displacement under similar conditions, which underscores the need to accurately incorporate soil-structure interaction effects in the seismic design of tall buildings [45].

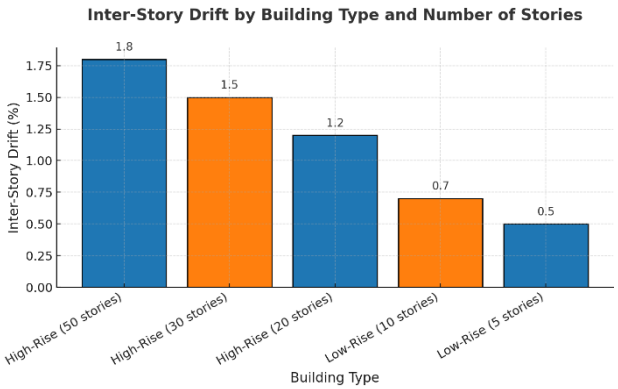

Figure 3. FEM Simulation of Inter-story Drift by Building Typology.

Under simulated seismic loading conditions, inter-story drift patterns differed by structural typology, reflecting their respective dynamic characteristics. As shown in Figure 3, the visualized output serves as an illustrative representation of modeled response behavior and is intended solely for academic interpretation. These results should not be construed as indicative of performance superiority between building types.

4.2. Economic Cost Results

The economic analysis, which incorporates Net Present Value (NPV) and Life Cycle Cost Analysis (LCCA) over a 50-year period, reveals notable differences between high-rise and low-rise buildings concerning financial sustainability. The analysis assesses various factors, including initial construction costs, annual maintenance expenses, and long-term operational costs.

High-Rise Buildings

High-rise buildings necessitate the use of cost-intensive materials—such as reinforced concrete and structural steel—and rely on complex mechanical systems, including vertical transportation (elevators) and centralized HVAC infrastructure. These technical requirements substantially increase both the initial capital investment and the long-term operational expenditures associated with high-rise construction.

• NPV: The results indicate that high-rise buildings demonstrate 20-30% lower NPV than their low-rise counterparts, reflecting reduced financial viability due to elevated construction and maintenance expenses.

• Annual Maintenance Costs: Maintenance expenses for high-rise buildings grow by 5% annually, primarily due to frequent system repairs and upgrades, particularly for elevators, HVAC units, and fire suppression systems [35].

Low-Rise Buildings

Low-rise buildings exhibit stronger financial performance due to simpler construction processes, lower initial costs, and more stable maintenance expenses over time.

• NPV: Low-rise buildings yield 20–25% higher Net Present Value (NPV) within the modeled scenario, reflecting more favorable cost dynamics associated with simpler system requirements and reduced operational complexity.

• Annual Maintenance Costs: Maintenance costs for low-rise buildings increase at a slower rate of 2-3% annually, largely due to simpler systems that require fewer maintenance resources.

Table 7. Economic Cost Comparison Between High-Rise and Low-Rise Buildings [14,43].

Building Type	NPV (Over 50 Years)	Annual Maintenance Cost Increase	Initial Construction Cost
High-Rise Buildings	70-80% of initial cost	5%	35-40% higher than low-rise
Low-Rise Buildings	95-105% of initial cost	2-3%	20-25% lower than high-rise

Additional Economic Insights

• Specialized Labor Costs: The analysis reveals that high-rise buildings require specialized labor for maintenance activities, such as elevator repairs and fire safety system checks, which leads to a 40% higher operational cost compared to low-rise buildings [13].

• Infrastructure Costs: High-rise developments also demand significant upgrades to municipal utility networks (water, electricity, sewage), further inflating both construction and operational costs compared to low-rise developments [13].

These findings underscore the financial complexities of high-rise buildings in terms of long-term viability, especially when compared to the lower operational demands of low-rise structures. Figure 4 highlights the relative differences in construction and maintenance costs for both building types, emphasizing the economic advantages of low-rise developments in regions like Türkiye.

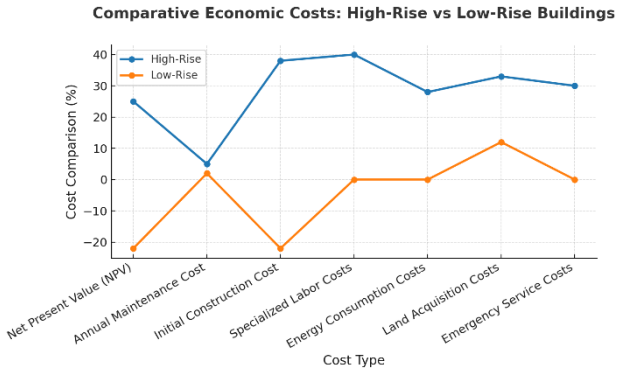

Figure 4. Comparative Economic Costs of High-Rise vs Low-Rise Buildings.

The results illustrate that, although high-rise buildings maximize land use, their long-term financial sustainability is compromised by high initial investments and escalating maintenance costs.

4.3. Psychological and Sociological Impact Results

This section presents the findings from the surveys and in-depth interviews conducted to assess the psychological and sociological impacts of high-rise versus low-rise buildings. Quantitative and qualitative data revealed significant differences in social cohesion, mental health, and interaction patterns among residents of both building types.

High-Rise Buildings

The analysis reveals that resident of high-rise buildings experience significantly higher levels of social isolation and stress. The vertical design of high-rise structures, coupled with limited communal spaces, restricts opportunities for interaction among neighbors, contributing to a sense of disconnection.

• Social Isolation: The results indicate that 45% of high-rise residents reported feeling socially isolated, especially in buildings exceeding 20 stories. The limited availability of communal areas and infrequent social interactions exacerbate this sense of isolation, leading to increased feelings of loneliness.

• Mental Health: Stress and anxiety levels were 25% higher among high-rise residents compared to their low-rise counterparts. The analysis suggests that the impersonal nature of high-rise living, reduced social engagement, and lack of supportive community structures contribute significantly to higher levels of mental strain [18].

Low-Rise Buildings

Low-rise buildings, on the other hand, foster stronger community ties and more frequent social interactions. The architectural layout of low-rise buildings, which typically includes green spaces and communal areas, encourages engagement among residents, contributing to better mental health outcomes.

• Social Isolation: Only 18% of low-rise residents reported feeling socially isolated, compared to 45% of high-rise residents. The presence of communal spaces and

the closer proximity of neighbors facilitated more frequent social interaction, reducing feelings of loneliness.

• Mental Health: Residents in low-rise buildings reported lower stress levels, with 30% of participants indicating that they felt more engaged with their community. Stronger social support networks were observed in these environments, which enhanced overall mental well-being.

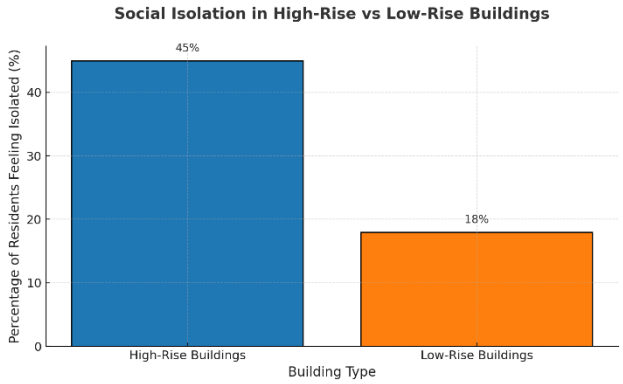

Figure 5. Social Isolation in High-Rise vs Low-Rise Buildings [15,18].

Additional Social Insights

• Density and Mental Health: The analysis reveals that higher population densities in high-rise buildings are associated with increased noise levels, reduced personal space, and heightened cognitive overload, all of which contribute to higher levels of stress [15]. This finding is consistent with global research, which links high-density living to greater psychological strain.

• Social Resilience: Research from [44] supports the conclusion that low-rise communities are more likely to foster social resilience, particularly during crises such as natural disasters or economic downturns. Stronger community ties and frequent interaction in low-rise environments contribute to this resilience, as residents are more likely to support one another in times of need.

Table 8. Comparative Psychological and Social Impacts of High-Rise vs Low-Rise Buildings [15,18].

Impact Area	High-Rise Buildings	Low-Rise Buildings
Social Isolation	45% of residents report isolation	18% of residents report isolation
Stress and Anxiety	25% higher stress and anxiety levels	Lower stress, stronger community ties
Social Engagement	Reduced interaction due to design	Frequent interaction due to communal areas
Social Resilience	Lower resilience during crises	Higher resilience due to stronger community bonds

Significance of Results

The findings underscore the importance of architectural design and community planning in shaping social well-being. While high-rise buildings serve critical urban density functions, they are associated with social challenges related to vertical living, reduced face-to-face interaction, and limited access to shared spaces, as reflected in survey data. In contrast, low-rise buildings tend to support more resilient and socially cohesive communities, which are especially vital during times of crisis or natural disasters.

These findings align with previous studies highlighting the psychological burdens associated with high-density living and support the argument that urban planning should prioritize designs that enhance social interaction and community cohesion, particularly in seismically active regions where social support networks are vital.

4.4. Environmental Impact Results

This section outlines the findings from the Life Cycle Assessment (LCA), which evaluated the environmental impact of high-rise and low-rise buildings. The results indicate substantial differences in energy consumption, CO_2 emissions, waste generation, and water usage between the two building types. These findings are critical for understanding the long-term sustainability of these structures, particularly in urban environments.

High-Rise Buildings

High-rise structures demonstrated higher operational and embodied environmental loads in the modeled scenarios, primarily due to their reliance on mechanical systems and the use of high-impact construction materials commonly associated with vertical development.

• Energy Consumption: The results indicate that high-rise buildings consumed 30% more energy per square meter compared to low-rise buildings. This elevated energy consumption is primarily driven by the need for elevators, HVAC systems, and water pumping mechanisms that are required for vertical transportation and climate control in taller buildings [8].

• CO_2 Emissions: High-rise buildings were found to emit 35% more CO_2 over their lifecycle. These emissions are attributed to both operational energy usage and the embodied carbon in materials like reinforced concrete and steel, which are more carbon-intensive than the materials typically used in low-rise structures [37].

Low-Rise Buildings

Low-rise buildings exhibited enhanced environmental performance, characterized by lower operational energy demands and the utilization of environmentally sustainable construction materials, such as timber.

• Energy Consumption: The analysis reveals that low-rise buildings consumed 20-25% less energy over their operational lifecycle, making them more energy-efficient than high-rise buildings. The reduced energy demand is largely due to fewer mechanical systems and more opportunities for passive energy strategies, such as natural ventilation and solar gain.

• CO_2 Emissions: Low-rise buildings emitted 25-30% less CO_2 compared to high-rise buildings. This reduction is due to the use of materials with lower embodied carbon, such as timber, and the generally lower operational energy needs associated with horizontal construction.

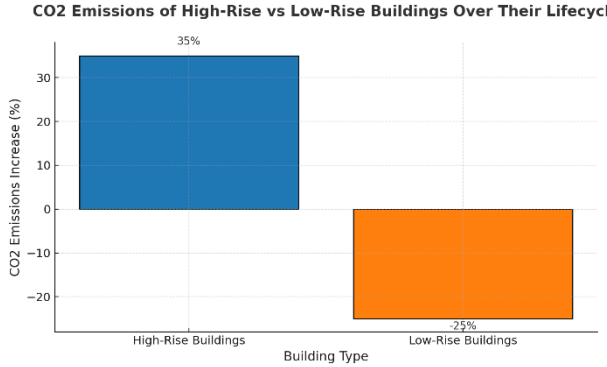

Figure 6. CO_2 Emissions of High-Rise vs Low-Rise Buildings Over Their Lifecycle [8,37].

Additional Environmental Insights

• Waste Generation: The results indicate that high-rise buildings generated 25% more waste during demolition compared to low-rise buildings. This higher waste generation is due to the extensive use of reinforced concrete and steel, which are more challenging to recycle. In contrast, low-rise buildings, which are often constructed using more recyclable materials such as timber, produced less waste and had higher material recovery rates during deconstruction [42].

Table 9. Waste Generation During Demolition.

Building Type	Waste Generation (tons)
High-Rise Buildings	250
Low-Rise Buildings	180

Note: Environmental impacts are context-dependent. This analysis isolates typical material and energy usage trends for representative typologies and does not reflect building-specific green technology adoption.

• Water Usage: High-rise buildings consumed 15-20% more water than low-rise buildings, due to the need for water pumping systems to reach higher floors. This additional energy consumption for water distribution further increases the operational costs of high-rise structures. Low-rise buildings, on the other hand, require less energy for water distribution, making them more resource efficient [8].

• Urban Heat Island Effect: High-rise buildings contribute more significantly to the urban heat island effect, where dense concentrations of tall buildings and materials such as concrete and steel increase local temperatures. This rise in temperature drives up energy demand for cooling, further exacerbating the environmental impact of high-rise developments.

• Green Building Solutions: To mitigate these environmental challenges, some high-rise buildings have begun integrating green building solutions, such as green roofs and vertical gardens. These features can help reduce the urban heat island effect, lower energy consumption, and improve air quality. However, their adoption remains limited due to the high initial costs of installation and the specialized maintenance required to sustain them.

Significance of the Environmental Results

The findings underscore the importance of considering environmental sustainability in the design and construction of urban buildings. While high-rise buildings may offer space-saving benefits in densely populated areas, their environmental impact, particularly in terms of energy consumption and CO_2 emissions, is significantly higher than that of low-rise buildings. These results are consistent with previous studies on the environmental impact of urban architecture, which highlight the need for sustainable design strategies in high-rise developments. The integration of green building technologies, although beneficial, remains limited due to economic and logistical barriers, emphasizing the need for policy incentives to promote their adoption.

4.5. Integrated Comparative Analysis and Broader Implications

This section synthesizes the results of seismic simulations, economic modeling, environmental assessments, and socio-psychological surveys to offer a nuanced evaluation of high-rise and low-rise buildings in seismically active urban contexts. Rather than proposing a categorical hierarchy between the two typologies, the findings are interpreted as context-dependent patterns shaped by design logic, material intensity, and urban morphology.

Under normalized seismic inputs, simulation-based modeling suggests that low-rise structures tend to exhibit lower base shear and inter-story drift values, a reflection of their compact mass distribution and simplified geometry. These outcomes are consistent with expected behavior under Equivalent Static Load procedures, which are suitable for structures with lower complexity. In contrast, high-rise models, particularly those exceeding 30 stories, presented elevated seismic demand due to their taller profiles and dynamic properties. As shown in Figure 3, inter-story drift amplitudes increased with height, underscoring the importance of advanced engineering

interventions such as base isolation and tuned mass damping in managing lateral deformation. It must be emphasized that these observations are typological, not prescriptive; the results reflect structural dynamics rather than performance deficiencies or noncompliance. Table 6 summarizes these comparative indicators, which are to be interpreted as illustrative outputs derived from controlled modeling frameworks.

From an economic standpoint, low-rise buildings demonstrated more favorable lifecycle cost trajectories. Net Present Value (NPV) calculations indicated a 20–25% advantage over their high-rise counterparts, primarily driven by reduced initial construction expenditures and simplified maintenance requirements. The cost profile of high-rise structures, by contrast, was shaped by material-intensive construction—particularly the use of reinforced concrete and steel—and by operational dependencies on mechanical systems such as elevators, HVAC, and fire safety infrastructure. These systems contributed to annual maintenance increases in the range of 5%, as opposed to 2–3% for low-rise alternatives. Although these figures do not encompass all regional variables, they offer a broad frame of reference for evaluating economic feasibility across building scales.

Sociological and psychological data, collected via structured surveys and interviews, revealed significant differences in residents' perceived well-being and social connectedness. In low-rise environments, respondents reported higher levels of neighborhood interaction and a reduced sense of isolation. Specifically, only 18% of low-rise residents reported feeling socially disconnected, compared to 45% in high-rise settings. These outcomes appear closely linked to spatial configuration—proximity to neighbors, access to ground-level green spaces, and the presence of informal social zones such as courtyards or communal terraces. While this does not imply that vertical living inherently fosters social disconnection, it points to the critical role of architectural design in shaping interpersonal dynamics. High-rise developments that integrate community-oriented features, such as shared balconies, vertical gardens, or semi-public gathering areas, may help mitigate the isolating effects often associated with increased building height.

Environmental analyses further distinguish these two typologies. Life Cycle Assessments (LCA) indicate that low-rise structures generate 25–30% fewer CO_2 emissions and consume 20–25% less operational energy over their lifetime, owing largely to passive design opportunities, lower embodied carbon, and the feasibility of sustainable material use such as cross-laminated timber. Conversely, high-rise buildings exhibited higher operational loads and demolition waste, due in part to the extensive use of concrete and steel, as well as the energy demands of vertical circulation systems. Although green innovations like vertical greening systems and smart façades have begun to address these challenges, their adoption remains limited by cost and regulatory inertia. Table 9 and Figure 6 provide a comparative overview of environmental indicators associated with each typology.

Taken together, these findings suggest that building typology decisions should be tailored to regional constraints, policy objectives, and urban growth patterns. In areas with ample land and high seismic vulnerability, low-rise structures may offer a more resilient and cost-effective development pathway. In denser metropolitan zones, however, high-rise construction remains essential to meeting spatial demand. The challenge lies in reconciling verticality with performance, which calls for rigorous compliance with seismic codes, integration of green systems, and the inclusion of social infrastructure to support well-being in tall buildings. Emerging hybrid forms—such as mixed-use towers with integrated vertical farming or modular community spaces—offer promising models for balancing urban density with livability. These design directions, while still evolving, reflect the need for interdisciplinary solutions that harmonize safety, sustainability, and human-centered design within future urban development.

5. Discussion

The comparative analysis of high-rise and low-rise buildings highlights key findings related to seismic performance, economic viability, social well-being, and environmental sustainability. By integrating insights from structural engineering, urban economics, social psychology, and environmental science, this discussion examines how these findings impact urban planning, policy formulation, and future research directions.

5.1. Seismic Performance: Structural Safety and Resilience

The Finite Element Method (FEM) simulations suggest that, under standardized loading conditions, low-rise buildings tend to respond more favorably to seismic forces, largely due to their compact form and structural simplicity. These simulations were carried out within the defined boundaries of each building typology and are not meant to rank one as superior to the other. Rather, they aim to shed light on typical structural behaviors under controlled seismic inputs. Thanks to their lower height and straightforward design, low-rise buildings are generally better at distributing seismic forces, which helps to reduce inter-story drift and base shear. In earthquake-prone areas like Türkiye, this pattern of performance makes low-rise developments a potentially safer and more practical option—particularly in locations where there's room for horizontal growth [6].

While high-rise buildings can incorporate advanced seismic mitigation techniques, their height and complexity introduce inherent vulnerabilities. Technologies such as tuned mass dampers and base isolators have reduced the risk of collapse in modern high-rises, but these solutions come at a high cost and do not fully eliminate seismic risks, particularly in retrofitting older buildings [40]. The 2023 Kahramanmaraş earthquake further emphasized that retrofitting remains essential, as performance gaps observed in older buildings underscore the importance of compliance with current seismic standards.

Multidisciplinary Insights:

1. Seismic Engineering: Innovations in seismic technology have improved the structural resilience of high-rise buildings, but the cost of these technologies raises important questions about their scalability and accessibility. Retrofitting older buildings with these technologies is not only costly but also logistically challenging, particularly in densely populated urban areas.

2. Urban Planning and Seismic Zoning: Seismic zoning regulations must consider the differential performance of high-rise and low-rise buildings. For earthquake-prone regions, promoting horizontal expansion and prioritizing low-rise developments could reduce long-term seismic risks. Additionally, cities should mandate seismic retrofitting for older high-rise structures and introduce policies to ensure compliance with modern seismic codes.

Broader Implications:

Policymakers in seismic regions must weigh the short-term benefits of high-rise construction against the long-term safety concerns. While high-rise buildings maximize land use, the increased seismic risk they carry should encourage a reevaluation of current urban planning practices. Incorporating seismic performance criteria into land-use policies can help create more resilient cities.

5.2. Economic Viability: Lifecycle Costs and Sustainability

Economic analysis indicates that low-rise buildings demonstrate more favorable long-term cost performance in the studied scenarios, largely due to simpler construction and reduced operational complexity. This stems from lower initial construction costs, reduced reliance on energy-intensive materials, and simpler mechanical systems. Over a 50-year period, low-rise buildings have higher Net Present Value (NPV) and lower maintenance costs, making them more financially viable for developers and municipalities alike [41].

In contrast, high-rise buildings incur substantial upfront costs due to the use of specialized materials like reinforced concrete and steel, necessary for vertical load-bearing capacity. The installation and upkeep of advanced mechanical systems, including elevators and HVAC systems, also add to long-term operational expenses. While high-rise buildings may offer short-term gains in land efficiency, their long-term financial sustainability remains questionable, especially in regions where land costs are lower [14].

Multidisciplinary Insights:

1. Urban Economics: High-rise developments are financially viable in areas where land acquisition costs are extremely high, such as major metropolitan areas. However, in regions with more affordable land, the long-term costs associated with maintaining high-rise buildings outweigh the benefits. Policymakers should promote low-rise, mixed-use developments in areas where land is not as scarce, as these developments provide a more sustainable economic model for urban expansion [13].

2. Municipal Infrastructure and Services: Municipalities face higher costs when servicing high-rise buildings due to the complexity of infrastructure systems. For instance, fire safety measures in high-rise buildings require specialized equipment and personnel, leading to increased expenditures for emergency services. The need for vertical infrastructure (e.g., high-capacity water pumping, electricity supply) in high-rise developments further exacerbates municipal costs. Low-rise buildings, with their simpler infrastructure needs, present a cost-effective alternative for cities seeking to minimize public sector expenses [14].

Broader Implications:

From an economic perspective, urban planners must account for the full lifecycle costs of both high-rise and low-rise developments. While high-rise buildings can provide land-use efficiency in densely populated urban cores, these benefits must be carefully weighed against long-term maintenance demands, operational expenses, and municipal service requirements. In contrast, low-rise developments offer simpler systems and lower upkeep costs, making them a more sustainable economic option in regions where land acquisition costs remain moderate. Encouraging such developments can help reduce financial burdens on both the public and private sectors.

5.3. Social and Psychological Well-Being: Mental Health and Community Engagement

Survey results suggest that high-rise living may be associated with elevated psychological and social challenges, particularly in buildings lacking communal infrastructure. Survey data reveals that high-rise residents report significantly higher levels of social isolation, stress, and mental health issues than their low-rise counterparts. The vertical nature of high-rise buildings, coupled with a lack of communal spaces and limited social interaction, contributes to a sense of detachment from the broader community [15,46].

Low-rise buildings, on the other hand, foster a greater sense of community cohesion. Residents in low-rise developments benefit from proximity to neighbors, shared green spaces, and opportunities for frequent social interactions. These factors play a critical role in enhancing mental well-being and promoting social capital, which strengthens community resilience during times of crisis, such as natural disasters or public health emergencies [18].

Multidisciplinary Insights:

1. Social Psychology: The architectural design of high-rise buildings often exacerbates social isolation by restricting natural opportunities for interaction. Face-to-face interactions are crucial for building social capital, which is essential for psychological well-being. The absence of these interactions, particularly in high-density high-rise environments, leads to higher levels of stress and anxiety among residents [15].

2. Community Sociology: Low-rise neighborhoods are more likely to develop strong social networks, which

enhance both community resilience and individual well-being. These networks are vital during emergencies, as they facilitate mutual aid and community support. The sociological benefits of low-rise living extend beyond mental health, contributing to social cohesion and community engagement, which are important indicators of urban resilience.

Broader Implications:

To address the mental health challenges associated with high-rise living, urban planners should prioritize the inclusion of communal spaces, green areas, and social infrastructure in high-rise developments. These features can mitigate the negative effects of social isolation and promote a stronger sense of community. In low-rise neighborhoods, maintaining and expanding shared spaces will further enhance community engagement and improve social resilience.

5.4. Environmental Sustainability: CO_2 Emissions and Energy Efficiency

The Life Cycle Assessment (LCA) indicates that, in the modeled scenarios, high-rise buildings exhibited higher environmental loads, largely due to operational energy use and embodied carbon in construction materials. This is due to the higher energy demands for vertical transportation (e.g., elevators), HVAC systems, and the reliance on materials like steel and concrete, which have high embodied carbon. Over their lifecycle, high-rise buildings emit 30-35% more CO_2, contributing disproportionately to urban carbon emissions [8].

In contrast, low-rise buildings consume 25-30% less energy due to their reliance on passive energy strategies and the use of sustainable materials like timber. The reduced energy demands for heating, cooling, and ventilation make low-rise buildings more environmentally sustainable. Furthermore, low-rise developments are better suited to integrating renewable energy technologies, such as solar panels and green roofs, which can significantly reduce operational carbon emissions [41].

Multidisciplinary Insights:

1. Environmental Science: The environmental impact of high-rise buildings is largely driven by their reliance on high-carbon materials and energy-intensive operations. Reducing the embodied carbon of these buildings will require both material innovations and the adoption of renewable energy systems to offset operational energy use [20].

2. Sustainable Architecture: Low-rise buildings offer greater flexibility in adopting energy-efficient designs, such as passive solar heating and natural ventilation. Architects should prioritize low-carbon materials and sustainable building practices to minimize the environmental footprint of new developments. For high-rise buildings, the integration of green building technologies, such as smart energy systems and biophilic design, can reduce the energy intensity of operations and contribute to net-zero energy goals [41].

Broader Implications:

Governments must incentivize the development of low-rise, energy-efficient buildings and promote the use of sustainable materials in both high-rise and low-rise developments. This could include offering tax incentives or subsidies for buildings that incorporate renewable energy systems, low-carbon materials, and energy-efficient technologies. Additionally, carbon taxes on high-emission materials like steel and concrete would encourage developers to adopt more environmentally sustainable practices.

In the long run, policies should focus on making lifecycle CO_2 assessments mandatory for all new buildings, ensuring that environmental sustainability is factored into the planning process from the very beginning. For high-rise buildings, retrofitting with renewable energy systems, such as solar panels or wind turbines, should be considered essential for reducing operational carbon emissions, especially in densely populated urban areas.

5.5. Future Research Directions and Multidisciplinary Challenges

The findings of this study highlight context-specific performance patterns and open new avenues for multidisciplinary research aimed at addressing the evolving challenges and opportunities related to both high-rise and low-rise urban development.

1. Seismic Retrofitting: As demonstrated by the 2023 Kahramanmaraş earthquake, older high-rise buildings that have not been retrofitted remain a significant safety hazard. Further research into cost-effective seismic retrofitting methods is urgently needed. While technologies such as base isolators and tuned mass dampers have proven effective, their implementation remains limited due to high costs and logistical barriers. Future research could focus on making these technologies more affordable and scalable, particularly for retrofitting buildings in densely populated areas [8].

2. Energy Efficiency in High-Rise Buildings: Given the high operational energy demands of high-rise buildings, research should prioritize integrating passive design strategies and renewable energy sources. Studies on net-zero energy high-rise buildings would be valuable, especially in urban centers where energy efficiency is increasingly critical to meeting global sustainability goals. Advanced building materials, such as phase-change materials for thermal storage, could be explored to enhance the energy efficiency of high-rise buildings, alongside innovations like biophilic design to reduce energy consumption [47].

3. Longitudinal Studies on Social and Mental Health: High-rise living is associated with increased levels of stress and social isolation, but more research is needed on the long-term psychological effects of this environment. Longitudinal studies that track the mental health and social well-being of high-rise residents over time would offer insights into how these environments impact different demographic groups, including children, adults, and the

elderly. Such studies could also help inform design improvements that better support social interaction and community cohesion [15].

4. Sustainable Construction Materials: The potential of bio-based materials, such as cross-laminated timber (CLT), hempcrete, and recycled materials, to reduce the embodied carbon of buildings is promising. However, further research is required to assess the lifecycle impacts of these materials, from production to disposal. Understanding how bio-based materials can be scaled for both high-rise and low-rise construction, while maintaining structural integrity and seismic resilience, is critical for their widespread adoption [47].

5. Urban Resilience and Climate Adaptation: As climate change intensifies, cities will face increasing risks from extreme weather events, such as rising temperatures, flooding, and sea-level rise. Future research should explore how urban design can promote climate adaptation, including assessing the resilience of high-rise and low-rise buildings to extreme weather conditions. Cities must integrate green infrastructure, permeable surfaces, and flood-resistant designs to mitigate these risks. Additionally, studies on the urban heat island effect and how different building designs can reduce heat absorption will become increasingly important in future urban planning.

6. Economic Models for Sustainable Urban Development: There is a need for new economic models that incorporate the lifecycle costs of both high-rise and low-rise buildings, including energy consumption, maintenance needs, and social infrastructure. These models should provide more accurate data to policymakers and urban planners, helping them make evidence-based decisions about the most sustainable and cost-effective forms of urban development. Future research should also focus on financing mechanisms that can support the development of net-zero energy buildings and climate-resilient urban infrastructure.

5.6. Broader Policy Implications

The findings of this study hold meaningful implications for urban policy and development strategies, particularly in seismic-prone regions and areas pursuing long-term sustainability goals. Importantly, the policy recommendations outlined here are not based solely on structural modeling; instead, they emerge from a comprehensive synthesis of economic analysis, environmental assessment, and sociological evidence. Based on this integrated perspective, the following recommendations are proposed:

1. Seismic Safety and Urban Design: In suitable contexts—particularly seismic-prone regions where land availability allows—policymakers may consider prioritizing low-rise developments to reduce long-term seismic risk. Enhancing safety also requires stricter enforcement of building codes for high-rise structures, including mandatory seismic retrofitting for older buildings that were constructed under outdated standards. Incentive programs that support the development of low-rise, seismically resilient buildings could be especially effective in areas with moderate land acquisition costs, where horizontal expansion is more feasible.

2. Economic Incentives for Low-Rise Developments: Municipalities should offer tax incentives or subsidies for developers who prioritize low-rise, energy-efficient buildings. These developments provide long-term economic benefits by reducing maintenance and operational costs for both private developers and public services. Furthermore, policies should promote affordable housing in low-rise neighborhoods to enhance social equity and urban resilience.

3. Social Infrastructure in High-Rise Buildings: To mitigate the social isolation and mental health challenges associated with high-rise living, urban planners should consider designing buildings that integrate communal spaces, green areas, and recreational facilities. Policies should require the inclusion of these features in new high-rise developments, ensuring that residents have access to social infrastructure that supports community interaction and well-being. Retrofitting existing high-rise buildings with green spaces and social amenities could also be a cost-effective way to improve the quality of life for residents in dense urban areas.

4. Environmental Sustainability and Green Building Codes: Governments are encouraged to adopt enhanced green building standards that incorporate lifecycle carbon assessments and promote the use of sustainable materials in both high-rise and low-rise construction. Economic instruments such as carbon pricing or targeted taxes on high-emission materials—like steel and concrete—can incentivize a shift toward low-carbon construction practices. Additionally, financial support for net-zero energy buildings, including subsidies or tax credits for integrating renewable energy systems such as solar panels and wind turbines, could accelerate the adoption of environmentally responsible building solutions.

5. Climate-Resilient Urban Design: As climate change increases the frequency of extreme weather events, cities must invest in climate-resilient infrastructure. This includes flood defenses, urban cooling strategies, and renewable energy systems that can withstand the impacts of climate change. Both high-rise and low-rise buildings should be designed with climate adaptation in mind, incorporating flood-resistant foundations, permeable surfaces, and green roofs to reduce the urban heat island effect. Policymakers should also explore opportunities for public-private partnerships to fund the development of climate-resilient infrastructure in both new and existing urban areas.

6. Conclusion

This study offers a detailed, context-sensitive comparison of high-rise and low-rise buildings, addressing their relative strengths and limitations in terms of seismic performance, economic sustainability, social and psychological well-being, and environmental impact. The

findings underscore the necessity of adopting a multidisciplinary approach to urban development, integrating insights from engineering, economics, social sciences, and environmental studies to guide future policy and planning decisions.

Seismic Performance and Resilience

In earthquake-prone regions like Türkiye, the seismic resilience of buildings is paramount. This study confirms that low-rise buildings—defined in TBDY-2018 as structures under 15 stories or 60 meters—exhibit more favorable seismic response characteristics due to their simpler geometry and lower mass. These attributes enable more effective distribution of seismic forces, resulting in reduced inter-story drift and base shear, which are key indicators of structural stability. Accordingly, low-rise developments may offer strategic advantages in regions where horizontal expansion is feasible.

In contrast, high-rise buildings face inherently greater seismic challenges due to their height, flexibility, and complex load paths. Although modern seismic engineering techniques—such as tuned mass dampers and base isolators—have significantly improved the performance of new tall buildings, these technologies are not always feasible for retrofitting older structures, especially in dense urban settings. The 2023 Kahramanmaraş earthquake highlighted the need for enhanced seismic retrofitting, particularly for buildings constructed before current codes were enacted [37].

The seismic modeling presented in this study was conducted within typology-specific analytical boundaries, in line with TBDY-2018 requirements. High-rise buildings were analyzed using nonlinear dynamic methods, while low-rise structures followed equivalent static procedures. As such, the results are not used for direct performance ranking but to illustrate expected behavior patterns within each category under controlled conditions.

Urban planners may consider encouraging low-rise development in areas where land use and seismic risk allow, without disregarding the functional necessity of high-rise construction in dense metropolitan areas. The emphasis, therefore, should be on strict code compliance, context-sensitive design, and the systematic retrofitting of existing building stock to enhance overall urban resilience.

Economic Sustainability

The economic analysis conducted in this study illustrates that low-rise buildings are more cost-effective over their lifecycle. Life Cycle Cost Analysis (LCCA) and Net Present Value (NPV) calculations reveal that low-rise developments have lower construction and operational costs due to their simpler design and use of less energy-intensive materials. For instance, low-rise buildings tend to have 20-25% higher NPV over a 50-year period compared to high-rise structures, making them more financially viable in the long run.

In contrast, high-rise buildings require significant upfront investments in specialized materials such as reinforced concrete and steel, along with complex mechanical systems like elevators, HVAC, and fire suppression systems. These systems, while necessary for vertical development, increase both the initial construction costs and long-term maintenance expenses. Additionally, operational costs for high-rise buildings tend to escalate over time, as advanced systems require frequent maintenance and upgrades [14]. For example, annual maintenance cost increases for high-rise buildings range from 5-7%, higher than the 2-3% for low-rise developments.

This creates financial challenges not only for developers but also for municipalities, which bear the brunt of maintaining the infrastructure needed to support high-rise living. Emergency services, utility maintenance, and fire safety measures are more costly and complex for high-rise buildings, placing an additional strain on public resources. As cities continue to grow vertically, the long-term financial sustainability of high-rise developments may present challenges—particularly in areas where vertical density is not a pressing necessity or where land acquisition costs remain moderate.

Urban planners should take these long-term financial implications into account when considering new developments. Developing low-rise, mixed-use neighborhoods in areas with moderate land costs offers a more sustainable economic model than high-rise construction. These developments require lower maintenance and infrastructure costs, benefiting both private investors and municipalities.

Social and Psychological Well-Being

The social and psychological impacts of building design are often overlooked in urban planning, but they are critical for fostering livable communities. Survey data from Istanbul and Ankara reveal that residents of high-rise buildings experience higher levels of social isolation, stress, and anxiety compared to those in low-rise environments. Limited communal spaces and reduced neighborly interaction contribute to these challenges. The lack of communal spaces in many high-rise buildings, combined with limited opportunities for neighborly interaction, contributes to a sense of anonymity and disconnection. Surveys from cities like Istanbul and Ankara show that nearly 45% of high-rise residents report feelings of isolation, compared to just 18% in low-rise communities [15].

On the other hand, low-rise developments promote stronger social cohesion through the availability of shared green spaces, courtyards, and community centers. These features encourage frequent social interaction, which enhances mental well-being and helps build social capital—a critical asset during times of crisis. Studies in urban resilience suggest that neighborhoods with high levels of social cohesion are better equipped to recover from disasters such as earthquakes and public health emergencies, as residents are more likely to provide mutual support [18].

The findings highlight the need for urban planners to incorporate social infrastructure into high-rise developments. Designing buildings with communal areas, recreational spaces, and green areas can help mitigate the negative social and psychological effects of vertical living. Additionally, retrofitting older high-rise buildings to include more communal facilities could improve the quality of life for residents and foster greater community engagement.

Environmental Impact and Sustainability

In the modeled scenarios, low-rise buildings demonstrate environmental performance advantages, particularly in operational energy use and material emissions. Life Cycle Assessments (LCA) indicate that low-rise buildings generate 25-30% lower CO_2 emissions over their lifespan. This is due to their use of sustainable materials like cross-laminated timber (CLT) and energy-efficient designs that support natural ventilation and solar energy integration. These features make low-rise buildings better suited to meet net-zero energy targets.

In contrast, high-rise buildings are responsible for 30-35% more CO_2 emissions due to the extensive use of energy-intensive materials like steel and concrete, as well as the increased energy demands of elevators, HVAC systems, and other infrastructure required for vertical living [33]. High-rise developments remain essential in dense urban cores, but they require targeted green interventions to mitigate environmental load. Moving forward, the integration of energy-efficient technologies—such as solar panels, wind turbines, and smart building systems—will be critical to reducing the carbon footprint of vertical development.

To support this transition, governments must implement green building regulations that require developers to conduct lifecycle carbon assessments for new projects. Financial incentives for using low-carbon construction materials and integrating renewable energy systems will be crucial in reducing the overall environmental impact of urban development. Retrofitting existing high-rise buildings with green technologies could also help offset their long-term carbon emissions, making them more compatible with global sustainability goals.

Policy Implications and Future Directions

This study outlines key policy directions aimed at enhancing seismic resilience, economic sustainability, environmental responsibility, and social well-being within the context of urban development. The implementation of targeted regulations and incentive-based frameworks may offer a balanced approach to addressing the challenges associated with high-rise construction, while fostering more resilient and adaptive urban growth trajectories.

1. Seismic Safety: In regions prone to earthquakes, low-rise developments may be prioritized in areas where land availability and seismic risk align. At the same time, the enforcement of stricter seismic building codes remains essential for both new and existing structures, regardless of typology. Seismic retrofitting programs for older high-rise buildings may be incentivized through tax breaks or subsidies to improve overall urban resilience.

2. Economic Incentives: Policymakers should encourage the development of low-rise, mixed-use neighborhoods by offering tax incentives or development grants for projects that incorporate sustainable materials and energy-efficient designs. These neighborhoods can offer long-term financial and social benefits, while reducing the maintenance burden on public infrastructure.

3. Social Infrastructure: To mitigate the social isolation associated with high-rise living, new developments must include communal spaces, green areas, and recreational facilities. These features may be recommended as part of urban planning guidelines for all future high-rise projects, with retrofitting initiatives for older buildings to improve community well-being.

4. Environmental Regulations: Governments are encouraged to adopt enhanced green building standards that prioritize the use of low-carbon materials and energy-efficient technologies. Policies that promote net-zero energy buildings and incentivize renewable energy systems will be essential in meeting global climate targets.

While individual studies have addressed specific aspects such as social isolation, mental health, seismic resilience, or environmental sustainability, comprehensive studies that integrate all these factors—as this paper does—are relatively rare, especially in the context of Türkiye.

This research fills a significant gap by providing a holistic comparison of high-rise and low-rise buildings, considering the intertwined effects of seismic vulnerability, economic factors, environmental impact, and, importantly, psychological and social well-being.

The interlinked findings across seismic, economic, environmental, psychological, and sociological dimensions present a strong case for prioritizing low-rise buildings, particularly in regions with high seismic risk and available land. Low-rise structures offer enhanced seismic resilience, economic benefits through lower costs and higher long-term value, reduced environmental impact, and improved psychological and social well-being for residents.

Urban planning and policy decisions should consider these interconnected factors to promote sustainable and resilient cities. By encouraging low-rise developments that incorporate sustainable materials, energy-efficient designs, and communal spaces, Türkiye can work toward addressing seismic risks, reducing environmental degradation, enhancing economic sustainability, and fostering cohesive communities.

This study underscores the need for an integrated approach to urban development that balances structural safety, economic feasibility, environmental impact, and social well-being. By adopting evidence-based planning strategies, cities can create resilient, sustainable, and livable environments. Adopting such an integrated

perspective will contribute to the creation of urban environments that are not only structurally sound and economically viable but also environmentally responsible and socially enriching. While these findings offer valuable comparative insights, further region-specific analyses and long-term empirical studies are recommended to inform localized urban planning strategies.

7. References

[1] O. Hansu and A. Oğuz, "Seismic Risk, Structural Vulnerabilities, and Retrofitting Solutions: Lessons from the 2023 Kahramanmaraş Earthquake," *Osmaniye Korkut Ata University Journal of The Institute of Science and Technology*, vol. 8, no. 3, pp. 1427–1452, 2025. [Online]. Available: https://doi.org/10.47495/okufbed.1573919

[2] AFAD (Disaster and Emergency Management Authority), "2023 Kahramanmaraş earthquake report," Disaster and Emergency Management Authority (AFAD), Türkiye, 2023. [Online]. Available: https://www.afad.gov.tr.

[3] T. Okada, "Development and present status of seismic evaluation and seismic retrofit of existing reinforced concrete buildings in Japan," *Proc. Japan Acad. Ser. B, Phys. Biol. Sci.*, vol. 97, no. 10, 2021. [Online]. Available: https://doi.org/10.2183/pjab.97.021.

[4] R. Kant and M. S. Thakur, "Study on seismic performance of reinforced concrete high-rise building with buckling restrained braces dissipation devices," *E3S Web Conf.*, 2024. [Online]. Available: https://doi.org/10.1051/e3sconf/202450503001.

[5] X. Wu and D. Lin, "Seismic assessment of high-rise buildings through dynamic nonlinear analysis," *Ann. Geophys.*, 2022. [Online]. Available: https://doi.org/10.4401/ag-8770.

[6] M. Benek and S. Aktan, "Seismic risk evaluation of existing reinforced concrete buildings: A case study for Çanakkale-Türkiye," *J. Adv. Res. Nat. Appl. Sci.*, 2024. [Online]. Available: https://doi.org/10.28979/jarnas.1467032.

[7] X. Zhang and H. Far, "Beneficial and detrimental impacts of soil-structure interaction on seismic response of high-rise buildings," *Adv. Struct. Eng.*, 2024. [Online]. Available: https://doi.org/10.1177/13694332241255747.

[8] United Nations Environment Programme (UNEP), "2021 Global Status Report for Buildings and Construction: Towards a zero-emission, efficient, and resilient buildings sector," UNEP, 2021. [Online]. Available: https://www.unep.org/resources/report/2021-global-status-report-buildings-and-construction.

[9] A. Oğuz and O. Hansu, "Disaster Governance and Recovery Efficiency in Türkiye and Japan: A Comparative Analysis of Post-Earthquake Reconstruction," SETSCI Conference Proceedings, vol. 23, pp. 126–134, 2025. [Online]. Available: https://doi.org/10.36287/setsci.23.56.001.

[10] Kandilli Observatory, "Seismic activity and building vulnerability in Türkiye," Bogazici University, Kandilli Observatory and Earthquake Research Institute, 2021. [Online]. Available: https://www.koeri.boun.edu.tr.

[11] R. W. Wassmer, "Do higher land costs for new single-family housing inhibit economic activity in U.S. metropolitan areas?" *Econ. Dev. Q.*, vol. 35, no. 4, pp. 325–337, 2021. [Online]. Available: https://doi.org/10.1177/08912424211006174.

[12] M. Damlakhi, "Evaluation of low-rise neighborhoods and high-rise neighborhoods in the context of new urbanism," *Soc. Sci. Dev. J.*, 2022. [Online]. Available: https://doi.org/10.31567/ssd.551.

[13] World Bank, *Lifelines: The Resilient Infrastructure Opportunity*. World Bank, 2019. [Online]. Available: https://www.worldbank.org/en/news/infographic/2019/06/17/lifelines-the-resilient-infrastructure-opportunity.

[14] Turkish Statistical Institute (TÜİK), "Construction cost index, December 2024," Turkish Statistical Institute, 2024. [Online]. Available: https://data.tuik.gov.tr/en.

[15] Z. Kan, M. Kwan, M. Ng, and H. Tieben, "The impacts of housing characteristics and built-environment features on mental health," *Int. J. Environ. Res. Public Health*, vol. 19, no. 5, 2022. [Online]. Available: https://doi.org/10.3390/ijerph19095143.

[16] S. Kalantari and M. Shepley, "Psychological and social impacts of high-rise buildings: A review of the post-occupancy evaluation literature," *Hous. Stud.*, vol. 36, no. 7, pp. 1147–1176, 2020. [Online]. Available: https://doi.org/10.1080/02673037.2020.1752630.

[17] World Health Organization, "Social isolation and loneliness among older people: Advocacy brief," WHO, 2021. [Online]. Available: https://www.who.int/publications/i/item/9789240030749.

[18] N. Nzimande and F. Morris-Kolawole, "Does size really matter for the place attachment of high-rise and low-rise housing estates? A Budapest case study," *Sustainability*, 2024. [Online]. Available: https://doi.org/10.3390/su16031195.

[19] World Health Organization, *Depression and Other Common Mental Disorders: Global Health Estimates*. WHO, 2017. [Online]. Available: https://www.who.int/publications/i/item/depression-global-health-estimates.

[20] A. Oğuz and O. Hansu, "Climate-Adaptive Modular Micro-Living for Urban Regeneration: A Passive Design and Low-Carbon Construction Framework," SETSCI Conference Proceedings, vol. 23, pp. 149–154, 2025. [Online]. Available: https://doi.org/10.36287/setsci.23.62.001.

[21] AFAD (Disaster and Emergency Management Authority), "Türkiye Bina Deprem Yönetmeliği (TBDY-2018)," T.C. İçişleri Bakanlığı Afet ve Acil Durum Yönetimi Başkanlığı, Ankara, 2018. [Online]. Available: https://www.resmigazete.gov.tr/eskiler/2018/03/20180318M1-2.htm.

[22] International Code Council, "2018 International Building Code (IBC)," 2018. [Online]. Available: https://codes.iccsafe.org/content/IBC2018/chapter-2-definitions.

[23] Rockpanel, "High-rise buildings and fire safety," 2023. [Online]. Available: https://www.rockpanel.co.uk/product-benefits/firesafety/high-rise-buildings.

[24] R. Gifford, "The consequences of living in high-rise buildings," *Architectural Science Review*, vol. 50, no. 1, pp.

2–17, 2007. [Online]. Available: https://doi.org/10.3763/asre.2007.5002.

[25] H. Lee, "Psychological characteristics of high-rise residents," *International Journal of Sustainable Building Technology and Urban Development*, vol. 5, no. 1, pp. 10–20, 2014. [Online]. Available: https://doi.org/10.1080/2093761X.2014.876905.

[26] L. Jing, "Environmental impact of two types of residential building," *Urban Environment & Urban Ecology*, 2003.

[27] W. Xu, C. Jimenez-Bescos, and J. K. Calautit, "Evaluating the impact of neighbouring structures on a high-rise residential block's performance," *Building Simulation Conference Proceedings*, 2021. [Online]. Available: https://doi.org/10.26868/25222708.2021.30210.

[28] R. Rambabu, "Base isolation and energy dissipating system in earthquake resistant building design," *CVR J. Sci. Technol.*, 2024. [Online]. Available: https://doi.org/10.32377/cvrjst2603.

[29] M. R. B. Karimi and M. C. Geneş, "Optimized values for lead core rubber bearings for minimum response quantities," in *Proc. 6th Int. Conf. Civil Eng., Archit. Urban Planning Elites*, 2023. [Online]. Available: https://doi.org/10.33422/6th.caueconf.2023.08.10.

[30] M. Noureldin and J. Kim, "Simplified life cycle cost estimation of low-rise steel buildings using fundamental period," *Sustainability*, vol. 15, no. 3, 2023. [Online]. Available: https://doi.org/10.3390/su15032706.

[31] N. Ding, T. Chen, Y. Zhu, and Y. Lu, "State-of-the-art high-rise building emergency evacuation behavior," *Physica A: Stat. Mech. Appl.*, vol. 561, 2021. [Online]. Available: https://doi.org/10.1016/j.physa.2020.125168.

[32] L. Ma, R. Azari, and M. Elnimeiri, "A building information modeling-based life cycle assessment of the embodied carbon and environmental impacts of high-rise building structures: A case study," *Sustainability*, 2024. [Online]. Available: https://doi.org/10.3390/su16020569.

[33] International Energy Agency (IEA), "High-rise refurbishment," IEA Reports, 2022. [Online]. Available: https://www.iea.org/reports/high-rise-refurbishment.

[34] M. Sarcheshmehpour and H. Estekanchi, "Life cycle cost optimization of earthquake-resistant steel framed tube tall buildings," *Structures*, vol. 30, pp. 585–601, 2021. [Online]. Available: https://doi.org/10.1016/j.istruc.2021.01.038.

[35] United Nations Environment Programme (UNEP), "2022 Global Status Report for Buildings and Construction," UNEP, 2022. [Online]. Available: https://www.unep.org/resources/publication/2022-global-status-report-buildings-and-construction.

[36] United States Geological Survey (USGS), "Urban seismic hazards," USGS, 2023. [Online]. Available: https://www.usgs.gov/programs/earthquake-hazards/science/urban-seismic-hazards.

[37] The Global Footprint Network, "Ecological footprint of urban buildings," Global Footprint Network, 2022. [Online]. Available: https://www.footprintnetwork.org.

[38] A. K. Chopra, *Dynamics of Structures: Theory and Applications to Earthquake Engineering*. Englewood Cliffs, NJ, USA: Prentice Hall, 2012.

[39] *Eurocode 8: Design of Structures for Earthquake Resistance—Part 1: General Rules, Seismic Actions, and Rules for Buildings,* European Committee for Standardization, 2004.

[40] E. Budak, H. Sucuoglu, and O. Celik, "Response parameters that control the service, safety, and collapse performances of a 253 m tall concrete core wall building in Istanbul," *Bull. Earthq. Eng.*, vol. 21, no. 1, 2022. [Online]. Available: https://doi.org/10.1007/s10518-022-01527-4.

[41] F. Shadram and J. Mukkavaara, "Improving life cycle sustainability and profitability of buildings through optimization: A case study," *Buildings*, vol. 12, no. 4, 2022. [Online]. Available: https://doi.org/10.3390/buildings12040497.

[42] B. R. Viswalekshmi and D. Bendi, "A comprehensive model for quantifying construction waste in high-rise buildings in India," *Waste Manage. Res.*, 2023. [Online]. Available: https://doi.org/10.1177/0734242X231178227.

[43] UN-Habitat, *Enhancing Urban Safety and Security: Global Report on Human Settlements 2007*. UN-Habitat, 2007. [Online]. Available: https://unhabitat.org/sites/default/files/2020/09/grhs.2007.6.pdf.

[44] P. T. Thoi, T. H. Nguyen, and E. Harms, "Spaces of social capital across pandemic time: COVID-19 responses in Ho Chi Minh City's high-rise and low-rise neighborhoods," *City & Community*, 2023. [Online]. Available: https://doi.org/10.1177/15356841231198458.

[45] W. Dawood, M. Nazim, O. El-Mahdy, and M. Adam, "Soil-structure interaction assessment for seismic performance of high-rise RC building on piled-raft foundation," *Eng. Res. J. (Shoubra)*, 2024. [Online]. Available: https://doi.org/10.21608/erjsh.2024.263591.1274.

[46] K. Lai, C. Sarkar, S. Kumari, M. Y. Ni, J. D. Gallacher, and C. Webster, "Calculating a national anomie density ratio: Measuring the patterns of loneliness and social isolation across the UK's residential density gradient using results from the UK Biobank study," *Landsc. Urban Plan.*, vol. 215, 2021. [Online]. Available: https://doi.org/10.1016/j.landurbplan.2021.104194.

[47] World Green Building Council (WorldGBC), "Advancing net zero status report 2021," WorldGBC, 2021. [Online]. Available: https://worldgbc.org/article/worldgbc-details-built-environment-progress-to-achieving-net-zero-in-latest-report/.

Dicle University
Journal of Engineering
https://dergipark.org.tr/tr/pub/dumf
duje.dicle.edu.tr

Research Article

AI-driven anomaly detection for fraud prevention in project monitoring

Mehmet Tahir SANDIKKAYA[1*], Onur Behzat TOKDEMİR[2, 3]

[1] Istanbul Technical University, Department of Computer Engineering, sandikkaya@itu.edu.tr, Orcid No: 0000-0002-9756-603X
[2] Istanbul Technical University, Department of Civil Engineering, otokdemir@itu.edu.tr, Orcid No: 0000-0002-4101-8560
[3] Istanbul Technical University, AI Center, otokdemir@itu.edu.tr, Orcid No: 0000-0002-4101-8560

ARTICLE INFO

Article history:

Received 13 March 2025
Received in revised form 26 October 2025
Accepted 29 October 2025
Available online 30 December 2025

Keywords:

Cybersecurity, Anomaly Detection, Data Poisoning Attacks, Fraudulent Reporting Detection, Insider Threat Detection, Project Management

Doi: : 10.24012/dumf.1656802

* Corresponding author

ABSTRACT

Accurate tracking of project progress is crucial for timely delivery, cost control, and fraud prevention. Issues in progress reporting, whether due to real mistakes, employee inefficiencies, or internal threats, present considerable risks to major projects. This study aims to examine statistical and machine learning techniques to identify data inconsistencies, fraudulent reporting, and other anomalies in project tracking. Utilizing a dataset of 118 weekly snapshots, including genuine and tainted data, this research assesses the effectiveness of the interquartile range, isolation forest, and an ensemble approach in detecting anomalies. The results underscore the strengths and weaknesses of statistical and machine learning models while proposing an optimal detection framework for effective project management.

Introduction

Large-scale construction projects require thorough coordination from several workflows involving numerous subcontractors and vast data reports [1–3]. Proper progress monitoring is important, as both accidental and intentional discrepancies as well as weak reporting, require workarounds and adjustments that lead to delays, increase likelihood of going over budget, and cause conflicts over contracts. Traditional project management tools like Critical Path Method (CPM) and Program Evaluation and Review Technique (PERT) are effective for scheduling; however, they lack real-time fraud detection and anomaly identification capabilities. The benefits of anomaly detection are often ignored in between numerous tasks to be accomplished by limited technical man-hours. This study examines the use of statistical approaches and machine learning algorithms for anomaly detection in construction project management and their use for decision support systems.

Machine learning (ML) methods have been increasingly used for construction progress monitoring and control [4, 5]. The construction industry can benefit if anomalies can be detected and addressed early in large projects and tight timeframes. The construction industry suffers from anomalies like demurrage, breaches, misappropriation of resources, and unintentional data breaches. Making conscious performance decisions via ML methods in projects make project stakeholders more risk-free.

Traditional methods for monitoring construction progress rely on manual inspections, analysis of past data, and auxiliary rule-based systems. These approaches have varying degrees of success, but generally lag behind the complexity and variability associated with mega construction projects. These widely applied techniques include CPM and PERT. Hybrid techniques are more adaptive in construction [6] while predictive features are mostly missing. However, these techniques are often lengthy, error-prone and cannot handle uncertainties. Moreover, classical methods might overlook hints, which, could be an early indicator of the emergence of anomalous behavior [7].

ML, therefore, is promising in monitoring progress in construction by providing automated, data-driven solutions. Supervised and unsupervised learning algorithms have a long history of successfully identifying anomalies in data. Anomaly detection can be more accurate if supervised models such as decision trees, random forests, and SVMs on labeled data are utilized. They are trained on past data to

learn normal behavior, and then can identify deviations from the learned behaviors as anomalies [8, 9]. Some studies that utilize random forest have been used to create dashboards to predict the construction delay, and their recall values reached above 90% in some cases [9]. However, accessing project-specific data history where the number of normal instances is large enough to correctly identify anomalies is far from a practical reality.

Algorithms like autoencoders and K-means clustering are used under unsupervised learning, a standard approach to locating outliers. Autoencoders have attracted attention for investigating complex and high-dimensional data in construction. They are able to recover when they encounter small but significant outliers, i.e., anomalous or rare events in the data set featuring an increased activity in the transaction rate in the project, in addition to the addition of non-viable project timelines to the data set [10]. Another example is the one where K-means clustering is used to find out the major risk factors that contribute to the delay of construction processes, which aids the risk-management process [11].

Many other works propose case studies of using ML for fault detection to enhance construction progress tracking. For example, the use of autoencoder neural networks in identifying irregular investment trends and project durations in the Kuwait Construction Market demonstrates the deviations from typical market activities that lead to additional cost [10]. The predictive analysis utilizing ML algorithms has achieved wide acceptance for designating potential VOs and issuing early alerts such that construction delays can be avoided [9]. Such applications demonstrate the merits of ML in streamlining operations and defining more effective temporary organizational structures.

The integration of ML in construction progress monitoring provides numerous benefits. Especially in construction projects where early detection of anomalies can save time and reduce costs, ML can process extensive datasets quickly and accurately, identifying anomalies and patterns that may be missed by traditional techniques [7]. In addition, ML models can learn iteratively, which means that ML models can adapt their learning in response to changes during the project, therefore increasing their predictive accuracy over time [12]. Predicting delays and cost overages with machine learning models [13] allows project managers and stakeholders to prevent and react to possible complaints early on. It is an advantage in complex infrastructural projects where it is critical to avoid any delays. This might greatly impact the timings and project costs [14]. Machine Learning also enables effective resource allocation and scheduling, which ensures the end project delivery on time while sticking to the budget [7].

The existing anomaly detection methods cannot directly embrace the natural progress of the stages of a construction project. From a project management perspective, each stage is tied either loosely or tightly to previous stages; the progress of a stage has a warm-up, peak, and tailing time, and the progress might get stuck occasionally. To be able to handle these, the data from progress reports are preprocessed to reveal if the sane and natural expectations of any progress (e.g., the amount of reinforced concrete and reinforcement used have to be proportional to the design documents) are met.

This study evaluates the ability of statistical and ML-based techniques to identify anomalies in construction progress tracking. This research uses 118 weekly dataset snapshots with artificially introduced anomalies to mimic fraudulent reporting and insider threats. IQR, isolation forest, and an ensemble method were compared to evaluate their performance. This reinforces the conclusion that proposed approaches outperform standard methods in terms of accuracy and ease of adaptation and provide a more robust framework for anomaly detection. Such insights also shed light on the merits of integrating these ideas into project management software solutions, in a manner to promote visibility and reduce exposure to data manipulation risks that can plague large construction projects.

The examination is conducted systematically, incorporating data collection, preprocessing, anomaly detection, and evaluation (Figure 1). By utilizing this structured framework, we can methodically identify inconsistencies that might be used to qualitatively compare traditional statistical analysis methods with more advanced ML-based methods.

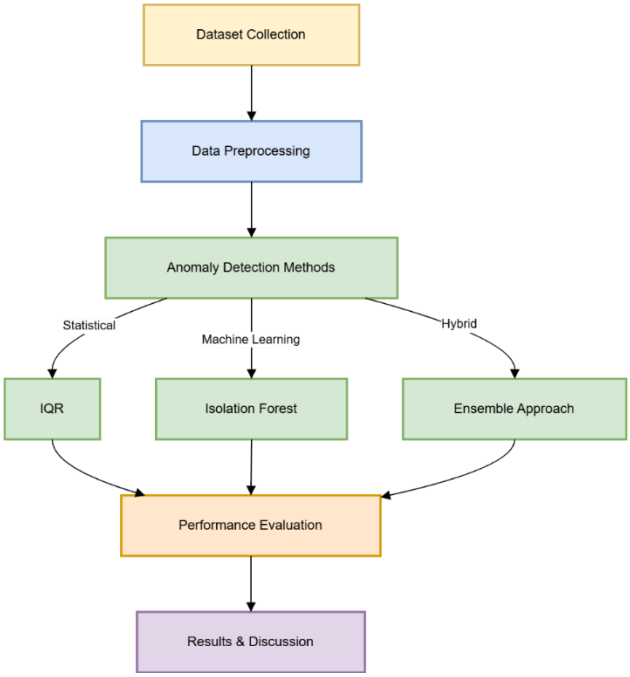

Figure 1 Methodology of the study

Related Work

The construction industry is adopting the digital transformation, emphasizing Industry 4.0, and is increasingly critical in implementing cybersecurity measures against insider threats or intrusions on construction sites and mega projects. However, this shift has incorporated digital technologies, exposing construction sites to risks. Comprehensive cybersecurity spans multiple strategies and technologies. A key aspect of

this approach is creating a cyber risk assessment framework leveraging machine learning methodologies, enabling continuous monitoring and updates for scenario parameters to undertake proactive risk mitigation tailored to industry-relevant specifications [15]. Moreover, the collaboration of cyber-physical systems (CPSs) improves the resilience and authenticity of the smart building initiatives, helping with real-time data gathering, tracking, and appropriate risk assessment and decision-making [16]. RFID-based systems for intrusion detection enable real-time monitoring and alerts of unauthorized entry into restricted areas, enhancing safety and efficiency on construction sites [17].

In addition, the high precision of potential hazard identification and safety improvement of computer vision and 4D Building Information Modeling (BIM)-based spatio-temporal analysis are applied to intrusion detection in hazardous areas [18]. The construction industry can also learn from critical infrastructure protection efforts and use well-established processes to promote better cybersecurity practices [19]. In addition, data security and privacy management can safeguard sensitive data against unauthorized access and attacks, maximizing risk assessment and resource allocation [20]. Using a vulnerability assessment framework based on the common vulnerability scoring system (CVSS) to identify and address vulnerabilities in autonomous site monitoring systems before deploying cyber-physical systems on-site enables decision-makers to prioritize critical metrics [21]. These steps help ensure a safer construction site while minimizing digitization risk, making buildings safer and more efficient.

Few machine learning techniques have acted as catalysts for anomaly detection to the forefront of cybersecurity, i.e., isolation forest, one-class SVM, autoencoders, Gaussian mixture model (GMM), and interquartile range (IQR). As an unsupervised learning approach, isolation forest identifies steep changes tied to cyberattacks with high accuracy and few false positives in the smart grid cybersecurity domain [22]. It has also demonstrated strong web traffic anomaly detection results with high precision and recall [23, 24]. One-class SVM is another unsupervised model that can help detect smooth changes and general clustering, but is less effective for catching abrupt anomalous events [22].

These deep learning techniques through autoencoders enable handling very complex and multidimensional data, thereby creating a stable framework to manage the anomaly detection process in dynamic environments like cybersecurity, removing false positives, and significantly improving the detection process [25, 26]. Statistical GMM-based outlier detection is used by modeling the typical behavior of the system that could serve as a pattern to detect the cyber threats [25]. A well-known statistical method for outlier identification is the Interquartile Range, which gives the spread of the middle 50% of data. But it struggles in more complex, high-dimensional cybersecurity data scenarios.

Integrating these models into cybersecurity paradigms has proven to enhance detection rates, reduce false positives, accelerate response times, and improve the overall efficiency of the framework in comparison to legacy rule-based systems [26]. When appropriately tailored to specific new cybersecurity applications, they can provide robust and tunable protection against sophisticated intrusions, showing the importance of model selection and tuning in practical use cases [27, 28].

Helping to prevent fake reporting and discrepancies in data, project delays, workforce allocation, and false progress reporting in large-scale construction projects using advanced technologies and methodologies. The Kuwait construction market was analyzed by autoencoder neural networks, which provide a generic approach in that they train historical data to learn common patterns, so that deviations from normal patterns can be detected that could indicate inefficiency or fraudulent behavior [10].

Another study proposes rule-based forward chaining-based techniques and states that the techniques have improved the systems for project monitoring, thereby optimizing fraud detection and control mechanisms, which were left unaddressed mainly by traditional project management software, which utilized planning and scheduling to gain control over the project [29]. As such, Computer Vision and Internet of Things (IoT) systems for automated construction progress monitoring present a potential route for real-time data collection and processing to reduce divergences between anticipated and actual progress and avoid delays and budget overruns [30, 31].

Another study [32] argues that advancements in statistical pattern recognition techniques allow for the classification of the construction activity monitoring model based on multiple scenarios that may arise. This is particularly crucial given the apparent information technology usage gap in the construction industry, as information technology has shown promising potential in its application to progress measurement, with potential for automation of progress information generation, making it timelier with respect to decision making and mitigation of risk in fraud, and ultimately enhancing project control [33]. Incorporating these new analytical frameworks and technology can create a better strategy, improve efficiency, and detect fraud in mega construction projects.

Relevant studies specific to financial fraud detection in the construction domain include many perspectives. Most of the time, these studies focus on embracing the root of the fraudulent activity, then preventing it. A study that incorporates a questionnaire to model the influence factors on external financial auditors, so that more accurate and independent audits could be possible [34]. Another study, which also conducts a questionnaire with the experts, focuses on the protection of the project data [35]. The study compiles best practices for security against external threats that could be conducted in the organization. Another study, which expands fraudulent data manipulation beyond the construction domain, utilizes Bayesian Nash Equilibrium to predict better strategies to protect data [36]. The study considers not only outsiders but also misuse or insider

attacks. In contrast to those, the proposed approach focuses on the detection of the fraudulent reporting of project data.

Methodology and Dataset

A large-scale construction project dataset was analyzed over 193 weeks, with reliable data available from the 62nd week onward. At the beginning of the project, the project suffered from budget-related issues and could not progress as planned. Therefore, the dataset consists of 118 healthy weekly snapshots, covering planned, acquired, and realized progress metrics for over 350 tasks. These tasks were categorized into six major groups: concrete works, electrical works, finishing works, façade, mechanical works, and insulation. Additionally, the total progress is included.

Planned progress stands for the expected completion percentage based on the project schedule, acquired progress stands for the self-reported completion percentage provided by subcontractors or project managers, and realized progress stands for the validated completion percentage after independent verification.

The six categories of tasks include:

- Concrete Works: Foundations, structural elements, and reinforced concrete components.
- Electrical Works: Power distribution, panel installations, and wiring.
- Finishing Works: Interior detailing, painting, tiling, and carpentry.
- Façade: Cladding, external insulation, and waterproofing.
- Mechanical Work: Heating, ventilation, and air conditioning (HVAC) systems, plumbing, and mechanical piping.
- Insulation: Thermal and acoustic insulation layers.

Even though the original dataset includes higher resolution data, progress tracking at weekly intervals was selected to tradeoff between data granularity and computation load. Daily tracking would result in too much noise that could prevent meaningful outlier detection, while monthly tracking might average out abnormal patterns. So that, it could be too late to prevent project delays. By processing the data points weekly, we can quickly compare the progress of our anomalies while maintaining a helpful anomaly detection framework. The proposed methods are applied to the cleaned and preprocessed dataset. This preprocessing step was required to increase the robustness of statistical and ML-based anomaly detection. Figure 2 plots the total acquired value per week in each major group to sketch a sample from the dataset.

As there were no recorded fraudulent activities in the dataset, a simulation approach is taken: a practical, real-world, adversarial, data poisoning attack. The poisoned data is injected into the dataset to assess the robustness of relevant anomaly detection. This attack consisted of seven manipulated snapshots, each of which was carefully designed to insert anomalies that would only be latent in a typical project management system. Six of these snapshots were manipulated so that only a single task group was affected, which simulated slightly deceitful acts or system-wide inconsistencies that could occur due to purposeful falsification or human error during data entry. The seventh snapshot, however, was constructed to be more aggressive, changing all task groups at once to mimic massive reporting fraud or a systemic failure in project monitoring.

For visual comparison, the same data in Figure 2 after insider modification is sketched in Figure 3. One can notice that the difference is faint and could hardly be noticed by the naked eye.

This approach indicates that the statistical and ML models could differentiate between the actual project variance and the artifacts added afterwards. The situations in practice at a construction site can cause anomalies such as fraudulent reporting, mismanagement, or even cyber threats. This study aims to achieve an integrated evaluation of the practical and useful anomaly detection methods by integrating localized data manipulations. The proposed method is evaluated whether the automated systems can identify unusual behaviors by determining whether the variations are irrelevant or indicative of a fraud.

Statistical approach: interquartile range (IQR)

The interquartile range is a statistical method used to detect anomalies by identifying values that deviate significantly from the mean of a distribution. IQR detects outliers in numerical data. Therefore, it is appropriate to identify progress deviations in construction reporting. The IQR works as follows:

The first and third quartiles $(Q1, Q3)$ are computed. They represent 25th and 75th percentiles of the values, where they are the lower and upper boundaries of normal values. Then, the IQR is calculated based on the difference between the first and third quartiles as $IQR = Q3 - Q1$. Any value outside the range is determined as outliers after the boundaries are defined as follows:

$$Lower\ Bound = Q1 - (k \times IQR)$$

$$Upper\ Bound = Q3 + (k \times IQR)$$

k is a scaling factor that sets the sensitivity of outlier detection. Even though the typical value of $k = 1.5$, the natural fluctuations of construction projects require a higher value. Therefore, $k = 4.8$ is selected based on the construction projects' erraticism.

The IQR method was selected as a baseline anomaly detection technique due to its simplicity and interpretability. IQR provides transparent anomaly detection without requiring training data. Additionally, IQR is effective when the data is skewed. Construction progress data often contains nonlinear distributions, making mean-based methods unreliable. IQR is not sensitive to extreme values. Moreover, it is non-parametric and can detect significant deviations without requiring extensive computation.

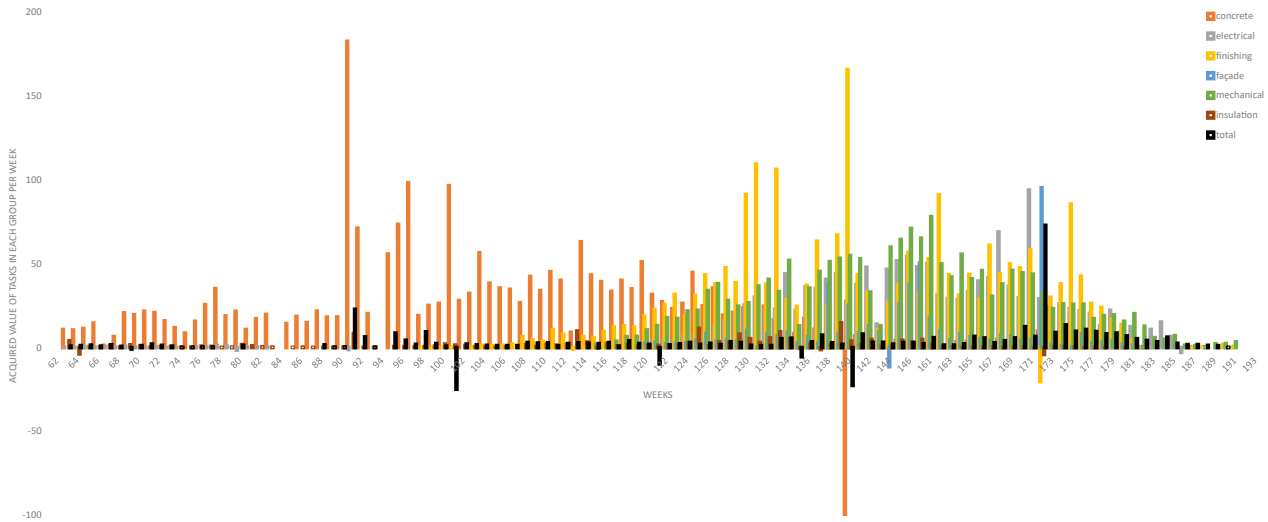

Figure 2 Actual acquired values per week

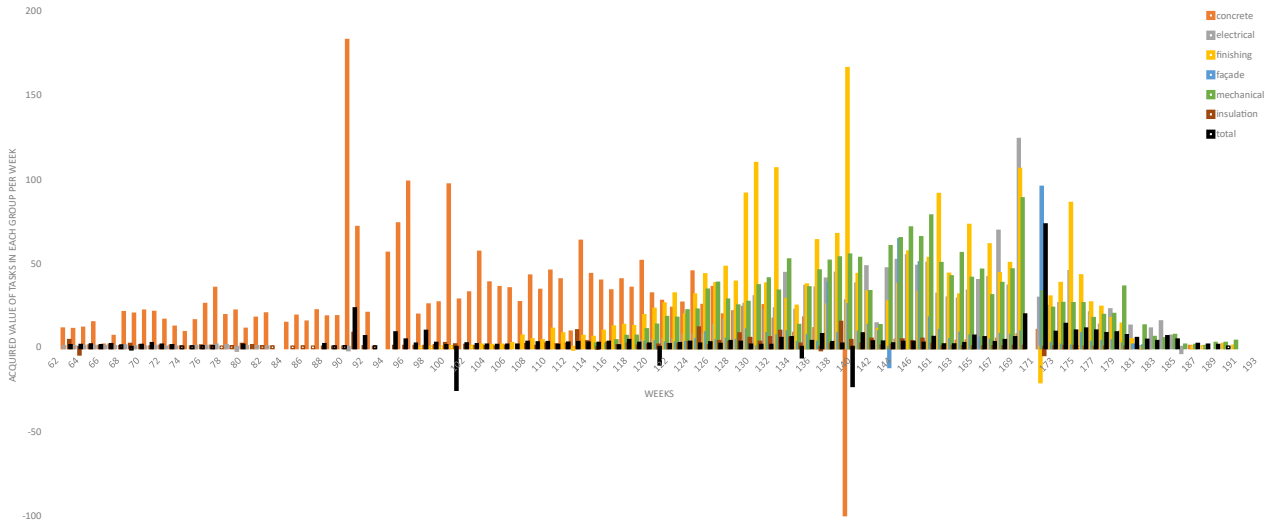

Figure 3 Modified acquired values per week

Table 1 below presents the confusion matrix and standard metrics during the detecting of fake instances.

Table I Confusion matrix and relevant metrics of fake instances for IQR

		Detected	
		Real	Fake
Actual	Real	92	19
	Fake	1	6
Accuracy		0.8305	
Precision		0.2400	
Recall		0.8571	
F1 score		0.3750	

It is seen that IQR successfully flags large deviations. However, its high false positive rate indicates that not all flagged anomalies are genuine. This suggests that, even though statistical approach could build a handy baseline detection system, contextual variations in construction progress (e.g., milestone-based completions) might be misclassified as anomalies.

Machine learning approach: isolation forest (IF)

The isolation forest (IF) algorithm is an unsupervised ML method for anomaly detection in high-dimensional data. It randomly partitions data and measures how quickly an instance becomes isolated. Anomalies tend to be isolated in fewer partitions than normal data points as they differ from normal data. In other words, an ensemble of randomly generated decision trees is built and the anomalies are identified based on their isolation depth.

The algorithm is as follows. The dataset is randomly split into multiple subgroups. Then a decision tree is built by selecting a random feature and a random split value at each node for each subgroup. Anomalous instances require fewer splits to be isolated because they do not stay together with the others. Anomaly scoring is computed based on the average depth required to isolate a point. A lower depth (indicates fewer splits) indicates a higher likelihood of an anomaly. The formula for the anomaly score for a data point x is calculated as follows.

$$s(x,n) = 2^{-\frac{E(h(x))}{c(n)}}$$

$E(h(x))$ is the average depth of x across all trees, and $c(n)$ is the normalization factor based on tree depth for a given dataset size n.

Isolation forest is utilized for anomaly detection as it is efficient and scalable. $O(n.logn)$ time complexity makes it useful for large datasets. As it is an unsupervised model, labelling is not a necessity. This is suitable for real-world construction progress data as labelled anomaly prediction data is not realistic. Again, akin to IQR, isolation forest can also handle nonlinear data. This is desirable due to the fact that the data may include sudden variations. Its robustness against high-dimensionality is beneficial since construction tracking involves multiple parameters (planned, acquired, and realized progress). Furthermore, isolation forest is not being affected by feature scaling.

The confusion matrix and standard metrics for fake instance detection are provided in Table 2, below. It is observed that isolation forest has higher precision and fewer false positives than IQR. It has similar recall to IQR, so that, determining actual anomalies around the same rate. Finally, F1-score has improved, indicating a more balanced detection capability. One could conclude that it can effectively distinguish irregular yet valid milestones from genuinely fraudulent instances. However, some categories showed higher misclassification rates because of project-specific fluctuations in progress, again as in the IQR approach. For instance, milestone-based tasks (e.g., façade completion) sometimes seemed unusual when legitimate progress jumps occurred.

The limitations of both methods yield to an ensemble approach that combined statistical and machine learning methods to enhance detection accuracy.

Ensemble approach

The interquartile range method is significant and isolation forest provides enhanced results. IQR performs better in discovering extreme deviations but results in a large number of false positives. On the other hand, isolation forest yields a refined detection mechanism; yet, it presents sudden jumps based on milestones as anomalies. An ensemble approach could solve the problems while providing a trade-off between the two levels of accuracy and sensitivity owed to the complementary characteristics of both approaches.

Table II Confusion matrix and relevant metrics of fake instances for IF

		Detected	
		Real	Fake
Actual	Real	100	11
	Fake	1	6
Accuracy		0.8983	
Precision		0.3529	
Recall		0.8571	
F1 score		0.5000	

Using an ensemble of multiple models lessens the deficiencies of singular models. In this study, the ensemble method is proposed with the intention of reducing false positives, enhancing recall, and improving decision confidence. Cross-validating flagged anomalies reduces false positives where legitimate milestone completions were misclassified. Recall enhances when significant irregularities could be consistently detected. Finally, providing a layered detection mechanism, where multiple models confirm an anomaly classification enhances confidence.

Two ensemble scenarios are tested:

1. Inclusive Ensemble: A data point is flagged as an anomaly if IQR **or** IF detected it as an outlier.

2. Consensus Ensemble: A data point is flagged only if IQR **and** IF detected it as an anomaly.

Scenario 1

Any snapshot detected as an anomaly by either method is flagged. The confusion matrix and standard metrics for fake instance detection are provided in Table 3, below.

Table III Confusion matrix and relevant metrics of fake instances for the inclusive ensemble scenario

		Detected	
		Real	Fake
Actual	Real	89	22
	Fake	0	7
Accuracy		0.8136	
Precision		0.2414	
Recall		1.0000	
F1 score		0.3889	

Scenario 2

A snapshot was flagged only if both methods detected an anomaly. The confusion matrix and standard metrics for fake instance detection is provided in Table 4, below.

Table IV Confusion matrix and relevant metrics of fake instances for the consensus ensemble scenario

		Detected	
		Real	Fake
Actual	Real	103	8
	Fake	2	5
Accuracy		0.9153	
Precision		0.3846	
Recall		0.7143	
F1 score		0.5000	

It is observed that Scenario 1 ("Inclusive") detected all actual anomalies (100% recall) but suffered from more false positives, lowering precision. Scenario 2 ("Consensus") achieved the best balance, reducing false positives while maintaining high accuracy and F1-score. As a matter of fact, two scenarios could be put together where an inclusive approach warns human actors as a decision support system, and a consensus approach is considered as a more serious alert that requires investigation.

By combining statistical and machine learning techniques, the ensemble approach provides a robust and scalable framework for anomaly detection in construction project tracking. Early fraud detection is one of the main advantages, as this reduces the reliance on manual inspections and creates a more automated, data-driven system to detect and scrutinize anomalies in progress reporting. Also, given its ability to correlate the suspicious behavior with the project, it can easily work with the project management packages like Primavera, MS Project, or in-house project management packages to ensure timely alerts are triggered. The method is also extremely scalable, so it is computationally cheap to apply across construction sites in real time, which allows companies to control all their large-scale operations and make better decisions.

Discussion and Practical Implications

Interquartile range and other statistical techniques are effective at detecting large anomalies but tend to generate false positives. This leads to false investigations and decreased trust in the system. Machine learning based isolation forest, on the other hand, finely detects anomaly with a focus on localized patterns and distance from the average.

Since both scenarios have their advantages and disadvantages, ensemble methods bring the best of both worlds. The combination of statistical approach with machine learning approach brings high recall with low false positive rates. The output of the ensemble approach, which remarkably decreases likely false alarms, could be a primary information during project decision making.

The findings on the early detection of anomalies let project managers to take early action. In addition, real-time identification of workforce inefficiencies, delays or disruptions make room for proactive reorganization of the project tasks. The proposed approaches could be easily integrated into existing project management tools, like Primavera or MS Project. In this case, the need for manual monitoring and missing unnoticed anomalies would be reduced. Moreover, insider manipulations, either to report artificial progress or to gain financial benefit, could be noticed; therefore, ends up with more trustworthy project reporting.

The potential of machine learning could grow larger in anomaly detection in construction project management. Static rule-based monitoring could be replaced with automated tools and present a steadily approach learning from the fluctuating conditions of the projects. This ensures that any outliers, whether due to misreporting, or fraudulent activity, could be noticed. Thus, project managers could shift from problem solving afterwards to averting problems beforehand. The proposed approach might have optimizing effects on other industrial projects. Moreover, financial accountability of projects could be enhanced. In the future, the proposed tool integrated to other project management tools together with real-time monitoring data could produce better predictions and lead to more intelligent, digitized project management.

The proposed approach is probably one of the many possibilities of the application of artificial intelligence in the construction domain. Even though the proposed approach utilizes two fundamental methods in an ensemble approach, in the availability of more data, combining autoencoders with other machine learning methods may improve the output of anomaly detection [9, 10]. Future developments may provide continuous information flow where potential anomalies could be identified before they develop into critical issues, thereby their effects could be timely mitigated [7, 14]. Further enhancements might be enabled by integrating additional contextual data, such as productivity measures of the subcontractors and their financial history. This could improve the model output by being aware of not only the project-related data but also other affecting factors. To provide validity to the proposed approach, presented historical study could be implemented in large construction sites and compared hand in hand with conventional methods. Practical deployment could also point several constraints that cannot be foreseen in this paper.

Conclusion

This paper present that anomaly detection could be realized via statistical and machine learning methods in the construction industry. The interquartile range offers a basic approach for defining an outlier; however, this leads to many false positives. Isolation forest produces more data-driven approach so that it decreases the number of false positives. The first ensemble method provides perfect detection at the cost of more false positives. The second ensemble method, on the other hand, provides the least number of false positives. Therefore, hybrid ensemble methods seem to improve accuracy, reduces false positives and presents a desirable solution for practical construction monitoring.

From project managers perspective, utilizing AI-based anomaly detection is useful for resource optimization and timely risk management. Early anomaly detection improves proactiveness in decision-making, leaves room for taking action before delays become costly. So that, keeping projects on track. AI tools could be more valuable as the construction projects grow bigger and become more sophisticated.

A promising future focus could be introducing interpretability to AI-driven tools for the construction sector. Even though the automated detection mostly provides useful output, the models are imperfect. The untrustworthy black boxes could be replaced by more transparent tools by developing explainable methods with the same functionality. Finally, developed methods could be integrated into building information modeling systems and integrated sensor data flow from the project site could be used to further optimize a digital information system of construction project management. Broadening the use of AI in construction progress tracking could pave the way for the industry to make a major leap towards improved efficiency, and risk mitigation. Project monitoring might shift the construction sector to an intelligent and robust state by embracing data-driven automation.

References

[1] Jin, S. (2024). Measuring complexity in mega construction projects: fuzzy comprehensive evaluation and grey relational analysis. Engineering, Construction and Architectural Management. https://doi.org/10.1108/ecam-07-2024-0951

[2] Zhao, X., Liu, Y., Lang, X., Liu, K., Yang, X., & Liu, L. (2024). Study on the Characteristics and Operational Mechanisms of Industry–University–Research Collaborative Innovation in Megaprojects: The Case from China. Systems. https://doi.org/10.3390/systems12120553

[3] Xiang, P., Yang, Y., Yan, K., & Jin, L. (2024). Identification of Key Safety Risk Factors and Coupling Paths in Mega Construction Projects. Journal of Management in Engineering. https://doi.org/10.1061/jmenea.meeng-5926

[4] Mostofi, F., Toğan, V., & Tokdemir, O. B. (2025). A cost estimation recommendation system for improved contingency management in construction projects. Neural Computing & Applications 37, 3521–3538. https://doi.org/10.1007/s00521-024-10740-y

[5] Mostofi, F., Tokdemir, O. B., & Toğan, V. (2024). Generating synthetic data with variational autoencoder to address class imbalance of graph attention network prediction model for construction management. (2024). https://doi.org/10.1016/j.aei.2024.102606

[6] Shyam, R., & Tiwari, S. (2025). A Comprehensive Review of Machine Learning and Multi-Criteria Decision Analysis in Construction Delay Management. International Research Journal on Advanced Science Hub. https://doi.org/10.47392/irjash.2025.002

[7] Manu, B. A. (2024). Leveraging Artificial Intelligence for optimized project management and risk mitigation in construction industry. World Journal of Advanced Research and Reviews. https://doi.org/10.30574/wjarr.2024.24.3.4026

[8] Zapata-Cortes, O., Serna, M. D. A., Zapata-Cortés, J. A., & Restrepo-Carmona, J. A. (2024). Machine Learning Models and Applications for Early Detection. Sensors. https://doi.org/10.3390/s24144678

[9] Nishat, M. M., Neraas, S. M., Marsov, A., & Olsson, N. O. E. (2024). Prediction of project activity delays caused by variation orders: a machine-learning approach. https://doi.org/10.1088/1755-1315/1389/1/012038

[10] Al-Sabah, B., & Anbarjafari, G. (2024). Anomaly Detection in Kuwait Construction Market Data Using Autoencoder Neural Networks. Information. https://doi.org/10.3390/info15080424

[11] Al-Bataineh, F., Khatatbeh, A. A., & Alzubi, Y. (2024). Unsupervised machine learning for identifying key risk factors contributing to construction delays. Organization, Technology and Management in Construction: An International Journal. https://doi.org/10.2478/otmcj-2024-0014

[12] Alhasan, A. M. A., & Alawadhi, E. K. E. (2024). Evaluating the Impact of Artificial Intelligence in Managing Construction Engineering Projects. The Journal of Engineering Sciences and Information Technology. https://doi.org/10.26389/ajsrp.k090724

[13] Mostofi, F., Toğan, V., Ayözen, Y., & Tokdemir, O. B. (2022). Predicting the Impact of Construction Rework Cost Using an Ensemble Classifier. Sustainability, 14 (22), 14800. https://doi.org/10.3390/su142214800

[14] Gajera, R. (2024). The Impact of SmartPM's Ai-Driven Analytics on Predicting and Mitigating Schedule Delays in Complex Infrastructure Projects. International Journal of Scientific Research in Science, Engineering and Technology. https://doi.org/10.32628/ijsrset24115101

[15] Yao, D., & Soto, B. G. de. (2024). Cyber Risk Assessment Framework for the Construction Industry Using Machine Learning Techniques. Buildings. https://doi.org/10.3390/buildings14061561

[16] Li, S., & Zhu, A. (2024). Integrating Wireless Sensor Networks in Construction Project Risk Management: A Cyber-Physical Approach to Enhancing Robustness and Security in Smart Building Developments. https://doi.org/10.1109/wrcsara64167.2024.10685736

[17] Yang Z., Xiaocheng Y. & Yongmei Y., "Design and implementation of RFID-based construction restricted area intrusion detection system," Proc. SPIE 13160, Fourth International Conference on Smart City Engineering and Public Transportation (SCEPT 2024), 1316002 (16 May 2024); https://doi.org/10.1117/12.3030396

[18] Tran, S. V.-T., Lee, D., Bao, Q. L., Yoo, T., & Jo, J. (2023). A Human Detection Approach for Intrusion in Hazardous Areas Using 4D-BIM-Based Spatial-Temporal Analysis and Computer Vision. Buildings. https://doi.org/10.3390/buildings13092313

[19] Soto, B. G. de, Georgescu, A., Mantha, B. R. K., Turk, Z., Maciel, A., & Sonkor, M. S. (2022). Construction cybersecurity and critical infrastructure protection: new horizons for Construction 4.0. Journal of Information Technology in Construction. https://doi.org/10.36680/j.itcon.2022.028

[20] Saah, A. E. N., Yee, J.-J., & Choi, J.-H. (2023). Securing Construction Workers' Data Security and Privacy with Blockchain Technology. Applied Sciences. https://doi.org/10.3390/app132413339

[21] Sonkor, M. S., Xu, X., Prieto, S. A., & Soto, B. G. de. (2022). Vulnerability Assessment of Construction Equipment: An Example for an Autonomous Site Monitoring System. Proceedings of the 39th ISARC, Bogotá, Colombia, https://doi.org/10.22260/isarc2022/0040

[22] Kochergin, S. V., Artemova, S., Bakaev, A. A., Mityakov, E. S., Vegera, Z. G., & Maksimova, E. (2024). Cybersecurity of smart grids: Comparison of machine learning approaches training for anomaly detection. Russian Technological Journal. https://doi.org/10.32362/2500-316x-2024-12-6-7-19

[23] Chua, W., Pajas, A. L. D., Castro, C. L. B. de, Panganiban, S. P., Pasuquin, A. J., Purganan, M. J., Malupeng, R., Pingad, D. J., Orolfo, J. P., Lua, H. H., & Velasco, L. C. (2024). Web Traffic Anomaly Detection Using Isolation Forest. Informatics (Basel). https://doi.org/10.3390/informatics11040083

[24] Yılmazer Demirel, D. and Sandikkaya, M.T. (2023) ACUM: An Approach to Combining Unsupervised Methods for Detecting Malicious Web Sessions. 2023 8th International Conference on Computer Science and Engineering (UBMK), Burdur, Turkiye, pp. 288-293, https://doi.org/10.1109/UBMK59864.2023.10286727

[25] Manavadaria, M. S., Srinivas, T. A. S., Ahamed, S. K., Amshavalli, M., Nadaf, A. B., & Varadharajan, B. (2024). Anomaly Detection Algorithms in Cybersecurity. Advances in Computational Intelligence and Robotics Book Series. https://doi.org/10.4018/979-8-3693-7540-2.ch013

[26] Sharma, R., & Grover, M. (2024). Enhancing Cybersecurity with Machine Learning: Evaluating the Efficacy of Isolation Forests and Autoencoders in Anomaly Detection. https://doi.org/10.1109/iccpct61902.2024.10673338

[27] Ness, S., Eswarakrishnan, V., Sridharan, H., Shinde, V., Janapareddy, N. V. P., & Dhanawat, V. (2025). Anomaly Detection in Network Traffic using Advanced Machine Learning Techniques. IEEE Access. https://doi.org/10.1109/access.2025.3526988

[28] Bhuiyan, M. R. I., Faraji, M. R., Tabassum, M. N., Ghose, P., Sarbabidya, S., & Akter, R. (2024). Leveraging Machine Learning for Cybersecurity: Techniques, Challenges, and Future Directions. Edelweiss Applied Science and Technology. https://doi.org/10.55214/25768484.v8i6.2930

[29] Abas, A., Oshoiribhor, O. E., & John-Otumu M. A. (2017). Rule Based Forward Chaining Technique for Detecting and Controlling Fraud in Project Monitoring System. International Journal of Software Engineering & Applications. https://doi.org/10.5121/IJSEA.2017.8503

[30] Wang, K., Zhao, Z., Deng, R., & Mao, Y. (2023). Automated Construction Progress Monitoring and Controlling Framework Based on Computer Vision and Internet of Things System. 2023 6th International Conference on Electronics Technology (ICET). https://doi.org/10.1109/icet58434.2023.10211573

[31] Shamsollahia, D., Moselhib, O., & Khorasanic, K. (2022). Construction Progress Monitoring and Reporting using Computer Vision Techniques – A Review. 39th International Symposium on Automation and Robotics in Construction (ISARC 2022).

[32] Abdel-Wahhab, O., & Elazouni, A. (2010). Progress Monitoring of Construction Projects Using Statistical Pattern Recognition. https://doi.org/10.1061/41109(373)121

[33] Jin, X., & Le, Y. (2014). Monitoring Construction Projects Using Information Technologies. Proceedings of the 17th International Symposium on Advancement of Construction Management and Real Estate, pp. 1011-1020. https://doi.org/10.1007/978-3-642-35548-6_104

[34] Hansen, S. Setiono, B., Handayani, S., & Dewobroto, W. S. (2025). Influence Factor Model for Fraud Detection in Construction Companies' Financial Statements. Journal of Legal Affairs and Dispute Resolution in Engineering and Construction. https://doi.org/10.1061/JLADAH.LADR-1301

[35] Tambwe, O. T., Aigbavboa, C. O., Akinradewo, O. I., & Adekunle, P. A. (2025). Measures to Address Cyber-Attacks in Construction Project Data Management Processes: A Cybersecurity Perspective. IET Information Security. https://doi.org/10.1049/ise2/7398742

[36] Lalropuia, K. C., Goyal, S., de Soto, B. G., Yao, D., Sonkor, M. S. (2025). Mitigating Malicious Insider Threats to Common Data Environments in the Architecture, Engineering, and Construction Industry: An Incomplete Information Game Approach. Journal of Cybersecurity and Privacy. https://doi.org/10.3390/jcp5010005

Dicle University
Journal of Engineering
https://dergipark.org.tr/tr/pub/dumf
duje.dicle.edu.tr

Araştırma Makalesi / Research Article

Hekimoğlu Ali Paşa Türbesi'nin Mevcut Durum Tahkiki Ve Taşıyıcı Kemere Takviye Önerisi

Actual Structural Condition Assessment of Hekimoğlu Ali Pasha Tomb and Reinforcement Recommendation for the Supporting Arch

Erdinç Önen[1]
[1]beonen@gmail.com
ORCID: https://orcid.org/0009-0000-5544-2883

MAKALE BİLGİLERİ

Makale Geçmişi:

Geliş 24 Nisan 2025
Revizyon 21 Ekim 2025
Kabul 24 Ekim 2025
Online 30 Aralık 2025

Anahtar Kelimeler:

Hekimoğlu Ali Paşa Türbes Kültürel Miras, Yığma Yapı, Güçlendirme, Kesmetaş Kemerin Takviyesi

ÖZ

İstanbul Fatih ilçesi Davut Paşa mahallesinde yer alan türbe, I. Mahmud'un sadrazamlarından Hekimoğlu Ali Paşa tarafından 1730 – 1754 yılları arasında Çuhadar Ömer Ağa ve Hacı Mustafa Ağa adında iki mimara yaptırılmıştır. Makalede, tarihi değere sahip bu değerli yapının mevcut yapısal durum değerlendirmesi yapılarak gerekli görülen takviyeler önerilmiştir. Özellikle yapının ortasında bulunan ve beklenen depremde dayanımı sınır değerlere ulaşması ve hatta aşması öngörülen mevcut kemerin takviyesi için önerilen yine aynı malzemeden yapılacak takviye bir kemere dikkat çekilmiştir.

ARTICLE INFO

Article history:

Received 24 April 2025
Received in revised form 21 October 2025
Accepted 24 October 2025
Available online 30 December 2025

Keywords:

Hekimoğlu Ali Pasha Tomb, Cultural Heritage, Masonry Structure Reinforcement, Stone Arch Reinforcement

Doi: 10.24012/dumf.1683039

ABSTRACT

The tomb, located in the Davut Pasha neighborhood of Fatih district, İstanbul, was built by two architects named Çuhadar Ömer Ağa and Hacı Mustafa Ağa between 1730 and 1754 by Hekimoğlu Ali Pasha, one of the grand viziers of Mahmud I. In the article, the current structural condition of this valuable historical building was evaluated and necessary reinforcements were suggested. Particular attention was drawn to an additional arch made of the similar material, which is recommended for the reinforcement of the existing arch, which is located in the middle of the building and whose strength is expected to reach or even exceed the limit values in the expected earthquake.

* Sorumlu Yazar

1. Giriş

Hekimoğlu Ali Paça Külliyesi, İstanbul ili, Fatih İlçesi'nde, Davutpaşa- Kocamustafapaşa mahalleleri arasında 1730-1754 yılları arasında inşa edilmiştir. Sadrazamlardan Hekimoğlu Ali Pasa tarafından, mimarlar Çuhadar Ömer Ağa ve Hacı Mustafa Ağa' ya yaptırılan külliye; cami, tekke, şadırvan, türbe, sebil, kütüphane ve çeşmeden oluşmaktadır.

Türbenin Hekimoğlu Ali Paça caddesine bakan cephesi, yapıya sonradan eklenmiş olan çatı saçağına kadar mermer ile kaplıdır (Resim 2, 4). Taşıyıcı beden duvarları ise 1 sıra taş ve 2 sıra tuğladan oluşan almaşık örgü ile inşaa edilmiştir (Resim 6). Günümüzde türbenin avlu cephesinde, ahşap sütunlar ve kemerlerle oluşturulmuş, şadırvanın örtüsüyle bütünlesen bir sundurma bulunmaktadır (Resim 5). Türbenin iç cepheleri tamamen sıva ile kaplıdır. İç kısmın ortasındaki kemer ise kesmetaş örgüdür (Resim 7). Kubbeye geçiş tromplarla sağlanmıştır, trompların altları mukarnas konsolludur (Resim 8). Yapının eski fotoğraflarında görüldüğü üzere kubbe tuğla örgülüdür (Resim 1, 2).

Resim 1- Bahçeden eski bir görünüş

Resim 2- Yol tarafından eski bir görünüş

Giriş cephesi ve girişin sol yan duvar kalınlığı 110cm, caddeye bakan duvar ve sağ yan duvar kalınlığı, mermer kaplama hariç, 82cm'dir. Yaklaşık 6,0 metre çapındaki basık kubbenin kalınlığı yaklaşık 40 cm'dir. Kubbenin iç yüzeyi çimento esaslı sıva tabakası ile dış yüzeyi ise kurşun kaplama ile örtülüdür (Resim 7, 4). Yapı duvarlarında ve kubbede kılcal çatlaklar dışında belirli bir hasara veya oturmaya rastlanmamıştır (Resim 6, 7).

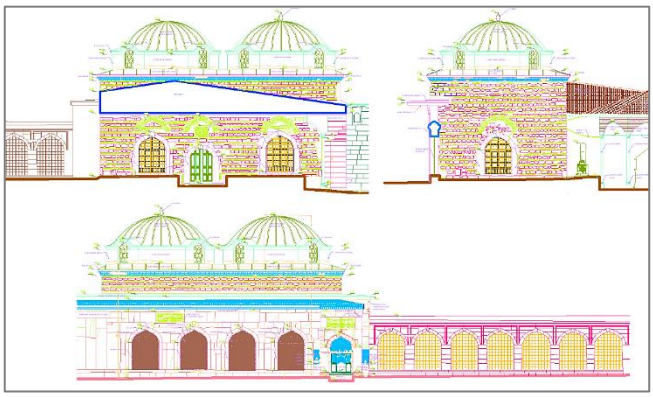

Resim 3- Çizim- bahçeden yol tarafından ve yandan görünüşler

Resim 4- Yol tarafından görünüş

Resim 5- Bahçeden görünüş

Resim 6- Bahçeden görünüş

Resim 7- Kemer

Resim 8- Kubbe ve tromblar

2. Malzeme

Doğal taş veya tuğlanın, bir bağlayıcı harçla beraber kullanılması ile oluşan yapım tarzına kârgir (yığma) adı verilir. Çevre şartlarına ve zamanın ilerlemesiyle oluşan yaşlanma etkilerine göre de farklı özellikler gösterebilen kârgir malzemenin basınca karşı davranışı iyi sayılırken, kesmeye ve çekmeye karşı zayıftır. Taşıyıcı yığma duvarların mukavemeti, bağlayıcı harcın mukavemetine eşdeğer kabul edilebilir, zira oluşan yükler karşısında tuğla veya taş birimlerden önce harç güç tükenmesine erişir [3].

Taşıyıcı duvarlar 1 sıra taş ve 2 sıra tuğladan oluşan almaşık örgü, kubbe ise tuğla örgüdür. Kemerin malzemesi kesme taştır. Yığma yapı elemanlarının harç ile birlikte tek bir malzeme özelliği gösterdiği kabul edilerek, Elastisite modülü ve birim ağırlık kabulleri yapılmıştır. Taşıyıcı elemanların dayanım değerleri tablosu için 3 farklı referanstan faydalanılmıştır (Tablo 4); 2017 Tarihi Yapılar İçin Deprem Risklerinin Yönetim Kılavuzu (Tablo 3a, 3b) [5] ile 2018 Türkiye Bina Deprem Yönetmeliği (TBDY Tablo 1, 2, 3, 4) [10] ve Edirne'de bulunan ve 1478 yılında inşa edilmiş olan Merkez Evliya Kasımpaşa Camii yapısının su taşkını ve deprem risklerine yönelik olarak yapılan güçlendirme çalışmalarına ait makale [23].

Tablo 1- Kargir Birimlerin Delik Oranlarına Göre Gruplandırılması (TBDY Tablo 11.1)

Kargir Birim Cinsi(*)	Grup I	Grup II
Tuğla	$\alpha \le$ %35	%35 < $\alpha \le$ %50
Beton	$\alpha \le$ %35	%35 < $\alpha \le$ %50

Tablo 2- Yığma Taşıyıcı Duvarların Karakteristik Basınç Dayanımı, fk (TBDY Tablo 11.2)

Birim-Birim Sınıfı	Harç sınıfı	Harç basınç dayanımı, f_m (MPa)*	Kargir birim basınç dayanımı, f_b (MPa)					
			5	10	15	20	25	30
Grup I	Genel amaçlı harç	M10-M20	3.4-4.2	5.5-6.8	7.3-9.0	8.9-11.0	10.4-12.9	11.9-14.6
		M2.5-M9	2.2-3.3	3.6-5.3	4.8-7.1	5.9-8.7	6.9-10.1	7.8-11.5
		M1-M2	1.7-2.1	2.8-3.4	3.7-4.5	4.5-5.5	5.2-6.4	5.9-7.3
Grup II ve Kesme taş		M10-M20	2.8-3.4	4.5-5.5	6.0-7.4	7.3-9.0	8.5-10.5	9.7-12.0
		M2.5-M9	1.8-2.7	3.0-4.4	3.9-5.8	4.8-7.1	5.6-8.3	6.4-9.4
		M1-M2	1.4-1.7	2.3-2.8	3.0-3.7	3.7-4.5	4.3-5.3	4.9-6.0

Tablo 3- Duvarların Başlangıç Kesme Dayanımları, fvko (MPa) (TBDY Tablo 11.3)

Kargir birim	Genel amaçlı harç(*)		İnce tabaka harç
Tuğla	M10-M20	0.30	0.30
	M2.5-M9	0.20	
	M1-M2	0.10	
Beton	M10-M20	0.20	0.30
Gazbeton	M2.5-M9	0.15	0.30
Doğal veya Yapay Taş	M1-M2	0.10	Kullanılamaz

Tablo 3a- Yığma duvar malzemesinin mekanik özellikleri (TYDRY Tablo 6.1; Magenes, Penna, 2009)

Duvar türü	Basınç dayanımı fm (MPa)	Kayma dayanımı To (kPa)	Elastisite modülü E (MPa)	Kayma modülü G (MPa)	Birim hacm ağırlığı (Kn/m³)
Moloz taşlı yığma duvar	0,60 ~ 0,90	20 ~ 32	690 ~ 1050	115 ~ 175	19
Kaba yonu taşlı yığma duvar	1,10 ~ 1,60	35 ~ 51	1020 ~ 1440	170 ~ 240	20
Kesme taşlı iyi bağlantılı yığma duvar	1,50 ~ 2,00	56 ~ 74	1500 ~ 1980	250 ~ 330	21
Kireç harçlı tuğla yığma duvar	1,80 ~ 2,80	60 ~ 92	1800 ~ 2400	300 ~ 400	18

Tablo 3b- Yığma duvar malzemesinin Tablo 6.1.de verilen mekanik parametrelerine harç, duvar işçiliğine ve duvarın enine bağlantılarının özelliklerine bağlı kullanılabilecek düzeltme katsayıları (TYDRY Tablo 6.2)

Duvar düzeni	İyi bağlayıcı harç	İyi düzenlenen derzli duvar	Enine bağlantılı duvar	Harç enjeksiyonlu duvar	Donatılı sıva ile güçlendirilmiş duvar
Moloz taşlı yığma duvar	1,50	1,30	1,50	2,00	2,00
Kaba yonu taşlı yığma duvar	1,40	1,20	1,50	1,70	2,00
Kesme taşlı iyi bağlantılı yığma duvar	1,30	1,10	1,30	1,50	1,50
Kireç harçlı tuğla yığma duvar	1,30	-	1,30	1,50	1,50

Tablo 4- Analizde kullanılan malzeme değerleri

Taşıyıcı Elemanların farklı referanslara göre fiziksel değerleri	Türkiye Bina Deprem Yönetmeliği [10]		Tarihi Yapılar İçin Deprem Risklerinin Yönetim Kılavuzu (Tablo 6.1, 6.2; Magenes, Penna, 2009) [5]		Merkez Evliya Kasımpaşa Camii [23]	
	Tuğla ve taş örgü duvar	Kesme taş kemer	Tuğla ve taş örgü duvar	Kesme taş kemer	Tuğla ve taş örgü duvar	Kesme taş kemer
(TDBY Tablo 11.1) Kargir Birimlerin Delik Oranına Göre Gruplandırılması	Grup I					
(TDBY Tablo 11.2) Harç basınç dayanımı, f_m (MPa)	M1 - M2	M1 - M2				
(TDBY Tablo 11.2) Kargir birim basınç dayanımı, f_b (MPa)	5,00	10,00				
(TDBY Tablo 11.2) Yığma Taşıyıcı Duvarların Karakteristik Basınç Dayanımı, f_k (MPa)	1,90	2,55	1,80	2,20	2,00	2,00
(TDBY Tablo 11.3) Duvarların Başlangıç Kesme Dayanımları, f_{dko} (MPa)	0,10	0,10	0,06	0,06	0,16	0,20
(TDBY 11.2.9) Duvar karakteristik kesme dayanımı, Denk.11.1; $f_{dk} = f_{dko} + 0.4\sigma_d \leq 0.10\, f_b$ (Mpa)	0,50	1,00				
(TDBY 11.2.13) Esneklik Sabiti - Taşıyıcı duvarların elastisite modülü, $E_{dtv} = 750 f_k$ (MPa)	1425	1913	1800	1980	1500	1500
(TDBY 11.2.13) Duvar kayma modülü, $G_{dtv} = \%40 E_{dtv}$ (Mpa)	570	765	300	330	600	600
Kütle Yoğunluğu - Özkütle (kg/m3)	1800	2520	1800	2100		
Poisson Oranı	0,20	0,20				

3. Model ve mevcut durum tahkiki

Bu safhada öncelikle yerinde incelemeler ve geometrik olarak gözlemler yapılmış, yapının taşıyıcı sistemi ve yük aktarımının hangi elemanlar vasıtasıyla gerçekleştiği incelenmiştir. Sayısal modellemenin amacı, yapının tamamının, belli bir bölümünün ya da taşıyıcı sistem elemanlarının çeşitli yük veya çevresel etkiler altında gerçek davranışının belirlenmesini sağlamaktır. Sayısal analizlerle elde edilen gerilme dağılımı yapının davranışı hakkında bilgiler verir, ancak modelden elde edilen gerilme değerleri mutlak veri olarak tanımlanamaz. Tarihi yapıların ve anıtların taşıyıcı sistemi çoğunlukla çok karmaşıktır. Bu nedenle, yapıyı modellemek için birçok sadeleştirmenin yapılması zorunludur. En doğru sonucu veren model her zaman en basit olanıdır. Doğrusal analiz veya malzemenin doğrusal elastik davranışı, taşıcıyı sistem elemanlarında meydana gelen şekil değiştirmenin sadece uygulanan yükün şiddeti ilgili olduğu anlamına gelir ve aşağıdaki kabullere dayanır;

1.Gerilmenin şiddeti arttıkça, bunun sonucunda ortaya çıkan birim şekil değiştirme miktarı da doğrusal oranda artar,

2. Gerilmenin şiddeti azaldıkça, birim şekil değiştirme miktarı da aynı doğrusal oranda azalır,

3. Malzeme homojen ve süreklidir.

Birçok malzeme için küçük gerilme değerlerinde doğrusal gerilme-birim şekil değiştirme kabulü geçerlidir. Yığma yapı elemanları da genellikle, izotropik doğrusal elastik malzeme özellikleri göz önünde bulundurularak modellenirler [20].

Yapılan analiz ve değerlendirmelerde 2018 Türkiye Bina Deprem Yönetmeliği (TBDY Bölüm 11 Deprem Etkisi Altında Yığma Bina Taşıyıcı Sistemlerinin Tasarımı İçin Özel Kurallar) [10] ile 2017 Tarihi Yapılar İçin Deprem Risklerinin Yönetim Kılavuzu'ndan yararlanılmıştır [5]. 2018 Türkiye Bina Deprem Yönetmeliği'ne göre yığma, binalar, DD-2 deprem yer hareketinin etkisi altında Kontrollü Hasar (KH) performans hedefini sağlayacaktır (TBDY Bölüm 3.5.1.2). DD-2 Deprem Yer Hareketi, spektral büyüklüklerin 50 yılda aşılma olasılığının %10 ve buna karşı gelen tekrarlanma periyodunun 475 yıl olduğu seyrek deprem yer hareketini nitelemektedir (TBDY Bölüm 2.2.2). Bu düzey, can güvenliğini sağlamak üzere bina taşıyıcı sistem elemanlarında çok ağır olmayan ve çoğunlukla onarılması mümkün olan hasar düzeyine karşı gelmektedir (TBDY Bölüm 3.4.3) [10].

Yapı sonlu elemanlar yöntemi ile, yığma duvar kompozit bir malzeme olarak kabul edilerek, makro modelleme tekniği kullanılarak, SAP2000 programı ile modellenmiştir. Duvarlar katı eleman, kubbeler ise alan eleman olarak modellenmiştir (Resim 9, 9a).

Modelde kullanılan sonlu eleman boyutlarının, duvardaki tuğla ya da taş eleman boyutlarının en fazla 3-4 katı kadar olması koşulu ile sistem homojen olarak ifade edilebilir. Genel olarak yığma duvarlarda kullanılan harcın mukavemeti, duvarın mukavemetine eşdeğer durumdadır. Güç tükenmesi harç ile tuğla veya taş arasında gerçekleşir [17].

Model 918 adet katı eleman ve 765 adet alan elemandan oluşmuştur (Resim 9).

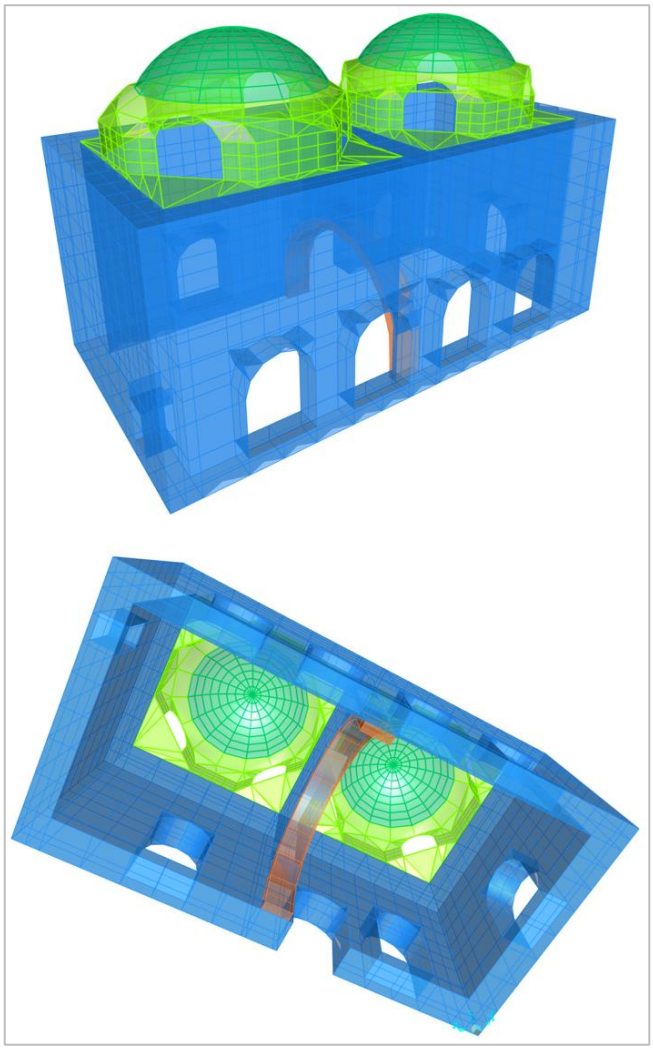

Resim 9- Yapının Modeli

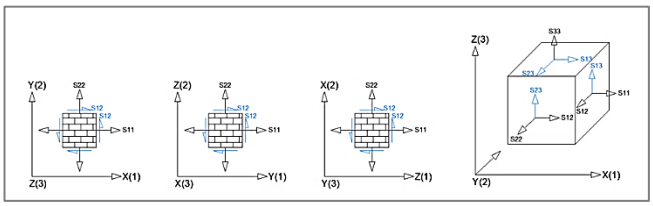

Resim 9a- Kabuk elemanlarda gerilmeler; S11 yatay eksen doğrultusundaki gerilmeleri, S22 düşey eksen doğrultusundaki gerilmeleri, S12 ve S21 ise kayma gerilmelerini gösterir. Katı elemanlarda gerilmeler; S11- X yönündeki depremlerde X ekseni doğrultusundaki gerilmeleri, S22- Y yönündeki depremlerde Y ekseni doğrultusundaki gerilmeleri, S33 ise düşey gerilmeleri ifade eder. Negatif gerilme değeri basınç gerilmesini, pozitif değer ise çekme gerilmelerini gösterir. S13-S23 kayma gerilmeleridir ve negatif veya pozitif olmaları sadece kaymanın yönüyle ilgilidir.

Analizde kullanılan Eşdeğer deprem yükü yöntemi, yüklerin hesabında yapı ve zemine ilişkin periyot değerleri gibi dinamik parametrelerin kullanılması nedeniyle, sadece birinci modun dikkate alındığı dinamik bir yöntem olarak kabul edilir ve sadece Yönetmelikte belirtilen, yapımızın da bu şartlara uyduğu, aşağıdaki bina sınıfları için kullanılabilir [4];

i. Yapının Kullanım Sınıfı, BKS=2 (Tablo 5a, TBDY Tablo 3.1),

ii. Deprem Tasarım Sınıfı, DTS=1 (S_{DS}=1,107>0,75, Tablo 5b, TBDY Tablo 3.2)

iii. Bina Yükseklik Sınıfı, BYS=7 (Kubbe yüksekliği= 10,50mt, Tablo 5c, TBDY Tablo 3.3)

iv. Eşdeğer Deprem Yükü Yöntemi 'nin Uygulanabileceği Binalar (Tablo 6, TBDY Tablo 4.4)

Mevcut durum değerlendirmesi yapılırken, gerilmeler R katsayısı ile azaltılmış deprem etkilerinden, yer değiştirmeler ise azaltılmamış deprem etkilerinden elde edilir [5] (Tablo 9, 10).

Tablo 5a- Bina Kullanım Sınıfları ve Bina Önem Katsayıları (TBDY Tablo 3.1)

Bina Kullanım Sınıfı	Binanın Kullanım Amacı	Bina Önem Katsayısı (I)
BKS = 2	**İnsanların kısa süreli ve yoğun olarak bulunduğu binalar** Alışveriş merkezleri, spor tesisleri, sinema, tiyatro, konser salonları, ibadethaneler, vb.	1.2

Tablo 5b- Deprem Tasarım Sınıfları (TBDY Tablo 3.2)

DD-2 Deprem Yer Hareketi Düzeyinde Kısa Periyot Tasarım Spektral İvme Katsayısı (S_{DS})	Bina Kullanım Sınıfı	
	BKS = 1	BKS = 2, 3
$0.75 \le S_{DS}$	DTS = 1a	DTS = 1

Tablo 5c- Bina Yükseklik Sınıfları ve Deprem Tasarım Sınıflarına Göre Tanımlanan Bina Yükseklik Aralıkları (TBDY Tablo 3.3)

Bina Yükseklik Sınıfı	Bina Yükseklik Sınıfları ve Deprem Tasarım Sınıflarına Göre Tanımlanan Bina Yükseklik Aralıkları [m]		
	DTS = 1, 1a, 2, 2a	DTS = 3, 3a	DTS = 4, 4a
BYS = 7	$7 < H_N \le 10.5$	$10.5 < H_N \le 17.5$	

Tablo 6- Eşdeğer Deprem Yükü Yöntemi 'nin Uygulanabileceği Binalar (TBDY Tablo 4.4)

Bina Türü	İzin Verilen Bina Yükseklik Sınıfı	
	DTS = 1, 1a, 2, 2a	DTS = 3, 3a, 4, 4a
Her bir katta burulma düzensizliği katsayısının $\eta_{bi} \le 2.0$ koşulunu sağladığı ve ayrıca **B2** türü düzensizliğinin olmadığı binalar	BYS ≥ 4	BYS ≥ 5
Diğer tüm binalar	BYS ≥ 5	BYS ≥ 6

Eşdeğer Deprem Yükü Yöntemi, birbirine dik (X) ve (Y) deprem doğrultularında binaya etkiyen depremler için ayrı ayrı uygulanacaktır (TBDY 4.7). Gözönüne alınan deprem doğrultusunda, binanın tümüne etkiyen toplam eşdeğer deprem yükü (taban kesme kuvveti) aşağıdaki formülle hesaplanır;

$$V_{tE} = m_t * S_{aR}(T_p) \ge 0.04 m_t * I * S_{DS} * g \qquad \text{Denklem 4.19}$$

Burada $S_{aR}(T_p)$, gözönüne alınan deprem doğrultusunda binanın hâkim doğal titreşim periyodu Tp gözönüne alınarak hesaplanan Azaltılmış Tasarım Spektral İvmesini göstermektedir. S_{DS} kısa periyot için tasarım spektral ivme katsayısı, mt ise binanın toplam kütlesine karşı gelmektedir [10] (Tablo 7);

Tablo 7- Gözönüne alınan deprem doğrultusunda ve azaltılmamış deprem yükleri altında yapının tümüne etkiyen toplam eşdeğer deprem yükü (taban kesme kuvveti) hesabı

2018 TÜRKİYE BİNA DEPREM YÖNETMELİĞİ VE AFAD DEPREM HARİTASI VERİLERİNE GÖRE DATALAR VE TABAN KESME KUVVETİ HESABI		
Bina Kütlesi (G+n*Q) m_t (Programdan)	657,67	Ton
Bina Yüksekliği h	10,50	mt
(TDBY Bolum 11.1.2) Yığma Bina Türü	a	
(TDBY Bolum 2.2) Deprem Yer Hareketi Düzeyi	DD-2	
(TDBY Bolum 3.5.1.2) Performans Hedefi	KH	
(TDBY Tablo 15.1) Bilgi Düzeyi Katsayisi	1	
(TDBY Tablo 16.1) Zemin sinifi	ZD	
(Türkiye Deprem Tehlike Haritaları Raporundan) Kısa periyot harita spektral ivme katsayısı - Ss =	1,01	
(Türkiye Deprem Tehlike Haritaları Raporundan) 1.0 saniye periyot için harita spektral ivme katsayısı - S_1 =	0,279	
(Türkiye Deprem Tehlike Haritaları Raporundan) Yatay Elastik Tasarım Spektrumu - T_L =	6	sn
(Türkiye Deprem Tehlike Haritaları Raporundan) Kısa periyot bölgesi için Yerel Zemin Etki Katsayısı - F_S =	1,096	
(Türkiye Deprem Tehlike Haritaları Raporundan) 1.0 saniye periyot için Yerel Zemin Etki Katsayısı F_1 =	2,042	
(TDBY Denklem 2.1, Tablo2.1, AFAD Raporundan) Tasarım spektral ivme katsayısı - $S_{DS} = S_S * F_S$	1,1070	
(TDBY Denklem 2.1, Tablo2.1, AFAD Raporundan) 1.0 saniye periyot için tasarım spektral ivme katsayısı - $S_{D1} = S_1 * F_1$	0,5697	
(TDBY Tablo3.1) Bina Kullanim Sinifi - BKS	2	
(TDBY Tablo3.1) Bina Onem Katsayisi - I	1,2	
(TDBY Tablo3.2) Deprem Tasarım Sınıfı - DTS	1	
(TDBY Tablo 4.1) Bina Tasiyici Sistemi; Donatısız Yığma Bina	E22	
(TDBY Tablo 4.1) Taşıyıcı Sistem Davranış Katsayısı - R =	1	
(TDBY Tablo 4.1) Dayanım Fazlalığı Katsayısı - D =	1,5	
Kubbe yüksekliği=	10,5	mt
(TDBY Tablo 3.3) (TDBY Tablo 3.3) İzin Verilen Bina Yükseklik Sınıfları - BYS =	7	
(TDBY Tablo 4.4) Eşdeğer Deprem Yükü Yöntemi kullanılabilirlik durumu;	Kullanılabilir	
TDBY 2018_Denklem 2.3_Yatay tasarım spektrumu köşe periyodu TA = 0.2*(S_{D1}/S_{DS})	0,103	sn
TDBY Denklem 2.3_Yatay tasarım spektrumu köşe periyodu TB = S_{D1}/S_{DS}	0,515	sn
Hakim doğal titreşim periyodu (Programdan) T	0,1346	sn
TBDY Denklem 4.1_Deprem Yükü Azaltma Katsayısı; T ≤ T_B ise; $R_a(T)$=D+[R/I-D]*T/T_B	1,33	
TBDY Denklem 2.2_Yatay elastik tasarım spektral ivmesi (TL=6sn); $T_A \le T \le T_B$ ise; $S_{ae}(T) = S_{DS}$	1,107	
TBDY Denklem 4.8_Yatay doğrultuda azaltılmış deprem yükleri'nin belirlenmesi için kullanılacak azaltılmış tasarım ivme spektrumu'nun belirli bir T doğal titreşim periyodu için ordinatı olan azaltılmış tasarım spektral ivmesi; $S_{aR}(T) = S_{ae}(T)/R_a(T)$	0,835	
TBDY Denklem 4.19_Gözönüne alınan (X) deprem doğrultusunda, binanın tümüne etkiyen toplam eşdeğer deprem yükü (taban kesme kuvveti) hesabı;		
Hesap; $V_{tE}^{(X)} = m_t * S_{aR}(T_p^{(X)})$ =	549,200	Ton
Şart; $V_{tE}^{(X)} \ge 0.04 m_t * I * S_{DS} * g$ =	342,808	Ton
Programdan; Ex =	531,869	Ton

Performans analizi yük kombinasyonları seçilirken, yatayda birbirine dik doğrultulardaki deprem etkilerinin birleştirilmesi ile binalarda düşey deprem etkisi dikkate alınmıştır (TBDY Bölüm 4.4, Denklemler 4.9, 4.10 ve 4.11) [10];

$E_d^H = E_d^X + 0{,}3E_d^Y$; $E_d^H = 0{,}3E_d^X + E_d^Y$ Denklem 4.9

$E_d^Z = (2/3)S_{DS} * G$ Denklem 4.10

$G+Q+0{,}2S+E_d^H+E_d^Z$ Denklem 4.11

Tablo 8- Analizde kullanılan yük kombinasyonları

Kombinasyonlar	G	EX	EY	EZ	Deprem etkisini içeren yük birleşimleri
G + Ex + 0,3Ey + 0,3Ez	1,22	1	0,3	0,3	TBDY 2018- 4.4.2_Yatayda Birbirine Dik Doğrultulardaki Deprem Etkilerinin Birleştirilmesi (Denklem 4.9); Ed(H) = ± Ed(X) ± 0,3Ed(Y) Ed(H) = ± 0,3Ed(X) ± Ed(Y) TBDY 2018- 4.4.3.2 ve 4.4.4.1_Düşey deprem etkisi (Denklem 4.10 ve 4.11); $E_d^{(Z)} = (2/3)*S_{DS}*G$ $G + Q + 0{,}2*S + E_d^{(H)} + 0{,}3* E_d^{(Z)}$ $G \pm E_d^{(X)} \pm 0{,}3E_d^{(Y)} + [0{,}3*(2/3)*S_{DS}]*G$ $G \pm 0{,}3E_d^{(X)} \pm E_d^{(Y)} + [0{,}3*(2/3)*S_{DS}]*G$
G + 0,3Ex + Ey + 0,3Ez	1,22	0,3	1	0,3	
G + Ex - 0,3Ey + 0,3Ez	1,22	1	-0,3	0,3	
G - Ex + 0,3Ey + 0,3Ez	1,22	-1	0,3	0,3	
G - Ex - 0,3Ey + 0,3Ez	1,22	-1	-0,3	0,3	
G + 0,3Ex - Ey + 0,3Ez	1,22	0,3	-1	0,3	
G - 0,3Ex + Ey + 0,3Ez	1,22	-0,3	1	0,3	
G - 0,3Ex - Ey + 0,3Ez	1,22	-0,3	-1	0,3	

--> G ± Ex ± 0,3Ey ± 0,3Ez = G ± Ex ± 0,3Ey ± 0,3*[(2/3)*S_{DS}*G] = (1+0,3*2/3*Sds)G ± Ex ± 0,3Ey = 1,22 G ± Ex ± 0,3Ey

--> G ± 0,3Ex ± Ey ± 0,3Ez = G ± 0,3Ex ± Ey ± 0,3*[(2/3)*S_{DS}*G] = (1+0,3*2/3*Sds)G ± 0,3Ex ± Ey = 1,22 G ± 0,3Ex ± Ey

--> S_{DS} = 1,107 --> G katsayısı = (1+0,3*2/3*Sds) = 1,22

Taşıyıcı sistem güvenliğinin değerlendirilmesinde yapıda hasarın (elastik ötesi şekil değiştirmelerin) küçük olması durumunda dayanıma göre değerlendirme uygun düşerken, hasarın göçmeye sebep olmayan biçimde ve kontrollü olması kaydıyla büyük olması durumunda şekil değiştirmeye göre değerlendirmenin kullanımı tercih edilir. Ancak, uygun deprem yükü azaltma katsayısı kullanarak, kuvvete dayalı değerlendirmenin kullanım sınırını genişletmek ve uygun sınır değerleri tanımlayarak şekil değiştirmeye dayalı tasarımı bu tür hasar durumunda da uygulamak mümkündür (Resim 9b, Tablo 9, 10) [5].

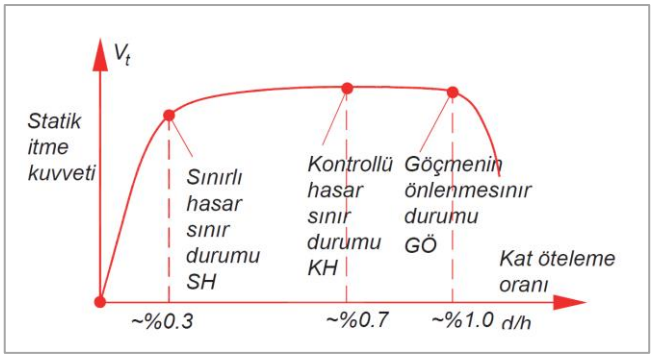

Resim 9b- Statik itme eğrisi ve sınır durumları (TRDBY Şekil 6.17)

Tablo 9- Önerilen hedef performans düzeyleri (TYDRY Tablo 6.3)

TARİHİ YAPILARIN ÖNEMİNE GÖRE SEÇİLEBİLECEK PERFORMANS DÜZEYLERİ	Ulusal öneme sahip tarihi yapı Grup I	Evrensel öneme sahip tarihi yapı	
	DD-3 (50/%50, 72 yıl) Sınırlı hasar düzeyi (SH)	DD-2 (50/%10, 475 yıl) Sınırlı hasar düzeyi (SH)	DD-3 (50/%2, 2475 yıl) Sınırlı hasar düzeyi(SH)
Yerel öneme sahip tarihi yapı Grup II	DD-3 (50/%50, 72 yıl) Kontrollü hasar düzeyi (KH)	DD-2 (50/%10, 475 yıl) Kontrollü hasar düzeyi (KH)	DD-1 (50/%2, 2475 yıl) Kontrollü hasar düzeyi (KH)
	DD-3 (50/%50, 72 yıl) Göçmenin önlenmesi düzeyi (GÖ)	DD-2 (50/%10, 475 yıl) Göçmenin önlenmesi düzeyi (GÖ)	DD-1 (50/%2, 2475 yıl) Göçmenin önlenmesi düzeyi (GÖ)

Tablo 10- Performans düzeyleri ile ilgili hesap yöntemleri ve gerilme, yerdeğiştirme sınırları (TYDRY Tablo 6.4)

Performans düzeyi	Hesap yöntemi ve sınırlar
Sınırlı hasar sınır durumu (SH)	1. Doğrusal hesap yöntemi kullanılıyor; a) Düşey yük ve azaltılmamış öngörülen deprem etkisinde bulunan hesap dayanımları aşılmıyor. b) Azaltılmamış deprem etkisinde öteleme oranı 0,3% sınırını aşmıyor.
Kontrollü hasar sınır durumu (KH)	1. Doğrusal hesap yöntemi kullanılıyor; a) Düşey yük ve Ra ≤3 ile azaltılmış öngörülen deprem etkisinde bulunan hesap dayanımları aşılmıyor. b) Azaltılmamış deprem etkisinde öteleme oranı 0,7% sınırını aşmıyor. 2. Doğrusal olmayan hesap yöntemi kullanılıyor; a) Öteleme oranı 0,7% sınırını aşmıyor. b) Malzemelerin şekil değiştirme kapasiteleri aşılmıyor.
Göçme öncesi sınır durumu (GÖ)	1. Doğrusal hesap yöntemi kullanılıyor; a) Düşey yük ve Ra ≤3 ile azaltılmış öngörülen deprem etkisinde bulunan hesap dayanımları belirli bir oranda (~1,5 katı) aşılabilir. b) Azaltılmamış deprem etkisinde öteleme oranı 1% sınırını aşmıyor. 2. Doğrusal olmayan hesap yöntemi kullanılıyor; a) Öteleme oranı 1% sınırını aşmıyor. b) Malzemelerin şekil değiştirme kapasiteleri sınırlı oranda (~1,2 katı) aşılabilir.

i. Yer değiştirmeye göre değerlendirme

Mevcut durum değerlendirmesi yapılırken yer değiştirmeler azaltılmamış deprem etkilerinden elde edilir (Taşıyıcı Sistem Davranış Katsayısı, R=1, TYDRY 2017, Tablo 10). Buna göre taşıyıcı kemerin üst noktasında gerçekleşen yerdeğiştirmeler görülüyor (Resim 10). Bu değerlere göre hesapladığımız yerdeğiştirme oraları ise, %0,7 sınır değerinin altında kalıyor. Buna göre yapı deprem etkisi altında büyük bir sorun yaşamıyor.

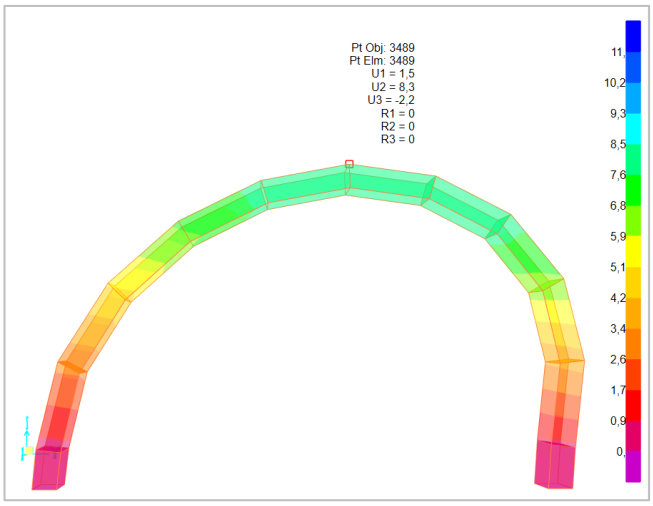

Resim 10- Y yönü ağırlıklı (G+0,3Ex+Ey+0,3Ez) yüklemesi altında maximum yerdeğiştirme kemerin üst noktasında; 8,3mm. Yer değiştirme oranı = Yatay yönde yer değiştirme miktarı/Kemerin Yüksekliği= 8,30mm/4500mm=0,18%<0,70%; sınır değerinin altında

Resim 11- Kubbeleri taşıyan mevcut kemer

ii. Dayanıma göre değerlendirme

Mevcut durum değerlendirmesi yapılırken, gerilmeler azaltılmış deprem etkilerinden elde edilir (Taşıyıcı Sistem Davranış Katsayısı, R=2,5, TYDRY 2017, Tablo 10), ancak burada riskleri daha açık görebilmek için analiz azaltılmamış deprem yüklerine göre yapılmıştır (R=1). Buna göre en büyük gerilmeler kemerde oluşuyor (Resim 9a, 11, 12, 13).

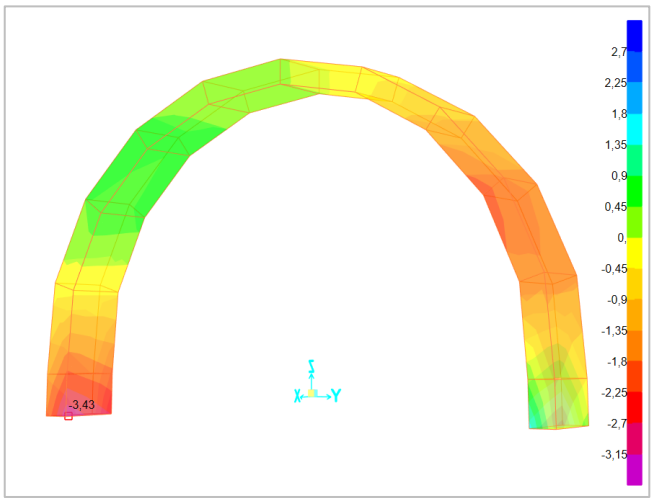

Resim 12- Y yönü ağırlıklı (G+0,3Ex+Ey+0,3Ez) yüklemesiyle kemerde oluşan (S33) basınç gerilmeleri; kemerin alt bölgesinde oluşan basınç gerilmeleri >2,55MPa; sınır değerin üstünde (Tablo 4)

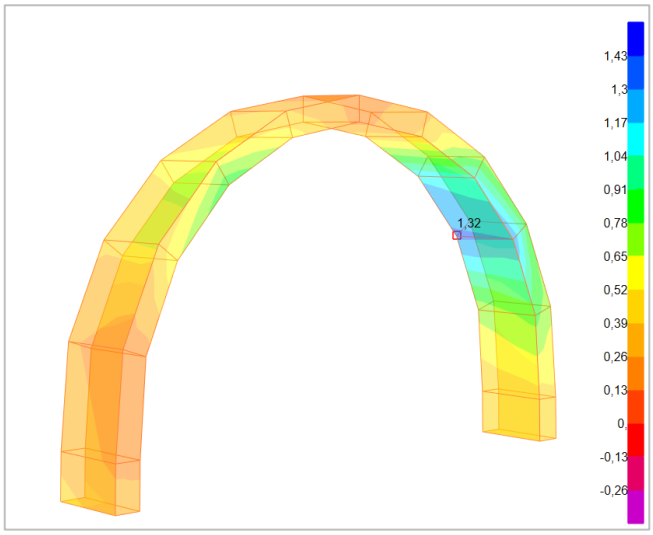

Resim 13- Y yönü ağırlıklı (G+0,3Ex+Ey+0,3Ez) yüklemesiyle oluşan (S23) kayma gerilmeleri, kemerin kayma bölgesinde oluşan gerilmeler>1,00MPa; sınır değerin üstünde (Tablo 4)

4. Taşıyıcı kemer için takviye önerisi

Taşıyıcı sistemin, yapıya etki eden düşey ve yatay yükleri zemine güvenli bir şekilde ve herhangi bir hasara sebep olmadan aktarması gerekir. Bu iletim yollarının birden daha fazla olmasının sağlanmasıyla deprem gibi dış etkiler altında yapının aniden toptan göçmesi belirli ölçüde önlenebilir [6].

Analizde taşıyıcı duvarlarda oluşan gerilmeler genel olarak sınır değerlerin altında kalmış olsa da yapının ortasında bulunan taşıyıcı kemer Y yönündeki deprem etkisine karşı riskli görünmüştür (Resim 12, 13). Bu duruma karşı mevcut kemerin altına aynı özgün malzeme kullanarak ve aynı

ölçülerde yeni bir kemer inşaa edilmesi önerilmiştir. Restorasyon Mimarları bu öneriye yeni kemerin özgün kemerden ayırt edilemeyeceği nedeniyle karşı çıkmış, mevcut kemerin başka bir şekilde, örneğin çelik konstrüksiyon ile takviye edilip edilemeyeceğini sormuştur. Buna karşı, fiziksel özellikleri çok farklı 2 ayrı malzemenin birbirleriyle uyumlu çalışmayacağı, üstelik Elastisite modülü çok yüksek olan çelik malzemenin özellikle deprem sırasında kesmetaşa zarar vereceği açıklanmıştır. Uluslararası koruma kurallarının yer aldığı 1964 tarihli Venedik Tüzüğü'nün temel ilkelerden biri, koruma müdahalelerinin tarihi yapıların belge ve estetik değerlerini gözeten bir yaklaşımla uygulanmasıdır. Geleneksel malzeme ve tekniklerle inşa edilmiş olan tarihi yapıların onarımlarının özenli olması, yapılacak müdahalelerin, plan düzenini, görünümünü, malzeme ve yapım sistemlerini değiştirmemesi istenmektedir ki bu kriteri tamamen karşılayan önerimiz uygulanmak üzere kabul görmüştür [5].

Tüzüğün bir diğer ilkesi de kullanılan tekniklerin denenmiş ve uzun erimde tarihi yapıya uygun oldukları belirlenmiş olmasını ister. Bu kritere en muhteşem örnek Mimar Sinan'ın 1573 yılında Bayezid Camii'nin mevcut kemerine yeni bir kemer ilave ederek taşıyıcı sistemi güçlendirmesidir [15, 16, 17] (Resim 14).

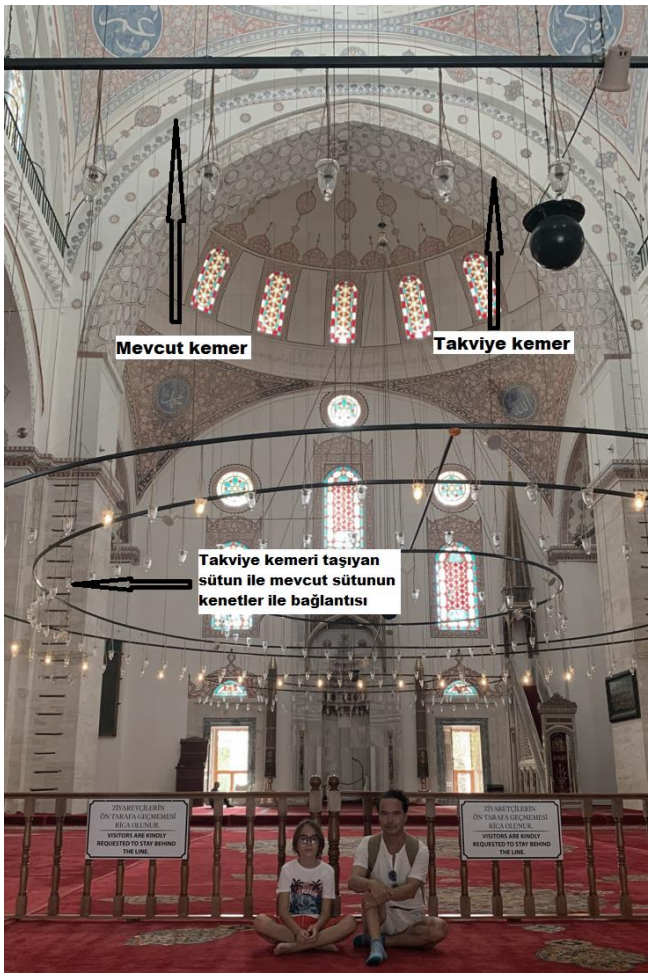

Resim 14- Mimar Sinan'ın eserlerinin adlarını veren Tuhfetü'l-Mi'mârin 'den, Bayezid Camii'nin içlerinde O'nun tarafından bir kemer inşa edilerek desteklendiği öğrenilir. Bu kaynakta "…ve İstanbul'da Merhum Sultan Bayezid'in Cami-i Şerifi bir kemer-i cedidle istihkam bulmuştur, fi sene 981 (1573/74) …" denilmektedir [15].

Diyarbakır Keçi Burcu sütun ve kemerlerine sonraki dönemde kesmetaş ile uygulanan takviye de yapılan öneriye uygun bir örnek olarak gösterilebilir [21] (Resim 14/1).

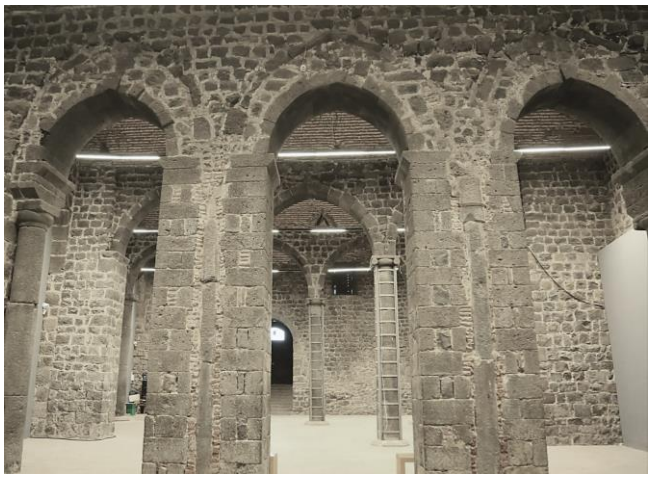

Resim 14/1- Sütunlara ve kemerlere sonraki dönemde kesmetaş ile yapılan takviye ile arka kısımda görünen günümüzde yapılmış, deprem sırasında sütunlara yarardan çok zarar verecek olan çirkin görünümlü metal takviye. Mardin Kapı'nın doğusunda yontulmuş olan kaya kitlesinin üstüne inşa edilmiş olan ve içerisinde 11 adet kemer bulunana Keçi Burcu, inşa tarihi bilinmemekle beraber 1223 yılında Mervanoğulları tarafından onarılmıştır [21].

Yapının mevcut sivri kemerine önerilen takviye kemerin yapım şartlarını aşağıdaki gibi belirleyebiliriz (Resim 15, 16);

- Takviye kemerde kullanılacak kesme taşın menşei, görünümü bozmayacak şekilde, mevcuttaki taş ile aynı olacaktır. Onarılacak veya restore edilecek eski eserin bünyesine konacak taşın, eserin yapıldığı devrin tekniğine ve Vakıflar Genel Müdürlüğü Eski Eser Birim Fiyat Tariflerine uygun olarak üretilip konması esastır [22].

- Temel kısmı, mevcut zemin örselenmeden, dikkatlice ve Mühendis nezaretinde açılacak, temel taşının boyutuna, kemer taşının genişliği olan 30cm'den az olmamak üzere, zeminin durumuna göre Mühendis karar verecektir.

- Takviye kemerin kalıbı mevcut kemerin altında sivri kemer oluşturacak şekilde m1 ve m2 merkezli 2 adet daireden oluşacak, taşların kesim yönlerinin nirengi noktası bu merkezler olacaktır (Merkezlerden çembere çizilen yarıçap çizgileri, taşların kesim yönüdür) (Resim 16),

- Takviye kemerin, mevcut kemer ile kaynaşması ve yatay yüklere karşı birlikte çalışabilmesi için, dış sırtı, mevcut kemerin iç sırtına oturacak ve derz genişliği 2-4mm'yi geçmeyecek şekilde doğal hidrolik bağlayıcı kireç harcı kullanılarak örülecektir.

Bu kurallara, İstanbul'da 1883 yılında kurulan Mülkiye Mühendis Mektebi'nde Kargir Usul'i İnşaatı dersi muallimi mimar Ali Talat'ın 1911 yılında kaleme aldığı ''Kargir İnşaat ve Eşkali'' kitabındaki kemer tarifi de eklemelidir [2];

- "Kemeri oluşturan tuğla ya da kesme taş gibi malzemelerin bir bütün olarak davranması ve dayanıklı olması için birleşim yerlerini oluşturan derzlere özel bir istikamet verilmelidir.

- Takviye kemer malzemesinin derzleri kemerin iç karnına bir düzen içinde dizilir ki bu durumda taşların köşelerinde birer dik açı meydana gelir. Bu durumda bir taşın dış sırtı, iç karında kalan sırtından daha geniş olacağından taş yerinden çıkmayacak ve sabit kalması sağlanmış olacaktır.

- Kemere verilecek şekil belirlendikten sonra kemeri oluşturan taşların gerçek boyutlu kalıplarının hazırlanması gerekir. Bunun için düz bir döşeme üzerinde birebir ölçekte kemerin iç karnı ile dış sırtı ve derz yönleri gerçekte olacakları gibi çizilir ve her taş için gereken gövde kalıpları bu şekilde elde edildikten sonra taşlara şekil verilir." [2]

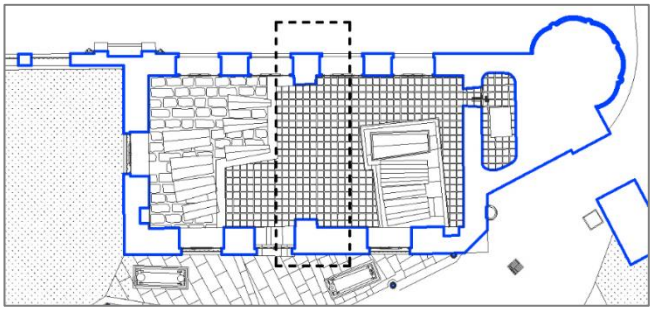

Resim 15- Kubbeleri taşıyan kemerin yerleştiği kısmın plan görünüşü

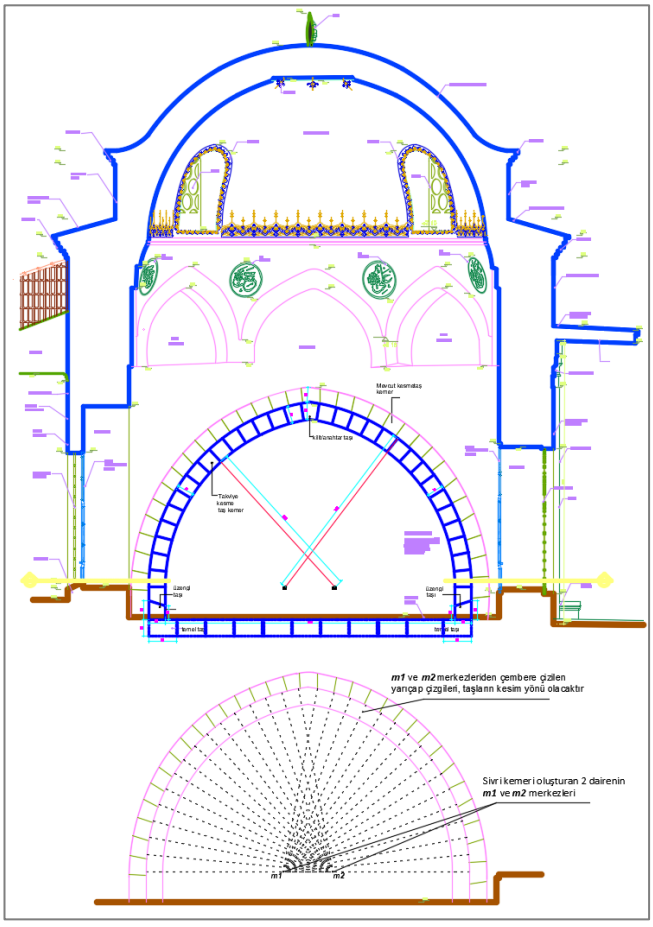

Resim 16- Mevcut sivri kemerin altına önerilen takviye kemer detay çizimleri

5. Takviye kemerin modele eklenmesi ve yapıya katkısı

Takviye kemer, mevcut kemerin hemen altına, yük iletim noktaları mevcutla kesişecek şekilde adapte edilmiştir. Malzeme özellikleri olarak tamamen aynı, ölçüleri ise mevcut kemerin taşları ile birbirine tamamen uyumludur (Resim 16a).

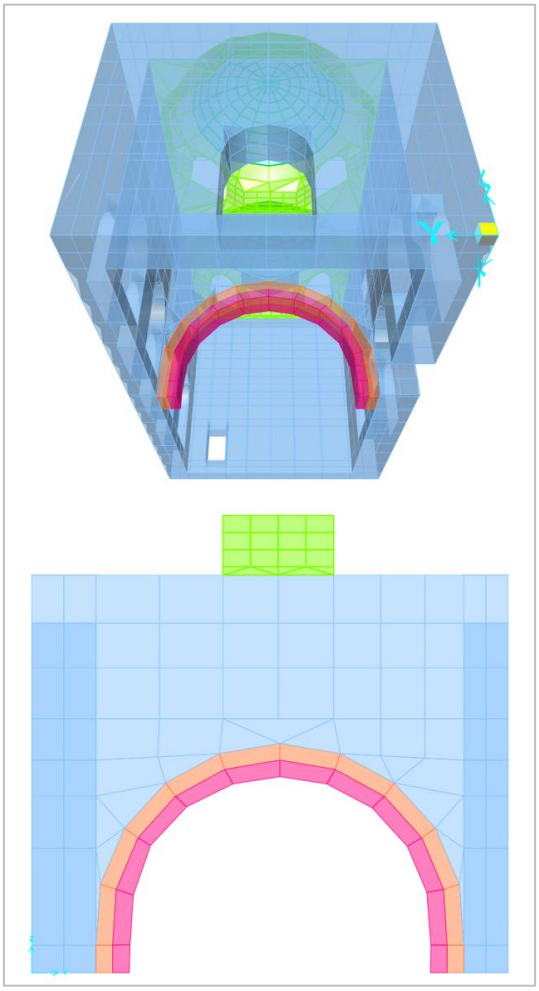

Resim 16a- İlave kemerin modele eklenmesi

Mevcut yapının modları ile takviye önerisi doğrultusunda modele eklenen kemer ile oluşan modları karşılaştırdığımızda, takviye kemerin modele eklenmesinden sadece Y yönündeki hâkim periyodun etkilendiği, X yönündeki hâkim periyodda ise önemli bir değişiklik olmadığı görülmüştür (Resim 17, 18). Bu nedenle takviye kemerin yapımıyla yapıda oluşan yer değiştirme oranları ve gerilme dağılımlarının mevcut durum ile kıyaslaması sadece Y yönü yüklemeleri için yapılmıştır.

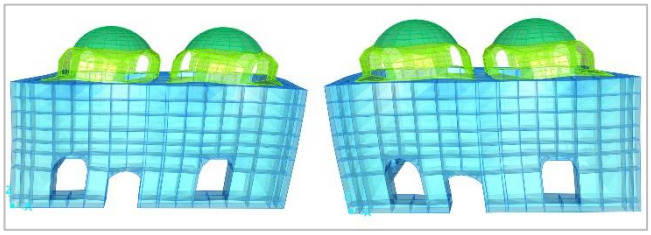

Resim 17- Solda X yönü hâkim periyod (Mod 2, T=0,13459sn) iken, sağda takviye kemer ile X yönü hâkim periyod değişmiyor (Mod 2, T=0,134sn)

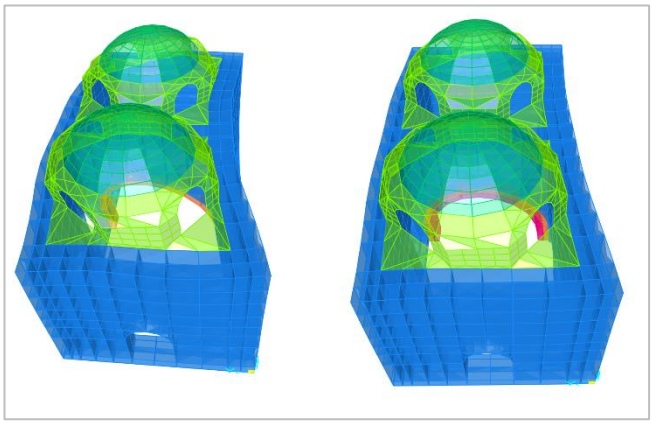

Resim 18- Solda Y yönü hâkim periyod (Mod 1, T=0,16964sn) iken, sağda takviye kemer ile Y yönü hâkim periyod azalıyor (Mod 1, T=0,15736sn)

Takviye kemerin modele eklenmesiyle kemerde, duvarlarda ve kubbelerde depremden dolayı oluşan yer değiştirme ve gerilme değerleri azalıyor (Resim 19, 20, 21, 22, 23, 24);

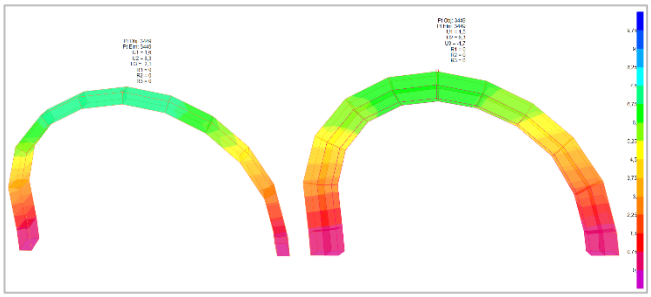

Resim 19- Solda Y yönü (G+0,3Ex+Ey+0,3Ez) yüklemesiyle kemer üst noktasında oluşan yer değiştirme yatayda 8,30mm iken, sağda takviye kemerin mevcut kemerin hemen altına aynı genişlik ve malzeme özellikleri atanarak modele eklenmesi ile yatayda 6,30mm'ye düşüyor

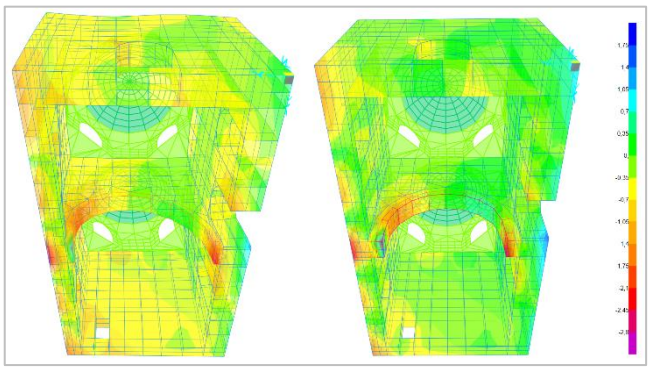

Resim 20- Solda Y yönü (G+0,3Ex+Ey+0,3Ez) yüklemesiyle kemerde oluşan en büyük (S33) basınç gerilmesi 3,48MPa iken, sağda takviye kemer ile 2,92MPa (>2,55MPa); sınır değere daha yakın

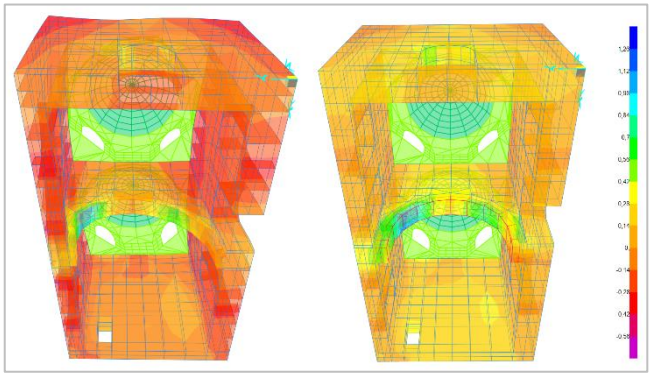

Resim 21- Solda Y yönü (G+0,3Ex+Ey+0,3Ez) yüklemesiyle kemerde oluşan en büyük (S23) kayma gerilmesi 1,47MPa iken, sağda takviye kemer ile 1,36MPa (>1,00MPa); sınır değere daha yakın

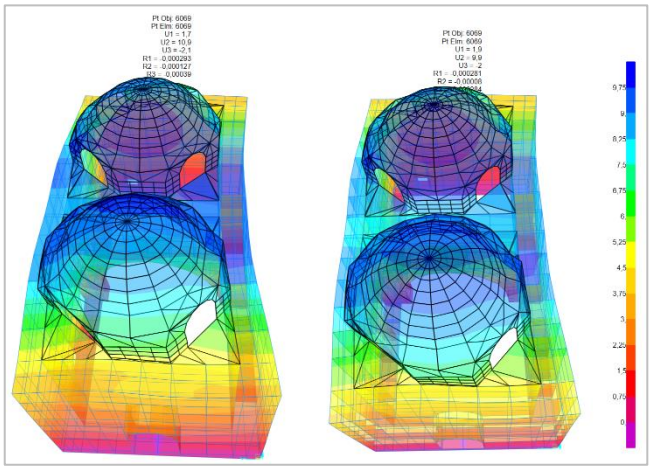

Resim 22- Solda Y yönü (G+0,3Ex+Ey+0,3Ez) yüklemesiyle duvarda ve kubbelerde oluşan yer değiştirmeler (10,9mm), sağda takviye kemer ile duvarda ve kubbelerde oluşan yer değiştirmeler azalıyor (9,9mm)

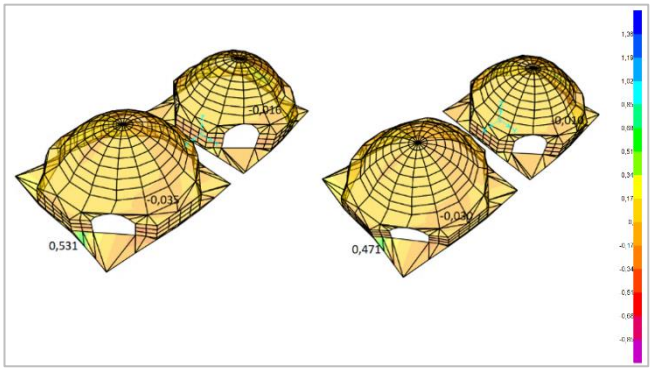

Resim 23- Solda Y yönü (Ey) yüklemesiyle duvarda oluşan S12 kayma gerilmeleri (MPa), sağda takviye kemer ile S12 kayma gerilmeleri azalıyor

6. Sonuç

1730 – 1754 yılları arasında Hekimoğlu Ali Paşa tarafından yaptırılan türbenin güçlendirilmesi için, mevcut kemerinin hemen altına bitişik olarak, aynı malzeme ve ölçülerde, mevcut kemer ile birlikte çalışacak yeni bir kemer tasarlanmış ve yapıya olabilecek katkıları gösterilmiştir. Türbenin restorasyonu sırasında uygulanmak üzere kabul gören önerimiz tarihi yapının geleceğe güvenle devrine katkı sağlayacaktır.

Tarih yapılarda müdahalelerin pek çoğu, yapıda görülen bir hasarı gidermek için yapılır. Bazı durumlarda yapının restorasyonu yapılırken, taşıyıcı sistemin düşey ve yatay yükler altındaki güvenliği incelenerek, hasar bulunmayan elemanlarda da bir sağlamlaştırma müdahalesi önerilebilir. Bir yapıda hasar olmaması, her zaman yapının yeterli taşıyıcı sistem güvenliğine sahip olduğuna işaret etmez. Mevcut durumda hasarlı olan tarihi yapıya müdahale edildiği gibi, restorasyonuna karar verilen bir tarihi yapıda hasar olmasa bile, taşıyıcı sistem güvenliğinin incelenmesi ve yetersiz bulunduğunda gerekli takviyenin yapılması önerilir [5].

Eğer yapının depremde zarar görebileceği öngörülüyorsa, gerekli takviye, "estetik değerini gözeten bir yaklaşımla, geleneksel malzeme ve teknikle, plan düzenini, görünümünü, malzeme ve yapım sistemini değiştirmeden" ve "geleneksel konumuna, kompozisyonuna, dengesine ve çevresiyle olan bağıntısına zarar gelmeyecek" [19] şekilde, yapının geleceğe güvenle devri adına ve yapı ayaktayken yapılmalıdır. Yapılacak olan müdahale yapıyı güncel şartnamelere uygun hale getirmese de onun deprem dayanımını artıracaktır.

7. Kaynaklar

[1] Ahunbay, Z., Tarihi Çevre Koruma ve Restorasyon, 2007

[2] Mülkiye Mühendis Mektebi'nde Kargir Usul'i İnşaatı dersi muallimi mimar Ali Talat, Kargir İnşaat ve Eşkali, 1911, (Koruma Akademisi Yayınları tarafından tercümesiyle yayınlandı, 2022)

[3] Tarihi Ahşap Sütunlu Camilerin Sonlu Elemanlar Analizi ile Taşıyıcı Sistem Performansının Belirlenmesi, 2010, Aslı Er Akan

[4] Durutürk G., Yalvaç Hamidiye Cami Deprem Analizi, Süleyman Demirel Üniversitesi, İnşaat Mühendisliği Anabilim Dalı, 2012

[5] Tarihi Yapılar İçin Deprem Risklerinin Yönetim Kılavuzu, İstanbul Valiliği, T.C. Başbakanlık Vakıflar Genel Müdürlüğü, 2017

[6] Celep Z., Deprem Mühendisliğine Giriş ve Depreme Dayanıklı Yapı Tasarımı, 2019

[7] Bayraktar A., Depremin Faydaları ve Depremden Korunmanın Yapı Tasarımları, 2020

[8] Bayülke N., Depremlerde Hasar Gören Yapıların Onarımı ve Güçlendirilmesi, 1984

[9] Sesigür H., Çelik O. C., Çılı F., Tarihi Yapılarda Taşıyıcı Bileşenler, Onarım ve Güçlendirme, İstanbul Bülten, 2007

[10] Türkiye Bina Deprem Yönetmeliği, 2018

[11] Ural A., Kara M. E., Kenet ve Zıvanaların Yığma Duvarların Kesme Davranışına Etkisi, 5. Tarihi Eserlerin Güçlendirilmesi ve Geleceğe Güvenle Devredilmesi Sempozyumu, 2015

[12] Kara H. G., Tarihi Yığma Yapıların Taşıyıcı Sistemleri, Güvenliğinin İncelenmesi, Onarımı ve Güçlendirilmesi, İstanbul Teknik Üniversitesi, 2009

[13] Bayülke N., Yığma Yapılar, Taş ve Tuğla, 2018

[14] Bayraktar A., Yığma Yapı Mühendisliğinin Gelişim Tarihi, 2011

[15] Eyice S., İstanbul'da Sultan II. Bayezid Külliyesi, Sanat Tarihi Araştırmaları Drg, 1990

[16] Bozdoğan M., Ovalı P. K., Özkan S., Mimar Sinan'ın "Koruma" Anlayışı Ve Günümüzde Sinan'ın Eserlerini "Koruma" Anlayışı (Edirne Örneği), 2006

[17] Dabanlı Ö., Tarihi Yığma Yapıların Deprem Performansının Belirlenmesi, İstanbul Teknik Üniversitesi, İnşaat Mühendisliği Anabilim Dalı, 2008

[18] Değirmenci İ., Sarıbıyık M., Tarihi Yapıların Güçlendirilmesinde Yenilikçi Yaklaşımlar ve FRP Malzemelerin Kullanımı, 2015

[19] Venedik Tüzüğü, 1964

[20] Can H., Ünay A. İ., Tarihi Yapıların Deprem Davranışını Belirlemek İçin Sayısal Analiz Yöntemleri, 2011

[21] Çidam, Feride Burcu, Diyarbakır Kent Dokusunun Turizm Ve Rekreasyon Kaynaklarının Peyzaj Mimarlığı Açısından Değerlendirilmesi, Keçi Burcu, 2007

[22] Kültür Ve Turizm Bakanlığı Birim Fiyat Analiz Ve Tarifleri

[23] Yıldırım S., Mahdavi A., İlki A., Erkuş B., Tonguç Y.İ., 550 Yıllık Bir Tarihi Camiinin Su Taşkını ve Deprem Risklerine Karşı Korunması, 2021

Dicle University
Journal of Engineering
https://dergipark.org.tr/tr/pub/dumf
duje.dicle.edu.tr

Araştırma Makalesi / Research Article

Mardin'in Eryeri Mahallesinde Bulunan Geleneksel Evlerin Yapısal Koruma Sorunları

The Structural Conservation Problems of the Traditional Houses in Eryeri, Mardin

Yasemin ERCAN GÜNDÜZ[1*], Mine TURAN[2], Engin AKTAŞ[3]

[1] Yıldız Teknik Üniversitesi, Mimarlık Fakültesi, mimaryaseminercan@gmail.com, ORKİD: https://orcid.org/0000-0002-6623-0955
[2] İzmir Yüksek Teknoloji Enstitüsü, Mimarlık Fakültesi, mineturan@iyte.edu.tr, ORKİD: https://orcid.org/0000-0002-7418-9577
[3] İzmir Yüksek Teknoloji Enstitüsü, Mühendislik Fakültesi, enginaktas@iyte.edu.tr, ORKİD: https://orcid.org/0000-0002-5706-2101

MAKALE BİLGİLERİ

Makale Geçmişi:

Geliş 30.04.2025
Revizyon 10.10.2025
Kabul 14.10.2025
Online 30.12.2025

Anahtar Kelimeler:

Geleneksel Mardin Evleri, yapısal hasarlar, yapım sistemleri, koruma sorunları, belgeleme

ÖZ

Mardin evleri, geleneksel yapım sistemleri ve yerel malzeme kullanımı ile Güneydoğu Anadolu Bölgesi'nin geleneksel ev tipolojisinin önemli bir parçasıdır. Zaman içerisinde kullanıcıları tarafından değişime uğrayan yapılar, yapısal hasarların onarımı aşamasında ve kullanım alanlarının kontrolsüz genişletilmesi sırasında istenmeyen müdahalelere maruz kalmaktadır. Bu tür müdahaleler yapısal koruma sorunlarına neden olmaktadır. Bu çalışma kapsamında Mardin ili Artuklu ilçesine bağlı Eryeri mahallesinde bulunan ve geleneksel yapım tekniklerini barındıran konutlar yapısal koruma sorunları çerçevesinde incelenmiştir. Alanda seçilen sekiz yığma taş yapının yapım sistemleri, malzeme kullanımları ve mevcut yapısal hasarları, yapıların geçirdiği değişim aşamaları ile belgelemiştir. Mardin ili ve çevresinde bulunan benzer yapım tekniklerini barındıran tarihi yapılar ve köyler de bu kapsamda incelenmiş, karşılaştırma çalışması yapılmıştır. Yapısal elemanların kayıpları ile sonuçlanan yıkımlar, bakımsızlık ve yapılara eklenen betonarme ekler en yaygın yapısal koruma sorunları olarak belirlenmiştir. Koruma planlaması kapsamında betonarme eklerin önlenmesi, fazla yüke sebep olan eklerin kaldırılması hususu önemlidir.

ARTICLE INFO

Article history:

Received 30.04.2025
Received in revised form 10.10.2025
Accepted 14.10.2025
Available online 30.12.2025

Keywords:

Traditional Mardin Houses, structural failures, construction systems, conservation problems, documentation

Doi: 10.24012/dumf.1687885

* Sorumlu Yazar

ABSTRACT

Mardin houses are a significant part of the traditional house typology of the Southeastern Anatolia with their traditional construction systems and use of local materials. Buildings that have been changed by their users over time are exposed to undesirable interventions during the repair phase of structural failures and the expansion of their usage areas. These intervetions cause structural preservation problems. Within the scope of this study, houses located in Eryeri neighborhood of Artuklu district of Mardin province and containing traditional construction techniques were examined within the framework of structural conservation problems. The construction systems, material usage and structural failures of eight stone masonry buildings selected in the area were documented, along with the stages of change that the structures have gone through. Historical buildings and villages with similar construction techniques in Mardin province and its surroundings were also examined in this context and a comparison study was made. Demolitions resulting in loss of the structural elements, neglect, and reinforced concrete annexes addes to the buildings are the most crucial structural conservation problems. Within the scope of conservation planning, it is important to prevent reinforced concrete additions and remove that additions that cause overload.

Giriş

Türkiye'de son 20 yıldır tartışılan, kırsal mirasın tescili ve koruma amaçlı imar planlarının hazırlanması sürecinin doğru ve planlı bir şekilde yürütülmesi üzerinde durulması gerekilen önemli konulardan birisidir. Kırsal mimarinin kent mimarisi kadar ön planda olmaması, genellikle belirli bir plan veya program olmadan inşa edilmesi ve sürekli müdahalelere maruz kalması gerek yetkililer gerekse maliklerce yeterli desteğin verilmemesi gibi çeşitli nedenler kırsal mirası korumanın önünde engel oluşturmaktadır [1].

Tarihi yapılara uygulanabilecek yapısal müdahaleler konusunda Koruma Yüksek Kurulunun belirlediği çeşitli ilke kararları vardır. Yapının koruma durumu dikkate alınarak bakım, basit onarım ve esaslı onarım gereklilikleri belirlenmektedir [2]. Tarihi yapılara deprem sonrasında müdahale edilmesi [3] ve güçlendirilmeleri [4] konuları da ilke kararlarında ele alınmıştır. Diğer yandan tarihi yapıların güçlendirilmesi konusundaki ilk kapsamlı ulusal belge olarak, Vakıflar Genel Müdürlüğünce yayınlanmış olan, deprem risklerinin yönetimi kılavuzu gösterilebilir [5]. Kılavuz farklı disiplinlerden koruma uzmanları arasında dil birliği sağlamakta; gerek yığma, gerekse ahşap yapılar için yapısal belgeleme, analiz ve müdahale süreçleriyle ilgili yönlendirmeler yapmaktadır. Acil müdahaleler olarak payanda yerleştirme, askıya alma ve sargılama tariflenmiştir. Basit onarım kapsamına cephedeki mimari öğelerin, kaplamanın, sıvanın özgüne uygun olarak yenilenmesi dahil edilmiştir. Esaslı onarım kapsamı ise her bir yapı elemanı türü için ayrıntılandırılmıştır. Ulusal ölçekteki söz konusu yapısal onarım ilkelerini ve kılavuzunu dikkate alan, ülkemizin farklı yörelerindeki geleneksel yapım sistemlerinin özgün niteliklerini, yaygın hasarlarını ve çağdaş müdahale sorunlarını dikkate alan, yöreye özel yapısal envanterin oluşturulmasını, analiz kapsamının ve müdahale türlerinin belirlenmesini yönlendiren ayrıntılı çalışmalara gereksinim vardır.

Tarihi kiliseler, manastırlar, camiler, medreseler, hanlar, hamamlar, çarşılar, çeşmeler ve geleneksel evler gibi ekonominin gelişimini ve refah düzeyini gösteren mimari eserlerin yoğun bir şekilde bulunduğu Mardin, Güneydoğu Anadolu bölgesinde Gaziantep, Şanlıurfa ve Diyarbakır'ın yanı sıra kendine özgü kentsel ve kırsal mimarisiyle öne çıkıyor [6]. Özgün konut dokusunun günümüze kadar korunabildiği nadir kentlerden biri olan Mardin'de görülen eğimli yerleşim sistemi kırsal alanlarda da karşımıza çıkmaktadır [7].

Mardin'in Artuklu ilçesine bağlı Eryeri mahallesinde yer alan evler, geleneksel Mardin evlerinin yapım sistemlerinden, malzeme kullanımlarından, yörenin kültüründen ve tipolojisinden etkilenerek şekillenmiştir. Ölçek bakımından Mardin evlerine kıyasla daha küçük olmaları sebebiyle mekan çeşitliliğinde ve taş işçiliğinde geleneksel Mardin evlerinin izleri nadir olarak görülse de bölgede incelenmek üzere seçilen tüm evler Mardin evleri ile aynı yapım tekniği ve malzeme ile inşa edilmiştir [8]. Bölgede oluşturulan ortak mimari kültür zaman içerisinde değişime uğramıştır ve uğramaya devam etmektedir. Yapısal hasarların incelendiği evler günümüze ulaşmış olsada istenmeyen müdahaleler sonucunda yapılar bütünlüğünü ve özgünlüğünü kaybetmiştir. Özellikle betonarme ilaveler ile yapıların taşıdığı yük miktarının, herhangi bir statik hesaplama yapılmadan, kontrolsüzce arttığı görülmektedir. Kırsal alanlarda koruma sorunlarına bir örnek olan Eryeri, yok olmakta olan bir kültür mirasının korunması ve yaşatılması adına önem teşkil etmektedir.

Evlerin İncelenmesi

Eryeri, Mardin şehir merkezine 7 km uzaklıkta yer alan yakın bir köydür. Günümüze kadar Mardin'in mimari mirası ile ilgili çok sayıda çalışma yapılmış olmasına rağmen Eryeri ile ilgili bilimsel bir çalışma bulunmamaktadır. Geleneksel Mardin Evleri'nin izlerini taşıyan Eryeri'nde daha önce herhangi bir restorasyon çalışması yapılmamıştır. Kendi haline bırakılmış bu köyün evleri niteliksiz betonarme ilavelerle sarmalanmıştır. Bu gibi koruma sorunları sebebiyle evlerin özgünlükleri ve bütünlükleri tehdit altındadır.

Geleneksel Eryeri Evleri özelinde hazırlanan çalışmada koruma sorunları strüktürel bağlamda incelenip, temel sebepler yapılan karşılaştırmalı çalışmalar ile belirlenmiştir. Bu kapsamda yapılan ilk koruma çalışması olması sebebiyle çalışma Mardin ve çevre köyler için önemlidir.

Çalışma kapsamında kütle kompozisyonları, yapısal elemanlar, yapısal değişiklikler, yapım aşamaları ve yapısal hasarları içeren envanter fişleri hazırlanmıştır. Şekil 1, 2, 3 ve 4 'te 3 numaralı ve 4 numaralı evlerin incelenmesi sırasında tamamlanan envanter fişleri yer almaktadır.

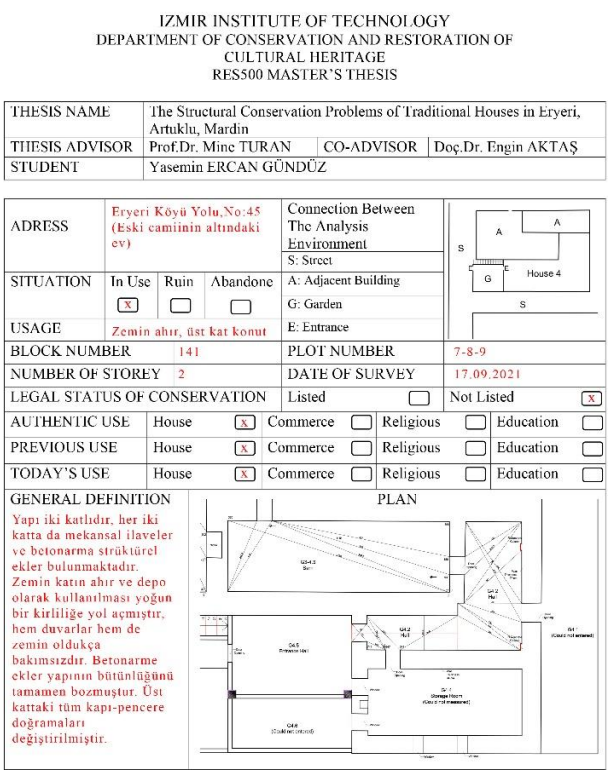

IZMIR INSTITUTE OF TECHNOLOGY
DEPARTMENT OF CONSERVATION AND RESTORATION OF CULTURAL HERITAGE
RES500 MASTER'S THESIS

THESIS NAME	The Structural Conservation Problems of Traditional Houses in Eryeri, Artuklu, Mardin		
THESIS ADVISOR	Prof.Dr. Minc TURAN	CO-ADVISOR	Doç.Dr. Engin AKTAŞ
STUDENT	Yasemin ERCAN GÜNDÜZ		

ADRESS	Eryeri Köyü Yolu,No:45 (Eski camiinin altındaki ev)			Connection Between The Analysis Environment S: Street	A, A, S, C, G, House 4, S
SITUATION	In Use [X]	Ruin [ ]	Abandone [ ]	A: Adjacent Building	
				G: Garden	
USAGE	Zemin ahır, üst kat konut			E: Entrance	
BLOCK NUMBER	141			PLOT NUMBER	7-8-9
NUMBER OF STOREY	2			DATE OF SURVEY	17.09.2021
LEGAL STATUS OF CONSERVATION				Listed [ ]	Not Listed [X]
AUTHENTIC USE	House [X]	Commerce [ ]	Religious [ ]	Education [ ]	
PREVIOUS USE	House [X]	Commerce [ ]	Religious [ ]	Education [ ]	
TODAY'S USE	House [X]	Commerce [ ]	Religious [ ]	Education [ ]	

GENERAL DEFINITION

Yapı iki katlıdır, her iki katta da mekansal ilaveler ve betonarma strüktürel ekler bulunmaktadır. Zemin katın ahır ve depo olarak kullanılması yoğun bir kirliliğe yol açmıştır, hem duvarlar hem de zemin oldukça bakımsızdır. Betonarme ekler yapının bütünlüğünü tamamen bozmuştur. Üst kattaki tüm kapı-pencere doğramaları değiştirilmiştir.

PLAN

Şekil 1. Envanter fişinin birinci sayfası

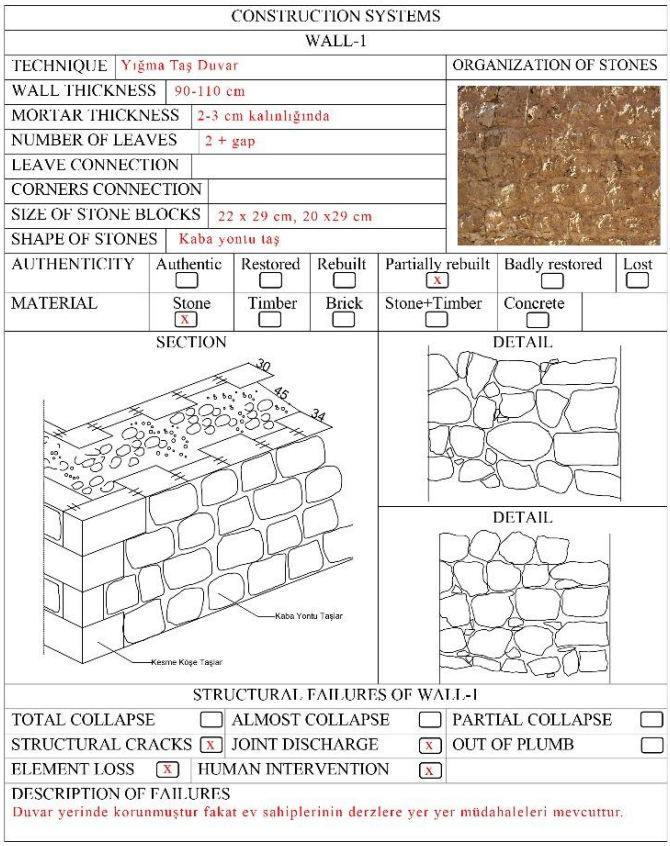

Şekil 2. Envanter fişinin ikinci sayfası

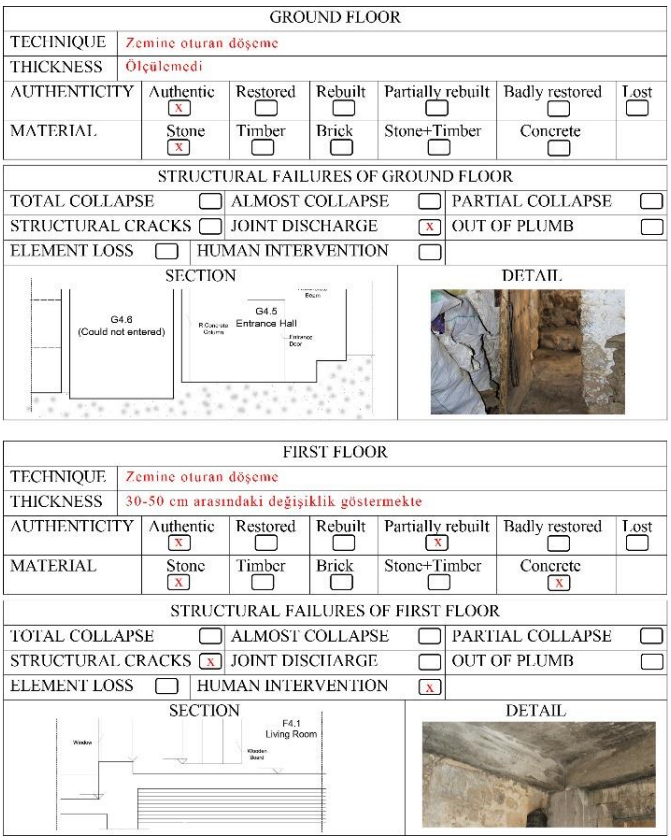

Şekil 3. Envanter fişinin üçüncü sayfası

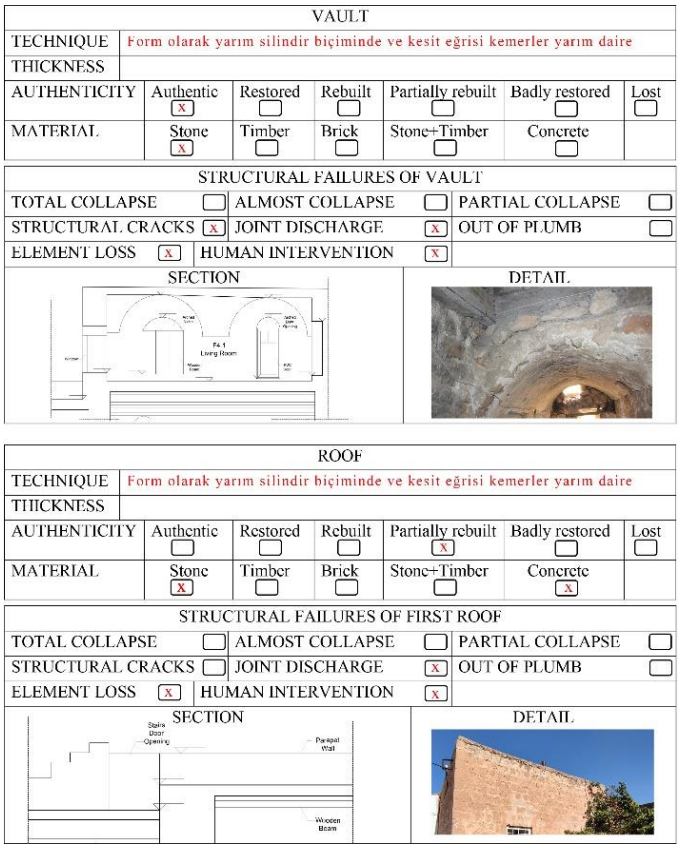

Şekil 4. Envanter fişinin dördüncü sayfası

Envanter fişlerinin yanı sıra yapılan malzeme ve yapım tekniği analizleri sırasında kullanılmak üzere üç boyutlu görselleştirme çalışmaları hazırlanmıştır. Yapıların tüm detayları incelenmiştir, belirli aralıklarla gerçekleştirilen arazi çalışmaları sonuçları değerlendirilmiştir. Çalışma sonunda seçilen yapılar hem kendi aralarında hem de çevre köylerde tespit edilen benzer yapılar ile karşılaştırılmıştır.

Şekil 5'te işaretlendiği üzere, çalışma kapsamında incelenmiş sekiz evden altısı su kanalının doğusunda ve diğer ikisi su kanalının batısında yer almaktadır.

Şekil 5. Çalışma alanı ve evlerin konumlanışı.

1 Numaralı Ev

1 numaralı ev iki katlı yığma taş bir yapıdır ve katların birbirinden bağımsız girişleri vardır: Zemin katın girişi güneydoğuda, birinci katın girişi ise kuzeydoğudadır. Arazinin oldukça eğimli olmasından kaynaklı olarak Şekil

6'da görüldüğü üzere güney ve batı cephesinden bakıldığında iki katlı, kuzeyden ve doğudan bakıldığında ise tek katlı olarak görülmektedir.

Şekil 6. 1 numaralı ev.

Şekil 7'de birinci kat planı yer verilen 1 numaralı ev, zemin katta bir oda ve birinci katta üç odadan oluşur: G1.1, F1.1, F1.2 ve F1.3. G1.1 çatı örtüsü beşik tonozdur. F1.1, evin ana yaşam alanıdır ve Şekil 8'de F1.1'in çatısının tamamen çöktüğü görülmektedir. Birinci katın duvarının zemin katın dış yüzeyinden geriye doğru çekilmiş olması evin iki katının farklı yapım evrelerine işaret eder. Zemin katta beşik tonoz ve birinci katta ahşap tavan örtü olmak üzere iki farklı üst örtü bulunduğu görülmektedir. Yapının taşıyıcı duvarları 90-100 cm kalınlığındadır. Duvarlar kaba yontma taşlar ve harçlı moloz bir çekirdekten oluşmaktadır. Tüm taşlar 2-3 cm kalınlığında harçla birleştirilmiş ve dış duvarlar sıvasızdır.

1 numaralı ev üç farklı yapım dönemi sunar: Birinci dönemi kütlenin tek katlı olarak inşa edilmesidir. Birinci katın, zemin kattaki duvarlara benzer yapım teknikleriyle ancak ahşap tavan üst örtü gibi farklı taşıyıcı elemanlarla ilavesi ikinci dönemde yapılmıştır. Üçüncü ve son dönem ise, yapıya bitişik olarak inşa edilen tandır ve kümes gibi bölümlerin ve birinci kattaki bölme duvarların ilavelerini kapsar.

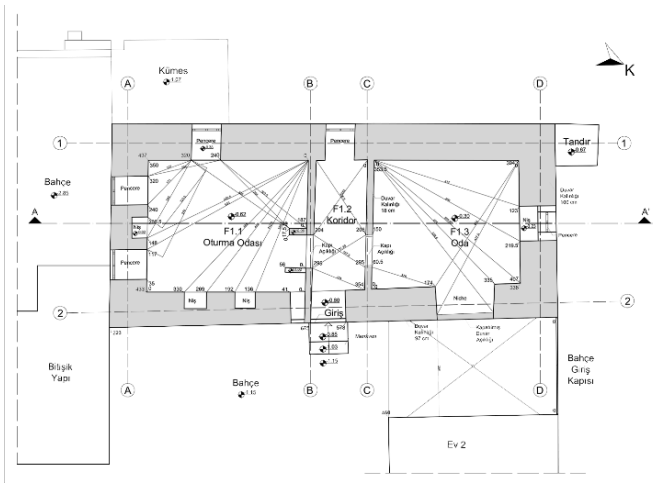

Şekil 7. 1 numaralı evin birinci kat planı.

Yapısal koruma sorunları açısından detaylı olarak incelendiğinde; 1 numaralı evde acil müdahale gerektiren ciddi yapısal problemler var. İlk hasar F1.1'deki çatının tamamen çökmesidir. Bu oda tüm hava koşullarına açıktır ve bu durum daha fazla yapısal hasara sebep olacaktır. Öte yandan, zemin kat ile aynı dönemde inşa edilmediği anlaşılan birinci katın sonraki dönemlerde yapıya ilavesi, zemin katın özgün beşik tonoz örtüsüne ekstra yük binmesine sebep olmaktadır. Herhangi bir mühendislik hesaplaması yapılmadan yapılan bu ilaveler beşik tonoz örtüde veya bu örtüyü taşıyan yığma duvarlarda yapısal çatlaklar gibi olası hasarlara yol açabilir.

Şekil 8. 1 numaralı evin F1.1 odası ve çöken çatısı.

2 Numaralı Ev

2 numaralı ev iki katlı yığma taş bir yapıdır. Şekil 9'da yer alan giriş kat planında yer aldığı üzere 1 numaralı ev ile ortak L şeklinde büyük bir bahçesi vardır. Şekil 10'da görülen sivri kemerle taçlandırılmış kapı bu bahçenin ana giriş kapısıdır. Giriş kapısından girildiğinde 1 numaralı ev doğuda, 2 numaralı ev batıda yer alır. Evin iki katı bağımsız girişlere sahiptir. Zemin katın girişi güney cephesinde olup, aynı cephenin doğu tarafında birinci kata ulaşmak için bir merdiven bulunmaktadır.

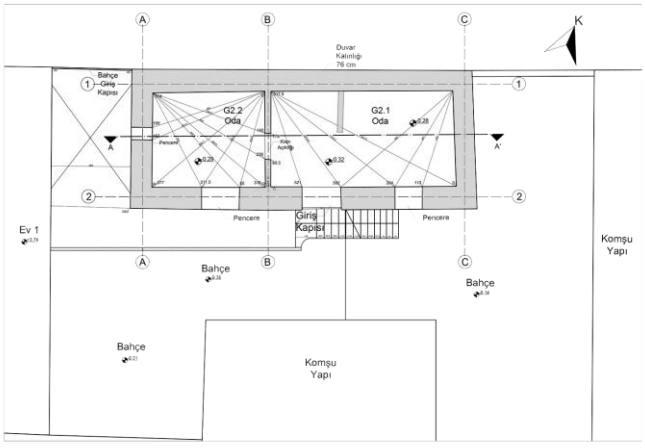

Şekil 9. 2 numaralı evin giriş kat planı.

2 numaralı evin düşey yapı elemanları ağırlıklı olarak 70-75 cm kalınlığındaki taşıyıcı duvarlardır. 1. Tip duvar olarak sınıflandırılan bu duvarlar, dış yüzeyde çeşitli küçük moloz taşlardan ve harçlı moloz çekirdekten oluşmaktadır. Tüm taşlar harçla birleştirilir ve harç kalınlığı 2 cm civarındadır. Evin zemin katının iç duvarlarındaki sıva ve boya tabakaları, duvarlardaki bozulmalar sayesinde gözle görülmektedir. Şekil 11'de görüldüğü üzere sıvanın kalınlığı 3 cm civarındadır. Duvarların dış yüzeyleri sıvasızdır ve cephede

yapılan harç onarım tadilatları sırasında harç taşların üzerine bilinçsizce yayılmıştır.

Şekil 10. 2 numaralı ev ve bahçe giriş kapısı.

Şekil 11. 2 numaralı evin duvar harç ve sıva katmanları.

İki farklı yapım dönemi görülür. İlk dönem, yapının yığma taş duvarlar ve çapraz tonoz ile örtülü zemin kat ve ahşap tavan ile örtülü birinci kat olarak inşa edilmesini içerir. Birinci katın ahşap üst yapısının özgünlüğü tartışılır. Taşıyıcı elemanlar patinalıdır ancak yapım tekniği özgün görünmemektedir. Birinci kata erişim için kullanılan merdiven de özgün değildir. Bu iki belirsiz durum sebebiyle birinci katın sonradan ilave edilmiş olma olasılığı yüksektir. Zemin katta ve birinci katta yer alan tuğla yığma duvar şeklinde inşa edilen bölme duvarların ilavesi ikinci dönemde yapılmıştır.

Yapısal koruma sorunları açısından detaylı olarak incelendiğinde acil müdahale gerektiren yapısal hasarlar görülmektedir. Özellikle giriş kat duvarlarında harçlarının boşaldığı ve tonoz örtünün yapısal çatlakları görülmektedir.

3 ve 4 Numaralı Evler

Şekil 12'de yer alan üç boyutlu görselleştirme çalışmasında 3 numaralı ve 4 numaralı evler yer almaktadır. Sol kısımda yer alan tek katlı ve üst örtüsü olmayan yapı 3 numaralı evdir. Sağ kısımda yer alan ve birbirinden bağımsız iki farklı kat girişleri bulunan yapı ise 4 numaralı evdir. Bu evler bitişik nizamlıdır ve Şekil 13'te yer alan giriş kat planında G3-4.3 olarak adlandırılan ortak bir mekana sahiptirler.

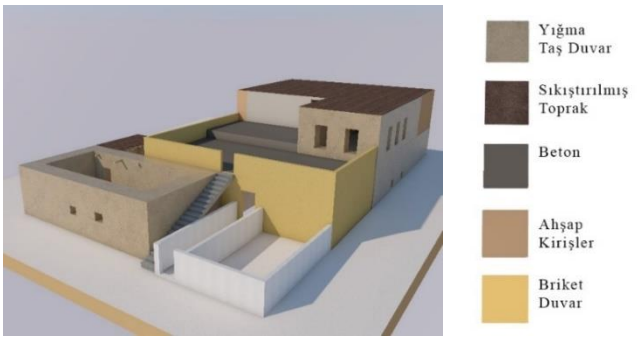

Şekil 12. 3 ve 4 numaralı evlerin üç boyutlu malzeme görselleştirme çalışması.

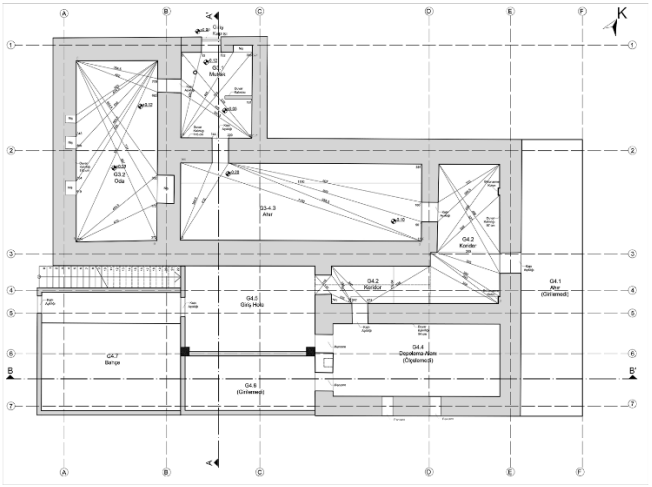

Şekil 13. 3 ve 4 numaralı evlerin giriş kat planı.

3 numaralı ev iç ve dış yüzeyleri sıvalı yığma taş duvarlar ile inşa edilmiştir. Duvar kalınlıkları yaklaşık 100 cm'dir. Evin girişi kütlenin kuzey kısmındadır ve üç odadan oluşmaktadır. Şekil 14'te boyutları yaklaşık 8,34 m x 3,72 m olan ve yaşam alanı olarak kullanılan oda görülmektedir. Bu evde mutfak veya tuvalet için ıslak hacim mevcut değildir.

Şekil 14. 3 numaralı ev ve yıkılan üst örtüsü.

4 numaralı ev içeride sıvalı, dış cephelerde sıvasız olacak şekilde kalınlıkları 80-95 cm aralığında olan yığma taş duvarlardan oluşmaktadır. Duvarların kalınlıklarının birbirinden farklı olması, bu iki bitişik nizam evin inşa dönemlerinin farklı olmasına dair bir ipucu verebilir.

3 ve 4 numaralı evler dönemsel eklere sahiptir. Özelikle 4 numaralı ev kütle kompozisyonunu değiştiren üst kat ilavesi, beton kolon ve kirişler gibi yapısal elemanların ve mimari elemanların eklenmesi gibi değişikliklere sahiptirler. 3 numaralı ev uzun yıllar önce terkedilmiştir. Sahipleri bu evi terk ettikten sonra bazen depo bazen de hayvanlar için ahır olarak kullanmıştır. Kullanım süresince duvar ilaveleri yapılmıştır fakat günümüze sadece yıkıntıları ulaşmıştır. Yapının üst örtüsü 1 ve 2 numaralı odalarda tamamen çökmüştür ve her türlü hava koşuluna açıktır.

4 numaralı evin yapısal aşamaları, kullanılan malzemelerin farklı olması ile çok net bir şekilde okunmaktadır. Şekil 15'te yer alan güney cephesi kütle kompozisyonu olarak üç ana evreye sahiptir. Birinci dönem yığma taş duvarlı, tonoz üst örtülü, kemerli pencereleri ile iki katlı kütlenin inşa edildiği dönemdir. İkinci dönem ilavesi olarak betonarme taşıyıcı sistem ile ilave edilen ön kısımdır. Son dönem de ise üst kata erişimi sağlayan merdivenin değişimi, ön kısma bahçe duvarı örülmesi gibi ilaveler görülür.

Şekil 15. 4 numaralı yapının güney cephesi.

Yapısal koruma sorunları açısından detaylı olarak incelendiğinde; 3 numaralı yapının iki odasının da çatısı çökmüştür. Bu alan, çatı kaplamalarının kaybı nedeniyle tüm olumsuz hava koşullarına maruz kalmıştır. Yığma taş duvarlarda şakulden kayma görülmüştür. 4 numaralı evde yalnızca küçük çatlaklar görülmektedir. Bunlar dışında gözle görülür yapısal hasar mevcut değildir fakat yapıya gelen ekstra yükler önemli yapısal sorunlara sebep olabilir.

5 Numaralı Ev

5 numaralı ev iki katlı yığma taş bir yapıdır. Kuzeydoğusunda geniş bir avlusu vardır (Şekil 16). Zemin katın girişi güneydoğuda, birinci katın girişi kuzeydoğudadır. Birinci katta, ana kapının hemen karşısında bir giriş kapısı daha bulunmaktadır. Şekil 17'de arazinin eğimli yapısı görülmektedir. Yapı zemin katta bir oda ve birinci katta üç odadan oluşur.

Yapıdaki düşey yapı elemanlar zemin kattaki 90-100 cm kalınlığındaki taşıyıcı duvarlardır. Dış yüzlerde çeşitli boyutlarda kaba yontma taşlardan ve harçlı moloz çekirdekten oluşmaktadır. Tüm taşlar harçla birleştirilmiştir ve harç kalınlığı 2-3 cm civarında olup duvarların dış yüzeyleri sıvasızdır.

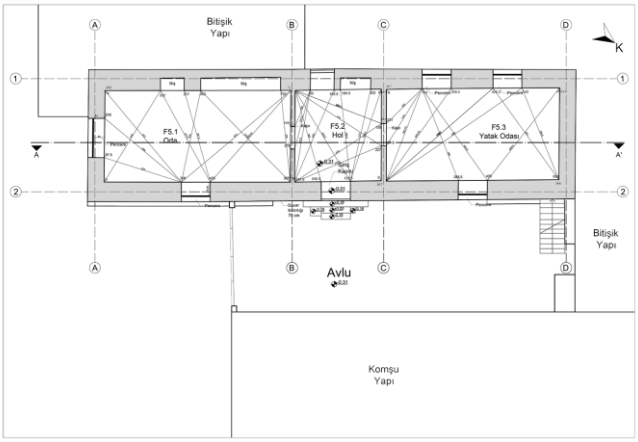

Şekil 16. 5 numaralı evin birinci kat planı.

Şekil 17. 5 numaralı evin kuzeydoğu cephesi.

5 numaralı yapı birinci katın eklenmesi ile ikinci bir yapım dönemine işaret eder. Bu değişime işaret eden iki iz vardır. İlk iz iki katın duvar kalınlık farklarıdır. Zemin katta 90-100 cm kalınlığında olan duvarlar ve birinci katta 76 cm kalınlığındadır. İkinci iz, Şekil 18'de yer alan taşıyıcı elemanlarındaki farklılıktır. Zemin kat beşik tonoz ile örtülürken, birinci kat betonarme örtü sistemine sahiptir. Bu verilere ek olarak zemin kat ile birinci kat arasında bir düşey sirkülasyon elemanı bulunmamaktadır. Her iki bölümün giriş kapıları ayrıdır.

5 numaralı ev üç farklı aşama sunar: İlk aşama, kütlenin yığma taş duvarlar ve beşik tonoz örtü ile tek katlı olarak inşa edilmesidir. İkinci aşama, üç odadan oluşan birinci katın eklenmesidir. Bu katta bulunan duvarlar zemin kattakine benzer şekilde yığma taş duvarlar ile örülmüştür fakat betonarme taşıyıcı elemanlarının bulunması açısından farklılaşmaktadır. Üçüncü ve son aşama, beton merdiven yapılması, teras çatıdaki korkuluk duvarlarının, bahçe duvarlarının ve metal bahçe kapısının eklenmesini kapsar. Bu aşamada yapısal ilaveler yapılmamıştır.

Yapısal koruma sorunları açısından detaylı olarak incelendiğinde acil müdahale gerektiren ciddi yapısal hasarlar yoktur. Birinci katın betonarme ilaveleri, zemin katın beşik tonoz ve yığma duvarlarına ekstra yük getirmiştir. Herhangi bir mühendislik hesabı yapılmadan yapılan bu ilaveler, gelecekte beşik tonoz veya yığma duvarlarda yapısal hasarlara yol açabilir.

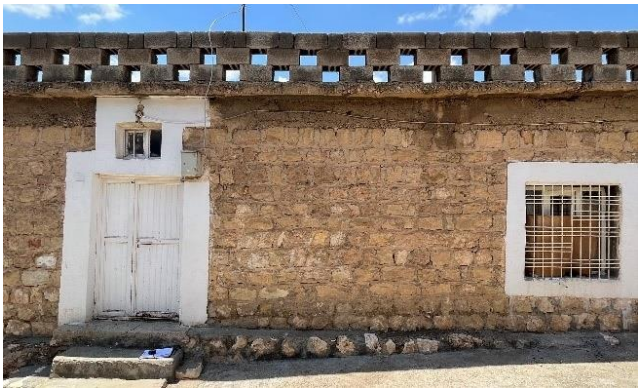

Şekil 18. Birinci katın ek çizgisi ve betonarme üst örtüsü.

6 ve 7 Numaralı Evler

6 ve 7 numaralı evler ortak bir eyvanın güneyinde ve kuzeyinde konumlanmıştır. Şekil 19'da görülen ana giriş kapısından ulaşılan eyvanın üzeri beşik tonoz ile örtülüdür. 6 numaralı ev tek katlı ve 7 numaralı ev iki katlıdır.

Şekil 19. Güneydoğu cephesi ve eyvanın giriş kapısı.

Şekil 20'de kat planı verilen 6 numaralı ev dört bölümden oluşur. İki bölüm beşik tonoz ile örtülüdür. Düşey yapısal elemanları, esas olarak 90-110 cm kalınlıklarındaki taşıyıcı duvarlardır. Duvarlar dış yüzeylerinde çeşitli boyutlarda kaba kesme taşlar ve harçlı moloz çekirdekten oluşmaktadır. Tüm taşlar 2-3 cm kalınlığında harçla birleştirilmiştir. Duvarların iç yüzeylerine kireç sıva uygulanmıştır. Dış yüzeylerinde ise yer yer onarımlarda kullanılan kireç sıva izleri görülmektedir.

7 numaralı ev, sahipleri tarafından uzun zamandır kullanıma kapatıldığı için detaylı inceleme yapılamadı. Birbirinden bağımsız iki kattan oluşan evde girişler yapının batı cephesinde yer alır. Zemin kat iki odadan oluşurken yapıya sonradan ilave edilen birinci katta üç oda bulunmaktadır. 12 basamaktan oluşan bir taş merdiven, 6 numaralı evin damına ve 7 numaralı evin birinci katına çıkar. Dönem eki olan birinci kat, briket yığma duvarlara sahiptir. Zemin katın üst örtüsü beşik tonoz, birinci katın üst örtüsü ise ahşap tavan döşemedir. Yapının düşey yapısal elemanları yığma taş duvarlardır. Zemin katın doğu duvarının kalınlığı 103 cm'dir. Pencere açıklığından görüldüğü kadarıyla içeride başka duvarlar vardır fakat ölçülememiştir. Bazı bölümlerde iç duvarlarda kireç sıva ve boya görülmektedir. Duvarlarının dış yüzeyleri sıvasızdır.

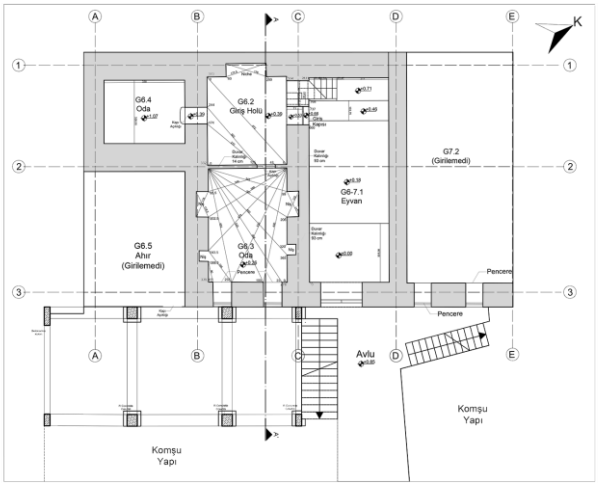

Şekil 20. 6 ve 7 numaralı evlerin giriş kat planı.

6 numaralı evdeki ana değişiklik, güneyde iki odanın eklenmesidir. Bu iki odalı eklenti, Şekil 21'de görüldüğü gibi tavan yükseklik farkından çok net olarak anlaşılmaktadır.

Şekil 21. 6 numaralı evin ek kısımları.

7 numaralı evdeki en büyük değişiklik, birinci katın eklenmesidir. Taşıyıcı duvarlar zemin katta taş yığma, birinci katta briket yığmadır. Zemin kat beşik tonoz ile örtülüyken, birinci kat ahşap tavan ile örtülüdür. Zemin katın genişliği 5,21 metre civarında iken birinci katın genişliği yaklaşık 3,7 metredir. Bu farklılık kat ilavesi sebebiyle zemin katın tonoz üst örtüsünün beklenmeyen bir yük ile karşılaşması gibi başka bir yapısal sorunu tartışmaya açmaktadır. Bir diğer önemli konu, 6 numaralı ve 7 numaralı evlerin ortak alanı olan evyanın üst örtüsü olan tonozun bir

bölümünün üst kata erişmek amacıyla eklenen merdiven sebebiyle yapısal müdahaleye uğramasıdır. Şekil 22'de görüldüğü gibi hem merdiven tavan yüksekliğinin standart boyutlardan oldukça kısa olması hem de düzensiz bir biçimde inşa edilmesi gibi ipuçları merdivenin yapıya sonradan ilave edildiğini kanıtlayabilir. Merdiven açıklığı için gerekli alanın özgün tonoz yapısını deforme ederek sağlanması hem malzeme eksikliğine hem de yapısal hasarına neden olmuştur.

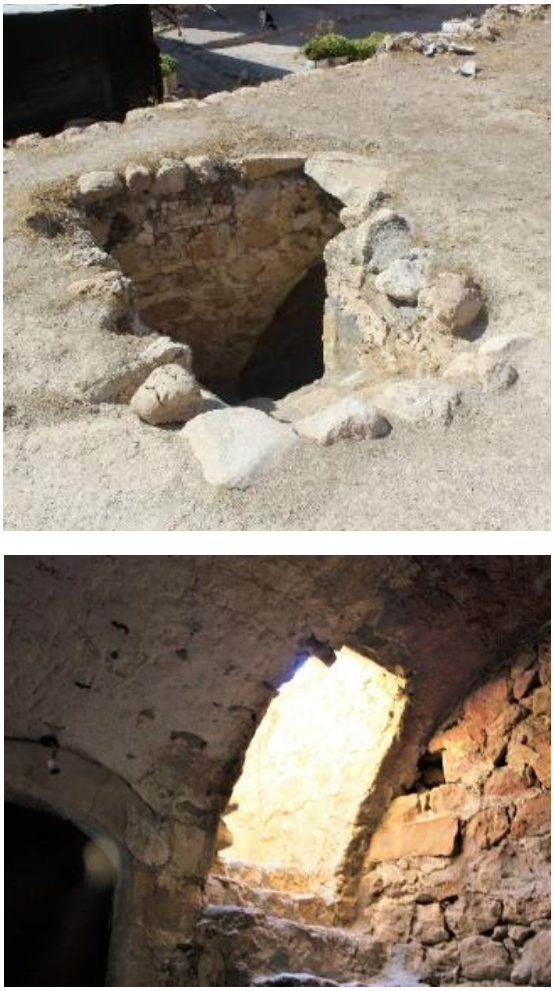

Şekil 22. Merdivenin damdan ve eyvandan görünüşü.

Yapısal koruma sorunları açısından detaylı olarak incelendiğinde 6 numaralı yapının ilave kısımları olan G6.4 ve G6.5'in çatısı kısmen çökmüştür. Çatının çökmesinin ana nedeni çatının uygun yapısal elemanlarla desteklenmemiş olmasıdır. Bir diğer önemli neden ise bakımsızlık ve sismik faaliyetlerin yaratabileceği hasarlar olabilir. Yapı yığma taş duvarların alt kotlarında oluşan derz boşlukları dışında iyi durumdadır. Derz boşalmalarının olası nedeni, yapıların doğu cephesi olan ön cephesine eklenen beton döşeme nedeniyle artan rutubettir.

7 numaralı evin yapısal sorunları beşik tonozun merkezine uygulanan kütle ilavesinin yükü nedeniyle ilerleyen yıllarda ortaya çıkabilir. Binaya gelen bu fazladan yük, çökme, yapısal çatlaklar gibi önemli yapısal sorunları çıkarabilir. Birinci katta bulunan iki odanın çatısı tamamen çökmüştür. Yapı, tahribatlar ve derin çatlaklar nedeniyle zayıf olarak değerlendirilmektedir.

8 Numaralı Ev

8 numaralı ev Şekil 23'te yer alan giriş kat planında görüldüğü üzere büyük bir avlu ve iki farklı bölümden oluşan iki katlı bir kompleks yapıdır. Avlunun kuzeybatısında ahır ve kümes alanını ve kuzeydoğusunda beşik tonoz ile örtülü yaşam alanları bulunmaktadır (Şekil 24). Yapının zemin katındaki düşey yapı elemanları 70-80 kalınlığındaki taşıyıcı duvarlardır. Dış yüzeyde çeşitli büyüklükteki taşlardan ve harçlı moloz çekirdekten oluşmaktadır. Taşlar arasında 1-2 cm kalınlığında harç görülmektedir. Duvarların dış yüzeyleri sıvasızdır.

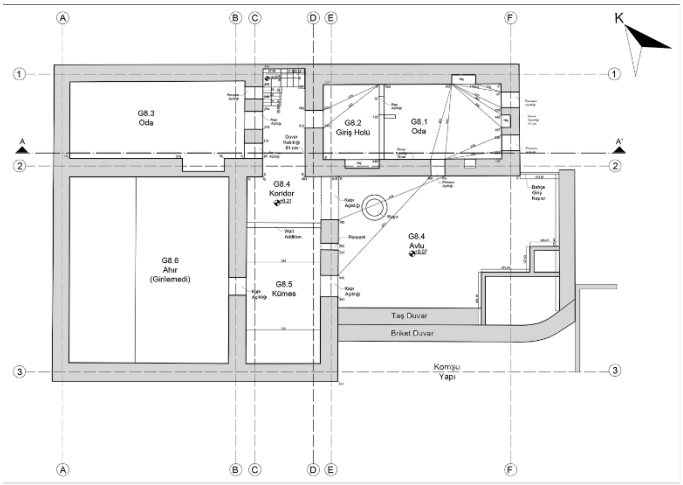

Şekil 23. 8 numaralı evin giriş kat planı.

Şekil 24. 8 numaralı ev ve avlusu.

Yapının ana değişikliği, merdivenleri ile birinci katın ve takibinde ikinci katın eklenmesidir. Ek bölümlerin duvarları briket yığma duvar olarak yapılmıştır. Birinci katın batı cephesinin dış duvarı zemin kat duvarıyla aynı eksende değildir. Bu durum duvar yüklerinin duvarlara değil tonoza aktarılmasına neden olur. Parapetin taş cinsi zemin kattan farklıdır ve bu farklılık evin yapısal bütünlüğünü bozmaktadır.

8 numaralı ev taş duvarlar ve beşik tonozlarla oluşan zemin katın inşasını içeren ilk dönem ve briket yığma duvarlar ile birinci katın eklenmesini içeren ikinci dönemin izlerini taşır.

Zemin kattaki bölme duvarlarının ilaveleri birinci katın yapımı ile aynı zamanda olabilir ancak bu konuda somut bir bilgi yoktur. Avlu üzerine tuvalet eklenmesi de aynı evrede değerlendirilebilir ancak bu somut bir kanıtla desteklenmemektedir.

Evlerin Karşılaştırılması

Bu çalışma kapsamında incelenen sekiz evin tüm yapısal özelliklerinin karşılaştırılması ve yapıların sınıflandırılması aşamasında veri olarak kullanılmak üzere alanda doldurulan envanter fiş verilerinin genel değerlendirmesi Tablo 1'de özetlenmiştir. Evlerin kütle kompozisyonları, yapısal elemanları, yapısal değişimleri ve mevcut korunma durumları, yapısal hasarları karşılaştırılarak yapısal sorunlar ve nedenleri değerlendirilmiştir.

Tablo 1. Sekiz evin yapısal özelliklerinin karşılaştırılması.

		İncelenen Yapılar	Ev 1	Ev 2	Ev 3	Ev 4	Ev 5	Ev 6	Ev 7	Ev 8
	Kat Sayısı	Özgün	1	2	1	2	1	1	1	1
		Dönem Eki	1	-	-	-	1	-	1	1
		Mevcut	2	2	1	2	2	1	2	2
		Zemin Döşemesi	Zemine Oturan Döşeme (Taş)							
Zemin Kat	Üst Örtü	Eleman	Taş Tonoz	Taş Tonoz	Ahşap Tavan	Taş Tonoz	Taş Tonoz	Taş Tonoz	Taş Tonoz	Taş Tonoz
		Kalınlık	Gözlemlenemedi							
		Mevcut Durumu	Korunmuş Özgün	Korunmuş Özgün	Kısmen Çökmüş	Korunmuş Özgün	Korunmuş Özgün	Korunmuş Özgün	Korunmuş Özgün	Korunmuş Özgün
	Duvarlar	Yığma Taş	✓	✓	✓	✓	✓	✓	✓	✓
		Kalınlık (cm)	90-100	70-75	100-110	80-95	90-100	90-110	95-105	70-80
		Yığma Briket	✓	✓	-	✓	✓	-	✓	✓
		Kalınlık (cm)	17-19	19-20	-	19-20	19-20	-	19-20	19-20
Birinci Kat	Üst Örtü	Eleman	Ahşap Tavan	Ahşap Tavan	-	Taş Tonoz	Beto-narme	-	Ahşap Tavan	Beton-arme
		Mevcut Durumu	Kısmen Çökmüş	Hasarlı Özgün	-	Korunmuş Özgün	Hasar Yok	-	Kısmen Çökmüş	Hasar Yok
	Duvarlar	Yığma Taş	✓	✓	-	✓	✓	-	-	-
		Kalınlık (cm)	90-100	70-75	-	80-95	75-85	-	-	-
		Yığma Briket	✓	✓	-	✓	✓	-	✓	✓
		Kalınlık (cm)	17-19	19-20	-	19-20	17-20	-	19-20	19-20
		Çatı Kaplaması	Sıkıştı-rılmış Toprak	Şap	Sıkıştı-rılmış Toprak	Şap	Beton	Sıkıştı-rılmış Toprak	Şap	Beton

Yapısal koruma nedenlerine odaklanıldığında evlerde ortak olarak izlenen 4 farklı strüktürel problem listelenmiştir.

● Birinci Tip: Tonozlara dönem ilaveleri.

Ev 1, 2, 5, 7, 8; 1. kat eklentileri mevcuttur. Bu birinci katlardaki duvar düzenleri, orijinal zemin kat planını takip etmemektedir, ancak bir taraftan girintilidir. Birinci katın uzunlamasına duvarlarından biri ise zemin katın üzerindeki özgün tonozun üzerine oturmaktadır (Şekil 25).

● İkinci Tip: Şekil 26'da örnekleri görülen taşıyıcı duvarların yanına kolon, kiriş, döşeme gibi beton yapı elemanlarının eklenmesi.

3 ve 7 numaralı evler hariç sekiz evin altısında bu tip bir yapısal sorun görülmektedir. Bunlar, mekanların genişletilmesi veya mekan sayısının arttırılması gibi maliklerin ihtiyaçlarına göre eklenmiştir. Bu eklemeler genellikle taş yığma taşıyıcı elemanlara temas etmektedir. Bu eklemeler, deprem gibi sismik hareketler sırasında sorunlara yol açabilir.

Şekil 25. Özgün tonoz üzerine binen yüklerin gösterimi.

Şekil 26. Yapılara eklenen betonarme elemanlar.

● Üçüncü Tip: Evlerin çatılarının tamamen veya kısmen çökmesidir.

Bu tip yapısal sorun sekiz evden dördünde görülmektedir: Ev 1, 3, 6 ve 7. Çöken çatıların tamamı ahşaptır. Hiçbir tonoz örtü çökmemiştir. Bu yapıların hiçbirinde koruyucu örtü yoktur: Hava şartlarına tamamen açıktırlar. Duvarların üst kısımlarında ise çökmenin olduğu yerlerde yağmur suyuna maruz kalmasından dolayı derz boşalması görülmektedir. Öte yandan duvarların üst kısımlarında sıva dökülen kısım fazla nem gösterir.

● Dördüncü Tip: Taşıyıcı duvar ve üst örtülerde yapısal çatlaklar.

Bu tip yapısal sorun sekiz evin tamamında görülmektedir. Bu çatlaklardan bazıları oldukça geniştir. Çatlaklar genişliklerine göre 2 cm'den dar ve 2 cm'den geniş olmak üzere iki grupta incelenmiştir. Bu çatlakların olası nedenleri sismik kuvvetler, doğal yaşlanma, beklenmeyen yükler ve bakım eksikliğidir.

Çalışma kapsamında incelenen sekiz yapı Şekil 27'de işaretlenen ve en yakın kırsal alanlar olan Eryeri, Eskikale, Çiftlikköy, Acar mahalleleri ve Mardin il merkezindeki benzer yapılarla da karşılaştırılmıştır [8]. Benzer yapım tekniklerini ve koruma sorunlarını görüntülenmiştir. Yığma taş duvarlar, beşik ve çapraz tonoz kullanımı, kemerli kapı ve pencereler Eryeri evleri ile başlıca benzerliklerdir. Eskikale ve Mardin'de ise taş işçiliği Eryeri evlerine göre daha süslüdür.

Eryeri'nde gözlenen yapısal hasarlar bu alanlarda da görülmektedir: zemin katın tonozlarına kat ilaveleri, taşıyıcı duvarlara kolon, kiriş, döşeme gibi betonarme yapı elemanları ilavesi, çatıların tamamen veya kısmen çökmesi ve taşıyıcı duvarlar ve üst örtülerdeki yapısal çatlaklar vb.

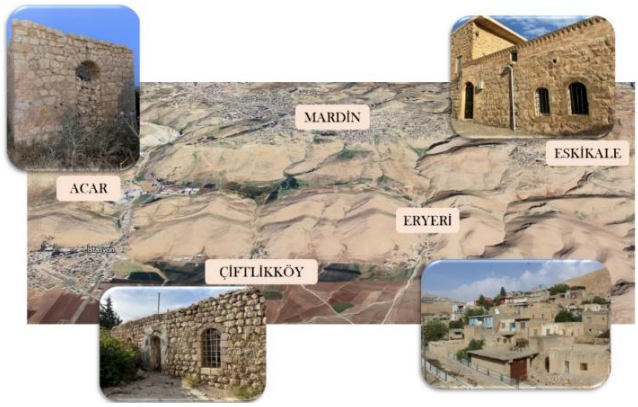

Şekil 27. Karşılaştırma yapılan köylerin Mardin'e ve Eryeri'ne göre konumları.

Sonuç

Yamaça dayanan, bir veya iki katlı, zemin katların kayalık arazinin içine oyulduğu, yığma taş duvarların ana kaya ile bütünleştiği Eryeri konutları özgünlüklerini önemli oranda korumuşlardır. Coğrafyaya ve kültüre özel yapım geleneğinin devamlılığını temsil etmektedirler. Duvar kesitleri üç katmanlı veya iki katmanlıdır. Çekirdek moloz taş ve harç örgülü, kaplama kaba yonu taştır. Üst yapılar beşik tonoz, çapraz tonoz veya ahşap döşemedir. Teras çatılar sıkıştırılmış toprakla tamamlanmıştır ve dam adı verilir. Saptanan müdahaleler basit onarım ve acil müdahale kapsamını aşan, esaslı onarımın gerektirdiği analitik yaklaşımdan yoksun, ancak özgün yapım sistemini dönüştüren niteliktedir. Genellikle bir veya iki kattan oluşan evlerde, kütle düzeni düşey yönde genişletilerek kat ilaveleri yapılmaktadır. Özgün yapı elemanlarındaki yük dağılımını, özgün elemanların yapısal davranışını ve yeni eklenenlerle ilişkisini dikkate almayan niteliksiz müdahaleler yaygındır.

Bu çalışma kapsamında sunulan kırsal konutların yapım özelliklerinin ve yapısal koruma durumlarının belirlenmesi yöntemi, Mardin kırsalı özelindeki müdahalelerin planlanmasına yön verecek, aynı zamanda kırsal konutlarda yaygın olarak uygulanan niteliksiz yapısal müdahalelerin incelenmesi ve önlenmesi konularında halihazır rehber ve ilkelerin geliştirilmesine de ışık tutacaktır.

Teşekkür

Bu çalışma 2022IYTE-1-0028 numaralı İzmir Yüksek Teknoloji Enstitüsü, Bilimsel Araştırma Projesi tarafından desteklenmiştir.

Kaynaklar

[1] Eres, Z., "Türkiye'de Planlı Kırsal Yerleşmelerin Tarihsel Gelişimi ve Erken Cumhuriyet Dönemi Planlı Kırsal Mimarisinin Korunması Sorunu", Doktora Tezi, Fen Bilimleri Enstitüsü, İstanbul Teknik Üniversitesi, İstanbul, 2008.

[2] T.C. Kültür Bakanlığı, Kültür ve Tabiat Varlıklarını Koruma Yüksek Kurulu, "660 Nolu İlke Kararı: Taşınmaz Kültür Varlıklarının Gruplandırılması, Bakım ve Onarımları", Ankara, 05.11.1999. https://korumakurullari.ktb.gov.tr/Eklenti/18338,660-nolu-ilke-kararipdf.pdf?0 (Erişim: 10.10.2025)

[3] T.C. Kültür ve Turizm Bakanlığı, Kültür Varlıklarını Koruma Yüksek Kurulu, "35 Nolu İlke Kararı: Depremde Hasar Gören Tescilli Taşınmaz Kültür Varlıkları ile Sit Alanları Etkileşim-Geçiş Sahalarındaki Yapılarda Yapılacak Uygulamalara İlişkin Kültür Varlıklarını Koruma Yüksek Kurulu İlke Kararı", Ankara, 10.04.2012. https://teftis.ktb.gov.tr/TR-263815/35-nolu-ilke-karari-depremde-hasar-goren-tescilli-tasinmaz-kultur-varliklari-ile-sit-alanlari-ve-etkilesim-gecis-sahalarindaki-yapilarda-yapilacak-uygulamalara-iliskin.html (Erişim: 10.10.2025)

[4] T.C. Kültür ve Turizm Bakanlığı, Kültür Varlıklarını Koruma Yüksek Kurulu, "2878 No'lu İlke Kararı: Korunması Gerekli Taşınmaz Kültür Varlıklarının Güçlendirilmesi İlke Kararı", Ankara, 27.12.2023. https://www.resmigazete.gov.tr/eskiler/2024/01/20240113-13.pdf (Erişim: 10.10.2025)

[5] Ahunbay, Z., Aköz, F., Altay, G., Arun, G., Celep, Z., Erberik, M. A., İlki, A., Ünal, Z. G., Aydemir, O., Kuran, F., Şimşek, M., Ünlügedik, S., Çelik, S., Atasagun, F. D., Kaya, Y., Uçar, Y. & Olgun, N., Tarihi Yapılar İçin Deprem Risklerinin Yönetimi Kılavuzu, T.C. Başbakanlık Vakıflar Genel Müdürlüğü, Ankara, 2016.

[6] Halifeoğlu, F. M., Dalkılıç, N., "Mardin-Savur Geleneksel Kent Dokusu ve Evleri", Uludağ Üniversitesi Mühendislik-Mimarlık Fakültesi Dergisi, Vol. 11, Issue 1, 2006.

[7] Tunçer, M., "Mardin'in Korunması ve UNESCO Dünya Miras Listesi'ne Girmesi", İdeal Kent, Sayı 9, syf: 94-113, 2013.

[8] Alioğlu, F., "Mardin Şehir Dokusu ve Evler", Tarih Vakfı, İstanbul, 2000.

Soyukaya, N., Özgür, M., Kaya, F., Han, Z., Savaş, B., Alpay, E., "Mardin Kültür Envanteri", Mardin Valiliği İl Kültür ve Turizm Müdürlüğü, 2013.

Beyazıt, D., "Mardin Ortaçağ İslam Mimarisi", Albert Gabriel, 2006.

Dicle University
Journal of Engineering
https://dergipark.org.tr/tr/pub/dumf
duje.dicle.edu.tr

Araştırma Makalesi / Research Article

Diyarbakır Surlarında Tuğla Malzemenin Kullanım Teknikleri ile SEM/EDX (Taramalı Elektron Mikroskobu/Enerji Dağılımlı X-Işını Spektroskopisi) Analizlerinin Değerlendirilmesi

Evaluation of Brick Material Usage Techniques and SEM/EDX (Scanning electron microscopy/Energy dispersive X-ray spectroscopy) Analyses on the City Walls of Diyarbakır

Nursen IŞIK [1]* , Ronay OKUTMUŞTUR [2]

[1] Dicle University, Architecture Department, isikcn@gmail.com, Orcid No: 0000-0002-6125-1896
[2] Dicle University, Architecture Department, ronayokutmustur19@gmail.com, Orcid No: 0000-0001-7439-7651

MAKALE BİLGİLERİ

Makale Geçmişi:

Geliş 29 Temmuz 2025
Revizyon 9 Ekim 2025
Kabul 10 Ekim 2025
Online 30 Aralık 2025

Anahtar Kelimeler:

Anahtar kelime 1, Tuğla 2, Diyarbakır Surları 3 SEM-EDX Analizi 4.Örgü Tekniği 5.İstif Tekniği.

ÖZ

Geleneksel yığma yapılar, geçmiş dönemlerde insanların bulundukları yöreye yakın yerlerden temin edebildikleri malzemelerle yapı inşa etmeleri sonucunda meydana gelmişlerdir. İnsanların yakın çevrelerinden elde edebildikleri doğal malzemeler taş ve ahşap gibi yapı malzemeleri iken, bu malzemelerin bulunmadığı yörelerde toprak kökenli olan kerpiç ve tuğla gibi malzemeler üretilmiştir. Kerpiç malzemenin zamanla dış hava koşullarına karşı dayanıksız olduğunun tespit edilmesi sebebiyle bu malzeme tarihsel süreçte yerini tuğlaya bırakmıştır. Tuğla; kil, killi toprak ve suyun bir araya getirilerek şekillendirilmesi, kurutulması ve pişirilmesi ile meydana getirilen bir malzemedir. Diyarbakır kenti Türkiye'nin güneydoğusunda yer alan tarihi bir kenttir. Kentte pek çok uygarlık hüküm sürmüş ve bu uygarlıklar kente önemli mimari eserler bırakmışlardır. Bu eserlerden en önemlisi UNESCO Kültürel Miras Listesi'nde yer alan Diyarbakır surlarıdır. Bu çalışmada tarihi surların 4 ana kapısından seçilen Mardin Kapı ile Yeni Kapı arasındaki sur duvarları ve burçlarda tuğla malzemenin kullanıldığı yapı elemanları incelenmiştir. İncelenen yapı elemanlarında tuğla malzemenin kullanım alanları, istif ve örgü biçimleri alan çalışmasıyla gözlemsel olarak tespit edilmiş ve fotoğraflarla belgelenmiştir. Belirlenen bölgede sur duvarları ve burçlarda kullanılan tuğla malzemenin içeriğinin analiz edilmesi amacıyla seçilen 63 ve 64 numaralı burçlardan tuğla numuneleri alınarak SEM/EDX analizleri yapılmıştır. Deney sonuçları grafikler halinde değerlendirilmiştir.

ARTICLE INFO

Article history:

Received 29 July 2025
Received in revised form 9 October 2025
Accepted 10 October 2025
Available online 30 December 2025

Keywords:
keyword 1, Brick; 2. Diyarbakır city walls;3. SEM/EDX (Scanning electron microscopy/Energy dispersive X-ray spectroscopy); 4. Bonding technique;5 Stacking technique.

Doi: 10.24012/dumf.1753428

* Sorumlu Yazar

ABSTRACT

Traditional masonry structures were developed because of people constructing buildings using materials obtained from nearby sources. In areas where natural materials like stone and wood were available, these were used for construction. In regions where such materials were not present, earth-based materials like adobe and brick were produced. Over time, adobe was found to be unsuitable for withstanding external weather conditions, and it was gradually replaced by brick. Brick is a material made by shaping, drying, and firing a mixture of clay, clay soil, and water.
Diyarbakır is a historic city located in southeastern Turkey. It has been ruled by various civilizations, each leaving significant architectural heritage. The Diyarbakır city walls, included in the UNESCO World Heritage list, are the most notable among these This study examines the brick materials used in the walls and towers between the Mardin Gate and the New Gate of the historic city walls. The stacking and bonding patterns of the brick material in the studied structural elements were observed and documented with photographs. To analyze the structure of the brick material employed in the walls and towers of the selected region, brick samples were collected from Towers 63 and 64 for SEM/EDX analysis. The experimental outcomes were analyzed using graphical representations.

Giriş

Toprak esaslı yapı malzemeleri, tarih boyunca insanların yaşadıkları coğrafyalarda doğal taş gibi yapı hammaddelerinin yeterli miktarda bulunmadığı durumlarda başvurdukları önemli bir çözüm olmuştur. Bu bağlamda, en erken dönemlerden itibaren kullanılan ilk malzemelerden biri kerpiçtir. Kerpiç, su ile yoğrulmuş kilin belirli bir form verilerek kalıplanması ve güneşte kurutulmasıyla elde edilen, ısıl işlem görmemiş bir yapı malzemesidir. Kerpiç, üretimi ve uygulanması kolay olması nedeniyle tarih boyunca yaygın şekilde kullanılmıştır; ancak dış hava koşullarına karşı düşük dayanımı, özellikle yağmur ve dona karşı hassasiyeti, zamanla bu malzemenin yerini daha dayanıklı bir alternatif olan tuğlaya bırakmasına neden olmuştur [1].

Tuğla, kerpicin gelişmiş bir formu olarak kabul edilmekte olup, balçık veya kil karışımının kalıplanarak kurutulması ve ardından yüksek sıcaklıklarda pişirilmesiyle elde edilir. Türk Dil Kurumu, tuğlayı "balçığın kalıba dökülerek kurutulmasından sonra pişirilmesiyle elde edilen yapı malzemesi" olarak tanımlamaktadır [2]. Arkeolojik bulgulara göre tuğla ilk kez Neolitik Dönemde kullanılmaya başlanmış; bu döneme ait en eski örnekler, Ürdün Nehri kıyısında bulunmuş ve yaklaşık 26×10×10 cm boyutlarında, elle şekillendirilmiş amorf bloklardan oluşmuştur [3].

Tuğla üretim süreci hammadde hazırlığı, şekillendirme, kurutma, pişirme ve ambalajlama olmak üzere beş temel aşamadan oluşmaktadır. Bu süreçlerde kullanılan en uygun toprak türleri ise genellikle killi topraklardır. Killer; fiziksel, kimyasal ve mineralojik özellikleri açısından oldukça farklılık gösterebilmekte ve bu özellikler tuğlanın performansını doğrudan etkilemektedir [4][5]. (Tablo 1)

Tablo 1. Tuğla yapımında kullanılan killerin kimyasal bileşimleri[6]

Kimyasal Bileşim	SiO_2	Al_2O_3	Fe_2O_3	MgO	CaO	Na_2O	K_2O	MnO	Kızdırma Kaybı
%	30-50	12-30	4-7	0-6	0-35	0-6	0-2	0-2	0-14

Tuğla hammaddesinde özellikle illit, kaolinit ve montmorillonit türü killer tercih edilirken, bu killerin yapısında genellikle silisyum (Si), alüminyum (Al), demir (Fe), kalsiyum (Ca), magnezyum (Mg), potasyum (K) ve sodyum (Na) gibi elementler yer almaktadır [6]. Bu elementler, tuğlanın fiziksel özellikleri ile yüksek sıcaklıkta fırınlanma sonrası dayanıklılığı üzerinde belirleyici rol oynamaktadır.

Kaolinit killerinde alüminyum ve silisyum elementleri bulunurken; montmorillonit, illit ve klorit killerinde demir ve magnezyum başta olmak üzere farklı elementler bulunmaktadır [4][5]. (Tablo 2)

Tablo 2. Kimyasal bileşimlerine göre killerin sınıflandırılması [6].

Kimyasal Bileşim (%)	SiO_2	Al_2O_3	Fe_2O_3 FeO	MgO	CaO	KO	Na
Gibsit	-	30-35	-	-	-	-	-
Kaolin	44-47	37	0,5-1,0	0,3	0,3	0-1,5	0-1,5
İllit	47-52	22-30	2,0-7,0	0-1,0	0-1,0	6,0-8,0	0-1,0
Muskovit	45	38	-	-	-	12	-
Montmorillonit	50-56	16-20	1,0-4,0	3,0-6,0	1,0-3,0	0-0,5	0-2,0
Klorit	20-30	15-25	1,0-4,0	3,0-3,5	0,3	-	-

Türkiye'nin güneydoğusunda yer alan Diyarbakır ili, kültürel, tarihsel ve mimari mirasıyla Anadolu'nun en önemli kentlerinden biridir. Kentin tarihi kimliğinin oluşturan Suriçi Bölgesi, yaklaşık 5.5 kilometre uzunluğundaki UNESCO Dünya Kültür Mirası Listesi'nde yer alan surlarla çevrilidir. Suriçi Bölgesi ve surlar, Roma, Bizans, Artuklu, Akkoyunlu ve Osmanlı dönemlerine ait izleri barındırmaktadır [7]. Surlar, genellikle yöresel ve mukavemeti yüksek bazalt taş malzemeyle inşa edilmiştir. 82 burçtan oluşan Diyarbakır Surlarında burçlar ve sur duvarlarında bazalt taş malzeme dışında tuğla malzeme özellikle tonoz, kubbe, kemer ve pandantif gibi yatay taşıyıcı elemanları ile süslemelerde kullanılmıştır.

Çalışma, surların güney ve batısında yer alan Mardin Kapı ile Yeni Kapı arasındaki sur duvarları ve burçları kapsayan alanla sınırlandırılmıştır. Mardin Kapı ile Yeni Kapı arasında yer alan tüm burçlardaki tuğla malzeme kullanım alanları saha çalışmasıyla tespit edilmiştir. Diyarbakır surlarında kullanılan tuğla malzemeye yönelik detaylı analizlerin yer aldığı akademik ve literatür çalışmalarının sınırlı olması, bu çalışmanın önemini artırmakta ve bilimsel literatüre katkı sunmaktadır. Ayrıca, bu tür malzemelerin niteliklerinin anlaşılması, mevcut yapının korunması ve gelecekte yapılacak restorasyon çalışmaları açısından büyük önem arz etmektedir.

Bu çalışmanın amacı, daha önce kapsamlı biçimde ele alınmamış bir konu olan Diyarbakır tarihi surlarında tuğla malzemenin kullanım alanları ve tekniklerini belgelemektir. Ayrıca Mardin Kapı ve Yeni Kapı arasında tüm burçlar yapım ve örgü tekniği açısından değerlendirilmiştir. Saha çalışmasında yer alan 63 ve 64 numaralı burçlardan alınan tuğla numunelerin kimyasal özellikleri incelenmesi amacıyla taramalı Elektron Mikroskobu (SEM) ve Enerji Dağılımlı X-Işını Spektroskopisi (EDX) analizleri yapılmıştır.

2. Materyal ve Metot

Diyarbakır surları kayalık bir zeminde Dicle Nehri'nden yaklaşık olarak 100 m yukarda inşa edilmiştir. Surlar üzerinde yer aldığı topografyaya uygun olarak şekillendirilmiş ve tarihi Suriçi bölgesini çevrelemiştir [7].

Diyarbakır Surları günümüzdeki şeklini 4. yüzyıl ortalarında almıştır [8]. Surlar, tarih boyunca stratejik ve askeri işlevlerinin yanı sıra kültürel ve estetik değerleriyle de dikkat

çekmiştir. Günümüzde işlevselliğini sürdüren dört ana kapıya sahiptir: Dağ (Harput) Kapı, Mardin (Tell) Kapı, Urfa (Rum) Kapı ve Yeni Kapı [10]. (Şekil 1).

Şekil 1. Diyarbakır Suriçi Bölgesi (KAİP, 2012)

Araştırma kapsamında, Diyarbakır surlarının Mardin Kapı ile Yeni Kapı arasında yer alan bölümü çalışma alanı olarak seçilmiştir. Bu bölüm, sur yapısının mimari çeşitliliği ve farklı dönem yapı tekniklerini yansıtması bakımından özel bir önem taşımaktadır. Çalışmada, söz konusu sur kesitinde yer alan tuğla kullanım alanları, örgü teknikleri, yapısal ve süsleyici işlevleri detaylı biçimde fotoğraflanmış ve belgelendirilmiştir. Tuğlanın, özellikle tonoz, kemer, kubbe, ve hatılların mevcut durumu ve tekniklerinin yerinde gözlemlendiği saha çalışması yapılmıştır. Saha çalışmalarında fotoğraflarla belgelenmiş, Mardin Kapı ve Yeni Kapı arasındaki alanda seçilen burçlardan alınan tuğla malzemeler üzerinde analizler yapılmıştır. Malzeme analizleri yapılan tuğla malzemenin yapım ve örgü tekniği ile desteklenen çalışma, yapı tekniklerinin tarihsel sürekliliğini ve değişimini ortaya koymayı amaçlamaktadır.

Belgeleme çalışmaları sonrası, Mardin Kapı ile Yeni Kapı arasındaki sur duvarları ve burçlarındaki kısmen hasar görmüş olan 63 ve 64 numaralı burçlar detaylı olarak incelenmiştir. Hasar durumları ve tuğla kullanımı açısından veri sağlayabilecek nitelikte olan iki burç, analitik incelemeler için örnekleme alanı olarak belirlenmiştir. Her iki burçtan toplamda 12 adet tuğla numunesi alınmıştır (63 numaralı burçtan 8 adet, 64 numaralı burçtan 4 adet). Numune alımı sırasında, yapıya zarar verilmeden ve özgünlüğü korunacak şekilde yüzeyden ayrılmış kopuk veya zayıflamış tuğla parçaları tercih edilmiştir.

Alınan numuneler, Dicle Üniversitesi Bilim ve Teknoloji Uygulama ve Araştırma Merkezi (DÜBTAM) laboratuvarına getirilmiş ve burada mikro-yapısal ve kimyasal analizlere tabi tutulmuştur. Deneysel çalışmalar, FEI QUANTA FEG 250 marka ve modeline sahip Taramalı Elektron Mikroskobu (SEM) cihazı ile gerçekleştirilmiştir. Cihaz, yüksek çözünürlüklü görüntüleme ve elementel bileşen analizlerini bir arada yapabilen Enerji Dağılımlı X-Işını Spektroskopisi (EDX) donanımına sahiptir. Analizler, cihazın düşük vakum, yüksek vakum ve ESEM (Environmental SEM) modlarında çalışabilme kapasitesi sayesinde, iletken olmayan ve nemli numunelerde de sorunsuz şekilde yürütülebilmiştir.

SEM görüntüleriyle numunelerin yüzey morfolojileri, gözeneklilik oranları, kristalin yapıları ve mikro çatlakları belirlenmiş; EDX verileri ile oksijen (O), silisyum (Si), alüminyum (Al), magnezyum (Mg), kalsiyum (Ca), demir (Fe), potasyum (K), sodyum (Na) ve bazı örneklerde karbon (C), titanyum (Ti) ve kükürt (S) gibi elementlerin varlığı ve yüzdesel dağılımı tespit edilmiştir. Bu analizler, tuğla malzemelerin hammadde kaynaklarının belirlenmesi, pişirme koşullarının anlaşılması ve bozulma süreçlerinin değerlendirilmesi açısından önemli veriler sunmuştur.

Bu kapsamlı metodoloji, Diyarbakır Surlarında kullanılan tuğla malzemenin tarihsel bağlam içinde fiziksel ve kimyasal özelliklerinin değerlendirilmesini mümkün kılarak, yapının korunması ve restorasyonuna yönelik bilimsel veri üretmeyi amaçlamaktadır. Ayrıca, literatürde eksikliği hissedilen tuğla malzemenin yerel mimarideki rolü ve özgün teknik uygulamaları hakkında yeni bir bakış açısı sunmaktadır.

2.1 Tuğla malzemenin kullanım alanları ve teknikleri

Diyarbakır Surlarının Mardin Kapı ile Yeni Kapı arasında yer alan güneydoğu kesimi, topografik koşullara bağlı olarak mimari biçimlenme açısından bazı farklılıklar göstermektedir. Bu bölümde, sur duvarlarının genel olarak daha zayıf kesitli, burçlar arasındaki mesafenin ise daha geniş olduğu tespit edilmiştir. İncelenen alan içerisinde toplamda 16 adet burç yer almakta olup, bu burçlar arasında kalan sur duvarlarında ve burç yapılarında tuğla malzemenin belirli yapı elemanlarında kullanıldığı görülmektedir. [11]. (Şekil 2)

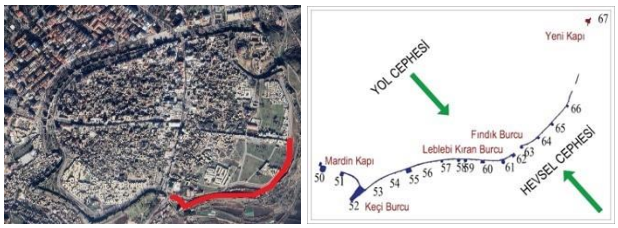

Şekil 2. Mardin Kapı ile Yeni Kapı arası sur duvarları ve konumu

Yapılan saha çalışmaları kapsamında, surlardaki tuğla kullanımı, mimari işlevleri doğrultusunda düşey taşıyıcı elemanlar ve yatay taşıyıcı elemanlar olmak üzere iki temel gruba ayrılmıştır:

- **Düşey Taşıyıcı Elemanlar**: Duvarlar ve taşıyıcı ayaklar.
- **Yatay Taşıyıcı Elemanlar**: Kemerler, tonozlar, kubbeler, hatıllar ile örtü geçiş elemanları olan tromp ve pandantifler.

Yapı elemanları içerisinde tuğla malzeme, duvar ve ayaklarda sınırlı düzeyde kullanılmış olup, bu alanlarda esas yapı malzemesi olan bazalt taşı ile almaşık örgü (Alternating Masonary) tekniğiyle uygulanmıştır. Taş ve tuğla malzemenin birlikte kullanımı, tarihi yapılarda estetik ve yapısal nedenlerle tercih edilen bir tekniktir. Bu yöntem, malzemeler arası yük dağılımının dengelenmesine katkı

sunarken, aynı zamanda yapının deprem gibi yatay yükler karşısındaki performansını artırabilmektedir [12], (Şekil 3).

Şekil 3. 51 numaralı burç duvarı ve 52 numaralı burç (Keçi Burcu) taşıyıcı ayağında almaşık örgü halinde tuğla malzeme kullanımı (2024)

Kemer, kubbe ve tonoz gibi yatay taşıyıcı elemanlarda tuğla malzemenin kullanımının daha yoğun olduğu görülmektedir. Bu tür elemanlarda tuğla, taş malzemeye göre daha hafif, daha kolay şekillendirilebilir ve yüksek sıcaklık direncine sahip olması nedeniyle tercih edilmiştir. Surlardaki bu elemanlarda, yatay istif düz örgü (horizontal stacked bond) tekniği yaygın şekilde uygulanmıştır. Özellikle tonoz ve kubbe elemanlarında, yatay düzlemde dizilmiş tuğlalar, iç içe geçmiş yük aktarım sistemine katkı sunacak şekilde düzenlenmiştir.

Surların kemer elemanlarında ise tuğla kullanımı genellikle çift sıra, yer yer tek sıra olarak düzenlenmiştir. Bu uygulamalarda tercih edilen örgü biçimi, literatürde kılıcına örgü (soldier course) olarak adlandırılmaktadır. Bu teknik, tuğlaların uzun eksenlerinin düşey olarak yerleştirilmesiyle elde edilen bir örüntüdür ve özellikle dar açıklıkların geçilmesinde ya da yük aktarımının doğrudan olması istenen alanlarda tercih edilir [13]. Ayrıca, kare planlı mekânlardan dairesel örtü sistemlerine geçişi sağlayan tromp ve pandantif elemanlarında da yer yer tuğla kullanımı gözlemlenmiştir. Bu bölgelerde, hem geometrik dönüşümün sağlanması hem de ağırlığın daha hafif bir malzeme aracılığıyla aktarılması amacıyla tuğla tercih edilmiştir. Özellikle pandantif yüzeylerinde dışa doğru eğik yerleştirilmiş tuğlalarla oluşturulan örüntüler, yapısal işlevin yanı sıra sınırlı düzeyde estetik etki de yaratmaktadır. Diyarbakır surlarında tuğla malzemenin yaygın kullanım alanı hatıl, tonoz ve kubbe gibi yapı elemanlarında genellikle yatay istif düz örgü tekniği görülmektedir (Şekil 4).

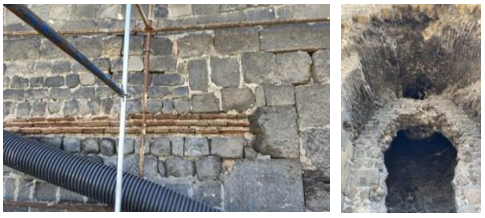

Şekil 4. 55-56 numaralı burçlar arasındaki hatılda ve 59 numaralı burç tonozunda yatay istif düz örgü tekniği ile kullanılan tuğla malzeme (2024)

Kemerlerde genellikle çift sıra, yer yer tek sıra halinde dizildiği tespit edilen tuğla malzeme bu yapı elemanında ise kılıcına örgü tekniği yer almıştır (Şekil 5, Şekil 6, Şekil 7, Şekil 8).

Şekil 5. 52 numaralı burç (Keçi Burcu) kubbe pandantiflerinde (2024) ve 62 numaralı burç (Leblebikıran Burcu) tromplarında tuğla malzeme kullanımı

Şekil 6. 57 numaralı burç kubbesinde yatay istif düz örgü tekniği ile kullanılan tuğla malzeme (2024)

Şekil 7. 53 numaralı burç kemerinde çift sıra halinde kılıcına örgü tekniği ile tuğla malzeme kullanımı (2024)

Şekil 8. 55 numaralı burçta yatay-düşey istif ve dışa çıkıntılı-eğik açılı tuğla malzeme kullanımı [12]

Tuğla malzemenin özellikle yapısal işlev taşıyan alanlarda kullanılması, bu malzemenin Diyarbakır surlarında süsleme amacı dışında taşıyıcı ve işlevsel amaçla tercih edildiğini göstermektedir. Bununla birlikte, 63 numaralı burç gibi bazı yapılarda, tuğlanın yatay ve düşey istiflerle oluşturduğu tonoz ve kubbe yüzeylerinde kısmen estetik amaçlı yerleştirildiği gözlemlenmiştir. Bu yönüyle, tuğla kullanımı yalnızca teknik bir tercih değil, aynı zamanda dönemin mimari estetiğinin bir uzantısı olarak da değerlendirilebilir.

Diyarbakır Surlarında tuğla malzemenin kullanımı, büyük ölçüde yapı elemanının fonksiyonuna ve yapım tekniğine bağlı olarak çeşitlenmektedir. Özellikle kemer, tonoz ve kubbe gibi mimari elemanlarda tercih edilen tuğla malzeme, sur yapısının taşıyıcılığını artıran ve yapım sürecini kolaylaştıran bir malzeme olarak işlev görmüştür (Tablo 3).

Tablo 3. Mardin Kapı ile Yeni Kapı arası sur duvarları ve burçlarda tuğla malzemenin kullanıldığı yapı elemanları

Burç No	Burç ve Sur Duvarlarının Konumu	Düşey Taşıyıcılarda		Yatay Taşıyıcılarda Kullanımı			
		Duvar	Ayak	Hatıl	Kemer	Tonoz	Kubbe
50 No'lu Burç		-	-				-
51 No'lu Burç	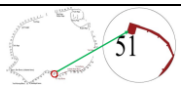		-				-
52 NO'LU BURÇ		-					
53 No'lu Burç	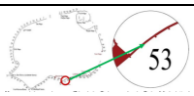	-	-	--			--
53-55 No'lu Burç Arası			-	-	-	-	-
55 No'lu Burç	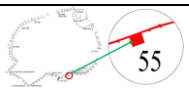		-	-			
56 No'lu Burç	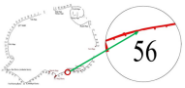	-	-	-		--	--
57 No'lu Burç	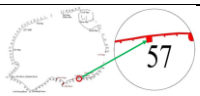	-	-	-		-	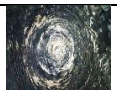
58 No'lu Burç	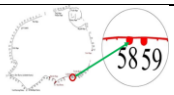		--			-	
59 No'lu Burç	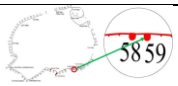	-	-	-			
60 No'lu Burç	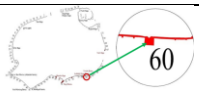	-	--	-			
61 No'lu Burç	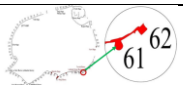	-	-	-			-
62 No'lu Burç	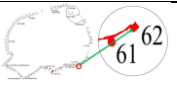		-	-			
63 NO'LU BURÇ	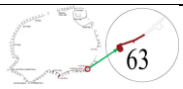	-	-	-			
64 NO'LU BURÇ	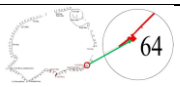	-	--	-			
65 No'lu Burç	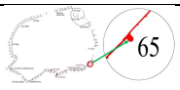	-	-	--			
66 No'lu Burç	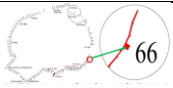	-	-	-			-

3. Bulgular

Diyarbakır Surlarında Mardin Kapı ve Yeni Kapı arasındaki burçlarla sınırlandırılan çalışma alanında, tuğla malzemenin içeriğinin tespit edilmesi amacıyla SEM/EDX analizi yapılmıştır. Analizler için seçilen iki burçtaki (63-64 numaralı burç) harman tuğlalardan analizler için numuneler alınmıştır (Şekil 9, Şekil 10).

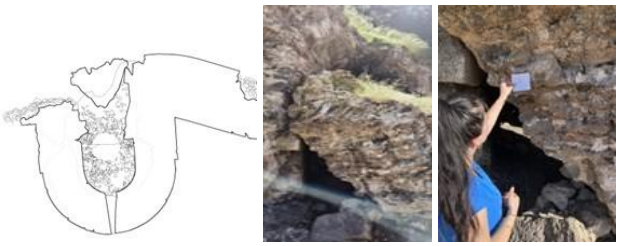

Şekil 9. 63 numaralı burçtan (Fındık Burcu) numune alınması

Şekil 10. 64 numaralı burçtan numune alınması

63 numaralı burç (Fındık Burcu) ile 64 numaralı burçlardan alınan harman tuğla numuneleri üzerinde yapılan SEM/EDX analizleri, tuğla malzemelerinin iç yapısını ve bileşenlerini tespit etmek amacıyla gerçekleştirilmiştir. Çalışma, Dicle Üniversitesi Bilim Teknoloji Uygulama ve Araştırma Merkezi'nde QUANTA FEG 250 marka cihaz ile yapılmıştır. Analiz, numunelerin iç yapısını belirlemek ve bileşenlerin oranlarını saptamak için üç farklı basınç aralığında gerçekleştirilmiştir. SEM görüntüleri, numunelerin gözenekli, kristal ve heterojen yapıda olduğunu göstermektedir. EDX analizi ise her numunede bulunan elementlerin miktarını belirlemiştir (Şekil 11).

Şekil 11. SEM[1]-EDX[2] analizlerinde kullanılan cihaz

63 numaralı burçtan (Fındık Burcu) alınan 8 adet, 64 numaralı burçtan alınan 4 adet harman tuğla numunesinin SEM/EDX verileri sonuçları tablo haline getirilmiştir.

63-1 numaralı numune üzerinde yapılan SEM gözlemleri, numunenin gözenekli yapıda ve heterojen bir dokuya sahip olduğunu ortaya koymuştur. (Görüntülerdeki boşluklar gözenekliliği göstermektedir). Bu durum, numunenin yapısal özelliklerinin, içerdiği elementlerin dağılımına ve dokusal heterojenliğine bağlı olarak değişkenlik gösterdiğini işaret etmektedir. (Şekil 12).

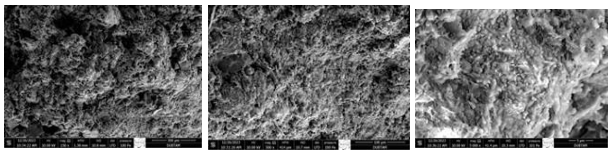

Şekil 12. 63-1 numaralı numunenin SEM görüntüleri

EDX analiz sonuçlarına göre, 63-1 numunesinde tespit edilen başlıca elementler sırasıyla oksijen (O)**,** magnezyum (Mg)**,** alüminyum (Al)**,** silisyum (Si)**,** kalsiyum (Ca) ve demir (Fe) olmuştur. Bu elementler, tuğla üretiminde kullanılan hammaddelerin yanı sıra, numunenin mineralojik bileşenlerinin ve bileşik yapılarının da belirleyicileri olarak değerlendirilebilir.

Numunenin kimyasal yapısı incelendiğinde, oksijen (O) en yüksek oranda bulunan element olarak tespit edilmiştir. Oksijenin yüksek orandaki varlığı, numunede bulunan silikat bileşenlerinin ve oksitlerin tuğlanın yapısal bileşiminde önemli bir rol oynadığını göstermektedir. Bu, numunenin termal ve mekanik dayanıklılığını artıran bir özellik olarak değerlendirilebilir. Düşük miktarda magnezyumun olması, numunede az miktarda magnezyum içeren minerallerin bulunduğunu göstermektedir. Bu durum, tuğlanın kimyasal kararlılığını etkileyebilir ve mukavemet özellikleri üzerinde değişkenlik yaratabilir. Alüminyum (Al), Silisyum (Si), Kalsiyum (Ca) elementlerin, seramik ve inorganik malzeme yapılarında bulunan bileşiklerdir. Özellikle silikat yapısının önemli bileşenleri olan silisyum ve alüminyum, tuğlanın dayanıklılığını ve estetik özelliklerini etkileyen elementlerdir. Demir (Fe)**,** **g**enellikle inorganik malzemelerin rengini etkileyen ve yapısal bütünlüğü sağlayan elementtir. Demirin (Fe) varlığı, numunenin oksidasyon özellikleri ve mekanik dayanıklılığı açısından önemlidir.

Yapılan SEM/EDX analizleri, 63-1 numaralı harman tuğlasının heterojen bir yapıya sahip olduğunu ve içeriğinde silikat ve oksit bileşenlerinin baskın olduğunu ortaya koymuştur. Oksijenin yüksek orandaki varlığı, numunenin kimyasal dayanıklılığını ve mekanik özelliklerini etkileyebilecek önemli bir faktör olarak değerlendirilmiştir. Öte yandan, magnezyumun düşük oranı, bu tür numunelerde genellikle beklenen magnezyum içeren mineral oranlarının düşük olduğunu ve numunede daha az magnezyum bileşiği içerdiği görülmektedir. Bu analizler, harman tuğla üretiminde kullanılan hammaddelerin kimyasal bileşimlerinin malzeme özelliklerini doğrudan etkileyebileceğini ve tuğla üretim sürecinin optimize

[1] SEM: Taramalı Elektron Mikroskobu

[2] EDX: Enerji Dağılımlı X-Işını Spektroskopisi

edilmesinde önemli bir rol oynayabileceğini göstermektedir (Şekil 13).

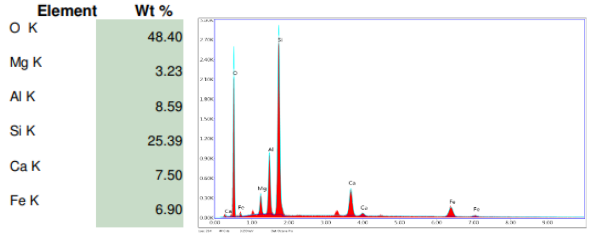

Şekil 13. 63-1 numaralı numunenin EDX verileri

63-2 numaralı numune üzerinde yapılan taramalı elektron mikroskobu (SEM**)** incelemeleri, numunenin gözenekli, kristal ve heterojen yapıya sahip olduğunu göstermektedir. Bu gözlemler, numunenin yapısının farklı fazlardan ve bileşiklerden oluştuğunu, bunun da tuğlanın mekanik ve termal özelliklerinin heterojen olmasına yol açabileceğini düşündürmektedir (Şekil 14).

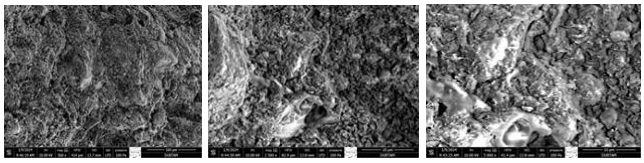

Şekil 14. 63-2 numaralı numunenin 500x, 2500x ve 5000x SEM görüntüleri

EDX analizi sonucunda, 63-2 numaralı numune içerisinde Oksijen (O), Sodyum (Na), Magnezyum (Mg), Alüminyum (Al), Silisyum (Si), Potasyum (K), Kalsiyum (Ca), Titanyum (Ti) ve Demir (Fe) elementleri tespit edilmiştir: . Bu elementler, numunenin mineralojik bileşenlerinin ve kimyasal yapısının çeşitliliğini ortaya koymaktadır.

Oksijen (O), numunede en yüksek oranda bulunan element olarak tespit edilmiştir. Oksijen, özellikle silikat ve oksit bileşenlerinde önemli bir yapı taşıdır ve bu durum, numunenin yapısal olarak oksitli ve silikat bileşenlerden zengin olduğunu göstermektedir. Yüksek oksijen içeriği, tuğlanın dayanıklılığını ve termal özelliklerini artırabilir. Titanyum (Ti), numunede en düşük oranda bulunan element olarak belirlenmiştir. Titanyum, özellikle seramik ve inorganik malzeme yapılarında düşük miktarlarda bulunan bir elementtir. Bu, numunede titanyum bileşenlerinin sınırlı olduğunu ve bunun numunenin kimyasal kararlılığını büyük ölçüde etkilemeyeceğini göstermektedir. Titanyum, genellikle malzeme yüzeyinde belirli özellikler oluşturabilen bir elementtir, ancak burada fazla yer tutmamaktadır. Sodyum (Na), özellikle silikat yapılarında ve bazı alkali metal bileşiklerinde yer alır. Yüksek sıcaklıklarda ve özellikle tuğla üretiminde, sodyum bileşenlerinin varlığı, tuğlanın mukavemetini ve termal dayanıklılığını etkileyebilir. Magnezyum (Mg): genellikle inorganik malzemelerde yer alan ve seramik malzemelerin dayanıklılığını artıran bir elementtir. 63-2 numunesinde tespit edilen magnezyum, numunenin dayanıklılığını ve termal kararlılığını artıran bir faktör olabilir. Alüminyum (Al) ve Silisyum (Si) silikat bileşiklerinin ana bileşenleridir. Bu elementlerin varlığı, numunenin silika-alümina yapısına sahip olduğunu ve bu bileşiklerin numunenin mekanik özelliklerini ve ısıya dayanıklılığını önemli ölçüde etkileyebileceğini göstermektedir. Potasyum (K), seramik malzemelerin yapısında ve bileşiklerinde rastlanan bir diğer alkali metal elementidir. Bu elementin varlığı, numunenin kimyasal özelliklerini etkileyebilir ve ısıya karşı direnç kazandırabilir. Kalsiyum (Ca) silikat yapılarında ve kalsiyum oksit bileşiklerinde bulunan bir elementtir. Kalsiyum, tuğlanın dayanıklılığını ve fiziksel özelliklerini önemli ölçüde iyileştirebilir. Demir (Fe), inorganik malzemelerin rengini etkileyebilecek ve yapısal bütünlüğü artırabilecek bir elementtir. Numunedeki demir oranı, tuğlanın oksidasyon özelliklerini ve genel dayanıklılığını etkileyebilir.

Numunenin gözenekli yapısı, onun hafiflik ve dayanıklılık arasında bir denge sağladığını gösterebilir. Bu tür bir yapı, malzemenin termal özelliklerini etkileyebilir ve ısıya karşı dirençli olmasına katkıda bulunabilir. Aynı zamanda, heterojen yapılar, malzemenin farklı bileşenlerden oluştuğunu ve her bir bileşenin tuğlanın genel özelliklerine farklı etkilerde bulunabileceğini göstermektedir.

63-2 numaralı numune, silikat ve oksit bileşiklerinden zengin bir yapıya sahip olup, mineralojik açıdan heterojen özellikler göstermektedir. Oksijen (O) ve alüminyum (Al), silisyum (Si) gibi elementlerin yüksek oranları, tuğlanın termal ve mekanik dayanıklılığını artıran faktörler olarak değerlendirilebilir. Potasyum (K) ve sodyum (Na) gibi alkali metallerin varlığı ise, özellikle numunenin kimyasal stabilitesini ve yüksek sıcaklık koşullarına karşı dayanıklılığını olumlu yönde etkileyebilir. Titanyum (Ti) gibi elementlerin düşük oranları, numunenin özellikleri üzerinde sınırlı bir etkiye sahipken, silikat yapılarının dominant olması, malzemenin dayanıklılığını pekiştiren bir etken olarak öne çıkmaktadır. Bu analizler, numunenin yapısal ve kimyasal özelliklerinin harman tuğla üretimi için önemli bir parametre olduğunu ve bu özelliklerin numunenin mekanik ve termal dayanıklılığını doğrudan etkilediğini göstermektedir (Şekil 15).

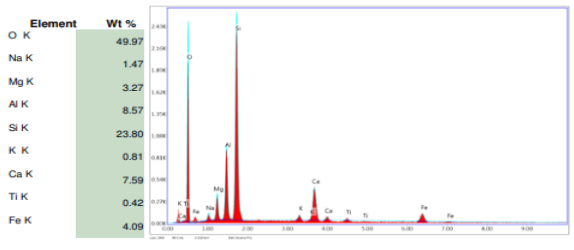

Şekil 15. 63-2 numaralı numunenin EDX verileri

63-3 numaralı numunenin SEM görüntülerinde numunenin gözenekli, kristal ve heterojen yapıda olduğu tespit edilmiştir (Şekil 16).

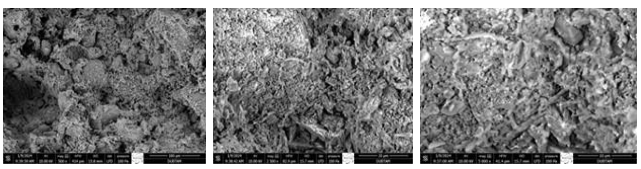

Şekil 16. 63-3 numaralı numuneni 500x, 2500x ve 5000x SEM görüntüleri

EDX ile yapılan analiz sonucunda, 63-3 numaralı numune içerisinde Oksijen (O), sodyum (Na), magnezyum (Mg), alüminyum (Al), silisyum (Si), potasyum (K), kalsiyum (Ca) ve demir (Fe) elementler tespit edilmiştir. Analiz sonuçlarına göre, numune içerisindeki en yüksek oranda bulunan element oksijen (O) olurken, en düşük oranda bulunan element magnezyum (Mg) olarak belirlenmiştir.

Oksijen (O), en baskın element olarak bulunmuştur. Numunedeki oksijen oranının yüksek olması, yapının büyük ölçüde oksit ve silikat bileşiklerinden oluştuğunu göstermektedir. Oksijenin varlığı, özellikle silisyum (Si), alüminyum (Al), kalsiyum (Ca) ve demir (Fe) gibi elementlerle birlikte çeşitli metal oksitlerin ve alüminosilikat fazlarının oluşumuna işaret eder. Bu durum, tuğlanın yüksek sıcaklıklara karşı dayanıklılığını artırmakta ve yapısal bütünlüğünü sağlamaktadır [14]. Silisyum (Si) ve Alüminyum (Al) tuğla yapımında sıklıkla karşılaşılan ve kil kökenli hammaddelerden kaynaklanan ana bileşenlerdir. Bu elementler, silikat minerallerinin (örneğin kuvars, feldspat) ve alüminosilikat fazlarının (örneğin mullit) oluşumuna göstermektedir. Bu tür fazlar, malzemenin hem mekanik dayanımını hem de yüksek sıcaklıktaki kararlılığını güçlendirir [15].Potasyum (K) ve Sodyum (Na), çoğunlukla feldspat grubu mineraller aracılığıyla yapıya katılır. Bu elementler seramik üretiminde akışkanlaştırıcı olarak görev yapar ve sinterleme sıcaklığını düşürerek eriyik fazın oluşumunu kolaylaştırır [16]. Ayrıca cam fazların oluşumuna katkı sağlayarak gözenekliliği azaltabilir ve yüzey düzgünlüğünü iyileştirebilir. Kalsiyum (Ca) elementi, genellikle kalsit ($CaCO_3$) veya kalsiyum silikat bileşenleri şeklinde bulunur. Kalsiyum, tuğla içerisinde hidrolik özelliklerin oluşmasına katkı sağlayabilir ve bağlayıcılık özelliklerini güçlendirir [17] . Bazı kalsiyumlu fazlar, ürünün suya karşı dayanımını artırabilir. Demir (Fe) elementi genellikle Fe_2O_3 (hematit) formunda bulunur ve tuğlaya karakteristik kırmızımsı-kahverengi renk kazandırır. Aynı zamanda demir oksitler, pişme davranışını etkileyebilir. Yüksek oranda demir (Fe) içeren yapılar, oksidatif koşullarda daha düşük sıcaklıklarda sinterleme sağlayabilir [18]. Magnezyum (Mg), numune içerisinde en düşük oranda bulunan element olarak tespit edilmiştir. Genellikle dolomit, talk, veya klorit gibi minerallerden gelen magnezyum (Mg), düşük konsantrasyonda olsa bile malzemenin ısıl genleşmesini ve refrakter özelliklerini etkileyebilir [14]. Ancak bu numunede düşük oranda bulunması, magnezyumun (Mg) yapısal etkiye katkısının sınırlı olduğunu göstermektedir.

63-3 numaralı harman tuğla numunesi, klasik seramik malzemelerin yapısal özelliklerine sahip bir kompozisyon göstermektedir. Oksijen, silisyum ve alüminyumun yüksek oranları, silikat ve alümin silikat fazlarının baskın olduğunu ve bu fazların tuğlanın mekanik ve termal dayanıklılığını artırdığını ortaya koymaktadır. Sodyum ve potasyum gibi alkali metallerin varlığı, sinterleme sürecinde eriyik oluşumunu kolaylaştırarak ürünün yoğunluğunu ve yüzey kalitesini artırabilir. Kalsiyumun bağlayıcı özellikleri ve demirin oksidatif ortamlarda renk ve sinterleme davranışına etkisi malzemenin performansını doğrudan etkilemektedir. Magnezyumun düşük oranı ise refrakter özelliklerin sınırlı düzeyde olduğunu göstermektedir. Ancak genel kimyasal kompozisyon, numunenin yapı malzemesi olarak kullanılabilirliğini destekleyen özelliklere sahip olduğunu göstermektedir (Şekil 17).

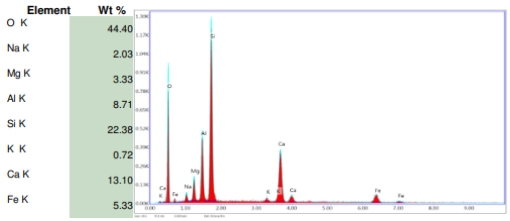

Şekil 17. 63-3 numaralı numunenin EDX verileri

63-4 numaralı tuğla numunesi üzerinde gerçekleştirilen Taramalı Elektron Mikroskobu (SEM) analizleri, numunenin mikro-yapısal açıdan gözenekli, kristal yapılı ve heterojen bir morfolojiye sahip olduğunu ortaya koymuştur. Bu durum, malzemenin üretim sürecinde kullanılan ham madde karışımı ile pişirme koşullarının bir sonucu olarak değerlendirilebilir[19].Gözenekli yapı, su emme kapasitesini artırarak malzemenin tuz hasarına ve donma-çözülme döngülerine karşı hassas hale gelmesine neden olabilir [20] (Şekil 18).

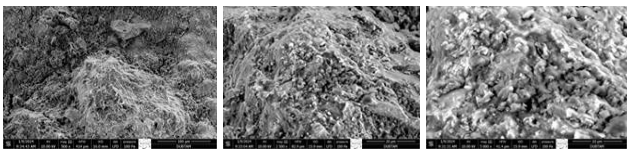

Şekil 18. 63-4 numaralı numunenin 500x, 2500x ve 5000x SEM görüntüleri

EDX analizlerinde, tuğlanın kimyasal bileşimi hakkında önemli veriler sunmuştur. Analiz sonuçlarına göre, numune içerisinde karbon (C), oksijen (O), sodyum (Na), magnezyum (Mg), alüminyum (Al), silisyum (Si), potasyum (K), kalsiyum (Ca), titanyum (Ti) ve demir (Fe) elementleri tespit edilmiştir. Bu elementler, geleneksel pişmiş toprak yapı malzemelerinde yaygın bileşenlerdir ve çoğunlukla kil minerallerinden veya katkı malzemelerinden kaynaklanmaktadır [21]. Analizde en yüksek oranda bulunan elementin karbon (C) olması, organik kalıntıların varlığına, karbonatlı bileşiklere ya da atmosferik kirleticilerin yüzeyde birikmesine işaret edebilir. Karbonun yüksek oranlarda bulunması, ayrıca pişirme sürecinin tam anlamıyla tamamlanmamış olabileceğini ya da düşük sıcaklıkta pişirmenin söz konusu olduğunu da düşündürebilir [22]. Ayrıca, titanyum (Ti) elementinin en düşük oranda bulunması, bu elementin doğal kil mineralleri içinde eser miktarda yer aldığını göstermektedir.

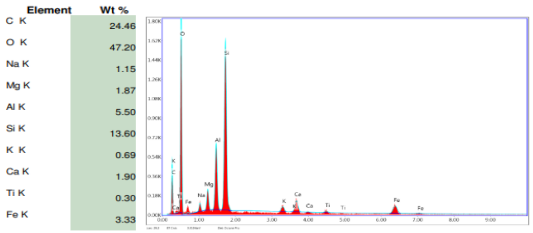

Şekil 20. 63-4 numaralı numunenin EDX verileri

63-5 numaralı numunenin taramalı elektron mikroskobu (SEM) görüntüleri incelendiğinde, malzemenin gözenekli, kristal ve heterojen bir yapıya sahip olduğu belirlenmiştir. Gözeneklilik, yapı malzemelerinin mekanik dayanımını ve çevresel etkilere karşı direncini doğrudan etkileyen önemli bir parametre olup, özellikle tarihi yapı elemanlarında bozulma süreçlerinin anlaşılması açısından kritik bir göstergedir [21]. Numunenin heterojen yapısı ise, kullanılan ham madde çeşitliliğini ve üretim sürecinde farklı mineral bileşenlerin katkısını işaret etmektedir (Şekil 21).

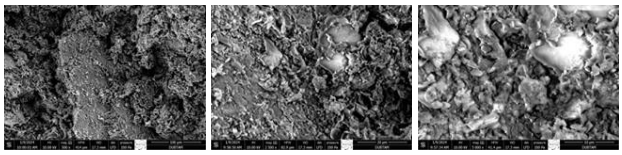

Şekil 21. 63-5 numaralı numunenin 500x, 2500x ve 5000x SEM görüntüleri

EDX analizlerinde, numune içerisinde oksijen (O), sodyum (Na), magnezyum (Mg), alüminyum (Al), silisyum (Si), potasyum (K), kalsiyum (Ca) ve demir (Fe) elementlerinin bulunduğu tespit edilmiştir. Bu elementlerin varlığı, malzemenin esas olarak silikat esaslı bir matris yapısına sahip olduğunu ve doğal taş ya da harç kökenli bir malzemeden oluştuğunu göstermektedir [23]. Numune içerisinde en yüksek oranda bulunan elementin oksijen (O) olması, silikat ve alüminat fazların yoğunluğunu desteklemektedir. Silisyum (Si) ve alüminyum (Al) varlığı ise kuvars, feldspat ve kil minerallerinin varlığına işaret edebilir. Kalsiyum (Ca) içeriği, kireç bağlayıcılı fazların veya karbonatlı bileşenlerin (ör. kalsit) katkısını düşündürmektedir. Sodyum (Na) ve potasyum (K) düşük oranlarda tespit edilmiş olup, bu durum alkali feldspat minerallerinden ya da ikincil çökelmelerden kaynaklanabilir [24]. Demir (Fe) varlığı ise mineralojik açıdan hematit veya goetit gibi demir oksit fazlarının katkısına işaret etmektedir. Özellikle potasyumun (K) en düşük oranda bulunması, malzemenin mineralojik kompozisyonunun feldspat açısından sınırlı olduğunu düşündürmektedir. Bu tür kimyasal dağılımlar, tarihi yapı malzemelerinin üretim tekniği, kullanılan ham madde kaynağı ve zamanla maruz kaldığı çevresel etkiler hakkında önemli bilgiler sunmaktadır [25] (Şekil 22).

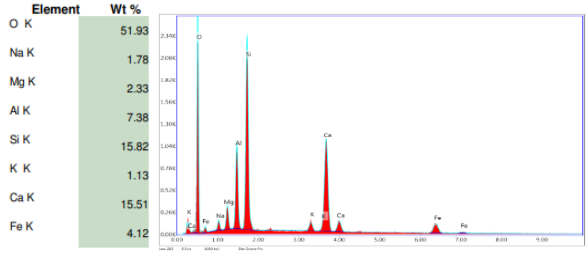

Şekil 22. 63-5 numaralı numunenin EDX verileri

63-6 numaralı numunenin taramalı elektron mikroskobu (SEM) görüntüleri incelendiğinde, malzemenin gözenekli, kristal ve heterojen bir yapıya sahip olduğu belirlenmiştir. Gözeneklilik, yapı malzemelerinin dayanıklılığını olumsuz yönde etkileyebilen ve özellikle nem, tuz kristalleşmesi ile donma-çözülme gibi bozulma süreçlerine karşı hassasiyeti artıran bir özelliktir [21] Kristal ve heterojen yapının ham madde çeşitliliği ve üretim sürecindeki farklı mineral fazların bir arada bulunduğuna işaret etmektedir (Şekil 23).

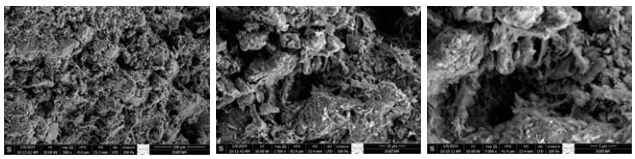

Şekil 23. 63-6 numaralı numunenin 500x, 2500x ve 5000x SEM görüntüleri

EDX analizlerinde, numune içerisinde oksijen (O), sodyum (Na), magnezyum (Mg), alüminyum (Al), silisyum (Si), potasyum (K), kalsiyum (Ca) ve demir (Fe) elementleri tespit edilmiştir. Analiz verilerine göre en yüksek oranda bulunan element oksijen (O) olurken, en düşük oranda potasyum (K) saptanmıştır. Oksijenin yüksek oranda bulunması, malzemenin esas olarak oksit ve silikat fazlarından oluştuğunu göstermektedir (Şekil 24). Bu durum, silisyum (Si), alüminyum (Al), kalsiyum (Ca) ve demir (Fe) ile farklı metal oksitlerin ve alüminosilikat minerallerinin oluşumuna işaret etmektedir. Bu tür fazların varlığı, malzemenin yüksek sıcaklıklara karşı kararlılığını artırarak pişirme sürecinde yapısal bütünlüğün korunmasına katkı sağlar [14]. Silisyum (Si) ve alüminyum (Al), kil kökenli hammaddelerden gelen temel bileşenler olup, kuvars, feldspat ve mullit gibi minerallerin oluşumunu destekler. Bu fazlar, tuğla veya seramik esaslı malzemelerin mekanik dayanımını güçlendirmekte ve termal kararlılığını artırmaktadır [15]. Sodyum (Na) ve potasyum (K), feldspat minerallerinden gelen alkali elementlerdir. Potasyumun en düşük oranda bulunması, bu mineral fazların sınırlı katkısına işaret etmektedir. Bununla birlikte, düşük miktarlarda bile bu elementler sinterleme sıcaklığını düşürerek cam faz oluşumuna katkı sağlayabilir ve gözeneklilik üzerinde etkili olabilir [16]. Kalsiyum (Ca), kalsit veya kalsiyum silikat fazlarıyla ilişkili olup, bağlayıcılık özelliklerinin güçlenmesine ve suya karşı dayanımın artmasına katkıda bulunabilir [17]. Demir (Fe) ise genellikle hematit (Fe_2O_3) formunda bulunur; malzemeye kırmızımsı kahverengi rengini verirken aynı zamanda pişme davranışını da etkileyebilir (Mackenzie & Bowden, 1999). Magnezyum (Mg), dolomit veya kil mineralleriyle ilişkili olup düşük oranlarda dahi malzemenin ısıl genleşme ve refrakter özelliklerine katkı sağlayabilir (Kingery vd., 1976). Ancak bu numunede nispeten sınırlı bir miktarda bulunması, yapısal etkiye katkısının düşük olduğunu göstermektedir.

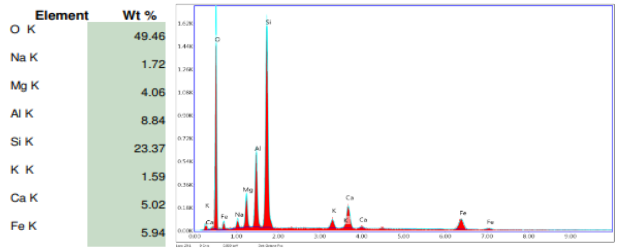

Şekil 24. 63-6 numaralı numunenin EDX verileri

63-7 numaralı numunenin taramalı elektron mikroskobu (SEM) görüntülerine göre, malzemenin gözenekli, kristal ve heterojen bir yapıya sahip olduğu görülmüştür. Gözenekli yapı, malzemenin dayanıklılığını ve çevresel etkilere (ör. nem, tuz kristalleşmesi, donma-çözülme) karşı hassasiyetini doğrudan etkileyen önemli bir özelliktir [21] Kristal ve heterojen yapı ise farklı mineral bileşenlerin bir arada bulunduğunu, hammaddenin çeşitli kaynaklardan geldiğini ve pişirme sürecinde çoklu fazların oluştuğunu göstermektedir.

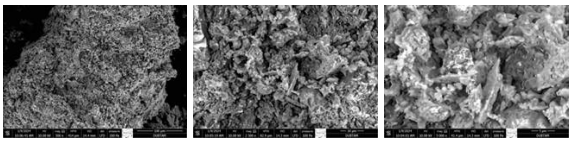

Şekil 25. 63-7 numaralı numunenin 500x, 2500x ve 5000x SEM görüntüleri

EDX analizlerinde, numune içerisinde oksijen (O), sodyum (Na), magnezyum (Mg), alüminyum (Al), silisyum (Si), potasyum (K), kalsiyum (Ca) ve demir (Fe) elementleri tespit edilmiştir. Analiz bulgularına göre en yüksek oranda bulunan element oksijen (O) olurken, en düşük oranda potasyum (K) belirlenmiştir.

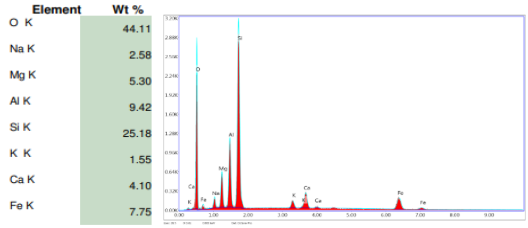

Şekil 26. 63-7 numaralı numunenin EDX verileri

63-8 numaralı numunenin taramalı elektron mikroskobu (SEM) görüntülerinde, malzemenin kristal ve heterojen bir yapıya sahip olduğu belirlenmiştir. Kristal yapının varlığı, hammadde kaynaklı mineral fazların belirginliğine ve pişirme sürecinde kristalizasyonun etkin rolüne işaret etmektedir [21] (Şekil 27)

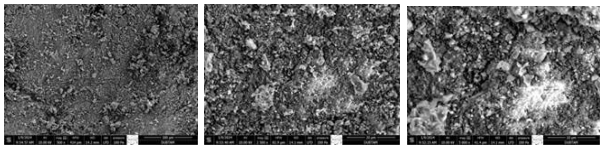

Şekil 27. 63-8 numaralı numunenin 500x, 2500x ve 5000x SEM görüntüleri

EDX analizlerinde, numunede oksijen (O), sodyum (Na), magnezyum (Mg), alüminyum (Al), silisyum (Si), potasyum (K), kalsiyum (Ca), titanyum (Ti) ve demir (Fe) elementleri tespit edilmiştir. Analiz bulgularına göre en yüksek oranda oksijen (O) bulunurken, en düşük oranda titanyum (Ti) saptanmıştır. Oksijenin yüksek oranda bulunması, malzemenin esas olarak oksit ve silikat fazlarından oluştuğunu göstermektedir. Silisyum (Si) ve alüminyum (Al) varlığı, kuvars, feldspat ve mullit gibi silikat ve alüminosilikat minerallerinin oluşumuna işaret eder. Bu tür fazların varlığı, malzemenin hem mekanik dayanımını hem de yüksek sıcaklıktaki kararlılığını artırmaktadır [15]. Sodyum (Na) ve potasyum (K), feldspat kökenli alkali elementler olup, seramik üretiminde akışkanlaştırıcı rol üstlenir. Sinterleme sıcaklığını düşürerek eriyik faz oluşumuna katkı sağlamakta ve cam faz oluşumunu destekleyerek gözeneklilik üzerinde etkili olmaktadırlar [16] Kalsiyum (Ca), genellikle kalsit ($CaCO_3$) ya da kalsiyum silikat fazları ile ilişkili olup, bağlayıcı özelliklerin güçlenmesine katkı sağlar. Aynı zamanda malzemenin suya karşı dayanımını artırabilir [17]. Demir (Fe), genellikle hematit (Fe_2O_3) formunda bulunur ve malzemeye kırmızımsı kahverengi rengini verirken, pişme davranışını da etkileyebilmektedir [18].Numune içerisinde en düşük oranda tespit edilen titanyum (Ti), genellikle kil mineralleri içerisinde eser miktarda bulunan bir elementtir. TiO_2, düşük konsantrasyonlarda bulunsa da malzemeye beyazlık derecesi kazandırabilir ve renk üzerinde ikincil etkiler oluşturabilir [27]. Bu nedenle, titanyumun düşük oranda bulunması, yapının mineralojik kompozisyonu üzerinde sınırlı bir etkiye sahip olduğunu göstermektedir (Şekil 28).

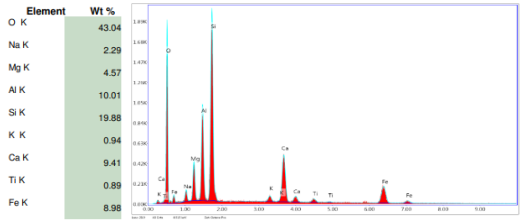

Şekil 28. 63-8 numaralı numunenin EDX verileri

64-1 numaralı numunenin taramalı elektron mikroskobu (SEM) görüntülerinde, malzemenin gözenekli, kristal ve heterojen bir yapıya sahip olduğu belirlenmiştir. Gözenekli yapı, malzemenin mekanik dayanımını olumsuz etkileyebilen ve çevresel etkilere (ör. nem, tuz kristalleşmesi, donma-çözülme döngüleri) karşı hassasiyetini artıran bir özelliktir [21] Kristal ve heterojen yapı ise, hammaddenin mineralojik çeşitliliğini ve pişirme sürecinde farklı fazların oluşumunu ortaya koymaktadır (Şekil 29)

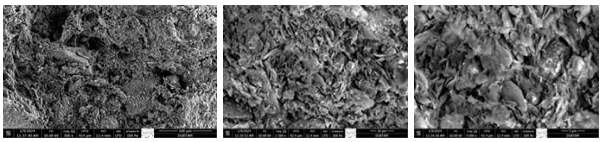

Şekil 29. 64-1 numaralı numunenin 500x, 2500x ve 5000x SEM görüntüleri

EDX analiz sonucunda, numune içerisinde oksijen (O), sodyum (Na), magnezyum (Mg), alüminyum (Al), silisyum (Si), potasyum (K), kalsiyum (Ca) ve demir (Fe) elementleri tespit edilmiştir. Bulgulara göre en yüksek oranda oksijen (O), en düşük oranda ise sodyum (Na) bulunmuştur.

Oksijenin yoğunluğu, malzemenin esas olarak oksit ve silikat fazlarından oluştuğunu göstermektedir. Silisyum (Si) ve alüminyum (Al) varlığı, kuvars, feldspat ve mullit gibi minerallerin oluşumuna işaret etmektedir. Bu fazlar, malzemenin yüksek sıcaklık dayanımını artırmakta ve mekanik kararlılığını güçlendirmektedir [15]. Sodyum (Na)

ve potasyum (K), genellikle feldspat mineralleri aracılığıyla yapıya katılmaktadır. Bu elementler seramik pişirimi sırasında eriyik faz oluşumuna katkı sağlamakta, sinterleme sıcaklığını düşürmekte ve gözenekliliği azaltarak yüzey özelliklerini iyileştirmektedir [16]. Ancak bu numunede sodyumun en düşük oranda bulunması, bu etkinin sınırlı olabileceğini göstermektedir. Kalsiyum (Ca), kalsit ($CaCO_3$) veya kalsiyum silikat fazlarıyla ilişkili olup, bağlayıcılık özelliklerini güçlendirir ve malzemenin suya karşı dayanımını artırabilir [17]. Demir (Fe), genellikle hematit (Fe_2O_3) formunda bulunmakta; tuğlaya kırmızımsı kahverengi rengini kazandırmakta ve pişme davranışını etkilemektedir [18]. Magnezyum (Mg) ise düşük oranlarda dahi refrakter özelliklere ve ısıl genleşme davranışına katkıda bulunabilir [14]. Genel olarak, 64-1 numunesinin element dağılımı, silikat esaslı yapı malzemelerine özgü tipik bir kompozisyon ortaya koymaktadır. Oksijen, silisyum ve alüminyumun baskınlığı, malzemenin esas yapısal matrisini oluştururken; kalsiyum, demir ve alkali elementler (Na, K) ise bağlayıcı, renk ve pişme özelliklerini etkilemektedir (Şekil 30).

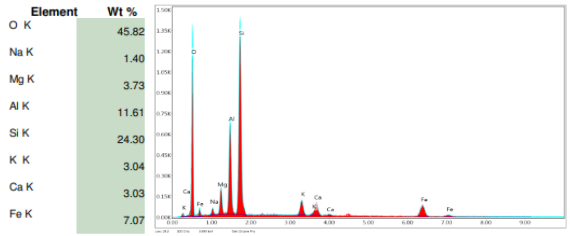

Şekil 30. 64-1 numaralı numunenin EDX verileri

64-2 numaralı numunenin taramalı elektron mikroskobu (SEM) incelemeleri sonucunda, malzemenin gözenekli, kristal ve heterojen bir yapıya sahip olduğu tespit edilmiştir. Gözenekli yapı, suyun ve çözünmüş tuzların malzeme bünyesine nüfuzunu kolaylaştırarak bozunma süreçlerini hızlandırabilmektedir [15] Kristal ve heterojen doku ise, kullanılan hammaddenin mineralojik çeşitliliğini ve pişirme esnasında farklı fazların oluşumunu yansıtmaktadır (Şekil 31).

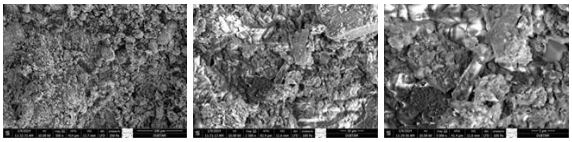

Şekil 31. 64-2 numaralı numunenin 500x, 2500x ve 5000x SEM görüntüleri

EDX analizlerinde, 64-2 numunesinde oksijen (O), sodyum (Na), magnezyum (Mg), alüminyum (Al), silisyum (Si), kükürt (S), kalsiyum (Ca) ve demir (Fe) elementleri belirlenmiştir. Bu elementler arasında en yüksek oranda oksijen (O), en düşük oranda ise magnezyum (Mg) tespit edilmiştir. Oksijenin oksit ve silikat esaslı bir matris yapısına sahip olduğunu göstermektedir. Silisyum (Si) ve alüminyum (Al), kuvars, feldspat ve kil minerallerinden türeyen fazların varlığını ortaya koymakta; bu fazlar malzemenin mekanik dayanıklılığını ve yüksek sıcaklık performansını belirlemektedir [15]. Kalsiyum (Ca), kalsiyum silikat veya kalsit kaynaklı bileşenlerin malzeme bünyesine katkısını işaret etmektedir. Bu fazlar, bağlayıcılık özelliklerini desteklerken, aynı zamanda malzemenin suya karşı dayanıklılığını artırmaktadır [17] Demir (Fe) ise genellikle hematit (Fe_2O_3) formunda bulunmakta ve tuğla ile seramiklerde gözlenen kırmızımsı renklenmeyi sağlamaktadır [18] Numunede düşük oranda tespit edilen magnezyum (Mg), yapıya refrakter özellik kazandırabilmekte, fakat düşük seviyelerde bulunması nedeniyle bu etkinin sınırlı olduğu düşünülmektedir [14]. Ayrıca, bu numunede diğer örneklerden farklı olarak kükürt (S) varlığı dikkat çekmektedir. Kükürt, genellikle çevresel etkiler sonucu (ör. sülfat tuzlarının kristalleşmesi) malzemeye sonradan taşınan bir bileşen olarak değerlendirilmektedir. Sülfat tuzlarının malzeme içerisinde birikmesi, genleşme ve çatlama gibi bozulmalara yol açabilmektedir [26].

64-2 numunesinin elementel bileşimi, oksit ve silikat esaslı tipik bir yapı malzemesi kompozisyonuna işaret etmekle birlikte; kükürt varlığı, çevresel tuz etkilerine maruz kalındığını göstermektedir. Bu durum, numunenin bozulma süreçlerine açık olduğunu ve özellikle sülfat kaynaklı degradasyona karşı hassasiyet taşıdığını ortaya koymaktadır (Şekil 32).

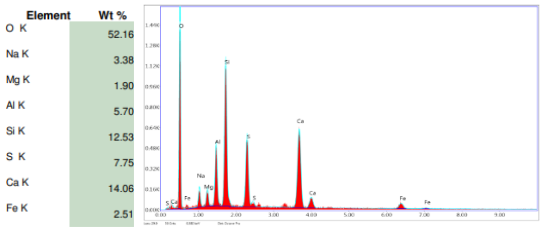

Şekil 32. 64-2 numaralı numunenin EDX verileri

64-3 numaralı burçtan alınan 3 numaralı numunenin SEM görüntülerine bakılarak numunenin gözenekli, kristal ve heterojen yapıda olduğu tespit edilmiştir (Şekil 33).

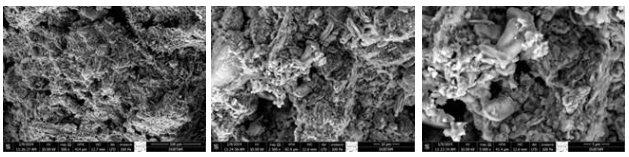

Şekil 33. 64-3 numaralı numunenin 500x, 2500x ve 5000x SEM görüntüleri

64 numaralı burçtan alınan 3 numaralı numunenin taramalı elektron mikroskobu (SEM) incelemeleri sonucunda, malzemenin gözenekli, kristal ve heterojen bir yapıya sahip olduğu belirlenmiştir. Gözenekli doku, malzemenin mekanik dayanımını zayıflatmakla birlikte nem ve tuz taşınımını kolaylaştırarak bozulma süreçlerini hızlandırabilmektedir [21]. Kristal ve heterojen yapı ise, hammaddenin mineralojik çeşitliliğini ve üretim sürecinde farklı fazların oluştuğunu göstermektedir.

EDX analizlerinde 64-3 numunesinde oksijen (O), sodyum (Na), magnezyum (Mg), alüminyum (Al), silisyum (Si), potasyum (K), kalsiyum (Ca) ve demir (Fe) elementleri tespit edilmiştir. Bu elementler arasında en yüksek oranda oksijen (O), en düşük oranda ise sodyum (Na) bulunmuştur.

Oksijenin yoğun miktarda bulunması, malzemenin oksit ve silikat esaslı bileşiklerden oluştuğunu göstermektedir. Silisyum (Si) ve alüminyum (Al), kuvars ve kil kökenli minerallerden türeyen fazların varlığına işaret eder; bu fazlar hem mekanik dayanıklılığı artırmakta hem de yüksek sıcaklık direncini desteklemektedir [15]. Kalsiyum (Ca), genellikle kalsit veya kalsiyum silikat fazları şeklinde bulunarak bağlayıcılık özelliklerine katkı sağlar ve malzemenin suya karşı dayanımını güçlendirir [17]. Demir (Fe), genellikle hematit (Fe_2O_3) formunda bulunmakta olup tuğlaya kırmızımsı rengini vermekte ve pişme davranışını etkilemektedir [18]. Potasyum (K) ve sodyum (Na) gibi alkali elementler ise çoğunlukla feldspat minerallerinden kaynaklanmakta ve seramiklerde akışkanlaştırıcı rol üstlenerek sinterleme sıcaklığını düşürmektedir [16]. Ancak bu numunede sodyumun en düşük oranda bulunması, alkali katkının sınırlı kaldığını göstermektedir.

64-3 numunesi, oksit ve silikat esaslı bir yapı malzemesi karakteri sergilemekte; düşük orandaki sodyum içeriği ise malzemenin mineralojik kompozisyonunda alkali feldspat katkısının sınırlı olduğunu işaret etmektedir. Bu durum, numunenin pişme koşulları ve hammaddenin mineralojik yapısı hakkında bilgi vermektedir (Şekil 34).

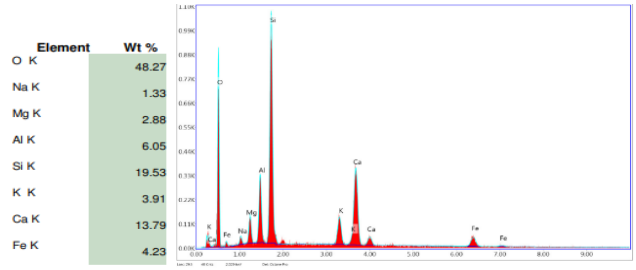

Şekil 34. 64-3 numaralı numunenin EDX verileri

64-4 numaralı numunenin taramalı elektron mikroskobu (SEM) görüntüleri incelendiğinde, malzemenin gözenekli, kristal ve heterojen bir yapıya sahip olduğu belirlenmiştir. Gözenekli doku, nem ve tuz taşınımını kolaylaştırarak malzemenin bozulma süreçlerine açık hale getirmekte; kristal ve heterojen yapı ise mineralojik çeşitliliği ve üretim sürecinde farklı fazların oluşumunu yansıtmaktadır [21

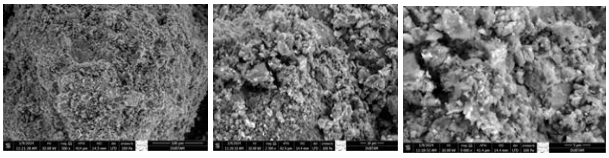

Şekil 35. 64-4 numaralı numunenin 500x, 2500x ve 5000x SEM görüntüleri

SEM-EDX analiz sonuçlarına göre numune içeriğinde sekiz temel element tespit edilmiştir: oksijen (O) %51,80; kalsiyum (Ca) %16,32; silisyum (Si) %13,38; alüminyum (Al) %6,26; demir (Fe) %5,16; potasyum (K) %2,94; magnezyum (Mg) %2,18 ve sodyum (Na) %1,96. Bu sonuçlara göre, en yüksek oranda bulunan element oksijen (O), en düşük oranda bulunan element ise sodyum (Na) olmuştur.

Analizler sonucunda, oksijen miktarının fazla olması, malzemenin oksit ve silikat esaslı bir yapıya sahip olduğunu göstermektedir. Silisyum (Si) ve alüminyum (Al) varlığı, kuvars, feldspat ve kil kökenli minerallerden türeyen fazların olduğunu düşündürtmektedir. Bu fazların yüksek sıcaklık dayanımı ve mekanik direnç açısından önemli olduğu bilinmektedir [15].

Kalsiyum (Ca), %16,32 oranı ile oldukça belirgin olup, kalsit veya kalsiyum silikat kökenli fazların olabileceğini göstermektedir. Bu fazların, bağlayıcı özellikleri destekleyerek malzemenin suya karşı mukavemetini arttıracağı düşünülmektedir.[17]. Demir (Fe), %5,16 oranında bulunmuş olup genellikle hematit (Fe_2O_3) formunda gözlenir. Bu element, tuğla ve harçlarda kırmızımsı renklenmeye neden olurken aynı zamanda pişme davranışını etkileyebilmektedir [18] Potasyum (K) ve sodyum (Na) gibi alkali elementler, düşük oranlarda tespit edilmiştir. Bu elementler çoğunlukla feldspat kökenli olup, seramiklerde sinterleme sıcaklığını düşürerek camsı fazların oluşumunu kolaylaştırmaktadır [16]. Ancak bu numunede düşük seviyelerde bulunmaları, alkali katkının sınırlı olduğunu göstermektedir. Magnezyum (Mg) ise %2,18 oranında tespit edilmiş olup, refrakter özelliklere kısmi katkı sağlayabilmektedir [14]

64-4 numunesi oksit ve silikat esaslı tipik bir yapı malzemesi bileşimi sergilemekte; özellikle yüksek orandaki kalsiyum elementi, malzemenin bağlayıcılık özelliklerinin güçlü olduğunu göstermektedir. Buna karşın düşük sodyum ve potasyum oranları, alkali katkının sınırlı kaldığını ve camsı faz oluşumunun düşük seviyelerde gerçekleştiğini ortaya koymaktadır (Şekil 35).

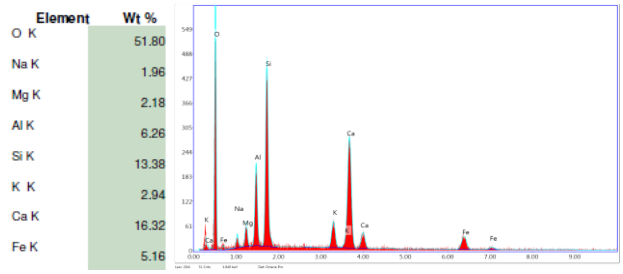

Şekil 34. 64-4 numaralı numunenin EDX verileri

Tablo 4. 63 Numaralı Burç (Fındık Burcu) Numuneleri için SEM/EDX Analiz Sonuçları

Numune	Tespit Edilen Elementler	En Yüksek Oranda Bulunan Element	En Düşük Oranda Bulunan Element	Özellikler
63-1	O, Mg, Al, Si, Ca, Fe	O (oksijen)	Mg (magnezyum)	Gözenekli, heterojen yapıda
63-2	O, Na, Mg, Al, Si, K, Ca, Ti, Fe	O (oksijen)	Ti (titanyum)	Gözenekli, kristal, heterojen yapıda
63-3	O, Na, Mg, Al, Si, K, Ca, Fe	O (oksijen)	Mg (magnezyum)	Gözenekli, kristal, heterojen yapıda
63-4	C, O, Na, Mg, Al, Si, K, Ca, Ti, Fe	C (karbon)	Ti (titanyum)	Gözenekli, kristal, heterojen yapıda
63-5	O, Na, Mg, Al, Si, K, Ca, Fe	O (oksijen)	K (potasyum)	Gözenekli, kristal, heterojen yapıda
63-6	O, Na, Mg, Al, Si, K, Ca, Fe	O (oksijen)	K (potasyum)	Gözenekli, kristal, heterojen yapıda
63-7	O, Na, Mg, Al, Si, K, Ca, Fe	O (oksijen)	K (potasyum)	Gözenekli, kristal, heterojen yapıda
63-8	O, Na, Mg, Al, Si, K, Ca, Ti, Fe	O (oksijen)	Ti (titanyum)	Kristal, heterojen yapıda

Tablo 5. 64 Numaralı Burç (64 Burcu) Numuneleri için SEM/EDX Analiz Sonuçları

Numune	Tespit Edilen Elementler	En Yüksek Oranda Bulunan Element	En Düşük Oranda Bulunan Element	Özellikler
64-1	O, Na, Mg, Al, Si, K, Ca, Ti, Fe	O (oksijen)	Ti (titanyum)	Gözenekli, kristal, heterojen yapıda
64-2	O, Na, Mg, Al, Si, K, Ca, Fe	O (oksijen)	Ti (titanyum)	Gözenekli, kristal, heterojen yapıda
64-3	O, Na, Mg, Al, Si, K, Ca, Fe	O (oksijen)	Ti (titanyum)	Gözenekli, kristal, heterojen yapıda
64-4	O, Na, Mg, Al, Si, K, Ca, Fe	O (oksijen)	Ti (titanyum)	Gözenekli, kristal, heterojen yapıda

4. Sonuç ve Öneriler

İnsanlık tarihinin erken dönemlerinden itibaren toprak, kerpiç ve tuğla gibi, doğal yapı malzemeleri yaygın olarak kullanılmıştır. Kerpiç malzeme, dış hava koşullarına karşı savunmasız kalırken, tuğla malzemenin üretim süreçleri teknolojinin gelişimiyle ana yapı malzemesi olarak kullanımını yaygınlaştırmıştır. Tuğla malzemenin tarihsel kökeni, Neolitik Dönem'e kadar gitmekte olup, Ürdün Nehri'nin kıyısında bulunan en eski tuğla kalıntıları, tuğla üretiminin başlangıcına dair önemli kanıtlar sunmaktadır. Bu dönemden itibaren tuğla, Anadolu, Mezopotamya, İran, Orta Asya, Mısır ve Osmanlı İmparatorluğu gibi medeniyetlerde yaygın olarak kullanılmıştır [28]

Tuğla üretiminde, en uygun hammaddeler illit ve kaolinit cinsi killerdir. Bu killer, yapısında silisyum (Si), alüminyum (Al), demir (Fe), magnezyum (Mg), kalsiyum (Ca), potasyum (K) ve sodyum (Na) gibi temel elementleri bulundurur (Çolak et al., 2020). Diyarbakır, Türkiye'nin güneydoğusunda yer alan tarihi ve kültürel zenginliklere sahip bir kent olup, surları ve Hevsel Bahçeleri ile UNESCO Dünya Mirası Listesi'nde yer almaktadır. Diyarbakır surları, 4. yüzyıl ortalarına tarihlenmekte olup, Mardin Kapı ile Yeni Kapı arasındaki sur duvarları, tuğla malzemenin yapısal olarak kullanıldığı önemli örnekler sunmaktadır.

SEM Analizleri, Diyarbakır surlarındaki tuğla malzemelerinin bileşim ve yapısal özellikleri hakkında derinlemesine bilgiler sunmaktadır. Yapılan analizler, her numunenin kimyasal bileşenlerini ve yapısal özelliklerini ortaya koymuş, bu malzemelerin zamanla maruz kaldığı çevresel etkiler ve üretim teknikleri hakkında önemli ipuçları sağlamıştır. Analizleri yapılan numunelerin birçoğunda tuğlanın heterojen yapıda olduğu tespit edilmiştir. Bu, malzemenin üretim sürecinde kullanılan ham maddelerin ve yapı taşlarının farklı mineral ve elementlerden oluştuğunu ve bunların çeşitli oranlarda bir araya geldiğini göstermektedir

SEM görüntülerinde tüm numunelerin gözenekli yapıda olduğu belirlenmiştir. Gözeneklilik, tuğlanın fiziksel dayanıklılığını ve izolasyon özelliklerini etkileyebilir. Özellikle iç mekanizmalarda kullanılan ham maddelerin birbirleriyle etkileşimini gösteren önemli bir parametre olarak değerlendirilir. Gözeneklilik, tuğlanın ısı yalıtımı gibi özelliklerini etkilerken, heterojen yapı, tuğlanın mikro yapısal dayanıklılığını ve çevresel etkilere karşı dayanıklılığını artırmıştır.

Oksijen (O), tüm numunelerde en yüksek oranda bulunan element olarak tespit edilmiştir. Bu durum, tuğla malzemelerinin genel yapısında yüksek oranda oksijen içeren bileşiklerin bulunduğunu göstermektedir. Elementel bileşim ve özellikle Oksijen (O) oranının yüksekliği, tuğlanın silikat bazlı bir yapıya sahip olduğunu doğrulamaktadır. Tuğlanın iç yapısının zamanla oluşmuş, belirli derecede kristalleşmiş yapılar içerdiğini, bu yapının dayanıklılığa etki edeceği düşünülmektedir.

Magnezyum (Mg) ve titanyum (Ti) gibi elementlerin düşük oranları, üretim koşullarının farklı olduğunu ve organik bileşiklerin kullanımının sınırlı olduğunu göstermektedir. Titanyum (Ti), bazı numunelerde en düşük oranda bulunan element olarak dikkat çekmektedir. Özellikle 63 numaralı burçtan alınan numunelerde, Titanyum en düşük konsantrasyona sahip element olarak öne çıkarken, 64 numaralı burç örneklerinde de Titanyum oranı benzer şekilde düşük bulunmuştur.

Bu bulgular, Diyarbakır surlarının tuğla malzemelerinin korunması ve restorasyonu sürecinde dikkate alınması gereken önemli faktörler sunmaktadır. Ayrıca, yapılan analizlerin sonuçları, tarihsel yapılar için uygun malzeme seçiminde yol gösterici olacaktır.

Dicle Üniversitesi Bilim Teknoloji Uygulama ve Araştırma Merkezi'nde (DÜBTAM) gerçekleştirilen SEM/EDX analizleri, Diyarbakır surlarından alınan tuğla numunelerinin içeriği hakkında önemli bilgiler sunmaktadır. Analiz sonuçlarına göre, numunelerin genel olarak kristal, heterojen ve gözenekli yapıya sahip olduğu tespit edilmiştir. Bu yapılar, tuğla malzemesinin zaman içinde fiziksel özelliklerini korunma durumlarını ve çevresel koşullara adaptasyon durumunu göstermektedir. Bazı numunelerde büyük boşluklar, çatlaklar ve mikro hasarlar gözlemlenmiş olup, bu durum, malzemenin uzun süreli kullanım ve çevresel etkiler sonucu hasar gördüğünü göstermektedir.

EDX analizleri, tuğla malzemesinin hammaddesi olan killerin kimyasal bileşimlerini doğrulamaktadır. Oksijen (O) ve silisyum (Si) elementlerinin yüksek oranda bulunması, tuğlanın genellikle silikat ve alüminat yapısına sahip olduğunu göstermiştir. Potasyum (K) ve sodyum (Na) elementlerinin düşük oranları, kullanılan ham maddenin özelliklerini ve üretim sürecinin doğasını yansıtmaktadır. Ayrıca, Titanyum (Ti) ve Karbon (C) gibi elementlerin varlığı, tuğla malzemesinin üretim sürecinde kullanılan ham maddelerin çeşitliliğine işaret etmektedir. Özellikle karbon (C) elementinin varlığı, tuğla malzemesinin ateşle etkileşimi sonucunda oluşmuş olabilir, bu da surlarda ateş yakılmasının tuğla yapısını nasıl etkileyebileceğine dair önemli ipuçları sunmaktadır. Kükürt (S) elementinin varlığı ise, 64 numaralı burçta farklı bir ham maddenin kullanıldığını veya çevresel faktörlerin etkisiyle kimyasal değişimlerin yaşandığını düşündürmektedir.

Öneriler

Diyarbakır surlarının tarihi ve kültürel önemi göz önüne alındığında, tuğla malzemenin özgün niteliklerinin korunması açısından oldukça önemlidir. Bu bağlamda, şu önerilerde bulunulabilir:

Kimyasal Bileşenlerin Korunması: Yapılacak restorasyon çalışmalarında, tuğla malzemesinin kimyasal bileşenlerinin korunması gerektiği vurgulanmalıdır. SEM/EDX analizlerinin sonuçları, tuğlanın ham maddesinin ve üretim tekniklerinin tarihsel bir bağlamda önemli olduğunu göstermesi nedeniyle, restore edilecek malzemenin bu kimyasal bileşimlere sadık kalınarak seçilmesi önerilmektedir.

Yapısal Stabilite: Surların yapısal bütünlüğünü sağlamak amacıyla, tuğla malzemenin gözenekli yapısının, restorasyon sırasında fiziksel özelliklerinin yeniden ele alınması gerekmektedir. Malzemenin su buharı geçirgenliği ve ısı yalıtımı özelliklerinin korunması için uygun restorasyon malzemeleri kullanılmalıdır.

İklimsel ve Çevresel Faktörler: Diyarbakır surları, aşırı sıcaklık değişimleri ve nemli iklim koşullarıyla karşı karşıya kalmaktadır. Bu nedenle, tuğla malzemesinin kimyasal dayanıklılığını artırmak için çevresel faktörlerin etkileri göz önünde bulundurulmalıdır. Restorasyon çalışmaları sırasında, tuğla malzemesinin asidik etkilere karşı korunması önemlidir

Sürekli İzleme ve Bakım: Restorasyon sonrası tuğla malzemesinin uzun vadeli dayanıklılığını sağlamak için düzenli izleme ve bakım çalışmalarına ihtiyaç vardır. Bu, yapının korunmasında kritik bir adım olacak ve surların özgün özelliklerinin gelecekte de korunmasına yardımcı olacaktır.

Sonuç olarak; yapılan çalışma Diyarbakır Surlarında kullanılan tuğla malzemenin tarihsel kökeni, yapısal özellikleri ve kimyasal bileşimini kapsamlı bir biçimde ele alarak, literatürde sınırlı düzeyde incelenmiş bir konuya katkı sağlamaktadır. Elde edilen bulgular, bölgenin özgün yapı malzemelerinin daha derinlemesine anlaşılmasına imkân tanımakta ve mevcut araştırmalara kıyasla yeni veriler sunarak bilimsel özgünlük ortaya koymaktadır. Bu yönüyle çalışma, hem kültürel miras yapı malzemeleri üzerine yapılan akademik araştırmaların genişletilmesine hem de restorasyon alanındaki disiplinler arası yaklaşımlara katkı sunmaktadır. Bununla birlikte, analizlerden elde edilen sonuçlar yalnızca Diyarbakır surlarının korunmasına değil, aynı zamanda benzer özellikler taşıyan kültürel miras yapılarına yönelik gelecekteki restorasyon uygulamalarına da yol gösterici niteliktedir. Çalışmanın ortaya koyduğu veriler, restorasyon süreçlerinde malzeme seçimi, koruma teknikleri ve sürdürülebilir müdahale yöntemleri açısından uygulamaya yönelik somut katkılar sağlamaktadır. Dolayısıyla bu araştırma, akademik literatüre ve kültürel mirasın korunmasına yönelik pratik uygulamalara iki yönlü bir katkı sağlayacağı düşünülmektedir.

Etik kurul onayı ve çıkar çatışması beyanı

"Hazırlanan makalede etik kurul izni alınmasına gerek yoktur"

"Hazırlanan makalede herhangi bir kişi/kurum ile çıkar çatışması bulunmamaktadır"

Yazar Katkıları

-Işık; Çalışma konsepti ve tasarım, verilerin analizi ve yorumlanması, Taslağın oluşturulması, Revizyon

-Okutmuştur; Veri toplama, Saha Çalışması

Teşekkür

Deneysel çalışmaların uygulanmasında sağlanan finansal destek için (Proje No: MİMARLIK.24.003) Dicle Üniversitesi Bilimsel Araştırma Projeleri Koordinatörlüğü'ne (DÜBAP) ve SEM/EDX analizlerinin uygulanmasında sağladıkları laboratuvar imkanları için Dicle Üniversitesi Bilim ve Teknoloji Uygulama ve Araştırma Merkezi'ne (DÜBTAM) teşekkür ederiz.

Kaynaklar

[1] Ö. Bakırer, "Selçuklu Öncesi ve Selçuklu Dönemi Anadolu mimarisinde tuğla kullanımı". Ankara: Orta Doğu Teknik Üniversitesi Yayını. 1981.

[2] M. Ağatekin, M., F.T.Filiz, (2022). "21. yy. yapı pratiğinde tuğlanın biçimsel ve işlevsel dönüşümleri". *Karadeniz Uluslararası Bilimsel Dergi*, 1(56), 17-29. https://doi.org/10.17498/kdeniz.1194194 17-29, 2022.

[3] J.Fiala, M.Mikolas, K.,Krejsova,. "Full brick, history and future". *IOP Conference Series: Earth and Enviromental Science,* 2019. https://doi.org 10.1088/1755-1315/221/1/012139

[4] G. Özışık, "*Yapı mühendisliğinde tuğla elemanlar ve yapı sistemleri".* İstanbul: Birsen Yayınevi.2000.

[5] A. G. Güzel, "*Ponza katkılı tuğla üretimi ve bu tuğlaların mekanik ve boşluk özelliklerinin incelenmesi".* İstanbul: İstanbul Teknik Üniversitesi Fen Bilimleri Enstitüsü.Yayımlanmamış Doktora Tezi.1993

[6] A.Ç. Öztürk, "*Tuğla üretiminde termik santral atığı puzolanik uçucu küllerin değerlendirilmesi üzerine bir araştırma".* Doktora Tezi, Mimar Sinan Güzel Sanatlar Üniversitesi Fen Bilimleri Enstitüsü, İstanbul. 2001.

[7] R. Okutmuştur, N, Işık. (2023). Diyarbakır Suriçi Bölgesi Mardin Kapı-Yeni Kapı Arası sur duvarlarında tuğla malzemenin kullanım alanları ile yapısal sorunların tespiti ve değerlendirilmesi. *III. International Architecture Symposium,* ,275-288. Diyarbakır.2023.

[8] C. Parla, "*Türk-İslam şehri olarak Diyarbakır".* Ankara: Hacettepe Üniversitesi Sosyal Bilimler Enstitüsü.Yüksek Lisans Tezi. 1990.

[9] unesco.org. (2024, Nisan 20). UNESCO: https://whc.unesco.org/archive/2015/whc15-39com-19-en.pdf , Erişim Tarihi 25.07.2025

[10] N. Işık, F.M. Halifeoğlu, M.Ş. Güler, "Tarihi Diyarbakır sur kapılarındaki yapısal hasarların georadar (GPR) yöntemiyle belirlenmesi: Urfa Kapı örneği". *Dicle University Journal of Engineering*, 101-109. 2022.

[11] F.M. Halifeoğlu, "Diyarbakır surlarının mimari özellikleri ve yapım tekniği". *Uluslararası Diyarbakır Surları Sempozyumu*.s. 115-129. Diyarbakır: Kültür Sanat Yayınları. 2012.

[12] Diyarbakır Rölöve Anıtlar Bölge Müdürlüğü Arşivi. 2023.

[13]] A. Petruccelli, *Understanding Islamic Architecture*. Routledge.2008.

[14] W. David Kingery, H. K. Bowen, Donald R. Uhlmann "*Introduction to Ceramics, 2nd Edition*" ISBN: 978-0-471-47860-7 . 1976.

[15] A. Elimbi, C.N. Djangang, M.A. Dika, & A. B. Tchamba, Use of kaolinite clay in the production of ceramic bricks. *Ceramics International*, 37(5), 1627–1633.2011.

[16] R. Siddique, & J. Klaus, Influence of mineral admixtures on the properties of high-performance concrete. *Construction and Building Materials*, 23(5), 2077–2086**,** 2009.

[17] M. H. Zhang, & O.E, Gjørv, Microstructure of the interfacial zone between lightweight aggregate and cement paste. *Cement and Concrete Research*, 30(6), 839–845.2000.

[18] K. J. Mackenzie. & M. E. Bowden, The role of iron oxides in the color of fired clays. *Applied Clay Science*, 14(1–3), 283–298,1999.

[19] X. Zhou, L. Zhang, , & H. Liu, "Microstructure of Fired Bricks Analyzed by SEM." *Construction and Building Materials*, 35, 167–174. 2012

[20] P.Lopez-Arce, A. Zornoza-Indart, A. "Evaluation of Porosity and Pore Structure in Historic Bricks by Mercury Intrusion Porosimetry." *Journal of Cultural Heritage*, 11(1), 58–64, 2010.

[21] A.Moropoulou, A. Bakolas, , & S. Anagnostopoulou, "Evaluation Of Porosity And Pore Structure In Historic Bricks *By Mercury Intrusion Porosimetry*" 2003.

[22] M, Singh, S. K Das, & B. Bhattacharyya, "Effect of Carbon on Microstructure and Properties of Fired Clay Bricks." *Ceramics International*, 33(6), 851–857.2007.

[23] K.L. Gauri, & J. K. Bandyopadhyay, *Carbonate stone: chemical behavior, durability, and conservation*. John Wiley & Sons. 1999.

[24] M. Stefanidou, I, Papayianni, The role of aggregates on the structure and properties of lime mortars. *Cement and Concrete Composites,* 27:914-919, 2005.

[25] F G Dimes, J. Ashurst Conservation of Building and Decorative Stone ISBN 9780750638982 Pages 466, *Publisher by Routledge.* May 6, 1998.

[26] A. E. Charola, Salts in the deterioration of porous materials: An overview. *Journal of the American Institute for Conservation*, 39 (3), 327–343.2000.

[27] W. A Deer, R. A., Howie, & J. Zussman, *An Introduction to the Rock-Forming Minerals*. 2nd edition. Longman Scientific & Technical, London.1992.

[28] W. P. James Campbell is Fellow in Architecture and History of Art, *Queen' College*, Cambridge,2003.

KAİP. Koruma Amaçlı İmar Planı Diyarbakır Büyükşehir Belediyesi Arşivi, 2012

Dicle University
Journal of Engineering
https://dergipark.org.tr/tr/pub/dumf
duje.dicle.edu.tr

Araştırma Makalesi/Research Article

Tuğla Üretiminden Kaynaklı Küresel Isınma Potansiyelinin Çevresel Ürün Beyanları Verileri Bağlamında İncelenmesi

Investigation of Global Warming Potential of Brick Production in the Context of Environmental Product Declarations Data

Yusuf Eşidir[1*], Arzuhan Burcu Gültekin[2], Hüseyin Yılmaz Aruntaş[3], Çiğdem Belgin Dikmen[4]

[1] Gazi Üniversitesi, Fen Bilimleri Enstitüsü, İnşaat Mühendisliği (Teknoloji Fakültesi) Anabilim Dalı, yusufesidir@gmail.com
ORCID: https://orcid.org/0000-0003-0221-729X

[2] Gazi Üniversitesi, Mimarlık Fakültesi, Mimarlık Bölümü, arzuhanburcu@gazi.edu.tr
ORCID: https://orcid.org/0000-0003-1246-6468

[3] Gazi Üniversitesi, Teknoloji Fakültesi, İnşaat Mühendisliği Bölümü, aruntas@gazi.edu.tr
ORCID: https://orcid.org/0000-0001-6417-629X

[4] Yozgat Bozok Üniversitesi, Mühendislik-Mimarlık Fakültesi, Mimarlık Bölümü, cbelgin.dikmen@gmail.com
ORCID: https://orcid.org/0000-0001-5975-1552

MAKALE BİLGİLERİ

Makale Geçmişi:

Geliş 4 Ağustos 2025
Revizyon 10 Ağustos 2025
Kabul 10 Ağustos 2025
Online 30 Aralık 2025

Anahtar Kelimeler:

Yaşam döngüsü değerlendirme, tuğla, yapı malzemeleri, küresel ısınma, iklim değişikliği

ÖZ

Son yüzyılda hız kazanan nüfus artışı, sanayileşme ve kentleşme süreçleri, yapılaşma ihtiyacını önemli ölçüde artırmıştır. Bu gelişmeler, yapı malzemelerine olan talebin artmasına ve dolayısıyla inşaat sektöründe daha fazla malzeme kullanımına yol açmıştır. Ancak yapı malzemelerinin üretim süreçleri, özellikle sera gazı salımları açısından çevresel etkiler doğurmakta ve küresel ısınma ile iklim değişikliği gibi küresel sorunları tetiklemektedir. Tarihi oldukça eski dönemlere dayanan tuğla, günümüzde de yaygın şekilde kullanılan temel yapı malzemelerinden biridir. Bu çalışmada, tuğla üretiminin çevresel etkileri incelenmiş; özellikle üretim kaynaklı salımların küresel ısınma üzerindeki etkisi ilgili veriler ışığında değerlendirilmiştir. Araştırma kapsamında, Yaşam Döngüsü Değerlendirme (YDD) yaklaşımı temel alınarak hazırlanmış olan ve ISO 21930 ile ISO 14025 standartlarına uygun olarak yayımlanmış Çevresel Ürün Beyanları (EPD) analiz edilmiştir. Bu belgelerde yer alan Küresel Isınma Potansiyeli (GWP) verileri üzerinden değerlendirmeler yapılmıştır. Yapılan analizler sonucunda, 1 ton tuğla üretiminin yaklaşık 230 ila 250 kg CO_2-eşdeğer sera gazı salımına neden olduğu belirlenmiştir. Bu salımların azaltılması için, özellikle pişirme aşamasında olmak üzere tüm üretim sürecinde enerji verimliliği yüksek teknolojilerin kullanılması önerilmektedir. Ayrıca, Türkiye'de faaliyet gösteren tuğla üreticilerinin EPD belgesi edinmelerinin, çevresel sürdürülebilirliğe katkı sağlayacağı sonucuna ulaşılmıştır.

ARTICLE INFO

Article history:

Received 4 August 2025
Received in revised form 10 August 2025
Accepted 10 August 2025
Available online 30 December 2025

Keywords:

Life cycle assessment, brick, construction materials, global warming, climate change

ABSTRACT

The rapid growth in population, industrialization, and urbanization over the past century has significantly increased the demand for built environments. This surge has led to a greater need for construction materials, consequently intensifying their environmental impact, particularly in terms of greenhouse gas emissions that contribute to global warming and climate change. Bricks, which have been used as a fundamental building material since ancient times, remain widely utilized in modern construction. This study investigates the environmental impact of brick production, focusing on its contribution to global warming through data-driven analysis of emissions. Within the scope of the research, Environmental Product Declarations (EPDs) prepared in accordance with ISO 21930 and ISO 14025 standards were examined. These documents, based on the Life Cycle Assessment (LCA) methodology, provided the Global Warming Potential (GWP) values used in the analysis. The findings indicate that producing one ton of bricks results in approximately 230 to 250 kg of CO_2-equivalent emissions. To mitigate this impact, it is recommended that advanced and energy-efficient technologies be implemented throughout the production process, particularly during the firing phase. Additionally, encouraging brick manufacturers in Türkiye to obtain EPD certification could significantly support environmental sustainability.

Doi: 10.24012/dumf.1758146

* Sorumlu Yazar

Giriş

Küresel ölçekte binalardan ve inşaat faaliyetlerinden kaynaklı CO_2 salımların artması inşaat sektöründe yapısal değişimin kaçınılmaz olduğunu göstermektedir. 2021 yılında binaların kullanımından kaynaklı salımlar 10 $GtCO_2$ civarında rekor seviyeye ulaşmıştır [1]. Bu seviye COVID-19 pandemisinin yaşandığı 2020 yılına nazaran %5, bir önceki en yüksek seviye olan 2019 yılına nazaran %2 daha yüksek olmuştur. Yapı malzemelerinin (beton, çelik, alüminyum, cam ve tuğla) üretiminden kaynaklı salımların ise 3,6 $GtCO_2$ seviyesinde olduğu tahmin edilmektedir [1]. 2021 yılında binalardan kaynaklı CO_2 salımları, toplam salımların %37'sine tekabül etmektedir [1].

Tuğla, binaların yapımında kullanılan en temel yapı malzemelerinden biridir. Tuğlalar, binalarda daha çok iç mekân ile dış mekânı ayıran dış duvarlarda ve mekânların fonksiyonlara göre bölünmesini sağlayan iç duvarlarda temel yapı bileşeni olarak kullanılmaktadır. Tuğla üretim endüstrisi, yüksek miktarda hammadde ve enerji gereksinimi nedeniyle birçok çevresel etkiye ve oldukça fazla CO_2 salımına sebep olmaktadır [2]-[7].

Çevresel Ürün Beyanları (EPD), bir üretim sürecinin ya da ürünün "beşikten mezara" çevresel performansını ölçerek ortaya koyan Yaşam Döngüsü Değerlendirme (YDD) metodolojisi kullanılarak hazırlanmaktadır. YDD metodolojisinde hammadde çıkarılması, endüstriyel üretim aşamaları, paketleme ve nakliye süreçleri ayrı ayrı ele alınarak enerji kullanımı ve salımların miktarı belirlenmektedir. YDD metodolojisi, yapı malzemelerinin çevresel etkisinin belirlenmesi amacıyla son yıllarda revaçta olan ve küresel ölçekte kabul görerek standartlaşmış etkili bir yöntemdir.

YDD metodolojisi, yapı malzemelerinin çevresel etkilerinin kıyaslanabilir bir biçimde ortaya koyulmasını sağlamaktadır. Fonksiyonel birimlerle ifade edilen yapı malzemelerinin yaşam döngüsünün tüm aşamalarında gösterdiği çevresel performans, YDD metodolojisi kullanılarak hazırlanan EPD'ler ile objektif ve kıyaslanabilir kriterlere göre ortaya konmaktadır. "TS ISO 21930: 2021: Yapılarda ve inşaat mühendisliği işlerinde sürdürülebilirlik - Yapı malzemelerinin ve hizmetlerinin çevresel beyanları için temel kurallar" [8] ve "ISO 14025: 2008: Çevre etiketleri ve beyanları - Tip III çevre beyanları - Prensipler ve prosedürler" [9] standartlarına göre hazırlanan Çevresel Ürün Beyanları ISO 14040 serisi standartların [10] uygulanması ve bağımsız otoriteler tarafından kontrol edilerek kabul edilmesi ile ürünlerin çevresel etkilerini objektif ve bağımsız bir şekilde açıklamalarını sağlamaktadır.

EPD'lerde analizlerde kullanılan farklı YDD metotlarına bağlı olarak farklı çevresel etkiler hesaplanmaktadır. Başlıca YDD metotları, küresel metotlar olan IMPACT ve ReCiPe; Avrupa metotları olan CML-IA, Avrupa Fiyatları, Ekolojik Kıtlık, Çevresel Ayak İzi (EF), EN 15804 + A2, EPD, EPS2015d, EPS 2015dx; Kuzey Amerika metotları olan BEES ve TRACI'dir [11]. Analiz sonucunda elde edilmek istenen göstergelere ve çalışmanın yapıldığı coğrafi konuma göre bu metotlar arasında tercih yapılabilmektedir. Metotlara göre farklılık göstermekle birlikte yaşam döngüsü etki değerlendirmesi sonucunda farklı çevresel etki kategorilerinde ürünlerin ya da süreçlerin çevresel etkileri hesaplanmaktadır. Bu etki kategorileri başlıca Küresel Isınma Potansiyeli (GWP), Ozon Tabakasını İnceltme Potansiyeli (ODP), Asidifikasyon Potansiyeli (AP), Ötrofikasyon Potansiyeli (EP), Kirli Hava Potansiyeli (SP), Troposferik Ozonun Oluşum Potansiyeli (POCP), Abiyotik Tükenme Potansiyeli – Elementler (ADPE), Abiyotik Tükenme Potansiyeli – Fosil Yakıtlar (ADPF) olarak sıralanabilmektedir. Bunların haricinde etki kategorileri de mevcuttur. Bu çalışma kapsamında yalnızca bu etki kategorilerinden biri olan Küresel Isınma Potansiyeli (GWP) etki kategorisine odaklanılmıştır.

GWP olarak kısaltılan küresel ısınma potansiyeli, bir sera gazının atmosferde ne kadar süre aktif kaldığını dikkate alarak, molekülden moleküle göreceli gücünü tanımlamak için kullanılan bir terimdir. Günümüzde kullanılan küresel ısınma potansiyelleri 100 yıl üzerinden hesaplanmaktadır. Karbondioksit 100 yıllık GWP'si 1 olan referans gaz olarak alınmaktadır [12].

Bu çalışma, tuğlanın üretim aşamalarında kullanılan malzeme ve enerjinin analizinin yapılması yoluyla CO_2 salımların sebep olduğu küresel ısınma potansiyelinin tespit edilmesini ve yapım sürecinde enerji kullanımını ve karbon salımını azaltacak öneriler geliştirilmesini amaçlamaktadır. Çalışma kapsamında veri kaynağı olarak tuğla ile ilgili hazırlanan EPD'lerde yer alan veriler kullanılmıştır. Çalışma kapsamında tuğla ile ilgili 9 farklı EPD'de yer alan GWP verileri derlenerek kıyaslanmış ve değerlendirmeler yapılmıştır.

Çalışmanın temel araştırma sorusu, farklı ülkelerde üretilen kil esaslı tuğlaların EPD'lerde beyan edilen GWP değerlerinin hangi aralıkta değiştiği ve bu değerler arasındaki farklılıkların üretim teknolojisi, enerji kaynağı ve coğrafi koşullar ile nasıl ilişkilendirilebileceğidir. Bu araştırma sorusundan yola çıkarak çalışmanın hipotezi, yüksek enerji verimliliğine sahip üretim teknolojilerini kullanan tuğla üreticilerinin GWP değerlerinin, geleneksel üretim teknolojilerini kullananlara kıyasla anlamlı derecede daha düşük olacağıdır.

Yöntem ve Veri

Çalışma kapsamında tuğla üretimi sürecinden kaynaklanan sera gazı salımlarının küresel ısınma üzerindeki etkisinin belirlenmesi amacıyla YDD metodolojisi kullanılarak hazırlanan ve tuğla üretiminden kaynaklı çevresel etkilere ortaya koyan EPD'lerden GWP verileri derlenerek analizler gerçekleştirilmiştir. YDD metodolojisi, bir ürünün, üretimi için kullanılan ham maddelerin tedarikinden, kullanımı, kullanım ömrü sonunda işlenmesi, geri dönüşümü ve nihaî bertarafına kadar yaşamı boyunca (beşikten mezara), çevresel boyutlarını ve muhtemel çevresel etkilerini (kaynakların kullanımı ve salımların çevresel sonuçları gibi) incelemektedir [10]. EPD'ler, önceden belirlenmiş parametreler kullanılarak sayısallaştırılmış çevresel veriler ve ilgili olduğu durumlarda ek çevresel bilgiler sağlayan çevresel beyanlar olarak tanımlanmaktadır [9].

Tablo 1. Tuğla ile ilgili EPD'lere dair genel bilgiler

	Üretici	**Ülke**	**EPD Kapsamı**	**Yazılım Aracı**	**Veritabanı**
[13]	Shaw Brick	Kanada	Beşikten kapıya (A1-A3)	Belirtilmemiş	Ecoinvent, US LCI
[14]	Brick Industry Association	Kanada	Beşikten kapıya (A1-A3)	Simapro	Ecoinvent
[15]	Brick Development Association (BDA) Ltd	Birleşik Krallık	Beşikten kapıya (A1-A5+C2-C4+D)	Simapro	Ecoinvent
[16]	Calstar Brick	ABD	Beşikten mezara (A1-C4)	Gabi	Belirtilmemiş
[17]	Saray Tuğla	Türkiye	Beşikten kapıya (A1–A3+A4+C+D)	Simapro	Ecoinvent
[18]	Marshalls Bricks	Birleşik Krallık	Beşikten kapıya (A1-A3)	Belirtilmemiş	Ecoinvent
[19]	Kingscourt Brick	İrlanda	Beşikten mezara (A1-C4)	Ecochain	Ecoinvent
[20]	Heluz Brick	Çek Cumhuriyeti	Beşikten kapıya (A1-A3+C+D)	Gabi	Ecoinvent
[21]	Bundesverband der Deutschen Ziegelindustrie e.V.	Almanya	Beşikten mezara (A1-C4)	Gabi	Gabi Database

Çalışma kapsamında tuğla üreticisi firmalara ait 9 adet EPD incelenmiştir. Bu EPD'lerin üretici firma isimleri, üretim yapılan ülkeler, EPD'nin hangi yaşam döngüsü evrelerini kapsadığı, analizlerde yararlanılan yazılım araçları ve kullanılan veri tabanlarına ilişkin bilgilere Tablo 1'de yer verilmiştir. EPD seçim kriterleri olarak; (i) belgenin ISO 21930 ve ISO 14025 standartlarına uygun olarak hazırlanmış olması, (ii) yayımlanma tarihinin 2012–2024 yılları arasında olması, (iii) tuğla ürün grubunu temsil etmesi, (iv) yaşam döngüsü evreleri ve veri kalitesine dair bilgilerin beyan edilmiş olması ve (v) veri setinin üreticiye özgü veya ülke ortalamasını temsil etmesi esas alınmıştır. Bu ölçütlere uymayan veya eksik veri içeren EPD'ler çalışma kapsamına dahil edilmemiştir.

İncelenmiş olan farklı EPD belgelerinde kullanılan Ürün Kategori Kuralları (PCR-Product Category Rules) ve YDD metotlarının çeşitliliği nedeniyle bu EPD'lerde yer alan çevresel etki kategorisi verilerinin doğrudan karşılaştırılması hatalı bir yaklaşımdır. Dolayısıyla bu verilerin bağlamsal olarak kullanılması ve yorumlanması gerektiği göz önünde bulundurulmalıdır.

Çalışma kapsamında yalnızca Küresel Isınma Potansiyeli (GWP) etki kategorisine odaklanılmış olması ise metodolojik bir tercihtir. GWP dışındaki asidifikasyon, ötrofikasyon, ozon tabakası tükenmesi gibi diğer çevresel etki kategorilerinin de önemli olduğu bilinmekle birlikte, bu çalışmada konu sınırlılığı ve EPD'lerde yer alan çevresel etki kategorilerinin kullanılan YDD metotlarına göre farklılaşmaları sebebiyle kapsam dışı bırakılmıştır.

İncelenen EPD'lerden bazıları yaşam döngüsü evrelerinin tümünü, bazıları üretim ve kullanım evrelerini, bazıları ise yalnızca üretim evresini ele almıştır. Bu çalışma kapsamında yalnızca tuğla üretiminin küresel ısınmaya katkısı dikkate alındığından, tüm incelenen EPD'lerden A1 (Hammadde temini), A2 (Hammaddenin fabrika sahasına nakliyesi), A3 (Üretim) evrelerine ait veriler derlenmiştir. A1-A3 evrelerini kapsayan veriler, hammadde temininden mamul bir ürün olan tuğlanın elde edilmesine kadar olan aşamadaki salımları yansıtmaktadır.

Tablo 2. Tuğla üreticisi firmalar için hesaplanan dönüşüm faktörleri

Üretici	**Beyan Edilen Birim**	**Ağırlık (kg)**	**Dönüşüm Faktörü**
Shaw Brick	1 m^3	2060	0,48
Brick Industry Association	1 m^3	2120	0,47
Brick Development Association (BDA) Ltd	1 ton	1000	1
Calstar Brick	1 tuğla	1,9	524,91
Saray Tuğla	1 m^2	126	7,94
Marshalls Bricks	1000 tuğla	2375	0,42
Kingscourt Brick	1 ton	1000	1
Heluz Brick	1 ton	1000	1
Bundesverband der Deutschen Ziegelindustrie e.V.	1 ton	1000	1

EPD'ler hazırlanırken belli bir fonksiyonel birime göre salım değerleri hesaplanmaktadır. Bu fonksiyonel birim 1 adet, 1 m^2, 1 m^3 veya 1 ton tuğla olabilmektedir. İncelenen EPD'lerde beyan edilen fonksiyonel birimler bu şekilde farklılık gösterebilmektedir. Kıyaslama yapılabilmesi için beyan edilen birimlerin hepsinin aynı birime çevrilmesi

gerekmektedir. Bunu yapabilmek için Tablo 1'de verilen üretici firmaların dönüşüm faktörleri hesaplanmıştır. Beyan edilen fonksiyonel birimlere ve bu birimlerin "1 ton tuğla" üretimi ile eşdeğer birime çevrilmesi için kullanılan dönüşüm faktörlerine Tablo 2'de yer verilmiştir.

Dönüşüm faktörleri hesaplanırken birim hacim ağırlık değeri kullanılmıştır. Örneğin Shaw Brick'in EPD'sinde $1m^3$ tuğlanın ağırlığının 2060 kg olduğu belirtilmiştir. Dolayısıyla 1000/2060=0,4854 dönüşüm faktörü olarak hesaplanmış ve Shaw Brick'in EPD'sinde yer alan GWP değeri, 0,4854 ile çarpılarak 1 ton tuğla için hesaplanmıştır. Diğer beyan edilen fonksiyonel birimler de benzer şekilde ağırlık-hacim hesabı yapılarak elde edilmiştir.

Bulgular ve Tartışma

Çalışma kapsamında 9 EPD, öncelikli olarak malzeme içerikleri bakımından incelenmiştir. Tuğlaların hammadde kompozisyonlarına Tablo 3'te yer verilmiştir. Kil esaslı tuğlaların malzeme içeriği büyük oranda kil ve şisten oluşmaktadır. Tabloda yer alan üretici firmalardan Calstar Brick, kum ve uçucu kül karışımından oluşan ve pişirilmeyen tuğla çeşidi üretmektedir. Saray tuğla da el yapımı tuğla olarak tabir edilen ve pişirme işleminin olmadığı tuğla çeşidini üretmektedir. Marshalls Bricks ise agrega ve çimento karışımından tuğla üretmektedir.

Bu üç tuğla çeşidi her ne kadar tuğla olarak isimlendirilmiş olsa da kil esaslı malzemeden oluşan ve fırında pişirilen tuğlalardan farklı bir yapı malzemesidir. Bu üç malzemeye de fikir vermesi açısından kıyaslamada yer verilmiştir. Ancak diğer 6 EPD klasik anlamda tuğla üretimine dair bilgileri içermektedir. Bu 6 EPD kil tuğla üretim aşamaları olan hammadde temini, hammadde hazırlanması, şekillendirme, kurutma, pişirme ve ambalajlama aşamalarını içermektedir.

9 farklı tuğla firmasının üretim kaynaklı CO_2 salımları sonucu oluşan GWP değerleri Şekil 1'de sunulmuştur. Görüldüğü gibi standart kil tuğla üreten 6 firma arasında en yüksek GWP değerine 350 $kgCO_2$-eşd ile Shaw Brick tuğlaları, en düşük GWP değerine 194,58 $kgCO_2$-eşd Heluz Brick firmasının ürettiği tuğlalar sahiptir. 1 ton kil tuğla üretiminde ortalama 244 $kgCO_2$-eşd GWP oluşmaktadır. En düşük değer ortalamanın %20 altında, en yüksek değer ise ortalamanın %44 üzerindedir.

İncelenen Çevresel Ürün Beyanları (EPD) arasında, Brick Industry Association tarafından Amerika Birleşik Devletleri ve Kanada'daki ortalama üretim verilerine, Brick Development Association tarafından Birleşik Krallık'taki 46 firmanın ortalama üretim verilerine ve Bundesverband der Deutschen Ziegelindustrie e.V. tarafından Almanya'nın ulusal ortalama üretim verilerine dayanılarak hazırlanmış belgeler yer almaktadır. Bu üç ülke arasında en yüksek GWP değerine 255,55 $kgCO_2$-eşd ile Almanya, en düşük GWP değerine 213 $kgCO_2$-eşd ile Birleşik Krallık sahiptir. En düşük değer ortalama değer olan 235,3 $kgCO_2$-eşd değerinin %10 altında, en yüksek değer ise %8,6 üzerindedir. Bu sonuçlardan anlaşıldığı gibi ülke ortalamalarını yansıtan değerlerde daha az sapma olmaktadır.

En düşük GWP değerine sahip olan Heluz Brick üreticisinin EPD'si incelendiğinde, fabrikalarında yüksek teknoloji kullandıklarını ve bazı ürün çeşitlerinin "Nature plus" adlı ekolojik üretim sertifikasına sahip olduğunu beyan etmiş oldukları dikkat çekmektedir. Firmanın sahip olduğu 3 fabrikanın ortalama verileri kullanılarak hazırlanan EPD'de, fabrikaların birinde (Hevlin II) Avrupa'nın en gelişmiş fırınlarından birinin kullanıldığı belirtilmektedir.

Tuğla üretiminden kaynaklanan sera gazı salımlarının küresel ısınma üzerine etkisinin incelendiği bu çalışma ile tuğla üretiminin GWP değerine ilişkin yaklaşık bir salım değeri ve mertebesi elde edilmeye çalışılmıştır. Bununla birlikte çalışmanın birtakım sınırlılıklarının olduğu da göz önünde bulundurulmalıdır. İncelenen EPD'ler farklı YDD metotları kullanılarak ve farklı varsayımlar altında oluşturulmuştur. EPD'lerin hepsinde farklı Ürün Kategori Kuralları (PCR-Product Category Rules) kullanılmıştır. Üretimde kullanılan fırınların ve yakıtların cinsi, fabrikanın hammadde sahasına uzaklığı, kullanılan makine-ekipmanların farklılıkları gibi birçok husus EPD'lerde beyan edilmemekte, EPD'yi düzenleyen kişilerde ham veri olarak bulunmaktadır. Bunun yanı sıra çalışma kapsamında yalnızca bir etki kategorisi olan GWP değerine odaklanılmıştır. Çevresel etkilerin miktarı yalnızca GWP değeriyle sınırlı olmadığından diğer etki kategorilerinin de incelenmesi önemlidir. Dolayısıyla bu EPD'lerin birebir kıyaslanması mümkün olmasa da tuğla üretiminin küresel ısınma üzerine etkisinin hangi mertebede olduğuna dair fikir edinilmesi açısından çalışmanın faydalı olacağı düşünülmektedir.

Tablo 3. Farklı firmalara ait tuğlaların malzeme içerikleri

	Üretici	**Malzeme İçeriği**
[13]	Shaw Brick	%67 kil, %32 şist, %1 baryum manganez, kromoks ve diğer katkı maddeleri
[14]	Brick Industry Association	%94,9 kil ve şist, %3,7 kül, tuğla kırıntısı ve diğer ikincil katkılar, %0,9 pigment, %0,5 katkı maddesi
[15]	Brick Development Association (BDA) Ltd	%92 kil ve şist, %6 kum, %2 inorganik katkı maddesi
[16]	Calstar Brick	%55,8 kum, %37,1 uçucu kül, %5,9 su
[17]	Saray Tuğla	%99 kil, %1 katkı maddesi
[18]	Marshalls Bricks	%85-89 agrega, %8-11 çimento, %2-4 su, %0-1 inorganik pigment ve polimerler
[19]	Kingscourt Brick	Büyük oranda kil, az miktarda şeker kamışı ve kum
[20]	Heluz Brick	%99,6 kil, %0,4 talaş ve saman külü
[21]	Bundesverband der Deutschen Ziegelindustrie e.V.	%85 kil, %8 kum, %7 manganez, demir oksit, perdah, diğer katkı maddeleri

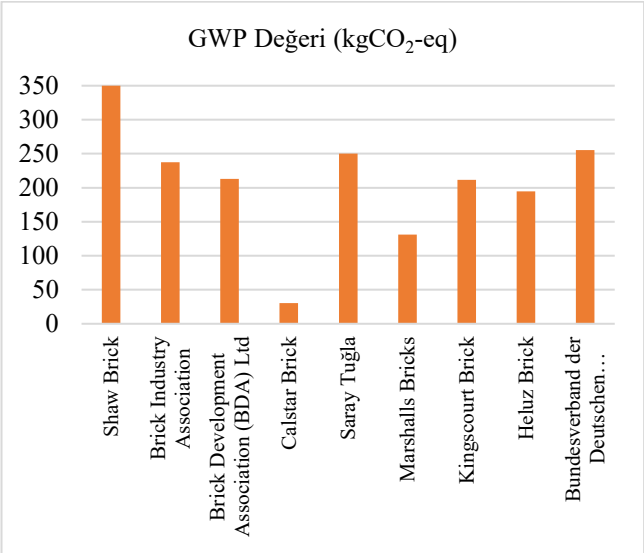

Şekil 1. Farklı firmalara ait tuğlaların GWP değerleri

Sonuç ve Öneriler

Bu çalışmanın amacı, tuğla üretiminin küresel ısınma üzerine etkisinin belirlenerek bu etkinin azaltılmasına yönelik bazı öneriler geliştirilmesidir. Bu kapsamda 9 adet tuğla üreticisinin EPD'sindeki GWP değerleri analiz edilmiştir. Söz konusu 9 firmanın 3 tanesi klasik kil tuğla yapımından farklı üretim yöntemi kullandığı için bu çalışmanın kapsamı dışında tutulmuştur. Geri kalan 6 firmanın tuğla üretimi verilerini içeren EPD'nin üç tanesinde üretildikleri ülkelerin ortalama üretim verileri, diğer üçünde ise fabrika verileri kullanılmıştır. Buna göre bütün veriler dikkate alındığında 1 ton tuğla üretiminin yaklaşık 244 $kgCO_2$-eşd, ABD, Kanada, Birleşik Krallık ve Almanya'nın ortalama verileri dikkate alındığında 235 $kgCO_2$-eşd sera gazı salımına sebep olarak küresel ısınmaya katkı sağladığı tespit edilmiştir. Dolayısıyla, 1 ton tuğla üretiminden yaklaşık 230-250 $kgCO_2$-eşd mertebesinde sera gazı salımını ortaya çıktığı söylenebilir. Türkiye'de tuğla üretimi yapan firmaların elde edilen bu değeri kullanarak kendi üretimlerinin küresel ısınmaya katkısını kıyaslamaları mümkün görülmektedir.

Sonuç olarak, tuğla üretiminden kaynaklı sera gazı salımlarının azaltılarak küresel ısınmaya daha az katkı sağlanması için fabrikalarda gelişmiş teknolojilerin, özellikle gelişmiş teknolojiye sahip fırınların kullanılması gerektiği kanaatine ulaşılmıştır. Türkiye'de üretim yapan tuğla fabrikalarının da kendi çevresel etkilerini objektif biçimde ortaya koydukları EPD belgelerine sahip olmasının, sektörün yeşil dönüşümüne katkı sağlayacağı düşünülmektedir.

Türkiye'de 2023 yılında yayımlanan "Yeşil Mutabakat Eylem Planı" ve "İklim Değişikliği ile Mücadele Stratejisi ve Eylem Planı" kapsamında yapı malzemeleri sektöründe düşük karbonlu üretim tekniklerinin teşvik edilmesi hedeflenmektedir. Ayrıca, EPD sahibi ürünlerin kamu ihalelerinde tercih edilmesine yönelik düzenlemeler gündemdedir. Bu bağlamda, tuğla üreticilerinin EPD belgesi edinmesi hem yasal uyum hem de uluslararası pazarda rekabet gücü açısından stratejik önem taşımaktadır.

Etik kurul onayı ve çıkar çatışması beyanı

Hazırlanan makalede etik kurul izni alınmasına gerek yoktur. Hazırlanan makalede herhangi bir kişi/kurum ile çıkar çatışması bulunmamaktadır.

Yazar Katkıları

Yazarlar çalışma konsepti ve tasarımı, literatür taraması, veri toplama, verilerin analizi ve yorumlanması, sonuçların değerlendirilmesi, taslağın oluşturulması, yazım denetimi ve içerik açısından makalenin revizyonu süreçlerine ortak katkı sağlamıştır.

Teşekkür

Bu çalışma Türkiye Bilimsel ve Teknolojik Araştırma Kurumu (TÜBİTAK) Bilim İnsanı Destekleme Programları (BİDEB) 2211-A kapsamında desteklenmiştir.

Bu çalışma Gazi Üniversitesi Bilimsel Araştırma Projeleri Koordinasyon Birimi tarafından FDK-2025-9615 nolu proje kapsamında desteklenmiştir.

Kaynaklar

[1] United Nations Environment Programme (2022). 2022 Global Status Report for Buildings and Construction: Towards a Zero-emission, Efficient and Resilient Buildings and Construction Sector. Nairobi.

[2] Buchanan, A. H., & Honey, B. G. (1994). Energy and carbon dioxide implications of building construction. Energy and Buildings, 20(3), 205-217.

[3] Oka, T., Suzuki, M., & Konnya, T. (1993). The estimation of energy consumption and amount of pollutants due to the construction of buildings. Energy and buildings, 19(4), 303-311.

[4] Koomey, J. G., Martin, N. C., Brown, M., Price, L. K., ve Levine, M. D. (1998). Costs of reducing carbon emissions: US building sector scenarios. Energy Policy, 26(5), 433-440.

[5] Treloar, G. J., Love, P. E., & Holt, G. D. (2001). Using national input/output data for embodied energy analysis of individual residential buildings. Construction Management and Economics, 19(1), 49-61.

[6] Imran, M. A., Baten, M. A., Nahar, B. S., ve Morshed, N. (2014). Carbon dioxide emission from brickfields around Bangladesh. International Journal of Agricultural Research, Innovation and Technology (IJARIT), 4(2355-2020-1574), 70-75.

[7] Bhat, M. S., Afeefa, Q. S., Ashok, K. P., & Bashir, A. G. (2014). Brick kiln emissions and its environmental impact: A Review. Journal of Ecology and the Natural Environment, 6(1), 1-11.

[8] TS ISO 21930: 2021: Yapılarda ve inşaat mühendisliği işlerinde sürdürülebilirlik - Yapı malzemelerinin ve hizmetlerinin çevresel beyanları için temel kurallar

[9] ISO 14025:2006: Çevre etiketleri ve beyanları - Tip III çevre beyanları - Prensipler ve prosedürler

[10] TS EN ISO 14040:2007: Çevre yönetimi - Hayat boyu değerlendirme - İlkeler ve çerçeve

[11] PRé Sustainability. "SimaPro Database Manual Methods Library" PRé Sustainability. Amersfoort, Hollanda. 8 Ekim 2025 [online] URL: https://simapro.com/wp-content/uploads/2025/04/DatabaseManualMethods.pdf

[12] Eurostat (2024). "Glossary:Global-warming potential (GWP)". 26 Ağustos 2024 [Online] URL: https://ec.europa.eu/eurostat/statistics-explained/index.php?title=Glossary:Global-warming_potential_(GWP)

[13] Shaw Brick (2022). Environmental Product Declaration. 5 Şubat 2024 [Online] URL: https://pcr-epd.s3.us-east-2.amazonaws.com/836.Shaw_Brick_Clay_Brick_EPD.pdf

[14] The Brick Industry Association (2020). Environmental Product Declaration. 5 Şubat 2024 [Online] URL: https://bowerstonshale.com/wp-content/uploads/2022/04/EPD.pdf

[15] The Brick Development Association (2019). Environmental Product Declaration. 5 Şubat 2024 [Online] URL: https://www.brick.org.uk/uploads/downloads/breg-en-epd-000002-v4.pdf

[16] CalStar Brick (2012). Environmental Product Declaration. 28 Ağustos 2024 [Online] URL: http://mts.sustainableproducts.com/CalStar%20EPD%20Document_Final.pdf

[17] Saray Tuğla (2022). Environmental Product Declaration. 5 Şubat 2024 [Online] URL: https://api.environdec.com/api/v1/EPDLibrary/Files/b58415f9-dfdd-4e00-9041-08dabb52e166/Data

[18] Marshalls Brick (2021). Environmental Product Declaration. 28 Ağustos 2024 [Online] URL: https://media.marshalls.co.uk/image/upload/epd-final-v3.pdf

[19] Kingscourt Brick (2021). Environmental Product Declaration. 28 Ağustos 2024 [Online] URL: https://www.igbc.ie/wp-content/uploads/2021/07/EPD-Kingscourt-Brick-12-07-2021-EPDIE-21-51.pdf

[20] Heluz Brick (2015). Environmental Product Declaration. 28 Ağustos 2024 [Online] URL: https://api.environdec.com/api/v1/EPDLibrary/Files/9448332d-b3e5-4f7c-8234-08d941d5f1c9/Data

[21] Bundesverband der Deutschen Ziegelindustrie e.V. (2021). Environmental Product Declaration. 28 Ağustos 2024 [Online] URL: https://ziegel.de/sites/default/files/2021-11/A88_2021_2_Dachziegel%20%28inklusive%20Zubehoer%29%20EN%2015804%20A2-000084.pdf

Dicle University
Journal of Engineering
https://dergipark.org.tr/tr/pub/dumf
duje.dicle.edu.tr

Review Article

Understanding the Root Causes of Construction Claims: A Narrative Review of Determinants and Preventive Strategies

Mehmet Kürşad BAHAT[1*], Sema ERGÖNÜL[2]

[1] Istanbul Medipol University, Graduate School of Natural and Applied Sciences, Construction Management and Law Program, mkbahat@gmail.com, Orcid No: 0009-0008-8600-8279
[2] Mimar Sinan Fine Arts University, Department of Architecture, sema.ergonul@msgsu.edu.tr, Orcid No: 0000-0002-8222-4694

ARTICLE INFO

Article history:

Received 6 August 2025
Received in revised form 22 October 2025
Accepted 29 October 2025
Available online 30 December 2025

Keywords:

construction claims, construction disputes, claim cause, claim prevention, claim resolution.

Doi: 10.24012/dumf.1759763

* Corresponding author

ABSTRACT

Construction projects are inherently vulnerable to claims due to their multifaceted nature, involvement of multiple stakeholders, complex contracts, and dynamic site conditions. Claims are common issues within the construction industry, often leading to disputes and significantly impacting the successful delivery of projects. Facing many claims increases the resource requirements necessary for project completion, resulting in resource wastage. This research undertakes a narrative review to identify, classify, and interpret the determinants of construction claims by aggregating evidence from 21 peer-reviewed papers and graduate theses published between 2006 and 2024. The sources were selected through non-systematic searches from Scopus, Web of Science, Google Scholar, and Türkiye's National Thesis Center, with priority given to research that had examined claim causation and resolution explicitly. The analysis demonstrated that the most common reasons for the generation of claims were ambiguities in the contracts, deficiencies in designs, delayed payments, and inadequate communication among the stakeholders. Particular roles were often overlapping or shared among the consultants (defective or incomplete designs), the contractors (mismanagement of the site, resource deficiencies), and the employers (scheduling expectations that could not possibly be met, financial constraints). While no single party could be held solely accountable in many cases, the data emphasized the interdependent nature of claim triggers. The research concludes that the reciprocal mitigation of claim generation necessitates a systems-based approach involving strong frameworks for contracts, improved coordination among stakeholders, planning during the preliminary stages, and the integration of advanced technologies.

Introduction

The construction sector is very important for the economic growth of countries around the world. It contributes to the creation of residential buildings, infrastructure development, and public works, hence significantly supporting the well-being, health, and living standards of people [1].

The interconnectivity with other sectors supports industrial operations and improves social well-being, so that placing greater emphasis on the crucial role of this sector beyond direct accountability [2]. It is a significant source of employment because of the interconnected input-output relations, which closely link it with the rest of the economy [3]. Its significant engagement towards economic progress and stability makes it a major factor of global economic growth [4]. Its diverse support for economic expansion, job creation, and cross-sectoral connections is key to sustainable development and social wellness. Knowledge of construction industry dynamics and the study of factors affecting it is critical.

Construction works are inherently complicated tasks involving multidisciplinary coordination, uncertainty, and many stakeholders whose interests often conflict. Such features make the construction industry highly prone to claims and disputes, which are likely to seriously affect project performance on time, cost, and quality factors [5, 6]. In construction works, a claim is defined as a request for compensation made by one of the parties in reaction to the failure of the other party to satisfy contractual terms [7]. If a claim left unresolved, such a claim can escalate into a dispute requiring legal intervention or third-party decision mechanisms [8, 9].

Claims and consequent claim-related disputes are common in the construction industry, and reducing project performance. They may occur due to numerous factors, such as contractual ambiguities, project accelerations, delays, changes, additional work, and site condition changes [10]. They are also destabilizing factors that significantly impact the completion of construction works within their schedule [11].

Understanding the causes of claims is essential as it is the basic step towards their relief [12]. Empirical studies have supported the idea that it is essential to identify the primary reasons behind construction claims to develop strategies to lessen or eliminate them [13, 14]. Performing data analysis focusing on issues of concern with suggestions for claims

mitigation in construction processes is vital for effectively managing claims. In this regard, it is essential to understand the core reasons behind claims arising during construction works and examine their impacts on project outcomes. After that one can yield lower project costs and durations, increased productivity, fewer claims and disputes, and better customer satisfaction [15].

Overall, the body of literature underscores the persistent and evolving nature of claims in construction projects. This study aims to provide a structured, comprehensive, and up-to-date synthesis of the literature on the causes of construction claims and disputes, identify the main claim causes, and suggested solutions to mitigate claims.

Methodology

This narrative review synthesizes published literature on the causes and resolution strategies of construction claims through a non-systematic review of the literature.

As this study is designed as a narrative review, the selection of literature was intentionally selective and interpretive rather than exhaustive; the included studies were chosen based on their perceived relevance and contribution to understanding the causes and mitigation strategies of construction claims, rather than through a systematic search protocol.

The study supported by thematic analysis. Relevant publications were reviewed to extract recurring themes and patterns, which were then classified into categories of causes of construction claims.

Selection criteria and inclusion scope

A total of 21 studies published between 2006 and 2024 were selected in this review for the main claim reasons, with guided by the following inclusion criteria:

- The study must explicitly focus on the causes of construction claims/disputes (as claim successor).
- The publication must be a peer-reviewed journal article, or graduate thesis (master's or PhD level).
- The full text must be available in English or Turkish.
- Studies must include qualitative or quantitative data relevant to claim causation, classification, or resolution strategies.

Research studies that addressed claims only superficially or lacked empirical evidence or a coherent theoretical framework were excluded from the review.

Data sources and search strategy

The literature was sourced from academic databases such as Scopus, Web of Science, Google Scholar, and the National Thesis Center (Türkiye). Keywords used included: "construction claims", "construction dispute causes", and "construction claim classification". Boolean operators and date filters were applied to focus the search on relevant studies within the 2004–2024 timeframe to meet the last two decades.

Data extraction and coding process

Each included study was carefully reviewed, and data were extracted on the following aspects:

- Geographic location and publication year,
- Research methodology (e.g., survey, case study, expert judgment),
- Identified claim causes,
- Proposed mitigation or resolution strategies.

Findings

This study examined 21 key articles published between 2006 and 2024 to identify, categorize, and interpret the reasons for construction claims. The findings reveal consistent themes across geographies, research methodologies, and stakeholder perspectives. Table 1 presents all the reasons for claims included in these studies and shows the breadth of challenges encountered in construction projects.

Table 1. The total list involves all causes of claims mentioned in the 21 selected studies.

References	Causes of Claims/Disputes
Zaneldin (2006) [6]	Change or variation orders, Delay caused by owner, Oral change orders by owner, Delay in payments by owner, Low price of contract due to high competition, Changes in material and labor costs, Owner personality, Variations in quantities, Subcontracting problems, Delay caused by contractor, Contractor is not well organized, Contractor financial problems, Bad quality of contractor's work, Government regulations, Estimating errors, Scheduling errors, Design errors or omissions, Execution errors, Bad communication between parties, Subsurface problems, Specifications and drawings inconsistencies, Termination of work, Poorly written contracts, Suspension of work, Accidents, Planning errors.
Doloi et al. (2012) [16]	Site accidents due to lack of safety measures, Lack of motivation for contractor (e.g., no incentive for early finish), Use of improper or obsolete construction methods, Delay in material delivery by vendors, Ambiguity in specifications and conflicting interpretations by parties, Poor labor productivity, Lack of control over subcontractor, Inadequate experience of contractor, Non-availability of drawings/designs on time, Slow decision from owner, Unrealistic time schedule imposed in contract, Poor site management and supervision, Extreme weather conditions, Lack of skilled operators for specialized equipment, Inefficient use of equipment, Poor coordination among parties, Delay in material procurement by contractor, Rework due to change of design or deviation order, Rework due to errors in execution, Frequent change of subcontractor, Increase in scope of work, Improper storage of materials leading to damage, Obtaining permissions from local

	authorities, Delay in approval of completed work by client (stage passing), Consultant or architect's reluctance for change, Poor means of contracting, Improper planning of contractor during bidding stage.
Cakmak and Cakmak (2014) [5]	Variations initiated by the owner, Change of scope, Late giving of possession, Acceleration, Unrealistic expectations, Payment delays, Delays in work progress, Time extensions, Financial failure of the contractor, Technical inadequacy of the contractor, Tendering, Quality of works, Design errors, Inadequate/incomplete specifications, Quality of design, Availability of information, Ambiguities in contract documents, Different interpretations of the contract provisions, Risk allocation, Other contractual problems, Adversarial / controversial culture, Lack of communication, Lack of team spirit, Site conditions, Unforeseen changes, Weather, Legal and economic factors, Fragmented structure of the sector.
Olanrewaju and Anavhe (2014) [15]	Variations, Extension of time, Fluctuations, Mistakes and discrepancies in contract documents, Re-measurement, Inadequate site investigation, Inaccurate design, Late information release, Instructional changes, Failure to give possession on time, Differing site conditions, Acts of God (force majeure), Political instability, Import and customs delays, Mistakes in bills of quantities, Unbalanced bidding, Unfair evaluation of claims, Poor communication, Ambiguity in contract terms, Lack of coordination among parties, Incomplete drawings, Delayed approval, Employer interference, Mistakes in tender, Changes in scope of work, Suspension of work, Unfavorable economic policies, Delays in payment, Bankruptcy or financial failure of contractor, Material shortages, Labour problems, Equipment failure, Poor weather conditions.
Hadikusumo and Tobgay (2015) [17]	Adverse geological occurrence, Change in quarry site (inadequate boulders), Differing sub-surface condition leading to design changes, Delay in handing over site from preceding contract work, Delay in making site available for the next phase, Late notice to proceed/delay in handing over access roads, Formal/directed changes by the owner, Constructive changes at site (due to alternative methods/materials), Floods, landslides, heavy monsoon effects, Loss of productivity and rework due to natural disasters, Contractual ambiguities or missing clauses, Conflict or omission in technical specifications.
Apte and Pathak (2016) [7]	Delay in supply of drawings, Delay in handing over the site, Delay in supply of materials, Delay in payments, Delay in starting work, Delay in completing the work, Work done but not measured and paid, Refund of maintenance deposit, Extra overheads due to extension of time, Idle machinery and idle labor costs, Design errors, Inadequate or incomplete specifications, Inadequate design information, Inadequate bid information, Inadequate time for bid preparation, Change in work scope, Changes in plans and specifications during construction, Insufficient plans and specifications, Extra items and variations, Non-granting of completion by engineer, Poor site management and administration, Ambiguities in contract documents, Different interpretations of contract provisions, Unbalanced bidding, Employer's lack of construction knowledge, Accidents, Natural calamities, Increase in material/fuel costs, Court intervention, Weather conditions, Unforeseen ground conditions, Defective or insufficient plans and specifications, Owner interference, Late approvals, Liaisoning and permit problems, Disruption due to owner's inaction, Late deliveries or site access issues, Bad weather, Subsurface water not indicated in documents, Loose or soft material instead of sound material, Excessive groundwater or moisture, Unusable existing materials, Unexpected high water table, Sub-roofing different than anticipated, Ineffective drainage systems, Presence of boulders, Presence of unusual materials.
Mishmish and El-Sayegh (2016) [18]	Poorly written contract, Inadequate documentation, Inadequate site investigation before bidding, Delay in granting possession of site, Late issue of instruction/clarification, Variations (employer/engineer initiated), Third-party interference, Measurement-related issues, Inconsistencies in specifications and drawings, Payment-related issues, Defects in works, Different perceptions in assessment, Unforeseen conditions, Delay caused by contractor, Termination/suspension of works, Acceleration.
Yildizel et al. (2016) [19]	Low quality of completed works, Late payment by the owner, Poor site management by the project management company, Poorly prepared contracts, Design mistakes, Unskilled workers, Inflation, Fluctuation in foreign currency, Poor application projects, Lack of skilled subcontractors, Low tender bids, Inaccurate project cost estimation, Late decisions of owner, Unrealistic contract period, Severe weather conditions, Severe construction site conditions, Late approval time of application projects by the owner, Unproductive labor, Scope changes in the project, Violation of contract clauses, Financial problems of the contractor, Lack of national standards, Poor quality of construction materials, Late evaluation of completed works, Communication errors, Lack of equipment, Fluctuation of labor and material cost during construction, Delay from local authorities for any permissions, Poorly prepared bill of quantity documents, Unforeseen problems, Planning mistakes.

Ataker (2018) [20]	Change or variation orders, Delay caused by owner, Delay in payments by owner, Low price of contract due to high competition, Changes in material and labor costs, Variations in quantities, Subcontracting problems, Delay caused by contractor, Contractor is not well organized, Contractor financial problems, Bad quality of contractor's work, Government regulations, Estimating errors, Scheduling errors, Design errors or omissions, Execution errors, Bad communication between parties, Subsurface problems, Specifications and drawings inconsistencies, Termination of work, Poorly written contracts, Suspension of work, Accidents, Planning errors, Inadequate tender documents, Unrealistic project durations, Bureaucratic delays, Site access problems, Employer's unclear expectations, Legal disputes.
Assaf et al. (2019) [21]	Change or variation orders, Delay caused by owner, Oral change orders by owner, Delay in payments by owner, Low price of contract due to high competition, Changes in material and labor costs, Owner personality, Variations in quantities, Subcontracting problems, Delay caused by contractor, Contractor is not well organized, Contractor financial problems, Bad quality of contractor's work, Government regulations, Estimating errors, Scheduling errors, Design errors or omissions, Execution errors, Bad communication between parties, Subsurface problems, Specifications and drawings inconsistencies, Termination of work, Poorly written contracts, Suspension of work, Accidents, Planning errors.
Malki and Alam (2020) [22]	Change or variation orders, Delay in payments to contractors and resulting cash problems during construction, Inadequate time for bidding and insufficient investigation before bidding, Delay approval of shop drawings, instructions and decision, Estimating errors, Specifications and drawings incompatible, Sudden change in material cost, Unexpected change in material prices, Scheduling errors, Design errors or omissions, Contractor is not well organized, Shortage in contractor resources, Stakeholders involved in the project, Lack of communication between parties, Low contract price due to strong competition, Suspension of work, Delay of owner representative/advisor in inspection of work, Shortage of designer experience in construction projects, Unexpected events, Subcontracting problems, Contractor financial problems, Shortage of contractor experience in construction projects, Bad quality of contractor's work, Termination of work, Relatively low profitability of the construction industry.
Temiz (2020) [23]	Errors in project documents and drawings, Incomplete project documents, Unclear and inconsistent project information, Delays in delivery of project documents, Unrealistic project duration, Changes requested during the project, Delays in approvals and permits, Differences in interpreting contract articles, Poorly prepared and ambiguous contracts, Inadequate planning and scheduling, Delay in payment, Financial problems of parties, Lack of communication between project participants, Low qualification of technical staff, Inexperience of contractor, Disputes in scope of work, Disputes regarding unit prices, Unexpected ground conditions, Delay in land delivery, Bureaucratic obstacles, Deficiencies in control and supervision, Late delivery of materials and equipment, Legal and legislative changes during project implementation.
Alqershy and Kishore (2021) [24]	Change in project scope, Delay in payment, Design errors, Discrepancies in contract documents, Delay in approvals, Delay in site access, Price escalation of materials, Substandard workmanship, Poor planning and scheduling, Shortage of materials, Poor communication among parties, Subcontractor-related problems, Owner's interference, Inadequate site investigation, Delay in drawings, Inaccurate cost estimation, Adverse weather conditions, Unrealistic deadlines, Inadequate equipment or resources, Frequent design changes, Change in laws or regulations, Delay in decision-making, Conflicts between stakeholders, Force majeure events.
Tanriverdi et al. (2021) [25]	Unrealistic contract durations, Incomplete or unclear contract documents, Ambiguous specifications and drawings, Late approvals, Design changes during construction, Delay in payments, Inadequate planning, Unclear scope of work, Poor communication between parties, Inadequate coordination between project stakeholders, Lack of experience of project participants, Inadequate site investigation, Material delivery delays, Unforeseen ground conditions, Inadequate documentation, Unrealistic cost estimates, Legal and regulatory issues, Delay in site handover, Poor contract management, Owner's late decisions, Conflict in responsibilities, Bureaucratic delays, Unexpected events (e.g., weather), Financial difficulties of contractor, Inadequate risk allocation.
Tuna (2021) [26]	Delay in payment, Design changes during construction, Unclear contract conditions, Inadequate project planning, Late delivery of materials, Inconsistent project documents, Errors and omissions in design, Inadequate site investigation, Poor communication between parties, Lack of coordination between stakeholders, Subcontractor-related issues, Unforeseen ground conditions, Delay in approvals, Legal and regulatory changes, Financial difficulties of contractor, Unrealistic project schedule, Deficient contract documents, Changes in laws and standards, Weather conditions, Delay in land acquisition, Conflicts over scope of work, Lack of technical staff, Poor quality of workmanship, Price escalation, Bureaucratic delays.

Muhammuddin et al. (2022) [9]	Unclear contract documents, Ambiguous specifications, Poor communication between parties, Inadequate project planning, Unrealistic time schedules, Design errors and omissions, Delay in decision-making, Delay in payments, Late site possession, Inadequate site investigation, Change orders during construction, Poor contract administration, Substandard workmanship, Inaccurate cost estimates, Poor coordination among stakeholders, Legal and regulatory issues, Unforeseen ground conditions, Shortage of materials or resources, Bureaucratic delays, Owner interference, Delay in approvals, Force majeure events, Financial difficulties of contractor, Unfair risk allocation, Inadequate stakeholder engagement, Lack of proper supervision, Lack of dispute resolution mechanisms.
Wang et al. (2022) [27]	Poor communication, Poor coordination, Ambiguous contract documents, Design errors and omissions, Change orders, Delay in decision-making, Lack of clarity in responsibilities, Inadequate information flow, Unclear project scope, Delay in approvals, Inconsistent documentation, Errors in construction drawings, Misunderstanding of contract terms, Inadequate documentation of changes, Poor record-keeping, Conflict of interest among stakeholders, Ineffective contract management, Differing interpretations of specifications.
Kikwasi (2023) [12]	Design changes, Poor site management and supervision, Delay in payment, Delay in approval of materials, Drawings or sample submissions, Change of construction methods, Change of materials, Adverse weather conditions, Inadequate contractor experience, Inadequate planning, Accidents, Inadequate site investigations, Delay in handing over the site, Escalation of material prices, Delay in providing information, Variations in quantities, Errors in contract documents, Unclear contract provisions, Delay in decision-making, Financial difficulties, Poor communication, Unforeseen site conditions, Errors and omissions in design.
Sherif and Abdelalim (2023) [28]	Design errors and changes, Poor communication, Delay in approvals, Delay in site access, Delay in material delivery, Delay in payments, Inadequate planning and scheduling, Contractor financial issues, Incomplete drawings, Inaccurate project documentation, Discrepancies in contract documents, Owner's late decisions, Unclear scope definition, Coordination problems among stakeholders, Errors in specifications, Weather-related delays, Ineffective change management, Subcontractor performance issues, Lack of documentation for delay events.
Silva et al. (2023) [8]	Poor communication between stakeholders, Inadequate planning and scheduling, Design errors and omissions, Incomplete or unclear contract documents, Delay in payments, Changes during construction, Unclear allocation of responsibilities, Unrealistic contract durations, Inadequate risk allocation, Inadequate site investigation, Inaccurate cost estimates, Delay in approvals, Poor coordination among parties, Force majeure events, Bureaucratic delays, Owner interference, Subcontractor problems, Poor contract administration, Discrepancies in specifications and drawings, Financial difficulties of stakeholders, Legal and regulatory changes, Delay in site possession, Conflicts over scope, Lack of stakeholder engagement.
Antoniou and Tsioulpa (2024) [29]	Design errors or omissions, Change orders, Inaccurate cost estimation, Contractor's financial difficulties, Delay in approvals, Poor site management, Inadequate project planning, Late payments, Lack of clarity in contract clauses, Errors in specifications, Unforeseen site conditions, Inadequate risk management, Subcontractor performance issues, Poor communication among stakeholders, Unclear project scope, Lack of coordination, Bureaucratic delays, Material delivery delays, Regulatory and legal changes, Ambiguities in contract terms, Owner interference, Adverse weather conditions, Conflicting stakeholder objectives, Delay in decision-making.

As evident from Table 1, construction claims have continued to be an endemic issue in the construction industry, and studies over the years indicate that most of the reasons have continued to be remarkably consistent, although some new ones have appeared with shifts in project environments. Variation or change orders (most often mentioned across nearly all the studies conducted to date) is one of the most common reasons mentioned in almost all the studies. Decisions made by owners, project scope that may not be clearly stated, or unexpected site conditions, lead to change orders. Unless addressed carefully, these changes may disrupt schedules and budgets, providing an invitation to claims and disputes [6, 29]. Complementary to this, owner delays in payments have continued to be a significant issue. These delays place contractors in an unwanted financial position and may lead to work stoppages or lead contractors to initiate claims for the recovery of costs [5, 8].Another ongoing issue that continues to prevail in the literature includes inadequate design and documentation. Errors on the drawings, incomplete specifications, and conflicting data are all typical claim initiators. When approvals take time or designs keep altering during construction, misunderstandings and delays almost become inevitable [5, 28]. Additionally, most researchers observe that poorly drafted or unclear contracts act as one of the major sources of claims. Ambiguous clauses or missing information provide too much scope for various interpretations, and as such, misunderstandings between parties tend to develop [18, 27]. A study examining 346 construction-related court cases in Turkiye between 2018 and 2021 reveals that superstructure projects are most prone to legal conflict, with financial issues (debit and credit) accounting for nearly half of all cases. Contracts involved were poorly drafted or

verbal, contributing to misunderstandings and disputes [30]. A study on public infrastructure projects in Turkiye identified and prioritized 29 suspension risks by combining a systematic review with focus-group discussions involving 20 experts from the public and private sectors and a fuzzy survey. The most critical risks are contractual uncertainties from constant contract changes, financial losses tied to litigation/ alternative dispute resolution, and administrative difficulties in securing financing when projects are re-started [31].

Table 2 lists the 21 considered studies in chronological order with a summary of their geographical scope, main construction claim causes, methods of study, and proposed preventative or corrective measures. Zaneldin [6], one of the pioneering and preliminary studies on construction claims in the United Arab Emirates (UAE), identified change orders, delayed payments, faulty designs, and contractual issues as the main reasons. With a structured survey approach, the study highlighted the significance of timely payments and early coordination of stakeholders to avoid disputes. By utilizing regression analysis in Indian construction project claim causation, research by Doloi et al. [16] highlighted lack of commitment, poor planning, scope uncertainty, and inadequate site management as primary contributing factors. Detailed project scoping, commitment enhancement, and strategic planning were advisable as measures to avoid such disputes. Olanrewaju and Anavhe [15] in the research from Nigeria, named the primary reasons for construction claims as delays in payments, slow approvals, mismanagement, and cost overruns. From survey data, they suggest the detection of issues at an early stage, along with aggressive negotiation processes, to effectively manage emerging disputes. Cakmak and Cakmak [5], from the case of the Turkish construction industry, employed the Analytic Network Process (ANP) to reveal primary reasons for construction claims such as contractor ineffectiveness, faulty designs, and poorly written contracts. The study highlighted the potential of careful contractual wording and verification of designs during the initial stages. Hadikusumo and Tobgay [17] in their research on the construction of power plants in Bhutan, employed a case study and concluded that the primary triggers were differing site conditions, project delays, revisions in designs, and force majeure. They proposed negotiation procedures and a stronger investigation during the design phase. Apte and Pathak [7] conducted a review of the literature that found that most claims resulted from uncertain contracts, deviations in schedules, and unexpected site conditions. The authors supported the use of early notice provisions and careful documentation for bolstering claim defenses and prevention. Mishmish and El-Sayegh [18] surveyed road construction works in the UAE and pinpointed design changes, delays by the contractor, documentation deficiencies, and inadequate site investigation as the major reasons. The authors advocated better design documentation and better attention to investigatory work. Yildizel et al. [19] surveyed in Türkiye and identified low construction quality, tardy payments, inefficient site management, and design errors. Enhanced worker training and well-defined contractual structures were some of the remedies they suggested. Ataker [20] created game-theoretical modeling for the analysis of change order and compensation for delays in change order claims in the construction ventures of Turkey. The study illustrated that conflicting incentives and reactive attitudes between the employer and contractor would lead disputes to get out of hand. The thesis concluded that game theory can provide strategic recommendations for balanced and effective negotiation processes for construction contracting. Assaf et al. [21] conducted a thorough survey in Saudi Arabia, which identified change orders, design inconsistency, contractor delays, and contractual misunderstanding as common reasons. Structural control measures in design and systematic payment structures were the measures the authors proposed for managing the claim proactively. Temiz [23] conducted document analysis from the construction ventures of Turkey and determined that contractual vagueness, owner-initiated change, and contractor inefficiency were the common reasons for disputes. Contractual transparency and official training courses for the participants of the project achieved importance in the study. Malki and Alam [22] investigated the dynamics of the claim in the construction of Bahrain through the analysis of the survey data. The findings highlighted the influence of change orders, tardy payments, weak bidding processes, and design faults or omissions. The research encouraged stricter cost and scope controls and tougher pre-bid appraisal. Tanrıverdi et al. [25] used causal mapping for the analysis of Turkish projects and found that unrealistic expectations, contractual ambiguities, and design faults dominated claim formation. Their method brought forth the importance of stakeholder congruence and causal visualization for strategic planning. Alqershy and Kishore [24] synthesized an artificial neural network (ANN) model with survey research for analyzing dispute causation in Indian construction. Contract ambiguities, faulty planning, financial volatility, and design faults dominated their findings. They advocated the use of better-written contract phrases, sound financial planning, and enhanced managerial practices. Muhammuddin et al. [9] performed a systematic review of Indonesian construction activities and determined variation orders, cash retentions, design faults, and communication breakdowns as the main reasons for claims. Recommendations from them included the proper engagement of stakeholders and enhanced utilization of Building Information Modeling (BIM) for openness and coordination. Wang et al. [27] presented a generic scheme combining BIM with claim prevention measures. While not being specific to a particular region, the research linked BIM with fewer change orders, better documentation, and timely detection of conflicts, positioning the method as a proactive management tool. Silva et al. [8] performed an international systematic review, with the findings showing poor design of the contract, inefficient contractors, design faults, and slow payments as global claim inducers. The authors recommended better planning in the advanced stages and better contractual delineations for managing risks. Sherif and Abdelalim [28] studied Egyptian claims using the survey method. Shortcomings in designs, lapses in consultant work, owner-side delays, and inefficient contractors were common reasons. Solutions were the use of delay classification with enhanced communication and coordination of stakeholders, and the implementation of mediation tools. Kikwasi [12], in a correlation-based analysis conducted in Tanzania, identified variability,

delayed payments, slow decision-making, and defective documents as major sources of claims. Improved management of contracts, timely payment structures, and accuracy in documentation were presented as solutions to these issues. Global research by Antoniou and Tsioulpa [29] employed the Relative Importance Index (RII) for risk analysis. Scope alterations, delayed payments, design defects, and contractual issues were major findings. Project planning based on risk, the use of BIM, and alternative methods for resolving disputes were the major recommendations for minimizing construction claims.

Table 2. Summary of key reviewed studies, identified claim causes, and suggested solutions.

Author(s)	Year	Country /Region	Main Causes	Methodology	Proposed Solutions
Zaneldin [6]	2006	UAE	Change orders, delay caused by owner, payment delays, low price.	Survey	Enhanced contract/design and risk-sharing philosophy.
Doloi et al. [16]	2012	India	Lack of commitment, poor planning, unclear scope, and inefficient site management.	Regression Analysis	Defined scope, commitment, and planning.
Olanrewaju and Anavhe [15]	2014	Nigeria	Late payments, approvals delay approval delays, change orders, adjoining properties.	Survey	Participatory approach and timely payment.
Cakmak and Cakmak [5]	2014	Türkiye	Contractor issues, design errors, and contract ambiguities.	ANP	Clear contracts and improve design.
Hadikusumo and Tobgay [17]	2015	Bhutan	Differing site conditions, delays, design changes, and force majeure.	Case Study	Negotiation and design investigation.
Apte and Pathak [7]	2016	Global	Contract ambiguity, delays, scope changes, unforeseen conditions.	Literature Review	Clear contracts and proper documentation.
Mishmish and El-Sayegh [18]	2016	UAE	Variations, contractor delays, poor documentation, and inadequate site investigation.	Survey	Better design, qualified stakeholders, and accurate records.
Yildizel et al. [19]	2016	Türkiye	Low quality, late payments, poor site management, and design mistakes.	Survey	Skilled labor and clear contracts.
Ataker [20]	2018	Türkiye	Change claims, delay claims, and contract complexity.	Game Theory Model	Clear contracts and coordination.
Assaf et al. [21]	2019	Saudi Arabia	Change orders, design errors, contractor delays, contract issues.	Survey	Clear contracts and improve payment structure.
Temiz [23]	2020	Türkiye	Contract ambiguities, owner changes, and contractor inefficiency.	Survey	Contract clarity, effecting planning and management.
Malki and Alam [22]	2020	Bahrain	Change orders, payment delays, inadequate bidding time, and estimating errors.	Survey	Scope and cost control.
Tanriverdi et al. [25]	2021	Türkiye	Changes, unrealistic expectations, contract ambiguities, design errors, delays.	Causal Mapping	Improved design and clear contracts.
Tuna [26]	2021	Global	Payment delays, changes, unclear scope, contract ambiguities, and financial difficulties of contractors.	Literature review	Contract clarity and enhanced planning.
Alqershy and Kishore [24]	2021	India	Delays in approvals, changes, contract ambiguities, financial instability, unforeseen conditions.	ANN Modeling and Survey	Scope control and improved contracts.
Muhammuddin et al. [9]	2022	Global	Variation orders, delayed payments, design errors, and communication issues.	Systematic Literature Review	Clear contracts and enhanced communication.
Wang et al. [27]	2022	Global	Design errors, change orders, payment problems, and communication issues.	Conceptual Framework	BIM-based prevention.
Silva et al. [8]	2023	Global	Poor contract arrangements, changes, unforeseen conditions, and contract ambiguities.	Systematic Literature Review	Contract clarity and improved planning.

Sherif and Abdelalim [28]	2023	Egypt	Design errors, consultant issues, owner delays, contractor inefficiency.	Survey	Proper documentation and trained participants.
Kikwasi [12]	2023	Tanzania	Variations, payment delays, decision-making delays, design/documentation issues.	Correlation-Based Analysis	Contract clarity and enhanced site management.
Antoniou and Tsioulpa [29]	2024	Greece	Changes, payment delays, design errors, contract issues.	Survey, Risk Analysis	Improved design and consistent financial flow.

Results

This narrative review clarifies an overarching framework for construction claims, which occur due to the interaction of technical, contractual, managerial, financial, and environmental factors. The compilation of 21 studies from 2006 to 2024 indicates that these claims are by no means a sporadic phenomenon; instead, they are the outcome of an intricate interaction of various interdependent factors at all phases of the construction process.

A distinguishing observation of this synthesis is the repeated instances of contractual and design issues, which constantly appeared within different contexts. Poorly written contracts, ambiguous specifications, uncertainty regarding responsibility delineation, and incomplete project documentation were often repeated basic factors causing claims [7, 23, 29]. Errors of design resulting from consultant blunder, lack of coordination, or insufficiency of site investigation repeatedly surfaced [5, 8, 28]. These technical discrepancies primarily result in cost overruns, requiring financial repercussions and alterations to project schedules.

An important implication relates to delays taking place within financial and administrative processes, and notably, within payment systems. Delayed payments from employers and financial organizations are a widespread concern, often leading to cash flow interruptions, demands for additional payment, and longer project schedules [6, 15, 22]. These are all notably documented from research within the Middle East, Türkiye, and African contexts, and quite probably reflect entrenched systemic impediments to finance and purchasing. At the same time, continual references to unrealistic project schedules and inappropriate scheduling—particularly by contractors—highlight the need for accurate baseline scheduling [16, 25, 26].

Stakeholder misalignment has been noted to occur with considerable frequency and disruptiveness. Studies point to such incidents usually resulting from ineffective communications, lack of stakeholder engagement, or unclear project scope definitions. Such an issue is especially evident in large infrastructure projects, whereby various stakeholders—such as customers, consultants, contractors, and subcontractors—have varying perceptions of their respective objectives and responsibilities [12, 27]. In most cases, the absence of anticipatory management measures like early warning systems or collaborative contracting schemes allowed small problems to escalate into major project complexities.

From a perspective of assigning liability, the multi-label coding assessment in Table 1 suggests that the roots of claims could not be uniquely attributed to a specific stakeholder. Consultants were most commonly identified with technical shortcomings, contractors were implicated with problems of planning, site management, and financial shortcomings, and employers were implicated with regard to delay due to payments and administrative shortcomings. However, a significant percentage of the reasons could not be uniquely attributed to a specific entity. These findings point to the complex and interconnected natures of construction processes and hence highlight difficulties of fault assignment, suggesting the need for a systems-based approach to claim mitigation.

Notwithstanding variations in geographical, regulatory, and methodological settings among studies covered, some of the common preventive measures were uniformly emphasized. Elaboration and standardization of contract terms, including scope, allocation of responsibilities, and risk distribution, were mentioned most commonly. Multiple studies have shown that non-specific wording of contracts, deviations from written descriptions and drawings, and different interpretations of contract clauses are key sources of claims [5, 7, 8, 23, 29]. To prevent such risks, contracts were strongly recommended to be prepared on standardized templates with clearly defined deliverables, schedules, and change control procedures for scope modifications.

Among the commonly proposed strategies is to improve communication and coordination among stakeholders involved at different stages of the project. Studies in Türkiye [25, 26], in the UAE [18], and in Indonesia [9] revealed that poor communication of relevant information, long approval times, and fragmented interactions among contractors, consultants, and clients often escalated confusion, leading to official disputes. Many scholars [27, 28] have proposed adopting set communication protocols, conducting stakeholder engagement workshops, and adopting open reporting policies as sustainable ways of improving understanding and tackling problems ahead of time.

Another prevention-related theme is improved technical documentation and protocols for site investigations. Numerous studies have shown that faulty and incomplete drawings, unforeseen subsurface conditions, and a lack of proper technical specifications are the main technical reasons for claims [7, 12, 17-19]. Implications are proposed to include performing thorough pre-construction site analyses, incorporating geotechnical investigations, and having independent verification of design documents before mobilization.

Simultaneously, an increasing body of recent scholarly research has highlighted the need for combining digital tools with risk-informed planning methodologies for an

efficient handling of inherent complexities within environments prone to claims. BIM has particularly received widespread support for its ability to improve visualization, detect design conflicts, and facilitate collaborative documentation among stakeholders for a construction project [8, 9, 27]. Similarly, advanced computational methods, such as ANN, have been utilized for research, such as Alqershy and Kishore [24], to make predictions regarding possible claim instances based on risk factors and historical trends. These tools not only allow for prognostic functionality but also facilitate superior transparency and traceability in construction decision-making.

Several researchers [6, 15, 21] have highlighted the imperative importance of timely and trustworthy payment systems, pointing out that financial uncertainty due to delayed payments to contractors is a leading driver of disputes within construction contracts. Staggered payment arrangements, computerized invoice verification systems, and dispute adjudication boards have been recommended to be included among financial management practices aimed at preventing the incidence of claims.

Finally, there was a consensus on the need to put in place institutional structures for capacity-building and training programs for project stakeholders, with a focus on contract administration, risk management, and dispute avoidance. Studies in Türkiye [23, 26], in Saudi Arabia [21], and in India [7] have shown that insufficient understanding of contractual rights and responsibilities often led to reactive measures rather than anticipatory problem-solving approaches.

When looked at collectively, these findings support the view that minimizing claim frequencies requires an overarching and coherent strategy, tailored to each project's specific legal, technical, and organizational environments. Synergistic interaction among accurate contract terms, better communication, reliable design, technology, and stakeholder expertise appears to form the cornerstone of any lasting framework for claim management.

In many studies, construction claims have been divided into groups in order to better analyze them and to better reveal the relationships between them [5, 8, 16, 19, 21, 24, 25, 28, 29]. In an endeavor to examine factors of claims systematically, this study conducted an extensive content analysis of 21 peer-reviewed papers and graduate theses from the years 2006 to 2024. Analyzing each article in fine detail allowed for similar and thematically related factors to be consolidated, and hence, for an eventual list of factors to amount to 28. Finally, these factors were grouped into five main categories: factors external to the project, factors from employers, factors from contract documents, factors relating to contractual relationships, and factors from contractors. Table 3 demonstrates this categorization, wherein it not only lists how often each factor was mentioned within different studies but also offers a systematic framework for understanding the multifaceted nature of construction claims. A field study based on these identified causes will allow for analyzing their potential to lead to claims. This analysis can serve as a foundation for identifying the causes with the highest impact on claims and developing models to prevent them. Consequently, reducing claims in the construction sector and minimizing or preventing resource waste originating from claims may become feasible.

Table 3: Categories of main claim causes.

No	Category	Factors Causing Claims	References																						
			[6]	[16]	[5]	[15]	[17]	[7]	[18]	[19]	[20]	[21]	[22]	[23]	[24]	[25]	[26]	[9]	[27]	[12]	[28]	[8]	[29]
1	External Factors	Changes in Government Regulations and Laws	✓	✓	✓	✓			✓	✓	✓		✓		✓	✓	✓			✓			✓
2		Changes in Material Prices and/or Labor Costs	✓	✓	✓	✓	✓	✓		✓	✓	✓	✓		✓		✓						✓
3		Force Majeure			✓		✓	✓	✓	✓	✓		✓	✓	✓	✓	✓			✓		✓	✓
4		Unforeseen Ground Conditions	✓	✓	✓	✓	✓	✓		✓	✓		✓	✓	✓	✓	✓	✓	✓	✓		✓	✓
5	Employer-Related	Verbal Change Orders	✓								✓	✓					✓						
6		Written Change Orders	✓	✓	✓	✓		✓	✓	✓	✓	✓	✓	✓	✓	✓	✓	✓	✓	✓	✓	✓	✓
7		Acceleration, Suspension, and Restarting of Work			✓	✓			✓	✓	✓			✓	✓	✓	✓	✓			✓	✓	✓
8		Changes in Drawings and Specifications During Construction					✓	✓						✓	✓		✓						
9		Slow Decision-Making by the Employer	✓	✓		✓		✓					✓	✓	✓	✓			✓	✓	✓		
10		Delay in Site Handover		✓	✓		✓	✓	✓	✓	✓			✓	✓	✓		✓	✓	✓	✓	✓	✓
11		Deficiencies in Tender Documents				✓		✓		✓	✓								✓	✓			✓
12		Delay in Payments to the Contractor	✓	✓	✓	✓	✓	✓	✓	✓	✓	✓	✓	✓	✓	✓	✓	✓	✓	✓	✓	✓	✓

13	Contract Documents Related	Design Errors or Deficiencies	✓		✓		✓	✓	✓	✓	✓	✓	✓	✓	✓		✓	✓	✓	✓	✓	✓	✓
14		Poorly Written Contracts and Ambiguities	✓	✓	✓		✓	✓	✓	✓	✓	✓	✓	✓	✓	✓	✓	✓		✓		✓	✓
15	Contractual Relationship Related	Contract Termination or Suspension of Work	✓			✓	✓		✓		✓	✓	✓	✓	✓	✓				✓	✓		✓
16		Different Interpretations of Contract Provisions		✓	✓			✓	✓	✓	✓			✓		✓		✓	✓			✓	✓
17		Lack of Coordination and Communication Among Project Parties	✓	✓	✓			✓	✓	✓	✓	✓	✓	✓	✓	✓	✓	✓	✓		✓	✓	✓
18		Insufficient Time for Bid Preparation					✓	✓				✓	✓	✓			✓						
19		Low-Priced Contract Due to High Competition	✓			✓			✓		✓	✓	✓		✓		✓	✓				✓	
20	Contractor-Related	Subcontractor Issues	✓	✓		✓			✓		✓	✓	✓	✓	✓	✓	✓			✓	✓		
21		Poor Site Management and Administration		✓			✓	✓					✓		✓						✓		
22		Accidents	✓	✓			✓	✓		✓	✓		✓			✓							✓
23		Cost Estimation Errors	✓					✓			✓	✓	✓		✓		✓						
24		Errors in Work Schedule	✓					✓		✓	✓	✓		✓		✓	✓				✓	✓	
25		Insufficient Contractor Resources (Labor, Equipment, etc.)				✓		✓		✓		✓	✓		✓								✓
26		Financial Insufficiency of the Contractor	✓	✓	✓	✓			✓	✓	✓	✓	✓	✓	✓	✓	✓			✓		✓	✓
27		Poor Workmanship by the Contractor	✓	✓	✓	✓		✓	✓	✓	✓	✓		✓	✓	✓	✓			✓		✓	
28		Implementation Errors by the Contractor	✓			✓							✓	✓		✓				✓			✓

Implications

As mentioned above construction claims have been addressed in the literature both by category and by item. Here we present category-based and key item-based assessments of claims within the scope of the literature reviewed in our article.

Comparative perspectives on claim cause categories

Design related claim causes are frequently identified in the literature as significant contributors to disputes. These causes may include errors, omissions, incomplete specifications, or misaligned design intent, which can have cascading effects on project execution. Antoniou and Tsioulpa highlighted design deficiencies and scope inconsistencies among the higher-risk categories affecting contract performance in Greek public projects [29]. Likewise, Cakmak and Cakmak, through an ANP model, found inadequate specifications and design errors to be important triggers for disputes, although contractor- and contract-related causes carried slightly greater overall weight in their analysis [5]. Tanriverdi et al. also noted that under Design-Build contracts, design-related problems such as incomplete or delayed design information may contribute to disputes, often interacting with other factors such as contract provisions or people-related issues [25].

Claims attributed to project owners or their representatives are prevalent, particularly in cases involving scope changes, delayed payments, or delayed site access. This category appears prominently in the literature across various regions and project types. According to a study in the Indian construction industry, frequent change orders and delayed approvals by owners are primary drivers of claims [32]. These findings are supported by Assaf et al. who emphasized the high incidence of claims resulting from client-initiated variations in Saudi Arabia [21]. Silva et al. also reinforced that employer-driven changes are among the most repeated claim origins in the global literature [8].

Contractor-related claim causes—particularly delays in work progress, financial instability, and defects/substandard workmanship—are frequently identified as significant. In an ANP model, Cakmak and Cakmak found the contractor category to have the highest overall importance, with delays in progress and workmanship quality featuring among key sub-causes [5]. Consistently Antoniou and Tsioulpa list delays in work progress and contractor financial failure among the five highest-risk causes affecting contract performance in Greek public projects [29]. At the same time, evidence from Tanriverdi et al. indicates that, under Design–Build (FIDIC Yellow Book) arrangements, disputes typically emerge from causal chains in which contractor actions interact with pre-construction practices, people factors, and contract terms [25]; thus, the salience of contractor-driven causes

may be shaped by procurement form and contractual clarity rather than being uniformly secondary to design or owner categories.

The key causes and mitigation strategies

According to Table 2, the most repetitive drivers of construction claims seem to gather around a small set of claims that are seen often across different geographies and methods (surveys, case studies, literature reviews, causal mapping, and modeling such as ANP and ANN). First, change/variation orders are consistently cited [6, 8, 9, 12, 15, 18, 20, 21, 23, 25, 26, 24, 27]. Changes may stem from evolving client needs, design development or late clarifications, and they frequently interact with other drivers such as ambiguous contract wording, unclear scope, and weak documentation. Second, payment problems (late or delayed payments and unreliable cash flow) are repeatedly identified [6, 9, 12, 15, 19, 22, 26, 27, 29]. These issues may increase delays, intensify adversarial postures, and create leverage points for claims. Third, design-related deficiencies (design errors, late design, and documentation issues) are common precursors; they can trigger rework, change orders, and time impact [5, 9, 12, 17, 19, 21, 25, 27, 28]. Fourth, contractual quality problems—contract ambiguities, poor arrangements, and excessive complexity—recur across many studies and may manifest as interpretive gaps that parties exploit during performance [5, 7, 8, 20, 21, 23, 24, 25, 26]. Fifth, delays are almost always part of the picture whether they're caused by the owner, the contractor, or by slow approvals and decision making [6, 7, 12, 15, 17, 18, 20, 21, 24, 25, 28]. These often go together with the other issues mentioned earlier. Beyond that, there are several other factors that increase claims. These factors include shifting project scope, poor planning and site management, unexpected site conditions, weak communication, and problems on the contractors' end like inefficiency, budget troubles, unrealistic pricing, or not enough time to prepare a proper bid [6, 7, 9, 16, 17, 19, 22, 23, 26, 27, 28].

Preventive approaches in the literature largely map onto these claims and may be viewed as a layered risk reduction strategy. For change-related risk, the evidence repeatedly points to contract clarity and scope control: clearly drafted change and variation procedures, rigorous definition of scope at tender, and coordination mechanisms that reduce design evolution during construction [6, 8, 7, 9, 12, 16, 20, 21, 22, 23, 24, 25, 26]. Strengthening design quality (allowing adequate design time, employing competent designers, conducting design investigations and constructability reviews) may reduce downstream variations and design-triggered claims [5, 17, 19, 25, 28]. To address payment risk, studies recommend ensuring timely payment and consistent financial flow, sometimes through explicit payment structures and owner-side commitment [6, 9, 15, 19, 22, 26]. To address contractual ambiguity, the prevailing recommendation emphasizes the need for contracts that are clear, unambiguous, and internally consistent. These include explicitly defined roles, clearly articulated approval processes, notice requirements, and standardized documentation protocols. Equally important is maintaining accurate and contemporaneous records, ensuring that contract administration remains both traceable and auditable. It is also recommended to use contract clauses that have been successfully implemented before and standard contract forms if possible [5, 7, 8, 20, 21, 23, 24, 25, 26].

Where scheduling and approval processes pose challenges, proposed solutions consistently involve more rigorous planning and scheduling practices. The implementation of clear and timely decision-making and approval protocols, and the adoption of collaborative governance models—such as partnering approaches or risk-sharing frameworks—that set up negotiation and early engagement to promote timely resolution of issues [12, 15, 16, 20, 24, 28]. For site management and documentation/communication gaps, the literature accentuates accurate records, proper documentation practices, and improved communication, alongside qualified/trained stakeholders and skilled labor to ensure that procedures are understood and followed [9, 18, 19, 27]. When site conditions are uncertain, thorough pre-bid/site investigation and realistic pricing/estimating (including adequate bid time) may reduce risk of claims. Finally, some sources promote for technology-enabled coordination—particularly using BIM as a proactive approach to identifying clashes and scope gaps early in the process. By surfacing these issues upfront, such tools have the potential to reduce the frequency of design- and coordination-related variations and so as claims [9, 12, 21, 27, 29].

In synthesis, the studies indicate that claim prevention may be strengthened by aligning four interrelated and mutually reinforcing levers. First, contractual clarity, achieved through unambiguous provisions concerning scope, changes, payments, notices, and approvals. Second, design excellence and coordination, which involves early investment in design, thorough site investigation, constructability reviews, and the engagement of qualified design teams. Third, execution discipline, which covers realistic planning and scheduling, timely decision-making and payments, effective site management, and consistent documentation and communication. Fourth, risk-sharing and capability, which includes collaborative or negotiated project approaches, well-trained stakeholders, and, where appropriate, the use of BIM to support integrated and transparent information flow.

The primary sources of claims such as scope changes, payment disputes, design shortcomings, contractual ambiguities, and delays are often interrelated. The most resilient form of prevention is likely to come from a combined and coordinated application of these measures, rather than from any single intervention in isolation.

Based on the synthesis of the reviewed literature, a structured mapping of main claim causes, typical failure pathways, corresponding mitigation levers, and concrete actions to cite was developed. Table 4 summarizes these relationships, highlighting how contractual clarity, design excellence, execution discipline, and risk-sharing mechanisms can be operationalized to prevent the escalation of claims. As shown in the table common claim causes such as change/variation orders, payment delays, and design deficiencies typically follow identifiable failure pathways that culminate in disputes. By linking each cause to its 'primary lever' and specific preventive actions, the table provides a practical claim-avoidance framework.

Table 4: Main causes, failure pathways, and prevention levers/actions for claims.

Causes	Typical failure pathway	Primary lever(s) to pull	Concrete actions to cite
Change / variation orders	Evolving needs, late clarifications, or scope creep → undocumented/ambiguous changes → time/cost growth and claims	Contractual clarity; design excellence & coordination; execution discipline	Draft unambiguous change/variation clauses; require signed approvals before proceeding; define scope rigorously at tender; freeze design at milestones; perform constructability and coordination reviews; maintain contemporaneous records
Payment problems (delays / cash-flow unreliability)	Interrupted cash flow → slowed work and adversarial posture → delay and compensation claims	Contractual clarity; execution discipline; risk-sharing and capability	Set explicit payment schedules, certification steps, and consequences; track and meet payment deadlines; owner-side commitment mechanisms (e.g., funding proofs); define early escalation channels
Design deficiencies (errors, late design, doc gaps)	Rework and requests for information (RFIs) → variations and time impact → cost/time claims	Design excellence and coordination	Allocate adequate design time; engage qualified designers; perform site and design investigations; conduct constructability and clash reviews (building information modeling [BIM], where appropriate); issue clear, coordinated documents
Contract quality problems (ambiguity, inconsistency, excess complexity)	Ambiguity and inconsistency → divergent interpretations → notice/entitlement disputes → claim events	Contractual clarity	Use clear, internally consistent contracts; rely on standard forms and tested clauses where feasible; define roles, approvals, notices, and documentation protocols; simplify where possible; implement audit-ready administrative procedures
Delays (owner, contractor, slow approvals/decisions)	Schedule slippage at gates → concurrency/entitlement debates → time and cost claims	Execution discipline; contractual clarity; risk-sharing & capability	Build realistic schedules with float logic; set time-bound approval and decision requirements; define escalation ladders; maintain progress evidence (diaries, weather logs); establish partnering and early-issue resolution forums
Shifting project scope	Scope drift after tender → serial changes → cumulative impact claims	Contractual clarity; design excellence & coordination	Tighten scope definition and change thresholds; define price options and alternatives explicitly; hold pre-award scope-reconciliation workshops; enforce disciplined configuration control
Poor planning / site management	Inefficient sequencing and resourcing → disruption and inefficiency → prolongation/productivity claims	Execution discipline	Use baseline plus rolling-wave planning; conduct look-ahead planning and constraint removal; ensure qualified supervision; maintain daily reporting and issue logs; deliver pre-task briefings and method statements
Unexpected site conditions	Latent conditions → method changes and delay → variation/time claims	Design excellence and coordination; risk-sharing and capability	Conduct thorough pre-construction site investigations (e.g., geotechnical, utilities); use risk-allocation clauses for latent conditions; include contingency allowances; validate design assumptions through early contractor involvement (ECI); define discovery, reporting, and escalation protocols; plan for adaptive methods

Weak communication / documentation	Missing or late information → rework and disruption → dispute over scope/entitlement → prolonged claims	Execution discipline; contractual clarity	Establish document-control procedures; maintain RFI and submittal registers; standardize meeting minutes and transmittals; use a common data environment (CDE); enforce contemporaneous records (diaries, daily photos, correspondence logs)
Contractor-side issues (inefficiency, underpricing, short bid time)	Unrealistic offers or capability gaps → performance shortfalls → claims to recover losses	Execution discipline; risk-sharing and capability	Ensure realistic estimating and bidding durations; conduct pre-award capability checks; provide training and upskilling; issue early warnings of resourcing gaps; replan collaboratively where appropriate

Limitations

This research is a narrative review based on a non-systematic collection of 21 peer-reviewed articles and graduate theses published between 2006 and 2024. Although this analysis clarifies pertinent insights into explanatory factors leading to construction claims, some restrictions deserve consideration. The analysis does not include grey publications, unpublished data, and sources from outside of academic authorities, which can provide additional evidence to support construction claim causes and management. Though this review draws upon world sources, a considerable number of research articles focus mainly on a particular geographical area, e.g., the Middle East and Türkiye. While this can be considered as an advantage for the works to be done in the mentioned regions, as a consequence, this focal point may inhibit generalizability of results to diverse settings differing in construction techniques, regulations, or stakeholder relationships.

Conclusion

Claims remain a persistent and critical challenge within the construction industry. Insufficient attention to their underlying causes can lead to adverse outcomes for both projects and stakeholders. This narrative review highlights the multifaceted nature of construction claims, emphasizing that they rarely stem from a single stakeholder or isolated technical failure. Instead, they emerge from a systemic interplay of contractual ambiguity, financial mismanagement, deficient design coordination, and communication breakdowns across project lifecycles. A synthesis of 21 studies from 2006 to 2024 indicates that contract clarity, payment discipline, scope definition, and stakeholder alignment remain the cornerstones of claim prevention. While consultants were most frequently associated with technical deficiencies and design flaws, employers and contractors shared responsibility for financial delays and project mismanagement, respectively. Yet, a majority of causes could not be attributed solely to any single party, reflecting the interdependence of actors in the built environment. Across various contexts, prominent mitigation strategies include the implementation of clear and adaptive contract mechanisms, structured communication frameworks, integration of risk-based tools, and proactive institutional capacity-building. The findings derived from this research, supported by field evidence, may provide a base to prevent claim causes with the highest impact. Ultimately, such measures could contribute to minimizing resource wastage in the construction industry stemming from unresolved claims.

Ethics committee approval and conflict of interest statement

"There is no need to obtain permission from the ethics committee for the article prepared"

"There is no conflict of interest with any person / institution in the article prepared"

Authors' Contributions

Author 1: Study conception and design; Acquisition of data; Analysis and interpretation of data; Drafting of manuscript.

Author 2: Study conception and design; Grouping and categorization of claim factors; Support in preparing summary tables; Critical revision of the manuscript.

References

[1] M. Stan, "Issues concerning the dynamics of labor productivity at the level of the companies in Constanta County operating in the 'Construction' sector before and after the COVID-19 pandemic", *Technium Soc. Sci. J.*, vol. 25, pp. 225–241, 2021, DOI: 10.47577/tssj.v25i1.5095.

[2] C. S. Lean, "Empirical tests to discern linkages between construction and other economic sectors in Singapore", *Constr. Manag. Econ.*, vol. 19, no. 4, pp. 355–363, 2001, DOI: 10.1080/01446190010022686.

[3] H. Ren, H. Folmer, and A. J. Van Der Vlist, "What role does the real estate–construction sector play in China's regional economy?" *Ann. Reg. Sci.,* vol. 52, no. 3, pp. 839–857, 2014, DOI: 10.1007/s00168-014-0613-5.

[4] B. Ilhan and H. Yaman, "A comparative input-output analysis of the construction sector in Turkey and EU countries", *Eng. Constr. Archit. Manag.,* vol. 18, no. 3, pp. 248–265, 2011, DOI: 10.1108/09699981111126160.

[5] E. Cakmak and P. I. Cakmak, "An analysis of the causes of disputes in the construction industry using the analytical

network process", *Procedia Soc. Behav. Sci.*, vol. 109, pp. 183–187, 2014, DOI: 10.1016/j.sbspro.2013.12.441.

[6] E. K. Zaneldin, "Construction claims in United Arab Emirates: Types, causes, and frequency", *Int. J. Proj. Manag.*, vol. 24, no. 5, pp. 453–459, 2006, DOI: 10.1016/j.ijproman.2006.02.006.

[7] B. A. Apte and S. P. Pathak, "Review of types and causes of construction claims", *Int. J. Res. Civ. Eng.,* Architecture & Design, vol. 4, no. 2, pp. 43–50, 2016, https://iaeme.com/MasterAdmin/Journal_uploads/IJRCEAD/VOLUME_4_ISSUE_2/IJRCEAD_04_02_008.pdf.

[8] P. M. Silva, N. Domingo, and N. Ali, "Causes of disputes in the construction industry – a systematic literature review", *J. Financ. Manag. Prop. Constr.*, vol. 29, no. 2, pp. 193–210, 2023, DOI: 10.1108/jfmpc-03-2023-0012.

[9] N. N. Muhammuddin, M. Danuri , H. Hanid, and M. Mahanim, "Dispute occurrences during construction stages of building project: A systematic literature review", *J. Proj. Manag. Pract.*, vol. 2, no. 2, pp. 1–22, 2022, DOI: 10.22452/jpmp.vol2no2.1.

[10] M. T. A. Qershi, "Leading factors contributing to the generation of claims in the Indian Construction Industry-Consultant's perception", *Civ. Eng. Res. J.*, vol. 4, no. 4, 2018, DOI: 10.19080/cerj.2018.04.555642.

[11] A. Adeyemi and O. Segwabe, "Rank-Order analysis of factors causing claims on road construction projects in Botswana", *J. Adv. Perform. Inf. Value*, vol. 8, no. 2, pp. 58, 2016, DOI: 10.37265/japiv.v8i2.64.

[12] G. J. Kikwasi, "Claims in construction projects: how causes are linked to effects?", *J. Eng. Des. Technol.*, vol. 21, no. 6, pp. 1710–1724, 2023, DOI: 10.1108/JEDT-06-2021-0312.

[13] H. H. Shaikh, N. Y. Zainun, and S. H. Khahro, "Claims in construction projects: A comprehensive literature review", in *IOP Conference Series Earth and Environmental Science*, vol. 498, no. 1, pp. 012095, 2020 , DOI: 10.1088/1755-1315/498/1/012095.

[14] R. Asadi, J. O. B. Rotimi, and S. Wilkinson, "Investigating the relationship between reworks and contractual claims: The salience of contract conditions", *J. Leg. Aff. Disput. Resolut. Eng. Constr.,* vol. 14, no. 1, 2021, DOI: 10.1061/(asce)la.1943-4170.0000519.

[15] A. A. Olanrewaju and P. J. Anavhe, "Perceived claim sources in the Nigerian construction industry", *Built Environ. Proj. Asset Manag.,* vol. 4, no. 3, pp. 281–295, 2014, DOI: 10.1108/bepam-05-2013-0014.

[16] H. Doloi, A. Sawhney, K. Iyer, and S. Rentala, "Analysing factors affecting delays in Indian construction projects", *Int. J. Proj. Manag.,* vol. 30, no. 4, pp. 479–489, 2012, DOI: 10.1016/j.ijproman.2011.10.004.

[17] B. H. W. Hadikusumo and S. Tobgay, "Construction claim types and causes for a large-scale hydropower project in Bhutan", *J. Constr. Dev. Ctries*., vol. 20, no. 1, pp. 49–63, 2015, https://doaj.org/article/0b3e6298066b494485e6f13b0987669b.

[18] M. Mishmish and S. M. El-Sayegh, "Causes of claims in road construction projects in the UAE", *Int. J. Constr. Manag.*, vol. 18, no. 1, pp. 26–33, 2016, DOI: 10.1080/15623599.2016.1230959.

[19] S. Yildizel, E. Dogan, G. Kaplan, and A. Ergut, "Major constructional dispute causes in Turkey", *Arch. Civ. Eng.*, vol. 62, no. 4, pp. 193–204, 2016, DOI: 10.1515/ace-2015-0116.

[20] K. C. Ataker, "İnşaat projelerinde oyun teorisi yaklaşımıyla hak taleplerinin yönetimi", Yüksek lisans tezi, İstanbul Üniversitesi-Cerrahpaşa Lisansüstü Eğitim Enstitüsü, 2018.

[21] S. Assaf, M. A. Hassanain, A. Abdallah, A. M. Sayed, and A. Alshahrani, "Significant causes of claims and disputes in construction projects in Saudi Arabia", *Built Environ. Proj. Asset Manag.*, vol. 9, no. 5, pp. 597–615, 2019, DOI: 10.1108/bepam-09-2018-0113.

[22] Y. M. A. Malki and M. S. Alam, "Construction claims, their types and causes in the private construction industry in the Kingdom of Bahrain", *Asian J. Civ. Eng.,* vol. 22, no. 3, pp. 477–484, 2020, DOI: 10.1007/s42107-020-00326-z.

[23] E. Temiz, "Türkiye'deki yapım projelerinde anlaşmazlıklara neden olan faktörlerin analizi", Yüksek lisans tezi, İstanbul Teknik Üniversitesi, 2020.

[24] M. T. Alqershy and R. Kishore, "Construction claims prediction using ANN models: a case study of the Indian construction industry", *Int. J. Constr. Manag.,* vol. 23, no. 6, pp. 1097–1108, 2021, DOI: 10.1080/15623599.2021.1955322.

[25] C. Tanriverdi, G. Atasoy, I. Dikmen, and M. T. Birgonul, "Causal mapping to explore emergence of construction disputes", *J. Civ. Eng. Manag.*, vol. 27, no. 5, pp. 288–302, 2021, DOI: 10.3846/jcem.2021.14900.

[26] A. H. Tuna, "İnşaat projelerinde hak talepleri", Bitirme projesi, MEF Üniversitesi, 2021.

[27] J. Wang, S. Zhang, P. Fenn, X. Luo, Y. Liu, and L. Zhao, "Adopting BIM to facilitate dispute management in the construction industry: A conceptual framework development", *J. Constr. Eng. Manag.*, vol. 149, no. 1, 2022, DOI: 10.1061/(asce)co.1943-7862.0002419.

[28] A. Sherif and A. M. Abdelalim, "Delay analysis techniques and claim assessment in construction projects", *Int. J. Manag. Commerce Innov.*, vol. 10, no. 2, pp. 316–325, 2023, DOI: 10.5281/zenodo.7509156.

[29] F. Antoniou and A. V. Tsioulpa, "Assessing the delay, cost, and quality risks of claims on construction contract performance", *Buildings*, vol. 14, no. 2, pp. 333, 2024, DOI: 10.3390/buildings14020333

[30] M. Çevikbaş, "Identification of dispute sources in the construction industry via court files," *Turk. J. Civ. Eng.*, vol. 57, pp. 57–75, 2023, DOI: 10.18400/tjce.1224425.

[31] F. S. Demirci, O. Okudan, G. Demirdoğan, and Z. Işık, "Identifying and assessing suspension risks of public infrastructure projects," *Turk. J. Civ. Eng.*, vol. 37, no. 1, 2026, DOI: 10.18400/tjce.1647446.

[32] M. T. Alqershy and R. Kishore, "Claim causes and types in Indian construction industry – contractor's perspective," *Am. J. Civ. Eng. Archit.*, vol. 5, no. 5, pp. 196–203, 2017, DOI: 10.12691/ajcea-5-5-3

Dicle University
Journal of Engineering
https://dergipark.org.tr/tr/pub/dumf
duje.dicle.edu.tr

Araştırma Makalesi / Research Article

Geri Dönüşümlü Malzemeler ve Doğal Katkıların İnce-Daneli Zeminlerin Stabilizasyonundaki Etkisinin Taguchi Optimizasyon Yöntemi ile İncelenmesi

Investigation of the Effects of Recycled Materials and Natural Additives on the Stabilization of Fine-Grained Soils Using the Taguchi Optimization Method

Yasemin Pekdemir[1], Ahmet Şahin Zaimoğlu[2], Fatih Artuk [3*]

[1] Atatürk Üniversitesi, İnşaat Mühendisliği Bölümü, yasemin.pekdemir@outlook.com.tr
ORCID: https://orcid.org/0000-0001-7039-4998

[2] Atatürk Üniversitesi, İnşaat Mühendisliği Bölümü, zaimoglu@atauni.edu.tr
ORCID: https://orcid.org/0000-0001-5245-0212

[3] Atatürk Üniversitesi, İnşaat Mühendisliği Bölümü, fatih.artuk@atauni.edu.tr
ORCID: https://orcid.org/0000-0003-4798-9277

MAKALE BİLGİLERİ

Makale Geçmişi:

Geliş 14 Ağustos.2025
Revizyon 2 Eylül 2025
Kabul 18 Eylül 2025
Online 30 Aralık 2025

Anahtar Kelimeler:

Zemin stabilizasyonu, Taguchi Optimizasyon Yöntemi, kil, serbest basınç dayanımı

ÖZ

Artan yapılaşma, düşük taşıma kapasitesine sahip ince daneli zeminlerin mühendislik özelliklerinin iyileştirilmesini zorunlu kılmaktadır. Bu nedenle, katkı maddeleriyle yapılan zemin stabilizasyonu geoteknik mühendisliğinde yaygın bir yöntem haline gelmiştir. Son yıllarda ise katkıların etkinliğini artırmaya yönelik çeşitli deneysel tasarım ve optimizasyon çalışmalarının uygulanması önem kazanmıştır. Bu çalışmada, yüksek plastisiteli killi (CH) zeminin iyileştirilmesi amacıyla parametre olarak atık cam tozu (ACT), bazalt lif (BL), pirinç kabuğu külü (PK), geri dönüştürülmüş karbon karası (KK) ve kireç (K) katkı maddeleri kullanılarak, katkıların optimum düzeylerinin belirlenmesi ve serbest basınç dayanımına etkileri incelenmiştir. Bu parametrelerin seviyeleri ise ACT (%2–8), BL (%0,25–1), PK (%5–20), KK (%1–7) ve K (%2–8) olarak seçilmiştir. 7 günlük ve 28 günlük serbest basınç dayanımının maksimum olduğu değerleri ve optimum karışım oranları Taguchi Optimizasyon Yöntemi ile belirlenmiştir. Deneylerden elde edilen sonuçlar değerlendirildiğinde 7 günlük ve 28 günlük serbest basınç dayanımı üzerinde en etkili parametrenin kireç olduğu belirlenmiştir. Ayrıca, bu araştırma, katkı maddelerinin etkili şekilde optimize edilmesinin yalnızca zemin dayanımını artırmakla kalmadığını, aynı zamanda geri dönüşüm malzemelerinin inşaat mühendisliği uygulamalarına entegrasyonuna katkı sunduğunu göstermektedir.

ARTICLE INFO

Article history:

Received 14 August 2025
Received in revised form 2 September 2025
Accepted 18 September 2025
Available online 30 December 2025

Keywords:

Soil stabilization, Taguchi Optimization Method, clay, unconfined compressive strength

ABSTRACT

Increasing construction activities make it necessary to improve the engineering properties of fine-grained soils with low bearing capacity. In this context, the use of additives has emerged as a common and effective method for soil stabilization in geotechnical engineering. However, in recent years, the application of various experimental design and optimization methods to maximize the effectiveness of additives has become a remarkable trend. In this study, waste glass powder (WGP), basalt fiber (BF), rice husk ash (RHA), recycled carbon black (RCB), and lime (L) were selected as parameters to improve the properties of high plasticity clay (CH). The levels of these parameters were determined as follows: WGP (2%–8%), BF (0.25%–1%), RHA (5%–20%), RCB (1%–7%), and L (2%–8%). The optimum mixture ratios and the values of unconfined compressive strength (UCS) at 7 and 28 days were determined using the Taguchi Optimization Method. When the results obtained from the experiments were evaluated, it was determined that the most effective parameter on 7-day and 28-day unconfined compressive strength was lime. Furthermore, this research demonstrates that effective optimization of additives not only increases soil strength but also contributes to the integration of recycled materials into civil engineering applications.

Doi: 10.24012/dumf.1764248

* Sorumlu Yazar

Giriş

Nüfus artışı ve beraberinde gelen kentleşme, çoğu zaman yapıların sorunlu alt zeminler üzerine inşaa edilmesine neden olmuştur. Bu tür durumlarda, yapı güvenliğini ve performansını artırmak amacıyla zeminlerin mühendislik özelliklerini iyileştirmek için çeşitli zemin iyileştirme yöntemleri kullanılmaktadır. Geoteknik mühendisliğinde katkı maddelerinin zemin iyileştirme yöntemi olarak kullanımı, uzun yıllardır birçok araştırmacı tarafından incelenmiş ve bu alanda önemli çalışmalar yapılmıştır [1]-[6]. Son yıllarda, geleneksel yöntemlere ek olarak, çeşitli optimizasyon tekniklerinin kullanıldığı ve katkı maddelerinin etkili bir şekilde optimize edildiği çalışmalar literatürde yerini almıştır [7]-[14]. Bu kapsamda, optimizasyon yöntemleri kullanılarak hem zeminlerin iyileştirilmesi hem de maliyet etkin çözümlerin geliştirilmesi hedeflenmiştir. Bu doğrultuda, Olgun [13], killi bir zeminin geoteknik özelliklerini iyileştirmek amacıyla katkı maddelerinin optimizasyonunu gerçekleştirmiş ve bu maddelerin zeminin donma-çözülme davranışı üzerindeki etkilerini detaylı bir şekilde incelemiştir. Katkı maddelerinin optimizasyonunda ve sonuçların değerlendirilmesinde bir deneysel tasarım yöntemi olan Tepki Yüzey Metodolojisi (RSM) yöntemi kullanmıştır. Yapılan değerlendirmeler sonucunda donma-çözülmeye maruz kalmayan numunelerdeki serbest basınç dayanımı üzerindeki en etkili parametrenin kireç olduğunu, donma-çözülme işlemine maruz kalan numunelerde ise en etkili parametrenin pirinç kabuğu külü olduğunu belirtmiştir. Zaimoğlu [7], çalışmasında polipropilen elyafların ve bazı katkı malzemelerinin (borojips, uçucu kül ve çimento) ince daneli bir zeminin serbest basınç dayanımı üzerindeki etkisini araştırmıştır. Katkı maddelerinin optimizasyonunda ve sonuçların değerlendirilmesinde bir deneysel tasarım yöntemi olan Taguchi Optimizasyon Yöntemini kullanmıştır. Deneysel sonuçlarda, numunelerin serbest basınç dayanımını arttırmada en etkili malzemenin polipropilen elyaf olduğunu belirtmiştir. Ikeagwuani ve Nwonu [8], yüksek plastisiteli killi zeminlerin iyileştirilmesinde kullanılan talaş külü, taşocağı külü ve normal portland çimentosunun etkilerini Taguchi Optimizasyon Yöntemi ile incelemiş ve optimum katkı kombinasyonunu %20 talaş külü, %20 taşocağı külü ve %8 çimento olarak belirlemiştir. Nuruzzaman ve Hossain [15], atık cam tozunun killi zemin üzerindeki etkilerini incelemiş ve katkı ile maksimum kuru yoğunluğun arttığını, optimum nem içeriği ile plastisite ve şişme özelliklerinin azaldığını belirtmiştir. Ayrıca, kür uygulanmayan numunelerde dayanımın azaldığı, ancak cam tozunun içerdiği %10 kireç sayesinde belirli süre kür edilen numunelerde ek dayanım sağladığı ifade edilmiştir. Olufowobi vd. [16], atık cam tozu katkısının killi zeminin stabilizasyonuna etkisini Kaliforniya Taşıma Oranı (CBR) ve doğrudan kesme deneyleriyle incelemiş; %5 oranına kadar CBR değerinde artış, %10 oranında ise maksimum kohezyon ve içsel sürtünme açısı elde edildiği rapor edilmiştir. Gao vd. [17], farklı uzunluk ve oranlarda bazalt lif katkısının killi zeminde serbest basınç dayanımına etkisini incelemiş; dayanımın %0,25 oranında ve 12 mm lif uzunluğunda maksimuma ulaştığını, bu değerlerin üzerinde ise azalma gösterdiğini bildirmiştir. Tebaldi vd. [4], kireçle stabilize edilmiş zeminin donma-çözülme çevrimlerinin mekanik davranış üzerine etkisini incelemiştir. Araştırmanın sonuçlarında, kireçle stabilize edilmiş zeminlerin, kür süreleri arttıkça serbest basınç dayanımlarının arttığı ifade edilmiştir. Phanikumar ve Nagaraju [18], yüksek plastisiteli kilin uçucu kül ve pirinç kabuğu külü ile iyileştirilmesini incelemiş; artan katkı oranlarının 7 ve 28 günlük kür sürelerinde puzolanik reaksiyonların ilerlemesiyle serbest basınç dayanımında belirgin artışlar sağladığını belirtmiştir. Chhun [19], çimento stabilizasyonunun zeminin mühendislik özelliklerini iyileştirmede etkili bir yöntem olduğunu belirtmiştir. Çalışmada, geri dönüştürülmüş karbon karasının (rCB), çimento ile stabilize edilmiş kumun dayanım özelliklerine etkisini incelemiştir. Çalışmanın sonucunda, basınç dayanımının %3'e kadar artan rCB oranı, uzayan kür süresi ve azalan su/çimento (w/c) oranı ile yükseldiğini ve optimum rCB oranının %3 olduğunu belirtmiştir.

Bu çalışmada, yüksek plastisiteli killi bir zeminin geoteknik özelliklerini iyileştirmek amacıyla atık cam tozu (ACT), bazalt lif (BL), pirinç kabuğu külü (PK), geri dönüştürülmüş karbon karası (KK) ve kireç (K) katkılarının optimizasyonu ve serbest basınç dayanımı üzerindeki etkileri Taguchi Optimizasyon Yöntemi ile incelenmiştir. Bu çalışma, literatürde sınırlı sayıda bulunan çoklu katkı maddesi optimizasyonu çalışmalarına önemli bir katkı sunmaktadır. Atık cam tozu, bazalt lif, pirinç kabuğu külü, geri dönüştürülmüş karbon karası ve kireç gibi farklı katkı maddelerinin birlikte değerlendirilmesi ve Taguchi Optimizasyon Yöntemi ile serbest basınç dayanımı üzerindeki etkilerinin sistematik olarak incelenmesi, çalışmayı mevcut araştırmalardan ayıran temel özgünlük unsurudur. Ayrıca, geri dönüşüm malzemelerinin mühendislik uygulamalarına entegrasyonunu da içeren yaklaşım, hem zemin iyileştirme performansını artırmayı hem de sürdürülebilir inşaat malzemeleri kullanımına yönelik çözümler geliştirmeyi hedeflemektedir. Bu bağlamda, araştırmanın bulguları, zemin stabilizasyonu alanında hem akademik literatüre hem de pratik uygulamalara yeni ve özgün bir perspektif kazandırmaktadır.

Materyal ve Metot

Kil Zemin

Kil zemin Erzurum ilinin Kuzeydoğusunda yer alan Oltu ilçesinden alınmıştır (Şekil 1). Kil zeminin USCS sınıflandırma sistemine göre CH sınıfında olduğu belirlenmiştir. Kil zemine ait bazı geoteknik özellikler Tablo 1'de verilmiştir.

Şekil 1. Kil zemin (a- alınan yer, b-elenmiş hali)

Tablo 1. Kil zemine ait bazı geoteknik özellikler

Temel Özellikler	Kil zemin
Renk	Kırmızı
Likit Limit (%)	81
Plastik Limit (%)	31
Plastisite İndisi (%)	50
Sınıflandırma (USCS)	CH
Optimum Su İçeriği (%) *	23
Maksimum Kuru Birim Hacim Ağırlık (kN/m3) *	14,6

*Harvard Minyatür Kompaksiyon Deney

Atık Cam Tozu

Cam, tamamen geri dönüştürülebilir bir malzeme olup, temel bileşenleri soda, silis ve kireçten oluşmaktadır. Atık camların elenerek özel değirmenlerde öğütülmesiyle elde edilen ince tanecikli ürün, atık cam tozu olarak adlandırılmaktadır. Bu malzeme, hem mekanik özelliklerin iyileştirilmesine katkı sağlamakta hem de geleneksel hammaddelere kıyasla daha ekonomik olması nedeniyle güçlendirici ve katkı maddesi olarak değerlendirilmektedir. Bu çalışmada kullanılan atık cam tozu, özel bir firmadan temin edilmiştir (Şekil 2). Temin edilen atık cam tozuna ait bazı kimyasal özellikler, ilgili firma tarafından sağlanan verilere dayanarak Tablo 2'de sunulmuştur.

Şekil 2. Atık cam tozu

Tablo 2. Atık cam tozuna ait bazı kimyasal özellikler

Bileşen	Miktar (Ağırlıkça %)
SiO2	69,42
LOI	16,18
Al2O3	1,09
Fe2O3	0,48
CaO	8,27
MgO	4,25
Na2O	12,31

Bazalt lifi

Bazalt lif, yaklaşık 1300–1700 °C sıcaklıktaki özel fırınlarda bazalt taşının eritilerek lif formuna dönüştürülmesiyle elde edilen bir malzemedir. Üretim sürecinde ilave bir katkı maddesi gerektirmemesi, düşük üretim maliyeti sağlamaktadır [20]. Yüksek mekanik dayanımı, asidik ve alkalin ortamlara karşı üstün kimyasal direnci ile birlikte sıcaklık değişimlerine karşı gösterdiği yüksek dayanım sayesinde inşaat ve kompozit malzeme uygulamalarında yaygın olarak tercih edilmektedir. Ayrıca, bazalt lifler toksik olmayan, yanmaz yapıları ve kuru karışımlarla kolayca homojen şekilde karışabilme özellikleriyle öne çıkmaktadır. Bazalt lif katkı malzemesi, düşük maliyetleri, yeterli dayanımları ve kolay ulaşılabilirliği sayesinde geleneksel zemin güçlendirme yöntemlerine çevre dostu ve ekonomik bir alternatif olarak öne çıkmaktadır. Özellikle düşük taşıma gücüne sahip, yüksek sıkışabilirliğe sahip, şev problemleri ve sıvılaşma potansiyeli olan zeminlerin güçlendirilmesinde kullanılmaktadır. Bazalt lifleri, zemine rastgele dağıtılarak bitki kökleri gibi kenetlenme ve sürtünme direnci oluşturup zemin partiküllerinin hareketini engelleyerek taşıma kapasitesini artırır.

Deneysel çalışmalar, bazalt lif katkısının zeminin kayma mukavemeti, kohezyon ve içsel sürtünme açısı gibi mühendislik özelliklerini önemli ölçüde iyileştirdiğini göstermiştir. Ekonomik açıdan bakıldığında, bazalt lif üretimi cam lifine göre daha az enerji gerektirir, bu da üretim maliyetlerini düşürür. Ayrıca, çevresel düzenlemelere uyum maliyetlerini azaltabilen ve genel iyileştirme giderlerini potansiyel olarak düşürebilen çevre dostu ve doğal bir malzemedir [21]-[22].

Bu çalışmada kullanılan bazalt lif, özel bir firmadan temin edilmiştir (Şekil 3). Temin edilen bazalt life ait bazı teknik özellikler, ilgili firmadan sağlanan veriler doğrultusunda Tablo 3'te sunulmuştur.

Şekil 3. Bazalt lif

Tablo 3. Bazalt lifine ait bazı teknik özellikler

Özellik	Değer
Çekme Dayanımı (MPa)	4840
Elastisite Modülü (GPa)	89
Uygulama Sıcaklık limetleri (°C)	-260°C- +982
Ergime Sıcaklığı (°C)	1450
Özgül Ağırlık (gr/cc)	2,60-2,80
Elyaf Çapı (micron)	9-23
Bazalt Elyaf Uzunluğu (mm)	6

Pirinç Kabuğu Külü

Pirinç kabuğu külü (PKK), pirinç kabuklarının kontrollü bir şekilde yakılmasıyla elde edilen ve puzolanik özellikler sergileyen bir katkı malzemesidir. Yakma sürecinde yüksek oranda uçucu maddeler oluşmakta, selüloz ve lignin uzaklaştırılarak silis açısından zengin bir kül elde edilmektedir. Pirinç kabuğu, pirincin ağırlığının yaklaşık %20'sini oluşturmaktadır. Küresel ölçekte, çimento üretimi sırasında atmosfere salınan yüksek CO_2 emisyonları ve problemli zeminlerde yapılaşma gerekliliği gibi sorunlar göz önüne alındığında, zemin iyileştirme yöntemlerinde endüstriyel atıkların kullanımına yönelik araştırmalar önem kazanmaktadır.

Özellikle PKK, pirinç kabuklarının 500–800 °C aralığında yakılmasıyla elde edilen, yüksek oranda silisyum dioksit (SiO_2) içeren ve amorf yapıda olduğu zaman yüksek puzolanik aktivite gösteren çevre dostu ve biyolojik olarak parçalanabilir bir malzeme olarak öne çıkmaktadır. Yapılan çalışmalarda, PKK'nın reolojik özellikleri incelendiğinde; düşük su/bağlayıcı oranlarında harcın akışkanlığını azalttığı, plastik viskoziteyi artırdığı ve mini slump akma çapını düşürdüğü, buna karşın genel olarak grout karışımlarının

akışkanlık ve işlenebilirlik özelliklerini iyileştirdiği gözlemlenmiştir [23].

PKK'nın düşük maliyeti, kolay temin edilebilirliği ve atık malzemelerin değerlendirilmesiyle sağladığı ekonomik ve ekolojik faydalar dikkate alındığında, zemin iyileştirmesinde yeterli dayanım özellikleri sunarak etkin bir katkı malzemesi olarak kullanılabileceği vurgulanmaktadır [23].

Bu çalışmada kullanılan PKK, pirinç kabuklarının 600 °C sıcaklıkta yakılmasıyla elde edilmiş olup, özel bir firmadan temin edilmiştir (Şekil 4). Temin edilen pirinç kabuğu külüne ait bazı kimyasal özellikler, firma tarafından sağlanan verilere dayanılarak Tablo 4'te sunulmuştur.

Şekil 4. Pirinç kabuğu külü

Tablo 4. Pirinç kabuğu külüne ait bazı kimyasal özellikler

Bileşen	Miktar (Ağırlıkça %)
SiO2	91.81
Al2O3	0.27
Fe2O3	0.19
CaO	0.64
K2O	2.28
MgO	0.78
Na2O	0.09

Geri Dönüştürülmüş Karbon Karası

Atık lastiklerin geri dönüştürülmesi süreci iki aşamada gerçekleştirilmektedir. İlk aşamada lastikler mekanik olarak parçalanarak çelik teller ve lastik parçacıkları elde edilirken, ikinci aşamada piroliz yöntemi uygulanarak pirolitik yağ ve karbon karası üretilmektedir. Pirolitik yağ, özellikle enerji sektöründe alternatif bir yakıt olarak değerlendirilirken, farklı boyutlardaki karbon karası ise çeşitli endüstriyel alanlarda paketlenmiş formda kullanılmaktadır [24]. Bu çalışmada kullanılan geri dönüştürülmüş karbon karası, özel bir firmadan temin edilmiştir (Şekil 5). Temin edilen karbon karasına ait bazı kimyasal özellikler, ilgili firmadan sağlanan verilere dayanarak Tablo 5'te sunulmuştur.

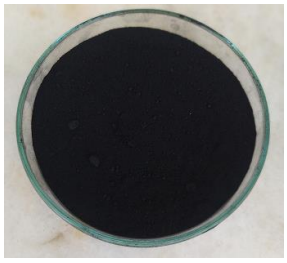

Şekil 5. Geri dönüştürülmüş karbon karası

Tablo 5. Pirinç kabuğu külüne ait bazı kimyasal özellikler

Bileşen	Miktar (Ağırlıkça %)
C	86.57
Na	2.88
Si	3.6
Au	3.32
S	3.64

Kireç

Kireç, kireç taşının (kalker) kalsinasyon işlemiyle elde edilen, kalsiyum bazlı bir malzemedir. Kimyasal bileşiminde genellikle kalsiyum karbonat ($CaCO_3$) veya magnezyum karbonat ($MgCO_3$) yer almakta olup; bunlara ek olarak demir, silisyum, alüminyum ve kükürt gibi elementler de çeşitli oranlarda bulunabilmektedir. Kirecin içeriğindeki kalsiyum, kil minerallerinde bulunan silis (SiO_2) ve alümin (Al_2O_3) ile reaksiyona girerek, kalsiyum-silikat hidrat (C-S-H), kalsiyum-alüminat hidrat (C-A-H) ve kalsiyum-alüminat-silikat hidrat (C-A-S-H) gibi yüksek dayanımlı çimentolaşma ürünlerinin oluşumunu sağlar. Bu reaksiyon ürünleri başlangıçta jel formundadır; kil parçacıklarının çevresini sararak boşlukları doldurur ve zamanla kristalleşerek sertleşir. Bu kristalleşme süreci, zeminin dayanımının kademeli olarak artmasına katkı sağlar ve bu dayanım artışı zamanla devam eder [25]. Kireç, kireç taşının (kalker) kalsinasyon işlemiyle elde edilen, kalsiyum bazlı bir malzemedir. Kimyasal bileşiminde genellikle kalsiyum karbonat ($CaCO_3$) veya magnezyum karbonat ($MgCO_3$) yer almakta olup; bunlara ek olarak demir, silisyum, alüminyum ve kükürt gibi elementler de çeşitli oranlarda bulunabilmektedir. Kirecin içeriğindeki kalsiyum, kil minerallerinde bulunan silis (SiO_2) ve alümin (Al_2O_3) ile reaksiyona girerek, kalsiyum-silikat hidrat (C-S-H), kalsiyum-alüminat hidrat (C-A-H) ve kalsiyum-alüminat-silikat hidrat (C-A-S-H) gibi yüksek dayanımlı çimentolaşma ürünlerinin oluşumunu sağlar. Bu reaksiyon ürünleri başlangıçta jel formundadır; kil parçacıklarının çevresini sararak boşlukları doldurur ve zamanla kristalleşerek sertleşir. Bu kristalleşme süreci, zeminin dayanımının kademeli olarak artmasına katkı sağlar ve bu dayanım artışı zamanla devam eder [25]. Manzoor ve Yousuf (2020), problemli zeminlerin iyileştirilmesinin yol, bina ve demiryolu gibi yapıların inşasında önemine dikkat çekmişlerdir. Geleneksel bir zemin stabilizatörü olan kireç, uzun yıllardır zemin özelliklerini iyileştirmek amacıyla kullanılmaktadır. Kireç stabilizasyon süreci, başlangıçta katyon değişimi ve flokülasyon (topaklanma) yoluyla zeminin plastisitesini ve işlenebilirliğini değiştirirken, uzun vadede puzolanik reaksiyonlar (C-S-H ve C-A-H oluşumu) ile dayanım ve kalıcılık sağlar. Kireç ilavesi, zeminin plastisitesini azaltırken (likit limit azalır, plastik limit artar), şişme potansiyelini ve sıkışabilirliğini düşürür; optimum nem içeriğini, taşıma kapasitesini, kayma mukavemetini, çekme dayanımını ve yorulma mukavemetini ise önemli ölçüde artırır. Maksimum kuru yoğunluk genellikle azalırken, geçirgenlik üzerindeki etkiler kireç içeriğine bağlı olarak değişkenlik göstermektedir [26].

Kireç stabilizasyonunun başlıca uygulama alanları arasında zemin altı iyileştirmeleri, kireç kolonları ile derin stabilizasyon, yol üstyapı tabakalarının stabilizasyonu ve baraj ile şev stabilizasyonu yer almaktadır. Genel olarak, kireç düşük maliyeti, kolay temin edilebilirliği ve sağladığı çevresel ile ekonomik faydalar nedeniyle problemli zeminlerin iyileştirilmesinde etkili ve tercih edilen bir yöntem olarak değerlendirilmektedir [26].

Bu çalışmada kullanılan sönmüş kireç, Erzurum ilinde faaliyet gösteren özel bir firmadan temin edilmiştir (Şekil 6). Sönmüş kirece ait bazı kimyasal özellikler, temin edildiği

firmadan alınan veriler doğrultusunda Tablo 6'da sunulmuştur.

Şekil 6. Kireç

Tablo 6. Şönmüş kirecin kimyasal özellikleri

Bileşen	Miktar (Ağırlıkça %)
Ca (OH)2	80-86
CaO + MgO	88
MgO	1-2

Taguchi Optimizasyon Yöntemi

Taguchi metodu, Genichi Taguchi tarafından geliştirilen istatistiksel bir optimizasyon tekniğidir [27].Bu metodun temel amacı, bir ürünün veya sürecin kalitesini artırmak, değişkenliği en aza indirmek ve süreç parametrelerini optimize etmektir [27]-[28]. Taguchi yaklaşımı, daha az deneme sayısı ile doğru sonuçlar elde etme kapasitesiyle bilinir ve eş zamanlı olarak birden fazla faktörü analiz etmeye olanak tanıyan sağlam ve verimli bir deneysel tasarım sunar [27]-[29]. Anahtar unsurları arasında ortogonal diziler (OA'lar), sinyal-gürültü (S/N) oranı ve kayıp fonksiyonu bulunur [28]- [30].

Taguchi metodolojisi, sistem tasarımı, parametre tasarımı ve tolerans tasarımı olmak üzere üç aşamalı bir süreçle ilerler [28]. Deneyler, belirli bir çıktı değişkeni üzerindeki etkiyi optimize etmek için girdi parametrelerinin ve bunların farklı seviyelerinin seçilmesiyle başlar [29]. Ortogonal diziler (OA'lar), faktörlerin ve seviyelerin belirlenmesine dayalı olarak deney sayısını önemli ölçüde azaltarak minimum deneme seti sağlar [27]-[28]- [29]. Sonuçların analizi için sinyal-gürültü (S/N) oranı kullanılır; bu oran, istenen performans karakteristiklerinin sapmasını değerlendirir ve genellikle "daha büyük daha iyi", "daha küçük daha iyi" veya "nominal en iyi" yaklaşımlarına göre hesaplanır [27]-[29]-[30]. Varyans analizi (ANOVA) ise her bir faktörün çıktı değişkeni üzerindeki yüzde katkısını ve önemini belirlemek için kullanılır [28]- [29]-[31].Bu çalışmada, beş parametreli ve her biri dört seviyeden oluşan değişkenler için L16 (4^5) tipi ortogonal dizi tercih edilmiş olup, ilgili deney düzeni Tablo 7'de sunulmaktadır.

Tablo 7. Ortogonal dizin L_{16} (4^5)

Deney No	Parametreler ve Deneylerin Yapılacağı Parametre Seviyeleri				
	F1	F2	F3	F4	F5
1	1	1	1	1	1
2	1	2	2	2	2
3	1	3	3	3	3
4	1	4	4	4	4
5	2	1	2	3	4
6	2	2	1	4	3
7	2	3	4	1	2
8	2	4	3	2	1
9	3	1	3	4	2
10	3	2	4	3	1
11	3	3	1	2	4
12	3	4	2	1	3
13	4	1	4	2	3
14	4	2	3	1	4
15	4	3	2	4	1
16	4	4	1	3	2

Tablo 7'de yer alan F1, F2, F3, F4 ve F5 sütunları, deneysel çalışmada değerlendirilen parametreleri temsil etmekte olup; her bir satırda yer alan sayısal değerler, ilgili parametrenin hangi seviyede uygulandığını göstermektedir.

Taguchi yöntemine göre oluşturulan bu deneysel tasarım tablosu, L16 ortogonal dizini olarak adlandırılmakta ve 16 satır ile en fazla 5 faktörü içerecek şekilde yapılandırılmıştır. Her satır, belirli parametre seviyelerinin bir kombinasyonunu temsil ederek, bu koşullar altında yürütülecek deneyleri tanımlamaktadır. Bu sistematik yaklaşım sayesinde, teorik olarak 4 seviyeli 5 parametre için yapılması gereken 1024 farklı deney yerine yalnızca 16 deney gerçekleştirilerek analiz yapılabilmekte, bu da zamandan ve kaynaklardan önemli ölçüde tasarruf sağlamaktadır. Bu kapsamda, çalışmada beş farklı parametre seçilmiştir: Atık Cam Tozu (ACT), Bazalt Lifi (BL), Pirinç Kabuğu Külü (PK), Geri Dönüştürülmüş Karbon Karası (KK) ve Kireç (K). Bu parametrelerin belirlenen seviyeleri Tablo 8'de ayrıntılı olarak sunulmaktadır.

Tablo 8. Parametreler ve seviyeleri

Parametreler	Seviyeler			
	1	2	3	4
(ACT)Atık Cam Tozu (%)	2.00 (ACT1)	4.00 (ACT2)	6.00 (ACT3)	8.00 (ACT4)
(BL) Bazalt Lifi (%)	0.25 (BL1)	0.50 (BL2)	0.75 (BL3)	1.00 (BL4)
(PK) Pirinç Kabuğu Külü (%)	5.00 (PK1)	10.00 (PK2)	15.00 (PK3)	20.00 (PK4)
(KK) Karbon Karası(%)	1.00 (KK1)	3.00 (KK2)	5.00 (KK3)	7.00 (KK4)
(K) Kireç (%)	2.00 (K1)	4.00 (K2)	6.00 (K3)	8.00 (K4)

Belirlenen parametreler ve bunlara ait seviyeler doğrultusunda oluşturulan ortogonal deney düzeni Tablo 9'da sunulmaktadır.

Tablo 9. Deneylerde kullanılan ortogonal dizin l16 (4^5)

Deney No	Parametreler ve Deneylerin Yapılacağı Parametre Seviyeleri				
	Atık Cam Tozu Oranı (%)	Bazalt Lifi Oranı (%)	Pirinç Kabuğu Külü Oranı (%)	Karbon Karası Oranı (%)	Kireç Oranı (%)
1	ACT1	BL1	PK1	KK1	K1
2	ACT1	BL2	PK2	KK2	K2
3	ACT1	BL3	PK3	KK3	K3
4	ACT1	BL4	PK4	KK4	K4
5	ACT2	BL1	PK2	KK3	K4
6	ACT2	BL2	PK1	KK4	K3
7	ACT2	BL3	PK4	KK1	K2
8	ACT2	BL4	PK3	KK2	K1
9	ACT3	BL1	PK3	KK4	K2
10	ACT3	BL2	PK4	KK3	K1
11	ACT3	BL3	PK1	KK2	K4
12	ACT3	BL4	PK2	KK1	K3
13	ACT4	BL1	PK4	KK2	K3
14	ACT4	BL2	PK3	KK1	K4
15	ACT4	BL3	PK2	KK4	K1
16	ACT4	BL4	PK1	KK3	K2

Ortogonal dizin doğrultusunda hazırlanan her bir deney kombinasyonuna ait numunelere, 7 ve 28 günlük kür sürelerinin tamamlanmasının ardından serbest basınç dayanımı deneyleri uygulanmıştır. Elde edilen deney verileri, Taguchi yöntemine özgü Sinyal/Gürültü (S/N) oranı analizleriyle değerlendirilmiş; böylece parametrelerin etkileri karşılaştırılarak en uygun ya da optimum kombinasyon belirlenmiştir.

Bu çalışmada, performansın maksimum düzeye çıkarılması hedeflenerek, "en büyük en iyi" yaklaşımına uygun S/N oranları, Denklem 1 temel alınarak hesaplanmıştır.

$$S/N_L = -10\ \log\left[\frac{1}{n}\sum_1^n \frac{1}{Y_i^2}\right] \quad (1)$$

Bu eşitlikte;

S/N_L: Performans istatistiği

n: Bir deney kombinasyonunda uygulanan deney tekrar sayısı

Yi: i. deneyin performans istatistiğidir.

Hedeflenen çıktının maksimum seviyeye ulaşması amaçlandığından, S/N oranını en yüksek düzeye taşıyan parametre seviyeleri, optimum seviyeler olarak kabul edilmiştir [32]. Elde edilen sonuçların güvenilirliğini değerlendirmek ve her bir parametrenin çıktılar üzerindeki etkisini nicel olarak belirlemek amacıyla varyans analizi (ANOVA) uygulanmıştır.

Serbest Basınç Deneyi

Serbest basınç deneyi ASTM D 2166'ya uygun olarak yürütülmüştür [33]. Bu deney için yükleme hızının ayarlanabildiği, bilgisayar kontrollü üç eksenli basınç deneyinin yükleme ünitesi kullanılmıştır (Şekil 7).

Şekil 7. Serbest basınç deney aleti

Tablo 9'da yer alan her bir deney kombinasyonu için, Harvard minyatür kompaksiyon cihazı kullanılarak ilgili karışımların optimum su muhtevaları belirlenmiştir. Belirlenen optimum su seviyesi ve maksimum kuru birim hacim ağırlığında 33mm çapında ve 71 mm yüksekliğinde üçer adet silindirik numuneler hazırlanmıştır. Numuneler ortalama sıcaklığı 23±1oC ve nem oranı %45 olan kontrollü laboratuvar ortamında, desikatör içerisinde 7 ve 28 gün süreyle kür edilmiştir. Kür işlemi tamamlanan numunelere serbest basınç dayanımı deneyleri uygulanmıştır. Bu deneylerde kırılan numunelere ait bazı görseller Şekil 8'de sunulmaktadır.

Şekil 8. Serbest basınç deneyinde kırılan bazı numune görselleri

Sonuç ve Tartışma

Kompaksiyon Deney Sonuçları

Harvard minyatür kompaksiyon deneyiyle elde edilen bulgular doğrultusunda, Tablo 9'daki her bir deneye ait optimum su muhtevası (wopt) ve maksimum kuru birim hacim ağırlığı (γkmax) değerleri belirlenmiş olup, bu veriler Tablo 10'da toplu biçimde sunulmuştur.

Tablo 10. Her bir deneye ait optimum su muhtevası ve maksimum kuru birim hacim ağırlığı

Deney No	**1**	**2**	**3**	**4**
wopt (%)	24	27	28	30
γkmax (kN/m3)	14,27	13,55	12,83	12,4
Deney No	**5**	**6**	**7**	**8**
wopt (%)	29	29	29	28
γkmax (kN/m3)	12,9	13,1	12,8	12,85
Deney No	**9**	**10**	**11**	**12**
wopt (%)	30	29	31	29
γkmax (kN/m3)	12,75	12,85	13,25	13,05
Deney No	**13**	**14**	**15**	**16**
wopt (%)	29	31	29	27
γkmax (kN/m3)	12,75	12,8	13,15	13,28

Serbest basınç deneylerinde, Tablo 10'da belirtilen su muhtevası ve maksimum kuru birim hacim ağırlığı değerleri esas alınarak hazırlanan numuneler kullanılmıştır.

7 günlük Serbest Basınç Deney Sonuçları

Çalışmada metot bölümünde belirtildiği gibi 7 gün kür süresi sonunda Tablo 9'daki her bir deney için yapılan serbest basınç deney sonuçları Tablo 11'de toplu biçimde verilmiştir.

Tablo 11. Serbest basınç dayanımı sonuçları (7gün)

Deney No	Serbest basınç Dayanımı (MPa)		
	1	2	3
1	0,62	0,67	0,73
2	1,05	1,06	1,05
3	1,13	1,19	1,07
4	1,16	1,13	1,09
5	1,02	0,94	1,11
6	1,11	1,22	1,33
7	1,26	1,14	1,38
8	0,61	0,61	0,61
9	0,97	0,91	0,84
10	0,42	0,39	0,46
11	0,98	1,04	1,10
12	1,10	1,14	1,19
13	1,19	1,18	1,20
14	1,26	1,25	1,25
15	0,49	0,51	0,54
16	1,06	1,01	1,11

Tablo 11'de verilen 7 günlük serbest basınç dayanım değerleri kullanılarak çizilen serbest basınç dayanımı- deney no ilişkisi Şekil 9'da gösterilmiştir.

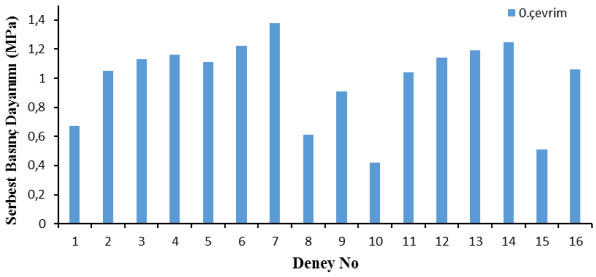

Şekil 9. Serbest basınç dayanımı- deney no ilişkisi (7 gün)

Tablo 11 ve Şekil 9 birlikte değerlendirildiğinde, 7 günlük kür süresi sonunda en düşük serbest basınç dayanımının 10 numaralı deneyde (%6 ACT, %0,50 BL, %20 PK, %5 KK, %2 K) 0,42 MPa, en yüksek serbest basınç dayanımının ise 7 numaralı deneyde (%4 ACT, %0,75 BL, %20 PK, %1 KK, %4 K) 1,38 MPa olarak elde edildiği tespit edilmiştir.

Tablo 11'de yer alan serbest basınç dayanımı verileri kullanılarak, her bir deney için S/N analizleri gerçekleştirilmiştir. Bu analizler sonucunda elde edilen S/N değerleri ile her bir parametre düzeyine karşılık gelen ortalama S/N oranları Tablo 12'de sunulmuştur.

Tablo 12. S/N değerleri (7 gün)

Deney No	Parametreler ve Seviyeleri					S/N
	ACT	BL	PK	KK	K	
1	ACT1	BL1	PK1	KK1	K1	-3,52
2	ACT1	BL2	PK2	KK2	K2	0,44
3	ACT1	BL3	PK3	KK3	K3	0,99
4	ACT1	BL4	PK4	KK4	K4	1,04
5	ACT2	BL1	PK2	KK3	K4	0,12
6	ACT2	BL2	PK1	KK4	K3	1,61
7	ACT2	BL3	PK4	KK1	K2	1,90
8	ACT2	BL4	PK3	KK2	K1	-4,32
9	ACT3	BL1	PK3	KK4	K2	-0,92
10	ACT3	BL2	PK4	KK3	K1	-7,57
11	ACT3	BL3	PK1	KK2	K4	0,27
12	ACT3	BL4	PK2	KK1	K3	1,14
13	ACT4	BL1	PK4	KK2	K3	1,51
14	ACT4	BL2	PK3	KK1	K4	1,96
15	ACT4	BL3	PK2	KK4	K1	-5,83
16	ACT4	BL4	PK1	KK3	K2	0,48
	Ortalama S/N Oranı					-0,67

Parametrelerin ve seviyelerinin deney sonuçlarına etkisini değerlendirmek amacıyla, seviyelere ait ortalama S/N oranları, Tablo 12'de yer alan S/N verileri kullanılarak hesaplanmıştır. Her bir parametre düzeyine karşılık gelen ortalama S/N oranları ise Tablo 13'te sunulmuştur. Tablo 13 incelendiğinde, en yüksek ortalama S/N değerinin kireç parametresinin 3. seviyesinde (%6) 1,31 olarak elde edildiği görülmektedir. Bu bulgu, kirecin 7 günlük serbest basınç dayanımı üzerinde en etkili parametre olduğunu ortaya koymaktadır.

Tablo 13. Ortalama S/N değerleri (7 gün)

	Ortalama S/N Etkileri				
	Atık Cam Tozu Oranı	Bazalt Lifi Oranı	Pirinç Kabuğu Külü Oranı	Karbon Karası Oranı	Kireç Oranı
1.seviye	-0,26	-0,70	-0,29	0,37	-5,31
2.seviye	-0,17	-0,89	-1,03	-0,53	0,47
3.seviye	-1,77	-0,67	-0,57	-1,50	1,31
4.seviye	-0,47	-0,42	-0,78	-1,03	0,85

Tablo 9'daki her bir deneyin 7 günlük serbest basınç dayanımına, parametrelerin (atık cam tozu, bazalt lif, pirinç kabuğu külü, karbon karası ve kireç) etkisini belirlemek amacıyla Varyans Analizi yapılmış ve elde edilen sonuçlar Tablo 14'te verilmiştir.

Tablo 14. Varyans analizi (ANOVA) tablosu (7 gün)

Parametre	Serbestlik derecesi (DOF)	Kareler Toplamı (S)	Varyans (V)	Varyans Oranı (F)	Net Toplam (S')	Oran P (%)
Atık Cam Tozu	3	6,68	2,23	8,10	5,86	4,44
Bazalt Lif	0	0,46	0,00	0,00	0,46	0,00
Pirinç Kabuğu Külü	0	1,19	0,00	0,00	1,19	0,00
Karbon Karası	3	7,65	2,55	9,27	6,82	5,16
Kireç	3	116,13	38,71	140,76	115,31	87,28
Diğer	6	1,65	0,28			3,12
Toplam	15	132,11				100,00

Tablo 14 incelendiğinde, bazalt lifi ve pirinç kabuğu külünün 7 günlük serbest basınç dayanımı üzerinde etkisinin ihmal edilebilir düzeyde olduğu (%0) belirlenmiştir. Buna karşılık, atık cam tozu, karbon karası ve kireç parametrelerinin aynı dayanım üzerinde sırasıyla %4,44, %5,16 ve %87,28 oranlarında etkili olduğu görülmektedir. Bu bulgular, kirecin serbest basınç dayanımı açısından en belirleyici parametre olduğunu açıkça ortaya koymaktadır.

Her bir parametre ve seviyelerinin 7 günlük serbest basınç dayanımı üzerindeki etkilerini gösteren Parametre-S/N oranı ilişkisi Şekil 10'da gösterilmiştir. Şekilde yatay eksen deneylerdeki ortalama S/N değerlerini göstermektedir.

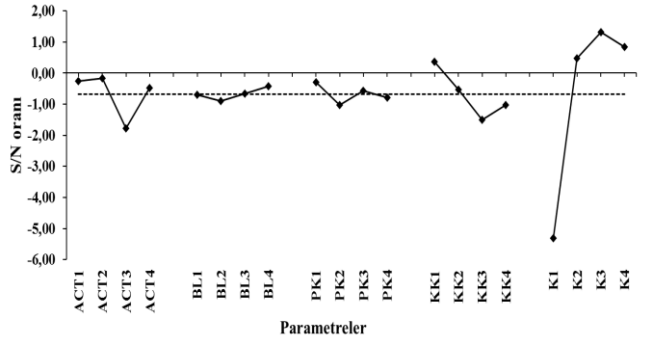

Şekil 10. Parametre – S/N oranı ilişkisi (7 gün)

Tablo 13, Tablo 14 ve Şekil 10 birlikte değerlendirildiğinde, 7 günlük serbest basınç dayanımı üzerinde en yüksek etkiye sahip parametrenin kireç olduğu açıkça görülmektedir. Elde edilen verilere göre, parametrelerin serbest basınç dayanımı üzerindeki etkinlik sırasına göre kireç, karbon karası, atık cam tozu, pirinç kabuğu külü ve bazalt lif şeklinde sıralanmaktadır. Bu sıralama, kirecin dayanım gelişimi açısından temel belirleyici rol oynadığını göstermektedir.

Şekil 10'da kirecin 7 günlük şerbest basınç dayanımı üzerinde özellikle 3. seviyeye kadar olan artışlarda (%6) genel olarak olumlu bir etki sağladığı görülmektedir. Bu artışa belli bir su muhtevasındaki killi zemine kireç ilave edildiğinde, kireç- su ve zemin içindeki silika ve alümina arasında meydana gelen puzolanik reaksiyonlar sonucunda oluşan katılaşmanın dayanım üzerindeki olumlu etkisinin neden olduğu düşünülmektedir [34].

KK parametresinin seviyelerinin artmasıyla birlikte 7 günlük serbest basınç dayanımında belirgin bir azalma meydana geldiği Şelil 10'da gözlemlenmektedir. Karbon karası, düşük ve orta seviyelerde zemin matrisinde mikro düzeyde dolgu malzemesi gibi davranarak dayanımı artırmıştır. Bu katkının karbon içeriği nedeniyle zemin bünyesinde boşlukları doldurması, geçirimsizliği artırması ve yük transferine katkı sunması beklenmektedir. Ancak yüksek katkı oranlarında, bağlayıcılık özelliği olmayan bu maddenin fazla kullanımı, zeminin kohezyonunu zayıflatmış ve dayanımı düşürmüştür. Benzer şekilde, Beheshti Germi [35] tarafından betonlar üzerinde gerçekleştirilen bir çalışmada da artan KK oranının betonun basınç dayanımı üzerinde olumsuz bir etki yarattığı ve dayanım değerlerinde düşüşe neden olduğu ifade edilmiştir. Bu durum, KK'nın belirli bir oranın üzerinde kullanıldığında bağ yapısını zayıflattığını göstermektedir.

Şekil 10 değerlendirildiğinde, ACT oranının %4'e karşılık gelen 2. seviyeye kadar artırılmasıyla 7 günlük serbest basınç dayanımında artış gözlemlendiği, bu seviyeden sonraysa dayanım değerlerinde genel bir azalma eğiliminin başladığı görülmektedir. Benzer bulgular, Çanakcı vd. [36] ve Geçkil vd. [37] tarafından yürütülen çalışmalarda da raporlanmıştır. Söz konusu araştırmalarda da belirli bir kür süresi sonunda ACT'nin yalnızca belirli bir orana kadar serbest basınç dayanımını artırdığı, bu eşik değerin aşılması durumunda ise dayanımın olumsuz yönde etkilendiği belirtilmiştir. Serbest basınç dayanımındaki bu iyileşmeler, ACT'nin puzolanik özellikleri ve zemin boşluklarını doldurarak karışımın mekanik davranışını geliştirmesinden kaynaklanmaktadır. Geçkil vd. [37] çalışmalarında esnek üstyapı tasarımlarında, %9 ACT ile iyileştirilen zeminlerde tabaka kalınlıklarının azaldığını ve ilk yapım maliyetlerinin %1,3 oranında düştüğünü; bu, 20 m genişliğinde ve 1000 m uzunluğundaki bir yol için yaklaşık önemli ölçüde bir maliyet tasarrufu sağlayabileceğini belirtmiştir. Bu bulgular, cam tozunun zemin boşluklarını doldurması ve puzolanik özellikleri sayesinde mekanik performansı artırdığını göstermektedir. Sonuç olarak, ACT, atık yönetimine katkı sağlayan, doğal kaynakları koruyan ve inşaat projelerinde maliyet ile çevresel etkileri azaltan çevre dostu bir zemin iyileştirme malzemesi olarak değerlendirilmektedir.

Şekil 10 incelendiğinde, PK (pirinç kabuğu külü) parametresinin seviyelerindeki artışın, 7 günlük serbest basınç dayanımı üzerinde genel olarak azalma eğilimi yarattığı gözlemlenmektedir. Bu durumu destekler nitelikte, Olgun [13] tarafından yürütülen çalışmada, donma-çözülme döngüsüne tabi tutulmayan numunelerde pirinç kabuğu külü için optimum oranın %5,85 olduğu ifade edilmiştir. Bu bulgu, PK'nın belirli bir düzeyin üzerinde kullanılmasının dayanım üzerinde olumsuz etki yaratabileceğini ortaya koymaktadır.

BL parametresinin artan seviyeleriyle birlikte 7 günlük serbest basınç dayanımında artış eğilimi Şekil 10' dan gözlemlenmektedir. Bu etki, bazalt liflerin zemin iç yapısında mikro çatlakların oluşumunu sınırlaması ve yük taşıma kapasitesini artırmasıyla ilişkili olduğu düşünülmektedir. Bu gözlem, Boz ve Sezer [38] tarafından yürütülen çalışmayla da uyumlu olup, ilgili araştırmada bazalt lif oranındaki artışın serbest basınç dayanımı üzerinde olumlu bir etki yarattığı ve dayanım değerlerinin yükseldiği ifade edilmiştir.

7 günlük serbest basınç dayanımının en yüksek seviyeye ulaştığı karışım oranlarını belirlemek amacıyla, Taguchi Optimizasyon Yöntemi uygulanmış ve bu doğrultuda beklenen dayanım değeri ile ilgili güven aralığı hesaplanarak Tablo 15'te sunulmuştur. Ayrıca, belirlenen optimum karışım oranlarına göre hazırlanan numuneler üzerinde doğrulama deneyleri gerçekleştirilmiş ve elde edilen sonuçların ortalama değeri yine aynı tabloda verilmiştir. Bu analiz, önerilen tasarım parametrelerinin dayanım üzerindeki etkisini doğrulamak açısından önemli bir değerlendirme sağlamaktadır.

Tablo 15. Optimum Deney Koşulları ve Beklenen Değerler

Optimum Koşullardaki Parametre ve Seviyeleri (%)					Optimum Şartlarda Beklenen Değer (S/N) / (MPa)	%95 Güven Aralığı (S/N)	Doğrulama Deney Sonucu (S/N) / (MPa)
ACT	BL	PK	KK	K			
4	1	5	1	6	2,85 / 1,39	1,95- 3,75	2,86 / 1,39

Tablo 15'te belirlenen optimum koşullarda elde edilen tahmini değerin doğruluğunu test etmek amacıyla, ilgili parametre ve seviyelere göre numune hazırlanmış, 7 günlük kür süresinin ardından serbest basınç dayanımı deneyi tekrar uygulanmıştır. Bu doğrulama deneyi sonucunda serbest basınç dayanımı 1,39 MPa olarak ölçülmüş, bu değere karşılık gelen S/N oranı ise 2,86 olarak hesaplanmıştır. %95 güven aralığına göre bu değerin 1,95 ile 3,75 arasında olması beklenmektedir. Dolayısıyla, elde edilen sonucun belirtilen güven aralığı içinde yer alması, Taguchi yöntemiyle yapılan tahminin (beklenen değerin) doğruluğunu teyit etmekte ve deneysel çalışmada parametreler arasında anlamlı bir etkileşim bulunmadığını göstermektedir.

28 günlük Serbest Basınç Deney Sonuçları

28 günlük kür süresi sonunda, Tablo 9'da yer alan her bir karışım için gerçekleştirilen serbest basınç deneylerinin sonuçları Tablo 16'da sunulmuştur. Bu değerlere dayanarak oluşturulan serbest basınç dayanımı ile deney numarası arasındaki ilişki grafiği ise Şekil 11'de gösterilmiştir.

Tablo 16. Serbest basınç dayanımı sonuçları (28 gün)

Deney No	Serbest basınç Dayanımı (MPa)		
	1	2	3
1	0,67	0,79	0,55
2	1,05	1,06	1,05
3	1,56	1,37	1,17
4	2,18	2,11	2,26
5	2,47	2,05	2,88
6	2,05	1,61	2,49
7	1,77	1,33	2,21
8	0,96	0,92	1,01
9	1,76	1,55	1,97
10	0,67	0,67	0,67
11	2,39	1,92	2,87
12	1,36	1,31	1,40
13	1,63	1,72	1,54
14	2,03	2,00	1,97
15	0,83	0,79	0,87
16	1,20	1,14	1,26

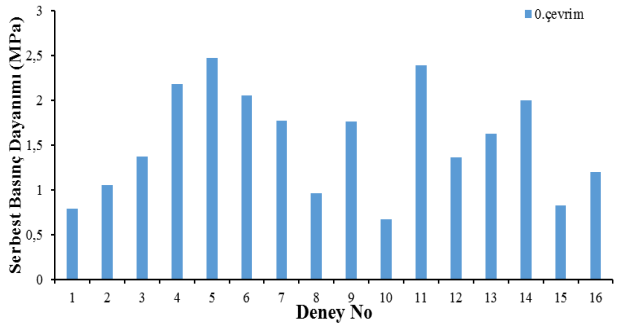

Şekil 11. Serbest basınç dayanımı-deney no ilişkisi (28 gün)

Tablo 16 ve Şekil 11 birlikte değerlendirildiğinde, 28 günlük kür süresi sonunda en düşük serbest basınç dayanımı değerinin 10 numaralı karışımda (%6 ACT, %0,50 BL, %20 PK, %5 KK, %2 K) 0,67 MPa olarak elde edildiği, en yüksek dayanım değerinin ise 5 numaralı karışımda (%4 ACT, %0,25 BL, %10 PK, %5 KK, %8 K) 2,47 MPa olarak ölçüldüğü görülmektedir.

Tablo 16' da verilen serbest basınç deney sonuçları kullanılarak her bir deneye ait S/N analizleri yapılmıştır. Yapılan analiz sonucunda hesaplanan S/N değerleri ile parametrelerin ortalama S/N değerleri Tablo 17' de toplu halde verilmiştir.

Tablo 17. S/N Değerleri (28 gün)

Deney No	Parametreler ve Seviyeleri					S/N
	ACT	BL	PK	KK	K	
1	ACT1	BL1	PK1	KK1	K1	-3,95
2	ACT1	BL2	PK2	KK2	K2	0,44
3	ACT1	BL3	PK3	KK3	K3	2,46
4	ACT1	BL4	PK4	KK4	K4	6,77
5	ACT2	BL1	PK2	KK3	K4	7,47
6	ACT2	BL2	PK1	KK4	K3	5,63
7	ACT2	BL3	PK4	KK1	K2	4,13
8	ACT2	BL4	PK3	KK2	K1	-0,34
9	ACT3	BL1	PK3	KK4	K2	4,72
10	ACT3	BL2	PK4	KK3	K1	-3,51
11	ACT3	BL3	PK1	KK2	K4	7,06
12	ACT3	BL4	PK2	KK1	K3	2,64
13	ACT4	BL1	PK4	KK2	K3	4,20
14	ACT4	BL2	PK3	KK1	K4	6,02
15	ACT4	BL3	PK2	KK4	K1	-1,65
16	ACT4	BL4	PK1	KK3	K2	1,55
Ortalama S/N Oranı						2,73

Parametrelerin ve bunlara ait seviyelerin sonuç üzerindeki etkilerini değerlendirmek amacıyla, Tablo 17'de yer alan S/N değerleri kullanılarak her seviyeye ait ortalama S/N değerleri hesaplanmıştır. Elde edilen bu ortalama S/N değerleri, her bir parametre için ayrı ayrı olmak üzere Tablo 18'de sunulmuştur.

Tablo 18. Ortalama S/N değerleri (28 Gün)

Ortalama S/N Etkileri					
	Atık Cam Tozu Oranı	Bazalt Lifi Oranı	Pirinç Kabuğu Külü Oranı	Karbon Karası Oranı	Kireç Oranı
1.seviye	1,43	3,11	2,57	2,21	-2,36
2.seviye	4,22	2,14	2,22	2,84	2,71
3.seviye	2,73	3,00	3,21	1,99	3,73
4.seviye	2,53	2,65	2,90	3,87	6,83

Tablo 18 incelendiğinde, en yüksek ortalama S/N değerinin kireç parametresinin 4. seviyesinde (%8) 6,83 olarak elde edildiği görülmektedir. Bu bulgu, 28 günlük serbest basınç dayanımı üzerinde en belirgin etkiye sahip parametrenin kireç olduğunu ortaya koymaktadır.

Tablo 9'daki her bir deneyin 28 günlük basınç dayanımına, parametrelerin (ACT, BL, PK, KK ve K) etkisini belirlemek için Varyans Analizi yapılmış ve sonuçlar Tablo 19'da verilmiştir.

Tablo 19. Varyans analizi (ANOVA) tablosu (28 Gün)

Parametre	Serbestlik derecesi (DOF)	Kareler Toplamı (S)	Varyans (V)	Varyans Oranı (F)	Net Toplam (S')	Oran P (%)
Atık Cam Tozu	3	15,83	5,28	7,11	13,60	6,68
Bazalt Lif	0	2,27	0,00	0,00	2,27	0,00
Pirinç Kabuğu Külü	0	2,19	0,00	0,00	2,19	0,00
Karbon Karası	3	8,47	2,83	3,81	6,25	3,07
Kireç	3	174,87	58,29	78,56	172,64	84,79
Diğer	6	4,45	0,74			5,47
Toplam	15	203,62				100,00

Tablo 19 incelendiğinde, bazalt lifi ve pirinç kabuğu külü parametrelerinin 28 günlük serbest basınç dayanımı üzerindeki etkisinin oldukça sınırlı olduğu (%0) görülmektedir. Buna karşılık, atık cam tozu, karbon karası ve özellikle kireç parametresinin dayanım üzerinde belirgin etkiler gösterdiği; bu etkinin sırasıyla %6,68, %3,07 ve %84,79 oranlarında olduğu tespit edilmiştir. Bu sonuçlar, uzun vadeli dayanım performansında en etkili bileşenin kireç olduğunu açıkça ortaya koymaktadır.

Her bir parametre ile bu parametrelere ait seviyelerin 28 günlük serbest basınç dayanımı üzerindeki etkilerini yansıtan Parametre–S/N oranı ilişkisi Şekil 12'de grafiksel olarak sunulmuştur. Şekilde yer alan yatay eksen, ilgili deneylerde elde edilen ortalama S/N değerlerini temsil etmekte olup, parametrelerin dayanım üzerindeki katkı düzeylerinin karşılaştırılmasına olanak sağlamaktadır.

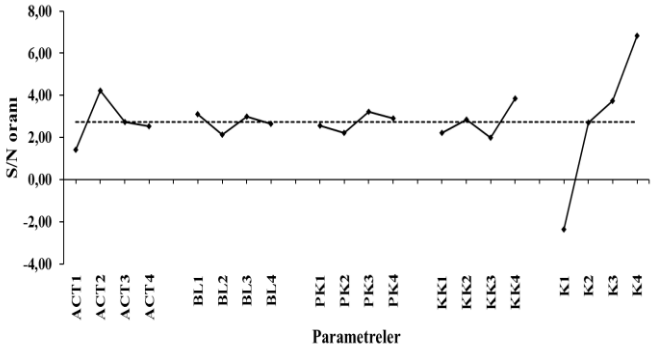

Şekil 12. Parametre – S/N oranı ilişkisi (28 gün)

Tablo 18, Tablo 19 ve Şekil 12 birlikte değerlendirildiğinde, 28 günlük serbest basınç dayanımı üzerinde en yüksek etkiye sahip parametrenin kireç olduğu açıkça görülmektedir. Elde edilen bulgular doğrultusunda, parametrelerin dayanım üzerindeki etkinlik sırasına göre şu şekilde sıralanmaktadır: kireç, atık cam tozu, karbon karası, pirinç kabuğu külü ve bazalt lif. Bu sıralama, özellikle kirecin uzun vadeli mekanik performans açısından belirleyici bir rol üstlendiğini ortaya koymaktadır.

Şekil 12 incelendiğinde, 28 günlük serbest basınç dayanımının ACT 'nun %4'e karşılık gelen 2. seviyeye kadar artış gösterdiği, bu seviyenin üzerinde ise dayanımın azalma eğilimine girdiği gözlemlenmektedir. Bu durum, cam tozunun ince yapısı sayesinde zeminin boşluklarını doldurarak daha sıkı bir yapı oluşturması ve içeriğindeki silis nedeniyle puzolanik reaksiyonlara girerek C-S-H bileşiklerinin oluşumunu teşvik etmesiyle açıklanabilir. Ancak, %4 seviyesinin üzerindeki oranlarda cam tozu fazlası, bağ yapısının bozulmasına ve homojenliğin azalmasına neden olarak dayanımı düşürmüştür. Benzer şekilde, Çanakcı vd. [36] ile Güllü vd. [3] tarafından gerçekleştirilen çalışmalarda da 28 günlük kür süresi sonunda atık cam tozunun belirli bir orana kadar serbest basınç dayanımını artırdığı; ancak bu oranın aşılması durumunda dayanım üzerinde olumsuz etkiler oluştuğu belirtilmiştir.

28 günlük serbest basınç dayanımının Pirinç kabuğu külü katkısı, %15'e kadar olan oranlarda dayanımı artırmış, bu oranın üzerindeki katkılarda ise düşüş gözlemlenmiştir. PK'nın yüksek oranda amorf silis içermesi, özellikle 28 günlük kür sürecinde puzolanik reaksiyonları desteklemiş ve dayanımı olumlu etkilemiştir. Ancak yüksek oranda PK kullanımı, kalsiyum içeriği yetersiz olan bir matris oluşturmuş ve bu da yeterli çimentolaşma ürünlerinin oluşmasını engelleyerek dayanımı azaltmıştır. Bu bulgu, Phanikumar ve Nagaraju [18] tarafından yapılan çalışmayla örtüşmektedir. Söz konusu araştırmada, pirinç kabuğu külü ile stabilize edilen killi zeminlerde 28 günlük kür sonunda dayanım değerlerinin, artan PK oranlarıyla birlikte yükseldiği belirtilmiştir. Elde edilen bu sonuçlar, mevcut çalışmadaki bulgularla paralellik göstermekte olup, PK'nin belirli bir orana kadar dayanım üzerinde olumlu etkiler yarattığını ortaya koymaktadır.

BL parametresinin seviyeleri arttıkça 28 günlük serbest basınç dayanımında düşüş gözlemlenmektedir (Şekil 12). Bu durum, Küçükosmanoğlu [39] tarafından yürütülen çalışmayla da desteklenmektedir. Söz konusu araştırmada, bazalt lifin killi zemine ağırlıkça %0,20 oranında ilave edilmesinin dayanımı en üst düzeye çıkardığı, ancak bu oranın üzerine çıkıldığında dayanımın azalmaya başladığı belirtilmiştir. Bu azalma, bazalt liflerin numune içerisinde boşluk (dren) oluşturmasıyla açıklanmakta; ayrıca lif oranının artmasıyla birlikte zemin içerisinde yığılma ve topaklanmalar meydana geldiği, bu durumun da homojen bir dağılımı engelleyerek dayanımı olumsuz etkilediği ifade edilmektedir.

Şekil 12 incelendiğinde, K ve KK parametrelerinin artan seviyeleriyle birlikte 28 günlük serbest basınç dayanımında genel bir artış eğilimi gözlemlenmektedir. Literatürde yer alan önceki çalışmalar da bu bulguları destekler niteliktedir. Özellikle zemine ağırlıkça %1 ila %9 oranında kireç ilave edilmesinin, zeminin dayanım özelliklerini belirgin şekilde

iyileştirdiği ve artan kireç oranlarının mukavemeti artırdığı ifade edilmiştir [40]-[41]. Ayrıca atık araç lastiklerinden geri dönüşüm ürünü olarak elde edilen siyah karbonun (SC), zayıf yol taban zemininin stabilizasyonunda kullanılmasının esnek yol üst yapı tabaka kalınlıklarına ve maliyetine etkilerini Geçkil vd. [37] tarafından araştırılmıştır. Zemine ağırlıkça %2,5 ila %20 oranlarında siyah karbon (SC) ilave edilerek deneyler yapmış; serbest basınç deneyleri sonucunda, en yüksek mukavemet değerlerinin %10 SC içeren karışımlardan elde edildiğini belirtmiştir. Bu oranın, mukavemeti 1 günlük kür sonunda 1,82 kat, 7 günlük kür sonunda ise 2,14 kat artırdığını ifade etmiştir. AASHTO 1993 metoduna göre yapılan üstyapı tasarımında, %10 SC ile stabilize edilen zeminler için üstyapı kalınlığının saf zemine göre 1 günlük kürde %10, 7 günlük kürde ise %15,25 oranında azaldığı bulunmuştur. Ekonomik analizler, bu azalmanın yol yapım maliyetlerini önemli ölçüde düşürdüğünü ortaya koymuştur; örneğin, 7 günlük kür uygulanan %10 SC katkılı zeminlerde üstyapı maliyetleri %14,37 oranında azalmış, bu da 1000 metre uzunluğunda ve 20 metre genişliğinde bir yolda önemli ölçüde bir tasarruf sağlayabileceğini göstermiştir. Sonuç olarak, siyah karbonun yol taban zemini stabilizasyonunda kullanılması, hem zemin taşıma gücünü artırarak üst yapı maliyetlerini düşürmekte hem de atıkların değerlendirilmesiyle çevre ve ülke ekonomisine katkı sağlamaktadır. Bu doğrultuda, mevcut çalışmada elde edilen sonuçların önceki araştırmalarla tutarlı olduğu ve kireç ile karbon karasının dayanım üzerinde olumlu etkiler yarattığı söylenebilir.

28 günlük serbest basınç dayanımının en yüksek olduğu değeri ve bu değere karşılık gelen optimum karışım oranlarını belirlemek amacıyla Taguchi Optimizasyon Yöntemi uygulanmıştır. Bu yöntemle elde edilen beklenen dayanım değeri ile %95 güven aralığı hesaplanarak Tablo 20'de sunulmuştur. Ayrıca, belirlenen optimum karışım oranlarına göre hazırlanan numuneler üzerinde doğrulama deneyi gerçekleştirilmiş olup, elde edilen deneysel sonuçların ortalama değerleri de aynı tabloda verilmiştir. Bu doğrulama çalışması, tahmin edilen dayanım ile deneysel veriler arasındaki uyumu ortaya koyarak optimizasyon sürecinin güvenilirliğini desteklemektedir.

Tablo 20. Optimum deney koşulları ve beklenen değerler

Optimum Koşullardaki Parametre ve Seviyeleri (%)					Optimum Şartlarda Beklenen Değer (S/N) /(MPa)	%95 Güven Aralığı (S/N)	Doğrulama Deney Sonucu (S/N) / (MPa)
ACT	BL	PK	KK	K			
4	0,25	15	7	8	9,46/2,97	7,98-10,95	8,40/2,63

Tablo 20'de belirtilen optimum koşullarda elde edilen tahmini değerin doğruluğunu değerlendirmek amacıyla, ilgili parametre ve seviyelere uygun olarak numune hazırlanmış ve 28 günlük kür süresinin ardından serbest basınç dayanımı deneyi yeniden uygulanmıştır. Deney sonucunda elde edilen serbest basınç dayanımı 2,63 MPa olarak ölçülmüş, bu değere karşılık gelen S/N oranı ise 8,40 olarak hesaplanmıştır. %95 güven aralığı kapsamında bu değerin 7,98 ile 10,95 arasında olması gerektiği dikkate alındığında, elde edilen sonucun bu aralıkla uyumlu olduğu görülmektedir. Bu durum, Taguchi yöntemiyle yapılan tahminlerin güvenilirliğini ortaya koymakta ve deneysel çalışmalar sırasında parametreler arasında anlamlı bir etkileşimin bulunmadığını göstermektedir.

Sonuç ve Değerlendirme

Yapılan deneysel çalışmaların değerlendirilmesi sonucunda, hem 7 günlük hem de 28 günlük kür sürelerinde elde edilen serbest basınç dayanımı sonuçları değerlendirildiğinde, **kireç (K)** katkısının hem 7 hem de 28 günlük kür sürelerinde serbest basınç dayanımını en fazla artıran parametre olduğu gözlemlenmiştir. Bu etkinin temel nedeni, kirecin içerdiği kalsiyum hidroksit ($Ca(OH)_2$) bileşiğinin, kil zemin içerisinde bulunan silis (SiO_2) ve alümina (Al_2O_3) gibi reaktif minerallerle reaksiyona girerek puzolanik bağlayıcı ürünler (C-S-H, C-A-H ve C-A-S-H) oluşturmasıdır. Bu çimentolaşma ürünleri, başlangıçta jel formundayken zamanla kristalleşerek zemin matrisinde daha sıkı, dayanıklı ve kohezyonu yüksek bir yapı meydana getirmiştir. Ayrıca, bu reaksiyonlar zemindeki boşlukları doldurmuş ve permeabiliteyi azaltarak mekanik performansı iyileştirmiştir. Özellikle uzun kür sürelerinde bu kimyasal reaksiyonların daha etkin hale gelmesi, 28 günlük dayanım artışını belirgin biçimde açıklamaktadır. Dolayısıyla kireç hem erken yaşta hem de zamanla gelişen bağlayıcı etkisiyle zemin stabilizasyonunda en etkili katkı maddesi olmuştur. Buna karşın, her iki kür süresi için de bazalt lif (BL) ve pirinç kabuğu külü (PK) katkılarının serbest basınç dayanımına olan etkilerinin sınırlı düzeyde kaldığı belirlenmiştir. Bu durum, lif katkılarının daha çok sünekliği artırmaya yönelik işlev göstermesi ve PK'nın pozolanik reaksiyonlarının sınırlı katkı süresinde yeterince aktive olmamasıyla ilişkilendirilebilir.

7 günlük kür süresi için elde edilen optimum katkı kombinasyonu sırasıyla atık cam tozu (ACT) %4, bazalt lif (BL) %1, pirinç kabuğu külü (PK) %5, geri dönüştürülmüş karbon karası (KK) %1 ve kireç (K) %6 olup, bu karışımla 1,39 MPa serbest basınç dayanımı elde edilmiştir. Bu sonuç, erken yaş dayanımında özellikle kireç ve ACT katkılarının pozitif etkisini ortaya koymaktadır.

28 günlük kür süresi sonucunda ise optimum katkı oranları ACT %4, BL %0,25, PK %15, KK %7 ve K %8 olarak belirlenmiştir. Bu kombinasyonla elde edilen maksimum serbest basınç dayanımı 2,63 MPa olarak ölçülmüştür. Dayanımın zamanla artması, puzolanik reaksiyonların ilerlemesi ve katkıların zemin iç yapısıyla daha iyi etkileşim kurmasıyla açıklanabilir. Özellikle kireç oranındaki artış ve PK oranının yükseltilmesi, uzun vadeli dayanım açısından olumlu katkılar sağlamıştır.

Yapılan deneysel çalışmaların değerlendirilmesi sonucunda, özellikle kireç katkısının zemin iyileştirme çalışmalarında en

etkili parametre olduğunu ortaya koymaktadır. Kirecin bağlayıcılık özelliği sayesinde zemin matrisinde daha kararlı ve dayanıklı bir yapı elde edilmesi, gerçek saha koşullarında zeminlerin taşıma gücünü ve uzun vadeli stabilitesini artırma potansiyeli taşımaktadır. Bu durum, özellikle altyapı projelerinde (yol, dolgu, temel altı uygulamaları vb.) yaygın olarak karşılaşılan düşük dayanımlı zeminlerin iyileştirilmesinde fayda sağlayabilir.

Bunun yanında, bazalt lif ve pirinç kabuğu külü katkılarının erken yaş dayanımlarına sınırlı düzeyde etki ettiği, ancak kür süresi ilerledikçe özellikle PK'nın pozolanik reaksiyonlarının gelişmesiyle 28 günlük dayanım üzerinde olumlu katkı sunduğu belirlenmiştir. Bu durum, saha uygulamalarında lif katkılarının sünekliği artırma işlevi ile daha çok deformasyon kapasitesine katkı sağlayacağını, pozolanik malzemelerin ise uzun vadeli dayanım açısından avantajlı olacağını göstermektedir.

Elde edilen sonuçlar ayrıca, atık cam tozu ve geri dönüştürülmüş karbon karası gibi çevresel atıkların optimum oranlarda kullanılmasıyla hem dayanım değerlerinin yükseltilebileceğini hem de çevresel atıkların geri kazanımı yoluyla sürdürülebilir malzeme kullanımına katkı sağlanabileceğini ortaya koymuştur. Dolayısıyla, mühendislik uygulamalarında maliyet-etkin ve çevre dostu çözümler sunma potansiyeli taşımaktadır.

Sonuç olarak, deneysel bulgular; saha uygulamalarında özellikle kireç katkısının kısa ve uzun vadeli performans üzerindeki belirgin etkisinin, pozolanik katkıların zamanla artan dayanım katkısının ve atık malzemelerin sürdürülebilirlik açısından sağladığı avantajların dikkate alınması gerektiğini ortaya koymaktadır. Bu bağlamda, farklı katkı kombinasyonlarının proje hedefleri doğrultusunda seçilmesi, hem mühendislik performansının hem de çevresel sürdürülebilirliğin en üst düzeye çıkarılmasına olanak sağlayacaktır.

Kaynaklar

[1] Shibi, T. and Kamei, T., 2014. Effect of freeze–thaw cycles on the strength and physical properties of cement-stabilised soil containing recycled bassanite and coal ash. Cold Regions Science and Technology, 106, 36-45.

[2] Erol, A., 2007. C sınıfı uçucu kül katkılı siltlerin dayanım ve donma-çözülme direncinin deneysel olarak incelenmesi, Yüksek Lisans Tezi, Ege Üniversitesi, Fen Bilimleri Enstitüsü.

[3] Güllü, H., 2015. Unconfined compressive strength and freeze–thaw resistance of fine-grained soil stabilised with bottom ash, lime and superplasticiser. Road Materials and Pavement Design, 16(3), 608-634.

[4] Tebaldi, G., Orazi, M., Orazi, U. S., 2016. Effect of freeze—thaw cycles on mechanical behavior of lime-stabilized soil. Journal of Materials in Civil Engineering, 28(6), 06016002.

[5] Mohamed, A. A. M. S., Al-Ajamee, M., Kobbail, A., Dahab, H., Abdo, M. M., & Alhassan, H. E., 2022. A study on soil stabilization for some tropical soils. Materials Today: Proceedings, 60, 87-92.

[6] Prusinski, J. R., & Bhattacharja, S., 1999. Effectiveness of Portland cement and lime in stabilizing clay soils. Transportation research record, 1652(1), 215-227.

[7] Zaimoglu, A. S., 2015. Optimization of unconfined compressive strength of fine-grained soils modified with polypropylene fibers and additive materials. KSCE Journal of Civil Engineering, 19.3: 578-582.

[8] Ikeagwuani, C. C., & Nwonu, D. C., 2022. Optimization of Multi-additives for Expansive Soil Improvement Using Response Surface Methodology. Geotechnical and Geological Engineering, 40(4), 1809-1831.

[9] Mousavi, F., Atarodi, A., & Abdi, E., 2024. Optimization of polymer materials performance on improving mechanical properties of fine-grained soils of forest. Road Materials and Pavement Design, 25(7), 1426-1448.

[10] Gidebo, F. A., Kinoshita, N., & Yasuhara, H., 2024. Optimization of physical and strength performance of cellulose-based fiber additives stabilized expansive soil. Case Studies in Construction Materials, 20, e02851.

[11] Hamed, E., & Demiröz, A., 2024. Optimization of geotechnical characteristics of clayey soils using fly ash and granulated blast furnace slag-based geopolymer. Construction and Building Materials, 441, 137488.

[12] Winoto, V., & Keawsawasvong, S., 2022. Response surface methodology for optimizing stabilization of clay soils using bacterial calcium carbonate precipitation. Transportation Infrastructure Geotechnology, 9(6), 890-898.

[13] Olgun, M., 2013. The effects and optimization of additives for expansive clays under freeze–thaw conditions. Cold Regions Science and Technology, 93, 36-46.

[14] Chen, K., Wu, D., Zhang, Z., Pan, C., Shen, X., Xia, L., & Zang, J., 2022. Modeling and optimization of fly ash–slag-based geopolymer using response surface method and its application in soft soil stabilization. Construction and Building Materials, 315, 125723.

[15] Nuruzzaman, M., and Hossain, M. A., 2014. Effect of soda lime glass dust on the properties of clayey soil. Global Journal of Research In Engineering, 14(5), 17-22.

[16] Olufowobi, J., Ogundoju, A., Michael, B., Aderinlewo, O., 2014. Clay soil stabilisation using powdered glass. Journal of Engineering Science and Technology, 9(5), 541-558.

[17] Gao, L., Hu, G., Xu, N., Fu, J., Xiang, C., & Yang, C., 2015. Experimental study on unconfined compressive strength of basalt fiber reinforced clay soil. Advances in Materials Science and Engineering, 2015(1), 561293.

[18] Phanikumar, B. R. and Nagaraju, T. V., 2018. Effect of fly ash and rice husk ash on index and engineering properties of expansive clays. Geotechnical and Geological engineering, 36(6), 3425-3436.

[19] Chhun, K. T., Choo, H., Kaothon, P., & Yune, C. Y., 2020. Experimental study on the strength behavior of cement-stabilized sand with recovered carbon black. Geomechanics and Engineering, 23(1), 31-38.

[20] Türkel, U. M., 2019. Bazalt Fiber ve Çimento Katkısının Zayif Zeminlerin Geoteknik Özelliklerine Etkisinin Araştırılması, Yüksek Lisans Tezi, Düzce Üniversitesi Fen Bilimleri Enstitüsü.

[21] Sungur, A., & Keskin, N., 2021. Bazalt Lifi ile Güçlendirilmiş Killi Zeminin Mühendislik Özellikleri Üzerine Deneysel Araştırma. Avrupa Bilim ve Teknoloji Dergisi, (28), 895-899.

[22] Terzi, S., 2021. Killi zeminlerin kayma direncine bazalt fiberin katkısı, Yüksek Lisans Tezi, Sakarya Üniversitesi Fen Bilimleri Enstitüsü.

[23] Çınar, M., & Erbaşı, K., 2023. Zemin İyileştirmesinde Kullanılan Jet Grout Yönteminde Çimento Yerine İkame Edilen Atık Malzemelerin Mekanik ve Reolojik Özelliklerine Etkisinin İncelenmesi: Literatür Araştırması. Osmaniye Korkut Ata Üniversitesi Fen Bilimleri Enstitüsü Dergisi, 6(2), 1742-1767.

[24] Işık, F. ve Akbulut, R. K., 2018. Geri Dönüştürülmüş Karbon Karasının Killi Zeminlerin Kıvam Limitlerine Etkisi. Journal of the Institute of Science and Technology, 8(2), 123-130.

[25] Dadanlar, A., 2019. Şişen killerin stabilizasyonunda katkı malzemesi olarak atık cam kullanımı. Yüksek Lisans Tezi, Hacettepe Üniversitesi, Fen Bilimleri Enstitüsü.

[26] Manzoor, S. O., & Yousuf, A., 2020. Stabilisationof soils with lime: A review. J. Mater. Environ. Sci, 11(10), 1538-1551.

[27] Benamrane, R., Bennouna, M. S., Fellah, M., & Sadek, K., 2024. The improvement of the tensile properties of alfa fibers using the Taguchi method. Industrial Crops and Products, 221, 119398.

[28] Karna, S. K., & Sahai, R., 2012. An overview on Taguchi method. International journal of engineering and mathematical sciences, 1(1), 1-7.

[29] Hisam, M. W., Dar, A. A., Elrasheed, M. O., Khan, M. S., Gera, R., & Azad, I., 2024. The versatility of the Taguchi method: Optimizing experiments across diverse disciplines. Journal of Statistical Theory and Applications, 23(4), 365-389.

[30] Rashid, K. M. J., 2023. Optimize the Taguchi method, the signal-to-noise ratio, and the sensitivity. Int J Stat Appl Math, 8(6), 64-70.

[31] Nagaraja, B., Almeida, F., Yousef, A., Kumar, P., Ajaykumar, A. R., & Al-Mdallal, Q., 2023. Empirical study for Nusselt number optimization for the flow using ANOVA and Taguchi method. Case Studies in Thermal Engineering, 50, 103505.

[32] Montgomery, D.C., 1991. Design and Analysis of Experiments, Arizona State University, John Wiley and Sons, N.Y., Chichester, Brisbane, Toronto Singapure, Ninth Edition, 1991.

[33] ASTM D 2166. Standard test method for unconfined compressive strength of cohesive soil, American Society for Testing and Materials, West Conshohocken, Pennsylvania, USA.

[34] Boz, A., 2017. Fiber ile donatılandırılmış kireç stabilize kilin donma çözünme etkisi öncesi ve sonrası mekanik özellikleri, Yüksek Lisans Tezi, Ege Üniversitesi, Fen Bilimleri Enstitüsü.

[35] Beheshti Germi, M. H., 2016. Geri dönüştürülmüş nano karbon karasının betonun bazı fiziksel ve mekanik özellikleri üzerine etkisi, Yüksek Lisan Tezi, Atatürk Üniversitesi, Fen Bilimleri Enstitüsü.

[36] Canakci, H., Aram, A. L., and Celik, F., 2016. Stabilization of clay with waste soda lime glass powder. Procedia engineering, 161, 600-605.

[37] Geçkil, T., Sarıcı, T., & Karabaş, B., 2021. Siyah karbon ile stabilize edilen taban zeminin yol esnek üst yapı maliyetine etkisi. Avrupa Bilim ve Teknoloji Dergisi, (23), 222-235.

[38] Boz, A. and Sezer, A., 2018. Influence of fiber type and content on freeze-thaw resistance of fiber reinforced lime stabilized clay. Cold Regions Science and Technology, 151, 359-366.

[39] Küçükosmanoğlu, M., 2019. Bazalt Fiberin Zemin İyileştirilmesinde Kullanımı, Yüksek Lisans Tezi, Sakarya Üniversitesi, Fen Bilimleri Enstitüsü.

[40] Abduljauwad, S. N., 1995. Improvement of plasticity and swelling potential of calcareous expansive clays. Geotechnical Engineering, 26(1).

[41] Aydın, S., 2010. Yenikent (Ankara) yerleşim alanı killerinin kireç ve uçucu külle geoteknik özelliklerinin iyileştirilmesi, Yüksek Lisans Tezi, Gazi Universitesi, Fen Bilimleri Enstitüsü.

Etik kurul onayı ve çıkar çatışması beyanı

Hazırlanan makalede etik kurul izni alınmasına gerek yoktur. Hazırlanan makalede herhangi bir kişi/kurum ile çıkar çatışması bulunmamaktadır.

Yazar Katkıları

Y.Pekdemir: Çalışma konsepti ve tasarım, deneysel çalışma, verilerin analizi ve yorumlanması, taslağın oluşturulması, revizyon. **A.Ş.Zaimoğlu:** Çalışma konsepti ve tasarım, verilerin analizi ve yorumlanması, taslağın oluşturulması**. F.Artuk:** Çalışma konsepti ve tasarım, deneysel çalışma, verilerin analizi ve yorumlanması, taslağın oluşturulması, revizyon.

Teşekkür

Bu makale Yasemin Pekdemir'in doktora tezi kapsamında üretilmiştir. Yazarlar Atatürk Üniversitesi Fen Bilimleri Enstitüsüne teşekkür etmektedir.

Dicle University
Journal of Engineering
https://dergipark.org.tr/tr/pub/dumf
duje.dicle.edu.tr

Araştırma Makalesi / Research Article

Tarihi Yapı Restorasyonunda Enerji Performansı Optimizasyonu: Cami Son Cemaat Bölüm Tasarımları İçin Simülasyon Temelli Bir Karşılaştırma

Energy Performance Optimization in Historic Building Restoration: A Simulation-Based Comparison of Design Alternatives for Mosque Porticoes

Ebru Ulaş Sarıaydın[1*]

[1] Eskişehir Teknik Üniversitesi, Mimarlık Bölümü, e.ebruulas@gmail.com

ORCID: https://orcid.org/0000-0002-9156-4674

MAKALE BİLGİLERİ

Makale Geçmişi:

Geliş 22 Ağustos 2025
Revizyon 26 Kasım 2025
Kabul 28 Kasım 2025
Online 30 Aralık 2025

Anahtar Kelimeler:

Bina Enerji Tüketimi, Simülasyon, İbadet Mekanı, Restorasyon, Tipoloji

ÖZ

İbadet mekanlarından cami tipolojisi, haftanın her günü ve aralıklı kullanım imkanı sunan bir fonksiyona sahiptir. Bu yoğun kullanım şeması enerji tüketiminde sürekliliği de beraberinde getirmektedir. Bu çalışma, cami yapılarında gerçekleştirilen restorasyon müdahalelerinden biri olan son cemaat bölümünün kapatılmasının bina enerji performansına etkisini araştırmış ve kurgulanacak tasarımlardaki tipoloji ve malzeme seçiminin enerji iyileştirmesi üzerindeki etkisini incelemiş, bu bağlamda tipoloji ve malzeme seçiminin enerji verimliliği üzerindeki potansiyel etkisini ortaya koymayı amaçlamıştır. Design Builder yazılımı kullanılarak oluşturulan bir cami modeli üzerine, literatürde yer alan son cemaat bölüm tipolojileri uygulanmış ve alternatifler, sayısal simülasyon tabanlı incelenmiştir. Aynı model üzerindeki son cemaat bölümü revizyon alternatiflerinin modelin enerji tüketimine etkisi karşılaştırmalı olarak sunulmuştur. Son cemaat bölümünün kapatılmasına dair literatürde yer alan iki temel tipoloji, son cemaat bölümünün tamamen cam ile kapatılması ve duvar ile çevrelenmesi şeklinde bulunmuştur. Malzeme tercihleri, cam yüzeyler için tek cam ve çift cam,cephe elemanları için ise taş, tuğla, betonarme ve ahşap duvar olarak sınırlandırılmıştır. Belirtilen cephe parametreleri doğrultusunda, model üzerinde 11 farklı senaryo geliştirilmiştir ve her senaryonun enerji tüketimi üzerindeki etkileri analiz edilmiştir. Senaryo karşılaştırmaları sonucunda, en yüksek enerji tasarrufu, son cemaat bölümünün çift cam malzeme kullanılarak tamamen saydam kurgulandığı senaryoda gözlenmiştir. En düşük iyileşme çıktısı ise ahşap kayıtlar üzerindeki tek camlı pencere tipolojisine aittir. Elde edilen bulgular, cami yapılarında gerçekleştirilecek restorasyon projelerinde son cemaat bölümü için uygulanacak malzeme ve tipoloji seçimlerinin enerji verimliliği açısından önemli sonuçlar doğurabileceğini göstermekte ve gelecek restorasyon projelerine rehberlik etmeyi hedeflemektedir.

ARTICLE INFO

Article history:

Received 22 August 2025
Received in revised form 26 November 2025
Accepted 28 November 2025
Available online 30 December 2025

Keywords:

Building Energy Consumption, Simulation, Place of Worship, Restoration, Typology

Doi: 10.24012/dumf.1770506

* Sorumlu Yazar

ABSTRACT

The mosque typology of worship spaces has a function that allows for use every day of the week and intermittent use. This intensive usage pattern also brings with it continuity in energy consumption. This study investigates the impact of closing the rear congregation section, one of the restoration interventions carried out in mosque structures, on the building's energy performance. It also examines the effect of typology and material selection in the designs to be developed on energy improvement, aiming to reveal the potential impact of typology and material selection on energy efficiency in this context. The final congregation section typologies found in the literature are applied to a mosque model created using Design Builder software, and alternatives are examined based on numerical simulations. The effect of the final congregation section revision alternatives on the model's energy consumption is presented comparatively. The two main typologies in the literature regarding the closure of the rear section are the complete closure of the rear section with glass and its enclosure with walls. Material preferences are limited to single and double glazing for glass surfaces and stone, brick, reinforced concrete, and wooden walls for facade elements. Based on the specified facade parameters, 11 different scenarios were developed on the model, and the effects of each scenario on energy consumption were analyzed. As a result of the scenario comparisons, the highest energy savings were observed in the scenario where the rear section of the mosque was designed to be completely transparent using double-glazed material. The lowest improvement output, on the other hand, was associated with single-pane window typology on wooden walls. The findings indicate that material and typology selections for the rear congregation area in restoration projects for mosque structures can have significant implications for energy efficiency and aim to guide future restoration projects.

Giriş

Birden fazla kullanıcı profiline ve yoğun kullanım programına sahip ibadet mekanları çok sayıda insanın aynı ortamda ibadet ettiği yerlerdir [1]. İbadet yerlerinde, oturma, ayakta durma, yürüme, hareket etme gibi eylemler bireysel veya toplu gerçekleştirilmekte, haftanın her günü, tüm gün kullanıma açık bulunmaktadır. Müslümanların ibadet yerleri olan camiler bulundukları bölgeye ve yapıldıkları döneme göre farklılıklar göstermektedir. Bununla birlikte tüm cami mekansal kurgularında harim, son cemaat bölümü ve kadınlar mahfili, cami içerisindeki ana ibadet alanlarını oluşturmaktadır. Caminin ana ibadet mekanı olan harim bölümü, ibadetin topluca gerçekleştirildiği bölümdür. Harim plan şeması içerisinde mihrap, minber ve kubbe bölümleri yer almakta ve kıble yönüne odaklı planlanmaktadır. Son cemaat bölümü, caminin giriş cephesinde yer almakta, harim ile dış mekan arasında geçiş alanı sağlamaktadır. Kadınlar mahfili, cami içerisinde kadın cemaatin ibadeti için ayrılmış özel bir mekandır. Harim bölümünün üst kotunda, korkuluklarla çevrili galeri formunda yer almakta olan bölüm genellikle giriş cephesine yakın konumlanmaktadır. Ayrı bir giriş ile kadın cemaatin ulaşımı sağlanmaktadır [2,3].

Camilerde günde beş vakit namaz kılınması sebebi ile yapı kullanım sürekliliği ve beraberinde bina içerisindeki enerji yükleri aktif olmaktadır. İbadet mekanlarında söz konusu olan enerji yükü, bu yapılar için verimli enerji tüketimi çalışmalarını beraberinde getirmektedir. Literatürde cami binaları üzerinde enerji performans iyileştirmesi araştırılan çalışmalardan Çelebi ve Arpacıoğlu [4], Konya ilindeki Selçuklu dönemi cami ve medreselerinin enerji performanslarını incelemiştir. Alaeddin Camii, Erdemşah Mescidi ve Şekerfüruş Mescidi olmak üzere 3 ibadet yapısı üzerinde,plan şekli, taşıyıcı sistem, cephe açıklıkları, hacim gibi mimari özellikler karşılaştırılmış, bu özelliklerin enerji yükleri üzerindeki etkisi tartışılmıştır. Nordin ve Misni [5], modern ve geleneksel cami tipolojilerinde iç mekan ısıl performans karşılaştırması sunmuştur. Çalışma içerisinde, yön, açıklık, kabuk sistemi gibi pasif tasarım unsurlarının bina ısıl performansı üzerindeki etkisi tartışılmış, iyi bir iç mekan termal performansı elde etmek için cami tasarımına yönelik stratejik yaklaşımlar önerilmiştir. Benzer problemler çerçevesinde yürütülmüş olan bir diğer çalışmada [6], Umman'daki geleneksel ve modern cami modelleri, sıcak-kurak iklim kapsamında incelenmiştir. İklim koşulları, yapı tipi ve mimari özelliklerin enerji tüketimi üzerindeki etkisi tartışılmıştır. Sunulan çalışmalar, pasif mimari tasarım ilkelerinin enerji tüketimi üzerindeki etkilerini analiz etmiştir.

Bununla birlikte, mevcut ibadet mekanlarına yönelik iyileştirme müdahalelerinin enerji performans sonuçlarını değerlendiren araştırmalar da literatürde yer almaktadır. Cami binaları üzerinde, enerji performans iyileştirme müdahaleleri araştırılan çalışmalardan Elshurafa ve ark. [7], camilerdeki çatı yüzeylerinde PV panel entegrasyonu ile yenilenebilir enerji kaynakları kullanarak iyileşme önermiştir. Suudi Arabistan'da gerçekleştirilen çalışmada, cami yapılarının genellikle ayrık nizam oturuma sahip olması, çevresel elemanların güneş alımına uygun pozisyon sunması ve nispeten cami çatı alanlarının geniş yüzeylere sahip olması sebepleri ile fotovoltaik panel kullanımı uygun bulunmuştur. Elshurafa ve ark.'nın [7] çalışma verilerine göre cami inşaatının erken evrelerinde, panel kullanımına dair planlama ve hesaplamalar yapıldığı takdirde cami elektrik tüketiminin tamamı PV paneller ile sağlanabilmektedir.

Cami içerisindeki iç mekan sıcaklıkları, aydınlatma performansı ve aydınlatma seviyelerinin iç mekan doluluk takibi ile yönetimi araştırılan bir başka çalışmada [8] akıllı kontrol sistemleri önerilmiştir. Kontrol sistemi ile kullanıcı yoğunluğuna göre iç ortam koşullarının optimizasyonu hedeflenen önerinin tüketim çıktısında, cami enerji tüketiminde önemli ölçüde azalma söz konusudur. Enerji verimliliği parametrelerinden biri olan doğal aydınlatma, Coşkuner Pamuk ve ark.'nın [9] çalışmasında camiler kapsamında ele alınmıştır. Konya'da bulunan üç farklı cami üzerinde iç mekan tasarımlarının doğal aydınlatmaya etkisi araştırılmıştır. Camilerdeki gün ışığı kontrolleri yaz dönemi iklim şartlarında, her cami özelinde belirli gün ve saatlerde yapılmıştır. Belirtilen kontroller cami üzerinden, konfor ölçüm cihazları ile sağlanmış, simülasyon modelleri gerçek veriler ile oluşturulmuştur. Çalışma sonucunda geçmiş ve bugüne dair cami tipolojisinde gelişen inşa teknikleri ve tasarım kriterlerinin, aydınlatma seviyesi ve iç yansıyan ışık artışı üzerinde etkin olduğu belirtilmiştir. Pencere ve cam çeşitliliği, yeni inşa yöntemleri ile sağlanan geniş açıklıklar ve iç duvar yüzeylerinde kullanılan gelişmiş yapı elemanları olanakları, doğal aydınlatmanın yapı içerisinde güçlü bir aydınlatma unsuru haline gelmesini sağlamıştır. Bu durum, yapay aydınlatma yükünün azalmasıyla birlikte bina enerji tüketiminin düşmesine yol açmıştır. Çeşitli kullanıcı tipi ve kullanıcı yoğunluğuna sahip olan camilerin iç mekan termal konforunu kabul edilebilir düzeylerde tutmayı amaçlayan bir diğer çalışmada [10] ise, pasif tasarım kriterlerinin belirlenmesine ve klima ekipmanı tipinin seçimine dair stratejiler değerlendirilmiştir. Müdahale senaryolarının oluşturulmasında Design Builder simülasyon yazılımı kullanılan çalışma kapsamında, ele alınan tasarım parametrelerinin bina enerji tüketimi üzerindeki etkisi karşılaştırılmıştır.

Sunulan literatür verilerine göre, ibadet mekanlarındaki enerji performansı iyileştirme çalışmaları iki ana başlıkta gruplandırılabilmektedir. Bu başlıklar; (1) camilerdeki pasif tasarım kararlarına bağlı performans artırımı ve (2) mevcut yapıya uygulanan restorasyon müdahaleleri sonucunda elde edilen enerji performans iyileştirmesi olarak ayrıştırılabilmektedir. Bu çalışma, mevcut yapıya uygulanan restorasyon müdahalelerini, son cemaat bölümü ölçeğinde ele almış ve bu bölümde gerçekleştirilen revizyonların binanın genel enerji performansı üzerindeki etkilerini analiz etmiştir. Özellikle enerji verimliliği amacı taşımayan ancak fiziksel müdahale yoluyla yapının bir bölümünde gerçekleşen restorasyon eylemlerinin enerji performansı açısından ne tür sonuçlar doğurduğunun belirlenmesi bu çalışmanın temel problemidir.

Çalışmanın amacı, camilerdeki son cemaat bölümünün kapatılmasına ilişkin literatürde yer alan veriler doğrultusunda, kapatma müdahalesi sonrasında ortaya çıkan yeni cephelerdeki doluluk-boşluk tipolojilerini belirlemek ve bu cephe uygulamalarının bina enerji tüketimi üzerindeki etkilerini analiz etmektir. Çalışma kapsamında, literatürde tespit edilen cami son cemaat bölümlerinin müdahaleler sonrası mevcut durumları incelenmiş ve elde edilen veriler doğrultusunda son cemaat bölümü cephe tipolojileri

geliştirilmiştir. Bu araştırmada, cami restorasyonlarındaki son cemaat bölümlerine uygulanan farklı kapatma yaklaşımları dikkate alınarak çeşitli uygulama senaryoları oluşturulmuştur. Bu senaryolar üzerinden, son cemaat bölümüne yapılan müdahalelerin, baz alınan modelin enerji tüketimi üzerindeki etkileri değerlendirilmiş ve müdahale türlerine bağlı olarak ortaya çıkabilecek enerji verimliliği potansiyelleri analiz edilmiştir.

Materyal ve Metod

Araştırma yöntemi üç adım olarak sunulmuştur. Mevcut çalışma, belirli kabullere dayalı oluşturulmuş kurgusal bir baz model üzerinde yürütülmüştür. Birinci adım, Design Builder yazılımı kullanılarak oluşturulan modelin tanıtımını içermektedir. İkinci adım, çalışmada sunulacak senaryo kurgusunun oluşturulmasına temel hazırlayan bir işlev taşımaktadır. Türkiye'de gerçekleştirilen cami restorasyonları ile bu restorasyonlarda uygulanan son cemaat bölümü cephe alternatiflerine ilişkin örnek araştırması; ulusal akademik yayınlar, yerel kurum raporları ve lisansüstü tezleri kapsayan Google Scholar veritabanı kapsamında sınırlandırılmış, ve bu yerel araştırma kapsamı, mevcut çalışmanın amaçları doğrultusunda yeterli ve uygun bir veri kaynağı sunmuştur. Bölümün üçüncü adımında ise literatür verileri doğrultusunda oluşturulan müdahale senaryolarının içerikleri paylaşılmıştır. Senaryolar çerçevesinde kabul olunan son cemaat bölümü kabuk tasarımı, kabuk bileşenin özellikleri, son cemaat bölümünün dolu-boş yüzey alanları ve bölüme ait cephedeki saydam yüzey oranları paylaşılmıştır.

Baz modelin tanımlanması

Design Builder simülasyon programı aracılığıyla performans analizleri gerçekleştirilecek baz model, aşağıda belirtilen ve Tablo 1'de detaylandırılan kabullere dayalı olarak tamamen kurgusal bir tasarımda oluşturulmuştur. Baz model, ayrık nizam oturum alanına sahip, zemin kat erkek cemaat alanı ve asma kat kadın cemaat alanı olmak üzere cami tipolojisine uygun tasarlanmıştır. Oluşturulan model, ikinci derece gün bölgesinde yer alan Bursa ili üzerinde varsayılmıştır. Derece gün birimi, 24 saatlik periyod içerisinde sıcak ve soğuk saat ölçümünü ifadelendirmektedir. Belirtilen konum Design Builder programı içerisinde seçilmiş ve böylece dış ortam iklim verileri Bursa iline göre oluşturulmuştur. Baz modele ait genel bilgiler Tablo 1'de paylaşılmıştır.

Tablo 1. Simülasyonda oluşturulan baz modele ait genel özellikler.

Binaya ait Genel Bilgiler			
	Zemin Kat	Asma Kat	Toplam
Toplam Kullanım Alanı (m^2)	169.50 (harim) 35.70 (son cemaat)	61.50	266.70
Kat Yüksekliği (m)	6.50 (harim) 2.80 (son cemaat)	2.40	
Hacim (m^3)	1 350.80	175.30	1 526.10
Toplam Pencere Alanı (m^2)			65.20
Saydamlık Oranı (%)			%25

Ayrık nizam olarak planlanmış baz modelin zemin katında erkek cemaat ibadet etmekte ve bu alan iki bölümden oluşmaktadır. 169.50 m^2 alana sahip harim bölümü yüksekliği 6.50 m iken geç gelen cemaat için ayrı bir mekan niteliği taşıyan son cemaat bölümü yüksekliği 2.80 m'dir. 169.50 m^2 harim bölümü ve 35.70 m^2 son cemaat bölümü bulunan zemin katın toplam kullanım alanı 205.20 m^2'dir. Son cemaat bölümünün üst kotunda yer alan, kadınlar için ibadet mekanı olan ve 61.50 m^2 kullanım alanına sahip kadınlar mahfili yüksekliği ise 2.40 m'dir (Tablo 1).

Çalışma içerisinde gerçekleştirilecek müdahaleler, son cemaat bölümü ölçeğinde sınırlandırılmıştır. Bu sebeple oluşturulan ve Tablo 2'de paylaşılan modelde kullanılmış ısıl geçirgenlik katsayıları, tüm senaryolarda ortak kullanılacak baz modele aittir.

Doğal taş olarak modellenen cephe elemanın iç ve dış yüzeyinde sıva bulunmamaktadır. 75 cm kalınlığında kullanılan taş malzemenin toplam ısı geçirme katsayısı 2.33 W/m^2K'dir. Yapı içerisinde kullanılan iç duvarlarda 9 cm kalınlığında düşey delikli tuğla ve sıva kullanılmış, bileşene ait toplam ısı geçirme katsayısı 3.46 W/m^2K olarak bulunmuştur. Zemin ve iç döşeme olarak ayrı kullanılan şablonlarda ahşap iç döşeme 2.46 W/m^2K iken zemin döşemesinin toplam ısı geçirme katsayısı 4.27 W/m^2K'dir. Camideki çatı boşluğu kullanılmayan alan olarak modellenmiş ve programdan seçilen şablon içeriğine ait toplam ısı geçirme katsayısı 4.96 W/m^2K olarak hesaplanmıştır (Tablo 2).

Tablo 2. Baz modele ait kabuk bilesen özellikleri

Kabuk bileşenleri		Kalınlık (cm)	Toplam Isı Geçirgenlik Katsayısı U (W/m^2K)
K1	Dış Duvar- Doğal Taş Malzeme	75	0.580
K2	İç Duvar- Düşey Dolgulu Tuğla/sıva	10	2.350
K3	İç Döşeme- Ahşap	19	2.460
K4	Zemin Döşemesi- Betonarme döşeme	40	4.270
K5	Çatı arası kullanılmayan kırma çatı		4.960
K6	Ahşap doğramalı tek camlı pencere (Meşe)		5.130
K7	Dış kapı		3.120
K8	İç kapı		2.820

Tasarlanan baz model cami binasında iki tip pencere kullanılmıştır. İlk tip pencere yüksekliği 1.55 metre, genişliği 1.00 metre ve parapet yüksekliği ise 0.80 metredir. İkinci tip pencere yüksekliği 2.45 metre, genişliği 1.00 metre ve parapet yüksekliği 0.80 metredir. Camideki tüm pencere çerçevelerinde meşe pencere doğraması kullanılmış, cam tercihi olarak 6 mm'lik tek cam seçilmiştir. Toplam kullanım alanı 266.70 m^2 olarak tanımlanan caminin cephesinde, 16 adet tip 1 pencere, 5 adet tip 2 pencere olmak üzere %25 oranında pencere açıklığı mevcuttur. Zemin kat ve asma kat cephelerinde farklılık gösteren pencere düzeni toplamda 65.20 m^2'lik alana sahiptir. Bina çelik dış kapı U değeri 3.12

W/m^{2}K iken ahşap iç kapılara ait toplam ısı geçirme katsayısı 2.82 W/m^{2}K olarak belirlenmiştir (Tablo 2). Tablo 2 ile paylaşılan kabuk bileşenleri baz model verilerini sunmaktadır.

Baz model üzerinde tanımlanan kullanıcı tipi, yoğunluğu ve kullanım çizelgesi, aydınlatma elemanlarının açık-kapalı kullanım çizelgeleri, bina ısıtma yöntemi ve ısıtılan zaman planlamaları Design Builder programı içerisine yazar tarafından tanımlanmıştır. Oluşturulan simülasyon modelinde bina aktivitesi olarak, ASHRAE [11] sekmesi altında paylaşılan dini ibadet mekanları seçilmiştir. Kullanıcı davranışı ve aydınlatma kabullerinde, Sarıaydın vd.'nin çalışmasında [12] paylaşılan, HOBO UX90-005 kullanıcı varlığı ve aydınlatma (on/off) kaydedicileri kullanılarak bir cami yapısı üzerinden elde edilmiş gerçek veriler referans alınmıştır. Oluşturulan kullanıcı yoğunluğu kabulü 1.29 kişi/m^2 olarak belirlenmiştir. Bina kullanım zaman çizelgesi, haftanın her günü, sabah 5.00 akşam 23.00 saatleri arası kullanım sunacak şekilde tasarlanmıştır. Oluşturulan çizelgede namaz saatlerine denk gelen aralıklarda, Cuma namazlarında ve ramazan ayını simgeleyen bir aylık sürede kullanıcı yoğunluğu artırılmıştır. Yapı içerisinde kullanılan ısıtma sistemi kabulü radyatör ısıtma olarak seçilmiş ve bina içi ısıtma çizelgesi, mevcut çalışmanın varsayımları doğrultusunda, kullanıcı zaman çizelgesi paralelinde hazırlanmıştır. Isıtma sisteminin çalışma kabulüne göre, cami kullanımının aktif olduğu 5.00-23.00 saatleri arasında cami ısıtma sistemi aralıksız çalıştırılmış ve diğer saatlerde tamamen kapatılılmıştır. Tasarlanan cami modelinde ele alınan kabuller bu bölümde paylaşılılmıştır. Baz modelin mevcut durumundaki enerji tüketim değerleri ise bulgular bölümünde paylaşılılmıştır. Senaryolar halinde aktarılan son cemaat bölüm müdahalelerinin etkisi baz model tüketim değerleri ile karşılaştırılarak sunulmuştur.

Son cemaat bölümü tipoloji araştırması

Scholar veri tabanında yürütülen literatür araştırması, mosque AND restoration AND "last congregation area" AND intervention anahtar kelimeleri ile son 5 yıl sınırlandırması ile yapılmıştır. Belirtilen arama sonucunda 14 farklı camiye ait restorasyon ve sismik analiz çalışmasına ulaşılmıştır. İncelenen 14 çalışma içerisinde cami son cemaat bölümüne ait bilgi ulaşılamayan 4 çalışmanın çıkarılması ile Tablo 3'te paylaşılan 10 cami üzerinde tipoloji çalışması yürütülmüştür. Literatür verileri doğrultusunda ulaşılan 10 caminin lokasyon farklılıkları gerekçesiyle son cemaat bölümü cephe yönelimleri birbirinden farklıdır. İncelenen camilerin bu çalışmaya dahiliyeti, son cemaat bölümü tipolojileri ile sınırlandırılmış ve camilere ait yönelim değişkeni çalışma içerisinde yok sayılmıştır. Bu çalışmada, tipoloji tespitlerinin karşılaştırılabilirliğini sağlamak amacıyla tüm senaryolar, aynı konum koşulları kabul edilerek oluşturulan tek bir model üzerinde denenmiştir. Bu yaklaşım, camilerin farklı yönlenmelerinden kaynaklı oluşabilecek ışık ve ısı kazanımı farklılıklarının etkisini gözardı edebilme olanağı sunmuştur.

Cami mimarisinin temel bileşenleri arasında yer alan harim ve son cemaat bölümleri, ibadet mekanının işlevsel bütünlüğünü tanımlayan ana unsurlardandır. Son cemaat bölümü, caminin cephe düzeninde önemli bir yer tutmaktadır. Bu nedenle, bu bölümde yapılacak revizyonlar caminin cephe ve işlev bütününü etkilemektedir. Literatür incelemesi sonucunda, Tablo 3'te lokasyon verileri ve referans kaynakları ile birlikte sunulan toplam 10 cami restorasyonunda son cemaat bölümüne yönelik çeşitli kapatma müdahaleleri tespit edilmiştir. Bu incelemeler sonucunda, son cemaat bölümlerinde gerçekleştirilen kapatma uygulamalarının cephe üzerinde üç farklı tipolojide ortaya çıktığı belirlenmiştir. Bu tiplojiler şu şekilde sıralanabilir; (G1) özgün camiye ait kolon/dikme kurgusunun ve aralarındaki boşluklu yapının korunması, (G2) dikmeler arası boşluğun tamamen cam ile kapatılması, (G3) dikmeler arasının pencereli duvar örgüsü ile kapatılması. Bu üç tipoloji, cami son cemaat bölümlerinde gerçekleştirilen farklı kapatma yaklaşımlarını temsil etmekte olup, bu çalışmada ele alınan enerji performans analizilerinin temel senaryolarını oluşturmaktadır (Tablo 3).

Şekil 1'de, son cemaat bölümü bulunan ve dikmeler arası boşluklara sahip yapının sembolik bir plan gösterimi sunulmuş, çalışma içerisindeki tipoloji farkları sembol üzerinden aktarılmıştır. G1 tipolojisinde, kolonlar arasında açıklıklar yer almakta; G2 tipolojisinde ise şema üzerinde kırmızı ile işaretlenen alanlar tamamen şeffaf cam yüzeylerle kapatılmaktadır. Üç akslı olarak tanımlanan bu sembolde, orta aksta giriş kapısı, yan akslarda ise şeffaf cam paneller bulunmaktadır. G3 kodu ile tanımlanan pencereli duvar tipolojisinde ise, kolon aralarının duvarla örülmesi ve bu duvarlar üzerinde kapı ile pencere boşluklarının oluşturulması durumu gösterilmektedir.

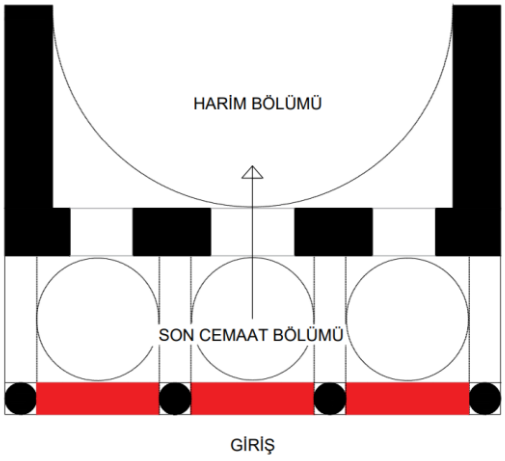

Şekil 1. Son cemaat mahalli sembolik plan gösterimi

Sembol anlatıma ek olarak, Tablo 3'te yer alan son cemaat bölümü kapatılmış camilerin tipoloji farklılıkları Şekil 2 üzerinde görselleştirilmiştir. Tipoloji ayrışmasında ilk sınıfı (Şekil 2a) oluşturan dikmeler arası boşluklu kullanım [13], [14], [15] tarihi caminin özgün kullanımındaki revak yapısını korumakta, cemaat için yarı açık kullanım alanı sunmaktadır. İncelenen 10 cami restorasyonun 4'ünde son cemaat bölümü yarı açık alan olarak kullanımına devam etmektedir.

İkinci sınıf olan dikmeler arasının tamamen cam malzeme ile kapatılmasında (Şekil 2b) [13], [16], [12] Erzurum Pervizoğlu Cami, Malatya Ulu Cami ve Eskişehir Alaaddin Bey Cami olmak üzere 3 kullanım örneğine sahiptir. Üç farklı tipoloji içerisindeki üçüncü grup olan dikmeler arasının duvar örgüsü ile kapatılmasında (Şekil 2c) Tyana Sinanbey Cami,

Sandıklı Ulu Cami ve Kastamonu Mehran Cami referans alınmıştır [17], [18], [19]. Örnekler üzerinde görülen farklı boyutlardaki cephe açıklıkları mevcut çalışma içerisinde iki tip pencere ölçüsü olarak belirlenmiş ve oluşturulan pencere detayları baz modelin tanımlandığı bölümde aktarılmıştır.

Tablo 3. Son cemaat bölümü verilerine ulaşılan camiler

No	Grup Kodu	Grup İçeriği	Cami İsmi	Konum Bilgisi	Referans Kaynak
1	G1	Özgün camiye ait kolon/dikme kurgusunun ve aralarındaki boşluklu yapının korunması	Caferiye Cami	Erzurum	[13]
2	G1		Murat Paşa Cami		
3	G1		Bekdemir Cami	Samsun	[14]
4	G1		Mirliva Muhammed Bey Cami	Bingöl Bağlarpınarı (Temran) Köyü	[15]
5	G2	Dikmeler arası boşluğun tamamen cam ile kapatılması	Pervizoğlu Cami	Erzurum	[13]
6	G2		Malatya Ulu Cami	Malatya/Battalgazi	[16]
7	G2		Alaaddin Bey Cami	Eskişehir	[12]
8	G3	Dikmeler arasının pencereli duvar örgüsü ile kapatılması	Tyana (Kemerhisar) Sinanbey Cami	Niğde İli, Bor İlçesi, Kemerhisar Kasabası	[17]
9	G3		Sandıklı Ulu Cami	Afyon Sandıklı	[18]
10	G3		Mehran Camii	Kastamonu ili Hacımuharrem Köyü	[19]

(a) Dikmeler arası boşluk senaryosuna (G1) örnek görsel-Erzurum Caferiye Cami

(b) Dikmeler arası tamamen cam senaryosuna (G2) örnek-Erzurum Pervizoğlu Cami

(c) Dikmeler arası pencere boşluklu duvar senaryosuna (G3) örnek-Afyon Sandıklı Ulu Cami

Şekil 2. Tipoloji ayrışmalarına örnek görseller

Senaryo kurguları

Araştırma yönteminin üçüncü adımında, literatür verileri sonucu ulaşılan cami son cemaat bölüm tipolojilerine ait senaryo detayları oluşturulmuştur. Senaryoların değerlendirmesinde değişken çeşitliliği hedeflenmekte ve bu sebeple oluşturulan tipolojiler içerisine malzeme alternatifleri dahil edilmektedir.

Dikmeler arasının tamamen cam ile kapatılması olarak tanımlanan G2 kodlu tipolojide, cam malzeme 2 alternatifli ele alınmaktadır. Kurgulanan senaryolarda kullanılan cam, tek cam ve çift cam olmak üzere 2 alternatifli simüle edilmektedir. Dikmeler arasının pencereli duvar örgüsü ile kapatılması olarak tanımlanan G3 kodlu tipolojide ise hem cam hem de cephe malzemesinde çeşitlilik ele alınmıştır. %20 oranında opak/saydam yüzey kabulü benimsenen bu tipolojide, saydam yüzeylerde tek cam ve çift cam alternatifleri kullanılırken opak yüzeylerde tuğla, taş, betonarme ve ahşap duvar kurguları modellenmiştir. Belirtilen alternatifler doğrultusunda oluşturulan senaryo kurgusu Şekil 3'de görselleştirilmiştir.

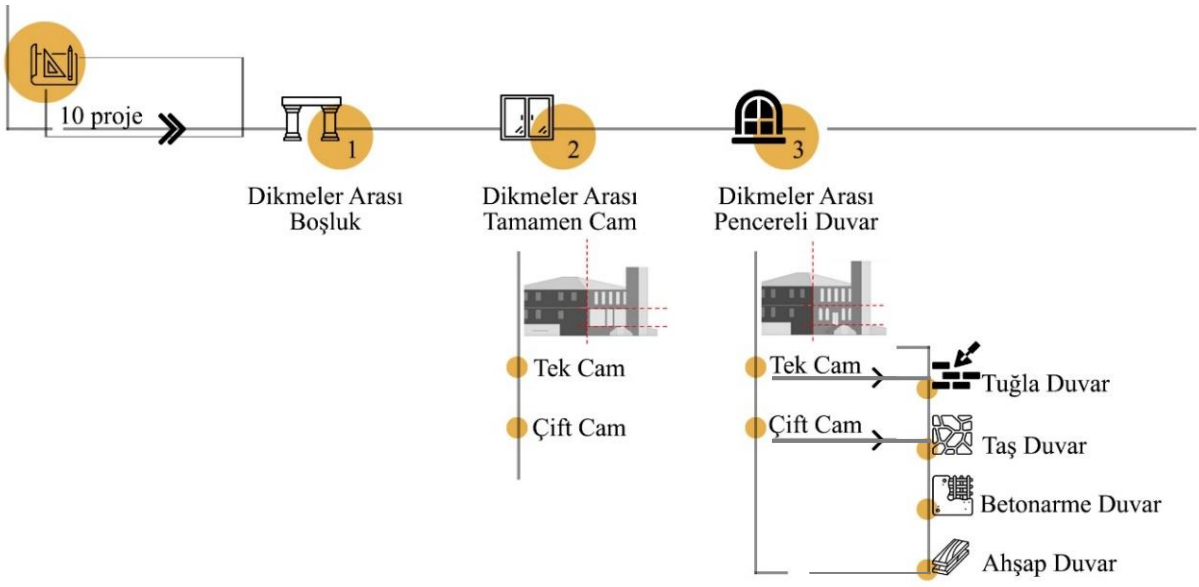

Şekil 3. Tipolojilere ait malzeme değişkenleri

Belirtilen değişkenler sonucu 11 farklı son cemaat bölüm senaryosu elde edilmiştir. Kurgulanan senaryolar, Tablo 2'de detayları paylaşılan baz model üzerinde gerçekleştirilmiştir. Böylece son cemaat bölümü dışındaki camiye ait tüm mekanlar ve mekanlara ait özellikler ortak olmakta, tek değişken son cemaat mekanına ait olmaktadır. Tek değişkenli model kurgusu sayesinde camiye ait enerji tüketimindeki değişiklikler, son cemaat bölümüne uygulanan müdahaleler ile ilişkilendirilebilmektedir. Tablo 4'te senaryo içerikleri paylaşılmıştır.

Tablo 4. Son cemaat senaryo içerikleri

Senaryo No	İçerik		
S1	(G1) Dikmeler arası boşluk		
S2	(G2) Dikmeler arası tamamen cam kurgu		Tek camlı
S3			Çift camlı
S4	(G3) Dikmeler arası pencereli duvar kurgusu	Tek Camlı	Tuğla duvar
S5			Taş duvar
S6			Betonarme duvar
S7			Ahşap duvar
S4'		Çift Camlı	Tuğla duvar
S5'			Taş duvar
S6'			Betonarme duvar
S7'			Ahşap duvar

Tablo 4'te aktarıldığı gibi 2 çeşit cam ve 4 çeşit cephe malzemesi alternatifleri sunulmaktadır. Tek camlı pencere ile kurgulanan S4-S7 senaryolarının çift camlı pencere senaryoları S4'-S7' olarak isimlendirilmekte ve toplamda 11 ayrı son cemaat senaryosu oluşturulmaktadır. Bulgular bölümünde her bir tipoloji ve belirtilen tipolojiye ait alternatif modellerin enerji tüketimine etkisi karşılaştırmalı olarak sunulmakta ve etki potansiyelleri yorumlanmaktadır.

Bulgular

Bu bölümde ilk olarak caminin özgün formu olarak kabul edilen dikmeler arası boşluklu, revak tipolojisinin korunduğu senaryoya (S1) ait enerji tüketimi paylaşılmıştır (Tablo 5). Bu senaryo, minimum müdahale içeriğine sahip olmasından dolayı baz model olarak kabul edilmiş ve diğer senaryoların yorumlanmasında referans niteliği taşımıştır. Tablo 3'te binaya ait ısıtma, soğutma, aydınlatma tekil enerji tüketimleri, bu tekil enerji yüklerinin toplam enerji tüketimindeki oranı (tekil yük dağılımı) ve toplam enerji tüketimi paylaşılmıştır. Enerji yüklerinin ayrı olarak belirtilmesi, senaryo değişikliklerinin tekil yüklere etkisini sunmaktadır.

Tablo 5. Senaryo 1'e ait bina enerji tüketim verileri

Senaryo No	Senaryo İçerik	Isıtma	Soğutma	Aydınlatma	Toplam Enerji Tüketimi
		(kWh/m^2-yıl)			
S1	Dikmeler arası boşluk	34.20	287.80	114.40	436.40
Tekil yük dağılımı		%8	%66	%26	%100

Çalışmanın referans noktası olarak kabul edilen ve herhangi bir müdahale uygulanmamış, dikmeler arası boşluklu yapıya sahip bina simülasyon verileri (S1) Tablo 5'teki gibidir. Paylaşılan veriler, boşluklu kullanıma sahip, yarı açık mekanlı cami yapısının bina enerji tüketim verilerini

sunmuştur. Bu veriler, son cemaate uygulanacak müdahale alternatiflerindeki değişimler için gereklidir. Yıllık toplam enerji tüketiminin %66'sı bina soğutma yükü kaynaklı bulunmuştur. En düşük enerji yükü ısıtma sistemine ait olup toplam bina enerji tüketiminde %8'lik bir paya sahiptir. Aydınlatma için tüketim miktarı ise toplam tüketimin %26'sına denk gelmektedir (Tablo 5).

Son cemaat bölümünün dış ortam koşullarından korunması amacıyla kapatılması, çalışma içerisinde iki ayrı kurguda ele alınmıştır. Dikmeler arasının tamamen cam ile kapatılması (Şekil 4a) ve dikmeler arasının duvar örgüsü ile kapatılması (Şekil 4b) iki farklı senaryo başlığı olarak test edilmektedir.

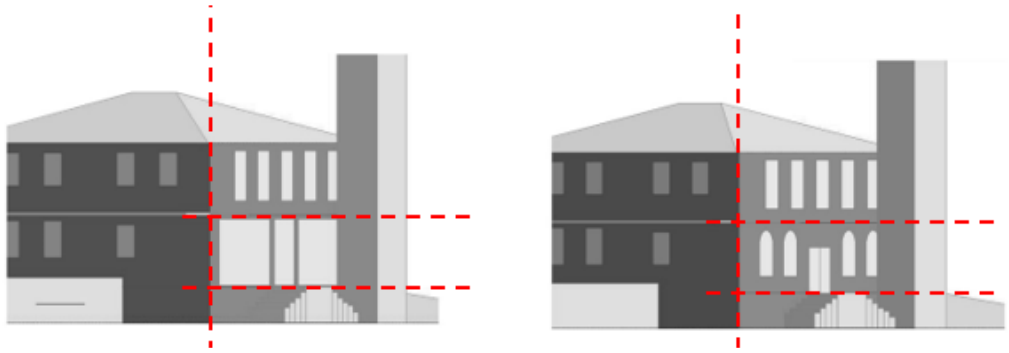

(a) Dikmeler arası cam (b) Dikmeler arası pencereli duvar

Şekil 4. Son cemaat bölümünün kapatılmasına ait senaryo görselleri

Tablo 6. Dikmeler arası tamamen cam ile kapatılmış senaryolara ait bina enerji tüketim verileri

Senaryo No	**Senaryo İçerik**		**Isıtma**	**Soğutma**	**Aydınlatma**	**Toplam Enerji Tüketimi**	**Baz Model Farkı**
				(kWh/m^2-yıl)			
S1	Dikmeler arası boşluk		34.20	287.80	114.40	436.40	
Tekil yük dağılımı			%8	%66	%26	%100	
S2	Dikmeler arası tamamen cam	Tek Camlı	45.70	233.80	114.40	393.90	
Tekil yük dağılımı			%12	%59	%29	%100	%10
S3		Çift Camlı	36.30	187.10	114.40	337.80	
Tekil yük dağılımı			%11	%55	%34	%100	%23

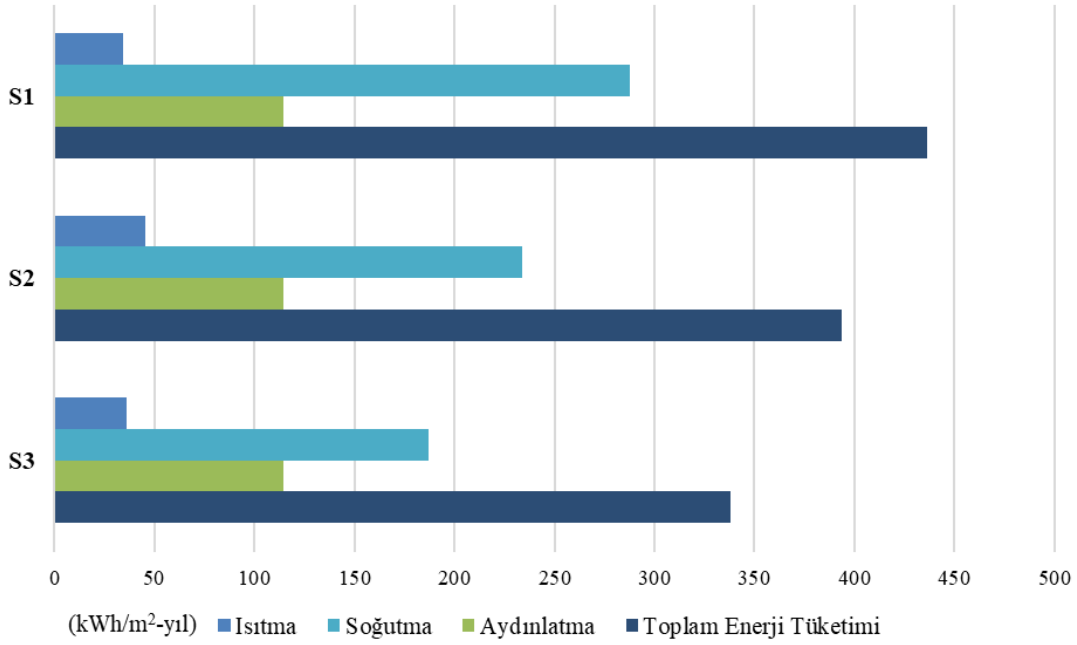

Şekil 5. Dikmeler arası tamamen cam ile kapatılmış senaryolara ait bina enerji tüketim grafiği (kWh/m2-yıl)

İlk kurgu olan dikmeler arasının restorasyon sonrası tamamen cam malzeme ile kapatılmasında malzeme alternatifi olarak tek camlı (S2) ve çift camlı (S3) kullanılmıştır. Tablo 6 sunumunda görüldüğü gibi dikmeler arasının cam malzeme ile kapatılması, binaya ait enerji tüketiminde iyileşme sağlamaktadır. Tek cam ve çift cam uygulamalarının her iki alternatifinde de baz model tüketiminde düşüş tespit edilmektedir. Dikmeler arasında tek cam ve çift cam uygulamalarının karşılaştırılmasına bakıldığında, tek cam kullanımında %10'luk iyileşme sağlanırken çift cam kullanımının bina enerji tüketimi iyileştirmesinde %23'lük oranda etki potansiyeli gözlenmektedir (Tablo 6). İki alternatifli senaryoda en yüksek enerji tüketimi soğutma kaynaklıdır. Çift cam kullanımında (S3) hem ısıtma hem de soğutma yükünde iyileşme sağlanmaktadır. Son cemaat bölümünün cam malzeme ile kapatılması bina ısıtma yükünde artışa, soğutma yükünde ise düşüşe sebep olmaktadır (Şekil 5). Bu durum, özgün yapıda ara mekan olarak konumlanan son cemaat bölümünden yapı iç mekanına ısı geçişinin varlığını ve bu mekanın kapatılması durumunda iç mekandaki sıcaklık değerlerinde düşüş gözleneceğini göstermektedir.

Dikmeler arası boşluklu kullanım (S1) ve dikmeler arasının tamamen cam ile kapalı kullanımlarında (S2-S3) yıllık aydınlatma enerji tüketimleri aynı hesaplanmıştır. Bu durum, simülayon modelindeki yapay aydınlatma sisteminin, varsayılan kullanım programı gereği günışığına duyarlı bir kontrol (daylight-linked dimming/on-off) mekanizması ile ilişkilendirilmemesi kaynaklıdır. Bu nedenle, iç mekana giren doğal ışık miktarındaki farklılıklar aydınlatma enerjisine yansımamış, sunulan tüm senaryolarda aynı tanımlı aydınlatma güç tüketim profili çalışmıştır. Günışığı kontrollü sistemler kullanılmadığı sürece, mimari açıklık ve şeffaflık değişkenlerinin elektrikli aydınlatma yüküne sınırlı etkisi Li ve Lam'in ve Reinhart'ın çalışmalarında belirtilmiştir [20, 21]. Ek olarak, çalışmada kullanılan cam alternatiflerinin görünür ışık geçirgenliği değerlerinin birbirine yakın olması ve son cemaat bölümündeki pencere alanının toplam kullanım alanı içerisindeki sınırlı oranı, günışığı katkısının aydınlatma yüküne etkisini azaltmıştır.

Ele alınan bir diğer tipoloji olan dikmeler arasının duvar ile kapatılması, çalışma içerisinde 4 farklı malzeme değişkeni ile kurgulanmaktadır. Tuğla, betonarme, ahşap ve taş malzemelerinin test edildiği senaryolara duvar üzerindeki pencere açıklıklarında tek ve çift cam alternatifleri dahil edilmiş ve 8 farklı senaryo elde edilmiştir. Tek cam kullanımı ile oluşturulan senaryoların baz model enerji tüketimindeki iyileştirme etkisi benzer bulunmuştur. Duvar malzemesinde taş seçimi ile %9, betonarme duvar sistemi ile %8, tuğla duvar örgüsü ile %7, ahşap duvar sisteminde %6 verim sağlamıştır. Dörtlü duvar malzeme alternatifi içerisinde enerji tüketimindeki en yüksek iyileşme oranı taş duvar ile en düşük iyileşme oranı ahşap duvar ile gözlenmiştir (Tablo 7).

Tablo 7. Senaryolara ait enerji tüketim verileri

Senaryo No	Senaryo İçerik			Isıtma	Soğutma	Aydınlatma	Toplam Enerji Tüketimi	Baz Model Farkı
				(kWh/m^2-yıl)				
S1	Dikmeler arası boşluk			34.20	287.80	114.40	436.40	
Tekil yük dağılımı				%8	%66	%26	%100	
S4	Dikmeler arası pencereli duvar	Tuğla Duvar	Tek Camlı	46.80	212.20	145.50	404.60	%7
Tekil yük dağılımı				%12	%52	%36	%100	
S5		Betonarme Duvar		43.50	212.90	145.50	401.90	%8
Tekil yük dağılımı				%11	%53	%36	%100	
S6		Ahşap Duvar		48.40	215.70	145.50	409.60	%6
Tekil yük dağılımı				%12	%53	%35	%100	
S7		Taş Duvar		42.80	207.90	145.50	396.10	%9
Tekil yük dağılımı				%11	%52	%37	%100	
S4'		Tuğla Duvar	Çift Camlı	38.80	176.40	145.50	360.70	%17
Tekil yük dağılımı				%11	%49	%40	%100	
S5'		Betonarme Duvar		50.20	179.70	145.50	375.30	%14
Tekil yük dağılımı				%13	%48	%39	%100	
S6'		Ahşap Duvar		40.40	179.60	145.50	365.60	%16
Tekil yük dağılımı				%11	%49	%40	%100	
S7'		Taş Duvar		34.80	171.70	145.50	352.00	%19
Tekil yük dağılımı				%10	%49	%41	%100	

Son cemaat bölümüne eklenen cephe üzerindeki pencerelerde çift cam kullanımının farklı duvar malzemelerindeki analizinde enerji tüketiminde en yüksek iyileşme yine taş duvar ile sağlanırken bu sefer sıralama tuğla, ahşap ve betonarme şeklindedir. En düşük iyileşme potansiyeli betonarme duvarda görülmekte olup cam malzeme değişiminin duvar seçimindeki iyileşme potansiyelinde etkin olduğu gözlenmektedir (Tablo 7). Tablo 7 ile aktarılan verilerin görsel aktarımı sunulan Şekil 6'da senaryolara bağlı en etkin değişim, soğutma yükünde gözlenmiştir. Baz modele göre soğutma yükünde en verimli iyileştirme çıktısı tuğla duvar uygulamasındadır. Baz model tüketim verileri ile

karşılaştırıldığında, son cemaat bölümünün kapatılması ısıtma yükünde artışa sebep olmuş ve tüketim farkı tüm senaryolarda gözlenmiştir. Bu farkın temel nedeni, ilk senaryo olarak sunulan baz modelde (S1) son cemaat bölümünün yarı açık bir mekan olarak değerlendirilmesi ve bu nedenle ısıtma yükü hesaplamalarına dahil edilmemiş olmasıdır. Son cemaat bölümün kapatıldığı alternatif senaryolarda, söz konusu alan koşullandırılmış hacme dahil olmakta ve bu nedenle ısıtma yükünde artış gözlenmektedir.

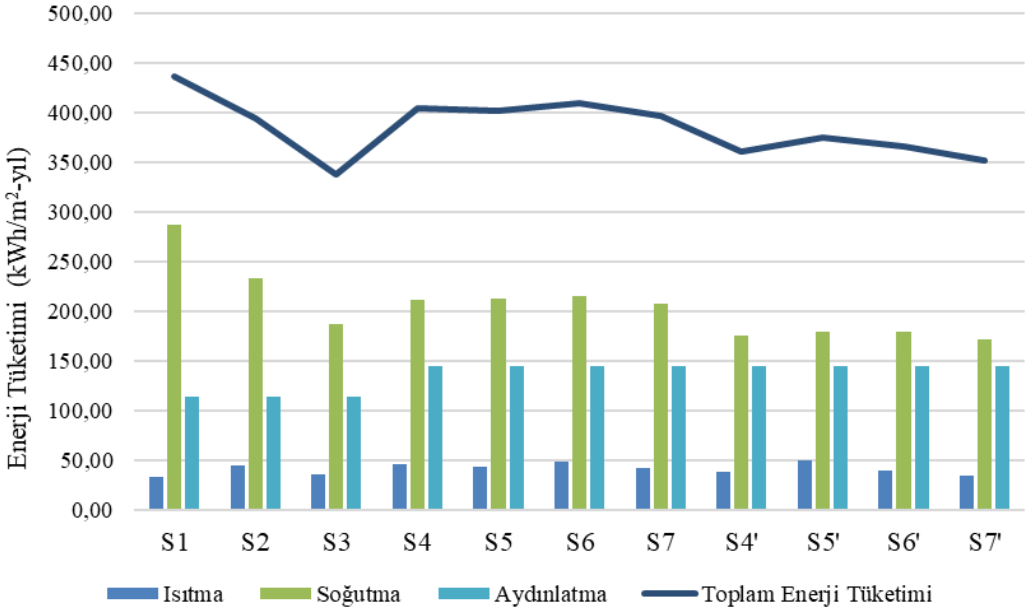

Şekil 6. Senaryolara ait enerji tüketim verileri

Aydınlatma yüküne dair genel değerlendirmede, S1-S3 senaryoları için aydınlatma kontrol algoritmasının günışığına duyarlı olmaması sebebi ile tüketim farkının gözlenmemesi bulgusu, dikmeler arası pencereli duvar kurguları için de geçerli bulunmuştur. Benzer şekilde S4-S11 senaryolarında duvar malzemesi, cam türü, pencere oranı ve geçirgenlik değerleri birbirinden farklı olsa da, günışığı katkısındaki bu değişimler iç mekan aydınlatma yüküne yansımamış ve ilgili senaryoların aydınlatma enerji tüketimleri ortak bir tüketim değeri olan 145.50 kWh/m²-yıl seviyesinde toplanmıştır. Toplam enerji tüketiminde ise en düşük tüketim değeri, S3 senaryosu doğrultusunda kurgulanan, dikmeler arasının çift cam ile kapatılması sonucu elde edilmiştir (Şekil 6). Tüm son cemaat kapatma senaryoları sonucunda ısıtma yükündeki artış ve soğutma yükündeki düşüş ortak bulgu niteliğindedir.

Tartışma

Enerji verimliliğinde tipoloji etkisi araştırılan çalışma bulgularında tipoloji ile birlikte malzeme seçiminin etki potansiyeli saptanmış ve çalışmaya ait tartışmada tipoloji-malzeme karşılaştırmaları birlikte ele alınmaktadır. Aynı tipolojinin farklı malzemeler ile kurgulandığı senaryolara ait veriler Şekil 7'de paylaşılmakta olup, tipolojide malzeme etkisi bu veriler ile ispatlanmaktadır.

Son cemaat bölümünün tuğla duvar ile kapatıldığı senaryodaki (S4) tek camlı pencere kullanımı baz model enerji tüketiminde %7 iyileşme sağlarken, çift camlı pencere uygulaması ile iyileşme oranı %17'e yükselmektedir. Betonarme duvarda iyileşme oranı çift camlı pencere ile %8'den %14'e yükselmekte, ahşap duvar üzerinde tek camlı pencere ile %6'dan %16'ya verim artışı gözlenmektedir. Aynı tutum taş duvarda da gerçekleşmekte olup, tek camlı pencere kullanılan duvar kurgusu ile %9 iyileşme sağlanırken çift camlı pencere kullanımı ile iyileşme yüzesi %19'a yükselmektedir. Tüm duvarlarda çift camlı pencere kullanımının yüksek potansiyel farkı ele alınan tipolojilerde ortak çıktı sunmaktadır. Mevcut çalışma içerisinde simülasyonu oluşturulan 11 senaryo modeli içerisinde en yüksek iyileşme (%23), son cemaat bölümündeki dikmeler arasının tamamen çift camlı pencere kullanılarak, saydam cephe söz konusu olan modele aittir (Şekil 7).

3 ayrı konsept çerçevesinde gerçekleştirilen 11 senaryo değerlendirmesine göre cam malzemesi olarak çift cam uygulamasının etkin enerji iyileştirme potansiyeli tüm senaryolarda teyit edilmiştir. Mevcut çalışmada ele alınan, dikmeler arası tamamen cam ve dikmeler arası açıklıklı duvar kurgusu karşılaştırmasında kullanılan cam malzemesinin potansiyeli gözlenmekte olup dikmeler arasının çift cam ile kapatılmasının, çift cam pencereli duvar örgü sistemi senaryolarına kıyasla toplam enerji tüketiminde daha yüksek iyileştirme sunduğu gözlenmektedir (Şekil 7). Bu durum, son cemaat bölümünün kapatılmasında tamamen şeffaf cephe projelendirmesinde kullanılan cam malzemenin önemini vurgulamaktadır.

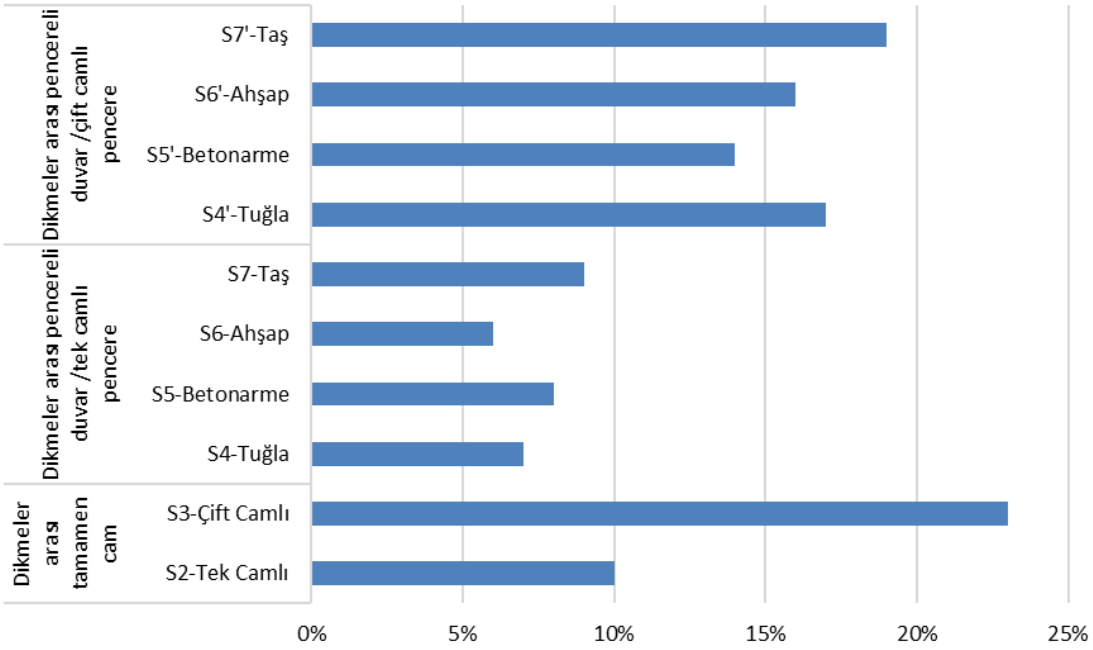

Şekil 7. Baz model enerji tüketimi üzerindeki tüm senaryoların iyileştirme oranları

Sonuç

Mimari koruma alanında tarihi yapıya uygulanacak müdahalelerin öncelikli dikkati özgün yapıya uyum odaklıdır. Uygulanacak yeni malzemenin özgün malzemeye uyumu, mevcut yapı görünüşünün önüne geçmeyecek niteliğe sahip olması, geri dönüştürülebilir imkan sağlaması mimari koruma kriterleri içerisindedir. Bu dikkatler doğrultusunda ele alınacak her proje kendi kapsamında değerlendirilecek olmakla birlikte, cam ve duvar kurgusu ile kapatma alternatiflerinin enerji iyileştirme potansiyelleri çalışma kapsamında örneklenmiştir.

Çalışma bulguları, cami mimarisinde yarı açık kullanıma sahip son cemaat bölümünün kapatılmasının, bina enerji tüketimi açısından anlamlı bir iyileştirme potansiyeline sahip olduğunu göstermektedir. Özellikle çalışma içerisinde sunulan tipoloji-malzeme karşılaştırmaları üzerinden elde edilen sonuçlar, malzeme seçiminin tipoloji kadar belirleyici olduğunu ortaya koymaktadır. Çalışma kapsamında, senaryolarla aktarılan veriler, son cemaat bölümünün tamamen çift cam malzeme ile kapatıldığı modelin diğer duvar kurgulu modellere kıyasla enerji tüketiminde en yüksek iyileşmeyi sağladığını göstermiştir. Bu durum, saydam cephe uygulamalarında kullanılan cam malzemenin enerji performansındaki önemini vurgulamaktadır. Çalışma içerisinde ele alınan tek ve çift cam sınırlılığı, cam teknolojisindeki gelişmeler göz önüne alındığında, gelecek çalışmalar için örnek niteliği taşımaktadır.

Sonuç olarak, mevcut cami restorasyonlarında kullanımına sıklıkla rastlanan son cemaat bölümü kapatma uygulamalarının enerji verimliliği açısından değerlendirilmesi, proje özelindeki karar verme süreçlerinde müdahale kararlarının önemini ve alınan kararların etki potansiyeline dair önemli bir rehber niteliği taşımaktadır. Bu bağlamda çalışma, farklı malzeme ve kurgu alternatiflerinin simülasyon temelli ön değerlendirmelerinin, koruma odaklı tasarım kararlarında enerji etkinliği açısından ne denli belirleyici olduğunu göstermektedir. Özgün yapının kimliğini koruma ilkesiyle uyumlu geliştirilecek enerji etkin müdahale planlamaları için sunulan bu örnek yaklaşımın, gelecekteki çalışmalara yön vermesi, müdahale tercihleri için altlık oluşturması beklenmektedir.

Etik Standartlar Beyanı

"Bu makalenin yazarı, bu çalışmada kullanılan materyal ve yöntemlerin etik kurul izni ve / veya yasal-özel izin gerektirmediğini beyan etmektedir. Bu çalışma, herhangi bir demografik veya kişisel olarak tanımlanabilir bilginin toplanmasını içermemiştir."

Çıkar Çatışması

"Yazar, bu makalede herhangi bir kişi/kurum ile çıkar çatışması bulunmadığını beyan etmektedir."

Kaynaklar

[1] A.B. Atmaca and G. Zorer Gedik, "Development of energy efficient design proposals for air-conditioned mosques: Temperate humid climate case," Heliyon, vol. 9, no. 10, pp. 1-15, October 2023, to be published. DOI: 10.1016/j.heliyon.2023.e20992

[2] D. Kuban, "Osmanlı Mimarisi," Yapı Kredi Yayınları, İstanbul, 2007.

[3] G. Goodwin, "A History of Ottoman Architecture," Thames and Hudson, 1993.

[4] N.G. Çelebi, Ü. Arpacıoğlu, "Evaluation of Energy Performance of Monumental Mosque and Masjids of the Anatolian Seljuk Period: The Case of Konya," Tasarım Kuram Dergisi, vol. 20, no. 42, 2024, pp. 123-135.

[5] N.I. Nordin, A. Misni, "A Comparative Study on the Indoor Thermal Performance of New and Old Mosques," Environment-Behaviour Proceedings Journal, vol 2, no 5, 2017.

[6] H. Al-Rasbi, M. Gadi, Energy Modelling of Traditional and Contemporary Mosque Buildings in Oman. Buildings, vol. 11, no. 7, 2021, pp. 1-20. https://doi.org/10.3390/buildings11070314

[7] A. M. Elshurafaa, A.M. Alsubaieb, A.A. Alabduljabbarb and S.A. Al-Hsaien, "Solar PV on mosque rooftops: Results from a pilot study in Saudi Arabia," Journal of Building Engineering, Vol. 25, September 2019, to be published. DOI:10.1016/j.jobe.2019.100809

[8] A.S.H. Abdallah, "Improved energy consumption and smart eco system for mosques in hot arid climates," Ain Shams Engineering Journal, vol. 14, no. 7, 2023, to be published. DOI:10.1016/j.asej.2022.101997

[9] A. Coşkuner Pamuk, İ.A. Taşdemir and Ü. Arpacıoğlu, "A comparative study on daylight performance of Konya Mosques built in Anatolian Seljuk and Ottoman period," ICONARP International Journal of Architecture & Planning, vol. 8, September 2020, to be published. DOI: 10.15320/ICONARP.2020.145

[10] W.F.M. Yusoff, "Indoor thermal comfort in modern mosque of tropical climate," ICONARP International Journal of Architecture and Planning, vol. 9, no. 2, September 2021, to be published. DOI:10.15320/ICONARP.2021.178

[11] ANSI/ASHRAE Standart 55. "Thermal Environmental Conditions for Human Occupancy," Atlanta, GA, 2013.

[12] E.U. Sarıaydın, B. Güçyeter and H.H. Halaç, "Planning the monitoring process and energy performance evaluation in historical buildings: The case of Tiryakizade Süleyman Ağa Mosque," Journal of the Faculty of Engineering and Architecture of Gazi University, vol. 39, no. 2, pp. 943-958, 2024, to be published. DOI:10.17341/gazimmfd.1218594

[13] İ. Kocaman and M. Gürbüz, "Enhancing seismic performance of historic mosques through retrofitting measures," Engineering Structures, Vol. 301, February 2024, to be published. DOI:10.1016/j.engstruct.2023.117245

[14] B. Ş. Şeker and M. Özkaynak, "Seismic assessment of Historical Timber Bekdemir Mosque," Journal of Multidisciplinary Engineering Science and Technology (JMEST), vol. 8, no.7, pp.14350-14357, July 2021.

[15] B. Bilgili and M. Efeoğlu, "Bingöl Bağlarpınarı (Temran) Köyü Mirliva Muhammed Bey Camii Ve Haziresi'nin koruma sorunları ve restorasyon önerileri" TÜBA-KED Türkiye Bilimler Akademisi Kültür Envanteri Dergisi, vol. 28, pp. 31-48, September 2023, to be published. DOI: 10.22520/tubaked.1274427

[16] A.A. Akyol, E. Aksoy and Y. K. Kadıoğlu, "Malatya Ulu Cami mimari, dekoratif ve yapısal malzemelerinin arkeometrik karakterizasyonu," Amisos, vol. 13, pp. 274-298, Decembe, 2022, to be published. DOI:10.48122/amisos.1175555

[17] E. Efe Yavaşcan, S. Akçaözoğlu and O. Doğanay, "Tyana (Kemerhisar) Sinanbey Cami koruma ve restorasyon önerisi," Nevşehir Hacı Bektaş Veli Üniversitesi SBE Dergisi, Vol. 13, pp. 286-314, October 2023, to be published. DOI:10.30783/nevsosbilen.1323137

[18] P. Usta, "Tarihi ve kültürel yapıların korunması ve incelenmesi; Sandıklı Ulu Cami Örneği," Journal of Architectural Sciences and Applications, vol. 4, no. 2, pp. 201-209, September 2019, to be published. DOI:10.30785/ mbud.431909

[19] E. Aksoy, "A forgotten structure in the rural setting of Kastamonu/Turkey: Documentation, restitution and restoration proposal for Mehran Mosque," Case Studies in Construction Materials, vol. 20, July 2024, to be published. DOI: 10.1016/j.cscm.2024.e03096

[20] D.H.W. Li and J.C. Lam, " Evaluation of lighting performance in office buildings with daylighting controls," Energy and Buildings, vol. 33, no. 8, pp. 793-803, 2001, to be published. DOI: 10.1016/S0378-7788(01)00067-6.

[21] C.F. Reinhart, " Lightswitch-2002: a model for manual and automated control of electric lighting and blinds," Solar Energy, vol. 77, no. 1, pp. 15-28, 2004, to be published. DOI: 10.1016/j.solener.2004.04.003.

Dicle University
Journal of Engineering
https://dergipark.org.tr/tr/pub/dumf
duje.dicle.edu.tr

Araştırma Makalesi / Research Article

Askı Maddesi Boyutunun Askı Maddesi Konsantrasyonu Üzerindeki Etkisinin Doğrusal Karma Regresyon Modeli ile Analizi

Analysis of the Effect of Suspended Sediment Particle Size on Suspended Sediment Concentration Using Linear Mixed-Effects Regression Model

Eyyup Ensar Başakın[1*]

[1] İstanbul Teknik Üniversitesi, İnşaat Mühendisliği Bölümü, basakin@itu.edu.tr
ORCID: https://orcid.org/0000-0002-9045-5302

MAKALE BİLGİLERİ

Makale Geçmişi:

Geliş 3 Eylül 2025
Revizyon 16 Ekim 2025
Kabul 19 Ekim 2025
Online 30 Aralık 2025

Anahtar Kelimeler:

Askı Maddesi, Karma Etki Modeli, Dane Çapı, Hidrolik

ÖZ

Açık kanal akımlarında askı maddesi miktarının artması hidrolik ve inşaat mühendisliği açısından önemli bir problemdir. Bu artış, rezervuar kapasitelerinin azalmasına, su yapılarının zamanla aşınmasına, su kalitesinin giderek bozulmasına ve sucul yaşam alanlarının zarara uğramasına yol açabilir. Bu nedenle, askı maddesi konsantrasyonunun doğru bir şekilde tahmin edilmesi, etkili sediment yönetimi, erozyon kontrolü ve su kaynakları sistemlerinin sürdürülebilirliği için kritik öneme sahiptir. Bu çalışmada, birden fazla laboratuvar deneyinden derlenmiş bir veri kümesi kullanarak, dane çapının askı maddesi konsantrasyonu üzerindeki etkisi araştırılmıştır. Geleneksel doğrusal regresyon (LM) temel tahminler sağlarken, deneysel gruplardaki farklılıklardan kaynaklanan değişkenliği yakalamada başarısız olur. Bunu ele almak için, dane çapı için rastgele etkilere sahip doğrusal karma etkili modeller (LMM) kullanıldı ve diğer hidrolik ve geometrik parametreleri (örneğin, debi, genişlik, derinlik, sıcaklık, eğim) sabit etkiler olarak ele alındı. LMM, LM modeli için 0.24 olan koşullu R^2 değeriyle karşılaştırıldığında yaklaşık 0.74'lük bir değer elde etmiş ve önemli ölçüde daha düşük Akaike bilgi kriteri ve Bayesçi bilgi kriteri değerleri göstererek üstün bir model uyumu göstermiştir. Sonuçlar, debi, eğim, derinlik ve dane çapının askı maddesi konsantrasyonunu önemli ölçüde etkilediğini, ancak yatak genişliği ve sıcaklığın etkilemediğini ortaya koymaktadır. Bu bulgular, birden fazla deneysel kaynaktan gelen sediment konsantrasyonu veri kümelerini analiz ederken grup düzeyinde rastgele etkilerin dahil edilmesinin gerekliliğini vurgulamaktadır.

ARTICLE INFO

Article history:

Received 3 September 2025
Received in revised form 16 October 2025
Accepted 19 October 2025
Available online 30 December 2025

Keywords:

Suspended Sediment, Mixed Model, Particle Size, Hydraulics

Doi: 10.24012/dumf.1776879

* Sorumlu Yazar

ABSTRACT

The increase in suspended sediment concentration (SSC) in open channel flows poses significant challenges in hydraulic and environmental engineering. Such increases can lead to reduced reservoir capacities, gradual abrasion of hydraulic structures, deterioration of water quality, and damage to aquatic habitats. Therefore, accurately predicting SSC is critical for effective sediment management, erosion control, and the sustainability of water resource systems. In this study, a dataset compiled from multiple laboratory experiments was utilized to investigate the effect of grain size on SSC. While traditional linear regression (LM) provided baseline estimates, it failed to account for the variability arising from differences among experimental groups. To address this, linear mixed-effects models (LMM) with random effects for grain size and fixed effects for other hydraulic and geometric parameters (e.g., discharge, width, depth, temperature, slope) were applied. The LMM achieved a conditional R^2 of approximately 0.74, compared to 0.24 for the LM model, and exhibited substantially lower Akaike and Bayesian information criterion values, indicating superior model performance. The results revealed that discharge, slope, depth, and grain size significantly influence SSC, whereas channel width and temperature showed no significant effects. These findings highlight the necessity of incorporating group-level random effects when analyzing sediment concentration datasets derived from multiple experimental sources.

Giriş

Nehirlerde veya yapay kanallarda meydana gelen katı madde birikimi önemli mühendislik problemlerine sebep olabilmektedir [1]. Rüzgâr veya yüzeysel akış aşındırmaları sonrası, yer değiştiren, nehirlere dahil olan ve zamanla su kütlelerinin içinde veya dibinde biriken, farklı dane boyutuna sahip partiküller sediment olarak adlandırılmaktadır. Nehir sedimentleri, amorf veya zayıf kristalli mineral parçacıkları, organik madde ve biyolojik maddelerden (biyofilmler, bakteriler, virüsler ve biyomakromoleküller) oluşan heterojen agregalar ve

bileşik yapılardır [2]. Nehirlerdeki akış hızlarının yükselmesi ile birlikte dibe çökmeyen ve su içinde taşınan, genellikle silt ve kil boyutundaki sedimentler ise askı maddesi olarak tanımlanmaktadır [3]. Yağış, kar erimesi, buzul erimesi ve yeraltı suyu akışının birleşimi, nehrin debisini kontrol eder ve bu da nehrin taşıma kapasitesini belirler. Yüksek akışlar, sedimenti askıda tutarak taşınmasına olanak tanır ve kanal erozyonu [4] yoluyla ek sediment girişlerine ve nehir yatağında depolanmış parçacıkların yeniden askıda kalmasına yol açabilir [5]. Bu parçacıkların, kum ve çakıl gibi kohezyonsuz malzemelerin veya çamur veya kil gibi kohezyonlu malzemelerin, doğal veya insan yapımı bir kanalda, bir akışkan içinde hareketi ise sediment taşınımı olarak tanımlanmaktadır [6]. Askı maddelerinin zamanla nehirlerde ve akabinde rezervuarlarda birikmesi sonucunda, doğal ekosistem ve mühendislik yapıları olumsuz şekilde etkilenebilmektedir. Aşırı konsantrasyonlar, su kalitesinde düşüşe, şeffaflığın ve güneş ışığının nüfuz etmesinde azalmaya ve balıkların ve diğer su canlılarının solungaçlarının tıkanmasına yol açtığı için nehir ekosistemleri ve su canlıları üzerinde olumsuz etkilere neden olabilir [7]. Bu parçacıklar suyun bulanıklığını artırmakla kalmaz, aynı zamanda arıtma süreçlerini zorlaştırarak maliyetleri de yükseltir [8]. Hidrolik ve su kaynakları mühendisliğinde, barajlar ve rezervuarlar gibi hidrolik yapıların kurulumundan önce, taşınan sediment hacminin tahmini önemli bir konudur. Bir rezervuarın ekonomik ömrü, sedimentlerin ölü hacmi doldurmasıyla ters orantılıdır. Sediment hacminin yanlış veya eksik tahmin edilmesi, yetersiz baraj kapasitesine neden olur ve bu da tarama gibi bakım ve temizlik prosedürleri gerektirir.

Nehir ekolojisi ve su kaynakları mühendisliği açısından, akarsu sistemi içindeki askı madde miktarı ve hareketini karakterize etmek ve bu hareketi yönlendiren doğal ve beşerî güçleri belirlemek önemlidir. Bu sebeple, farklı bağımsız değişken kombinasyonlarını kullanarak nehirlerdeki askı maddesi konsantrasyonunu tahmin etmeye yönelik birçok ampirik denklem geliştirilmiştir. Yang [9], geliştirdiği denklem sayesinde birim akım gücü, kayma hızı, suyun kinematik viskozitesi, katı madde çökelme hızı ve katı madde parçacık dane çapı değerlerini kullanarak askı maddesi konsantrasyonunu tahmin etmeye çalışırken, Molinas ve Wu [10], ise evrensel akım gücü tabirini kullanarak, geniş ve derin akarsulardaki sediment konsantrasyonunu tahmin etmek için ortalama akım hızı, akım derinliği, dane çapı, dane çökelme hızı, dane yoğunluğu ve yerçekimi ivmesi değişkenleri ile bir eşitlik elde etmişlerdir. Shu-Qing Yang [11] ise bu denklemleri geliştirerek katı madde konsantrasyonunu tahmin etmek için, ortalama akım hızı, derinlik, enerji eğimi, akışkan ve dane yoğunluğu, kinematik viskozite, dane çökelme hızı, dane çapı, kanal genişliği ve dane boyu derecesi değerlerini kullanmıştır. Bu denklemlerin yanı sıra doğrusal regresyon (DR) yöntemi ile askı maddesi konsantrasyonunun tahmin edilmesi de mümkündür. Ancak DR yönteminin bazı katı önkoşullara sahip olması (normal dağılım, çoklu doğrusal bağıntı vb.) kullanımını kısıtlamaktadır.

Askı maddesi konsantrasyonunu tahmin etmek için son yıllarda makine öğrenmesi yöntemleri de sıklıkla tercih edilmeye başlanmıştır. Türkiye'de askı maddesi konsantrasyonu çalışmalarında başı çeken araştırmacılardan olan Doğan [12], çalışmasında, laboratuvar deneyleri sonrasında elde ettiği veri setindeki askı maddesi konsantrasyonunu yapay sinir ağları (YSA) ve modifiye edilmiş Einstein yöntemini kullanarak tahmin etmiştir. Doğan [13], bir diğer çalışmasında ise, Aşağı Sakarya nehrinden elde edilen askı maddesi miktarını YSA ve bulanık mantık yöntemlerini kullanarak tahmin etmiştir. Çalışma sonunda, askı maddesi miktarını 0.781 R^2 değeri ile yüksek doğrulukta tahmin ettiğini raporlamıştır. Yine benzer şekilde literatürde birçok ML yöntemini kullanarak askı maddesi konsantrasyonunun tahmin eden çalışma mevcuttur [14,15,16]. Bu çalışmaların çoğu askı maddesi miktarını ya da konsantrasyonunu yüksek doğrulukta tahmin etmiş olsa da bağımsız girdilerin bağımlı değişkeni ne düzeyde etkilediğini araştırmada yetersiz kalabilmektedir.

Bağımsız girdilerin, bağımlı değişken üzerindeki etkileri istatistiksel olarak yorumlamak için önerilen bazı regresyon modelleri mevcuttur. Bu modeller doğrusal karma modeller (LMM) olarak adlandırılır ve modele sabit ve rasgele etkileri ekleyerek bir takım bağımsız değişkenlerin faktör olarak ele alınmasını mümkün kılar. Veri üretim süreci tasarımla belirlenen hiyerarşi ve bağımlılıkları içerdiğinde, LMM, sabit ve rassal etkileri aynı çatı altında ele alarak grup-içi ve gruplar-arası varyansı açıkça ayrıştırması, parametre yorumlanabilirliğini koruması ve eksik veriyi MAR varsayımı altında maksimum olabilirlik ile doğrudan ele alabilmesi nedeniyle hem sağlam bir kıyas çizgisi hem de pratik bir yaklaşım olmayı sürdürmektedir [17,18]. Nitekim LMM'ler için marjinal ve koşullu R^2 tanımlarının alan yazında standartlaşması da, uygunluk ve açıklayıcılık ölçütleri açısından bu modellerin süregelen önemini vurgulamaktadır [19]. Bu sayede grup içi etkileşimler modele daha doğru yansıtılır ve daha yüksek koşullu R^2 değerlerinin elde edilmesine olanak sağlanır.

Hava kirleticilerinin zamansal ve mekânsal olarak modellendiği bir çalışmada, LMM, rastgele orman (RF), XGBoost, LightGBM ve YSA modelleri kullanılmıştır. Farklı birçok bağımsız değişken kullanılan ve günlük/aylık/yıllık ölçekte tahmin yapılan çalışmada günlük ölçekte boosting modelleri en yüksek doğruluğa ulaşırken LMM hem rastgele hem mekânsal çapraz doğrulamada üçüncü olup RF ve YSA'yı geride bırakmıştır [20]. Hidrolojik bağlantılılık ve su kalitesi arasındaki ilişkinin incelendiği bir çalışmada, XGBoost ile LMM yöntemleri karşılaştırmalı olarak kullanılmıştır. XGBoost'un doğrusal olmayan etkileri yakalamada esnek olduğu; fakat veri hiperparametrelere karşı duyarlı olduğu, LMM'nin ise mekânsal farklılıkları rastgele etkiler ile iyi yakalayıp ilişkiyi izole ettiğini raporlamışlardır [21].

Gili vd. çok kademeli toprak örneklemesinde, saha/parsel/transekt/nokta düzeylerinde LMM kurularak rastgele etkiler birlikte modellenmiştir. Düzeltilmiş olasılık oran testleri ile daha zengin rastgele etki yapısının

gerekli olduğunu, böylece vejetasyon yamaları arasındaki farkların klasik ANOVA'nın kaçırdığı durumlarda yakalanıp sabit etki kestirimlerinin daha hassaslaştığını göstermiştir [22]. Sydney'de bulunan iki alt havzada toplam fosfor ve toplam azotun aylık ölçümlerini, zamansal otokorelasyon içeren doğrusal karma modeller ile tahmin edildiği bir diğer çalışmada, türbiditenin tek başına akımdan daha güçlü bir yordayıcı olduğu ve türbiditeye akıma dayalı türev değişkenler eklendiğinde hatanın belirgin biçimde azaldığı raporlanmıştır. LMM'ler klasik en küçük kareler regresyona göre hem daha düşük hata hem de belirsizliği önyargısız tahmin etme açısından üstün performans verdiği sonucuna varmışlardır [23]. Ayrıca LMM'ler, yağış tahmini [24], toprak su içeriği tahmini [25] ve içme suyundaki zararlı maddelerin tespiti [26] gibi alanlarda güncel olarak kullanılmıştır.

Bu çalışmada, Government of West Bengal [27], Daves [28], Ho [29] ve Mavis vd. [30] tarafından farklı zamanlarda yapılan deney örnekleri kullanılarak askı maddesi konsantrasyonunun LMM ile tahmin edilmesi amaçlanmıştır. Ayrıca klasik doğrusal regresyon modelleri ile mukayese yapılarak, LMM yönteminin üstün yönleri vurgulanmıştır. Çalışmada askı maddesi konsantrasyonun, dane çapı tarafından nasıl kontrol edildiği analiz edilmiş, bu değişkenler için sabit etki ve rasgele etki modelleri kurulmuştur. Bu modeller ışığında askı maddesi konsantrasyonunun fiziksel doğası daha anlaşılır hale gelmiştir.

Materyal ve Metot

Kullanılan veri seti Compilation of Alluvial Channel Data: Laboratory and Field adlı raporda bulunan deney setleri arasında yer almaktadır. Rapor William R. Brownlie tarafından 1981 yılında yazılmıştır [31]. Bu raporda 5263 adeti laboratuvar deneyi, 1764 adeti ise nehirlerden alınan ölçümlerden meydana gelen toplam 7027 veri mevcuttur. Veri setleri 9 adet bağımsız değişken ve bir adet bağımlı değişkenden meydana gelmektedir (Tablo 1).

Tablo 1. Veri setlerinde bulunan değişkenler ve birimleri

Değişkenler	Açıklama	Birim
Su Debisi	Birim alandan geçen, saniyedeki su hacmi	l/s
Kanal Genişliği	Akışın olduğu kanalın genişliği	m
Su Derinliği	Akış sırasında meydana gelen su derinliği	m
Enerji Eğimi	Birim ağırlıktaki suyun enerji kaybının akış yönündeki mesafeye oranı	‰
Dane Boyutu (medyan)	Sediment tane boyu dağılımında, kütlenin %50'sinin daha küçük, %50'sinin daha büyük olduğu tane çapıdır. Sediment boyut dağılımının ortanca değeri	mm
Dane Boyutu Geometrik Standart Sapması	Sediment tane boyunun geometrik standart sapması	mm
Katı Madde Özgül Yoğunluğu	Sediment yoğunluğunun, referans sıvının yoğunluğuna (genellikle 4 °C'deki saf su) oranı.	-
Askı Maddesi Konsantrasyonu	Sediment yükünün kütlesinin, su–sediment karışımının toplam kütlesine oranıdır. Kütle esasına göre ppm (parts per million) olarak ifade edilir.	ppm
Sıcaklık	Su sıcaklığı	℃
Yatak Şekli	Akarsu yatağı yüzeyinde akım ve sediment etkileşimi sonucunda oluşan morfolojik şekillerin genel adıdır. 0 ile 8 arasında değerler almakta.	-

Bu çalışmada, laboratuvar deney setleri kullanılmış ve askı maddesini konsantrasyonunu tahmin etmeye yönelik geliştirilen modellerde girdi olarak su debisi (debi), kanal genişliği (genişlik), su derinliği (derinlik), enerji eğimi (eğim), dane boyutu ve sıcaklığın kullanılması tercih edilmiştir. Kullanılan veri setlerinde yatak şekli aynı olan veriler tercih edilmiştir ve yatak şekli bağımsız değişken olarak modele dahil edilmemiştir. Ayrıca dane boyutu geometrik standart sapması ve katı madde özgül yoğunluğu da modellemede kullanılmamıştır. Çalışmada kullanılan bağımsız değişkenlerin seçimi için literatürde daha önce yapılan çalışmalardan faydalanılmıştır. Doğan [12] yaptığı çalışmada debi, eğim ve dane çapı değişkenlerini model dahil etmiştir. Bu çalışmada da benzer etkilerin araştırılması hedeflenmiştir. Ek olarak genişlik, derinlik ve sıcaklık değişkenleri de modellere dahil edilmiştir. Her ne kadar genişlik ve derinlik değerleri benzer etki yaratacağı belirtilse de [32] karma modellerin çoklu doğrusal bağıntıya karşı dayanıklı yapısı nedeniyle modele dahil edilmesi kararlaştırılmıştır. Modellemede kullanılan bağımsız değişkenlere ve bağımlı değişkene ait tanımlayıcı istatistikler Tablo 2 de paylaşılmıştır.

Tablo 2. Kullanılan veri setine ait tanımlayıcı istatistik bilgiler

Değişken	Mak.	Min.	Ortalama	Std. Sap.	Çarpıklık	Değişim Katsayısı (%)
Su Debisi (l/s)	165.6	0.87	32.41	26.4	1.88	81.46
Kanal Genişliği (m)	1.37	0.39	0.82	0.21	0.74	25.83
Su Derinliği	0.3	0.009	0.071	0.04	1.49	66.38
Enerji Eğimi	10.1	0.11	3.93	3.12	0.89	79.42
Dane Boyutu	4.18	0.15	2.24	1.25	0.03	55.84
Sıcaklık	44.4	1.5	25.5	5.57	-1.41	21.78
Konsantrasyon	2361	0.2	220.5	333	2.8	151.08

En yüksek değişim katsayısına sahip değişken askı maddesi konsantrasyonu onu takiben su debisi ve eğim olmuştur. Ayrıca çarpıklık değerleri incelendiğinde dane boyutu hariç diğer tüm değişkenlerin normal dağılımdan uzak olduğu yorumu yapılabilir. Analiz öncesi farklı birimlere sahip değişkenlerin analiz edilmesini kolaylaştırmak ve laboratuvar arası farklılardan kaynaklanan deneysel heterojenliğin azaltılması için tüm veriler standartlaştırılmıştır. Standartlaşma işlemi Denklem (1) yardımıyla gerçekleştirilmiştir.

$$z = \frac{x - \mu}{\sigma} \tag{1}$$

Burada: x standartlaştırılacak değer, μ değişkenin aritmetik ortalaması, σ değişkenin standart sapması z standartlaştırılmış değerdir. Tüm değişkenlere ait dağılımlar Şekil 1'de paylaşılmıştır. Grafikler

incelendiğinde neredeyse hiçbir değişkenin normal dağılmadığı teyit edilmiştir.

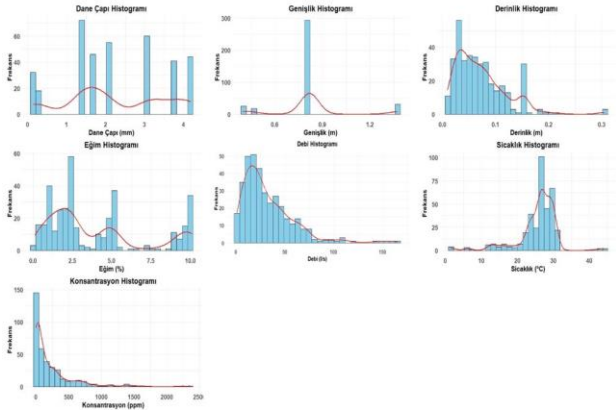

Şekil 1. Değişkenlere ait dağılımlar

Değişkenlerin standartlaştırılması sonrası kutu grafikleri elde edilerek, farklı birimlerdeki değişkenlerin daha kolay şekilde karşılaştırılması sağlanmıştır. Şekil 2'de verilen standartlaştırılmış kutu grafikleri, değişkenlerin göreli dağılım özelliklerini karşılaştırmalı olarak ortaya koymaktadır. Gözlemler, medyanların çoğunun 0 civarında kümelenmesiyle standardizasyonun tutarlı biçimde uygulandığını göstermektedir. Konsantrasyon değişkeni belirgin pozitif çarpıklık ve ağır üst kuyruk sergilemekte, çok sayıda yüksek aykırı değer içermektedir. Bu durum olası olay temelli piklere ve ağır kuyruk davranışına işaret eder. Benzer biçimde debi değişkeni de üst uçta yoğunlaşan aykırılarla pozitif çarpıklık göstermektedir. Sıcaklık ise alt uçta güçlü aykırılarla negatif çarpık bir yapı sergilemekte; bu örüntü, mevsimsel rejimler, sensör farklılıkları veya veri bütünleştirme kaynaklı sistematik etkilerin varlığını ima eder. Derinlikte orta düzey yayılım ve hafif pozitif çarpıklık gözlenirken, eğim dağılımı nispeten simetrik ve dar yayılımlıdır. Dane ise en dengeli dağılıma sahip olup aşırı uçlar sınırlıdır.

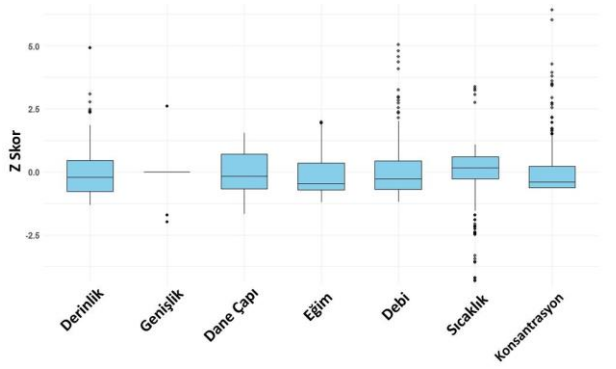

Şekil 2. Standartlaştırılmış verilere ait kutu diyagramları

Değişkenler arasındaki doğrusal ilişkilerin belirlenmesi için korelasyon matrisinden yararlanılmıştır (Şekil 3). Korelasyon katsayılarının hesaplanması için Sperman Korelasyon katsayısı kullanılmıştır. Çünkü Pearson korelasyon katsayısı verinin normal dağıldığı durumda kullanılabilmektedir. Ancak Sperman korelasyon katsayısı sıralı korelasyon hesabı yaptığı için parametrik olmayan bir testtir ve bu çalışmadaki veriler için daha uygundur.

Konsantrasyon ile dane çapı, derinlik ve debi arasında negatif anlamlı korelasyon mevcut iken sıcaklık ile anlamlı olmayan bir ilişki söz konusudur. Genişlik ve eğim ile ise pozitif anlamlı bir ilişki tespit edilmiştir. Korelasyon analizinde hidrolik değişkenler (debi, derinlik, eğim ve dane çapı) arasında yüksek düzeyde çoklu doğrusal bağlantı (eş doğrusallık) tespit edilmiştir. Özellikle debi-derinlik (ρ = 0.87), derinlik-eğim (ρ =-0.75) ve eğim-dane çapı (ρ = 0.57) ilişkileri, bu değişkenlerin birlikte kullanılması durumunda sabit etkilerin tahmininde belirsizlik yaratabileceğini göstermektedir. Ayrıca, farklı deney kurulumları ve araştırmacı grupları arasında sistematik varyasyonların bulunma olasılığı, yalnızca sabit etkilerle kurulan klasik regresyon modellerinin yetersiz kalabileceğini düşündürmektedir. Bu nedenle, grup düzeyindeki heterojenliği hesaba katan LMM tercih edilmesi uygun görülmüştür.

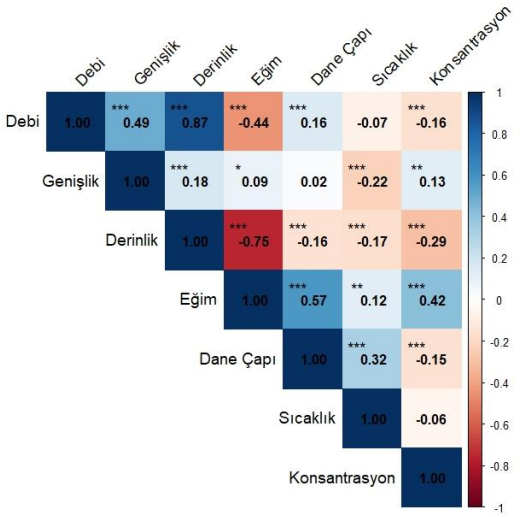

Şekil 3. Korelasyon tablosu (p<0.1*, p<0.05**, p<0.01***)

Çoklu Doğrusal Regresyon

Regresyon analizi, bir hedef değişkeni (bağımlı değişken) ile bir dizi açıklayıcı değişken (bağımsız değişkenler) arasındaki ilişkiyi araştırmak için kullanılan istatistiksel bir yöntemdir. Değişkenler arasında fonksiyonel bir ilişki kurmak için basit yöntemler sağladığı için en sık kullanılan istatistiksel yöntemlerden biridir. Doğrusal regresyon, bir veya daha fazla bağımsız değişkene dayanarak bağımlı değişkeni tahmin eden bir modelleme tekniğidir ve bu tür modeller bilinmeyen parametrelerine doğrusal olarak bağlı olduğundan pratik uygulamalarda en çok kullanılan istatistiksel modeldir. Doğrusal regresyon modeli, basit doğrusal regresyon ve çoklu doğrusal regresyon modeli olmak üzere iki formdan oluşur. Özünde, çoklu doğrusal regresyonlar, birden fazla açıklayıcı değişken içeren sıradan en küçük kareler regresyonunun bir uzantısıdır. Basit regresyon analizi Denklem (2)'de tanımlandığı gibidir.

$$Y = \beta_0 + \beta_1 X_1 + \varepsilon \quad (2)$$

Y bağımlı değişken, X_1 bağımsız değişken, β_0 sabit terim ya da kesişim parametresi, β_1 eğim katsayısı ve ε ise hata terimi ya da artık olarak adlandırılır. Hata terimi, modelin açıklayamadığı kısmı yani tesadüfi hatayı gösterir. Hata teriminin çoğunlukla normal dağılıma sahip olduğu varsayılır, yani ortalaması sıfır ve varyansı sabittir. Çoklu doğrusal regresyona ait genel form Denklem (3)'te verilmiştir.

$$Y = \beta_0 + \beta_1 X_1 + \beta_2 X_2 + \cdots + \beta_n X_n + \varepsilon, \quad i = 1, 2, 3 \ldots . n \tag{3}$$

Çoklu doğrusal regresyon analizi, sonuçlarının geçerliliğini ve güvenilirliğini sağlayan çeşitli temel varsayımlara dayanır. Bu varsayımların anlaşılması ve doğrulanması, doğru model yorumlama ve tahmin için çok önemlidir. Çoklu doğrusal regresyonun temel varsayımı, bağımlı değişken ile bağımsız değişkenler arasında doğrusal bir ilişkinin varlığıdır. Analiz, kalıntıların (gözlemlenen ve tahmin edilen değerler arasındaki farklar) normal dağılım gösterdiğini varsayar. Bağımsız değişkenlerin birbirleriyle çok yüksek oranda ilişkili olmaması esastır; bu duruma çoklu doğrusallık denir. Hata terimlerinin (kalıntıların) varyansı, bağımsız değişkenlerin tüm seviyelerinde tutarlı olmalıdır. Kalıntıların öngörülen değerlere göre dağılım grafiği, koni biçimli bir dağılım gibi, heteroskedastisiteye işaret edebilecek herhangi bir belirgin örüntü göstermemelidir. Hataların bağımsızlığı, doğrusal regresyon modelleri için bir diğer kritik varsayımdır. Artıkların (gözlemlenen ve tahmin edilen değerler arasındaki farklar) birbirleriyle ilişkili olmamasını sağlar. Bu, bir gözlemle ilişkili hatanın başka bir gözlemin hatasını etkilememesi gerektiği anlamına gelir. Hataların ilişkili olması, verilerdeki temel bir örüntünün veya eğilimin model tarafından gözden kaçırıldığına işaret edebilir.

Doğrusal Karma Model

Laird ve Ware [33] tarafından geliştirilen model, yalnızca sabit etkileri ve ilişkisiz hata varsayımını içeren klasik doğrusal regresyon modellerinin aksine, LMM, ilişkili ve bağımlı veriler için rastgele ve sabit etkilerin dahil edilmesiyle oluşturulabilir. Genellikle boylamsal ve gruplanmış veri kümeleri için uygulanırlar. Daha açık bir ifadeyle, LMM'ye iç içe geçmiş/hiyerarşik yapılar dahil edilebilir ve denek veya koşullara ait sonuçlar, rastgele terimler yardımıyla popülasyona genelleştirilebilir. LMM, yanıt değişkenini rastgele ve sabit etkilerle ilişkilendirir ve Denklem (4) ile ifade edilebilir.

$$Y_i = X_i\beta + Z_i u_i + \varepsilon_i \tag{4}$$

$$u_i \sim N(0, D)$$

$$\varepsilon_i \sim N(0, R_i)$$

Y_i i. birime ait gözlemlenen yanıt (bağımlı değişken) değerlerinin vektörü, X_i sabit etkiler tasarım matrisi, β sabit etkilerin katsayıları, Z_i rassal etkiler tasarım matrisi, u_i rassal etkiler vektörü, ε_i hata terimi (modelin açıklayamadığı varyans).

Öncelikle, hata terimleri (ε_i) ortalaması sıfır olan ve varyansı R_i ile ifade edilen normal bir dağılıma sahiptir. Yani modelin açıklayamadığı sapmalar rastgele dağılım gösterir ve farklı gözlemler arasında bu hataların kovaryans yapısı R_i matrisi ile tanımlanabilir. Bu matris simetrik ve pozitif tanımlıdır; böylece farklı varsayımlar veya yapılar için esneklik sağlar. Diğer yandan, rassal etkiler (u_i) sabit etkilerden farklı olarak bireyler arasındaki değişkenliği yansıtır ve istatistiksel bir dağılımdan geldiği kabul edilir. Bu etkiler de ortalaması sıfır ve varyans-kovaryans matrisi D olan normal bir dağılıma sahiptir. Bu D matrisi de simetrik ve pozitif tanımlıdır ve boyutu modele dâhil edilen rassal etki terimlerinin sayısına bağlıdır. Özetle, bu varsayımlar sayesinde model hem gözlemlerdeki rastgele hataları hem de bireyler arası farklılıkları istatistiksel olarak tanımlayarak daha esnek ve gerçekçi bir yapı sunar.

Model Seçim Kriterleri

En uygun regresyon modelinin belirlenmesi için literatürde bazı bilgi kriterleri kullanılmaktadır. Bu kriterlerin ana amacı model karmaşıklığı ile uyum kalitesini dengeleyen en uygun modelin belirlenmesini sağlamaktır. Başlıca kullanılan iki bilgi kriteri Akaike Bilgi Kriteri (AIC) ve Bayesian Bilgi Kriteridir (BIC). Bu kriterler Denklem (5) ve (6)'da tanımlanmıştır.

$$AIC = 2k - 2\ln(L) \tag{5}$$

$$BIC = k(\ln(\mathrm{n}) - 2\ln(L) \tag{6}$$

Denklem (4) ve (5)'te verilen n gözlem sayısını, k parametre sayısını ve L ise maksimum olasılık değerini belirtmektedir. Daha düşük AIC değeri, modelin hem iyi uyum sağladığını hem de gereksiz parametre eklemediğini gösterir. AIC, tahmin odaklı çalışmalar için uygun bir kriterdir ancak küçük örneklemlerde fazla parametre ekleme eğilimi gösterir. Bu durumda düzeltilmiş AIC (AICc) tercih edilir. BIC, AIC'den farklı olarak parametre sayısını daha ağır bir şekilde cezalandırır. Bu nedenle, büyük veri setlerinde daha sade modelleri tercih etme eğilimindedir. Daha düşük BIC değeri, veriye uygun ve gereksiz parametrelerden arındırılmış bir modeli işaret eder [34]. Her iki kriter de maksimum olabilirlik temelli çalışır, ancak odak noktaları farklıdır. AIC, genellikle tahmin doğruluğunu maksimize etmeye çalışırken, BIC model açıklayıcılığını ve sadeliğini ön plana çıkarır [35].

AIC ve BIC kriterleri iki veya daha fazla modelin karşılaştırılmasına olanak verirken, modellerin yeterliliğini/başarısını tek başına ölçen yöntemlerde mevcuttur. Bu yöntemlerden en sık kullanılanlardan ikisi Nash-Sutcliffe (NSE) [36] ve Kling-Gupta (KGE) [37] verimlilik katsayılarıdır. Bu iki katsayı eksi sonsuz ile bir arasında değerler almaktadır. Bir değerine yakın katsayılar modelin iyi tahminler yaptığına işaret ederken, 1 değerinden uzaklaşan (eksi negatife doğru) değerlerin ise kötüleşen modele işaret etmektedir. NSE ve KGE ye ait eşitlikler Denklem (8) ve (9)'da paylaşılmıştır.

Son olarak hataların ne kadar küçük olduğunun tespit edilmesi içinde ortalama karekök hatası (RMSE) metriği

kullanılmıştır. Bu metrik bir modeli tek başına değerlendirmede zayıf kalırken iki modelin karşılaştırmasında güçlü bilgiler sunabilmektedir. RMSE değerinin sıfıra yaklaşması modelin hatasız tahmin yapma eğiliminde olduğunu belirtir.

$$RMSE = \sqrt{\frac{\sum_{i=1}^{n}\left(K_i^{tahmin} - K_i^{gözlem}\right)^2}{n}} \quad (7)$$

$$NSE = 1 - \frac{\sum_{i=1}^{n}\left(K_i^{tahmin} - K_i^{gözlem}\right)^2}{\sum_{i=1}^{n}\left(K_i^{gözlem} - \overline{K}^{gözlem}\right)^2} \quad (8)$$

$$KGE = 1 - \sqrt{(r-1)^2 + (\alpha-1)^2 + (\beta-1)^2} \quad (9)$$

$$r = kor\left(K_{tahmin}, K_{gözlem}\right), \alpha = \frac{\sigma^{gözlem}}{\sigma^{tahmin}}, \quad \beta = \frac{\mu^{gözlem}}{\mu^{tahmin}}$$

Denklem (7), (8) ve (9)'da bulunan K_i^{tahmin} ve $K_i^{gözlem}$ i anındaki tahmin edilen ve gözlenen konsantrasyon değerini, $\overline{K}^{gözlem}$ gözlenen konsantrasyon değerlerinin ortalamasını, r gözlenen ve tahmin edilen konsantrasyonlar arasındaki korelasyon değerini, α değişkenliği, β ortalamadaki önyargıyı ve n toplam gözlem sayısını temsil etmektedir.

Bulgular ve Tartışma

Karma ve normal doğrusal modeller birlikte değerlendirildiğinde, bağımlı değişkeni açıklamada karma modelin çok daha güçlü ve güvenilir bir performans sergilediği görülmektedir. Sabit etkiler incelendiğinde, her iki modelde de debi ve eğim değişkenleri pozitif ve anlamlı etkiler göstermektedir. Tablo 6'da görüldüğü üzere LM modelinde debi katsayısı +171.21 ($p<0.001$) iken, Tablo 3'te sunulan LMM sonuçlarında bu değer +366.09'a ($p<0.001$) yükselmiştir. Benzer şekilde, eğim katsayısı LM modelinde +143.8 ($p<0.001$) iken, LMM modelinde +284.68 ($p<0.001$) olarak hesaplanmıştır. Bu bulgular, karma modelin sabit etkileri daha güçlü bir şekilde yakaladığını ve grup düzeyindeki rastgele farklılıkları hesaba katarak daha kararlı tahminler sunduğunu göstermektedir.

Derinlik değişkeni her iki modelde de anlamlı bir negatif etki sergilemektedir. LM modelinde katsayı -103.37 ($p<0.001$) iken, LMM modelinde bu değer -139.41 ($p<0.001$) olarak bulunmuştur. Bu durum, derinlik arttıkça bağımlı değişkenin azaldığını ortaya koymaktadır. Genişlik değişkeni LM modelinde anlamsız bir katsayıya sahipken ($p=0.344$), LMM modelinde negatif bir eğilim göstermiş ancak istatistiksel anlamlılık sınırında kalmıştır ($p=0.072$). Sıcaklık değişkeni ise LM modelinde anlamlı bir negatif etki gösterirken (-43.84; $p=0.008$), LMM modelinde anlamsız bulunmuştur ($p=0.380$). Bu fark, karma modelin rastgele etkileri hesaba katarak sıcaklığın etkisini daha gerçekçi şekilde değerlendirdiğini düşündürmektedir.

Tablo 3. Karma model (LMM, (1|dane)) sonuçları

Sabit Etkiler	Katsayı	Std. Hata	t değeri	p değeri
Sabit	253.08	80.83	3.13	0.012*
Debi	+366.09	27.06	13.53	<0.001***
Genişlik	-136.33	67.52	-2.02	0.072
Derinlik	-139.41	25.41	-5.49	<0.001***
Eğim	+284.68	18.65	15.27	<0.001***
Sıcaklık	13.58	15.47	0.88	0.380

Tablo 4. Karma modelde rastgele etkiler için varyans ve standart sapma değerleri

Rastgele Etkiler	Varyans	Std. Sapma
Dane Çapı	56.741	238.2
Artık	48.562	220.4

Modelin rastgele etkileri Tablo 4'te verilmiştir. Dane çapı bazlı rastgele kesişimlerin varyansı 56.741 ve standart sapması 238.2 olarak hesaplanmış, artık varyansı ise 48.562 ve standart sapması 220.4 olarak belirlenmiştir. Bu sonuçlar, dane çapı grupları arasında bağımlı değişken düzeyinde önemli farklılıklar olduğunu ve grup bazlı değişkenliğin modele dahil edilmesinin modelin açıklayıcılığını artırdığını göstermektedir.

Model performansı karşılaştırıldığında Tablo 7'de verilen LM sonuçlarına göre R^2=0.25 ve düzeltilmiş R^2=0.24 iken, Tablo 5'teki LMM sonuçlarında marjinal R^2=0.43 ve koşullu R^2=0.74 olarak hesaplanmıştır. Bu bulgular, sabit etkilerin varyansın %43'ünü, sabit ve rastgele etkilerin birlikte ise toplam varyansın %74'ünü açıkladığını göstermektedir. Ayrıca, AIC ve BIC kriterleri LMM modelinde (AIC=5065.7; BIC=5097) LM modeline (AIC=5228.95; BIC=5256.31) kıyasla daha düşük değerler almıştır, bu da karma modelin veri ile daha uyumlu olduğunu ortaya koymaktadır. RMSE değerleri incelendiğinde ise karma modelin LM'den daha düşük hata değerlerine sahip olduğu görülmektedir. Son olarak, karma modelin 0.646 NSE ve 0.787 KGE ile orta üstü tahminler ürettiği, LM'ninde benzer paternde olduğu ancak 0.586 NSE ve 0.686 KGE ile daha düşük performans sergilediği sonucuna ulaşılmıştır.

Genel olarak, bu sonuçlar karma modelin grup düzeyindeki rastgele etkileri hesaba katarak daha güçlü, kararlı ve gerçekçi tahminler sunduğunu göstermektedir. Debi ve eğim değişkenlerinin bağımlı değişken üzerinde en baskın pozitif etkiler olduğu, derinliğin ise anlamlı ve güçlü bir negatif etki gösterdiği her iki modelde de tutarlıdır. Ancak, karma modelin daha yüksek R^2 değerleri, daha düşük AIC/BIC kriterleri ve grup farklılıklarını yansıtan rastgele etkileri, bu yaklaşımın karmaşık veri yapılarında tercih edilmesi gerektiğini açıkça ortaya koymaktadır.

Tablo 5. Karma modele (LMM) ait performans metrikleri

Model Performansı	Değer
Marjinal R^2	0.43
Koşullu R^2	0.74
AIC	5065.7
BIC	5097.0
KGE	0.787
NSE	0.646
RMSE	96.28

Tablo 6. Normal doğrusal model (LM) sonuçları

Sabit Etkiler	Katsayı	Std. Hata	t değeri	p değeri
Sabit	220	15.19	14.52	0.001***
Debi	+171.21	31.82	5.38	<0.001***
Genişlik	-20.78	21.29	-0.95	0.344
Derinlik	-103.37	30.39	-3.4	<0.001***
Eğim	+143.8	21.31	6.75	<0.001***
Sıcaklık	-43.84	16.41	-2.67	0.008**

Tablo 7. Normal (LM) modele ait performans metrikleri

Model Performansı	Değer
R^2	0.25
Adj. R^2	0.24
AIC	5228.95
BIC	5256.31
KGE	0.686
NSE	0.586
RMSE	104

Şekil 4'te paylaşılan grafikte, sabit etkilerin hem klasik doğrusal model hem de karma doğrusal model kapsamında elde edilen katsayıları ve %95 güven aralıkları gösterilmektedir. Dikey kesikli çizgi sıfır noktasını işaret ederken, bu çizginin sağında kalan değerler pozitif, solunda kalanlar ise negatif etkileri ifade etmektedir. Elde edilen sonuçlar, değişkenlerin bağımlı değişken üzerindeki etkilerinin hem yönünü hem de büyüklüğünü açık bir şekilde ortaya koymaktadır.

Debi değişkeni, her iki modelde de güçlü ve pozitif bir etki göstermektedir. Özellikle LMM modelinde yaklaşık +400 civarında tahmin edilen katsayı, debideki artışın bağımlı değişken üzerinde oldukça belirgin bir artışa yol açtığını ortaya koymaktadır. LM modelinde bu değer yaklaşık +200 seviyesinde kalmakla birlikte yön açısından benzerlik göstermekte, ancak güven aralıklarının genişliği daha yüksek belirsizlik işaret etmektedir. Benzer şekilde, eğim değişkeni de her iki modelde pozitif etki sergilemiş, ancak LMM modeli daha yüksek (~+300) ve daha dar güven aralıklarıyla daha kararlı sonuçlar vermiştir. Bu durum, eğimin sistem dinamikleri üzerinde anlamlı bir pozitif etkiye sahip olduğunu güçlü bir şekilde desteklemektedir.

Sıcaklık değişkeni incelendiğinde hem LM hem de LMM modellerinde pozitif ama düşük katsayılarla temsil edilen bir etki gözlenmektedir (+10 civarı). Ancak güven aralıklarının sıfır çizgisine yakın olması, bu etkinin istatistiksel olarak anlamsız olduğunu göstermektedir. Diğer yandan genişlik değişkeni, LMM modelinde yaklaşık -200 civarında anlamlı bir negatif etki göstermekte, LM modelinde ise bu ilişki daha zayıf ve daha belirsiz bir şekilde gözlenmektedir. Bu bulgu, rastgele etkilerin dikkate alınmasının modelin hassasiyetini artırdığını ve değişkenin gerçek etkisini daha doğru yakaladığını ortaya koymaktadır. Derinlik değişkeni ise her iki modelde de negatif katsayılarla temsil edilmiş (-100 civarı) ve güven aralıkları sıfır çizgisinin dışında kalarak istatistiksel anlamlılığı desteklemiştir. Bu sonuç, derinlik arttıkça bağımlı değişkenin azalabileceğine işaret etmektedir.

Genel olarak, LMM modelinin özellikle debi, eğim ve genişlik değişkenlerinde daha dar güven aralıkları ve daha belirgin katsayılar sunması, karma veri yapılarında bu modelin daha güvenilir tahminler sağladığını göstermektedir. Bulgular, hidrodinamik değişkenlerin (özellikle debi ve eğim) bağımlı değişken üzerindeki kritik rolünü güçlü biçimde vurgulamakta; genişlik ve derinlik gibi morfometrik faktörlerin ise ters yönde etkiler oluşturabileceğini düşündürmektedir. Sıcaklığın etkisi ise nispeten sınırlı kalmıştır. Bu kapsamda, rastgele etkilerin dikkate alındığı karma modelleme yaklaşımının, sistemin karmaşık yapısını daha doğru yansıtarak daha kararlı ve güvenilir sonuçlar ürettiği söylenebilir.

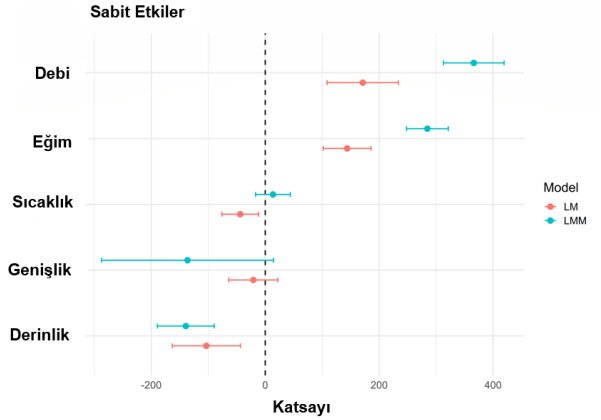

Şekil 4. Karma ve klasik doğrusal modellerde sabit etkilerin katsayı dağılımları ve güven aralıkları

Şekil 5'te paylaşılan grafik ise, karma modelde dane değişkenine ait rastgele kesim (intercept) tahminlerini ve bunların %95 güven aralıklarını göstermektedir. Yatay eksende rastgele kesim değerleri, dikey eksende ise dane grupları yer almaktadır. Sıfır noktasındaki kesikli çizgi, rastgele kesimlerin ortalama etkisini referans almaktadır.

Bazı dane gruplarının rastgele kesim değerleri pozitif tarafta, bazıları ise negatif tarafta yer almaktadır. Pozitif tarafta yer alan gruplar (örneğin 0.15, 1.41, 1.4 gibi dane değerleri), bağımlı değişken üzerinde ortalamanın üzerinde bir kesim etkisine sahiptir. Bu gruplar, modelde beklenen değeri yukarı yönlü kaydırmakta, yani daha yüksek bir tahmin değeri ile ilişkilendirilmektedir.

Negatif tarafta yer alan gruplar (örneğin 3.73 ve 4.18 dane değerleri), bağımlı değişken üzerinde ortalamanın altında bir kesim etkisine sahiptir; bu da bu grupların bağımlı değişken için daha düşük tahminlere neden olduğunu göstermektedir.

Güven aralıklarının genişliği, gruplar arasındaki tahmin belirsizliğini göstermektedir. Bazı gruplarda güven aralıkları oldukça dar olup tahminlerin daha kararlı olduğunu (örneğin dane=1.4), bazı gruplarda ise daha geniş aralıkların daha fazla belirsizliğe işaret ettiğini (örneğin dane=3.12) göstermektedir.

Genel olarak, bu sonuçlar dane gruplarının bağımlı değişken üzerindeki etkilerinde belirgin farklılıklar bulunduğunu ortaya koymaktadır. Özellikle negatif tarafta yer alan gruplar, bağımlı değişken düzeyinin ortalamanın altında kaldığı durumları açıklarken, pozitif tarafta yer alan gruplar ortalamanın üzerinde sonuçlar üreten grupları temsil etmektedir. Bu bulgu, rastgele etkilerin modele dahil edilmesinin neden gerekli olduğunu ve dane bazlı farklılıkların bağımlı değişken üzerindeki etkilerinin güçlü olduğunu göstermektedir.

Hidrolik açıdan değerlendirildiğinde, pozitif tarafta yer alan dane grupları (örneğin dane = 0.15, 1.4, 1.41) akış koşullarında daha yüksek enerjiye veya daha fazla askıda madde taşınımına uygun ortamları temsil ediyor olabilir. Bu gruplar, daha küçük dane çaplarıyla ilişkili olup akım içinde daha kolay süspansiyon sağlayabilir, dolayısıyla sistemde ölçülen değişken üzerinde daha yüksek tahminlere yol açabilir.

Buna karşılık, negatif tarafta kalan gruplar (örneğin dane = 3.12, 3.73, 4.18), daha iri dane çaplarıyla ilişkili olup akışta daha hızlı çöken veya daha düşük mobiliteye sahip taneleri ifade etmektedir. Bu durum, akımın bu gruplar üzerinde daha sınırlı bir etki yarattığını ve bağımlı değişkenin ortalamanın altında kalmasına neden olduğunu göstermektedir.

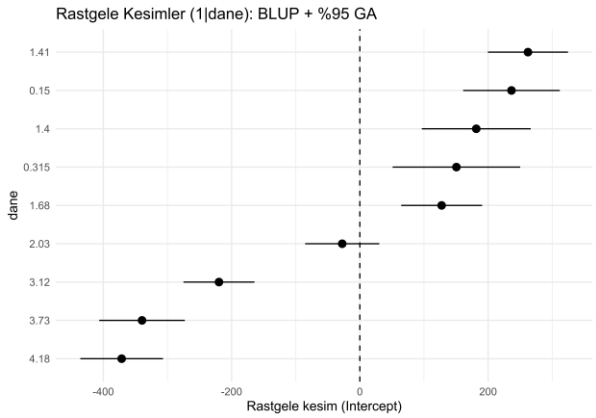

Şekil 5. Dane gruplarına ait rastgele kesim (intercept) tahminleri ve %95 güven aralıkları

Artıklar ile uydurulan değerlerin ilişkisini gösteren grafikler, normal doğrusal model ile karma modelin tahmin performanslarını karşılaştırmalı olarak ortaya koymaktadır (Şekil 6). LM modeline ait dağılım incelendiğinde artıkların belirgin bir U şeklinde dağıldığı görülmektedir. Bu durum, sabit varyans varsayımının ihlal edildiğini, yani modelde heteroskedastisite bulunduğunu ve hataların sistematik bir desen izlediğini göstermektedir. Ayrıca, bazı gözlemlerde artık değerlerinin oldukça yüksek seviyelere ulaşması, modelin uç noktaları yeterince temsil edemediğini ortaya koymaktadır. LMM modelinde ise artıkların dağılımı sıfır etrafında daha dengeli bir şekilde toplanmış ve sistematik sapmalar belirgin ölçüde azalmıştır. Eğrinin daha yatay bir seyir izlemesi, karma modelin veri yapısındaki karmaşık ilişkileri daha iyi yakalayabildiğini göstermektedir. Bununla birlikte, bazı uç gözlemlerin varlığı modelin tam uyumunu sınırlasa da LMM modelinin hataları önemli ölçüde azalttığı ve daha güvenilir tahminler sunduğu anlaşılmaktadır. Bu sonuçlar, karma modelin grup düzeyindeki rastgele etkileri hesaba katarak doğrusal modele kıyasla daha iyi bir uyum sağladığını ve daha kararlı bir performans sergilediğini açıkça ortaya koymaktadır.

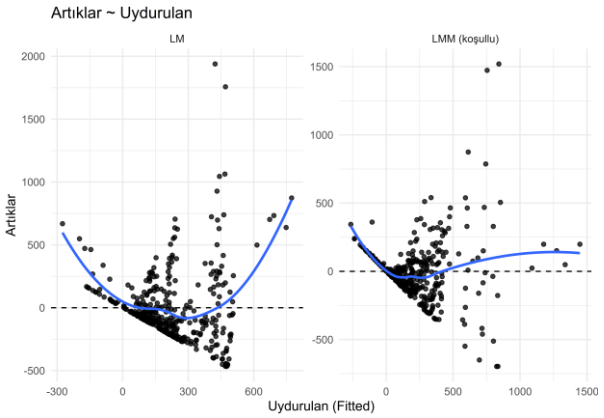

Şekil 6. LM ve LMM artıkları ile model tahminleri grafikleri

Karma modeller, grup düzeyinde değişkenlerin bulunduğu veri yapılarında klasik doğrusal modellere göre daha esnek, güvenilir ve genellenebilir bir yaklaşım sunar. Bu modellerin en önemli avantajlarından biri, kısmi havuzlama (partial pooling) ve shrinkage özelliğidir. Her grup için ayrı sabit katsayılar tahmin etmek yerine grup etkilerini genel ortalamaya doğru çeker ve özellikle gözlem sayıları az veya dengesiz olan seviyelerde aşırı uyumu önler. Bu yaklaşım, tahminlerin daha sağlam ve kararlı olmasını sağlar [38]. Ayrıca, rastgele kesimler ve rastgele eğimler sayesinde, örneğin "debi" gibi bir yordayıcının etkisinin grup seviyesine göre değişmesi modellenebilir. Bu sayede etkileşim terimleriyle karmaşık modeller kurmaya gerek kalmadan grup içi heterojenlikler yakalanabilir [39].

Karma modellerin bir diğer güçlü yönü, toplam varyansı grup içi ve grup arası bileşenlerine ayırarak, sınıf içi korelasyon katsayısı (ICC) hesaplamaya imkân tanımasıdır. ICC, bağımlı değişkendeki değişimin ne kadarının grup etkilerinden kaynaklandığını nicel olarak gösterir ve böylece grup yapısının açıklayıcılığı daha somut bir şekilde yorumlanabilir [40]. Bunun yanı sıra, karma modeller sabit etkilerin yalnızca mevcut gruplar için değil, benzer ancak gözlemlenmemiş yeni gruplar için de tahminler yapabilmesine olanak tanır; bu da sonuçların genellenebilirliğini artırır.

Bu modeller, dengesiz veri tasarımlarında da avantajlıdır. Bazı gruplarda çok az, bazılarında ise çok fazla gözlem bulunması klasik ANOVA veya OLS modellerinde ciddi sapmalara yol açarken, karma modeller bu dengesizliklere karşı daha dayanıklı çalışır [41]. Ayrıca, mevcut gruplar için en iyi doğrusal yansız tahmin ediciler (BLUP) tahminleri yaparak hem sabit hem de grup düzeyindeki rastgele sapmaları birlikte kullanır; böylece grup bazlı daha doğru ve hassas tahminler üretir [42].

Elde edilen sonuçların önemli kısmı literatürdeki çalışmalar ile desteklenmektedir. Lamb vd. [43], çok sayıda kanal verisini derleyerek kritik Shields gerilmesinin eğim arttıkça yükseldiğini göstermiştir. Bunun nedeni, eğim büyüdükçe bağıl pürüzlülüğün artması ve buna bağlı olarak yatak hız ile türbülans yapısının değişmesidir. Bu sonuç, modelimizde eğimin pozitif katsayıyla konsantrasyonu artırmasıyla tutarlıdır. Khosravi vd. [44] deneyleri, akım hızıyla (dolaylı olarak debi ve kayma gerilmesiyle) sediman taşınımı arasında güçlü bir ilişki olduğunu gösterir. Bu bulgu, çok kaynaklı veride LMM ile elde ettiğimiz debi ve eğimin pozitif ve baskın etkileriyle uyumludur.

Pratik Kullanım Alanları

LMM sonuçlarının gösterdiği desenler doğrudan uygulanabilir kararlara çevrilebilir ve pratikte önemli kullanım alanlarına hizmet edebilecektir. Debinin güçlü ve pozitif etkisi ile eğimin artırıcı rolü, yağışlı dönemlerde ve yüksek akım olaylarında su alma yapılarında ön-çöktürme hacminin ve modüler havuz sayısının artırılmasını, giriş yapılarına pik akımlar için yönlendirmeli ızgara ve by-pass hatlarının eklenmesini gerektirebilir. Bu hatların açma-kapama eşikleri istasyonlara özgü rastgele etkiler ışığında yerelleştirilebilir. Derinliğin negatif etkisi, çok seviyeli çekim yapılarında bulanıklık ve askı madde yükseldiğinde üst kotlardan kontrollü çekim senaryolarına öncelik verilmesini destekler. Rastgele etkilerin anlamlı bulunması, yukarı havzadaki tane gruplarına bağlı heterojenliğin işletmeye yansıtılmasını, örneğin ince dane baskın alt havzalar için daha sık numune alma, olay sırasında taşınabilir sensörlerin devreye alınması ve sediment havuzu bakımlarının bu pencerelere göre zamanlanmasını sağlar. Artık yapısının LMM'de daha sağlıklı olması, olay yüklerinin belirsizlik bantlarıyla izlenmesine ve taşkın kontrolünde yıl içi yük bütçesine göre şev koruma, tampon şerit ve geçici tutma yapılarının önceliklendirilmesine imkân verebilmektedir.

Sonuç

Bu çalışmada elde edilen sonuçlar, doğrusal karma etkili modellerin askı maddesi konsantrasyonunu tahmin etmede güçlü ve güvenilir bir yaklaşım sunduğunu açıkça ortaya koymuştur. Grup düzeyindeki rastgele etkilerin modele dahil edilmesi, özellikle dane çapına bağlı değişkenliği daha gerçekçi şekilde yansıtmayı sağlamış ve modelin açıklayıcılığını önemli ölçüde artırmıştır. Debi ve eğimin en belirgin pozitif etkiler, derinliğin ise negatif etki göstermesi, akarsu sistemlerindeki askı maddesi taşınım süreçlerinin hidrolik dinamiklerle sıkı ilişkisini vurgulamaktadır. Buna karşılık genişlik ve sıcaklık gibi değişkenlerin etkisinin sınırlı düzeyde kalması, bu parametrelerin sistem dinamiklerinde ikincil rol oynadığını göstermektedir.

Modelin rastgele etkiler kısmı, dane grupları arasındaki farklılıkların askı maddesi konsantrasyonunda önemli rol oynadığını göstermiştir. Özellikle küçük dane çapına sahip gruplarda daha yüksek konsantrasyon değerlerinin gözlenmesi, bu partiküllerin akımda daha uzun süre askıda kalabilme potansiyeli ile uyumludur. Bu bulgu, sediment yönetimi ve mühendislik tasarımlarında dane boyutunun dikkate alınmasının önemini ortaya koymaktadır.

Elde edilen bulgular, grup düzeyindeki heterojenliklerin modellenmesiyle elde edilen doğruluk artışını açıkça gösterse de ilerleyen çalışmalarda doğrusal olmayan karma modellerin (nonlinear mixed models) veya makine öğrenmesi tabanlı hibrit yaklaşımların kullanılması, askı maddesi konsantrasyonunun tahmin performansını daha da iyileştirebilir. Özellikle değişkenler arasındaki karmaşık ve doğrusal olmayan ilişkilerin modellenmesi, mevcut lineer yaklaşımların açıklamakta zorlandığı dinamik süreçlerin daha net anlaşılmasına katkı sağlayacaktır. Buna ek olarak, önsel bilgiyi ve grup düzeyi belirsizliği açıkça temsil ederek öngörü belirsizliğini bütüncül biçimde yayabilmek için Bayesyen hiyerarşik modellerin uygulanmasını gelecekteki çalışmalar için öneriyoruz. Bu tür gelişmiş modeller, su yapılarının tasarımı, sediment yönetimi, taşkın kontrolü ve ekosistem koruma stratejilerinde karar alma süreçlerine önemli katkılar sağlayacaktır.

Etik kurul onayı ve çıkar çatışması beyanı

Hazırlanan makalede etik kurul izni alınmasına gerek yoktur.

Hazırlanan makalede herhangi bir kişi/kurum ile çıkar çatışması bulunmamaktadır.

Kaynakça

[1] E. Shamaei and M. Kaedi, "Suspended sediment concentration estimation by stacking the genetic programming and neuro-fuzzy predictions," Appl Soft Comput, vol. 45, pp. 187–196, Aug. 2016, doi: 10.1016/j.asoc.2016.03.009.

[2] J. Lepesqueur, R. Hostache, N. Martínez-Carreras, E. Montargès-Pelletier, and C. Hissler, "Sediment transport modelling in riverine environments: on the importance of grain-size distribution, sediment density, and suspended sediment concentrations at the upstream boundary," Hydrol Earth Syst Sci, vol. 23, no. 9, pp. 3901–3915, Sep. 2019, doi: 10.5194/hess-23-3901-2019.

[3] M. Cieśla and R. Gruca-Rokosz, "Implications of suspended sediment in the migration of nutrients at the water-sediment interface in retention reservoirs," Sci Rep, vol. 14, no. 1, p. 24924, Oct. 2024, doi: 10.1038/s41598-024-76556-x.

[4] J. Park and J. R. Hunt, "Coupling fine particle and bedload transport in gravel-bedded streams," J Hydrol (Amst), vol. 552, pp. 532–543, Sep. 2017, doi: 10.1016/j.jhydrol.2017.07.023.

[5] J. Deng, B. Camenen, C. Legout, and G. Nord, "Estimation of fine sediment stocks in gravel bed rivers including the sand fraction," Sedimentology, vol. 71, no. 1, pp. 152–172, Jan. 2024, doi: 10.1111/sed.13132.

[6] A. Kumar, S. Hossain, S. Sen, S. Mohan, and K. Ghoshal, "Grain-size distribution in suspension under non-equilibrium conditions," International Journal of Sediment Research, vol. 39, no. 5, pp. 774–794, Oct. 2024, doi: 10.1016/j.ijsrc.2024.06.003.

[7] A. van Hamel, P. Molnar, J. Janzing, and M. I. Brunner, "Suspended sediment concentrations in Alpine rivers: from annual regimes to sub-daily extreme events," Hydrol Earth Syst Sci, vol. 29, no. 13, pp. 2975–2995, Jul. 2025, doi: 10.5194/hess-29-2975-2025.

[8] Š. Zezulka, B. Maršálek, E. Maršálková, K. Odehnalová, M. Pavlíková, and A. Lamaczová, "Suspended Particles in Water and Energetically Sustainable Solutions of Their Removal—A Review," Processes, vol. 12, no. 12, p. 2627, Nov. 2024, doi: 10.3390/pr12122627.

[9] C. T. Yang and J. B. Stall, "Unit Stream Power for Sediment Transport in Natural Rivers," Illinois State Water Survey, University of Illinois Water Resources Center, Research Report No. 88, July 1974. [Online]. Available: https://www.researchgate.net/publication/237395916_Unit_Stream_Power_for_Sediment_Transport_in_Alluvial_Rivers

[10] A. Molinas and B. Wu, "Transport of sediment in large sand-bed rivers," Journal of Hydraulic Research, vol. 39, no. 2, pp. 135–146, 2001, doi: 10.1080/00221680109499814.

[11] S.Q. Yang, "Sediment transport capacity in rivers," Journal of Hydraulic Research, vol. 43, no. 2, pp. 131–138, Jan. 2005, doi: 10.1080/00221686.2005.9641229.

[12] E. Doğan, "Katı Madde Konsantrasyonunun Yapay Sinir Ağlarını Kullanarak Tahmin Edilmesi," Teknik Dergi, vol. 20, no. 96, pp. 4567–4582, 2009.

[13] E. Dogan, "Suspended Sediment Load Estimation in Lower Sakarya River By Using Artificial Neural Networks, Fuzzy Logic and Neuro-Fuzzy Models," 2005,

[14] G. Çeribaşı and E. Doğan, "Aşağı Sakarya Nehrindeki Askı Maddesi Miktarının Esnek Yöntemler ile Tahmini," Karaelmas Fen ve Mühendislik Dergisi, vol. 6, no. 2, pp. 351–358, 2016

[15] Ö. Terzi and T. Baykal, "Dalgacık- GEP Modeli ile Akarsularda Askıda Katı Madde Miktarı Tahmini," Süleyman Demirel Üniversitesi Fen Bilimleri Enstitüsü Dergisi, vol. 19, no. 2, pp. 39–45, 2015, doi: 10.19113/sdufbed.89396.

[16] A. Ülke, S. Özkul, and G. Tayfur, "Ampirik Yöntemlerle Gediz Nehri İçin Askıda Katı Madde Yükü Tahmini," Teknik Dergi, vol. 22, no. 107, pp. 5387–5407, 2011,

[17] J. G. Ibrahim and G. Molenberghs, "Missing data methods in longitudinal studies: a review," *TEST*, vol. 18, no. 1, pp. 1-43, May. 2009, doi.org/10.1007/s11749-009-0138-x

[18] A. J. Carnoli, P. oude Lohuis, Lutgarde M.C. Buydens, G. H. Tinnevelt, and J. J. Jansen, "Linear Mixed-Effects models in chemistry: A tutorial," Analytica Chimica Acta, vol. 1304, pp. 342444–342444, Mar. 2024, doi: https://doi.org/10.1016/j.aca.2024.342444.

[19] S. Nakagawa and H. Schielzeth, "A General and Simple Method for Obtaining R2 from Generalized Linear Mixed-Effects Models," Methods in Ecology and Evolution, vol. 4, no. 2, pp. 133–142, Dec. 2012, doi: https://doi.org/10.1111/j.2041-210x.2012.00261.x.

[20] T.-L. Liu, B. Flückiger, and K. de Hoogh, "A comparison of statistical and machine-learning approaches for spatiotemporal modeling of nitrogen dioxide across Switzerland," Atmospheric Pollution Research, vol. 13, no. 12, p. 101611, Dec. 2022, doi: https://doi.org/10.1016/j.apr.2022.101611.

[21] S. Yang, G. Yang, B. Li, and R. Wan, "Water quality improves with increased spatially surface hydrological connectivity in plain river network areas," Journal of Environmental Management, vol. 377, p. 124703, Mar. 2025, doi: https://doi.org/10.1016/j.jenvman.2025.124703.

[22] A. A. Gili, E. J. Noellemeyer, and M. Balzarini, "Hierarchical linear mixed models in multi-stage sampling soil studies," Environmental and Ecological Statistics, vol. 20, no. 2, pp. 237–252, Aug. 2012, doi: https://doi.org/10.1007/s10651-012-0217-0.

[23] J. S. Lessels and T. F. A. Bishop, "Estimating water quality using linear mixed models with stream discharge and turbidity," Journal of Hydrology, vol. 498, pp. 13–22, Aug. 2013, doi: https://doi.org/10.1016/j.jhydrol.2013.06.006.

[24] F. Belhaj et al., "Predicting precipitation and NDVI utilization of the multi-level linear mixed-effects model and the CA-markov simulation model," Clim Serv, vol. 38, p. 100554, Apr. 2025, doi: 10.1016/j.cliser.2025.100554.

[25] E. Barca, D. De Benedetto, and A. M. Stellacci, "Contribution of EMI and GPR proximal sensing data in soil water content assessment by using linear mixed effects models and geostatistical approaches," Geoderma, vol. 343, pp. 280–293, Jun. 2019, doi: 10.1016/j.geoderma.2019.01.030.

[26] K. RK. Dilrukshi et al., "Determining bad actors: A linear mixed effects model approach to elucidate behavioral toxicity of metal mixtures in drinking water," Ecotoxicol Environ Saf, vol. 287, p. 117296, Nov. 2024, doi: 10.1016/j.ecoenv.2024.117296.

[27] Government of West Bengal, "Study on the Critical Tractive Force Various Grades of Sand," Annual Report of the River Research Institute, West Bengal, Publication No. 26, Part I, 1965. [Online]. Available: https://www.aloki.hu/pdf/1704_98379863.pdf

[28] T. R. Daves, "Summary of experimental data for flume tests over fine sand," Department of Civil Engineering, University of Southampton, 1971. [Online]. Available: https://conservancy.umn.edu/bitstreams/a279845d-26e8-4409-ab42-d3b7b17be30f/download

[29] P.- Y. Ho, "Abhängigkeit der Geschiebebewegung von der Kornform und der Temperatur," Preussische Versuchsanstalt für Wasser-, Erd- und Schiffbau, Berlin, Mitt., Heft 37 (43 pp.), 1939. [Online]. Available: https://public.ucrlib.aspace.cdlib.org/repositories/5/archival_objects/607416

[30] F. T. Mavis, T.-Y. Liu, and E. Soucek, "The transportation of detritus by flowing water—II," University of Iowa Studies in Engineering, Bulletin 11 (New Series No. 341), University of Iowa, Iowa City, IA, 1937. [Online]. Available: https://iro.uiowa.edu/view/pdfCoverPage?download=true&filePid=13811796880002771&instCode=01IOWA_INST

[31] W. R. Brownlie, "Compilation of alluvial channel data: Laboratory and field," W. M. Keck Laboratory of Hydraulics and Water Resources, California Institute of Technology, Pasadena, CA, Report No. KH-R-43B, November 1981. [Online]. Available: https://authors.library.caltech.edu/records/deqcj-g7748/latest

[32] E. Doğan, "Akarsularda Taşınan Toplam Katı Madde Miktarının Yapay Zekâ Metotları ile Tahmin Edilmesi," Doktora Tezi, Sakarya Üniversitesi Fen Bilimleri Enstitüsü, 2008.

[33] N. M. Laird and J. H. Ware, "Random-Effects Models for Longitudinal Data," Biometrics, vol. 38, no. 4, p. 963, Dec. 1982, doi: 10.2307/2529876.

[34] J. Zhang, Y. Yang, and J. Ding, "Information criteria for model selection," WIREs Computational Statistics, vol. 15, no. 5, Sep. 2023, doi: 10.1002/wics.1607.

[35] Q. Liu, M. A. Charleston, S. A. Richards, and B. R. Holland, "Performance of Akaike Information Criterion and Bayesian Information Criterion in Selecting Partition Models and Mixture Models," Syst Biol, vol. 72, no. 1, pp. 92–105, May 2023, doi: 10.1093/sysbio/syac081.

[36] J. E. Nash and J. V. Sutcliffe, "River flow forecasting through conceptual models part I — A discussion of principles," Journal of Hydrology, vol. 10, no. 3, pp. 282–290, Apr. 1970, doi: https://doi.org/10.1016/0022-1694(70)90255-6.

[37] H. V. Gupta, H. Kling, K. K. Yilmaz, and G. F. Martinez, "Decomposition of the mean squared error and NSE performance criteria: Implications for improving hydrological modelling," Journal of Hydrology, vol. 377, no. 1–2, pp. 80–91, Oct. 2009, doi: https://doi.org/10.1016/j.jhydrol.2009.08.003.

[38] A. Gelman and J. Hill, Data Analysis Using Regression and Multilevel/Hierarchical Models. Cambridge: Cambridge University Press, 2006. doi: 10.1017/CBO9780511790942.

[39] D. J. Barr, R. Levy, C. Scheepers, and H. J. Tily, "Random effects structure for confirmatory hypothesis testing: Keep it maximal," J Mem Lang, vol. 68, no. 3, pp. 255–278, Apr. 2013, doi: 10.1016/j.jml.2012.11.001.

[40] S. Nakagawa and H. Schielzeth, "Repeatability for Gaussian and non-Gaussian data: a practical guide for biologists," Biological Reviews, vol. 85, no. 4, pp. 935–956, Nov. 2010, doi: 10.1111/j.1469-185X.2010.00141.x.

[41] José C. Pinheiro and Douglas M. Bates, Mixed-Effects Models in S and S-PLUS. in Statistics and Computing. New York: Springer-Verlag, 2000. doi: 10.1007/b98882.

[42] C. R. Henderson, "Best Linear Unbiased Estimation and Prediction under a Selection Model," Biometrics, vol. 31, no. 2, p. 423, Jun. 1975, doi: 10.2307/2529430.

[43] M. P. Lamb, W. E. Dietrich, and J. G. Venditti, "Is the critical Shields stress for incipient sediment motion dependent on channel-bed slope?," Journal of Geophysical Research, vol. 113, no. F2, May 2008, doi: https://doi.org/10.1029/2007jf000831.

[44] K. Khosravi, Amir, L. Mao, J. F. Rodriguez, P. M. Saco, and A. D. Binns, "Experimental Analysis of Incipient Motion for Uniform and Graded Sediments," Water, vol. 13, no. 13, pp. 1874–1874, Jul. 2021, doi: https://doi.org/10.3390/w13131874.